BUCKLING AND POSTBUCKLING BEHAVIOR OF UNBALANCED AND UNSYMMETRIC LAMINATED GRAPHITE/EPOXY PLATES

Vol 1

by

DAVID WARREN JENSEN

B.S., Brigham Young University
(1980)
S.M., Massachusetts Institute of Technology
(1981)

SUBMITTED TO THE DEPARTMENT OF AERONAUTICS AND ASTRONAUTICS
IN PARTIAL FULFILLMENT OF THE REQUIREMENTS FOR
THE DEGREE OF

DOCTOR OF PHILOSOPHY

at the

MASSACHUSETTS INSTITUTE OF TECHNOLOGY

February 1986

Signature of Author _____
Department of Aeronautics and Astronautics
January 10, 1986

Certified by _____
Prof. John Dugundji
Thesis Supervisor

Certified by _____
Prof. James W. Mar
Thesis Committee

Certified by _____
Prof. Paul A. Lagace
Thesis Committee

Certified by _____
Prof. Edward F. Crawley
Thesis Committee

Accepted by _____
Prof. Harold Y. Wachman
Chairman, Departmental Graduate Committee

BUCKLING AND POSTBUCKLING BEHAVIOR OF UNBALANCED AND UNSYMMETRIC LAMINATED GRAPHITE/EPOXY PLATES

by

DAVID WARREN JENSEN

Submitted to the Department of Aeronautics and Astronautics on January 10, 1986 in partial fulfillment of the requirements for the Degree of Doctor of Philosophy

ABSTRACT

An experimental and analytical investigation has been conducted on the buckling and postbuckling behavior of generally anisotropic graphite/epoxy laminated plates. The elastic (mechanical) couplings inherent in unbalanced and unsymmetric laminates have been isolated and studied. These include bending-stretching, stretching-shearing/bending-twisting, and stretching-twisting couplings. Square 254 mm laminates were manufactured from Hercules AS4/3501-6 graphite/epoxy pre-impregnated tape. Experimental techniques were employed to test the plates in uniaxial compressive loading to failure with clamped, simply-supported, and free edges. Out-of-plane deflection, in-plane strain, and end-shortening displacement measurements were obtained. The test program consisted of two layups which served as control cases, three layups which isolated various elastic couplings described above, and six additional layups which contained varying amounts of all of the couplings. Both Rayleigh-Ritz and finite element linear analytical solutions were used to predict the buckling loads and mode shapes. The Rayleigh-Ritz analysis was extended to the nonlinear regime, by including von Kármán's large deflection strain-displacement relations, to predict the compressive postbuckling (pre-failure) behavior. The results show that the introduction of elastic couplings reduces the buckling loads, although the concept of bifurcation takes on new meaning. Laminates with free sides exhibit classical wide-column buckling behavior based on the reduced bending stiffness. Stretching-twisting coupling and the stretching-shearing/bending-twisting coupling combination introduce twisting in the deflection pattern in a similar fashion. Also, at least two stable equilibrium configurations exist at certain load levels for laminates which have bending-stretching coupling, restrained sides, and an effective aspect ratio greater than 0.7. Both first bending, with a superimposed third bending component, and second bending modes were observed for such laminates.

Thesis Supervisor: John Dugundji
Title: Professor of Aeronautics and Astronautics

ACKNOWLEDGEMENTS

The culmination of the past few years' research efforts with this final document inspires me to reflect on the many contributions of those who have assisted in its successful completion, either directly or indirectly. First, and foremost, I wish to express thanks to my thesis committee: Professors John Dugundji, Paul Lagacé, James Mar, and Ed Crawley. I am especially indebted to Prof. Dugundji, committee chairman, for his masterful approach in helping me to discover the fundamental principles of mechanics, particularly those pertaining to the buckling and vibration of composite plates and shells. Likewise, I am grateful to Professors Mar, lab director, and Lagacé, principle investigator, for exposure to the advancing technologies of composite materials and for support in the Technology Laboratory for Advanced Composites (TELAC). In spite of Prof. Lagacé's youth, his traditionalistic rituals provided an excellent training in the methodology of experimental research. Likewise, I am thankful to Prof. Crawley, whose young energetic professionalism provided the critical direction and encouragement during my "formative" years at MIT. I also wish to thank Professors Pian and Witmer for their supporting academic training and insight.

The support staff also deserves a round of applause. Laboratory techniques were patiently taught by Al Supple, Don

Weiner, and Earl Wassmouth. Carl Varnerin assisted in the acquisition and setup of laboratory equipment. The bureaucratic barriers were eased with the administrative skills of Ping Lee and Debra Smith.

Several graduate students also deserve recognition for their cooperation. Encouragement was provided by officemate Hatem Daken, who, by leading the way, showed that it was indeed possible to finish. However, no TELAC thesis is complete without mention of Tony Vizzini, who masterminded the text processor and equation editor used to prepare this document, wrote most of the original BASIC programs which were tailored for our data acquisition and reduction, and functioned frequently as a ready reference manual. Marc DiNardo contributed in a multitude of ways over the past two years, for which I am indebted, including designing and constructing the transducer rack and cart assembly and providing invaluable assistance during the different experimental phases. Pierre Minguet, author of the original version of the nonlinear Rayleigh-Ritz program, assisted with debugging the same and made timely comments concerning modifications thereof. Cheng Wang, who worked overtime to ensure that it would be ready prior to the completion of this thesis, wrote the finite element program. Doug Finch, who preceded me, designed and constructed the compressive loading jig for preliminary buckling work.

I would especially like to acknowledge the hundreds of hours of assistance provided by several undergraduate

students. The tooling construction and manufacturing team was composed of Marc DiNardo, Mary Claire Froelich, Peter Falatyn, and Chris Winters. The testing crew consisted of Marc DiNardo (by then a graduate student), Mary Claire Froelich, Peter Falatyn, Bob Yancey, Giancarlo Filippazzo, and Pao-hua Kuo. Particular thanks go to John Sultana, Gail Marie Sadlo, and many other laboratory members who provided general assistance. However, a special recognition is reserved for Pao-hua Kuo, who not only assisted in the testing and data reduction, but also prepared almost all of the figures in this thesis document (which number in the hundreds) and was dedicated enough to endure to the very end, laboring long hours during the final crunch.

Thanks are extended to many friends, particularly the Westgate gang, who were always prepared and willing to help.

Last, but certainly not least, I would like to thank my family. My parents can never be thanked enough for their sacrifices and examples. My two sons, Joshua (going on five) and Brady (almost three), provided the stimuli for finishing quickly, and the enthusiasm and excitement which made the duration most satisfying. Finally, I am forever indebted to my wife, GayLynn (whom I love very dearly), for forfeiting her career to join me here in pursuit of this goal, and supporting me in every possible way during the past few years, making this not only possible, but truly enjoyable.

FOREWORD

This research was performed in the Technology Laboratory for Advanced Composites (TELAC) of the Department of Aeronautics and Astronautics at the Massachusetts Institute of Technology. This work was sponsored by the Boeing Military Airplane Company under Contract No. BMAC P.O. AA0045. Messrs. Jack Avery and Robert Waner are the contract monitors. The thesis committee comprised Professors John Dugundji, James W. Mar, Paul A. Lagacé, and Edward F. Crawley.

TABLE OF CONTENTS

TABLE OF CONTENTS (Continued)

TABLE OF CONTENTS (Continued)

LIST OF FIGURES

LIST OF FIGURES (Continued)

LIST OF FIGURES (Continued)

LIST OF FIGURES (Continued)

LIST OF FIGURES (Continued)

LIST OF FIGURES (Continued)

LIST OF FIGURES (Continued)

LIST OF FIGURES (Continued)

LIST OF FIGURES (Continued)

LIST OF FIGURES (Continued)

LIST OF TABLES

LIST OF TABLES (Continued)

NOMENCLATURE

A	Elastic stretching matrix
$(AR)_e$	Effective aspect ratio
a	Plate length in the x-direction
B	Elastic coupling matrix
b	Plate width in the y-direction
D	Elastic bending matrix
F_i	Beam function used in Rayleigh-Ritz analysis
G	Matrix for finite element formulation
H	Matrix for finite element formulation
J	Jacobian matrix
k	Element stiffness matrix
k_i	Transducer spring stiffness
$K_{r_{ij}}$	Elements of Rayleigh-Ritz stiffness matrices
L	Loading matrix
M	Moment resultant
N	Stress resultant
$\bar{N}_i$	Buckling loads
N_u, N_v, N_w	Number of assumed modes in the x, y, and z directions, respectively
P_i	Displacement transducer force
P_{oi}	Initial transducer force
q_i	Generalized displacements
Q	Transverse shear
R	Force multiplier matrix for finite element formulation

NOMENCLATURE (Continued)

S_σ	Surface over which tractions are applied
T	Applied tractions
U	Strain energy
u	Displacement in the x-direction (end-shortening)
V	Volume
v	Displacement in the y-direction
W	Work done by external forces
w	Deflection in the z-direction (out-of-plane)
x,y,z	Plate coordinates
α	Correction factor for non-linear Rayleigh-Ritz analysis
β	Stress parameters in the finite element formulation
$\alpha_i, \gamma_i, \chi_i$	x-components of Rayleigh-Ritz assumed shape functions
$\beta_i, \delta_i, \psi_i$	y-components of Rayleigh-Ritz assumed shape functions
Δ	Increment of
∇	Gradient of
ε°	Strain at plate midplane
ε	Strain
Φ	Assumed displacements for finite element analysis
γ	Shearing strain
θ	Lamination angle (with respect to the x-axis)
κ	Curvature
λ	Eigenvalue for buckling problem
$\partial/\partial x$	Partial derivative with respect to x

NOMENCLATURE (Continued)

Π_P	Total potential energy
Π_R	Total energy based on Hellinger-Reissner Principle
σ	Stress
$(\tilde{})$	Prescribed boundary displacements
$[\ ]_S$	Symmetric laminate
$[\ ]_T$	Total laminate
$(\ )_n$	Indicates normal direction
$(\ )_{ns}$	Indicates tangential direction
/	Ply interface
//	Room temperature bondline

CHAPTER 1

INTRODUCTION

Advanced composite materials, such as carbon fiber reinforced plastics, are revolutionizing the design of modern aerospace structures by yielding significant weight reductions for given structural requirements of stiffness and strength, as well as providing performance advantages, e.g., aeroelastic tailoring via bending-torsion coupling. However, when laminated in certain formats, these materials have been shown to introduce elastic couplings into the mechanical behavior which require more careful analysis than is usually necessary for traditional isotropic or orthotropic materials [1,2]. For example, employing unbalanced laminates (which do not have a ply oriented at $-\theta$ for every one oriented at $+\theta$, e.g. $[45/0]_S$) to improve aeroelastic efficiency, a procedure referred to as aeroelastic tailoring [3], results in coupling between the bending and twisting behavior of a laminate, as well as between the in-plane stretching and shearing. The complexity increases further for unsymmetric laminates which couple the stretching (membrane) and bending (flexural) response. In fact, the use of unsymmetric laminates can result in fully anisotropic behavior in that the bending, stretching, shearing, and twisting responses become completely coupled.

There may be applications where the unique elastic (mechanical) couplings of unsymmetric laminates provide aeroelastic or other advantages which can be effectively utilized in a structure. However, such dissymmetries also arise "naturally" during the design process. This is most likely to occur in panels with tapered thickness in which individual plies are dropped off. Due to design constraints, these are often dropped off in an unsymmetric fashion. Delamination of plies, in an otherwise symmetric laminate, can also create local dissymmetries which can affect the residual strength and stiffness of a structure.

The buckling and postbuckling behavior of these unsymmetric laminates is important inasmuch as many structural components experience significant compressive loads during their lifetime. In fact, conventional aircraft wing panels are often designed to operate predominantly in the postbuckled region. Although great strides have been taken in seeking an understanding of the response of laminated composites in assorted structural configurations, a firm grasp of many of the fundamental mechanisms which govern their behavior has not yet been realized.

In general, the elastic couplings inherent in unbalanced and unsymmetric laminates reduce their structural stiffness. Consequently, the buckling loads are reduced and the postbuckling response becomes more compliant. In fact, unsymmetric laminates mandate reconsideration of the concept of bifurcation buckling, since out-of-plane deflections begin

with the onset of load [4].

Unsymmetric plates generally possess fully populated elastic matrices, and, therefore, exhibit every possible type of elastic (mechanical) coupling in a complex interwoven fashion. The mechanical behavior of such laminates is somewhat analogous to that of plates with an initial curvature or flat plates loaded eccentrically. In each of these cases, the out-of-plane deflections begin simultaneously with the application of the load. Also, since the neutral bending surface is shifted from the center in unsymmetric laminates, the critical buckling load is reduced substantially. However, unsymmetric laminates are different in that there may not be any definable neutral surface.

A recent review of the current state of the art in buckling and postbuckling of laminated composite plates by Leissa [5] suggests that a better understanding of the effects of the elastic couplings inherent in generally anisotropic laminates is needed. The early development of the theories governing the buckling and postbuckling behavior of plates and a review of the current state of the art is summarized in Chapter 2.

This research effort consists of an extensive experimental and analytical investigation into the general buckling and postbuckling behavior of unbalanced and unsymmetric laminated graphite/epoxy plates. The principle objective was to isolate and study the effects of various elastic couplings. Laminates which possessed different types

and amounts of elastic couplings were tested in uniaxial compression with clamped, simply-supported, and free side boundary conditions and clamped loaded ends. The same laminates were analyzed with both Rayleigh-Ritz and hybrid finite element analyses.

Descriptions of the formulations of the analytical methods employed in this investigation are contained in Chapter 3. Two different theoretical techniques were implemented to predict the buckling loads and mode shapes and the postbuckling behavior of the plates being studied in this work. The first analysis was based on the Rayleigh-Ritz assumed modes energy method involving a direct minimization of the total potential energy of the system. The second type of analysis performed was a finite element formulation based on a 32 degrees-of-freedom hybrid semi-Loof element developed recently for the express application of thin composite plates and shells [6,7]. Both linear and nonlinear Rayleigh-Ritz and linear finite element analyses were performed using these techniques to predict the critical buckling loads and mode shapes and the postbuckling (i.e., large displacement) behavior.

The experimental operation is outlined in Chapter 4 beginning with a discussion of the test matrix and laminate notation. A total of 75 laminated plates were manufactured using a two-step curing/bonding technique. Symmetric sublaminates, manufactured using standard procedures, were bonded together at room temperature to form the desired

unsymmetric laminates. This two-step operation was necessary in order to produce flat unsymmetric laminates at room temperature and is described in detail including the preparation of unidirectional sublaminates, room-temperature bonding, and laminate instrumentation. This is followed by a description of the test fixture, the data acquisition equipment, and a detailed outline of the testing procedure. The final section describes the methods used to reduce the experimental data.

A description and presentation of some typical results from the present investigation, including both experimental data and analytical predictions, is contained in Chapter 5. Load versus out-of-plane deflection data, load versus strain data, isodeflection contour maps, and graphs of the applied load versus longitudinal in-plane displacement are presented. The critical buckling loads and failure data are also tabulated, along with information about the failure loads and apparent failure mechanisms. In addition to the data presented in this chapter, a complete collection of graphs from the experimental data are included in several appendices.

A correlation of the results with a discussion of their meaning is presented in Chapter 6. Specific conclusions drawn in Chapter 6 are summarized in Chapter 7, along with recommendations for further work.

CHAPTER 2

PREVIOUS WORK

2.1 Overview

Without question, Leonhard Euler can be regarded as the father of the theory of elastic stability [8]. However, Bryan has been widely recognized as the one first responsible for extending this theory to plate buckling almost 150 years later, in 1891 [9]. His contemporary, Kirchhoff, was simultaneously developing the theory which governs the large deflection (postbuckling) behavior of plates [10]. Timoshenko became one of Bryan's early followers, with an extension of plate stability theory to approximate solutions for cases where rigorous solutions were not possible [11-13]. Meanwhile, von Kármán was influential in refining the theory of large deflections of plates [14].

Since that time, Timoshenko and Gere have compiled one of many textbooks on the subject of elastic stability containing scores of classic examples [15], with a chapter devoted to the buckling of plates. Likewise, von Kármán's theory is summarized in many texts including the classic reference by Timoshenko and Woinowsky-Krieger [16]. These classic works describe the fundamental mechanisms and equations governing the buckling and postbuckling behavior of general plates.

Since this early development of the basic theories, an immense amount of research has been performed on the buckling and postbuckling behavior of isotropic plates. In 1981, for example, Leissa [17] mentioned the availability of approximately 2000 references in the open literature concerning isotropic plate buckling. During the past few decades, this early theoretical and experimental work has been extended to orthotropic plates, with recent contributions from Stein [18,19], Jones and Morgan [20], and others, in such depth, that, in general, the buckling and postbuckling behavior of orthotropic plates are fairly well understood.

2.2 Laminates with Elastic Couplings

A comprehensive summary of the current state of the art in buckling and the postbuckling behavior of composites has been compiled recently by Leissa [5], with a review of almost 400 works relating specifically to composites performed in the intervening period. Most of these publications deal with symmetric, balanced composite plates. In general, composites have been shown to have reduced buckling loads due to various elastic couplings, yet still exhibit significant postbuckling strength.

Anisotropic and generally unsymmetric laminated plates introduce elastic couplings which complicate the buckling and postbuckling behavior and corresponding theoretical predictions. Unsymmetric laminates, for example, exhibit

elastic (mechanical) coupling between the in-plane (membrane) and out-of-plane (flexural) behaviors. Reissner and Stavsky [21] were the first to investigate the theoretical membrane-flexural couplings inherent in unsymmetric laminated plates (the general category of membrane-flexural coupling includes stretching-bending, stretching-twisting, and shearing- twisting couplings). Since that time, comparatively little work has been done, either analytically or experimentally, on such laminated composite plates. Nevertheless, an understanding of the buckling and postbuckling behavior of unbalanced and unsymmetric laminated composite plates is important, as pointed out by Jones [22], and as noted in Chapter 1 of this document.

The work which has focused on anisotropic plates, e.g., Ashton [23-26], Kicher and Mandell [27], Starnes [28,29], Turvey and Wittrick [30], Chia [31], and others, has been primarily restricted to specially orthotropic, midplane symmetric, antisymmetric, and/or cross-ply laminates, mostly with simply-supported boundary conditions. Such laminates have simplified constitutive relations and behavior. Also, most of the work has been analytical, with only a handful of experimental verifications. Ashton and Love [26] investigated the buckling of an antisymmetric angle-ply laminate, $[+45_{10}/-45_{10}]_T$, which displays stretching-twisting coupling, and found the experimental buckling load to be approximately half of the predicted value. Kicher and Mandell [27] likewise presented experimental buckling results for a variety of

plates, which included both unbalanced and unsymmetric laminates, as did Lagace et al. [32] and Chailleux et al. [33]. These works were limited to the linear buckling problem of laminates. More recently, Chia has assembled an invaluable collection of analytical work on the nonlinear analysis of plates, including applications to the postbuckling of unsymmetric composite plates [31].

Leissa [5] concluded from a Lockheed design guide [34] that bending-twisting couplings always decrease the buckling loads, and that the magnitude of this decrease is greater for longer plates. However, he later showed that, based on Mandell's results, this was not always true. Among the conclusions concerning the behavior of unsymmetric laminates reached by these various investigators are the facts that the membrane-flexural couplings significantly decrease the buckling loads and that a reduced bending stiffness, as defined in Chapter 6, improves the accuracy of a prediction based on the uncoupled bending equations. Additionally, Stein [18] showed that in-plane boundary conditions were important for laminates loaded in shear. An extension of this idea would imply that the behavior of laminates with stretching-shearing or shearing-twisting coupling loaded in compression would also be very dependent on the in-plane boundary conditions.

As indicated, the experimental studies to date have considered the linear buckling problem of unsymmetric laminates. However, the concept of bifurcation buckling takes

on an entirely new meaning when consideration of the concept is extended to include unsymmetrically laminated composite plates. The bending-stretching coupling terms, B_{ij}, introduced in unsymmetric laminates cause out-of-plane deflections, w, to initiate simultaneously with the application of the compressive load. All of the analyses performed to date have assumed a uniform axial compressive load prior to buckling. However, the applied stress will begin to deviate from this original ideal uniformity as soon as any out-of-plane deformation is introduced [15].

Ordinarily, bifurcation buckling loads are calculated as a standard eigenvalue problem. However, for nonlinear behavior it is difficult, at best, to establish an appropriate criterion for determination of the critical "buckling" load. While an approximation can still be obtained by this means for unsymmetric laminates, it appears to be more appropriate to calculate the load-deflection curves directly and compare these to the experimentally measured load-deflection curves. This would provide a compatible approach for comparing analytical and experimental buckling solutions for unsymmetrically laminated composite plates, rather than considering a buckling load which experimentally has little, if any, meaning.

Most of the research efforts noted here (as well as others) are summarized in the recent monograph by Leissa [5] mentioned above. However, compared to the vast number of possible configurations of unsymmetric laminates, relatively

little progress has been made to date on this subject. From this it is clear that further work is necessary to gain a better understanding of the effects of the elastic couplings inherent in unbalanced and unsymmetric laminates on the buckling behavior of these plates and extend this to the postbuckling regime.

CHAPTER 3

ANALYSIS

Two different analytical techniques were implemented to predict the buckling loads and mode shapes and the postbuckling behavior of the unbalanced and unsymmetric laminated graphite/epoxy plates investigated in this work. The first analysis was based on the Rayleigh-Ritz assumed modes energy method involving a direct minimization of the total potential energy of the system. The second type of analysis performed was a finite element formulation using a hybrid semi-Loof element developed recently for application to thin composite plates and shells. Linear analyses were performed using these techniques to predict the critical buckling loads and mode shapes. The Rayleigh-Ritz analysis was extended to predict the postbuckling, or large displacement (i.e., nonlinear), behavior.

For the linear part of the problem, both of these analytical formulations reduce to a standard eigenvalue problem which produces theoretical predictions of the critical buckling loads and their corresponding mode shapes. Upon including the nonlinear terms from the strain displacement relations, the analyses can be extended to the large deflection arena, enabling prediction of the large out-of-plane displacements and internal stresses at prescribed

load levels.

It should be noted that general unsymmetric laminates do not exhibit classical bifurcation buckling behavior. The bending-stretching coupling inherent in such laminates causes normal out-of-plane displacements to initiate simultaneously with the application of the compressive load. A nonlinear analysis is thus required, even for the "linear" (prebuckled) region. However, a "pseudo" buckling value can be determined analytically using linear plate theory. Although this "pseudo" elastic buckling load does not necessarily correspond to any apparent location on the load-displacement curve, it can be related to an experimental buckling load determined from a Southwell plot [35-37].

A detailed description of each of these two approaches is included in the following sections, as developed for the right-handed Cartesian coordinate system defined in Figure 3.1.

3.1 Rayleigh-Ritz Analysis

The Rayleigh-Ritz analysis involves a direct minimization of the total potential energy of the system. By assuming a set of "n" linearly independent mode shapes to represent the deflections u, v, and w as defined in Figure 3.1, the continuous plate, which theoretically has an infinite number of degrees of freedom, is approximated by an n-degrees-of-freedom model in terms of the "n" generalized

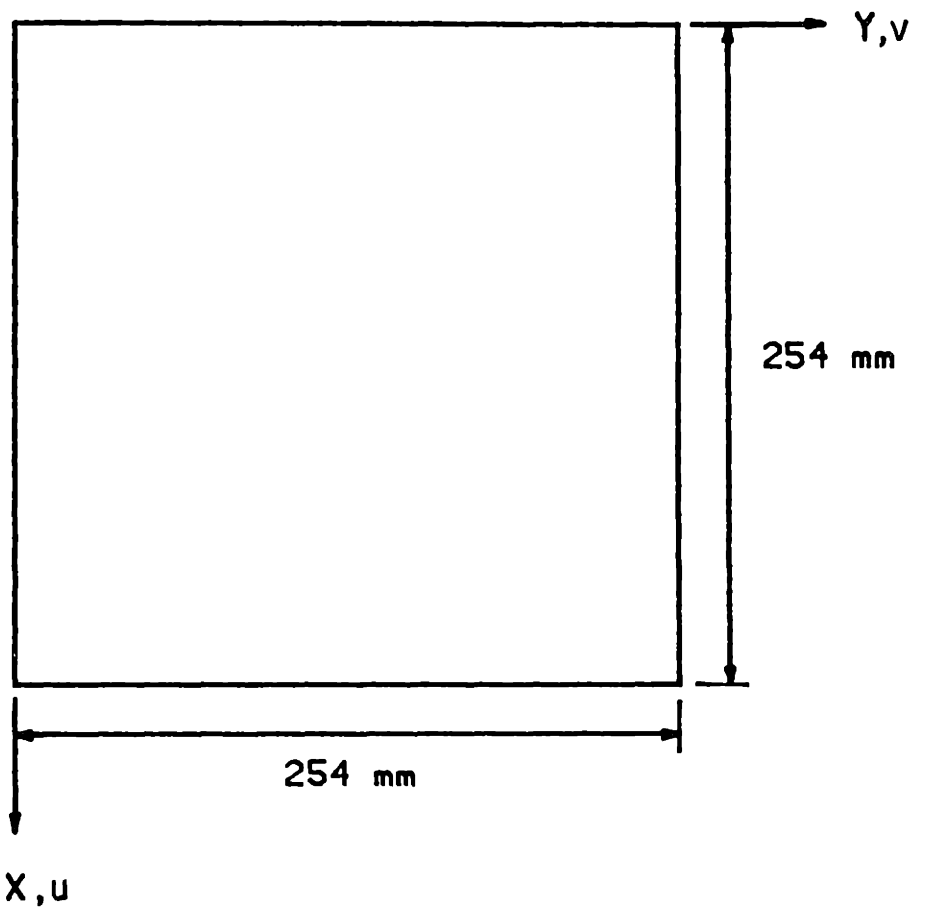

FIGURE 3.1 Definition of Coordinate System

coordinates (q_i). The governing differential equations are consequently reduced to a set of algebraic equations which can be solved numerically. Due to the additional constraints imposed by including only a finite number of degrees of freedom, the model is inherently stiffer than the actual structure. Consequently, the predicted critical buckling loads will represent an upper bound, while the resulting deflections will represent lower bounds.

The only restriction on the Rayleigh-Ritz method is the requirement that each of the assumed displacement functions satisfy the geometric boundary conditions. The accuracy of the Rayleigh-Ritz technique is dependent on the choice of assumed modes and can be improved by carefully selecting the most appropriate mode shapes which satisfy the geometric boundary conditions and/or by increasing the number of assumed displacement functions employed. For the laminates analyzed in this investigation, an attempt was made to isolate the minimum number of modes necessary to satisfactorily predict the buckling loads and mode shapes and adequately model the postbuckling behavior.

3.1.1 Formulation

The internal potential (strain) energy for any structural system is determined by integrating the product of the internal stresses and strains over the volume:

$$U = \frac{1}{2} \iiint \sigma\varepsilon \, dV \tag{3.1}$$

For a general laminated composite plate, the strain energy expresssion is simplified by integrating over the thickness of the laminate and introducing the laminate constitutive relations between the applied loads and moments and the in-plane strains and curvatures, which are given by [38]:

$$\begin{Bmatrix} N_x \\ N_y \\ N_{xy} \end{Bmatrix} = \begin{bmatrix} A_{11} & A_{12} & A_{16} \\ A_{21} & A_{22} & A_{26} \\ A_{61} & A_{62} & A_{66} \end{bmatrix} \begin{Bmatrix} \varepsilon_x^\circ \\ \varepsilon_y^\circ \\ \gamma_{xy}^\circ \end{Bmatrix} + \begin{bmatrix} B_{11} & B_{12} & B_{16} \\ B_{21} & B_{22} & B_{26} \\ B_{61} & B_{62} & B_{66} \end{bmatrix} \begin{Bmatrix} \kappa_x \\ \kappa_y \\ \kappa_{xy} \end{Bmatrix} \tag{3.2}$$

and

$$\begin{Bmatrix} M_x \\ M_y \\ M_{xy} \end{Bmatrix} = \begin{bmatrix} B_{11} & B_{12} & B_{16} \\ B_{21} & B_{22} & B_{26} \\ B_{61} & B_{62} & B_{66} \end{bmatrix} \begin{Bmatrix} \varepsilon_x^\circ \\ \varepsilon_y^\circ \\ \gamma_{xy}^\circ \end{Bmatrix} + \begin{bmatrix} D_{11} & D_{12} & D_{16} \\ D_{21} & D_{22} & D_{26} \\ D_{61} & D_{62} & D_{66} \end{bmatrix} \begin{Bmatrix} \kappa_x \\ \kappa_y \\ \kappa_{xy} \end{Bmatrix} \tag{3.3}$$

where $\{N\}$ and $\{M\}$ contain the in-plane stress and moment resultants, $\{\varepsilon^\circ\}$ and $\{\kappa\}$ contain the in-plane strains and curvatures, and $[A]$, $[B]$, and $[D]$ represent the symmetric elastic in-plane, coupling, and out-of-plane stiffness properties of the laminated plate as determined from classical laminated plate theory, respectively.

These relations assume a linear strain distribution through the thickness of the laminate, such that:

$$\varepsilon_x = \varepsilon_x^o + z\kappa_x \tag{3.4}$$

where ε^o refers to the strain at the reference plane, z refers to the distance from the reference plane, and κ refers to the local curvature component. It should be noted that the laminate midplane is the plane of reference throughout this work.

Transverse shear is neglected in these formulations. Normally, shear deformation increases the flexibility of the structure. However, its effect has been shown to be negligible for laminates with a thickness-to-width ratio of less than 0.02 [39,40]. The laminates investigated in this study had a thickness-to-width ratio of less than 0.006, which underscores the validity of this assumption.

By using Equations 3.2, 3.3, and 3.4 in the general energy expression of Equation 3.1, the resulting expression for the internal strain energy of a general laminated composite plate in terms of the elastic matrices can be obtained:

$$U = \frac{1}{2}\int\int\left(\{\varepsilon^o\}^T[A]\{\varepsilon^o\}+2\{\varepsilon^o\}^T[B]\{\kappa\}+\{\kappa\}^T[D]\{\kappa\}\right)dxdy \tag{3.5}$$

In order to generalize the analytical formulation, it is

necessary to introduce the full nonlinear strain-displacement relations. These have been separated into linear and nonlinear components for the sake of convenience and future reference:

$$\{\varepsilon^{\circ}\} = \{\varepsilon^{\circ}\}_{L} + \{\varepsilon^{\circ}\}_{NL} \tag{3.6}$$

or,

$$\begin{Bmatrix} \varepsilon_x^{\circ} \\ \varepsilon_y^{\circ} \\ \gamma_{xy}^{\circ} \end{Bmatrix} = \begin{Bmatrix} \frac{\partial u}{\partial x} \\ \frac{\partial v}{\partial y} \\ \frac{\partial u}{\partial y} + \frac{\partial v}{\partial x} \end{Bmatrix}_{L} + \begin{Bmatrix} \frac{1}{2}\left(\frac{\partial w}{\partial x}\right)^2 \\ \frac{1}{2}\left(\frac{\partial w}{\partial y}\right)^2 \\ \frac{\partial w}{\partial x}\ \frac{\partial w}{\partial y} \end{Bmatrix}_{NL} \tag{3.7}$$

The corresponding curvature-displacement relations, which are the same for the linear and nonlinear cases, are given by:

$$\begin{Bmatrix} \kappa_x \\ \kappa_y \\ \kappa_{xy} \end{Bmatrix} = \begin{Bmatrix} -\frac{\partial^2 w}{\partial x^2} \\ -\frac{\partial^2 w}{\partial y^2} \\ -2\frac{\partial^2 w}{\partial x \partial y} \end{Bmatrix} \tag{3.8}$$

Placing these relations into the expression for the strain energy, Equation 3.5, yields an extremely long expression for the total strain energy of deformation, which can be broken up into six primary recognizable components:

$$U = \sum_{i=1}^{6} U_i \tag{3.9}$$

The first three components in the total expression for the internal strain energy are the linear terms which are used in both the linear buckling analysis and the nonlinear postbuckling analysis. Specifically, the first component, U_1, represents the linear contribution to the strain energy due to the in-plane extensional deformation:

$$\begin{aligned} U_1 = \frac{1}{2}\iint\Big\{ & A_{11}\left(\frac{\partial u}{\partial x}\right)^2 + 2A_{12}\left(\frac{\partial u}{\partial x}\right)\left(\frac{\partial v}{\partial y}\right) + A_{22}\left(\frac{\partial v}{\partial y}\right)^2 \\ & + 2A_{16}\left(\frac{\partial u}{\partial x}\right)\left(\frac{\partial u}{\partial y} + \frac{\partial v}{\partial x}\right) + 2A_{26}\left(\frac{\partial v}{\partial y}\right)\left(\frac{\partial u}{\partial y} + \frac{\partial v}{\partial x}\right) \\ & + A_{66}\left(\frac{\partial u}{\partial y} + \frac{\partial v}{\partial x}\right)^2 \Big\} dxdy \end{aligned} \tag{3.10}$$

The second term, U_2, represents the linear contribution to the deformation energy due to the elastic material coupling between in-plane stretching and out-of-plane bending. This linear term is unique to unsymmetric laminates:

$$U_2 = -\frac{1}{2}\int\int\Bigg\{ 2B_{11}\left(\frac{\partial u}{\partial x}\right)\left(\frac{\partial^2 w}{\partial x^2}\right) + 2B_{12}\left[\left(\frac{\partial u}{\partial x}\right)\left(\frac{\partial^2 w}{\partial y^2}\right) + \left(\frac{\partial v}{\partial y}\right)\left(\frac{\partial^2 w}{\partial x^2}\right)\right]$$

$$+ 2B_{22}\left(\frac{\partial v}{\partial y}\right)\left(\frac{\partial^2 w}{\partial y^2}\right) + 4B_{66}\left(\frac{\partial u}{\partial y} + \frac{\partial v}{\partial x}\right)\left(\frac{\partial^2 w}{\partial x \partial y}\right) \qquad (3.11)$$

$$+ 2B_{16}\left[2\left(\frac{\partial u}{\partial x}\right)\left(\frac{\partial^2 w}{\partial x \partial y}\right) + \left(\frac{\partial u}{\partial y} + \frac{\partial v}{\partial x}\right)\left(\frac{\partial^2 w}{\partial x^2}\right)\right]$$

$$+ 2B_{26}\left[2\left(\frac{\partial v}{\partial y}\right)\left(\frac{\partial^2 w}{\partial x \partial y}\right) + \left(\frac{\partial u}{\partial y} + \frac{\partial v}{\partial x}\right)\left(\frac{\partial^2 w}{\partial y^2}\right)\right]\Bigg\} dx dy$$

The third term, U_3, represents the linear contribution to the internal strain energy due to the out-of-plane bending. This is the only component of the strain energy necessary for the linear buckling analysis of symmetric plates:

$$U_3 = \frac{1}{2}\int\int\Bigg\{ D_{11}\left(\frac{\partial^2 w}{\partial x^2}\right)^2 + 2D_{12}\left(\frac{\partial^2 w}{\partial x^2}\right)\left(\frac{\partial^2 w}{\partial y^2}\right) + D_{22}\left(\frac{\partial^2 w}{\partial y^2}\right)^2$$

$$+ 4D_{16}\left(\frac{\partial^2 w}{\partial x^2}\right)\left(\frac{\partial^2 w}{\partial x \partial y}\right) + 4D_{26}\left(\frac{\partial^2 w}{\partial y^2}\right)\left(\frac{\partial^2 w}{\partial x \partial y}\right) \qquad (3.12)$$

$$+ 4D_{66}\left(\frac{\partial^2 w}{\partial x \partial y}\right)^2\Bigg\} dx dy$$

The remaining three components represent the nonlinear contributions to the strain energy and provide the essential information for the postbuckling (large deflection) analysis.

The first of these nonlinear components, U_4, represents the nonlinear contribution to the strain energy due to the geometrical coupling between the in-plane stretching and the out-of-plane bending deformations introduced in the large deflection regime:

$$U_4 = \frac{1}{2}\iint\Big\{ A_{11}\left(\frac{\partial u}{\partial x}\right)\left(\frac{\partial w}{\partial x}\right)^2 + A_{12}\left[\left(\frac{\partial u}{\partial x}\right)\left(\frac{\partial w}{\partial y}\right)^2 + \left(\frac{\partial v}{\partial y}\right)\left(\frac{\partial w}{\partial x}\right)^2\right]$$

$$+ A_{16}\left[2\left(\frac{\partial u}{\partial x}\right)\left(\frac{\partial w}{\partial x}\right)\left(\frac{\partial w}{\partial y}\right) + \left(\frac{\partial u}{\partial y} + \frac{\partial v}{\partial x}\right)\left(\frac{\partial w}{\partial x}\right)^2\right] \qquad (3.13)$$

$$+ A_{26}\left[2\left(\frac{\partial v}{\partial y}\right)\left(\frac{\partial w}{\partial x}\right)\left(\frac{\partial w}{\partial y}\right) + \left(\frac{\partial u}{\partial y} + \frac{\partial v}{\partial x}\right)\left(\frac{\partial w}{\partial y}\right)^2\right]$$

$$+ A_{22}\left(\frac{\partial v}{\partial y}\right)\left(\frac{\partial w}{\partial y}\right)^2 + 2A_{66}\left(\frac{\partial u}{\partial y} + \frac{\partial v}{\partial x}\right)\left(\frac{\partial w}{\partial x}\right)\left(\frac{\partial w}{\partial y}\right)\Big\}dxdy$$

The next component, U_5, represents the nonlinear contribution to the potential energy due to the combined action of material coupling between the in-plane stretching and out-of-plane bending with the geometrically large displacement behavior. This nonlinear term is unique to unsymmetric laminates:

$$U_5 = -\frac{1}{2}\int\int\Big\{ B_{11}\left(\frac{\partial w}{\partial x}\right)^2\left(\frac{\partial^2 w}{\partial x^2}\right) + B_{12}\left[\left(\frac{\partial w}{\partial x}\right)^2\left(\frac{\partial^2 w}{\partial y^2}\right) + \left(\frac{\partial w}{\partial y}\right)^2\left(\frac{\partial^2 w}{\partial x^2}\right)\right]$$

$$+ B_{22}\left(\frac{\partial w}{\partial y}\right)^2\left(\frac{\partial^2 w}{\partial y^2}\right) + 4B_{66}\left(\frac{\partial w}{\partial x}\right)\left(\frac{\partial w}{\partial y}\right)\left(\frac{\partial^2 w}{\partial x \partial y}\right) \tag{3.14}$$

$$+ 2B_{16}\left[\left(\frac{\partial w}{\partial x}\right)^2\left(\frac{\partial^2 w}{\partial x \partial y}\right) + \left(\frac{\partial w}{\partial x}\right)\left(\frac{\partial w}{\partial y}\right)\left(\frac{\partial^2 w}{\partial x^2}\right)\right]$$

$$+ 2B_{26}\left[\left(\frac{\partial w}{\partial x}\right)^2\left(\frac{\partial^2 w}{\partial x \partial y}\right) + \left(\frac{\partial w}{\partial x}\right)\left(\frac{\partial w}{\partial y}\right)\left(\frac{\partial^2 w}{\partial y^2}\right)\right]\Big\}dxdy$$

The final component of internal strain energy, U_6, contains the higher order terms which represent the postbuckling stiffening due to the large deflections:

$$U_6 = \frac{1}{2}\int\int\Big\{ \frac{1}{4}A_{11}\left(\frac{\partial w}{\partial x}\right)^4 + \frac{1}{2}\left(A_{12}+2A_{26}\right)\left(\frac{\partial w}{\partial x}\right)^2\left(\frac{\partial w}{\partial y}\right)^2$$

$$+ A_{16}\left(\frac{\partial w}{\partial x}\right)^3\left(\frac{\partial w}{\partial y}\right) + A_{26}\left(\frac{\partial w}{\partial x}\right)\left(\frac{\partial w}{\partial y}\right)^3 \tag{3.15}$$

$$+ \frac{1}{4}A_{22}\left(\frac{\partial w}{\partial y}\right)^4\Big\}dxdy$$

In addition to the potential energy stored as internal strain energy in the plate, the potential energy attributable to the work performed by the externally applied loads must also be accounted for. This is obtained by integrating the

vector product of the applied tractions and the corresponding displacements over the surface of the plate where tractions are applied, S_σ:

$$W = \iint_{S_\sigma} \{q\}^T \{T\}\, ds \tag{3.16}$$

where $\{T\}$ represents the applied tractions and $\{q\}$ contains the corresponding generalized displacements.

For the case of a thin plate loaded in uniaxial compression and referenced at x equals 0, as shown in Figure 3.1, the work expression reduces to a line integral of the product of the in-plane force resultant, N_x, along the boundary and the corresponding axial displacement, u, in the form:

$$W = \int N_x\, u(a,y)\, dy \tag{3.17}$$

This expression was employed in the nonlinear analysis.

However, for the linear analysis, the following expression for the work energy in terms of the shortening, which is equivalent to the above expression in the variational case, was used:

$$W = -\frac{1}{2} \iint N_x \left(\frac{\partial w}{\partial x}\right)^2 dxdy \tag{3.18}$$

This enabled simplification of the ensuing eigenvalue problem.

In addition to the six components of the elastic potential energy and the work energy due to the applied axial load, the influence of lateral spring forces was included to model the effect of the out-of-plane deflection measurement transducers used in the experiment. Nine such transducers were employed at the locations shown in Figure 3.2. The transverse force exerted by a transducer on the plate can be expressed generically as:

$$P_i = P_{oi} - k_i w_i \tag{3.19}$$

where P_{oi} represents the initial force due to the compressed spring in the i^{th} transducer, k_i represents the stiffness of the corresponding spring, and w_i represents the out-of-plane deflection at the same location. This can be expressed explicitly for the actual transducers used in the experimental portion of this investigation as:

$$P_I = 2.10 - 0.0827\ w_i \tag{3.20}$$

$$P_{II} = 5.89 - 0.116\ w_i \tag{3.21}$$

where P_I (expressed in Newtons) represents the force exerted by each of the transducers in the upper and lower rows (i.e., at x equal to a/4 and 3a/4) which have a working range of

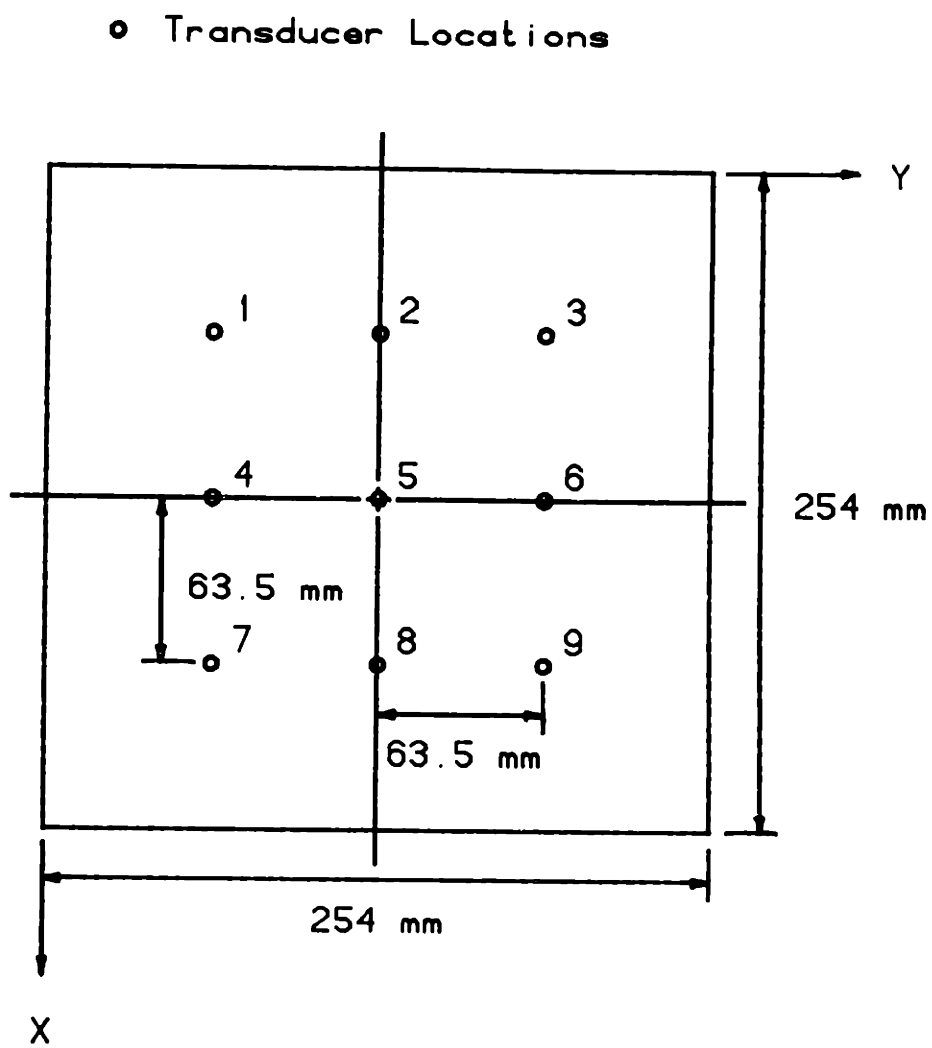

FIGURE 3.2 Illustration showing Transducer Locations on Plate

± 25.4 mm, P_{II} (also expressed in Newtons) represents the force exerted by each of the transducers in the middle row (i.e., at x equal to a/2) which have a working range of ± 50.8 mm, and w_i represents the local out-of-plane deflection in millimeters. These are based on values specified by the transducer manufacturer. For the linear transducer springs, the associated contributions to the internal strain energy and work energy are determined to be:

$$U_T = \frac{1}{2} \sum_{i=1}^{9} k_i w_i^2 \tag{3.22}$$

and

$$W_T = \sum_{i=1}^{9} P_{oi} w_i \tag{3.23}$$

where w_i represents the out-of-plane deflection at the location of the i^{th} transducer. These influences were added directly to the corresponding linear stiffness matrix and load vector.

The total potential energy of the system, Π_p, is the difference between the total internal strain energy of deformation and the work performed by the externally applied loads:

$$\Pi_p = U - W \tag{3.24}$$

For this particular case, accounting for the effect of the transducers, the governing expression for the total potential energy is given by:

$$\Pi_P = \sum_{i=1}^{6} U_i - W + U_T - W_T \tag{3.25}$$

In the Rayleigh-Ritz analysis, it is assumed that the deflection behavior can be adequately modelled by a series of separable displacement functions of the form:

$$u = \sum_i \bar{u}_i \alpha_i(x)\beta_i(y)$$

$$v = \sum_i \bar{v}_i \gamma_i(x)\delta_i(y) \tag{3.26}$$

$$w = \sum_i \bar{w}_i \chi_i(x)\psi_i(y)$$

where α_i, γ_i, and χ_i represent the assumed shape function distributions in the x-direction, β_i, δ_i, and ψ_i represent the assumed shape function distributions in the y-direction, and $\bar{u}_i$, $\bar{v}_i$, and $\bar{w}_i$ represent the unknown amplitudes of the corresponding assumed mode shapes. This can be expressed

generically in terms of the generalized coordinates, q_i, as:

$$u = \sum_{i=1}^{N_u} q_i \phi_i(x,y)$$

$$v = \sum_{i=N_u+1}^{N_u+N_v} q_i \phi_i(x,y) \qquad (3.27)$$

$$w = \sum_{i=N_u+N_v+1}^{N_u+N_v+N_w} q_i \phi_i(x,y)$$

where N_u, N_v, and N_w are the number of modes assumed for u, v, and w, respectively.

Upon substituting the assumed displacement shape functions expressed in Equation 3.26, into the expresssion for the total potential energy of the structure, Equation 3.25, the expression can be rewritten in terms of the generalized coordinates, q_i, as:

$$\Pi_P = \sum_{i=1}^{6} U_i(\{q\}) - W(\{q\}) + U_T(\{q\}) - W_T(\{q\}) \qquad (3.28)$$

The strain energy components, U_i, are now functions of the associated stiffness terms, $K_{r_{ij}}$, as follows:

$$U_1 = \frac{1}{2} \sum_{i=1}^{M} \sum_{j=1}^{M} K_{1_{ij}} q_i q_j \tag{3.29}$$

$$U_2 = \frac{1}{2} \sum_{i=1}^{M} \sum_{j=P}^{N} K_{2_{ij}} q_i q_j \tag{3.30}$$

$$U_3 = \frac{1}{2} \sum_{i=P}^{N} \sum_{j=P}^{N} K_{3_{ij}} q_i q_j \tag{3.31}$$

$$U_4 = \frac{1}{2} \sum_{i=1}^{M} \sum_{j=P}^{N} \sum_{k=P}^{N} K_{4_{ijk}} q_i q_j q_k \tag{3.32}$$

$$U_5 = \frac{1}{2} \sum_{i=P}^{N} \sum_{j=P}^{N} \sum_{k=P}^{N} K_{5_{ijk}} q_i q_j q_k \tag{3.33}$$

$$U_6 = \frac{1}{2} \sum_{i=P}^{N} \sum_{j=P}^{N} \sum_{k=P}^{N} \sum_{l=P}^{N} K_{6_{ijkl}} q_i q_j q_k q_l \tag{3.34}$$

$$U_T = \frac{1}{2} \sum_{i=P}^{N} \sum_{j=P}^{N} K_{T_{ij}} q_i q_j \tag{3.35}$$

where M is the combined number of assumed modes for u and v, P=M+1, and N is the total combined number of assumed modes for u, v, and w. The stiffness terms are given in Appendix A.

3.1.2 Linear (Buckling) Problem

The linear stability problem is solved by invoking the principle of stationary total potential energy:

$$\delta \Pi_p = 0 \tag{3.36}$$

where Π_p for the linear problem is simplified to:

$$\Pi_p = \sum_{i=1}^{3} U_i - W \tag{3.37}$$

It should be noted that the transducer forces were neglected in the linear problem, since they do not affect the buckling loads [41].

Placing the assumed separable displacement functions into the potential energy expression and minimizing yields a standard eigenvalue problem, in terms of the critical buckling value, $\bar{N}_x$, as shown:

$$[K]\{q\} = \bar{N}_x[L]\{q\} \tag{3.38}$$

where [K] and [L] represent the resulting stiffness and loading matrices. In order to enhance the solution procedure, these stiffness and loading matrices in the eigenvalue problem were partitioned between the in-plane and out-of-plane

coordinates:

$$\left[\begin{array}{c|c} [K_1] & [K_2] \\ \hline [K_2^T] & [K_3] \end{array}\right]\left\{\begin{array}{c} \{q_{uv}\} \\ \hline \{q_w\} \end{array}\right\} = \bar{N}_x \left[\begin{array}{c|c} [0] & [0] \\ \hline [0] & [L_w] \end{array}\right]\left\{\begin{array}{c} \{q_{uv}\} \\ \hline \{q_w\} \end{array}\right\} \qquad (3.39)$$

The solution of the eigenvalue problem, Equation 3.38, was simplified by observing that only the lower diagonal partition in the loading matrix was populated. This allowed the size of the eigenvalue problem to be significantly reduced through a process involving partitioning and simple matrix algebra. The resulting reduced eigenvalue problem is of the form:

$$\left[[K_3] - [K_2]^T[K_1]^{-1}[K_2]\right]\{q_w\} = \bar{N}_x[L_w]\{q_w\} \qquad (3.40)$$

This reduces the solution procedure from an eigenvalue problem of order (N,N) where N equals the sum of N_u, N_v, and N_w, to essentially that of a matrix inversion of order (M,M) where M equals the sum of N_u and N_v, coupled with an eigenvalue problem of order (N_w,N_w).

After obtaining a solution for $\{q_w\}$, if desired, the relative modal amplitudes (generalized coordinates) associated with the u and v deflections can be reconstructed using the relation:

$$\{q_{uv}\} = -\left[[K_1]^{-1}[K_2]\right]\{q_w\} \tag{3.41}$$

The critical buckling load, $\bar{N}_x$, and mode shape, $\{q\}$, determined in this manner should correspond to that obtained experimentally via the Southwell method.

3.1.3 Nonlinear (Postbuckling) Problem

The solution procedure for the full nonlinear problem is based on a direct minimization of the total potential energy of the system using a structural optimization search technique for any given load [42,43]. The nonlinear equations were solved using a modified Newton-Raphson iterative solution technique. The Newton-Raphson method was selected because it ensures rapid convergence at each iteration. However, since it requires inverting the Jacobian matrix at each step, it is primarily applicable to problems with only a few degrees of freedom.

Beginning with the linear solutions for the displacements, $\{q\}_o$, based on the lowest few natural buckling modes (eigenvalues), the corresponding local minima were determined using the full nonlinear equations. In order for a local minimum to exist, the gradient of the potential energy function must be zero:

$$\left\{\nabla \Pi_p\right\} = \left\{\frac{\partial \Pi_p}{\partial q_j}\right\} = 0 \tag{3.42}$$

According to the Newton-Raphson method, the value of the function for which an extrema is sought, represented here by the gradient of the potential energy, $\nabla\Pi_P$, at step k+1 is obtained by incrementing the value of the function at step k with an estimate of the root given by the product of the Jacobian matrix and the corresponding displacement vector at step k:

$$\{\nabla\Pi_P\}_{k+1} = \{\nabla\Pi_P\}_k + [J]_k\{\Delta q\}_k \tag{3.43}$$

where the Jacobian matrix, [J], is given by:

$$[J] = \frac{\partial\nabla\Pi_P}{\partial q_i} = \frac{\partial^2\Pi_P}{\partial q_i \partial q_j} \tag{3.44}$$

The gradient at step k+1 goes to zero if and only if the increment is chosen such that:

$$\{\nabla\Pi_P\}_k + [J]_k\{\Delta q\}_k = 0 \tag{3.45}$$

Thus, the normal increment in the displacements at step k, $\{\Delta q\}_k$, is determined by multiplying the gradient by the inverted Jacobian matrix:

$$\{\Delta q\}_k = -[J]_k^{-1}\{\nabla\Pi_P\}_k \tag{3.46}$$

For the unmodified Newton-Raphson method, this represents the actual increment to be added to the displacements at the k^{th} step. For the modified Newton-Raphson method employed, this represents a search vector which indicates the initial direction of optimum descent in the value of the potential energy functional, Π_p. The next step requires finding the actual minimum of the potential energy function along the direction of this search vector.

The solution procedure is generalized by determining a correction factor, α, which provides a better estimate for the displacement increment and, thus, optimizes the solution procedure. This factor was found by solving for the roots of the expression:

$$\frac{\partial \Pi_p}{\partial \alpha}(q + \alpha \Delta q) = 0 \tag{3.47}$$

The displacement estimates at step k+1 are then updated by adding the revised increment to the old estimate:

$$\{q\}_{k+1} = \{q\}_k + \alpha_k \{\Delta q\}_k \tag{3.48}$$

This procedure is repeated until the desired convergence is achieved. For the laminated plates presented in this investigation, two convergence criteria were employed. Convergence was assumed when either the normalized gradient was less than 0.005:

$$\frac{\sum_i \left| \nabla \Pi_{P_i} \right|}{N_u+N_v+N_w} < 0.005 \tag{3.49}$$

or when the normalized gradient was less than 0.1 and the normalized displacement increment was less than 0.00001:

$$|\alpha|_k \frac{\sum \left| \Delta q_i \right|_k}{\sum \left| q_i \right|_k} < 0.00001 \tag{3.50}$$

The entire procedure is then repeated beginning with each of the lowest few modes from the linear solution. The resulting local minima are then compared in order to ascertain which solution represents the global minimum of the energy functional. A listing of the Rayleigh-Ritz source code is presented in Appendix B.

3.1.4 Boundary Conditions

In general, the following four boundary conditions must be prescribed along each boundary (i.e., at x=0,a and y=0,b): first, either the normal in-plane displacement or the corresponding applied traction; second, either the tangential in-plane displacement or the applied shear load; third, either the out-of-plane slope or the applied moment; and, fourth, either the out-of-plane displacement or a combination of the applied twisting moment and transverse shear (i.e. the

Kirchhoff condition).

For the Rayleigh-Ritz analysis, only the geometric boundary conditions need to be satisfied. Thus, along the clamped loaded ends, the essential boundary conditions are that the variation of the displacement, δu, in the loading direction (x) must be zero for the linear case or prescribed for the nonlinear case; similarly, the out-of-plane slope, $\partial w/\partial x$, and displacement, w, must be zero along these clamped boundaries. Along the sides, three types of boundary conditions were investigated. For the free case, there are no restrictions; for the simply-supported case, only the out-of-plane displacement, w, must be zero; and, for the clamped case, both the out-of-plane slope, $\partial w/\partial y$, and deflection, w, are required to be zero.

3.1.5 Modal Selection

The most critical step in the Rayleigh-Ritz method is the selection of assumed modes. Linear combinations of components from both geometric and trigonometric series were chosen to represent each of the displacements, u, v, and w, in order to allow the full effects of any elastic (mechanical) couplings to be adequately represented. Previous work provided a basis for the modes finally selected. The modes chosen for this investigation are identified as follows.

The first component of the axial in-plane (u) mode represents the uniform stretching (1 mode). This was coupled

with modes which allowed the sides of the plate to contract or expand in the plane in an unrestricted manner (4 modes). The last components used in the u-modes represent a partial double trigonometric series to model the expected in-plane behavior (16 modes). Thus, a total of 21 modes were used to represent the u-deflection:

$$u = q_1\left(\frac{x}{a}\right) + \sum_{n=1}^{4} q_{n+17}\left(\frac{x}{a} - \frac{1}{2}\right)\cos\left(\frac{n\pi y}{b}\right) + \sum_{m=1}^{4}\sum_{n=1}^{4} q_{4(m-1)+n+1}\sin\left(\frac{m\pi x}{a}\right)\cos\left((2n-1)\frac{\pi y}{b}\right) \tag{3.51}$$

The first two components of the v-deflection represent Poisson's effect and the in-plane shear, respectively. The remaining terms are analagous to those discussed above. Therefore, a total of 22 modes were used to represent the v-deflection:

$$v = q_{22}\left(\frac{y}{b}\right) + q_{23}\left(\frac{x}{a}\right) + \sum_{m=1}^{4} q_{m+39}\cos\left(\frac{m\pi x}{a}\right)\left(\frac{y}{b} - \frac{1}{2}\right) + \sum_{m=1}^{4}\sum_{n=1}^{4} q_{4(m-1)+n+23}\cos\left(\frac{m\pi x}{a}\right)\sin\left((2n-1)\frac{\pi y}{b}\right) \tag{3.52}$$

The assumed modes for the w-deflection depend on the side boundary conditions, unlike the u and v assumed modes. For

the laminates with clamped side boundary conditions, the out-of-plane deflections were represented by beam functions in both x and y (9 modes total):

$$w_{clamped} = \sum_{m=1}^{3} \sum_{n=1}^{3} q_{3(m-1)+n+43} F_m\left(\frac{x}{a}\right) F_n\left(\frac{y}{b}\right) \qquad (3.53)$$

where F_k represents the standard beam functions [44] given by:

$$F_k = \cosh\left(\frac{\alpha_k x}{a}\right) - \cos\left(\frac{\alpha_k x}{a}\right) - \gamma_k\left[\sinh\left(\frac{\alpha_k x}{a}\right) - \sin\left(\frac{\alpha_k x}{a}\right)\right] \qquad (3.54)$$

The coefficients for the beam functions are listed in Table 3.1.

For the laminates with simply-supported side boundary conditions, beam functions were again used for the x-components of w, but trigonometric functions were used for the y-components of w:

$$w_{simple} = \sum_{m=1}^{3} \sum_{n=1}^{3} q_{3(m-1)+n+43} F_m\left(\frac{x}{a}\right) \sin\left(\frac{n\pi y}{b}\right) \qquad (3.55)$$

These modes enable the complex buckling patterns and large displacement behavior to be properly represented, allowing the full effects of coupling between the in-plane

TABLE 3.1

BEAM FUNCTION COEFFICIENTS EMPLOYED IN RAYLEIGH-RITZ ANALYSIS

k	α_k	γ_k
1	4.7300407448627[a]	0.98250221457624[a]
2	7.8532046240958	1.00077731190727
3	10.995607838002	0.99996645012541
4	14.137165491257	1.00000144989766
5	17.278759657400	0.99999993734438
6	20.420352245626	1.00000000270759

[a] Values from Reference 44.

extension and shear and the out-of-plane bending and twisting to be exhibited. The analysis indicated that these series, although incomplete, adequately represent the predominant contributions to the in-plane behavior (i.e., the u and v displacements). These modes were found to be the most important for the laminates studied in this investigation.

The laminates tested with free side boundary conditions were found to behave according to classical wide-column theory. Therefore, the linear and nonlinear Rayleigh-Ritz analyses were not performed for that type of side boundary conditions. The analysis technique used for laminates with free side bounddary conditions is described in Chapter 6.

3.2 Finite Element Analysis

The finite element method, while similar in principle to the Rayleigh-Ritz technique, has two major differences. The primary distinction between the two formulations is that the structure is discretized in the finite element method into smaller regions enabling the application of generic mode shapes, whereas global mode shapes must be predetermined for a genuine Rayleigh-Ritz analysis. A hybrid plate element [6,7,45,47], based on an extended Hellinger-Reissner principle, was determined to be the most useful for this type of investigation. The 32 degree-of-freedom semi-Loof element implemented in the analysis is illustrated in Figure 3.3, in terms of the natural coordinates, ξ and η. For the finite

element analysis, the plate was discretized into a five by five grid as shown in Figure 3.4. This represents a total of 408 degrees of freedom.

The second major difference between the Rayleigh-Ritz analysis and the particular finite element method employed is the energy principle upon which each is based. The hybrid plate element used in this investigation originates from the Hellinger-Reissner principle. However, since equilibrium is forced to be satisfied in the integral sense the Hellinger-Reissner principle reduces to the following form for the buckling problem:

$$\Pi_R = \sum_n \left\{ \iint \left[\frac{1}{2}[\{N\}^T\{M\}^T] \begin{bmatrix} [A] & [B] \\ [B]^T & [D] \end{bmatrix}^{-1} \begin{Bmatrix} \{N\} \\ \{M\} \end{Bmatrix} + \frac{1}{2}\left[\frac{\partial w}{\partial x} \; \frac{\partial w}{\partial y}\right] \begin{bmatrix} \bar{N}_x & \bar{N}_{xy} \\ \bar{N}_{xy} & \bar{N}_y \end{bmatrix} \begin{Bmatrix} \frac{\partial w}{\partial x} \\ \frac{\partial w}{\partial y} \end{Bmatrix} \right] dxdy \qquad (3.56)$$

$$+ \int_s \left[N_n \tilde{u}_n + N_{ns} \tilde{u}_{ns} + Q_n \tilde{w} - M_n \left(\frac{\partial \tilde{w}}{\partial n}\right) - M_{ns} \left(\frac{\partial \tilde{w}}{\partial s}\right) \right] ds \Bigg\}$$

where, N_n and N_{ns} refer to the in-plane forces on the boundary, Q_n is the transverse shear on the boundary, and M_n and M_{ns} represent the bending moment on the boundary, with the subscript n referring to the normal direction and the subscript ns referring to the tangential direction. The prescribed boundary displacements, denoted by $\tilde{(\ )}$, are given

o Displacements u, v, and w
- Rotation $w_{,n}$

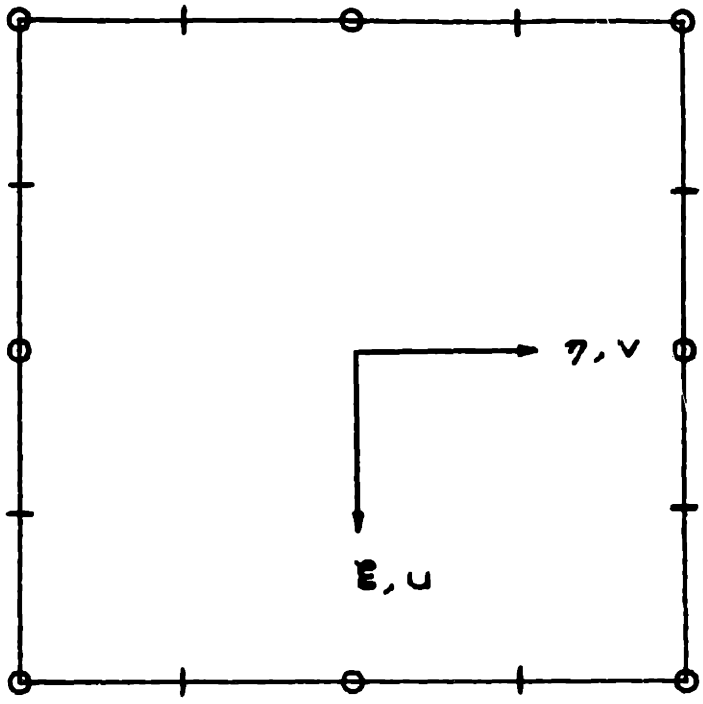

FIGURE 3.3 Illustration of 32 Degree of Freedom Semi-Loof Element

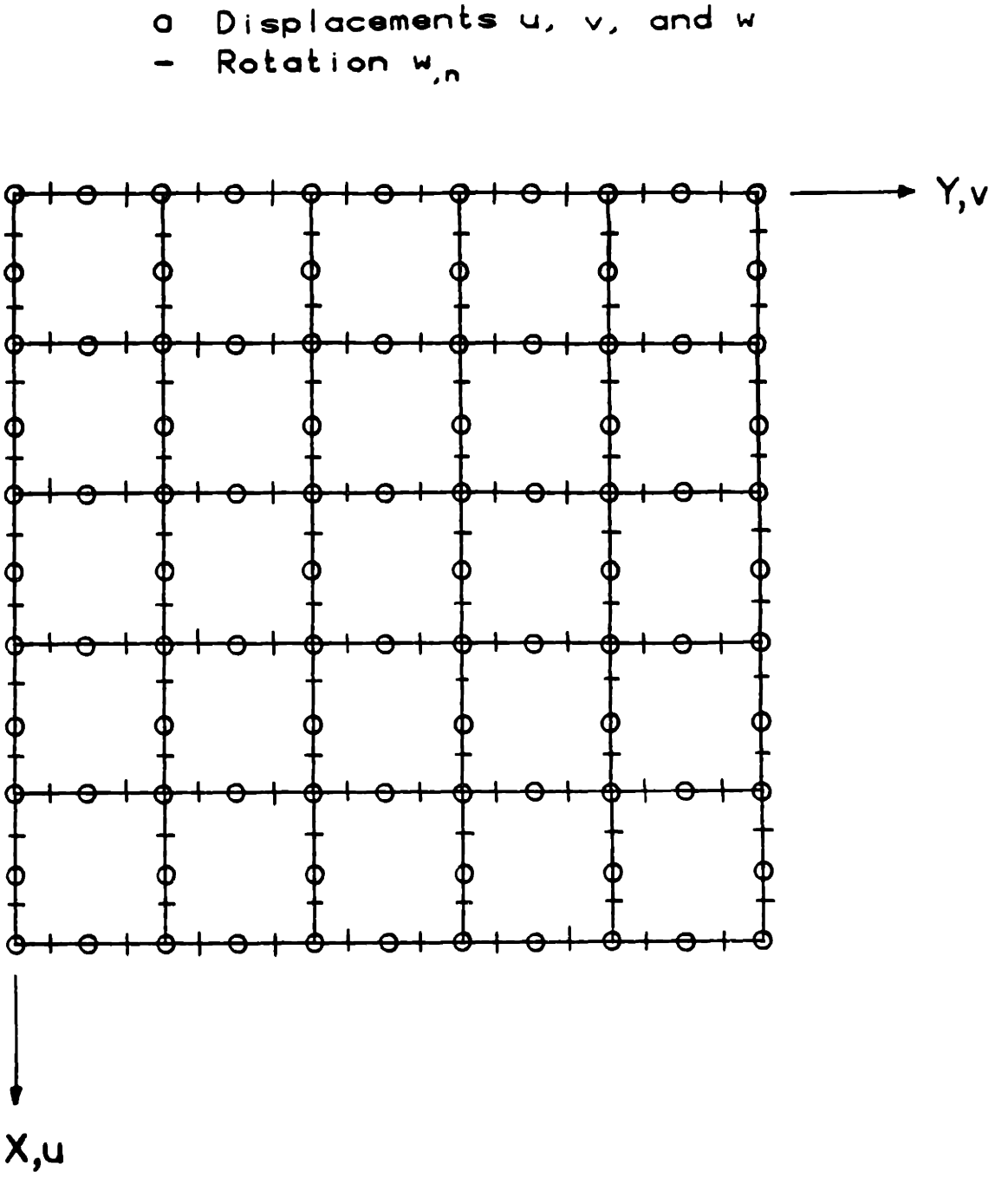

FIGURE 3.4 Illustration of Grid used in Finite Element Analysis

by:

$$\{w\} = \begin{Bmatrix} \tilde{w} \\ \frac{\partial \tilde{w}}{\partial n} \\ \frac{\partial \tilde{w}}{\partial s} \end{Bmatrix} \tag{3.57}$$

and

$$\{\tilde{u}\} = \begin{Bmatrix} \frac{\partial \tilde{u}}{\partial n} \\ \frac{\partial \tilde{u}}{\partial ns} \end{Bmatrix} \tag{3.58}$$

The problem was formulated by assuming 37 independent stress parameters (β):

$$\begin{Bmatrix} \{N\} \\ \{M\} \end{Bmatrix} = \begin{bmatrix} [P_N] & 0 \\ 0 & [P_M] \end{bmatrix} \{\beta\} = [P]\{\beta\} \tag{3.59}$$

The applied stress resultants were expressed in terms of a single eigenvalue, λ, by introducing the applied stress ratios, γ:

$$\begin{bmatrix} \bar{N}_x & \bar{N}_{xy} \\ \bar{N}_{xy} & \bar{N}_y \end{bmatrix} = \lambda \begin{bmatrix} \gamma_x & \gamma_{xy} \\ \gamma_{xy} & \gamma_y \end{bmatrix} = \lambda[Q] \tag{3.60}$$

The out-of-plane displacement field, w, was assumed to be of the form:

$$w = \{\Phi_I\}^T\{q\} \tag{3.61}$$

where Φ_i represent the assumed displacement shapes. The corresponding prescribed boundary displacements were likewise assumed to be of the form:

$$\begin{Bmatrix} \tilde{\{u\}} \\ \tilde{\{w\}} \end{Bmatrix} = \begin{bmatrix} [\Phi_u] & 0 \\ 0 & [\Phi_w] \end{bmatrix}\{q\} = [\Phi]\{q\} \tag{3.62}$$

Finally, the boundary forces can be identified as:

$$\{T\} = \begin{Bmatrix} N_n \\ N_{ns} \\ Q_n \\ -M_n \\ -M_{ns} \end{Bmatrix} = [R]\{\beta\} \tag{3.63}$$

Placing these assumed distributions into Equation 3.56 yields a revised energy formulation in terms of these matrices as:

$$\Pi_R = \sum_n \left[\frac{1}{2}\{\beta\}^T[H]\{\beta\} + \frac{1}{2}\lambda\{q\}^T[L]\{q\} + \{\beta\}^T[G]\{q\}\right] \tag{3.64}$$

where:

$$[H] = \iint [P]^T \begin{bmatrix} A & B \\ B^T & D \end{bmatrix}^{-1} [P] \, dxdy \tag{3.65}$$

$$[L] = \iint [S]^T [Q] [S] \, dxdy \tag{3.66}$$

and

$$[G] = \int [R]^T [\Phi] \, dS \tag{3.67}$$

The total energy is minimized with respect to the stress parameters, β:

$$\frac{\partial \Pi_R}{\partial \beta} = 0 \tag{3.68}$$

This results in a relation between the stress parameters, $\{\beta\}$, and the displacements, $\{q\}$:

$$\{\beta\} = [H]^{-1} [G] \{q\} \tag{3.69}$$

The resulting expression for the total energy is then simplified to:

$$\Pi_R = \sum_n \left\{ -\frac{1}{2} \{q\}^T [k] \{q\} + \frac{1}{2} \lambda \{q\}^T [L] \{q\} \right\} \tag{3.70}$$

where:

$$[k] = [G]^T[H]^{-1}[G] \tag{3.71}$$

Finally, the simplified total energy expression is minimized with respect to the displacements, {q}:

$$\frac{\partial \Pi_R}{\partial q} = 0 \tag{3.72}$$

to yield the standard eigenvalue problem in terms of the previously defined matrices:

$$[K]\{q\} = \bar{N}_x[L]\{q\} \tag{3.73}$$

As before, this can be solved for the critical buckling loads using standard eigenvalue solution techniques. A complete description of this formulation can be found in References 45 and 46.

This formulation permits extreme flexibility in the application to many structural problems. However, it was not extended to the nonlinear region for the laminates in this investigation, since it requires considerable more computation time than the Rayleigh-Ritz analysis. The linear finite element solution was used to verify the adequacy of the modes selected for the Rayleigh-Ritz analysis.

3.3 Implementation

The theoretical buckling load and mode shape predictions from the linear Rayleigh-Ritz and finite element analyses, as well as the predicted nonlinear behavior, for the laminates investigated are presented in Chapter 5. These analyses were implemented using FORTRAN programs with double precision on a VAX 11/782. The nondimensional integrations in the Rayleigh-Ritz analysis were performed using a second order Newton-Cotes integration technique with 21 integration steps. The elastic constants used in the analyses were based on the manufacturer's specifications on the VAX, as given in Table 3.2.

The following comparisons are based on the $[0_6//45_6]_T$ laminate with simply-supported sides. The finite element program, with 408 degrees of freedom, required approximately 350 seconds of CPU time to set up and solve the linear eigenvalue problem. The corresponding CPU time for the linear Rayleigh-Ritz analysis is 22 seconds. The nonlinear Rayleigh-Ritz analysis requires a nominal setup time for each problem equal to approximately 72 CPU seconds to set up the problem and solve one load case with a single trial vector. Thereafter, each calculation at a given load level requires approximately an additional 48 CPU seconds. For example, the nonlinear Rayleigh-Ritz calculations reported herein were performed at six discrete loads with one trial vector at the first two load levels, two trial vectors at the next two load

TABLE 3.2

MATERIAL PROPERTIES

Property	Material	
	Graphite/Epoxy[a]	Resin[b]
E_L [GPa]	139.3	1.7
E_T [GPa]	11.14	1.7
G_{LT} [GPa]	4.9	0.65
N_{LT}	0.3	0.3

[a] Hercules AS4/3501-6 preimpregnated graphite/epoxy tape (compressive values).

[b] Dexter HYSOL EA956 low-viscosity adhesive system.

levels, and three trial vectors at the highest two load levels. For this typical case, the total CPU time required was approximately 360 seconds.

CHAPTER 4

EXPERIMENT

An extensive experimental investigation was undertaken to observe the buckling and postbuckling behavior of several laminated plates which displayed the previously described elastic couplings. This chapter describes the entire experimental operation, beginning with a discussion of the test matrix and laminate notation. The manufacturing procedure is covered next, including a detailed description of the preparation of unidirectional sublaminates, room-temperature bonding, and final laminate preparation. The next section describes the actual tests, including a description of the test fixture, a review of the data acquisition equipment, a discussion of the preliminary tests and a detailed outline of the testing procedure. The final section describes the methods used to reduce the data.

4.1 Test Matrix and Laminate Notation

In general, there are five possible elastic couplings between the four types of mechanical deformation (extension, shear, bending and twisting). As previously mentioned, fully anisotropic laminates can exhibit coupling between all possible mechanical deformations caused by in-plane loads or

moments. These couplings are dependent upon the existence of terms in the constitutive relations between applied loads and moments and in-plane strains and curvatures. These couplings are identified in Table 4.1, along with the components of the A, B, or D matrix associated with each particular type of coupling.

Laminates were chosen that isolated most of the indicated couplings. This was achieved by allowing only the coupling coefficients associated with the desired elastic coupling to be nonzero. Shear-twisting coupling was not isolated in a laminate.

A subscript "T", in the laminate notation, denotes that the total laminate has been specified, in contrast to a subscript "S" which indicates that the arrangement is repeated symmetrically about the centerline. A double slash "//" indicates a room temperature bondline joining previously cured unidirectional sublaminates. This method of construction, described in the manufacturing section, was necessary in order to obtain flat unsymmetric laminates at room temperature. For the sake of consistency, this method of construction was employed throughout the manufacturing phase.

A basic specially-orthotropic laminate, $[0_3/90_3]_S$, was chosen to serve as a benchmark. This laminate does not exhibit any mechanical couplings. In addition to this basic construction, a $[0_3//90_3//90_3//0_3]_T$ laminate, which has the same number and orientation of plies and stacking sequence but utilizes the room temperature bondline construction, was

TABLE 4.1

POSSIBLE ELASTIC COUPLINGS AND ASSOCIATED MATRIX TERMS

Coupling Type	Nonzero Matrix Terms
1. Extension-Shear	A_{16}, A_{26}
2. Extension-Bending	B_{11}, B_{12}, B_{22}
3. Extension-Twisting	B_{16}, B_{26}
4. Shear-Bending	B_{16}, B_{26}
5. Shear-Twisting	B_{66}
6. Bending-Twisting	D_{16}, D_{26}

included to ascertain the effects of the room temperature bondline.

Three laminates were used to isolate the various mechanical couplings. An antisymmetric orthotropic laminate, $[0_3//90_3//0_3//90_3]_T$, exhibits coupling between the in-plane stretching and out-of-plane bending. Two types of laminates were manufactured using 0° and 45° sublaminates in the forms $[0_2//45_2//0_2//45_2//0_2]_T$ and $[0_2//45_2//0_2//-45_2//0_2]_T$. The first of these two layups is symmetric but unbalanced, resulting in bending-twisting and stretching-shearing couplings. The second laminate, which is balanced but unsymmetric, isolates the stretching-twisting coupling.

Additionally, a series of laminates was chosen with fully populated elastic matrices. These laminates possess all of the possible mechanical couplings. The degree of coupling was varied by changing the lamination angle, θ, of a $[0_6//\theta_6]_T$ laminate from 15° to 90° in 15° increments. A summary of the laminates chosen for this experimental investigation and the associated elastic couplings inherent in each are presented in Table 4.2.

Seven laminates of each type were manufactured using the techniques described in the manufacturing section, for a total of 75 laminates (only five of the $[0_3/90_3]_S$ laminate were manufactured). For all cases, the laminates were loaded in uniaxial compression along clamped ends. Three side boundary conditions were considered: clamped, simply-supported, and free.

TABLE 4.2

TEST LAMINATES AND ASSOCIATED ELASTIC COUPLINGS

Laminate	Mechanical Couplings				
	Extension–Shear	Extension–Bending	Extension–Twisting	Shear–Twisting	Bending–Twisting
$[0_3/90_3]_S$	–	–	–	–	–
$[0_3//90_3//90_3//0_3]_T$	–	–	–	–	–
$[0_3//90_3//0_3//90_3]_T$	–	Yes	–	–	–
$[0_2//45_2//0_2//45_2//0_2]_T$	Yes	–	–	–	Yes
$[0_2//45_2//0_2//-45_2//0_2]_T$	–	–	Yes	–	–
$[0_6//\theta_6]_T$	Yes	Yes	Yes	Yes	Yes

where θ = 15, 30, 45, 60, 75, & 90 degrees,

// indicates a room temperature bond line,

and T implies total laminate.

Early testing revealed a sensitivity in nominally identical laminates to external influences, such as boundary conditions and alignment, which resulted in a dichotomy in the observed deflection behavior. In order to further investigate this interesting phenomenon and try to gain a better understanding of its cause, five of each type of laminate were tested with clamped side boundary conditions. Only one of each type was tested with simply-supported side boundary conditions and one with free side boundary conditions. The test matrix is summarized in Table 4.3.

Due to the length of the standard notation for some of the laminate types investigated, a mnemonic scheme for identifying the laminates was devised. In this scheme, the letter "S" is used to denote the "symmetric", specially-orthotropic laminate, $[0_3/90_3]_S$. Likewise, the letter "T" denotes the equivalent "total" laminate, $[0_3//90_3//90_3//0_3]_T$, manufactured using the two-step process. The "unsymmetric" laminate of this family, $[0_3//90_3//0_3//90_3]_T$, is designated as "U". The $0_2/45_2$ combinations are referred to as "P" for the "positive" layup, $[0_2//45_2//0_2//45_2//0_2]_T$, and as "N" for the "negative" layup, $[0_2//45_2//0_2//-45_2//0_2]_T$. The $[0_6//\theta_6]_T$ family of laminates is designated by the letters "A" through "F" for θ equal to 15° through 90°, respectively. This notation, which is used in all of the tables in this report, is summarized in Table 4.4.

TABLE 4.3

LAMINATE TEST MATRIX

Laminate	Side Boundary Conditions		
	Clamped	Simply-Supported	Free
$[0_3/90_3]_S$	3[a]	1	1
$[0_3//90_3//90_3//0_3]_T$	5	1	1
$[0_3//90_3//0_3//90_3]_T$	5	1	1
$[0_2//45_2//0_2//45_2//0_2]_T$	5	1	1
$[0_2//45_2//0_2//-45_2//0_2]_T$	5	1	1
$[0_6//15_6]_T$	5	1	1
$[0_6//30_6]_T$	5	1	1
$[0_6//45_6]_T$	5	1	1
$[0_6//60_6]_T$	5	1	1
$[0_6//75_6]_T$	5	1	1
$[0_6//90_6]_T$	5	1	1

[a] Indicates number of specimens tested.

TABLE 4.4

SUMMARY OF LAMINATE NOTATION

Laminate Type	Layup
S	$[0_3/90_3]_S$
T	$[0_3//90_3//90_3//0_3]_T$
U	$[0_3//90_3//0_3//90_3]_T$
P	$[0_2//45_2//0_2//45_2//0_2]_T$
N	$[0_2//45_2//0_2//-45_2//0_2]_T$
A	$[0_6//15_6]_T$
B	$[0_6//30_6]_T$
C	$[0_6//45_6]_T$
D	$[0_6//60_6]_T$
E	$[0_6//75_6]_T$
F	$[0_6//90_6]_T$

4.2 Manufacturing Techniques

As mentioned, the 75 laminates in the test matrix were manufactured using a two-step operation. Since many of the desired layups were unsymmetric, a normal cure procedure would have resulted in warped (i.e., non flat) plates due to the mismatch of the thermal expansion coefficients through the thickness of the laminate.

The first step in manufacturing an unsymmetric laminate involved the preparation of symmetric sublaminates. In order to maintain consistency in the manufacturing process, all of the laminates, except those of the $[0_3/90_3]_S$ laminate type, were manufactured using the same two-part manufacturing process described below. In fact, all of the sublaminates manufactured for this study were unidirectional in nature; i.e., each set of plies with a particular ply orientation was manufactured as a separate subcomponent. The $[0_3/90_3]_S$ laminate was manufactured in a single step using the same technique as described in Section 4.2.1 for the unidirectional sublaminates.

Plies with the desired angular orientation were cut from 305 mm wide rolls of Hercules AS4/3501-6 preimpregnated tape, using standard TELAC (Technology Lab ratory for Advanced Composites) fixtures and procedures [47]. In addition to using the standard TELAC manufacturing tooling and equipment, several modifications were made and additional pieces of equipment were built to facilitate the heavy manufacturing

requirements.

The largest tooling constructed was a three-tiered curing assembly capable of curing 14 sublaminates simultaneously. Each tier consisted of a flat aluminum plate with an independent integrated vacuum system. The upper plate, designed to cure six laminates at a time, employed removable aluminum F-shaped dams with beveled outside corners to eliminate possible damage to the vacuum bagging. The lower two plates held four laminates each in a single row and employed cork dams exclusively. Each of the three plates was completely covered (except for the borders) with two layers of nonporous teflon between the aluminum plate and the dams to facilitate ease in cleanup after each cure.

4.2.1 Sublaminate Preparation

Unidirectional sublaminates were assembled by laying up the appropriate number of plies to form a 305 mm by 350 mm plate with the desired thickness (two, three, or six plies). The laminates were covered on each side with a layer of nylon peel-ply fabric coated with release agent. The peel-ply protected the laminates during the manufacturing process and textured the surface of the sublaminates to enhance the strength of the room temperature bondlines. Attempts to cure laminates with peel-ply on only one side in order to maintain a smooth surface for deflection scanning resulted in serious cracking during the postcure operation. Therefore, peel-ply

was used on both sides of all sublaminates.

These sublaminates were prepared for curing and cured in a standard TELAC cure process in a Baron-Blakeslee autoclave under 0.59 MPa applied pressure with a 762 mm Hg vacuum. The cure included a one hour hold at 116°C to allow flow of the resin, followed by a two hour hold at 177°C to set the resin. This cure cycle is illustrated in Figure 4.1. In an effort to eliminate any cure dependence in the results, one of each type of sublaminate was included in each cure, when possible.

After curing, the sublaminates were placed in a postcuring oven at 177°C for eight hours to drive the polymer cross-linking process of the thermosetting resin to completion. Aluminum shelves were constructed for the postcuring oven, so that all 14 sublaminates from each cure could be postcured simultaneously. A temperature distribution survey of the oven indicated excellent uniformity throughout, with temperature variations less than $\pm$2°C.

The cured sublaminates were machined to 292 mm square using a milling machine equipped with a diamond-grit cutting wheel and water cooling. Thickness measurements of the prepared sublaminates were taken at nine locations corresponding to the positions where deflection data would later be recorded, as shown in Figure 4.2.

A summary of the average thickness data for each sublaminate is provided in Table C.1 in Appendix C. It should be noted here that sublaminates with an average measured thickness which deviated by more than one-half of a ply

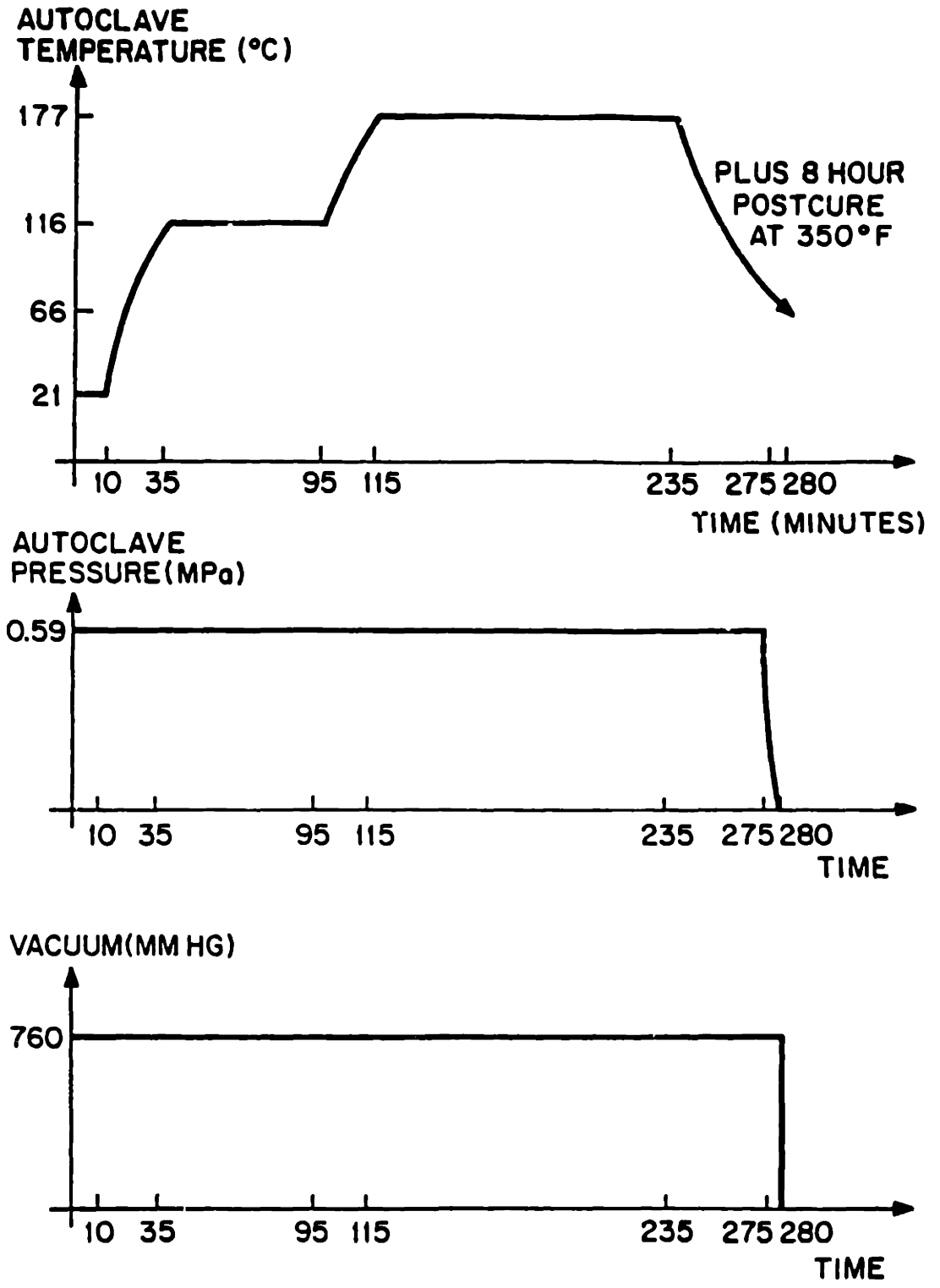

FIGURE 4.1 AS4/3501-6 Graphite/Epoxy Cure Cycle

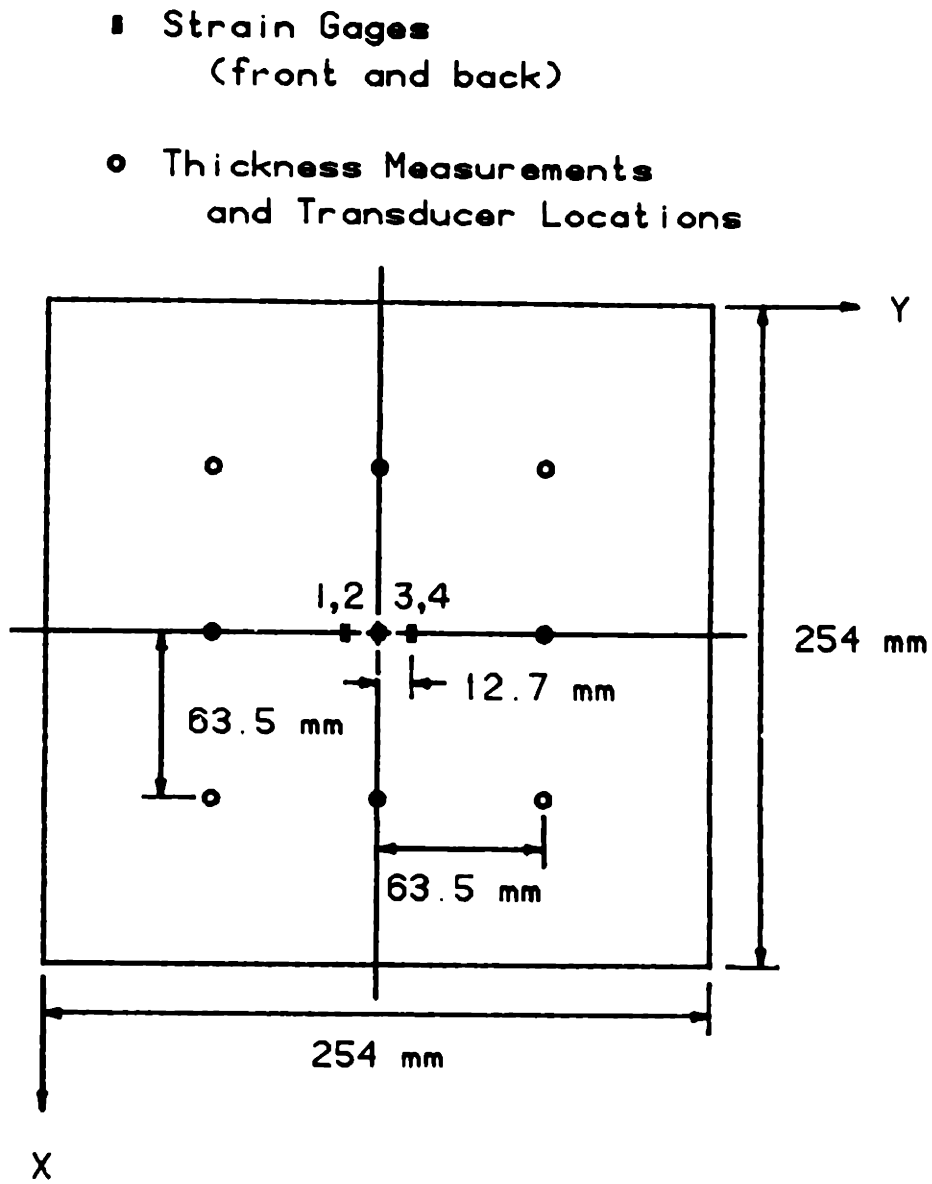

FIGURE 4.2 Illustration Identifying Strain Gage, Thickness Measurement, and Transducer Locations

thickness from the manufacturer's nominal value of 0.134 mm were rejected. Five laminates fell in this category. Consequently, they were set aside for use in preliminary testing.

This procedure resulted in excellent quality sublaminates with an average ply thickness of 0.134 mm for the 6-ply unidirectional sublaminates, 0.145 mm for the 2-ply and 3-ply unidirectional sublaminates, and 0.130 mm for the symmetric $[0_3/90_3]_S$ laminate. Although the overall average ply thickness was 0.137 mm, the manufacturer's nominal value of 0.134 mm was used for all theoretical calculations, so as to maintain a common reference.

4.2.2 Laminate Bonding

Once the sublaminates were completely manufactured, they were bonded together to form the desired finished laminates. Considerable efforts were undertaken to prevent the results from being dependent on the particular roll of graphite/epoxy prepreg, layup session, sublaminate cure, bonding cure, and the like. To eliminate any bias in the selection and matching of subcomponents, a randomization of the sublaminate identification numbers was performed. The resulting output was used to determine which sublaminates were bonded together to form each finished laminate.

The prepared sublaminates were bonded together at room temperature with Dexter HYSOL's EA956 low-viscosity adhesive

system, which has a tensile lap shear strength of 11.7 MPa. This adhesive system was recommended by the prepreg manufacturer, Hercules, Inc., for its compatibility with the AS4 graphite/epoxy shear characteristics.

Previous laminates manufactured using these room-temperature bonding techniques had a highly nonuniform bondline thickness [32]. In an attempt to control the bondline thickness, initial bonding tests were performed with microscopic solid glass spheres, ceramic particulate, or silica particulate mixed into the resin. Various combinations of particulate type, concentration, and compaction pressures were attempted, but none improved the thickness uniformity.

Photomicrography was used to investigate sections of the resulting bondlines. The basic conclusion was quickly reached that there was an insufficient quantity of large particulate with a controlled diameter. In order for this manufacturing technique to be feasible, particulate with a tighter size distribution must be used, since the smaller particles, which represent up to 90% of the particulate volume, increase the viscosity of the adhesive/particulate mixture (thus hampering the application of the epoxy), without contributing to thickness control. Since particulate with such a tight size distribution is very costly, the concept was abandoned and no particulate was added to the adhesive during the bonding operation. Instead, aluminum top plates were placed over the laminates during the bonding operation and 0.52 MPa pressure was applied to the top plates in order to control the bondline

thickness by preventing the laminates from bending.

Immediately prior to bonding, the sublaminates were cleaned with cheesecloth to remove any dust which had settled. After mixing the two-part epoxy using the manufacturer's recommended resin to hardener ratio of 100:58 by weight, each surface to be bonded was coated with a thin layer of the adhesive. The adhesive was spread over the surface of the laminate with wooden tongue depressors. The sublaminates were assembled in the proper stacking sequence and placed into a prepared bonding assembly. This consisted of a large aluminum plate, which had been covered with nonporous teflon, upon which cork dams had been constructed around the aluminum top plates. The top plates, which were slightly larger than the assembled laminates, assisted in ensuring that the resulting laminate was flat and encouraged a uniform thickness bondline. Nonporous teflon protected all metal surfaces from contacting the epoxy. Paper bleeder was placed above the laminate to absorb the excess epoxy and was separated from the laminate with a sheet of porous teflon. After placing the assembled laminates under the aluminum top plates, the entire assembly was covered with porcus teflon, fiberglass air breather, and vacuum bagging. An exploded view of the bonding assembly cross-section is shown schematically in Figure 4.3.

The completed assembly was placed into an autoclave, a full vacuum was drawn, and the chamber pressurized to 0.52 MPa. The cooling system was engaged to maintain the

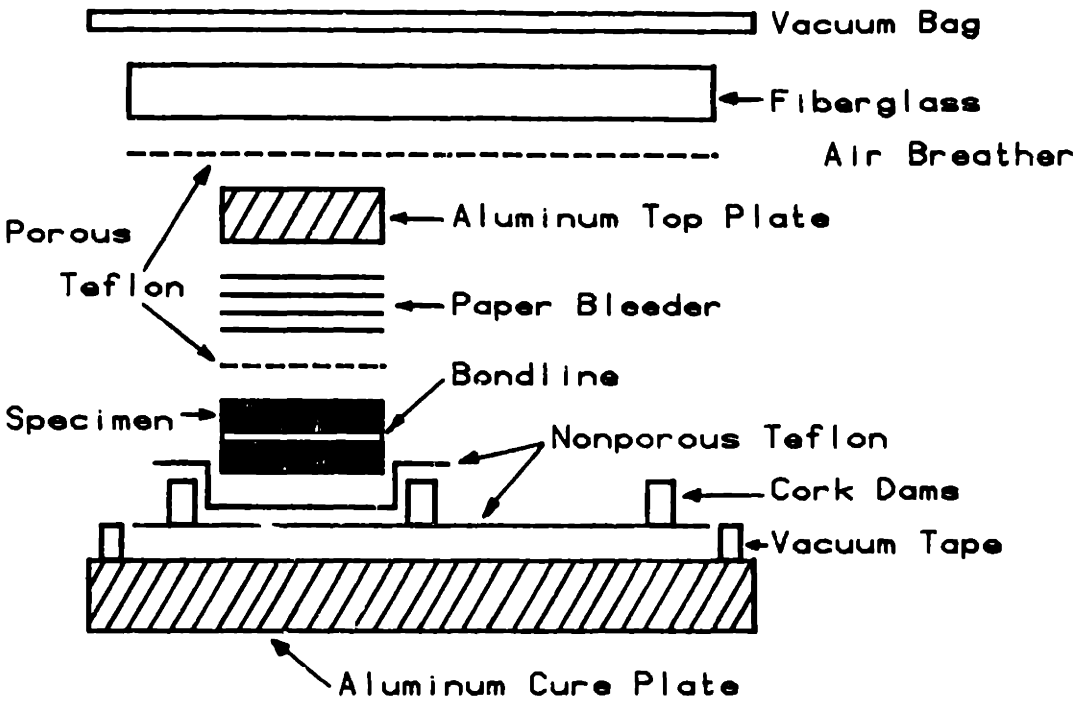

FIGURE 4.3 Schematic of Bonding Assembly Cross-Section

inside of the chamber at room temperature (25°C) during pressurization.

The bonding operation, from application of the epoxy to pressurization of the autoclave, took approximately 20 minutes. The adhesive manufacturer conservatively specified the pot life of the mixed epoxy as 30 minutes. The bonding setup time was minimized with the assistance of a quick-disconnect vacuum hookup and valve assembly.

In the autoclave, the plates were compacted for two hours, after which the pressure was released and the assembly was removed from the autoclave. However, the vacuum was maintained without interruption for an additional 22 hours in order to allow the epoxy to fully set. After this time had elapsed, the sublaminates were removed from the bonding setup. The laminates were left undisturbed on a shelf for a minimum of an additional five days to permit completion of the cure process.

The completed laminates were machined to their final dimensions of 279 mm by 279 mm. Thickness measurements were again taken at the previously described locations. For the $[0_3//90_3//90_3//0_3]_T$ and $[0_3//90_3//0_3//90_3]_T$ laminates, which had three bondlines each, the average bondline thickness was 0.024 mm with a coefficient of variation of 39%. For the $[0_2//45_2//0_2//45_2//0_2]_T$ and $[0_2//45_2//0_2//-45_2//0_2]_T$ laminates, which had four bondlines each, the average bondline thickness was 0.033 mm with a coefficient of variation of 36%. For the $[0_6//\theta_6]_T$ laminates, which had only a single

bondline each, the average bondline thickness was 0.036 with a coefficient of variation of 100%. Much of this variance is believed to be measurement dependent. For example, some of the laminates indicated a negative bondline thickness. This is clearly due to measurement error, possibly influenced by the textured surface of the sublaminates. For the laminates with multiple bondlines, the measurement dependence is averaged over the several bondlines, resulting in smaller coefficients of variation. Thus, the resulting average bondline thickness of 0.03 mm, which represents approximately one-fourth of a ply thickness, was considered to be very good. The laminate thickness data is tabulated in Table C.2 in Appendix C.

Using this manufacturing procedure, 75 test quality plates were produced for testing. Additionally, there were five plates manufactured with either an incorrect number of plies or damaged sublaminates. These were used for preliminary testing to determine the load and stroke limits and to establish the alignment and testing procedures.

4.2.3 Laminate Instrumentation

The final step in preparing the laminates for testing involved mounting strain gages on the specimens. Each of the plates was instrumented with two pairs of Micro Measurements EA-06-125AC-350 strain gages mounted back-to-back, as illustrated in Figure 4.2. Back-to-back strain gages allow

the data to be reduced into bending and stretching components. The gages were positioned 13 mm off-center horizontally to allow deflection measurements to be taken at the plate center. All of the gages had a gage factor of 2.07 ±0.5%.

Because of the nature of the design configuration mandated by the postbuckling test (i.e., with geometric symmetry and laminate inversion symmetry about the out-of-plane axis) the strain results were expected to have inversion symmetry; i.e., an inplane rotation of 180° would result in an identical configuration and, therefore, should yield identical strains. This implies that both sets of strain gages should exhibit identical readings, provided, of course, that the test fixture was properly aligned, the load was correctly introduced, and there were no antisymmetric modal components. Therefore, the redundant set of strain gages served as a partial measure of the accuracy of the test fixture alignment and load introduction.

4.3 Testing Techniques

In order that the buckling and postbuckling behavior of the selected laminates could be observed, a uniform axial compressive displacement was applied in a monotonically increasing manner (ramp) while measurements of the applied compressive load, surface strains, end-shortening displacement, and out-of-plane deflections were sampled. This

section describes the experimental test fixture and data acquisition equipment utilized in these postbuckling tests, as well as the actual procedure followed during testing.

4.3.1 Test Fixture

The test fixture employed in this study was originally constructed by Finch for buckling work on similar laminates [48]. It consists of a modular steel jig, illustrated in Figure 4.4, with interchangeable boundary conditions.

The jig, described in detail in Reference 4.48, was designed for easy installation and removal via the hydraulic grips of a 445 kN MTS 810 hydraulic testing machine, upon which all testing reported in this study was performed. In order to avoid problems due to friction, all sliding surfaces of the compressive loading jig were lubricated with Lubriplate Molybdenum-Lithium (MoS_2) No. 2 multi-purpose lubricant. For this investigation, several modifications were made to enhance the performance of the buckling jig. Most of these related to the data acquisition equipment and techniques and will be described in the succeeding sections.

One of the greatest difficulties encountered during preliminary testing involved the iterative trial and error alignment procedure of the plate in the test fixture. In order to facilitate frequent adjustments of the slope of the boundary conditions and make alignment of the boundary conditions more deterministic and monotonically convergent,

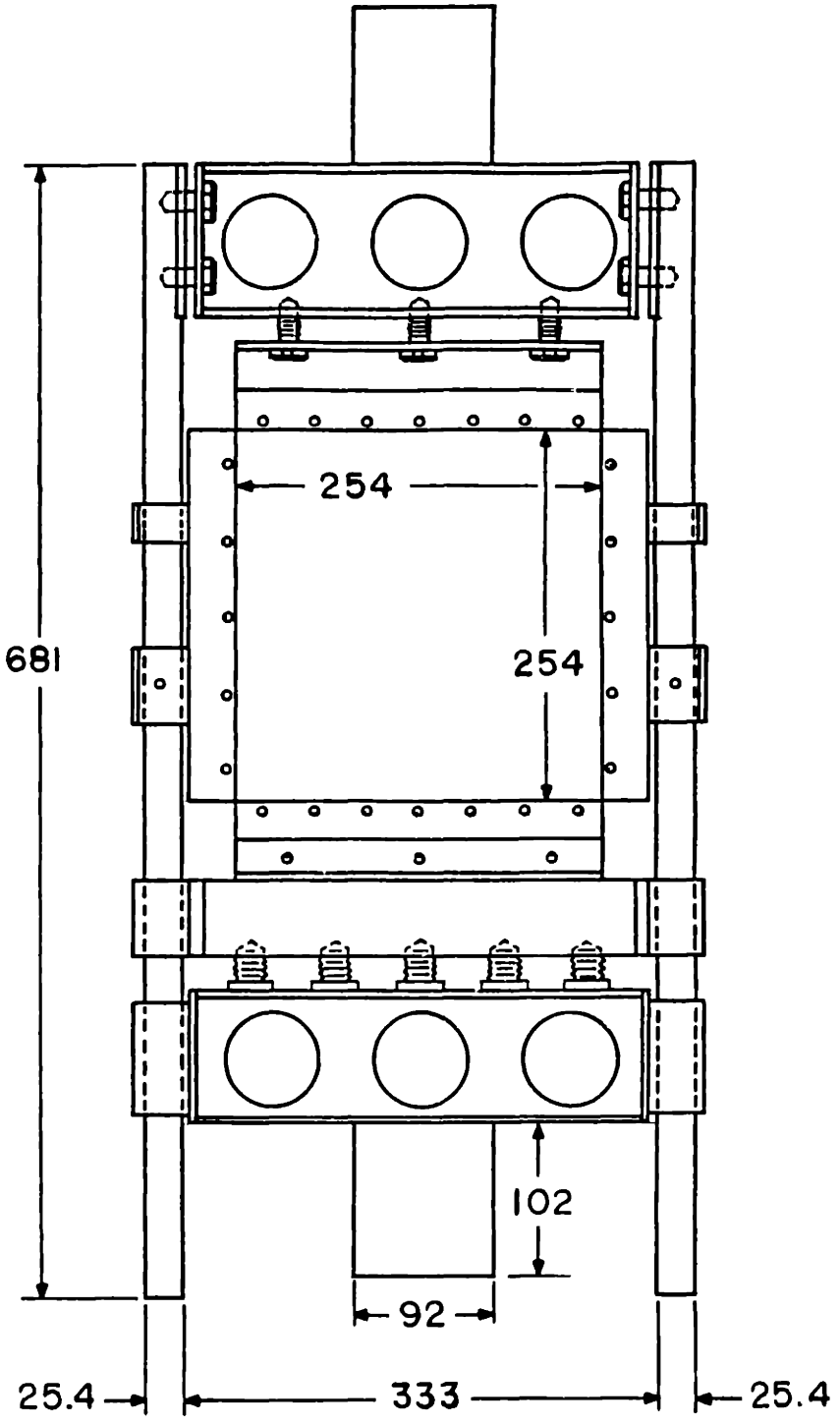

All dimensions in mm

FIGURE 4.4 Sketch of Compressive Loading Jig

screw adjusters were installed to replace the shim stock used previously. These slope alignment bolts are indicated in Figure 4.5, which shows how the clamped end boundary conditions were attached to the frame. The alignment procedure was also improved during initial testing as described in the procedure section. These enhancements significantly reduced the plate alignment time.

As mentioned previously, three different combinations of boundary conditions were employed in the tests. All of the plates were tested with clamped boundary conditions on the loaded ends. The sides were either clamped, simply-supported, or free. The clamped boundary conditions prevented out-of-plane deflection and twist, while permitting restricted in-plane sliding (it was impossible to eliminate all friction). The simply-supported boundary conditions additionally permitted out-of-plane rotation. Detailed schematics of the boundary conditions are shown in Figures 4.5 and 4.6.

The introduction of extraneous shear load transfer at the boundaries was minimized by applying two layers of 0.14 mm thick by 13 mm wide CHR-T Temp-R-Tape teflon tape to the borders of each plate and lubricating with the same molybdenum-lithium compound used in the buckling jig (Ashton and Love noted the presence of induced secondary stresses, which caused buckling loads to decrease by almost one-third. These undesireable stresses were reduced by attaching layers of teflon tape to the borders [49]). Additionally, the

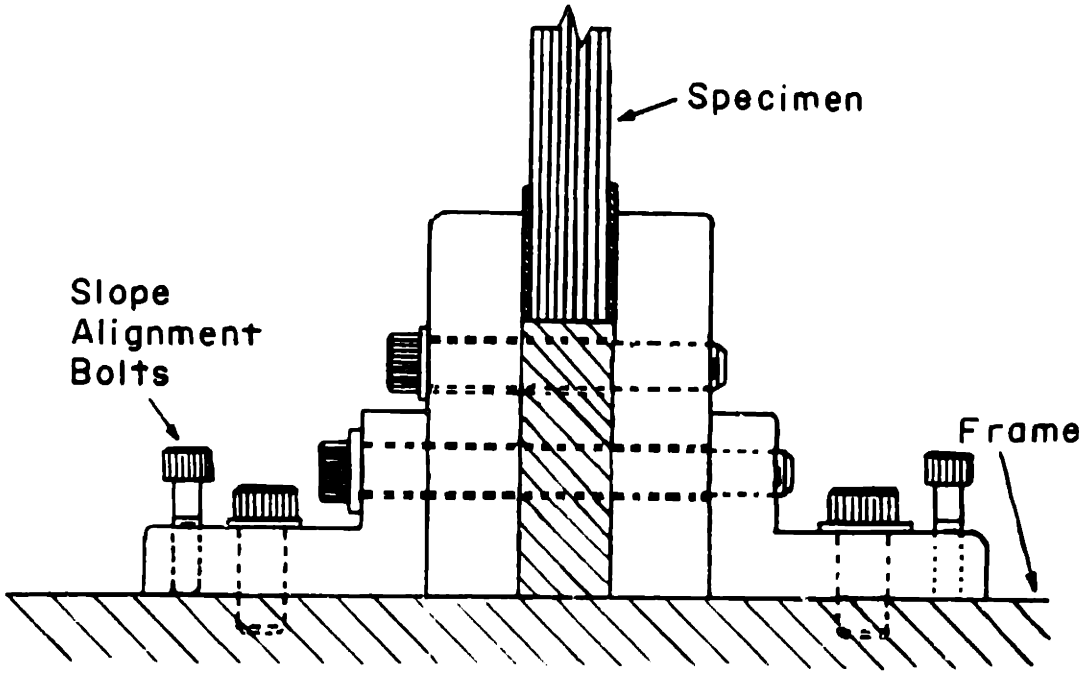

FIGURE 4.5 Sketch of Clamped End Boundary Conditions

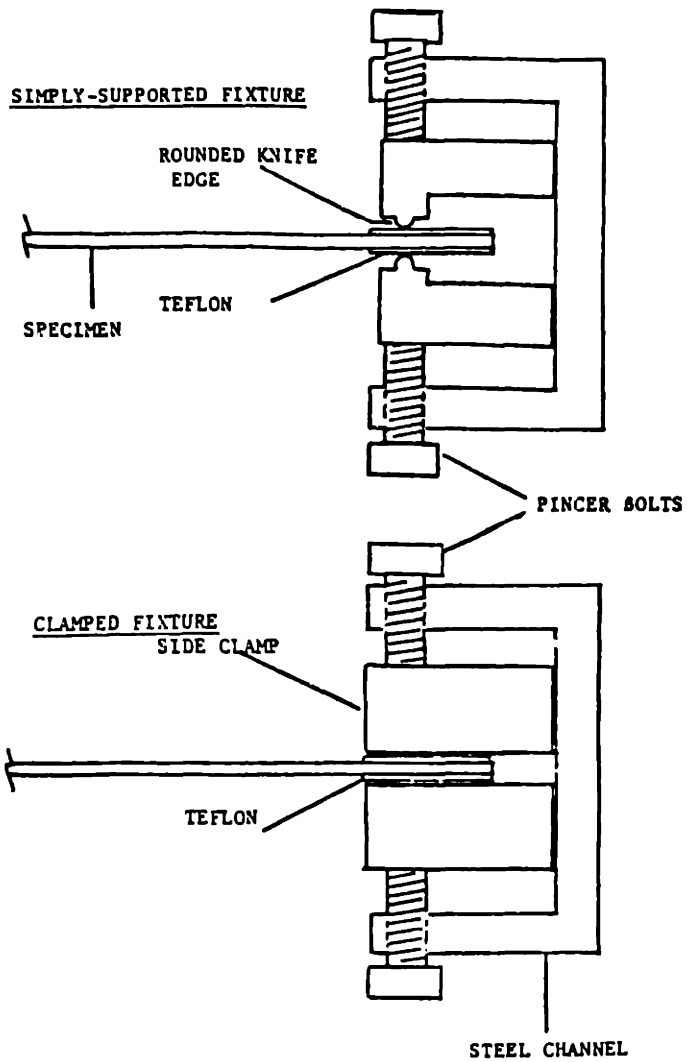

FIGURE 4.6 Sketch of Clamped and Simply-Supported Side Boundary Conditions

boundary conditions were only loosely clamped, thus minimizing the sliding friction between the plate and the boundary conditions.

4.3.2 Data Acquisition

Both in-plane and out-of-plane deformation measurements were recorded during testing. In-plane measurements included applied compressive load, end-shortening displacement, and back-to-back strain readings at two symmetric locations, as described previously. Out-of-plane deflection measurements were taken continuously at nine discrete locations. Scans of the deflected surface were also obtained at selected load levels. The equipment used to collect these data is described in the following paragraphs.

As described in the manufacturing section and shown in Figure 4.2, two sets of back-to-back strain gages were located 13 mm on either side of the vertical centerline. These strain readings were used to display the classical bifurcation buckling behavior (when it existed) and to determine an effective longitudinal elastic modulus, from which an approximation of the local longitudinal stress can be estimated. As mentioned previously, the second set of gages also provided an indication of the proper load introduction and plate alignment in the fixture, because of the geometric symmetry of the test and antisymmetry of the fibers about the loading axis. For example, an 180° in-plane rotation of the

plate should not affect the magnitude of the small deflection results, as observed from a fixed reference. However, the sense (±) of the strains would be dependent on the mode shape. (Noor, et al., implemented these considerations in a postbuckling analysis of composite plates in order to reduce computation time [49].)

To supplement the strain data, a ±25 mm Trans-Tek Model 354 gaging transducer (LVDT or Linear Variable Differential Transformer) with an accuracy of ±0.5% linearity was mounted on the side of the buckling jig, as shown in Figure 4.7. This provided a better measurement of the average relative end-shortening displacement as a function of the applied load, than the machine stroke. By measuring this locally, rather than using the testing machine head displacement, the inaccuracies due to slippage in the loading grips and play in the heads and test fixture were eliminated.

Two types of lateral displacement measurements, w, were taken during the test. The first type was obtained with the aid of a manually operated deflection tracker mounted on the front of the buckling fixture. The deflection tracker, also constructed by Finch and illustrated in Figure 4.8, employed a ±25 mm Sanborn type 7DCDT-1000 transducer mounted on a two degree-of-freedom scanning system [48]. Rigidly held within a Delrin plastic block, the LVDT slid freely along two parallel rods and was connected by a cord-pulley system to a rotary potentiometer, which was used to record the vertical position of the tracker. This vertical tracking unit slid within a

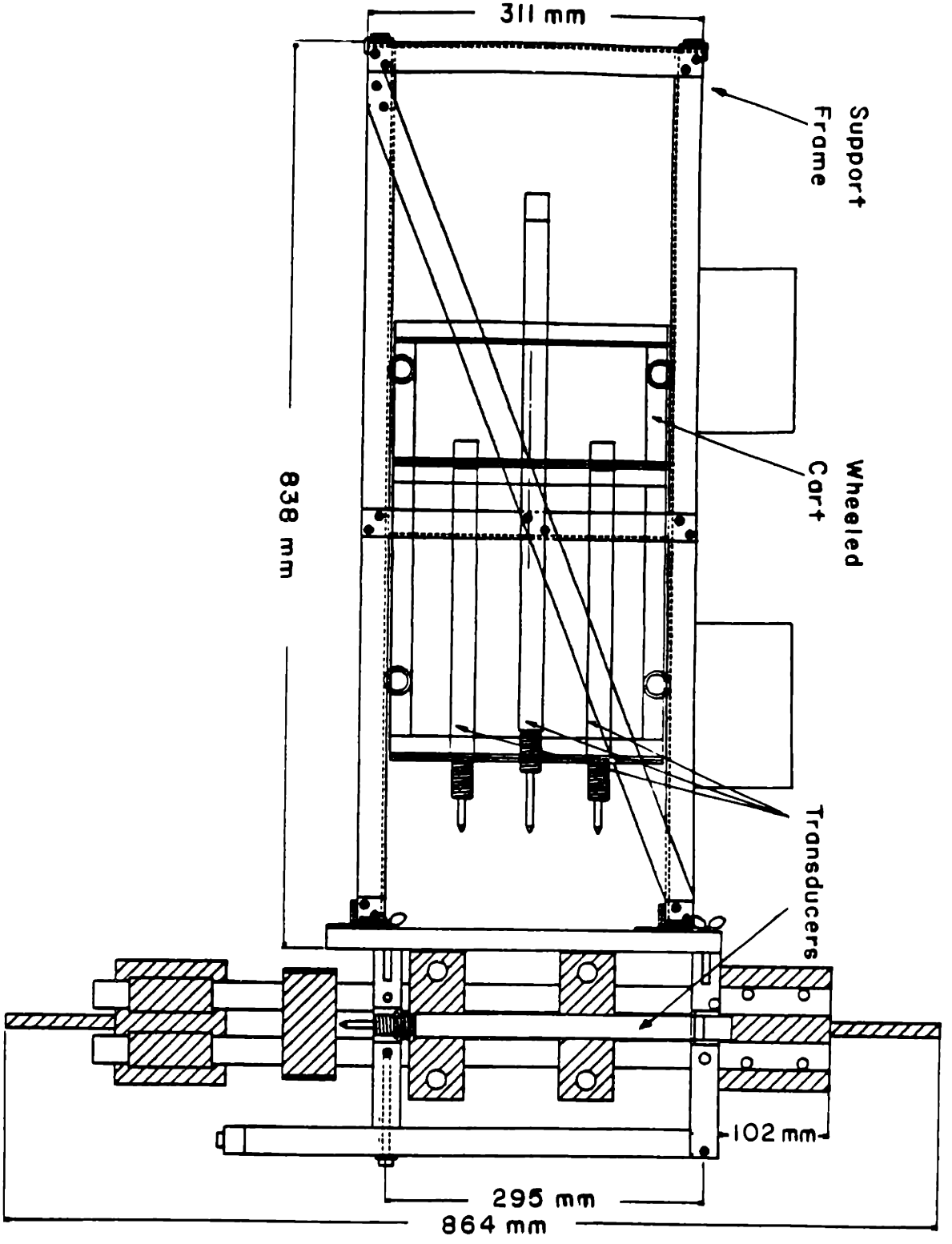

FIGURE 4.7 Illustration of Transducer Rack and Cart Assembly

pair of horizontal guide-channels and, thus, could be positioned anywhere along the plate width. In order to obtain consistent data, nine clamping positions were built into the horizontal guides at 25 mm intervals.

A general refurbishment of the scanner included bonding the transducer core, probe, and cap together with 5-minute epoxy to form an integrated probe that could maintain integrity during repeated tests. The springs which ensured probe contact with the plate had worn extensively and were consequently replaced with better springs. The first complete simulated test, performed with an aluminum plate, indicated significant noise in the scanning transducer signal. This noise was successfully eliminated by adding a one microfarad capacitor to the circuit in parallel with the signal.

At predetermined load levels, deflection measurements were sampled by a PDP-11/34 computer at 81 discrete locations, forming a nine by nine internal grid with 25.4 mm spacing, as illustrated in Figure 4.8. Fairly accurate isodeflection contour maps were generated from this data. Unfortunately, this technique required halting the test for approximately 20 minutes in order to collect the data. During this time, a noticeable drop in load (up to 0.9 kN) was generally witnessed. Therefore, after each scan, the load was completely released and the test was restarted. It should be noted that most of this load drop occurred prior to the collection of deflection data via the tracker, while switching data files on the computer. Only three cases actually

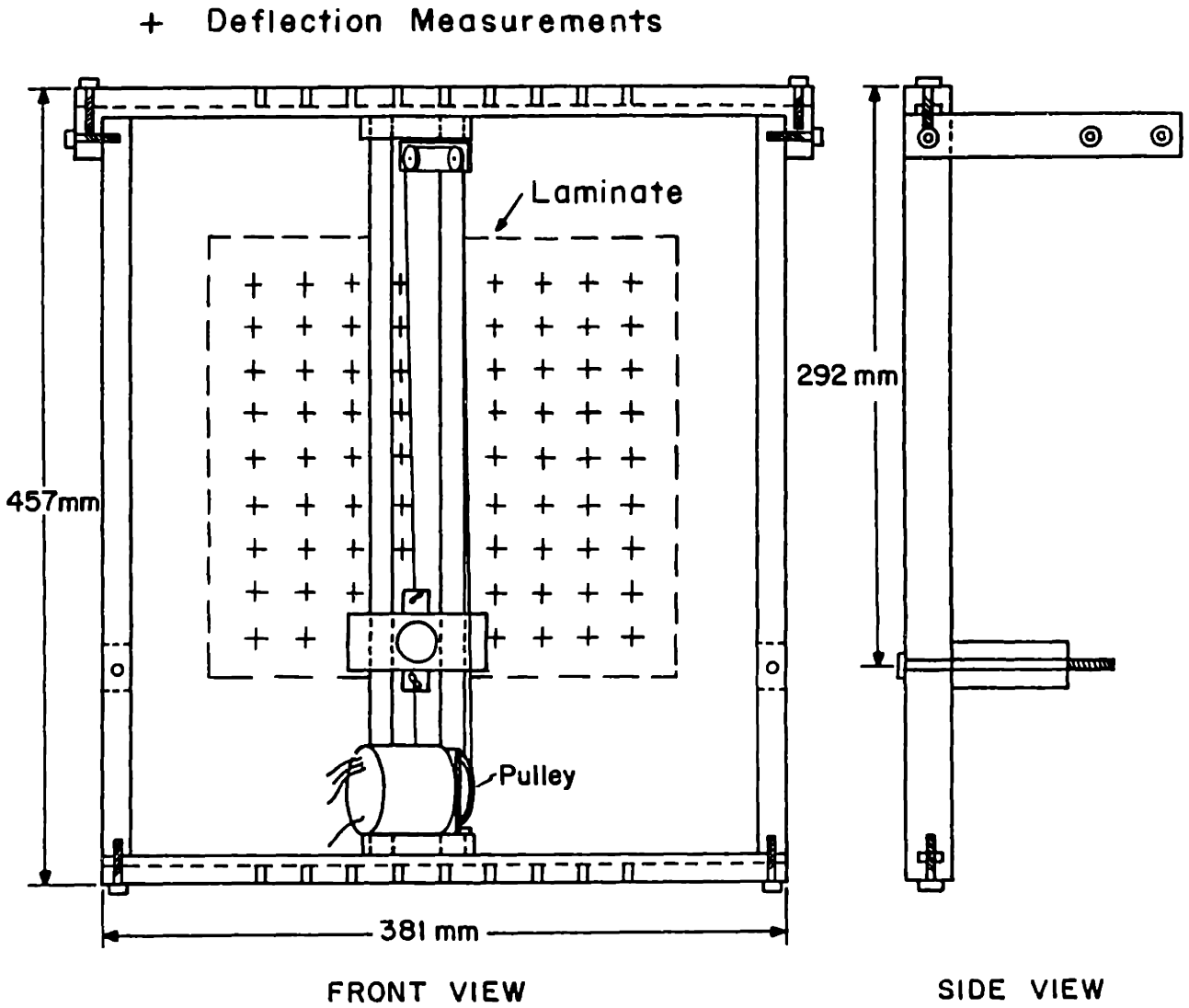

FIGURE 4.8 Sketch of Deflection Tracker

exceeded 0.5 kN of load drop during the scan. These were laminates $[0_6//15_6]_T$-2 (0.6 kN), $[0_6//15_6]_T$-F (1.2 kN), and $[0_3//90_3//90_3//0_3]_T$-5 (0.7 kN). The load drop in the remaining cases was considered to be negligible.

The data acquisition software was also specialized to facilitate the scanning process. The new version of scanning software took data within a prescribed "window". Sampling at the rate of 500 Hz, the software compared the value of the potentiometer reading with the predetermined value for a desired data point location. If the actual location of the transducer was within the prescribed tolerance, then the program saved the data corresponding to that point. At the end of each scan, the program determined if all of the data points had been properly stored. If not, then the program requested that another scan be made at that location. Thus, the resulting data file contained only the desired 81 data points, composing a nine by nine grid. Since the data were all within a tolerance of approximately $\pm$0.65 mm, the approximations and inaccuracies introduced through interpolation were negligibly small.

The second type of lateral deflection measurements consisted of continuous out-of-plane deflection data obtained at nine discrete locations using an array of LVDT's. A modular rack and cart assembly, shown in Figure 4.7, was designed and constructed along with the associated electronics and cables necessary to provide power to the transducers and route the signals to the analog-to-digital converters which

fed directly into the PDP-11/34 computer for data storage.

The cart held six ±25 mm Trans-Tek DC-DC Model 354 gaging transducers (three in the upper row and three in the lower row) and three ±51 mm Trans-Tek DC-DC Model 355 gaging transducers (in the center row) spaced 64 mm apart forming a three by three square grid, as shown in Figure 4.2. The ±25 mm transducers and the scanning transducer were powered by a ±12 VDC 200 MA Trans-Tek Model D12.200 fixed voltage power supply, while the ±51 mm transducers were powered by a ±15 VDC 100 MA Trans-Tek Model D15.100 fixed voltage power supply. The cart rolled within a rack which supported it in a fixed position relative to the buckling jig.

In summary, the test setup enabled automatic computerized data acquisition of 16 channels of information. These channels contained data from the nine deflection transducers in the rack, an end-shortening displacement (stroke) transducer, four strain gages, and the testing machine load cell. A switch allowed data to be taken from the scanning transducer and potentiometer on the deflection tracker mounted on the front of the test fixture. Splitter cables were constructed and employed to allow simultaneous signals to be sent to the computer and the X-Y plotter (for alignment purposes) or to a voltmeter (for signal verification and observation during loading). The information was necessarily stored in two separate files, each containing eight channels of information, during each phase of testing. This resulted in as many as 12 computer data files per laminate tested.

Table 4.5 identifies the information stored in each of the channels.

4.3.3 Preliminary Tests

Before testing any of the specimens, the testing equipment and proposed testing procedures needed to be validated and refined. To accomplish these purposes, the five specimens with manufacturing defects were tested to failure using the proposed testing procedures. All of the data obtained from these initial tests was carefully examined prior to full-scale testing. These preliminary tests assisted in the development of a standard testing procedure, substantiated the usefulness and accuracy of the data acquisition equipment, and instilled confidence that productive full-scale testing could begin.

One of the most important consequences of the initial tests, other than gaining some experience and a qualitative feel for the deflection behavior and expected failure loads, was the standardized testing procedure checklist, outlined in Appendix D. A quick glance over the checklist reveals the many tedious steps involved in the process of calibrating the scanner, transducers and jig, installing and aligning the plate, and running the actual multiphase test for each laminate. Following such a checklist ensured that all of the steps were completed in a consistent and proper sequence. A summary sheet of critical information for the test was also

TABLE 4.5

COMPUTER DATA FILE STRUCTURE

TELAC Channel Notation	Raw Data Files		Reduced Data File	Scan Data File
	File 1	File 2		
Load	P [lb]	P [lb]	P [lb]	P [lb]
Strain	T_4 [in]	T_1 [in]	w_c/P [in/lb]	T_1 [in]
Stroke	T_5 [in]	T_2 [in]	w_c [in]	T_2 [in]
Gage 1	T_6 [in]	T_3 [in]	-	T_3 [in]
Gage 2	ε_2 [in]	Stroke [in]	$(\varepsilon_1+\varepsilon_4)/2$	Stroke [in]
Gage 3	ε_3 [in]	T_7 [in]	$(\varepsilon_2+\varepsilon_3)/2$	y [in]
Gage 4	ε_4 [in]	T_8 [in]	$\varepsilon_1-\varepsilon_4$	x [in]
Gage 5	ε_1 [in]	T_9 [in]	$\varepsilon_2-\varepsilon_3$	w_s [in]

Key:

P	Refers to the total applied load.
T_i	Refers to transducer i.
ε_i	Refers to strain gage i.
w_c^i	Refers to the deflection at the center of the plate as measured by the center transducer.
"Stroke"	Refers to the end-shortening displacement.
x,y	Refer to the position of the scanner.
w_s	Refers to the deflection as measured by the scanner.

made up for each laminate prior to testing. These data sheets facilitated collection of data offsets and other important parameters and accelerated the testing procedure.

The only major problem discovered during this preliminary testing was noise in the strain gage data. The source of this noise was believed to be a combination of several possible factors. The most predominant of these factors seemed to be a "floating voltage" in the analog-to-digital (A/D) interface. The effects of this problem were partially mitigated by grounding the A/D plugs and installing additional dummy plugs into the interface. The strain gage noise was further reduced by coating the tips of the Cinch electrical connectors with solder, in the circuit which carried the strain signals into the analog-to-digital converters. This caused a significant improvement in the quality of the data transmission, enhanced the mechanical connection, and facilitated calibration of the strain gages.

4.3.4 Testing Procedure

After the preliminary tests were completed, the entire test setup was realigned and calibrated in preparation for full-scale testing. The steps involved during each phase of testing, beginning with preparation of the specimen and concluding with removal of the specimen from the fixture after failure, are summarized in the checklist of Appendix D.

Prior to each testing session, the buckling jig was

carefully installed in the testing machine. Alignment of the fixture was assured by lining up the steel tabs with one side of the hydraulic grips.

In order to facilitate alignment of the boundary conditions, an aluminum plate was installed in the fixture by clamping the upper and lower borders in the boundary conditions. The boundary conditions were completely loosened from the frame. The deflection tracker was used to obtain position readings at the four corners of the plate with the plate at the extreme forward and rearward limits to determine the maximum range of available travel. The plate was then placed as close as possible to the center of this range. The boundary condition bolts were partially tightened, corner position readings were taken with the scanner, and the boundary conditions were adjusted by gently tapping with a hammer until the plate was centered. This procedure was repeated until the boundary condition bolts were securely tightened to the frame.

Once the translational degree of freedom was correctly aligned, the scanner was used to determine the slope of the upper and lower boundary conditions, which would ideally be zero. Vertical profiles of the two extreme horizontal stations were made with the deflection tracker and recorded on graph paper on an MTS Model 431 X-Y recorder. Excellent resolution was made possible by greatly amplifying the output signal.

The slope alignment procedure involved adjusting the

previously described slope alignment bolts and examining profiles taken at the horizontal extremes (i.e., at the points y equal to 25.4 mm and 228.6 mm as referenced to Figure 4.2) in an iterative manner. However, the slope alignment was coupled to the position alignment, generally necessitating a realignment of the position, and so on. Nevertheless, the procedure was deterministic and converged monotonically, enabling a reasonable alignment of the boundary conditions. The four corners of the plate were aligned to within ± 0.04 mm relative to a plane parallel to the deflection tracker and the slope of the boundary conditions was correct to within $\pm 0.2°$.

After fixing the upper and lower boundary conditions, the next step was to adjust the side boundary conditions. This was accomplished by sliding the boundary conditions in close to the plate and finger tightening the pincer bolts. This established a loosely clamped configuration for the plate in the boundary conditions. The side boundary conditions were then securely clamped to the frame. It was not possible to measure or adjust the slope of the side boundary conditions with the equipment used. However, this slope is not as critical as the slope of the loaded ends, and, once seated, the actual slope of the side boundary conditions theoretically remained constant for all of the tests.

With the aluminum plate loaded in the test fixture, all of the data acquisition equipment and software was operationally verified and calibrated. The potentiometer which measures the vertical location (x) of the scanning

transducer on the deflection tracker was calibrated by attaching a precision scale to the aluminum plate. Scans were made at two horizontal stations equidistant from the vertical centerline. The signal voltage from the voltmeter and the number of computer units read directly from the computer were recorded at 25.4 mm intervals corresponding to the locations where data would later be recorded. The position measurements were averaged for each x-location and inserted via a data statement into the data acquisition program. These values were used by the program during scanning to identify the appropriate data points to be stored.

The nine transducers in the stationary array, the stroke transducer, and the scanning transducer were each calibrated using a series of Van Keuren Grade 3 cylindrical gage blocks with a tolerance of ± 0.000008 mm/mm. Although each transducer had a unique calibration factor, the deflection response was extremely linear (within $\pm 0.5\%$) in all cases for displacements in the desired range. High frequency squealing of the transducers in the array was almost completely eliminated by installing rubber cushions on the transducer attachment mounts.

Finally, after all of the boundary conditions had been correctly positioned and completely aligned, the aluminum plate was removed from the jig by loosening only the front halves of the boundary conditions from the frame. The rear halves, which remained fixed, served as a permanent reference plane for alignment of the graphite/epoxy plates. The

composite plates had a textured surface finish and a nonuniform thickness, which complicated their alignment directly.

Before inserting the composite plates into the buckling fixture, it was necessary to insert the probe into the scanning transducer and zero the load reading of the testing machine. Two layers of 0.14 mm thick by 13 mm wide CHR-T Temp-R-Tape teflon tape were applied to each of the borders on the plate. These borders were lubricated with Lubriplate Molybdenum-Lithium No. 2 multi-purpose lubricant to minimize friction which would otherwise introduce shear into the laminate. The plate was then inserted loosely in the upper and lower boundary conditions.

In this configuration, and with the testing machine in stroke control, the plate was loaded to approximately 0.9 kN to insure that the plate was properly seated in the upper and lower boundary conditions. The upper and lower boundary condition bolts were tightened approximately 1/16 turn beyond finger tight (initial seating), after which the load was released.

Corner readings were taken with the deflection tracker and the position of the boundary conditions was adjusted as necessary. An average of the final voltage readings at the four corners was used as an initial offset to be subtracted from the raw voltage readings obtained from the scans. This offset accounts for the relative position of the plate with respect to the zero position of the scanning transducer. At

this point, the upper and lower boundary conditions were securely clamped to the frame.

The side boundary conditions were aligned as with the aluminum plate and clamped tightly to the frame. After initializing the data acquisition software, the strain gages were balanced and calibrated. The initial strain gage offsets, if any, were recorded.

At this stage, the load was again brought to approximately 0.9 kN to assure proper seating of the plate and promptly released. Two of the load introduction bolts were hand tightened as much as possible, after which the resulting excess load was released by lowering the testing machine head. The other bolts were not used.

The transducer array was positioned against the plate, with the transducers compressed to the center of their available range. Initial offsets, which accounted for the relative voltage output from the compressed transducers, were recorded for later subtraction from the data.

After the plate was carefully aligned in the test fixture, a complete deflection scan of the plate was taken using the deflection tracker. This consisted of vertical scans at nine horizontal positions spaced at 25 mm intervals. This initial scan defined the shape of the plate prior to introduction of the load and included the initial deformation caused by the lateral forces imposed by the rack of stationary transducers. These forces were included in the Rayleigh-Ritz analysis described in the previous chapter. The magnitudes of

these forces were specified by the manufacturer and are reported in the analysis chapter as Equations 3.20 and 3.21.

After the initial deflection mapping was completed, the machine stroke rate was set to 0.42 millimeters per minute and the data sampling rate to once every 0.25 seconds. The initial stroke was recorded and the plate was loaded until the deflection at the center of the plate reached a value equivalent to one-half of the plate thickness.

Significant divergence of the strain readings of the back-to-back gages has been shown to occur at center plate deflections of less than one-half of the plate thickness [48]. Since this behavior indicates that buckling has taken place, the load necessary to cause the plate to deflect half of the plate thickness was defined as the stability "limit load".

The "limit load", as defined, and stroke values were recorded, and a surface scan was performed with the deflection tracker in the same manner as described above. The load was then released by returning the stroke to its original setting. Data acquisition was reinitialized with the data sampling rate set to once every 0.40 seconds and the entire loading procedure was repeated with scans taken at the predetermined load levels.

For the first laminate of each type and boundary condition, the loading was halted only at the limit load. A scan was taken as before, the load was released, and the plates were loaded to failure. Failure was defined as the

point where the load-carrying capability of the laminate decreased significantly. In general, a sudden drop of more than 30% in the load occurred at failure. Thereafter, laminates of the same type and with the same boundary conditions were scanned at higher loads for laminate types which had developed an interesting mode shape during the initial test. In all cases, the center deflection of the plate was monitored during the test, using the previously described splitter cables and a voltmeter. This technique was also used to monitor when a change in mode shape occurred. After each scan, the load was released and data acquisition was reinitialized. The laminate was loaded continuously to failure after the final scan. Marks were recorded in the data files when noises, indicative of damage, were heard.

At failure, the machine stroke was halted and the maximum load and stroke were recorded. The transducer cart was withdrawn from the plate, and the plate was labeled and photographed in its fully deflected shape. The machine stroke was returned to zero and the plate was removed from the jig. This process was repeated for each of the three side boundary conditions.

Early results from nominally identical laminates displayed both primary and secondary buckling modes at similar load levels. This caused some concern about the sensitivity of the behavior to various parameters. In order to investigate the source of this behavior, the last specimen of each type tested with clamped side boundary conditions was

halted and scanned at multiples of 4.5 kN. In an attempt to balance the force of the transducers and determine the effect of the small transverse load applied by the nine transducers, a somewhat unorthodox experiment was performed. During the second phase of testing of these laminates, a modest transverse force was applied (by hand) repeatedly to the center of the plate in the opposite direction of the forces applied by the transducers in the array. The results are described in the following chapter.

4.4 Data Reduction

The experimentally obtained data was reduced into meaningful information with the aid of several specially tailored computer programs which were developed to complement the standard TELAC software package [50]. The following paragraphs describe the types of data reduction performed.

The first phase of data reduction involved snipping the extraneous values from the data files; i.e., those which were recorded prior to the start of the test or after failure of the laminate, which was defined by a sudden significant decrease in its load-carrying ability. Then, by assuming a linear strain distribution through the thickness,

$$\varepsilon_x = \varepsilon_x^o + z\kappa_x \tag{4.1}$$

the strain data was reduced into its stretching component or

mid-plane strain, ε_x^o, where

$$\varepsilon_x^o = \frac{\varepsilon_x^{front} + \varepsilon_x^{back}}{2} \tag{4.2}$$

and its bending strain component, $h\kappa_x$, (which is linearly proportional to the curvature, κ_x), where

$$h\kappa_x = \varepsilon_x^{front} - \varepsilon_x^{back} \tag{4.3}$$

and h is the laminate thickness.

Although a discussion of an effective longitudinal modulus is somewhat academic for unsymmetric laminates, nevertheless, the local experimental effective "modulus", N_x/ε_x^o, was determined for each laminate by performing linear regressions on the stress versus mid-plane strain data. (A more detailed description of the meaning of this parameter can be found in the results chapter.) The following criteria were selected and employed to establish the correct linear region of the plot. First, the slope was required to be positive. Second, the correlation coefficient needed to exceed 0.9. Third, the linear region had to consist of at least 20 data points. This corresponded to five seconds of loading (loaded at a rate of 0.42 millimeter per minute) during the first phase of the test or eight seconds during the subsequent phases. Fourth, the selected linear region had to begin

within the first 100 data points. This corresponded to 25 seconds after load introduction for the first phase tests and 40 seconds after load introduction for the subsequent tests.

Examination of the results indicated that even these criteria were insufficient for much of the data and a certain degree of subjectivity was still required in determining the effective modulus parameter. This problem, which was anticipated apriori, was the justification for mounting the end-shortening transducer to the compressive loading jig in the experiment. The corresponding estimates for an effective modulus based on this average strain data over the entire length of the specimens were also calculated for comparison purposes.

The "pseudo" buckling loads were also back-calculated for each plate from the center deflection data using the technique developed by Southwell [35,36]. The critical "pseudo" buckling load is defined as the inverse of a least-squares fit of the curve representing the lateral deflection divided by the load plotted against the lateral deflection. This works extremely well for an isotropic column and reasonably well for composite plates. A word of caution is that Southwell's method gives accurate results only for deflections which are small compared to the plate thickness [37].

Considerable attention was given to verifying the transformation of data, required prior to calculating the isodeflection contour levels. The contour plotting program was modified to enable a correction to be made to the location

where data was measured. This was necessary for all deflection measurements obtained before the renovation of the scanner. Prior to that time, the scanner was slightly twisted and had a small horizontal offset. Comparisons of the corrected versus uncorrected contour plots showed that the effect of this correction was negligible. Nevertheless, the correction was made to all of the early data for the sake of accuracy. Isodeflection contours were generated based on the data from the deflection tracker. Contour maps were plotted showing the isodeflection contours.

Plots were also prepared of the "load versus lateral deflection, w" data from the nine stationary transducers, "load versus end-shortening displacement, u" data from the stroke transducer, and "load versus strain" data from the four strain gages. Representative graphs of the results are included in the following chapter.

CHAPTER 5

RESULTS

This chapter contains a presentation of typical results from the investigation, including both experimental data and analytical predictions. The types of experimental data obtained in this investigation and presented herein include the load versus out-of-plane deflection (P vs. w) data, the load versus longitudinal strain (P vs. ε) data, the load versus longitudinal in-plane displacement (P vs. u) data, and isodeflection (w) contour maps. The critical buckling loads (P_{cr}) and information about the failure values and failure mechanisms are presented in the final sections. In addition to the data presented in this chapter, a complete collection of the experimental graphs for each laminate are included in the appendices of this report: P vs. w in Appendix E, P vs. ε in Appendix F, P vs. u in Appendix G, and the isodeflection contour maps in Appendix H.

Where applicable, the theoretical predictions based on the linear and nonlinear Rayleigh-Ritz (52 modes) and linear finite element (408 degrees of freedom) analyses, are presented alongside the corresponding typical experimental results. The theoretical curves using the nonlinear Rayleigh-Ritz analysis were generated from calculations performed at multiples of load, P, equal to 4.5 kN (up to

27.0 kN). Failure stresses were not considered in the analysis.

Aside from the more subtle deflection components caused by the various elastic couplings, two general types of postbuckling behavior were observed on a global scale during the testing of laminates with restrained side boundary conditions. Most of these laminates exhibited a primary global bending mode throughout the entire range of compressive loading beginning with the application of the load and continuing to failure. Some of the laminates, however, transitioned, either smoothly or with a snap, into a secondary bending mode. In either case, components of twisting modes and higher bending modes were often superimposed on the deflection pattern. Table 5.1 summarizes the dominant longitudinal bending component just prior to failure for each of the laminates tested with restrained side boundary conditions (i.e., clamped or simply-supported). All of the laminates tested with free side boundary conditions exhibited only the primary bending mode.

5.1 Load versus Out-of-Plane Deflection, w

The out-of-plane deflection (w) readings were recorded at each of the nine transducer locations as described in Chapter 4, producing nine continuous load versus deflection (P vs. w) curves for each of the laminates tested. Observations relating to this experimental data and

TABLE 5.1

DOMINANT BENDING COMPONENT AT FAILURE

Laminate Type	Side Boundary Conditions						
	Clamped					Simply-Supported	Free
	1[a]	2	3	4	5		
S	1	1	1	1	1	1	1
T	1	1	1	1	1	1	1
U	2	2	1	1	1	1	1
P	1	1	1	1	1	1	1
N	1	1	1	1	1	1	1
A	1	1[b]	1	1[b]	1	1[b]	1
B	1	1[b]	1	1[b]	1	1[b]	1
C	2	1	2	1	2	2	1
D	2	1	1	1	1	2	1
E	2	2	1	1	2	1	1
F	2	2	1	1	1	1	1

[a] Identifies specimen number.
[b] Indicates beginning of transition into second mode.

correlations with the theoretical predictions are included in this section.

Symmetry considerations of the applied load, test geometry and fiber antisymmetry about the center of the laminate with respect to the loading direction dictate that a one-to-one correspondence should exist between antisymmetric transducer locations during first bending mode behavior[49]. That is, the deflection at location 1, as shown in Figure 3.2, should correspond identically to the deflection at location 9. Likewise, the deflection at location 2 should correspond identically to the deflection at location 8. Similarly, the deflection at location 3 should correspond identically to the deflection at location 7. Finally, the deflection at location 4 should correspond identically to the deflection at location 6. Thus, only five of the transducers should provide unique information about the first mode behavior. The theoretical predictions bear out these symmetry arguments, and, therefore, only the first five locations are indicated on the theoretical plots.

The redundant transducers in the experiment ensured symmetric lateral loading, served as an indicator of the accuracy of the test, and measured the introduction of secondary modal components into the deflection pattern. These effects can be separated by first examining the results from the symmetric laminates which contain no inherent mechanical couplings. For such laminates, the symmetry argument extends to all four corners; i.e., in addition to the above

relationships, the deflections at locations 1, 3, 7, and 9 should all be equal.

The following sections present typical load versus out-of-plane deflection results for the laminates tested with clamped, simply-supported, and free side boundary conditions, respectively. A complete set of experimental load versus out-of-plane deflection results for all of the laminates is contained in Appendix E.

5.1.1 Clamped Sides

A close examination of the $[0_3/90_3]_S$ and $[0_3//90_3//90_3//0_3]_T$ laminates with clamped side boundary conditions shows that while the experimental data were not absolutely perfect, the results were very repeatable between tests and the proper trends can be observed. For example, a typical experimental load versus deflection plot is shown in Figure 5.1 for the $[0_3/90_3]_S$-1 laminate, along with the corresponding theoretical prediction from the nonlinear Rayleigh-Ritz analysis.

A comparison of the out-of-plane deflection for the $[0_3//90_3//90_3//0_3]_T$-2 laminate in Figure 5.2 with the $[0_3/90_3]_S$-1 laminate in Figure 5.1 shows the primary effect of the room temperature bondlines. The $[0_3//90_3//90_3//0_3]_T$ laminates, which have three room temperature bondlines, were both stiffer, due to the increased thickness and consequently increased moments of inertia, and ultimately stronger than the

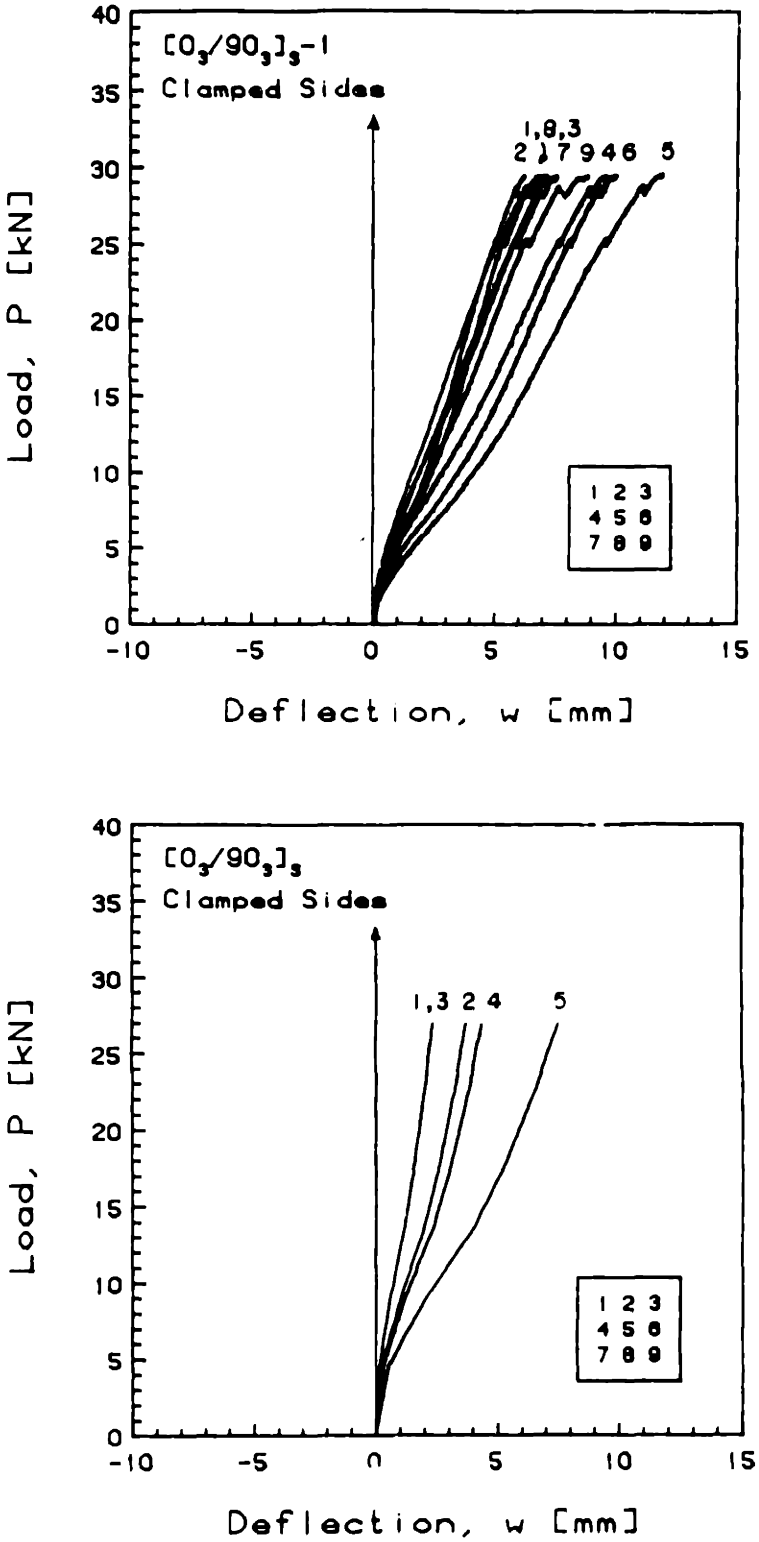

FIGURE 5.1 Experimental (top) and Predicted (bottom, via Rayleigh-Ritz) Plots of Applied Compressive Load versus Out-of-Plane Deflection for the $[0_3/90_3]_S$-1 Laminate with Clamped Side Boundary Conditions

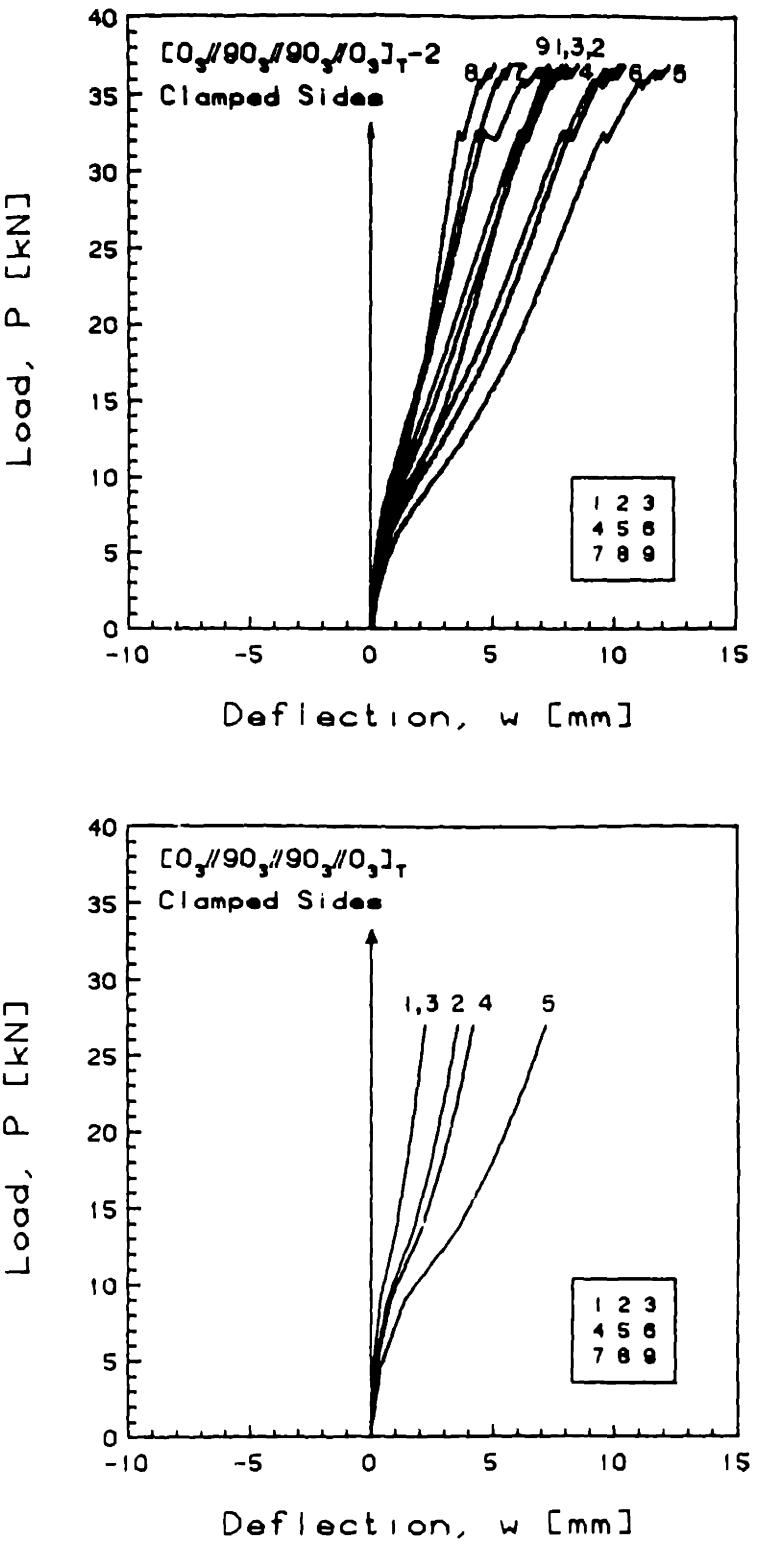

FIGURE 5.2 Experimental (top) and Predicted (bottom, via Rayleigh-Ritz) Plots of Applied Compressive Load versus Out-of-Plane Deflection for the $[0_3//90_3//90_3//0_3]_T$-2 Laminate with Clamped Side Boundary Conditions

$[0_3/90_3]_S$ laminates. This trend was also predicted by the nonlinear Rayleigh-Ritz analysis for these particular laminate types, as can be recognized in these same figures.

Switching one of the 90_3 sublaminates with the adjacent 0_3 sublaminate in the laminate type just discussed results in a $[0_3//90_3//0_3//90_3]_T$ laminate with an identical A_{ij} matrix, averaged D_{11} and D_{22} terms, and the introduction of bending-stretching coupling in the form of B_{11} and B_{22} with magnitudes of 22.4 kN. A typical load versus out-of-plane deflection example of this laminate type, with clamped side boundary conditions, which remained in the first mode, is shown in Figure 5.3, along with the theoretical prediction. However, this laminate type also exhibited secondary buckling as shown in Figure 5.4 for the $[0_3//90_3//0_3//90_3]_T$-1 laminate with clamped side boundary conditions. This particular laminate snapped rather abruptly into a clean second bending mode (without any twisting or shearing), since the related elastic couplings were not present in this laminate.

It is the introduction of bending-stretching coupling which apparently encourages the formation of this secondary buckling to occur. The experimentally observed secondary buckling behavior can be characterized as initially following the primary bending mode, and then transitioning, either smoothly or with a snap, into a secondary mode. Typically, experimental readings from the upper row of deflection transducers matched the corresponding deflection data from the laminates which remained in the first mode until failure. The

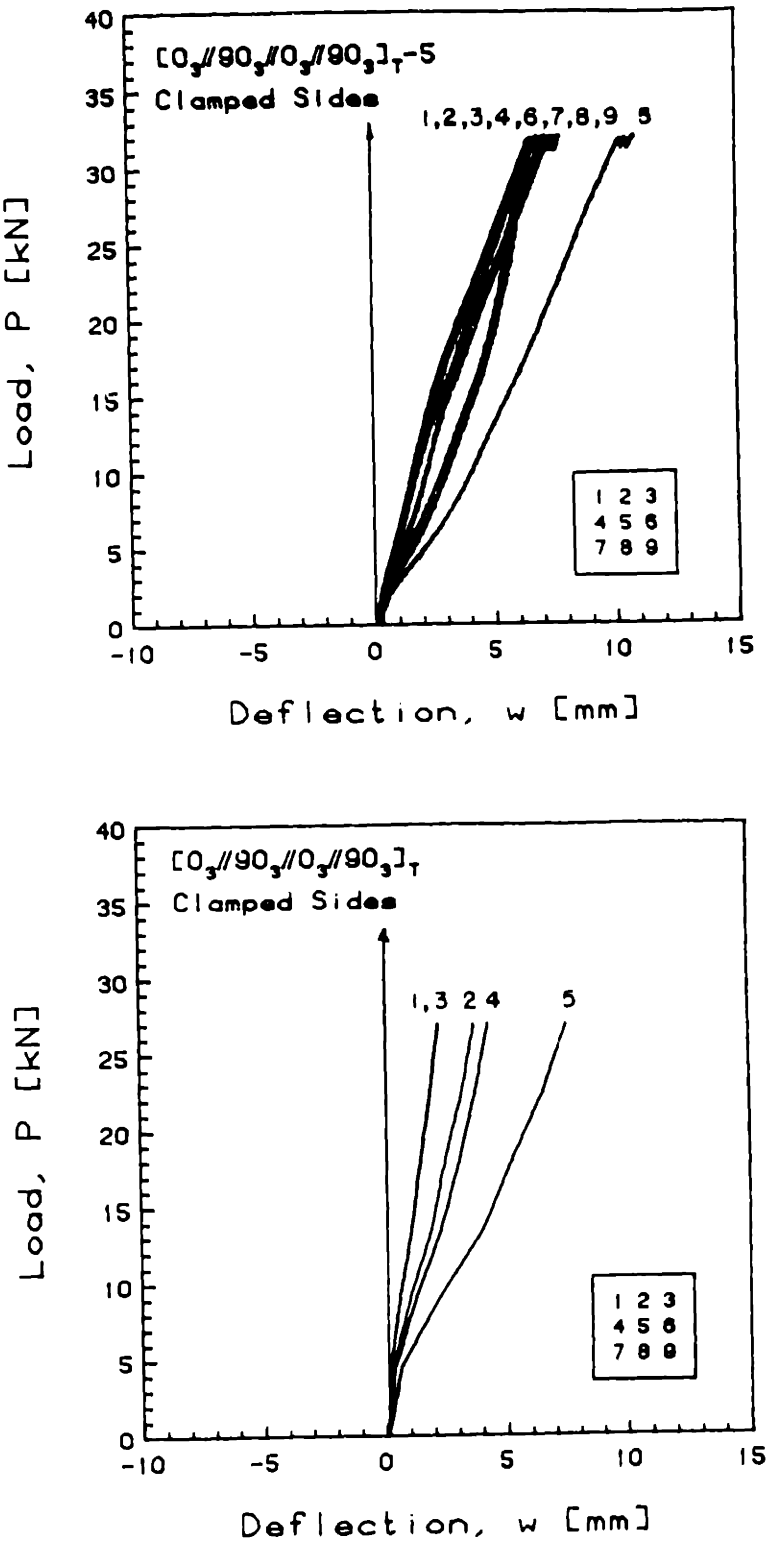

FIGURE 5.3 Experimental (top) and Predicted (bottom, via Rayleigh-Ritz) Plots of Applied Compressive Load versus Out-of-Plane Deflection for the $[0_3//90_3//0_3//90_3]_T$-5 Laminate with Clamped Side Boundary Conditions

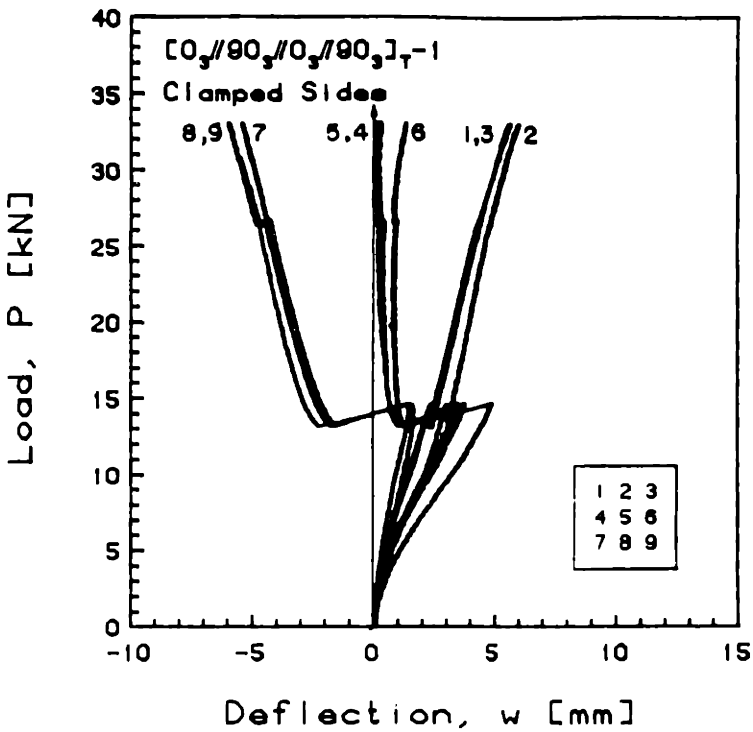

FIGURE 5.4 Experimental Plot of Applied Compressive Load versus Out-of-Plane Deflection for the $[0_3//90_3//0_3//90_3]_T$-1 Laminate with Clamped Side Boundary Conditions

nonlinear Rayleigh-Ritz energy analysis did not predict any second mode behavior to occur at a minimum energy level. A summary of the experimentally observed secondary buckling loads for all of the laminates tested is presented in Table 5.2.

Stretching-shearing and bending-twisting couplings are present in the $[0_2//45_2//0_2//45_2//0_2]_T$ laminates. These couplings introduce shearing and twisting into the deflection pattern. Since this laminate is symmetric, there are no structural (elastic) couplings between the in-plane behavior and the out-of-plane behavior. Although the shearing deflections are not readily evidenced from the experimental load versus out-of-plane deflection data in Figure 5.5, both the theoretical out-of-plane deflection data and the experimental isodeflection contour maps (see Section 5.4) reflect this behavior, since the theoretical prediction for location 1 is distinctly apart from locations 2 and 3.

A similar laminate type investigated reversed the orientation of one of the 45_2 sublaminates in the above laminate to balance the laminate, eliminating the stretching-shearing and bending-twisting couplings, and replacing them with stretching-twisting couplings. Results from a typical example are shown in Figure 5.6 for the $[0_2//45_2//0_2//-45_2//0_2]_T$-1 laminate. These laminates exhibited behavior extremely similar to the $[0_2//45_2//0_2//45_2//0_2]_T$ laminates. Analytically, there was less twist in the deflection pattern, but, experimentally,

TABLE 5.2

MEASURED SECONDARY BUCKLING LOADS FOR LAMINATES WITH RESTRAINED SIDE BOUNDARY CONDITIONS

Laminate	Experimental Secondary Buckling Load [kN]
U_1	14.6
U_2	10.4
C_1	10.0
C_3	6.5
C_5	6.8
C_{Simple}	7.2
D_1	5.0
D_{Simple}	5.8
E_1	3.0
E_2	5.0
E_5	5.8
F_1	5.0
F_2	4.0

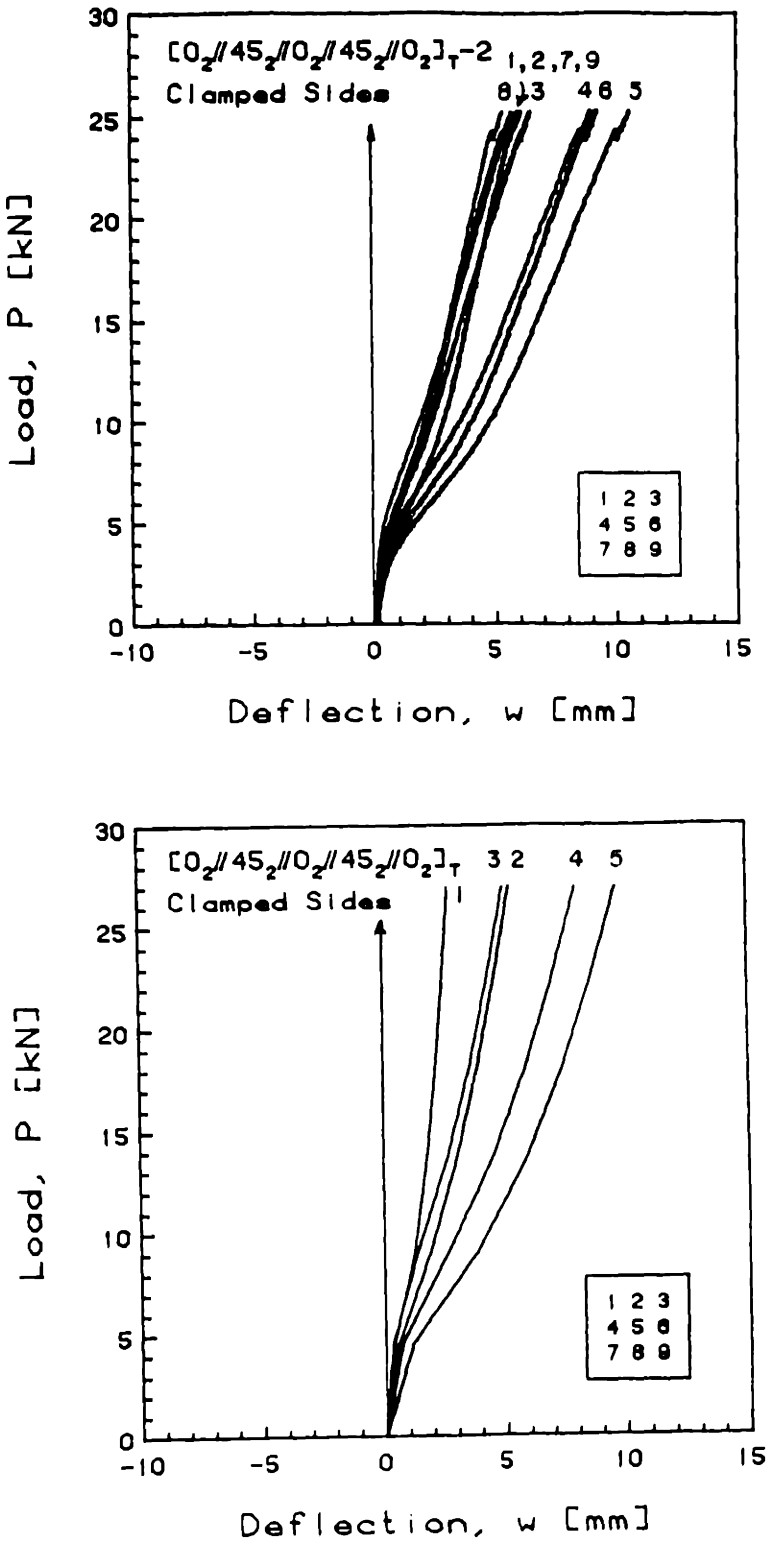

FIGURE 5.5 Experimental (top) and Predicted (bottom, via Rayleigh-Ritz) Plots of Applied Compressive Load versus Out-of-Plane Deflection for the $[O_2//45_2//O_2//45_2//O_2]_T$-2 Laminate with Clamped Side Boundary Conditions

this was not readily noticeable. This can be partially reconciled by realizing that the the stretching-shearing coupling response is tied into the bending-twisting coupling response (in the $[0_2//45_2//0_2//45_2//0_2]_T$ laminates), because the nonlinear large deflections geometrically couple together the in-plane and out-of-plane behaviors. Thus, these two laminates effectively have the same couplings.

The final laminate type investigated was the family of $[0_6//\theta_6]_T$ laminates, where θ varied from 15° to 90° in 15° increments. These laminates, with fully coupled elastic matrices, revealed the effects of altering the lamination angle, θ, in a particular laminate configuration. The experimental results for the first laminate type in this family, specifically $[0_6//15_6]_T$-5, are shown in Figure 5.7. Because the magnitude of the couplings are relatively small, compared to the other laminates in this family, this laminate type is the closest to being symmetric. In this case, both the experimental data and the theoretical predictions are quite clean and correlate rather well, as is true for the symmetric laminates previously discussed.

When θ was increased to 30°, the deflection behavior was often relatively free of twisting or second mode components, as seen in Figure 5.8 for laminate $[0_6//30_6]_T$-5. This data agreed quite well with the theoretical predictions from the Rayleigh-Ritz analysis shown in the same figure. The analysis also indicates the presence of a rather substantial amount of twist in the deflection behavior. However, although none of

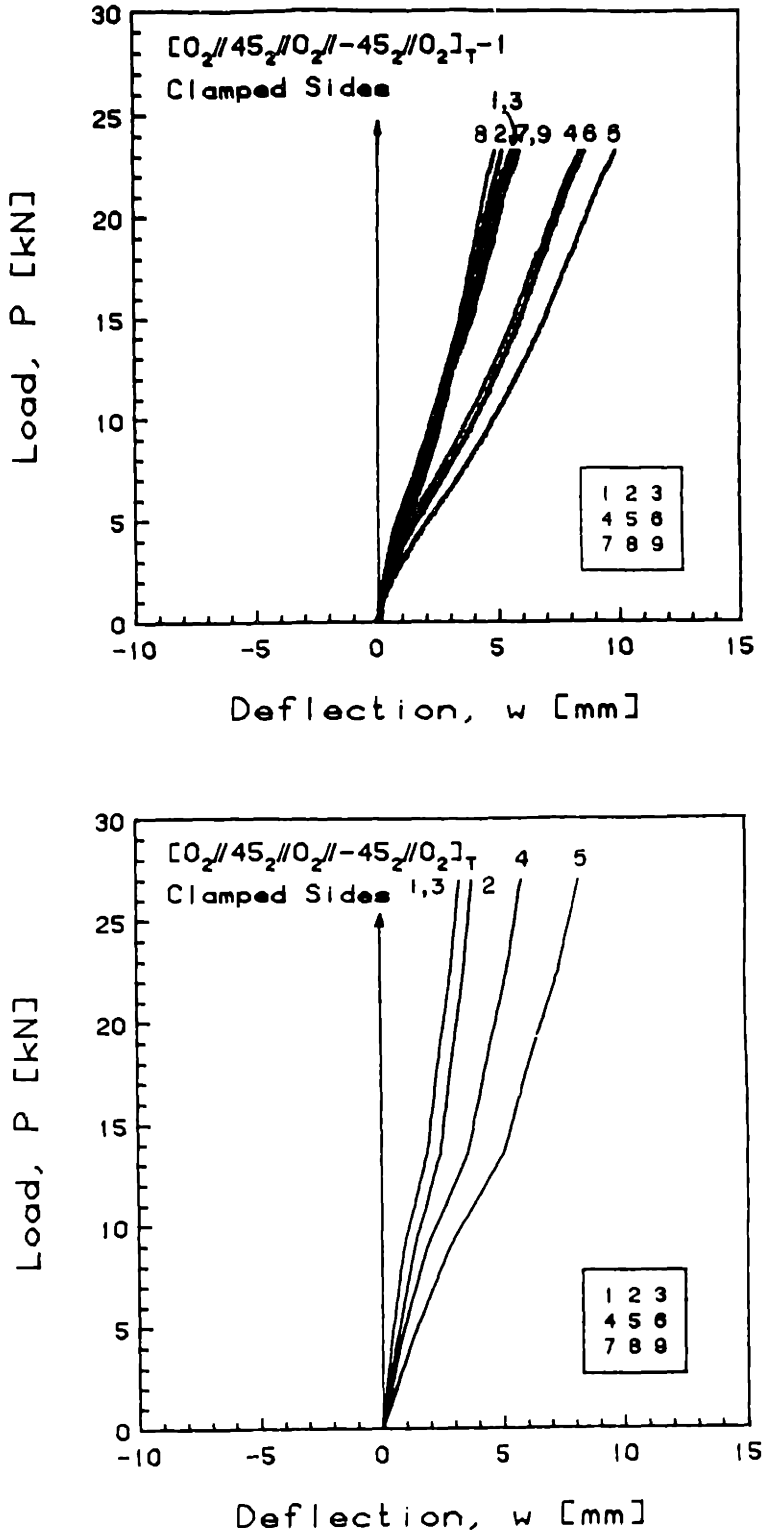

FIGURE 5.6 Experimental (top) and Predicted (bottom, via Rayleigh-Ritz) Plots of Applied Compressive Load versus Out-of-Plane Deflection for the $[O_2//45_2//O_2//-45_2//O_2]_T$-1 Laminate with Clamped Side Boundary Conditions

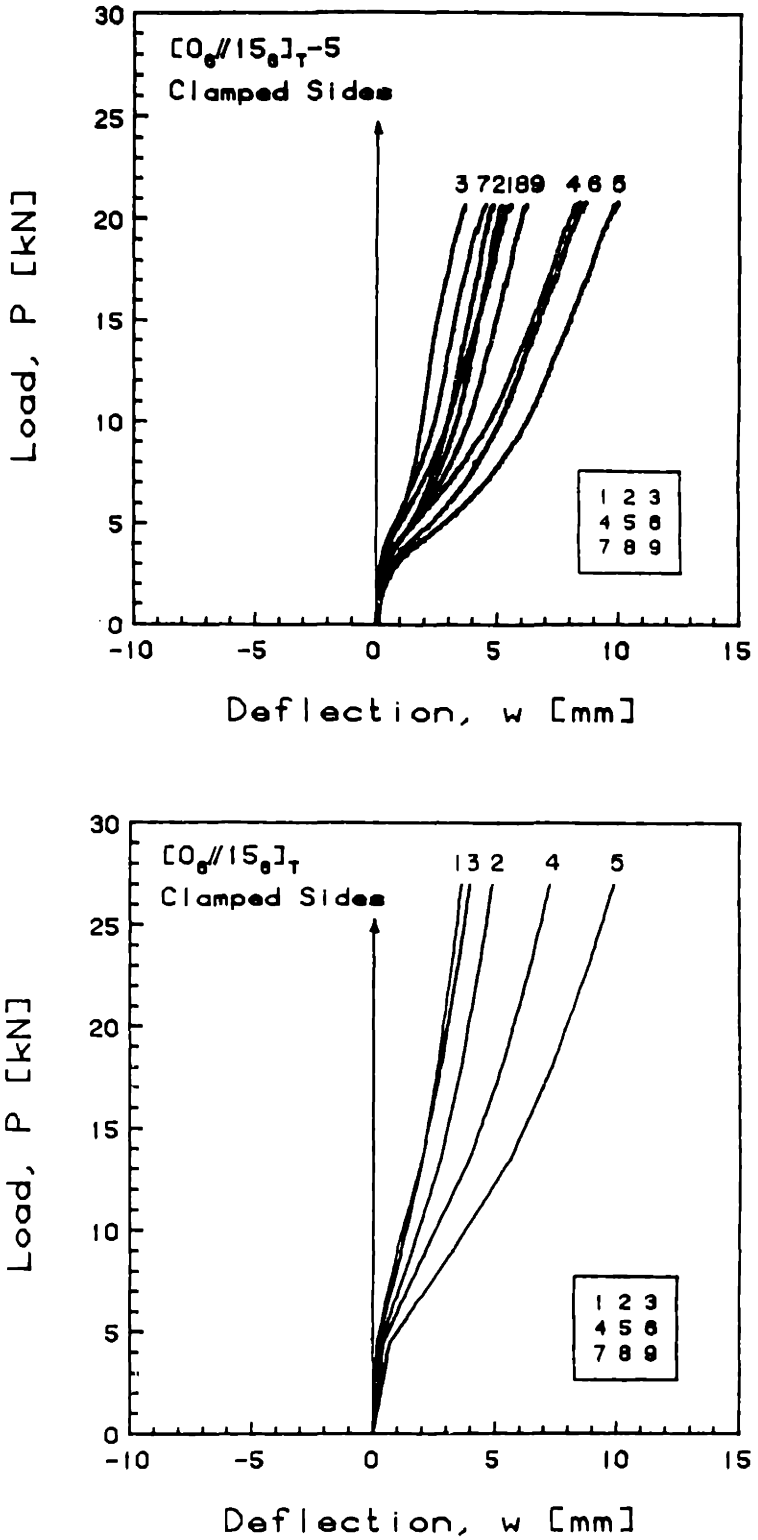

FIGURE 5.7 Experimental (top) and Predicted (bottom, via Rayleigh-Ritz) Plots of Applied Compressive Load versus Out-of-Plane Deflection for the $[0_6//15_6]_T$-5 Laminate with Clamped Side Boundary Conditions

the $[0_6//30_6]_T$ laminates buckled into a secondary bending mode, some of the specimens, such as $[0_6//30_6]_T$-2 shown in Figure 5.9, exhibited discernible twisting and the partial introduction of higher bending modes, as evidenced by the difference between the transducer readings at locations at 1, 2, and 3.

The most interesting results come from the $[0_6//45_6]_T$ laminates, which displayed the most extreme vicissitudes in behavior, both experimentally and analytically. The load versus out-of-plane deflection results for the $[0_6//45_6]_T$-4 laminate with clamped side boundary conditions are shown in Figure 5.10. Although this laminate remained in the primary bending mode, there was a large deviation from the analytically predicted behavior. Unlike most of the other laminates, the analysis predicted a surprisingly twisted second mode behavior at high loads, with locations 2, 3, and 4 exceeding the center deflection. This bimodal behavior is indicative of an extreme sensitivity to some of the coupling parameters. It may also indicate that an insufficient number of w-modes were used in the analysis to be able to accurately predict the actual higher bending components observed. On the other hand, it underscores the concept of the existence of two equilibrium configurations at similar energy levels.

A third bending mode component was also observed in some of the laminates of this type. This is evidenced by the fact that the out-of-plane deflections at locations 4 and 6 peaked at only a third of the way to failure, while all of the

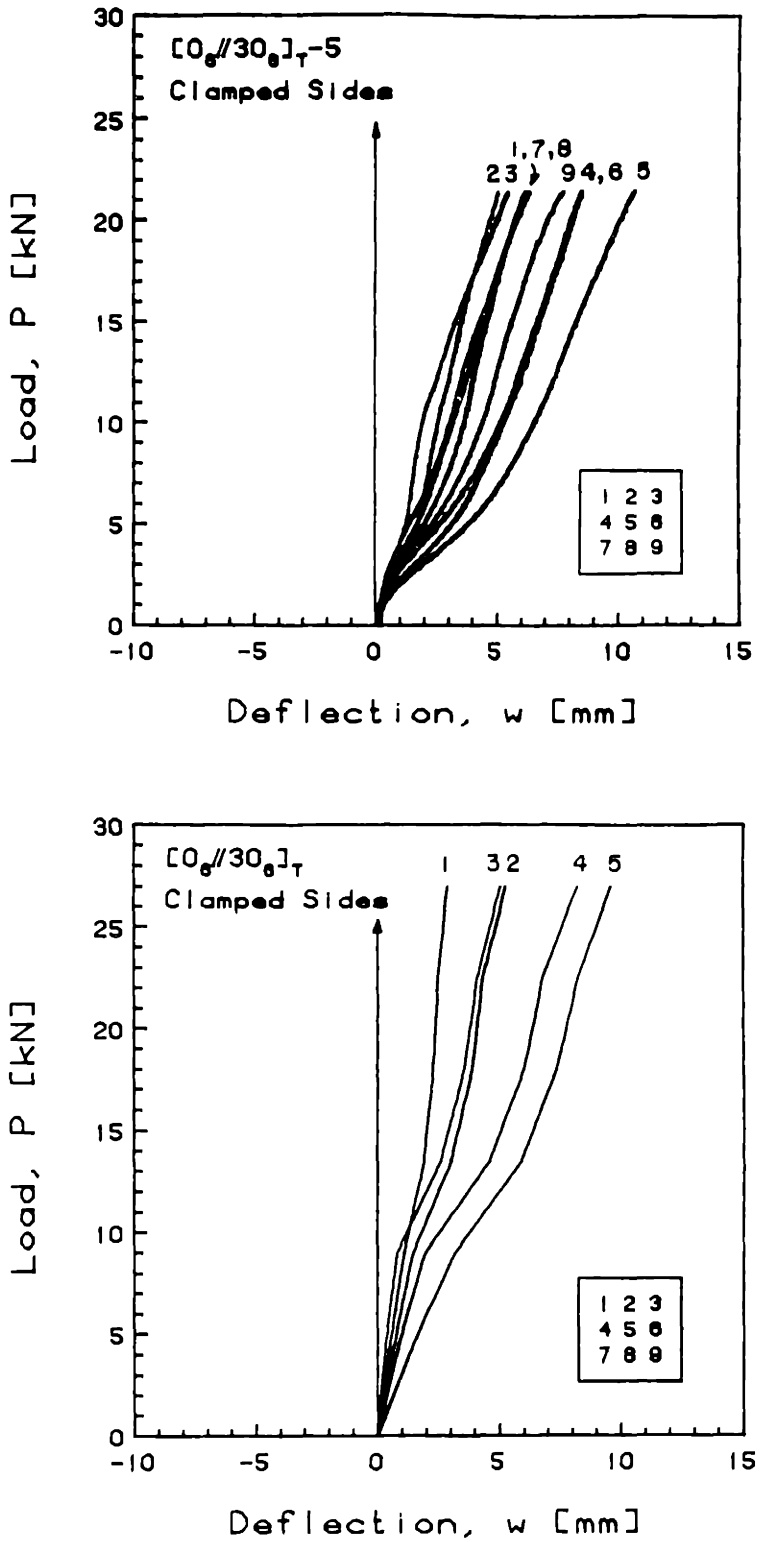

FIGURE 5.8 Experimental (top) and Predicted (bottom, via Rayleigh-Ritz) Plots of Applied Compressive Load versus Out-of-Plane Deflection for the $[0_6//30_6]_T$-5 Laminate with Clamped Side Boundary Conditions

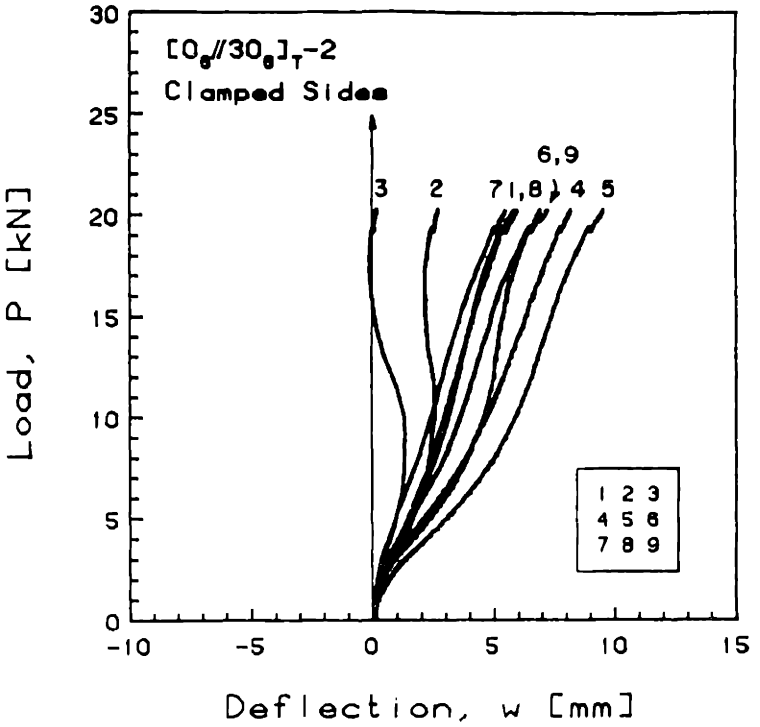

FIGURE 5.9 Experimental Plot of Applied Compressive Load versus Out-of-Plane Deflection for the $[0_6//30_6]_T$-2 Laminate with Clamped Side Boundary Conditions

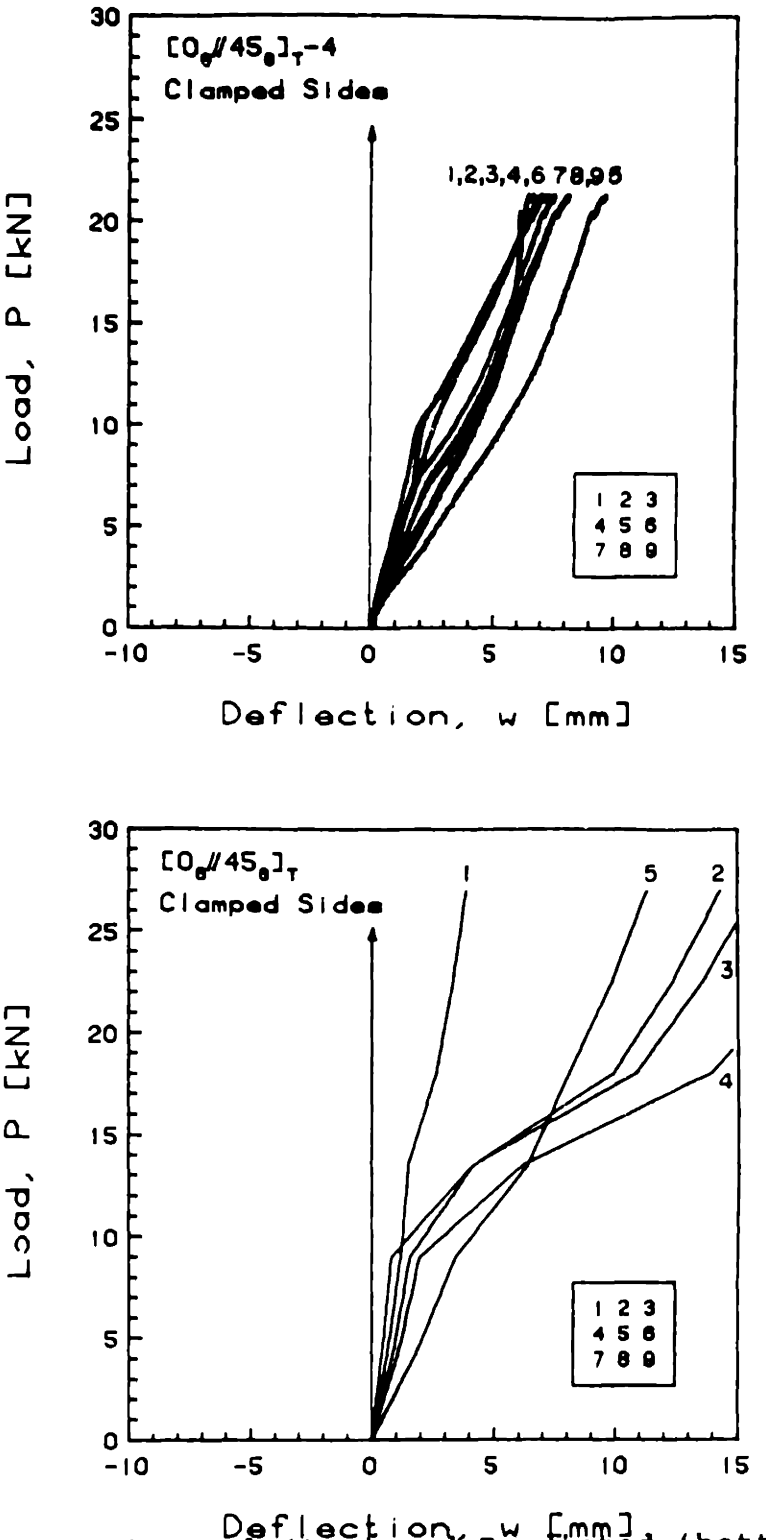

FIGURE 5.10 Experimental (top) and Predicted (bottom, via Rayleigh-Ritz) Plots of Applied Compressive Load versus Out-of-Plane Deflection for the $[0_6//45_6]_T$-4 Laminate with Clamped Side Boundary Conditions

remaining locations continued to see an increase in deflection. This component was superimposed on the deflection behavior of every laminate of this type which remained in the first bending mode. A comparison with the $[0_3//90_3//0_3//90_3]_T$-5 out-of-plane deflection behavior previously examined in Figure 5.3 reveals that although the corresponding locations never peak prior to failure, nevertheless, an increase in stiffness is observed at those locations. This implies that the bending-stretching couplings are responsible for this behavior.

The experimental behavior of the fifth specimen of this type tested with clamped side boundary conditions is shown in Figure 5.11. This particular laminate preferred the secondary bending mode, once the second instability load level was attained. A third nominally identical laminate, $[0_6//45_6]_T$-1, whose experimental behavior is shown in the same figure, snapped rather abruptly from one stable equilibrium configuration to the other.

It is germane to note that all of the shearing and twisting couplings peak at 45°. As θ continues to increase, the magnitudes of these couplings decrease. However, the bending-stretching couplings continue to increase.

During the second phase of testing of the $[0_6//60_6]_T$-5 laminate with clamped side boundary conditions (shown in Figure 5.12), the manually-applied lateral force revealed the existence of a shallow or soft region on the load equilibrium path, as evidenced by the fact that the primary bending mode

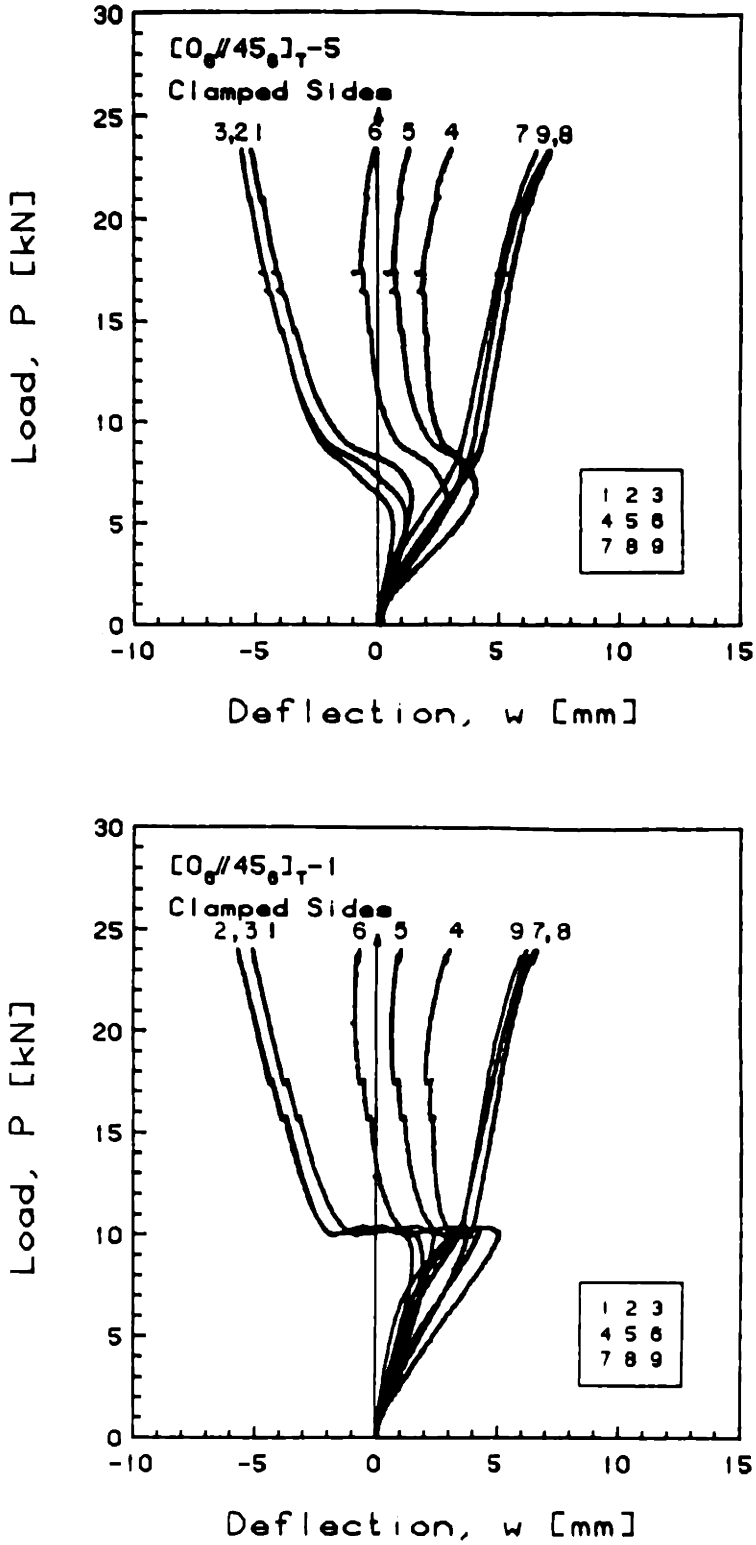

FIGURE 5.11 Experimental Plots of Applied Compressive Load versus Out-of-Plane Deflection for the $[O_6//45_6]_T$-5 (top) and $[O_6//45_6]_T$-1 (bottom) Laminates with Clamped Side Boundary Conditions

could be changed from first to second mode by applying a very small lateral force. However, for this particular laminate, the secondary bending mode did not represent a stable equilibrium position. The primary bending mode prevailed throughout the subsequent phases of the test, with a third bending mode component superimposed on the deflection behavior after approximately 9 kN. This is observed in the figure, by comparing the deflections at location 5 with the deflections at positions 4 and 6. The theoretical prediction displays a sensitivity to the strong couplings in this laminate, as indicated by the changing slopes and crossing of the lines not previously encountered in other laminates. However, the results from the first $[0_6//60_6]_T$ specimen tested with clamped side boundary conditions, exhibited in Figure 5.13, show that a secondary bending mode was preferred for that particular laminate, which was nominally identical to the one just considered.

As the lamination angle, θ, was increased to 75° in this laminate family, the stretching-shearing and bending-twisting couplings continued to cause the deflection response to twist, as seen by comparing locations 1 and 3 for the $[0_6//75_6]_T$-3 laminate tested with clamped side boundary conditions, shown in Figure 5.14. Comparison of locations 4 and 6 with location 5 in the same figure reveals the superimposed third bending mode component.

The next two graphs show the load versus deflection, w, data for the $[0_6//75_6]_T$-5 case, with clamped side boundary

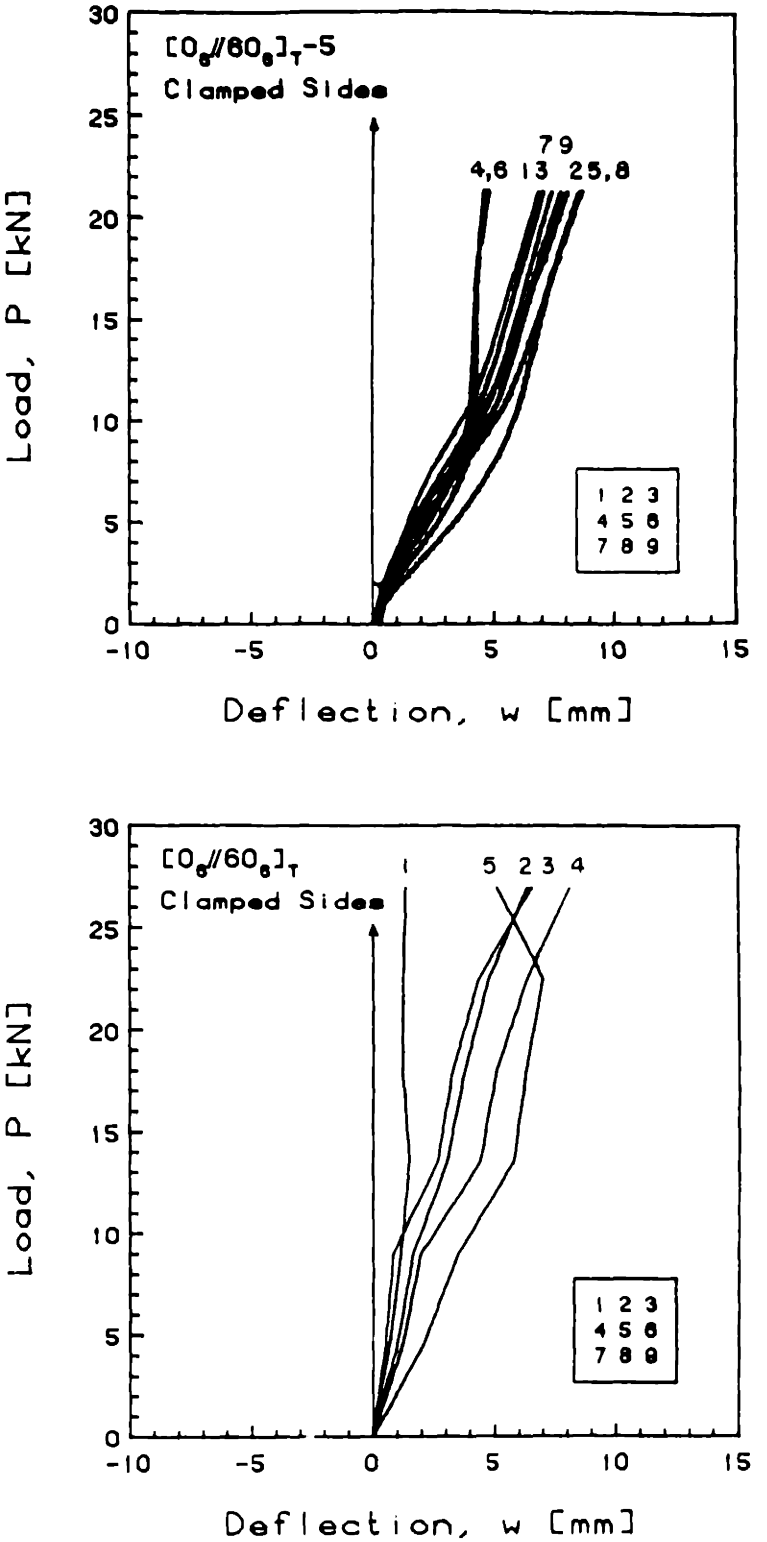

FIGURE 5.12 Experimental (top) and Predicted (bottom, via Rayleigh-Ritz) Plots of Applied Compressive Load versus Out-of-Plane Deflection for the $[0_6//60_6]_T$-5 Laminate with Clamped Side Boundary Conditions

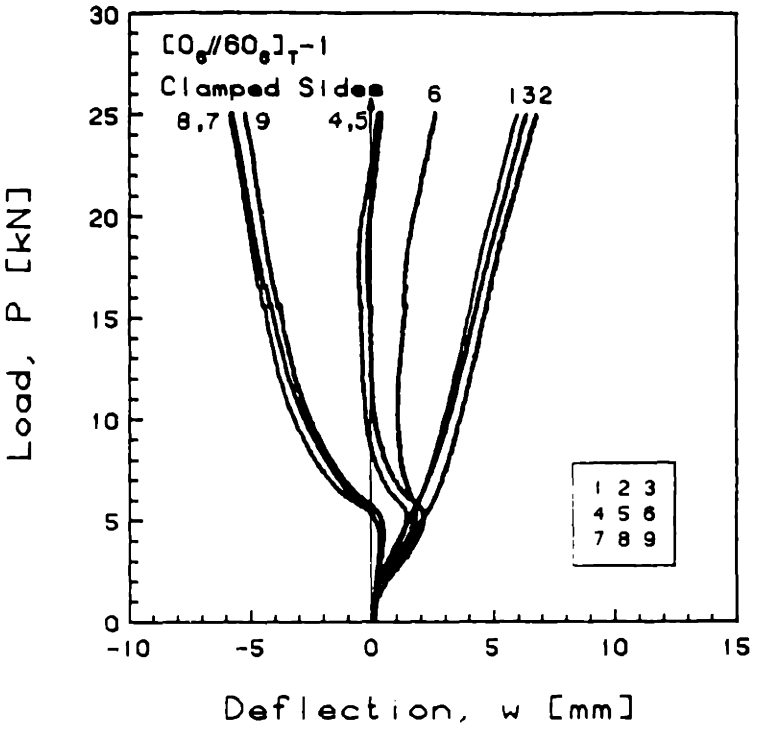

FIGURE 5.13 Experimental Plot of Applied Compressive Load versus Out-of-Plane Deflection for the $[0_6//60_6]_T$-1 Laminate with Clamped Side Boundary Conditions

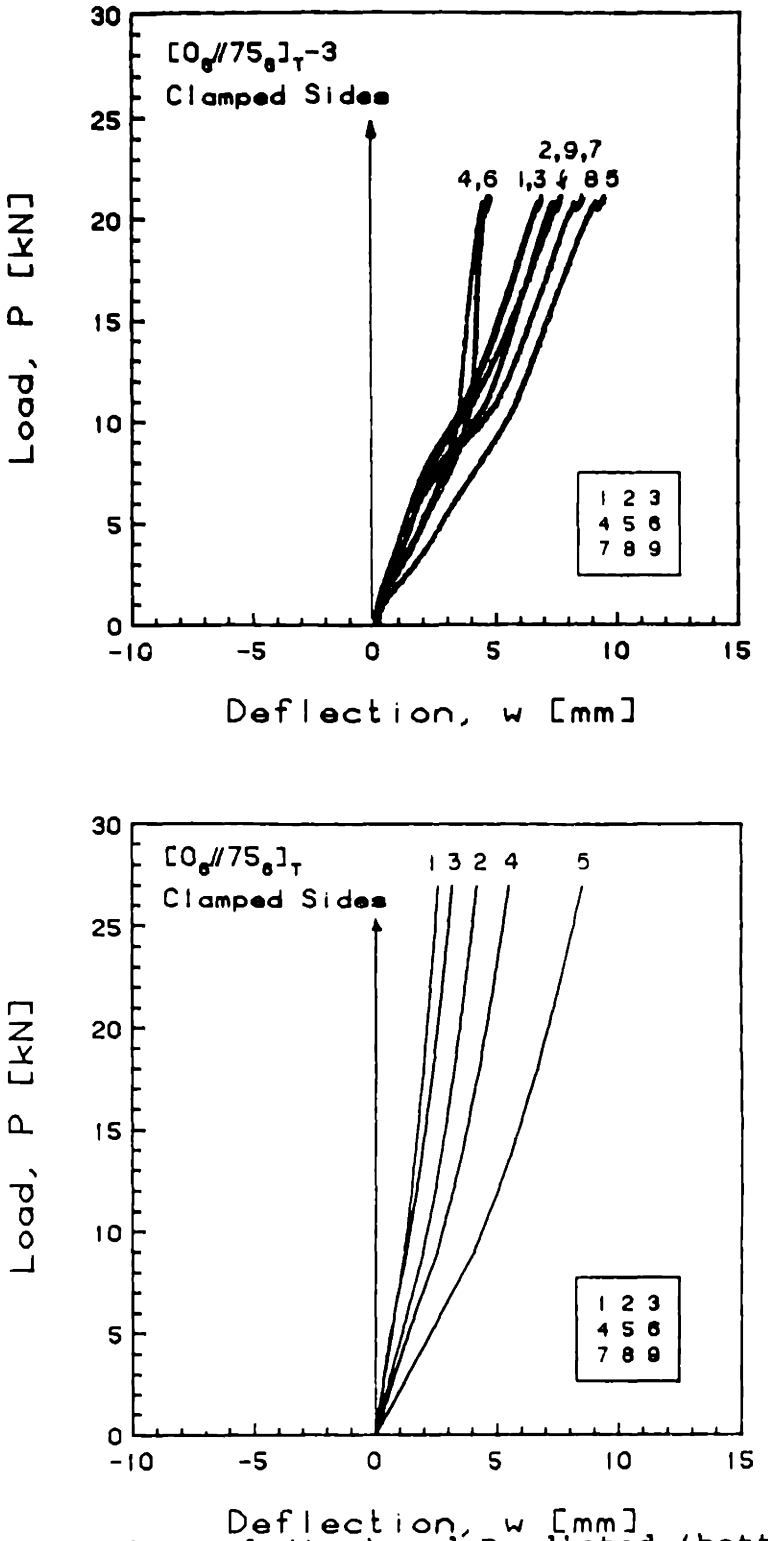

FIGURE 5.14 Experimental (top) and Predicted (bottom, via Rayleigh-Ritz) Plots of Applied Compressive Load versus Out-of-Plane Deflection for the $[0_6//75_6]_T$-3 Laminate with Clamped Side Boundary Conditions

conditions during the various phases of the experimental test. For this particular laminate, the initially preferred mode shape was the primary bending mode, as seen in the upper portion of Figure 5.15. During the next phase of the test, with the manually-applied lateral force, the laminate shifted into the secondary mode, as seen in the lower portion of Figure 5.15. A comparison of these two sets of curves reveals the two stable equilibrium configurations which exist at 9 kN. In Figure 5.16 it is indicated that although the primary bending mode was initially preferred, in the final phase of the test, the secondary bending mode clearly dominated. This near equality of preference is another verification of the close proximity of the energy levels associated with the two different modes in this load region.

The final laminate type tested with clamped side boundary conditions was the $[0_6//90_6]_T$ laminate. The elastic properties of this laminate were similar to the $[0_3//90_3//0_3//90_3]_T$ laminates, already discussed, except that the $[0_6//90_6]_T$ laminates had nominally twice the bending-stretching coupling as the $[0_3//90_3//0_3//90_3]_T$ laminates. The other elastic constants in these two types of laminates were identical (except for a slight difference due to the additional thickness of the room temperature bondlines in the $[0_3//90_3//0_3//90_3]_T$ laminates). The out-of-plane deflection behavior of the $[0_6//90_6]_T$-5 laminate is depicted in Figure 5.17. For this $[0_6//90_6]_T$-5 laminate, it was observed that although a stable second mode could be induced

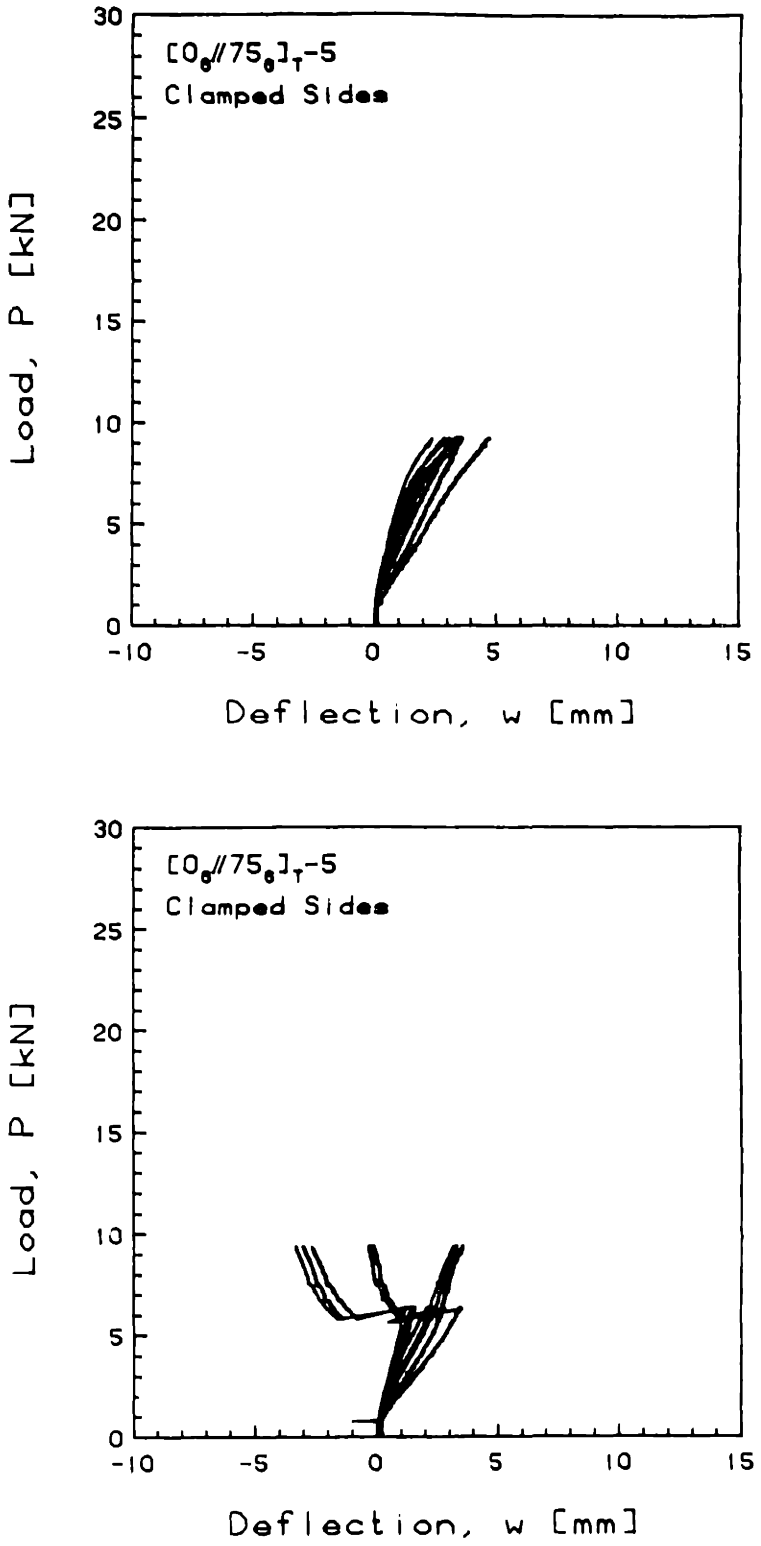

FIGURE 5.15 Experimental Phase I (top) and II (bottom) Plots of Applied Compressive Load versus Out-of-Plane Deflection for the $[0_6//75_6]_T$-5 Laminate with Clamped Side Boundary Conditions

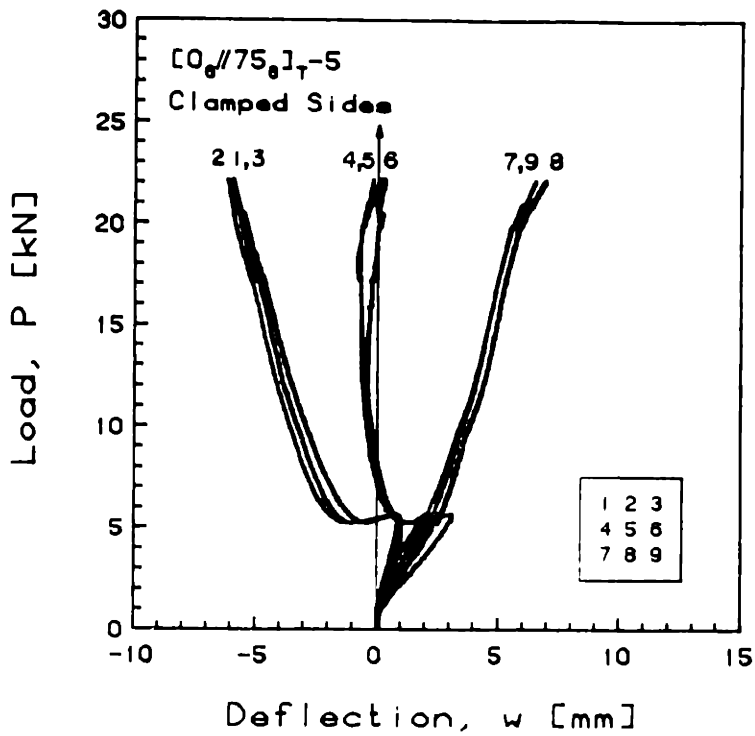

FIGURE 5.16 Experimental Phase III Plot of Applied Compressive Load versus Out-of-Plane Deflection for the $[0_6//75_6]_T$-5 Laminate with Clamped Side Boundary Conditions

with a little coaxing, the dominant mode, during subsequent phases of the test, was the primary bending mode, with a superimposed third bending mode component. Other nominally identical laminates preferred the secondary mode independent of any outside influence. For example, as shown in Figure 5.18, the $[0_6//90_6]_T$-2 laminate displays a dominant secondary bending mode beginning near the predicted secondary instability point.

5.1.2 Simply-Supported Sides

Only one of each type of laminate was tested with simply-supported side boundary conditions. Therefore, all of the experimental load versus out-of-plane deflection results for these laminates are included here for consideration. In general, the behavior of the laminates with simply-supported sides was very similar to the laminates tested with clamped side boundary conditions. Also, the agreement with the nonlinear Rayleigh-Ritz analysis was exceptionally good for the laminates with simply-supported side boundary conditions.

One of the major distinctions between the laminates tested with simply-supported side boundary conditions and those tested with clamped sides was that the simply-supported side boundary conditions allowed larger out-of-plane deflections. Additionally, the difference between the analytical out-of-plane deflection predictions for the laminates with clamped side boundary conditions versus those

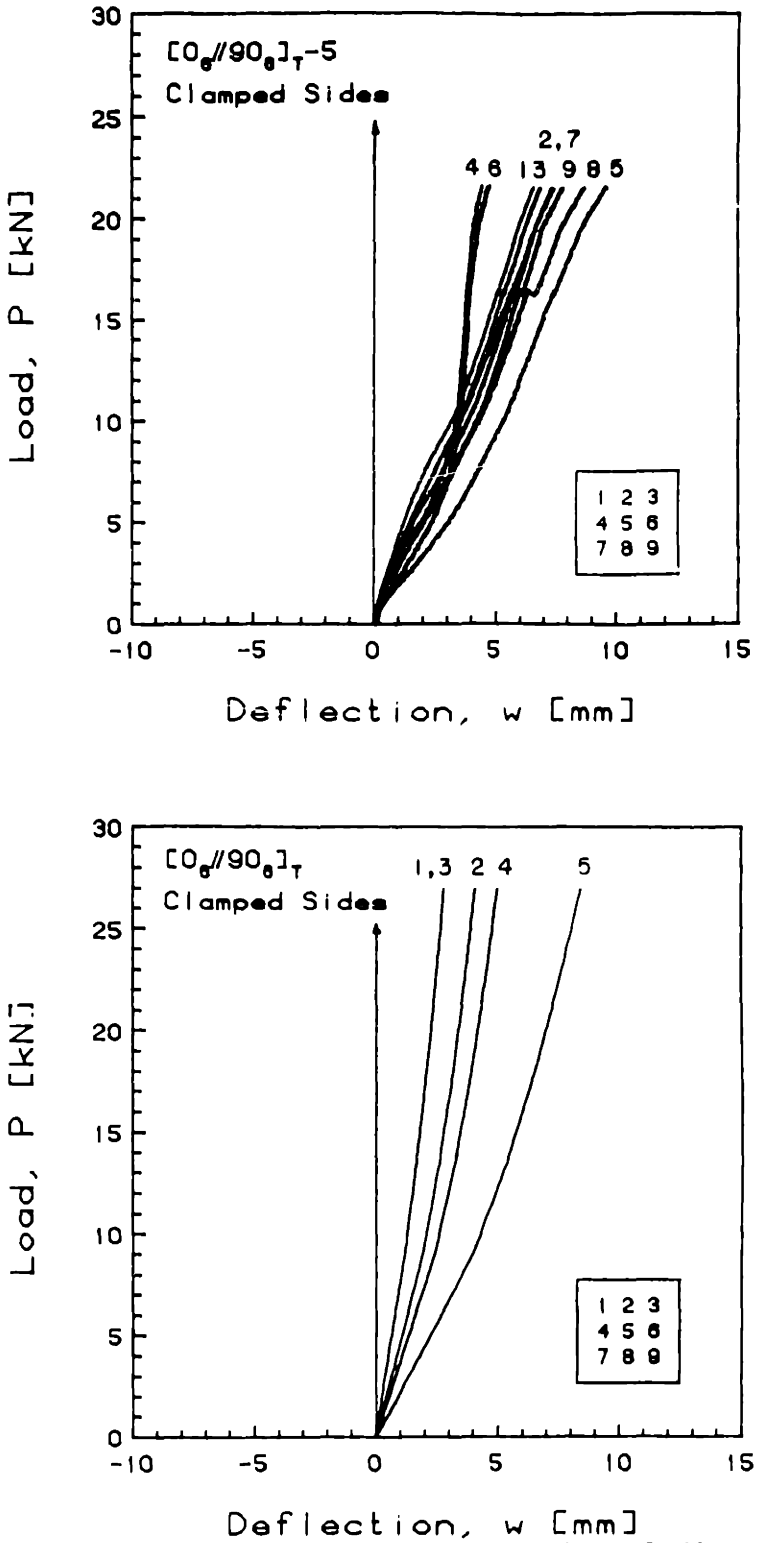

FIGURE 5.17 Experimental (top) and Predicted (bottom, via Rayleigh-Ritz) Plots of Applied Compressive Load versus Out-of-Plane Deflection for the $[0_6//90_6]_T$-5 Laminate with Clamped Side Boundary Conditions

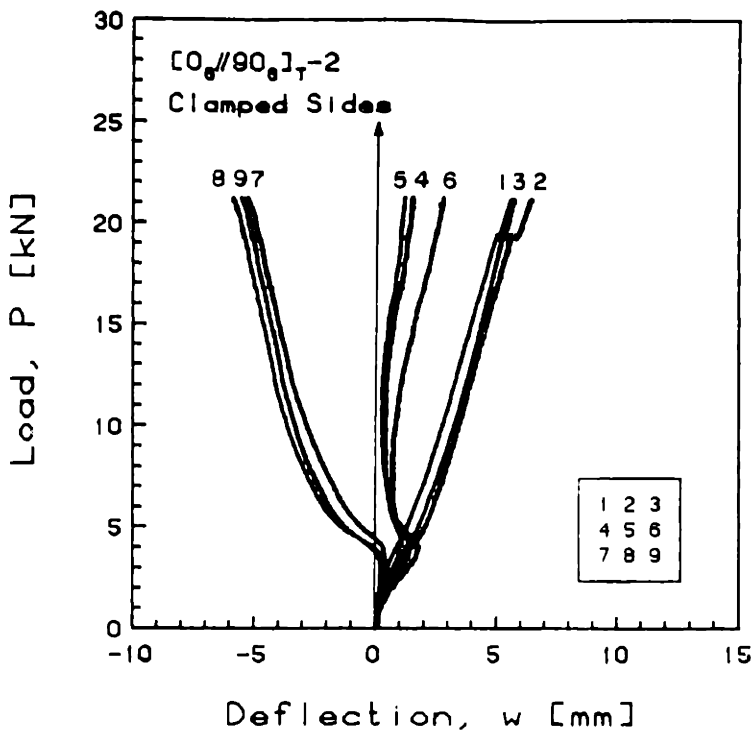

FIGURE 5.18 Experimental Plot of Applied Compressive Load versus Out-of-Plane Deflection for the $[0_6//90_6]_T$-2 Laminate with Clamped Side Boundary Conditions

with simply-supported side boundary conditions were more substantial than the experimentally measured equivalents. A likely explanation for this is that the clamped side boundary conditions in the experiment allowed some rotation at the edges of the plate, partially assimilating simply-supported side boundary conditions.

The experimental results and theoretical predictions for the $[0_3/90_3]_S$ laminate tested with simply-supported side boundary conditions are shown in Figure 5.19. The $[0_3//90_3//90_3//0_3]_T$ laminate, whose results are plotted in Figure 5.20, shows that the bondlines only slightly stiffen the laminates. This is similar to the behavior observed for the nominally identical laminates tested with clamped side boundary conditions.

The bending-stretching couplings, inherent in the $[0_3//90_3//0_3//90_3]_T$ laminates, cause a modest effect on the deflection behavior, as shown in Figure 5.21, by lowering the buckling load and increasing the deflections slightly. A comparison of the theoretical predictions for this laminate with the symmetric $[0_3//90_3//90_3//0_3]_T$ laminate reveals only a limited added compliance. Nevertheless, this effect is greater for laminates tested with simply-supported side boundary conditions than for the corresponding laminates tested with clamped side boundary conditions. Although no secondary mode was observed for this laminate, such behavior could be reasonably anticipated if more laminates were tested, since the behavior was generically similar to that displayed

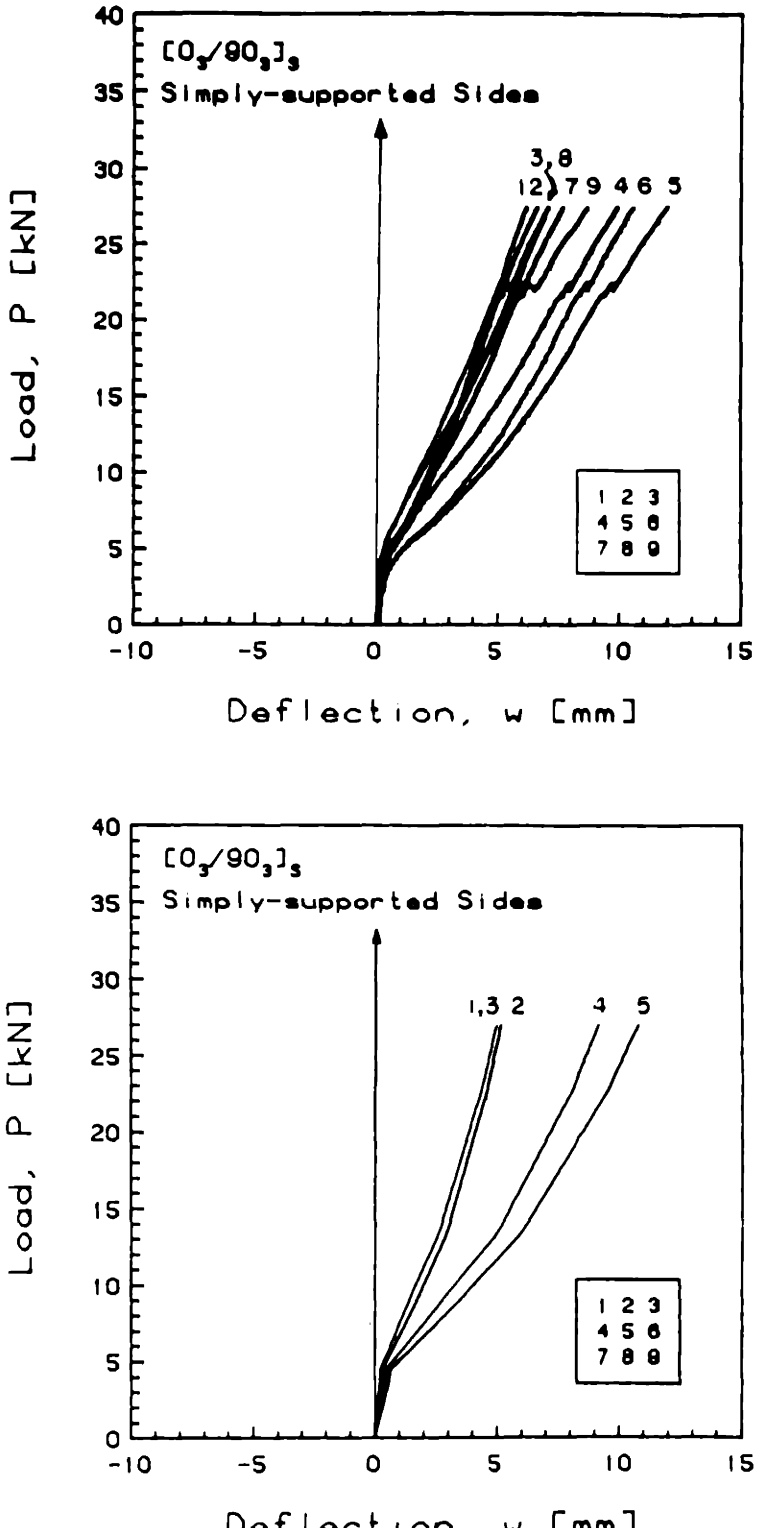

FIGURE 5.19 Experimental (top) and Predicted (bottom, via Rayleigh-Ritz) Plots of Applied Compressive Load versus Out-of-Plane Deflection for the $[0_3/90_3]_S$ Laminate with Simply-Supported Side Boundary Conditions

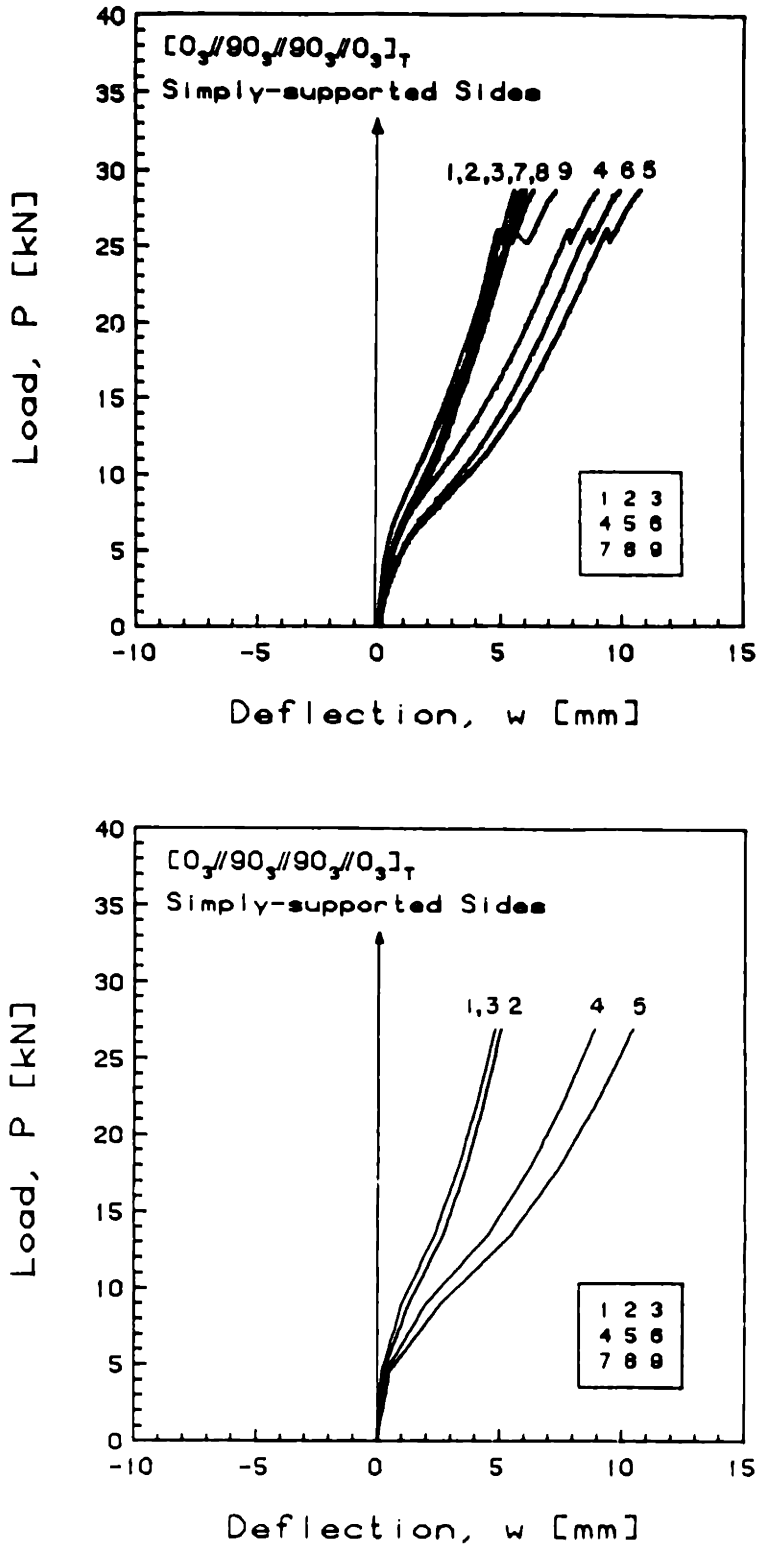

FIGURE 5.20 Experimental (top) and Predicted (bottom, via Rayleigh-Ritz) Plots of Applied Compressive Load versus Out-of-Plane Deflection for the $[0_3//90_3//90_3//0_3]_T$ Laminate with Simply-Supported Side Boundary Conditions

by nominally identical laminates tested with clamped side boundary conditions where both modes were observed.

For the $[0_2//45_2//0_2//45_2//0_2]_T$ and $[0_2//45_2//0_2//-45_2//0_2]_T$ laminates tested with simply-supported side boundary conditions, the experimental results are quite similar to each other (see Figures 5.22 and 5.23) while the analytical predictions indicate some subtle differences, such as the slight twist discernible in Figure 5.22 for the $[0_2//45_2//0_2//45_2//0_2]_T$ laminate due to the difference between the transducer readings at locations 1 and 3. Again, these curves are generically similar to those for the laminates tested with clamped side boundary conditions, but the laminates with simply-supported side boundary conditions exhibit less twist.

In the $[0_6//\theta_6]_T$ family of laminates, again, the behavior was similar to that observed for the laminates with the clamped side boundary conditions. For example, the $[0_6//15_6]_T$ laminate (Figure 5.24) tested with simply-supported side boundary conditions had deflections similar to those examined previously in Figure 5.7 for laminate $[0_6//15_6]_T$-5 tested with clamped side boundary conditions. Both of these laminates correlated well with the analytical solution for simply-supported side boundary conditions, plotted in Figure 5.24.

The $[0_6//30_6]_T$ laminate tested with simply-supported side boundary conditions demonstrated behavior remarkably similar to that of a nominally identical laminate tested with clamped

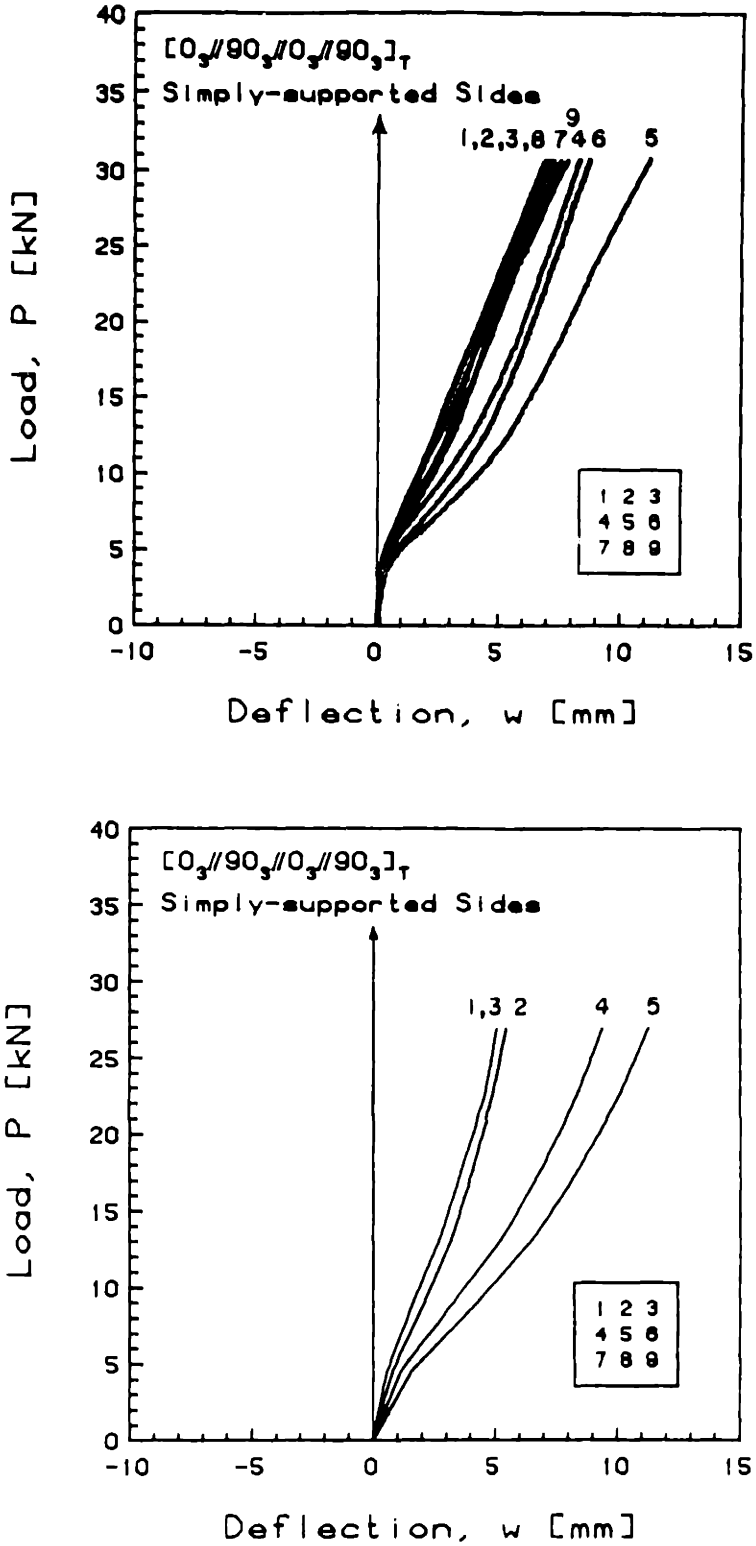

FIGURE 5.21 Experimental (top) and Predicted (bottom, via Rayleigh-Ritz) Plots of Applied Compressive Load versus Out-of-Plane Deflection for the $[0_3//90_3//0_3//90_3]_T$ Laminate with Simply-Supported Side Boundary Conditions

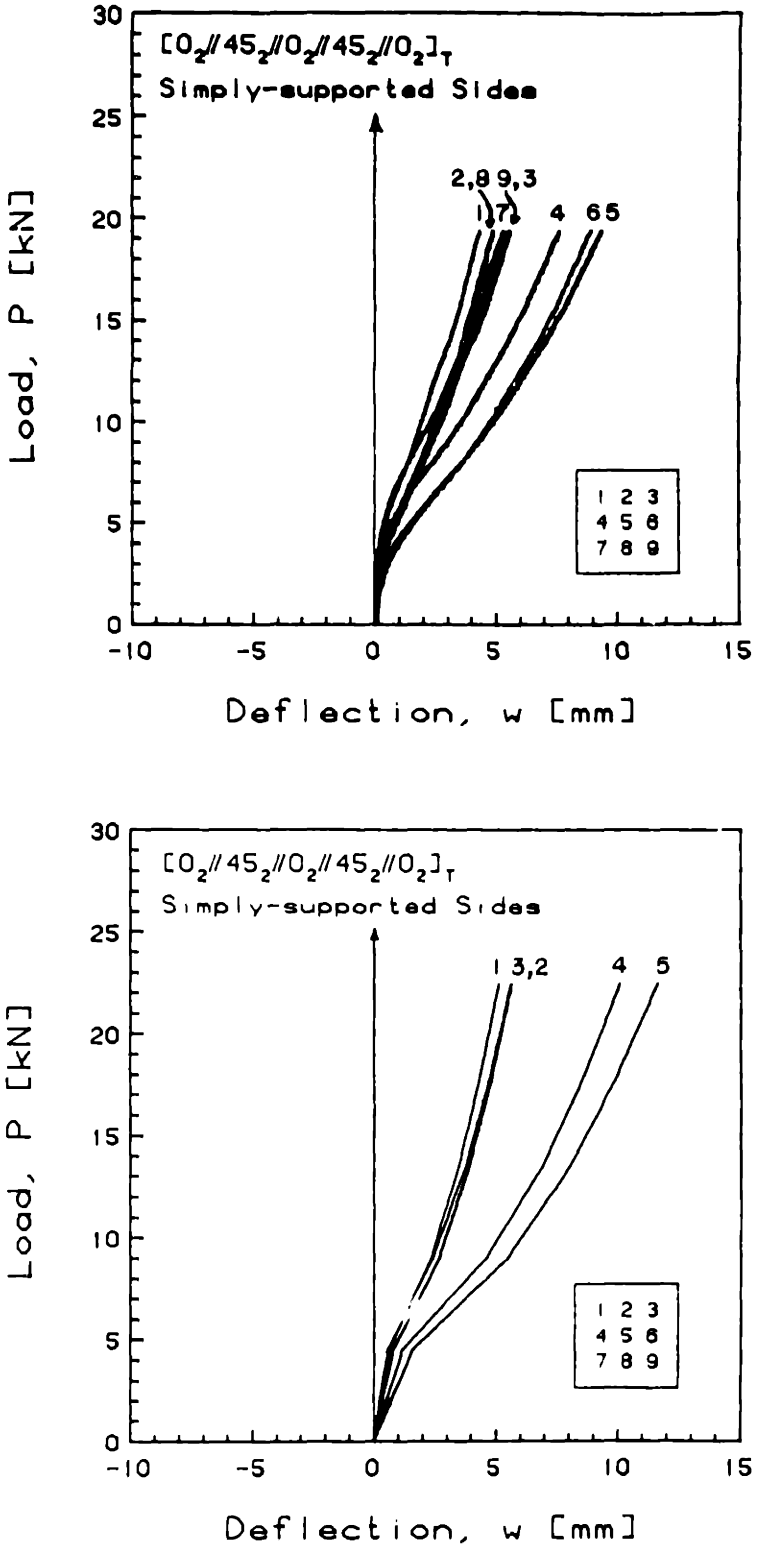

FIGURE 5.22 Experimental (top) and Predicted (bottom, via Rayleigh-Ritz) Plots of Applied Compressive Load versus Out-of-Plane Deflection for the $[0_2//45_2//0_2//45_2//0_2]_T$ Laminate with Simply-Supported Side Boundary Conditions

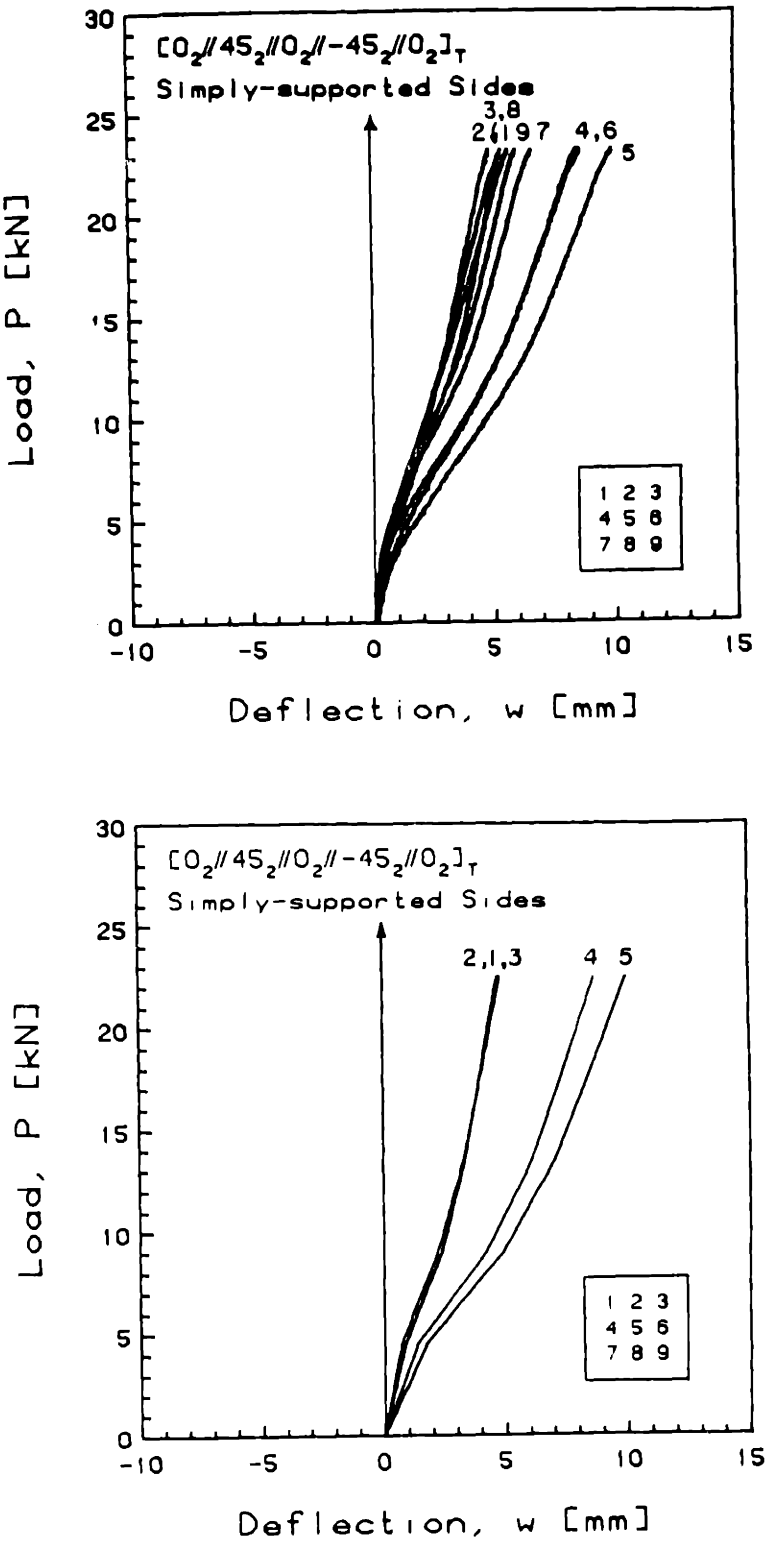

FIGURE 5.23 Experimental (top) and Predicted (bottom, via Rayleigh-Ritz) Plots of Applied Compressive Load versus Out-of-Plane Deflection for the $[0_2//45_2//0_2//-45_2//0_2]_T$ Laminate with Simply-Supported Side Boundary Conditions

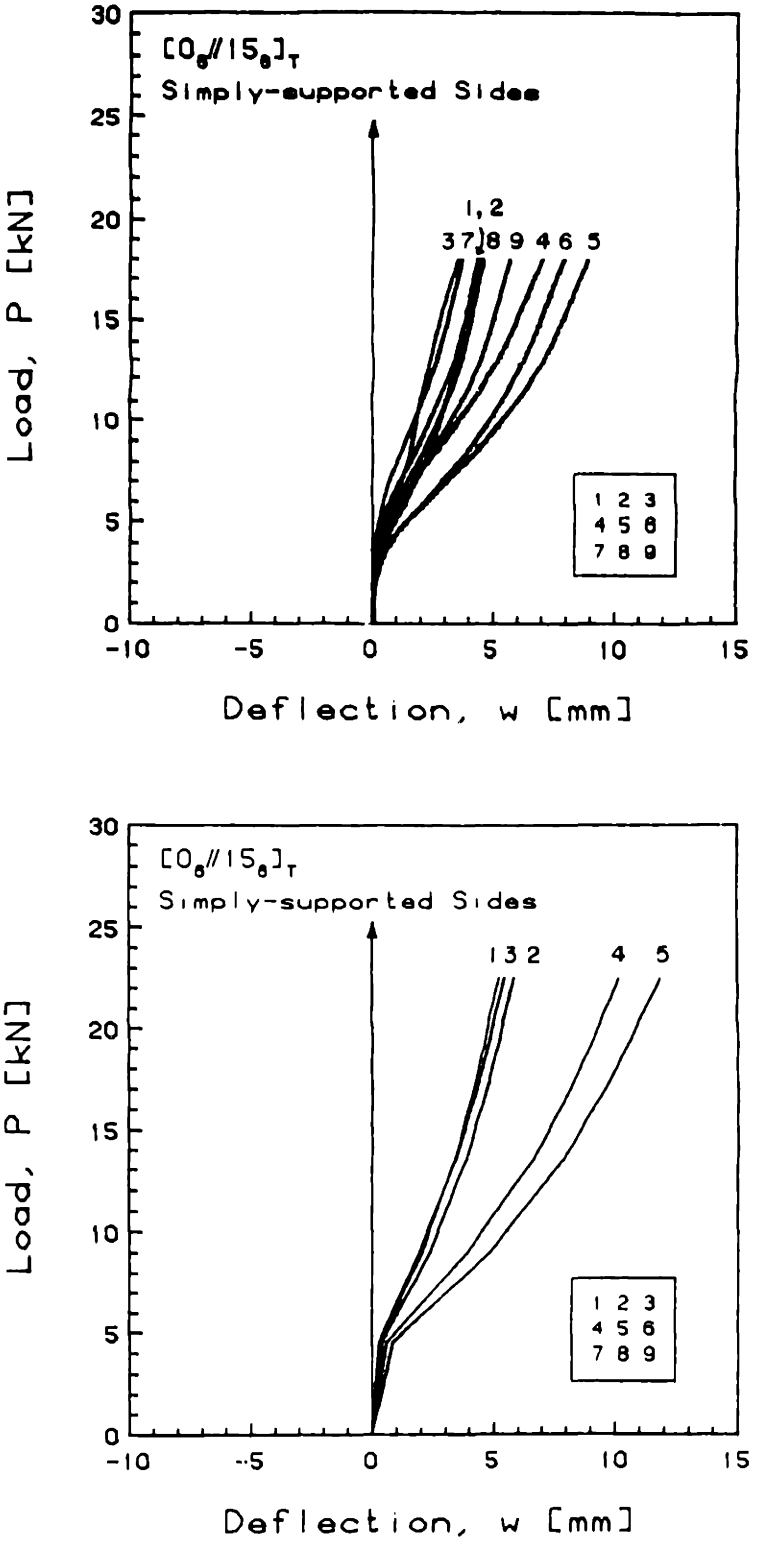

FIGURE 5.24 Experimental (top) and Predicted (bottom, via Rayleigh-Ritz) Plots of Applied Compressive Load versus Out-of-Plane Deflection for the $[0_6//15_6]_T$ Laminate with Simply-Supported Side Boundary Conditions

side boundary conditions, $[0_6//30_6]_T$-2 (see Figure 5.8). The behavior of the simply-supported version, shown in Figure 5.25, revealed larger deflections, but the deflection patterns were almost identical and showed twisting effects, as evidenced by the difference between the deflections at locations 1, 2, and 3. As before, this twisting was not assumed in the nonlinear Rayleigh-Ritz analysis.

One of the laminates tested with simply-supported side boundary conditions which exhibited an interesting deflection behavior was the $[0_6//45_6]_T$ laminate. The simply-supported version buckled into the second mode, as did several of the clamped versions (compare Figures 5.26 and 5.11). The two responses, once again, are extremely similar. However, the analytical predictions for the $[0_6//45_6]_T$ laminate with simply-supported side boundary conditions were much less twisted than the predictions for the same laminate with clamped side boundary conditions, previously discussed. The simply-supported version predicted only a first mode behavior, similar to the predictions for the other laminates.

Since second mode behavior was still not predicted to represent the minimum energy for this configuration, the theoretical plot, shown in Figure 5.26 for this laminate, does not correlate well with the experimentally observed behavior. Interestingly enough, however, it does qualitatively resemble the first mode behavior of nominally identical laminates tested with clamped side boundary conditions, such as that of laminate $[0_6//45_6]_T$-4 depicted in Figure 10, indicating that

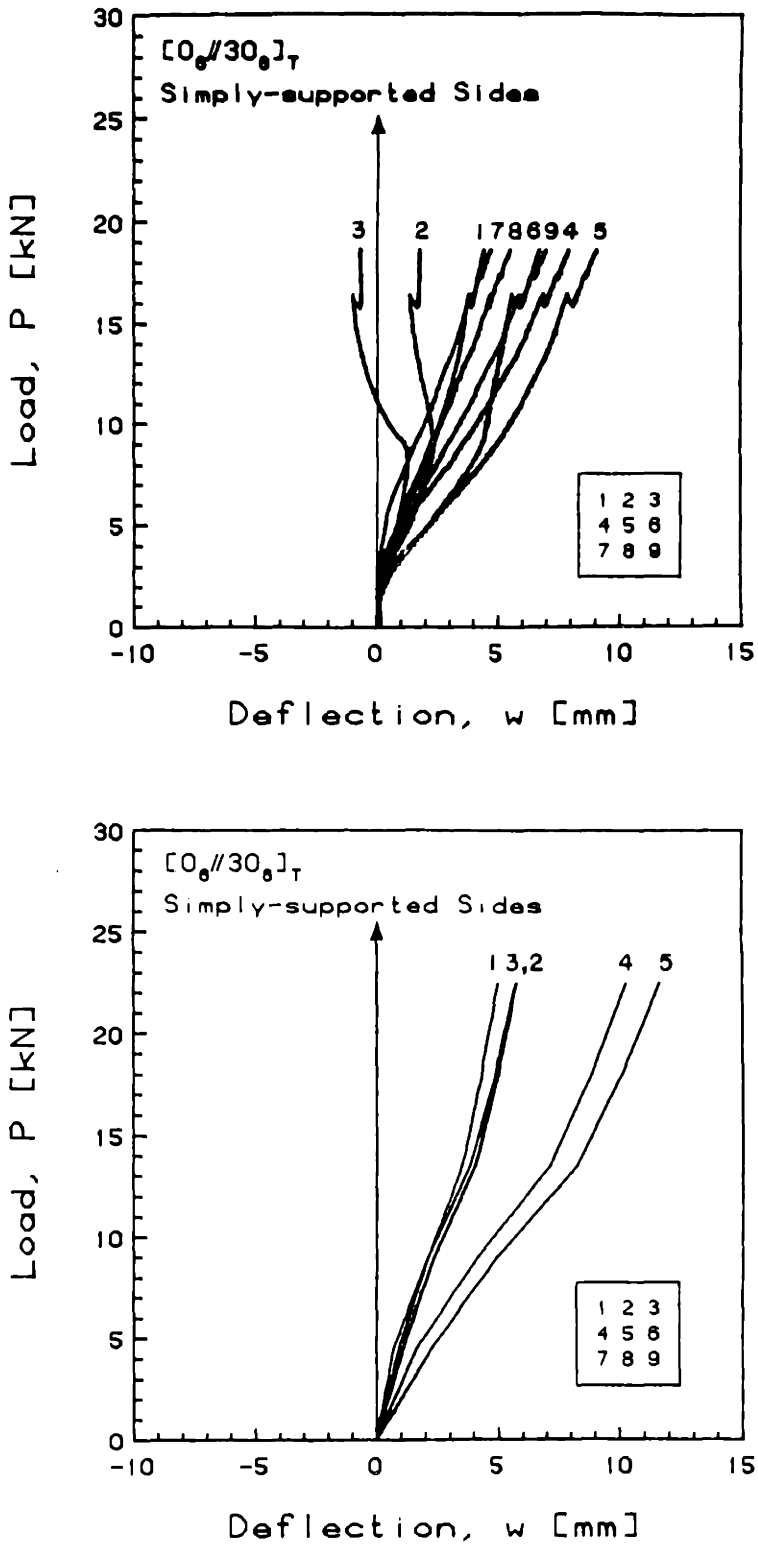

FIGURE 5.25 Experimental (top) and Predicted (bottom, via Rayleigh-Ritz) Plots of Applied Compressive Load versus Out-of-Plane Deflection for the $[0_6//30_6]_T$ Laminate with Simply-Supported Side Boundary Conditions

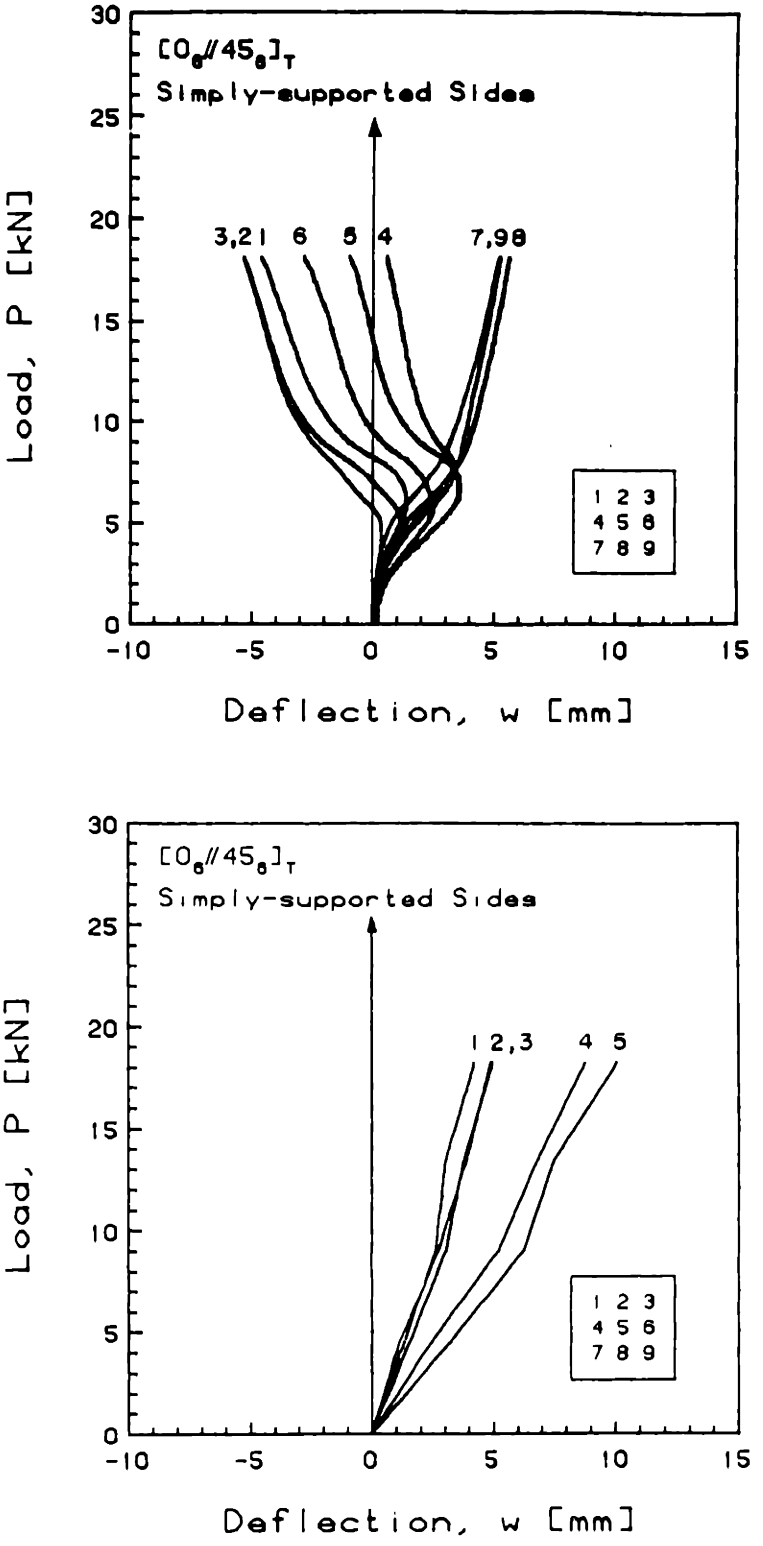

FIGURE 5.26 Experimental (top) and Predicted (bottom, via Rayleigh-Ritz) Plots of Applied Compressive Load versus Out-of-Plane Deflection for the $[O_6//45_6]_T$ Laminate with Simply-Supported Side Boundary Conditions

some of the inherent coupling mechanisms were adequately modelled in the analysis.

Likewise, the $[0_6//60_6]_T$ laminate tested with simply-supported side boundary conditions snapped into a secondary bending mode. Its behavior, shown in Figure 5.27, correlates better with its clamped counterpart in Figure 5.13 than with the theoretical predictions.

Another interesting case was the $[0_6//75_6]_T$ laminate where the analysis predicted the changes in stiffness observed experimentally, especially above 10 kN. The experimental and analytical results for that laminate, which, again, correlate very well, are shown in Figure 5.28.

The remaining laminate tested with simply-supported side boundary conditions, $[0_6//90_6]_T$ (shown in Figure 5.29), displayed a behavior very similar to some of the clamped laminates of the same type (e.g., see Figure 5.17). The experimental and theoretical load versus deflection curves correlate very well for this laminate. Comparison of the theoretical solution in Figure 5.29 with the corresponding solution for clamped side boundary conditions, in Figure 5.17, shows the theoretical stiffening due to the additional fixity of the clamped boundary conditions. However, laminates tested with both types of side boundary conditions exhibited behavior which corresponds more closely to the theoretical solution for simply-supported side boundary conditions. Again, this indicates that the clamped side boundary conditions were more compliant than was predicted by the analysis.

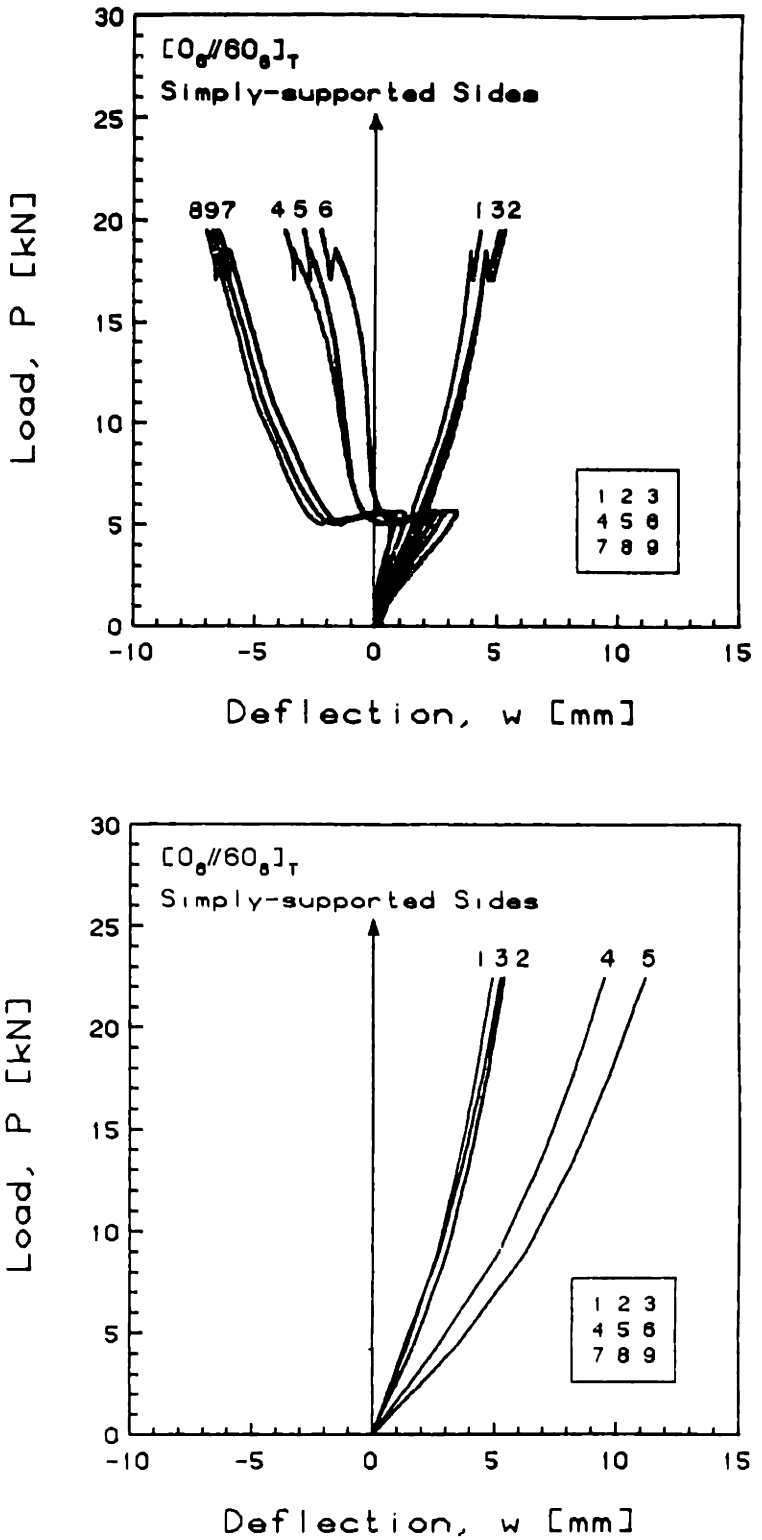

FIGURE 5.27 Experimental (top) and Predicted (bottom, via Rayleigh-Ritz) Plots of Applied Compressive Load versus Out-of-Plane Deflection for the $[0_6//60_6]_T$ Laminate with Simply-Supported Side Boundary Conditions

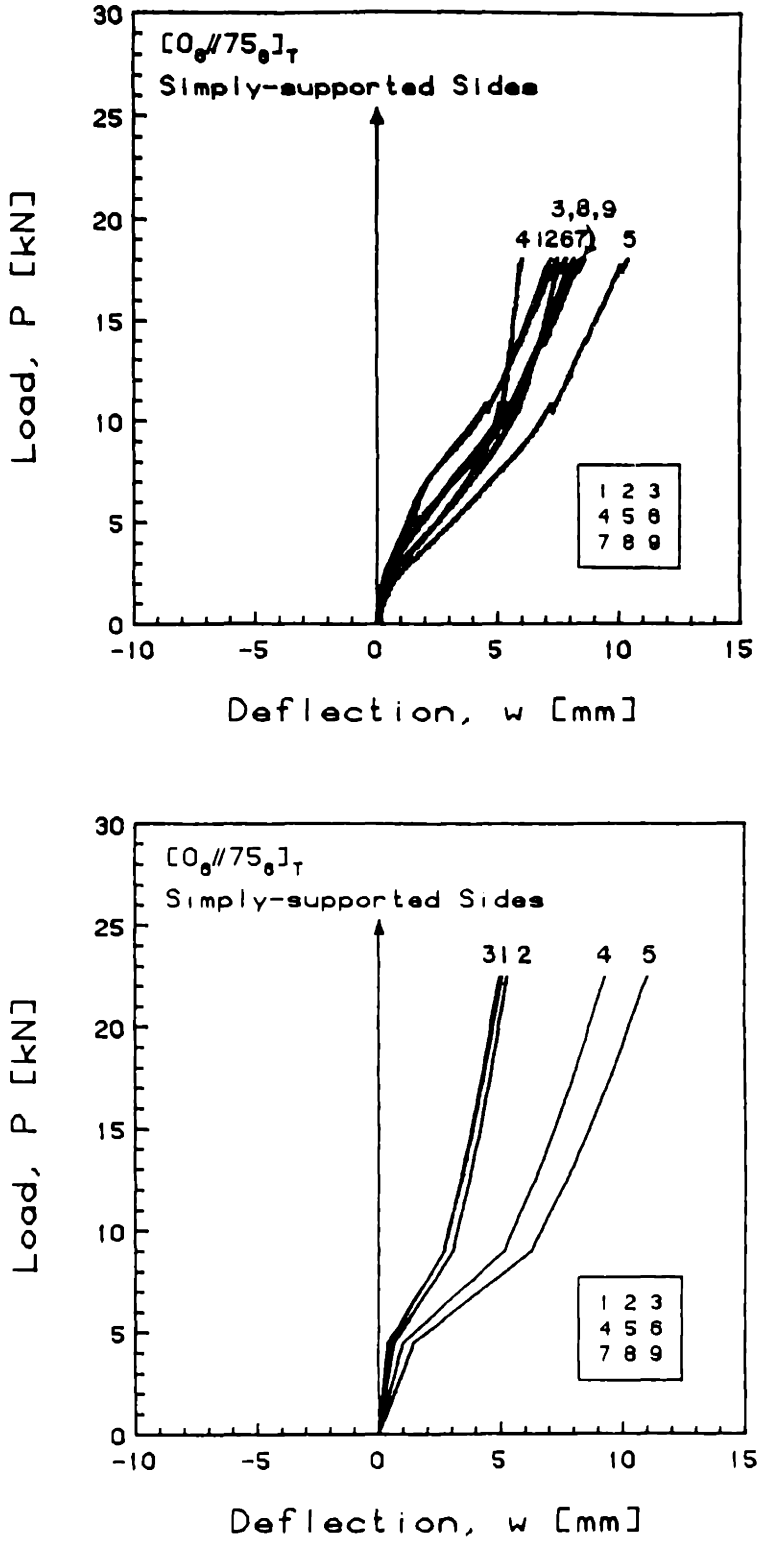

FIGURE 5.28 Experimental (top) and Predicted (bottom, via Rayleigh-Ritz) Plots of Applied Compressive Load versus Out-of-Plane Deflection for the $[0_6//75_6]_T$ Laminate with Simply-Supported Side Boundary Conditions

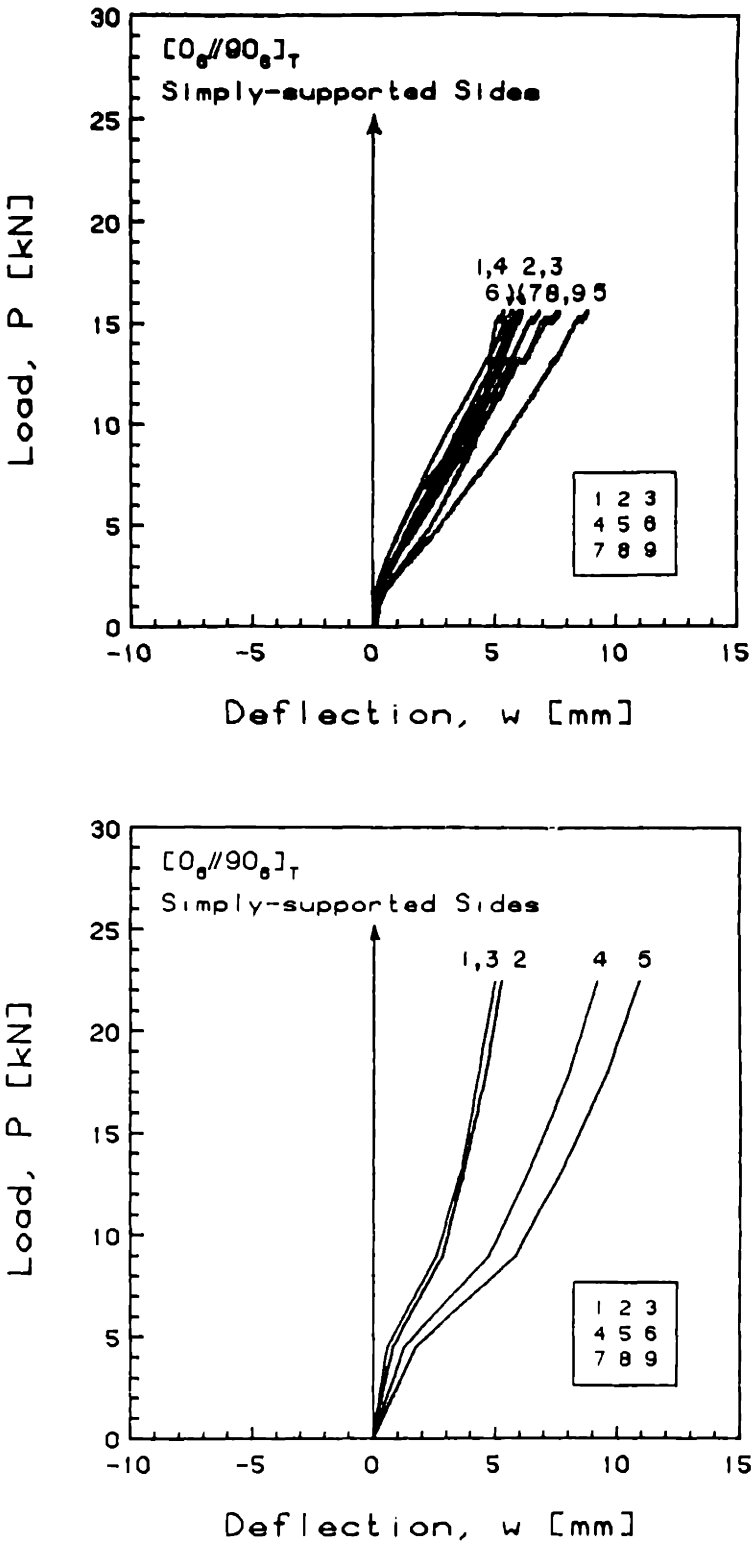

FIGURE 5.29 Experimental (top) and Predicted (bottom, via Rayleigh-Ritz) Plots of Applied Compressive Load versus Out-of-Plane Deflection for the $[0_6//90_6]_T$ Laminate with Simply-Supported Side Boundary Conditions

5.1.3 Free Sides

Graphs of the experimental load versus out-of-plane deflection, w, for each of the laminates tested with free side boundary conditions are also included here for completeness, since only one of each type of laminate was tested with free side boundary conditions. For example, Figure 5.30 presents this data for the $[0_3/90_3]_S$ laminate. Here, it is obvious that no postbuckling stiffening of the plate occurred. This is, therefore, a classical bifurcation buckling problem almost completely defined by the critical buckling load alone.

A quick glance at Figures 5.30 and 5.31 reveals the effect of the room temperature bondline on these two otherwise nominally identical laminates tested with free side boundary conditions. Compared with the $[0_3/90_3]_S$ laminate, the $[0_3//90_3//90_3//0_3]_T$ laminate has a larger bending stiffness, and consequently larger moment of inertia. It therefore exhibits increased stiffness and a higher buckling load.

The $[0_3//90_3//0_3//90_3]_T$ laminate in Figure 5.32 shows how bending-stretching coupling reduces the primary bending stiffness, by shifting the neutral axis (as discussed in depth in Section 6.3). However, the buckling load is slightly lower than expected from the longitudinal bending stiffness, D_{11}, alone. Otherwise, the out-of-plane deflections were so large that any effects due to the elastic couplings were overshadowed.

Comparison of the $[0_2//45_2//0_2//45_2//0_2]_T$ and

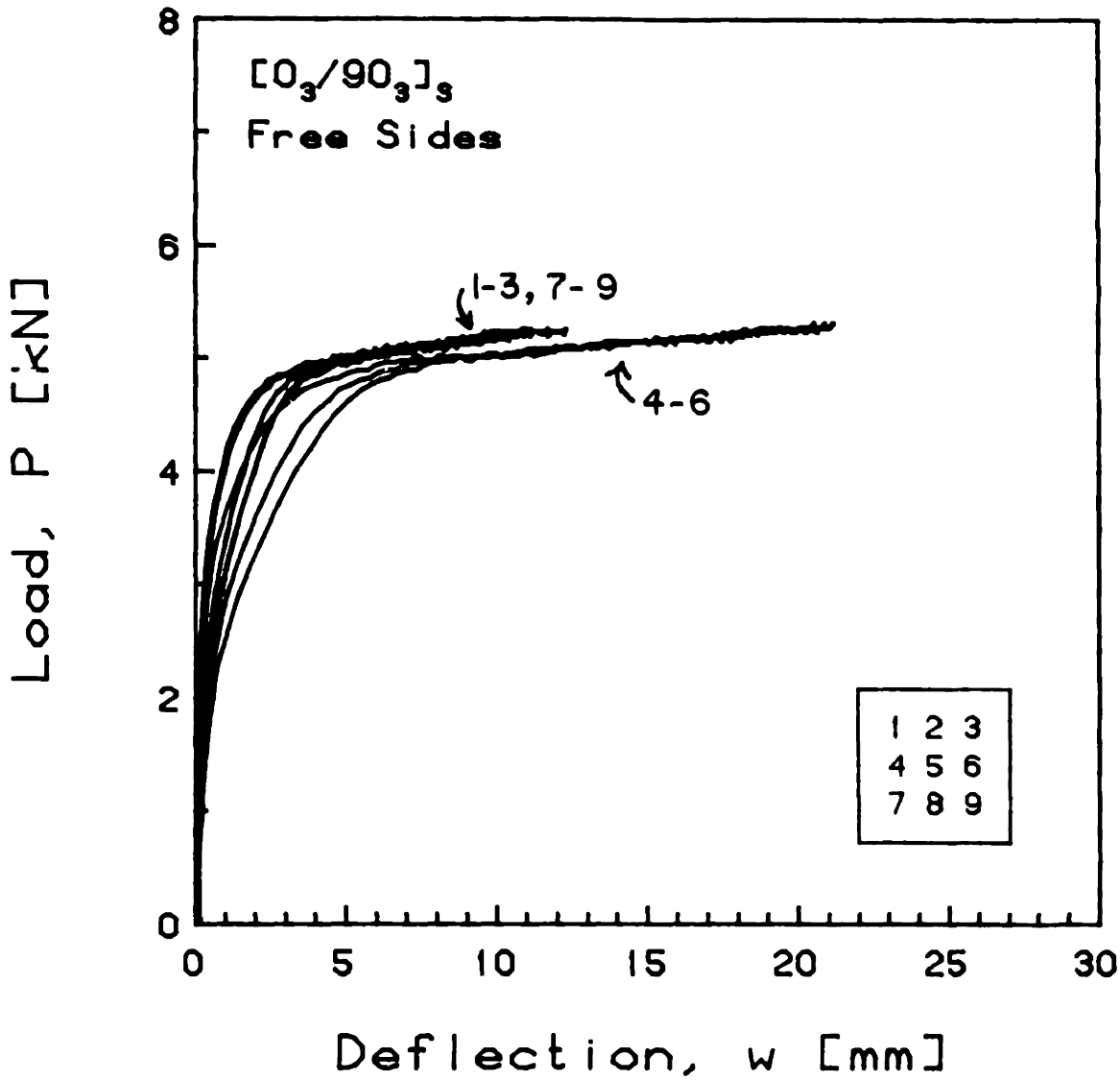

FIGURE 5.30 Experimental Plot of Applied Compressive Load versus Out-of-Plane Deflection for the $[0_3/90_3]_S$ Laminate with Free Side Boundary Conditions

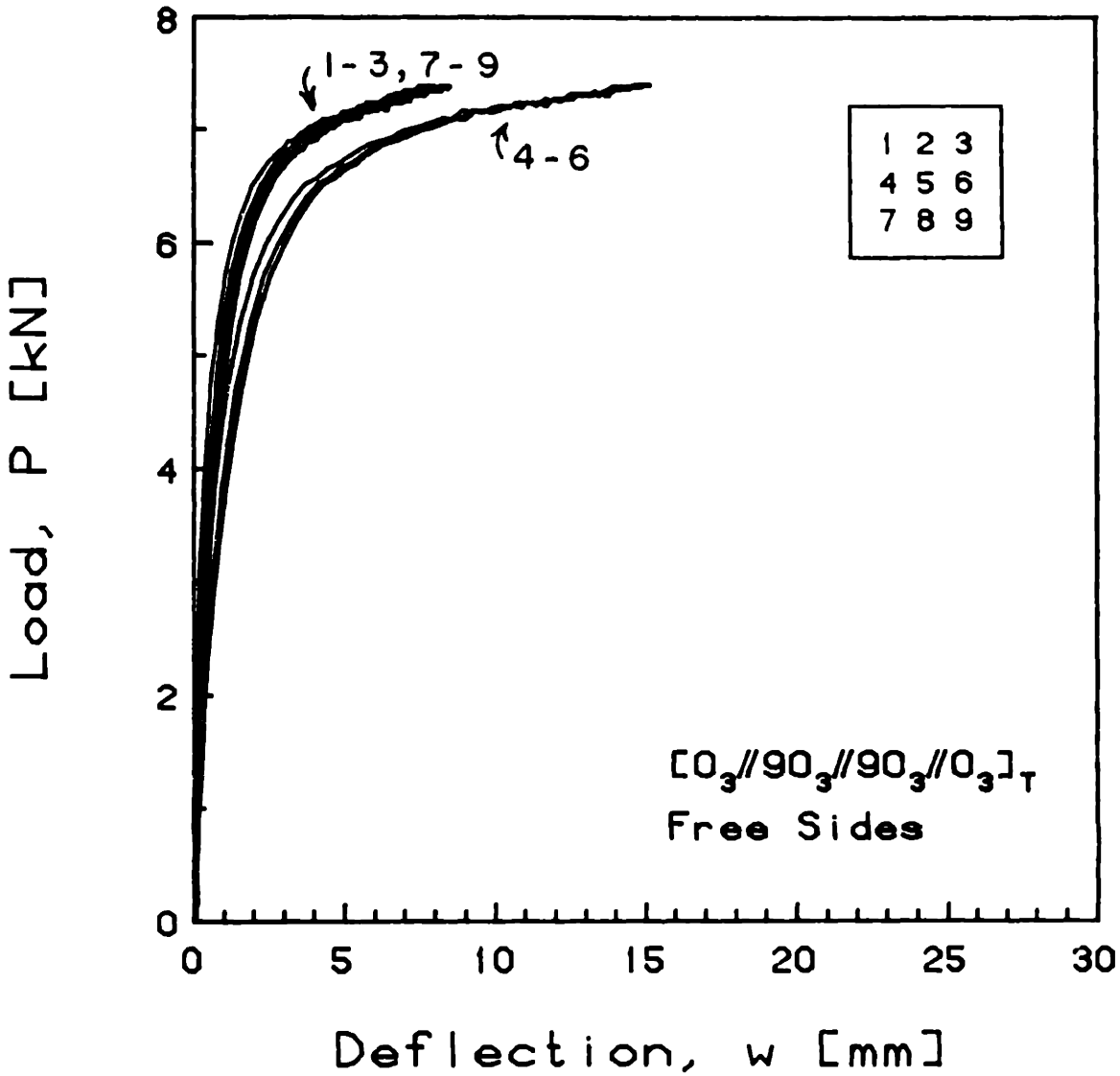

FIGURE 5.31 Experimental Plot of Applied Compressive Load versus Out-of-Plane Deflection for the $[0_3//90_3//90_3//0_3]_T$ Laminate with Free Side Boundary Conditions

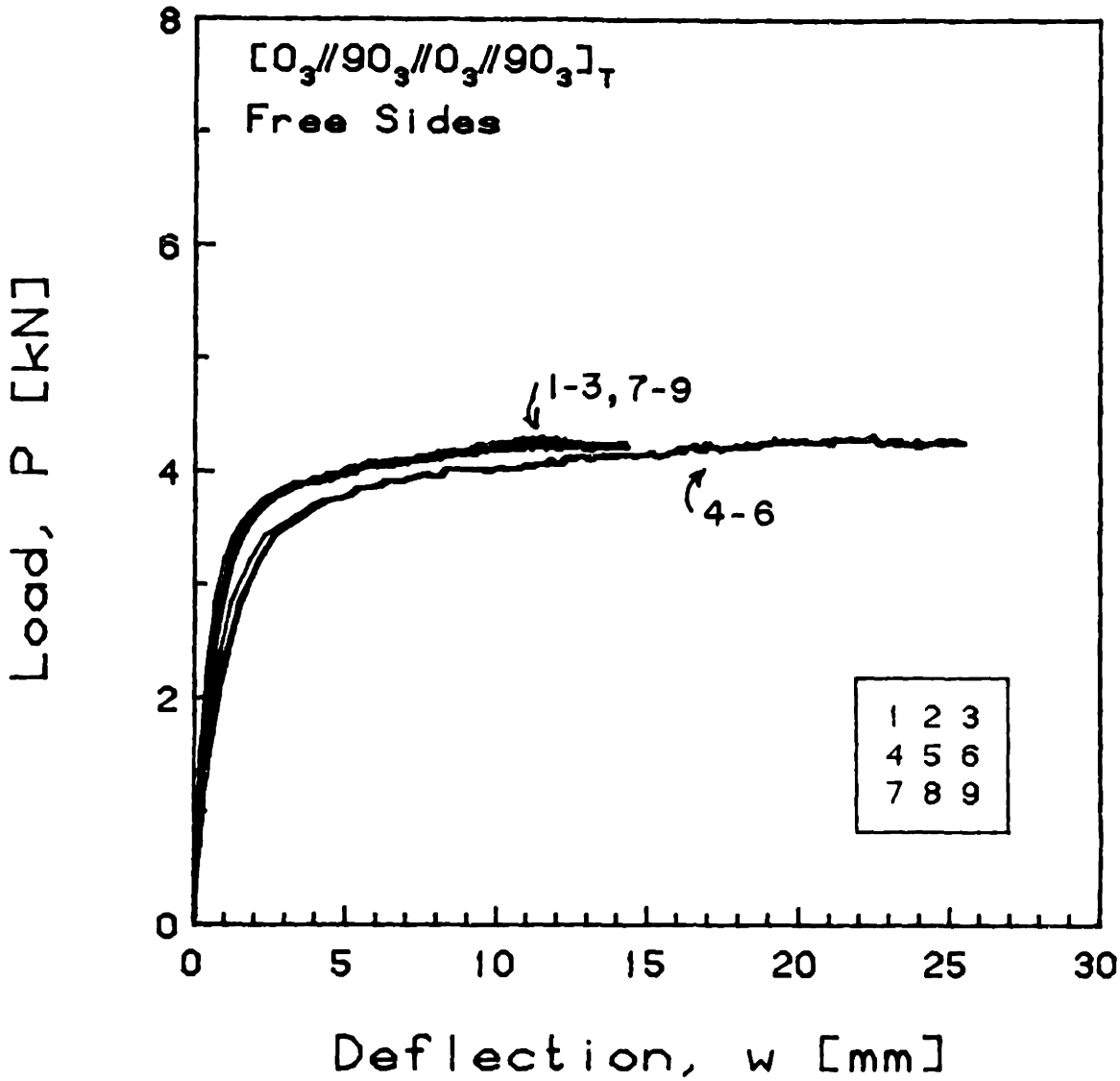

FIGURE 5.32 Experimental Plot of Applied Compressive Load versus Out-of-Plane Deflection for the $[0_3//90_3//0_3//90_3]_T$ Laminate with Free Side Boundary Conditions

$[0_2//45_2//0_2//-45_2//0_2]_T$ laminates tested with free side boundary conditions (Figures 5.33 and 5.34, respectively) reinforces the perception that in-plane/out-of-plane elastic coupling (i.e., manifest by the existence of B_{ij}, referred heretofore to as membrane-flexural coupling) reduces the buckling load even more than the longitudinal bending stiffness (D_{11}) can account for alone. The $[0_2//45_2//0_2//-45_2//0_2]_T$ laminate, which possessed a modest amount of stretching-twisting coupling, buckled approximately 10% lower than the $[0_2//45_2//0_2//45_2//0_2]_T$ laminate, which had nominally identical elastic properties other than the shearing- and twisting- couplings.

Finally, as θ was increased from 15° to 90° in the $[0_6//\theta_6]_T$ laminates, the buckling load steadily decreased along with the reduced longitudinal bending stiffness, D_{11}. The load versus out-of-plane deflection behavior for these laminates is shown in Figures 5.35 through 5.40.

5.2 Load versus Longitudinal Strain, ε

Since an anisotropic plate has an undefinable elastic axis due to the existence of different B-matrix couplings, the definition of the longitudinal modulus of the specimen becomes arbitrary with respect to the axis system and centerline as defined. Therefore, in order to compare theoretical calculations with experimental measurements, the ratio of the applied load resultant, N_x, to the longitudinal strain at the

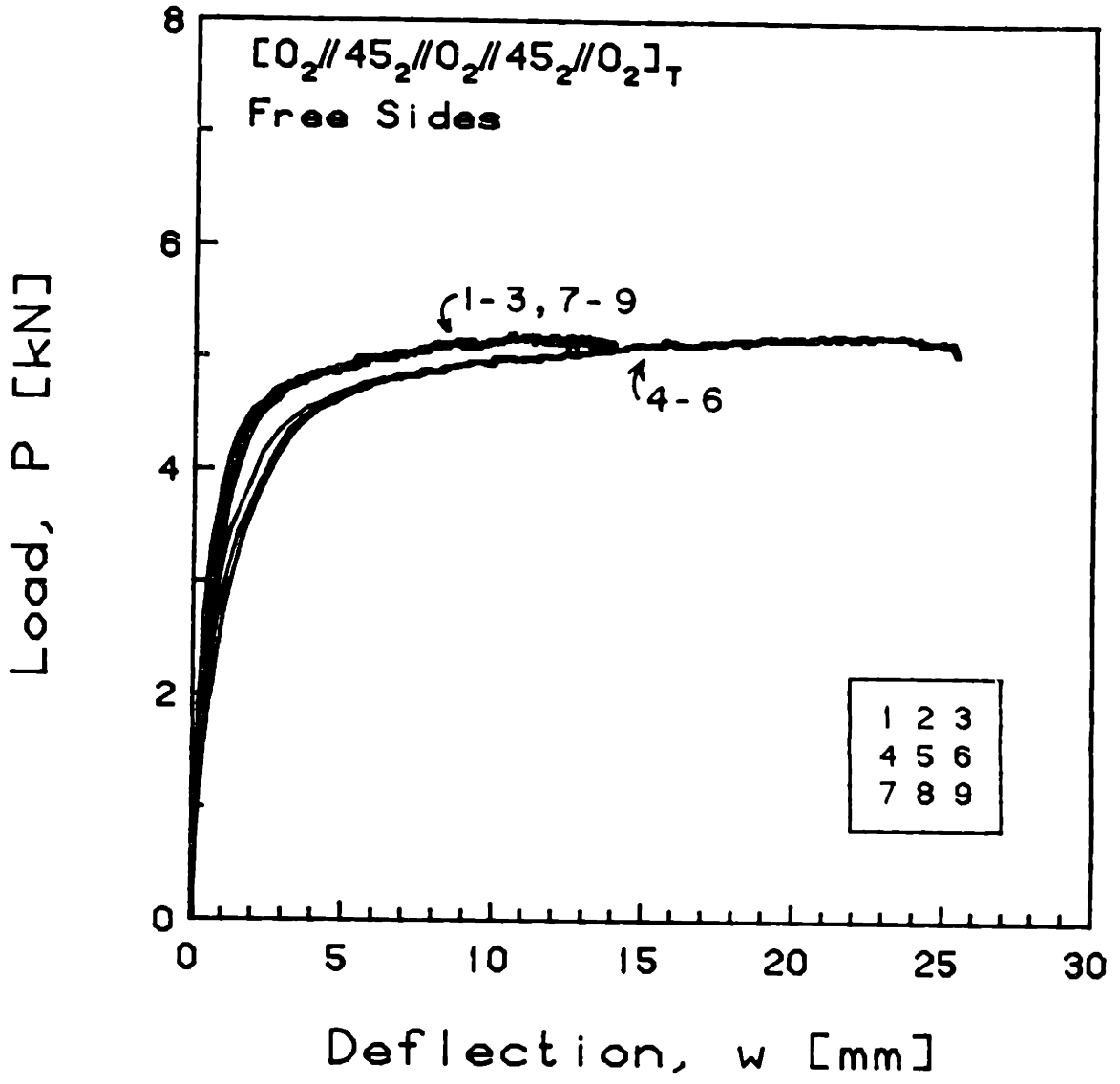

FIGURE 5.33 Experimental Plot of Applied Compressive Load versus Out-of-Plane Deflection for the $[0_2//45_2//0_2//45_2//0_2]_T$ Laminate with Free Side Boundary Conditions

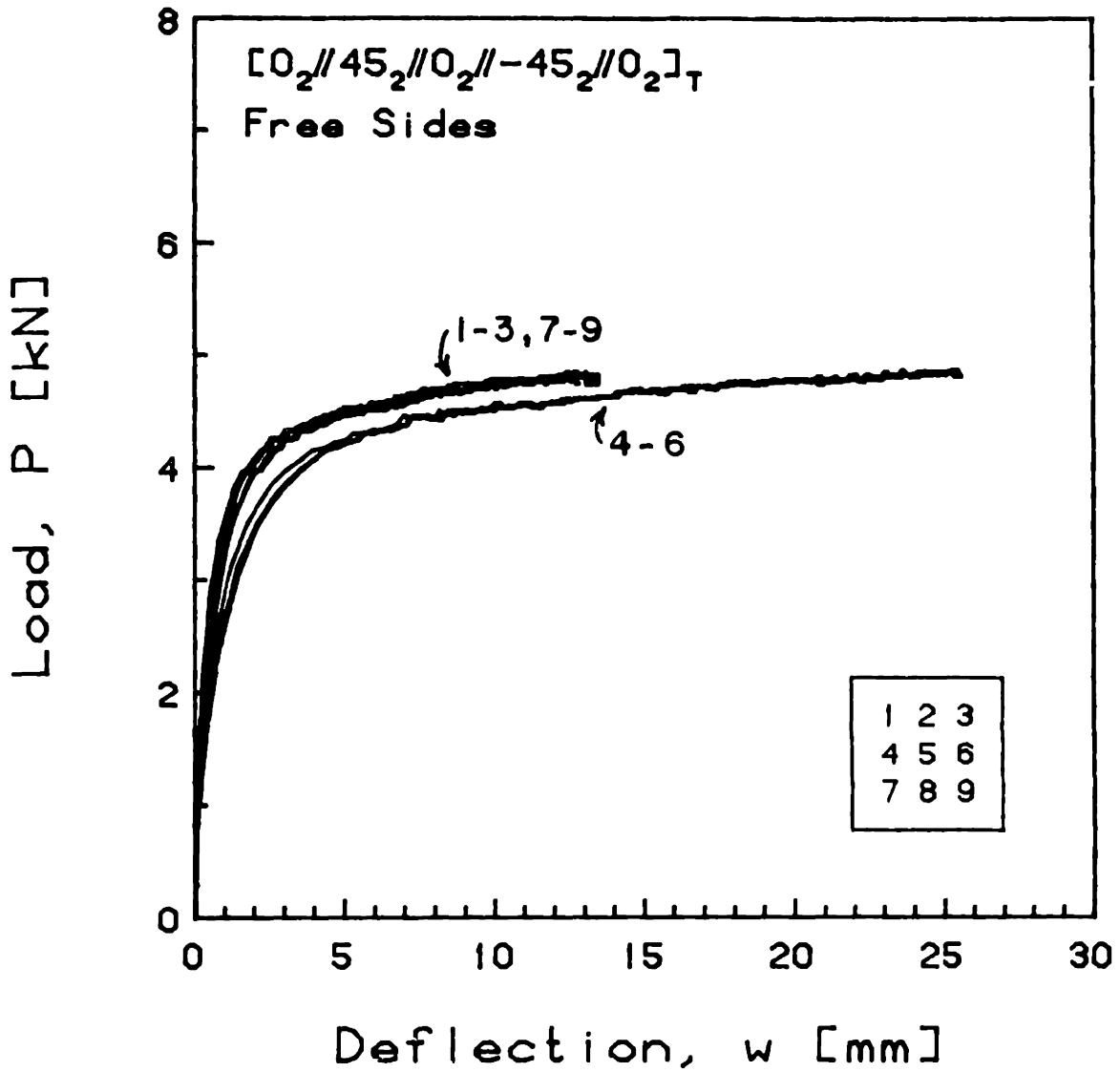

FIGURE 5.34 Experimental Plot of Applied Compressive Load versus Out-of-Plane Deflection for the $[O_2//45_2//O_2//-45_2//O_2]_T$ Laminate with Free Side Boundary Conditions

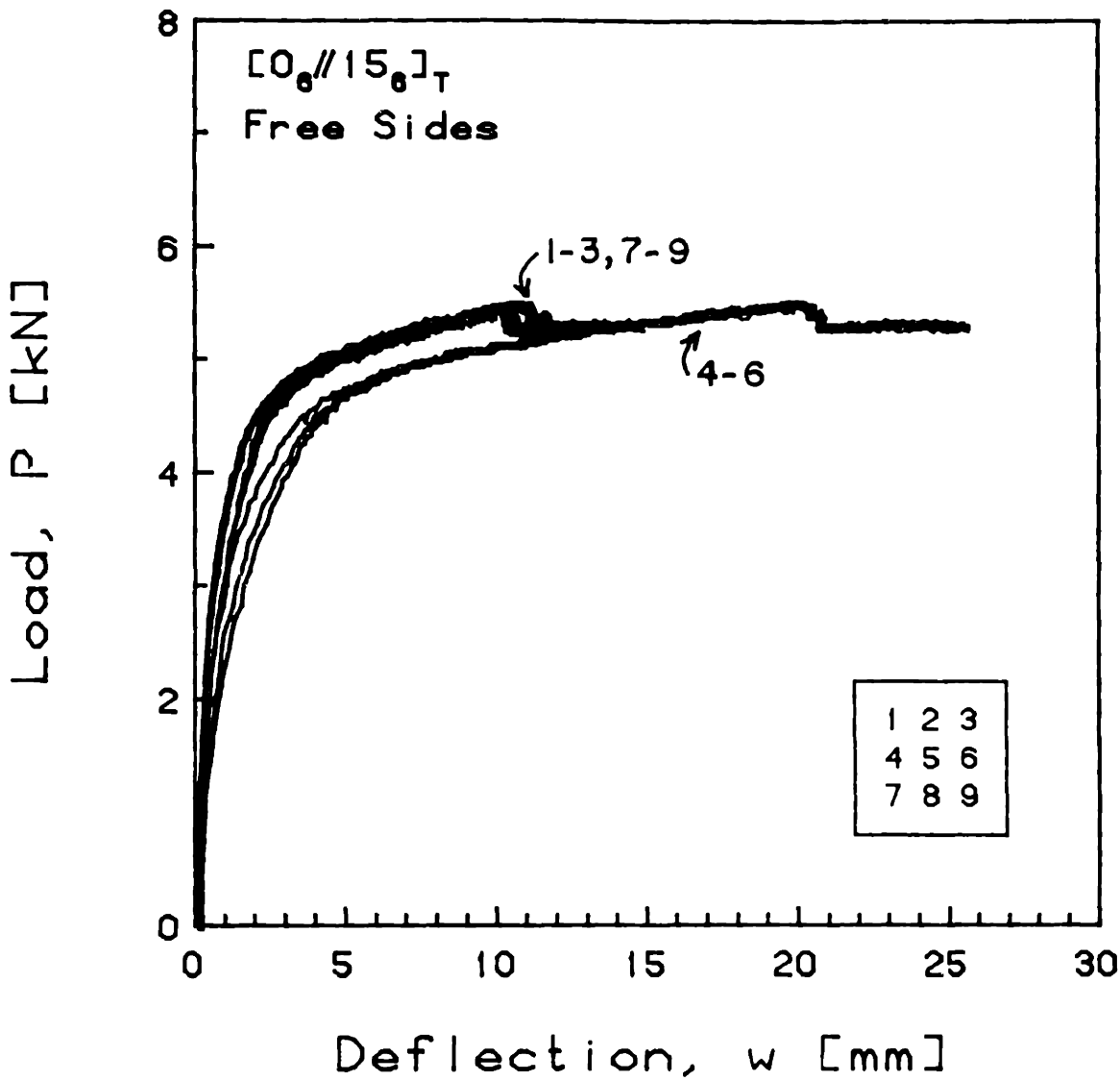

FIGURE 5.35 Experimental Plot of Applied Compressive Load versus Out-of-Plane Deflection for the $[0_6//15_6]_T$ Laminate with Free Side Boundary Conditions

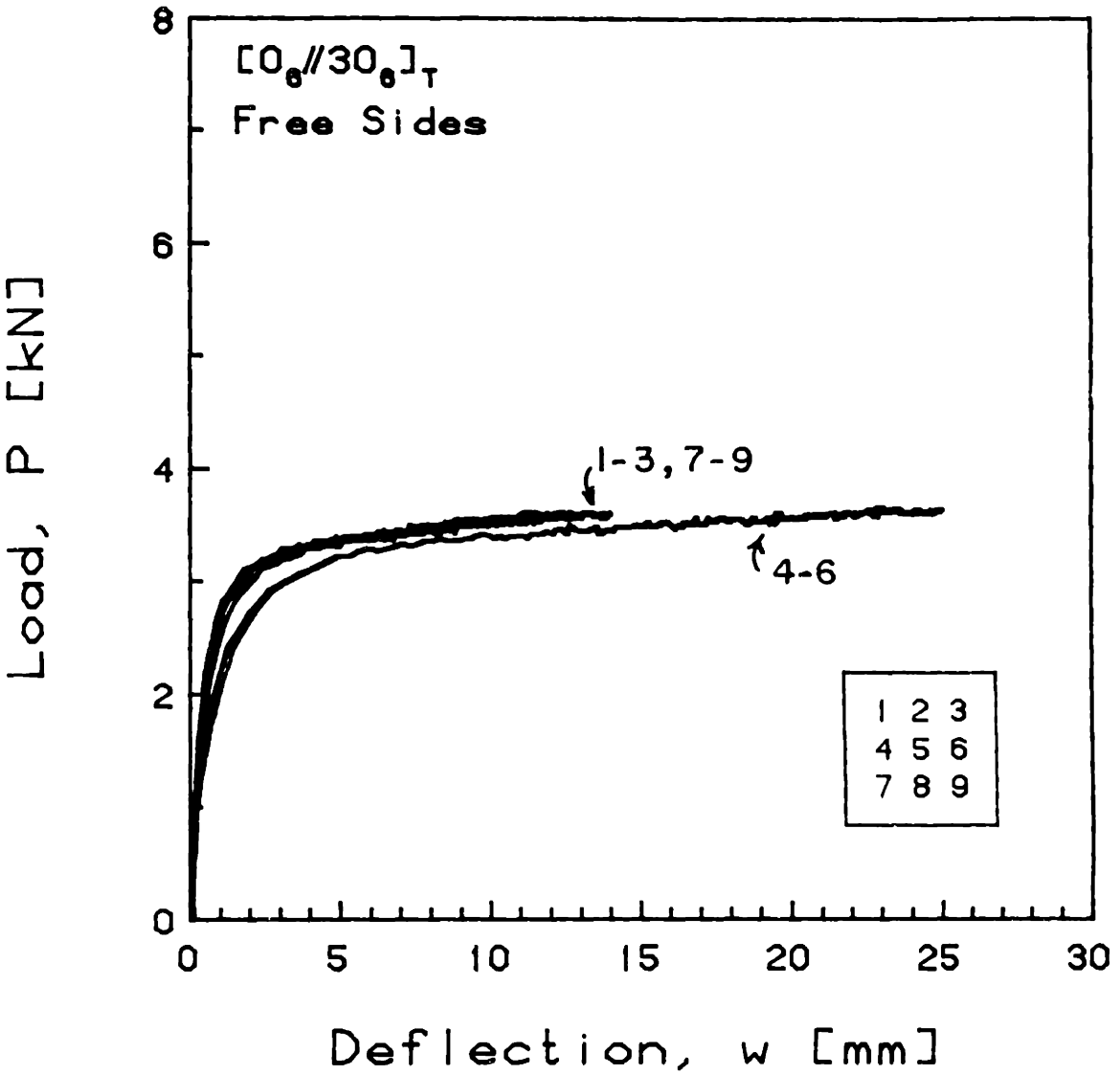

FIGURE 5.36 Experimental Plot of Applied Compressive Load versus Out-of-Plane Deflection for the $[0_6//30_6]_T$ Laminate with Free Side Boundary Conditions

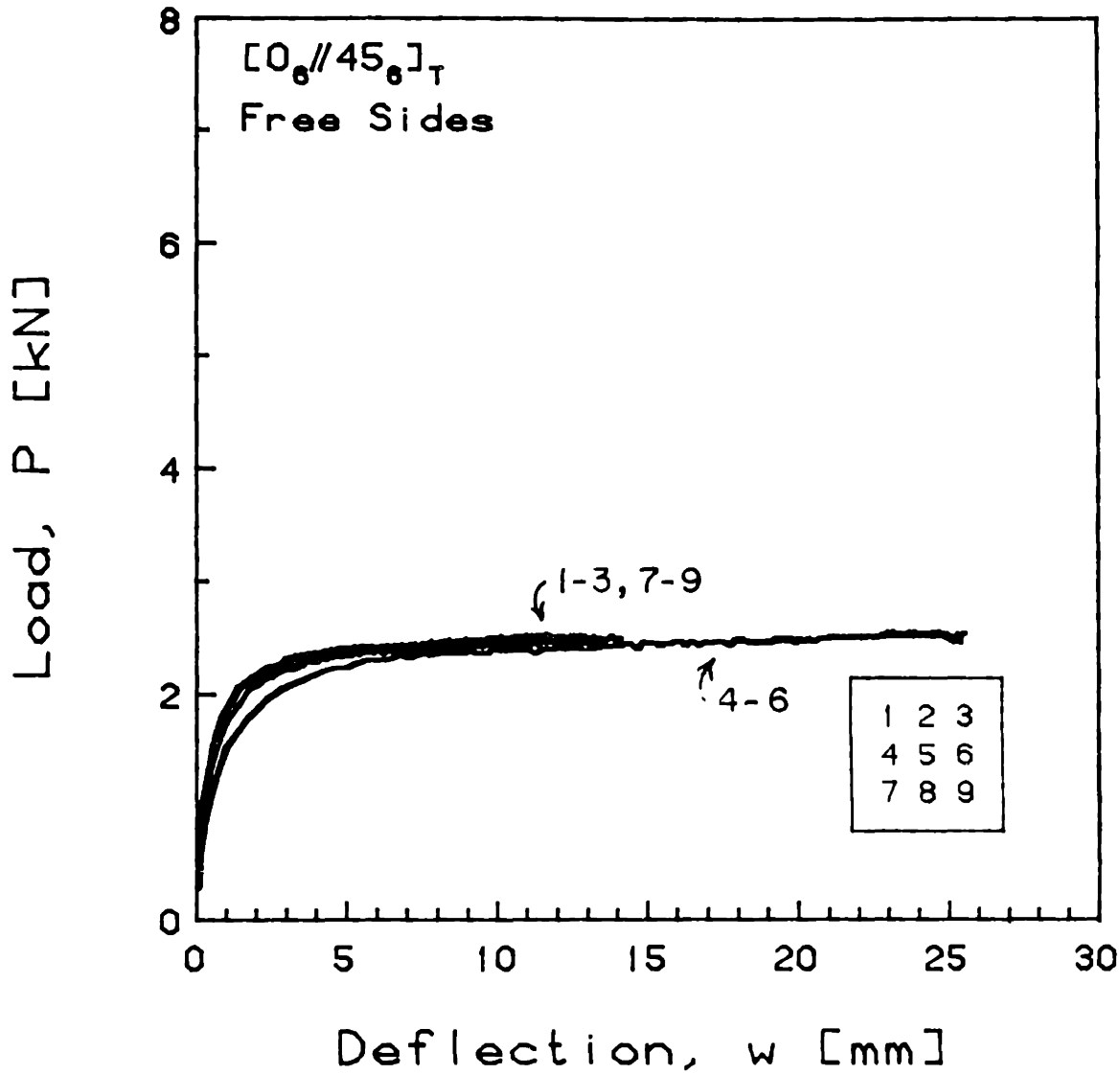

FIGURE 5.37 Experimental Plot of Applied Compressive Load versus Out-of-Plane Deflection for the $[0_6//45_6]_T$ Laminate with Free Side Boundary Conditions

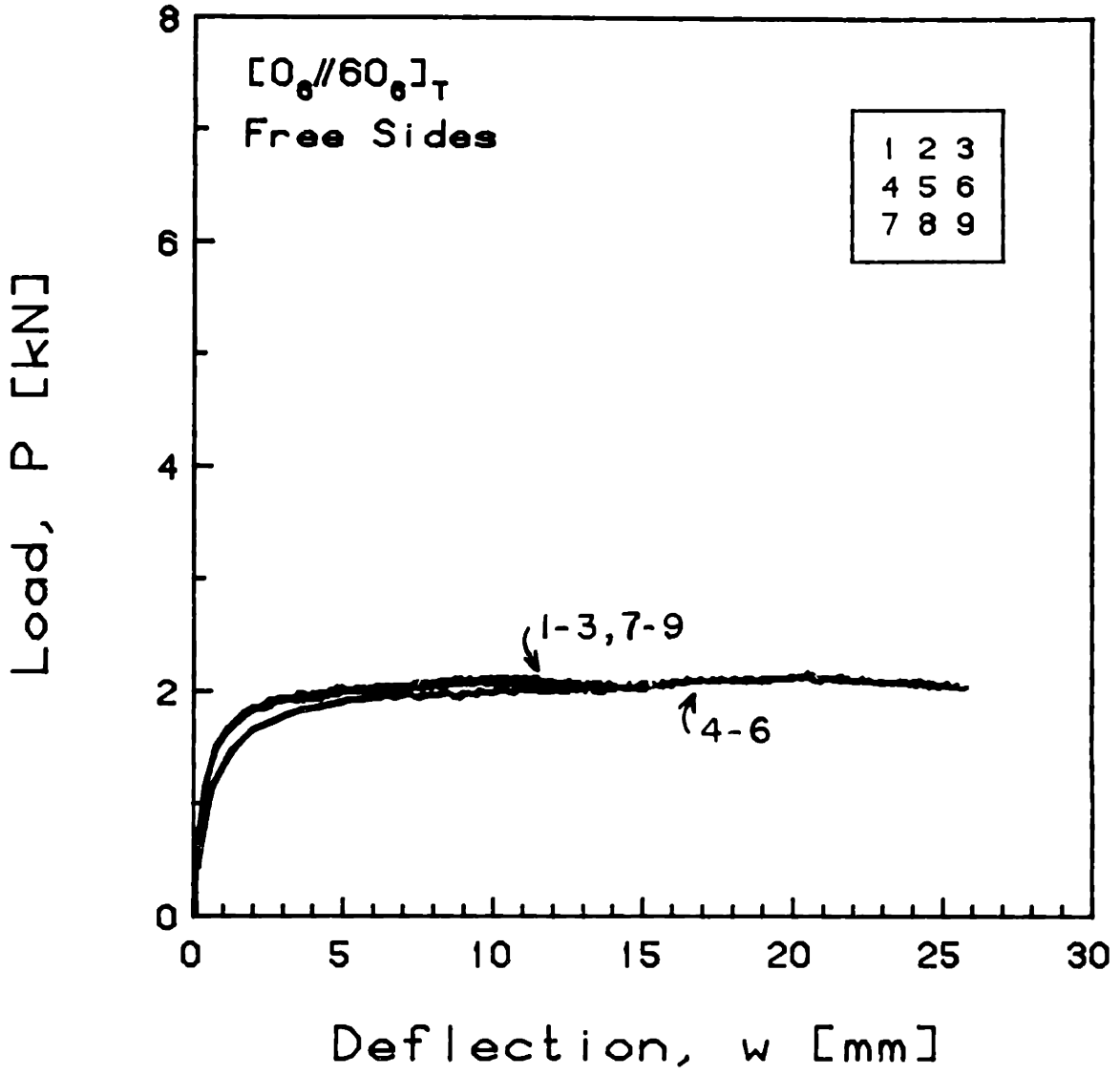

FIGURE 5.38 Experimental Plot of Applied Compressive Load versus Out-of-Plane Deflection for the $[0_6//60_6]_T$ Laminate with Free Side Boundary Conditions

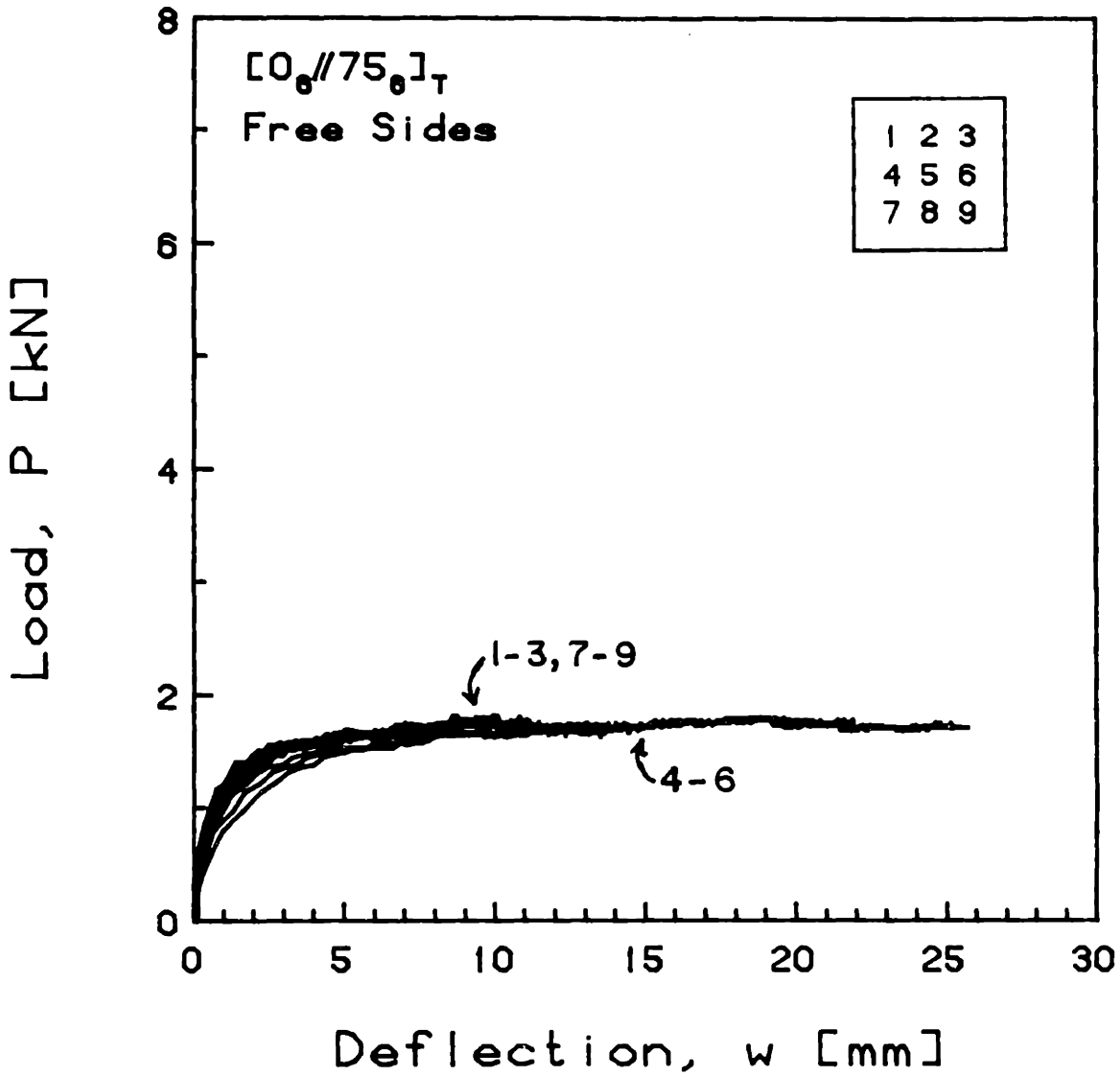

FIGURE 5.39 Experimental Plot of Applied Compressive Load versus Out-of-Plane Deflection for the $[0_6//75_6]_T$ Laminate with Free Side Boundary Conditions

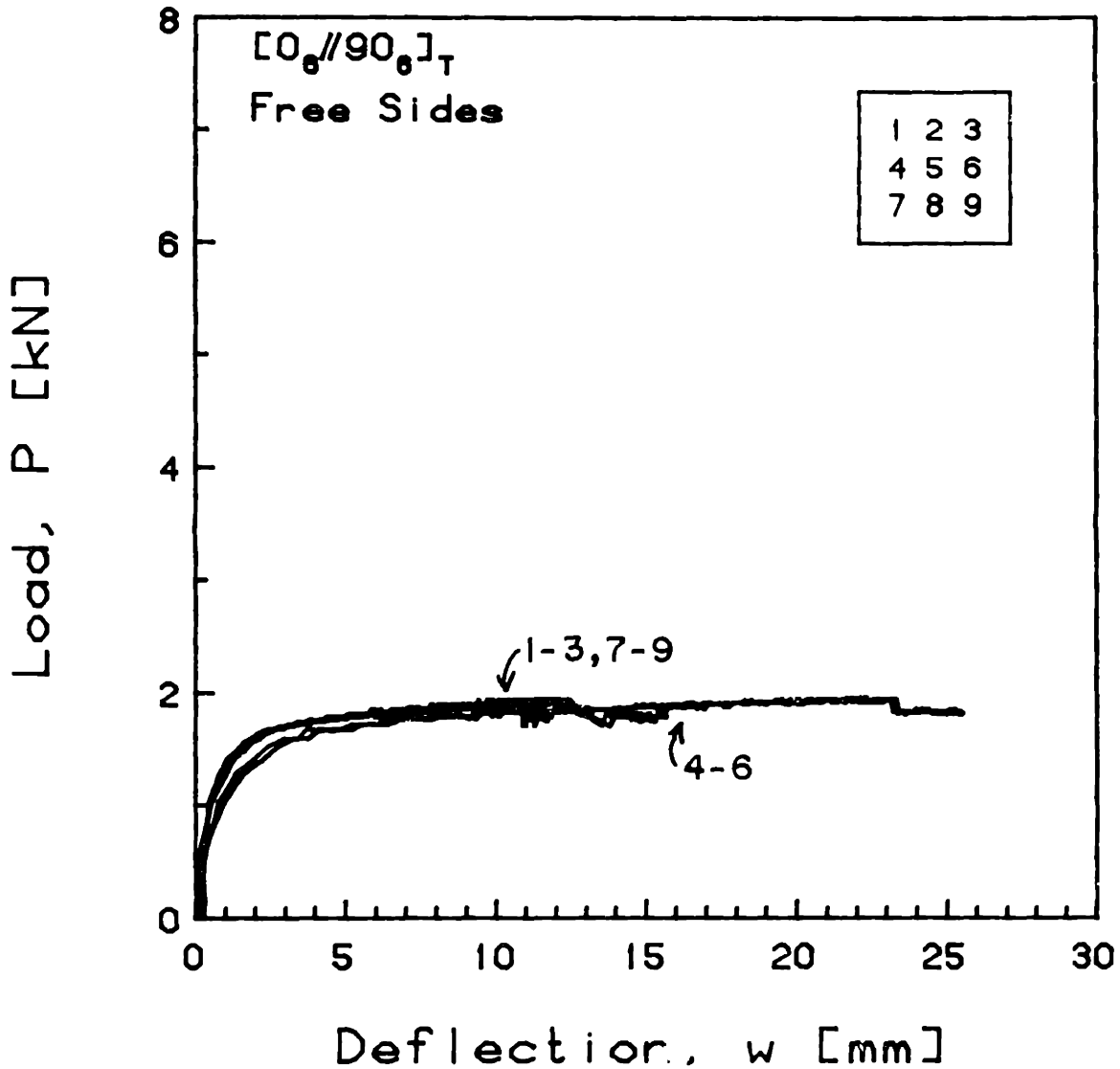

FIGURE 5.40 Experimental Plot of Applied Compressive Load versus Out-of-Plane Deflection for the $[0_6//90_6]_T$ Laminate with Free Side Boundary Conditions

laminate midplane, ε_x^o, has been chosen as a figure of merit [32]. This parameter can also be calculated analytically and will be referred to hereafter as the "effective modulus." The applied load resultant was determined by dividing the total applied load by the actual measured plate thickness. This is, in some sense, similar to the measurement of longitudinal material modulus. However, in compressively loaded structures, the buckling introduces some geometric influences which are not taken into consideration by this simple one-dimensional parameter.

For each of the laminates tested, the linear regions at the beginning of the load-strain curves were analyzed to determine the parameters N_x/ε_x^o. The midplane strain, ε_x^o, is determined by averaging the readings of the back-to-back strain gages. The local curvature, κ_x, which will later be referenced, is determined by subtracting these two readings and dividing by the laminate thickness. The experimentally determined ratios of N_x/ε_x^o are summarized in Table 5.3, along with the theoretical results which assume a uniform loading across the plate width.

Typical load versus strain results are presented in the following sections for laminates tested with clamped, simply-supported, and free side boundary conditions, respectively. Plots of the load versus strain results for all of the specimens are in Appendix F.

TABLE 5.3

EFFECTIVE MODULUS PARAMETER, N_x/ε_x

Laminate Type	Experimental[b] Side Boundary Conditions			Theoretical[b]
	Clamped	Simply-Supported	Free	
S	92.9 (27%)[a]	94.4	94.1	121.6
T	82.7 (16%)	68.1	65.7	121.8
U	67.1 (8.3%)	58.9	46.2	105.1
P	71.7 (10%)	79.9	56.9	120.5
N	75.0 (19%)	71.0	73.1	121.4
A	79.1 (13%)	87.1	64.0	132.8
B	51.8 (16%)	67.2	46.2	77.2
C	45.2 (7.8%)	61.3	24.6	59.5
D	40.6 (11%)	44.7	34.6	54.7
E	47.5 (18%)	51.1	24.7	53.8
F	50.3 (15%)	53.1	21.9	54.0

[a] Numbers in parentheses are coefficients of variation.
[b] All values expressed in kN/mm.

5.2.1 Clamped Sides

The results for the $[0_3/90_3]_S$-1 and $[0_3//90_3//90_3//0_3]_T$-4 laminates with clamped side boundary conditions are shown in Figures 5.41 and 5.42, respectively. The in-plane strain was slightly greater for the $[0_3//90_3//90_3//0_3]_T$ laminates than for the simpler $[0_3/90_3]_S$ laminates. Again, this is because the room temperature bondlines separated the plies, thus increasing the moment of inertia about both in-plane axes.

The effects of introducing bending-stretching coupling into the laminate can be observed in Figure 5.43 for the $[0_3//90_3//0_3//90_3]_T$-5 laminate tested with clamped side boundary conditions. The curvature near the center of the plate flattens out at high loads, while the in-plane strain simultaneously decreases. Thus, the strain gages, mounted slightly offset from the center, were located in local deflection "pockets". This corresponds to the load versus out-of-plane deflection results for this same laminate plotted in Figure 5.3 and is indicative of a local dimpling due to the impending onset of a global third bending mode component.

For all of the laminates which transitioned into a second bending mode shape, the trends observed in the load versus strain plots are similar to those for laminates with bending-stretching coupling. In fact, only laminates with bending-stretching coupling exhibited any secondary bending.

The similarities and differences in the strain data between first mode behavior and second mode behavior can be

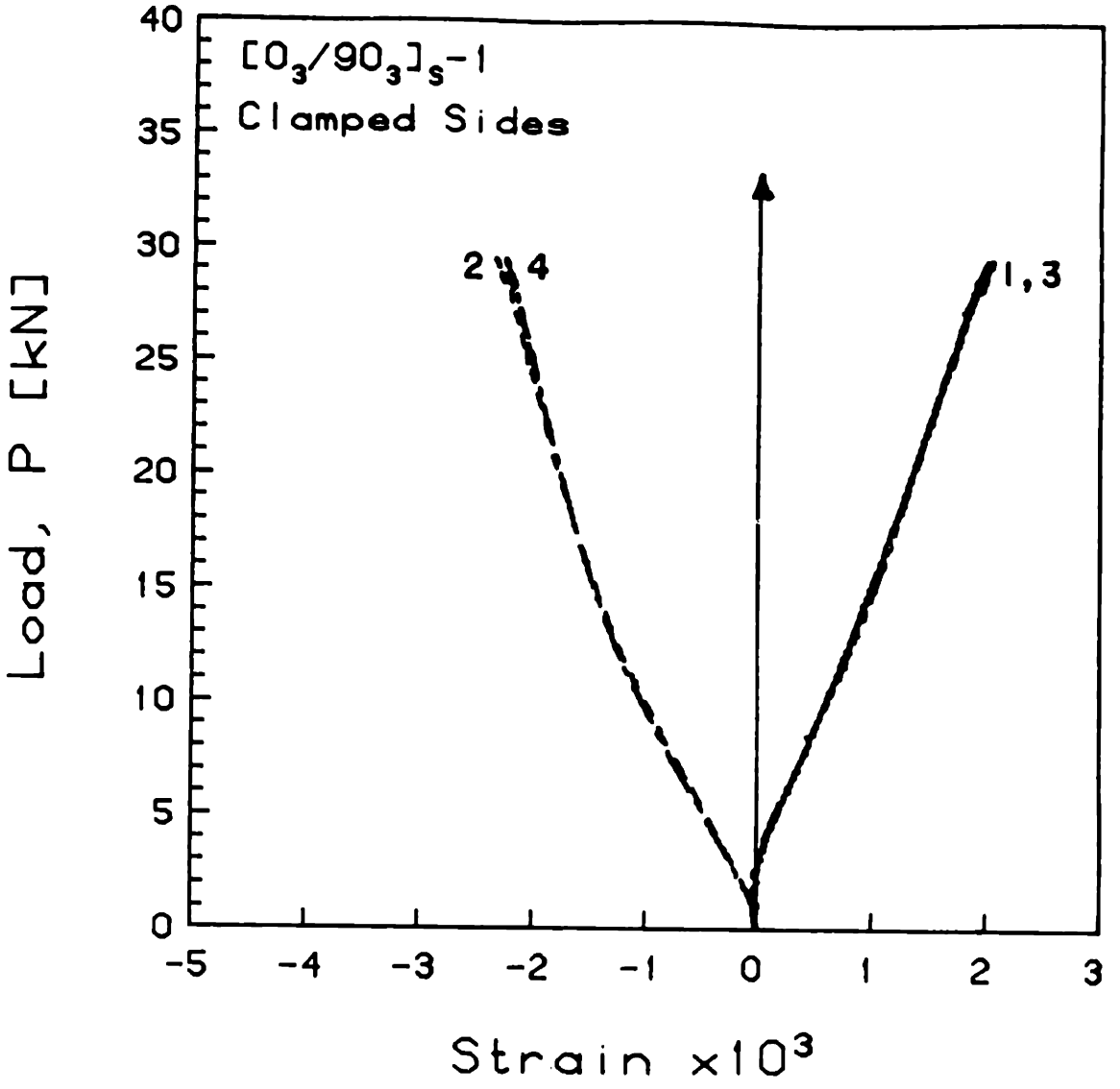

FIGURE 5.41 Experimental Plot of Applied Compressive Load versus Longitudinal Strain for the $[0_3/90_3]_s$-1 Laminate with Clamped Side Boundary Conditions

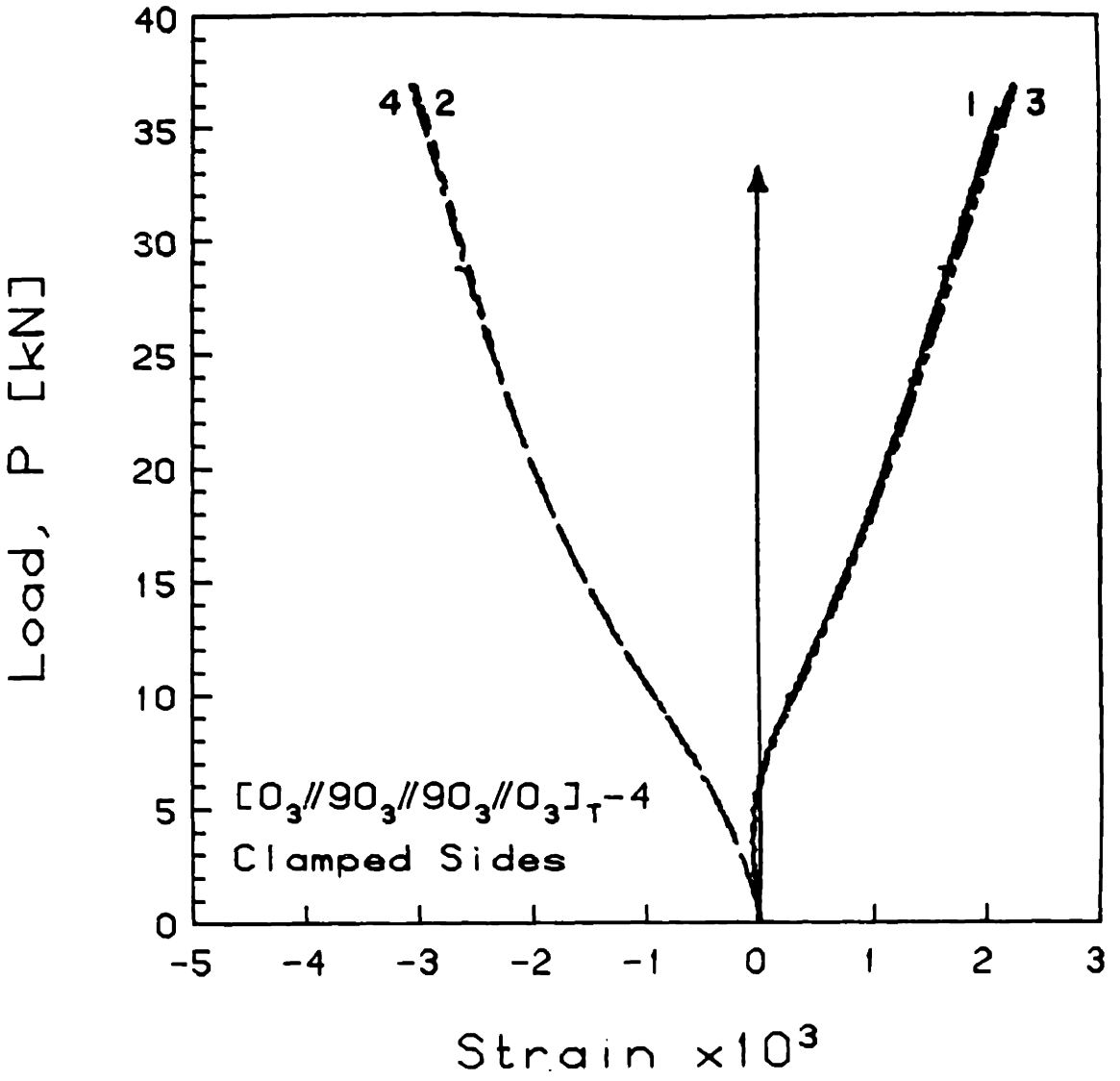

FIGURE 5.42 Experimental Plot of Applied Compressive Load versus Longitudinal Strain for the $[0_3//90_3//90_3//0_3]_T$-4 Laminate with Clamped Side Boundary Conditions

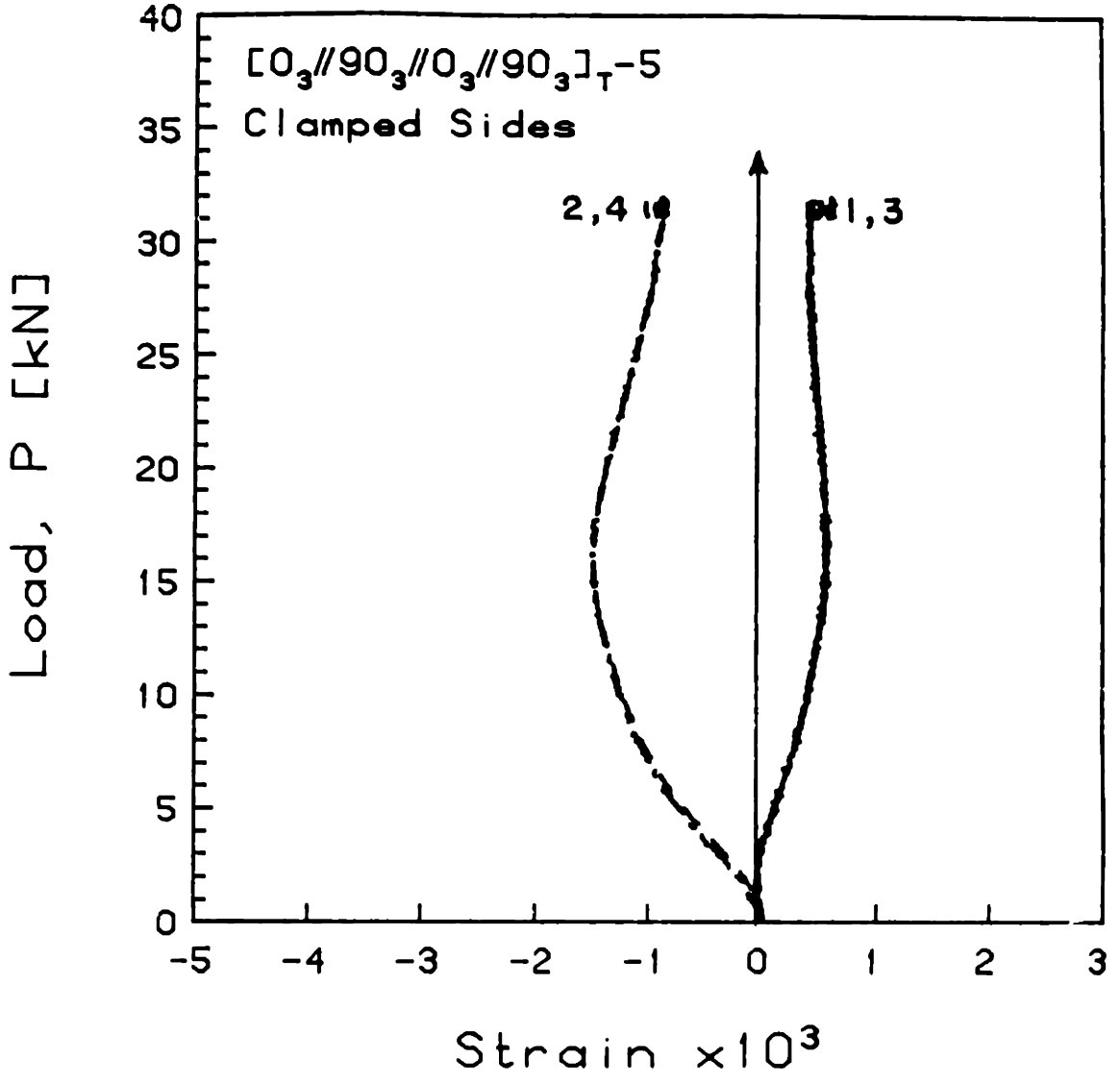

FIGURE 5.43 Experimental Plot of Applied Compressive Load versus Longitudinal Strain for the $[0_3//90_3//0_3//90_3]_T$-5 Laminate with Clamped Side Boundary Conditions

observed for typical results presented in Figures 5.43 for the laminate just considered and Figure 5.44 for the nominally identical $[0_3//90_3//0_3//90_3]_T$-2 laminate, which snapped into a second bending mode at approximately 10 kN. In the latter case, the surface strains snapped inward and approached zero, but did not cross. This indicates that the local curvature had almost disappeared and the corresponding local in-plane strain was also quite small. In the former case, however, in spite of the fact that no global bending transition had occurred, the average strains decrease. The strain gages were apparently in a region of low stress for these laminates, even though the total applied load was quite high. Thus, laminates of this type exhibited a local decrease in strain irrespective of the dominant global bending mode. The laminates which had little or no bending-stretching coupling did not display this reversal in the strain rates.

The effects of the stretching-shearing, bending-twisting, and stretching-twisting couplings were subtle and not readily evidenced in the load-strain data. All of the load versus strain curves for the $[0_2//45_2//0_2//45_2//0_2]_T$ and $[0_2//45_2//0_2//-45_2//0_2]_T$ laminates were almost identical to each other. Switching the orientation of one of the 45° sublaminates had only a minor effect on the local load versus strain behavior, in spite of altering the elastic coupling mechanisms. The in-plane strain and curvature were slightly less for the $[0_2//45_2//0_2//45_2//0_2]_T$ laminates than for the $[0_2//45_2//0_2//-45_2//0_2]_T$ laminates. For example, compare the

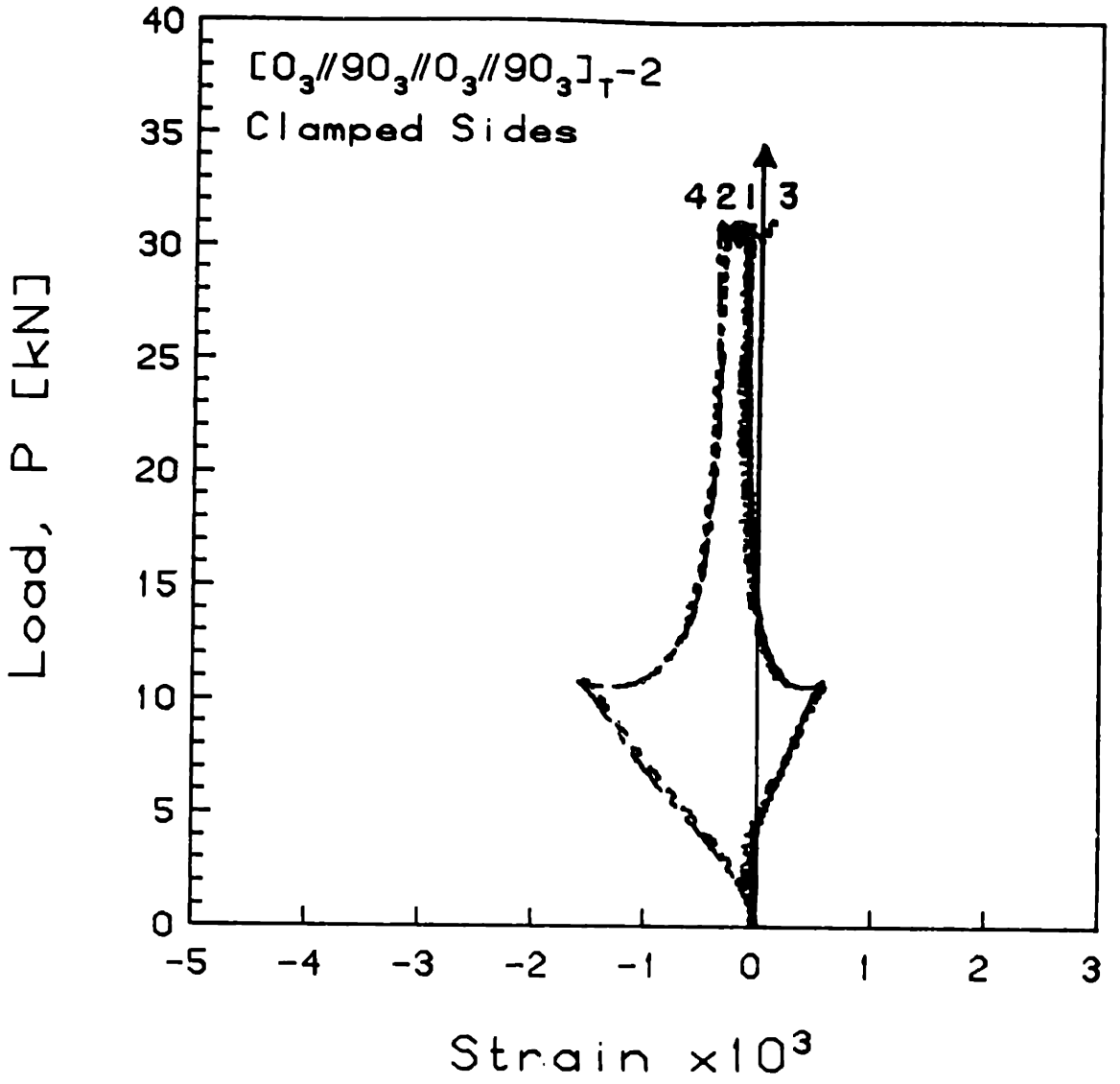

FIGURE 5.44 Experimental Plot of Applied Compressive Load versus Longitudinal Strain for the $[0_3//90_3//0_3//90_3]_T$-2 Laminate with Clamped Side Boundary Conditions

graphs in Figures 5.45 and 5.46 for specimens number 3 of each of these laminate types tested with clamped side boundary conditions, respectively. In general, the effects of the stretching-shearing, bending-twisting, and stretching-twisting couplings did not significantly affect the load versus strain behavior.

The series of load versus strain graphs presented in Figures 5.47 through 5.52 for laminates with clamped side boundary conditions show the effect on the local strain of increasing the lamination angle, θ, in the $[0_6//\theta_6]_T$ laminate family. The surface strains, measured near the center of the plate, clearly indicate the progression of development of a third bending mode component in the laminates as θ increases, for θ greater than 30°. As the fiber angle, θ, increases from 15° to 90°, the surface strains begin to reverse directions at progressively lower load levels. The figures show that the amount of curvature in the x-direction (load direction), represented by the difference between the surface strains, decreases with an increase in the layup angle, θ, as does the midplane, or average, strain. In fact, the average strain transitions from local compression to local tension and then becomes nearly nonexistent at high loads for these laminates with large lamination angles. This implies that a dimple is forming near the center of the plate, since a comparison with the load versus out-of-plane center deflection shows that the center deflection is always increasing for these laminates. The size and formation of these dimples is dependent on the

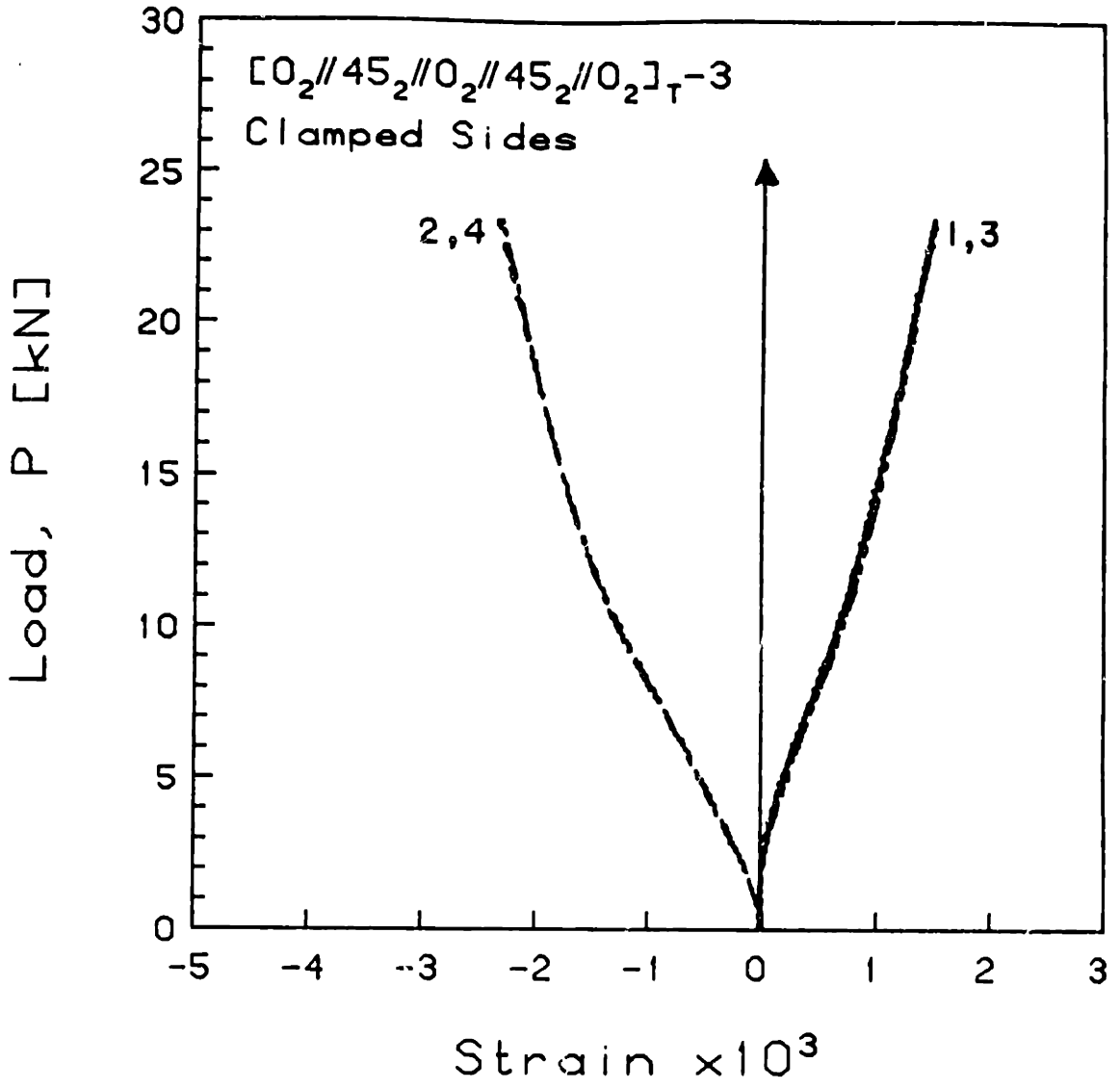

FIGURE 5.45 Experimental Plot of Applied Compressive Load versus Longitudinal Strain for the $[0_2//45_2//0_2//45_2//0_2]_T$-3 Laminate with Clamped Side Boundary Conditions

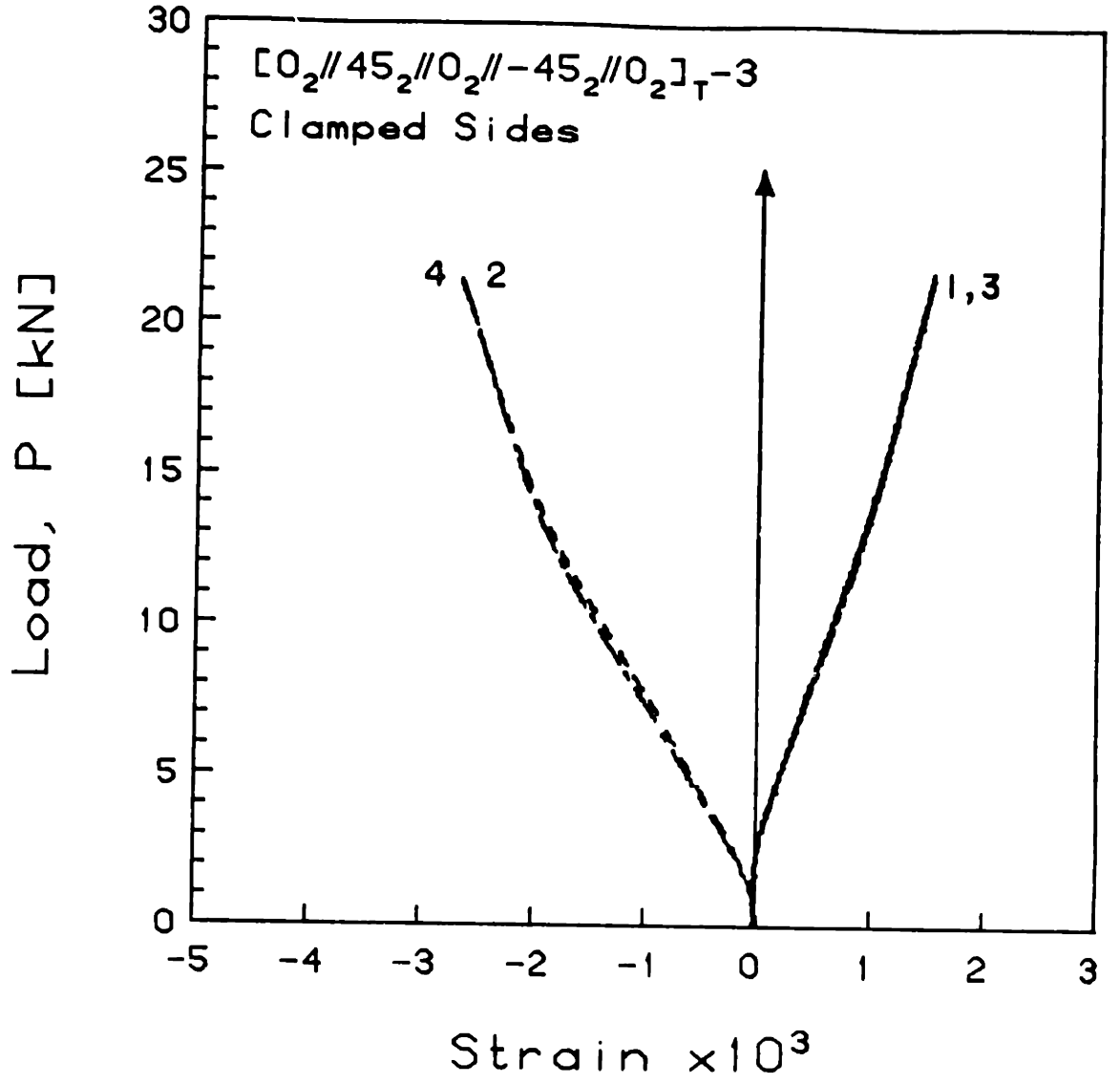

FIGURE 5.46 Experimental Plot of Applied Compressive Load versus Longitudinal Strain for the $[O_2//45_2//O_2//-45_2//O_2]_T$-3 Laminate with Clamped Side Boundary Conditions

magnitude of the various coupling parameters.

A comparison of the load versus strain response for laminates $[0_6//90_6]_T$-5 and $[0_3//90_3//0_3//90_3]_T$-5 (in Figures 5.52 and 5.43, respectively), tested with clamped side boundary conditions, show that the bending-stretching coupling effect alone was significant enough to be responsible for this behavior. The only difference between the elastic properties of these two laminate types is in the primary bending-stretching coupling terms (B_{11} and B_{22}). The theoretical values of these properties are exactly twice as large for the $[0_6//90_6]_T$ laminate as for the $[0_3//90_3//0_3//90_3]_T$ laminate. The other elastic coefficients in the constitutive relations for these two laminates are virtually identical, although the extra bondlines in the $[0_3//90_3//0_3//90_3]_T$ laminates do increase the bending stiffness ever so slightly. Consequently, any difference in behavior between these two laminates can be directly attributed to the increase in the bending-stretching coupling terms.

5.2.2 Simply-Supported Sides

In almost all cases, the local longitudinal bending strain component, $h\kappa_x$ (linearly proportional to the curvature), was slightly greater for the laminates with simply-supported side boundary conditions than for the laminates with clamped side boundary conditions. The in-plane

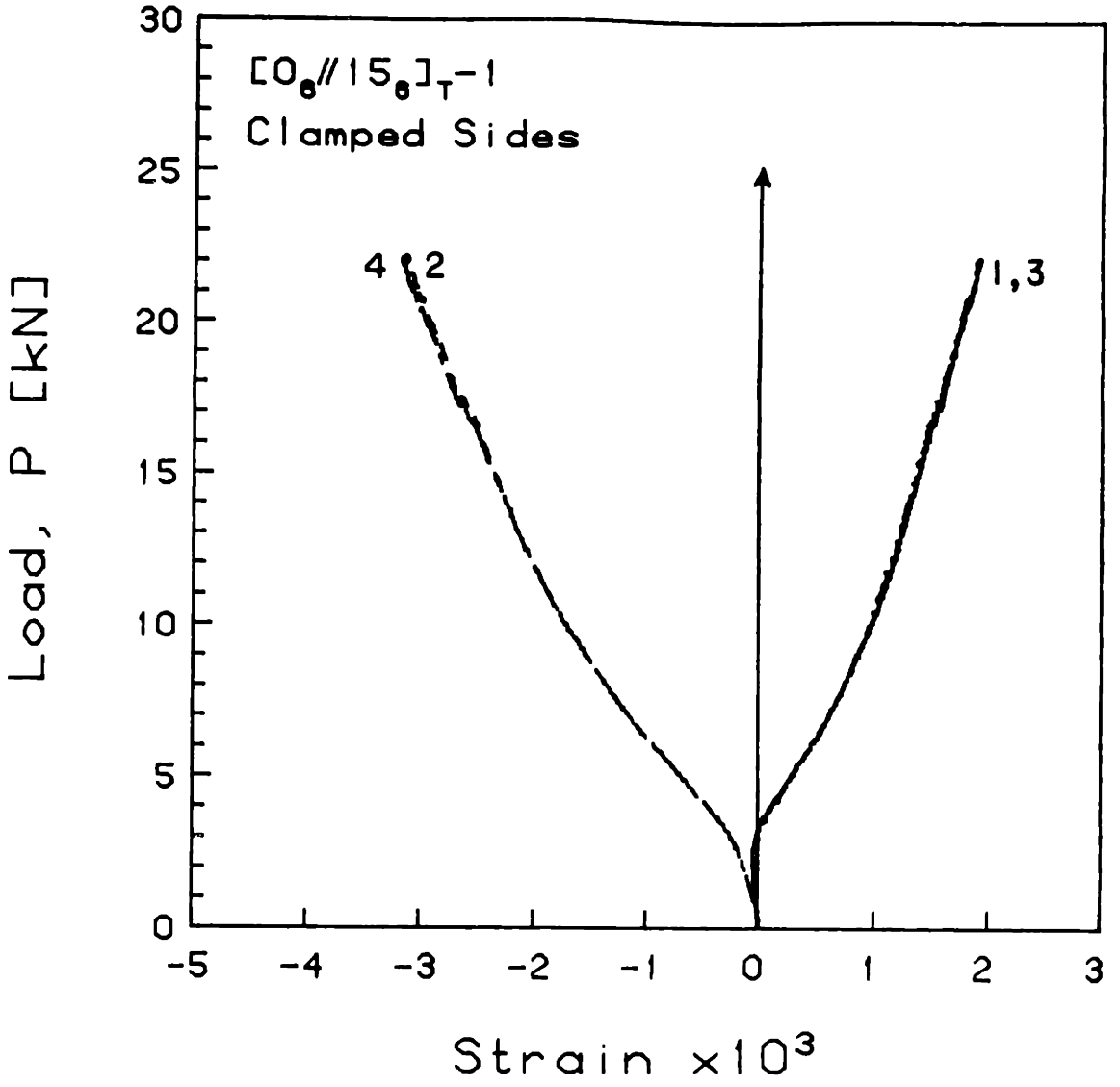

FIGURE 5.47 Experimental Plot of Applied Compressive Load versus Longitudinal Strain for the $[O_6//15_6]_T$-1 Laminate with Clamped Side Boundary Conditions

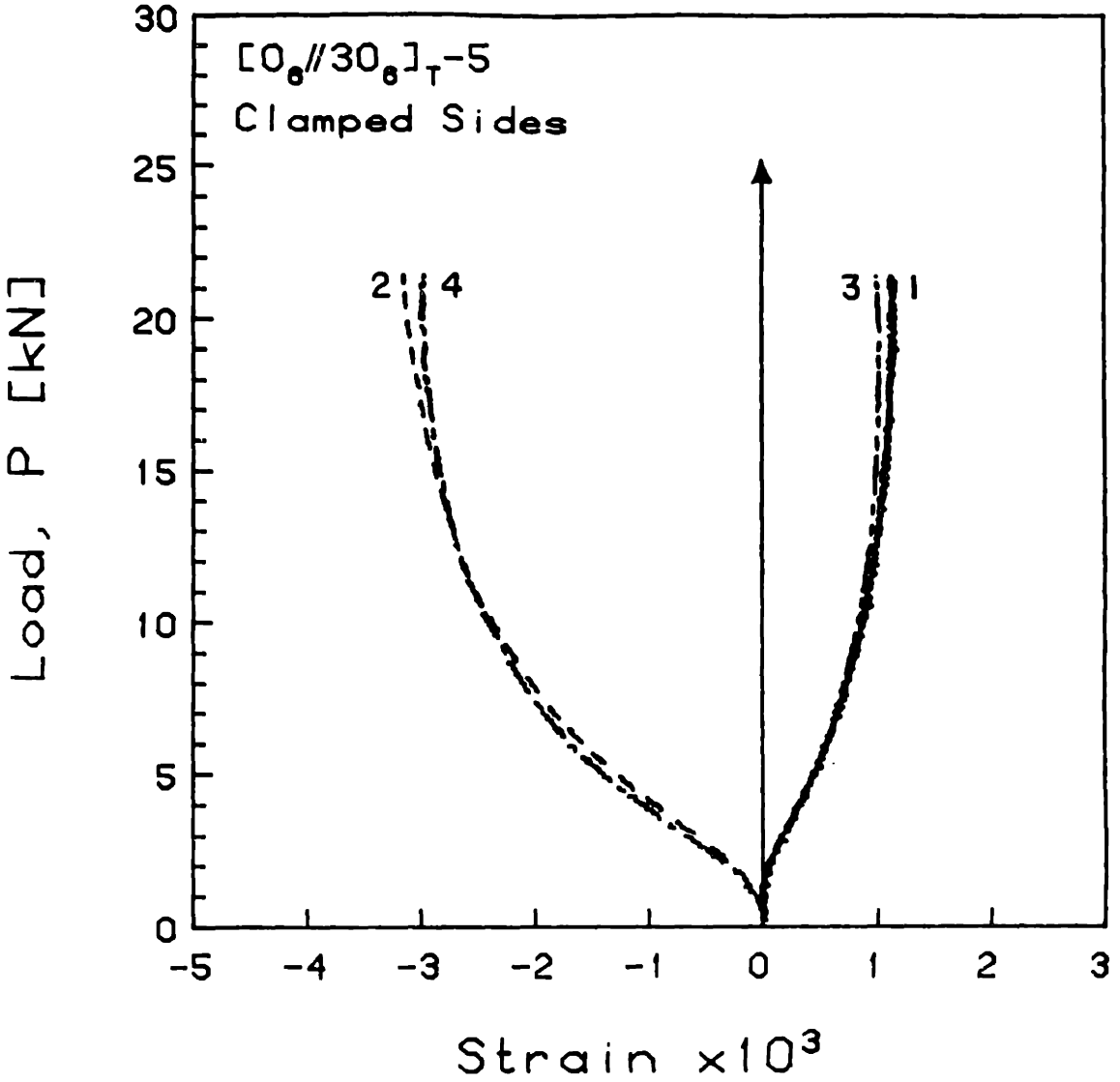

FIGURE 5.48 Experimental Plot of Applied Compressive Load versus Longitudinal Strain for the $[0_6//30_6]_T$-5 Laminate with Clamped Side Boundary Conditions

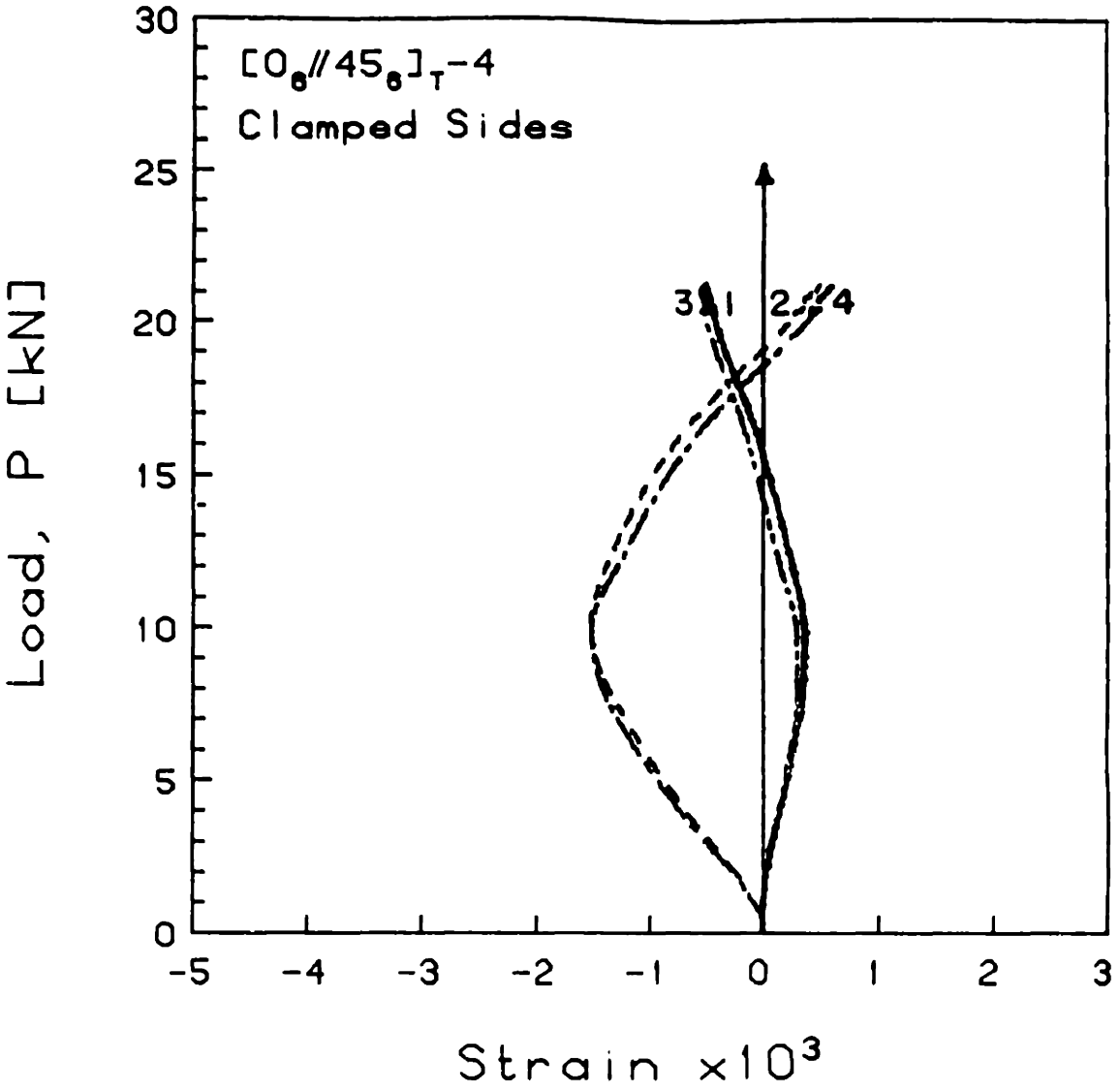

FIGURE 5.49 Experimental Plot of Applied Compressive Load versus Longitudinal Strain for the $[O_6//45_6]_T$-4 Laminate with Clamped Side Boundary Conditions

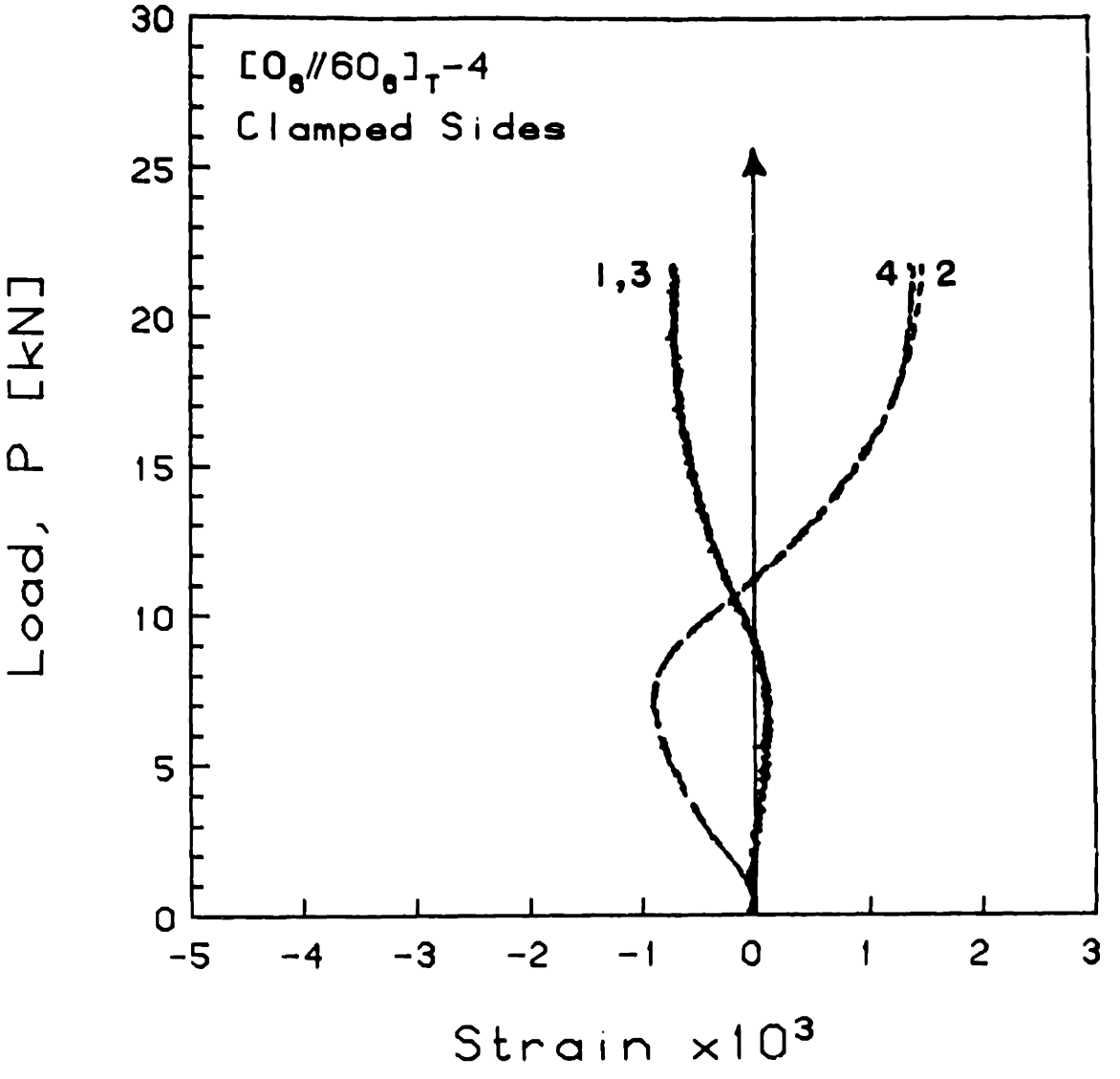

FIGURE 5.50 Experimental Plot of Applied Compressive Load versus Longitudinal Strain for the $[0_6//60_6]_T$-4 Laminate with Clamped Side Boundary Conditions

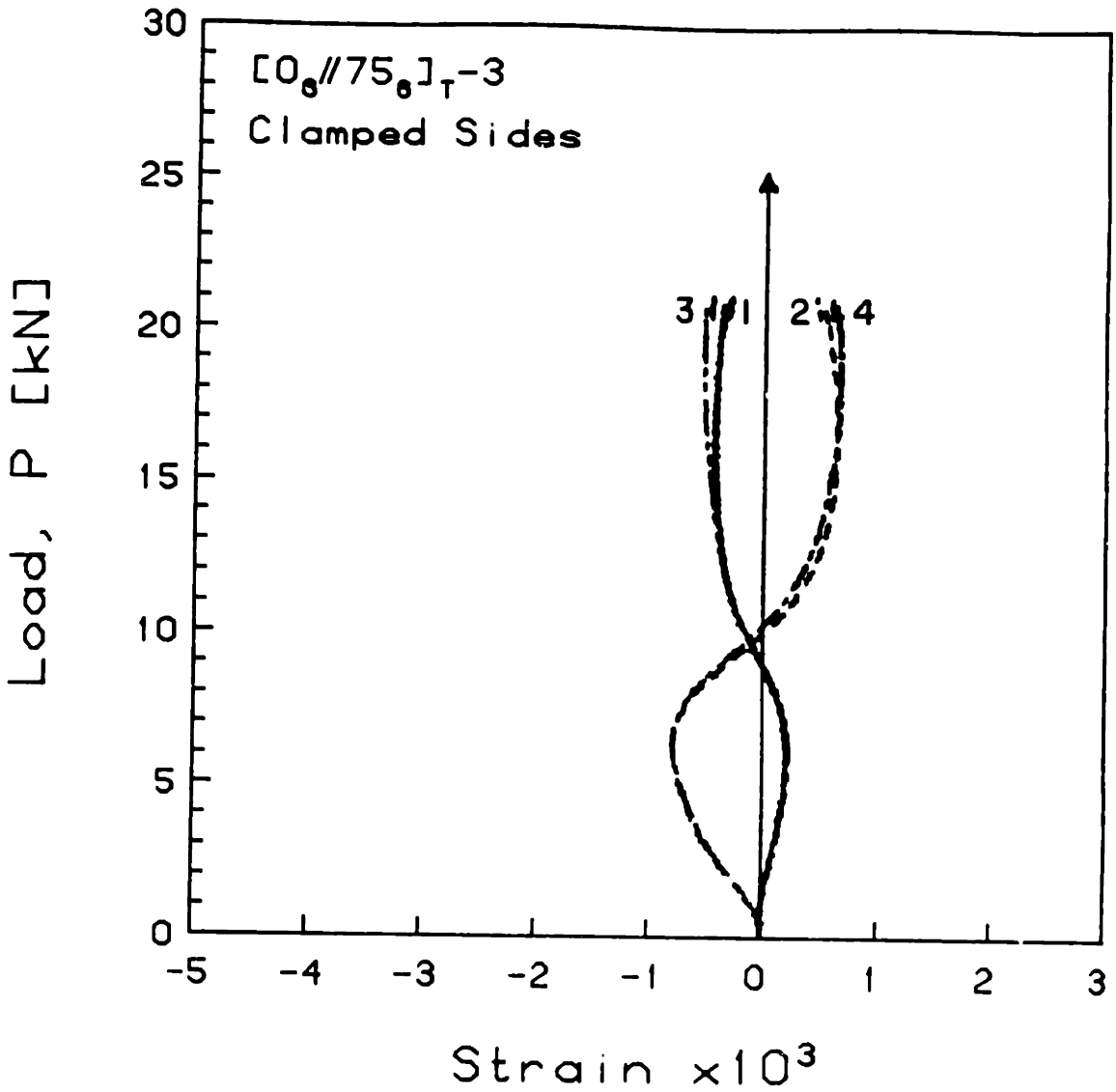

FIGURE 5.51 Experimental Plot of Applied Compressive Load versus Longitudinal Strain for the $[0_6//75_6]_T$-3 Laminate with Clamped Side Boundary Conditions

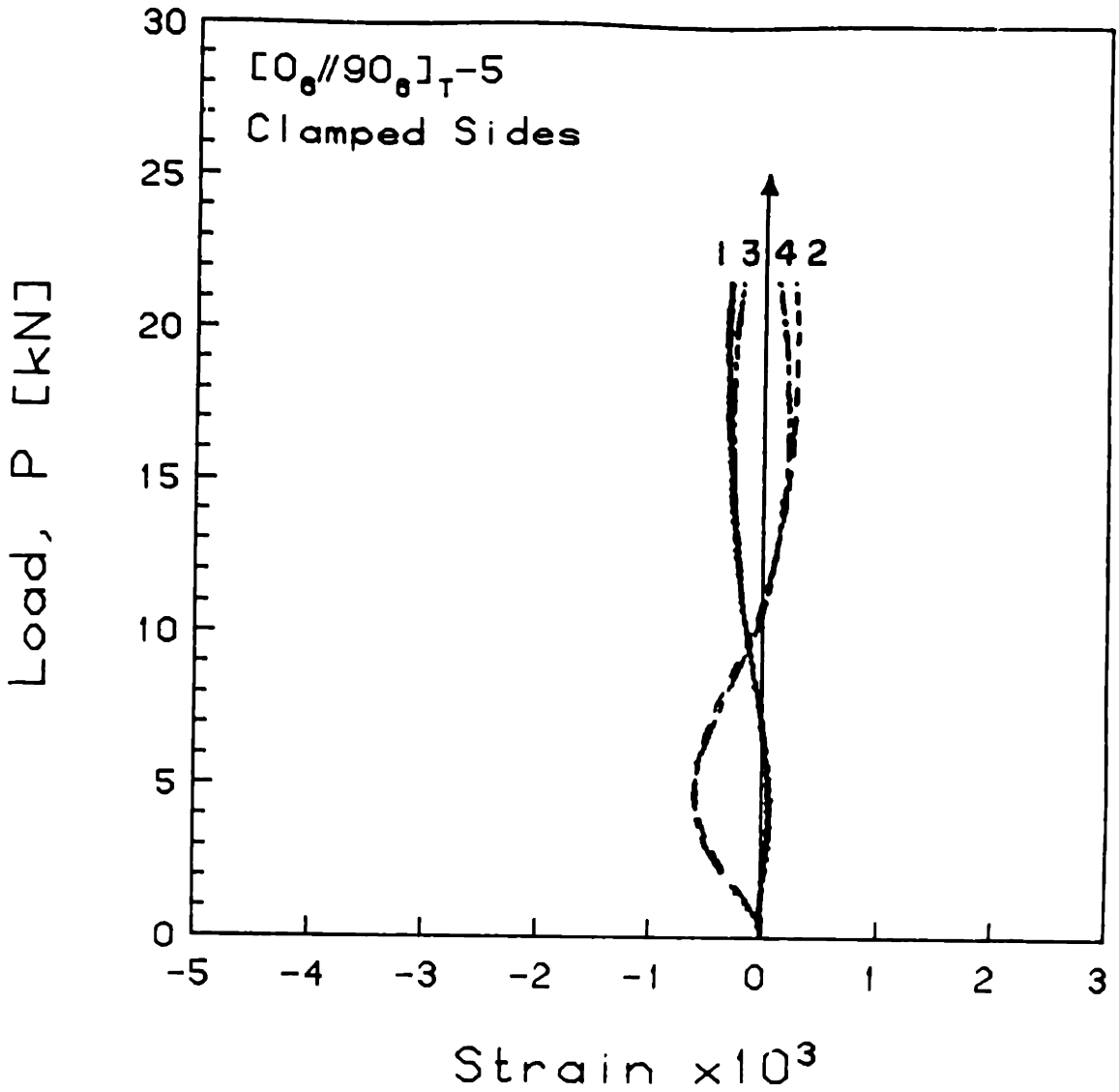

FIGURE 5.52 Experimental Plot of Applied Compressive Load versus Longitudinal Strain for the $[0_6//90_6]_T$-5 Laminate with Clamped Side Boundary Conditions

strain component, ε_x^o, was nearly the same for both types of partially restrained side boundary conditions. This slight effect can be observed for a typical case by carefully comparing the data from one of the symmetric laminates, $[0_3//90_3//90_3//0_3]_T$, in Figure 5.53 for the simply-supported case, with that presented in Figure 5.42 for the clamped case. Results from the antisymmetric laminate, $[0_3//90_3//0_3//90_3]_T$-5, are presented in Figure 5.54 and show how the bending-stretching coupling limits the growth of the local curvature component.

In general, the distinction between clamped and simply-supported side boundary conditions was not strongly apparent in the center of the plate. In fact, the load-strain curves for the $[0_2//45_2//0_2//-45_2//0_2]_T$ laminates (Figures 5.55 & 5.46) were almost identical for both clamped and simply-supported side boundary conditions, as were the curves for the $[0_6//15_6]_T$ (Figures 5.56 and 5.47) laminates.

5.2.3 Free Sides

As mentioned previously in the discussion of the load versus out-of-plane deflection results, the laminates with free side boundary conditions exhibited almost classical wide column buckling behavior. Figures 5.57, 5.58, and 5.59 show typical load versus strain plots for a symmetric laminate ($[0_3/90_3]_S$), an antisymmetric laminate ($[0_3//90_3//0_3//90_3]_T$), and a fully coupled laminate ($[0_6//45_6]_T$), respectively, with

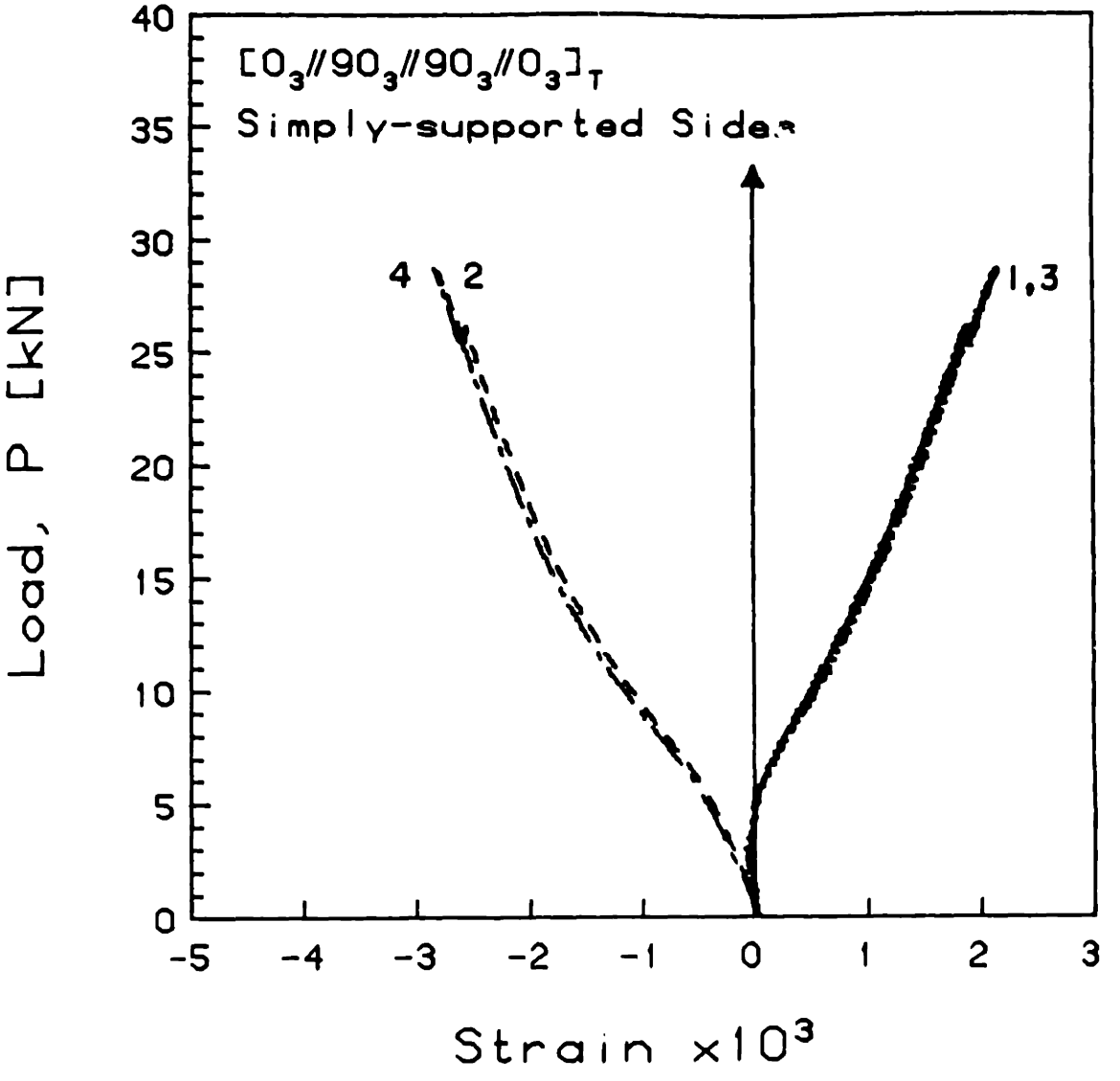

FIGURE 5.53 Experimental Plot of Applied Compressive Load versus Longitudinal Strain for the $[0_3//90_3//90_3//0_3]_T$ Laminate with Simply-Supported Side Boundary Conditions

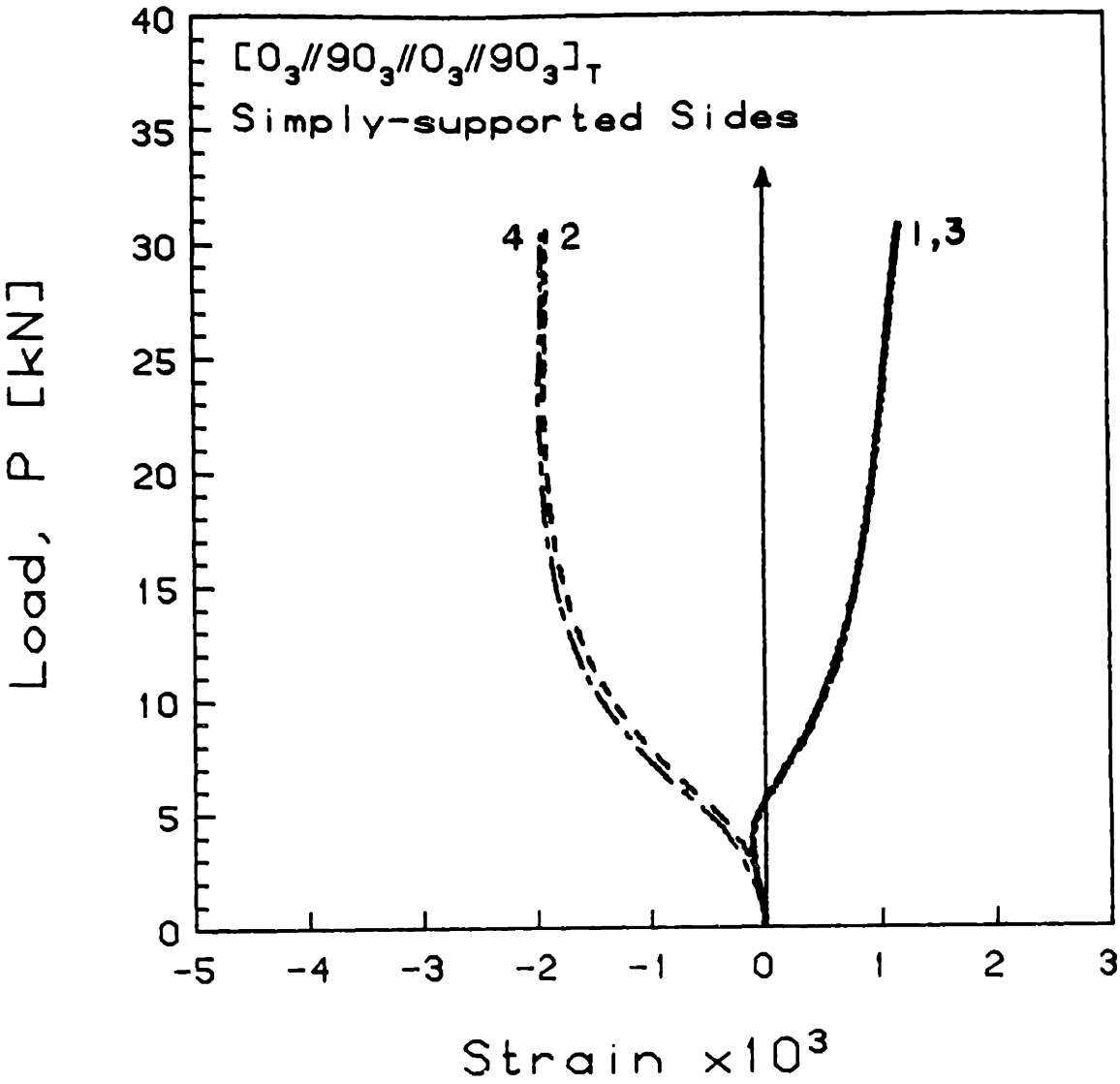

FIGURE 5.54 Experimental Plot of Applied Compressive Load versus Longitudinal Strain for the $[0_3//90_3//0_3//90_3]_T$ Laminate with Simply-Supported Side Boundary Conditions

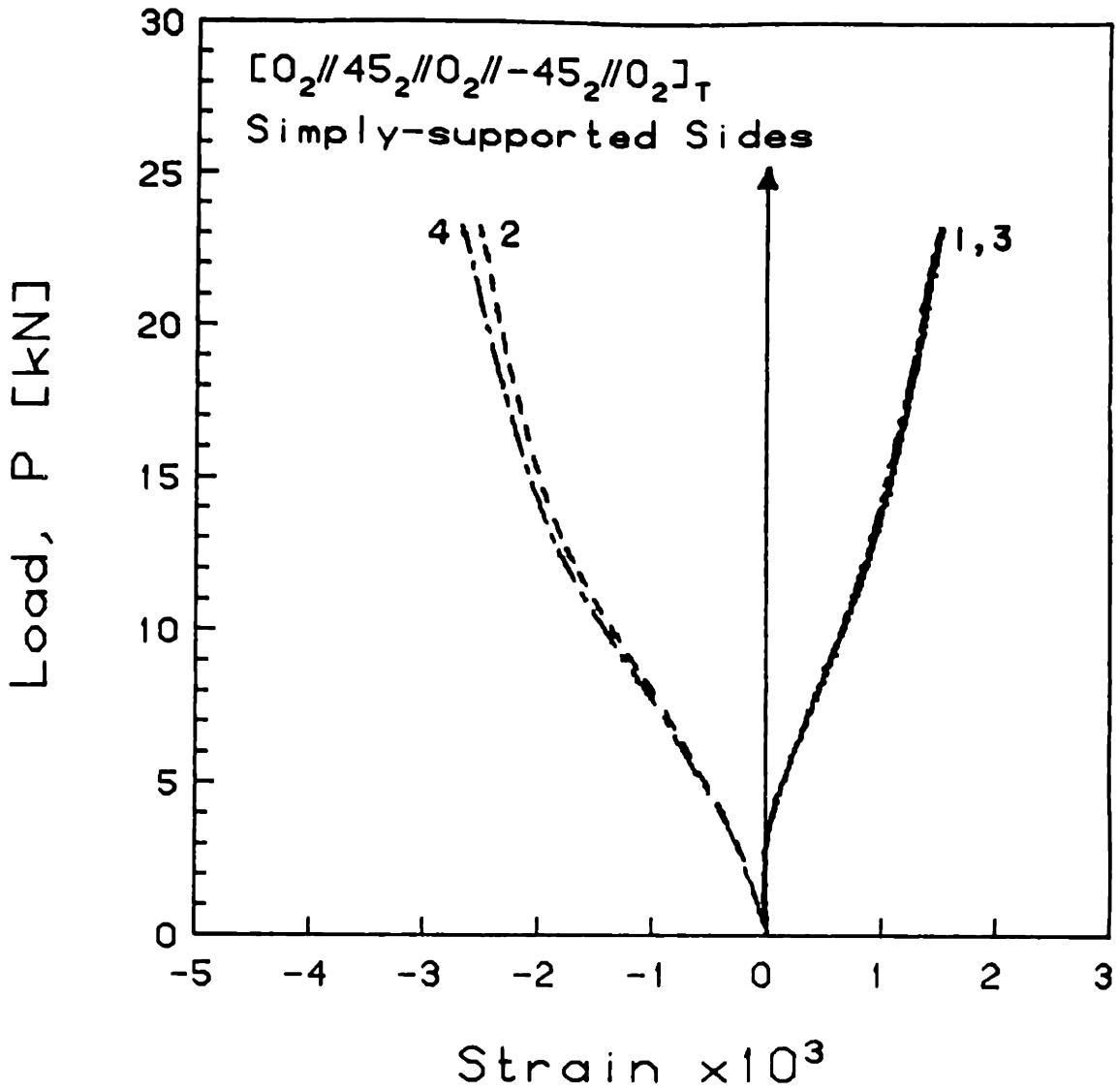

FIGURE 5.55 Experimental Plot of Applied Compressive Load versus Longitudinal Strain for the $[0_2//45_2//0_2//-45_2//0_2]_T$ Laminate with Simply-Supported Side Boundary Conditions

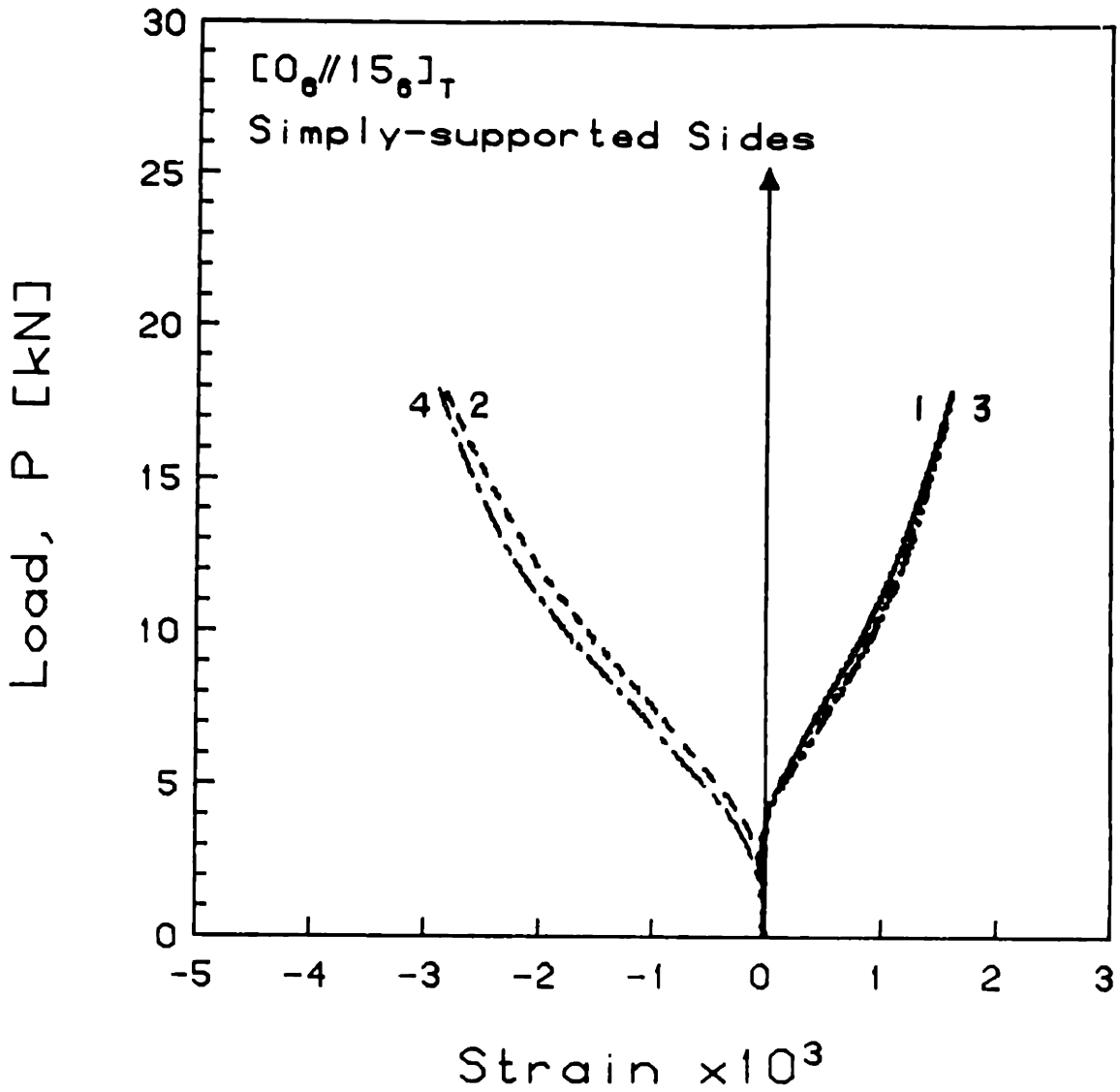

FIGURE 5.56 Experimental Plot of Applied Compressive Load versus Longitudinal Strain for the $[0_6//15_6]_T$ Laminate with Simply-Supported Side Boundary Conditions

free side boundary conditions. These graphs are typical of the behavior of all of the laminates tested with free sides and support the information already discussed for the load versus out-of-plane deflection data in that the behavior was governed almost exclusively by the longitudinal bending stiffness about the shifted neutral axis. In all cases of laminates tested with free side boundary conditions, the bifurcation was clearly evident in the strain data.

5.3 Load versus End-Shortening Displacement, u

The load versus end-shortening displacement results for the laminates tested with clamped and simply-supported side boundary conditions are summarized in this section. A complete collection of the experimental data is in Appendix G. End-shortening measurements were taken because it was recognized apriori that the local strain data would not provide a valid estimate of the effective modulus, whereas the total end-shortening represents an average value which should theoretically be more consistent. In a manner analogous to the calculation of an effective modulus from the load versus strain data, calculations were performed on the load versus end-shortening displacement data. However, in general, the results were independent of exhibited mode shape, laminate type, and boundary conditions, were too compliant, and had very large coefficients of variation. Therefore, the actual numbers are not very meaningful and are not reported herein.

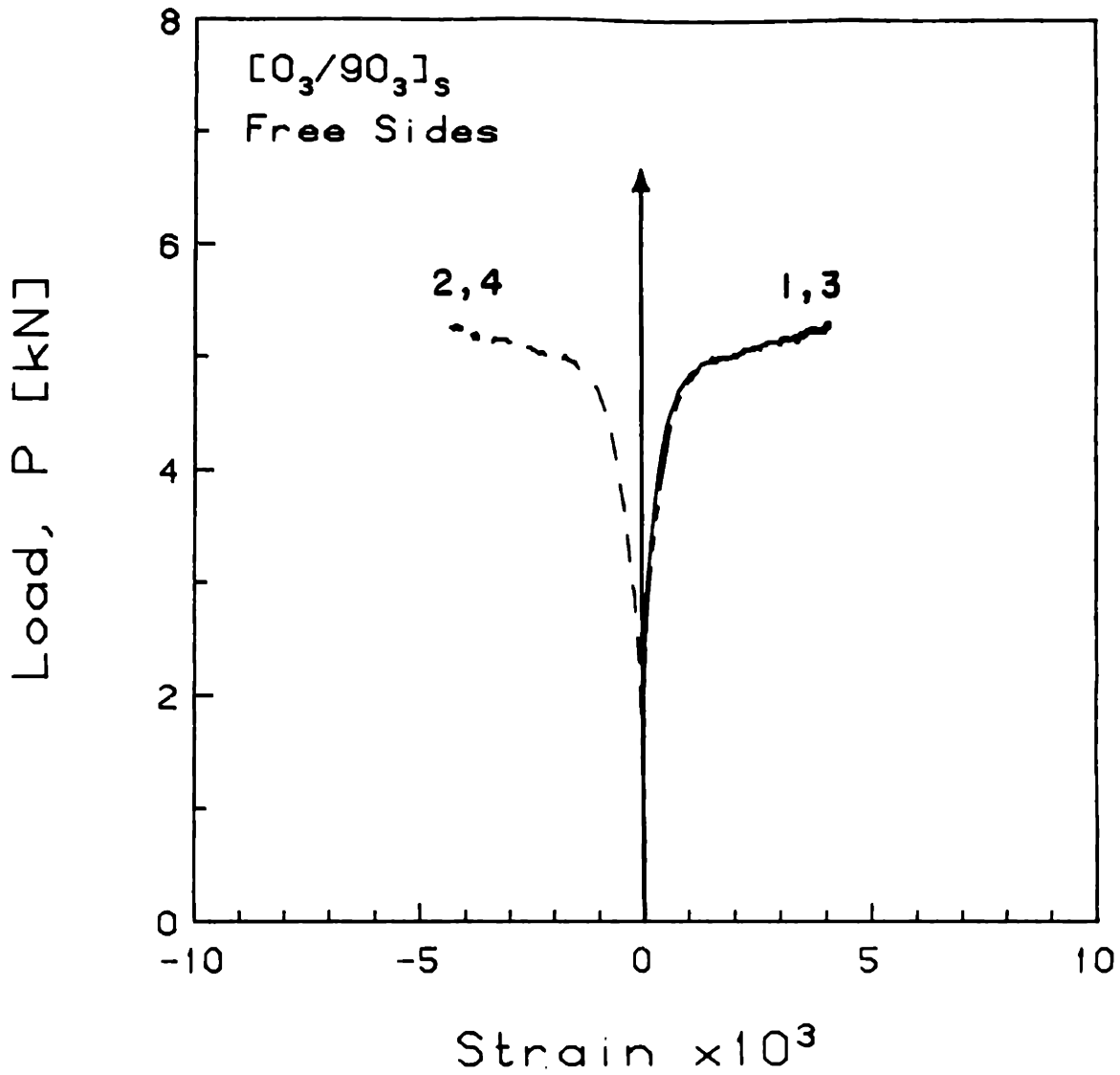

FIGURE 5.57 Experimental Plot of Applied Compressive Load versus Longitudinal Strain for the $[0_3/90_3]_S$ Laminate with Free Side Boundary Conditions

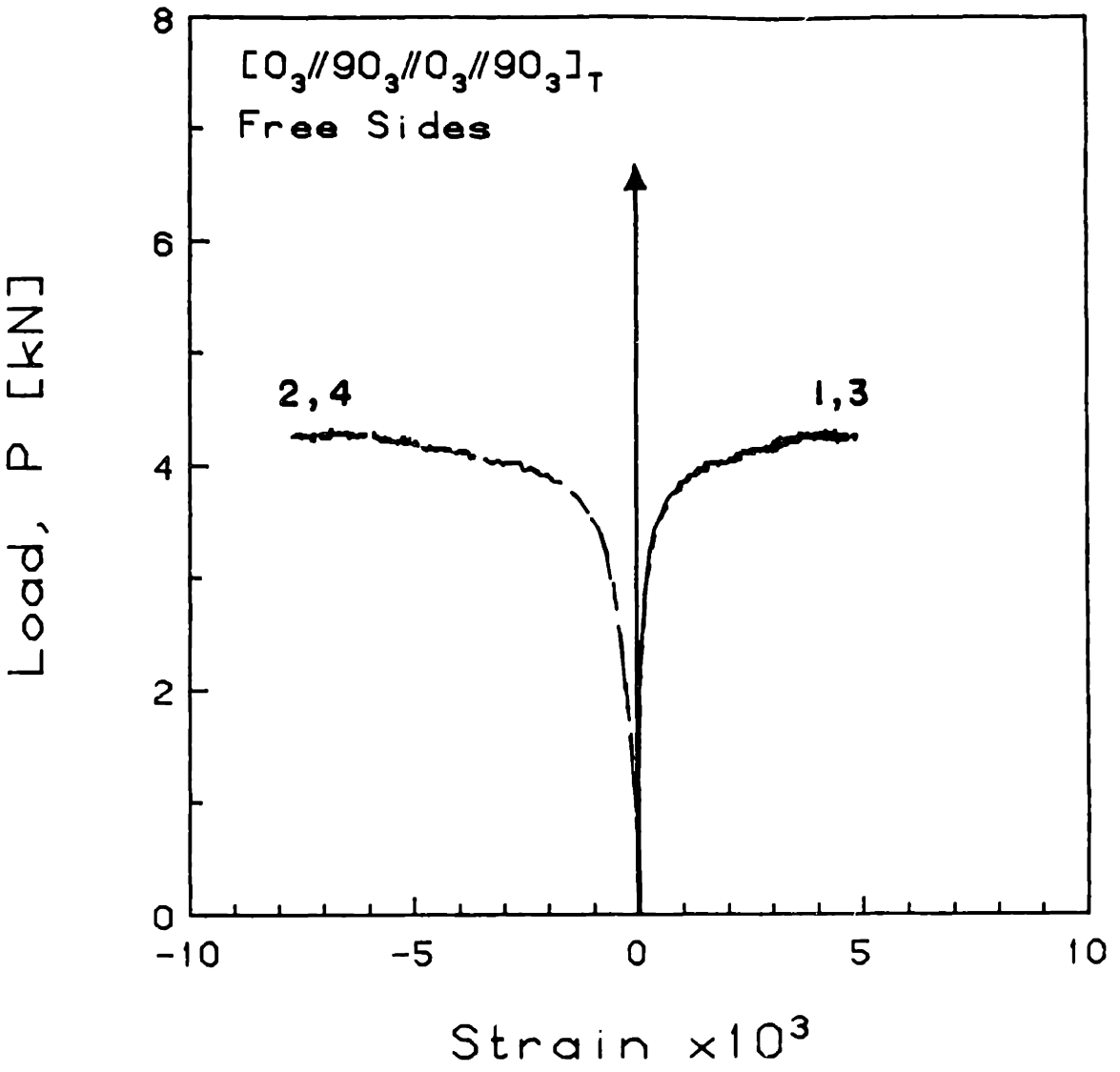

FIGURE 5.58 Experimental Plot of Applied Compressive Load versus Longitudinal Strain for the $[0_3//90_3//0_3//90_3]_T$ Laminate with Free Side Boundary Conditions

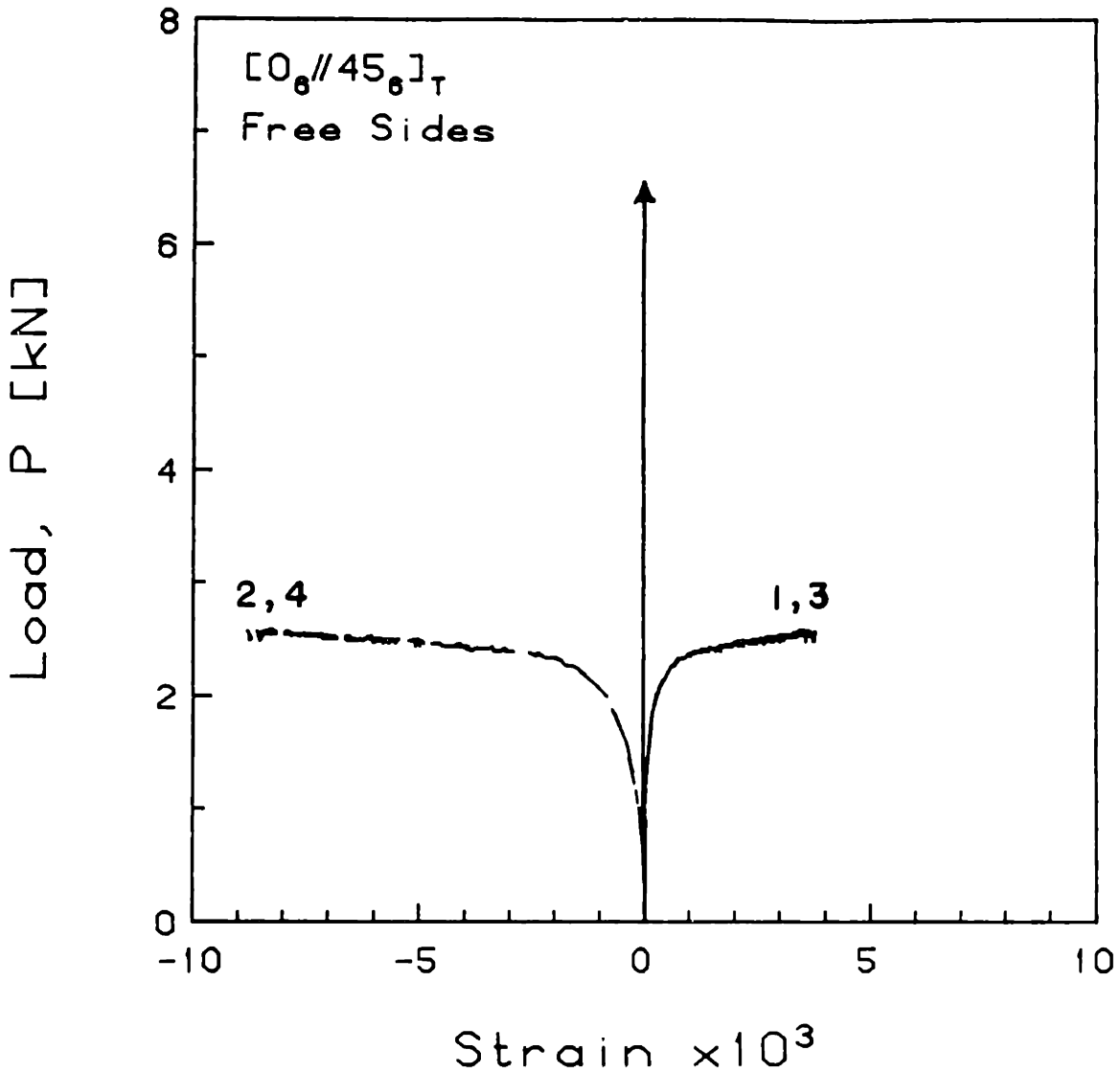

FIGURE 5.59 Experimental Plot of Applied Compressive Load versus Longitudinal Strain for the $[0_6//45_6]_T$ Laminate with Free Side Boundary Conditions

The experimental curves also indicated much more compliance than their theoretical counterparts, especially for the laminates with clamped sides. For example, the experimental and theoretical results for the $[0_3/90_3]_S$-1 laminate tested with clamped side boundary conditions, presented in Figure 5.60, show that the experimental end-shortening displacement data were excessively compliant. This extra compliance can be partially accounted for by considering the existence of additional compliance, due to the means by which the load was introduced, in series with the laminate.

The most interesting results were for the $[0_6//45_6]_T$ laminates. As before, the analytical predictions for this particular layup angle based on the Rayleigh-Ritz analysis exhibited the existence of an extreme softening; i.e., the analysis predicted an extremely large end-shortening displacement for this particular laminate only. Figure 5.61 shows the experimental results and Rayleigh-Ritz predictions for the $[0_6//45_6]_T$-4 laminate, respectively. However, the predictions for the same laminate with simply-supported side boundary conditions were much better behaved, as shown in Figure 5.62 for both the experimental results and Rayleigh-Ritz predictions.

On the other hand, all of the laminates tested with free side boundary conditions followed the same pattern of end-shortening, u, of the plate as a function of the applied load, P. Upon reaching the classical bifurcation (buckling)

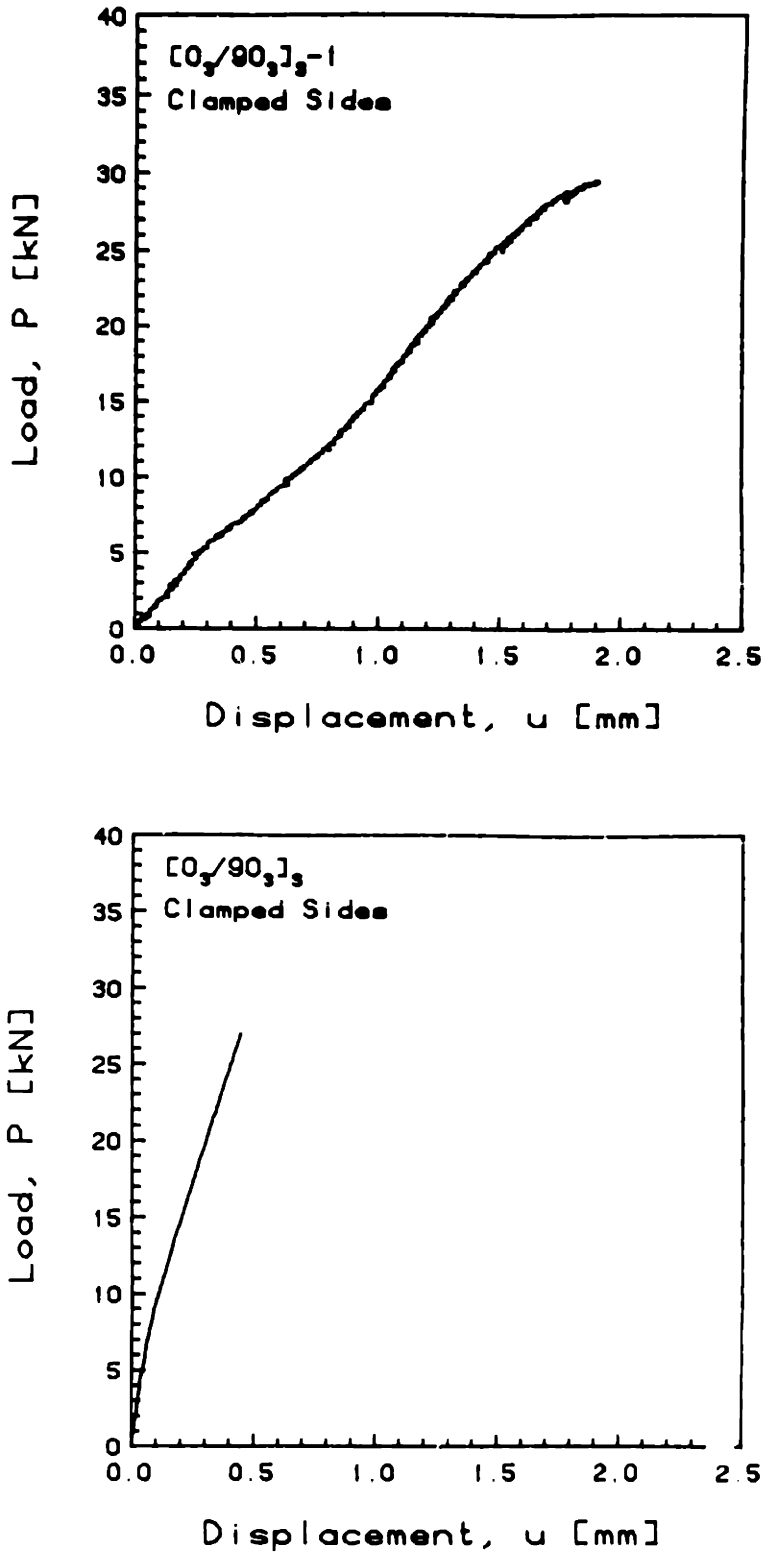

FIGURE 5.60 Experimental (top) and Predicted (bottom, via Rayleigh-Ritz) Plots of Applied Compressive Load versus End-Shortening Displacement for the $[0_3/90_3]_s$-1 Laminate with Clamped Side Boundary Conditions

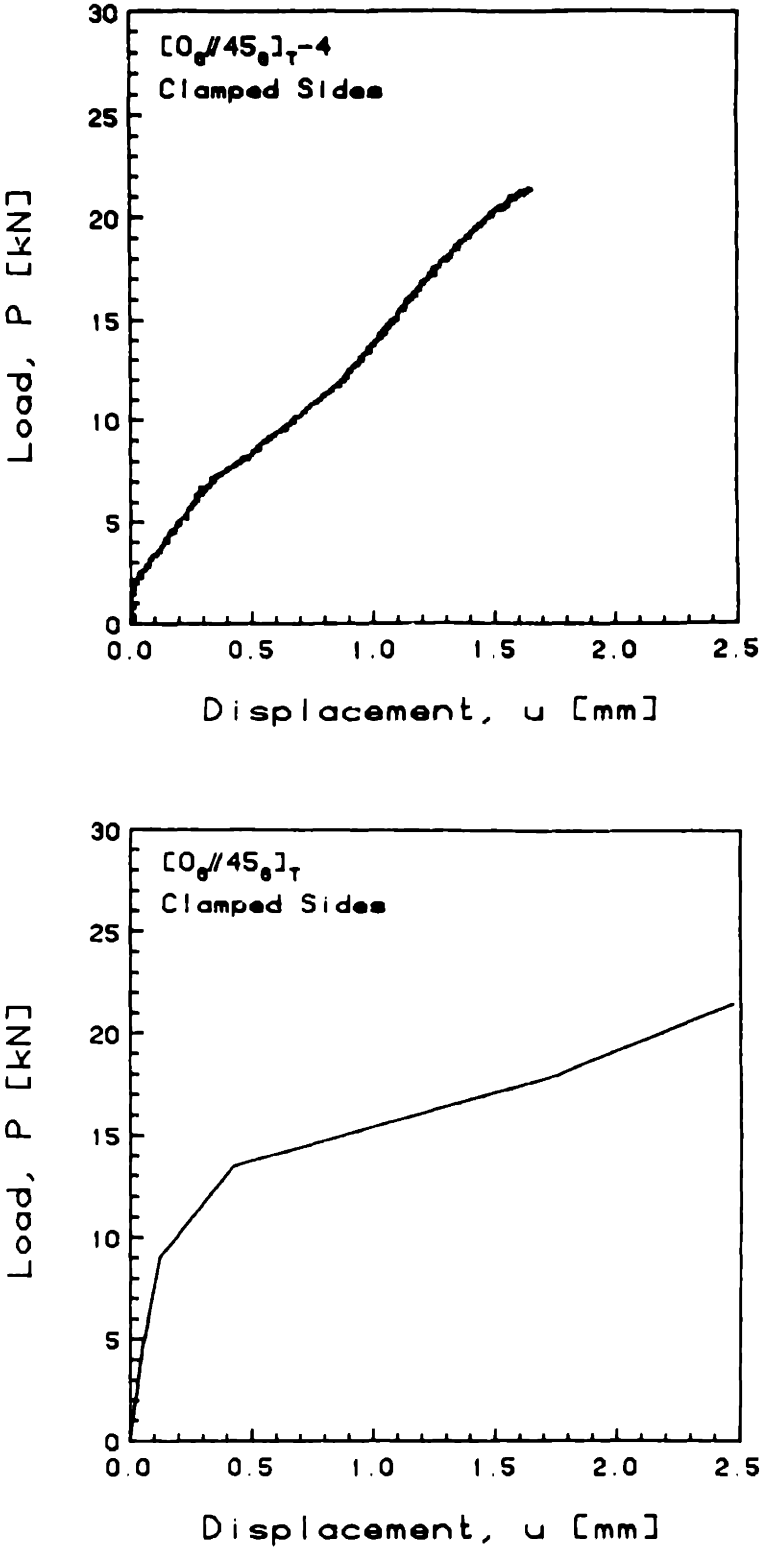

FIGURE 5.61 Experimental (top) and Predicted (bottom, via Rayleigh-Ritz) Plots of Applied Compressive Load versus End-Shortening Displacement for the $[0_6//45_6]_T$-4 Laminate with Clamped Side Boundary Conditions

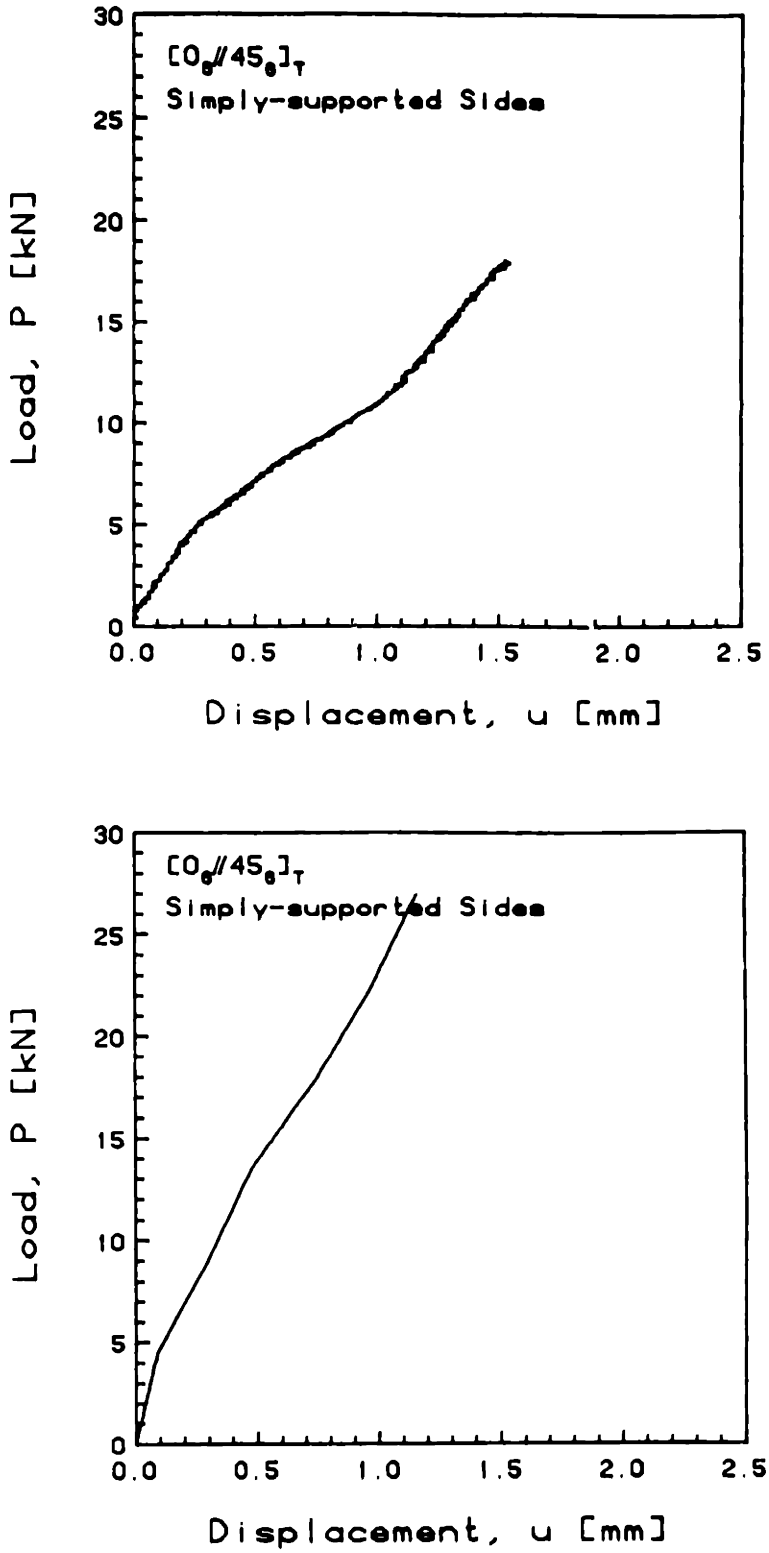

FIGURE 5.62 Experimental (top) and Predicted (bottom, via Rayleigh-Ritz) Plots of Applied Compressive Load versus End-Shortening Displacement for the $[O_6//45_6]_T$ Laminate with Simply-Supported Side Boundary Conditions

load, the end-shortening displacement, u, was essentially unrestricted by the laminate. Large displacements occurred with no increase in load-carrying capability. The classical wide-column buckling behavior was observed for all of these laminates, without any postbuckling stiffening. The load versus end-shortening displacement results for a typical laminate example are presented in Figure 5.63 for the $[0_3//90_3//0_3//90_3]_T$ laminate tested with free side boundary conditions.

5.4 Isodeflection Contour Maps

As described in Chapter 4, isodeflection contours were generated from the deflection tracker data taken at the limit load (as defined in Section 4.3) and during the succeeding phases for the fifth laminate of each type tested with clamped side boundary conditions. Maps were made using a nine by nine (internal) grid of deflection measurements for the experimental modes and the same grid for the analytical calculations. It should be pointed out that the nonlinear Rayleigh-Ritz analytical calculations for contour mapping were performed only at multiples of load equal to 9.0 kN, whereas the experimental contour data were obtained at either the previously defined limit load, or at approximate multiples of 4.5 kN. A complete set of the experimental isodeflection contour maps are in Appendix H.

Isodeflection contour maps, as predicted by the linear

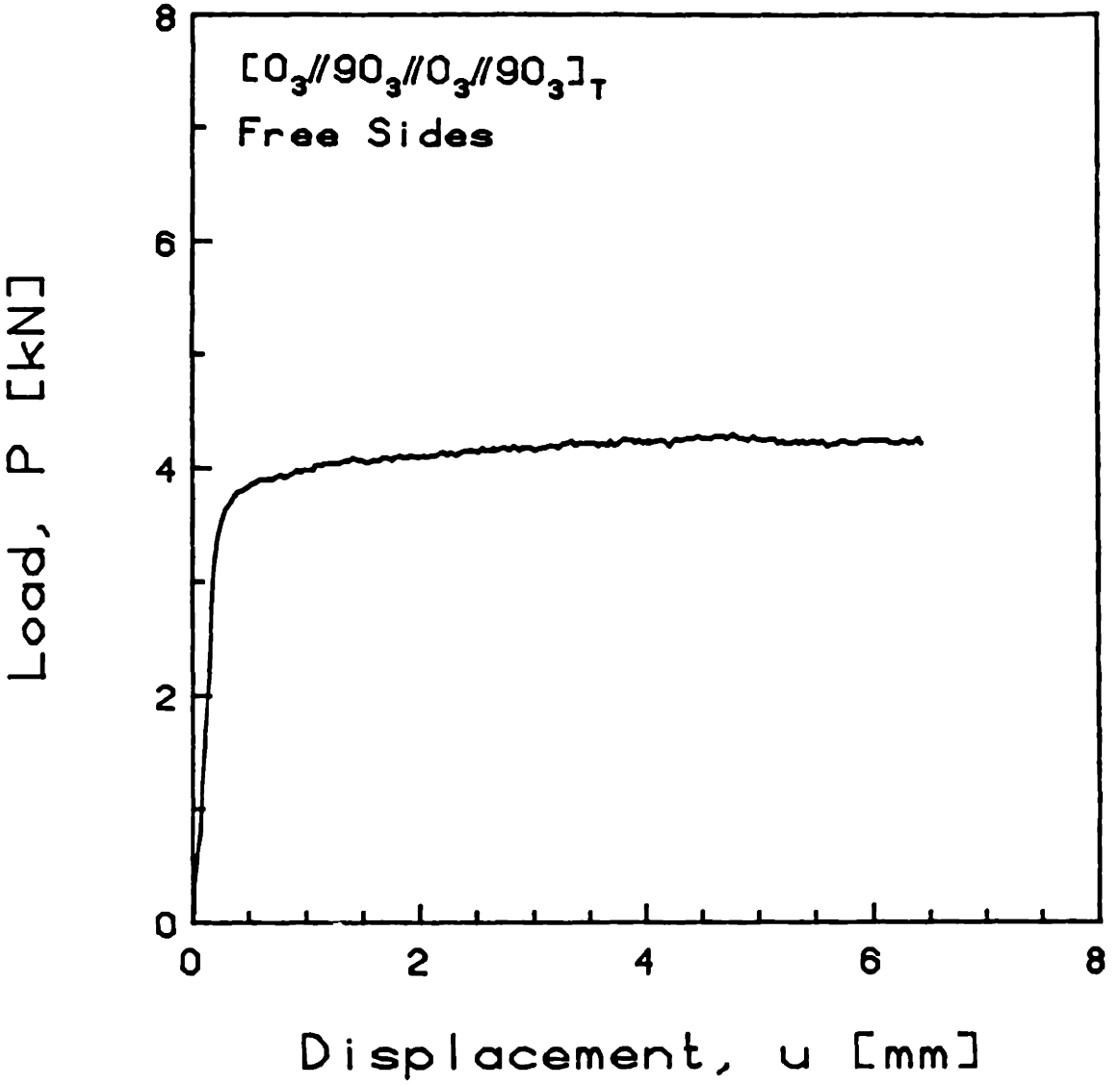

FIGURE 5.63 Experimental Plot of Applied Compressive Load versus End-Shortening Displacement for the $[0_3//90_3//0_3//90_3]_T$ Laminate with Free Side Boundary Conditions

Rayleigh-Ritz and the linear finite element analyses, are shown in Figure 5.64 for the $[0_6//45_6]_T$ laminate with simply-supported side boundary conditions. These contours, which are nearly identical, display predominantly a twisted first bending mode. Since both analyses predict the same general trends, the Rayleigh-Ritz choice of modes were considered to be adequate for extension to the nonlinear regime. A contour plot from the nonlinear Rayleigh-Ritz analysis, at 4.5 kN, is presented in Figure 5.65. This also has nearly the same shape.

A sampling of typical out-of-plane isodeflection contour maps is presented in this section to demonstrate the various types of behavior observed experimentally and predicted analytically. The isodeflection contours are plotted at 20%, 40%, 60%, and 80% of the normalized maximum deflection. The numbers in the center of these contour maps represent the magnitude of the deflection at that point in millimeters. The indicated experimental loads represent the average of the maximum and minimum loads observed during the course of the scanning operation. These isodeflection contours assist in the visualization of the out-of-plane deflection behavior of the laminates, as presented in Section 5.1. For the sake of compatibility with those results, only isodeflection contour maps which coincide with the laminates previously presented are included here for consideration.

As expected, isodeflection contours based on results from the symmetric laminates ($[0_3/90_3]_S$, $[0_3//90_3//90_3//0_3]_T$, and

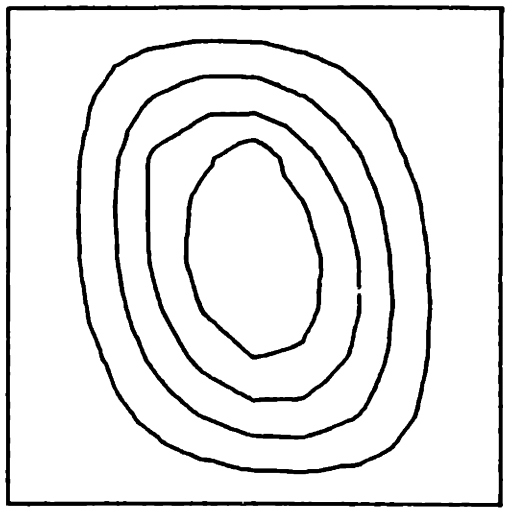

Linear Finite Element
$[0_6//45_6]_T$
Simply-supported Sides

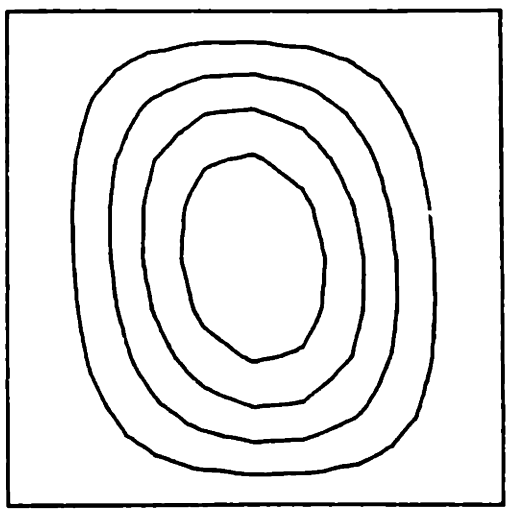

Linear Rayleigh-Ritz
$[0_6//45_6]_T$
Simply-supported Sides

FIGURE 5.64 Linear Finite Element (top) and Rayleigh-Ritz (bottom) Contour Maps for the $[0_6//45_6]_T$ Laminate with Simply-Supported Sides

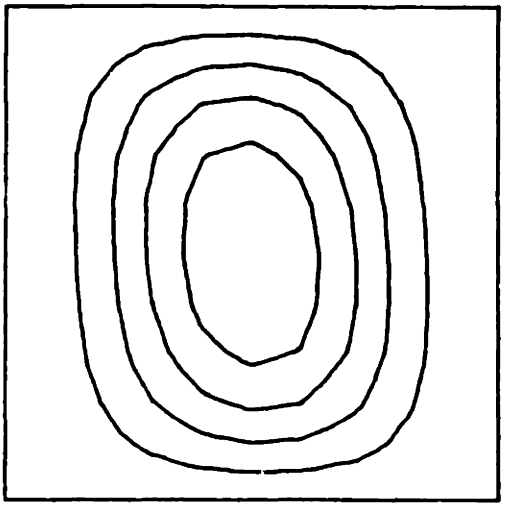

FIGURE 5.65 Nonlinear Rayleigh-Ritz Contour Map for the $[0_6//45_6]_T$ Laminate with Simply-Supported Sides

$[0_2//45_2//0_2//45_2//0_2]_T$) did not reveal any twist in the deflection behavior. An example of this symmetric behavior is shown in Figure 5.66 for the $[0_3//90_3//90_3//0_3]_T$-2 laminate tested with clamped side boundary conditions, with the equivalent predicted contour map at 9 kN based on the nonlinear Rayleigh-Ritz analysis.

The introduction of bending-stretching coupling into the laminate did not significantly affect the isodeflection contours. The slope in the y-direction was slightly shallower for the $[0_3//90_3//0_3//90_3]_T$ laminates than for the $[0_3//90_3//90_3//0_3]_T$ laminates, as observed from the theoretical plots in Figures 5.66 and 5.67 along with the experimental plots for specimens $[0_3//90_3//90_3//0_3]_T$-2 and $[0_3//90_3//0_3//90_3]_T$-5, respectively. However, the general deflection behavior was nearly identical in both cases, since no in-plane couplings exist in these laminates to introduce twisting.

The out-of-plane isodeflection contours from the $[0_2//45_2//0_2//45_2//0_2]_T$ and $[0_2//45_2//0_2//-45_2//0_2]_T$ laminates were somewhat more oval in shape than the contours from the orthotropic laminates, possibly due to the lower bending stiffness. Additionally, the mode shapes exhibited twisting due to the combination of geometric (large deflection) and bending-twisting coupling effects in the former laminate type, and due to stretching-twisting coupling in the latter laminate type. This effect is displayed in Figure 5.68 for the experimental isodeflection contour map from the

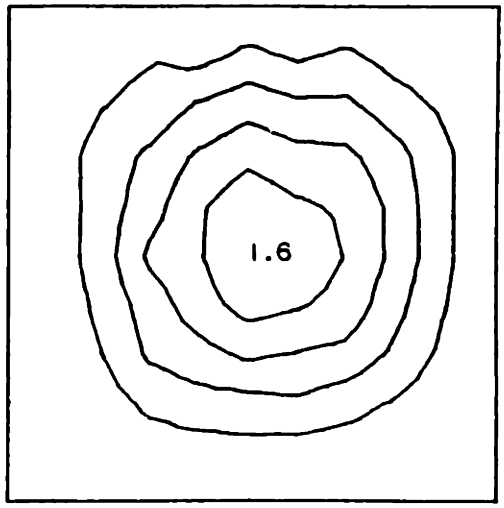

Experimental
$[0_3//90_3//90_3//0_3]_T$-2
Clamped Sides
5.3 kN

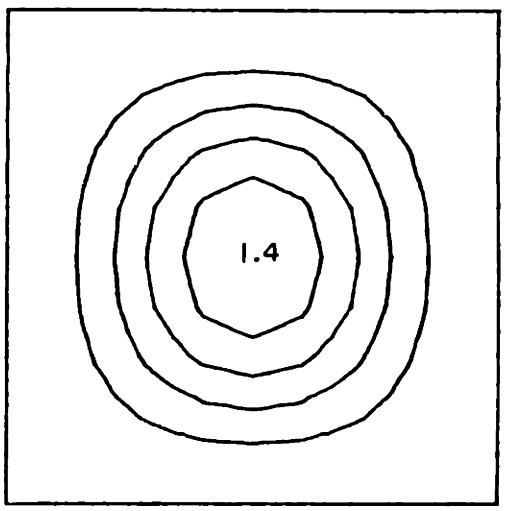

Rayleigh-Ritz
$[0_3//90_3//90_3//0_3]_T$
Clamped Sides
9.0 kN

FIGURE 5.66 Experimental (top) and Predicted (bottom, via Rayleigh-Ritz) Isodeflection Contour Maps for the $[0_3//90_3//90_3//0_3]_T$-2 Laminate with Clamped Side Boundary Conditions

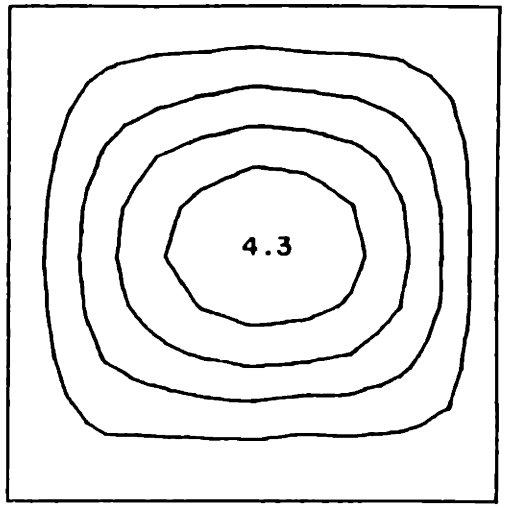

Experimental
$[0_3//90_3//0_3//90_3]_T$-5
Clamped Sides
8.9 kN

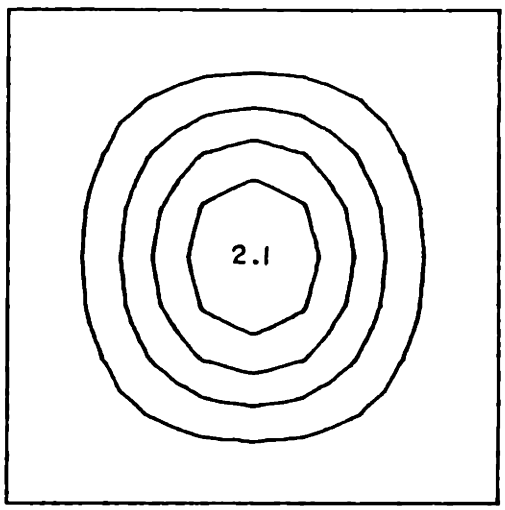

Rayleigh-Ritz
$[0_3//90_3//0_3//90_3]_T$
Clamped Sides
9.0 kN

FIGURE 5.67 Experimental (top) and Predicted (bottom, via Rayleigh-Ritz) Isodeflection Contour Maps for the $[0_3//90_3//0_3//90_3]_T$-5 Laminate with Clamped Side Boundary Conditions

$[0_2//45_2//0_2//45_2//0_2]_T$-2 laminate and in Figure 5.69 from the $[0_2//45_2//0_2//-45_2//0_2]_T$-1 laminate. In the analytical plots for these types of laminates, this twisting was not easily observed at low loads, i.e., near the "pseudo" buckling or limit loads. This implies that the twisting degrees-of-freedom in the nonlinear Rayleigh-Ritz analysis were too stiff.

The remaining isodeflection contour maps presented in this chapter come from the $[0_6//\theta_6]_T$ laminates, which inherently possess various combinations of all of the possible elastic couplings. For small lamination angles, θ, the effect of the bending-twisting coupling was evident from the twist in the mode shapes. For example, Figure 5.70 shows the isodeflection contour map for laminate $[0_6//15_6]_T$-5 tested with clamped side boundary conditions at 8.9 kN. As θ was increased to 30°, the couplings increased slightly, resulting in slightly more twist. This can be seen in Figure 5.71 for the $[0_6//30_6]_T$-5 laminate tested with clamped side boundary conditions at 8.7 kN and for the corresponding theoretical prediction at 9.0 kN.

A very interesting display of modal transition can be seen in Figures 5.72 through 5.74 for the $[0_6//45_6]_T$-5 laminate tested with clamped side boundary conditions at 3.8 kN, 8.4 kN, and 13.1 kN, along with the theoretical predictions at 9 kN and 18 kN. As the load was increased, the second mode began to appear in the upper right corner of the plate and rippled slowly across the plate as it developed into

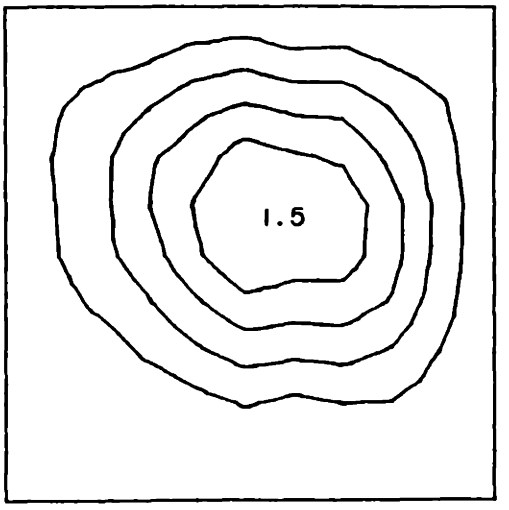

Experimental
$[0_2//45_2//0_2//45_2//0_2]_T$-2
Clamped Sides
3.7 kN

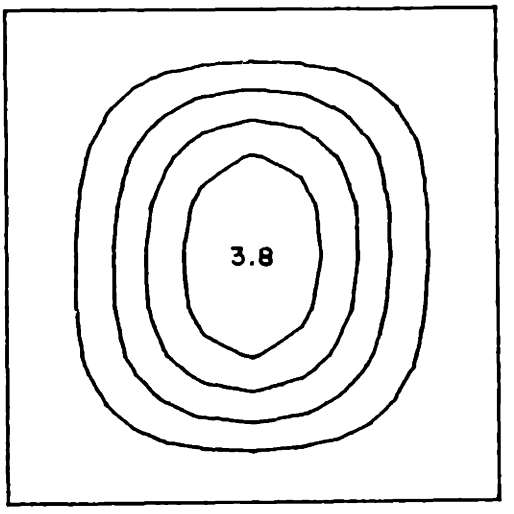

Rayleigh-Ritz
$[0_2//45_2//0_2//45_2//0_2]_T$
Clamped Sides
9.0 kN

FIGURE 5.68 Experimental (top) and Predicted (bottom, via Rayleigh-Ritz) Isodeflection Contour Maps for the $[0_2//45_2//0_2//45_2//0_2]_T$-2 Laminate with Clamped Side Boundary Conditions

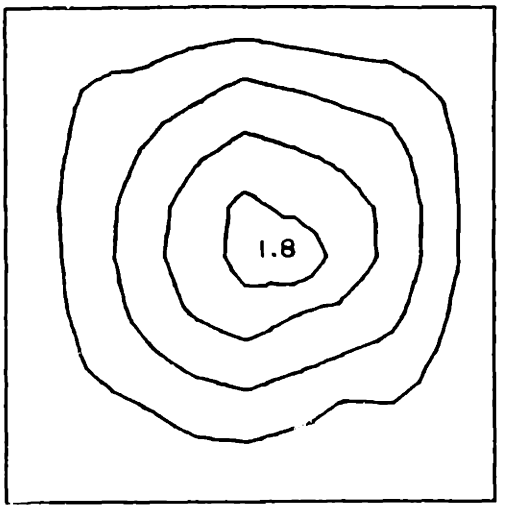

Experimental
$[0_2//45_2//0_2//-45_2//0_2]_T$-2
Clamped Sides
2.5 kN

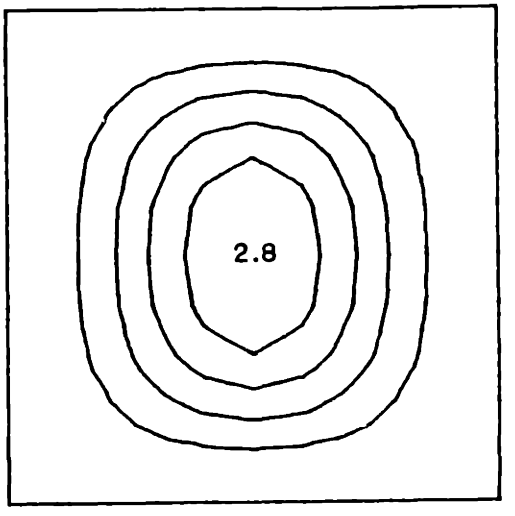

Rayleigh-Ritz
$[0_2//45_2//0_2//-45_2//0_2]_T$
Clamped Sides
9.0 kN

FIGURE 5.69 Experimental (top) and Predicted (bottom, via Rayleigh-Ritz) Isodeflection Contour Maps for the $[0_2//45_2//0_2//-45_2//0_2]_T$-2 Laminate with Clamped Side Boundary Conditions

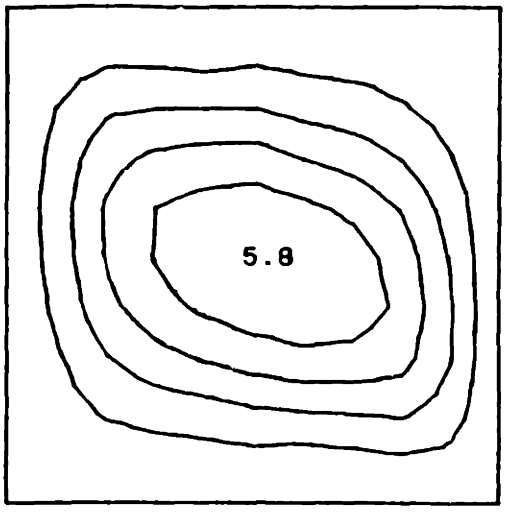

Experimental
$[0_6//15_6]_T$-5
Clamped Sides
8.9 kN

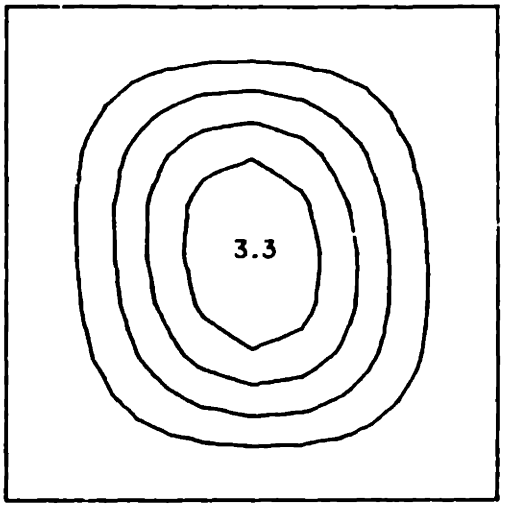

Rayleigh-Ritz
$[0_6//15_6]_T$
Clamped Sides
9.0 kN

FIGURE 5.70 Experimental (top) and Predicted (bottom, via Rayleigh-Ritz) Isodeflection Contour Maps for the $[0_6//15_6]_T$-5 Laminate with Clamped Side Boundary Conditions

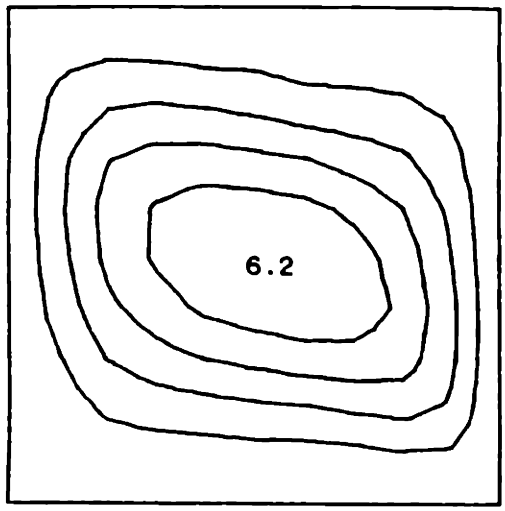

Experimental
$[0_6//30_6]_T$-5
Clamped Sides
8.7 kN

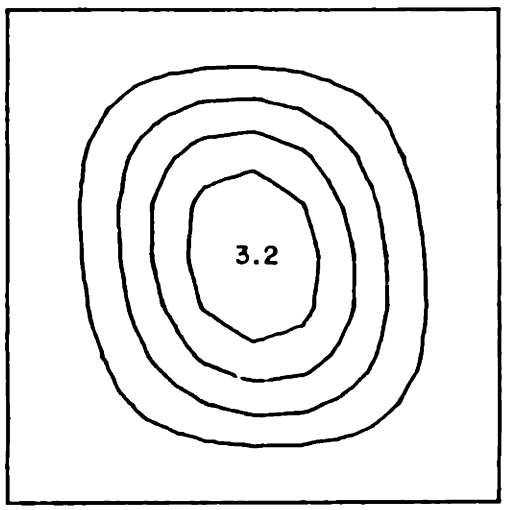

Rayleigh-Ritz
$[0_6//30_6]_T$
Clamped Sides
9.0 kN

FIGURE 5.71 Experimental (top) and Predicted (bottom, via Rayleigh-Ritz) Isodeflection Contour Maps for the $[0_6//30_6]_T$-5 Laminate with Clamped Side Boundary Conditions

a full second mode. The theoretical prediction at 9.0 kN correlates reasonably well with the earliest experimental contour map. However, at 18 kN the analysis is inadequately attempting to represent the higher mode behavior.

Another interesting phenomenon was exhibited by the $[0_6//60_6]_T$-5 laminate tested with clamped side boundary conditions. Figures 5.75 through 5.77 show the development of the third mode component, as discussed previously with regard to the load versus out-of-plane deflections, at 4.0 kN, 8.6 kN, and 13.1 kN, respectively, along with the theoretical predictions at 9 kN and 18.0 kN. This third mode component, most obvious in Figure 5.77, makes the isodeflection contours appear to be squeezed in the center. As pointed out in Section 5.1 and observed in Figure 5.77, the analysis did not predict any third bending mode components.

For θ equal to 75°, the fifth specimen was previously shown to exhibit two stable equilibrium positions at the same load level. Figures 5.78 and 5.79 show the isodeflection contour maps for these two modes, at 8.5 kN and 8.6 kN, respectively, and the analytical prediction at 9.0 kN. Again, a superimposed third bending mode component is readily observed in Figure 5.78.

The next two isodeflection contour maps also show two separate stable equilibrium modes for the $[0_6//90_6]_T$-5 laminate tested with clamped side boundary conditions. The second and third bending mode components observed experimentally at 8.7 kN and 13.0 kN, respectively, are

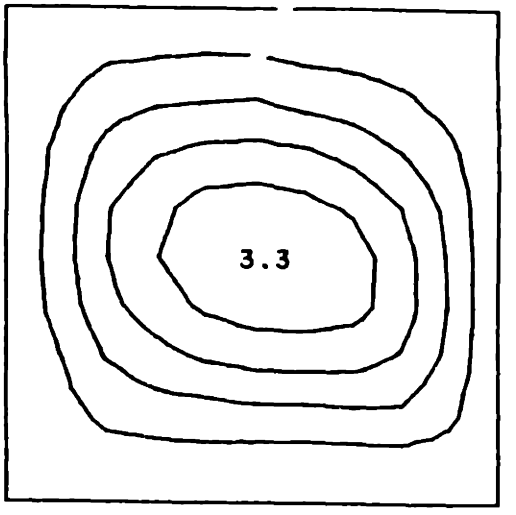

Experimental
$[0_6//45_6]_T$-5
Clamped Sides
3.8 kN

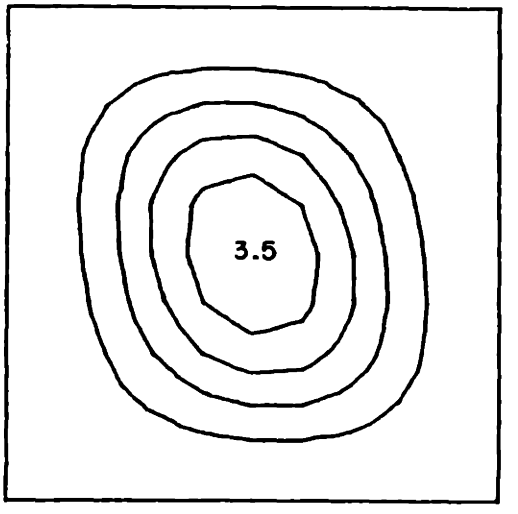

Rayleigh-Ritz
$[0_6//45_6]_T$
Clamped Sides
9.0 kN

FIGURE 5.72 Experimental Phase I (top) and Predicted (bottom, via Rayleigh-Ritz) Isodeflection Contour Maps for the $[0_6//45_6]_T$-5 Laminate with Clamped Side Boundary Conditions

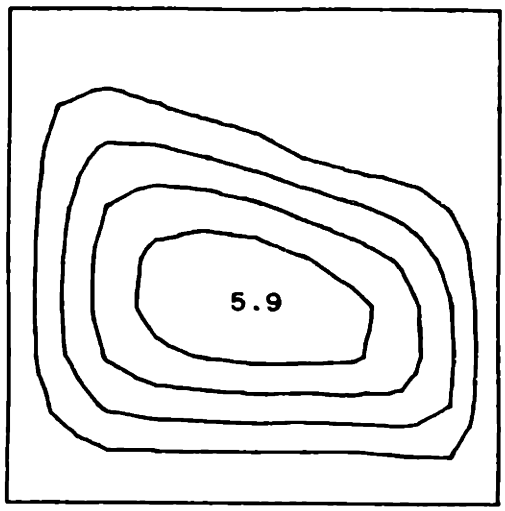

Experimental
$[0_6//45_6]_T$-5
Clamped Sides
8.4 kN

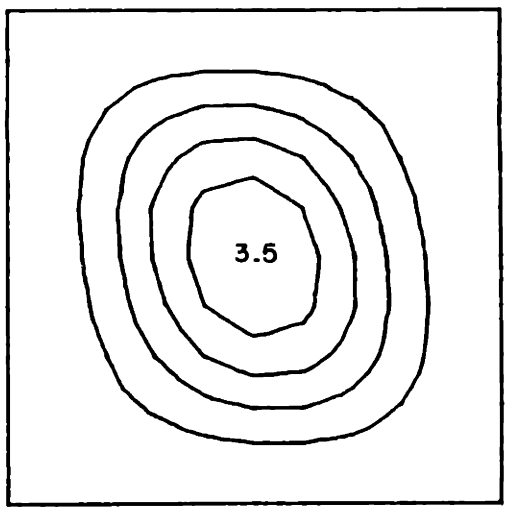

Rayleigh-Ritz
$[0_6//45_6]_T$
Clamped Sides
9.0 kN

FIGURE 5.73 Experimental Phase II (top) and Predicted (bottom, via Rayleigh-Ritz) Isodeflection Contour Maps for the $[0_6//45_6]_T$-5 Laminate with Clamped Side Boundary Conditions

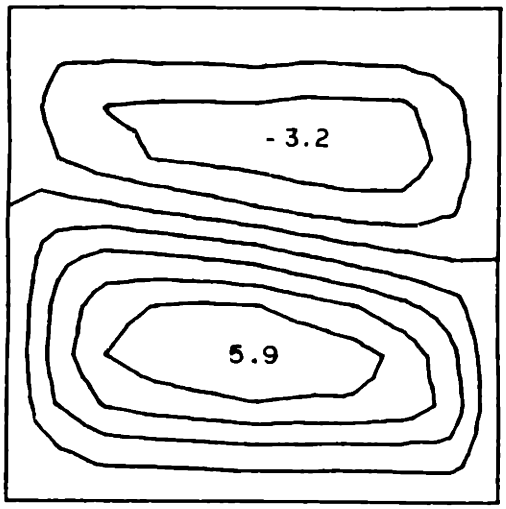

Experimental
$[0_6//45_6]_T$-5
Clamped Sides
13.1 kN

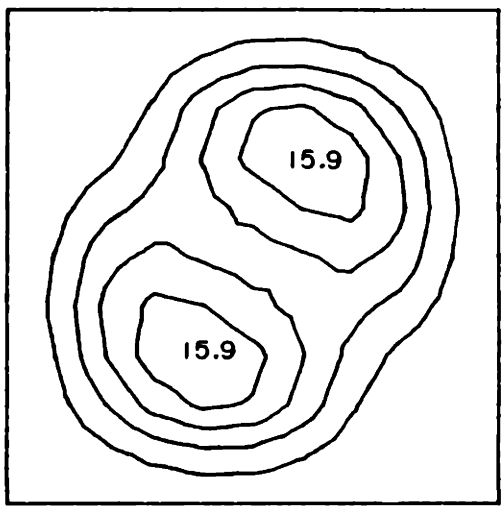

Rayleigh-Ritz
$[0_6//45_6]_T$
Clamped Sides
18.0 kN

FIGURE 5.74 Experimental Phase III (top) and Predicted (bottom, via Rayleigh-Ritz) Isodeflection Contour Maps for the $[0_6//45_6]_T$-5 Laminate with Clamped Side Boundary Conditions

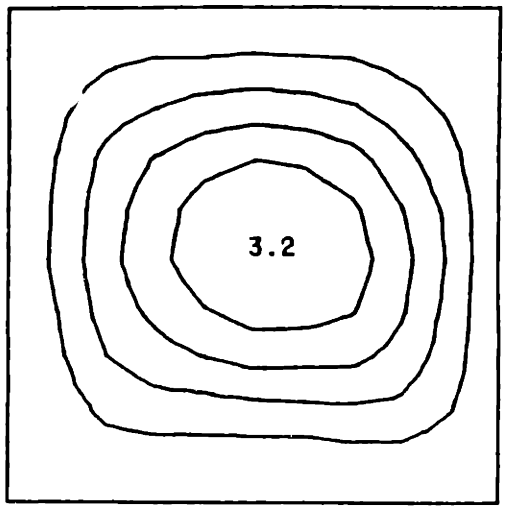

Experimental
$[0_6//60_6]_T$-5
Clamped Sides
4.0 kN

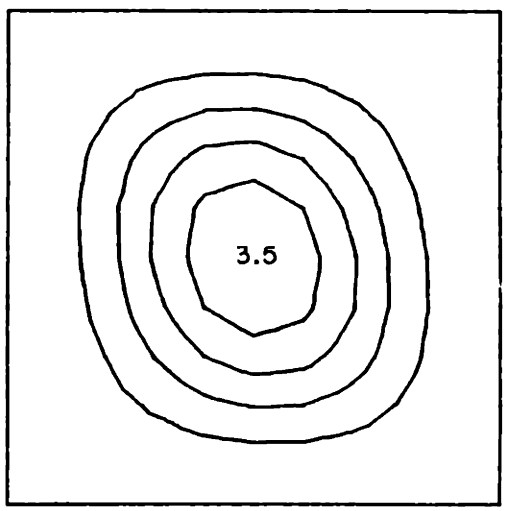

Rayleigh-Ritz
$[0_6//60_6]_T$
Clamped Sides
9.0 kN

FIGURE 5.75 Experimental Phase I (top) and Predicted (bottom, via Rayleigh-Ritz) Isodeflection Contour Maps for the $[0_6//60_6]_T$-5 Laminate with Clamped Side Boundary Conditions

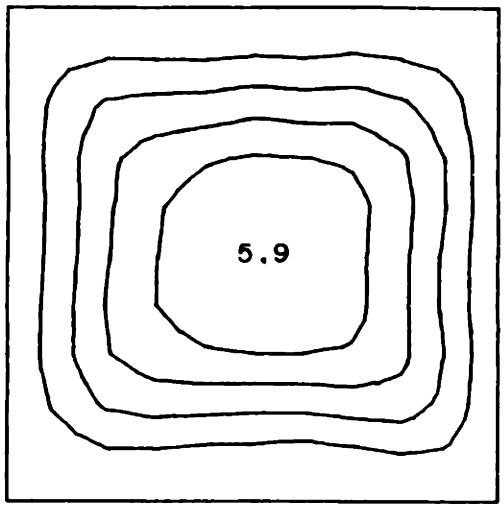

Experimental
$[0_6//60_6]_T$-5
Clamped Sides
8.6 kN

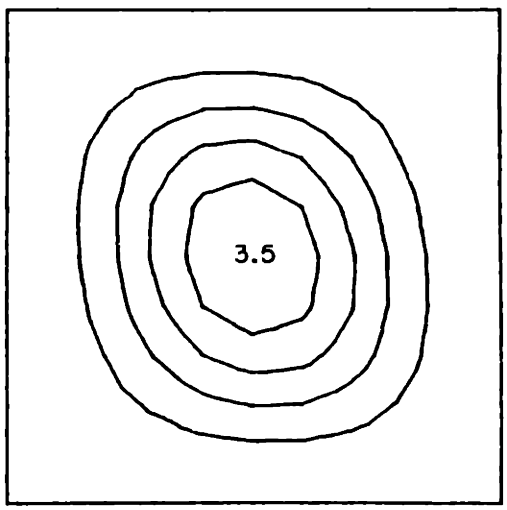

Rayleigh-Ritz
$[0_6//60_6]_T$
Clamped Sides
9.0 kN

FIGURE 5.76 Experimental Phase II (top) and Predicted (bottom, via Rayleigh-Ritz) Isodeflection Contour Maps for the $[0_6//60_6]_T$-5 Laminate with Clamped Side Boundary Conditions

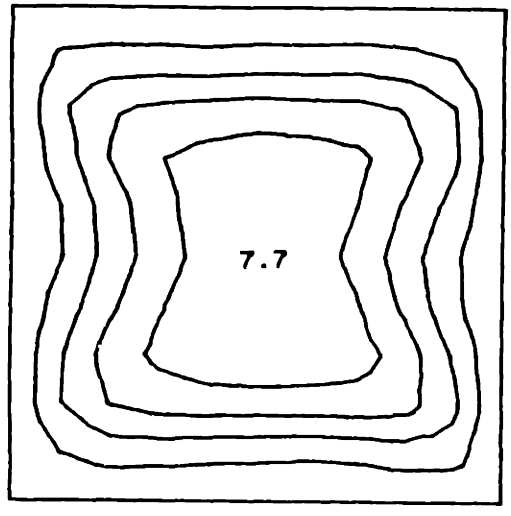

Experimental
$[0_6//60_6]_T$-5
Clamped Sides
13.1 kN

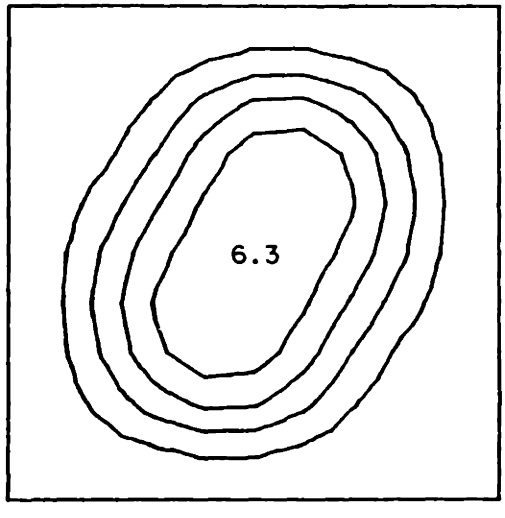

Rayleigh-Ritz
$[0_6//60_6]_T$
Clamped Sides
18.0 kN

FIGURE 5.77 Experimental Phase III (top) and Predicted (bottom, via Rayleigh-Ritz) Isodeflection Contour Maps for the $[0_6//60_6]_T$-5 Laminate with Clamped Side Boundary Conditions

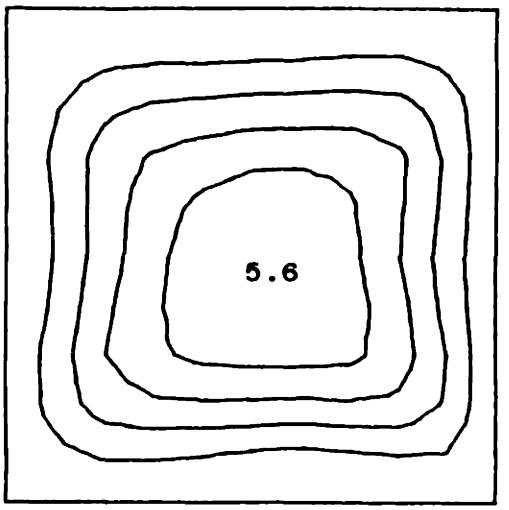

Experimental
$[0_6//75_6]_T$-5
Clamped Sides
8.5 kN

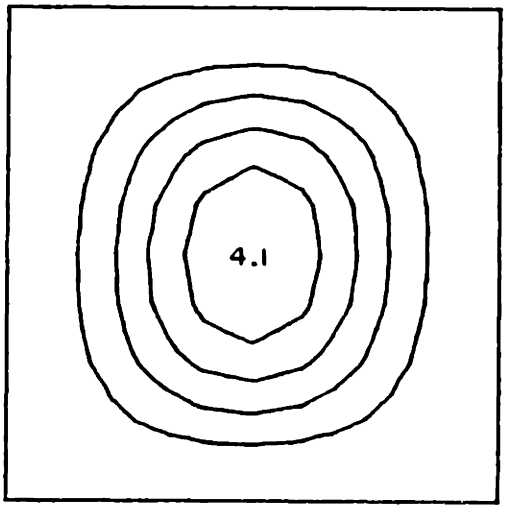

Rayleigh-Ritz
$[0_6//75_6]_T$
Clamped Sides
9.0 kN

FIGURE 5.78 Experimental Phase II (top) and Predicted (bottom, via Rayleigh-Ritz) Isodeflection Contour Maps for the $[0_6//75_6]_T$-5 Laminate with Clamped Side Boundary Conditions

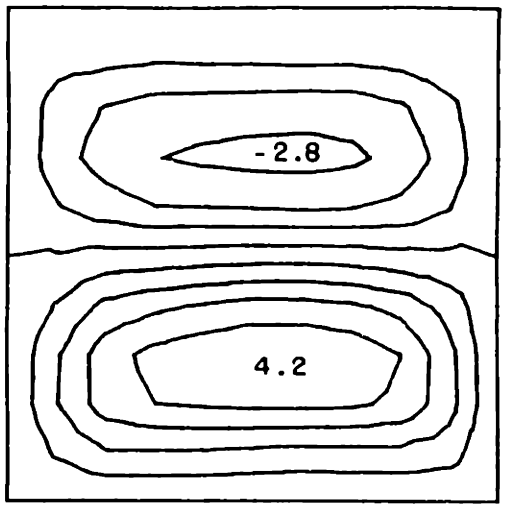

Experimental
$[0_6//75_6]_T$-5
Clamped Sides
8.6 kN

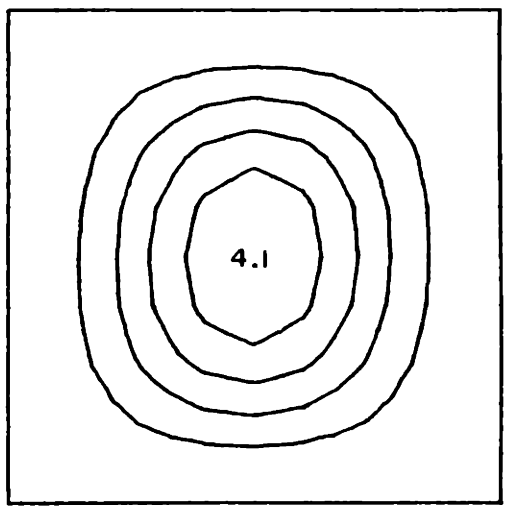

Rayleigh-Ritz
$[0_6//75_6]_T$
Clamped Sides
9.0 kN

FIGURE 5.79 Experimental Phase III (top) and Predicted (bottom, via Rayleigh-Ritz) Isodeflection Contour Maps for the $[0_6//75_6]_T$-5 Laminate with Clamped Side Boundary Conditions

apparent in Figure 5.80. However, the second mode position for this particular laminate was not a naturally preferred mode and was obtained only after applying the transverse counter-force, as discussed previously.

All of the isodeflection contour maps from the laminates with simply-supported side boundary conditions reinforced the findings already discussed in Section 5.1 and those presented above. However, each of the contour maps were biased to the right. This implies that a boundary condition error existed, possibly resulting in an applied moment at the left boundary. A typical contour map is shown in Figure 5.81 for the $[0_3//90_3//90_3//0_3]_T$ laminate tested with simply-supported side boundary conditions.

In summary, the isodeflection contour maps support the findings previously discussed, and assist in visualizing the deflection patterns and their modal components.

5.5 Buckling Loads

The experimentally observed and theoretically predicted primary and secondary buckling loads are summarized in Tables 5.4 and 5.5 for each of the laminates investigated with clamped and simply-supported side boundary conditions, respectively. As a reminder, the first mode experimental buckling values were calculated by the Southwell technique and do not necessarily correspond to any meaningful location on the load versus deflection curves, whereas the second mode

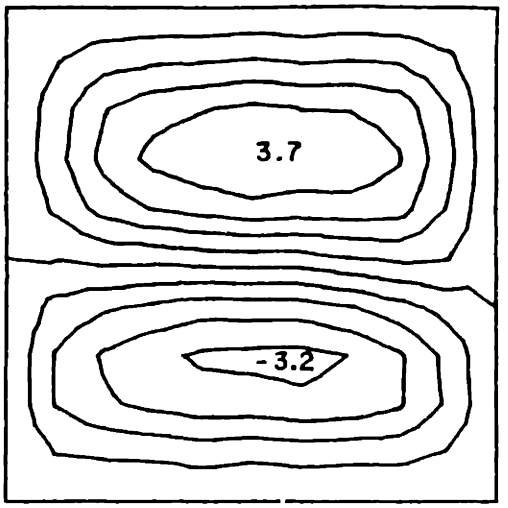

Experimental
$[0_6//90_6]_T$-5
Clamped Sides
8.7 kN

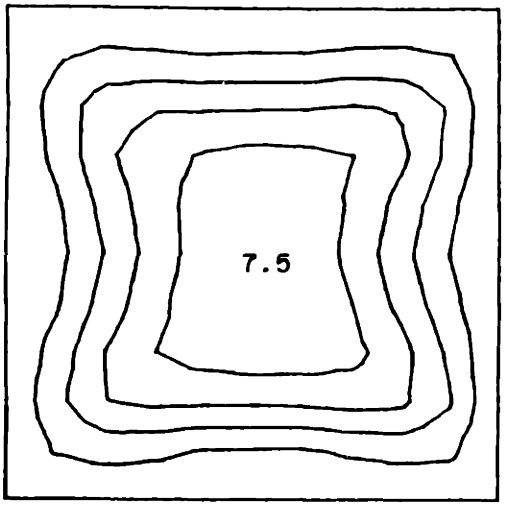

Experimental
$[0_6//90_6]_T$-5
Clamped Sides
13.0 kN

FIGURE 5.80 Experimental Phase II (top) and III (bottom) Isodeflection Contour Maps for the $[0_6//90_6]_T$-5 with Clamped Side Boundary Conditions

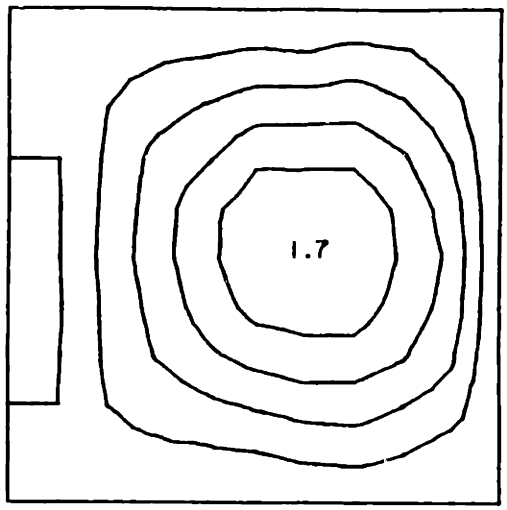

Experimental
$[0_3//90_3//90_3//0_3]_T$
Simply-supported Sides
4.6 kN

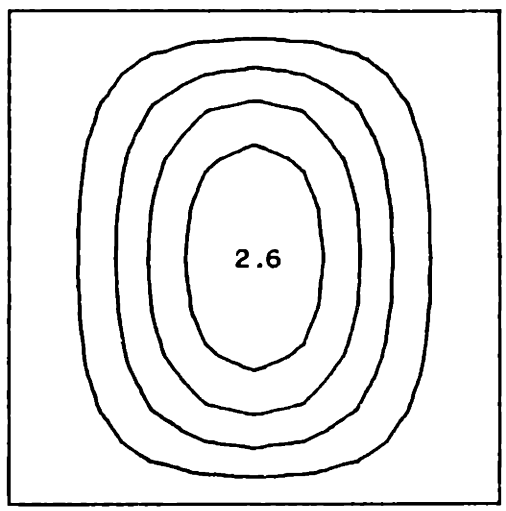

Rayleigh-Ritz
$[0_3//90_3//90_3//0_3]_T$
Simply-supported Sides
9.0 kN

FIGURE 5.81 Experimental (top) and Predicted (bottom, via Rayleigh-Ritz) Isodeflection Contour Maps for the $[0_3//90_3//90_3//0_3]_T$ Laminate with Simply-supported Side Boundary Conditions

instabilities, where the plate radically changed shape, were actually observed in the experiment.

The primary instability for laminates with membrane-flexural couplings is of value principally for comparative purposes. In general, the buckling loads determined via the Southwell method agree well with the predictions from both the linear Rayleigh-Ritz and finite element analyses. However, in almost all of the cases, the empirical results actually exceeded the predicted buckling loads. Also, interestingly enough, there was not any distinguishable difference between the experimental buckling loads for the two types of restrained side boundary conditions used. The analyses predict an increase in buckling load ranging from 10% to almost 60% for laminates with clamped sides over those with simply-supported sides (isotropic theory predicts an increase of 35%). In fact, the empirical buckling loads for the $[0_6//\theta_6]_T$ laminates were nearly the same for all values of θ while both of the analyses predicted a rather significant decrease (44% for clamped side boundary conditions and 60% for simply-supported side boundary conditions) in the buckling loads as θ changed from 15° to 90°. This raises a question as to the validity of a bifurcation buckling load for laminates with membrane-flexural couplings.

The secondary instability generally occurred at a compressive load level near the theoretically predicted value for the second linear buckling mode. The experimentally observed secondary instabilities were measured directly from

TABLE 5.4

PREDICTED AND MEASURED BUCKLING LOADS FOR LAMINATES WITH CLAMPED SIDE BOUNDARY CONDITIONS

Laminate Type	Mode	Buckling Loads [kN] Experiment	Rayleigh-Ritz	Finite Element
S	1	5.6[a] (17%)[c]	8.6	8.5
	2	-	14.8	13.6
T	1	11.5[a] (20%)	9.8	9.8
	2	-	17.0	15.6
U	1	9.8[a] (20%)	8.2	8.3
	2	12.7[b]	11.6	10.1
P	1	7.4[a] (21%)	6.0	5.9
	2	-	10.1	9.5
N	1	6.6[a] (26%)	5.5	5.4
	2	-	10.6	9.2
A	1	5.8[a] (8.1%)	7.2	7.2
	2	-	13.5	11.4
B	1	4.7[a] (21%)	5.2	5.3
	2	-	12.6	8.2
C	1	5.2[a] (27%)	4.3	4.4
	2	7.8[b]	11.4	6.3
D	1	4.5[a] (34%)	4.1	4.1
	2	5.3[b]	10.5	5.4
E	1	4.9[a] (31%)	4.1	4.1
	2	4.7[b]	9.9	5.1
F	1	5.5[a] (32%)	4.1	4.2
	2	4.5[b]	9.7	5.0

[a] Determined via the Southwell method.
[b] Observed during the test.
[c] Numbers in parentheses are coefficients of variation.

TABLE 5.5

PREDICTED AND MEASURED BUCKLING LOADS FOR LAMINATES WITH SIMPLY-SUPPORTED SIDE BOUNDARY CONDITIONS

Laminate Type	Mode	Buckling Loads [kN]		
		Experiment	Rayleigh-Ritz	Finite Element
S	1	7.1[a]	7.3	7.2
	2	-	12.4	12.5
T	1	11.9[a]	8.4	8.3
	2	-	14.2	14.3
U	1	6.6[a]	5.2	5.3
	2	-	10.4	9.2
P	1	6.1[a]	5.3	5.2
	2	-	8.5	8.5
N	1	7.9[a]	5.0	4.9
	2	-	8.9	7.8
A	1	5.5[a]	6.6	6.5
	2	-	10.9	9.7
B	1	4.9[a]	4.6	4.5
	2	-	10.8	7.5
C	1	5.4[a]	3.5	3.5
	2	8.6[b]	9.8	5.9
D	1	4.5[a]	3.0	2.9
	2	5.5[b]	8.5	5.0
E	1	5.6[a]	2.7	2.7
	2	-	7.6	4.6
F	1	4.4[a]	2.6	2.6
	2	-	7.3	4.5

[a] Determined via the Southwell method.
[b] Observed during the test.

the data. The associated critical load was defined as the load at which the rate of change in the deflection at the center of the plate with respect to the applied load went to zero, prior to reversal. This corresponds to a change in slope on the P vs. w graphs from positive (bulging) to negative (dimpling).

The laminates tested with free side boundary conditions displayed almost classical wide-column buckling behavior. Once the buckling load was reached, the laminates continued to deflect out-of-plane without any further increase in load. The tests, performed in stroke control, were continued until further end shortening would have damaged the test fixture. Total end shortening of the plates exceeded 25 mm and center plate deflections approached 50 mm. There was some cracking at the boundaries, but none of the plates actually broke during loading. The experimental maximum loads, which are equivalent to the buckling loads, are summarized in Table 5.6. There was not any postbuckling stiffening for the laminates with free sides.

5.6 Final Failure

It is important to note at the outset that none of the 75 laminates tested exhibited any fiber breakage. The apparent failure sequence, as deduced from observations during the tests and postmortem examinations, began with delamination at the room temperature bondline, followed by matrix cracking

TABLE 5.6

MEASURED BUCKLING LOADS FOR LAMINATES WITH FREE SIDE BOUNDARY CONDITIONS

Laminate Type	Experimental Buckling Loads[a] [kN]
S	5.32
T	7.41
U	4.32
P	5.22
N	4.87
A	5.52
B	3.65
C	2.59
D	2.17
E	1.83
F	1.96

[a] Maximum compressive load.

(parallel to the fibers), and eventually, to a sudden decrease in the load-carrying capability. This loss of strength was defined as failure.

The failure (or maximum) stress for each of the laminates tested with clamped side boundary conditions are presented in Tables 5.7 through 5.9, along with a notation as to which of the laminates exhibited second mode failures. The ultimate load carried by each plate is given in Table 5.7. The longitudinal end-shortening displacement at failure is given in Table 5.8. The maximum lateral deflection experienced at the center of the plate during the course of the test is given in Table 5.9. The maximum center deflection does not necessarily correspond to the maximum deflection in the plate for the laminates which buckled into a second mode prior to failure, since the center of the plate was near the nodeline.

The failure values for each of the nominally identical laminates tested with clamped side boundary conditions were very consistent for the plates which failed in similar modes. There was, however, a discernible distinction in the deflection data between those laminates which failed in the primary bending mode and those which transitioned into the secondary bending mode due to the nodeline near the center. The laminates tested with simply-supported side boundary conditions displayed similar results. No real failure values exist for the laminates tested with free sides. The test dat. was terminated at the point where the lateral deflection exceeded 25.4 mm.

TABLE 5.7

MAXIMUM COMPRESSIVE LOAD FOR SPECIMENS WITH CLAMPED SIDE BOUNDARY CONDITIONS

Laminate Type	Specimen Number[b]					Average[b]	
	1	2	3	4	5	Mode 1	Mode 2
S	29.5	30.7	27.2	-	-	29.1	-
T	36.1	36.9	30.7	36.9	29.1	34.0	-
U	33.1[a]	31.3[a]	25.9	30.5	32.0	29.5	32.2
P	23.2	25.3	23.5	24.5	23.3	23.9	-
N	23.3	20.6	21.8	21.9	21.9	21.9	-
A	22.2	18.7	18.4	18.5	20.8	19.7	-
B	23.1	20.3	21.1	20.4	21.4	21.2	-
C	24.0[a]	20.0	21.3[a]	21.4	23.4[a]	20.7	22.9
D	25.1[a]	20.2	23.3	21.6	21.4	21.6	25.1
E	22.2[a]	24.7[a]	21.1	21.0	22.2[a]	21.1	23.0
F	20.2[a]	21.2[a]	18.6	19.4	21.6	19.9	20.7

[a] Indicates dominate second bending component at failure.
[b] All loads expressed in kN.

TABLE 5.8

MAXIMUM LONGITUDINAL END-SHORTENING FOR SPECIMENS WITH CLAMPED SIDE BOUNDARY CONDITIONS

Laminate Type	Specimen Number[b]					Average[b]	
	1	2	3	4	5	Mode 1	Mode 2
S	1.9	1.7	1.7	-	-	1.8	-
T	1.8	1.9[a]	1.4	1.6	1.6	1.7	-
U	1.7[a]	1.7[a]	1.4	1.5	1.6	1.5	1.7
P	1.4	1.4	1.3	1.4	1.1	1.3	-
N	1.4	1.3	1.3	1.3	1.6	1.4	-
A	1.1	1.3	1.7	1.2	1.2	1.3	-
B	1.1	1.4	1.5[a]	1.4	1.4[a]	1.3	-
C	1.6[a]	1.4	1.6[a]	1.7	1.8[a]	1.6	1.7
D	1.7[a]	1.7[a]	1.6	1.7	1.5[a]	1.6	1.7
E	2.2[a]	1.8[a]	1.6	1.7	2.0[a]	1.7	2.0
F	1.9[a]	1.8[a]	1.4	1.7	1.5	1.5	1.9

[a] Indicates dominate second bending component at failure.
[b] All displacements expressed in mm.

TABLE 5.9

MAXIMUM LATERAL DEFLECTION AT PLATE CENTER FOR SPECIMENS WITH CLAMPED SIDE BOUNDARY CONDITIONS

Laminate Type	Specimen Number[b]					Average[b]	
	1	2	3	4	5	Mode 1	Mode 2
S	11.9	12.5	10.8	-	-	11.7	-
T	12.0[a]	12.3[a]	10.3	11.7	11.0	11.4	-
U	4.9[a]	3.3[a]	8.7	9.9	10.9	9.8	4.1
P	10.4	10.6	9.6	9.8	9.7	10.0	-
N	9.9	9.7	9.8	9.7	10.0	9.8	-
A	9.2	9.3	11.0	9.5	10.0	9.8	-
B	9.3[a]	9.6	11.0[a]	9.1	10.7[a]	9.9	-
C	5.1[a]	9.3	3.7[a]	9.7	4.1[a]	9.5	4.3
D	2.1[a]	8.9[a]	9.3	9.2	8.7[a]	9.0	2.1
E	2.9[a]	2.2[a]	9.5	9.8	3.2[a]	9.7	2.8
F	2.0[a]	1.7[a]	8.8	8.9	9.6	9.1	1.9

[a] Indicates dominate second bending component at failure.
[b] All deflections expressed in mm.

A summary of each of the three types of failure data described above is presented in Tables 5.10 through 5.12 for all of the boundary conditions investigated. The mean and coefficient of variation for each type of laminate tested with clamped side boundary conditions are also reported there. The data from the laminates tested with free side boundary conditions were arbitrarily truncated at the point where the lateral deflection at the center of the plate reached 25.4 mm.

Insufficient data were available to identify many significant trends within the failure data. The laminates with simply-supported side boundary conditions did, however, fail at lower load levels than the plates tested with clamped side boundary conditions.

TABLE 5.10

SUMMARY OF AVERAGE MAXIMUM COMPRESSIVE LOADS

Laminate Type	Side Boundary Conditions[c]			
	Clamped		Simply-Supported	Free
	Mode 1	Mode 2[a]		
S	29.1 (5.8%)[b]	-	27.5	5.3
T	34.0 (11%)	-	28.7	7.4
U	29.5 (11%)	32.2 (3.9%)	30.7	4.3
P	23.9 (3.8%)	-	19.4	5.2
N	21.9 (4.4%)	-	23.3	4.9
A	19.7 (8.6%)	-	17.9	5.5
B	21.2 (5.3%)	-	18.7[a]	3.7
C	20.7 (4.8%)	22.9 (6.2%)	18.1[a]	2.6
D	21.6 (5.8%)	25.1	19.6[a]	2.2
E	21.1 (0.6%)	23.0 (6.3%)	18.0	1.8
F	19.9 (7.8%)	20.7 (3.6%)	15.6	2.0

[a] Indicates dominate second bending component at failure.
[b] Numbers in parentheses are coefficients of variation.
[c] All loads expressed in mm.

TABLE 5.11

SUMMARY OF AVERAGE MAXIMUM LONGITUDINAL END-SHORTENING

Laminate Type	Side Boundary Conditions[c]			
	Clamped		Simply-Supported	Free
	Mode 1	Mode 2[a]		
S	1.8 (6.2%)[b]	-	1.7	4.2
T	1.7 (11%)	-	1.4	2.4
U	1.5 (7.1%)	1.7 (1.9%)	1.6	6.4
P	1.3 (9.1%)	-	1.5	6.3
N	1.4 (11%)	-	1.2	6.5
A	1.3 (17%)	-	1.3	6.2
B	1.3 (11%)	-	1.5	6.3
C	1.6 (9.3%)	1.7 (6.1%)	1.5[a]	6.4
D	1.6 (3.5%)	1.7	1.6[a]	6.6
E	1.7 (3.9%)	2.0 (10%)	1.5	6.9
F	1.5 (8.2%)	1.8 (1.8%)	1.4	6.6

[a] Indicates dominate second bending component at failure.
[b] Numbers in parantheses are coefficients of variation.
[c] All displacements expressed in mm.

TABLE 5.12
SUMMARY OF AVERAGE MAXIMUM LATERAL DEFLECTION AT CENTER OF PLATE

Laminate Type	Side Boundary Conditions[c]			
	Clamped		Simply-Supported	Free
	Mode 1	Mode 2[a]		
S	11.7 (7.4%)[b]	-	12.0	20.9
T	11.4 (6.9%)	-	10.8	15.2
U	9.8 (11%)	4.1 (26%)	11.2	25.5
P	10.0 (4.5%)	-	9.3	25.5
N	9.8 (1.3%)	-	9.9	25.4
A	9.8 (7.6%)	-	8.9	25.4
B	9.9 (8.7%)	-	9.1	25.5
C	9.5 (2.6%)	4.3 (17%)	3.6[a]	25.5
D	9.0 (3.2%)	2.1	3.3[a]	25.5
E	9.7 (2.3%)	2.8 (18%)	10.4	25.4
F	9.1 (4.9%)	1.8 (12%)	8.9	25.4

[a] Indicates dominate second bending component at failure.
[b] Numbers in parentheses are coefficients of variation.
[c] All deflections expressed in mm.

CHAPTER 6

DISCUSSION

Significant trends observed in the data are identified and interpreted in this chapter. A brief discussion of the experimental accuracy and analytical techniques employed, including comments on the differences observed between the results for specimens tested with clamped and simply-supported side boundary conditions, is presented, followed by a discussion of the effects of the room-temperature bondlines, bending-stretching coupling, the stretching-shearing/bending-twisting coupling combination, stretching-twisting coupling, and full coupling for laminates tested with restrained (clamped and simply-supported) side boundary conditions. The laminates tested with free side boundary conditions behaved according to classical wide-column theory, employing reduced bending stiffness parameters, and are discussed separately.

6.1 Overview

The experimental strain and lateral deflection results were very good. The load versus out-of-plane deflection data were the most informative. These were supported by the isodeflection contour maps, and, in a qualitative manner, by the load versus strain data.

However, the initial slope of the experimental load versus in-plane strain, which has been selected as an effective modulus parameter, showed a fairly large coefficient of variation for each laminate set and exhibited some inconsistencies with the analytical predictions. Two major factors contributed to these discrepancies. First, the mechanical couplings inherent in the laminates studied induce internal stresses and moments (other than the desired applied load, N_x) which would cause shearing, bending, and twisting were the plate not physically restrained. The presence of the boundary conditions restricts this motion by exerting additional forces and moments. Such effects were not included in the simple analytical predictions, which were based on the constitutive relations from classical laminated plate theory. For example, sliding friction at the boundaries induces the transverse stress resultant, N_y; clamping induces the corresponding moment, M_y; and so on. Second, due to the physical design of the buckling jig, the plates actually experienced a uniform end-shortening during loading, as opposed to a uniform load distribution. For this condition, as the center of the plate deflects outward due to mechanical couplings and initial imperfections, the in-plane stress is relieved in that region. The actual load distribution becomes sinusoidal even for an isotropic plate as soon as any out-of-plane deflection occurs [15]. For an anisotropic plate, the load distribution is expected to be even further distorted, since the couplings will cause immediate and

significant out-of-plane deflections beginning with the onset of loading. However, in determining the effective modulus parameters, a uniform applied load was assumed.

End-shortening displacement measurements should compensate for this nonuniform stress distribution because they represent an equivalent average strain over the entire length of the plate. For this reason, the total end-shortening displacement, u, was measured. However, the end-shortening displacement data seemed to be quite sensitive to miscellaneous compliance in the system, such as rotation of the plates in the end boundary conditions. Compared to the theoretical predictions, the end-shortening displacement measurements were approximately twice as compliant and had fairly large coefficients of variation.

A close examination of the load versus out-of-plane deflection results for the symmetric, specially orthotropic laminates, $[0_3/90_3]_S$ and $[0_3//90_3//90_3//0_3]_T$, tested with clamped side boundary conditions shows that while the experimental data were not absolutely perfect, the results were very good in general and quite consistent between specimens. For example, the typical experimental load versus deflection plot shown in Figure 5.1 for the $[0_3/90_3]_S$-1 laminate agrees rather well with the corresponding theoretical prediction from the nonlinear Rayleigh-Ritz analysis, also shown in Figure 5.1.

Small deviations from the theoretically imposed conditions of symmetry indicate the combined influence of

misalignment of the plate and/or the test fixture, improper positioning of the transducers, thickness variations in the plate, slightly incorrect fiber orientations, load introduction errors, boundary condition errors, and the like. The fact that all of these conditions combined leads only to an antisymmetry error of less than one millimeter of lateral deflection in the $[0_3/90_3]_S$ and $[0_3//90_3//90_3//0_3]_T$ laminates underscores the validity of the test methods employed and the experimentally acquired data. The theoretical predictions from the nonlinear Rayleigh-Ritz analysis were also quite reasonable as a whole, with the most error in the predictions for the laminates which exhibited second and third bending mode components. The lowest bifurcation buckling loads predicted by both the linear Rayleigh-Ritz and finite element analyses agreed quite well with the experimental observations.

Another important observation relates to the repeatability of tests. Juxtaposing the lower graph in Figure 5.15 with Figure 5.16 clearly demonstrates that the tests are very repeatable. The end points of the curves in the first figure fall precisely on the curves in the second figure. However, the early part of the curves do not match exactly. This discrepancy deserves a point of clarification. Apparently, the teflon tape on the borders of the plates is compressed as the plate bends during the first loading. When the load is released, the teflon tape does not spring back to its former thickness, resulting in slightly larger deflections

in the early parts of subsequent loadings.

In general, for all of the laminates studied with clamped side boundary conditions, the deflections predicted by the analysis were not as large as those observed experimentally. This was expected for several reasons. First, the actual boundary conditions are not truly clamped. The teflon tape on the borders of the graphite/epoxy specimens acts somewhat like a limited elastic support. Second, the analysis models only a finite number of degrees of freedom and is therefore inherently too stiff. Third the effects of loading eccentricities, material flaws, or other parameters combine to increase the experimental deflections. Nevertheless, in spite of these effects, the analytical predictions match the experimental observations reasonably well in almost all of the cases.

In fact, the experimental results from the simply-supported laminates agree well with the analysis. This point is demonstrated in Figure 5.19 for the $[0_3/90_3]_S$ laminate with simply-supported side boundary conditions. These experimental and analytical plots can be compared to Figure 5.1 for a nominally identical laminate tested with clamped side boundary conditions. The difference between the experimental and theoretical deflections for the laminate with clamped side boundary conditions is understandable since it is difficult to experimentally obtain true clamped boundary conditions.

It should also be noted that in some cases, the predicted

out-of-plane deflections for laminates with simply-supported side boundary conditions actually exceeded those observed experimentally. This can be explained by realizing that there is some friction at the boundaries, restricting the in-plane sliding degree of freedom allowed for in the analytical model.

The theoretical predictions from the nonlinear Rayleigh-Ritz analysis showed the proper trends in most cases. The linear finite element analysis verified that the assumed modes in the Rayleigh-Ritz analysis were sufficient to properly represent the first mode behavior. Thus, a nonlinear finite element analysis was not necessary for the laminates which remained primarily in the first mode. However, the selected Rayleigh-Ritz modes were shown to be too stiff to properly represent the second longitudinal bending mode and third longitudinal bending mode component behavior. Additional assumed modes would need to be included in the non-linear Rayleigh-Ritz analysis in order to satisfactorily model the out-of-plane deflections of these higher modes. However, the modes selected for the Rayleigh-Ritz analyses in this investigation should be more than adequate for laminates with less severe couplings than those studied herein. In fact, most laminates have much milder couplings and, therefore, probably will not exhibit the higher modes found to exist in some of the specialized laminates presented here. The Rayleigh-Ritz analyses described in Chapter 3 should be able to accurately model this behavior.

6.2 Room-Temperature Bondline Effects

As described in the manufacturing section of Chapter 4, the only difference between the first two types of laminates selected for this investigation was the method of manufacture. The first laminate, type $[0_3/90_3]_S$, was manufactured in a single cure using normal procedures. This type served as a benchmark, primarily for determination of the room-temperature bondline effects by comparison with the $[0_3//90_3//90_3//0_3]_T$ laminates, which consisted of cured symmetric sublaminates bonded together at room temperature. This two-step manufacturing technique was necessary to obtain flat unsymmetric laminates.

The thickness of the room-temperature bondlines increased the bending stiffness and ultimate strength of the laminates. The bondlines, treated essentially as spacers in the analysis, separated the load-carrying graphite/epoxy sublaminates. This resulted in larger longitudinal and transverse bending stiffnesses. This is verified by comparison of the load versus deflection, w, curves in Figures 5.1 and 5.2 for the $[0_3/90_3]_S$-1 and $[0_3//90_3//90_3//0_3]_T$-2 laminates, respectively, tested with clamped side boundary conditions; Figures 5.19 and 5.20 for the same laminate types tested with simply-supported side boundary conditions; and Figures 5.30 and 5.31 for the corresponding laminates tested with free side boundary conditions. Both the nonlinear Rayleigh-Ritz analysis and the experiment supported this finding. In general, as was

expected, the theoretical predictions were slightly stiffer than the corresponding experimentally observed deflections. Likewise, the membrane and bending strain components were greater for the $[0_3/90_3]_S$ laminates because of the smaller bending stiffness, as shown in Figures 5.41 and 5.42.

Since the increased stiffness reduced the out-of-plane deflections, the ultimate load was generally 17% greater for the $[0_3//90_3//90_3//0_3]_T$ laminates tested with clamped side boundary conditions, 4% greater for the single laminate tested with simply-supported side boundary conditions, and 40% greater for the single laminate tested with free side boundary conditions. Otherwise, the observed and predicted behavior were similar for the two types of laminates. As an aside, however, it is interesting to point out that both types of symmetric laminates failed at approximately the same out-of-plane deflection (w) values.

Thus, the room-temperature bondlines increase the bending stiffness and ultimate strength of the laminates. This can be properly accounted for analytically by modelling the bondline as an additional ply with the properties of the epoxy used in the bondline.

The principle failure mechanism begins with delamination at the room-temperature bondline, followed by separation of the fibers via matrix splitting. The failure is apparently governed by the large deflections inducing shear stresses which induce delamination at the bondlines. Thus, this failure mode is pertinent only to specimens which utilize the

room-temperature epoxy bondlines.

6.3 Bending-Stretching Coupling Effects

Two types of laminates isolated bending-stretching coupling: $[0_3//90_3//0_3//90_3]_T$ and $[0_6//90_6]_T$. The $[0_3//90_3//0_3//90_3]_T$ laminates were manufactured from sublaminates nominally identical to those used in the $[0_3//90_3//90_3//0_3]_T$ laminates, but with an antisymmetric stacking arrangement. This resulted in lower longitudinal bending stiffness, higher transverse bending stiffness, and the introduction of bending-stretching coupling due to the shifted neutral axis. These effects resulted in a dramatically different behavior from the symmetric laminates. Two of the six laminates tested with partially restrained side boundary conditions (clamped or simply-supported) buckled into a second longitudinal bending mode (for example, see Figure 5.4). For the other four laminates which maintained predominantly first mode behavior, a significant third bending component was superimposed. This is quite readily observed in Figure 5.3 for the $[0_3//90_3//0_3//90_3]_T$-5 laminate tested with clamped side boundary conditions and in Figure 5.21 for the same laminate type tested with simply-supported side boundary conditions. These second and third bending components were not predicted by the nonlinear Rayleigh-Ritz analysis.

One possible explanation for this, which is not sufficient in and of itself to explain this phenomenon, takes

into consideration the effective aspect ratio, $(AR)_e$, based on orthotropic plate theory, [18,51,52], where:

$$(AR)_e = \frac{a}{b}\left(\frac{D_{22}}{D_{11}}\right)^{\frac{1}{4}} \tag{6.1}$$

This effective aspect ratio takes into account the material orthotropy by modifying the geometric aspect ratio, a/b, by the fourth root of the ratio of the transverse to longitudinal bending stiffness. The effective aspect ratios for the laminate types studied in this investigation are tabulated in Table 6.1.

For the $[0_3//90_3//0_3//90_3]_T$ laminates, this effective aspect ratio was 50% greater than for the $[0_3//90_3//90_3//0_3]_T$ laminates. In fact, only laminates with an effective aspect ratio greater than 0.7 buckled into the longitudinal second bending mode. Conversely, at least one of each type which had an effective aspect ratio greater than 0.7 tested with restrained side boundary conditions buckled into the second mode; whereas, none of the laminates with an effective aspect ratio less than 0.7 buckled into the second mode. Therefore, the effective aspect ratio can be regarded as a significant parameter governing the postbuckling behavior of plates loaded in uniaxial compression.

Elastically, the $[0_6//90_6]_T$ laminates were similar to the $[0_3//90_3//0_3//90_3]_T$ laminates with two exceptions: one, having two fewer bondlines, the $[0_6//90_6]_T$ laminates were

TABLE 6.1

EFFECTIVE ASPECT RATIOS

Laminate Type	$(AR)_e$
S	0.686
T	0.682
U	1.000
P	0.624
N	0.624
A	0.546
B	0.610
C	0.741
D	0.878
E	0.970
F	1.000

slightly thinner, minimally affecting the bending stiffnesses; and, two, the $[0_6//90_6]_T$ laminates nominally had twice the bending-stretching coupling as the $[0_3//90_3//0_3//90_3]_T$ laminates. Again, two of the six laminates of this type tested with partially restrained side boundary conditions transitioned into a second longitudinal bending mode. Those which remained in the first longitudinal bending mode developed third longitudinal bending components.

Interestingly enough, the effective orthotropic aspect ratio, $(AR)_e$, was identically equal to 1.0 for both of these cases. However, the third bending mode component in the longitudinal direction was substantially stronger for the $[0_6//90_6]_T$ case, which had nominally twice the magnitude of bending-stretching coupling. Thus, the effective aspect ratio alone cannot account for these higher bending mode components, nor the timing of their introduction, as seen in Figures 5.3 and 5.17. Therefore, the bending-stretching coupling must be responsible for this effect.

Also, in the free case, the observed buckling load for the $[0_6//90_6]_T$ laminate was slightly less than half that observed for the $[0_3//90_3//0_3//90_3]_T$ laminate. These observations correspond roughly to the reduced bending stiffness, D_{11}^*, which takes into account all of the elastic couplings mechanisms. This is discussed in further detail in Section 6.6.

A comparison of Figures 5.3 and 5.21 shows that bending-stretching coupling plays less of a role in the

behavior of laminates with simply-supported side boundary conditions than those with clamped side boundary conditions. The more restrictive the boundary conditions are, the greater the influence of the coupling terms. That is to say, the more restrictive boundary conditions prohibit natural deflections at the edges and, thus, introduce stresses which amplify the effects of the coupling.

6.4 Stretching-Shearing/Bending-Twisting versus Stretching-Twisting Coupling Effects

The $[0_2//45_2//0_2//45_2//0_2]_T$ laminates isolated the stretching-shearing/bending-twisting coupling in the constitutive relations. Only pure first bending behavior was displayed by these laminates, regardless of the side boundary conditions. Although these laminates possessed both stretching-shearing and bending-twisting couplings, higher bending components were not observed. However, some twisting was observed in the load versus deflection curves, e.g., Figures 5.5 and 5.22, for typical laminates with clamped and simply-supported side boundary conditions, respectively. However, these effects were not significant enough from which to draw any meaningful conclusions. Similarly, the strain data in Figure 5.45 revealed little, except that the behavior was relatively symmetric as anticipated. The theoretical curves support the existence of a small amount of twisting which is greater for the laminates with clamped side boundary

conditions (Figure 5.5) than for the laminates with simply-supported side boundary conditions. Thus, once again it is shown that the more restrictive the side boundary conditions are, the higher the induced reaction stresses at the boundaries will be, and consequently, the more significant the effects of the coupling mechanisms.

The $[0_2//45_2//0_2//-45_2//0_2]_T$ laminates isolated the stretching-twisting coupling in the constitutive relations. These laminates also exhibited an almost pure first bending mode. Both the laminates tested with clamped side boundary conditions and the single laminate tested with simply-supported side boundary conditions were very closely represented by the theoretical predictions for the simply-supported side boundary conditions.

The experimental results for the $[0_2//45_2//0_2//45_2//0_2]_T$ and $[0_2//45_2//0_2//-45_2//0_2]_T$ laminates, tested with simply-supported side boundary conditions, are quite similar to each other; whereas, the analytical predictions reveal some subtle differences (see Figures 5.5 and 5.6). The experimental results for both of these laminates more closely resembled the $[0_2//45_2//0_2//-45_2//0_2]_T$ predictions than the $[0_2//45_2//0_2//45_2//0_2]_T$ predictions. This indicates that the effects of the stretching-shearing couplings were restricted at the boundaries. That is, the experimental laminates were not actually permitted to slide freely in the boundary conditions. Friction restricted this motion. This implication was also deduced from the clamped results, but to

a less convincing degree.

The strain data supported the claim that the bending strains were larger for the $[0_2//45_2//0_2//-45_2//0_2]_T$ laminates than for the $[0_2//45_2//0_2//45_2//0_2]_T$ laminates, although the corresponding out-of-plane deflections were less. This can be described as a flattened bending mode, compared to the usual sinusoidal distribution in the transverse direction.

The similarity between the results for the $[0_2//45_2//0_2//45_2//0_2]_T$ laminates and $[0_2//45_2//0_2//-45_2//0_2]_T$ laminates can be explained by considered the various coupling mechanisms involved. The geometrical nonlinearities due to the large deflections couple the in-plane and out-of-plane behaviors. Thus, the stretching-shearing structural coupling is geometrically married to the bending-twisting structural coupling in the $[0_2//45_2//0_2//45_2//0_2]_T$ laminates, resulting in behavior similar to the stretching-twisting coupling effects exhibited by the $[0_2//45_2//0_2//-45_2//0_2]_T$ laminates. Thus, the general conclusion can be drawn that when out-of-plane deflections become large, as in the postbuckling region, the geometric coupling between in-plane and out-of-plane behaviors causes the stretching-shearing/bending-twisting coupling combination to be effectively the same as the single stretching-twisting coupling.

6.5 Full Coupling Effects

This discussion deals with the $[0_6//\theta_6]_T$ series of

laminates which possess all of the possible elastic couplings in various degrees. It will be recalled from Chapter 4 that the fifth specimen of each type of laminate tested with clamped side boundary conditions underwent a three phase process with out-of-plane contour deflection data taken at 4.5 kN, 9.0 kN, and 13.5 kN. During the second part of the test, while applying a modest lateral force by hand to the center of the plate in the opposite direction of the transducers, several of the laminates buckled into a stable secondary mode, while other nominally identical laminates preferred the primary bending mode. This dichotomy was observed only for laminates with significant bending-stretching coupling; i.e., the $[0_3//90_3//0_3//90_3]_T$ laminates and laminates in the $[0_6//\theta_6]_T$ family, with θ greater than 30° (i.e., 45°, 60°, 75°, and 90°). As seen in Table 6.1, all of these laminates have an effective aspect ratio greater than 0.7.

During the subsequent phases of the test, without this gentle coaxing, some of the laminates followed the secondary mode path, while other laminates remained in the primary mode. This sheds some light on the paradox observed experimentally whereby nominally identical laminates exhibited strikingly different out-of-plane behavior. A region apparently exists on the load-deflection equilibrium path where the two mode shapes have nearly identical minimum energy requirements. The lateral forces applied by the displacement transducers mounted on the back of the test fixture were

sufficient to bridge the gap between the minimum energy levels of the two modes. In this region, the laminates were extremely sensitive to external forces. Misalignments, inherent flaws, or thickness variations can cause one mode to dominate over the other.

As can be seen in the sequence of load versus deflection, w, graphs for the $[0_6//\theta_6]_T$ laminates tested with clamped side boundary conditions, in Figures 5.7 through 5.18, there were many different types of deflection behavior exhibited by this family of laminates, which had fully-populated elastic matrices. Looking at Table 6.2, which lists the elastic properties for all of the laminate types studied in this investigation, it is interesting to note that as θ increases from 15° to 90°, the longitudinal bending stiffness (D_{11}) decreases steadily while the transverse bending stiffness (D_{22}) increases steadily, causing a corresponding increase in the effective aspect ratio from 0.55 to 1.00. Meanwhile, the shearing stiffness (A_{66}), twisting stiffness (D_{66}), and shearing-twisting coupling (B_{66}), as well as the Poisson's effects (A_{12}, B_{12}, and D_{12}) all peak at 45°; the longitudinal stretching-shearing (A_{16}), stretching-twisting (B_{16}), and bending-twisting couplings (D_{16}) peak at 30°; and the transverse stretching-shearing (A_{26}), stretching-twisting (B_{26}), and bending-twisting couplings (D_{26}) peak at 60°. Thus, as θ changes, the associated dominant coupling mechanisms also change, along with the effective aspect ratio. This results in a variety of observed behaviors.

TABLE 6.2

THEORETICAL LAMINATE ELASTIC PROPERTIES

Laminate Type	Elastic Matrix	Coefficient[a] 11	22	66	12	16	26
S	A	121.8	121.8	7.9	5.4	0	0
	B	0	0	0	0	0	0
	D	43.0	9.5	1.7	1.2	0	0
T	A	122.0	122.0	7.9	5.5	0	0
	B	0	0	0	0	0	0
	D	49.5	10.7	2.0	1.3	0	0
U	A	122.0	122.0	7.9	5.5	0	0
	B	22.4	-22.4	0	0	0	0
	D	30.1	30.1	2.0	1.3	0	0
P	A	136.9	33.1	23.4	21.4	17.3	17.3
	B	0	0	0	0	0	0
	D	29.7	4.5	2.8	2.4	1.6	1.6
N	A	136.9	33.1	23.4	21.4	0	0
	B	0	0	0	0	5.2	5.2
	D	29.7	4.5	2.8	2.4	0	0
A	A	212.4	18.8	14.2	11.7	23.9	2.1
	B	5.5	-0.3	-2.6	-2.6	-10.0	-0.9
	D	48.4	4.3	3.2	2.7	5.4	0.5
B	A	180.9	25.2	26.8	24.3	33.4	11.6
	B	18.7	-2.9	-7.9	-7.9	-13.9	-4.8
	D	41.2	5.7	6.1	5.5	7.6	2.6
C	A	148.6	44.8	33.1	30.6	25.9	25.9
	B	32.1	-11.1	-10.5	-10.5	-10.8	-10.8
	D	33.8	10.2	7.5	7.0	5.9	5.9
D	A	129.0	77.1	26.8	24.3	11.6	33.4
	B	40.3	-24.6	-7.9	-7.9	-4.8	-13.9
	D	29.4	17.5	6.1	5.5	2.6	7.6
E	A	122.5	108.6	14.2	11.7	2.1	23.9
	B	43.0	-37.8	-2.6	-2.6	-0.9	-10.0
	D	27.9	24.7	3.2	2.7	0.5	5.4
F	A	121.9	121.9	7.9	5.4	0	0
	B	43.3	-43.3	0	0	0	0
	D	27.7	27.7	1.8	1.2	0	0

[a] Elements of A, B, and D matrices are in units of [kN/mm], [kN], and [kN-mm], respectively, calculated with the midplane as reference.

In general, as θ increased, the observed deflection behavior became more compliant. At θ equal to 30°, for example, the stretching-shearing and bending-twisting couplings provoked a twisted mode shape for half of the laminates tested with restrained side boundary conditions, similar to that shown in Figure 5.9. At θ equal to or greater than 45°, second and third longitudinal bending components were observed for each of the layups. The load versus strain results also showed this softening behavior. For example, the introduction of the third bending component and its effect on the local strain is shown in Figures 5.47 through 5.52. As θ increased from 15° to 90°, both the midplane component and the bending component of the local strain slowly decreased, implying that the gages were located at a local inflection point, relatively free of stress. In fact, after 30°, the local longitudinal bending strain transitioned from positive curvature (bulge) to negative (dimple). As θ increased, this transition occurred at lower loads.

Figures 6.1 and 6.2 present the buckling loads for the $[0_6//\theta_6]_T$ laminates tested with clamped and simply-supported side boundary conditions, respectively. The finite element and Rayleigh-Ritz analyses agree exceptionally well with each other and with the experimental Southwell estimate for the first mode. A fairly substantial discrepancy exists between the Rayleigh-Ritz and finite element predictions for the second mode. The experimentally observed transitions into the second mode fall in between the two predictions, but are

generally closer to the finite element predictions. This is due to the fact that the Rayleigh-Ritz analysis only included three modes in each of the x and y directions, making it difficult to accurately predict higher mode behavior.

Thus, in summary, for θ equal to 15° or 30°, the longitudinal stretching-twisting couplings (B_{16}) dominate the behavior. At 45°, the shearing-twisting couplings (B_{66}) dominate the behavior, resulting in a very compliant response. The effective aspect ratio is important for θ greater than or equal to 45°. For θ greater equal to 60° or 75°, the transverse stretching-twisting couplings (B_{26}) dominate.

6.6 Free Sides

As pointed out repeatedly in Chapter 5 and in the previous few sections of this chapter, the laminates tested with free side boundary conditions displayed results reminiscent of classical column buckling. No postbuckling stiffening was observed for any of the laminates tested with free side boundary conditions. Therefore, the maximum loads were considered to be the buckling loads.

The behavior of the laminates in this configuration was governed primarily by the longitudinal bending stiffness, D_{11}. The buckling loads can be quite accurately predicted using a classical wide-column buckling criterion. For a column, the bending stiffness about the neutral axis is given

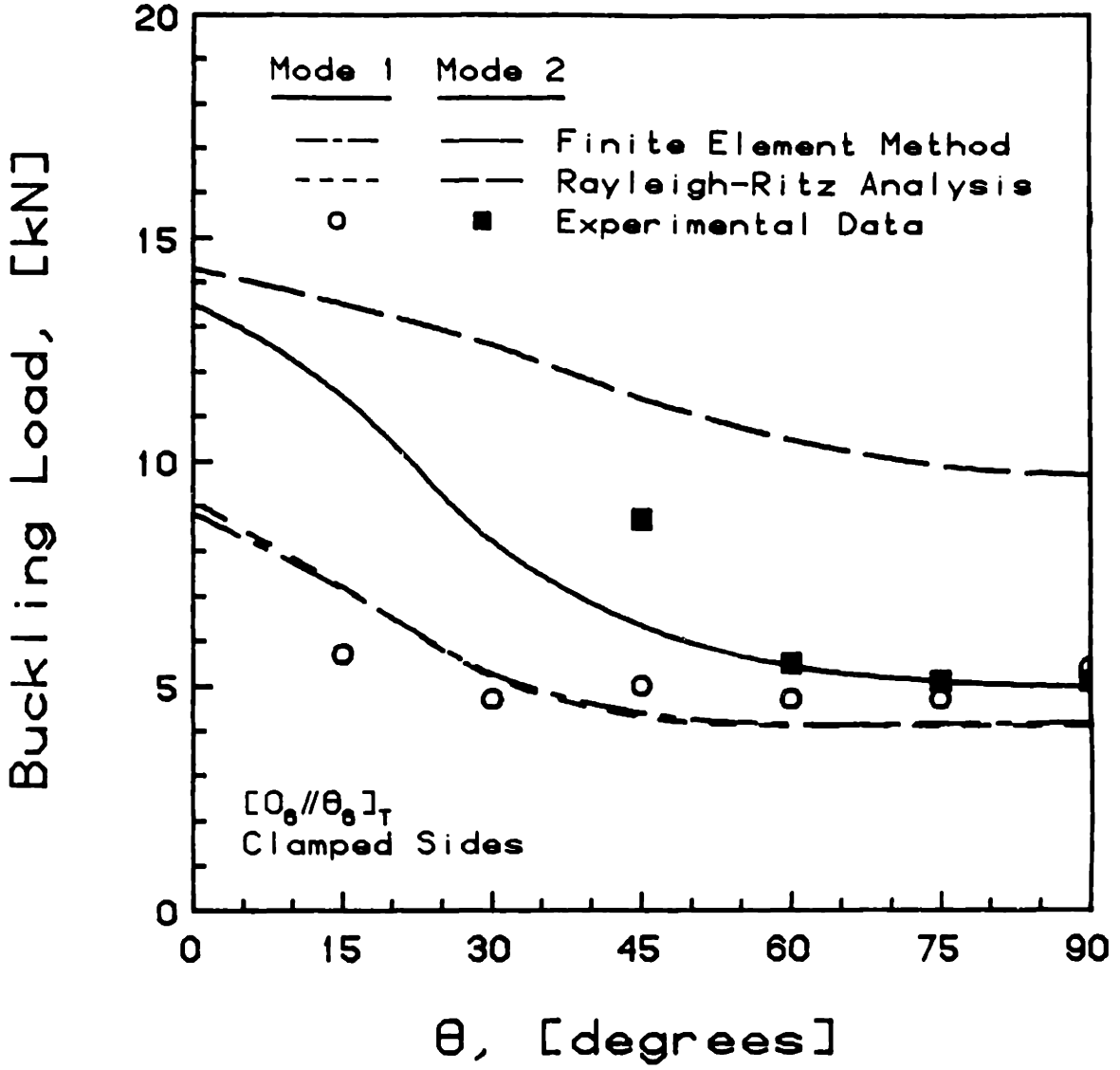

FIGURE 6.1 Predicted and Measured Buckling Loads for $[0_6//\theta_6]_T$ Laminates with Clamped Side Boundary Conditions

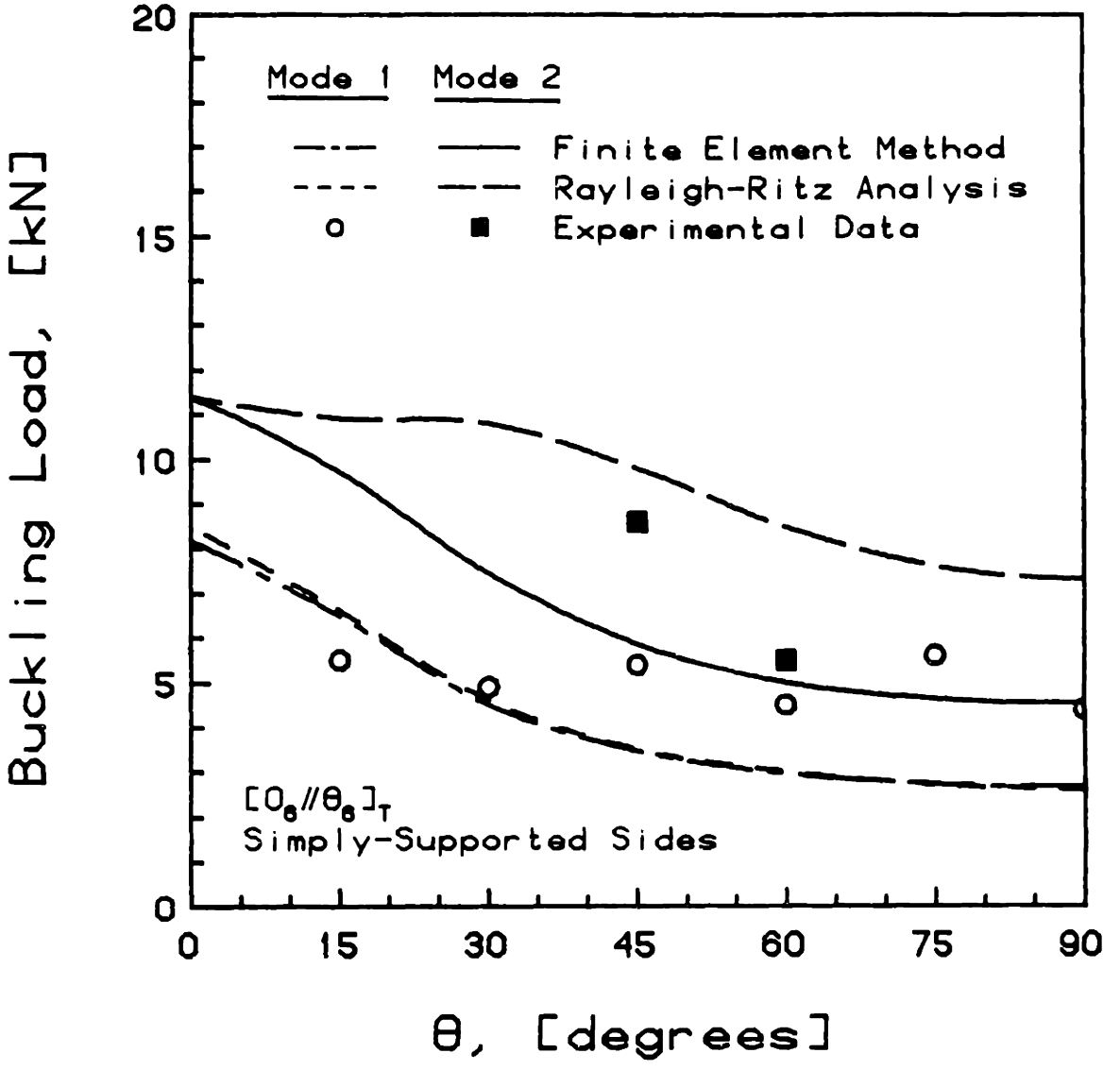

FIGURE 6.2 Predicted and Measured Buckling Loads for $[0_6//\theta_6]_T$ Laminates with Simply-Supported Side Boundary Conditions

by $\bar{D}_{11}$ [53], where:

$$\bar{D}_{11} = D_{11} - \frac{B_{11}^2}{A_{11}} \tag{6.2}$$

The accuracy is improved by replacing the longitudinal bending stiffness with an equivalent longitudinal bending stiffness for unsymmetric plates. The equivalent bending stiffness for a plate about a pseudo neutral surface is given by a reduced stiffness parameter, D_{11}^* [21,54,55,56], where:

$$[D^*] = [D] - [B]^T[A]^{-1}[B] \tag{6.3}$$

This is obtained by assuming that there are no variations in the in-plane stress resultants, {N}, during bifurcation buckling. These values are tabulated in Table 6.3.

The calculated buckling loads, based on the classical wide-column buckling expression for columns with clamped ends:

$$P_{cr} = \frac{4\pi^2 D_{11} b}{a^2} \tag{6.4}$$

are reported in Table 6.4 for each of the laminates investigated. Calculations were performed based on each of the longitudinal bending stiffness parameters, $\bar{D}_{11}$, and D_{11}^*. The experimental maximum loads for the laminates tested with

TABLE 6.3

REDUCED BENDING STIFFNESS PARAMETERS

Laminate Type	$\bar{D}_{11}$ [a]	D^*_{11} [b]
S	43.0[c]	43.0[c]
T	49.5	49.5
U	26.0	26.0
P	29.7	29.7
N	29.7	28.5
A	48.2	38.2
B	39.3	23.7
C	26.9	16.3
D	16.8	13.3
E	12.8	12.4
F	12.4	12.3

[a] $\bar{D}_{11}$ assumes existence of neutral axis.
[b] D^*_{11} assumes existence of neutral surface.
[c] All values are expressed in units of [kN-mm].

free sides are also reported in the same table.

The $[0_6//90_6]_T$ laminates, which were similar to the $[0_3//90_3//0_3//90_3]_T$ laminate (Figure 5.58), but with nominally twice the theoretical primary bending-stretching couplings, clearly demonstrated that the bending-stretching coupling shifts the neutral axis and, consequently, reduces the buckling load, as listed in Table 6.4.

Comparison of the $[0_2//45_2//0_2//45_2//0_2]_T$ and $[0_2//45_2//0_2//-45_2//0_2]_T$ laminates tested with free side boundary conditions (Figures 5.33 and 5.34, respectively) reinforces the perception that membrane-flexural elastic coupling (i.e., manifest by the existence of B_{ij}) reduces the buckling load even more than the longitudinal bending stiffness, D_{11}, can account for alone. The $[0_2//45_2//0_2//-45_2//0_2]_T$ laminate, which possessed a modest amount of stretching-twisting coupling, buckled approximately 4% lower than the $[0_2//45_2//0_2//45_2//0_2]_T$ laminate which had nominally identical elastic properties, except for the shearing- and twisting- couplings.

On the other hand, Figure 6.3 shows the exceptional agreement between the experimentally observed buckling loads and the wide-column theory predictions based on the generally anisotropic (D_{11}^*) reduced bending stiffness, as a function of θ in the $[0_6//\theta_6]_T$ family of laminates. Also presented in the same figure is the theoretical prediction based on the orthotropic bending stiffness ($\bar{D}_{11}$) calculated about an assumed neutral axis (i.e., such that B_{11} equals 0). This

TABLE 6.4

PREDICTED AND MEASURED BUCKLING LOADS FOR LAMINATES WITH FREE SIDE BOUNDARY CONDITIONS

Laminate Type	BUCKLING LOADS [kN]		
	Experiment	Wide-Column Theory	
	P^c	$\bar{P}^a$	P^{*b}
S	5.32	6.69	6.69
T	7.41	7.69	7.69
U	4.32	4.03	4.04
P	5.22	4.61	4.61
N	4.87	4.61	4.43
A	5.52	7.50	5.94
B	3.65	6.10	3.68
C	2.59	4.18	2.53
D	2.17	2.60	2.06
E	1.83	1.99	1.92
F	1.96	1.92	1.91

[a] Based on $\bar{D}_{11}$ (assumes existence of neutral axis).
[b] Based on D^*_{11} (assumes existence of neutral surface).
[c] Maximum compressive load.

does not agree well with the experimental observations. Thus, the laminates in this investigation tested with free side boundary conditions exhibited classical wide-column bifurcation buckling behavior and were governed by classical wide-column theory based on the reduced bending stiffness, D_{11}^{*}, which takes into account all of the membrane-flexural coupling mechanisms.

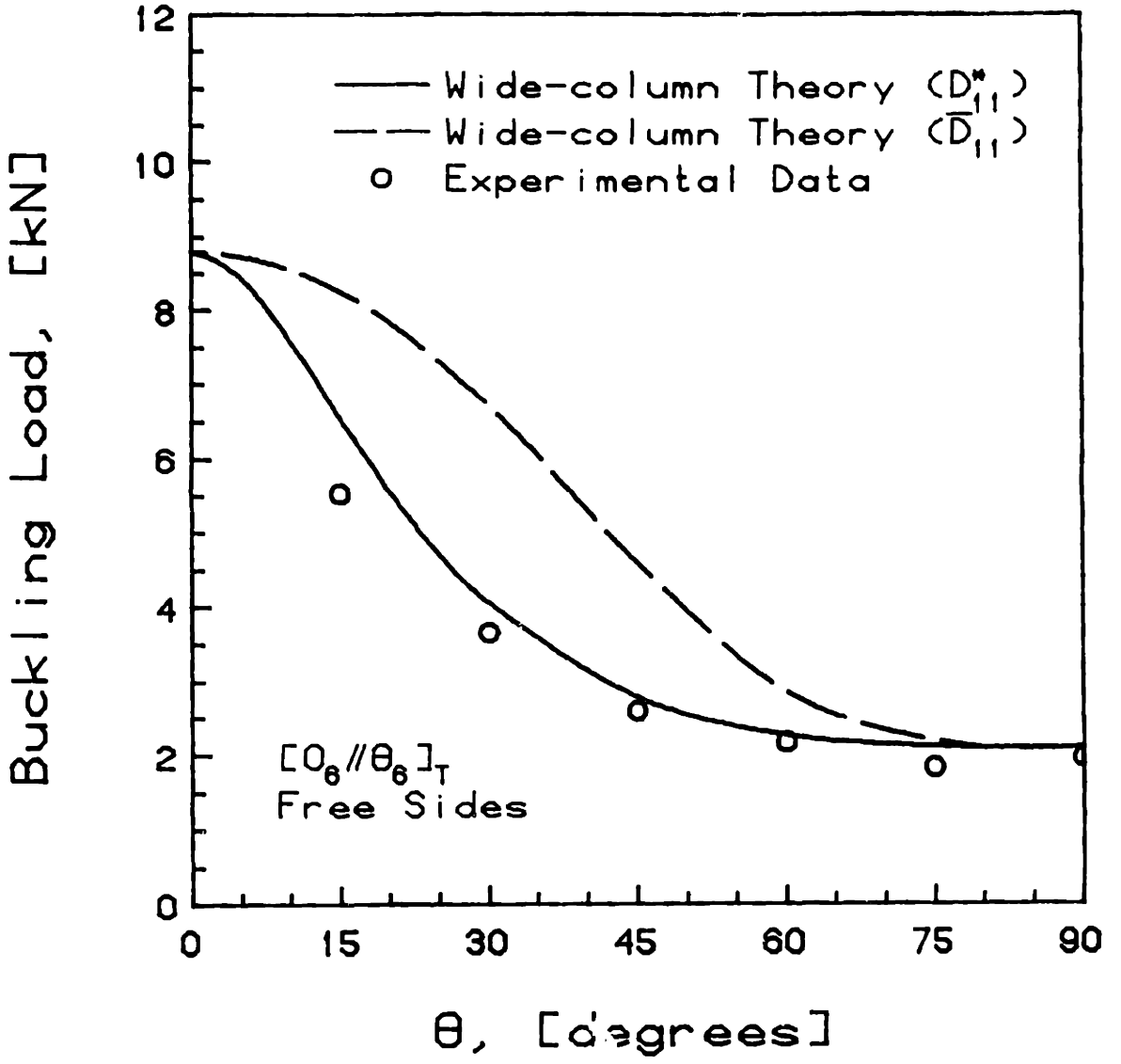

FIGURE 6.3 Predicted and Measured Buckling Loads for $[0_6//\theta_6]_T$ Laminates with Free Side Boundary Conditions

CHAPTER 7

CONCLUSIONS AND RECOMMENDATIONS

The buckling and postbuckling behavior of unbalanced and unsymmetric laminated graphite/epoxy plates loaded in compression with clamped, simply-supported, and free side boundary conditions and clamped loaded ends has been examined in this investigation. The primary focus of this work has been to better understand the influence of the various elastic couplings inherent in unbalanced and unsymmetric laminated graphite/epoxy plates and how the interaction of these couplings with the geometric boundary conditions and large deflection behavior affects the overall buckling and postbuckling behavior. Both experimental and analytical results have indicated that the existence of such couplings in the constitutive relations can significantly affect the buckling and postbuckling behavior of laminated graphite/epoxy plates. The following specific observations and conclusions can be drawn from the results obtained in this investigation:

1. The experimental methods employed produce reliable and repeatable strain and out-of-plane deflection data.

2. The laminates tested with clamped side boundary conditions in this study agreed more closely with the

theoretical predictions for the simply-supported side boundary conditions than with the theoretical predictions for the clamped side boundary conditions. This indicates that the edges were not completely clamped, due to the compliance of the teflon tape on the borders of the plates.

3. Friction at the boundaries, especially due to the normal force along the loaded ends, restricted in-plane sliding in the experiment, whereas the analysis assumed unrestricted in-plane freedom.

4. Room-temperature bondlines increase the bending stiffness and ultimate strength of the laminates by increasing the distance of the load-carrying graphite/epoxy sublaminates from the bending axis. This can be properly accounted for analytically by modelling the bondline as an additional ply.

5. The classical bifurcation buckling load does not necessarily correspond to any meaningful location on the load versus out-of-plane deflection curves for laminates with membrane-flexural couplings (B_{ij}) tested with restrained side boundary conditions. For these laminates, lateral deflections begin simultaneously with the application of compressive load due to the shifted neutral axis and effects of the elastic couplings.

6. Elastic (mechanical) couplings reduce the theoretically predicted and experimentally derived buckling loads.

7. The more restrictive the side boundary conditions are, the greater the influence of the coupling mechanisms, since restraining the boundaries of the plate prohibits the natural deflections at the edges. This restriction introduces stresses which, in turn, amplify the effects of the elastic coupling mechanisms.

8. The linear Rayleigh-Ritz and finite element analyses accurately predict the lowest bifurcation buckling load, as determined experimentally via the Southwell method.

9. The linear finite element analysis predictions for the second instability agree more closely with experimentally observed values than do predictions from the linear Rayleigh-Ritz analysis, since the Rayleigh-Ritz analysis, which used only three out-of-plane deflection (w) modes in each of the x and y directions, is inherently too stiff.

10. The effective aspect ratio, based on the material orthotropy, is a significant parameter affecting the postbuckling behavior of laminated composite plates loaded in uniaxial compression.

11. At least two stable equilibrium configurations exist for laminates which have bending-stretching coupling, an effective aspect ratio greater than 0.7, and partially restrained side boundary conditions. Nominally identical laminates which satisfy these criteria are extremely sensitive to external influences in the proximity of this secondary instability. Random variables, such as applied lateral forces, boundary conditions, and manufacturing variables, can cause one of these modes to dominate over the other.

12. Laminates which possess bending-stretching coupling, have an aspect ratio greater than 0.7, and partially restrained side boundary conditions exhibit a significant third longitudinal bending component superimposed on the first bending mode behavior.

13. Stretching-shearing coupling (A_{16}, A_{26}) introduces shearing stresses which cause the deflection shape to skew, and in combination with bending-twisting (D_{16}, D_{26}) couplings introduce twisting into the out-of-plane deflection.

14. Stretching-twisting (B_{16}, B_{26}) coupling flattens the primary bending mode shape of the plate.

15. The geometrically nonlinear large deflections typical in

postbuckling behavior couple together the combination of stretching-shearing (A_{16}, A_{26}) and bending-twisting (D_{16}, D_{26}) couplings in such a fashion that the results are virtually the same as those observed for laminates with stretching-twisting (B_{16}, B_{26}) coupling.

16. As θ changes from 15° to 90° in $[0_6//\theta_6]_T$ laminates, the associated dominant elastic coupling mechanisms change and the effective aspect ratio increases, resulting in a variety of observed behaviors: a) the first twisting mode components were most visible in the range of θ from 30° to 60°, where the related twisting coupling mechanisms dominate; and, b) the second and third longitudinal bending mode components were manifest for θ greater than or equal to 45°, where the reduced effective aspect ratio exceeds 0.7 and bending-stretching coupling is significant.

17. Symmetric, unbalanced, and unsymmetric laminated plates with free side boundary conditions all exhibit classical wide-column bifurcation buckling behavior and are governed by wide-column theory based on using the reduced bending stiffness parameter, which takes into account the elastic coupling mechanisms.

18. The extremely large deflections of laminates with free side boundary conditions overshadow any influence of

elastic shearing and twisting couplings in the postbuckling range.

19. The $[0_6//45_6]_T$ laminate has been identified as the one with the most critical elastic coupling mechanisms of those investigated herein. This laminate possesses the largest values of the elastic shearing (A_{66}), twisting (D_{66}), shearing-twisting (B_{66}), Poisson's stretching-stretching (A_{12}), Poisson's stretching-bending (B_{12}), and Poisson's bending-bending (D_{12}) couplings of the laminates investigated herein and also possesses significant bending-stretching (B_{11}) coupling. This results in the most exaggerated display of behavior.

20. Failure of the laminates investigated herein is a direct consequence of the construction process: failure is governed by the large deflections which induce shear stresses in the room-temperature bondlines and provoke delamination at these bondlines. This would not be expected to occur in laminates without such bondlines. Nevertheless, these laminates exhibited significant postbuckling strength.

Based on the results obtained herein, the following recommendations are made for further work:

1. Alternative techniques of improving bondline thickness

control should be investigated. A hydraulic press, which is capable of applying significantly higher pressures than an autoclave, could yield more satisfactory results.

2. The boundary conditions on the compressive loading jig should be redesigned and more carefully machined to facilitate alignment and improve accuracy. A rounded groove in the end boundary conditions, with matching rounded ends on the plates, and/or a rather compliant interface, such as a thin rubber strip, might also result in a more uniform applied displacement, reducing any undesirable twisting bias.

3. Additional improvements to the acquisition of meaningful in-plane data should be sought. Multitudes of strain gages could be employed. Alternatively, optical strain readings would have a lower marginal cost, be more versatile, and improve accuracy by eliminating the fixture compliance from the measurements.

4. Laminates should be tested with the lateral forces from the transducers pushing in the opposite direction to ascertain the influence of the direction of the forces.

5. The Rayleigh-Ritz modes should be extended to model second and third bending mode behavior by carefully

examining the predicted finite element shapes to determine the important modal contributions.

6. A nonlinear finite element analysis should be performed for a typical laminate with significant couplings, such as $[0_6//45_6]_T$, to gain a better understanding of the effect of the third bending mode component and the second mode behavior.

7. Additional $[0_6//45_6]_T$ laminates should be manufactured and tested to further investigate the mechanisms which caused the most interesting results for this particular laminate.

8. Cyclic tests should be performed on these same laminates over the transition region between first and second modes, to determine the significance of possible degradation of the stiffness after repeated modal transitions.

9. Configurations should be investigated which could yield more realistic and applicable failure data.

10. Thicker laminates of the form $[0_n//45_n]_T$ should be manufactured and tested in order to more definitively determine the effects of thickness on the coupling mechanisms which govern the buckling and postbuckling

behavior.

11. A symmetric laminate which has an effective aspect ratio greater than 0.7 should be manufactured and tested. Such a laminate would not exhibit any membrane-flexural couplings, thus isolating these two factors which have been shown to have a significant effect on the buckling and postbuckling behavior.

12. Additional tests of laminates with free side boundary conditions should not be performed. The results presented herein definitively identify their behavior.

13. This work should be extended to laminates with natural unsymmetries, such as ply-dropoffs, to laminated sandwich structures which require transverse shear considerations, and to stiffened plates, which locally possess more realistic boundary conditions.

14. Laminates with different geometric aspect ratios (i.e., a/b) should be investigated to ascertain how the geometry may alter the effects of the elastic couplings on the behavior as determined in this study.

REFERENCES

1. Jensen, D. W. and Crawley, E. F., "Frequency Determination Techniques for Cantilevered Plates with Bending-Torsion Coupling," AIAA J., Vol. 22, No. 3, pp. 415-420, March 1984.

2. Jensen, D. W., Crawley, E. F., and Dugundji, J., "Vibration of Cantilevered Graphite/Epoxy Plates with Bending-Torsion Coupling," J. Reinforced Plastics and Composites, Vol. 1, pp. 254-269, July 1982.

3. Sherrer, V. C., Hertz, T. J., and Shirk, M. H., "Wind Tunnel Demonstration of Aeroelastic Tailoring Applied to Forward Swept Wings," J. Aircraft, Vol. 18, pp. 976-983, November 1981.

4. Prabhakara, M. K., "Post-Buckling Behaviour of Simply-Supported Cross-Ply Rectangular Plates," Aeronautical Quarterly, Vol. 27, No. 4, pp. 309-316, 1976.

5. Leissa, A. W., "Buckling of Laminated Composite Plates and Shell Panels," Technical Report, AFWAL-TR-85-3069, 454 pp., June 1985.

6. Sumihara, K., "Thin Shell and New Invariant Elements by Hybrid Stress Method," Massachusetts Institute of Technology, Ph.D. Thesis, 203 pp., June 1983.

7. Pian, T. H. H., "Finite Elements Based on Consistently Assumed Stresses and Displacements," Finite Elements in Analysis and Design, Vol. 1, pp. 131-140, 1985.

8. Euler, L., "De Curvis Elasticis," Methodus Inveniendi Lineas Curvas Maximi Minimive Proprietate Gaudentes, Lausanne and Geneva, 1744.

9. Bryan, G. H., "On the Stability of a Plane Plate Under Thrusts in its Own Plane, with Applications to the 'Buckling' of the Sides of a Ship," Proc. London Mathematical Society, Vol. 22, pp. 54-67, 1891.

10. Kirchhoff, G. R., Mechanik, Second Edition, p. 450, 1877.

11. Timoshenko, S. P., Sur la Stabilité des Systémes Elastiques, Ann. Ponts et Chaussées, 1913.

12. Timoshenko, S. P., "Stability of Rectangular Plates with Stiffeners," Mem. Inst. Engrs. Ways of Commun., Vol. 89,

1915.

13. Timoshenko, S. P., Der Eisenbau, Vol. 12, 1921.

14. Karman, T. V., "Encyklopädie der Mathematischen Wissenschaften," Vol. IV, p. 349, 1910.

15. Timoshenko, S. P., and Gere J. M., "Buckling of Thin Plates," Theory of Elastic Stability, Second Edition, McGraw-Hill, pp. 348-439, 1961.

16. Timoshenko, S., and Woinowsky-Krieger, S., "Large Deflections of Plates," Theory of Plates and Shells, McGraw-Hill, Second Edition, pp. 396-428, 1968.

17. Leissa, A. W., "Buckling of Composite Plates," Composite Structures, Vol. 1, pp. 51-66, 1983.

18. Stein, M., "Postbuckling of Orthotropic Composite Plates Loaded in Compression," AIAA J., Vol. 21, No. 12, pp. 1729-1735, December 1983.

19. Stein, M., "Postbuckling of Long Orthotropic Plates in Combined Shear and Compression," AIAA J., Vol. 23, No. 5, pp. 788-794, May 1985.

20. Jones, R. M. and Morgan, H. S., "Buckling and Vibration of Cross-Ply Laminated Circular Cylindrical Shells," AIAA J., Vol. 13, No. 5, pp. 664-671, May 1975.

21. Reissner, E. and Stavsky, Y., "Bending and Stretching of Certain Types of Heterogeneous Aeolotropic Elastic Plates," Trans. ASME, J. Applied Mechanics, Vol. 9, pp. 402-408, 1961.

22. Jones, R. M. "Buckling and Vibration of Unsymmetrically Laminated Cross-Ply Rectangular Plates," AIAA J., Vol. 11, No. 12, pp. 1626-1632, 1973.

23. Ashton, J. E. and Waddoups, M.E., "Analysis of Anisotropic Plates," J. Composite Materials, Vol. 3, pp. 148-165, January 1969.

24. Ashton, J. E. and Waddoups, M.E., "Analysis of Anisotropic Plates II," J. Composite Materials, Vol. 3, pp. 470-479, July 1969.

25. Ashton, J. E., "Anisotropic Plate Analysis - Boundary Conditions," J. Composite Materials, Vol. 4, pp. 163-171, April 1970.

26. Ashton, J. E. and Love, T. S., "Experimental Study of the Stability of Composite Plates," J. Composite Materials,

Vol. 3, pp. 230-242, April 1969.

27. Kicher, T. P. and Mandell, J. F., "A Study of the Buckling of Laminated Composite Plates," AIAA J., Vol. 9, No. 4, pp. 605-613, April 1971.

28. Starnes, J. H. Jr. and Rouse, M., "Postbuckling and Failure Characteristics of Selected Flat Rectangular Graphite-Epoxy Plates Loaded in Compression," AIAA/ASME/ASCE/AHS 22nd SDM Conference, Atlanta, Georgia, April 1981.

29. Starnes, J. H. Jr., Knight, N. F. Jr., and Rouse, M., "Postbuckling Behavior of Selected Flat Stiffened Graphite-Epoxy Panels Loaded in Compression," AIAA J., Vol. 23, No. 8, pp. 1236-1246, August 1985.

30. Turvey, G. J. and Wittrick, W. H., "The Large Deflection and Postbuckling Behavior of Some Laminated Plates," Aeronautical Quarterly, Vol. 24, No. 2, pp. 77-86, 1973.

31. Chia, C. Y., Nonlinear Analysis of Plates, McGraw-Hill, New York, 422 pp., 1980.

32. Lagace, P. A., Jensen, D. W., and Finch, D. C., "Buckling of Unsymmetrical Composite Laminates," Composite Structures, Vol. 5, 1986.

33. Chailleux, A., Hans, Y., and Verchery, G., "Experimental Study of the Buckling of Laminated Composite Columns and Plates," Int. J. of Mechanical Sciences, Vol. 17, No. 8, pp. 489-498, 1975.

34. Fogg, L., "Stability Analysis of Laminated Materials," State of the Art Design and Analysis of Advanced Composite Materials, Lockheed California Company, Sessions I & II, 162 pp., 1981.

35. Southwell, R. V., "On the Analysis of Experimental Observations in Problems of Elastic Stability," Proc. Royal Society, London, Series A, Vol. 135, pp. 601-616, 1932.

36. Donnell, L. H., "On the Application of Southwell's Method for the Analysis of Buckling Tests," Stephen Timoshenko 60th Anniversary Volume, McGraw-Hill, pp. 27-38, 1938.

37. Roorda, J., "Some Thoughts on the Southwell Plot," ASCE, J. Engineering Mechanics Division, Vol. 93, No. EM6, 1967.

38. Tsai, S. W., and Hahn, H. T., Introduction to Composite Materials," Technomic Publishing Company, Connecticut,

457 pp., 1980.

39. Vinson, J. R. and Smith, A. P., Jr., "The Effect of Transverse Shear Deformation on the Elastic Stability of Plates of Composite Materials," Technical Report, AFOSR TR-75-1628, 77 pp., March 1975.

40. Shirakawa, K., "Effects of Shear Deformation and Rotatory Inertia on Vibration and Buckling of Cylindrical Shells," J. Sound and Vibration, Vol. 91, No. 3, pp. 425-437, 1983.

41. Gerard, G., "Minimum Weight Analysis of Orthotropic Plates Under Compressive Loading," J. Aerospace Sciences, Vol. 27, No. 64, pp. 21-26, January 1960.

42. Minguet, P., "Etude du Comportement Postcritique de Panneaux en Matériaux Composites," B.S. Thesis, Univ. de Liege, 1984.

43. Minguet, P., "Buckling of Graphite/Epoxy Sandwich Plates," Forthcoming S.M. Thesis, Massachusetts Institute of Technology, 1986.

44. Zhang, Y. and Matthews, F. L., "Postbuckling Behavior of Anisotropic Laminated Plates Under Pure Shear and Shear Combined with Compression Loading," AIAA J., Vol. 22, No. 2, pp. 281-286, February 1984.

45. Pian, T. H. H., Kang, D., and Wang, C., "Hybrid Plate Elements Based on Consistently Assumed Stresses and Displacements," to be published in Finite Element Methods for Plate and Shell Structures, Vol. 1: Element Technology, and Vol. 2: Formulations and Algorithms, edited by Hughes, T. J. R. and Hinton, E., Pineridge Press.

46. Wang, C., Forthcoming S.M. Thesis, Massachusetts Institute of Technology, 1986.

47. Lagace, P. A., and Brewer, J. C., TELAC Manufacturing Course Notes, Edition O-2, Technology Laboratory for Advanced Composites, TELAC Report 81-14, Massachusetts Institute of Technology, September 1981.

48. Finch, D. C., "The Buckling of Symmetric and Unsymmetric Composite Plates with Various Boundary Conditions," Technology Laboratory for Advanced Composites, TELAC Report 84-3, Massachusetts Institute of Technology, S.M. Thesis, February 1984.

49. Noor, A. K., Mathers, M. D., and Anderson, M. S., "Exploiting Symmetries for Efficient Postbuckling

Analysis of Composite Plates," AIAA J., Vol. 15, No. 1, pp. 24-32, 1977.

50. Vizzini, A. J., and Lagace, P. A., "TEBAS - TELAC Software User's Manual," TELAC Report No. 84-14-2, 1984.

51. Brunelle, E. J. and Oyibo, G. A., "Generic Buckling Curves for Specially Orthotropic Rectangular Plates," AIAA J., Vol. 21, No. 8, p. 1150-1156, August 1983.

52. Chandra, R. and Bavasu Raju, B., "Postbuckling Analysis of Rectangular Orthotropic Plates," Int. J. Mechanical Sciences, Vol. 15, pp. 81-97, 1973.

53. Dong, S. B., Pister, K. S., and Taylor, R. L., "On the Theory of Laminated Anisotropic Shells and Plates," J. Aeronautical Sciences, Vol. 29, pp. 969-975, 1962.

54. Chamis, C. C., "Buckling of Anisotropic Composite Plates," Proc. ASCE, J. Structural Division, Vol. 95, No. ST10, pp. 2119-2139, 1969.

55. Chamis, C. C., "Buckling of Anisotropic Plates, Closure and Errata," Proc. ASCE, J. Structural Division, Vol. 97, pp. 960-962, 1971.

56. Ashton, J. E., "Approximate Solutions for Unsymmetrical Laminated Plates," J. Composite Materials, Vol. 3, pp. 189-191, 1969.

APPENDIX A

RAYLEIGH-RITZ STIFFNESS MATRIX ELEMENTS

This appendix contains the generic stiffness matrix elements from the full nonlinear Rayleigh-Ritz analysis as given in Equations 3.29 through 3.35 in Chapter 3. However, when calculating the actual matrices, care must be taken to ensure that all of the permutations of the subscripts (i, j, k, and l) are properly accounted for.

The first three stiffness matrices, K_1, K_2, and K_3 are the linear stiffness matrices used in both the linear buckling and nonlinear postbuckling problems:

$$K_{1_{ij}} = A_{11} \int \alpha_i' \alpha_j' \, dx \int \beta_i \beta_j \, dy$$

$$+ 2A_{12} \int \alpha_i' \gamma_j \, dx \int \beta_i \delta_j' \, dy$$

$$+ A_{22} \int \gamma_i \gamma_j \, dx \int \delta_i' \delta_j' \, dy$$

$$+ 2A_{16} \int \alpha_i' \alpha_j \, dx \int \beta_i \beta_j' \, dy$$

$$+ 2A_{16} \int \alpha_i' \gamma_j' \, dx \int \beta_i \delta_j \, dy$$

$$+ 2A_{26} \int \gamma_i \alpha_j \, dx \int \delta_i' \beta_j' \, dy$$

$$+ 2A_{26} \int \gamma_i \gamma_j' \, dx \int \delta_i' \delta_j \, dy$$

$$+ A_{66} \int \alpha_i \alpha_j \, dx \int \beta_i' \beta_j' \, dy$$

$$+ 2A_{66} \int \alpha_i \gamma_j' \, dx \int \beta_i' \delta_j \, dy$$

$$+ A_{66} \int \gamma_i' \gamma_j' \, dx \int \gamma_i \delta_j \, dy \qquad \text{(A.1)}$$

$$K_{2_{ij}} = - 2B_{11} \int \alpha_i' \chi_j'' \, dx \int \beta_i \psi_j \, dy$$

$$- 2B_{12} \int \alpha_i' \chi_j \, dx \int \beta_i \psi_j'' \, dy$$

$$- 2B_{12} \int \gamma_i \chi_j'' \, dx \int \delta_i' \psi_j \, dy$$

$$- 2B_{22} \int \gamma_i \chi_j \, dx \int \delta_i' \psi_j'' \, dy$$

$$
\begin{aligned}
&- 4B_{66} \int \alpha_i \chi_j' \, dx \int \beta_i' \psi_j' \, dy \\
&- 4B_{66} \int \gamma_i' \chi_j' \, dx \int \delta_i \psi_j' \, dy \\
&- 2B_{16} \int \alpha_i' \chi_j' \, dx \int \beta_i \psi_j' \, dy \\
&- 2B_{16} \int \alpha_i \chi_j'' \, dx \int \beta_i' \psi_j \, dy \\
&- 2B_{16} \int \gamma_i' \chi_j'' \, dx \int \delta_i \psi_j \, dy \\
&- 2B_{26} \int \gamma_i \chi_j' \, dx \int \delta_i' \psi_j' \, dy \\
&- 2B_{26} \int \alpha_i \chi_j \, dx \int \beta_i' \psi_j'' \, dy \\
&- 2B_{26} \int \gamma_i' \chi_j \, dx \int \delta_i \psi_j'' \, dy
\end{aligned}
\qquad \text{(A.2)}
$$

$$
\begin{aligned}
K_{3_{ij}} = {} & D_{11} \int X_i'' X_j'' \, dx \int \psi_i \psi_j \, dy \\
& + 2D_{12} \int X_i'' X_j \, dx \int \psi_i \psi_j'' \, dy \\
& + D_{22} \int X_i X_j \, dx \int \psi_i'' \psi_j'' \, dy \\
& + 4D_{16} \int X_i'' X_j' \, dx \int \psi_i \psi_j' \, dy \\
& + 4D_{26} \int X_i X_j' \, dx \int \psi_i'' \psi_j' \, dy \\
& + 4D_{66} \int X_i' X_j' \, dx \int \psi_i' \psi_j' \, dy
\end{aligned}
\tag{A.3}
$$

The postbuckling stiffening information is stored in the nonlinear stiffness matrices, K_4, K_5, and K_6:

$$
\begin{aligned}
K_{4_{ij}} = {} & A_{11} \int \alpha_i' \chi_j' \chi_k' \, dx \int \beta_i \psi_j \psi_k \, dy \\
& + A_{12} \int \alpha_i' \chi_j \chi_k \, dx \int \beta_i \psi_j' \psi_k' \, dy \\
& + A_{12} \int \gamma_i \chi_j' \chi_k' \, dx \int \delta_i' \psi_j \psi_k \, dy \\
& + 2A_{16} \int \alpha_i' \chi_j' \chi_k \, dx \int \beta_i \psi_j \psi_k' \, dy \\
& + A_{16} \int \alpha_i \chi_j' \chi_k' \, dx \int \beta_i' \psi_j \psi_k \, dy \\
& + A_{16} \int \gamma_i' \chi_j' \chi_k' \, dx \int \delta_i \psi_j \psi_k \, dy \\
& + 2A_{26} \int \gamma_i \chi_j' \chi_k \, dx \int \delta_i' \psi_j \psi_k' \, dy \\
& + A_{26} \int \alpha_i \chi_j \chi_k \, dx \int \beta_i' \psi_j' \psi_k' \, dy
\end{aligned}
\qquad (A.4)
$$

$$+ A_{26} \int \gamma_i' X_j X_k \, dx \int \delta_i \psi_j' \psi_k' \, dy$$

$$+ A_{22} \int \gamma_i X_j X_k \, dx \int \delta_i' \psi_j' \psi_k' \, dy$$

$$+ 2A_{66} \int \alpha_i X_j' X_k \, dx \int \beta_i' \psi_j \psi_k' \, dy \qquad (A.4)$$

$$+ 2A_{66} \int \gamma_i' X_j' X_k \, dx \int \delta_i \psi_j \psi_k' \, dy$$

$$K_{5_{ij}} = - B_{11} \int X_i' X_j' X_k'' \, dx \int \psi_i \psi_j \psi_k \, dy$$

$$- B_{12} \int X_i' X_j' X_k \, dx \int \psi_i \psi_j \psi_k'' \, dy$$

$$- B_{12} \int X_i X_j X_k'' \, dx \int \psi_i' \psi_j' \psi_k \, dy$$

$$- B_{22} \int X_i X_j X_k \, dx \int \psi_i' \psi_j' \psi_k'' \, dy$$

$$
\begin{aligned}
&- 4B_{66} \int X_i' X_j X_k' \, dx \int \psi_i \psi_j' \psi_k' \, dy \\
&- 2B_{16} \int X_i' X_j' X_k' \, dx \int \psi_i \psi_j \psi_k' \, dy \\
&- 2B_{16} \int X_i' X_j X_k'' \, dx \int \psi_i \psi_j' \psi_k \, dy \\
&- 2B_{26} \int X_i' X_j' X_k' \, dx \int \psi_i \psi_j \psi_k' \, dy \\
&- 2B_{26} \int X_i' X_j X_k \, dx \int \psi_i \psi_j' \psi_k'' \, dy
\end{aligned}
\tag{A.5}
$$

$$
\begin{aligned}
K_{6_{ij}} = {} & \frac{1}{4} A_{11} \int X_i' X_j' X_k' X_l' \, dx \int \psi_i \psi_j \psi_k \psi_l \, dy \\
&+ \frac{1}{2}(A_{12} + 2A_{26}) \int X_i' X_j' X_k X_l \, dx \int \psi_i \psi_j \psi_k' \psi_l' \, dy \\
&+ A_{16} \int X_i' X_j' X_k' X_l \, dx \int \psi_i \psi_j \psi_k \psi_l' \, dy \\
&+ A_{26} \int X_i' X_j X_k X_l \, dx \int \psi_i \psi_j' \psi_k' \psi_l' \, dy \\
&+ \frac{1}{4} A_{22} \int X_i X_j X_k X_l \, dx \int \psi_i' \psi_j' \psi_k' \psi_l' \, dy
\end{aligned}
\tag{A.6}
$$

The stiffness contribution from the lateral transducer spring forces is given by K_T:

$$K_{T_{ij}} = \sum_{l=1}^{9} k_l \chi_i(x_l)\chi_j(x_l)\psi_i(y_l)\psi_j(y_l) \qquad (A.7)$$

The loading matrix elements for the linear Rayleigh-Ritz analysis are given by $L_{w_{ij}}$:

$$L_{w_{ij}} = \int \chi_i \chi_j \, dx \int \psi_i \psi_j \, dy \qquad (A.8)$$

APPENDIX B

RAYLEIGH-RITZ FORTRAN SOURCE CODE

This appendix contains a complete listing of the FORTRAN source code used in the linear and nonlinear Rayleigh-Ritz analyses. All of the applicable subroutines are included, except for the IMSL linear equation and eigenvalue solving packages. As described in Chapter 3, this program permits the calculation of local minima at different loads in any sequence, since the solution procedure is not incremental.

```
C=======================================================
C         POSTBUCKLING BEHAVIOR OF PLATES (V 7.2)
C                 Double Precision Version
C         David W. Jensen  (original program by Pierre Minguet)
C                         January 1986
C=======================================================
         IMPLICIT REAL*8 (A-H,O-Z)
         COMMON /MATRICES/ A(3,3),B(3,3),D(3,3)
         COMMON /NMODES/ NU,NV,NW,KU,LU,KV,LV,KW,LW,NM
         COMMON /STIFF/ XKEL(75,75),XKS(75,36,36),XKQ(82251),
     -     XKBL(75,36),XKBNL(36,36,36),XKF(36,36),XKT(36,36)
         COMMON /MODES/ XMODE(366),IMODE(366,2),SHAPE(45,21),
     -     XG(21),WEIGHT(21),NP,XL,YL
         COMMON /STRATES/ NC,TH(9),EP(9),EL(9),ET(9),XNULT(9),
     -     GLT(9),T,ELT,XT(9),XC(9),YT(9),YC(9),T6(9),XA,YA,
     -     XB,YB,XD
         DIMENSION Q(111),Q1(5,111),WT1(5),GRA1(5,111),Q0(36),
     -     S(111),GRA(111),HES(111,111),XLAM(36),VEC(36,36),
     -     SECU(9),XS(9),YS(9),SX(9),SY(9),TA(9),GE(111)
         CHARACTER*30 SPEC
         INTEGER*4 IT1(5)
C.........................................
C         CREATE ALL STIFFNESS MATRICES
C.........................................
         CALL ABD(IBCUV,IBCW,ILIN,ISYM,ITEST,ITRAN,SPEC)
         CALL CRWT
         CALL CRMODE(IBCUV,IBCW,ISYM)
         CALL CRKEL
         IF (ILIN.NE.1) THEN
           CALL CRKS
           CALL CRKQ
         ENDIF
         IF (ISYM.NE.1) THEN
           CALL CRKBL
           IF (ILIN.NE.1) THEN
             CALL CRKBNL
           ENDIF
         ENDIF
         CALL CRKF(ITRAN)
         IFT=0
C.........................................
C         READ LOAD CASE
C.........................................
  300    READ (5,*) PX,PY,TAU,PRES
         IF (PX.EQ.999) STOP
         READ (5,*) IQ,QQ
         Q0(IQ)=QQ
         READ (5,*) NMODE,IVAL,ISCAN
         IF (NMODE.GT.NW) NMODE=NW
C
C         NMODE=NUMBER OF DIRECTIONS TO TEST
C         IF IVAL=1 THEN FIND EIGENVECTORS
C
```

```
        N1=NU+NV
        ITRY=NMODE
        LIN=0
C*****************************************************************
C                                                                ***
C   MAIN LOOP STARTS HERE FOR DIFFERENT STARTING VECTORS         ***
C                                                                ***
C*****************************************************************
  190   DO 180 I=1,NM
          S(I)=0.D0
          GE(I)=0.D0
  180   Q(I)=0.D0
        ITER=0
C.................................................................
C        GENERATE LOAD VECTOR, SOLVE THE LINEAR PROBLEM,
C                AND FIND THE EIGENVECTORS.
C.................................................................
        CALL LOAD(PX,PY,TAU,PRES,GE,IBCUV,IBCW,ITRAN)
        IF (QQ.EQ.0.D0) LIN=1
        CALL LINEAR(Q,Q0,GE,ISYM,LIN)
        IF ((IVAL.EQ.1).AND.(ITRY.EQ.NMODE)) THEN
          CALL EIGEN(YL,XLAM,VEC,ISYM)
          IF ((ITRAN.EQ.1).AND.(IFT.EQ.0)) THEN
            DO 217 I=1,NW
            DO 217 J=I,NW
 217        XKF(I,J)=XKF(I,J)+XKT(I,J)
            WRITE(10,218)
 218        FORMAT(/' THE TRANSDUCER FORCES HAVE BEEN
     1        APPLIED.'/)
            IFT=1
          ENDIF
        ENDIF
C.................................................................
C  TEST THE DIRECTIONS CORRESPONDING TO DIFFERENT EIGENMODES
C.................................................................
        DO 220 I=1,NW
 220      S(NU+NV+I)=VEC(I,ITRY)
        WT=0.D0
        CALL LINESEARCH(Q,Q0,GE,S,ALPHA,ISYM,WT)
C.................................................................
C    IF THE DIRECTION MINIMIZES F(Q), THEN FIND A SOLUTION
C.................................................................
        IF (ABS(ALPHA).GE.1.E-3) THEN
          CALL SOLUTION(Q,Q0,GE,WT,GRA,ITER)
        ENDIF
        DO 210 I=1,NM
          GRA1(ITRY,I)=GRA(I)
  210     Q1(ITRY,I)=Q(I)          ! EIGENVECTOR
        WT1(ITRY)=WT                 ! ENERGY
        IT1(ITRY)=ITER                 !   ITERATIONS
        ITRY=ITRY-1
        IF (ITRY.GT.0) GO TO 190
C*****************************************************************
```

```
C                                                                      ***
C                          END OF LOOP                                 ***
C                                                                      ***
C            THE DIFFERENT SOLUTIONS ARE COMPARED                      ***
C                                                                      ***
C**********************************************************************
        XMIN=0.D0
        IM=0
        DO 230 K=1,NMODE
        IF (WT1(K).LT.XMIN) THEN
          XMIN=WT1(K)
          IM=K
        ENDIF
  230   CONTINUE
C
C         THE MINIMUM IS SAVED
C
        ZG=0.D0
        GMAX=0.D0
        IMAX=0
          DO 240 I=1,NM
            Q(I)=Q1(IM,I)
            GRA(I)=GRA1(IM,I)
            ZG=ZG+GRA(I)
            IF (ABS(GRA(I)).GT.GMAX) THEN
                GMAX=ABS(GRA(I))
                IMAX=I
          END IF
 240    CONTINUE
        ZG=ZG/NM
        WT=WT1(IM)
        ITER=IT1(IM)
C ******************************************************************
C ***                                                            ***
C ***         RECONSTRUCT DISPLACEMENT FIELDS : u,v,w            ***
C ***                                                            ***
C ******************************************************************
 245        CALL DISP(ISCAN,PX,Q,SPEC)
C.................................................
C         THE RESULTS ARE WRITTEN ON UNIT 10
C.................................................
        WRITE (10,249)
 249      FORMAT(1H1)
        DO 250 K=1,NMODE
 250      WRITE (10,255) IT1(K),K,WT1(K)
 255    FORMAT(' AFTER'I3' ITERATIONS, THE ENERGY OF MODE'I2,
     1    ' = 'G10.3)
        WRITE (10,108) PX,PY,TAU,PRES
        WRITE (10,*) ' '
        WRITE (10,256) QQ,IQ
 256    FORMAT(' INITIAL IMPERFECTION OF 'F8.4' IN MODE'I2/)
        WRITE (10,103) ZG,GMAX,IMAX
        WRITE (10,*) ' MODAL AMPLITUDES:'
```

```
      WRITE (10,*) ' '
      WRITE (10,*) ' U MODES:'
      WRITE (10,102) (Q(I),I=1,NU)
      WRITE (10,*) ' '
      WRITE (10,*) ' V MODES:'
      N1=NU+1
      N2=NU+NV
      WRITE (10,102) (Q(I),I=N1,N2)
      WRITE (10,*) ' '
      WRITE (10,*) ' W MODES:'
      N1=N2+1
      WRITE (10,102) (Q(I),I=N1,NM)
      WRITE (10,*) ' '
      WRITE (10,*) ' '
      WRITE (10,104) ITER, WT
C.....................................................
C       IF ITEST=1 THEN THE STRESSES ARE COMPUTED
C.....................................................
      IF (ITEST.EQ.1) THEN
        CALL RESIST(Q,Q0,SECU,XS,YS,SX,SY,TA)
        WRITE (10,106)
        DO 290 I=1,NC
          X=XS(I)/XL
          Y=YS(I)/YL
 290    WRITE (10,105) I,SECU(I),X,Y,SX(I),SY(I),TA(I)
      ENDIF
      GO TO 300
C*****
 102  FORMAT(5(G13.5,'   '))
 103  FORMAT(' AVERAGE GRADIENT ='G11.4' MAX COMPONENT =',
     -       G11.4,' FOR MODE'I3//)
 104  FORMAT(' AFTER'I3' ITERATIONS, THE LOWEST ENERGY IS',
     1   F10.5/)
 105  FORMAT(2X,I2,4X,6(G11.3))
 106  FORMAT(' LAYER ',2X,' SAFETY',8X,'X',10X,'Y',9X,'S1',
     -   9X,'S2',9X,'S6'/)
 108  FORMAT (/' APPLIED LOADS : PX =',F10.2,'     PY =',
     -   F10.2/,'                  PXY =',F10.2,
     -   '    PRESSURE =',F10.2/)
      END
C-------------------------------------------------------
C
C       MINIMUM SEARCHING BY NEWTON-RAPHSON METHOD
C
      SUBROUTINE SOLUTION(Q,Q0,GE,WT,GRA,IT)
      IMPLICIT REAL*8 (A-H,O-Z)
      COMMON /MATRICES/ A(3,3),B(3,3),D(3,3)
      COMMON /NMODES/ NU,NV,NW,KU,LU,KV,LV,KW,LW,NM
      COMMON /MODES/ XMODE(366),IMODE(366,2),SHAPE(45,21),
     -   XG(21),WEIGHT(21),NP,XL,YL
      COMMON /STRATES/ NC,TH(9),EP(9),EL(9),ET(9),XNULT(9),
     -   GLT(9),T,ELT,XT(9),XC(9),YT(9),YC(9),T6(9),XA,YA,
     -   XB,YB,XD
```

```
      DIMENSION Q(111),Q0(36),S(111),GRA(111),
     &     HES(111,111),GE(111)
      IT=0
      LIN=0
      IMAX=20
 20     CALL GRADIENT(Q,Q0,GE,ISYM,GRA)
        ZG=0.D0
        DO 30 I=1,NM
 30       ZG=ZG+ABS(GRA(I))
        ZG=ZG/NM
        IT=IT+1
        CALL HESSIEN(Q,Q0,HES,ISYM,LIN)
C
C       SOLVE:RESOLUTION OF HES*S=GRAD
C
        NN=NM
        CALL SOLVE(NN,GRA,HES,S)
        CALL LINESEARCH(Q,Q0,GE,S,ALPHA,ISYM,WT)
C
C       END IF ITERATIONS EXCESSIVE, OR IF GRADIENT OR
C         DISPLACEMENT INCREMENT IS SMALL
C
        IF (IT.GT.IMAX) RETURN
        ZQ=0.D0
        ZS=0.D0
        DO 50 I=1,NM
          ZQ=ZQ+ABS(Q(I))
 50       ZS=ZS+ABS(S(I))
        ZS=ZS*ABS(ALPHA)
      IF ((ZS/ZQ.LT.1.E-5).AND.(ZG.LT.0.1D0)) RETURN
      IF (ZG.LT.5.E-3) RETURN
      GO TO 20
      END
C-------------------------------------------------------------
      SUBROUTINE EIGEN(YL,XLAM,VEC,ISYM)
      IMPLICIT REAL*8 (A-H,O-Z)
      COMMON /MATRICES/ A(3,3),B(3,3),D(3,3)
      COMMON /NMODES/ NU,NV,NW,KU,LU,KV,LV,KW,LW,NM
      COMMON /STIFF/ XKEL(75,75),XKS(75,36,36),XKQ(82251),
     -   XKBL(75,36),XKBNL(36,36,36),XKF(36,36),XKT(36,36)
      DIMENSION XKA(666),XKB(666),VEC(36,36)
      DIMENSION XLAM(36),Q(111),WK(1368)
      DIMENSION X1(75,75),X2(75,36),X3(75,75)
C
C   PARTITION STIFFNESS MATRIX AND REDUCE
C
      NUV=NU+NV
      IUV=75
      IW=36
      DO 10 I=1,NUV
        DO 5 J=1,NW
   5      X2(I,J)=XKBL(I,J)*0.5D0
        X1(I,I)=XKEL(I,I)
```

```
            I1=I-1
            DO 10 J=1,I1
              X1(I,J)=XKEL(J,I)*0.5D0
   10       X1(J,I)=X1(I,J)
          DO 20 I=1,NW
            VEC(I,I)=XKF(I,I)
            I1=I-1
            DO 20 J=1,I1
              VEC(I,J)=XKF(J,I)*0.5D0
   20       VEC(J,I)=VEC(I,J)
C
          CALL REDUCE(X1,X2,VEC,X3,NUV,NW,IUV,IW)
C
C          CALCULATE LOAD MATRIX => WX*WX
C
          N2UV=2*NUV
          DO 50 I=1,NW
            I1=I+N2UV
            DO 50 J=I,NW
              J1=J+N2UV
              CALL INTEGRE2(S,I1,J1)
   50         X1(I,J)=-S
C
C          COMPUTE EIGENVALUES AND VECTORS
C   (TRUE FOR SYMMETRIC PLATES, PSEUDO FOR UNSYMMETRIC)
C
C          N1=NU+1
C          N2=NU+2
          IND=0
          DO 60 I=1,NW
          DO 60 J=1,I
            IND=IND+1
            XKA(IND)=VEC(J,I)
   60     XKB(IND)=X1(J,I)
          IJOB=2
          CALL EIGZS(XKB,XKA,NW,IJOB,XLAM,VEC,IW,WK,IER)
          WRITE (10,100)
  100     FORMAT (1H1,72(1H*))
          WRITE (10,*) ' IER=',IER
          WRITE (10,*) ' PERF=',WK(1)
          WRITE (10,*) ' '
          WRITE (10,*) ' EIGENVALUES AND VECTORS'
          WRITE (10,*) ' '
          DO 200 I=1,4
            IF (XLAM(I).EQ.0.D0) THEN
              WRITE(10,*) I,' *** NO SOLUTION ***'
              GO TO 200
            END IF
            P1=1.D0/XLAM(I)*YL
            WRITE (10,*) P1
            WRITE (10,*)
C
C          SCALE EIGENVECTORS (ARBITRARILY TO |V|=2 )
```

```
C
          ZV=0.D0
          DO 210 J=1,NW
 210      ZV=ZV+ABS(VEC(J,I))
          DO 220 J=1,NW
 220      VEC(J,I)=VEC(J,I)*2.*NW/ZV
          WRITE (10,*) (VEC(J,I),J=1,NW)
 200    WRITE (10,*) ' '
        RETURN
        END
C-------------------------------------------------------------
C
C         THE LINEAR PROBLEM IS SOLVED
C
        SUBROUTINE LINEAR(Q,Q0,GE,ISYM,LIN)
        IMPLICIT REAL*8 (A-H,O-Z)
        COMMON /MATRICES/ A(3,3),B(3,3),D(3,3)
        COMMON /NMODES/ NU,NV,NW,KU,LU,KV,LV,KW,LW,NM
        DIMENSION Q(111),Q0(36),GRA(111),HES(111,111),GE(111)
C
        CALL HESSIEN(Q,Q0,HES,ISYM,LIN)
        LIN=0
        DO 10 I=1,NM
 10     GRA(I)=GE(I)
        CALL SOLVE(NM,GRA,HES,Q)
        RETURN
        END
C-------------------------------------------------------------
C
C         GENERALIZED FORCES
C
        SUBROUTINE LOAD(PX,PY,TAU,PRES,GE,IBCUV,IBCW,ITRAN)
        IMPLICIT REAL*8 (A-H,O-Z)
        COMMON /MATRICES/ A(3,3),B(3,3),D(3,3)
        COMMON /NMODES/ NU,NV,NW,KU,LU,KV,LV,KW,LW,NM
        DIMENSION GE(111)
        PARAMETER (PI=3.141592654)
C
        GE(1)=PX
        GE(NU+1)=PY
        GE(NU+2)=TAU
        IF (IBCW.EQ.1) THEN
          IF (PRES.NE.0.D0) THEN
            IND=NU+NV
            DO 10 K=1,KW
              ZK=DFLOAT(K)
              DO 10 L=1,LW
                ZL=DFLOAT(L)
                IND=IND+1
                GE(IND)=PRES*XL*YL/ZK/ZL/PI**2
     &                  *(COS(ZK*PI)-1.D0)*(COS(ZL*PI)-1.D0)
 10         CONTINUE
          ENDIF
```

```
          ENDIF
          IND=1
          IF (TAU.NE.0.D0) THEN
            DO 20 K=1,KU
              ZK=DFLOAT(K)
              DO 20 L=JMOD(K,2),2*(LU-1)+JMOD(K,2),2
                ZL=DFLOAT(L)
                IND=IND+1
 20           GE(IND)=TAU/ZK/PI*((COS(ZK*PI)-1.D0)
     &                -(COS(ZK*PI)-1.D0)*COS(ZL*PI))
            IND=NU+2
            DO 30 L=1,LV
              ZL=DFLOAT(L)
              DO 30 K=JMOD(L,2),2*(KV-1)+JMOD(L,2),2
                ZK=DFLOAT(K)
                IND=IND+1
 30           GE(IND)=TAU/ZL/PI*((COS(ZL*PI)-1.D0)
     &                -(COS(ZL*PI)-1.D0)*COS(ZK*PI))
          ENDIF
          IF (ITRAN.EQ.1) THEN
            K=2*(NU+NV)+5*NW
            IND=NU+NV
            DO 40 I=1,NW
              IND=IND+1
              L=K+I
              CALL TRANSP(S,L)
 40           GE(IND)=GE(IND)+S
          ENDIF
          RETURN
          END
C+++++++++++++++++++++++++++++++++++++++++++++++++++++++++++++++++++++++
C
C          DETERMINES WORK PERFORMED BY TRANSDUCERS
C
          SUBROUTINE TRANSP(S,I)
          IMPLICIT REAL*8 (A-H,O-Z)
          COMMON /MODES/ XMODE(366),IMODE(366,2),SHAPE(45,21),
     -      XG(21),WEIGHT(21),NP,XL,YL
          S=0.D0
          I1=IMODE(I,1)
          I2=IMODE(I,2)
          K=(NP-1)/4
          DO 10 L=1,3
            IX=L*K+1
            P=0.00210D0
            IF (L.EQ.2) P=0.00589D0
            DO 10 M=1,3
              IY=M*K+1
 10       S=S+P*SHAPE(I1,IX)*SHAPE(I2,IY)
          RETURN
          END
C ***************************************************************
C ***                                                         ***
```

```
C ***          MATRIX REDUCTION SUBROUTINE PACKAGE          ***
C ***                                                       ***
C ***       FOR USE IN NONLINEAR POSTBUCKLING PROGRAM       ***
C ***                                                       ***
C *************************************************************
      SUBROUTINE REDUCE(A,B,C,D,NA,NC,IA,IC)
C
C CALCULATES C'(NC,NC)=C(NC,NC)-BT(NC,NA)*A-1(NA,NA)*B(NA,NC)
C
      IMPLICIT REAL*8 (A-H,O-Z)
      DIMENSION A(IA,1),B(IA,1),C(IC,1),D(IA,1)
C     INVERT A
      CALL INVERP(A,D,NA,IA)
C     CALCULATE A-1*B
      CALL MULT(D,B,A,NA,NA,NC,IA,IA,IA)
C     TRANSPOSE B
      DO 10 I=1,NC
      DO 10 J=1,NA
 10   D(I,J)=B(J,I)
C     CALCULATE BT*A-1*B
      CALL MULT(D,A,B,NC,NA,NC,IA,IA,IA)
C     CALCULATE C'
      DO 20 I=1,NC
      DO 20 J=1,NC
 20   C(I,J)=C(I,J)-B(I,J)
      RETURN
      END
C *************************************************************
C
      SUBROUTINE INVERP(A,AI,N,IA)
C
C INVERTS UP TO A 75 BY 75 MATRIX USING THE PIVOTING METHOD
C
      IMPLICIT REAL*8(A-H,O-Z)
      DIMENSION A(IA,IA), AI(IA,IA), IC(75), IR(75)
      IF((N.GT.IA).OR.(IA.GT.75)) THEN
        TYPE 5
  5     FORMAT(' INVERSION MATRIX IMPROPERLY DIMENSIONED')
        STOP
      ENDIF
C
C     INITIALIZATION
C
      DO 10 I=1,N
        IC(I)=I
        IR(I)=I
        DO 10 J=1,N
 10   AI(I,J)=A(I,J)
C
C     LOCATE LARGEST PIVOT ELEMENT
C
C       DET=1.0D0
        DO 120 K=1,N
```

```
          PIV=A(K,K)
          BIG=DABS(PIV)
          IP=K
          JP=K
          DO 20 I=K,N
          DO 20 J=K,N
            BIGG=DABS(A(I,J))
            IF(BIG.LT.BIGG) THEN
              BIG=BIGG
              PIV=A(I,J)
              IP=I
              JP=J
            ENDIF
 20       CONTINUE
          IF(DABS(PIV) .LE. 1.0D-37) THEN
            IRANK=K-1
            TYPE 30,IRANK
 30         FORMAT(' THE MATRIX BEING INVERTED HAS RANK = 'I4)
            STOP
          ENDIF
C
C     INTERCHANGE COLUMN OF PIVOT ELEMENT WITH K
C
C         DET=DET*PIV
          IF(K.NE.JP) THEN
C           DET=-DET
            DO 50 I=1,N
              TEMP=A(I,K)
              A(I,K)=A(I,JP)
 50           A(I,JP)=TEMP
            ITEMP=IC(K)
            IC(K)=IC(JP)
            IC(JP)=ITEMP
          ENDIF
C
C     INTERCHANGE ROW OF PIVOT ELEMENT WITH ROW K
C
          IF(K.NE.IP) THEN
C           DET=-DET
            DO 70 I=1,N
              TEMP=A(K,I)
              A(K,I)=A(IP,I)
 70           A(IP,I)=TEMP
            ITEMP=IR(K)
            IR(K)=IR(IP)
            IR(IP)=ITEMP
          ENDIF
C
C     PIVOT
C
          DO 90 I=1,N
          DO 90 J=1,N
 90       AI(I,J)=A(I,J)-A(I,K)*A(K,J)/PIV
```

```
          DO 100 I=1,N
            AI(I,K)=-A(I,K)/PIV
 100      AI(K,I)=A(K,I)/PIV
          AI(K,K)=1.0D0/PIV
          DO 110 I=1,N
          DO 110 J=1,N
 110      A(I,J)=AI(I,J)
 120    CONTINUE
C
C     OBTAIN CORRECT ORDER
C
        DO 130 I=1,N
          II=IC(I)
          DO 130 J=1,N
            JJ=IR(J)
 130    AI(II,JJ)=A(I,J)
        RETURN
        END
C ***************************************************************
C
        SUBROUTINE MULT(A,B,C,N1,N2,N3,IA,IB,IC)
C
C     COMPUTES C(N1,N3)=A(N1,N2)*B(N2,N3)
C
        IMPLICIT REAL*8(A-H,O-Z)
        DIMENSION A(IA,1),B(IB,1),C(IC,1)
        DO 10 I=1,N1
        DO 10 J=1,N3
  10      C(I,J)=0.D0
        DO 20 I=1,N2
        DO 20 J=1,N3
          IF(B(I,J).NE.0.D0) THEN
            X=B(I,J)
            DO 30 K=1,N1
  30        C(K,J)=C(K,J)+A(K,I)*X
          ENDIF
  20    CONTINUE
        RETURN
        END
C--------------------------------------------------------------
C
C             CREATION OF THE STIFFNESS MATRICES
C            ------------------------------------
C
C             KEL=LINEAR STRETCHING
C
        SUBROUTINE CRKEL
        IMPLICIT REAL*8 (A-H,O-Z)
        COMMON /MODES/ XMODE(366),IMODE(366,2),SHAPE(45,21),
     -    XG(21),WEIGHT(21),NP,XL,YL
        COMMON /MATRICES/ A(3,3),B(3,3),D(3,3)
        COMMON /NMODES/ NU,NV,NW,KU,LU,KV,LV,KW,LW,NM
        COMMON /STIFF/ XKEL(75,75),XKS(75,36,36),XKQ(82251),
```

```
     -     XKBL(75,36),XKBNL(36,36,36),XKF(36,36),XKT(36,36)
C
      NU1=NU+1
      N=NU+NV
      N1=N+1
      N2=N+NU
      N3=N2+1
      N4=N2+NV
C
C      A(1,1)*UX*UX
C
      DO 10 I=1,NU
      DO 10 J=I,NU
        CALL INTEGRE2(S,I,J)
        IF (I.NE.J) S=S*2.D0
 10     XKEL(I,J)=XKEL(I,J)+S*A(1,1)
C
C      A(1,2)*UX*VY
C
      DO 20 I=1,NU
      DO 20 J=NU1,N
        CALL INTEGRE2(S,I,J)
 20     XKEL(I,J)=XKEL(I,J)+S*A(1,2)*2.D0
C
C      A(1,3)*UX*(UY+VX)
C
      IF (ABS(A(1,3)).GE.1.E-6) THEN
        DO 30 I=1,NU
        DO 30 J=N1,N2
          CALL INTEGRE2(S,I,J)
          J1=J-N
          IF (I.EQ.J1) S=S/2.D0
          XKEL(I,J1)=XKEL(I,J1)+S*A(1,3)*2.D0
 30       XKEL(J1,I)=XKEL(J1,I)+S*A(1,3)*2.D0
        DO 40 I=1,NU
        DO 40 J=N3,N4
          CALL INTEGRE2(S,I,J)
          J1=J-N
 40       XKEL(I,J1)=XKEL(I,J1)+S*A(1,3)*2.D0
      ENDIF
C
C      A(2,2)*VY*VY
C
      DO 60 I=NU1,N
      DO 60 J=I,N
        CALL INTEGRE2(S,I,J)
        IF (I.NE.J) S=S*2.D0
 60     XKEL(I,J)=XKEL(I,J)+S*A(2,2)
C
C      A(2,3)*VY*(UY+VX)
C
      IF (ABS(A(2,3)).GE.1.E-6) THEN
        DO 70 I=N1,N2
```

```
            DO 70 J=NU1,N
              CALL INTEGRE2(S,I,J)
              I1=I-N
 70           XKEL(I1,J)=XKEL(I1,J)+S*A(2,3)*2.D0
            DO 80 I=N3,N4
            DO 80 J=NU1,N
              CALL INTEGRE2(S,I,J)
              I1=I-N
              IF (I1.EQ.J) S=S/2.D0
              XKEL(I1,J)=XKEL(I1,J)+S*A(2,3)*2.D0
 80           XKEL(J,I1)=XKEL(J,I1)+S*A(2,3)*2.D0
          ENDIF
C
C          A(3,3)*(UY+VX)**2
C
          DO 100 I=N1,N4
          DO 100 J=I,N4
            CALL INTEGRE2(S,I,J)
            I1=I-N
            J1=J-N
            IF (I1.NE.J1) S=S*2.D0
 100        XKEL(I1,J1)=XKEL(I1,J1)+A(3,3)*S
          RETURN
          END
C-------------------------------------------------------------
C
C               KS=NON-LINEAR STRETCHING
C
          SUBROUTINE CRKS
          IMPLICIT REAL*8 (A-H,O-Z)
          COMMON /MODES/ XMODE(366),IMODE(366,2),SHAPE(45,21),
     -      XG(21),WEIGHT(21),NP,XL,YL
          COMMON /MATRICES/ A(3,3),B(3,3),D(3,3)
          COMMON /NMODES/ NU,NV,NW,KU,LU,KV,LV,KW,LW,NM
          COMMON /STIFF/ XKEL(75,75),XKS(75,36,36),XKQ(82251),
     -      XKBL(75,36),XKBNL(36,36,36),XKF(36,36),XKT(36,36)
C
          NU1=NU+1
          N=NU+NV
          N1=N+1
          N2=N+NU
          N3=N2+1
          N4=2*N
          N5=N4+1
          N6=N4+NW
          N7=N6+1
          N8=N6+NW
C
          DO 10 I=1,NU
          DO 10 J=N5,N6
          DO 10 K=J,N6
            CALL INTEGRE3(S,I,J,K)
            J1=J-N4
```

```
          K1=K-N4
          IF (J1.EQ.K1) S=S/2.D0
          XKS(I,J1,K1)=XKS(I,J1,K1)+A(1,1)*S
10        XKS(I,K1,J1)=XKS(I,K1,J1)+A(1,1)*S
        DO 20 I=1,NU
        DO 20 J=N7,N8
        DO 20 K=J,N8
          CALL INTEGRE3(S,I,J,K)
          J1=J-N6
          K1=K-N6
          IF (J1.EQ.K1) S=S/2.D0
          XKS(I,J1,K1)=XKS(I,J1,K1)+A(1,2)*S
20        XKS(I,K1,J1)=XKS(I,K1,J1)+A(1,2)*S
        IF (ABS(A(1,3)).GE.1.E-6) THEN
          DO 30 I=1,NU
          DO 30 J=N5,N6
          DO 30 K=N7,N8
            CALL INTEGRE3(S,I,J,K)
            J1=J-N4
            K1=K-N6
30        XKS(I,J1,K1)=XKS(I,J1,K1)+A(1,3)*S*2.D0
        ENDIF
        DO 50 I=NU1,N
        DO 50 J=N5,N6
        DO 50 K=J,N6
          CALL INTEGRE3(S,I,J,K)
          IF (J.EQ.K) S=S/2.D0
          J1=J-N4
          K1=K-N4
          XKS(I,J1,K1)=XKS(I,J1,K1)+A(1,2)*S
50        XKS(I,K1,J1)=XKS(I,K1,J1)+A(1,2)*S
        DO 60 I=NU1,N
        DO 60 J=N7,N8
        DO 60 K=J,N8
          CALL INTEGRE3(S,I,J,K)
          IF (J.EQ.K) S=S/2.D0
          J1=J-N6
          K1=K-N6
          XKS(I,J1,K1)=XKS(I,J1,K1)+S*A(2,2)
60        XKS(I,K1,J1)=XKS(I,K1,J1)+S*A(2,2)
        IF (ABS(A(2,3)).GE.1.E-6) THEN
          DO 70 I=NU1,N
          DO 70 J=N5,N6
          DO 70 K=N7,N8
            CALL INTEGRE3(S,I,J,K)
            J1=J-N4
            K1=K-N6
70        XKS(I,J1,K1)=XKS(I,J1,K1)+S*A(2,3)*2.D0
        ENDIF
        IF (ABS(A(3,1)).GE.1.E-6) THEN
          DO 80 I=N1,N4
          DO 80 J=N5,N6
          DO 80 K=J,N6
```

```
            CALL INTEGRE3(S,I,J,K)
            I1=I-N
            J1=J-N4
            K1=K-N4
            IF (K1.EQ.J1) S=S/2.D0
            XKS(I1,J1,K1)=XKS(I1,J1,K1)+A(3,1)*S
 80         XKS(I1,K1,J1)=XKS(I1,K1,J1)+A(3,1)*S
          ENDIF
          IF (ABS(A(2,3)).GE.1.E-6) THEN
            DO 100 I=N1,N4
            DO 100 J=N7,N8
            DO 100 K=J,N8
              CALL INTEGRE3(S,I,J,K)
              I1=I-N
              J1=J-N6
              K1=K-N6
              IF (J.EQ.K) S=S/2.D0
              XKS(I1,J1,K1)=XKS(I1,J1,K1)+A(2,3)*S
 100          XKS(I1,K1,J1)=XKS(I1,K1,J1)+A(2,3)*S
          ENDIF
          DO 120 I=N1,N4
          DO 120 J=N5,N6
          DO 120 K=N7,N8
            CALL INTEGRE3(S,I,J,K)
            I1=I-N
            J1=J-N4
            K1=K-N6
 120      XKS(I1,J1,K1)=XKS(I1,J1,K1)+A(3,3)*S*2.D0
C
C          SYMMETRIC TERMS IN J AND K ARE ADDED
C
          NN=NW-1
          IF (NN.NE.0) THEN
            DO 130 I=1,N
            DO 130 J=1,NN
              JJ=J+1
              DO 130 K=JJ,NW
 130        XKS(I,J,K)=XKS(I,J,K)+XKS(I,K,J)
          ENDIF
          RETURN
          END
C-------------------------------------------------------------
C
C          KQ=NON-LINEAR STRETCHING
C
          SUBROUTINE CRKQ
          IMPLICIT REAL*8 (A-H,O-Z)
          COMMON /MODES/ XMODE(366),IMODE(366,2),SHAPE(45,21),
     -      XG(21),WEIGHT(21),NP,XL,YL
          COMMON /MATRICES/ A(3,3),B(3,3),D(3,3)
          COMMON /NMODES/ NU,NV,NW,KU,LU,KV,LV,KW,LW,NM
          COMMON /STIFF/ XKEL(75,75),XKS(75,36,36),XKQ(82251),
     -      XKBL(75,36),XKBNL(36,36,36),XKF(36,36),XKT(36,36)
```

```
      REAL*8 DE(5)
C
      N1=2*(NU+NV)+1
      N2=2*(NU+NV)+NW
      N3=N2+1
      N4=N2+NW
      DE(1)=24.D0/4.D0
      DE(2)=12.D0/4.D0
      DE(3)=4.D0/4.D0
      DE(4)=1.D0/4.D0
      DE(5)=6.D0/4.D0
      IND=0
      DO 10 I=N1,N2
      DO 10 J=I,N2
      DO 10 K=J,N2
      DO 10 L=K,N2
        IND=IND+1
        NEG=1
        IF (I.EQ.J) NEG=NEG+1
        IF (J.EQ.K) NEG=NEG+1
        IF (K.EQ.L) NEG=NEG+1
        IF ((J.NE.K).AND.(NEG.EQ.3)) NEG=5
        CALL INTEGRE4(S,I,J,K,L)
        XKQ(IND)=XKQ(IND)+A(1,1)*S*DE(NEG)
        I1=I+NW
        J1=J+NW
        K1=K+NW
        L1=L+NW
        CALL INTEGRE4(S,I1,J1,K1,L1)
10       XKQ(IND)=XKQ(IND)+A(2,2)*S*DE(NEG)
      IND=0
      COEF=(2.D0*A(1,2)+4.D0*A(3,3))/4.D0
      DO 20 I=N1,N2
      DO 20 J=I,N2
      DO 20 K=J,N2
      DO 20 L=K,N2
        IND=IND+1
        I1=I+NW
        J1=J+NW
        K1=K+NW
        L1=L+NW
        CALL INTEGRE4(S,I,J,K1,L1)
        IF (I.NE.J) S=S*2.D0
        IF (L.NE.K) S=S*2.D0
        XKQ(IND)=XKQ(IND)+S*COEF
        IF (K.NE.I) THEN
          CALL INTEGRE4(S,K,J,I1,L1)
          IF (K.NE.J) S=S*2.D0
          IF (I.NE.L) S=S*2.D0
          XKQ(IND)=XKQ(IND)+S*COEF
          IF ((J.EQ.K).AND.(K.EQ.L)) GO TO 20
          IF ((I.EQ.J).AND.(K.EQ.L)) GO TO 24
        ENDIF
```

```
            IF ((L.EQ.I).OR.(K.EQ.L)) GO TO 22
            CALL INTEGRE4(S,L,J,K1,I1)
            IF (L.NE.J) S=S*2.D0
            IF (K.NE.1) S=S*2.D0
            XKQ(IND)=XKQ(IND)+S*COEF
            IF ((I.EQ.J).AND.(J.EQ.K)) GO TO 20
 22           IF ((K.EQ.J).OR.(I.EQ.J)) GO TO 23
            CALL INTEGRE4(S,I,K,J1,L1)
            IF (I.NE.K) S=S*2.D0
            IF (J.NE.L) S=S*2.D0
            XKQ(IND)=XKQ(IND)+S*COEF
 23           IF ((L.EQ.K).OR.(I.EQ.J)) GO TO 24
            CALL INTEGRE4(S,I,L,K1,J1)
            IF (I.NE.L) S=S*2.D0
            IF (K.NE.J) S=S*2.D0
            XKQ(IND)=XKQ(IND)+S*COEF
            IF (J.NE.K) GO TO 20
 24           IF ((L.EQ.J).AND.(I.EQ.K)) GO TO 20
            CALL INTEGRE4(S,K,L,I1,J1)
            IF (K.NE.L) S=S*2.D0
            IF (I.NE.J) S=S*2.D0
            XKQ(IND)=XKQ(IND)+S*COEF
 20         CONTINUE
          IF (ABS(A(2,3)).GE.1.E-6) THEN
            IND=0
            DO 30 I=N1,N2
              II=I+NW
              DO 30 J=II,N4
              DO 30 K=J,N4
              DO 30 L=K,N4
                IND=IND+1
                CALL INTEGRE4(S,I,J,K,L)
                AA=3.D0
                IF ((J.NE.K).AND.(K.NE.L)) AA=6.D0
                IF ((J.EQ.K).AND.(K.EQ.L)) AA=1.D0
                XKQ(IND)=XKQ(IND)+S*A(2,3)*AA
                I1=I+NW
                IF (I1.NE.J) THEN
                  J1=J-NW
                  CALL INTEGRE4(S,J1,I1,K,L)
                  AA=3.D0
                  IF ((I1.NE.K).AND.(K.NE.L)) AA=6.D0
                  IF ((I1.EQ.K).AND.(K.EQ.L)) AA=1.D0
                  XKQ(IND)=XKQ(IND)+S*A(2,3)*AA
                ENDIF
                IF ((I1.EQ.K).OR.(J.EQ.K)) GO TO 50
                K1=K-NW
                CALL INTEGRE4(S,K1,J,I1,L)
                AA=3.D0
                IF ((I1.NE.J).AND.(I1.NE.L)) AA=6.D0
                IF ((I1.EQ.J).AND.(I1.EQ.L)) AA=1.D0
                XKQ(IND)=XKQ(IND)+S*A(2,3)*AA
 50             IF ((I1.EQ.L).OR.(K.EQ.L)) GO TO 30
```

```
                L1=L-NW
                CALL INTEGRE4(S,L1,J,K,I1)
                AA=3.D0
                IF ((J.EQ.K).AND.(I1.EQ.K)) AA=1.D0
                IF ((J.NE.K).AND.(I1.NE.K)) AA=6.D0
                XKQ(IND)=XKQ(IND)+S*A(2,3)*AA
 30           CONTINUE
            ENDIF
            IF (ABS(A(1,3)).GE.1.E-6) THEN
              IND=0
              DO 70 I=N3,N4
                II=I-NW
                DO 70 J=II,N2
                DO 70 K=J,N2
                DO 70 L=K,N2
                  IND=IND+1
                  CALL INTEGRE4(S,I,J,K,L)
                  AA=3.D0
                  IF ((J.EQ.K).AND.(K.EQ.L)) AA=1.D0
                  IF ((J.NE.K).AND.(K.NE.L)) AA=6.D0
                  XKQ(IND)=XKQ(IND)+S*A(1,3)*AA
                  I1=I-NW
                  IF (I1.NE.J) THEN
                    J1=J+NW
                    CALL INTEGRE4(S,J1,I1,K,L)
                    AA=3.D0
                    IF ((I1.EQ.K).AND.(K.EQ.L)) AA=1.D0
                    IF ((I1.NE.K).AND.(K.NE.L)) AA=6.D0
                    XKQ(IND)=XKQ(IND)+S*A(1,3)*AA
                  ENDIF
                  IF ((I1.EQ.K).OR.(J.EQ.K)) GO TO 90
                  K1=K+NW
                  CALL INTEGRE4(S,K1,J,I1,L)
                  AA=3.D0
                  IF ((J.EQ.I1).AND.(I1.EQ.L)) AA=1.D0
                  IF ((J.NE.I1).AND.(I1.NE.L)) AA=6.D0
                  XKQ(IND)=XKQ(IND)+S*A(1,3)*AA
 90                  IF ((I1.EQ.L).OR.(K.EQ.L)) GO TO 70
                  L1=L+NW
                  CALL INTEGRE4(S,L1,J,K,I1)
                  AA=3.D0
                  IF ((K.EQ.J).AND.(K.EQ.I1)) AA=1.D0
                  IF ((K.NE.J).AND.(K.NE.I1)) AA=6.D0
                  XKQ(IND)=XKQ(IND)+S*A(1,3)*AA
 70           CONTINUE
            ENDIF
            RETURN
            END
C-------------------------------------------------------------
C
C         KBL=LINEAR MATERIAL BENDING-STRETCHING COUPLING
C
            SUBROUTINE CRKBL
```

```
      IMPLICIT REAL*8 (A-H,O-Z)
      COMMON /MODES/ XMODE(366),IMODE(366,2),SHAPE(45,21),
     -   XG(21),WEIGHT(21),NP,XL,YL
      COMMON /MATRICES/ A(3,3),B(3,3),D(3,3)
      COMMON /NMODES/ NU,NV,NW,KU,LU,KV,LV,KW,LW,NM
      COMMON /STIFF/ XKEL(75,75),XKS(75,36,36),XKQ(82251),
     -   XKBL(75,36),XKBNL(36,36,36),XKF(36,36),XKT(36,36)
C
      N1=NU+1
      N2=NU+NV
      N3=N2+NU
      N4=N3+NV
      N5=N4+2*NW
      N6=N5+NW
      N7=N6+NW
      DO 10 I=1,NU
      DO 10 J=1,NW
        J1=J+N5
        CALL INTEGRE2(S,I,J1)
        XKBL(I,J)=XKBL(I,J)+S*B(1,1)*2.D0
        J1=J+N6
        CALL INTEGRE2(S,I,J1)
        XKBL(I,J)=XKBL(I,J)+S*B(1,2)*2.D0
        J1=J+N7
        CALL INTEGRE2(S,I,J1)
        XKBL(I,J)=XKBL(I,J)+S*B(1,3)*2.D0
        I1=I+N2
        J1=J+N5
        CALL INTEGRE2(S,I1,J1)
        XKBL(I,J)=XKBL(I,J)+S*B(1,3)*2.D0
        J1=J+N6
        CALL INTEGRE2(S,I1,J1)
        XKBL(I,J)=XKBL(I,J)+S*B(2,3)*2.D0
        J1=J+N7
        CALL INTEGRE2(S,I1,J1)
10    XKBL(I,J)=XKBL(I,J)+S*B(3,3)*2.D0
      DO 20 I=N1,N2
      DO 20 J=1,NW
        J1=J+N5
        CALL INTEGRE2(S,I,J1)
        XKBL(I,J)=XKBL(I,J)+S*B(1,2)*2.D0
        J1=J+N6
        CALL INTEGRE2(S,I,J1)
        XKBL(I,J)=XKBL(I,J)+S*B(2,2)*2.D0
        J1=J+N7
        CALL INTEGRE2(S,I,J1)
        XKBL(I,J)=XKBL(I,J)+S*B(2,3)*2.D0
        I1=I+N2
        J1=J+N5
        CALL INTEGRE2(S,I1,J1)
        XKBL(I,J)=XKBL(I,J)+S*B(1,3)*2.D0
        J1=J+N6
        CALL INTEGRE2(S,I1,J1)
```

```
            XKBL(I,J)=XKBL(I,J)+S*B(2,3)*2.D0
            J1=J+N7
            CALL INTEGRE2(S,I1,J1)
 20       XKBL(I,J)=XKBL(I,J)+S*B(3,3)*2.D0
          RETURN
          END
C-------------------------------------------------------------
C
C         KBNL=NON-LINEAR MATERIAL BENDING-STRETCHING COUPLING
C
          SUBROUTINE CRKBNL
          IMPLICIT REAL*8 (A-H,O-Z)
          COMMON /MODES/ XMODE(366),IMODE(366,2),SHAPE(45,21),
     -      XG(21),WEIGHT(21),NP,XL,YL
          COMMON /MATRICES/ A(3,3),B(3,3),D(3,3)
          COMMON /NMODES/ NU,NV,NW,KU,LU,KV,LV,KW,LW,NM
          COMMON /STIFF/ XKEL(75,75),XKS(75,36,36),XKQ(82251),
     -      XKBL(75,36),XKBNL(36,36,36),XKF(36,36),XKT(36,36)
C
          N1=2*(NU+NV)
          N2=N1+NW
          N3=N2+NW
          N4=N3+NW
          N5=N4+NW
          DO 10 I=1,NW
          DO 10 J=I,NW
          DO 10 K=1,NW
            I1=I+N1
            J1=J+N1
            K1=K+N3
            CALL INTEGRE3(S,I1,J1,K1)
            XKBNL(I,J,K)=XKBNL(I,J,K)+S*B(1,1)
            IF (I.NE.J) XKBNL(J,I,K)=XKBNL(J,I,K)+S*B(1,1)
            K1=K+N4
            CALL INTEGRE3(S,I1,J1,K1)
            XKBNL(I,J,K)=XKBNL(I,J,K)+S*B(1,2)
            IF (I.NE.J) XKBNL(J,I,K)=XKBNL(J,I,K)+S*B(1,2)
            IF (ABS(B(1,3)).GE.1.E-6) THEN
              K1=K+N5
              CALL INTEGRE3(S,I1,J1,K1)
              XKBNL(I,J,K)=XKBNL(I,J,K)+S*B(1,3)
              IF (I.NE.J) XKBNL(J,I,K)=XKBNL(J,I,K)+S*B(1,3)
            ENDIF
            I1=I+N2
            J1=J+N2
            K1=K+N4
            CALL INTEGRE3(S,I1,J1,K1)
            XKBNL(I,J,K)=XKBNL(I,J,K)+S*B(2,2)
            IF (I.NE.J) XKBNL(J,I,K)=XKBNL(J,I,K)+S*B(2,2)
            K1=K+N3
            CALL INTEGRE3(S,I1,J1,K1)
            XKBNL(I,J,K)=XKBNL(I,J,K)+S*B(1,2)
            IF (I.NE.J) XKBNL(J,I,K)=XKBNL(J,I,K)+S*B(1,2)
```

```
            IF (ABS(B(2,3)).GE.1.E-6) THEN
              K1=K+N5
              CALL INTEGRE3(S,I1,J1,K1)
              XKBNL(I,J,K)=XKBNL(I,J,K)+S*B(2,3)
              IF (I.NE.J) XKBNL(J,I,K)=XKBNL(J,I,K)+S*B(2,3)
            ENDIF
 10           CONTINUE
          DO 30 I=1,NW
          DO 30 J=1,NW
          DO 30 K=1,NW
            I1=I+N1
            J1=J+N2
            IF (ABS(B(1,3)).GE.1.E-6) THEN
              K1=K+N3
              CALL INTEGRE3(S,I1,J1,K1)
              XKBNL(I,J,K)=XKBNL(I,J,K)+S*B(1,3)*2.D0
            ENDIF
            IF (ABS(B(2,3)).GE.1.E-6) THEN
              K1=K+N4
              CALL INTEGRE3(S,I1,J1,K1)
              XKBNL(I,J,K)=XKBNL(I,J,K)+S*B(2,3)*2.D0
            ENDIF
            K1=K+N5
            CALL INTEGRE3(S,I1,J1,K1)
 30       XKBNL(I,J,K)=XKBNL(I,J,K)+S*B(3,3)*2.D0
C
C          SYMMETRIC INDICES ARE ADDED
C
          DO 50 I=1,NW
          DO 50 J=I,NW
          DO 50 K=J,NW
            DD=1.D0
            IF ((I.EQ.J).OR.(J.EQ.K)) DD=2.D0
            IF ((I.EQ.J).AND.(J.EQ.K)) GO TO 50
            XKBNL(I,J,K)=(XKBNL(I,J,K)+XKBNL(I,K,J)+XKBNL(J,I,K)
     -      +XKBNL(J,K,I)+XKBNL(K,I,J)+XKBNL(K,J,I))/DD
 50       CONTINUE
          RETURN
          END
C-------------------------------------------------------------
C
C          KF=LINEAR BENDING
C
          SUBROUTINE CRKF(ITRAN)
          IMPLICIT REAL*8 (A-H,O-Z)
          COMMON /MODES/ XMODE(366),IMODE(366,2),SHAPE(45,21),
     -      XG(21),WEIGHT(21),NP,XL,YL
          COMMON /MATRICES/ A(3,3),B(3,3),D(3,3)
          COMMON /NMODES/ NU,NV,NW,KU,LU,KV,LV,KW,LW,NM
          COMMON /STIFF/ XKEL(75,75),XKS(75,36,36),XKQ(82251),
     -      XKBL(75,36),XKBNL(36,36,36),XKF(36,36),XKT(36,36)
C
          N1=2*(NU+NV+NW)
```

```
      N2=N1+NW
      N3=N2+NW
      N4=N3+NW
      DO 10 I=1,NW
        I1=I+N1
        I2=I+N2
        I3=I+N3
        I4=I+N4
        DO 10 J=I,NW
          J1=J+N1
          CALL INTEGRE2(S,I1,J1)
          AA=2.D0
          IF (I.EQ.J) AA=1.D0
          XKF(I,J)=XKF(I,J)+S*D(1,1)*AA
          J2=J+N2
          CALL INTEGRE2(S,I1,J2)
          XKF(I,J)=XKF(I,J)+S*D(1,2)*AA
          CALL INTEGRE2(S,I2,J1)
          XKF(I,J)=XKF(I,J)+S*D(1,2)*AA
          CALL INTEGRE2(S,I2,J2)
          XKF(I,J)=XKF(I,J)+S*D(2,2)*AA
          J3=J+N3
          IF (ABS(D(1,3)).GE.1.E-6) THEN
            CALL INTEGRE2(S,I1,J3)
            XKF(I,J)=XKF(I,J)+S*D(1,3)*AA
            CALL INTEGRE2(S,I3,J1)
            XKF(I,J)=XKF(I,J)+S*D(1,3)*AA
          ENDIF
          IF (ABS(D(2,3)).GE.1.E-6) THEN
            CALL INTEGRE2(S,I3,J2)
            XKF(I,J)=XKF(I,J)+S*D(2,3)*AA
            CALL INTEGRE2(S,I2,J3)
            XKF(I,J)=XKF(I,J)+S*D(2,3)*AA
          ENDIF
          CALL INTEGRE2(S,I3,J3)
          XKF(I,J)=XKF(I,J)+S*D(3,3)*AA
          IF (ITRAN.EQ.1) THEN
            J4=J+N4
            CALL TRANSK(S,I4,J4)
            XKT(I,J)=XKT(I,J)+S*AA
          ENDIF
 10     CONTINUE
        RETURN
        END
C++++++++++++++++++++++++++++++++++++++++++++++++++++++++++++++++
C
C         DESTIFFENING DUE TO FORCE OF TRANSDUCERS
C
        SUBROUTINE TRANSK(S,I,J)
        IMPLICIT REAL*8 (A-H,O-Z)
        COMMON /MODES/ XMODE(366),IMODE(366,2),SHAPE(45,21),
     &    XG(21),WEIGHT(21),NP,XL,YL
        S=0.D0
```

```
      I1=IMODE(I,1)
      J1=IMODE(J,1)
      I2=IMODE(I,2)
      J2=IMODE(J,2)
      K=(NP-1)/4
      DO 10 L=1,3
        XK=0.0000827D0
        IF (L.EQ.2) XK=0.000116D0
        IX=L*K+1
        DO 10 M=1,3
          IY=M*K+1
10      S=S+XK*SHAPE(I1,IX)*SHAPE(I2,IY)*SHAPE(J1,IX)
     1    *SHAPE(J2,IY)
      RETURN
      END
C-----------------------------------------------------------
C
C       INTEGRATION SUBROUTINES
C
      SUBROUTINE INTEGRE2(S,I,J)
      IMPLICIT REAL*8 (A-H,O-Z)
      COMMON /MODES/ XMODE(366),IMODE(366,2),SHAPE(45,21),
     &   XG(21),WEIGHT(21),NP,XL,YL
      S=0.D0
      T=0.D0
      I1=IMODE(I,1)
      J1=IMODE(J,1)
      I2=IMODE(I,2)
      J2=IMODE(J,2)
      DO 10 K=1,NP
        T=T+WEIGHT(K)*SHAPE(I2,K)*SHAPE(J2,K)
 10   S=S+WEIGHT(K)*SHAPE(I1,K)*SHAPE(J1,K)
      S=S*T*XMODE(I)*XMODE(J)
      RETURN
      END
C
C
      SUBROUTINE INTEGRE3(S,I,J,II)
      IMPLICIT REAL*8 (A-H,O-Z)
      COMMON /MODES/ XMODE(366),IMODE(366,2),SHAPE(45,21),
     -   XG(21),WEIGHT(21),NP,XL,YL
      S=0.D0
      T=0.D0
      I1=IMODE(I,1)
      J1=IMODE(J,1)
      K1=IMODE(II,1)
      I2=IMODE(I,2)
      J2=IMODE(J,2)
      K2=IMODE(II,2)
      DO 10 K=1,NP
        T=T+WEIGHT(K)*SHAPE(I1,K)*SHAPE(J1,K)*SHAPE(K1,K)
 10   S=S+WEIGHT(K)*SHAPE(I2,K)*SHAPE(J2,K)*SHAPE(K2,K)
      S=S*T*XMODE(I)*XMODE(J)*XMODE(II)
```

```
      RETURN
      END
C
      SUBROUTINE INTEGRE4(S,I,J,II,JJ)
      IMPLICIT REAL*8 (A-H,O-Z)
      COMMON /MODES/ XMODE(366),IMODE(366,2),SHAPE(45,21),
     -   XG(21),WEIGHT(21),NP,XL,YL
      T=0.D0
      S=0.D0
      I1=IMODE(I,1)
      J1=IMODE(J,1)
      K1=IMODE(II,1)
      L1=IMODE(JJ,1)
      I2=IMODE(I,2)
      J2=IMODE(J,2)
      K2=IMODE(II,2)
      L2=IMODE(JJ,2)
      DO 10 K=1,NP
        T=T+WEIGHT(K)*SHAPE(I1,K)*SHAPE(J1,K)*SHAPE(K1,K)
     1     *SHAPE(L1,K)
 10   S=S+WEIGHT(K)*SHAPE(I2,K)*SHAPE(J2,K)*SHAPE(K2,K)
     1   *SHAPE(L2,K)
      S=S*T*XMODE(I)*XMODE(J)*XMODE(II)*XMODE(JJ)
      RETURN
      END
C*************************************************************
C
C                 CALCULATION OF ENERGY
C
      SUBROUTINE ENERGIE(Q,Q0,GE,WT,ISYM)
      IMPLICIT REAL*8 (A-H,O-Z)
      COMMON /MATRICES/ A(3,3),B(3,3),D(3,3)
      COMMON /NMODES/ NU,NV,NW,KU,LU,KV,LV,KW,LW,NM
      COMMON /STIFF/ XKEL(75,75),XKS(75,36,36),XKQ(82251),
     -   XKBL(75,36),XKBNL(36,36,36),XKF(36,36),XKT(36,36)
      COMMON /MODES/ XMODE(366),IMODE(366,2),SHAPE(45,21),
     -   XG(21),WEIGHT(21),NP,XL,YL
      REAL*8 Q(111),W(6),Q0(36),GE(111)
C
      W(1)=0.D0
      N=NU+NV
      DO 10 I=1,N
      DO 10 J=I,N
 10   W(1)=W(1)+XKEL(I,J)*Q(I)*Q(J)
      W(2)=0.D0
      DO 20 I=1,N
      DO 20 J=1,NW
        J1=J+N
        DO 20 K=J,NW
          K1=K+N
          W(2)=W(2)+XKS(I,J,K)*Q(I)*2.D0*Q0(J)*Q(K1)
 20   W(2)=W(2)+XKS(I,J,K)*Q(I)*Q(J1)*Q(K1)
      W(3)=0.D0
```

```
      INDICE=0
      DO 30 I=1,NW
        I1=I+N
      DO 30 J=I,NW
        J1=J+N
      DO 30 K=J,NW
        K1=K+N
      DO 30 L=K,NW
        INDICE=INDICE+1
        L1=L+N
        W(3)=W(3)+XKQ(INDICE)*4.D0*Q0(I)*Q(J1)*Q(K1)*Q(L1)
        W(3)=W(3)+XKQ(INDICE)*4.D0*Q0(I)*Q0(J)*Q(K1)*Q(L1)
 30     W(3)=W(3)+XKQ(INDICE)*Q(I1)*Q(J1)*Q(K1)*Q(L1)
      IF (ISYM.NE.1) THEN
        W(4)=0.D0
        DO 50 I=1,N
        DO 50 J=1,NW
 50     W(4)=W(4)-XKBL(I,J)*Q(I)*Q(N+J)
        W(5)=0.D0
        DO 60 I=1,NW
        DO 60 J=I,NW
        DO 60 K=J,NW
          W(5)=W(5)-XKBNL(I,J,K)*2.D0*Q0(I)*Q(J+N)*Q(K+N)
 60     W(5)=W(5)-XKBNL(I,J,K)*Q(I+N)*Q(J+N)*Q(K+N)
      ENDIF
      W(6)=0.D0
      DO 70 I=1,NW
      DO 70 J=I,NW
 70   W(6)=W(6)+XKF(I,J)*Q(I+N)*Q(J+N)
C
C       EXTERNAL LOADS
C
      WE=0.D0
      DO 80 I=1,NM
 80   WE=WE+GE(I)*Q(I)
C
      WT=(W(1)+W(2)+W(3)+W(4)+W(5)+W(6))/2.D0-WE
C     WRITE(2,100) (I,W(I),I=1,6),WE,WT
C 100 FORMAT(3(' W('I1')='G12.3),/,3(' W('I1')='G12.3),
C    &   /12X' WE='G12.3' WT='G12.3)
      RETURN
      END
C*************************************************************
C
C       CALCULATION OF THE GRADIENT OF THE ENERGY
C
      SUBROUTINE GRADIENT(Q,Q0,GE,ISYM,GRAD)
      IMPLICIT REAL*8 (A-H,O-Z)
      COMMON /MATRICES/ A(3,3),B(3,3),D(3,3)
      COMMON /NMODES/ NU,NV,NW,KU,LU,KV,LV,KW,LW,NM
      COMMON /STIFF/ XKEL(75,75),XKS(75,36,36),XKQ(82251),
     -   XKBL(75,36),XKBNL(36,36,36),XKF(36,36),XKT(36,36)
      COMMON /MODES/ XMODE(366),IMODE(366,2),SHAPE(45,21),
```

```
     -    XG(21),WEIGHT(21),NP,XL,YL
          REAL*8 Q(111),Q0(36),GR(6,111),GRAD(111),GE(111)
C
          N1=NU+NV
          N3=N1+1
          DO 5 I=1,NM
          DO 5 J=1,6
 5        GR(J,I)=0.D0
          DO 10 I=1,N1
          DO 10 J=I,N1
            GR(1,I)=GR(1,I)+XKEL(I,J)*Q(J)
 10       GR(1,J)=GR(1,J)+XKEL(I,J)*Q(I)
          DO 20 I=1,N1
          DO 20 J=1,NW
          DO 20 K=J,NW
            J1=J+N1
            K1=K+N1
            GR(2,I)=GR(2,I)+XKS(I,J,K)*Q(J1)*Q(K1)
            GR(2,I)=GR(2,I)+XKS(I,J,K)*Q0(J)*Q(K1)*2.D0
            GR(2,J1)=GR(2,J1)+XKS(I,J,K)*Q(I)*Q(K1)
            GR(2,K1)=GR(2,K1)+XKS(I,J,K)*Q(I)*Q0(J)*2.D0
 20       GR(2,K1)=GR(2,K1)+XKS(I,J,K)*Q(I)*Q(J1)
C
          IND=0
          DO 30 I=N3,NM
          DO 30 J=I,NM
          DO 30 K=J,NM
          DO 30 L=K,NM
            IND=IND+1
            GR(3,J)=GR(3,J)+XKQ(IND)*Q0(I-N1)*Q(K)*Q(L)*4.D0
            GR(3,K)=GR(3,K)+XKQ(IND)*(Q0(I-N1)*Q(J)*Q(L)
     -                *4.D0+Q0(I-N1)*Q0(J-N1)*Q(L)*4.D0)
            GR(3,L)=GR(3,L)+XKQ(IND)*(Q0(I-N1)*Q(K)*Q(J)
     -                *4.D0+Q0(I-N1)*Q0(J-N1)*Q(K)*4.D0)
            GR(3,I)=GR(3,I)+XKQ(IND)*Q(J)*Q(K)*Q(L)
            GR(3,J)=GR(3,J)+XKQ(IND)*Q(I)*Q(K)*Q(L)
            GR(3,K)=GR(3,K)+XKQ(IND)*Q(I)*Q(J)*Q(L)
 30       GR(3,L)=GR(3,L)+XKQ(IND)*Q(I)*Q(J)*Q(K)
          IF (ISYM.NE.1) THEN
            DO 40 I=1,N1
            DO 40 J=1,NW
              J1=J+N1
              GR(4,I)=GR(4,I)-XKBL(I,J)*Q(J1)
 40         GR(4,J1)=GR(4,J1)-XKBL(I,J)*Q(I)
            DO 60 I=1,NW
            DO 60 J=I,NW
            DO 60 K=J,NW
              I1=I+N1
              J1=J+N1
              K1=K+N1
              GR(5,J1)=GR(5,J1)-XKBNL(I,J,K)*Q0(I)*Q(K1)*2.D0
              GR(5,K1)=GR(5,K1)-XKBNL(I,J,K)*Q0(I)*Q(J1)*2.D0
              GR(5,I1)=GR(5,I1)-XKBNL(I,J,K)*Q(J1)*Q(K1)
```

```
            GR(5,J1)=GR(5,J1)-XKBNL(I,J,K)*Q(I1)*Q(K1)
 60       GR(5,K1)=GR(5,K1)-XKBNL(I,J,K)*Q(I1)*Q(J1)
         ENDIF
         DO 70 I=1,NW
         DO 70 J=I,NW
           J1=J+N1
           I1=I+N1
           GR(6,I1)=GR(6,I1)+XKF(I,J)*Q(J1)
 70      GR(6,J1)=GR(6,J1)+XKF(I,J)*Q(I1)
C
C         EXTERNAL LOADS
C
         DO 80 I=1,NM
           GRAD(I)=-GE(I)
           DO 80 J=1,6
 80      GRAD(I)=GRAD(I)+GR(J,I)/2.D0
         RETURN
         END
C*************************************************************
C
C         CALCULATION OF HESSIAN MATRIX
C
         SUBROUTINE HESSIEN (Q,Q0,HES,ISYM,LIN)
         IMPLICIT REAL*8 (A-H,O-Z)
         COMMON /MATRICES/ A(3,3),B(3,3),D(3,3)
         COMMON /NMODES/ NU,NV,NW,KU,LU,KV,LV,KW,LW,NM
         COMMON /STIFF/ XKEL(75,75),XKS(75,36,36),XKQ(82251),
     -     XKBL(75,36),XKBNL(36,36,36),XKF(36,36),XKT(36,36)
         COMMON /MODES/ XMODE(366),IMODE(366,2),SHAPE(45,21),
     -     XG(21),WEIGHT(21),NP,XL,YL
         REAL*8 Q(111),Q0(36),HES(111,111)
C
         N1=NU+NV
         N3=N1+1
         DO 5 I=1,NM
         DO 5 J=1,NM
 5         HES(I,J)=0.D0
         DO 10 I=1,N1
         DO 10 J=I,N1
           HES(I,J)=HES(I,J)+XKEL(I,J)
 10      HES(J,I)=HES(J,I)+XKEL(I,J)
         IF (LIN.NE.1) THEN
           DO 20 I=1,N1
           DO 20 J=1,NW
           DO 20 K=J,NW
             J1=J+N1
             K1=K+N1
             HES(I,J1)=HES(I,J1)+XKS(I,J,K)*Q(K1)
             HES(J1,I)=HES(J1,I)+XKS(I,J,K)*Q(K1)
             HES(I,K1)=HES(I,K1)+XKS(I,J,K)*(Q(J1)+Q0(J)*2.D0)
             HES(K1,I)=HES(K1,I)+XKS(I,J,K)*(Q(J1)+Q0(J)*2.D0)
             HES(J1,K1)=HES(J1,K1)+XKS(I,J,K)*Q(I)
 20        HES(K1,J1)=HES(K1,J1)+XKS(I,J,K)*Q(I)
```

```
          IND=0
          DO 30 I=N3,NM
          DO 30 J=I,NM
          DO 30 K=J,NM
          DO 30 L=K,NM
            IND=IND+1
            I1=I-N1
            J1=J-N1
            K1=K-N1
            L1=L-N1
            HES(I,J)=HES(I,J)+XKQ(IND)*Q(K)*Q(L)
            HES(I,K)=HES(I,K)+XKQ(IND)*Q(J)*Q(L)
            HES(I,L)=HES(I,L)+XKQ(IND)*Q(J)*Q(K)
            HES(J,K)=HES(J,K)+XKQ(IND)*(Q0(I1)*4.D0+Q(I))*Q(L)
            HES(J,L)=HES(J,L)+XKQ(IND)*(Q0(I1)*4.D0+Q(I))*Q(K)
            HES(K,L)=HES(K,L)+XKQ(IND)*(Q0(I1)*4.D0
     &                 *(Q(J)+Q0(J1))+Q(I)*Q(J))
            HES(J,I)=HES(J,I)+XKQ(IND)*Q(K)*Q(L)
            HES(K,I)=HES(K,I)+XKQ(IND)*Q(J)*Q(L)
            HES(L,I)=HES(L,I)+XKQ(IND)*Q(J)*Q(K)
            HES(K,J)=HES(K,J)+XKQ(IND)*(Q0(I1)*4.D0+Q(I))*Q(L)
            HES(L,J)=HES(L,J)+XKQ(IND)*(Q0(I1)*4.D0+Q(I))*Q(K)
            HES(L,K)=HES(L,K)+XKQ(IND)*(Q0(I1)*4.D0
     &                 *(Q(J)+Q0(J1))+Q(I)*Q(J))
30        CONTINUE
        ENDIF
        IF (ISYM.NE.1) THEN
          DO 40 I=1,N1
          DO 40 J=1,NW
            J1=J+N1
            HES(I,J1)=HES(I,J1)-XKBL(I,J)
40        HES(J1,I)=HES(J1,I)-XKBL(I,J)
          IF (LIN.NE.1) THEN
            DO 60 I=1,NW
            DO 60 J=I,NW
            DO 60 K=J,NW
              I1=I+N1
              J1=J+N1
              K1=K+N1
              HES(I1,J1)=HES(I1,J1)-XKBNL(I,J,K)*Q(K1)
              HES(I1,K1)=HES(I1,K1)-XKBNL(I,J,K)*Q(J1)
              HES(J1,I1)=HES(J1,I1)-XKBNL(I,J,K)*Q(K1)
              HES(J1,K1)=HES(J1,K1)-XKBNL(I,J,K)*(Q0(I)+Q(I1))
              HES(K1,I1)=HES(K1,I1)-XKBNL(I,J,K)*Q(J1)
60          HES(K1,J1)=HES(K1,J1)-XKBNL(I,J,K)*(Q(I1)+Q0(I))
          ENDIF
        ENDIF
        DO 70 I=1,NW
        DO 70 J=I,NW
          I1=I+N1
          J1=J+N1
          HES(I1,J1)=HES(I1,J1)+XKF(I,J)
70      HES(J1,I1)=HES(J1,I1)+XKF(I,J)
```

```
      DO 90 I=1,NM
      DO 90 J=1,NM
 90   HES(I,J)=HES(I,J)/2.D0
      RETURN
      END
C*************************************************************
C
C       DISPLACEMENT MODES CREATION
C
      SUBROUTINE CRMODE(IBCUV,IBCW,ISYM)
C
C       DISPLACEMENT MODES DERIVATIVES ARE DEFINED AND
C                 STORED IN THE FOLLOWING ORDER:
C   DU/DX, DV/DY, DU/DY, DV/DX, DW/DX, DW/DY, D2W/DX2,
C                 D2W/DY2, 2*D2W/DXDY, W
C
C*************************************************************
      IMPLICIT REAL*8 (A-H,O-Z)
      COMMON /MODES/ XMODE(366),IMODE(366,2),SHAPE(45,21),
     -   XG(21),WEIGHT(21),NP,XL,YL
      COMMON /MATRICES/ A(3,3),B(3,3),D(3,3)
      COMMON /NMODES/ NU,NV,NW,KU,LU,KV,LV,KW,LW,NM
      COMMON /STIFF/ XKEL(75,75),XKS(75,36,36),XKQ(82251),
     -   XKBL(75,36),XKBNL(36,36,36),XKF(36,36),XKT(36,36)
      REAL*8 AL(6),GA(6)
      PARAMETER (PI=3.14159265)
C
C       TX(X,K) =  COS((K-1)*X) - COS((K+1)*X)
C       TX2(X,K)= -((K-1)*PI)**2*COS((K-1)*X)
C     &                   +((K+1)*PI)**2*COS((K+1)*X)
C
      FX(X,K)=COSH(X)-COS(X)-GA(K)*(SINH(X)-SIN(X))
      FX1(X,K)=SINH(X)+SIN(X)-GA(K)*(COSH(X)-COS(X))
      FX2(X,K)=COSH(X)+COS(X)-GA(K)*(SINH(X)+SIN(X))
C
      NU=KU*LU+1
      NV=KV*LV+2
      NW=KW*LW
      IS=1
      IF (IBCUV.GT.3) THEN
        IBCUV=IBCUV-3
        NV=NV-1
        IS=0
      END IF
      IF (IBCUV.EQ.2) THEN
        NV=NV+4
        NU=NU+4
      END IF
      IF (IBCUV.EQ.3) THEN
        NV=NV+4
        NU=NU+4
      END IF
      IF (ISYM.EQ.0) THEN
```

```
            IF ((IBCW.EQ.2).OR.(IBCW.EQ.4)) THEN
              KK=KW
              LL=LW
              IF (KK.GT.4) KK=4
              IF (LL.GT.1) LL=1
              KL=KK*LL
              NU=NU+KL
              NV=NV+KL
            ENDIF
          END IF
          NM=NU+NV+NW
          WRITE(10,5) NU,NV,NW,NM
    5     FORMAT(' NU ='I2,3X'NV ='I2,3X'NW ='I2,5X'=>  NM='I3/)
          AL(1)=  4.7300407448627
          AL(2)=  7.8532046240958
          AL(3)= 10.995607838002
          AL(4)= 14.137165491257
          AL(5)= 17.278759657400
          AL(6)= 20.420352245626
          GA(1)=  0.98250221457624
          GA(2)=  1.00077731190727
          GA(3)=  0.99996645012541
          GA(4)=  1.00000144989766
          GA(5)=  0.99999993734438
          GA(6)=  1.00000000270759
C
C          CREATE THE SHAPE FUNCTIONS LIBRARY
C
          DO 10 I=1,NP
            X=PI*XG(I)
            IND=0
            ICOS=IND+1
            DO 11 K=0,6
              IND=IND+1
 11         SHAPE(IND,I)=COS(K*X)
            ISIN=IND+1
            DO 12 K=0,6
              IND=IND+1
 12         SHAPE(IND,I)=SIN(K*X)
            IFX=IND
            DO 13 K=1,6
              IND=IND+1
              X=XG(I)*AL(K)
 13         SHAPE(IND,I)=FX(X,K)
            IFX1=IND
            DO 14 K=1,6
              IND=IND+1
              X=XG(I)*AL(K)
 14         SHAPE(IND,I)=FX1(X,K)
            IFX2=IND
            DO 15 K=1,6
              IND=IND+1
              X=XG(I)*AL(K)
```

```
 15         SHAPE(IND,I)=FX2(X,K)
            FF=XG(I)-.5
            IND=IND+1
            ILIN=IND
            SHAPE(IND,I)=FF
            IND=IND+1
            IQUAD=IND
            SHAPE(IND,I)=FF*FF
            IND=IND+1
            ICUB=IND
            SHAPE(IND,I)=FF*FF*FF
            X=PI*XG(I)
            ISP=IND
            DO 16 K=1,4
              IND=IND+1
 16         SHAPE(IND,I)=COS(K*X)-1.+(1.-COS(K*PI))*XG(I)
            ISP1=IND
            DO 17 K=1,4
              IND=IND+1
 17         SHAPE(IND,I)= -K*PI*SIN(K*X)+1.-COS(K*PI)
 10       CONTINUE
C
C          REFERENCE INDEX:
C          ICOS, ISIN, IFX, IFX1, IFX2, ILIN, IQUAD, ICUB,
C          ISP, ISP1
c          WRITE(6,*) ' REFERENCE INDEX:'
c          WRITE(6,*) ICOS,ISIN,IFX,IFX1,IFX2
c          WRITE(6,*) ILIN,IQUAD,ICUB,ISP,ISP1
c          WRITE(6,*) ' SHAPE LIBRARY:'
c          DO 20 I=1,45
c 20         WRITE(6,25) I,(SHAPE(I,K),K=1,21,5)
c  25      FORMAT(I3,5F12.4)
C*************************************************************
C
C          CREATE DISPLACEMENTS MODES
C
C          DU/DX
C
           IND=1
           XMODE(IND)=1.D0/XL
           IMODE(IND,1)=1
           IMODE(IND,2)=1
           DO 30 K=1,KU
             JJ=JMOD(K,2)
             JK=2*(LU-1)+JJ
             DO 30 L=JJ,JK,2
               IND=IND+1
               XMODE(IND)=K*PI/XL
               IMODE(IND,1)=ICOS+K
               IMODE(IND,2)=ICOS+L
 30        CONTINUE
           IF (IBCUV.EQ.2) THEN
             DO 33 K=1,4
```

```
            IND=IND+1
            IMODE(IND,1)=ICOS+K
            IMODE(IND,2)=IQUAD
 33       XMODE(IND)=K*PI/XL
          END IF
          IF (IBCUV.EQ.3) THEN
            DO 35 L=1,4
              IND=IND+1
              IMODE(IND,1)=1
              IMODE(IND,2)=ICOS+L
 35         XMODE(IND)=1.D0/XL
          END IF
          IF (ISYM.EQ.0) THEN
            DO 36 K=1,KK
            DO 36 L=1,LL
              IND=IND+1
              XMODE(IND)=1.D0/XL
              IF (IBCW.EQ.1) THEN
                IMODE(IND,1)=ISP1+K
                IMODE(IND,2)=ISIN+L
              END IF
              IF (IBCW.EQ.2) THEN
                XMODE(IND)=AL(K)/XL
                IMODE(IND,1)=IFX2+K
                IMODE(IND,2)=ISIN+L
              END IF
              IF (IBCW.EQ.4) THEN
                XMODE(IND)=AL(K)/XL
                IMODE(IND,1)=IFX2+K
                IMODE(IND,2)=IFX+L
              END IF
 36         CONTINUE
          END IF
          IF(IND.NE.NU) GO TO 999
C
C          DV/DY
C
          IND=IND+1
          XMODE(IND)=1.D0/YL
          IMODE(IND,1)=1
          IMODE(IND,2)=1
          IF (IS.EQ.1) THEN
            IND=IND+1
            XMODE(IND)=0.D0
            IMODE(IND,1)=1
            IMODE(IND,2)=1
          END IF
          DO 40 L=1,LV
            JJ=JMOD(L,2)
            JK=2*(KV-1)+JJ
            DO 40 K=JJ,JK,2
              IND=IND+1
              XMODE(IND)=L*PI/YL
```

```
            IMODE(IND,1)=ICOS+K
 40       IMODE(IND,2)=ICOS+L
         IF (IBCUV.EQ.2) THEN
           DO 43 K=1,4
             IND=IND+1
             IMODE(IND,1)=ICOS+K
             IMODE(IND,2)=IQUAD
 43        XMODE(IND)=3.D0/YL
         END IF
         IF (IBCUV.EQ.3) THEN
           DO 45 K=1,4
             IND=IND+1
             IMODE(IND,1)=ICOS+K
             IMODE(IND,2)=1
 45        XMODE(IND)=1.D0/YL
         END IF
         IF (ISYM.EQ.0) THEN
           DO 46 K=1,KK
           DO 46 L=1,LL
             IND=IND+1
             XMODE(IND)=1.D0/YL
             IF (IBCW.EQ.1) THEN
               IMODE(IND,1)=ISIN+K
               IMODE(IND,2)=ISP1+L
             END IF
             IF (IBCW.EQ.2) THEN
               IMODE(IND,1)=IFX+K
               IMODE(IND,2)=ISP1+L
             END IF
             IF (IBCW.EQ.4) THEN
               XMODE(IND)=AL(K)/YL
               IMODE(IND,1)=IFX+K
               IMODE(IND,2)=IFX2+L
             END IF
 46        CONTINUE
         END IF
         IF(IND.NE.NU+NV) GO TO 999
C
C         DU/DY
C
         IND=IND+1
         XMODE(IND)=0.D0
         IMODE(IND,1)=1
         IMODE(IND,2)=1
         DO 50 K=1,KU
           JJ=JMOD(K,2)
           JK=2*(LU-1)+JJ
           DO 50 L=JJ,JK,2
             IND=IND+1
             XMODE(IND)=-L*PI/YL
             IMODE(IND,1)=ISIN+K
             IMODE(IND,2)=ISIN+L
 50        CONTINUE
```

```
      IF (IBCUV.EQ.2) THEN
        DO 53 K=1,4
          IND=IND+1
          IMODE(IND,1)=ISIN+K
          IMODE(IND,2)=ILIN
53      XMODE(IND)=2.D0/YL
      END IF
      IF (IBCUV.EQ.3) THEN
        DO 55 L=1,4
          IND=IND+1
          IMODE(IND,1)=ILIN
          IMODE(IND,2)=ISIN+L
55      XMODE(IND)=-L*PI/YL
      END IF
      IF (ISYM.EQ.0) THEN
        DO 56 K=1,KK
        DO 56 L=1,LL
          IND=IND+1
          IF (IBCW.EQ.1) THEN
            XMODE(IND)= L*PI/YL
            IMODE(IND,1)= ISP+K
            IMODE(IND,2)= ICOS+L
          END IF
          IF (IBCW.EQ.2) THEN
            XMODE(IND)=L*PI/YL
            IMODE(IND,1)=IFX1+K
            IMODE(IND,2)=ICOS+L
          END IF
          IF (IBCW.EQ.4) THEN
            XMODE(IND)=AL(K)/YL
            IMODE(IND,1)=IFX1+K
            IMODE(IND,2)=IFX1+L
          END IF
56      CONTINUE
      END IF
      IF(IND.NE.2*NU+NV) GO TO 999
C
C      DV/DX
C
      IND=IND+1
      XMODE(IND)=0.D0
      IMODE(IND,1)=1
      IMODE(IND,2)=1
      IF (IS.EQ.1) THEN
        IND=IND+1
        XMODE(IND)=1.D0/XL
        IMODE(IND,1)=1
        IMODE(IND,2)=1
      END IF
      DO 60 L=1,LV
        JJ=JMOD(L,2)
        JK=2*(KV-1)+JJ
        DO 60 K=JJ,JK,2
```

```
            IND=IND+1
            XMODE(IND)=-K*PI/XL
            IMODE(IND,1)=ISIN+K
            IMODE(IND,2)=ISIN+L
60        CONTINUE
        IF (IBCUV.EQ.2) THEN
          DO 63 K=1,4
            IND=IND+1
            IMODE(IND,1)=ISIN+K
            IMODE(IND,2)=ICUB
63        XMODE(IND)=-K*PI/XL
        END IF
        IF (IBCUV.EQ.3) THEN
          DO 65 K=1,4
            IND=IND+1
            IMODE(IND,1)=ISIN+K
            IMODE(IND,2)=ILIN
65        XMODE(IND)=-K*PI/XL
        END IF
        IF (ISYM.EQ.0) THEN
          DO 66 K=1,KK
          DO 66 L=1,LL
            IND=IND+1
            IF (IBCW.EQ.1) THEN
              XMODE(IND)=K*PI/XL
              IMODE(IND,1)=ICOS+K
              IMODE(IND,2)=ISP+L
            END IF
            IF (IBCW.EQ.2) THEN
              XMODE(IND)=AL(K)/XL
              IMODE(IND,1)=IFX1+K
              IMODE(IND,2)=ISP+L
            END IF
            IF (IBCW.EQ.4) THEN
              XMODE(IND)=AL(K)/XL
              IMODE(IND,1)=IFX1+K
              IMODE(IND,2)=IFX1+L
            END IF
66        CONTINUE
        END IF
        IF (IND.NE.2*(NU+NV)) GO TO 999
        IF (IBCW.EQ.3) GO TO 111
        IF (IBCW-2) 68,111,211
C*************************************************************
C                                                            ***
C                    SIMPLY-SUPPORTED                        ***
C                                                            ***
C*************************************************************
C
C         DW/DX
C
  68    DO 70 K=1,KW
        DO 70 L=1,LW
```

```
            IND=IND+1
            IMODE(IND,1)=ICOS+K
            IMODE(IND,2)=ISIN+L
 70       XMODE(IND)=K*PI/XL
C
C          DW/DY
C
          DO 80 K=1,KW
          DO 80 L=1,LW
            IND=IND+1
            IMODE(IND,1)=ISIN+K
            IMODE(IND,2)=ICOS+L
 80       XMODE(IND)=L*PI/YL
C
C          D2W/DX2
C
          DO 90 K=1,KW
          DO 90 L=1,LW
            IND=IND+1
            IMODE(IND,1)=ISIN+K
            IMODE(IND,2)=ISIN+L
 90       XMODE(IND)=-(K*PI/XL)**2
C
C          D2W/DY2
C
          DO 100 K=1,KW
          DO 100 L=1,LW
            IND=IND+1
            IMODE(IND,1)=ISIN+K
            IMODE(IND,2)=ISIN+L
 100      XMODE(IND)=-(L*PI/YL)**2
C
C          2*D2W/DXDY
C
          DO 110 K=1,KW
          DO 110 L=1,LW
            IND=IND+1
            IMODE(IND,1)=ICOS+K
            IMODE(IND,2)=ICOS+L
 110      XMODE(IND)=2.D0*K*L*PI*PI/XL/YL
C
C          W
C
          DO 120 K=1,KW
          DO 120 L=1,LW
            IND=IND+1
            IMODE(IND,1)=ISIN+K
            IMODE(IND,2)=ISIN+L
 120      XMODE(IND)=1.D0
C
C         WRITE(6,*) ' IBCW = 1',IND,IBCUV,IBCW,ISYM
          RETURN
C*************************************************************
```

```
C                                                                      ***
C                  CLAMPED SIMPLY-SUPPORTED                            ***
C                                                                      ***
C**********************************************************************
C
C         DW/DX
C
 111     DO 170 K=1,KW
         DO 170 L=1,LW
           IND=IND+1
           IMODE(IND,1)=IFX1+K
           IMODE(IND,2)=ISIN+L
 170     XMODE(IND)=AL(K)/XL
C
C         DW/DY
C
         DO 180 K=1,KW
         DO 180 L=1,LW
           IND=IND+1
           IMODE(IND,1)=IFX+K
           IMODE(IND,2)=ICOS+L
 180     XMODE(IND)=L*PI/YL
C
C         D2W/DX2
C
         DO 190 K=1,KW
         DO 190 L=1,LW
           IND=IND+1
           IMODE(IND,1)=IFX2+K
           IMODE(IND,2)=ISIN+L
 190     XMODE(IND)=(AL(K)/XL)**2
C
C         D2W/DY2
C
         DO 200 K=1,KW
         DO 200 L=1,LW
           IND=IND+1
           IMODE(IND,1)=IFX+K
           IMODE(IND,2)=ISIN+L
 200     XMODE(IND)=-(L*PI/YL)**2
C
C         2*D2W/DXDY
C
         DO 210 K=1,KW
         DO 210 L=1,LW
           IND=IND+1
           IMODE(IND,1)=IFX1+K
           IMODE(IND,2)=ICOS+L
 210     XMODE(IND)=2.D0*AL(K)*L*PI/XL/YL
C
C         W
C
         DO 220 K=1,KW
```

```
          DO 220 L=1,LW
            IND=IND+1
            IMODE(IND,1)=IFX+K
            IMODE(IND,2)=ISIN+L
 220      XMODE(IND)=1.D0
C         WRITE(6,*) ' IBCW = 2 OR 3',IND,IBCUV,IBCW,ISYM
          IF(IND.NE.2*(NU+NV)+6*NW) GO TO 1000
          RETURN
C*****************************************************************
C                                                                ***
C                          ALL CLAMPED                           ***
C                                                                ***
C*****************************************************************
C
C          DW/DX
C
 211      DO 270 K=1,KW
          DO 270 L=1,LW
            IND=IND+1
            IMODE(IND,1)=IFX1+K
            IMODE(IND,2)=IFX+L
 270      XMODE(IND)=AL(K)/XL
C
C          DW/DY
C
          DO 280 K=1,KW
          DO 280 L=1,LW
            IND=IND+1
            IMODE(IND,1)=IFX+K
            IMODE(IND,2)=IFX1+L
 280      XMODE(IND)=AL(L)/YL
C
C          D2W/DX2
C
          DO 290 K=1,KW
          DO 290 L=1,LW
            IND=IND+1
            IMODE(IND,1)=IFX2+K
            IMODE(IND,2)=IFX+L
 290      XMODE(IND)=(AL(K)/XL)**2
C
C          D2W/DY2
C
          DO 300 K=1,KW
          DO 300 L=1,LW
            IND=IND+1
            IMODE(IND,1)=IFX+K
            IMODE(IND,2)=IFX2+L
 300      XMODE(IND)=(AL(L)/YL)**2
C
C          2*D2W/DXDY
C
          DO 310 K=1,KW
```

```
          DO 310 L=1,LW
            IND=IND+1
            IMODE(IND,1)=IFX1+K
            IMODE(IND,2)=IFX1+L
 310      XMODE(IND)=2.D0*AL(K)*AL(L)/XL/YL
C
C          W
C
          DO 320 K=1,KW
          DO 320 L=1,LW
            IND=IND+1
            IMODE(IND,1)=IFX+K
            IMODE(IND,2)=IFX+L
 320      XMODE(IND)=1.D0
C
C         WRITE(6,*) ' IBCW >= 4',IND,IBCUV,IBCW,ISYM
          IF(IND.NE.2*(NU+NV)+6*NW) GO TO 1000
          RETURN
 999      WRITE(10,1010) NU,NV,IND
1000      WRITE(10,1020) NU,NV,NW,IND
1010      FORMAT(' ERROR IN U/V MODES: NU='I3' NV='I3
     1           ' IND='I3/)
1020      FORMAT(' ERROR IN W MODES: NU='I3' NV='I3
     1           ' NW='I3' IND='I3/)
          STOP
          END
C*************************************************************
C          MINIMUM SEARCHING IN S DIRECTION
C
          SUBROUTINE LINESEARCH(Q,Q0,GE,S,ALPHA,ISYM,W0)
          IMPLICIT REAL*8 (A-H,O-Z)
          COMMON /MATRICES/ A(3,3),B(3,3),D(3,3)
          COMMON /NMODES/ NU,NV,NW,KU,LU,KV,LV,KW,LW,NM
          COMMON /STIFF/ XKEL(75,75),XKS(75,36,36),XKQ(82251),
     -      XKBL(75,36),XKBNL(36,36,36),XKF(36,36),XKT(36,36)
          COMMON /MODES/ XMODE(366),IMODE(366,2),SHAPE(45,21),
     -      XG(21),WEIGHT(21),NP,XL,YL
          REAL*8 Q(111),S(111),W1(4),R(111),Q0(36),W(6),
     -      GE(111),AA(4)
C
C          CALCULATION OF ENERGY AT THE CURRENT POINT
C
          W0=0.D0
          CALL ENERGIE(Q,Q0,GE,W0,ISYM)
          ZS=0.D0
          ZQ=0.D0
          DO 5 I=1,NM
            ZQ=ZQ+ABS(Q(I))
 5        ZS=ZS+ABS(S(I))
          IF (ZQ.NE.0.D0) ZS=ZS/ZQ
C
C          IF NEAR MINIMUM THEN UNIT STEP
C
```

```
          IF (ZS.LE.1.E-2) THEN
            ALPHA=-1.D0
            GO TO 100
          ENDIF
C
C          F(Q) IS CALCULATED FOR ALPHA=-2,-1,1,2
C
          AA(1)=2.D0
          AA(2)=1.D0
          AA(3)=-1.D0
          AA(4)=-2.D0
           DO 20 K=1,4
            ALPHA=AA(K)
            DO 10 I=1,NM
 10         R(I)=Q(I)+ALPHA*S(I)
            CALL ENERGIE(R,Q0,GE,WT,ISYM)
 20       W1(K)=WT-W0
          CALL COEF(W1,A1,A2,A3,A4)
C
C          COEFFICIENT OF F'(Q)
C
          A1=4.D0*A1
          A2=3.D0*A2
          A3=2.D0*A3
          CALL ROOTS(A1,A2,A3,A4,ALPHA)
C
C          DISPLACEMENTS ARE INCREMENTED
C
 100      DO 30 I=1,NM
 30       Q(I)=Q(I)+ALPHA*S(I)
          RETURN
          END
C
C          POLYNOMIAL COEFFICIENTS ARE CALCULATED
C
          SUBROUTINE COEF(W,A1,A2,A3,A4)
          REAL*8 W(4)
          A4=-W(1)/12.D0+2.D0*W(2)/3.D0-2.D0*W(3)/3.D0
     1       +W(4)/12.D0
          A3=-W(1)/24.D0+2.D0*W(2)/3.D0+2.D0*W(3)/3.D0
     1       -W(4)/24.D0
          A2=W(1)/12.D0-W(2)/6.D0+W(3)/6.D0-W(4)/12.D0
          A1=W(1)/24.D0-W(2)/6.D0-W(3)/6.D0+W(4)/24.D0
          RETURN
          END
C
C          ROOTS AND STEP ALPHA ARE CALCULATED
C
          SUBROUTINE ROOTS(A1,A2,A3,A4,ALPHA)
          REAL*8 X(3),W(3)
          ALMAX=20.D0
          IMAX=100
          IT=0
```

```
      ZA=ABS(A1)+ABS(A2)+ABS(A3)+ABS(A4)
      A1=A1/ZA
      A2=A2/ZA
      A3=A3/ZA
      A4=A4/ZA
      XX=-20.D0
C
C      A FIRST ROOT IS FOUND
 20   DX=(A1*XX*XX*XX+A2*XX*XX+A3*XX+A4)
      DXD=3.D0*A1*XX*XX+2.D0*A2*XX+A3
      IT=IT+1
      IF (ABS(DXD).LE.1.E-9) THEN
        XX=1.05D0*XX
        GO TO 20
      ENDIF
      XX=XX-DX/DXD
      E=ABS(DX)
      F=ABS(DX/DXD)
C
C      IF NOT FOUND THEN ALPHA=1
C
      IF (IT.GE.IMAX) THEN
        ALPHA=-1.D0
        RETURN
      ENDIF
      IF ((F.GT.1.E-3).AND.(E.GT.1.E-3)) GO TO 20
C
C      THE POLYNOMIAL IS DIVIDED
C      AND THE NEXT TWO ROOTS ARE FOUND
C
      X(1)=XX
      A=A1
      B=A2+A*X(1)
      C=A3+B*X(1)
      IF (A.EQ.0.D0) THEN
        X(2)=-C/B
        X(3)=-C/B
        GO TO 40
      ENDIF
      DET=B*B-4.D0*A*C
      IF (DET.GE.0.D0) THEN
        X(2)=(-B-SQRT(DET))/2.D0/A
        X(3)=(-B+SQRT(DET))/2.D0/A
        GO TO 40
      ENDIF
      ALPHA=X(1)
C
C      IF THE ROOT DOES NOT MINIMIZE F(Q) THEN ALPHA=1
C
      IF (ABS(ALPHA).GT.ALMAX) ALPHA=-1.D0
      DW=(A1*XX*XX*XX*XX/4.D0+A2*XX*XX*XX/3.D0
     &    +A3*XX*XX/2.D0+A4*XX)*ZA
      IF (DW.GT.0.D0) ALPHA=-.1D0
```

```
      RETURN
 40   XMIN=1.D0+30.D0
C
C      THE DIFFERENT ROOTS ARE COMPARED
C
      ALPHA=X(1)
      DO 50 I=1,3
        IF (ABS(X(I)).GT.ALMAX) X(I)=ALMAX*X(I)/ABS(X(I))
        XX=X(I)
        W(I)=(A1*XX*XX*XX*XX/4.D0+A2*XX*XX*XX/3.D0
     &        +A3*XX*XX/2.D0+A4*XX)*ZA
        IF (W(I).LE.XMIN) THEN
          XMIN=W(I)
          ALPHA=X(I)
        ENDIF
 50   CONTINUE
      RETURN
      END
C*************************************************************
C
C                INTEGRATION WEIGHTS MATRIX
C
C     INTEGRATION POINTS AND WEIGHTS ARE CREATED
C     WITH SIMPSON'S RULE
C
      SUBROUTINE CRWT
      IMPLICIT REAL*8 (A-H,O-Z)
      COMMON /MODES/ XMODE(366),IMODE(366,2),SHAPE(45,21),
     -   XG(21),WEIGHT(21),NP,XL,YL
      IF (JMOD(NP,2).NE.1) NP=NP+1
      H=1.D0/DFLOAT(NP-1)
      DO 10 I=1,NP
 10   XG(I)=H*DFLOAT(I-1)
      H=H*SQRT(XL*YL)/3.D0
      WEIGHT(1)=H
      DO 20 I=2,NP,2
        WEIGHT(I)=4.D0*H
 20   WEIGHT(I+1)=2.D0*H
      WEIGHT(NP)=H
      RETURN
      END
C*************************************************************
C
C       CREATION OF A,B,D MATRICES
C
      SUBROUTINE ABD(IBCUV,IBCW,ILIN,ISYM,ITEST,ITRAN,SPEC)
      IMPLICIT REAL*8 (A-H,O-Z)
      CHARACTER*30 SPEC
      COMMON /MATRICES/ A(3,3),B(3,3),D(3,3)
      COMMON /NMODES/ NU,NV,NW,KU,LU,KV,LV,KW,LW,NM
      COMMON /STIFF/ XKEL(75,75),XKS(75,36,36),XKQ(82251),
     -   XKBL(75,36),XKBNL(36,36,36),XKF(36,36),XKT(36,36)
      COMMON /MODES/ XMODE(366),IMODE(366,2),SHAPE(45,21),
```

```
     -    XG(21),WEIGHT(21),NP,XL,YL
          COMMON /STRATES/ NC,TH(9),EP(9),EL(9),ET(9),XNULT(9),
     -    GLT(9),T,ELT,XT(9),XC(9),YT(9),YC(9),T6(9),XA,YA,
     -    XB,YB,XD
          DIMENSION H(3,3)
          PARAMETER (PI=3.141592654)
C
C          DATA ARE READ ON UNIT 1 AND COPIED ON UNIT 10
C
          WRITE(10,105)
 105      FORMAT(1H ,75(1H=)/1H ,T15,'POSTBUCKLING BEHAVIOR OF
     -    PLATES (V 7.2)'/1H ,75(1H=))
          READ (1,*) ISYM,NP,IBCUV,IBCW,ITRAN
          WRITE (10,100) ISYM,ITRAN,NP,IBCUV,IBCW
 100      FORMAT(' Coupling Terms Used (0=YES):',I2,T40,
     1    'Transducers Included (1=Yes):'I2//1H ,
     2    'Number of Integration Points:',I3,T40,
     2    'Boundary Conditions:',I2,' &',I2/)
          READ (1,*) ILIN,ITEST,XL,YL
          WRITE (10,110) XL,YL
 110      FORMAT(' Plate Dimensions: ',F8.2,' BY ',F8.2/)
          IF (ILIN.EQ.1) THEN
          WRITE(10,*) 'LINEAR SOLUTION'
          XA=0.D0
          YA=YL
          XB=XL
          YB=YL
          XD=XL
          READ (1,115) SPEC
          READ (1,*) NC
 115      FORMAT(A30)
          WRITE (10,120) NC, SPEC
 120      FORMAT (' Number of Layers:',I3,T40'Laminate ID =
     &    'A30/,/1H ,' THICKNESS',T16,'EL',
     &    T30,'ET',T43,'NU',T57,'G',T67,'THETA'/)
          DO 10 K=1,NC
            READ (1,*) EP(K),EL(K),ET(K),XNULT(K),GLT(K),TH(K)
            WRITE (10,130) EP(K),EL(K),ET(K),XNULT(K),
     1                     GLT(K),TH(K)
            READ(1,*) XT(K),XC(K),YT(K),YC(K),T6(K)
 10       TH(K)=TH(K)*PI/180.D0
 130      FORMAT (1H ,F8.3,T11,F10.3,T24,F10.3,T36,F10.3,
     -             T50,F10.3,T66,F5.2)
          WRITE (10,140)
 140      FORMAT(1H ,/1H ,'FAILURE STRESSES (TSAI-WU CRITERION)'
     -                  //,
     -           1H ,'     XT',T19,' XC',T34,' YT',T49,' YC',
     -               T66,'S'/)
          DO 5 K=1,NC
 5        WRITE (10,150) XT(K),XC(K),YT(K),YC(K),T6(K)
 150      FORMAT (1H ,F8.4,T14,F10.4,T29,F10.4,T44,F10.4,
     -              T59,F10.4)
C
```

```
C         A, B, AND D MATRICES ARE CALCULATED (TSAI-PAGANO)
C
          T=0.D0
          DO 15 K=1,NC
 15         T=T+EP(K)
          ZK=-T/2.D0
          DO 20 K=1,NC
            ZK1=ZK+EP(K)
            PSI=1.D0-XNULT(K)**2*ET(K)/EL(K)
            U1=(EL(K)+ET(K)+XNULT(K)*ET(K)*2.D0)/8.D0/PSI
            U2=(PSI*GLT(K)-XNULT(K)*ET(K))/2.D0/PSI
            U3=(EL(K)-ET(K))/2.D0/PSI
            U4=(EL(K)+ET(K)-2.D0*XNULT(K)*ET(K)
     &         -4.D0*PSI*GLT(K))/8.D0/PSI
            H(1,1)=3.D0*U1+U2+U3*COS(2.D0*TH(K))
     1             +U4*COS(4.D0*TH(K))
            H(2,2)=3.D0*U1+U2-U3*COS(2.D0*TH(K))
     1             +U4*COS(4.D0*TH(K))
            H(1,2)=U1-U2-U4*COS(4.D0*TH(K))
            H(2,1)=H(1,2)
            H(1,3)=0.5D0*U3*SIN(2.D0*TH(K))
     1             +U4*SIN(4.D0*TH(K))
            H(3,1)=H(1,3)
            H(2,3)=0.5D0*U3*SIN(2.D0*TH(K))
     1             -U4*SIN(4.D0*TH(K))
            H(3,2)=H(2,3)
            H(3,3)=U1+U2-U4*COS(4.D0*TH(K))
            DO 30 I=1,3
            DO 30 J=1,3
              A(I,J)=A(I,J)+H(I,J)*(ZK1-ZK)
              B(I,J)=B(I,J)+H(I,J)*(ZK1*ZK1-ZK*ZK)/2.D0
 30         D(I,J)=D(I,J)+H(I,J)*(ZK1*ZK1*ZK1-ZK*ZK*ZK)/3.D0
 20       ZK=ZK1
C
          WRITE (10,*) ' '
          WRITE (10,160)
          WRITE (10,*) ' '
          WRITE (10,*) 'A MATRIX'
          WRITE (10,*) ' '
          DO 11 I=1,3
 11       WRITE (10,400) (A(I,J),J=1,3)
          WRITE (10,*) ' '
          WRITE (10,*) 'B MATRIX'
          WRITE (10,*) ' '
          DO 12 I=1,3
 12       WRITE (10,400) (B(I,J),J=1,3)
          WRITE (10,*) ' '
          WRITE (10,*) 'D MATRIX'
          WRITE (10,*) ' '
          DO 13 I=1,3
 13       WRITE (10,400) (D(I,J),J=1,3)
          WRITE (10,*) ' '
          WRITE (10,160)
```

```
      WRITE (10,*) ' '
 400  FORMAT(3F15.6)
      READ (1,*) KU,LU,KV,LV,KW,LW
      WRITE (10,500) KU,LU,KV,LV,KW,LW
 500  FORMAT (' DEGREE OF U FIELD:',I2,' *',I2/
     -        ' DEGREE OF V FIELD:',I2,' *',I2/
     -        ' DEGREE OF W FIELD:',I2,' *',I2)
      WRITE (10,*) ' '
      WRITE (10,160)
      WRITE (10,*) ' '
 160  FORMAT (1H ,75(1H*))
      RETURN
      END
C*************************************************************
C
C       STRESSES CALCULATION AT INTEGRATION POINTS
C
      SUBROUTINE RESIST(Q,Q0,SECU,XS,YS,SX,SY,TA)
      IMPLICIT REAL*8 (A-H,O-Z)
      REAL*8 SECU(9),XS(9),YS(9),SX(9),SY(9),TA(9),Q(111),
     1       Q0(36)
      COMMON /MATRICES/ A(3,3),B(3,3),D(3,3)
      COMMON /NMODES/ NU,NV,NW,KU,LU,KV,LV,KW,LW,NM
      COMMON /STIFF/ XKEL(75,75),XKS(75,36,36),XKQ(82251),
     -  XKBL(75,36),XKBNL(36,36,36),XKF(36,36),XKT(36,36)
      COMMON /MODES/ XMODE(366),IMODE(366,2),SHAPE(45,21),
     -  XG(21),WEIGHT(21),NP,XL,YL
      COMMON /STRATES/ NC,TH(9),EP(9),EL(9),ET(9),XNULT(9),
     -  GLT(9),T,ELT,XT(9),XC(9),YT(9),YC(9),T6(9),XA,YA,
     -  XB,YB,XD
C
      N1=NU+NV
      N2=N1+NU
      N3=N2+NV
      N4=N3+NW
      N5=N4+NW
      N6=N5+NW
      N7=N6+NW
      DO 15 I=1,NC
 15   SECU(I)=0.D0
C
C       DISPLACEMENT GRADIENTS AND CURVATURES ARE
C       CALCULATED IN EACH POINT
C
      DO 10 I=1,NP
      DO 10 J=1,NP
        UX=0.D0
        DO 20 K=1,NU
 20     UX=UX+XMODE(K)*SHAPE(IMODE(K,1),I)
     1     *SHAPE(IMODE(K,2),J)*Q(K)
        VY=0.D0
        DO 30 K=1,NV
          K1=K+NU
```

```
 30         VY=VY+XMODE(K1)*Q(K1)*SHAPE(IMODE(K1,1),I)
     &                     *SHAPE(IMODE(K1,2),J)
            GA=0.D0
            DO 40 K=1,N1
              K1=K+N1
 40         GA=GA+XMODE(K1)*Q(K)*SHAPE(IMODE(K1,1),I)
     &                     *SHAPE(IMODE(K1,2),J)
            WX=0.D0
            WY=0.D0
            WXX=0.D0
            WXY=0.D0
            WYY=0.D0
            W0X=0.D0
            W0Y=0.D0
            DO 50 K=1,NW
              K1=K+N1
              K2=K+N3
              WX=WX+XMODE(K2)*Q(K1)*SHAPE(IMODE(K2,1),I)
     &             *SHAPE(IMODE(K2,2),J)
              W0X=W0X+XMODE(K2)*Q0(K) *SHAPE(IMODE(K2,1),I)
     &             *SHAPE(IMODE(K2,2),J)
              K2=K+N4
              WY=WY+XMODE(K2)*Q(K1) *SHAPE(IMODE(K2,1),I)
     &             *SHAPE(IMODE(K2,2),J)
              W0Y=WOY+XMODE(K2)*Q0(K) *SHAPE(IMODE(K2,1),I)
     &             *SHAPE(IMODE(K2,2),J)
              K2=K+N5
              WXX=WXX+XMODE(K2)*Q(K1) *SHAPE(IMODE(K2,1),I)
     &             *SHAPE(IMODE(K2,2),J)
              K2=K+N6
              WYY=WYY+XMODE(K2)*Q(K1) *SHAPE(IMODE(K2,1),I)
     &             *SHAPE(IMODE(K2,2),J)
              K2=K+N6
              WXY=WXY+XMODE(K2)*Q(K1) *SHAPE(IMODE(K2,1),I)
     &             *SHAPE(IMODE(K2,2),J)
 50         CONTINUE
C
C         EACH LAYER IS TESTED ON UPPER AND LOWER FACE
C
            Z=-T/2.D0
            DO 60 K=1,NC
              CALL TSAIWU(Z,UX,VY,GA,WX,WY,WXX,WYY,WXY,W0X,W0Y,
     -                    K,I,J,SECU,XS,YS,SX,SY,TA)
              Z=Z+EP(K)
              CALL TSAIWU(Z,UX,VY,GA,WX,WY,WXX,WYY,WXY,W0X,W0Y,
     -                    K,I,J,SECU,XS,YS,SX,SY,TA)
 60         CONTINUE
 10       CONTINUE
          END
C*************************************************************
C
C         FACTOR OF SAFETY IS CALCULATED IN A POINT
C         (TSAI-WU CRITERION)
```

```
C
      SUBROUTINE TSAIWU(Z,UX,VY,GA,WX,WY,WXX,WYY,WXY,
     -   W0X,WOY,K,I,J,SECU,XS,YS,SX,SY,TA)
      IMPLICIT REAL*8 (A-H,O-Z)
      COMMON /MODES/ XMODE(366),IMODE(366,2),SHAPE(45,21),
     -   XG(21),WEIGHT(21),NP,XL,YL
      COMMON /STRATES/ NC,TH(9),EP(9),EL(9),ET(9),XNULT(9),
     -   GLT(9),T,ELT,XT(9),XC(9),YT(9),YC(9),T6(9),XA,YA,
     -   XB,YB,XD
      REAL*8 SECU(9),XS(9),YS(9),SX(9),SY(9),TA(9)
C
C       DEFORMATIONS IN STRUCTURAL AXES ARE CALCULATED
C
      EX=UX+WX*WX/2.D0+W0X*WX-Z*WXX
      EY=VY+WY*WY/2.D0+W0Y*WY-Z*WYY
      EXY=(GA+WX*WY+W0X*WY+WX*W0Y-Z*WXY)/2.D0
C
C       ROTATION INTO FIBERS AXES
C
      CO=COS(TH(K))
      SI=SIN(TH(K))
      E1=CO*CO*EX+SI*SI*EY+2.D0*SI*CO*EXY
      E2=SI*SI*EX+CO*CO*EY-2.D0*SI*CO*EXY
      E6=(-SI*CO*EX+SI*CO*EY+(CO*CO-SI*SI)*EXY)*2.D0
C
C       STRESSES IN FIBERS AXES
C
      PSI=1.D0-XNULT(K)**2*ET(K)/EL(K)
      S1=(EL(K)*E1+ET(K)*XNULT(K)*E2)/PSI
      S2=(XNULT(K)*ET(K)*E1+ET(K)*E2)/PSI
      S6=GLT(K)*E6
C
C     FACTOR OF SAFETY IS CALCULATED
C      SAVED IF MAXIMUM IN THE LAYER
C
      BB= (1.D0/XT(K)-1.D0/XC(K))*S1
     &     +(1.D0/YT(K)-1.D0/YC(K))*S2
      AA=S1**2/XT(K)/XC(K)+S2**2/YT(K)/YC(K)+(S6/T6(K))**2
      IF (AA.EQ.0.D0) THEN
        SE=0.D0
        GO TO 30
      ENDIF
      SE=2.D0*AA/(-BB+SQRT(BB*BB+4.D0*AA))
 30   IF (SE.GE.SECU(K)) THEN
        SECU(K)=SE
        SX(K)=S1
        SY(K)=S2
        TA(K)=S6
        XI=(DFLOAT(I-1))*XL/DFLOAT(NP-1)
        ETA=(DFLOAT(J-1))*YL/DFLOAT(NP-1)
        XS(K)=XD*XI+XA*ETA+(XB-XA-XD)*XI*ETA
        YS(K)=YA*ETA+(YB-YA)*XI*ETA
      ENDIF
```

```
      RETURN
      END
C*************************************************************
C
      SUBROUTINE SOLVE(N,GRA,HES,S)
      IMPLICIT REAL*8 (A-H,O-Z)
      REAL*8 A(6216),DET(111),HES(111,111),GRA(111),S(111)
      INTEGER*4 ICH(222)
      NDIM=111
      ID=0
      M=1
      IND=0
      DO 10 I=1,N
      DO 10 J=1,I
        IND=IND+1
 10   A(IND)=HES(I,J)
      DO 20 I=1,N
 20   S(I)=GRA(I)
      CALL LEQ1S(A,N,S,M,NDIM,ID,ICH,DET,IER)
      RETURN
      END
C ***********************************************************
C ***                                                     ***
C ***      RECONSTRUCT DISPLACEMENT FIELDS : u,v,w        ***
C ***                                                     ***
C ***                 DAVID W. JENSEN                     ***
C ***                                                     ***
C ***                 SEPTEMBER 1985                      ***
C ***                                                     ***
C ***               FOR018 :  P vs. u                     ***
C ***               FOR019 :  P vs. w                     ***
C ***               FOR020 :  Contour Data                ***
C ***                                                     ***
C ***********************************************************
      SUBROUTINE DISP(ISCAN,PX,Q,SPEC)
      IMPLICIT REAL*8 (A-H,O-Z)
      COMMON /NMODES/ NU,NV,NW,KU,LU,KV,LV,KW,LW,NM
      COMMON /MODES/ XMODE(366),IMODE(366,2),SHAPE(45,21),
     1               XG(21),WEIGHT(21),NP,XL,YL
      CHARACTER*30 SPEC
      DIMENSION Q(111)
C
      M=2*(NU+NV)+5*NW
      N=M+NW
      WRITE(18,*) SPEC
      WRITE(19,*) SPEC
      WRITE(18,*) PX
      WRITE(19,*) PX
      IF (ISCAN.EQ.1) THEN
        WRITE(20,*) SPEC
        WRITE(20,*) PX
          DO 200 L=1,NP,2
          DO 200 K=1,NP,2
```

```
            W=0.0
            DO 100 I=1,NW
              I1=IMODE(I+M,1)
              I2=IMODE(I+M,2)
              I3=I+NU+NV
100           W=W+Q(I3)*SHAPE(I1,K)*SHAPE(I2,L)
200         WRITE(20,*) W
        ENDIF
        WRITE(18,*) Q(1)
        J=(NP-1)/4
        DO 500 K1=1,3
          K=K1*J+1
          DO 500 L1=1,3
            L=L1*J+1
            W=0.0
            DO 400 I=1,NW
              I1=IMODE(I+M,1)
              I2=IMODE(I+M,2)
              I3=I+NU+NV
400         W=W+Q(I3)*SHAPE(I1,K)*SHAPE(I2,L)
          WRITE(19,*) W
500     CONTINUE
        RETURN
        END
```

APPENDIX C

This appendix contains the average thickness values for the sublaminates in Table C.1 and the average thickness values for the assembled laminates in Table C.2.

TABLE C.1

SUBLAMINATE AVERAGE THICKNESS DATA

Laminate	Sublaminate[a]				Total Thickness[a]
	0_3	90_3	90_3	0_3	
T_1	0.436 (3.9%)	0.434 (3.6%)	0.419 (3.3%)	0.436 (4.4%)	1.816 (1.2%)
T_2	0.431 (3.0%)	0.443 (4.0%)	0.442 (2.8%)	0.440 (3.4%)	1.786 (1.0%)
T_3	0.433 (1.6%)	0.432 (3.6%)	0.427 (3.0%)	0.429 (4.2%)	1.762 (0.6%)
T_4	0.432 (3.7%)	0.439 (2.8$%)	0.437 (3.2%)	0.447 (3.1%)	1.848 (0.9%)
T_5	0.424 (2.6%)	0.413 (3.0%)	0.408 (6.4%)	0.429 (2.1%)	1.725 (0.6%)
T_S	0.428 (4.0%)	0.443 (1.9%)	0.414 (2.9%)	0.438 (3.2%)	1.797 (1.1%)
T_F	0.430 (2.8%)	0.413 (2.9%)	0.424 (4.0%)	0.432 (5.1%)	1.763 (0.9%)

[a] All thickness values in millimeters.

TABLE C.1 (Continued)

SUBLAMINATE AVERAGE THICKNESS DATA

Laminate	Sublaminate[a]				Total Thickness[a]
	0_3	90_3	0_3	90_3	
U_1	0.426 (2.1%)	0.432 (5.7%)	0.436 (6.4%)	0.435 (4.3%)	1.769 (0.5%)
U_2	0.426 (2.1%)	0.422 (5.3%)	0.428 (3.5%)	0.436 (3.7%)	1.788 (0.6%)
U_3	0.436 (2.5%)	0.433 (3.1%)	0.442 (3.6%)	0.436 (3.1%)	1.856 (1.0%)
U_4	0.454 (2.6%)	0.425 (2.8%)	0.438 (2.1%)	0.410 (4.4%)	1.824 (0.8%)
U_5	0.452 (2.2%)	0.429 (3.8%)	0.441 (2.6%)	0.431 (4.3%)	1.799 (0.6%)
U_S	0.447 (4.7%)	0.452 (3.3%)	0.441 (2.5%)	0.441 (4.0%)	1.896 (2.0%)
U_F	0.425 (3.8%)	0.430 (2.2%)	0.437 (3.0%)	0.428 (4.6%)	1.779 (0.6%)

[a] All thickness values in millimeters.

TABLE C.1 (Continued)

SUBLAMINATE AVERAGE THICKNESS DATA

Laminate	Sublaminate[a]					Total Thickness[a]
	0_2	45_2	0_2	45_2	0_2	
P_1	0.281 (6.4%)	0.299 (5.4%)	0.293 (3.4%)	0.291 (4.1%)	0.288 (5.9%)	1.581 (1.4%)
P_2	0.276 (5.4%)	0.295 (2.4%)	0.264 (4.5%)	0.291 (3.8%)	0.291 (6.9%)	1.641 (0.4%)
P_3	0.279 (3.6%)	0.304 (3.0%)	0.290 (3.1%)	0.274 (8.4%)	0.304 (9.9%)	1.616 (1.7%)
P_4	0.291 (5.5%)	0.300 (3.0%)	0.297 (11%)	0.296 (3.4%)	0.293 (5.1%)	1.617 (0.8%)
P_5	0.293 (8.2%)	0.294 (4.8%)	0.295 (4.7%)	0.276 (6.2%)	0.295 (6.1%)	1.591 (1.1%)
P_S	0.292 (5.5%)	0.292 (4.8%)	0.294 (2.4%)	0.270 (4.8%)	0.295 (5.4%)	1.566 (1.8%)
P_F	0.281 (3.9%)	0.301 (2.0%)	0.288 (3.8%)	0.312 (3.5%)	0.289 (6.2%)	1.589 (0.8%)

[a] All thickness values in millimeters.

TABLE C.1 (Continued)

SUBLAMINATE AVERAGE THICKNESS DATA

Laminate	Sublaminate[a]					Total Thickness[a]
	0_2	45_2	0_2	45_2	0_2	
N_1	0.279 (5.4%)	0.301 (3.0%)	0.281 (8.0%)	0.284 (6.7%)	0.286 (5.2%)	1.586 (2.3%)
N_2	0.289 (5.5%)	0.298 (4.7%)	0.290 (5.2%)	0.271 (6.6%)	0.282 (3.5%)	1.572 (1.3%)
N_3	0.312 (3.8%)	0.297 (5.1%)	0.291 (5.5%)	0.269 (5.6%)	0.294 (5.4%)	1.622 (1.4%)
N_4	0.289 (6.2%)	0.286 (5.2%)	0.290 (3.1%)	0.277 (5.8%)	0.283 (2.8%)	1.530 (0.7%)
N_5	0.288 (4.9%)	0.297 (3.4%)	0.299 (4.3%)	0.278 (4.7%)	0.298 (6.0%)	1.548 (1.5%)
N_S	0.286 (5.0%)	0.296 (4.1%)	0.288 (2.8%)	0.265 (4.2%)	0.304 (4.3%)	1.569 (1.2%)
N_F	0.295 (5.1%)	0.277 (7.6%)	0.285 (7.0%)	0.291 (5.2%)	0.284 (7.4%)	1.583 (0.8%)

[a] All thickness values in millimeters.

TABLE C.1 (Continued)

SUBLAMINATE AVERAGE THICKNESS DATA

Laminate	Sublaminate[a]		Total Thickness[a]
	0_6	15_6	
A_1	0.817 (1.7%)	0.768 (3.8%)	1.644 (0.7%)
A_2	0.807 (2.0%)	0.776 (3.5%)	1.613 (1.2%)
A_3	0.801 (1.3%)	0.807 (1.1%)	1.658 (1.1%)
A_4	0.806 (0.9%)	0.790 (1.4%)	1.606 (1.5%)
A_5	0.806 (0.6%)	0.776 (1.2%)	1.677 (5.6%)
A_S	0.819 (1.8%)	0.784 (2.9%)	1.656 (1.5%)
A_F	0.808 (1.0%)	0.786 (3.9%)	1.638 (2.7%)

[a] All thickness values in millimeters.

TABLE C.1 (Continued)

SUBLAMINATE AVERAGE THICKNESS DATA

Laminate	Sublaminate[a]		Total Thickness[a]
	0_6	30_6	
B_1	0.891 (1.8%)	0.791 (1.1%)	1.711 (0.7%)
B_2	0.794 (1.8%)	0.801 (1.6%)	1.597 (0.9%)
B_3	0.803 (1.4%)	0.811 (1.6%)	1.659 (2.8%)
B_4	0.801 (5.0%)	0.807 (1.5%)	1.634 (1.0%)
B_5	0.807 (2.1%)	0.803 (2.2%)	1.601 (0.8%)
B_S	0.793 (2.1%)	0.812 (1.7%)	1.621 (1.3%)
B_F	0.791 (1.6%)	0.817 (1.6%)	1.628 (2.1%)

[a] All thickness values in millimeters.

TABLE C.1 (Continued)

SUBLAMINATE AVERAGE THICKNESS DATA

Laminate	Sublaminate[a]		Total Thickness[a]
	0_6	45_6	
C_1	0.802 (2.7%)	0.791 (2.9%)	1.602 (1.4%)
C_2	0.798 (0.8%)	0.792 (2.7%)	1.618 (1.0%)
C_3	0.806 (1.2%)	0.789 (1.3%)	1.646 (1.0%)
C_4	0.765 (3.4%)	0.794 (1.4%)	1.614 (1.1%)
C_5	0.783 (2.2%)	0.789 (1.3%)	1.637 (1.7%)
C_S	0.792 (2.3%)	0.804 (1.2%)	1.631 (0.9%)
C_F	0.829 (1.6%)	0.819 (1.3%)	1.662 (0.8%)

[a] All thickness values in millimeters.

TABLE C.1 (Continued)

SUBLAMINATE AVERAGE THICKNESS DATA

Laminate	Sublaminate[a]		Total Thickness[a]
	0_6	60_6	
D_1	0.806 (0.9%)	0.866 (4.2%)	1.726 (2.6%)
D_2	0.762 (1.8%)	0.793 (1.8%)	1.702 (2.4%)
D_3	0.803 (3.0%)	0.862 (3.7%)	1.767 (1.1%)
D_4	0.799 (1.6%)	0.772 (3.1%)	1.674 (2.3%)
D_5	0.807 (2.6%)	0.802 (3.1%)	1.626 (1.2%)
D_S	0.811 (1.5%)	0.790 (1.8%)	1.624 (1.5%)
D_F	0.807 (1.5%)	0.787 (2.7%)	1.709 (2.2%)

[a] All thickness values in millimeters.

TABLE C.1 (Continued)

SUBLAMINATE AVERAGE THICKNESS DATA

Laminate	Sublaminate[a]		Total Thickness[a]
	0_6	75_6	
E_1	0.772 (1.0%)	0.807 (3.6%)	1.637 (1.5%)
E_2	0.881 (3.1%)	0.804 (2.0%)	1.749 (1.0%)
E_3	0.799 (2.4%)	0.810 (1.4%)	1.613 (0.5%)
E_4	0.802 (1.5%)	0.808 (1.9%)	1.611 (1.4%)
E_5	0.781 (3.1%)	0.811 (1.8%)	1.616 (0.7%)
E_S	0.786 (2.2%)	0.796 (1.4%)	1.614 (1.2%)
E_F	0.794 (1.6%)	0.807 (3.1%)	1.611 (1.1%)

[a] All thickness values in millimeters.

TABLE C.1 (Continued)

SUBLAMINATE AVERAGE THICKNESS DATA

Laminate	Sublaminate[a] 0_6	Sublaminate[a] 90_6	Total Thickness[a]
F_1	0.799 (2.1%)	0.801 (1.0%)	1.596 (0.8%)
F_2	0.804 (1.3%)	0.808 (1.7%)	1.622 (0.7%)
F_3	0.789 (1.0%)	0.816 (1.6%)	1.594 (0.6%)
F_4	0.778 (2.8%)	0.811 (3.6%)	1.589 (2.0%)
F_5	0.799 (2.0%)	0.812 (0.6%)	1.599 (0.8%)
F_S	0.805 (1.2%)	0.807 (1.6%)	1.616 (0.6%)
F_F	0.802 (0.7%)	0.809 (1.9%)	1.593 (0.8%)

[a] All thickness values in millimeters.

TABLE C.2

LAMINATE THICKNESS DATA

Laminate	Average Laminate Thickness[a]	Total Bondline Thickness[a]	Number of Bondlines	Average Bondline Thickness[a]
S_1	1.578 (1.8%)[b]	-	-	-
S_2	1.552 (2.8%)	-	-	-
S_3	1.557 (2.4%)	-	-	-
S_S	1.566 (1.3%)	-	-	-
S_F	1.565 (2.1%)	-	-	-
T_1	1.816 (1.2%)	0.091	3	0.030
T_2	1.786 (1.0%)	0.030	3	0.010
T_3	1.762 (0.6%)	0.041	3	0.014
T_4	1.848 (0.9%)	0.093	3	0.031
T_5	1.725 (0.6%)	0.051	3	0.017
T_S	1.797 (1.1%)	0.074	3	0.025
T_F	1.763 (0.9%)	0.065	3	0.022
U_1	1.769 (0.4%)	0.040	3	0.013
U_2	1.788 (0.6%)	0.076	3	0.025
U_3	1.856 (1.0%)	0.109	3	0.036
U_4	1.824 (0.8%)	0.097	3	0.032
U_5	1.799 (0.5%)	0.046	3	0.015
U_S	1.896 (1.9%)	0.117	3	0.039
U_F	1.779 (0.6%)	0.059	3	0.020

[a] All thickness values in millimeters.
[b] Numbers in parentheses are coefficients of variation.

TABLE C.2 (Continued)

LAMINATE THICKNESS DATA

Laminate	Average Laminate Thickness[a]	Total Bondline Thickness[a]	Number of Bondlines	Average Bondline Thickness[a]
P_1	1.581 (1.4%)[b]	0.137	4	0.034
P_2	1.641 (0.4%)	0.224	4	0.056
P_3	1.616 (1.7%)	0.165	4	0.041
P_4	1.617 (0.8%)	0.140	4	0.035
P_5	1.591 (1.1%)	0.138	4	0.034
P_S	1.566 (1.8%)	0.123	4	0.031
P_F	1.589 (0.8%)	0.118	4	0.030
N_1	1.586 (2.3%)	0.135	4	0.034
N_2	1.572 (1.3%)	0.142	4	0.036
N_3	1.622 (1.4%)	0.159	4	0.040
N_4	1.530 (0.7%)	0.005	4	0.001
N_5	1.548 (1.5%)	0.088	4	0.022
N_S	1.569 (1.2%)	0.131	4	0.033
N_F	1.583 (0.8%)	0.151	4	0.038

[a] All thickness values in millimeters.
[b] Numbers in parentheses are coefficients of variation.

TABLE C.2 (Continued)

LAMINATE THICKNESS DATA

Laminate	Average Laminate Thickness[a]	Total Bondline Thickness[a]	Number of Bondlines	Average Bondline Thickness[a]
A_1	1.644 (0.7%)[b]	0.059	1	0.059
A_2	1.613 (1.2%)	0.030	1	0.030
A_3	1.658 (1.1%)	0.050	1	0.050
A_4	1.606 (1.5%)	0.024	1	0.024
A_5	1.677 (5.6%)	0.095	1	0.095
A_S	1.656 (1.5%)	0.053	1	0.053
A_F	1.638 (2.7%)	0.044	1	0.044
B_1	1.711 (0.7%)	0.029	1	0.029
B_2	1.597 (0.9%)	0.002	1	0.002
B_3	1.659 (2.8%)	0.045	1	0.045
B_4	1.634 (1.0%)	0.026	1	0.026
B_5	1.601 (0.8%)	-0.009	1	-0.009
B_S	1.621 (1.3%)	0.016	1	0.016
B_F	1.628 (2.1%)	0.020	1	0.020

[a] All thickness values in millimeters.
[b] Numbers in parentheses are coefficients of variation.

TABLE C.2 (Continued)

LAMINATE THICKNESS DATA

Laminate	Average Laminate Thickness[a]	Total Bondline Thickness[a]	Number of Bondlines	Average Bondline Thickness[a]
C_1	1.602 (1.5%)[b]	0.014	1	0.014
C_2	1.618 (1.0%)	0.028	1	0.028
C_3	1.646 (1.0%)	0.051	1	0.051
C_4	1.614 (1.1%)	0.055	1	0.055
C_5	1.637 (1.6%)	0.065	1	0.065
C_S	1.631 (0.9%)	0.035	1	0.035
C_F	1.662 (0.8%)	0.014	1	0.014
D_1	1.726 (2.6%)	0.054	1	0.054
D_2	1.702 (2.3%)	0.147	1	0.147
D_3	1.767 (1.1%)	0.102	1	0.102
D_4	1.674 (2.3%)	0.103	1	0.103
D_5	1.626 (1.2%)	0.017	1	0.017
D_S	1.624 (1.5%)	0.023	1	0.023
D_F	1.709 (2.2%)	0.115	1	0.115

[a] All thickness values in millimeters.
[b] Numbers in parentheses are coefficients of variation.

TABLE C.2 (Continued)

LAMINATE THICKNESS DATA

Laminate	Average Laminate Thickness[a]	Total Bondline Thickness[a]	Number of Bondlines	Average Bondline Thickness[a]
E_1	1.637 (1.5%)[b]	0.058	1	0.058
E_2	1.749 (1.0%)	0.064	1	0.064
E_3	1.613 (0.5%)	0.040	1	0.040
E_4	1.611 (1.3%)	0.001	1	0.001
E_5	1.616 (0.7%)	0.024	1	0.024
E_S	1.614 (1.1%)	0.032	1	0.032
E_F	1.611 (1.1%)	0.010	1	0.010
F_1	1.596 (0.8%)	-0.004	1	-0.004
F_2	1.622 (0.7%)	0.010	1	0.010
F_3	1.594 (0.6%)	-0.007	1	-0.007
F_4	1.589 (1.9%)	0.000	1	0.000
F_5	1.599 (0.8%)	-0.012	1	-0.012
F_S	1.616 (0.6%)	0.004	1	0.004
F_F	1.593 (0.8%)	-0.018	1	-0.018

[a] All thickness values in millimeters.
[b] Numbers in parentheses are coefficients of variation.

APPENDIX D

TESTING PROCEDURE CHECKLIST

This is a reproduction of the actual checklist which was used to ensure that standardized procedures were followed while testing each of the laminates in this investigation:

__ A) Prepare Plate for Installation

- __ 1) Attach teflon tape to all borders of laminate (two layers).
- __ 2) Lubricate teflon tape (all surfaces).

__ B) Prepare Jig and Install Plate

- __ 1) Install probe.
- __ 2) Zero load reading.
- __ 3) Insert plate loosely in upper and lower boundary conditions.

__ C) Attach Upper and Lower Boundary Conditions to Plate

- __ 1) Load to approximately 890 N (Set Point).
- __ 2) Hand tighten upper and lower boundary conditions (horizontal bolts).
- __ 3) Loosely tighten with wrench (seat bolt + 1/16 turn).
- __ 4) Return stroke to zero (Set Point).

__ D) Position Upper and Lower Boundary Conditions with Respect to the Frame

__ 1) Read displacement (computer units and volts) and potentiometer readings (computer units) at four corners. [Adjust (if necessary) and repeat corner readings].
__ 2) Record scanner offset (average of four corner readings).
__ 3) Verify center transducer (No. 5) signal (first time only).
__ 4) Clamp upper and lower boundary conditions to frame (vertical bolts).

__ E) Align and Fix Side Boundary Conditions

__ 1) Align side boundary conditions (simultaneously hand tighten front and back).
__ 2) Clamp side boundary conditions to frame.

__ F) Update Database Information File ("GLOBAL")

__ G) Balance and Calibrate Strain Gages

__ 1) Attach strain gage wires.
__ 2) Adjust bridge excitation voltage (1 volt) on conditioner.
__ 3) Adjust amplifier balance (with excitation off).
__ 4) Turn excitation voltage on.
__ 5) Balance all four strain gages.
__ 6) Run calibration program ("ADCAL").
__ 7) Calibrate gain for each gage (13746 ohms shunt equals 2000 computer units).
__ 8) Record strain gage offsets (computer units).

__ H) Adjust Load Introduction

__ 1) Load to approximately 890 N to seat plate.
__ 2) Return stroke to zero.
__ 3) Align load introduction bolts (hand tighten).
__ 4) Release load to small compressive value (Set Point).

__ I) Determine Offsets

__ 1) Position transducer rack against plate.
__ 2) Switch electronics to "Rack".
__ 3) Record offsets for remaining channels ("ADCAL").

__ J) Scan Plate with No Load

__ 1) Switch electronics to "Scan".
__ 2) Run scanner data acquisition program ("SCAN").
__ 3) Switch electronics to "Rack".

__ K) Initialize Data Acquisition

__ 1) Run data acquisition program ("TDAK").
__ 2) Enter initial data offsets.
__ 3) Set interval between data points to 0.25 seconds.
__ 4) Record initial machine stroke.

__ L) Load to Stability "Limit Load"

__ 1) Reset memory.
__ 2) Start data acquisition.
__ 3) Increase stroke at rate of 0.42 millimeters/minute.
__ 4) Hold stroke when center transducer indicates a displacement equal to half of the plate thickness.
__ 5) Halt data acquisition and close files.
__ 6) Record maximum load and stroke.

__ M) Scan Plate at "Limit Load"

__ 1) Switch electronics to "Scan".
__ 2) Run scanning data acquisition program ("SCAN").
__ 3) Return machine stroke to zero.
__ 4) Switch electronics to "Rack".

__ N) Reinitialize Data Acquisition

__ 1) Run data acquisition program ("TDAK").
__ 2) Enter initial data offsets.
__ 3) Set interval between data points to 0.4 seconds.

__ O) Repeat Steps L, M and N for Scans at Higher Loads

__ P) Load to Failure

__ 1) Reset memory.
__ 2) Start data acquisition.
__ 3) Increase stroke at rate of 0.42 millimeters/minute.
__ 4) Record marks when audible damage occurs.
__ 5) Hold stroke when load drops significantly.
__ 6) Halt data acquisition and close files.
__ 7) Record maximum load and stroke.

__ Q) Photograph and Remove Plate

__ 1) Withdraw rack.
__ 2) Attach label and photograph plate.
__ 3) Return stroke to zero.
__ 4) Lower crosshead and turn pump off.
__ 5) Remove plate from jig.

APPENDIX E

LOAD VERSUS OUT-OF-PLANE DEFLECTION PLOTS

This appendix contains copies of all of the experimental load versus out-of-plane deflection plots. They are presented in the same order as discussed in the main text, i.e., according to the sequence summarized in Table 4.4. For the fifth laminate of each type, the early loading histories are also included. The results for laminates with clamped side boundary conditions are presented first, followed by those with simply-supported side boundary conditions, and, finally, the results for laminates with free sides.

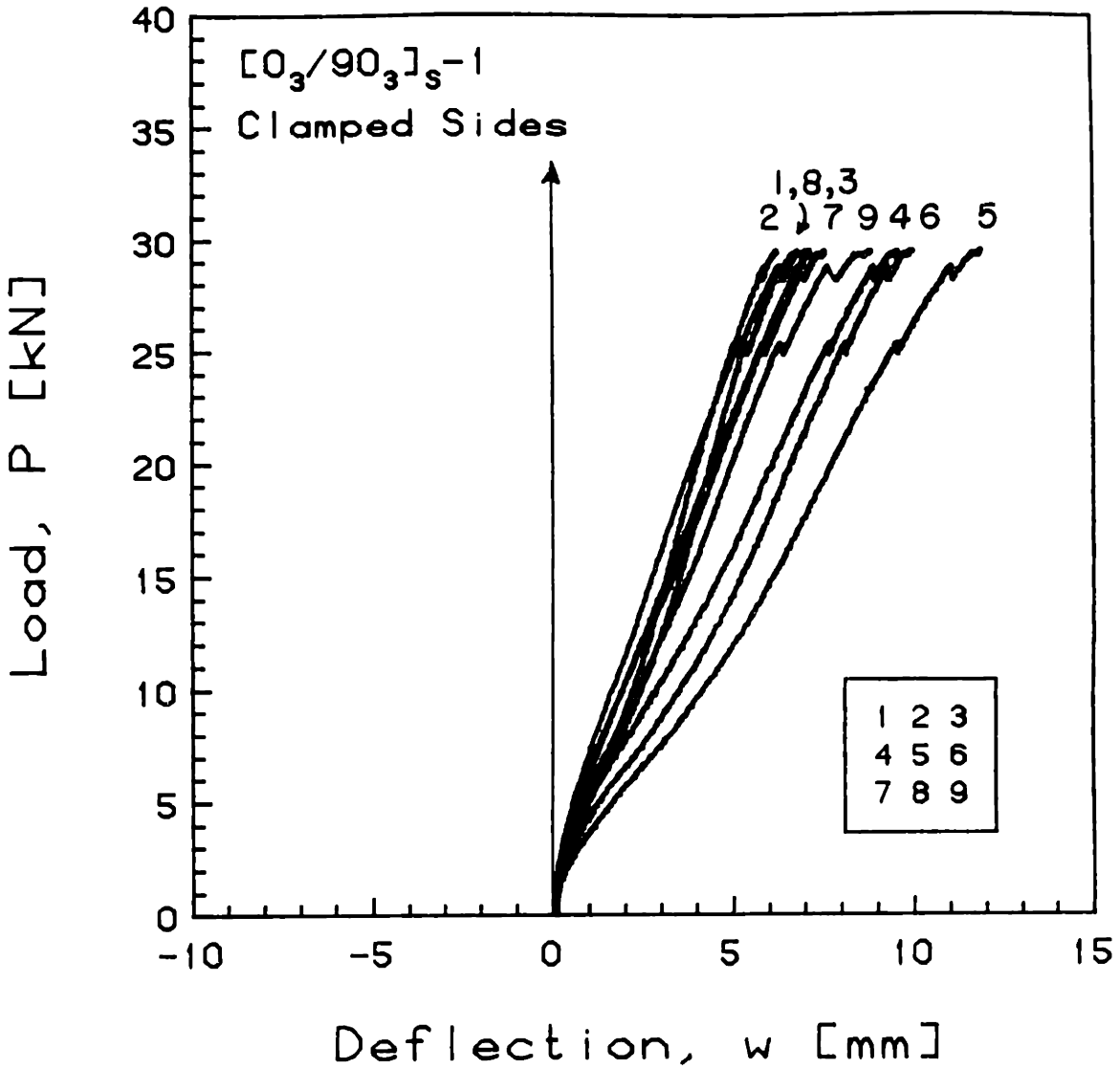

FIGURE E.1 Experimental Plot of Applied Compressive Load versus Out-of-Plane Deflection for the $[0_3/90_3]_S$-1 Laminate with Clamped Side Boundary Conditions

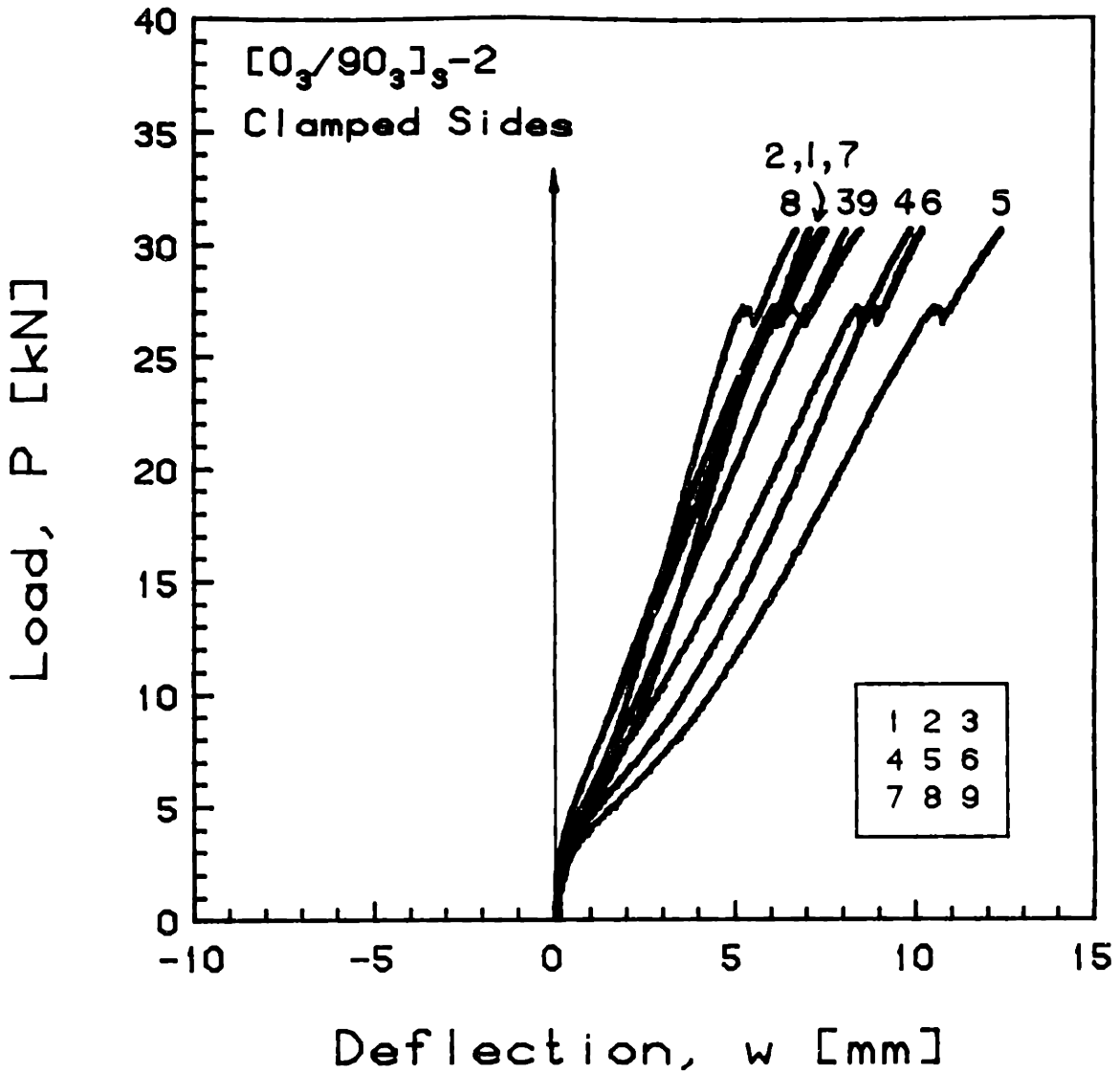

FIGURE E.2 Experimental Plot of Applied Compressive Load versus Out-of-Plane Deflection for the $[0_3/90_3]_s$-2 Laminate with Clamped Side Boundary Conditions

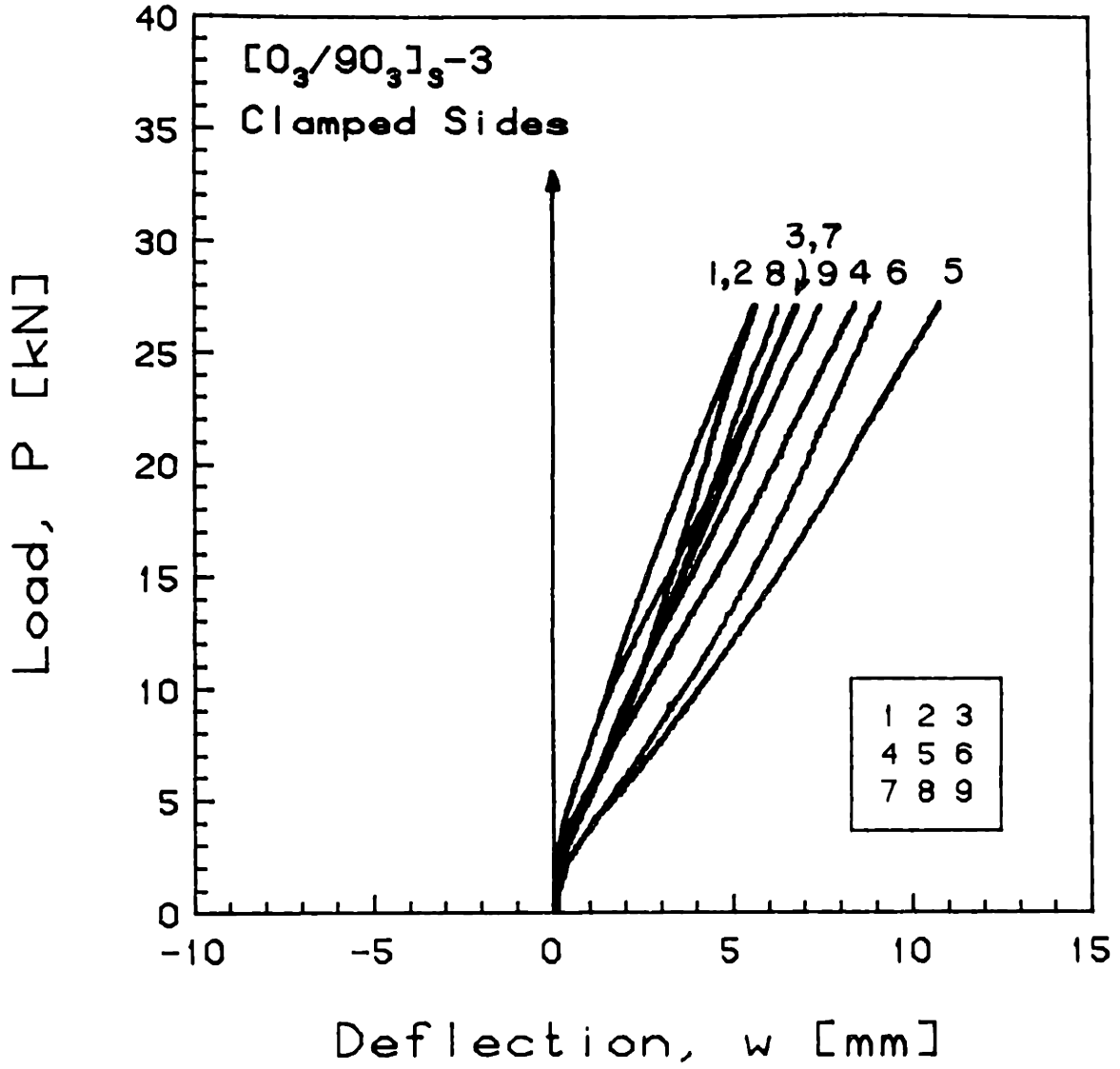

FIGURE E.3 Experimental Plot of Applied Compressive Load versus Out-of-Plane Deflection for the $[0_3/90_3]_S$-3 Laminate with Clamped Side Boundary Conditions

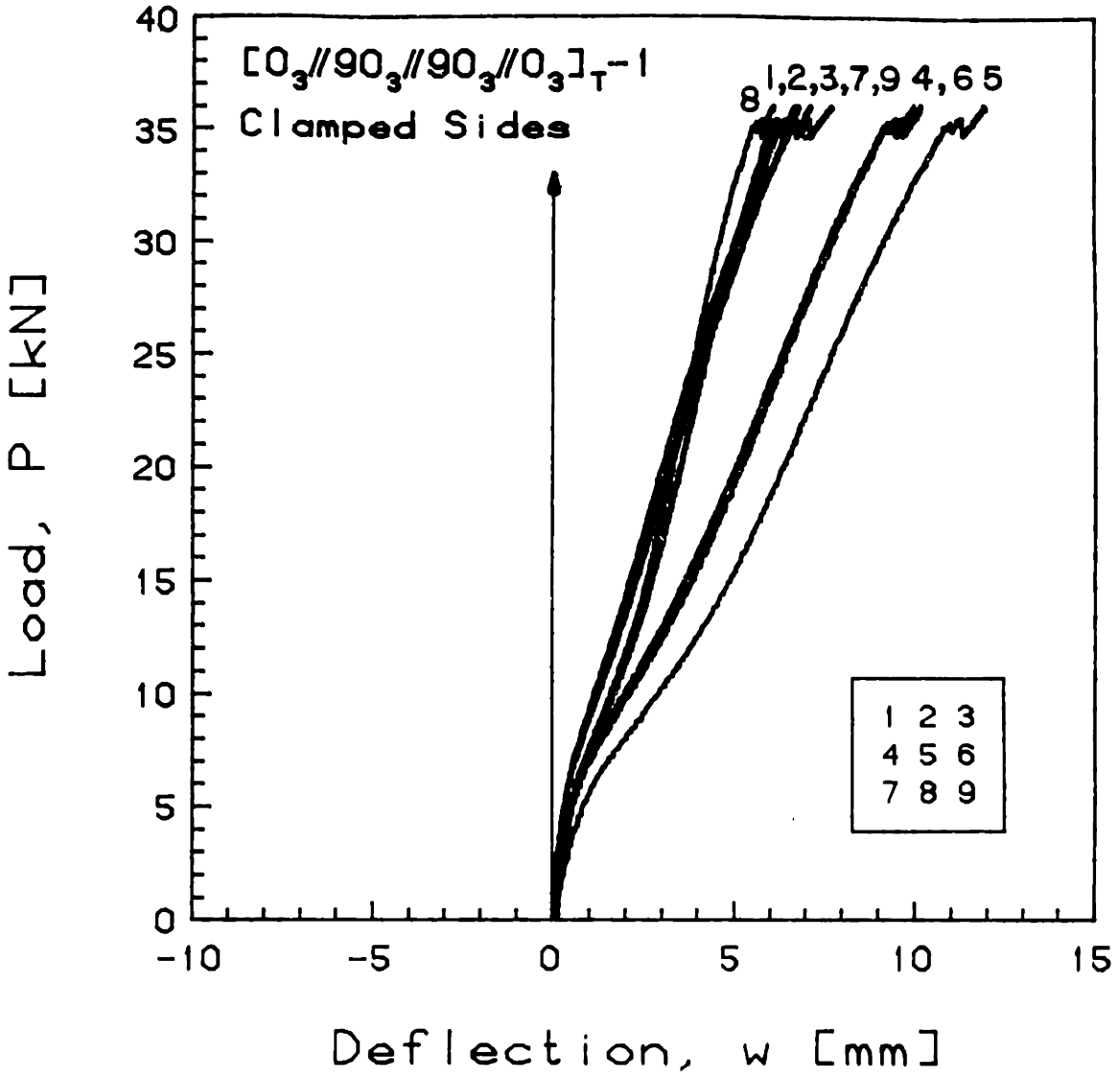

FIGURE E.4 Experimental Plot of Applied Compressive Load versus Out-of-Plane Deflection for the $[0_3//90_3//90_3//0_3]_T$-1 Laminate with Clamped Side Boundary Conditions

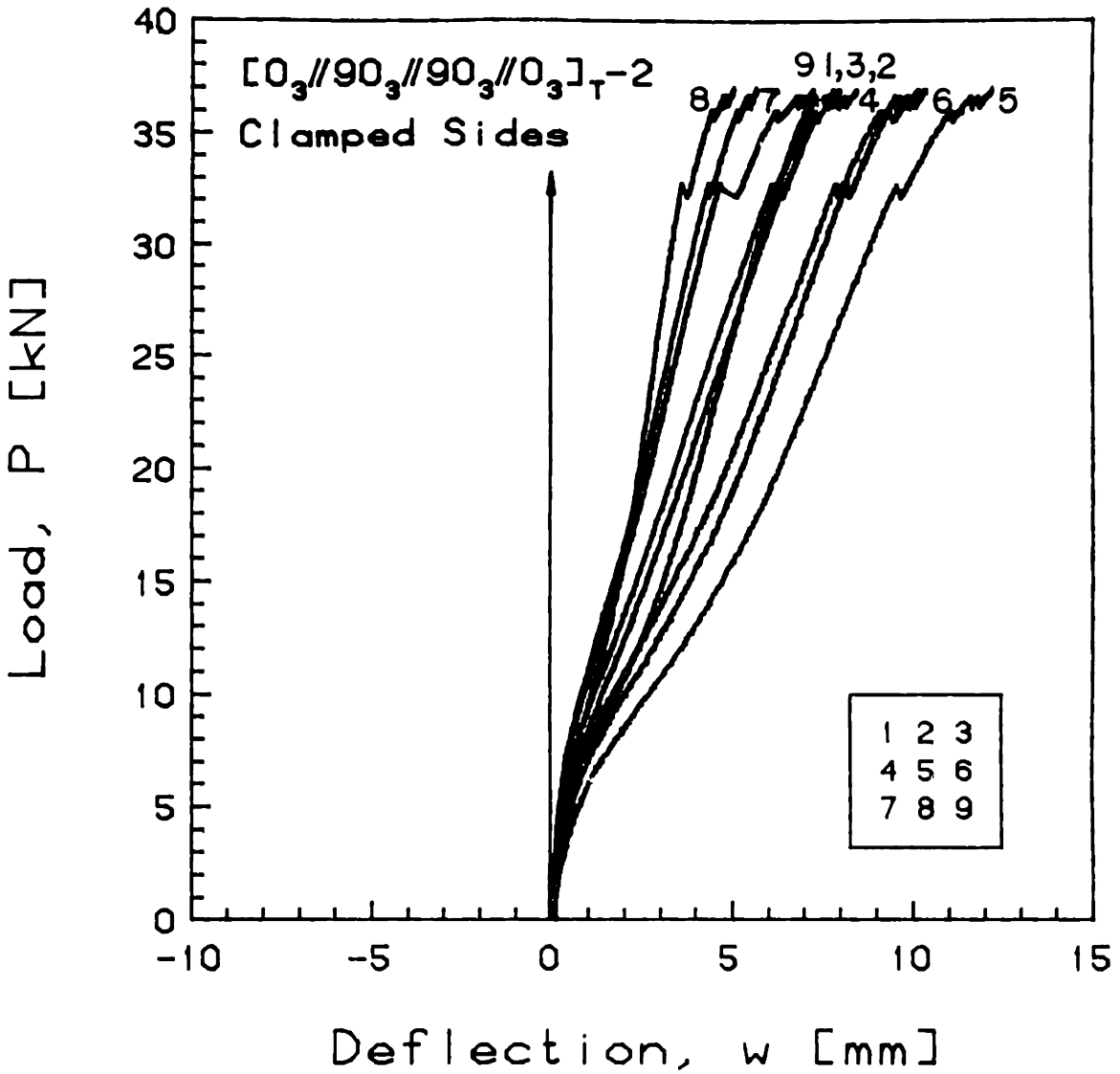

FIGURE E.5 Experimental Plot of Applied Compressive Load versus Out-of-Plane Deflection for the $[O_3//90_3//90_3//O_3]_T$-2 Laminate with Clamped Side Boundary Conditions

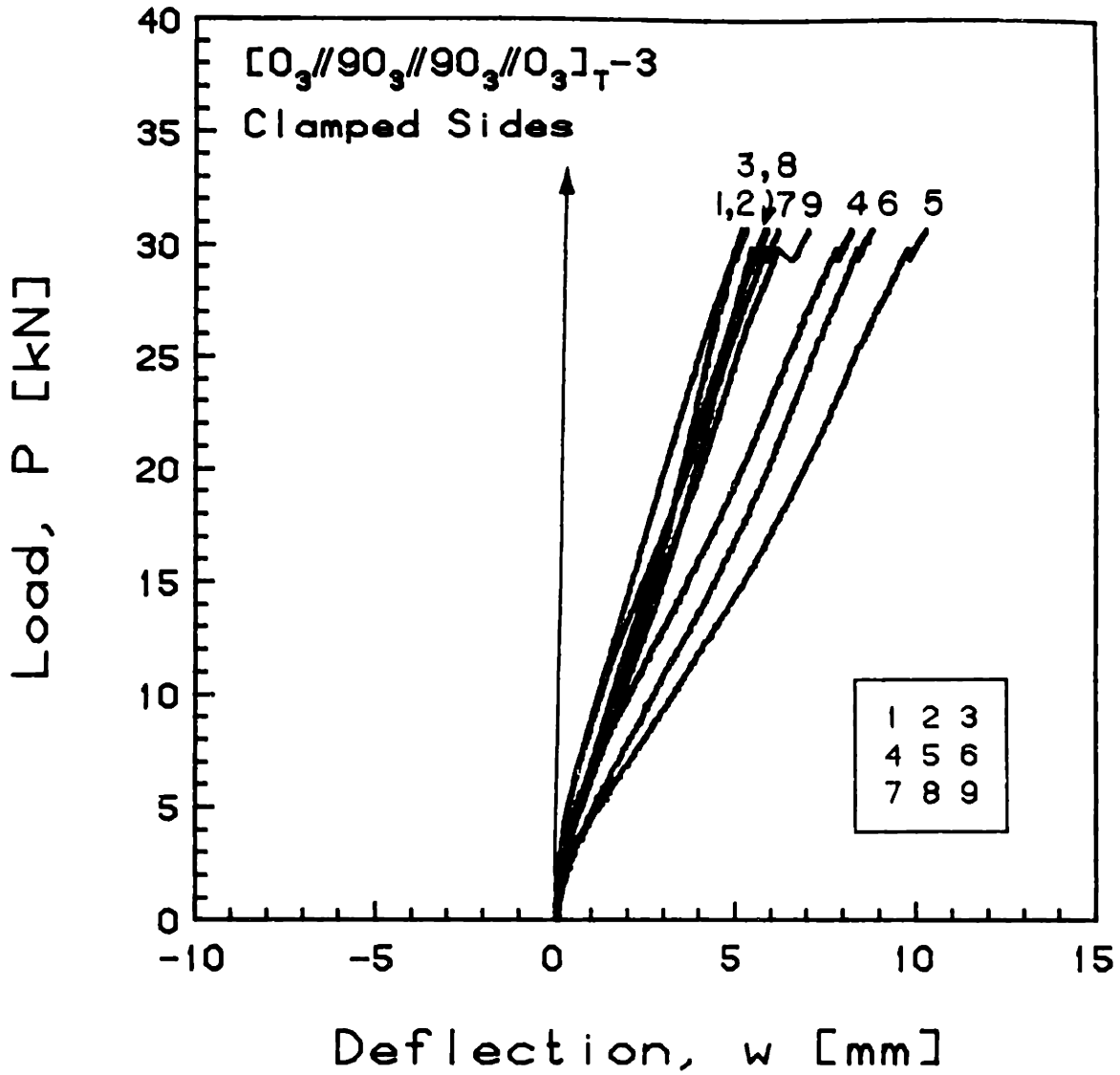

FIGURE E.6 Experimental Plot of Applied Compressive Load versus Out-of-Plane Deflection for the $[O_3//90_3//90_3//O_3]_T$-3 Laminate with Clamped Side Boundary Conditions

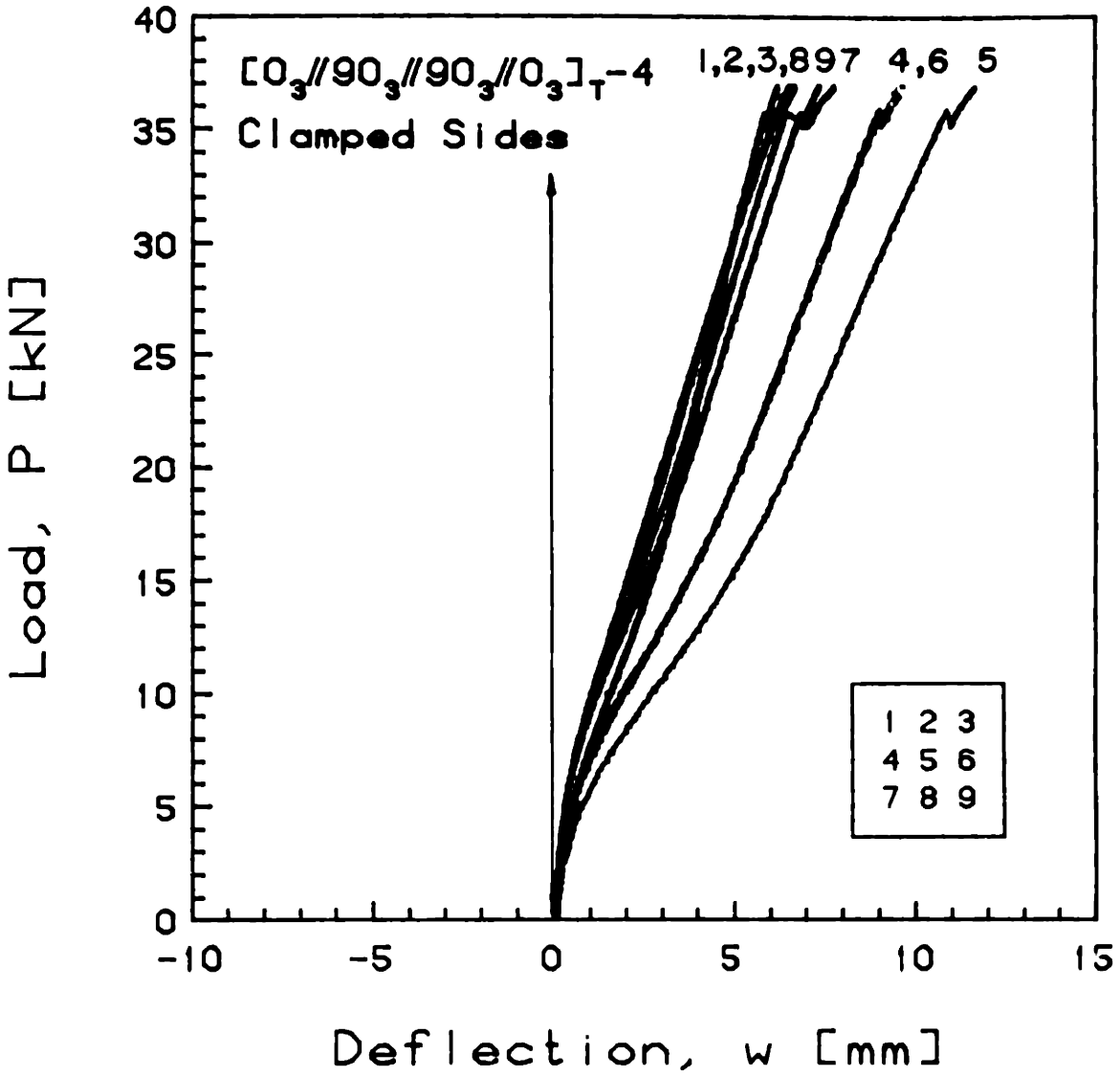

FIGURE E.7 Experimental Plot of Applied Compressive Load versus Out-of-Plane Deflection for the $[0_3//90_3//90_3//0_3]_T$-4 Laminate with Clamped Side Boundary Conditions

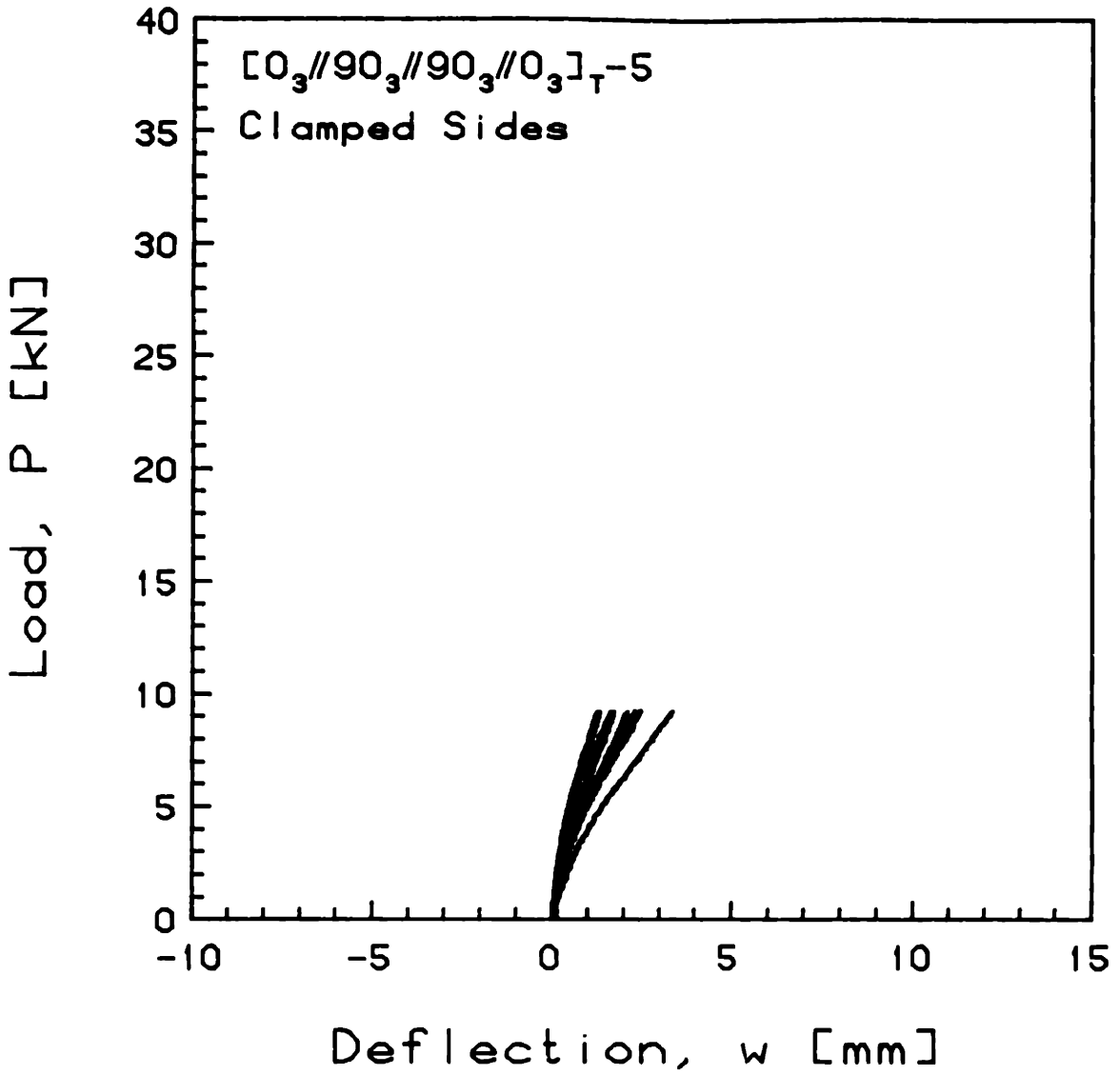

FIGURE E.8 Experimental Phase I Plot of Applied Compressive Load versus Out-of-Plane Deflection for the $[0_3//90_3//90_3//0_3]_T$-5 Laminate with Clamped Side Boundary Conditions

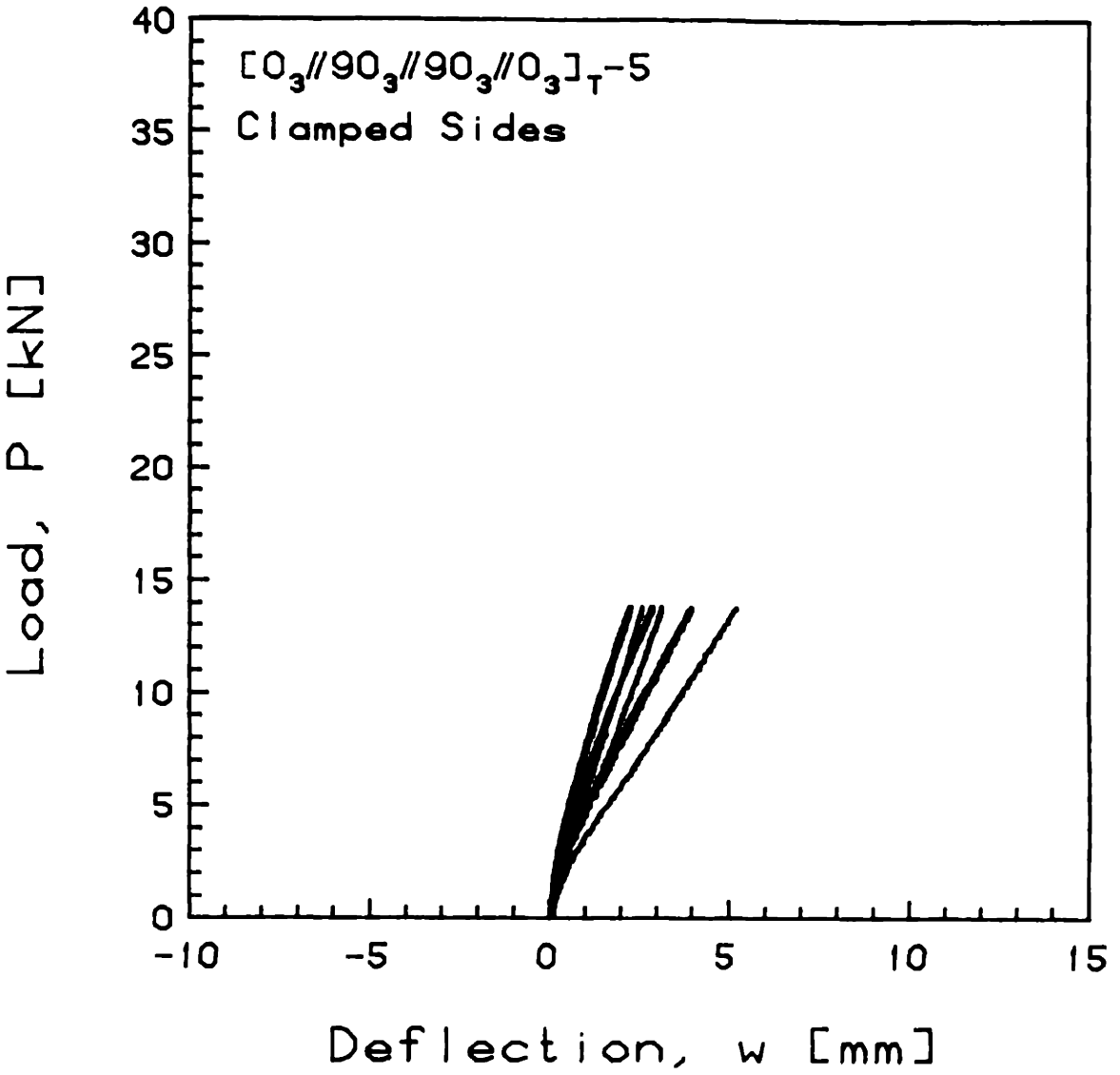

FIGURE E.9 Experimental Phase II Plot of Applied Compressive Load versus Out-of-Plane Deflection for the $[O_3//90_3//90_3//O_3]_T$-5 Laminate with Clamped Side Boundary Conditions

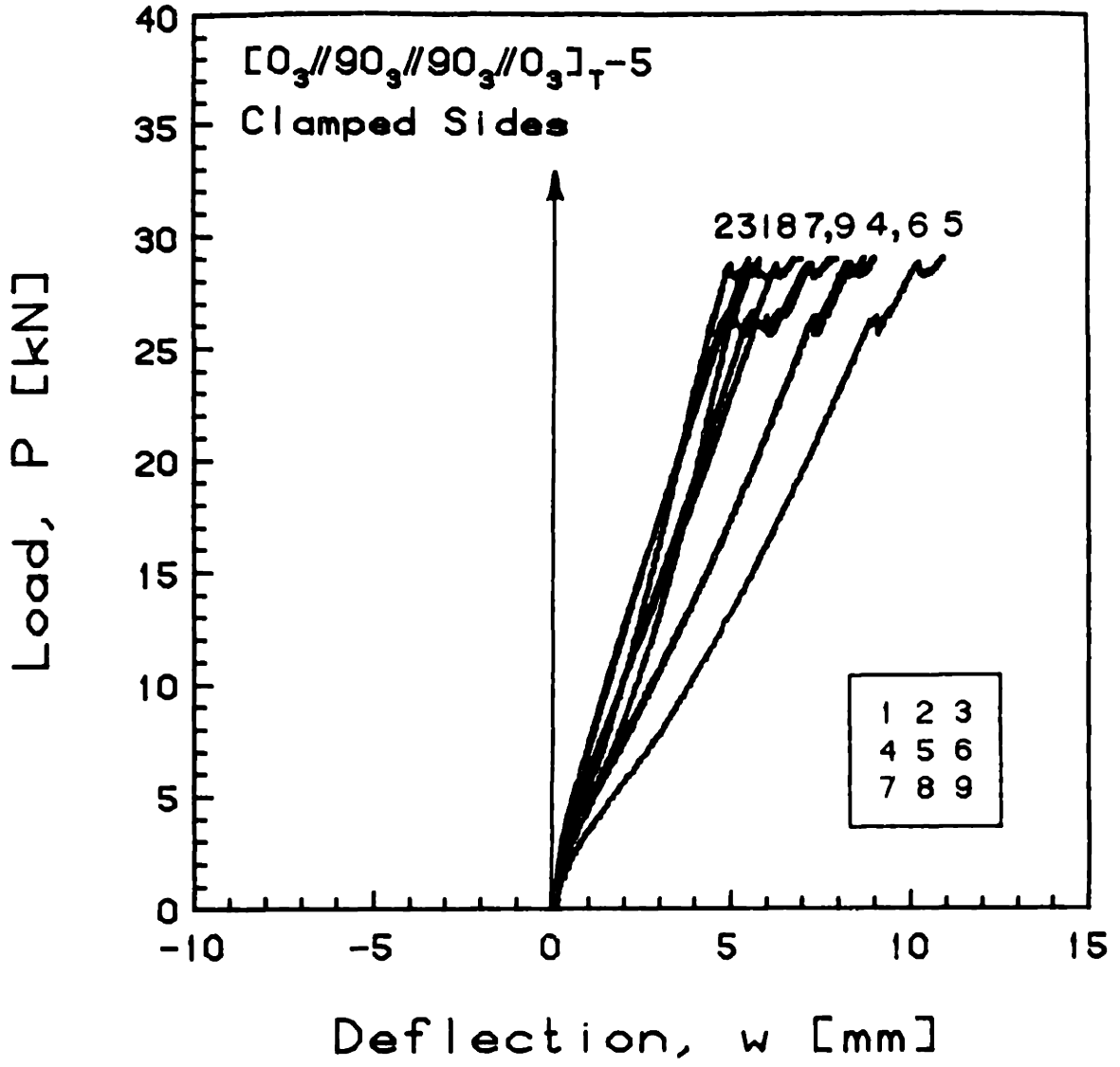

FIGURE E.10 Experimental Phase III Plot of Applied Compressive Load versus Out-of-Plane Deflection for the $[0_3//90_3//90_3//0_3]_T$-5 Laminate with Clamped Side Boundary Conditions

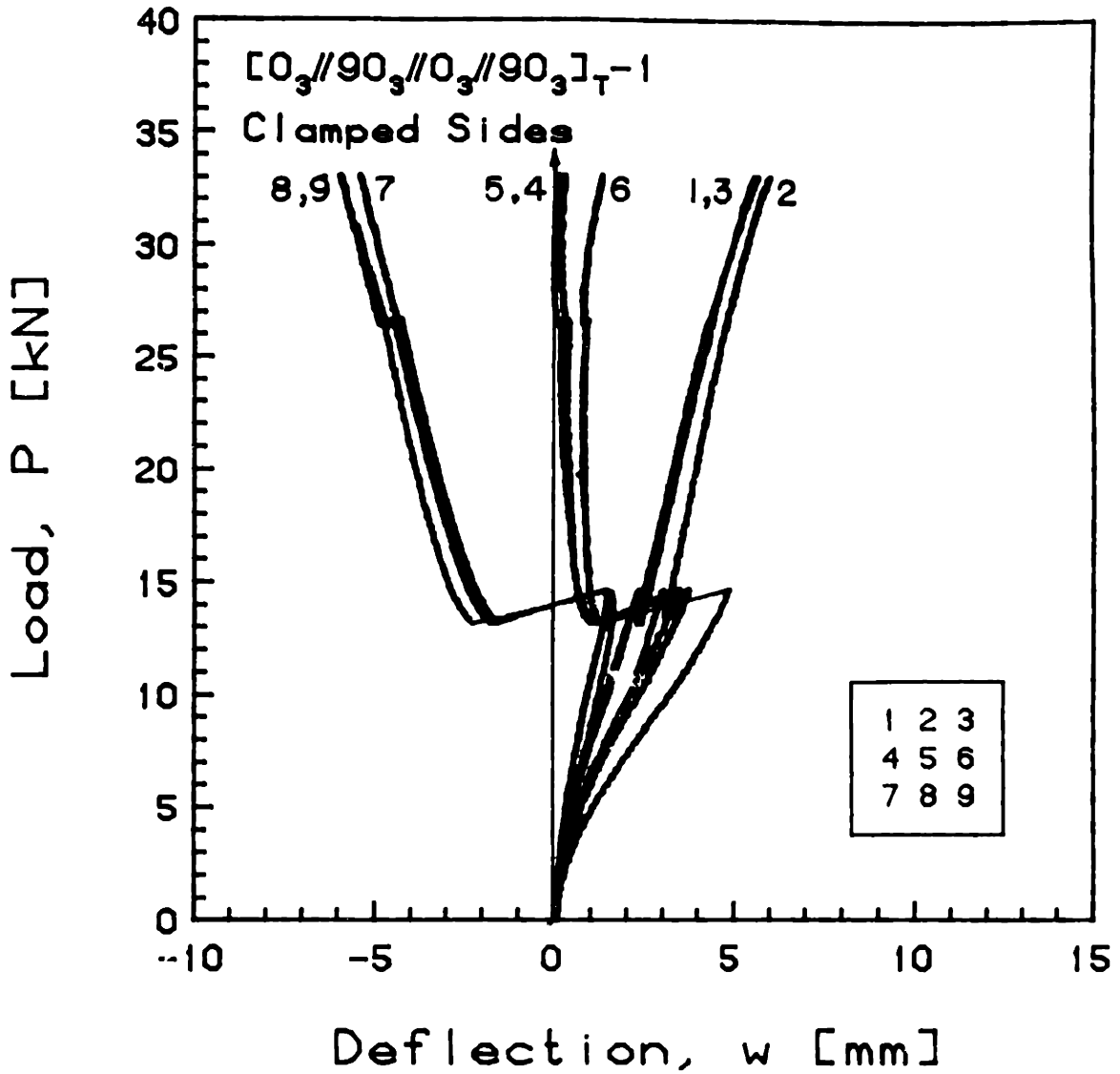

FIGURE E.11 Experimental Plot of Applied Compressive Load versus Out-of-Plane Deflection for the $[0_3//90_3//0_3//90_3]_T$-1 Laminate with Clamped Side Boundary Conditions

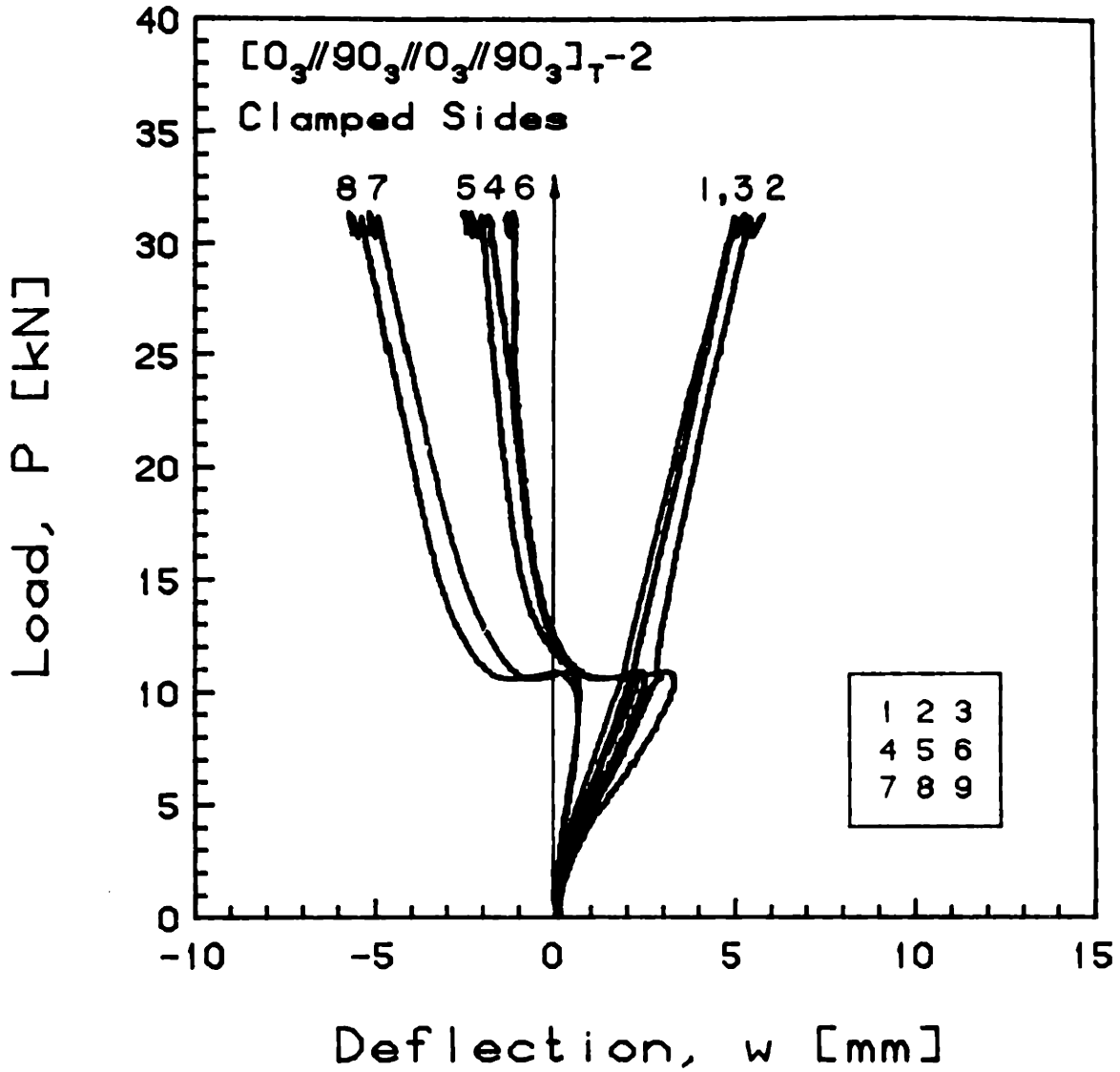

FIGURE E.12 Experimental Plot of Applied Compressive Load versus Out-of-Plane Deflection for the $[0_3//90_3//0_3//90_3]_T$-2 Laminate with Clamped Side Boundary Conditions

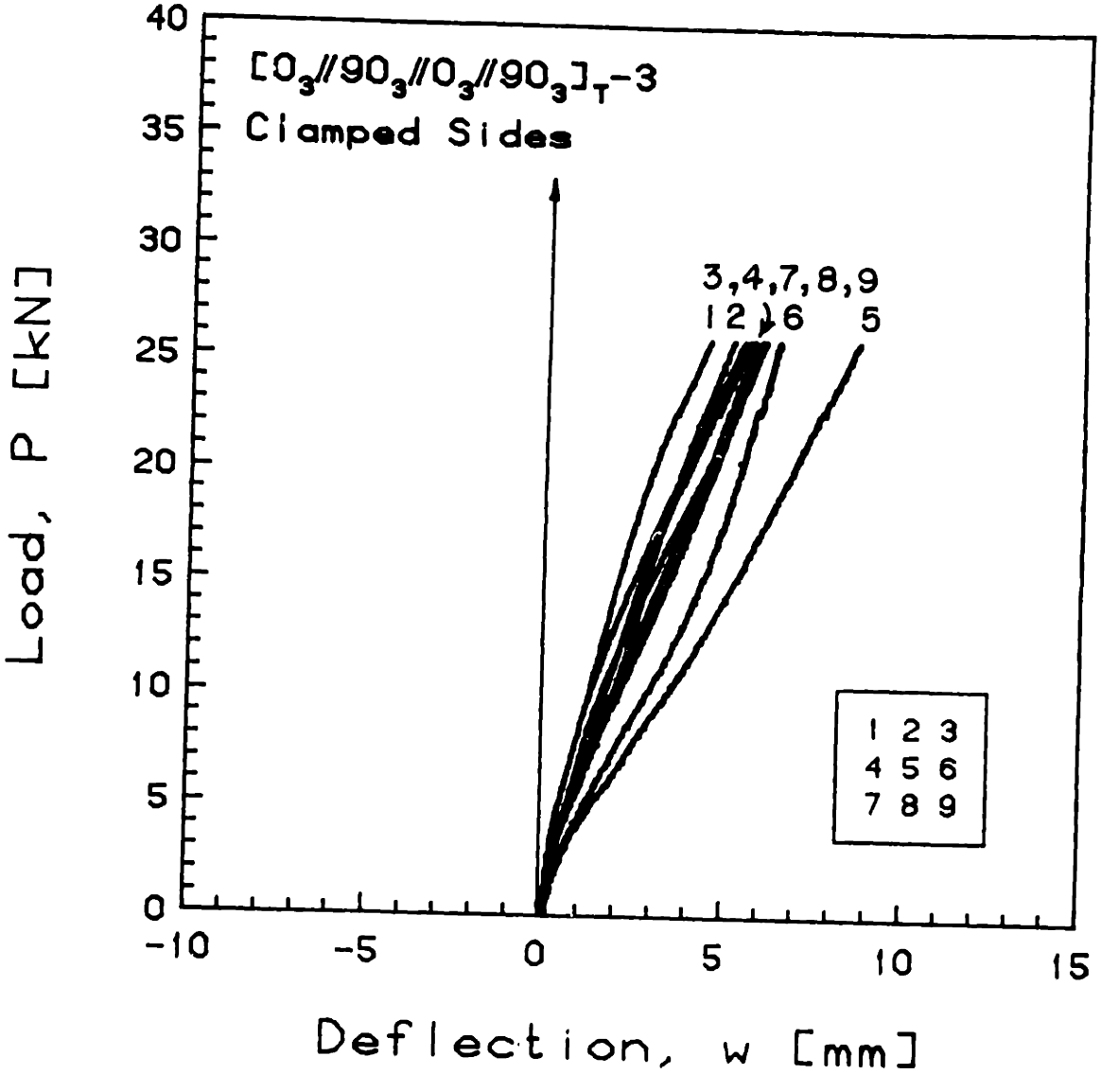

FIGURE E.13 Experimental Plot of Applied Compressive Load versus Out-of-Plane Deflection for the $[O_3//90_3//O_3//90_3]_T$-3 Laminate with Clamped Side Boundary Conditions

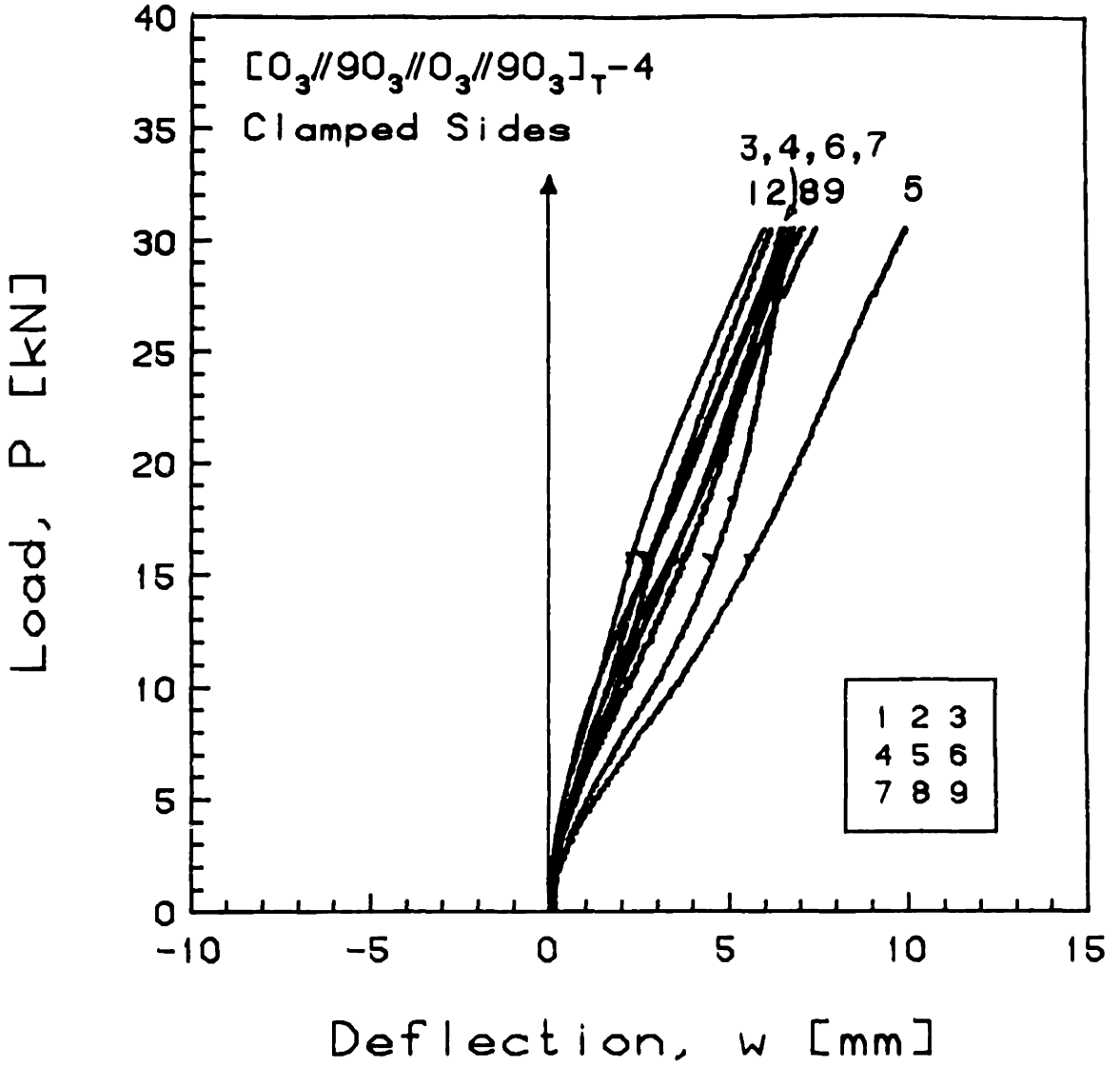

FIGURE E.14 Experimental Plot of Applied Compressive Load versus Out-of-Plane Deflection for the $[0_3//90_3//0_3//90_3]_T$-4 Laminate with Clamped Side Boundary Conditions

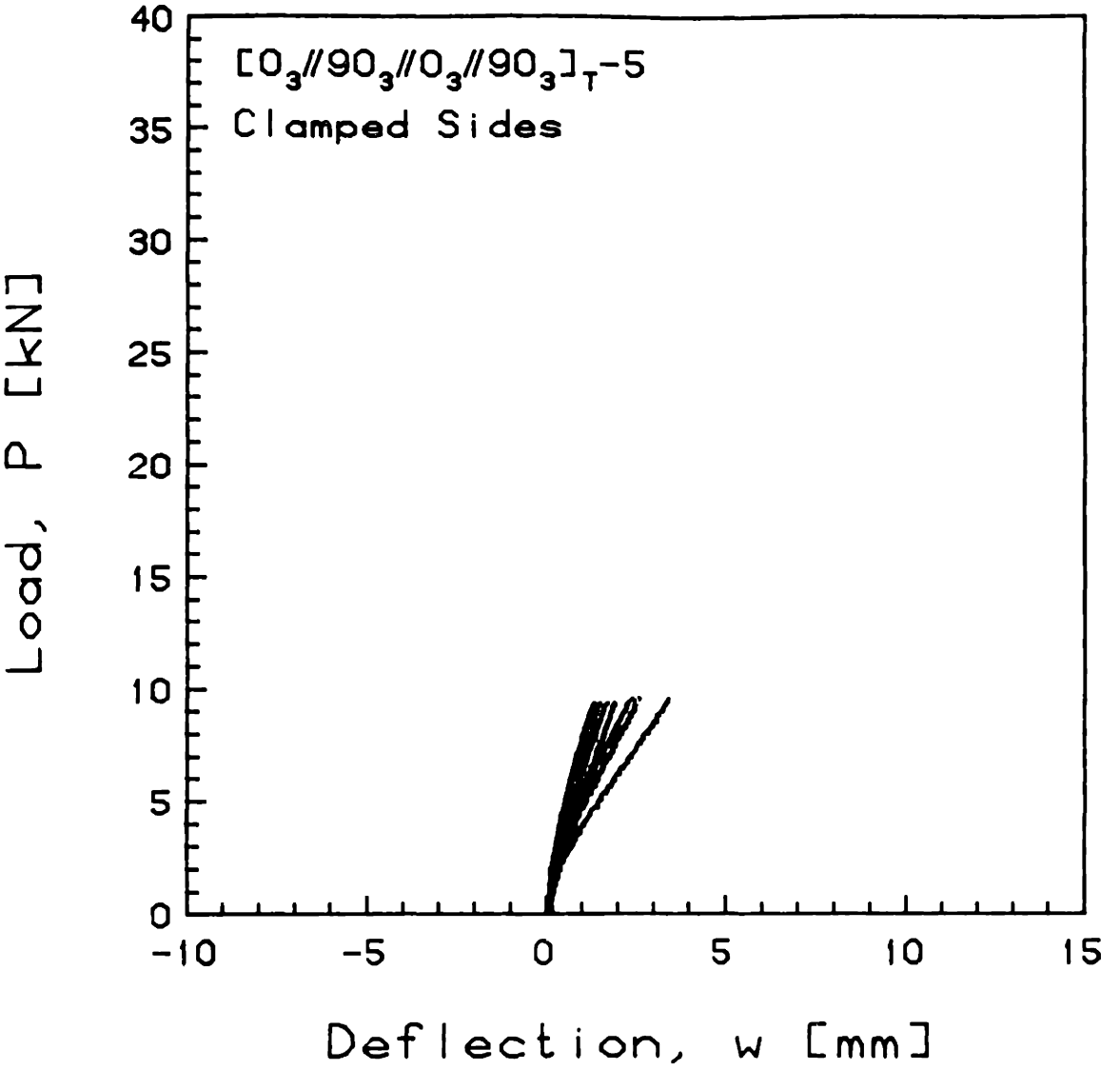

FIGURE E.15 Experimental Phase I Plot of Applied Compressive Load versus Out-of-Plane Deflection for the $[0_3//90_3//0_3//90_3]_T$-5 Laminate with Clamped Side Boundary Conditions

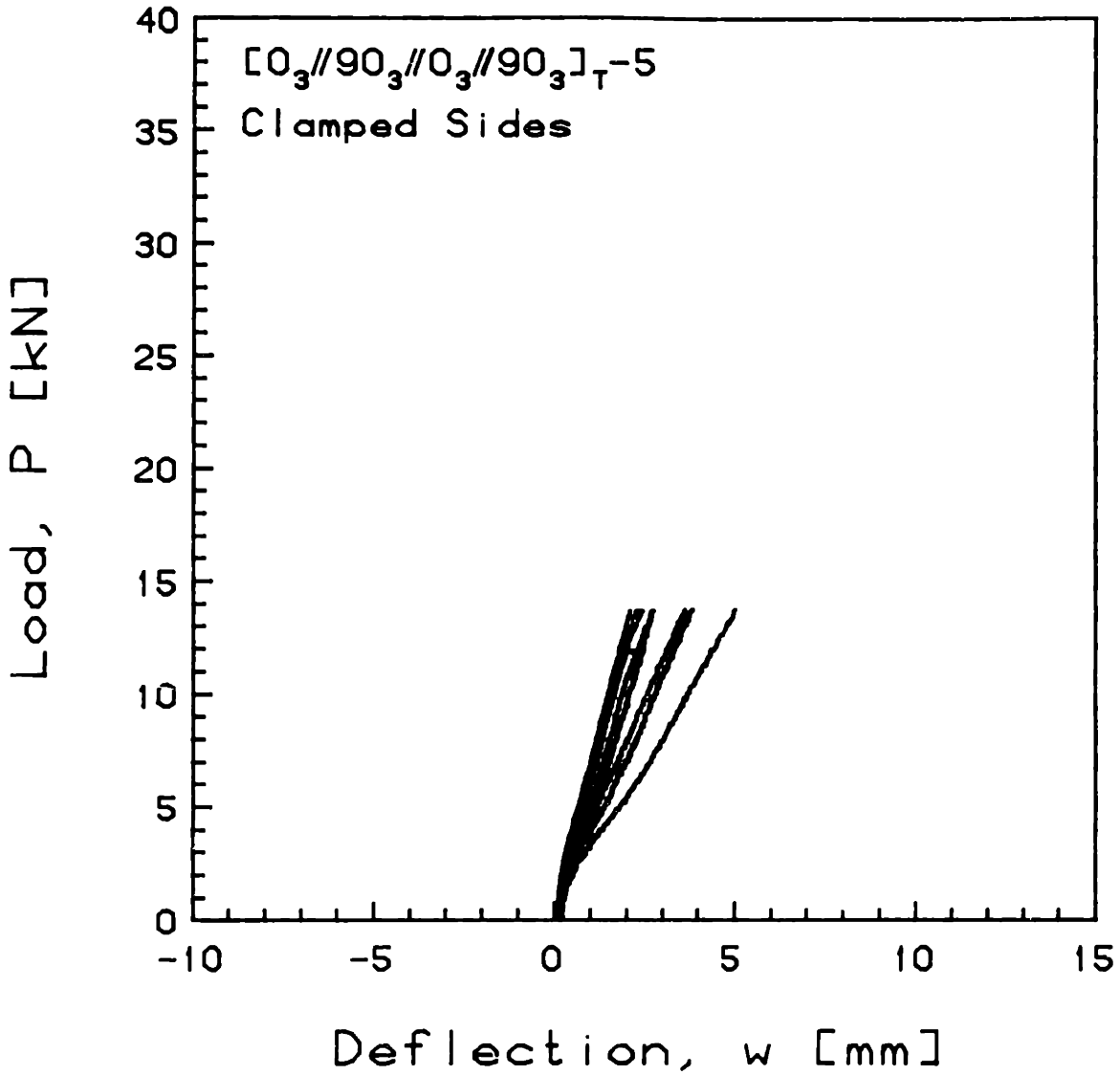

FIGURE E.16 Experimental Phase II Plot of Applied Compressive Load versus Out-of-Plane Deflection for the $[0_3//90_3//0_3//90_3]_T$-5 Laminate with Clamped Side Boundary Conditions

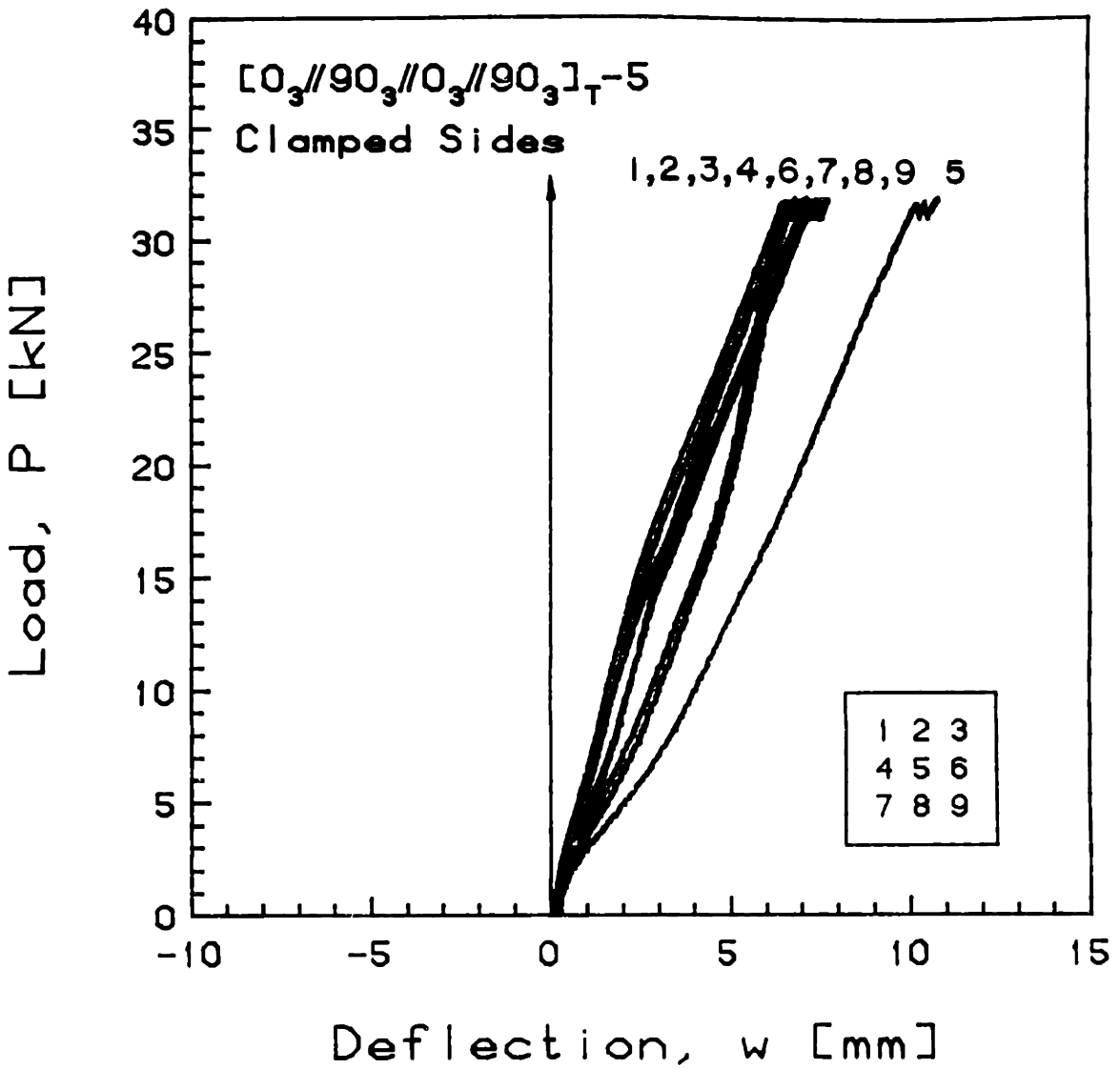

FIGURE E.17 Experimental Phase III Plot of Applied Compressive Load versus Out-of-Plane Deflection for the $[0_3//90_3//0_3//90_3]_T$-5 Laminate with Clamped Side Boundary Conditions

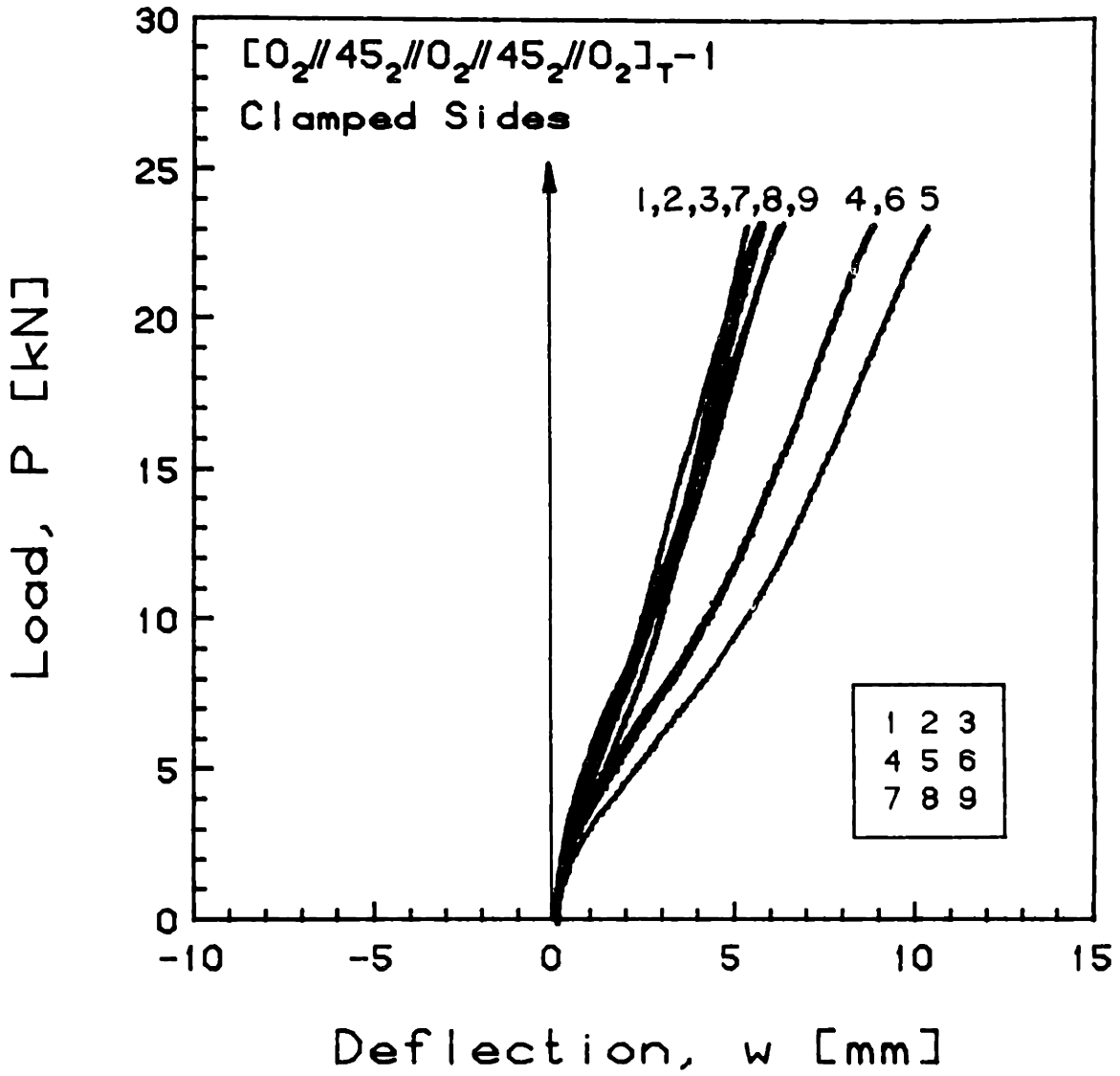

FIGURE E.18 Experimental Plot of Applied Compressive Load versus Out-of-Plane Deflection for the $[0_2//45_2//0_2//45_2//0_2]_T$-1 Laminate with Clamped Side Boundary Conditions

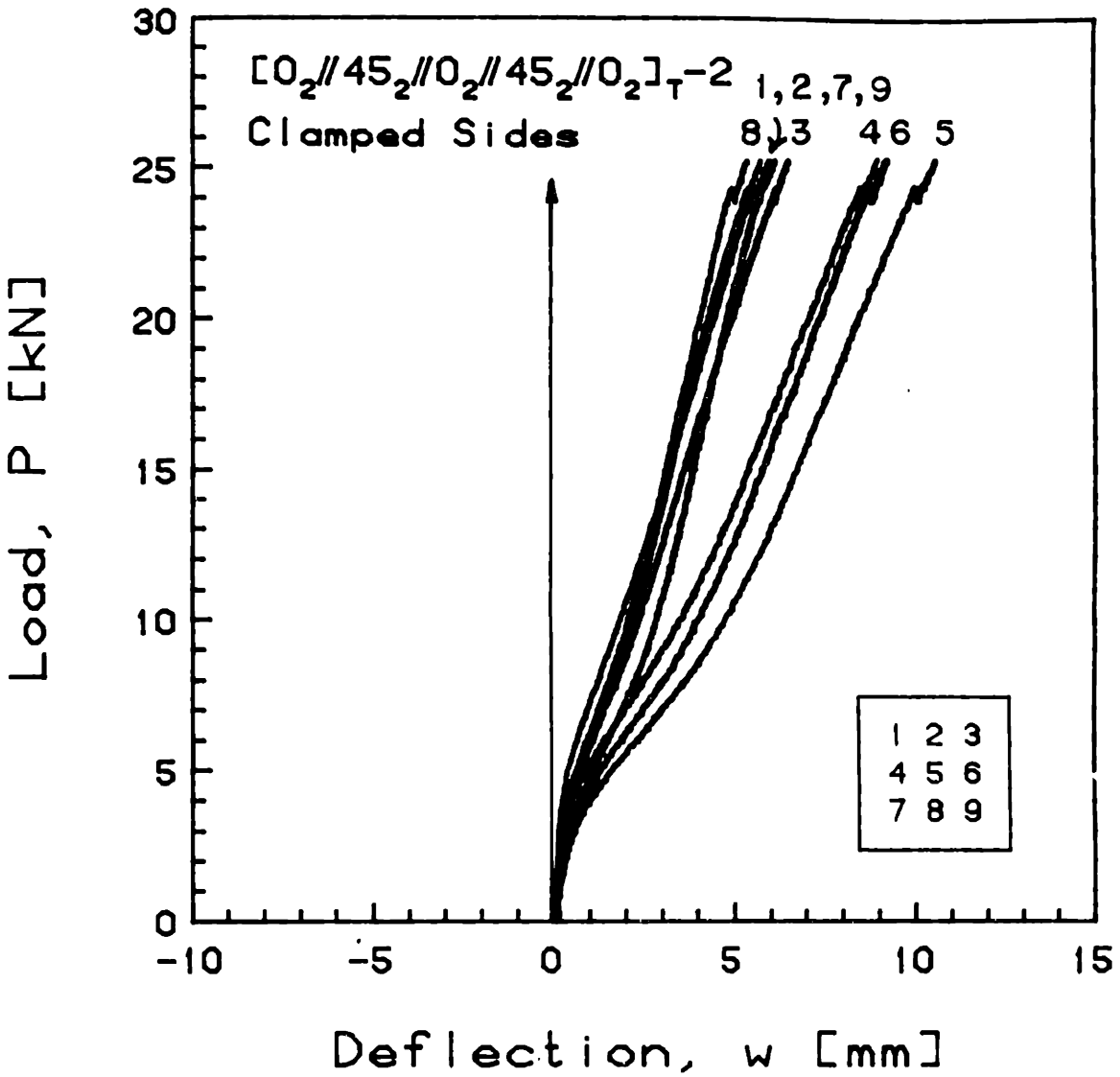

FIGURE E.19 Experimental Plot of Applied Compressive Load versus Out-of-Plane Deflection for the $[O_2//45_2//O_2//45_2//O_2]_T$-2 Laminate with Clamped Side Boundary Conditions

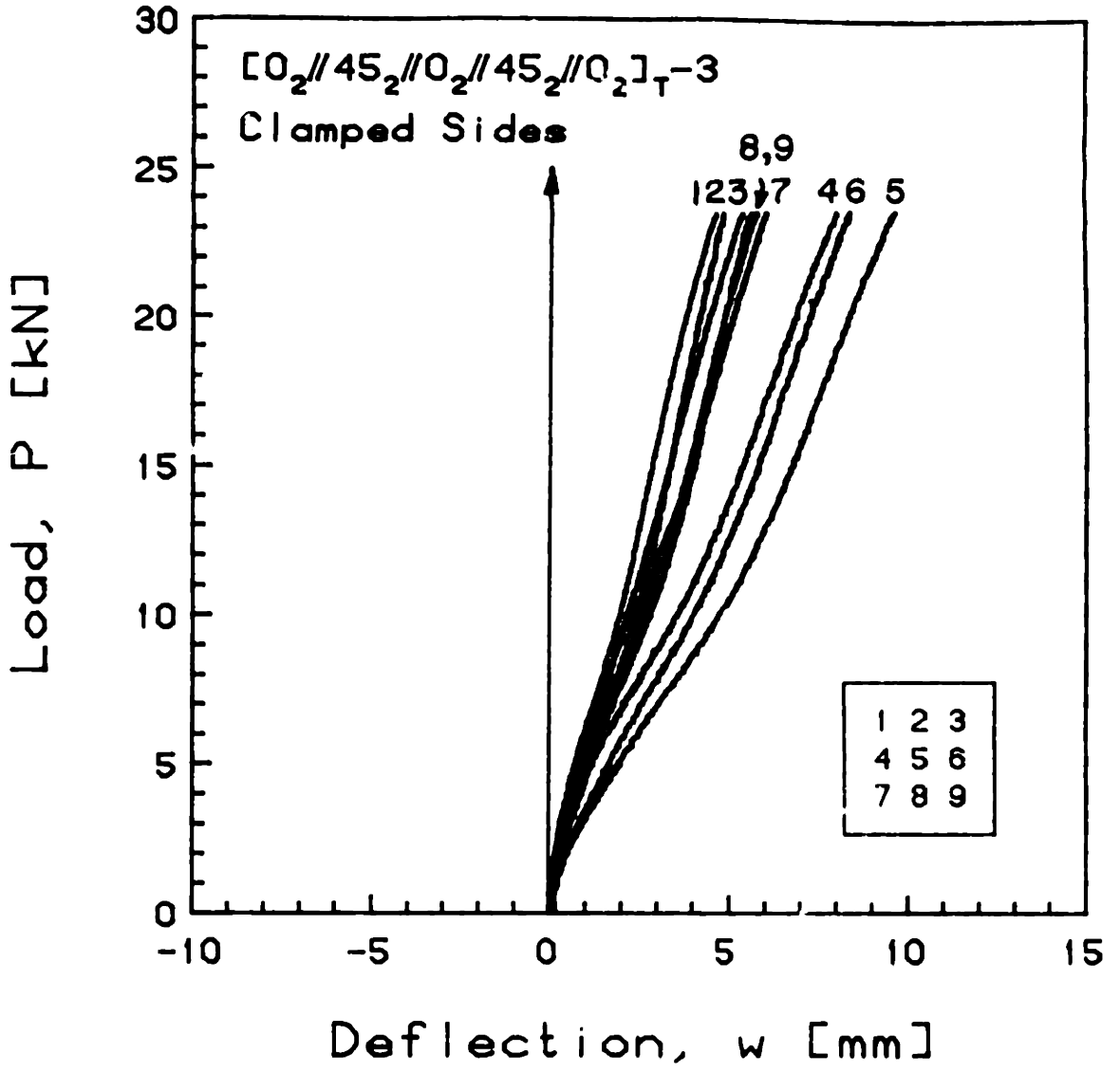

FIGURE E.20 Experimental Plot of Applied Compressive Load versus Out-of-Plane Deflection for the $[O_2//45_2//O_2//45_2//O_2]_T$-3 Laminate with Clamped Side Boundary Conditions

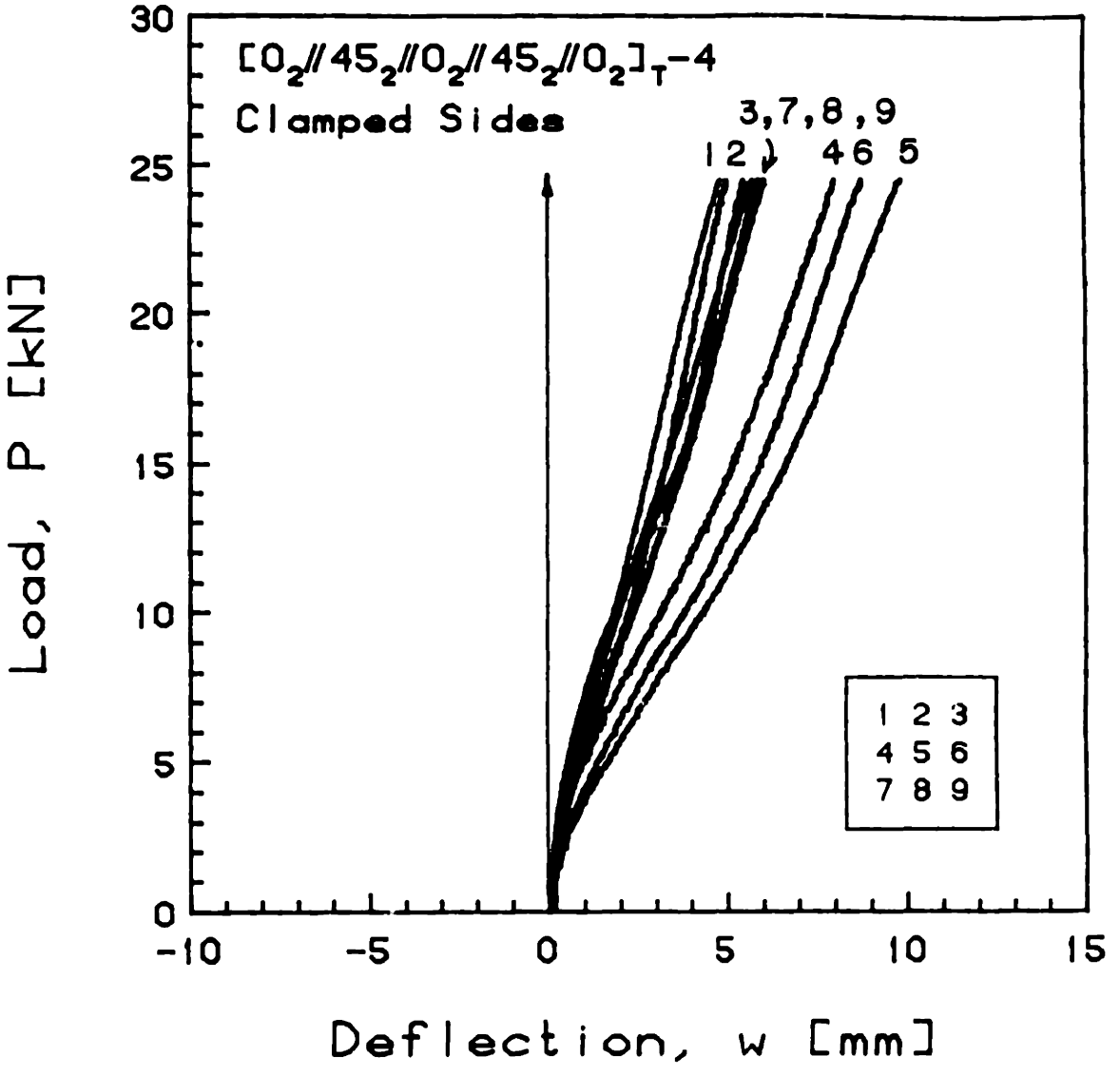

FIGURE E.21 Experimental Plot of Applied Compressive Load versus Out-of-Plane Deflection for the $[0_2//45_2//0_2//45_2//0_2]_T$-4 Laminate with Clamped Side Boundary Conditions

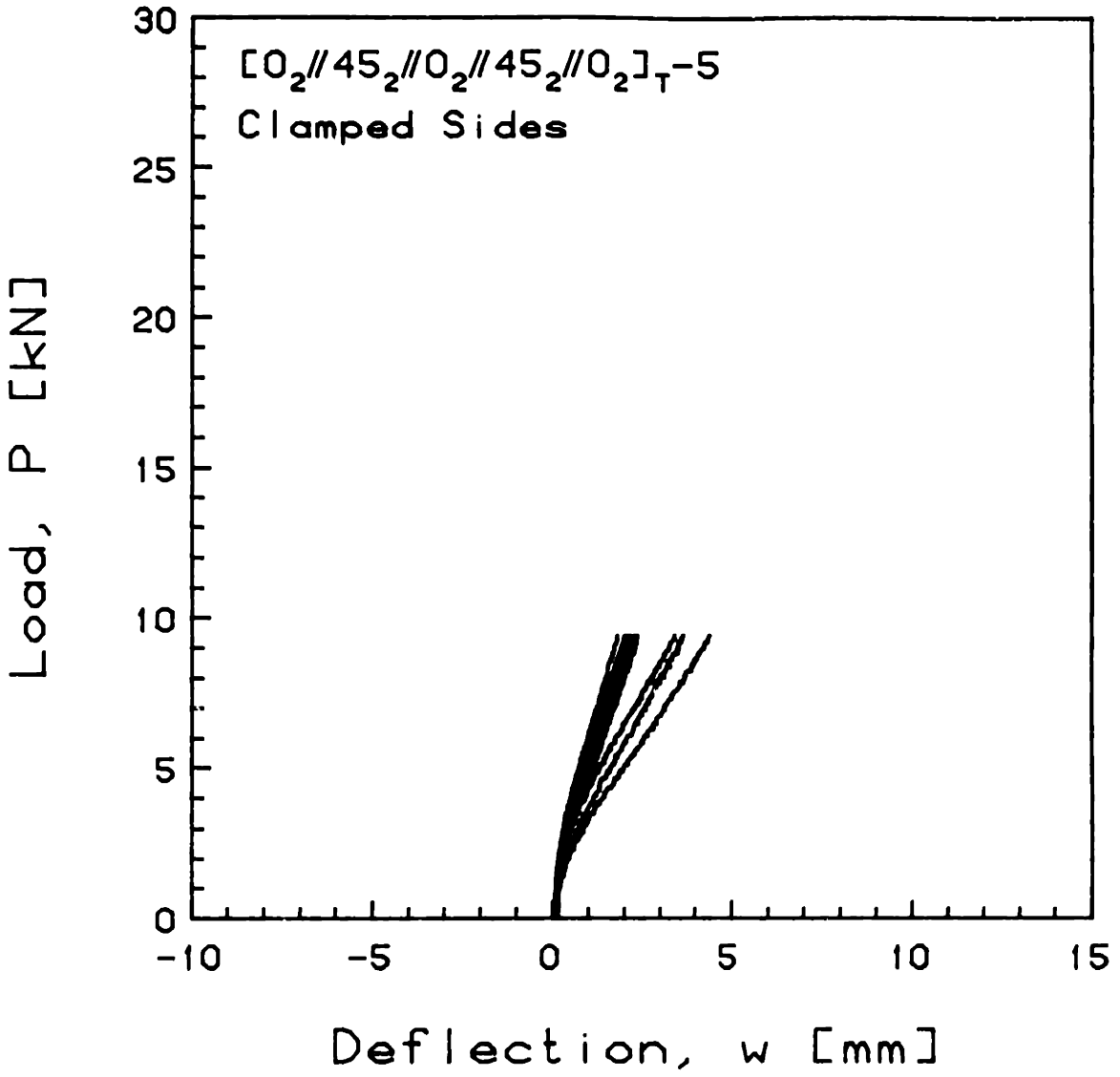

FIGURE E.22 Experimental Phase I Plot of Applied Compressive Load versus Out-of-Plane Deflection for the $[O_2//45_2//O_2//45_2//O_2]_T$-5 Laminate with Clamped Side Boundary Conditions

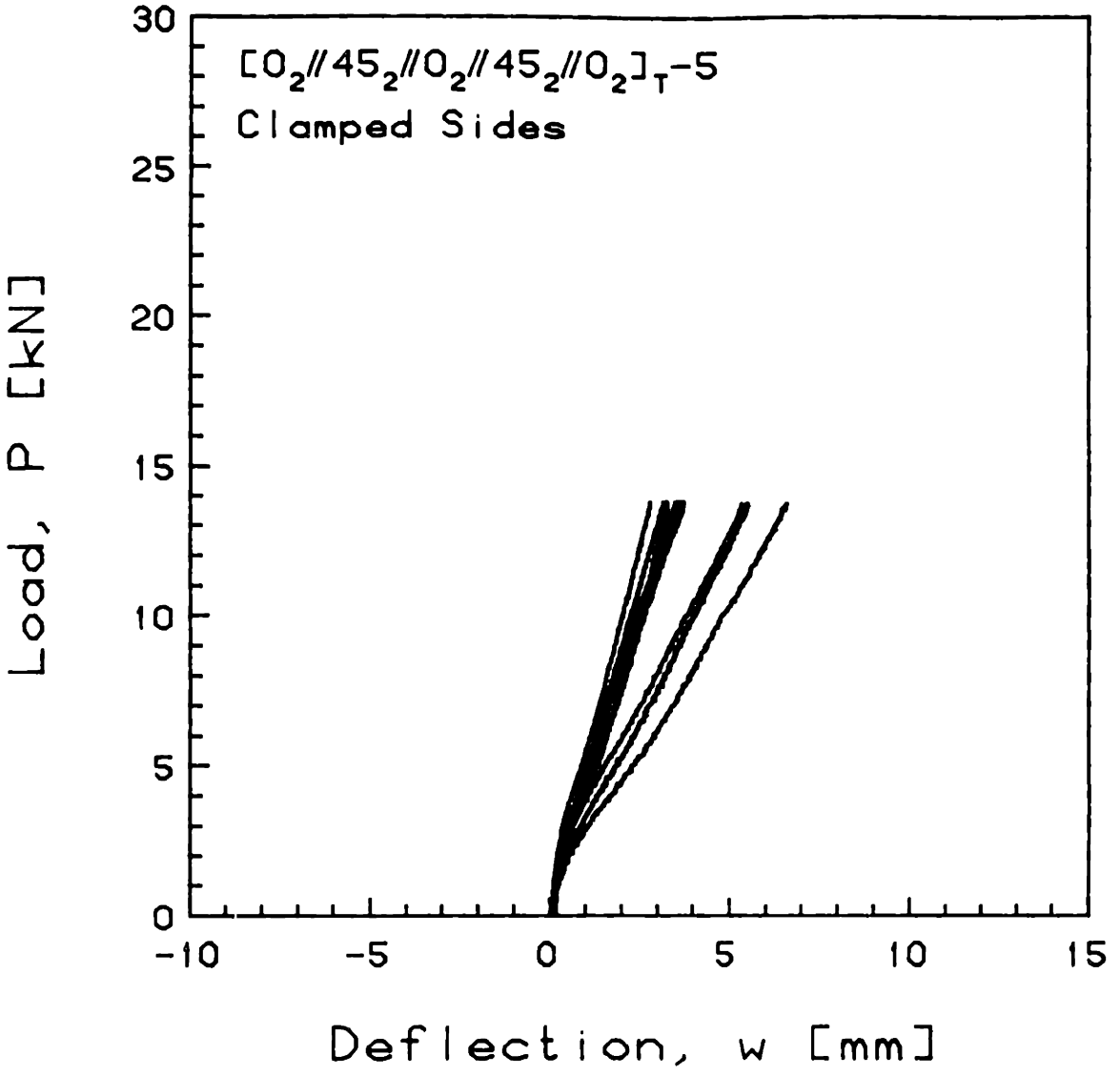

FIGURE E.23 Experimental Phase II Plot of Applied Compressive Load versus Out-of-Plane Deflection for the $[0_2//45_2//0_2//45_2//0_2]_T$-5 Laminate with Clamped Side Boundary Conditions

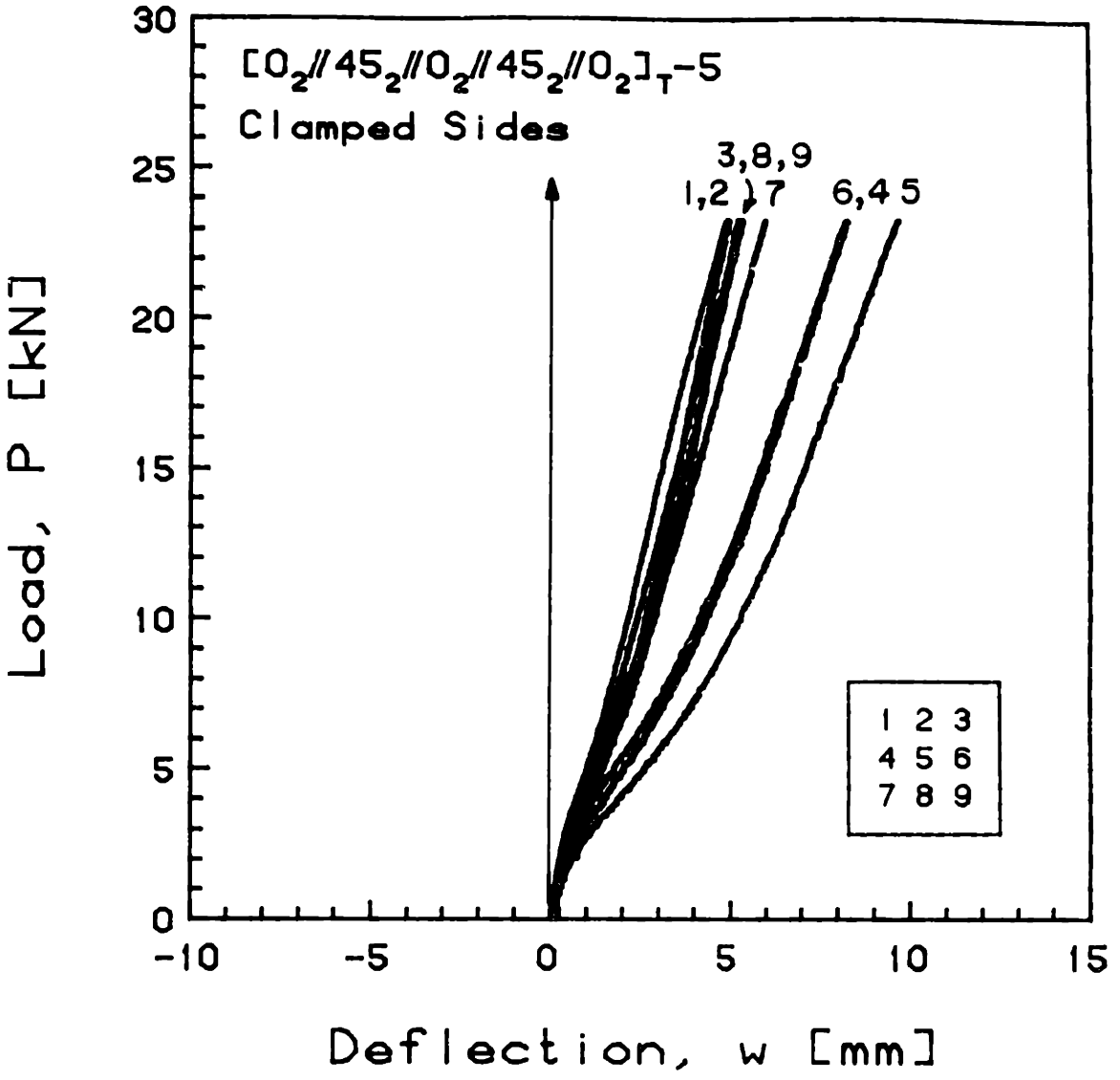

FIGURE E.24 Experimental Phase III Plot of Applied Compressive Load versus Out-of-Plane Deflection for the $[0_2//45_2//0_2//45_2//0_2]_T$-5 Laminate with Clamped Side Boundary Conditions

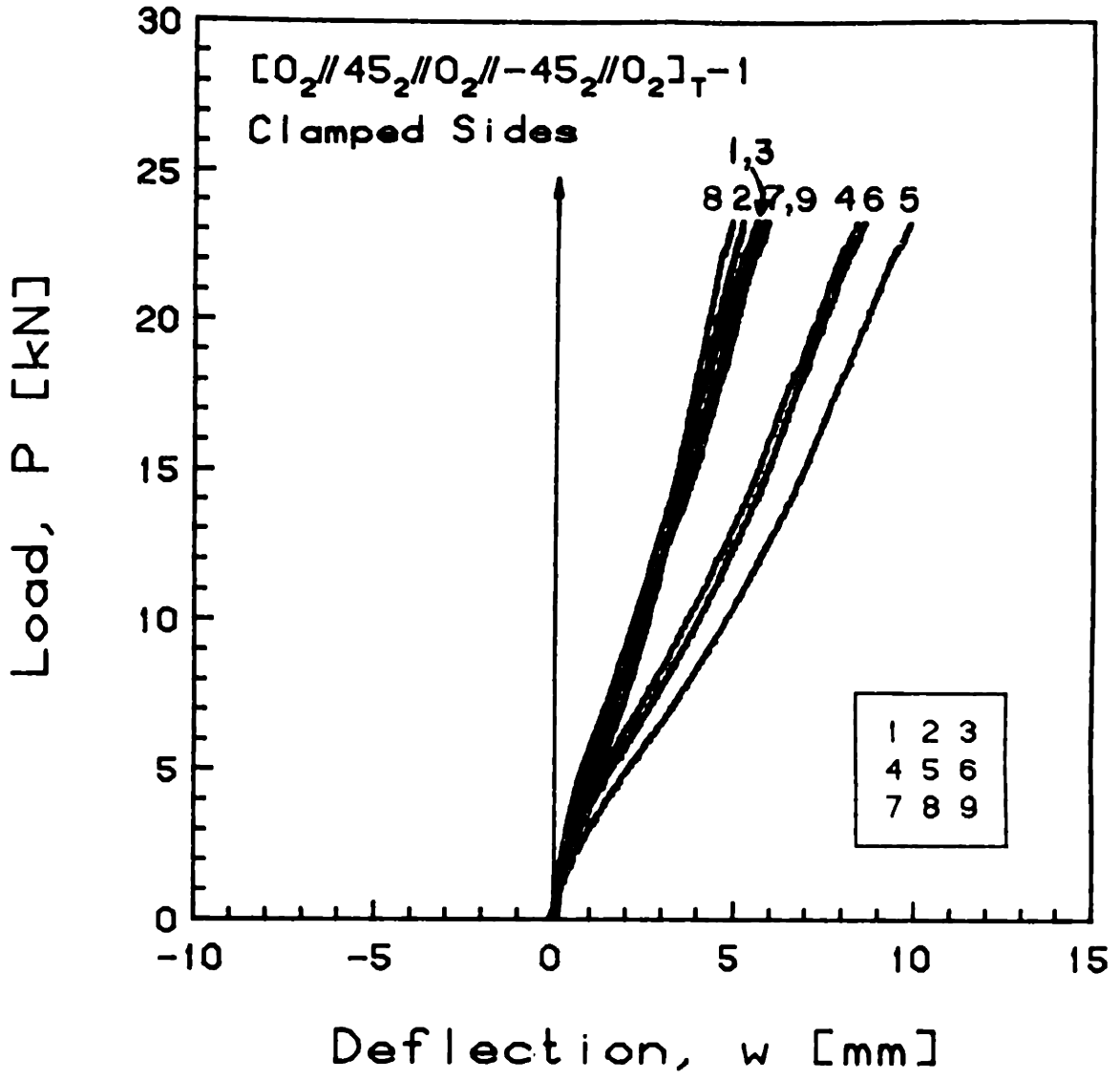

FIGURE E.25 Experimental Plot of Applied Compressive Load versus Out-of-Plane Deflection for the $[0_2//45_2//0_2//-45_2//0_2]_T$-1 Laminate with Clamped Side Boundary Conditions

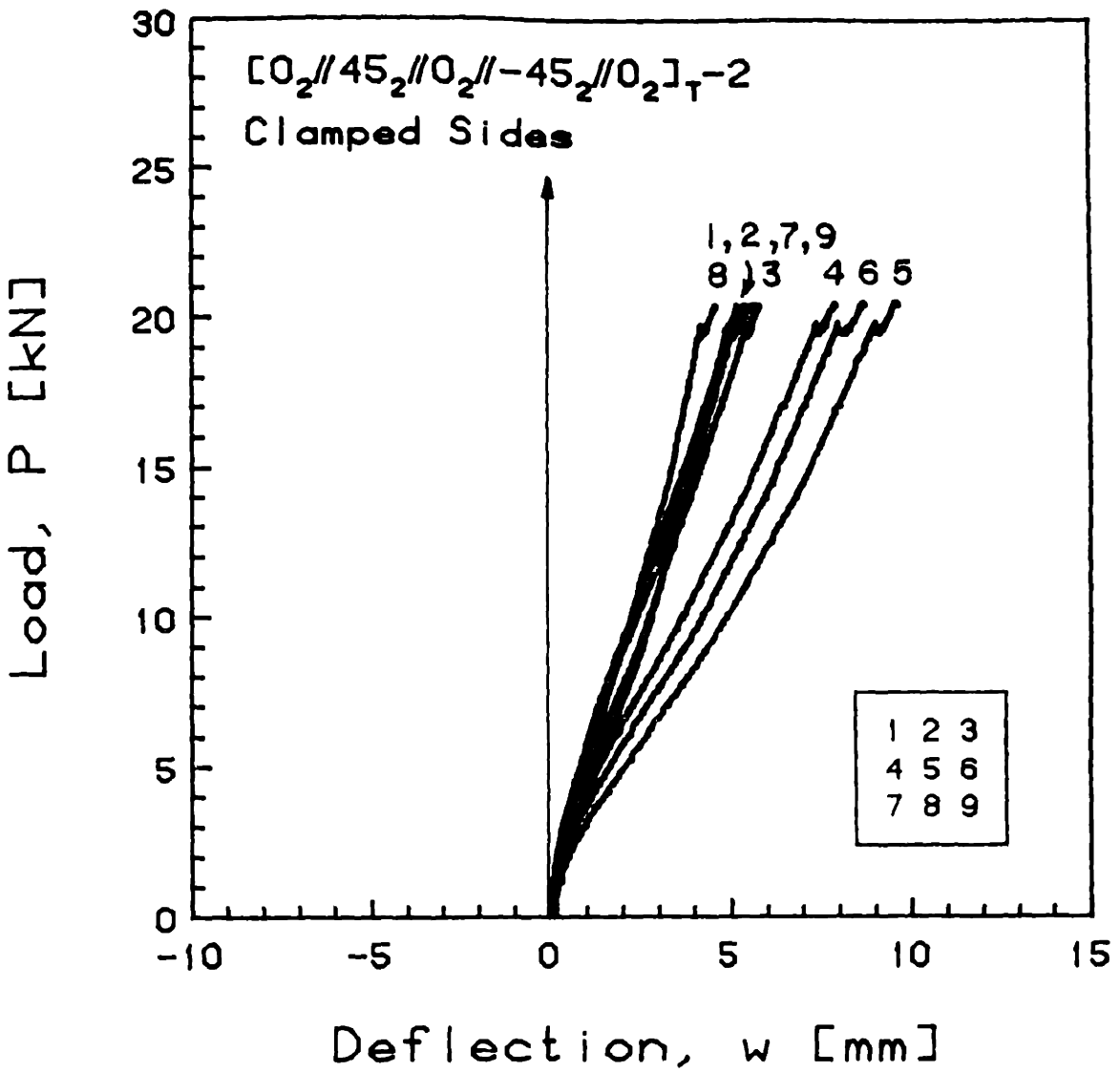

FIGURE E.26 Experimental Plot of Applied Compressive Load versus Out-of-Plane Deflection for the $[O_2//45_2//O_2//-45_2//O_2]_T$-2 Laminate with Clamped Side Boundary Conditions

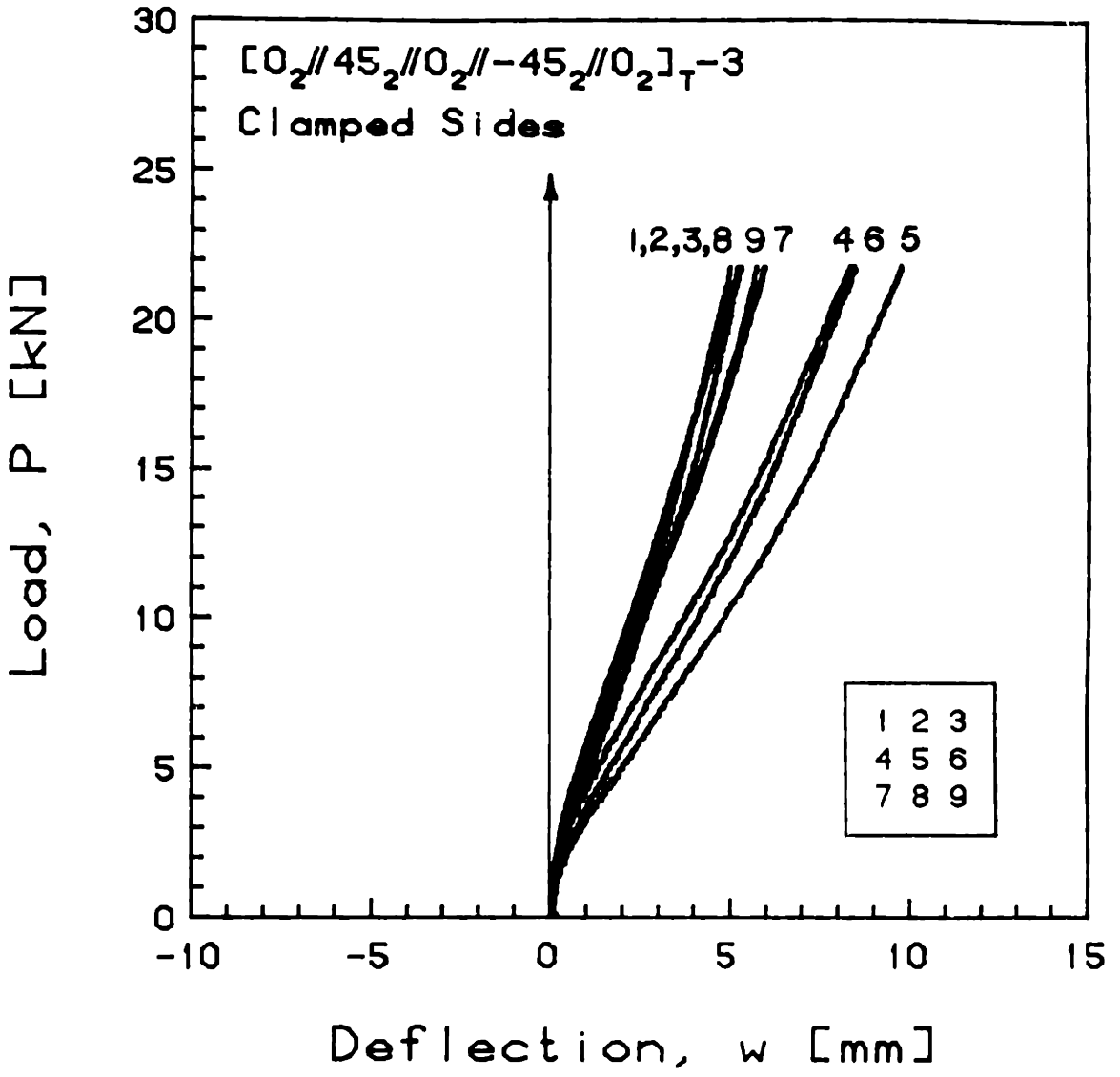

FIGURE E.27 Experimental Plot of Applied Compressive Load versus Out-of-Plane Deflection for the $[0_2//45_2//0_2//-45_2//0_2]_T$-3 Laminate with Clamped Side Boundary Conditions

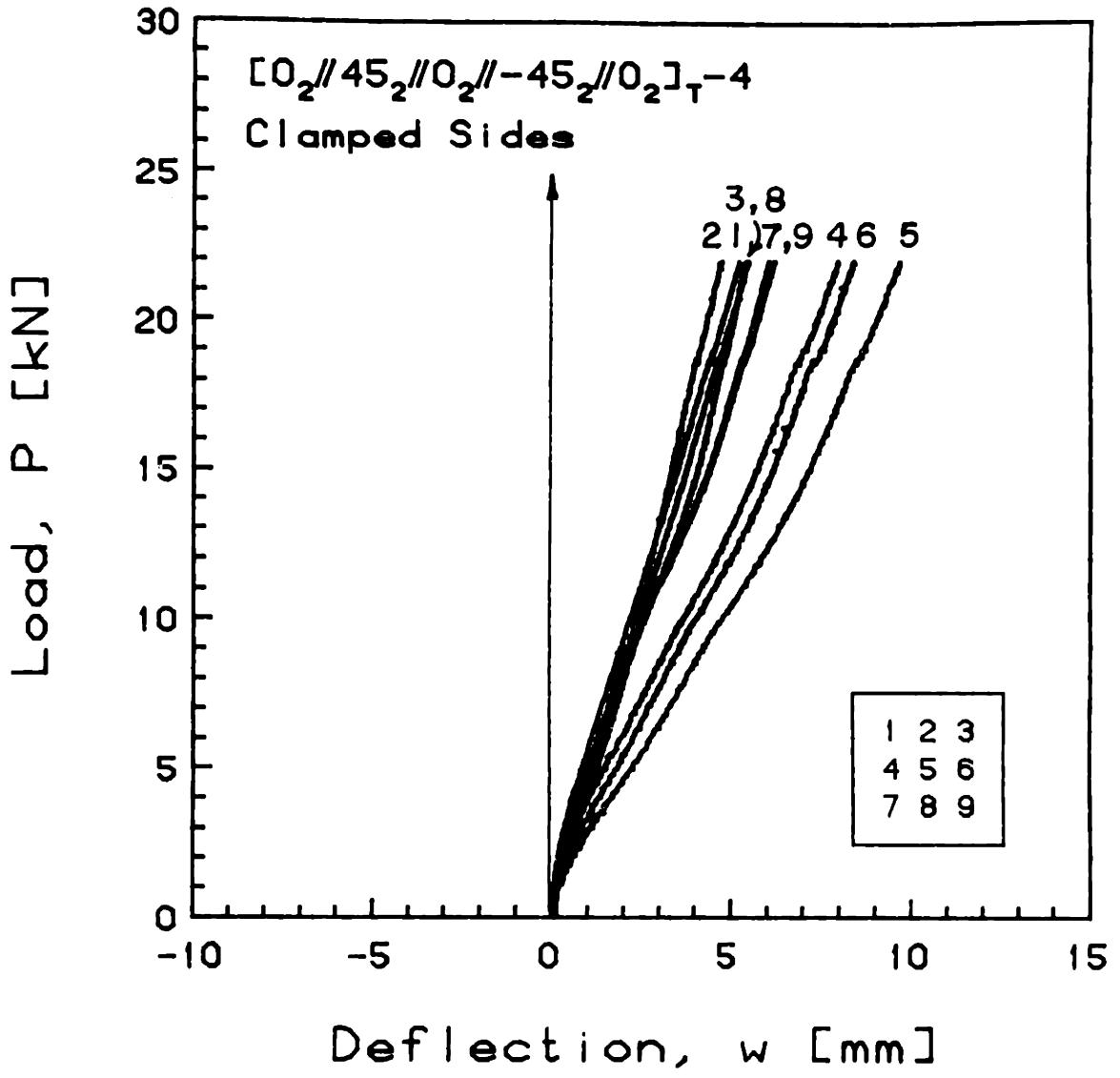

FIGURE E.28 Experimental Plot of Applied Compressive Load versus Out-of-Plane Deflection for the $[O_2//45_2//O_2//-45_2//O_2]_T$-4 Laminate with Clamped Side Boundary Conditions

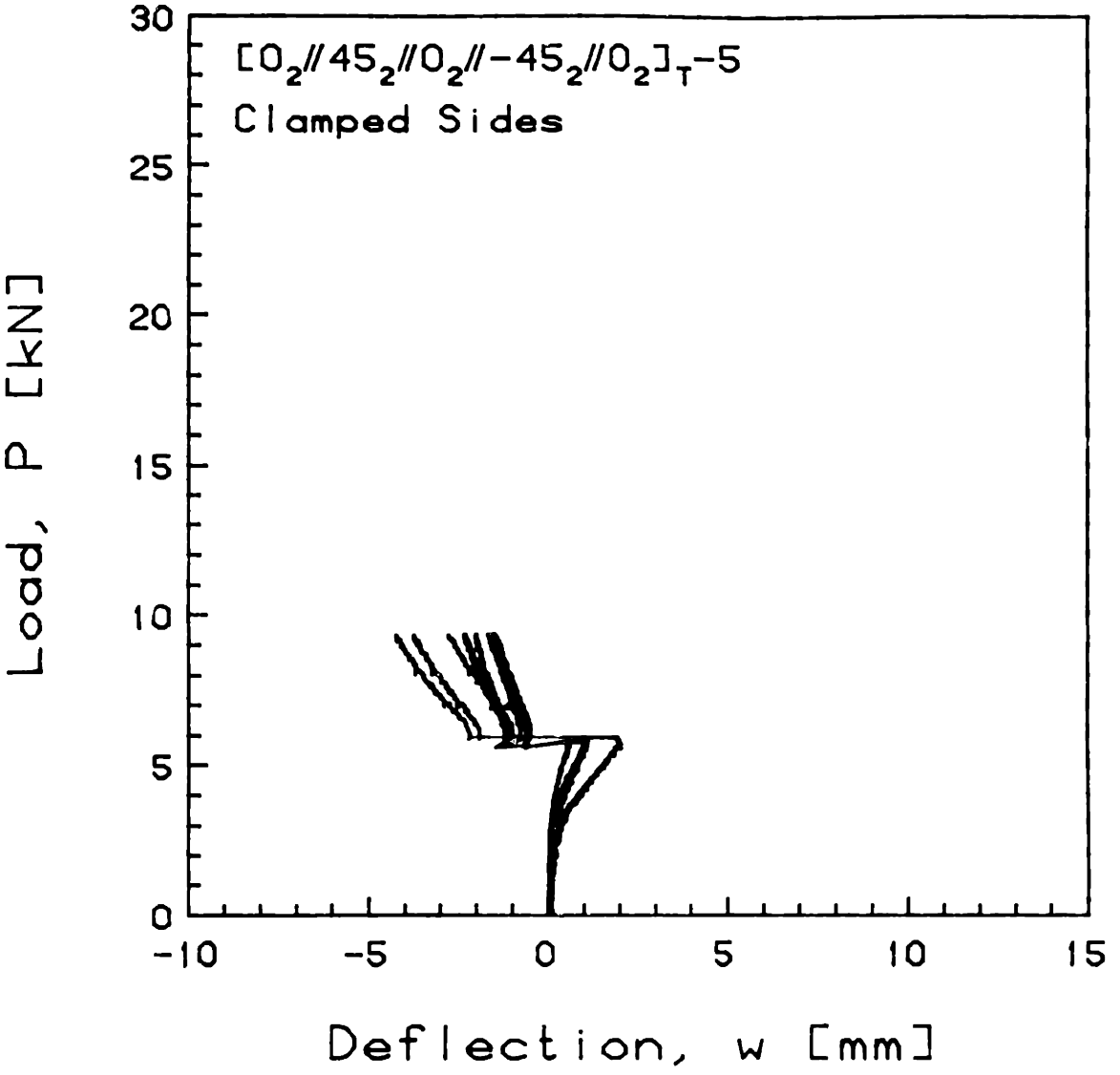

FIGURE E.29 Experimental Phase I Plot of Applied Compressive Load versus Out-of-Plane Deflection for the $[0_2//45_2//0_2//-45_2//0_2]_T$-5 Laminate with Clamped Side Boundary Conditions

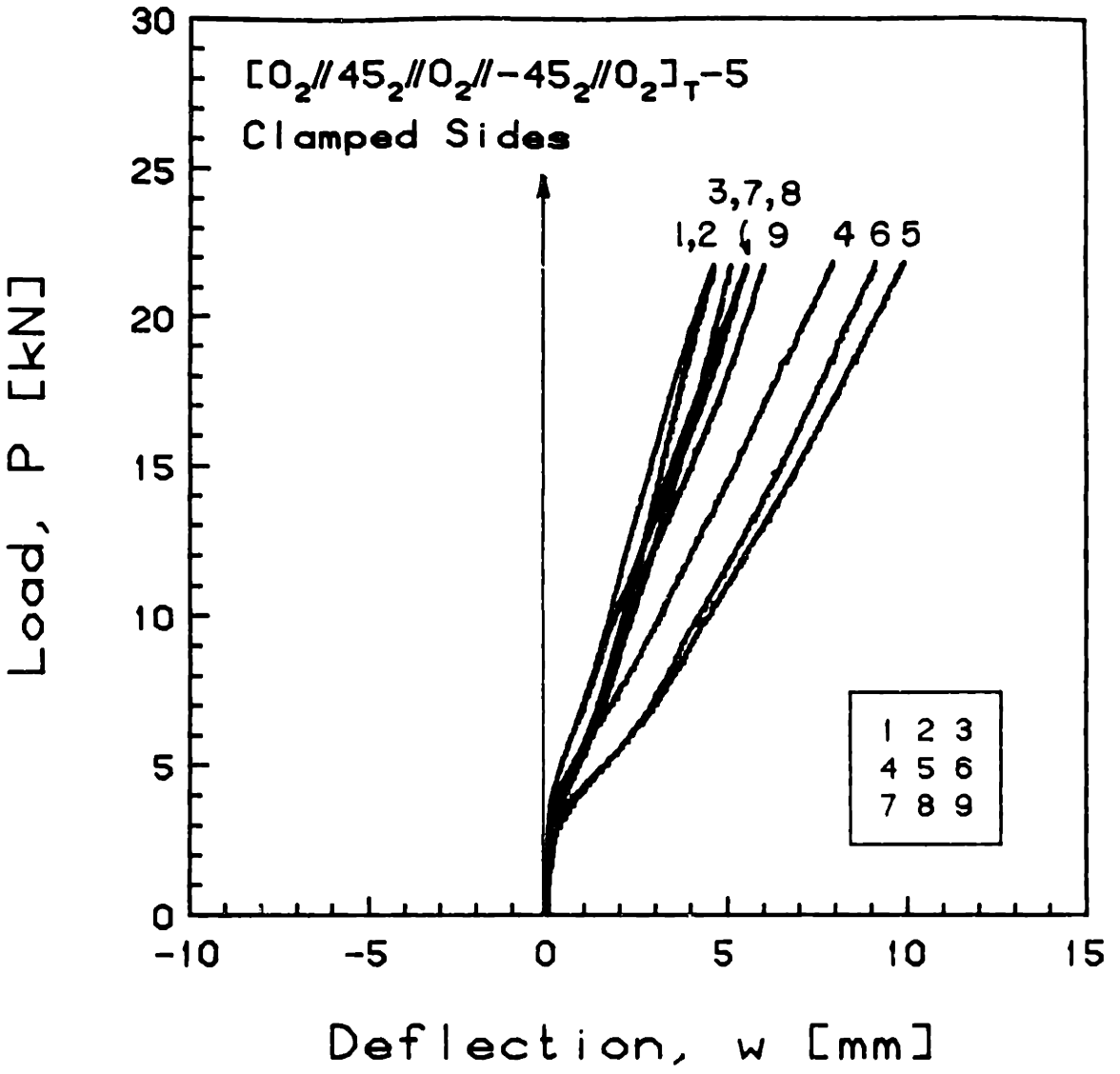

FIGURE E.30 Experimental Phase II Plot of Applied Compressive Load versus Out-of-Plane Deflection for the $[O_2//45_2//O_2//-45_2//O_2]_T$-5 Laminate with Clamped Side Boundary Conditions

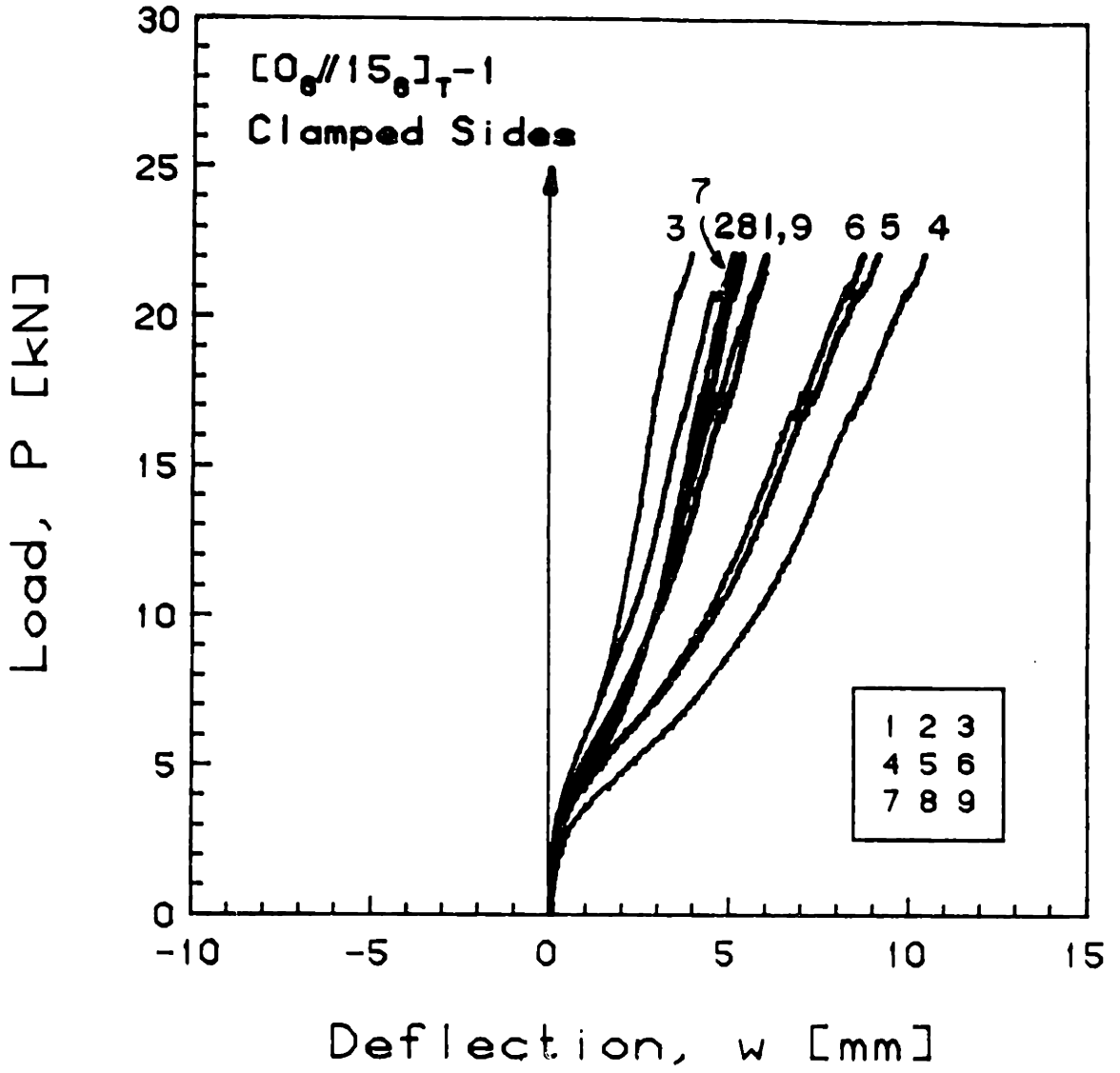

FIGURE E.31 Experimental Plot of Applied Compressive Load versus Out-of-Plane Deflection for the $[0_6//15_6]_T$-1 Laminate with Clamped Side Boundary Conditions

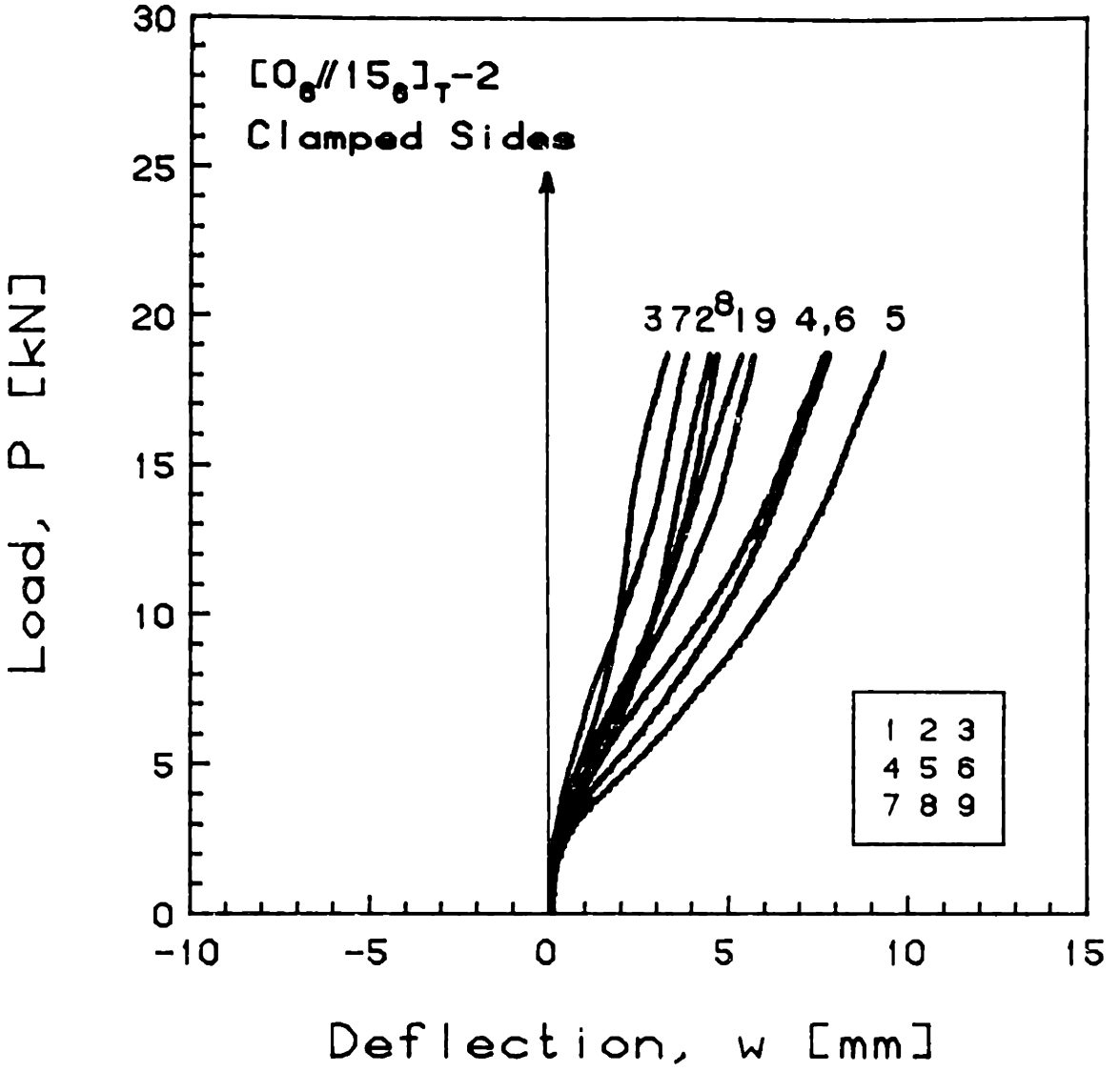

FIGURE E.32 Experimental Plot of Applied Compressive Load versus Out-of-Plane Deflection for the $[0_6//15_6]_T$-2 Laminate with Clamped Side Boundary Conditions

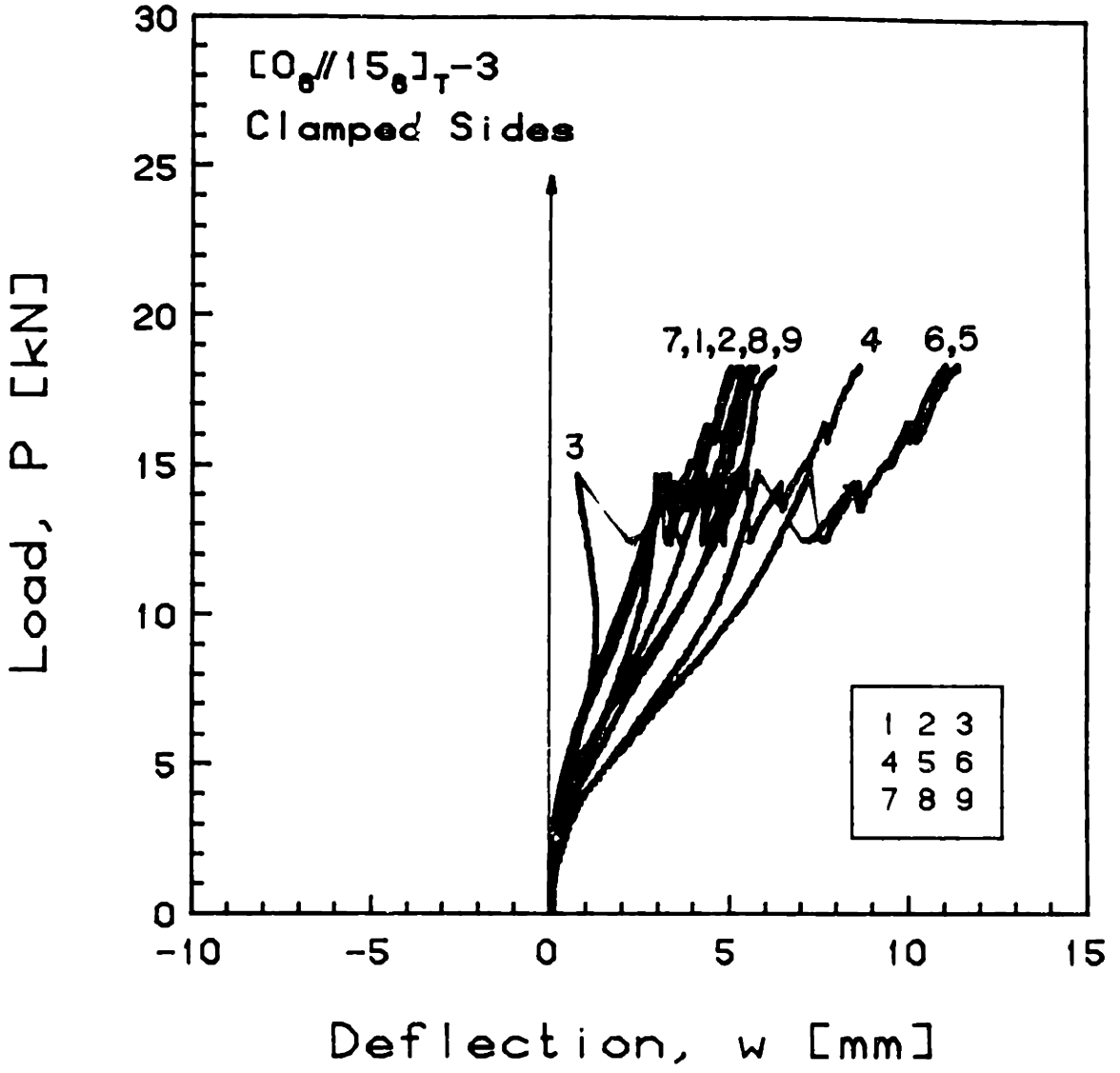

FIGURE E.33 Experimental Plot of Applied Compressive Load versus Out-of-Plane Deflection for the $[0_6//15_6]_T$-3 Laminate with Clamped Side Boundary Conditions

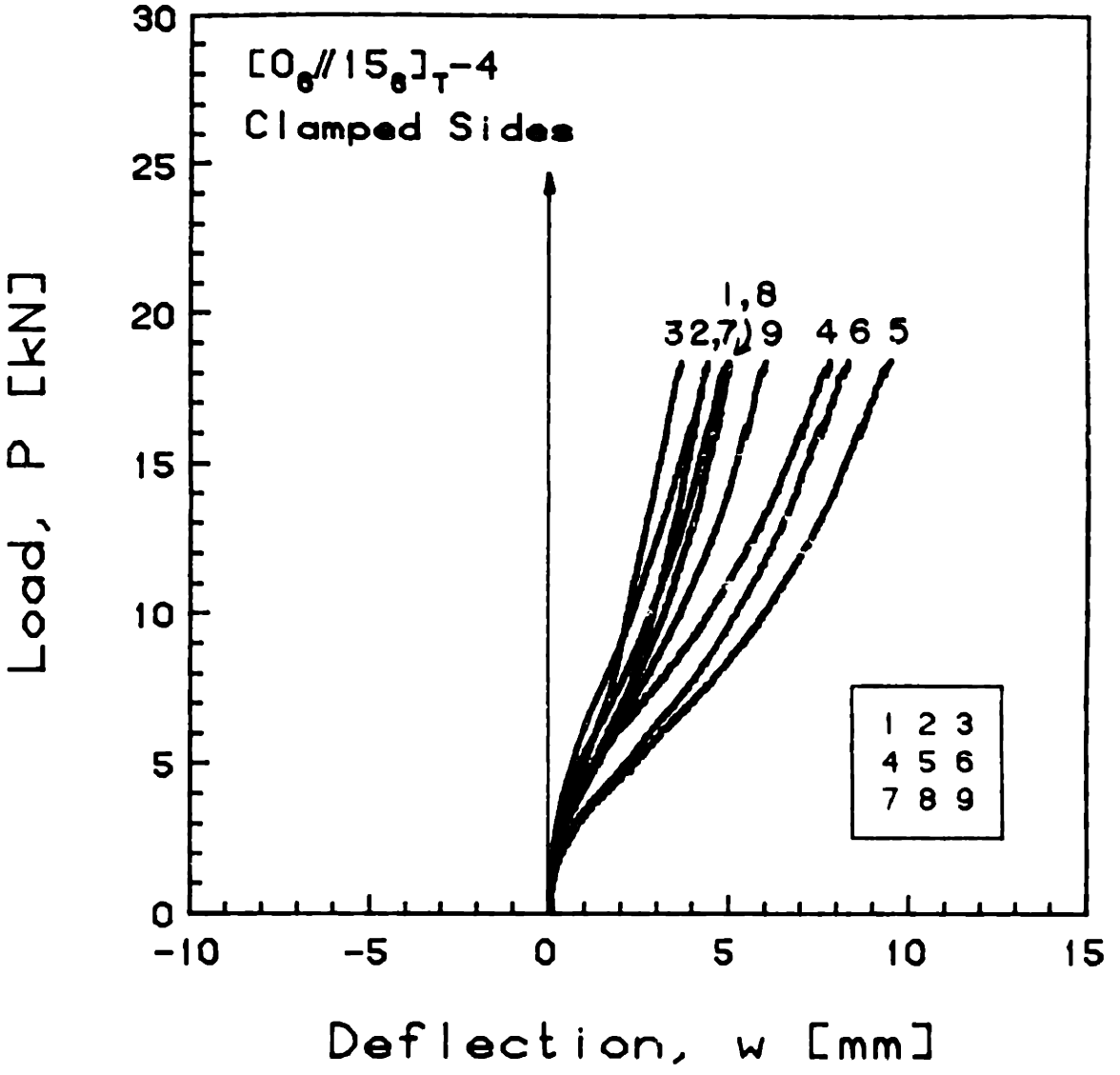

FIGURE E.34 Experimental Plot of Applied Compressive Load versus Out-of-Plane Deflection for the $[O_6//15_6]_T$-4 Laminate with Clamped Side Boundary Conditions

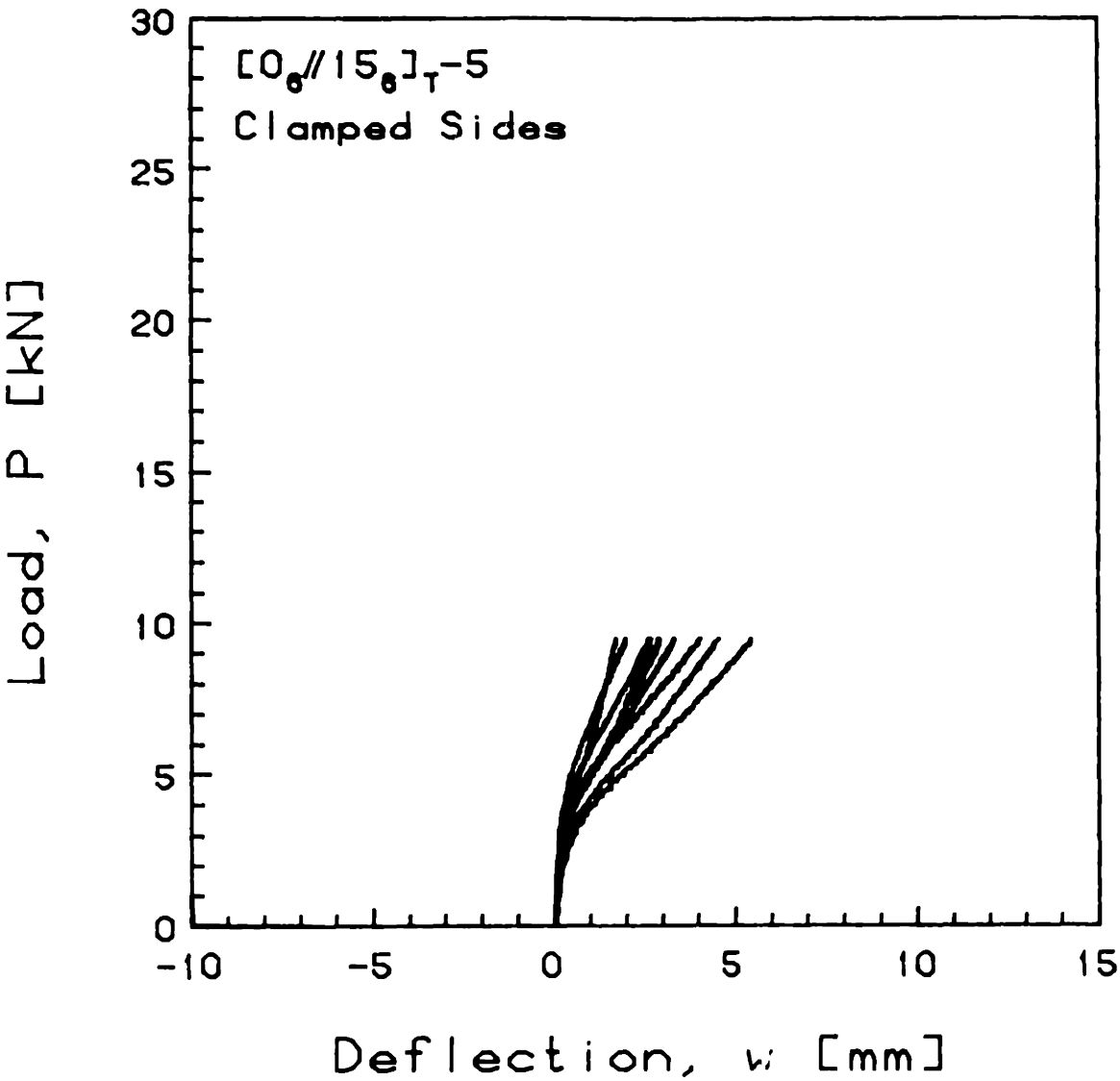

FIGURE E.35 Experimental Phase I Plot of Applied Compressive Load versus Out-of-Plane Deflection for the $[O_6//15_6]_T$-5 Laminate with Clamped Side Boundary Conditions

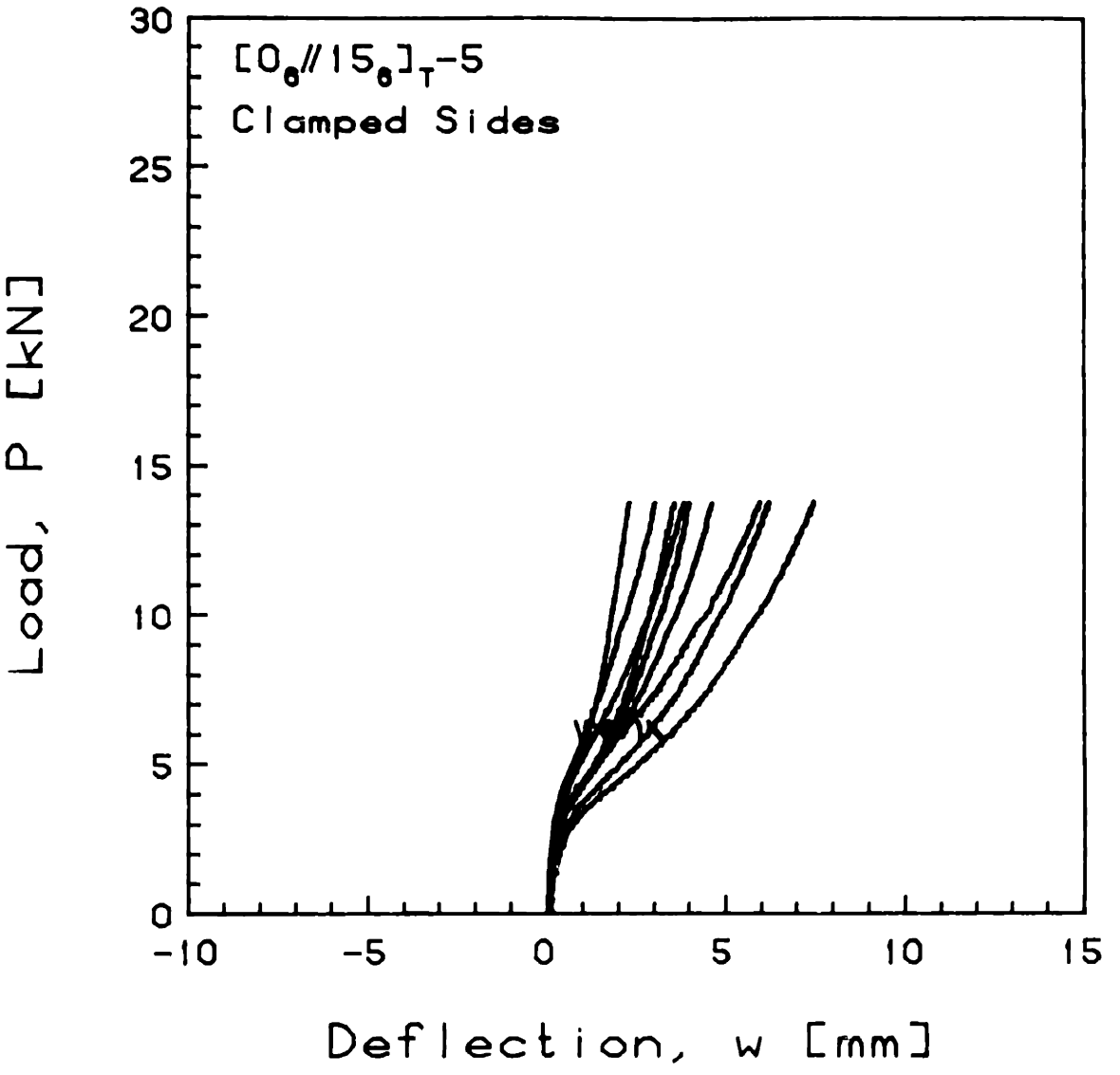

FIGURE E.36 Experimental Phase II Plot of Applied Compressive Load versus Out-of-Plane Deflection for the $[0_6//15_6]_T$-5 Laminate with Clamped Side Boundary Conditions

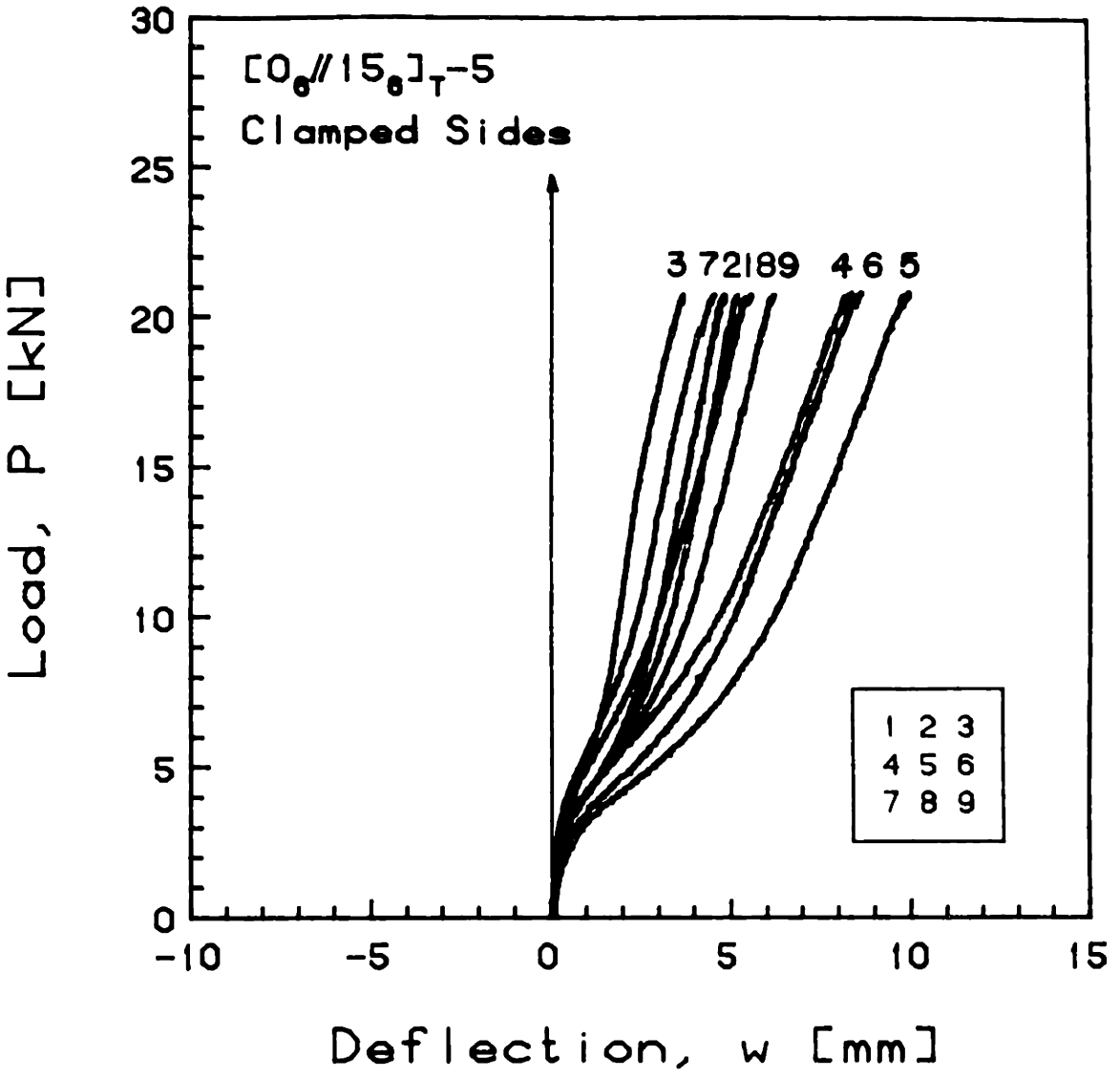

FIGURE E.37 Experimental Phase III Plot of Applied Compressive Load versus Out-of-Plane Deflection for the $[0_6//15_6]_T$-5 Laminate with Clamped Side Boundary Conditions

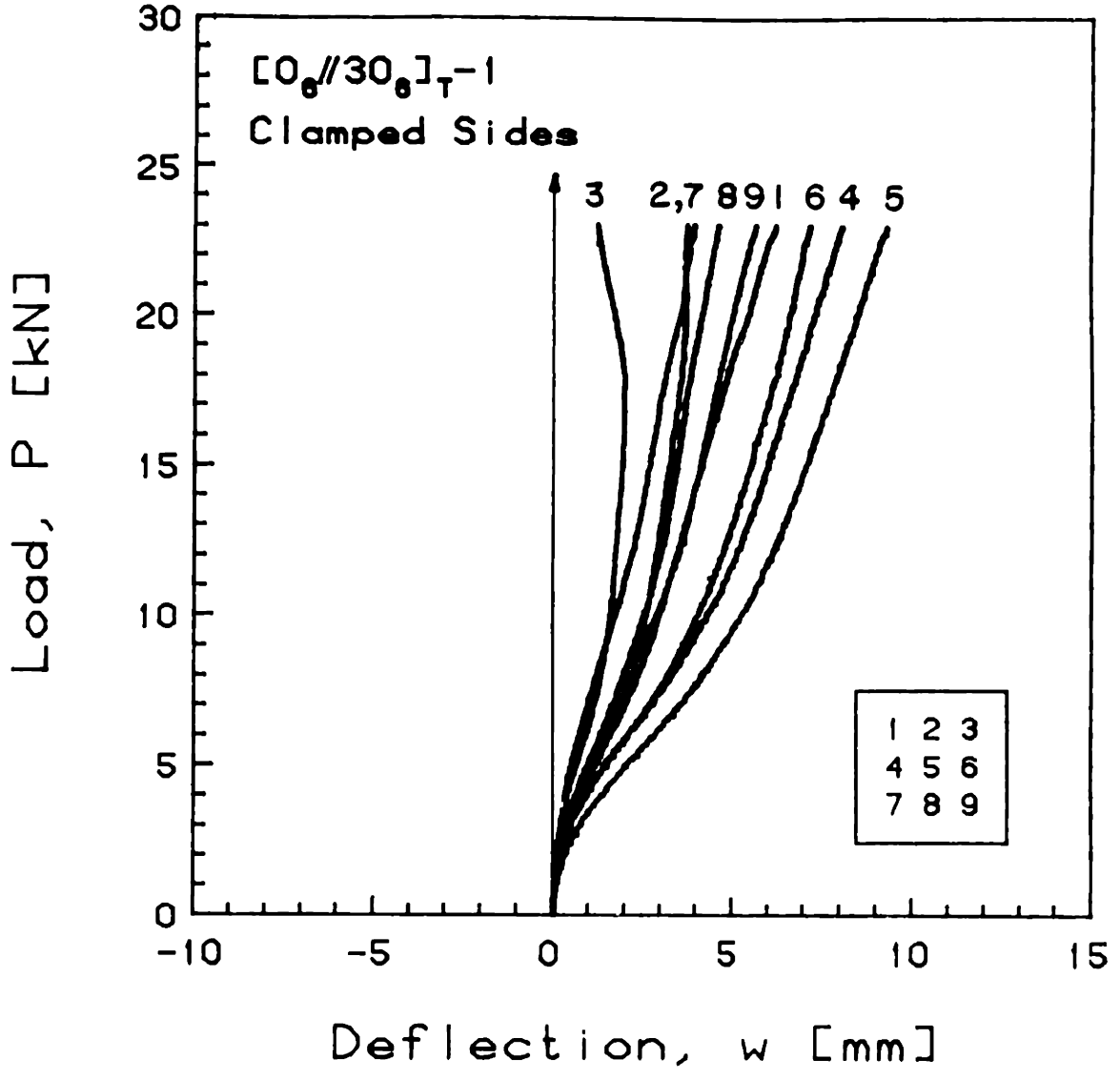

FIGURE E.38 Experimental Plot of Applied Compressive Load versus Out-of-Plane Deflection for the $[0_6//30_6]_T$-1 Laminate with Clamped Side Boundary Conditions

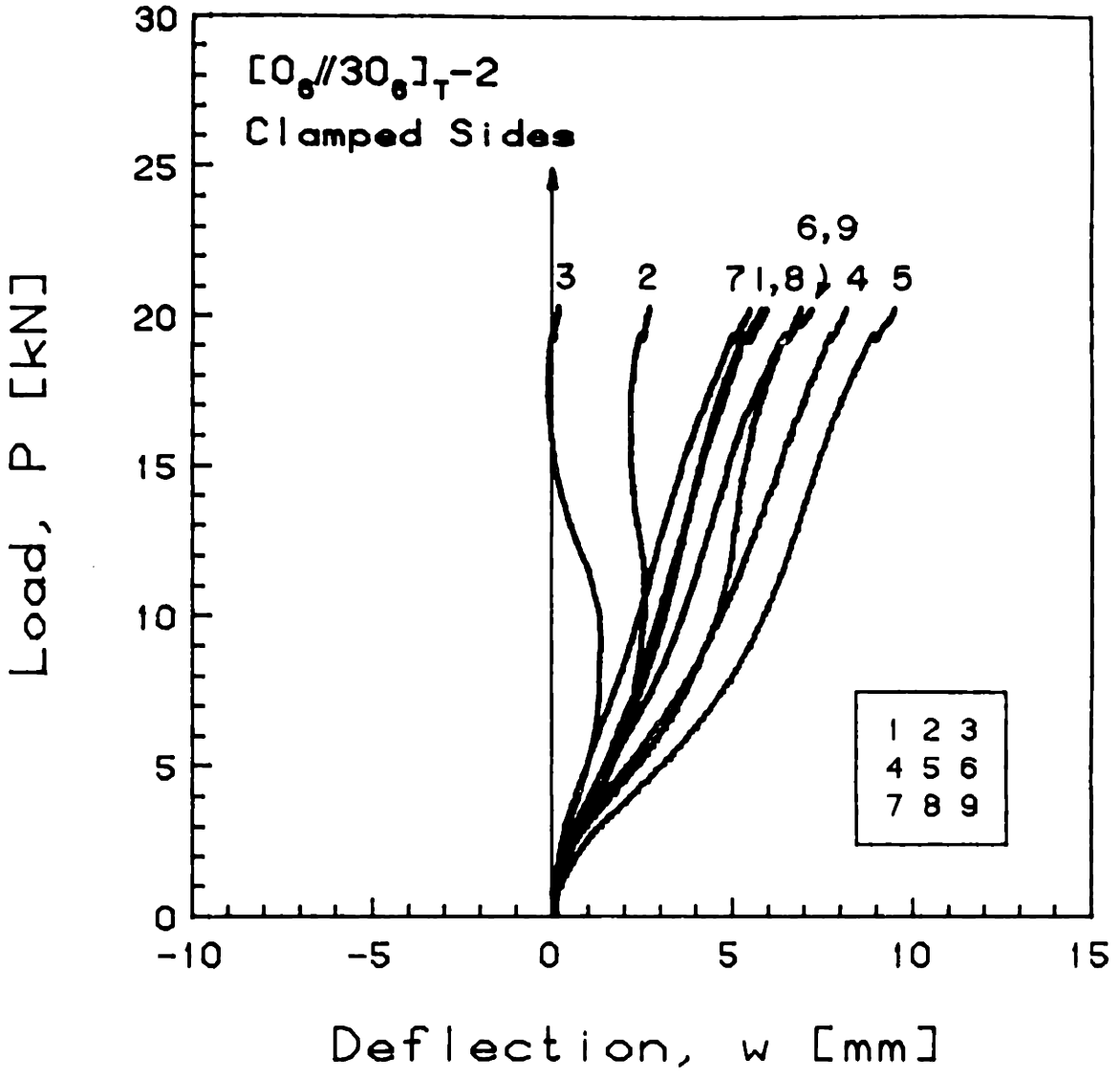

FIGURE E.39 Experimental Plot of Applied Compressive Load versus Out-of-Plane Deflection for the $[0_6//30_6]_T$-2 Laminate with Clamped Side Boundary Conditions

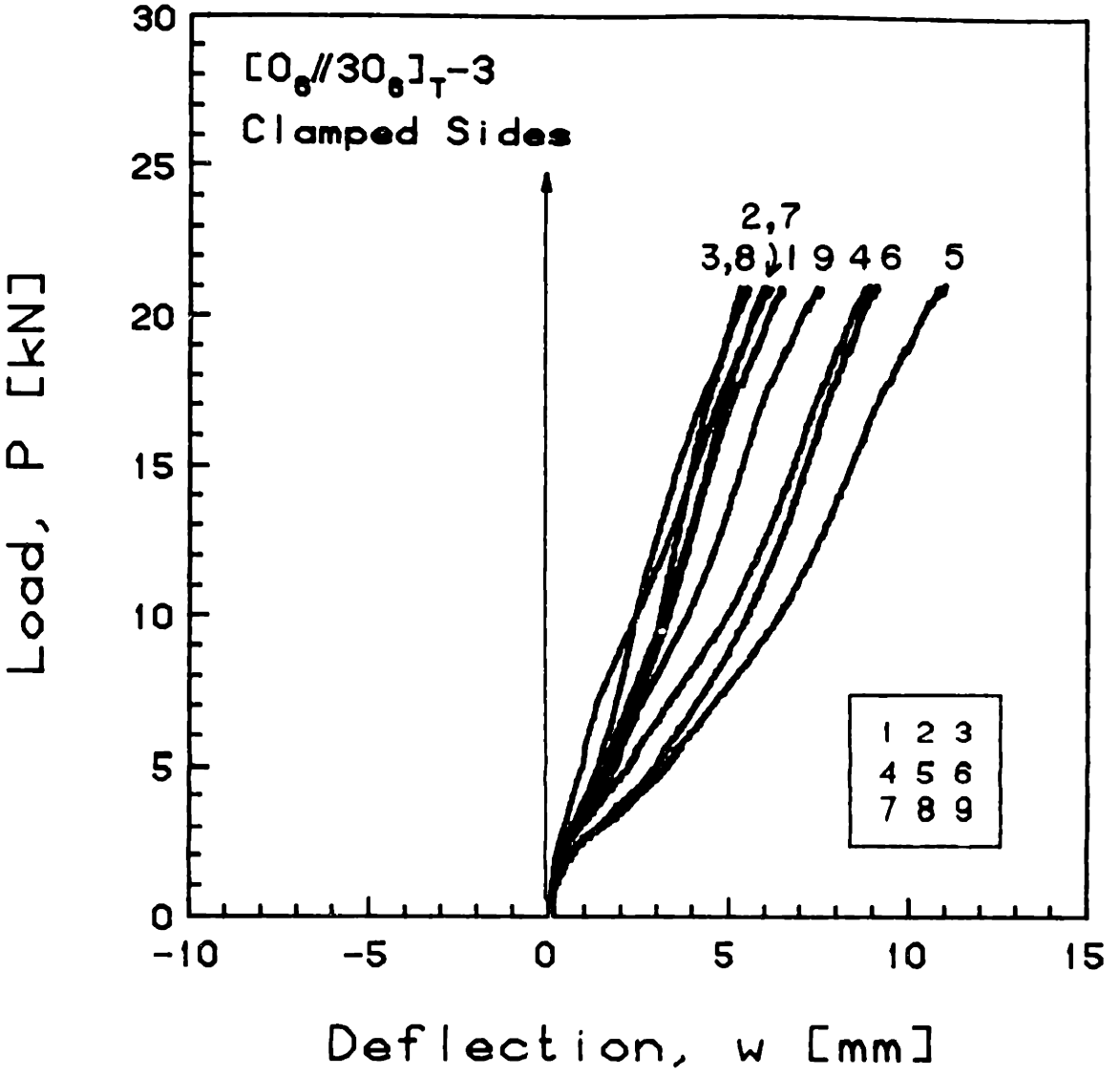

FIGURE E.40 Experimental Plot of Applied Compressive Load versus Out-of-Plane Deflection for the $[0_6//30_6]_T$-3 Laminate with Clamped Side Boundary Conditions

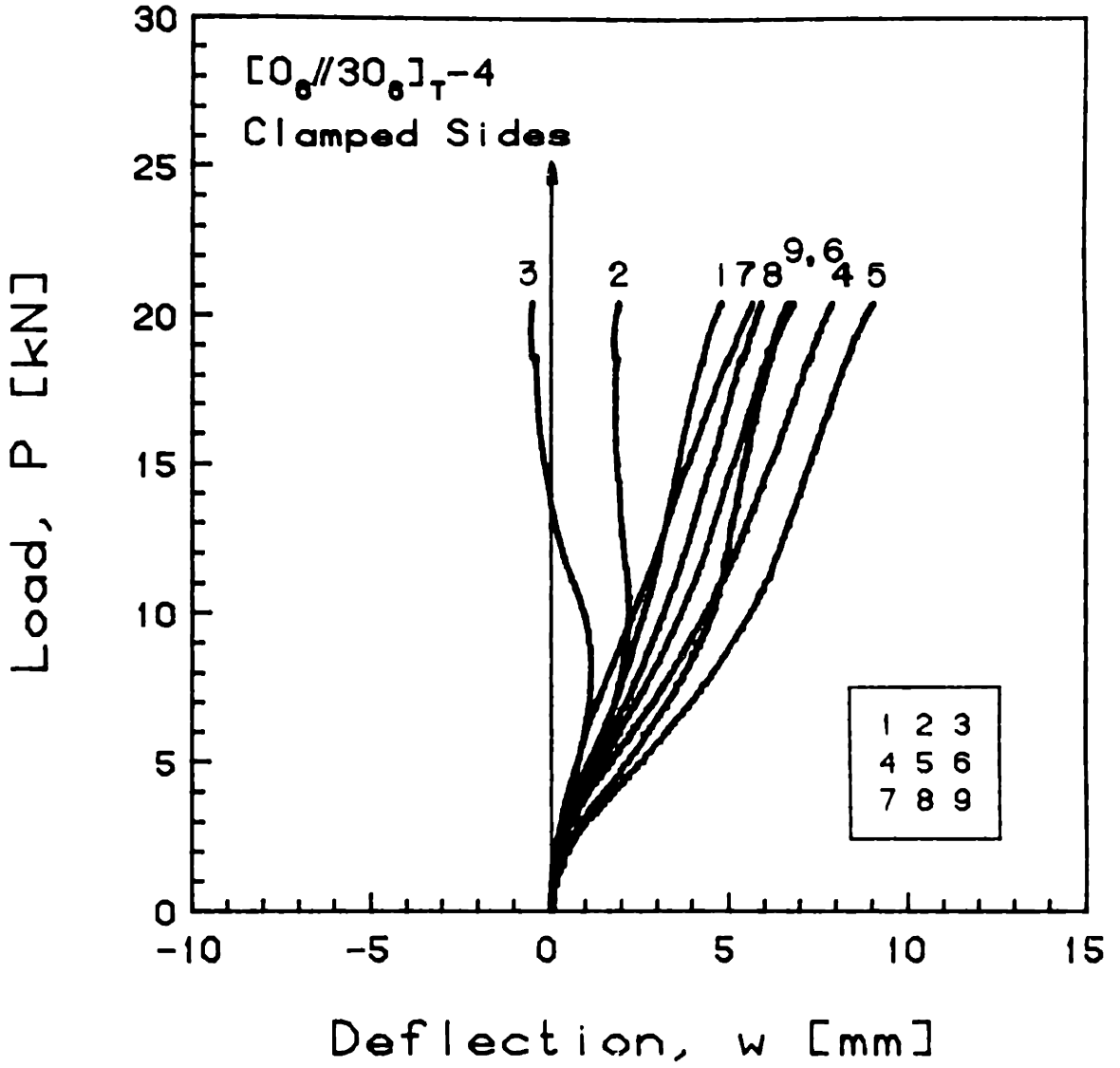

FIGURE E.41 Experimental Plot of Applied Compressive Load versus Out-of-Plane Deflection for the $[0_6//30_6]_T$-4 Laminate with Clamped Side Boundary Conditions

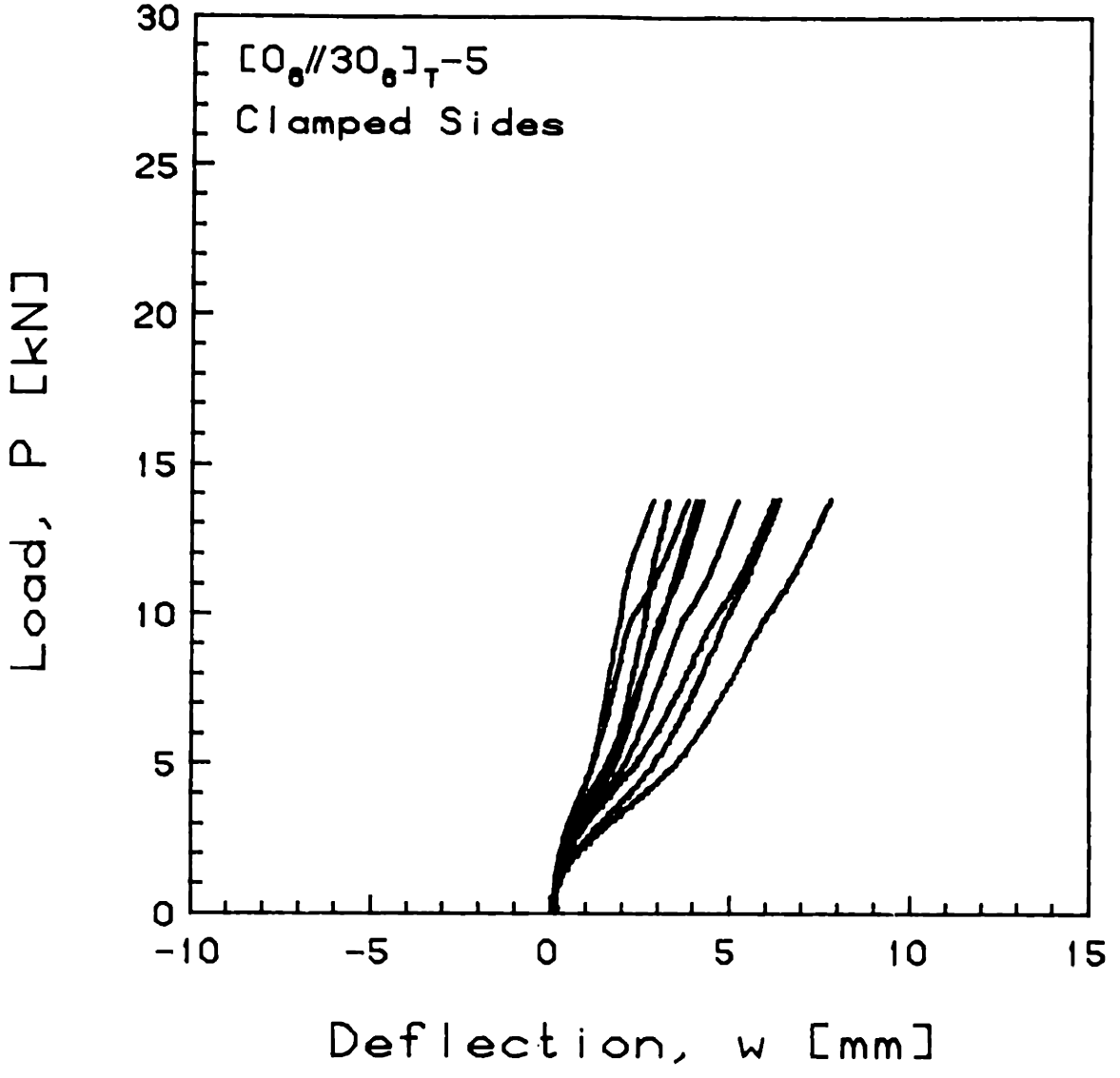

FIGURE E.42 Experimental Phase I Plot of Applied Compressive Load versus Out-of-Plane Deflection for the $[0_6//30_6]_T$-5 Laminate with Clamped Side Boundary Conditions

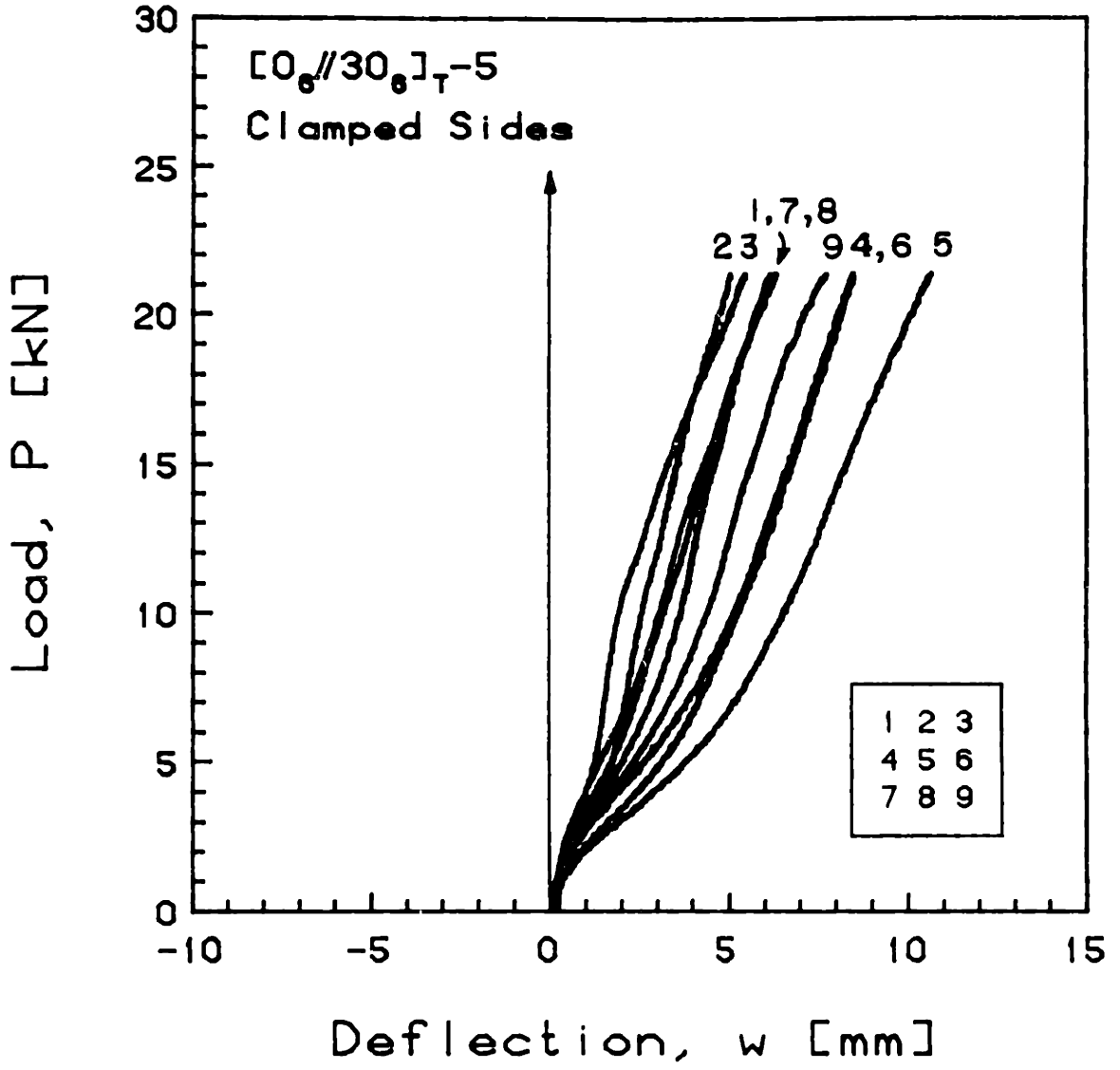

FIGURE E.43 Experimental Phase III Plot of Applied Compressive Load versus Out-of-Plane Deflection for the $[0_6//30_6]_T$-5 Laminate with Clamped Side Boundary Conditions

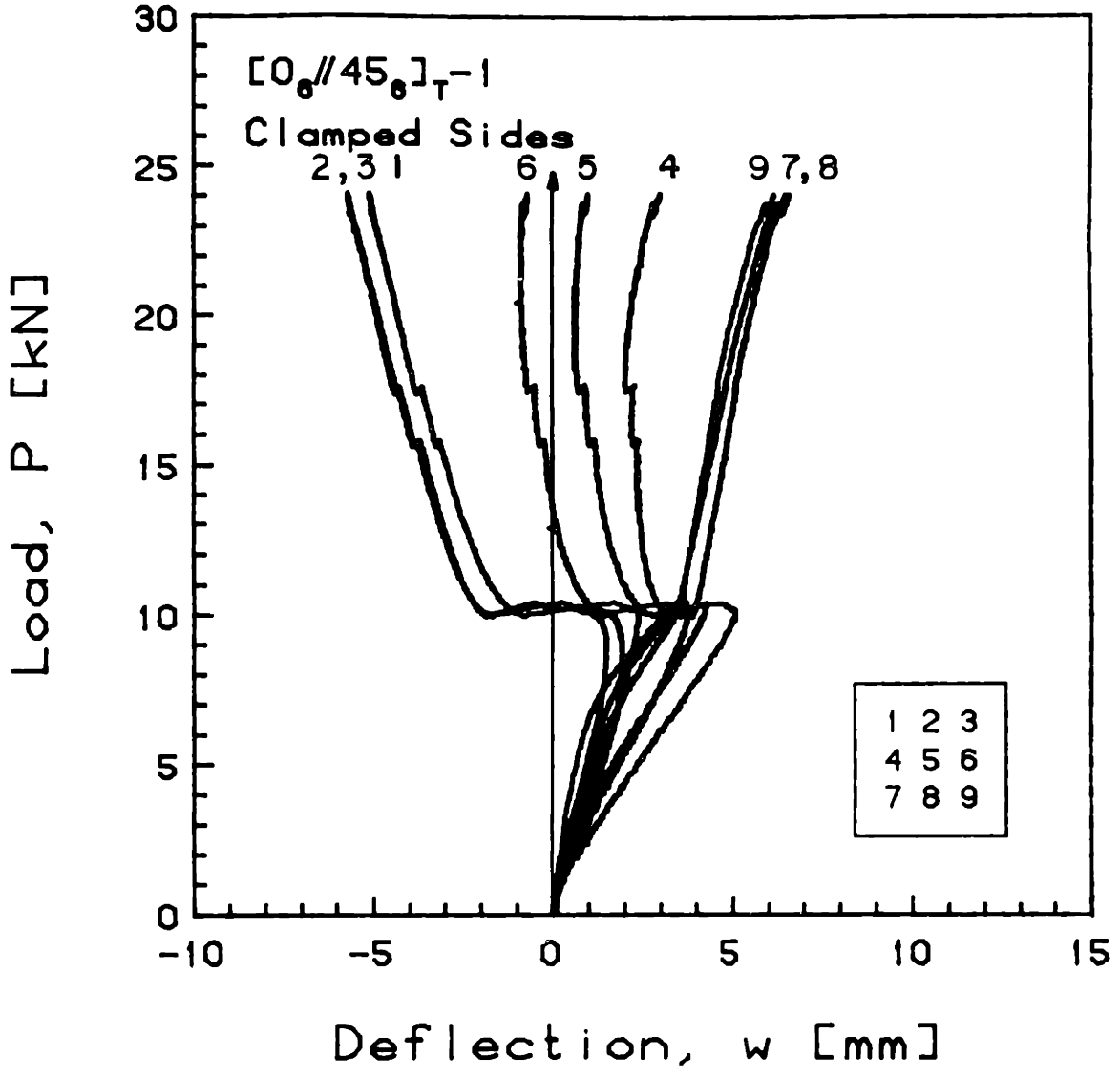

FIGURE E.44 Experimental Plot of Applied Compressive Load versus Out-of-Plane Deflection for the $[0_6//45_6]_T$-1 Laminate with Clamped Side Boundary Conditions

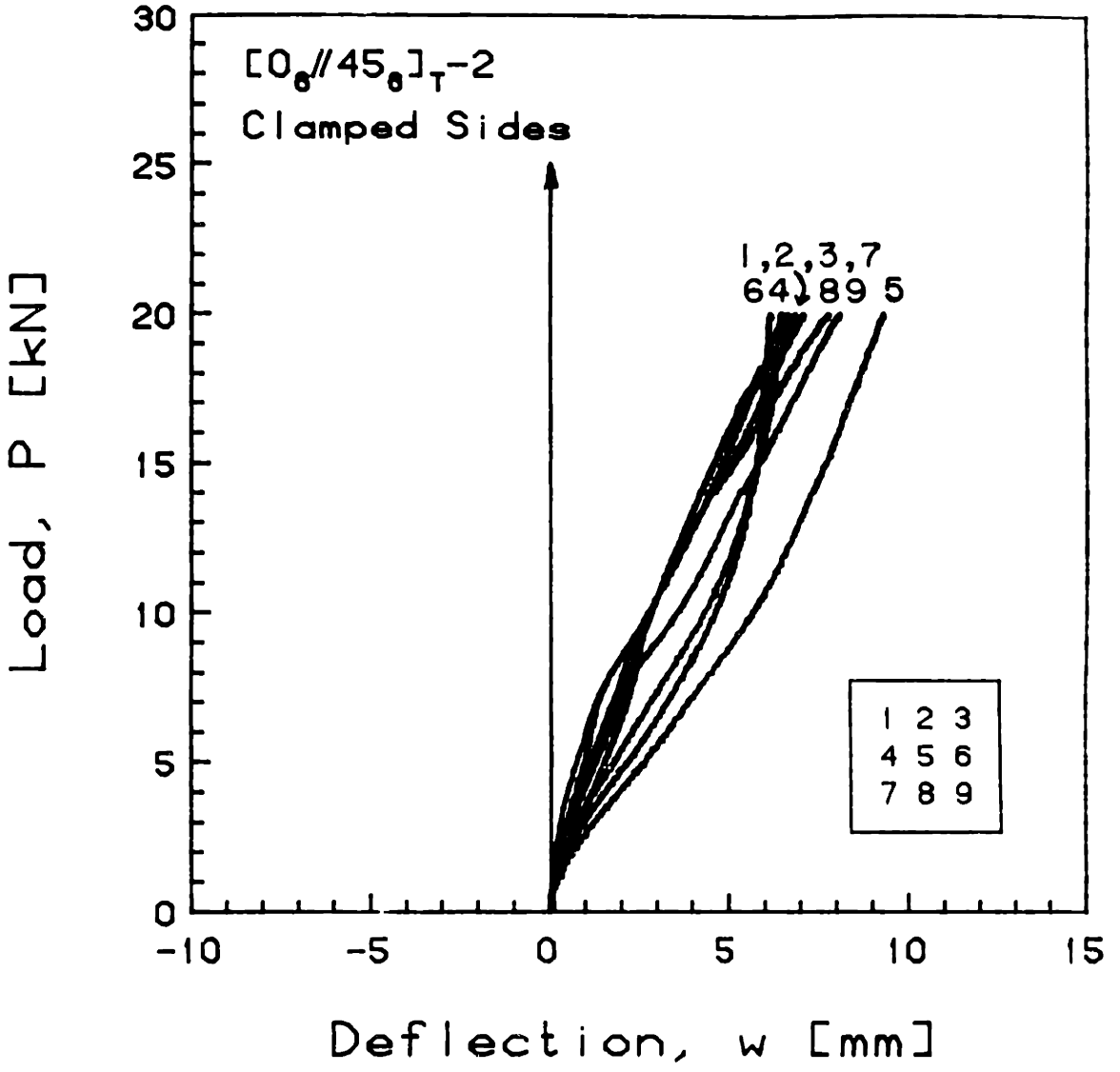

FIGURE E.45 Experimental Plot of Applied Compressive Load versus Out-of-Plane Deflection for the $[O_6//45_6]_T$-2 Laminate with Clamped Side Boundary Conditions

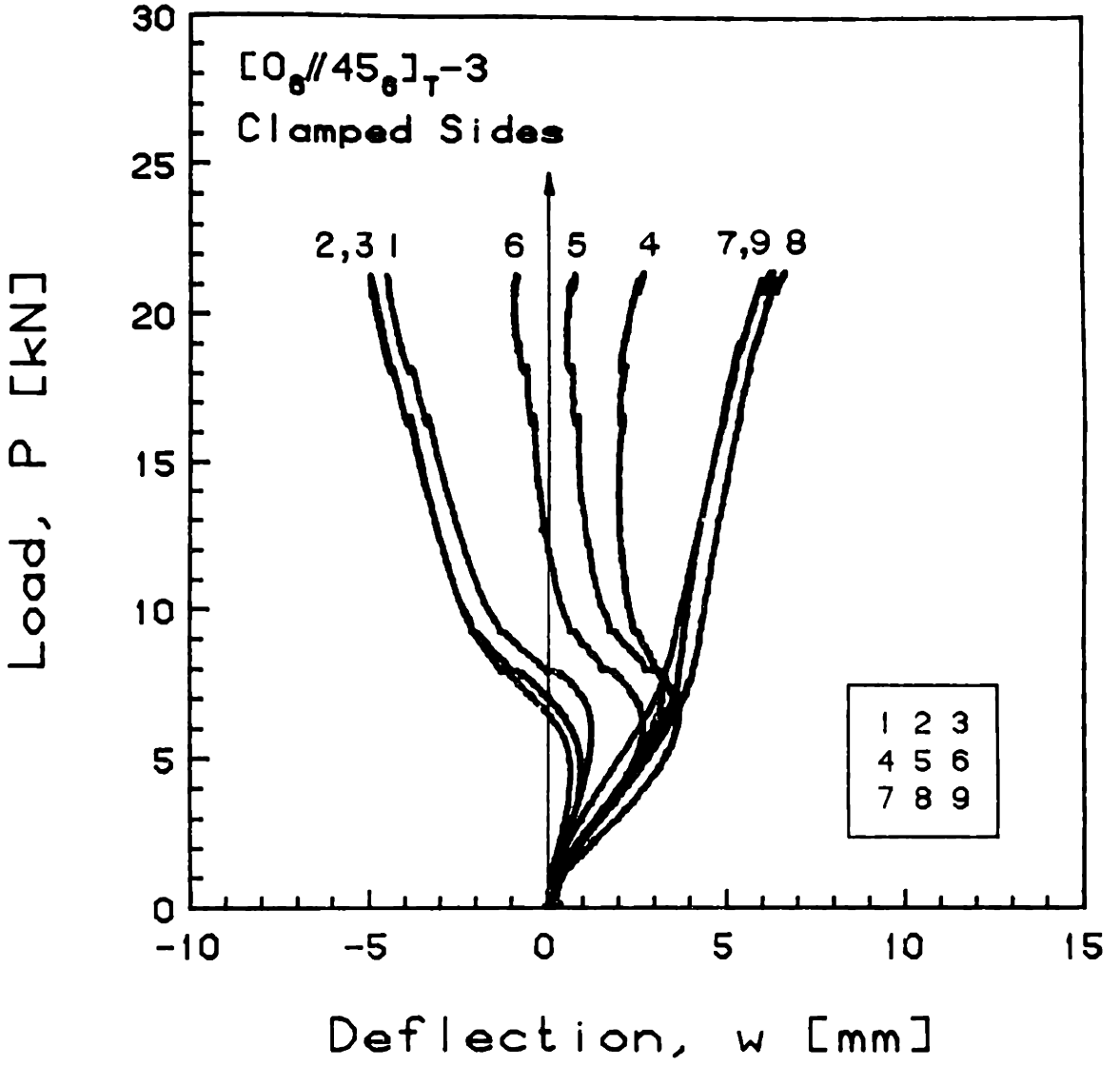

FIGURE E.46 Experimental Plot of Applied Compressive Load versus Out-of-Plane Deflection for the $[0_6//45_6]_T$-3 Laminate with Clamped Side Boundary Conditions

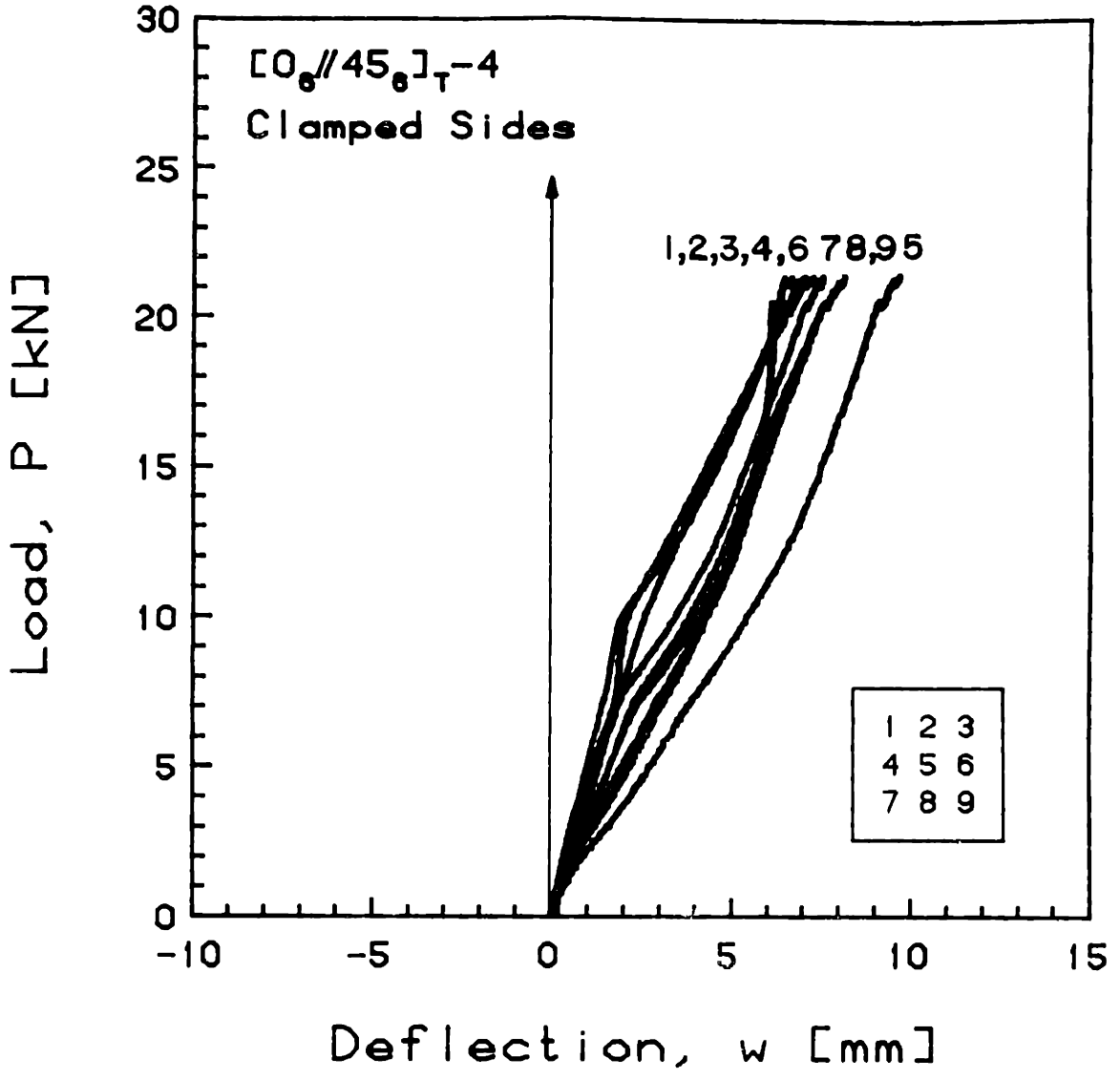

FIGURE E.47 Experimental Plot of Applied Compressive Load versus Out-of-Plane Deflection for the $[0_6//45_6]_T$-4 Laminate with Clamped Side Boundary Conditions

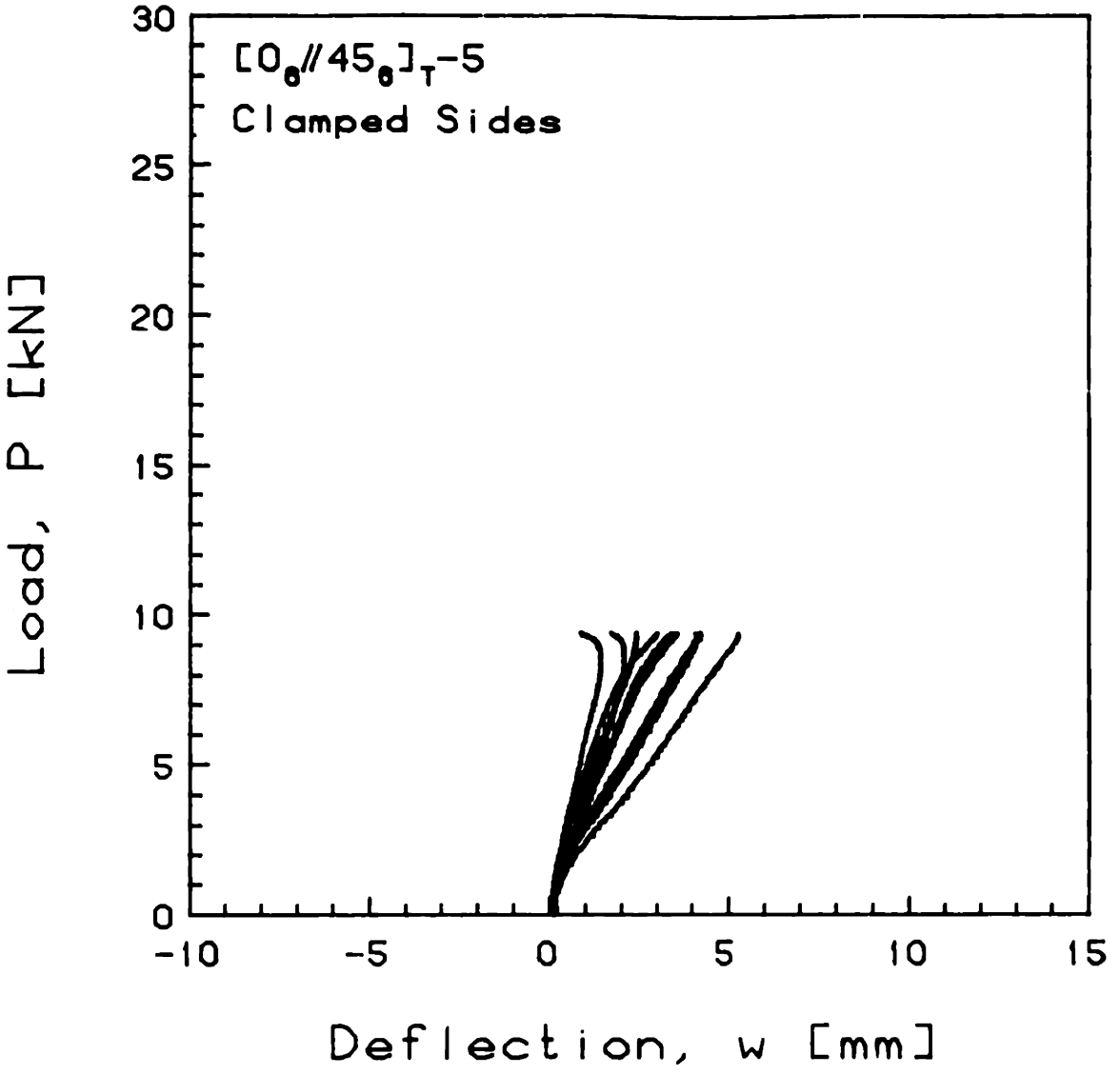

FIGURE E.48 Experimental Phase I Plot of Applied Compressive Load versus Out-of-Plane Deflection for the $[0_6//45_6]_T$-5 Laminate with Clamped Side Boundary Conditions

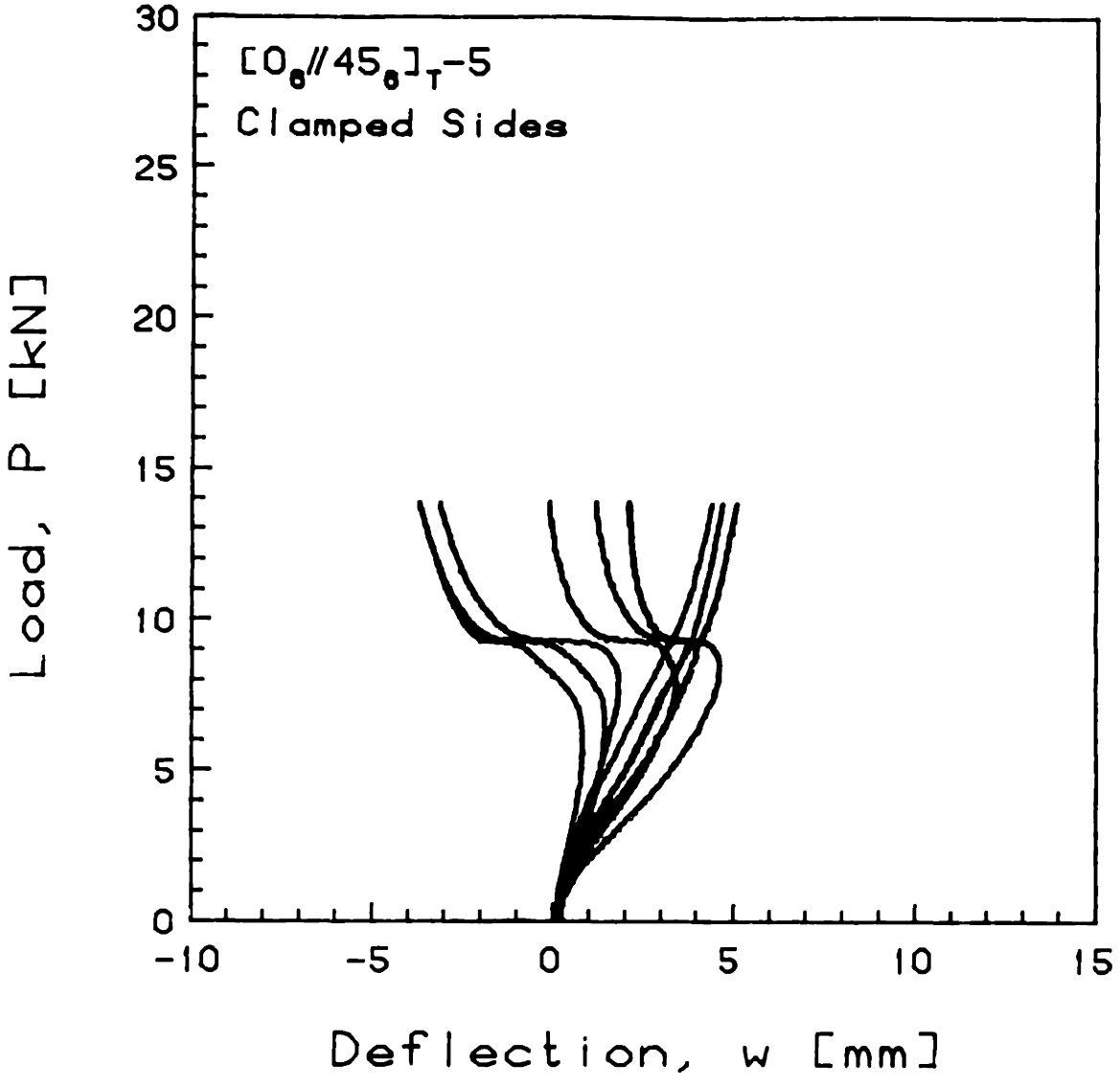

FIGURE E.49 Experimental Phase II Plot of Applied Compressive Load versus Out-of-Plane Deflection for the $[0_6//45_6]_T$-5 Laminate with Clamped Side Boundary Conditions

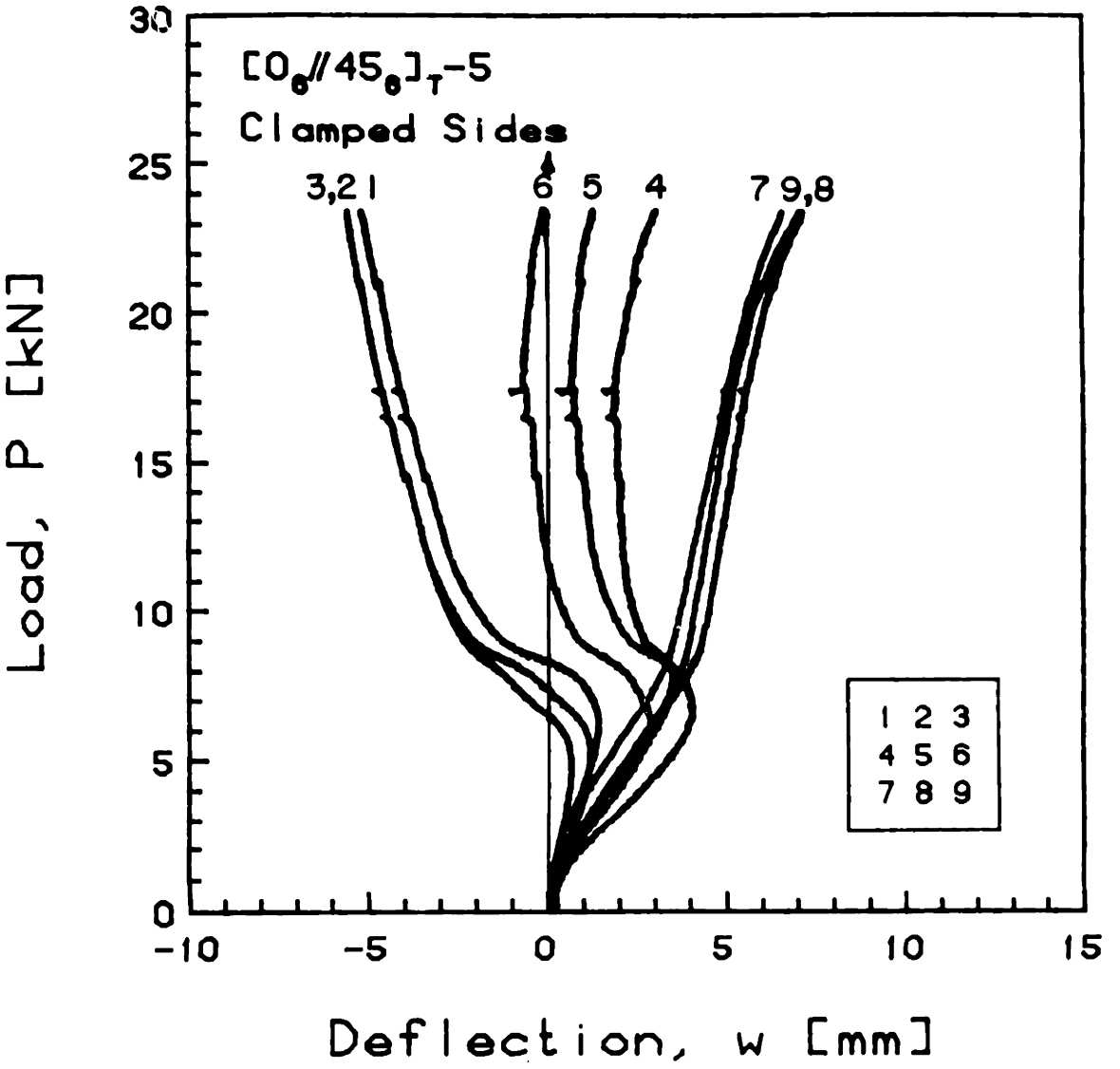

FIGURE E.50 Experimental Phase III Plot of Applied Compressive Load versus Out-of-Plane Deflection for the $[0_6//45_6]_T$-5 Laminate with Clamped Side Boundary Conditions

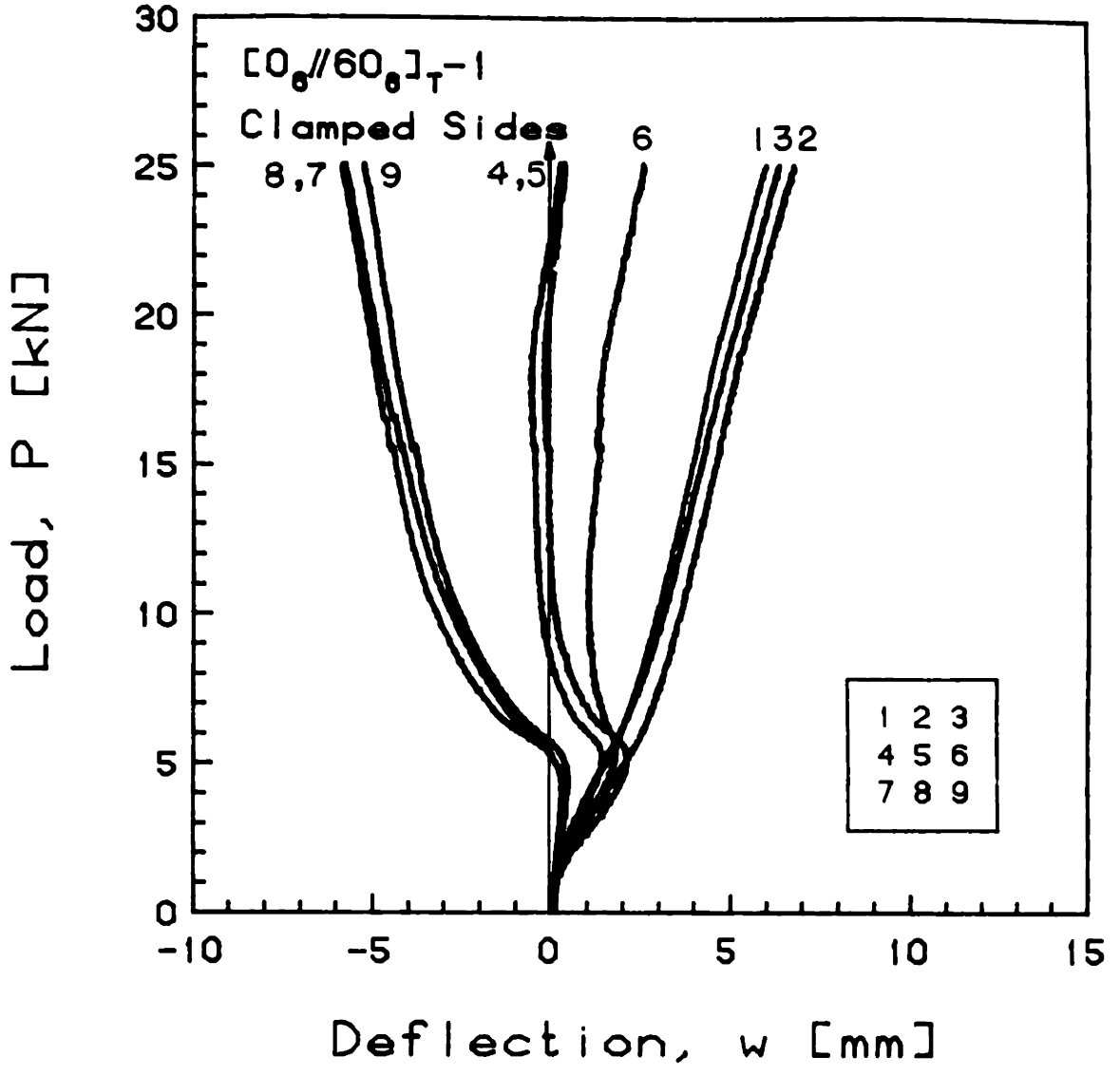

FIGURE E.51 Experimental Plot of Applied Compressive Load versus Out-of-Plane Deflection for the $[O_6//60_6]_T$-1 Laminate with Clamped Side Boundary Conditions

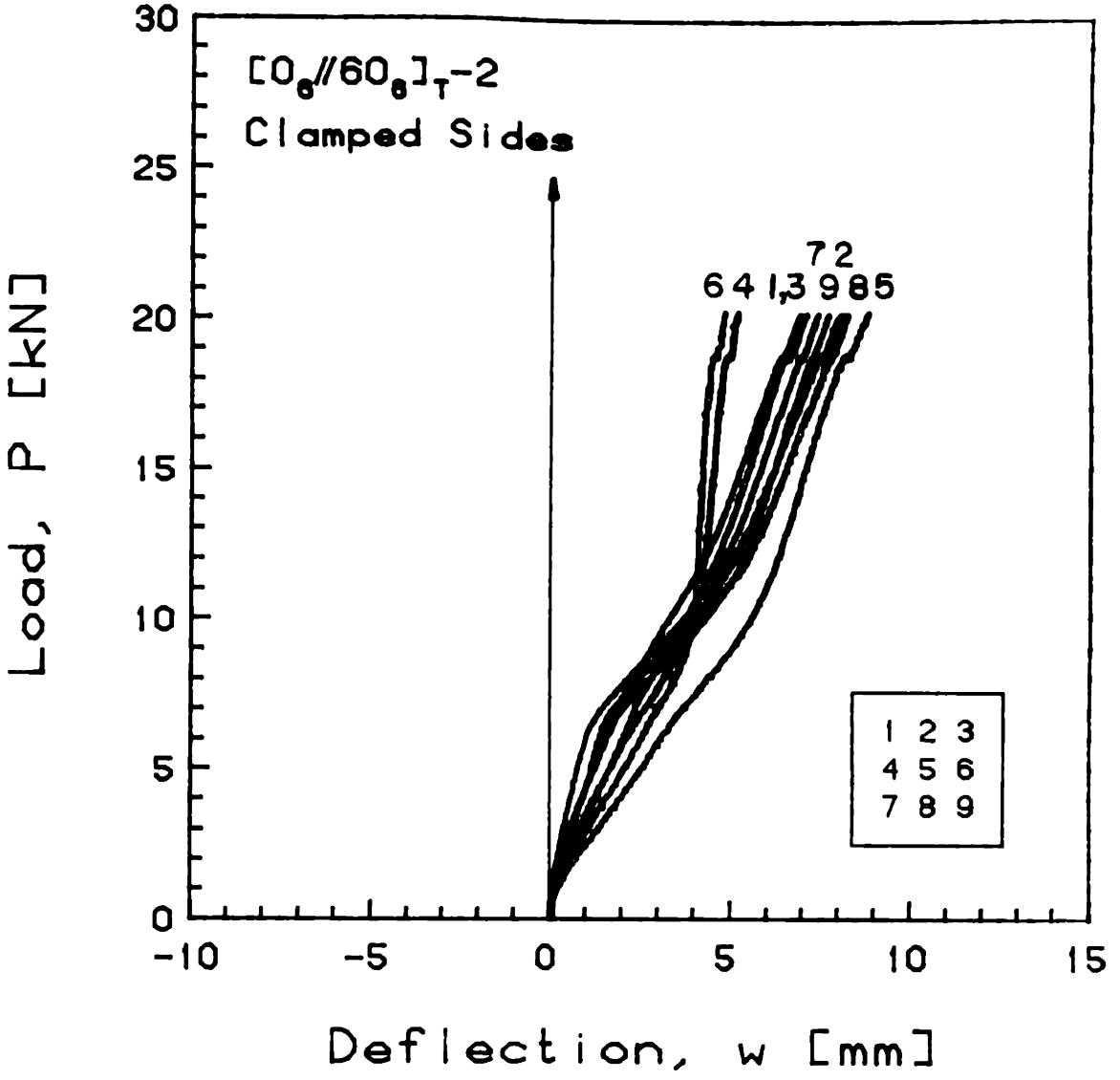

FIGURE E.52 Experimental Plot of Applied Compressive Load versus Out-of-Plane Deflection for the $[O_6//60_6]_T$-2 Laminate with Clamped Side Boundary Conditions

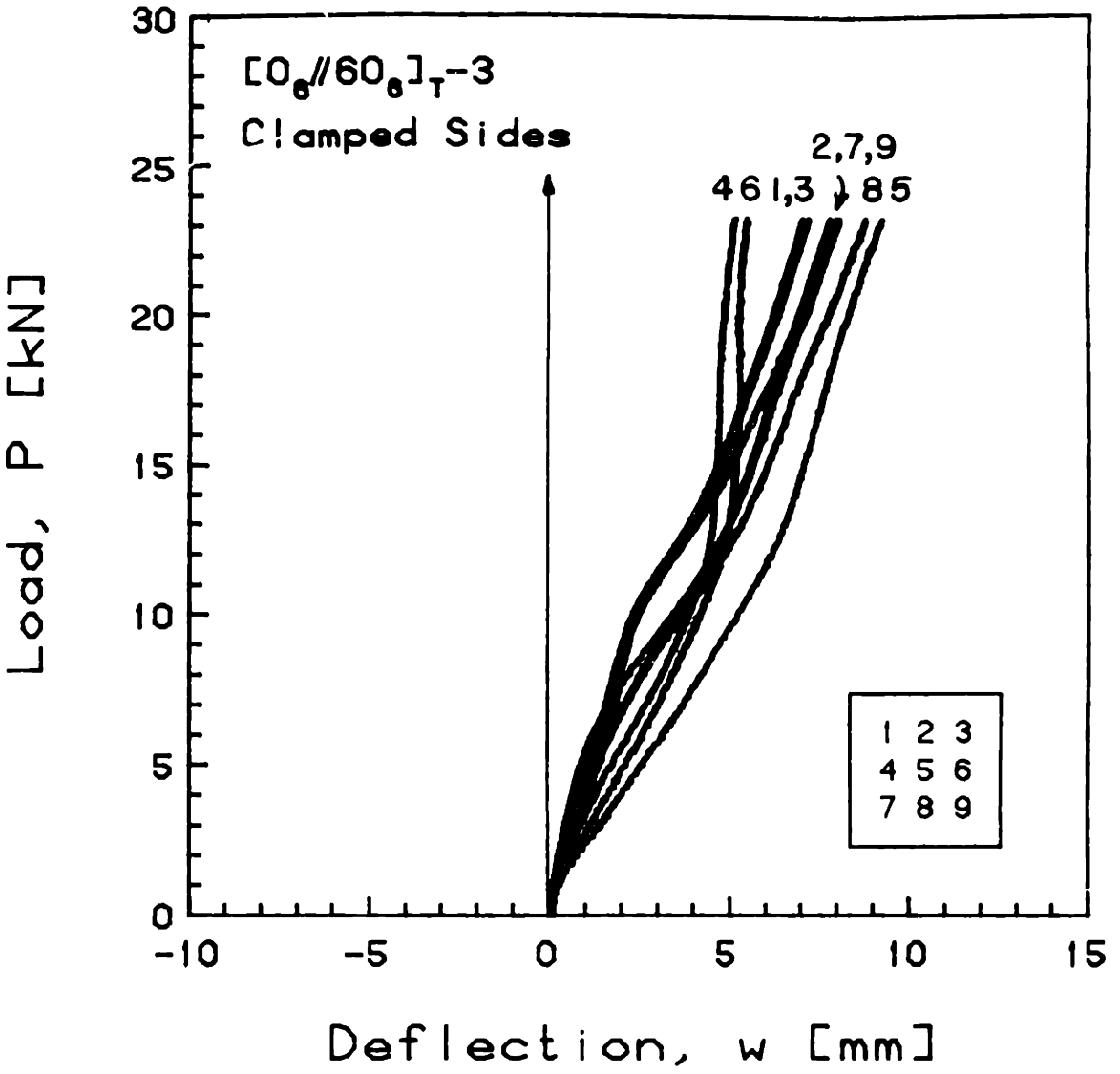

FIGURE E.53 Experimental Plot of Applied Compressive Load versus Out-of-Plane Deflection for the $[O_6//60_6]_T$-3 Laminate with Clamped Side Boundary Conditions

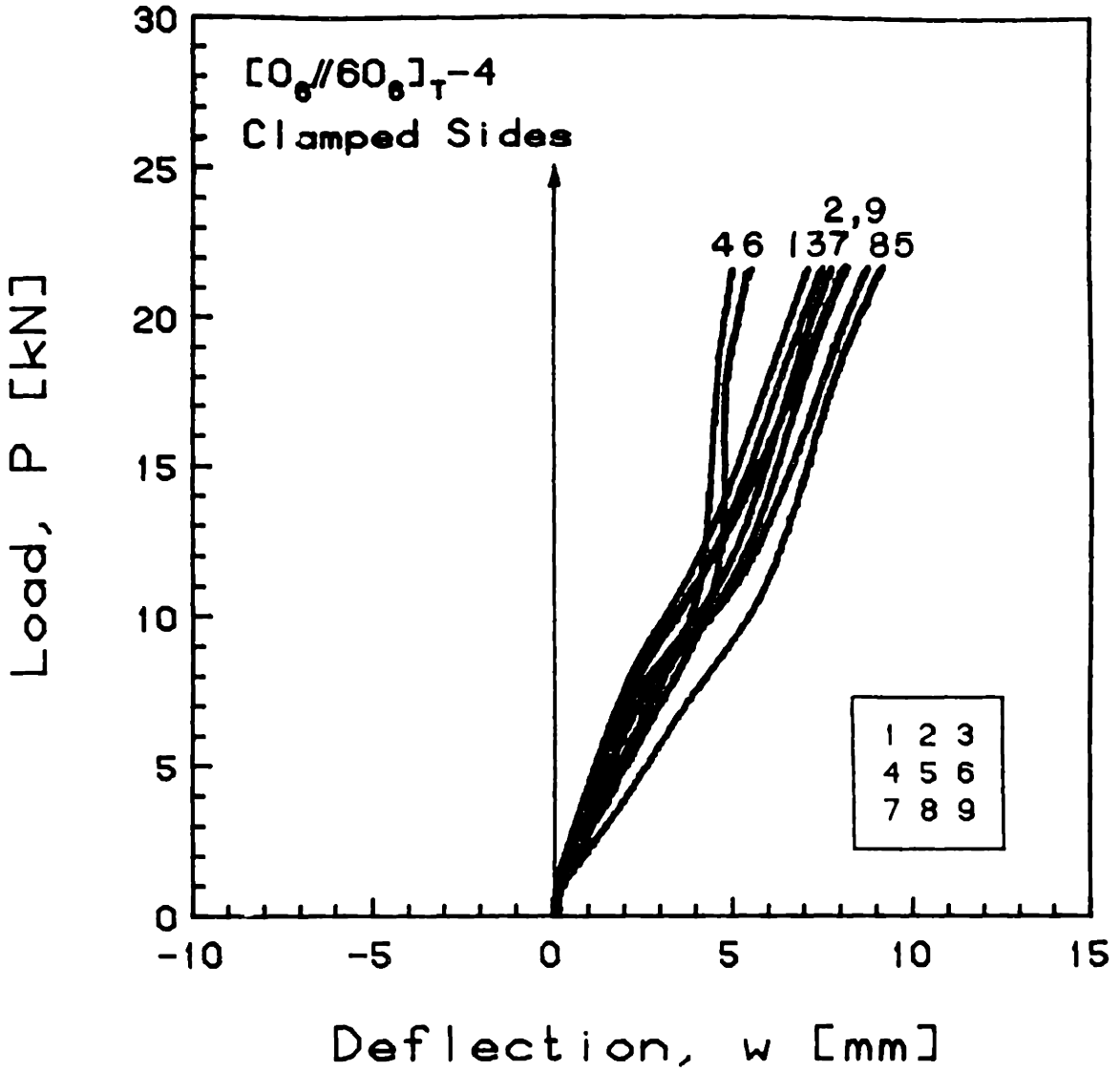

FIGURE E.54 Experimental Plot of Applied Compressive Load versus Out-of-Plane Deflection for the $[0_6//60_6]_T$-4 Laminate with Clamped Side Boundary Conditions

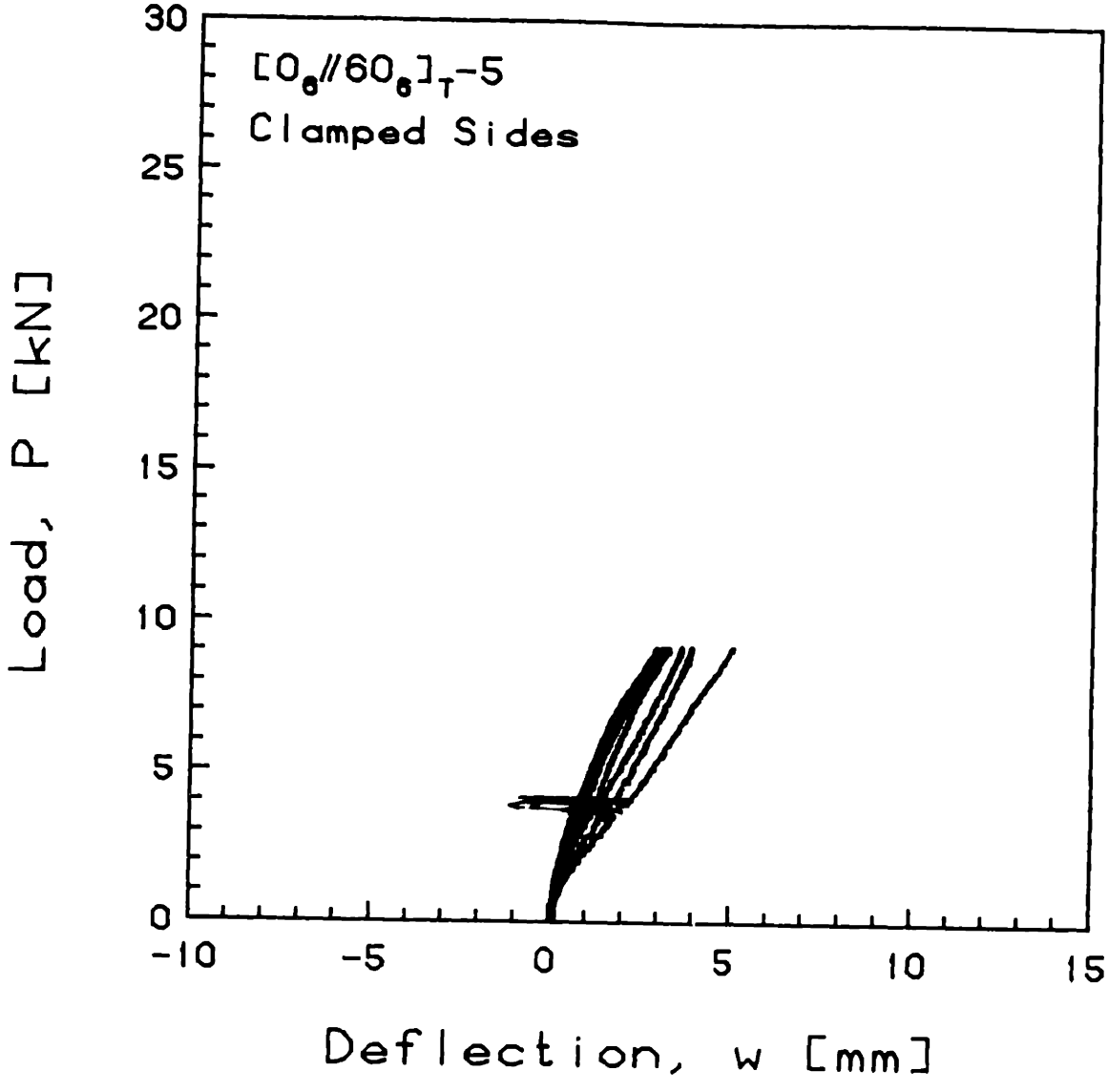

FIGURE E.55 Experimental Phase I Plot of Applied Compressive Load versus Out-of-Plane Deflection for the $[0_6//60_6]_T$-5 Laminate with Clamped Side Boundary Conditions

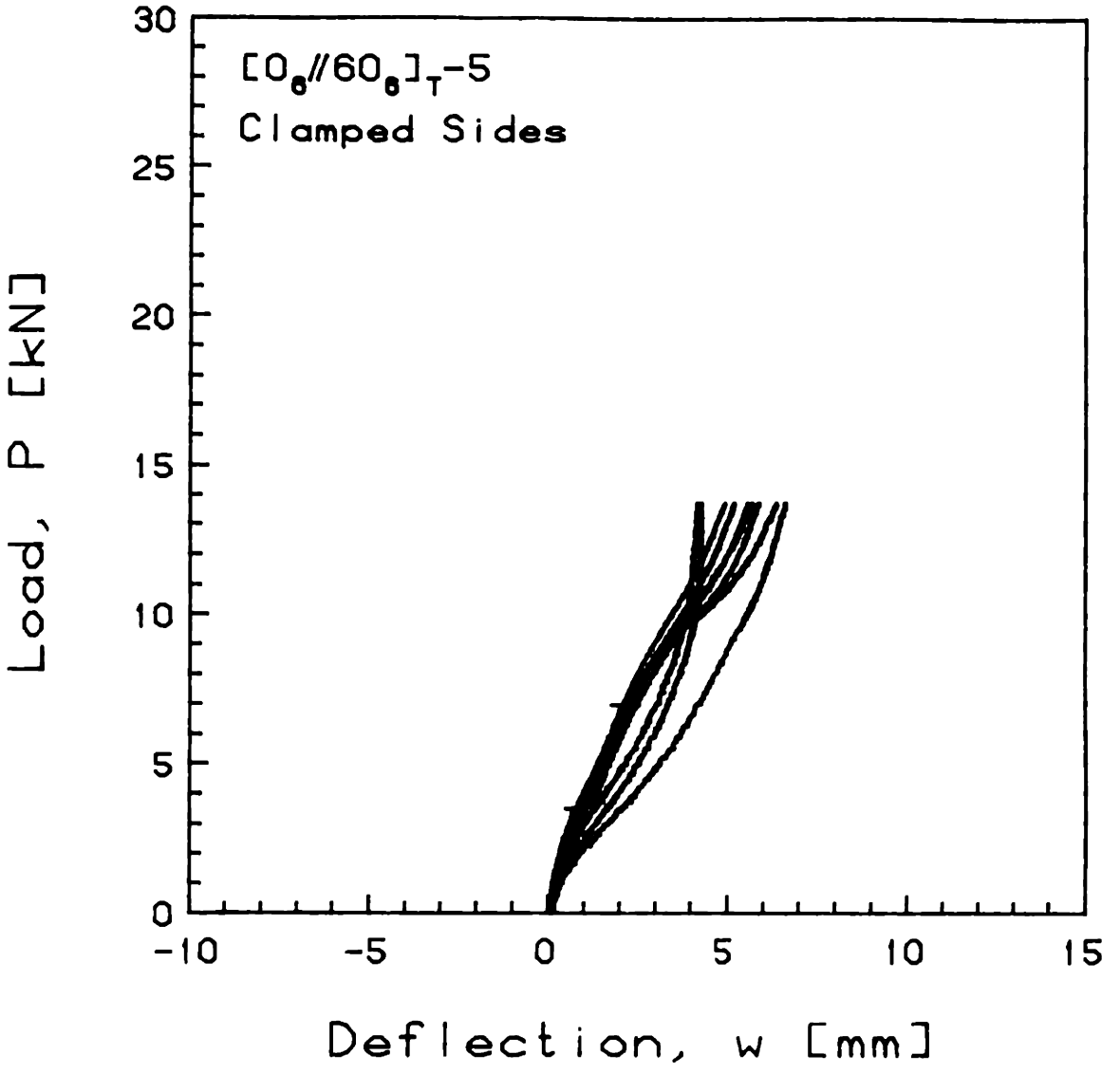

FIGURE E.56 Experimental Phase II Plot of Applied Compressive Load versus Out-of-Plane Deflection for the $[0_6//60_6]_T$-5 Laminate with Clamped Side Boundary Conditions

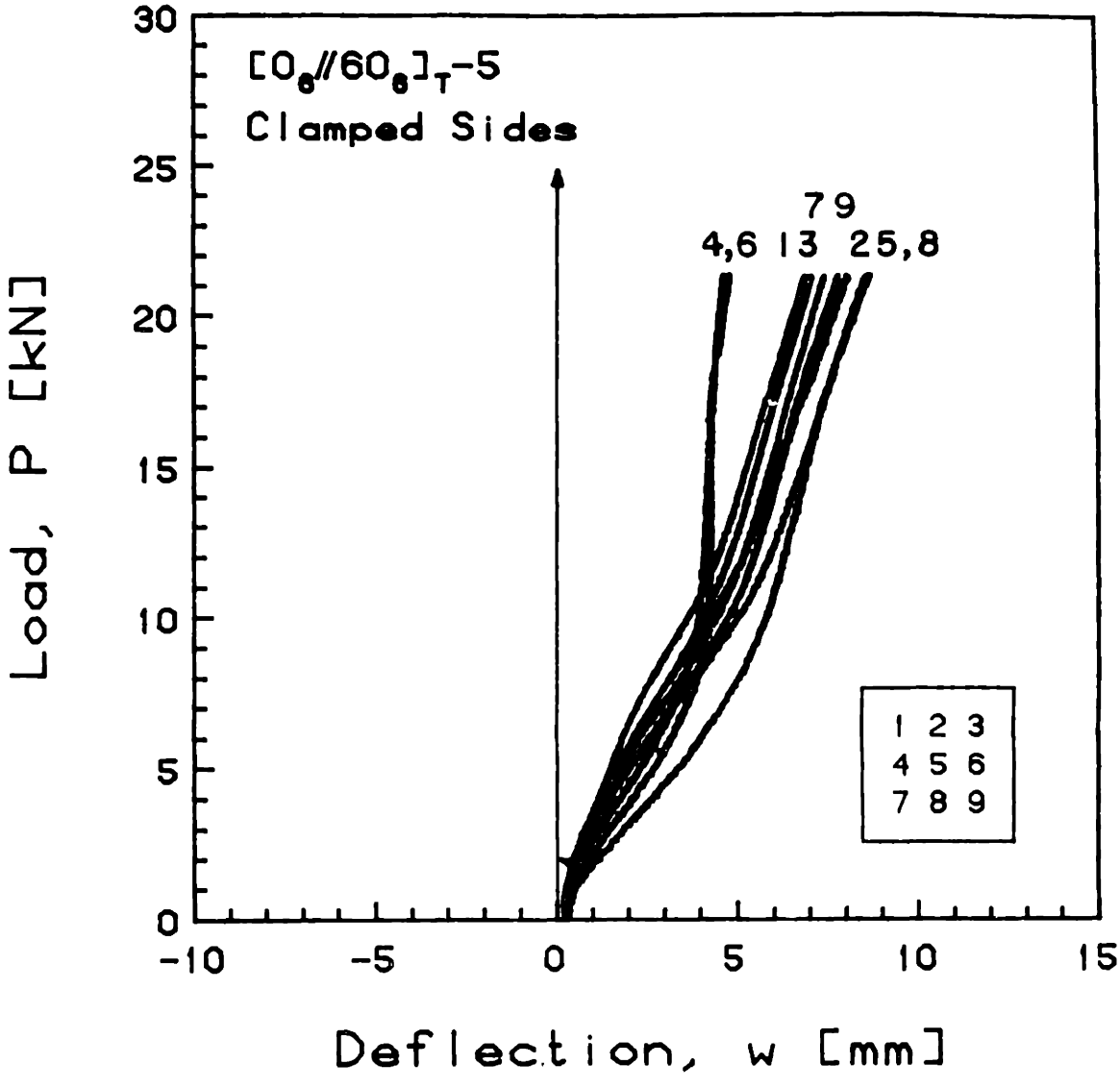

FIGURE E.57 Experimental Phase III Plot of Applied Compressive Load versus Out-of-Plane Deflection for the $[0_6//60_6]_T$-5 Laminate with Clamped Side Boundary Conditions

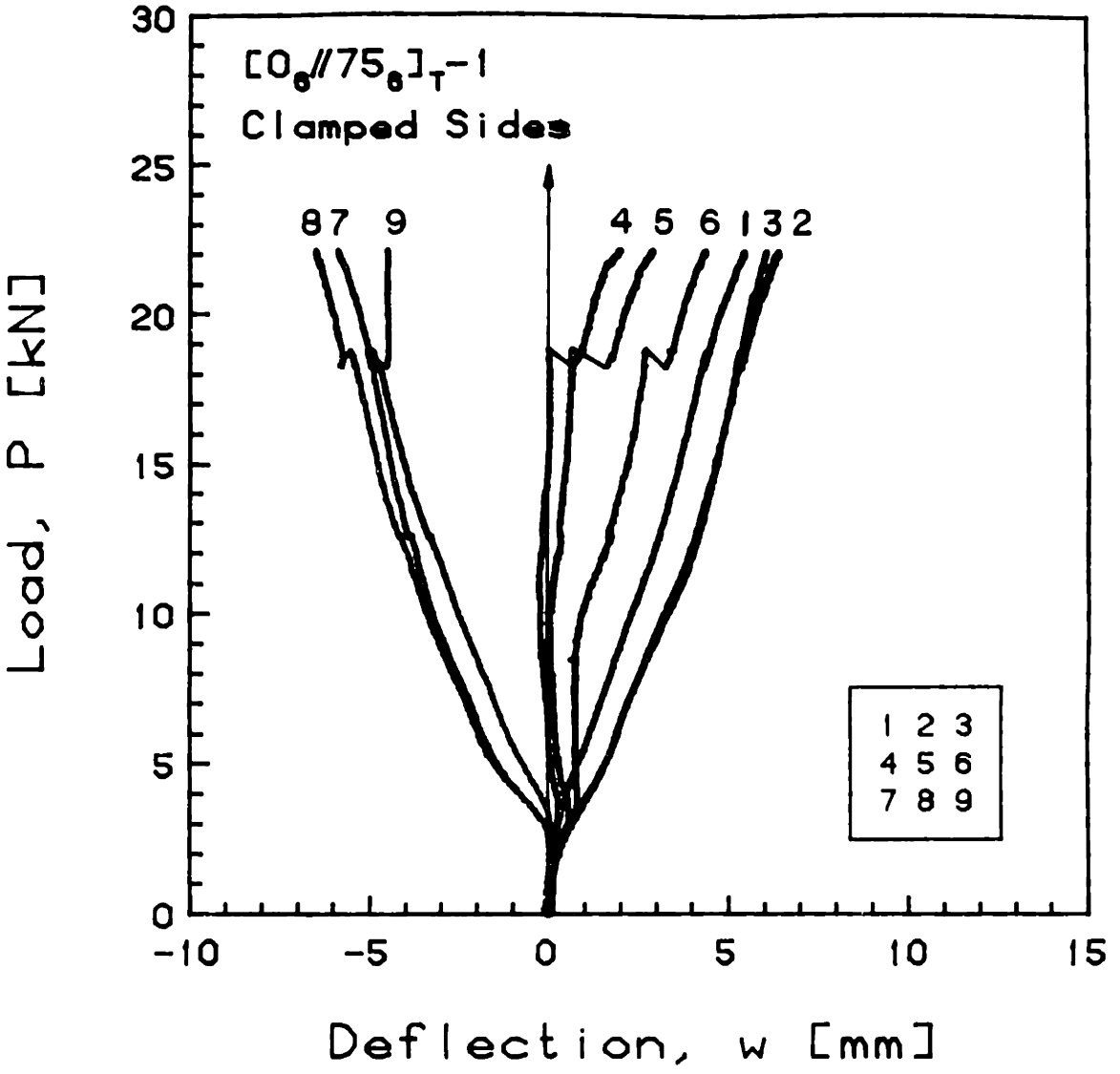

FIGURE E.58 Experimental Plot of Applied Compressive Load versus Out-of-Plane Deflection for the $[0_6//75_6]_T$-1 Laminate with Clamped Side Boundary Conditions

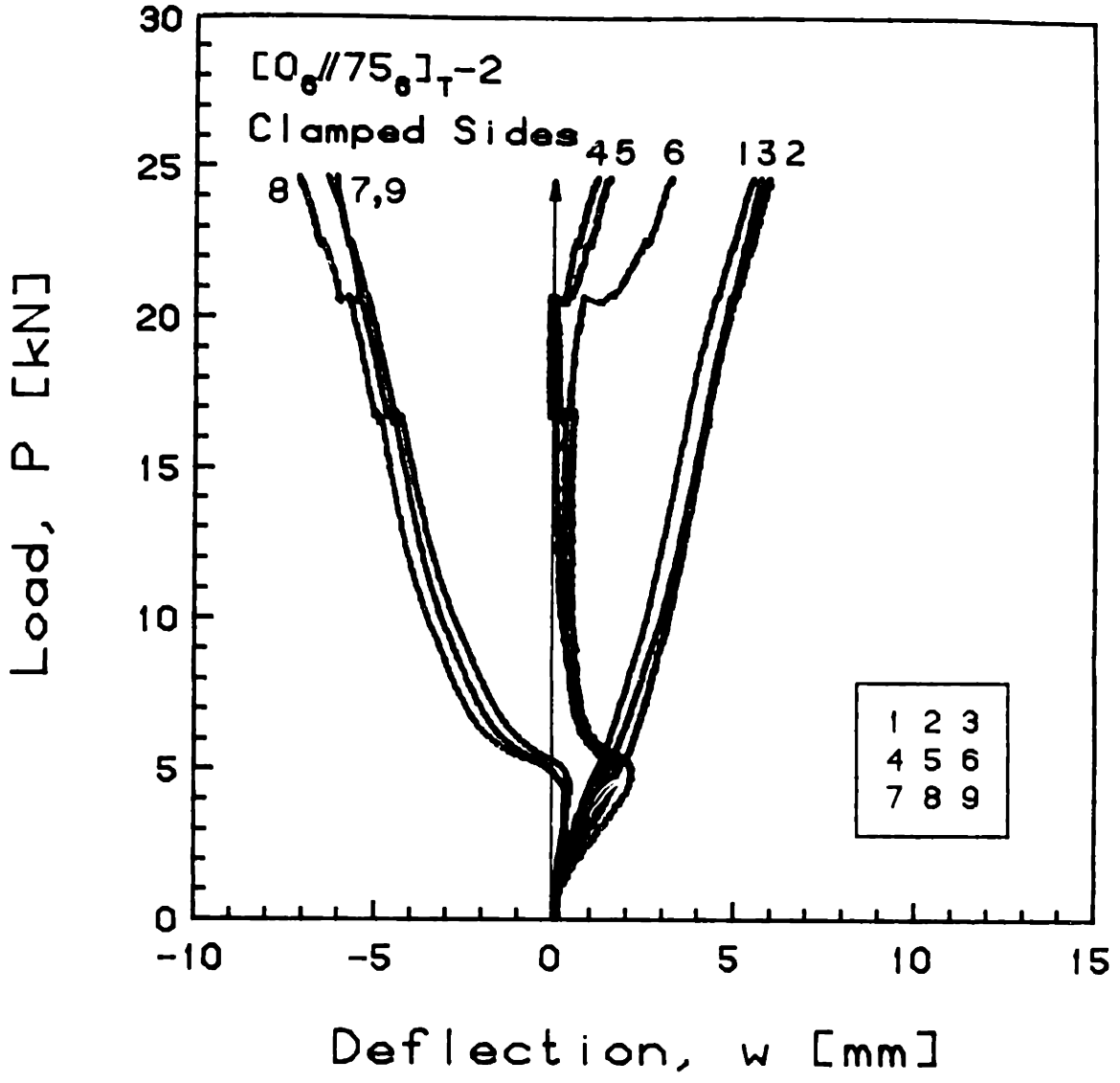

FIGURE E.59 Experimental Plot of Applied Compressive Load versus Out-of-Plane Deflection for the $[0_6//75_6]_T$-2 Laminate with Clamped Side Boundary Conditions

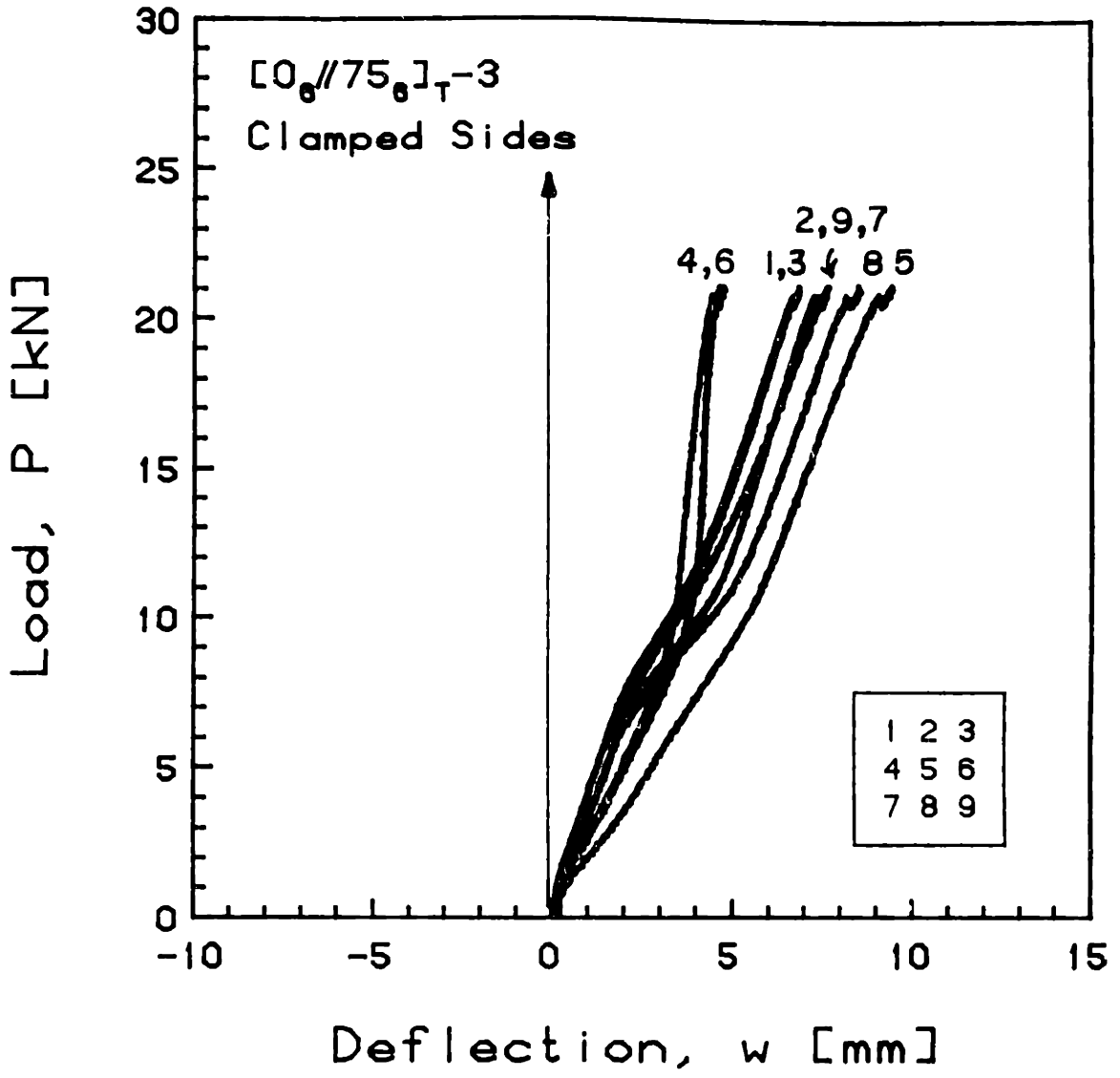

FIGURE E.60 Experimental Plot of Applied Compressive Load versus Out-of-Plane Deflection for the $[0_6//75_6]_T$-3 Laminate with Clamped Side Boundary Conditions

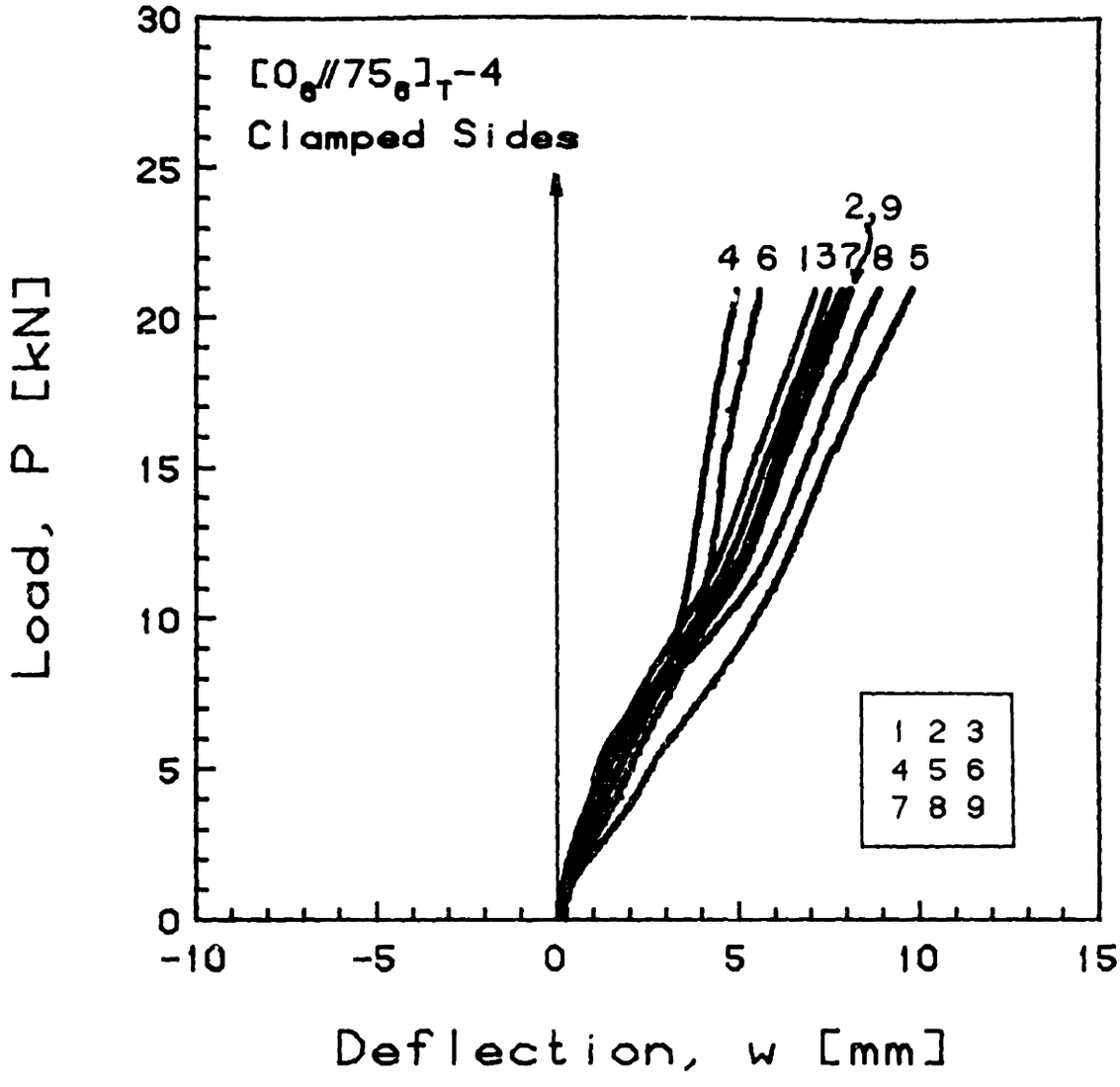

FIGURE E.61 Experimental Plot of Applied Compressive Load versus Out-of-Plane Deflection for the $[0_6//75_6]_T$-4 Laminate with Clamped Side Boundary Conditions

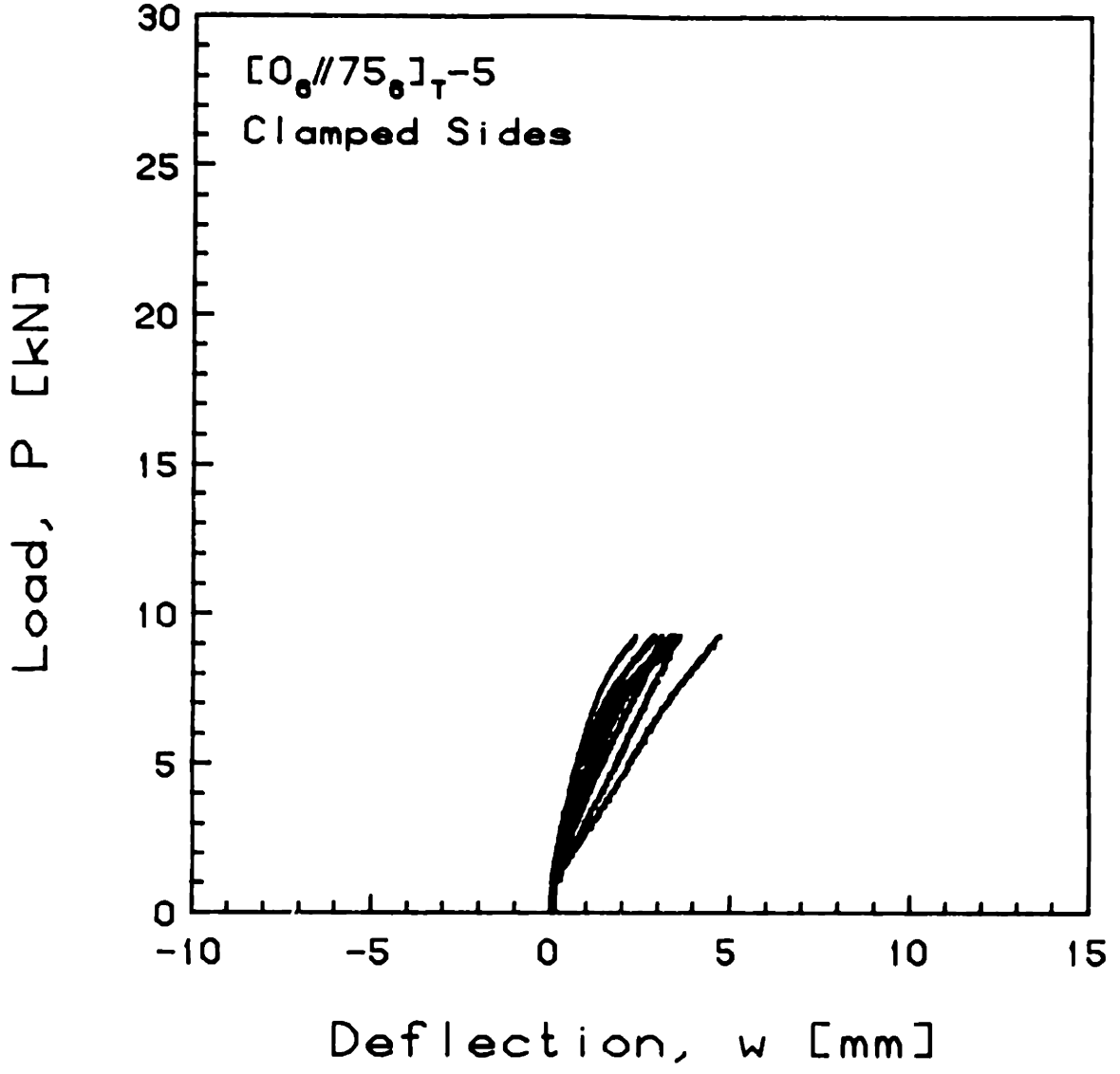

FIGURE E.62 Experimental Phase I Plot of Applied Compressive Load versus Out-of-Plane Deflection for the $[0_6//75_6]_T$-5 Laminate with Clamped Side Boundary Conditions

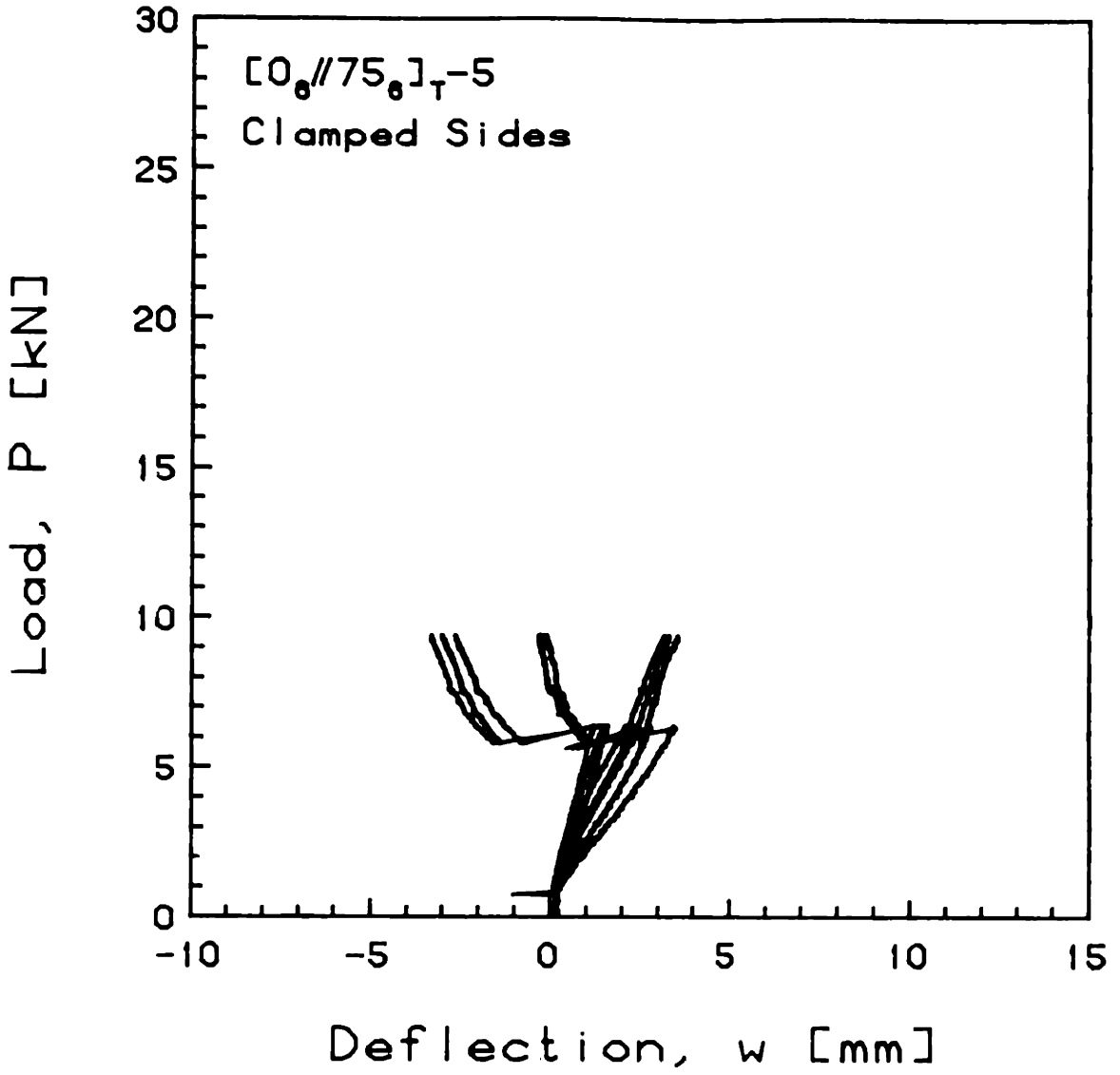

FIGURE E.63 Experimental Phase II Plot of Applied Compressive Load versus Out-of-Plane Deflection for the $[O_6//75_6]_T$-5 Laminate with Clamped Side Boundary Conditions

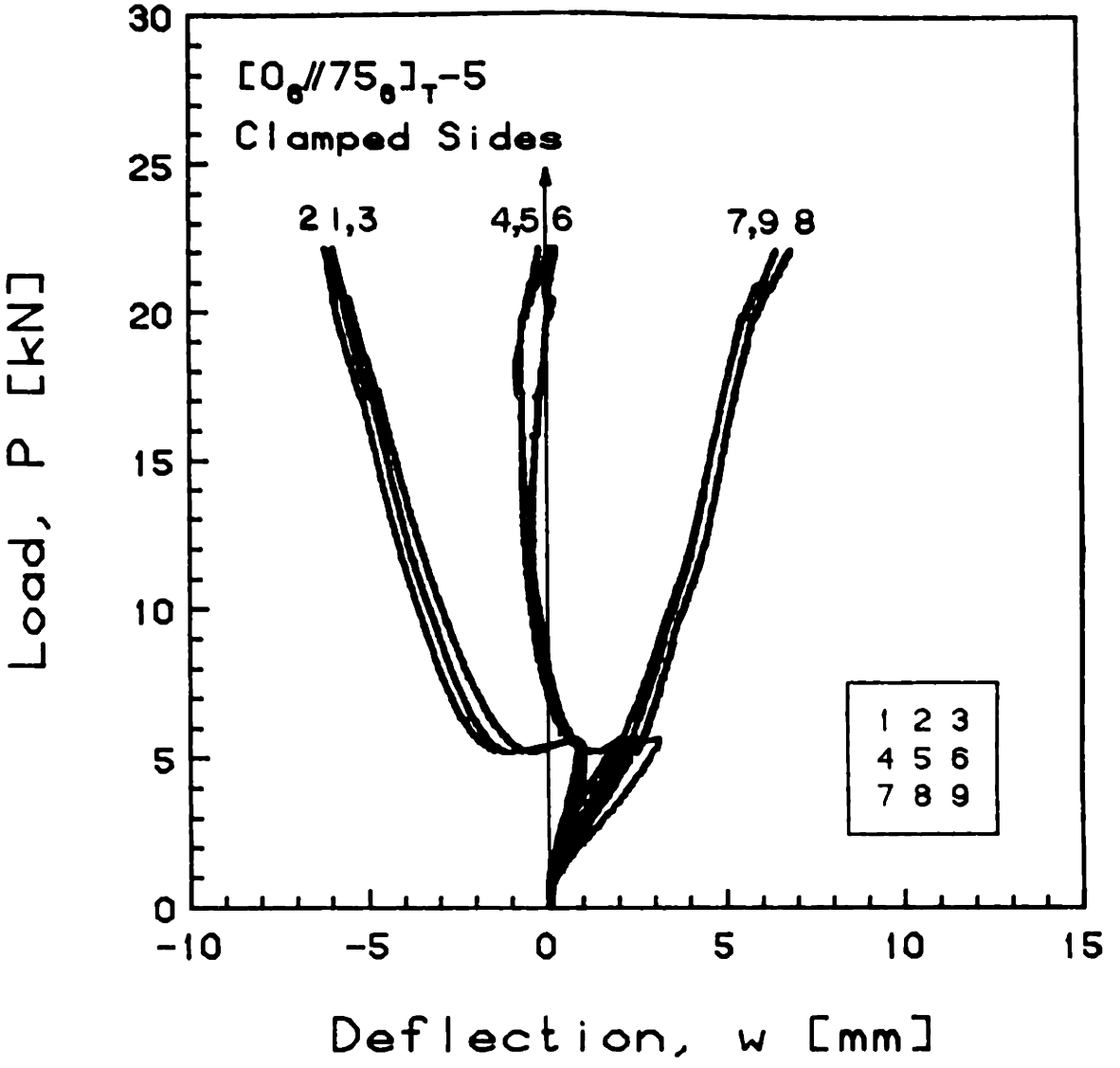

FIGURE E.64 Experimental Phase III Plot of Applied Compressive Load versus Out-of-Plane Deflection for the $[0_6//75_6]_T$-5 Laminate with Clamped Side Boundary Conditions

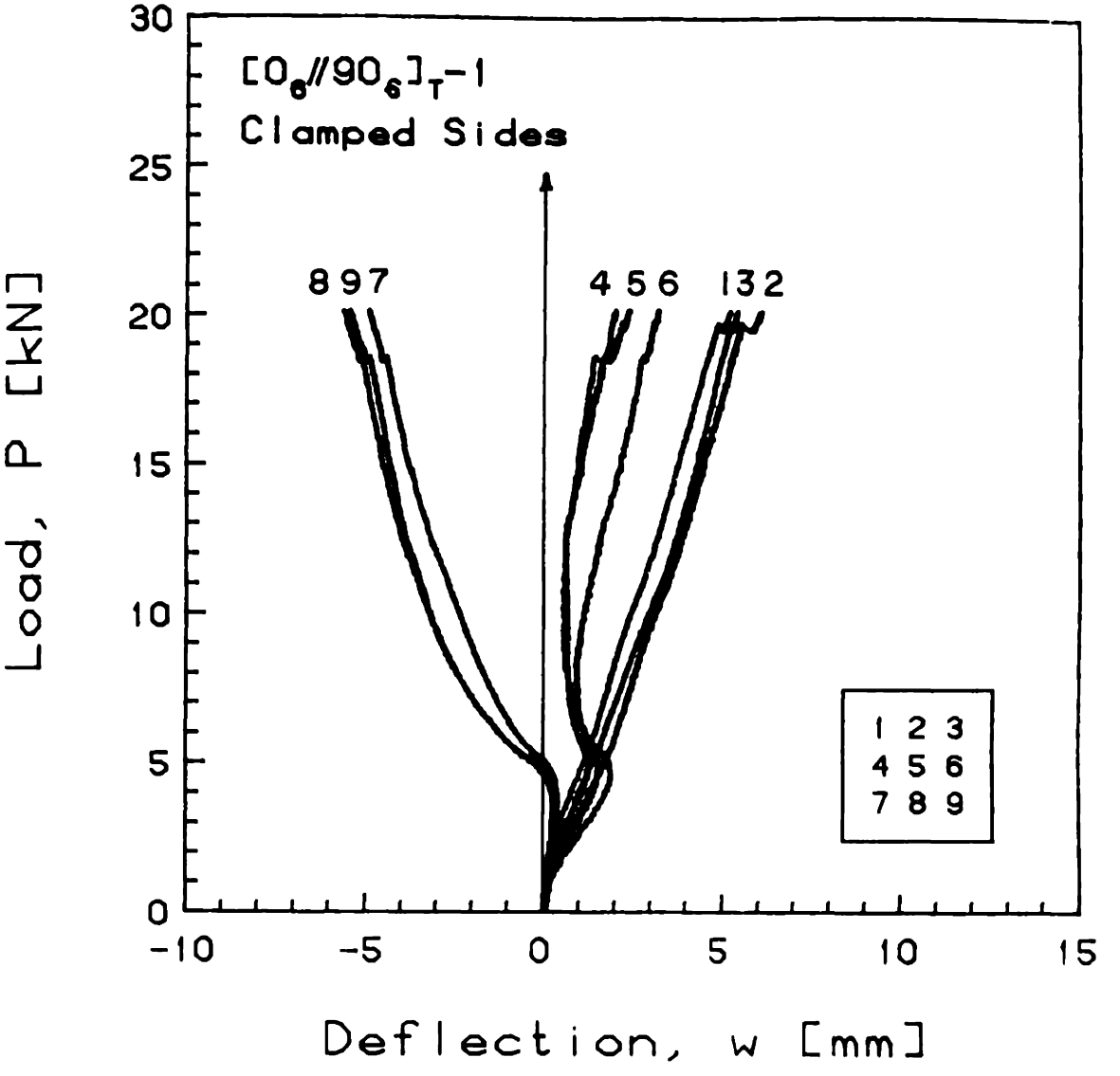

FIGURE E.65 Experimental Plot of Applied Compressive Load versus Out-of-Plane Deflection for the $[0_6//90_6]_T$-1 Laminate with Clamped Side Boundary Conditions

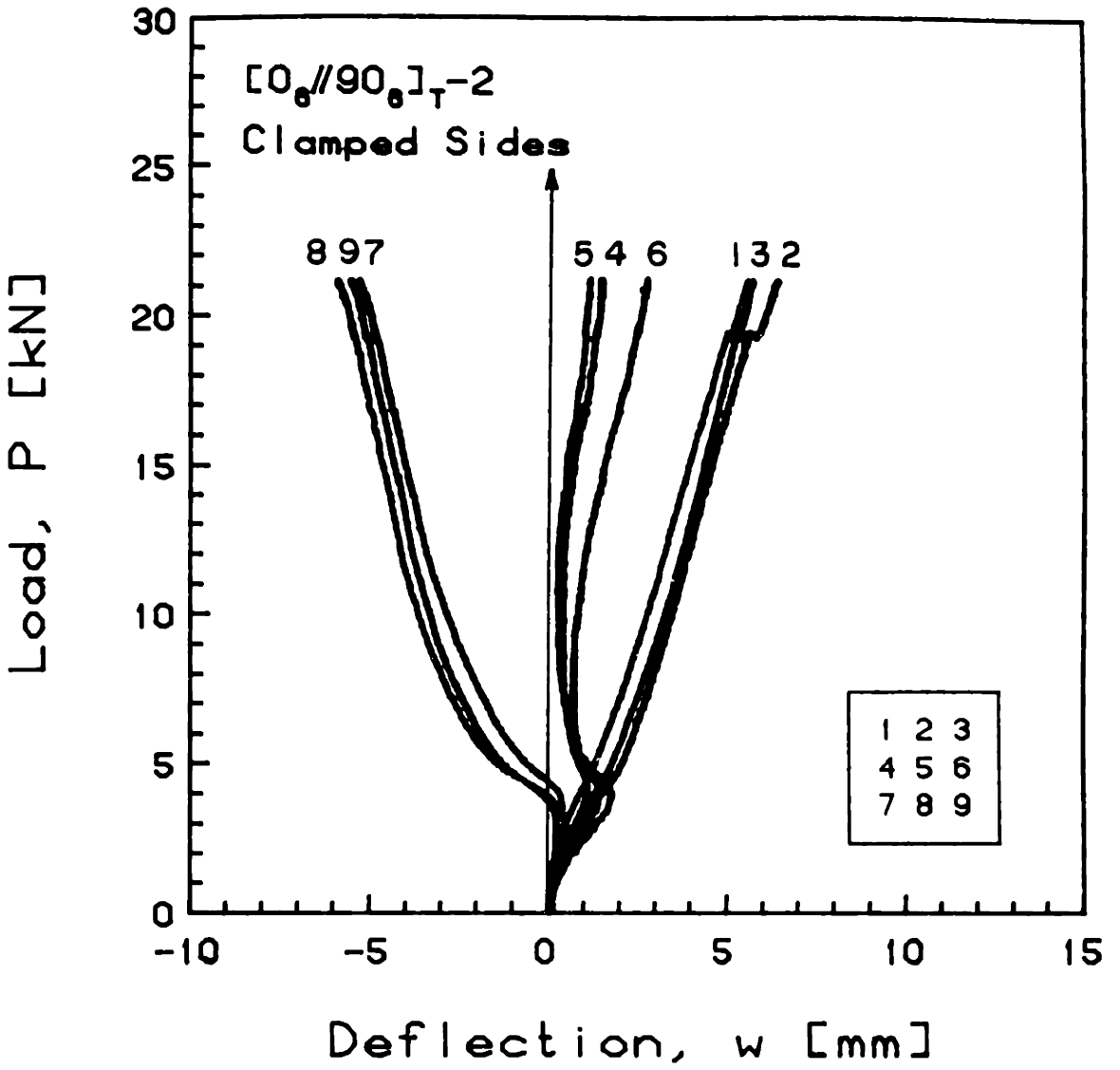

FIGURE E.66 Experimental Plot of Applied Compressive Load versus Out-of-Plane Deflection for the $[0_6//90_6]_T$-2 Laminate with Clamped Side Boundary Conditions

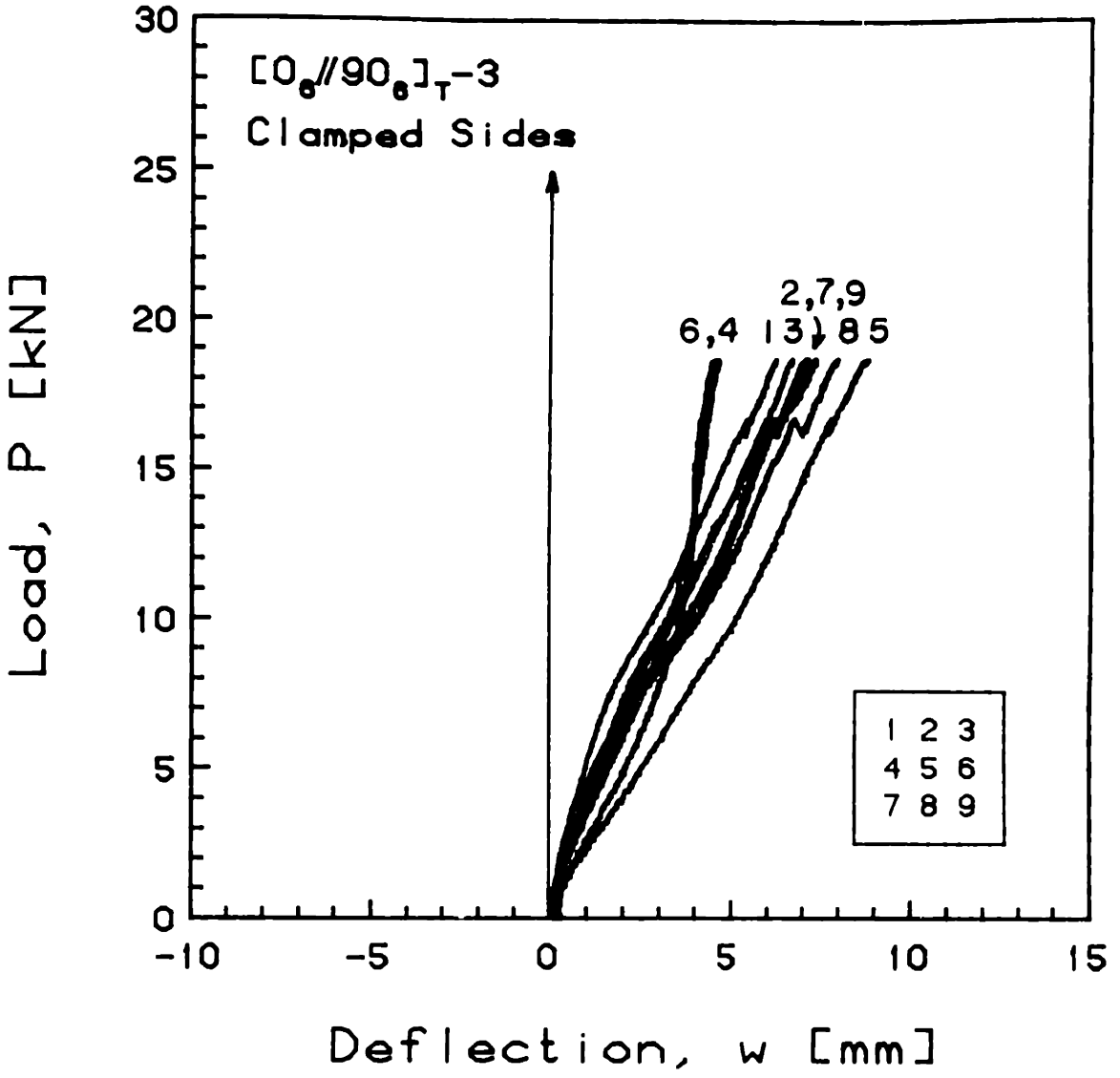

FIGURE E.67 Experimental Plot of Applied Compressive Load versus Out-of-Plane Deflection for the $[0_6//90_6]_T$-3 Laminate with Clamped Side Boundary Conditions

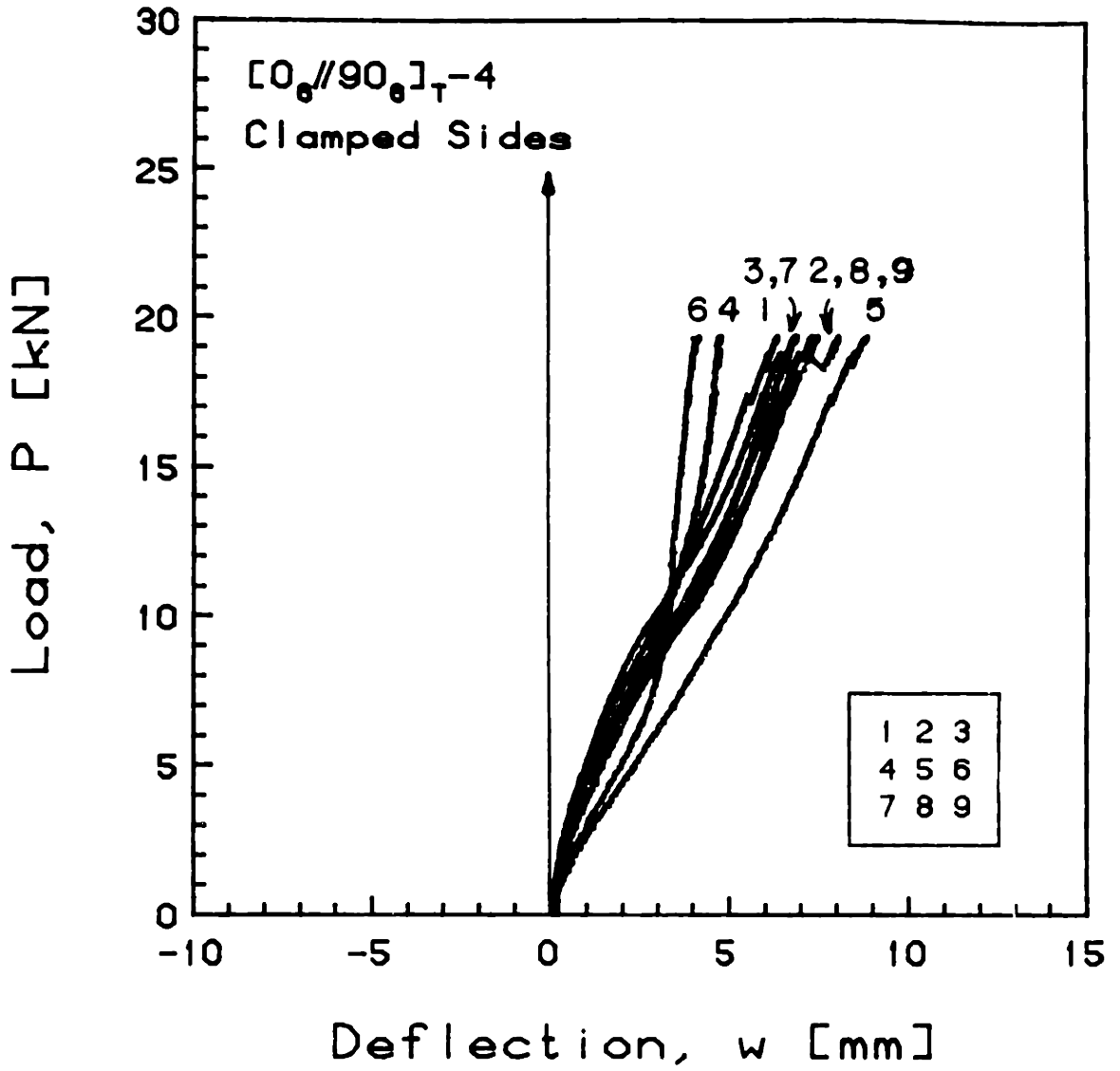

FIGURE E.68 Experimental Plot of Applied Compressive Load versus Out-of-Plane Deflection for the $[0_6//90_6]_T$-4 Laminate with Clamped Side Boundary Conditions

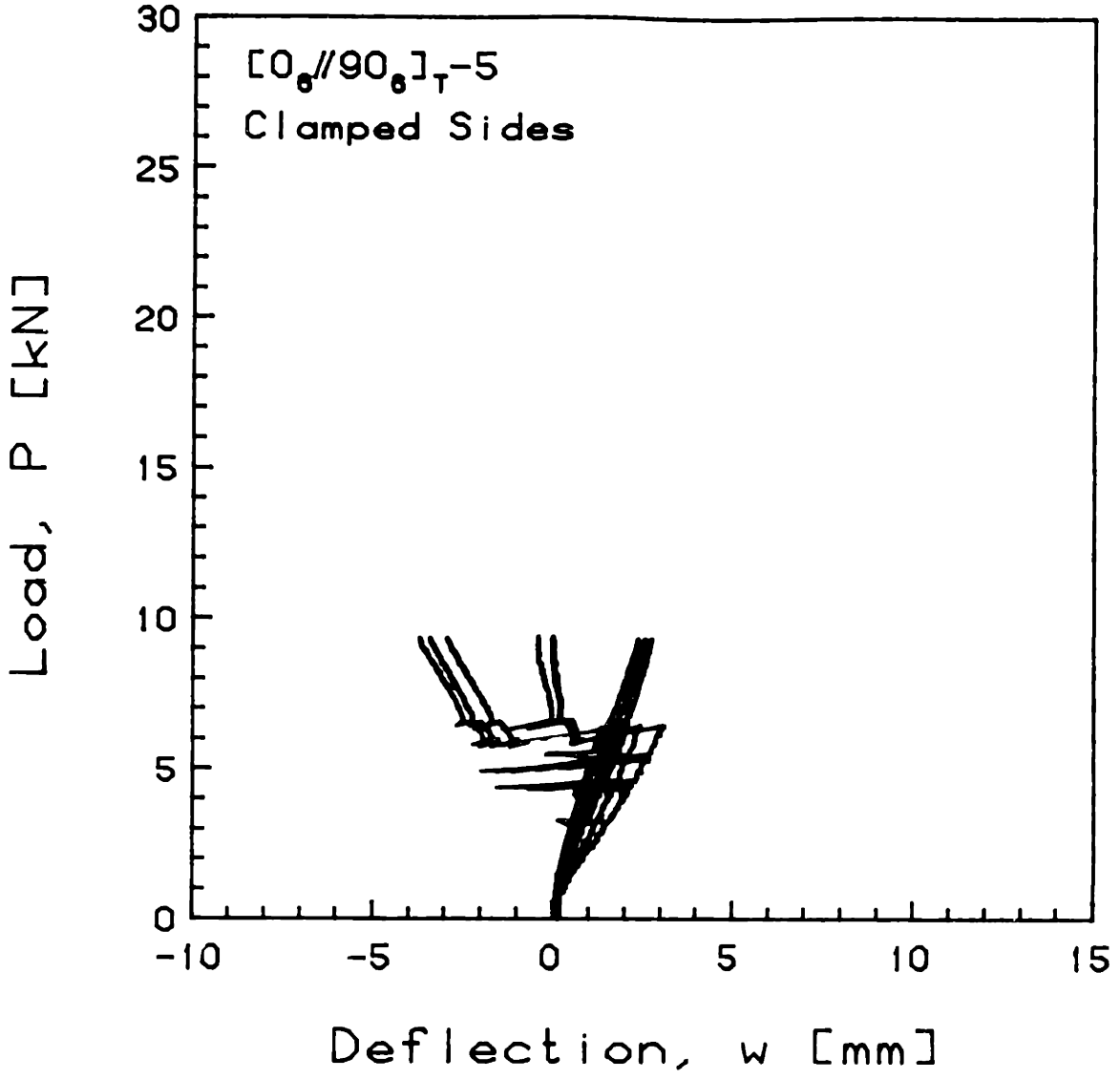

FIGURE E.69 Experimental Phase I Plot of Applied Compressive Load versus Out-of-Plane Deflection for the $[0_6//90_6]_T$-5 Laminate with Clamped Side Boundary Conditions

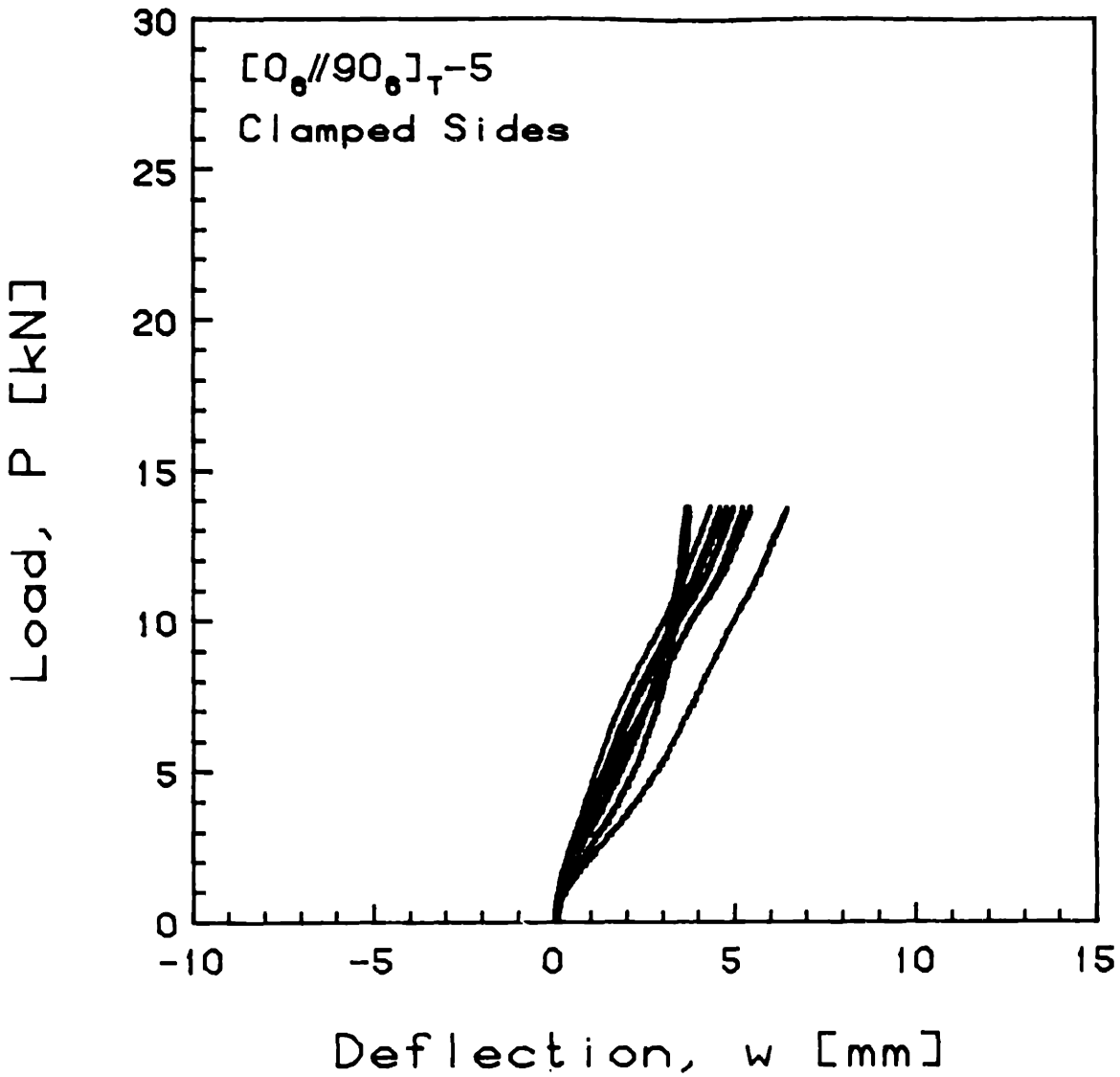

FIGURE E.70 Experimental Phase II Plot of Applied Compressive Load versus Out-of-Plane Deflection for the $[0_6//90_6]_T$-5 Laminate with Clamped Side Boundary Conditions

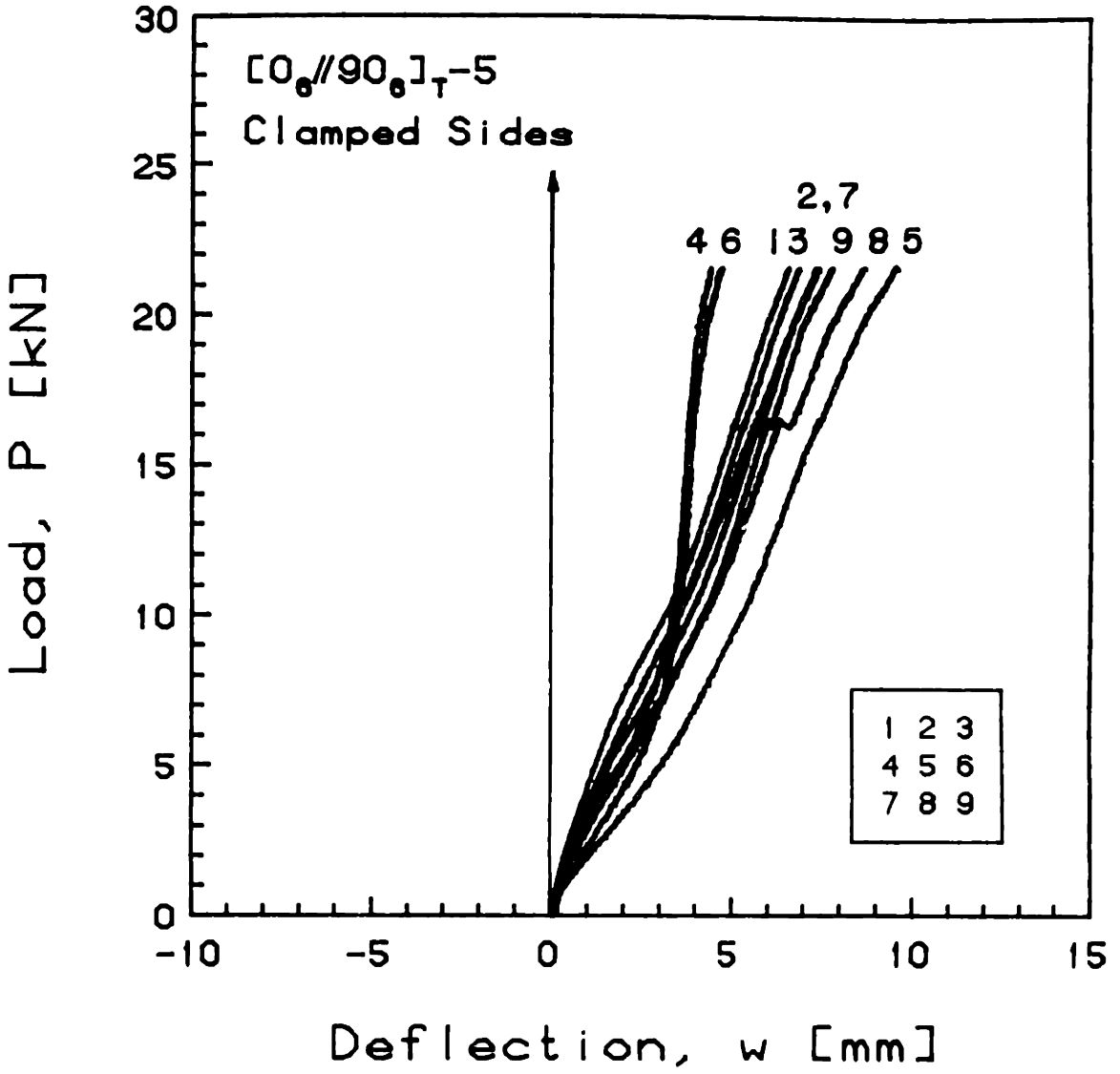

FIGURE E.71 Experimental Phase III Plot of Applied Compressive Load versus Out-of-Plane Deflection for the $[0_6//90_6]_T$-5 Laminate with Clamped Side Boundary Conditions

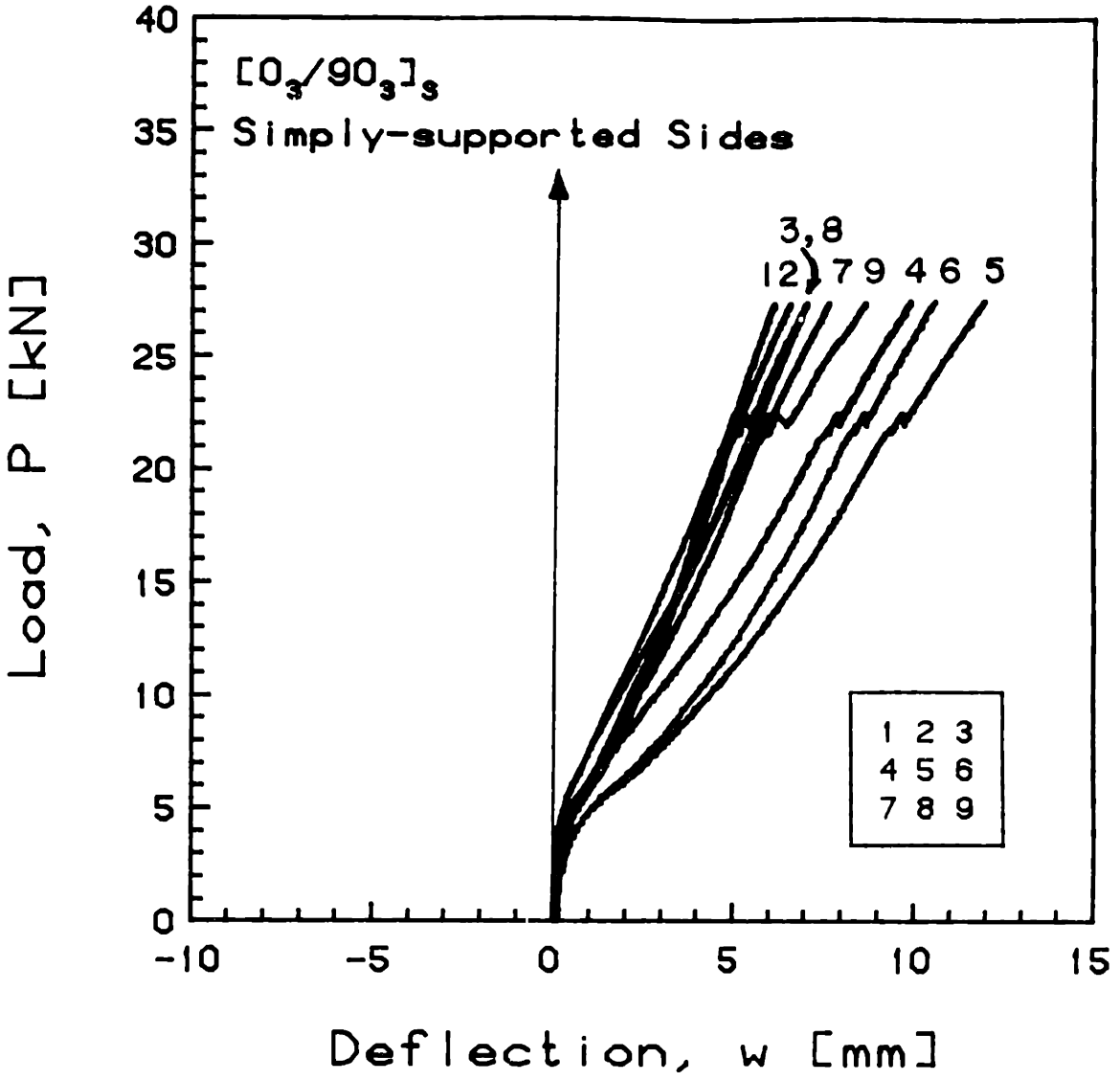

FIGURE E.72 Experimental Plot of Applied Compressive Load versus Out-of-Plane Deflection for the $[0_3/90_3]_S$ Laminate with Simply-Supported Side Boundary Conditions

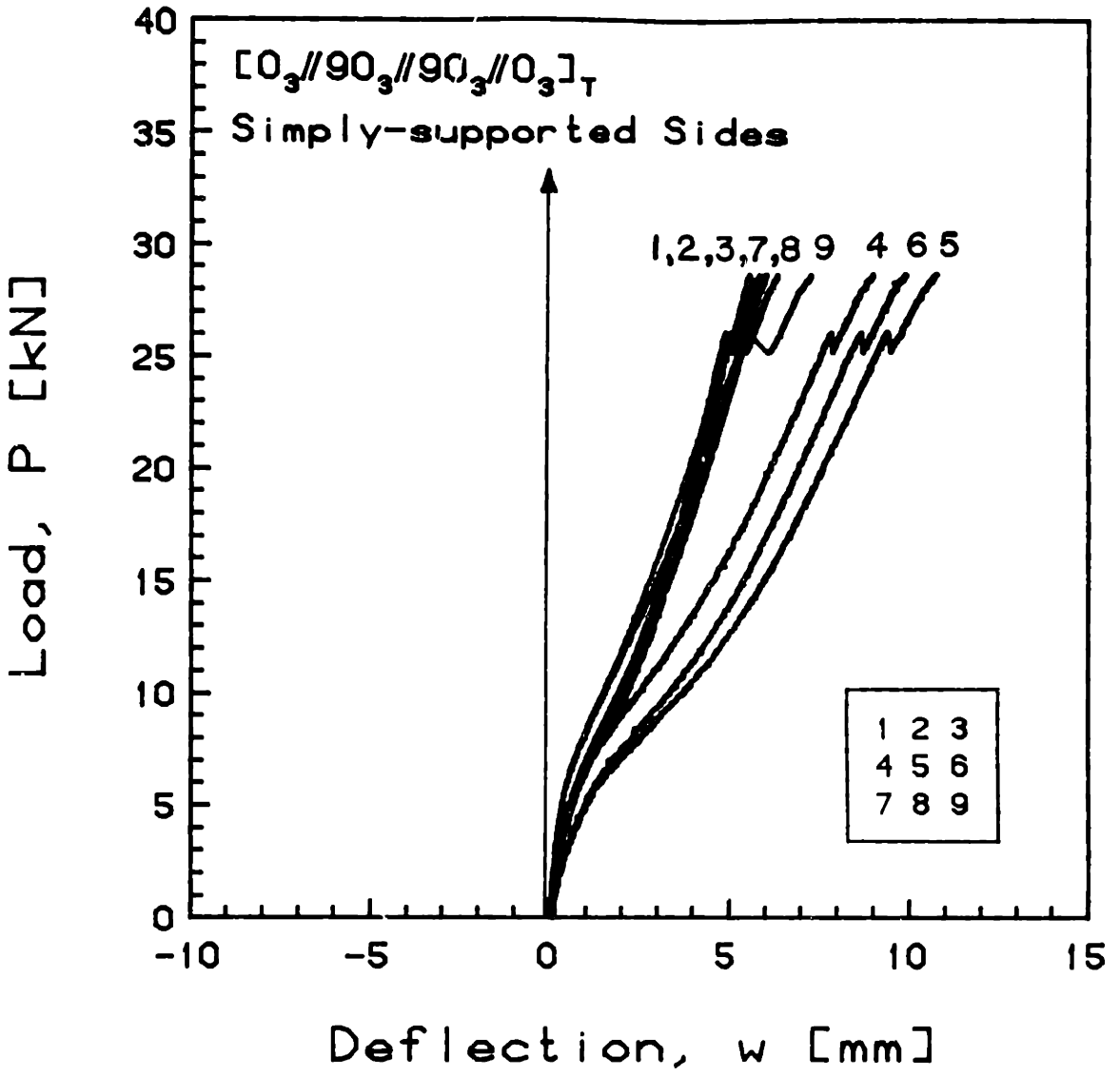

FIGURE E.73 Experimental Plot of Applied Compressive Load versus Out-of-Plane Deflection for the $[0_3//90_3//90_3//0_3]_T$ Laminate with Simply-Supported Side Boundary Conditions

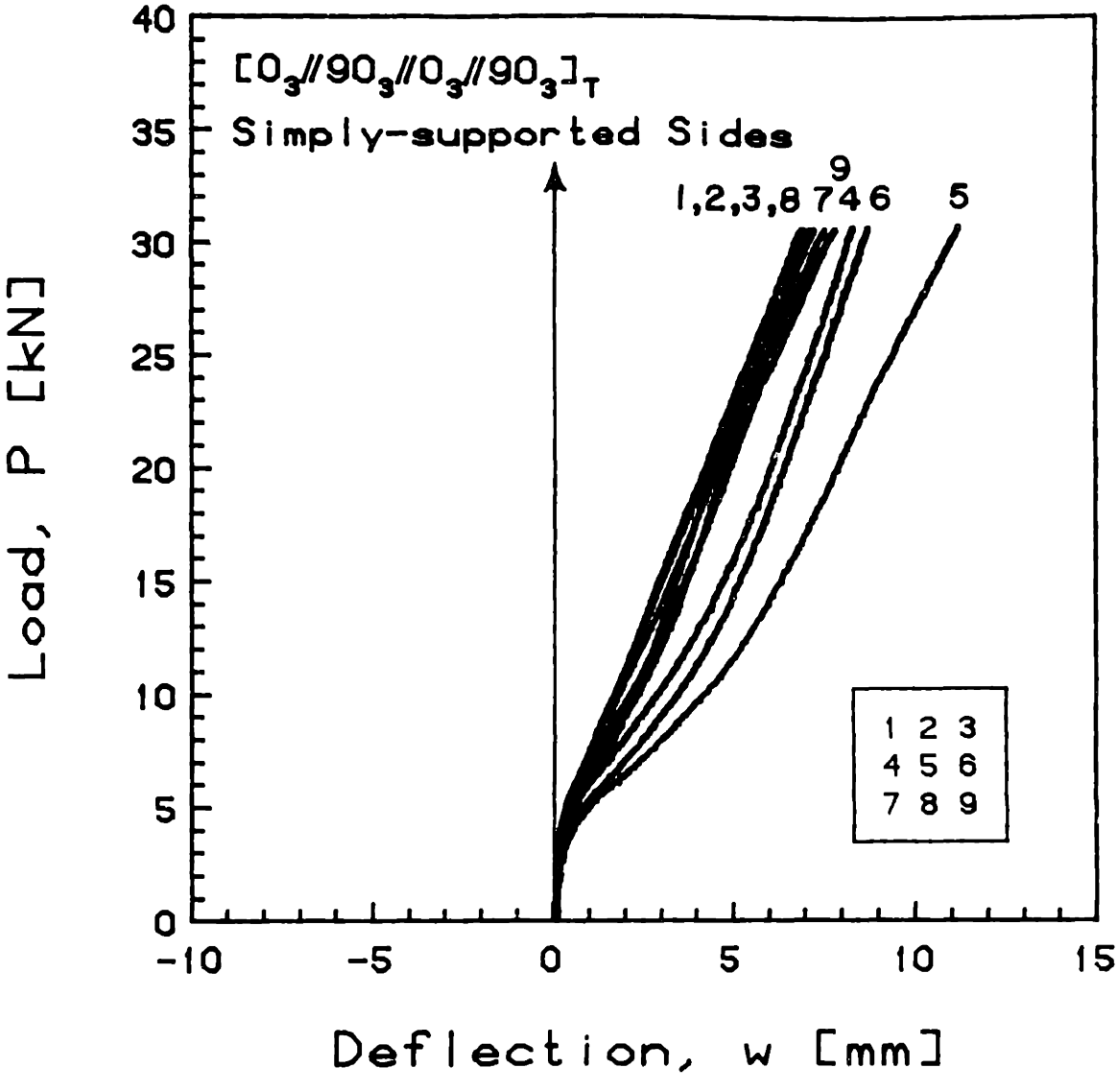

FIGURE E.74 Experimental Plot of Applied Compressive Load versus Out-of-Plane Deflection for the $[0_3//90_3//0_3//90_3]_T$ Laminate with Simply-Supported Side Boundary Conditions

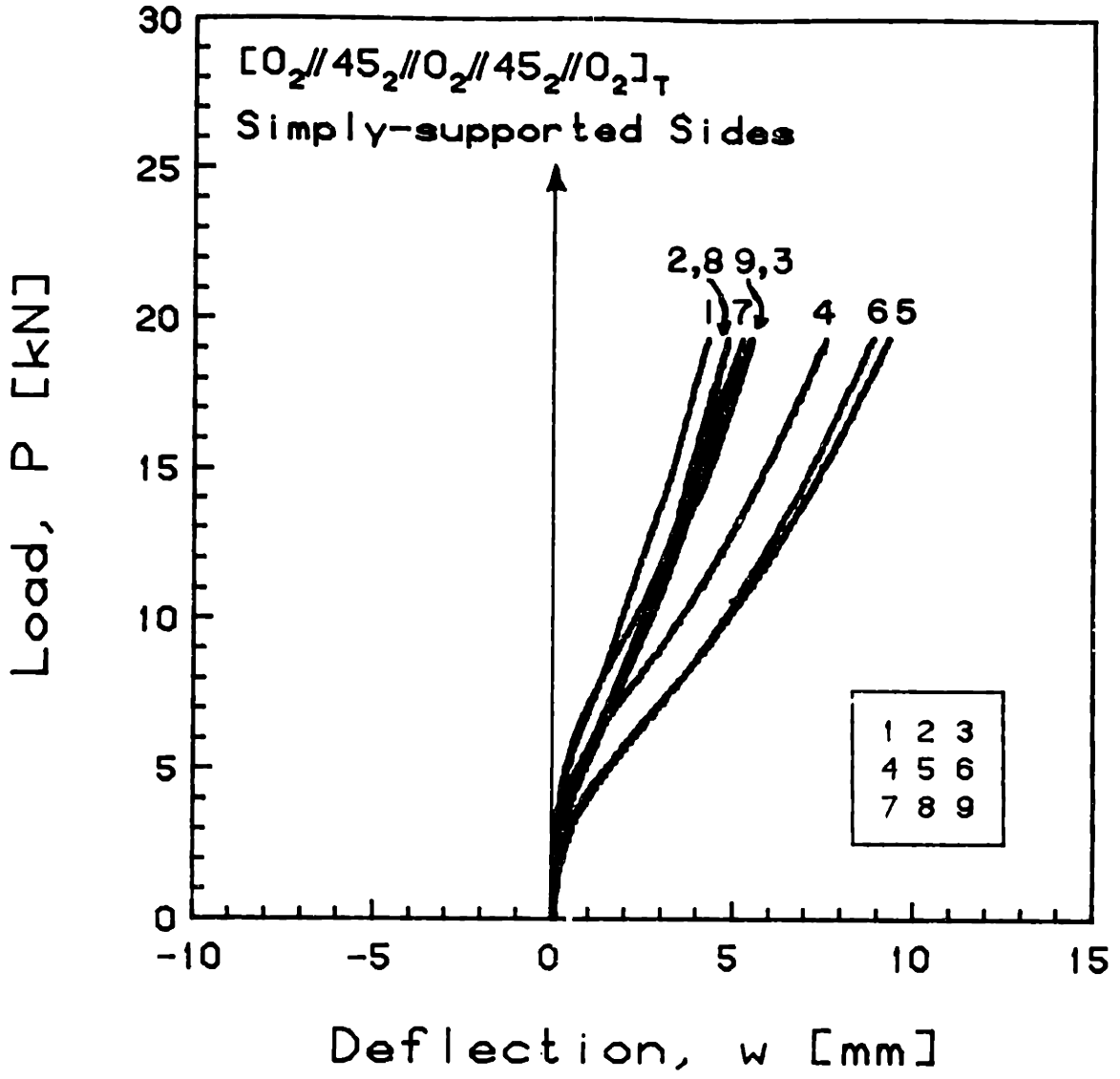

FIGURE E.75 Experimental Plot of Applied Compressive Load versus Out-of-Plane Deflection for the $[O_2//45_2//O_2//45_2//O_2]_T$ Laminate with Simply-Supported Side Boundary Conditions

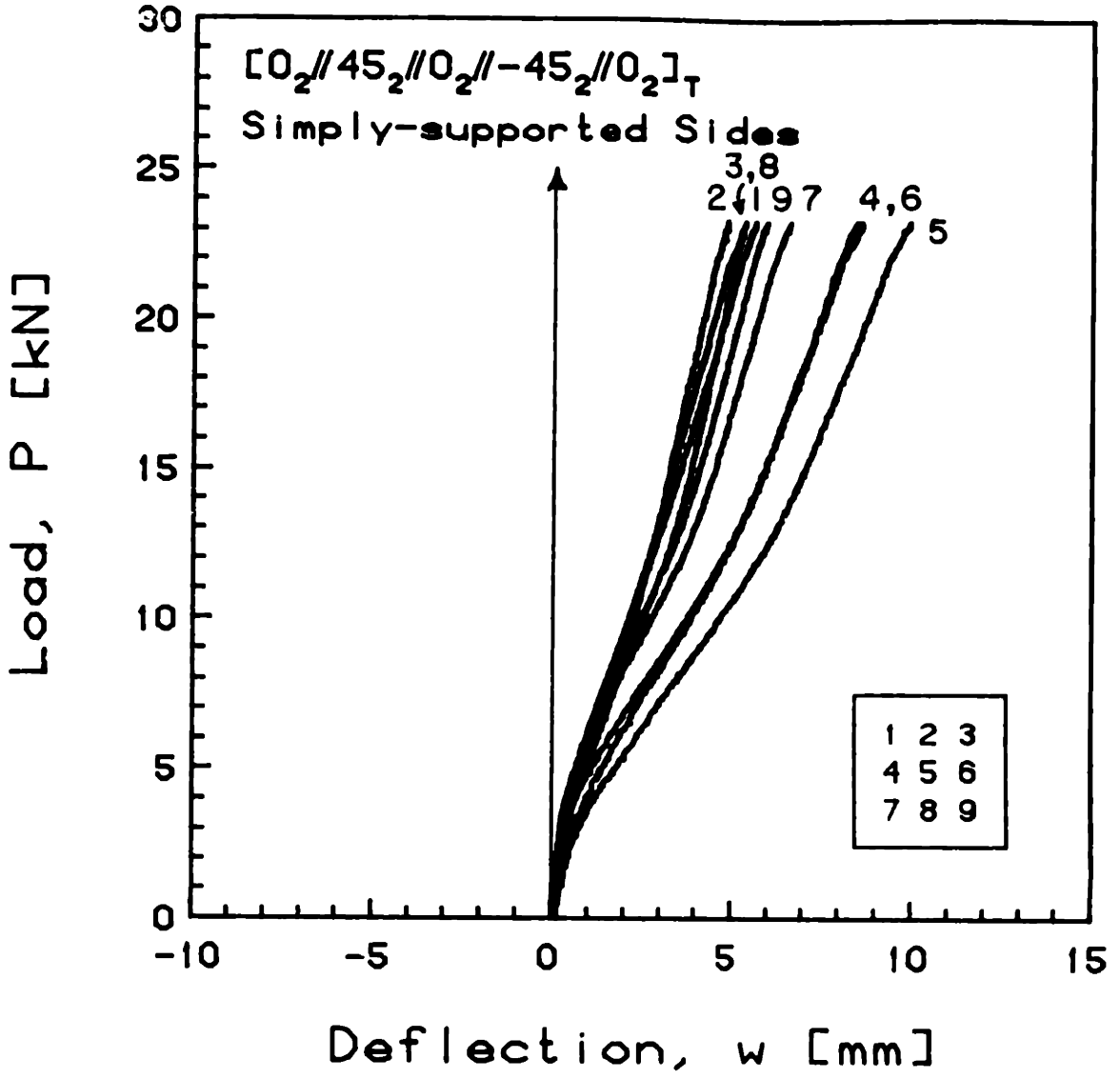

FIGURE E.76 Experimental Plot of Applied Compressive Load versus Out-of-Plane Deflection for the $[0_2//45_2//0_2//-45_2//0_2]_T$ Laminate with Simply-Supported Side Boundary Conditions

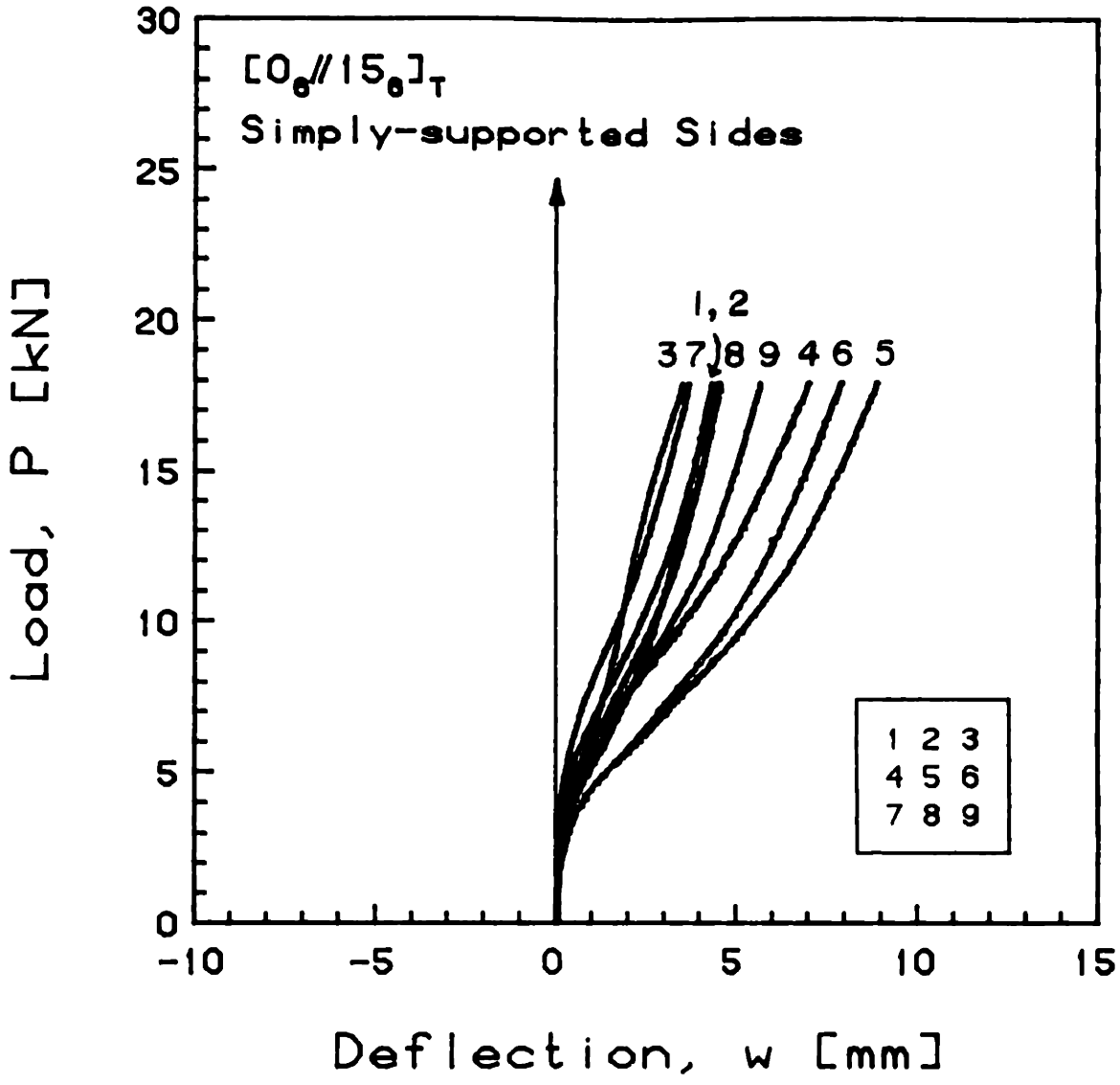

FIGURE E.77 Experimental Plot of Applied Compressive Load versus Out-of-Plane Deflection for the $[0_6//15_6]_T$ Laminate with Simply-Supported Side Boundary Conditions

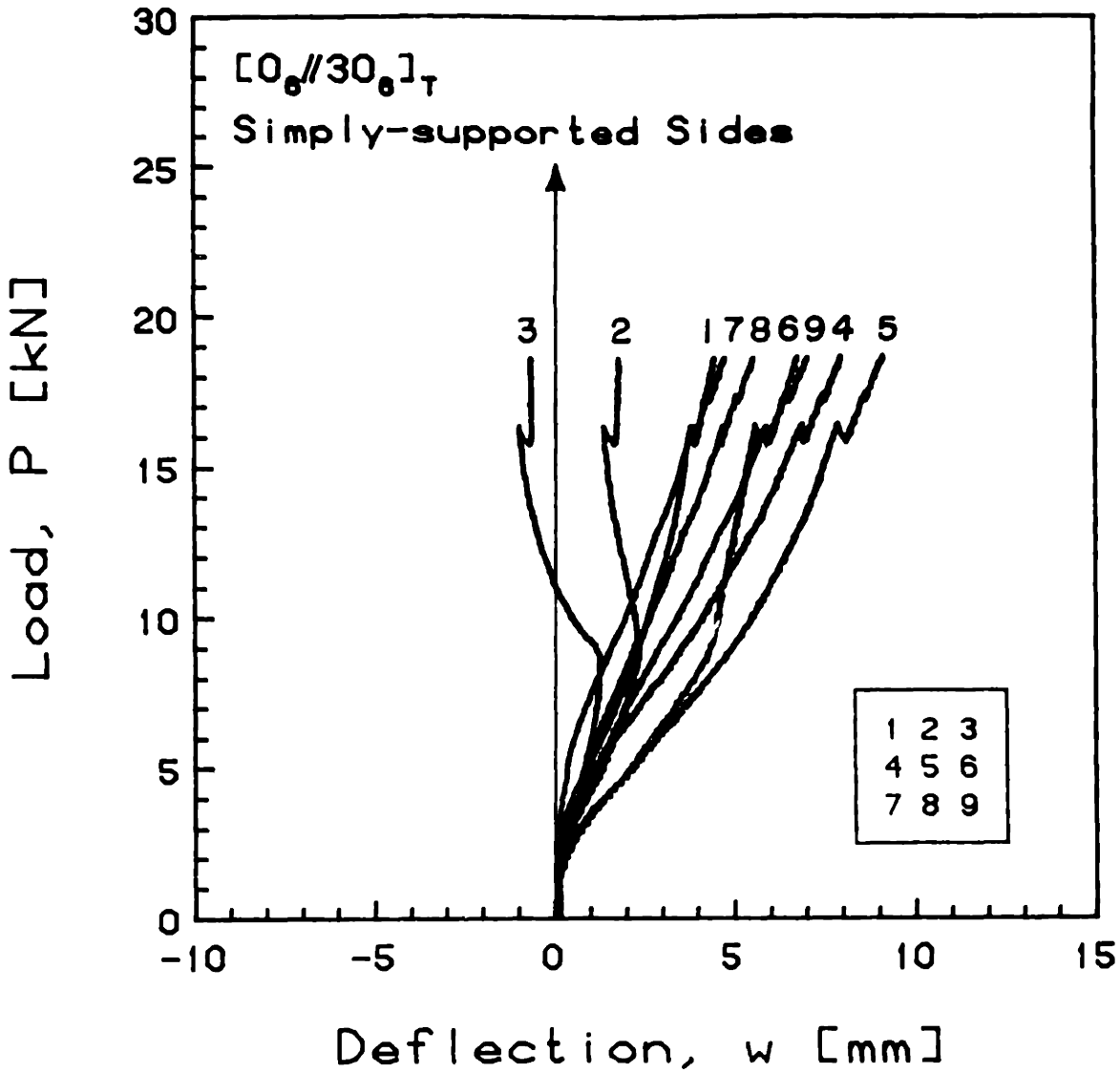

FIGURE E.78 Experimental Plot of Applied Compressive Load versus Out-of-Plane Deflection for the $[0_6//30_6]_T$ Laminate with Simply-Supported Side Boundary Conditions

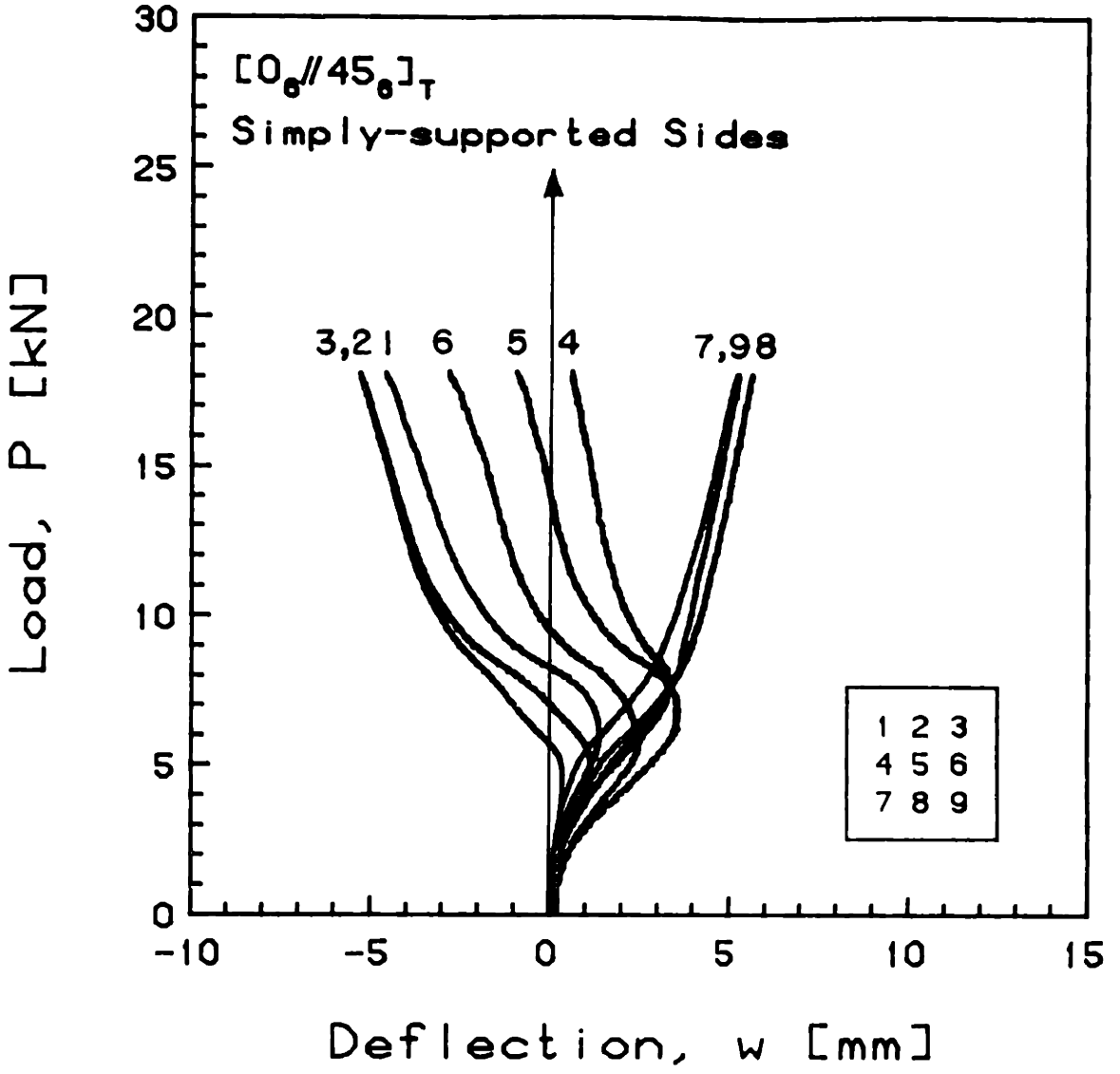

FIGURE E.79 Experimental Plot of Applied Compressive Load versus Out-of-Plane Deflection for the $[0_6//45_6]_T$ Laminate with Simply-Supported Side Boundary Conditions

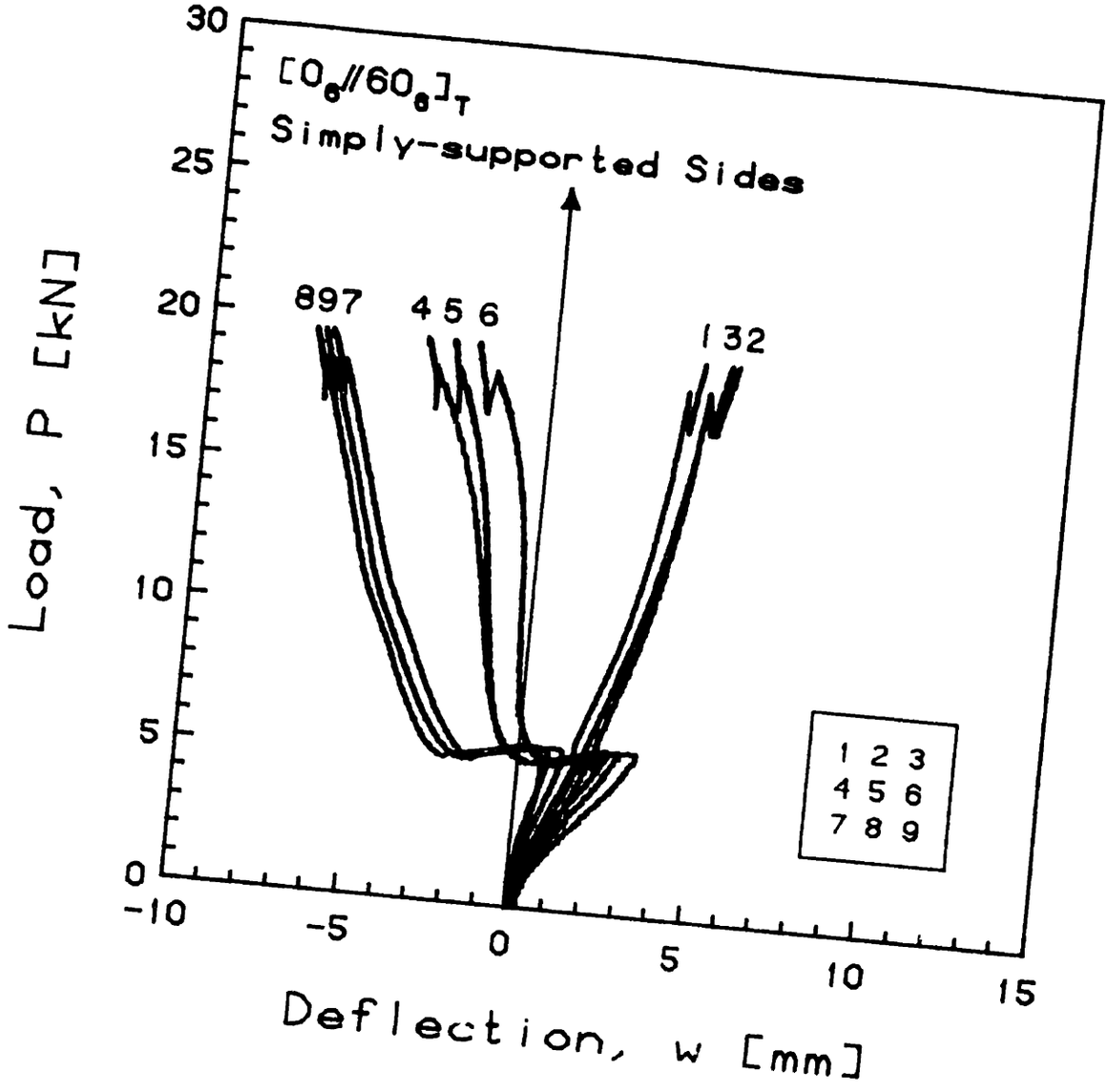

FIGURE E.80 Experimental Plot of Applied Compressive Load versus Out-of-Plane Deflection for the $[0_6//60_6]_T$ Laminate with Simply-Supported Side Boundary Conditions

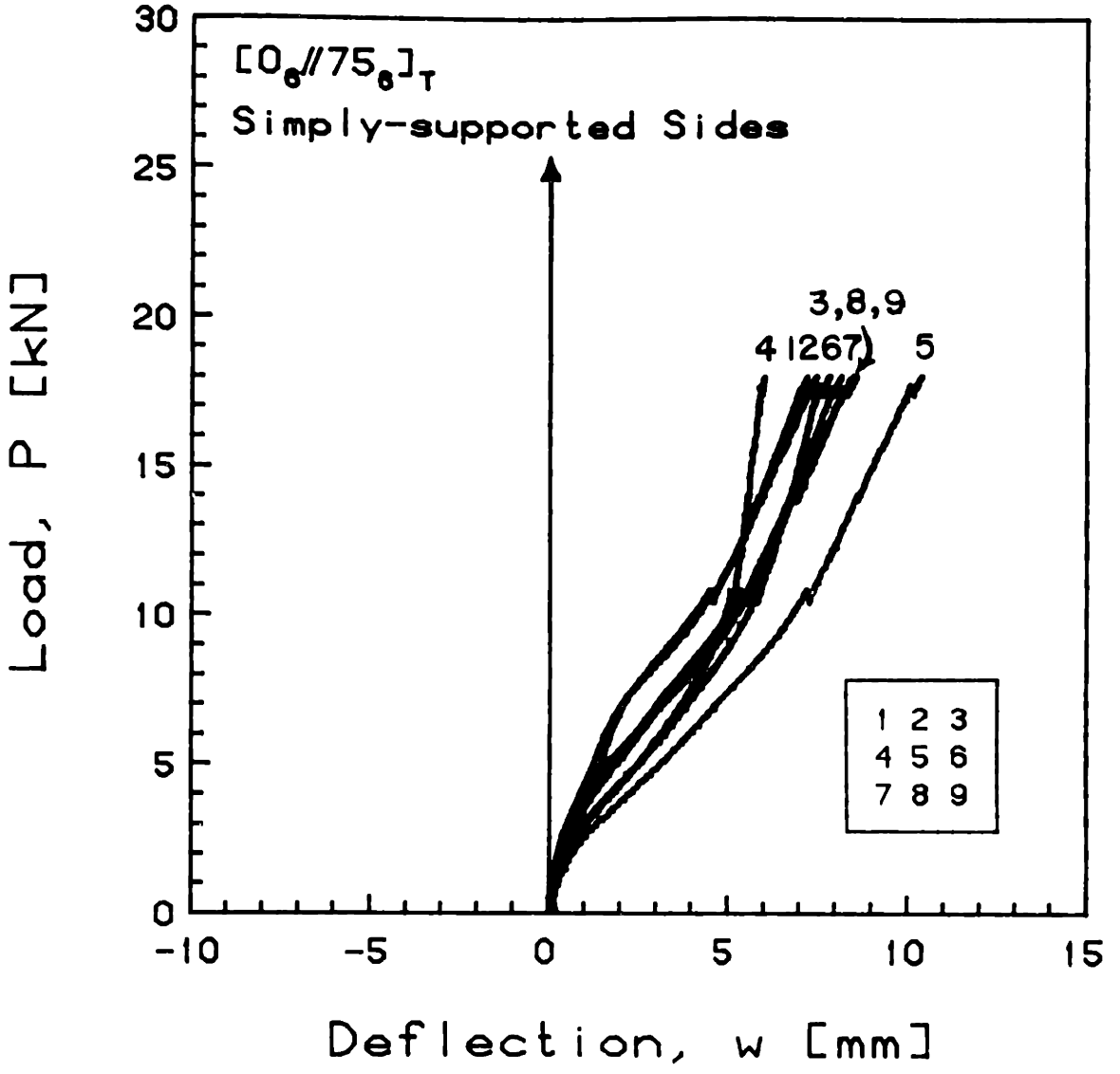

FIGURE E.81 Experimental Plot of Applied Compressive Load versus Out-of-Plane Deflection for the $[0_6//75_6]_T$ Laminate with Simply-Supported Side Boundary Conditions

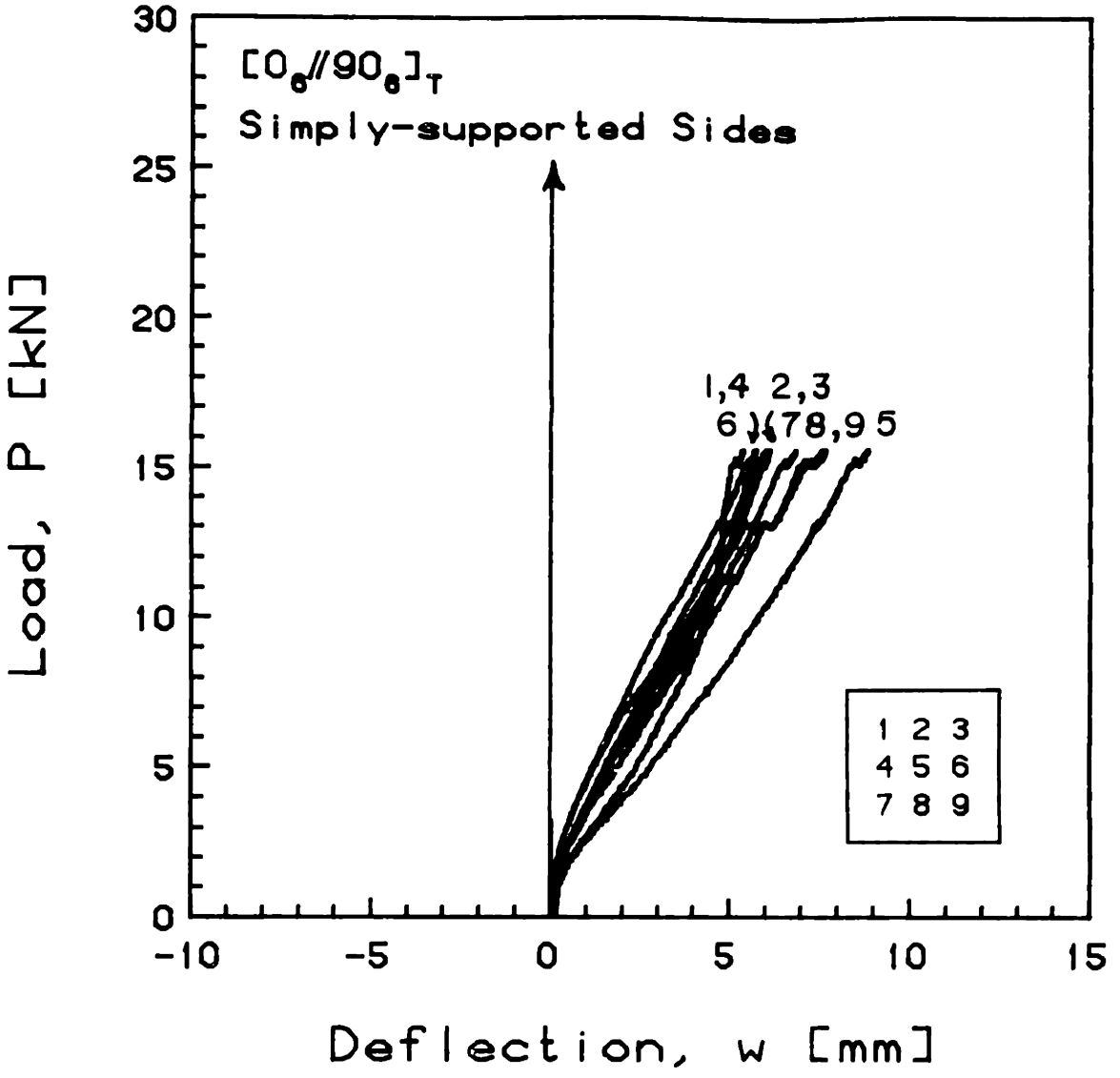

FIGURE E.82 Experimental Plot of Applied Compressive Load versus Out-of-Plane Deflection for the $[0_6//90_6]_T$ Laminate with Simply-Supported Side Boundary Conditions

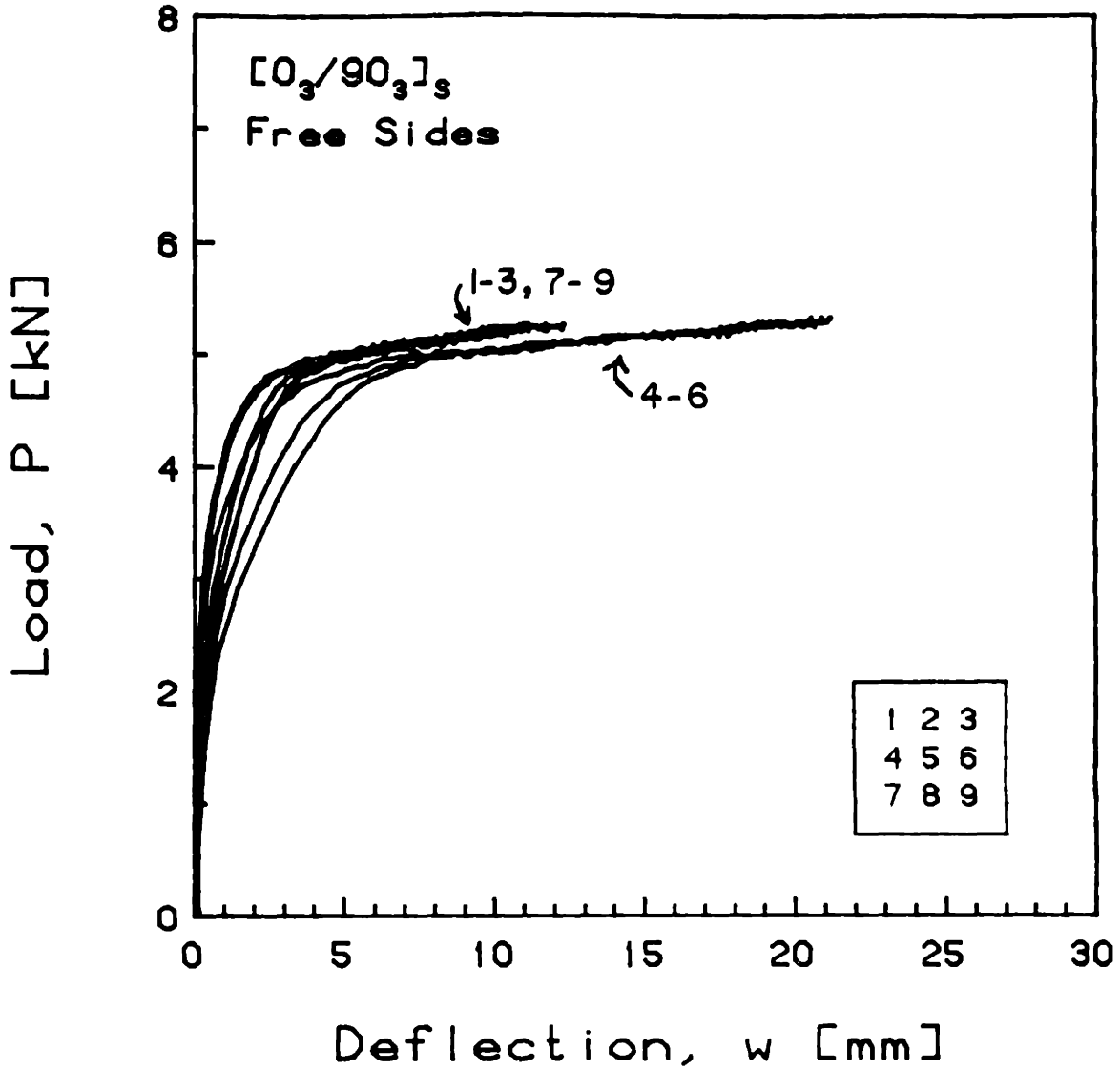

FIGURE E.83 Experimental Plot of Applied Compressive Load versus Out-of-Plane Deflection for the $[0_3/90_3]_S$ Laminate with Free Side Boundary Conditions

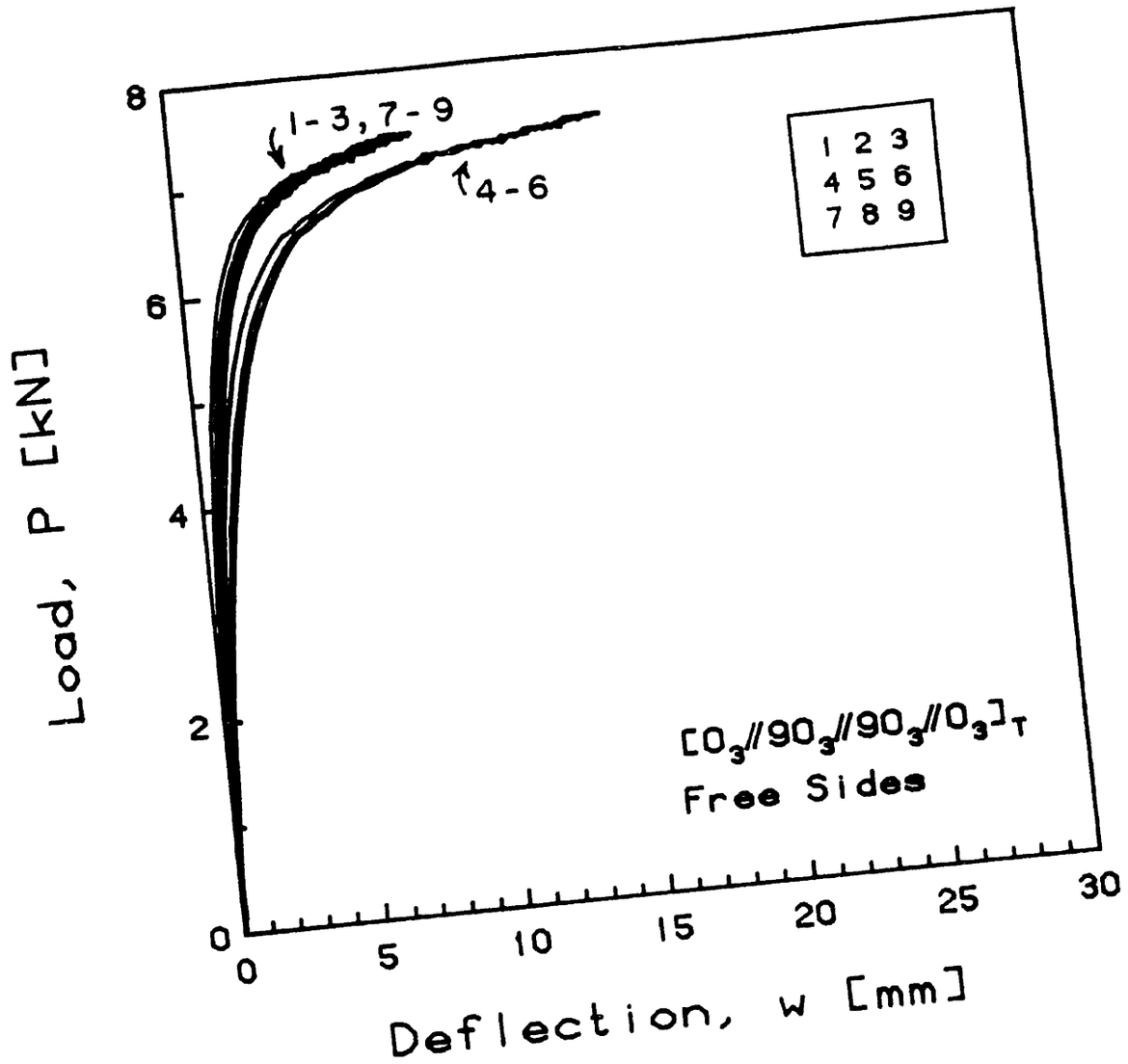

FIGURE E.84 Experimental Plot of Applied Compressive Load versus Out-of-Plane Deflection for the $[0_3//90_3//90_3//0_3]_T$ Laminate with Free Side Boundary Conditions

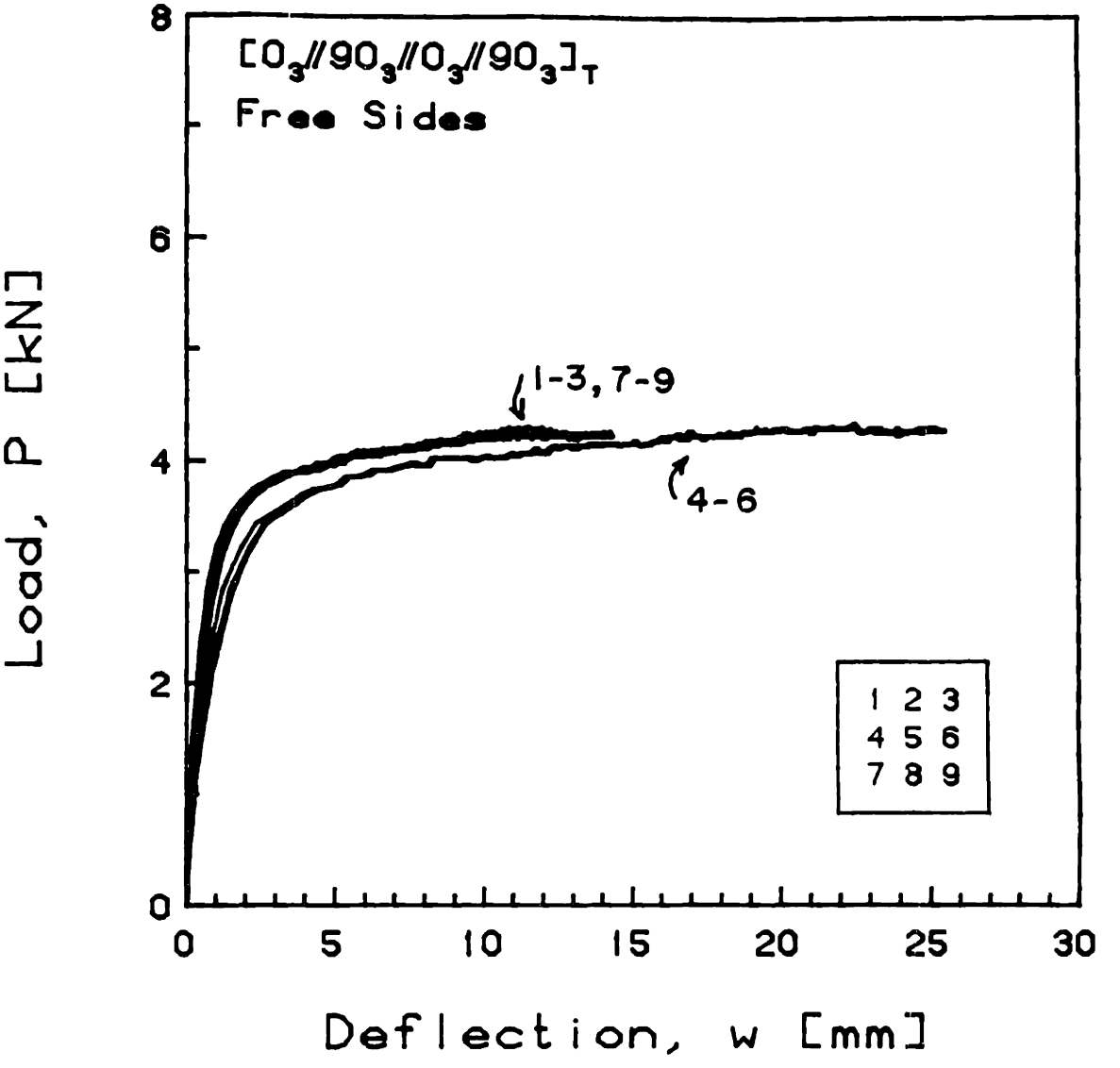

FIGURE E.85 Experimental Plot of Applied Compressive Load versus Out-of-Plane Deflection for the $[0_3//90_3//0_3//90_3]_T$ Laminate with Free Side Boundary Conditions

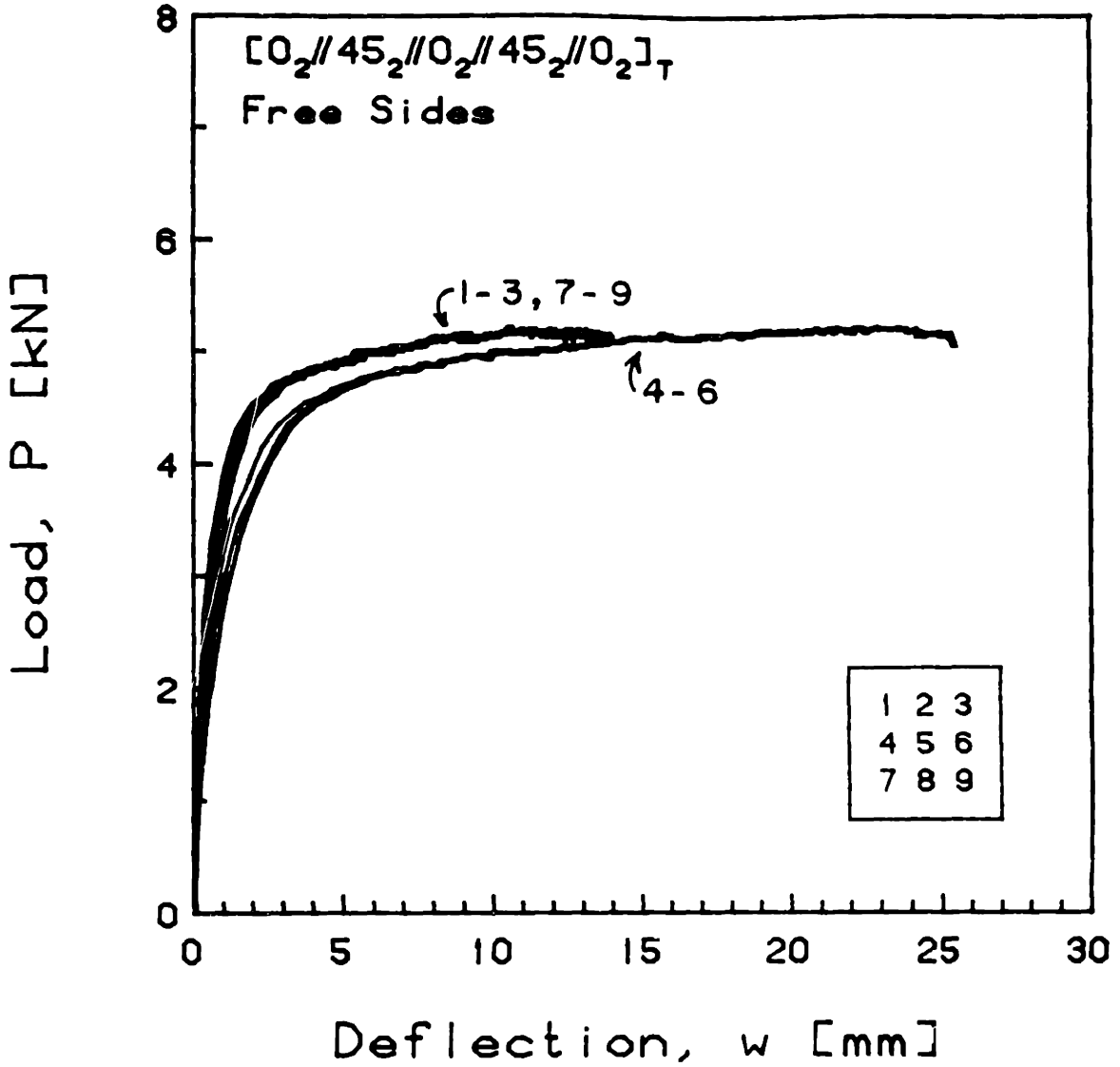

FIGURE E.86 Experimental Plot of Applied Compressive Load versus Out-of-Plane Deflection for the $[O_2//45_2//O_2//45_2//O_2]_T$ Laminate with Free Side Boundary Conditions

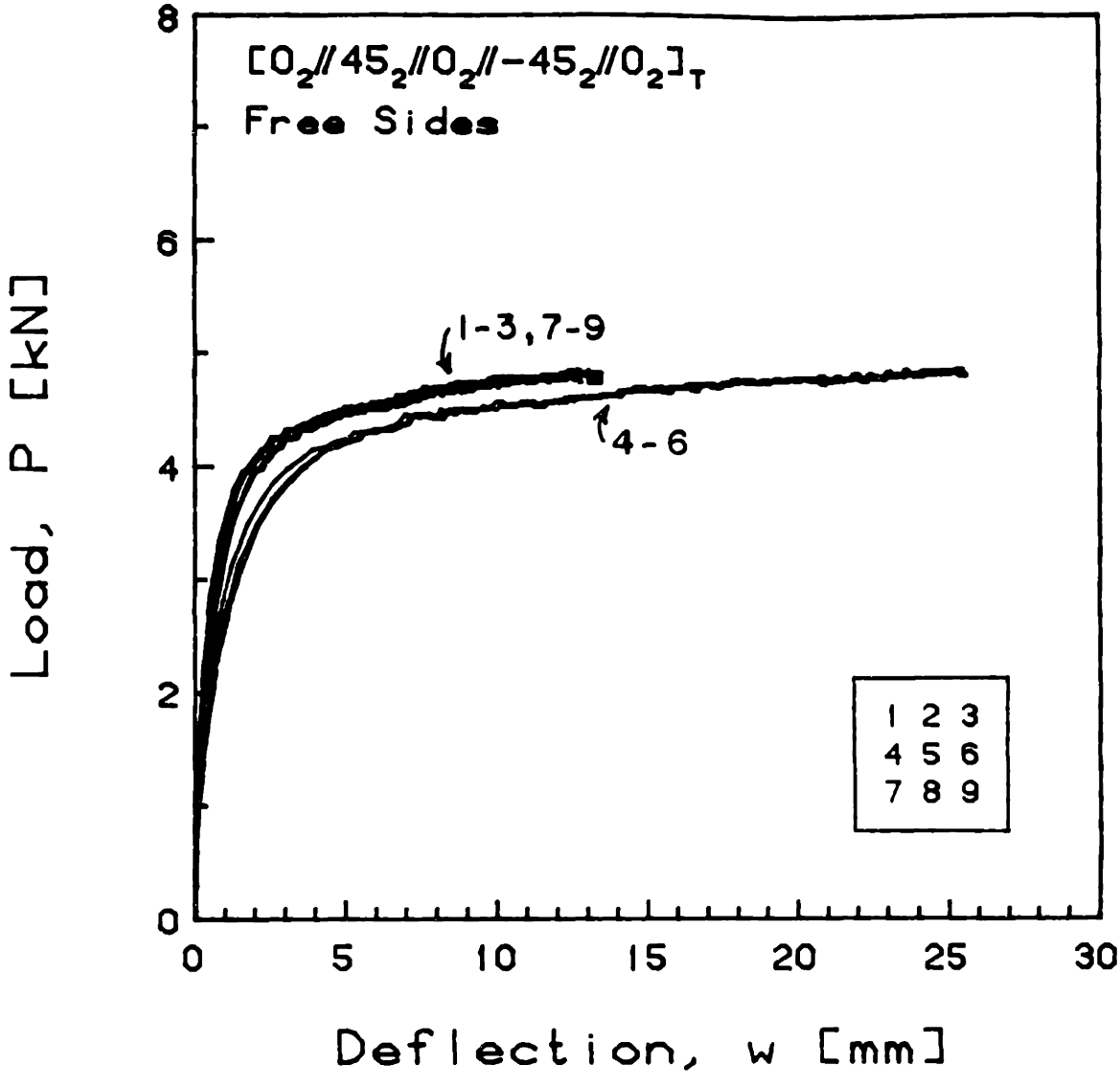

FIGURE E.87 Experimental Plot of Applied Compressive Load versus Out-of-Plane Deflection for the $[0_2//45_2//0_2//-45_2//0_2]_T$ Laminate with Free Side Boundary Conditions

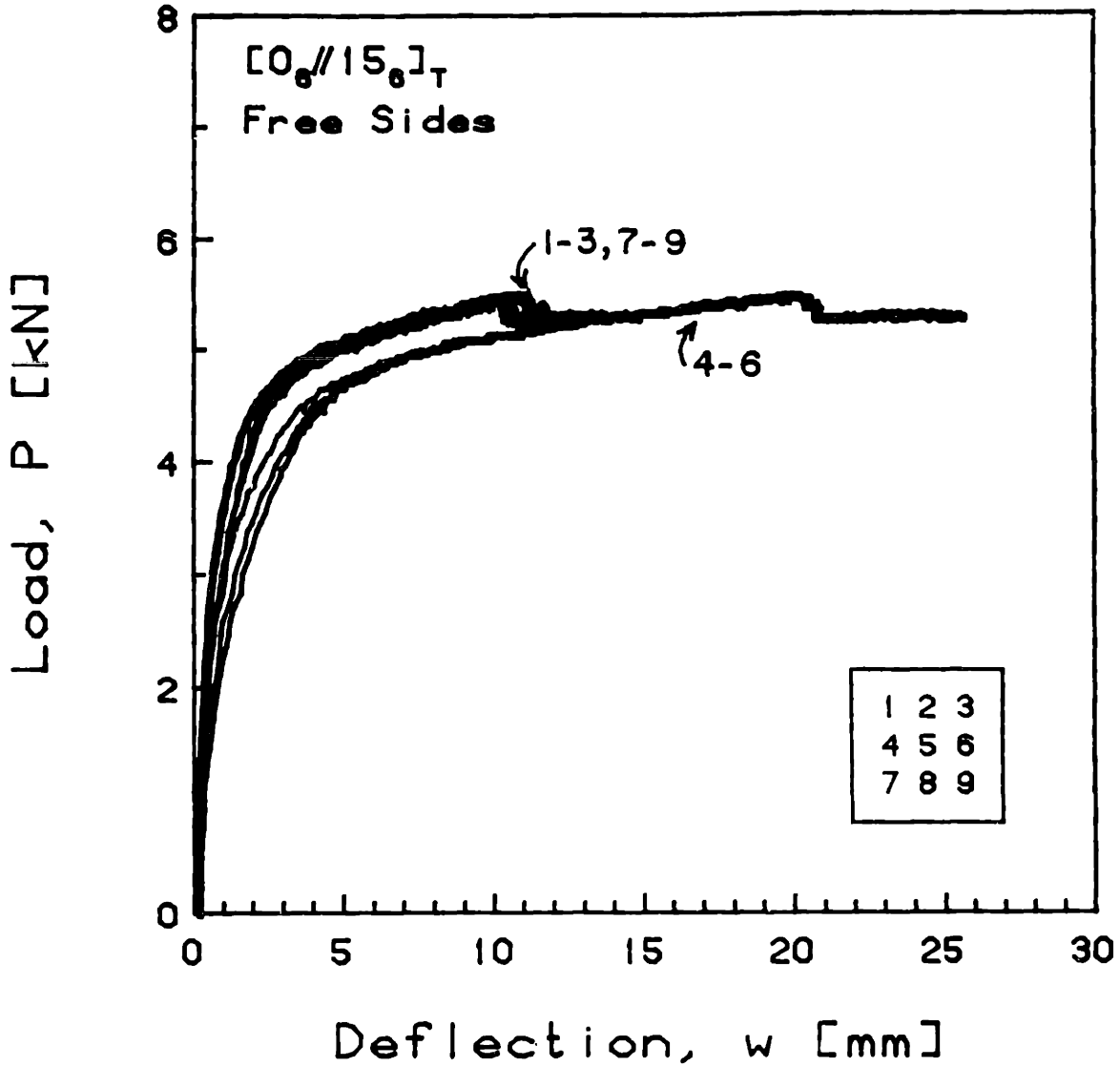

FIGURE E.88 Experimental Plot of Applied Compressive Load versus Out-of-Plane Deflection for the $[0_6//15_6]_T$ Laminate with Free Side Boundary Conditions

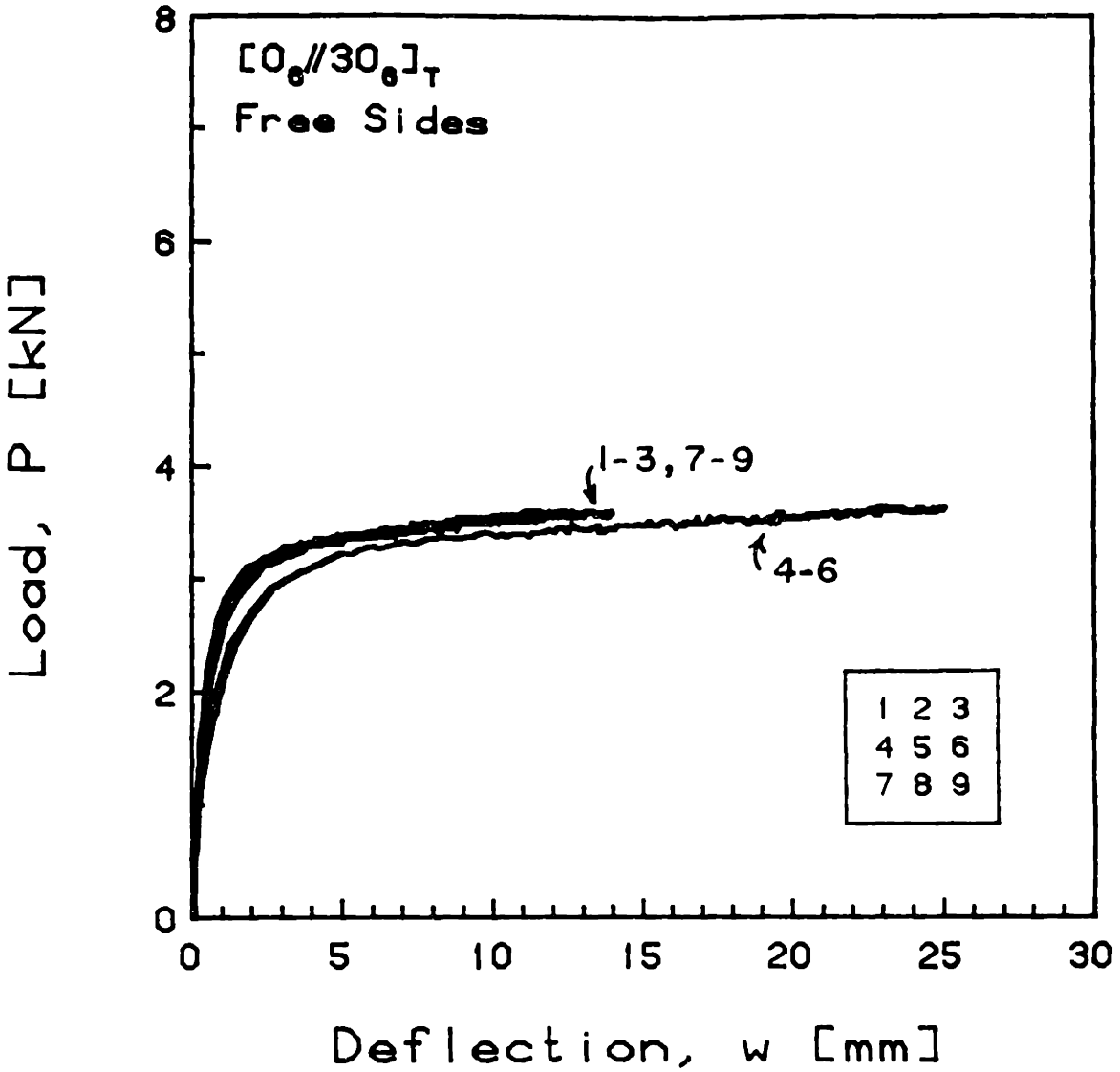

FIGURE E.89 Experimental Plot of Applied Compressive Load versus Out-of-Plane Deflection for the $[0_6//30_6]_T$ Laminate with Free Side Boundary Conditions

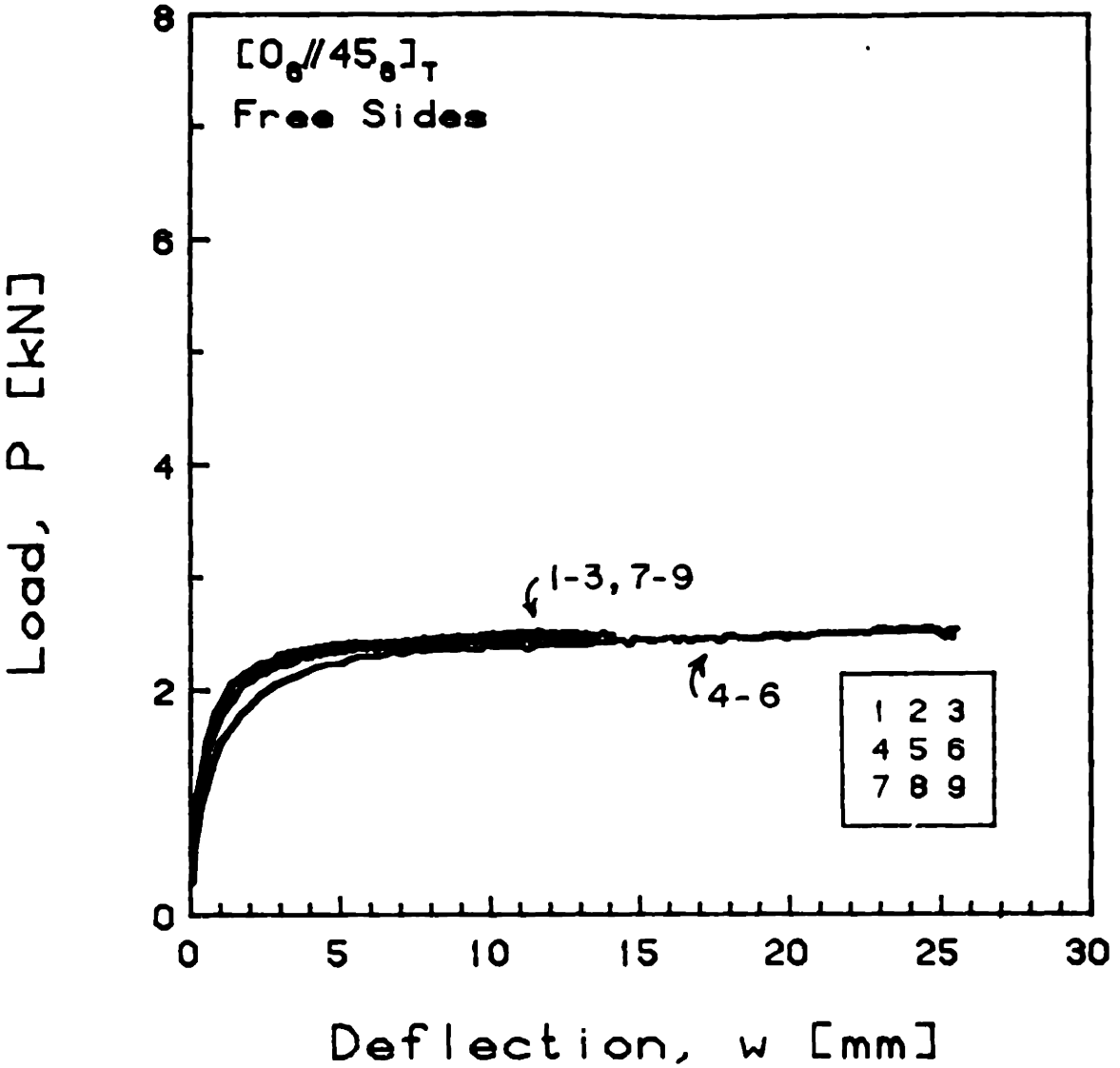

FIGURE E.90 Experimental Plot of Applied Compressive Load versus Out-of-Plane Deflection for the $[0_6//45_6]_T$ Laminate with Free Side Boundary Conditions

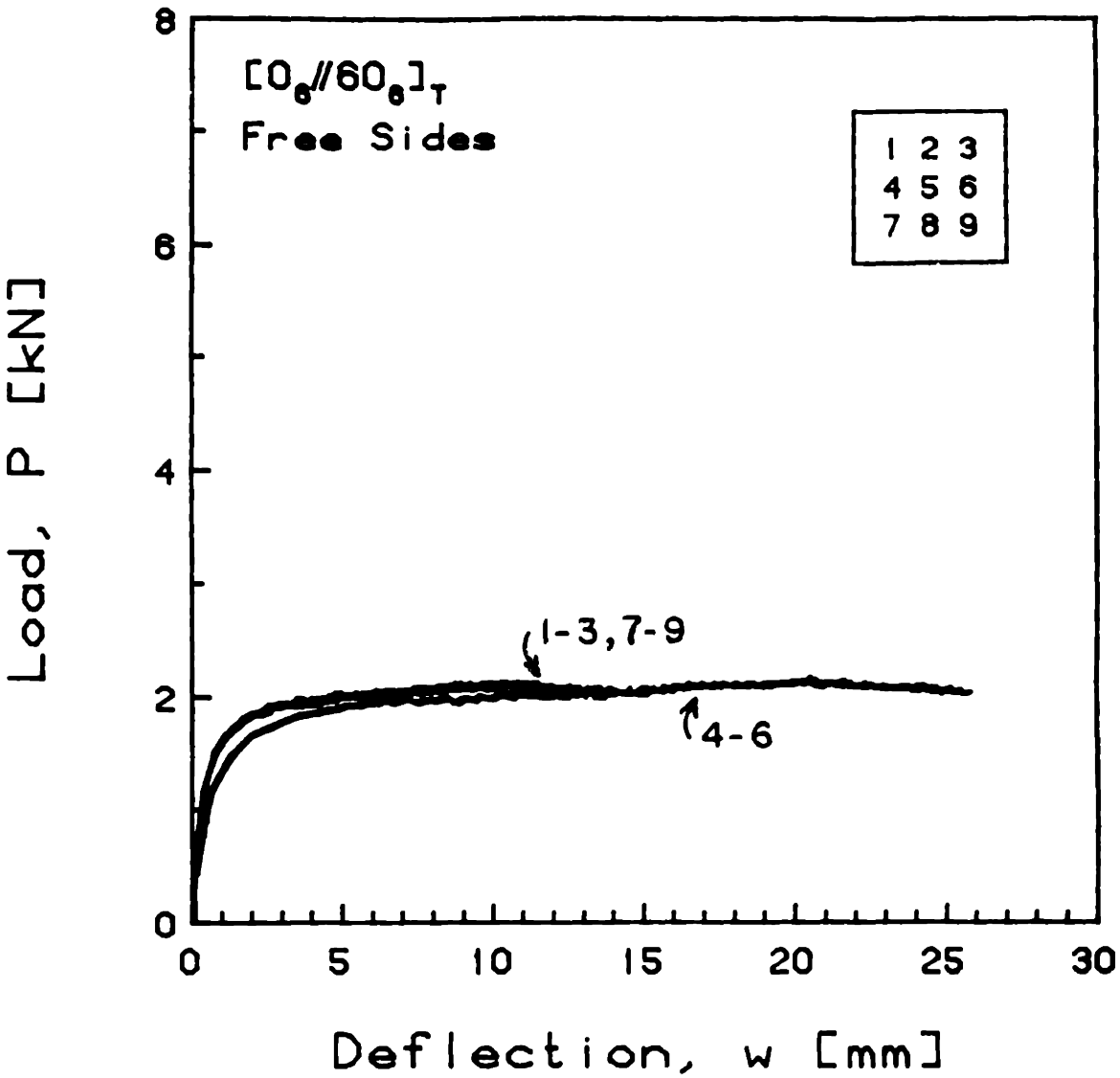

FIGURE E.91 Experimental Plot of Applied Compressive Load versus Out-of-Plane Deflection for the $[0_6//60_6]_T$ Laminate with Free Side Boundary Conditions

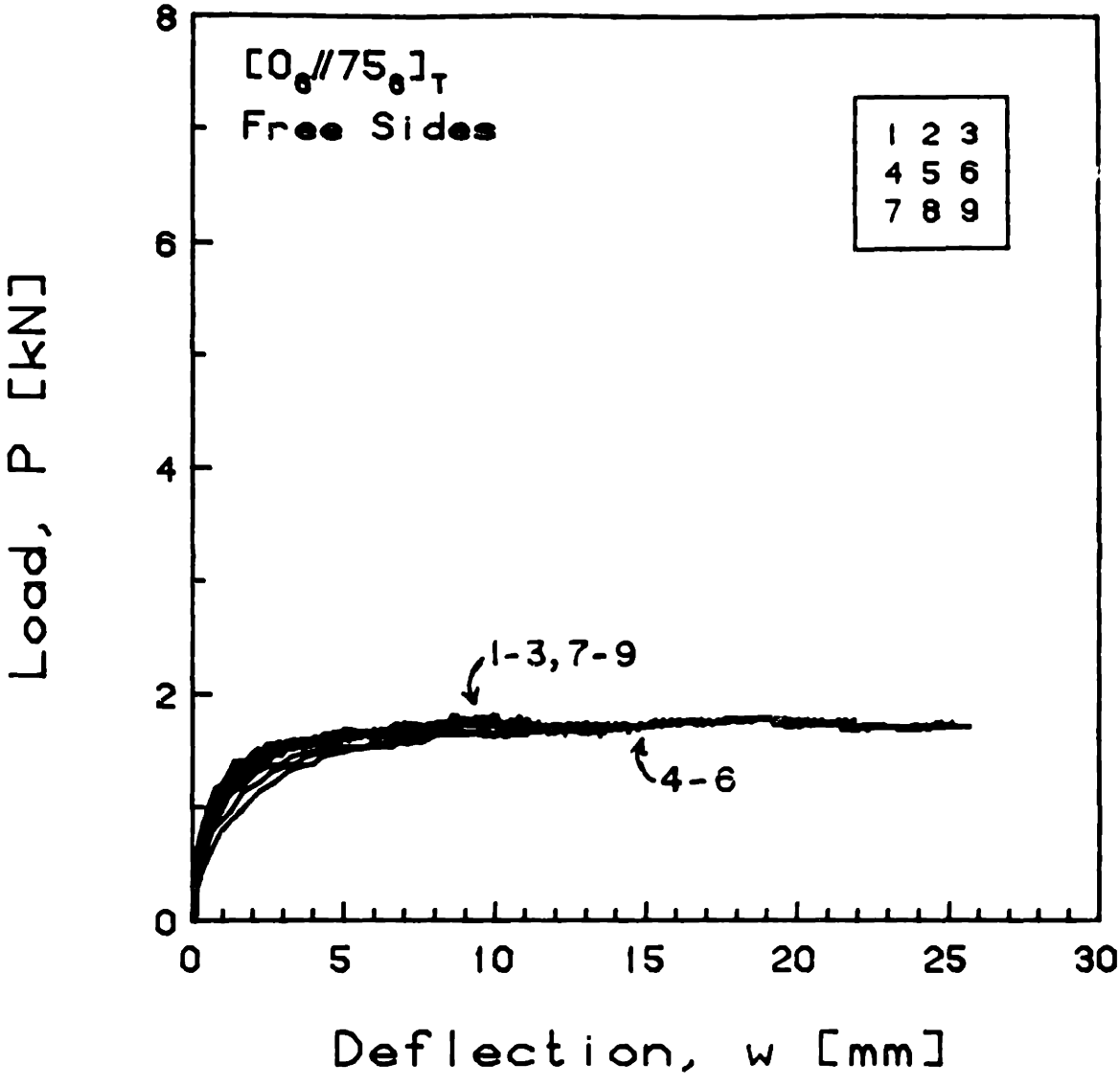

FIGURE E.92 Experimental Plot of Applied Compressive Load versus Out-of-Plane Deflection for the $[0_6//75_6]_T$ Laminate with Free Side Boundary Conditions

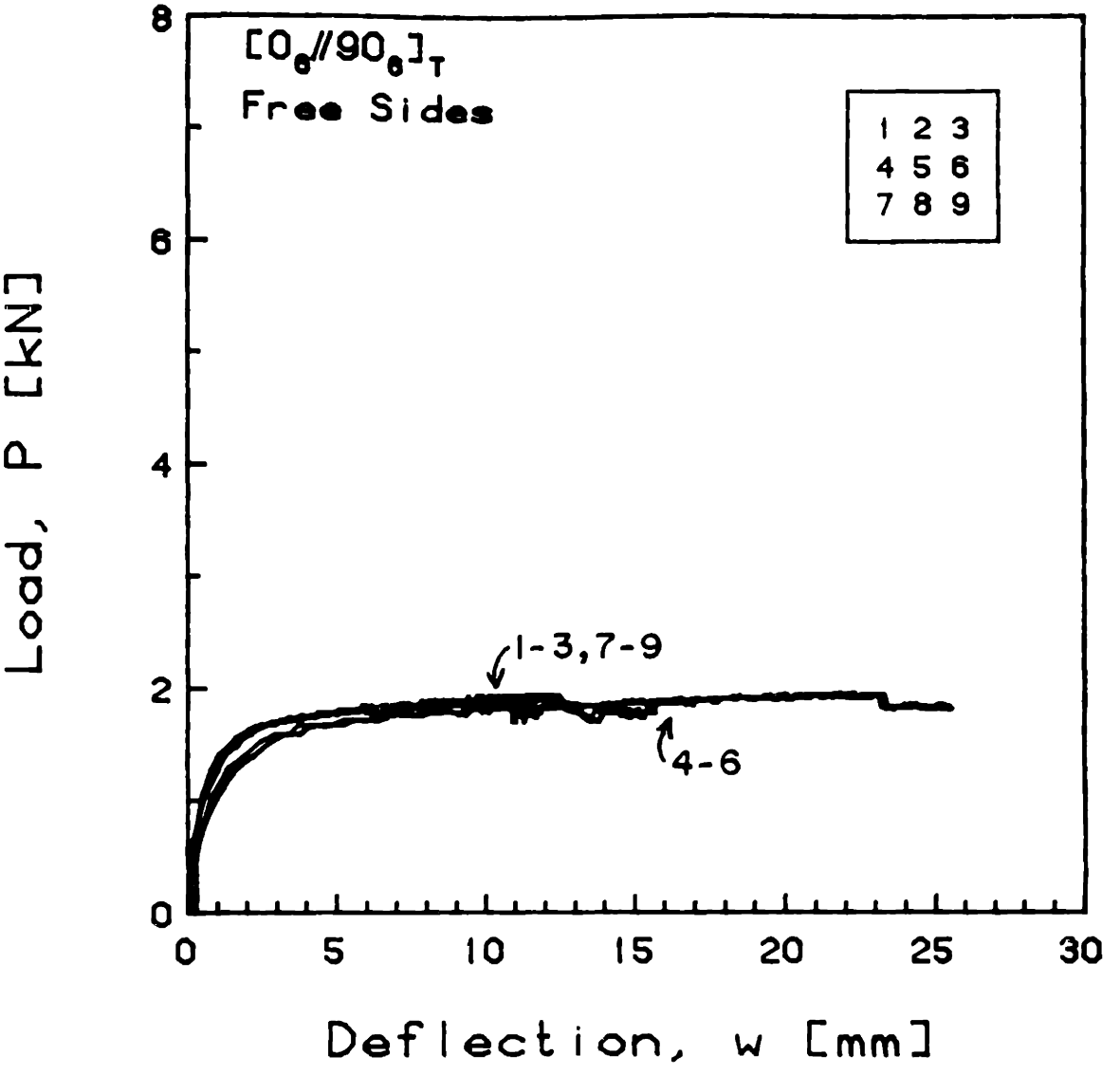

FIGURE E.93 Experimental Plot of Applied Compressive Load versus Out-of-Plane Deflection for the $[0_6//90_6]_T$ Laminate with Free Side Boundary Conditions

APPENDIX F

LOAD VERSUS LONGITUDINAL STRAIN PLOTS

This appendix contains copies of all of the experimental load versus longitudinal strain data plots. They are presented in the same order as discussed in the main text, i.e., according to the sequence summarized in Table 4.4. The results for laminates with clamped side boundary conditions are presented first, followed by those with simply-supported side boundary conditions, and, finally, the results for laminates with free sides.

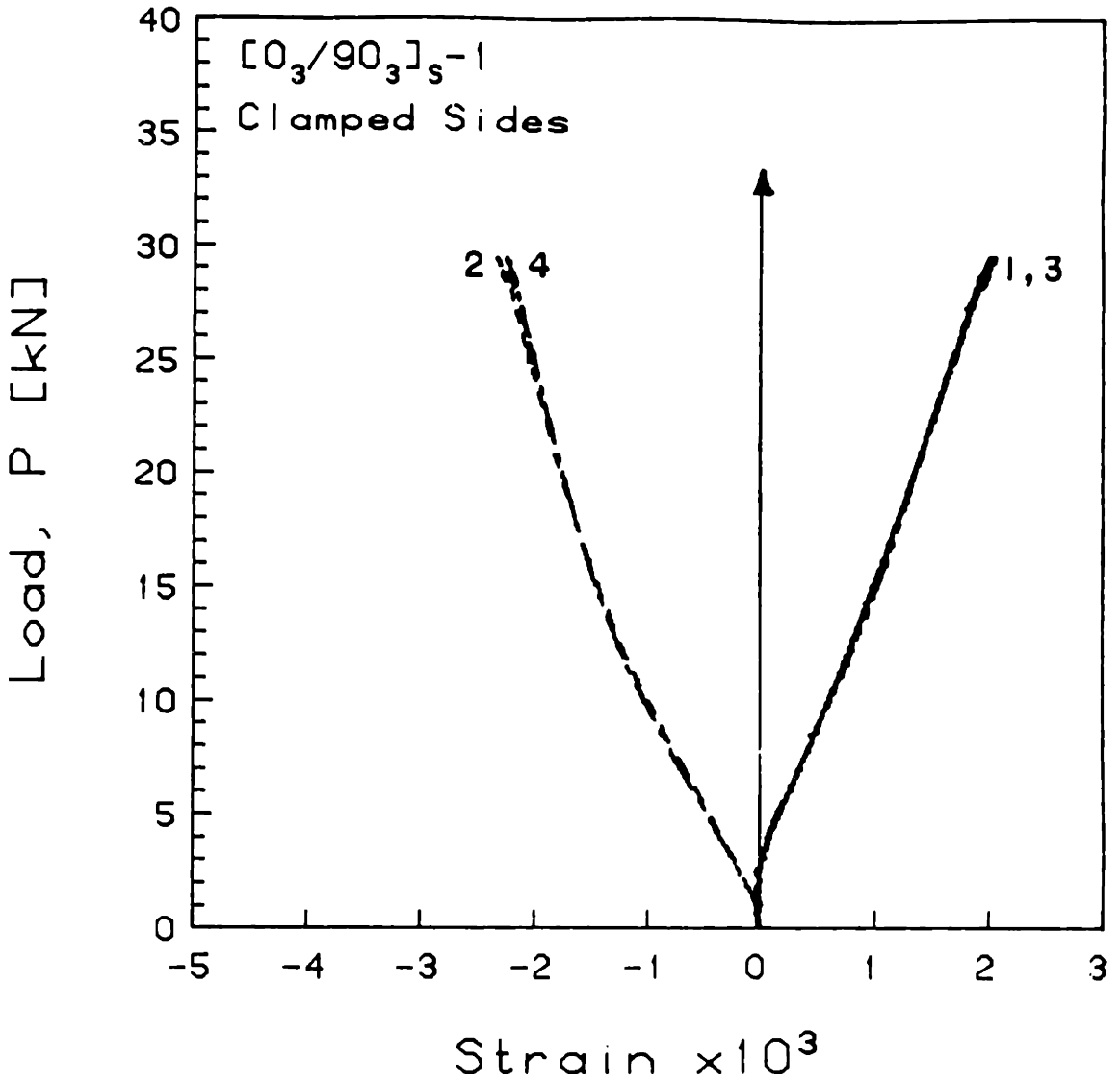

FIGURE F.1 Experimental Plot of Applied Compressive Load versus Longitudinal Strain for the $[0_3/90_3]_s$-1 Laminate with Clamped Side Boundary Conditions

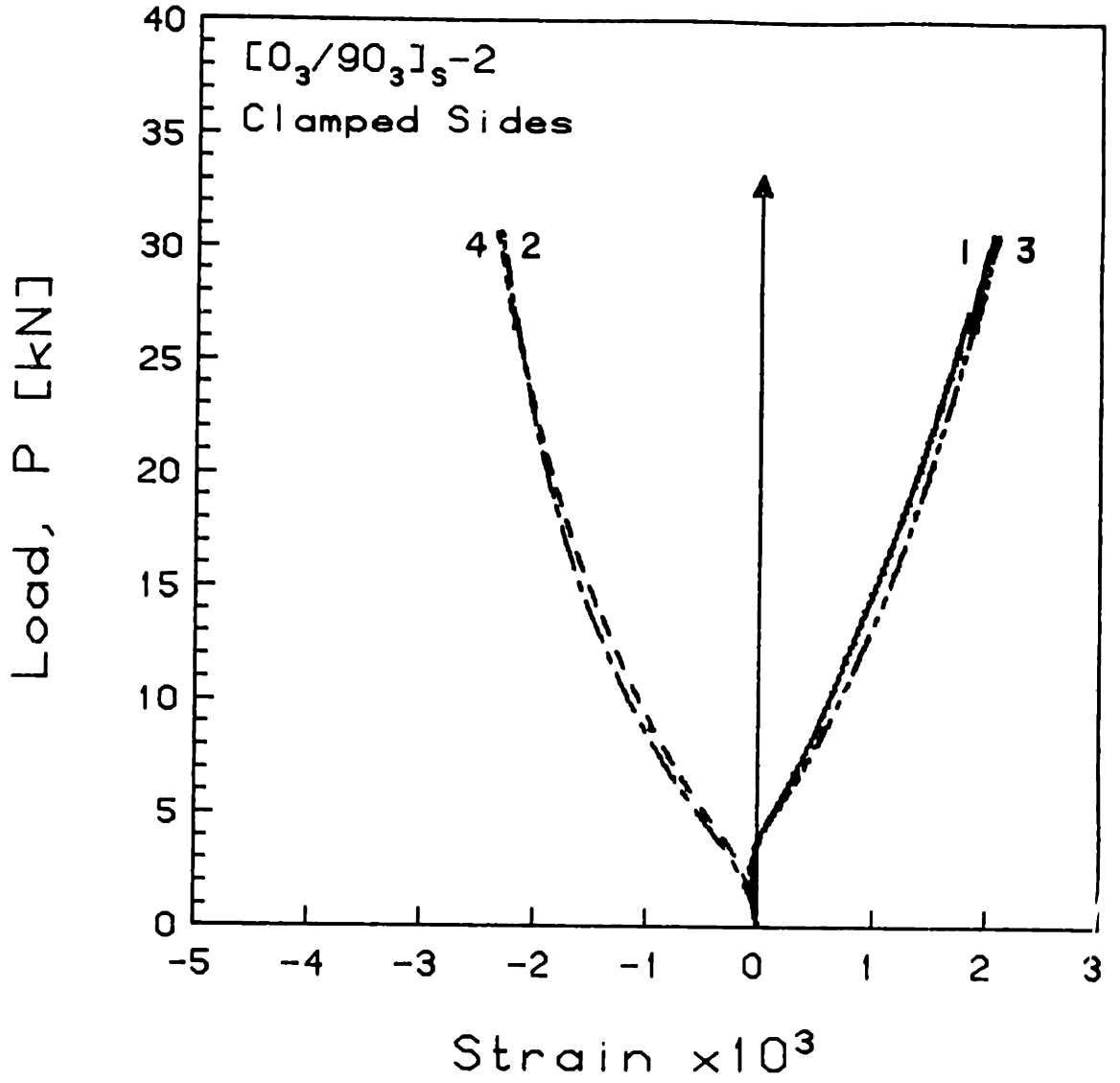

FIGURE F.2 Experimental Plot of Applied Compressive Load versus Longitudinal Strain for the $[0_3/90_3]_s$-2 Laminate with Clamped Side Boundary Conditions

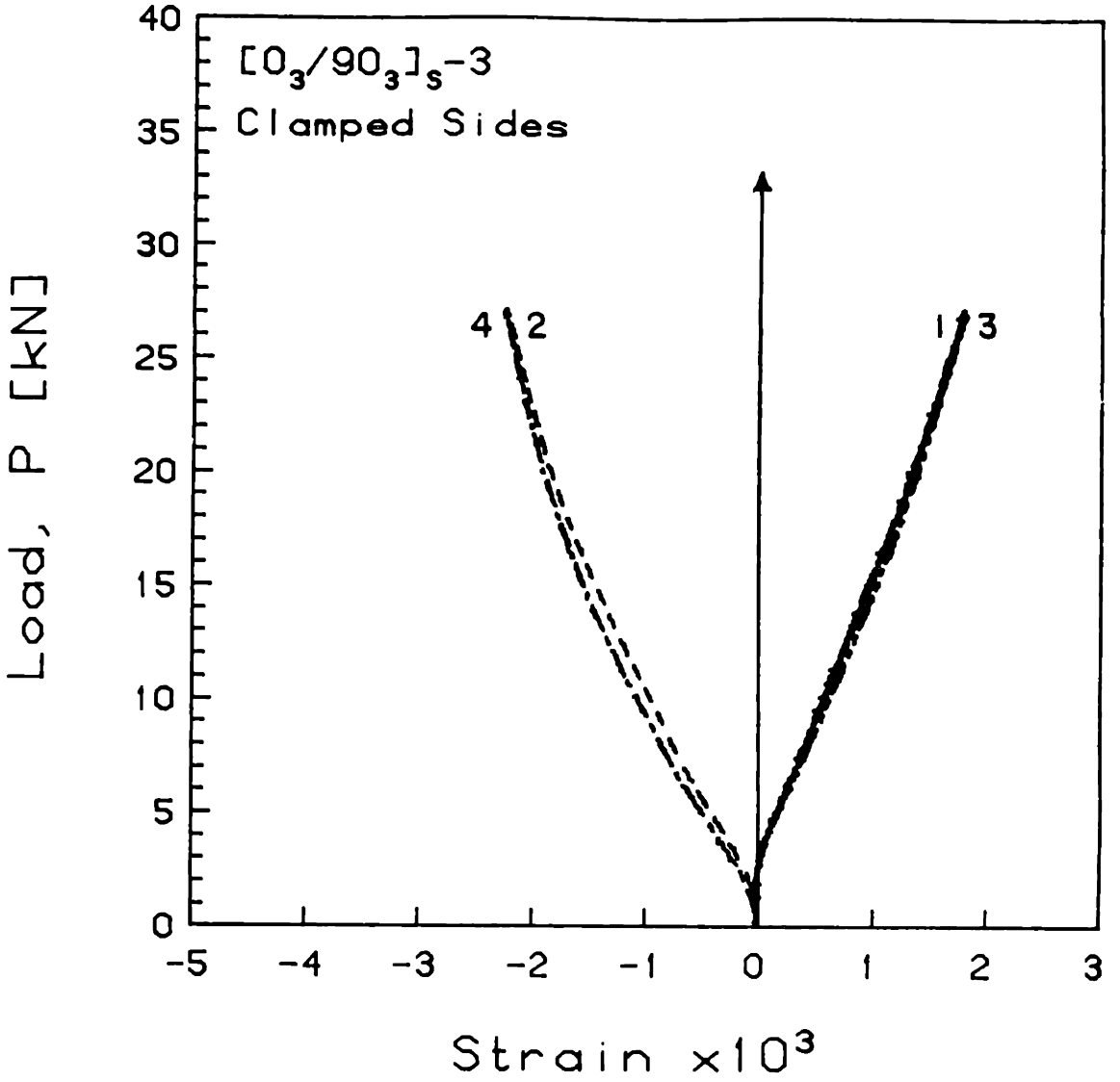

FIGURE F.3 Experimental Plot of Applied Compressive Load versus Longitudinal Strain for the $[0_3/90_3]_S$-3 Laminate with Clamped Side Boundary Conditions

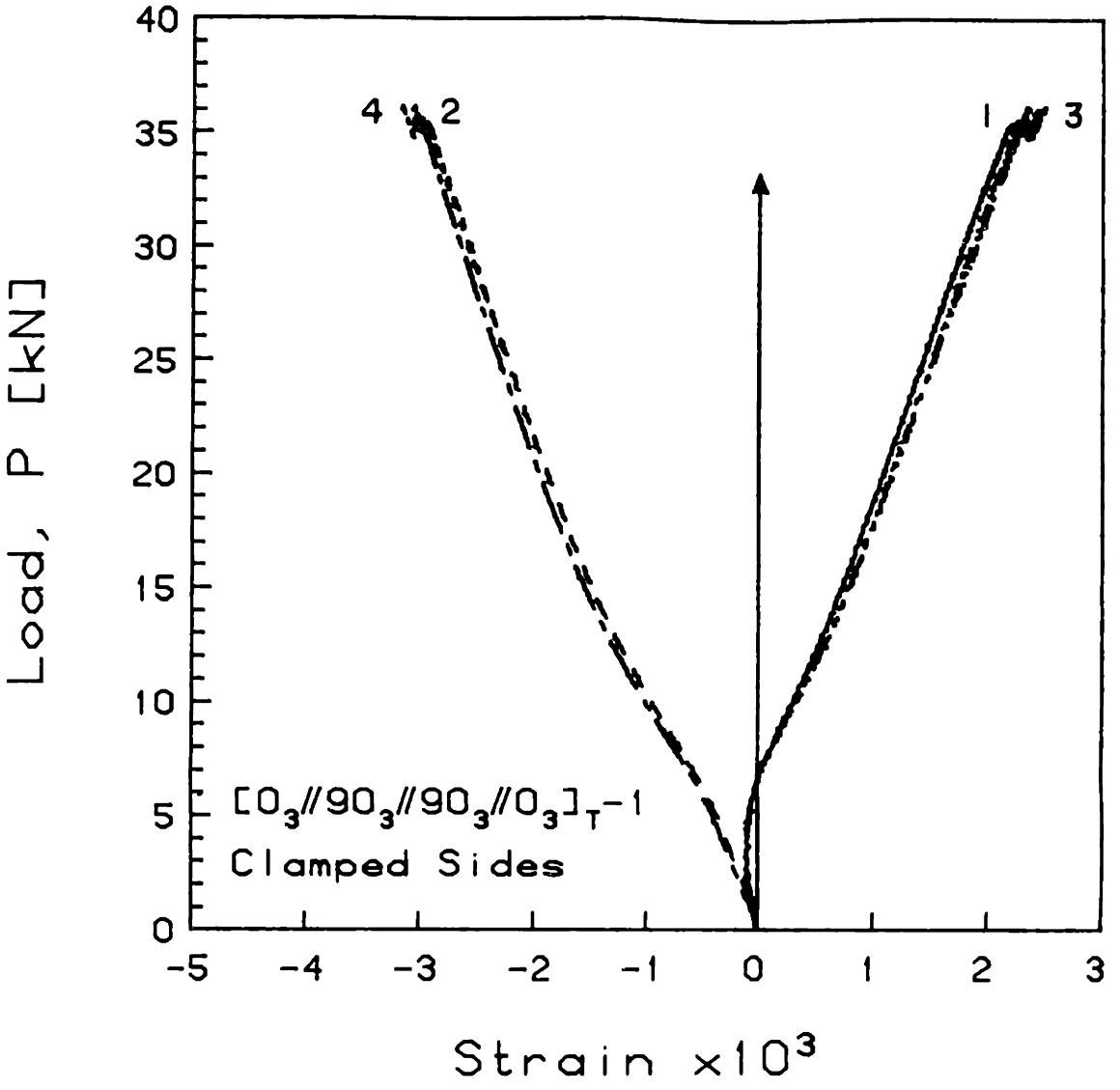

FIGURE F.4 Experimental Plot of Applied Compressive Load versus Longitudinal Strain for the $[0_3//90_3//90_3//0_3]_T$-1 Laminate with Clamped Side Boundary Conditions

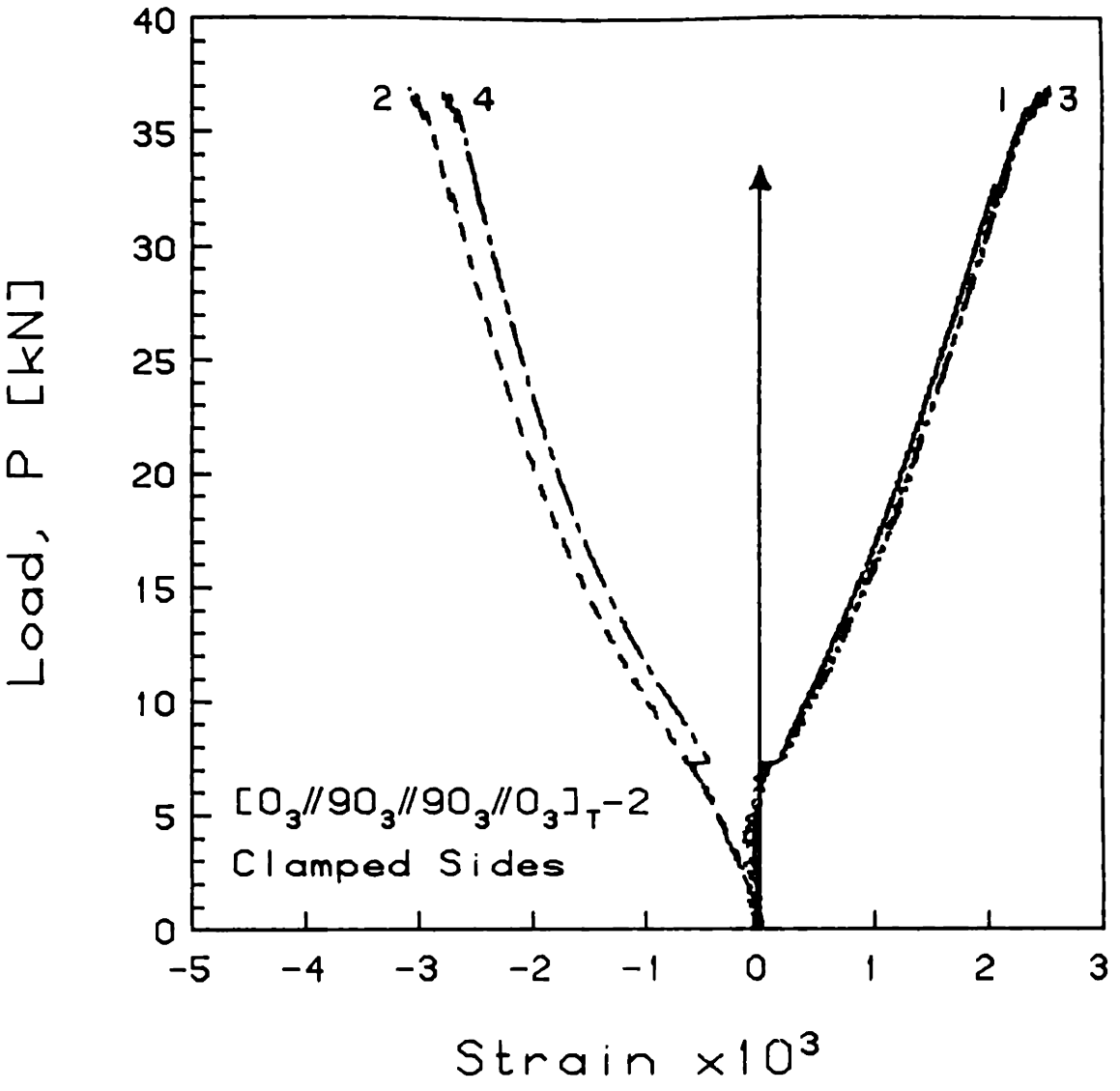

FIGURE F.5 Experimental Plot of Applied Compressive Load versus Longitudinal Strain for the $[0_3//90_3//90_3//0_3]_T$-2 Laminate with Clamped Side Boundary Conditions

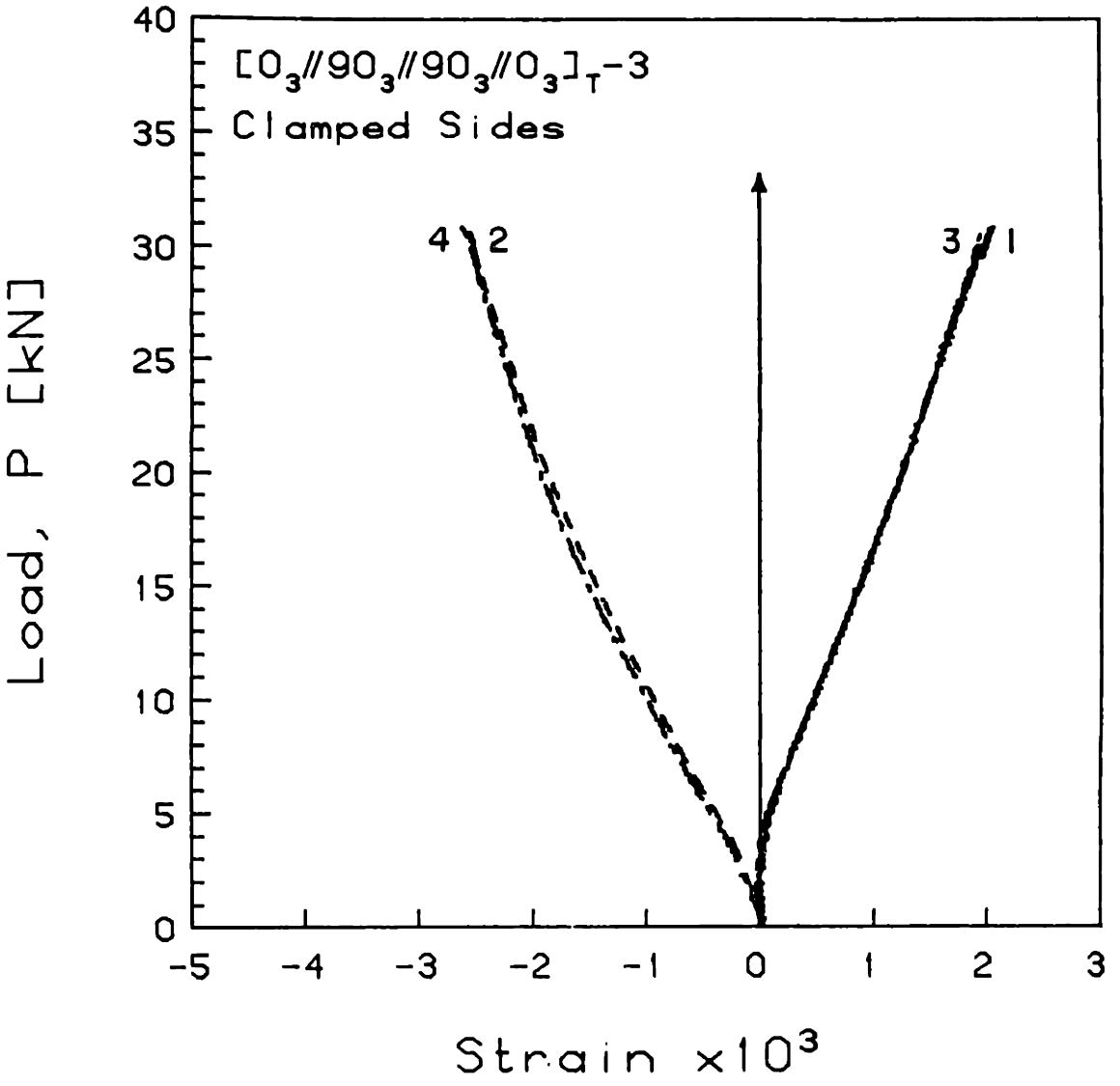

FIGURE F.6 Experimental Plot of Applied Compressive Load versus Longitudinal Strain for the $[0_3//90_3//90_3//0_3]_T$-3 Laminate with Clamped Side Boundary Conditions

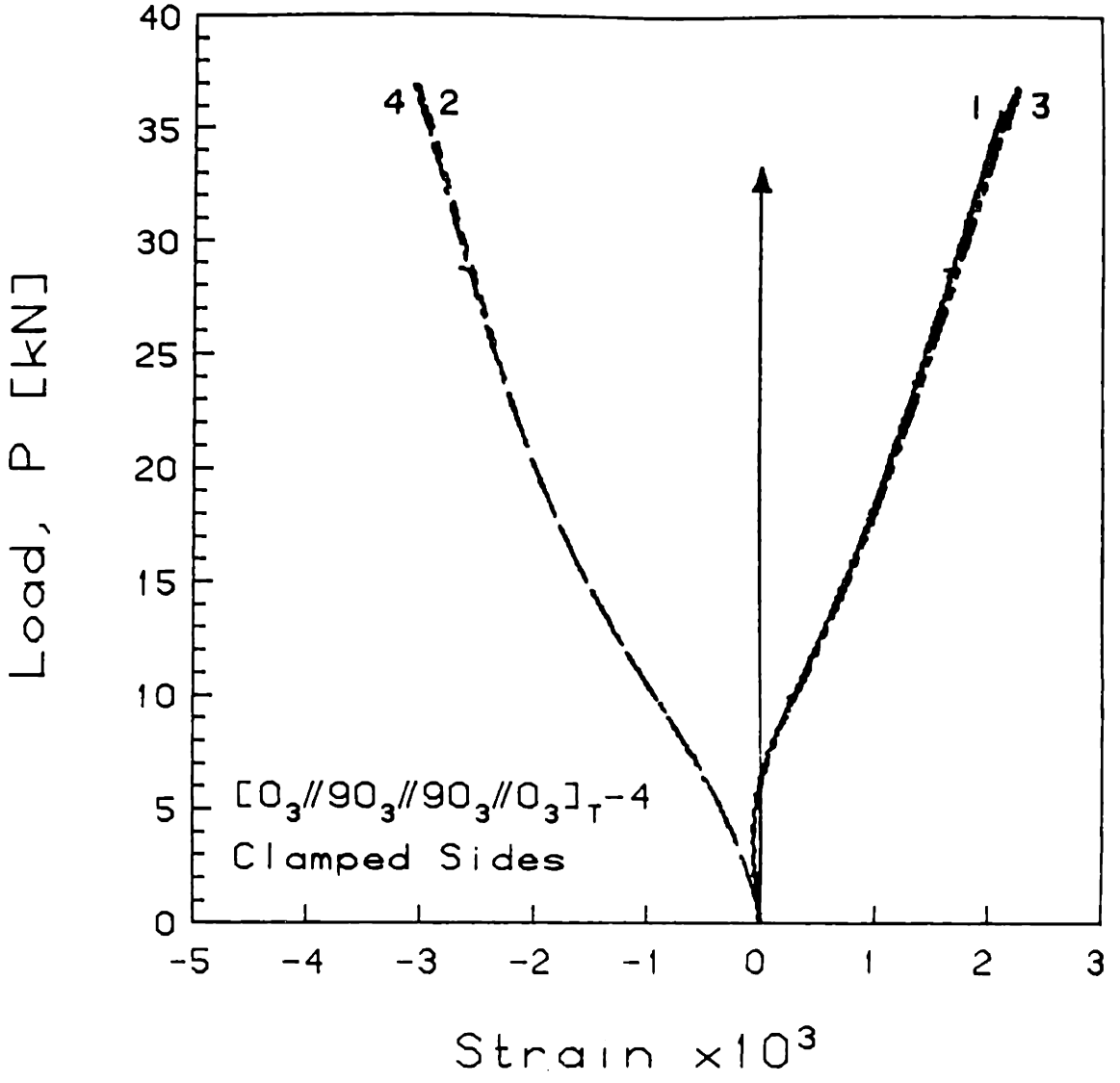

FIGURE F.7 Experimental Plot of Applied Compressive Load versus Longitudinal Strain for the $[0_3//90_3//90_3//0_3]_T$-4 Laminate with Clamped Side Boundary Conditions

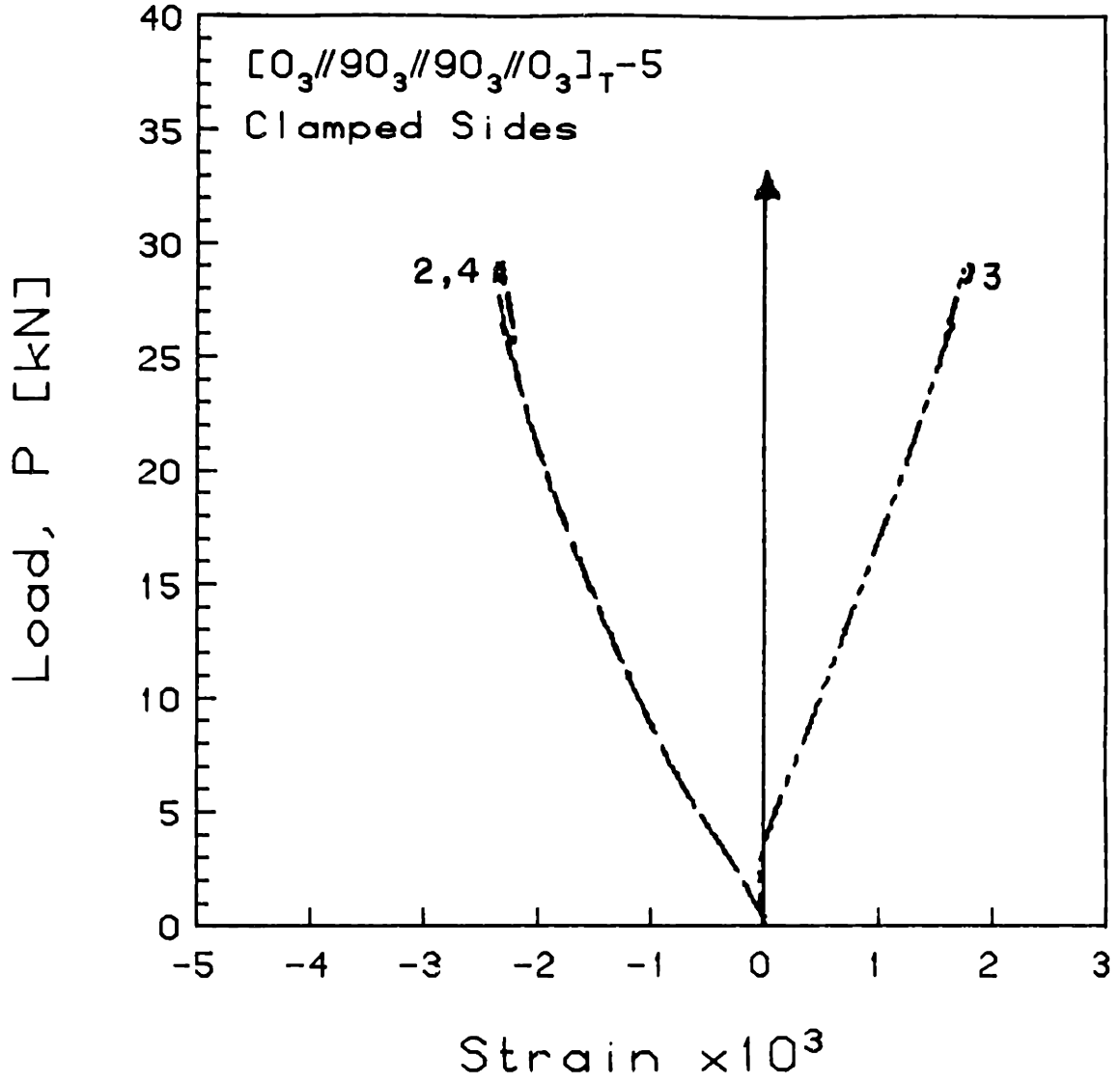

FIGURE F.8 Experimental Plot of Applied Compressive Load versus Longitudinal Strain for the $[0_3//90_3//90_3//0_3]_T$-5 Laminate with Clamped Side Boundary Conditions

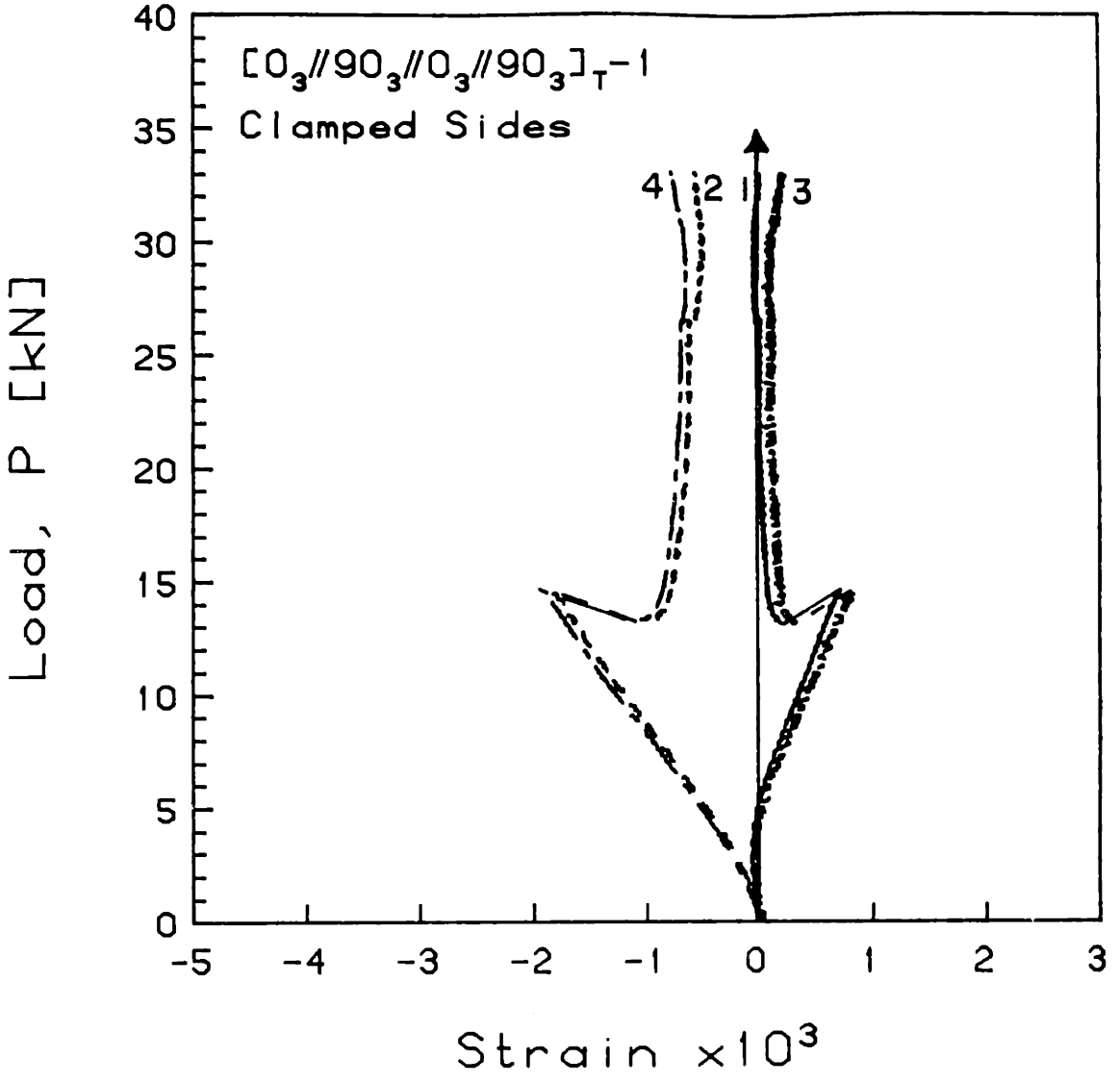

FIGURE F.9 Experimental Plot of Applied Compressive Load versus Longitudinal Strain for the $[0_3//90_3//0_3//90_3]_T$-1 Laminate with Clamped Side Boundary Conditions

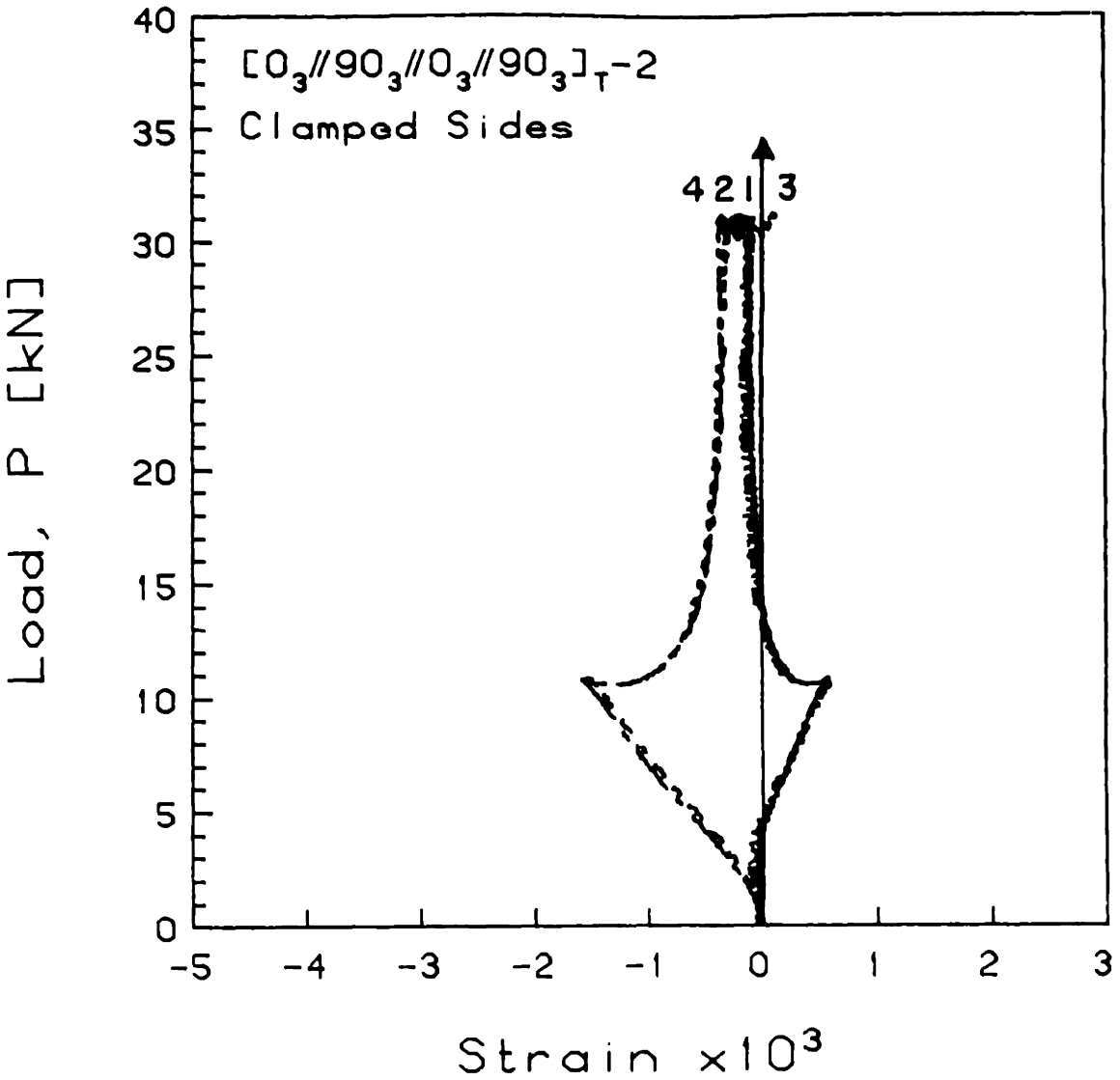

FIGURE F.10 Experimental Plot of Applied Compressive Load versus Longitudinal Strain for the $[0_3//90_3//0_3//90_3]_T$-2 Laminate with Clamped Side Boundary Conditions

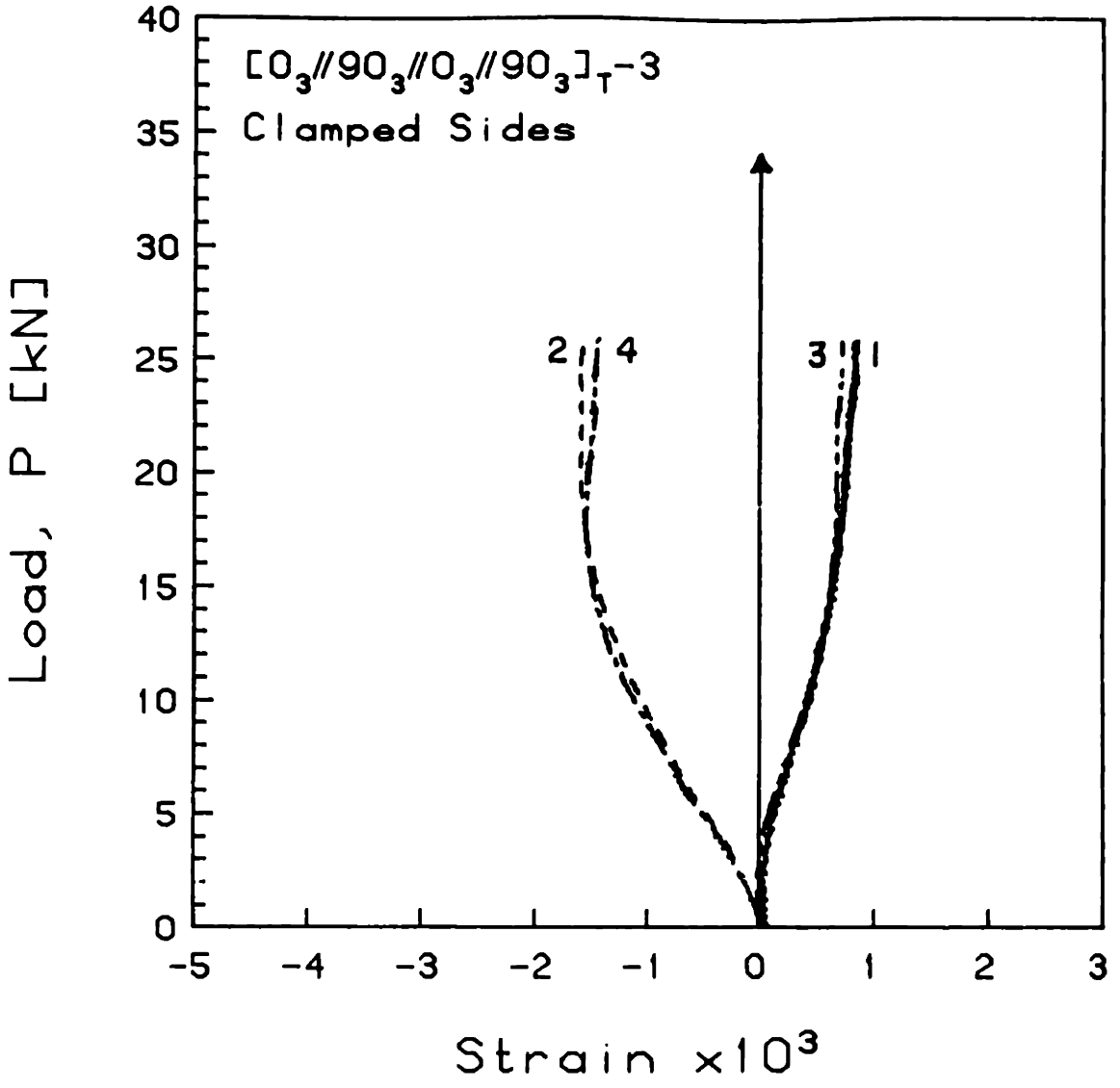

FIGURE F.11 Experimental Plot of Applied Compressive Load versus Longitudinal Strain for the $[0_3//90_3//0_3//90_3]_T$-3 Laminate with Clamped Side Boundary Conditions

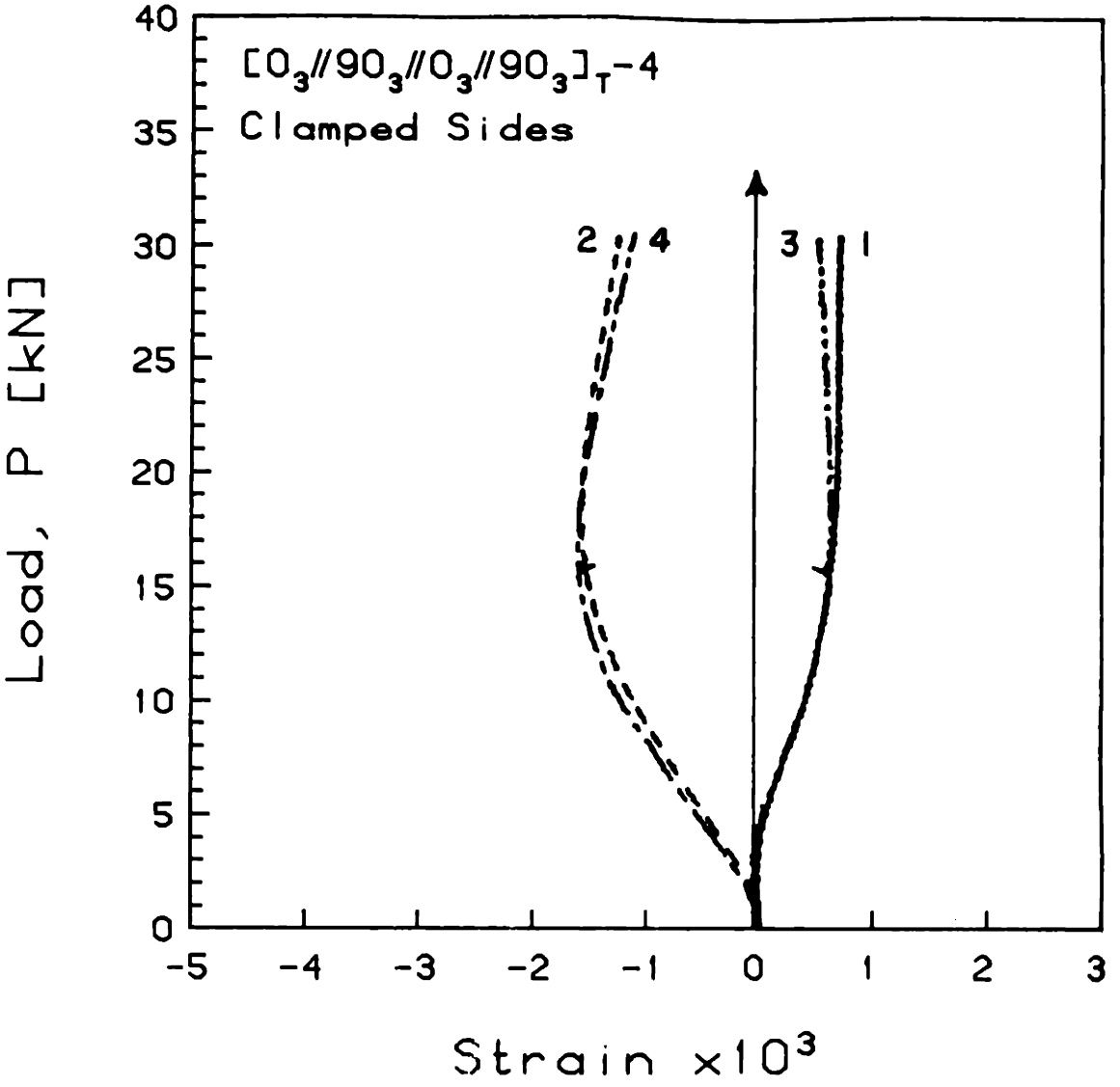

FIGURE F.12 Experimental Plot of Applied Compressive Load versus Longitudinal Strain for the $[0_3//90_3//0_3//90_3]_T$-4 Laminate with Clamped Side Boundary Conditions

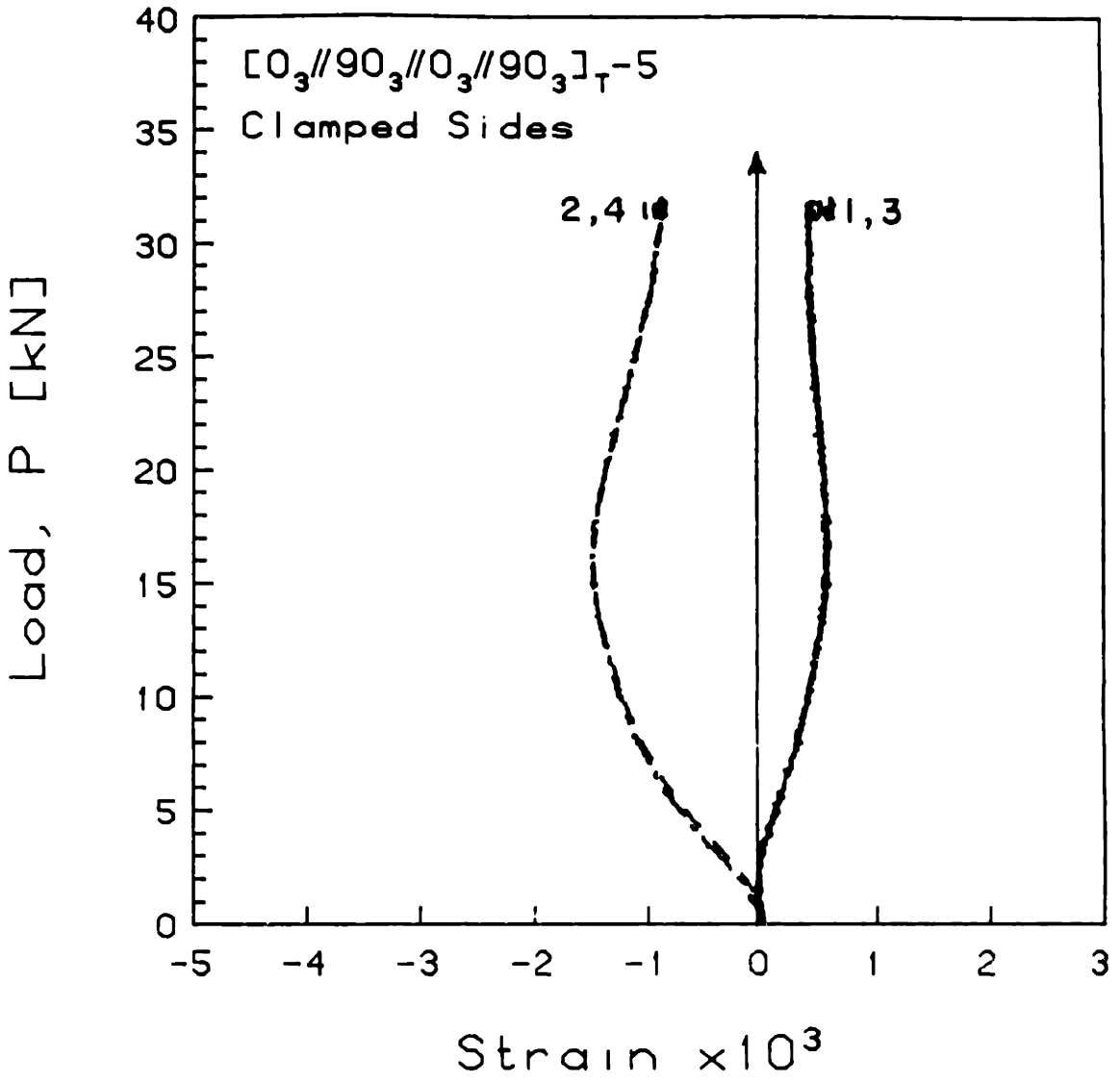

FIGURE F.13 Experimental Plot of Applied Compressive Load versus Longitudinal Strain for the $[0_3//90_3//0_3//90_3]_T$-5 Laminate with Clamped Side Boundary Conditions

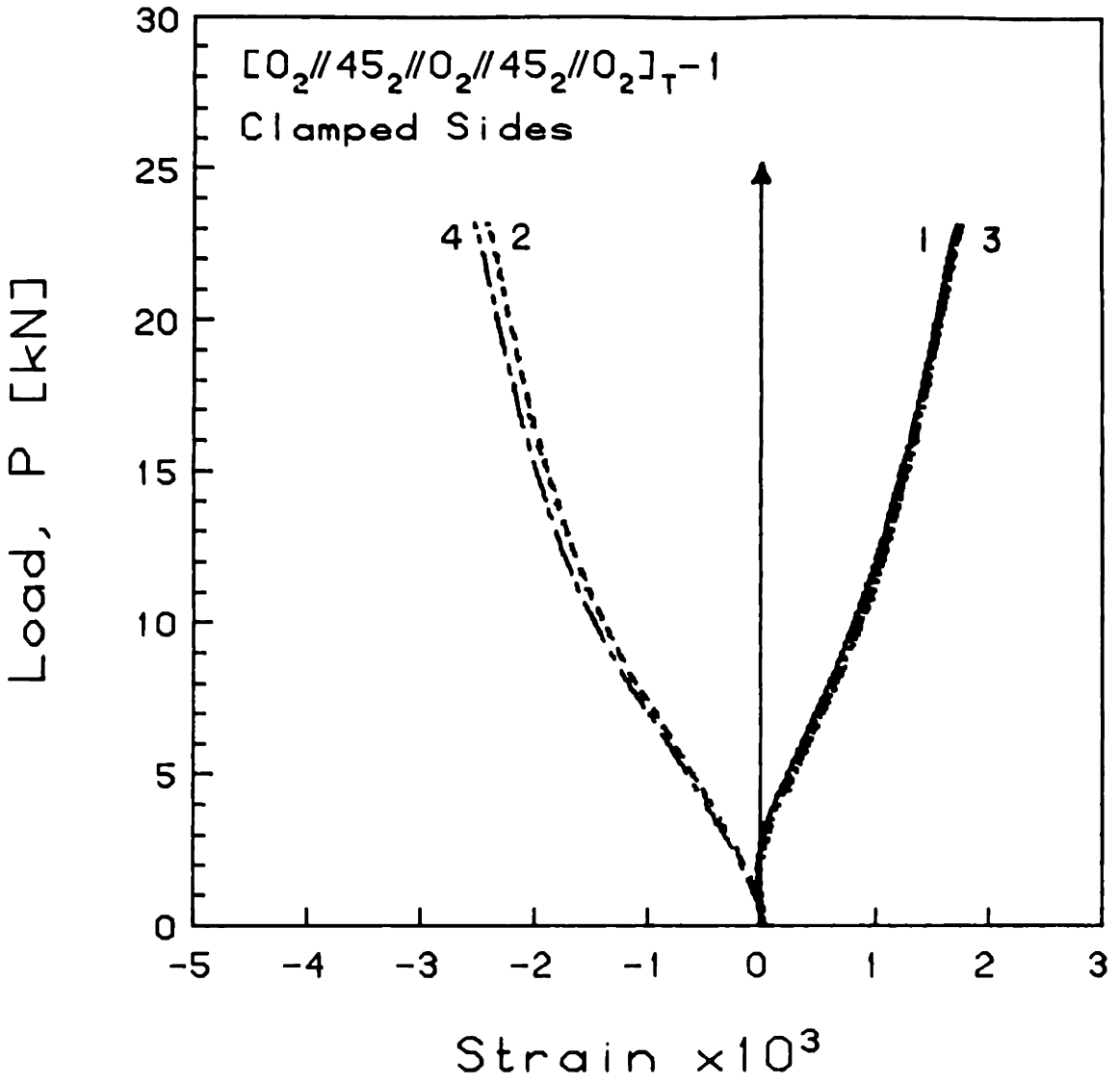

FIGURE F.14 Experimental Plot of Applied Compressive Load versus Longitudinal Strain for the $[O_2//45_2//O_2//45_2//O_2]_T$-1 Laminate with Clamped Side Boundary Conditions

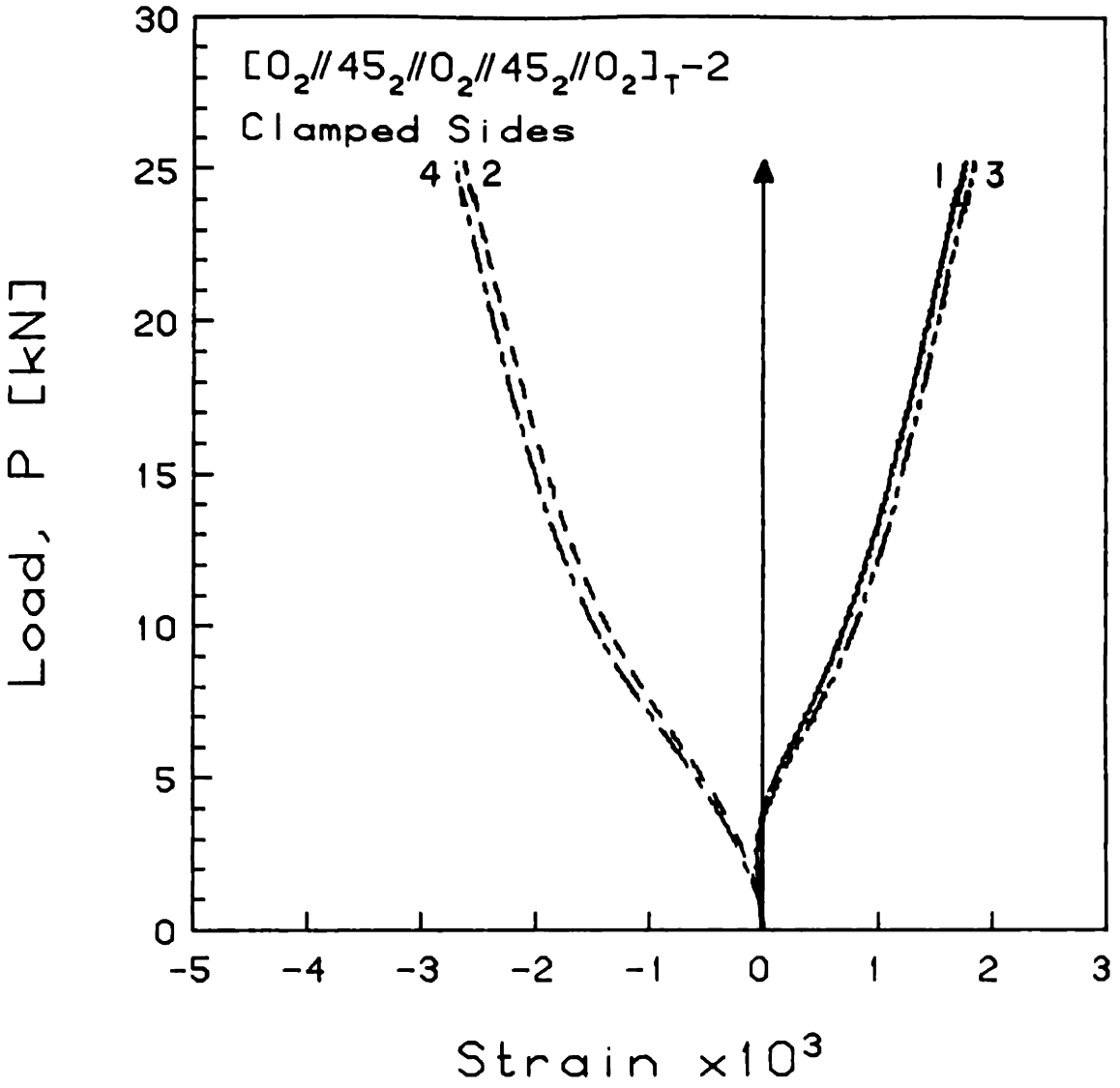

FIGURE F.15 Experimental Plot of Applied Compressive Load versus Longitudinal Strain for the $[0_2//45_2//0_2//45_2//0_2]_T$-2 Laminate with Clamped Side Boundary Conditions

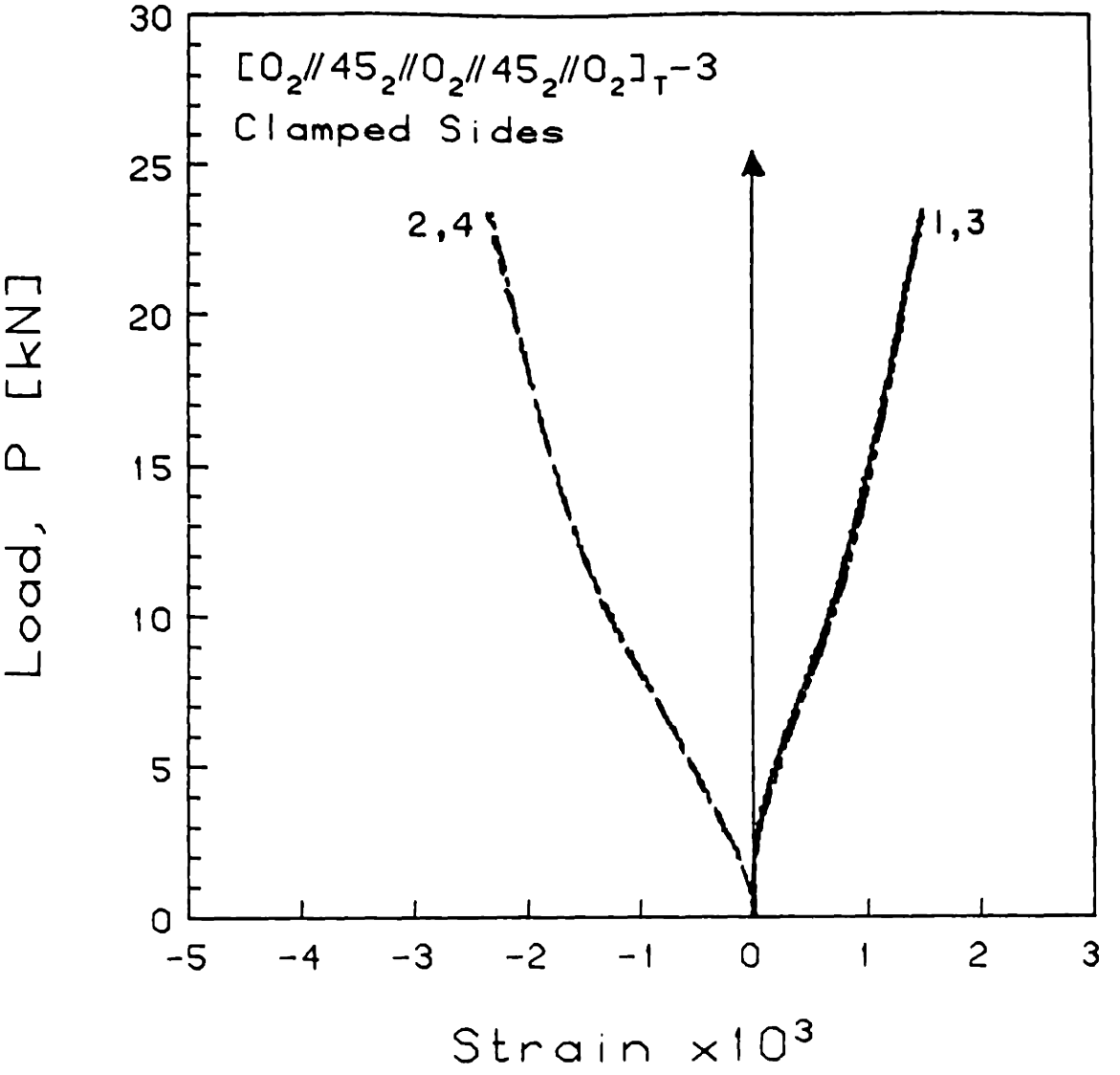

FIGURE F.16 Experimental Plot of Applied Compressive Load versus Longitudinal Strain for the $[0_2//45_2//0_2//45_2//0_2]_T$-3 Laminate with Clamped Side Boundary Conditions

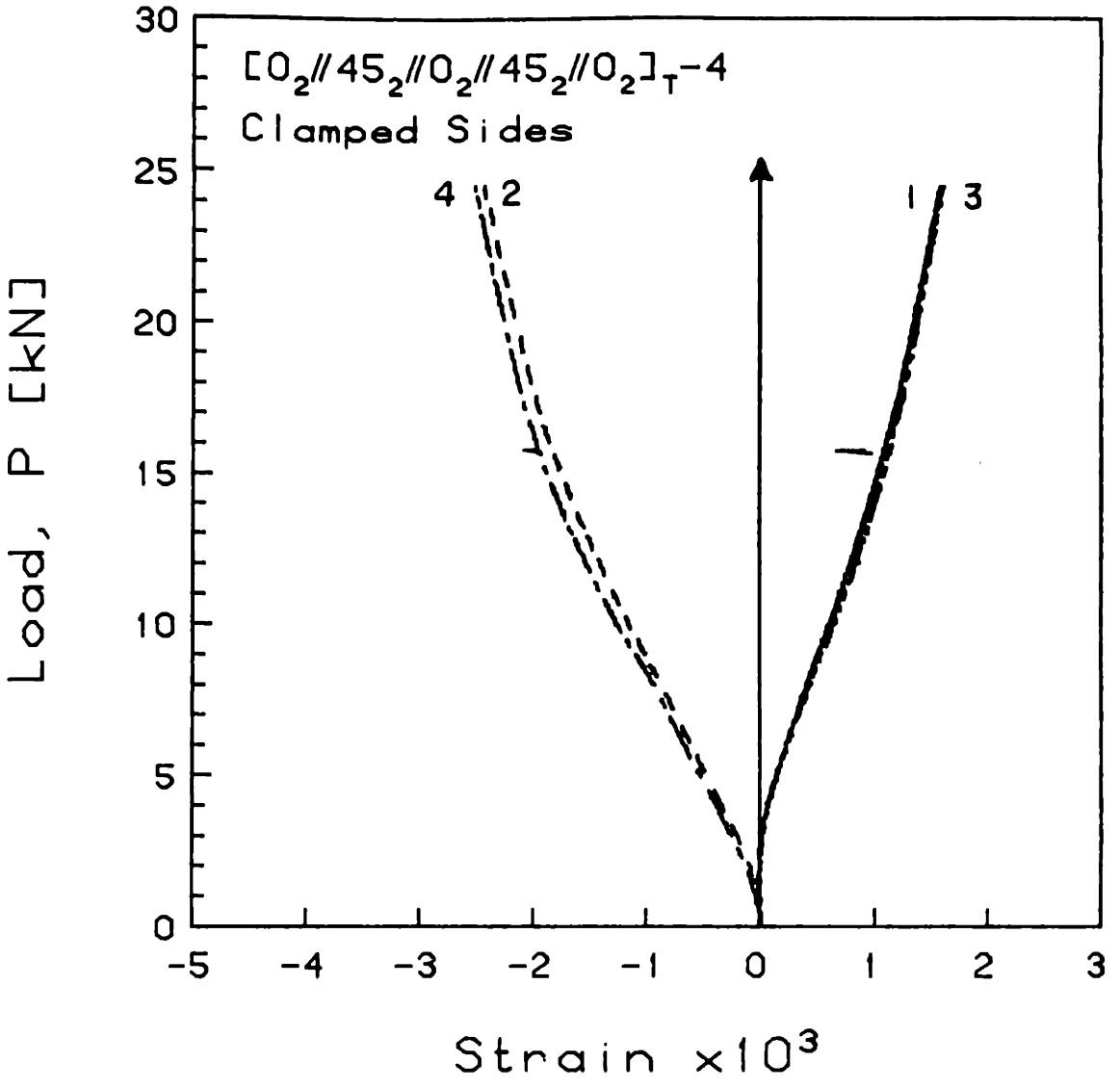

FIGURE F.17 Experimental Plot of Applied Compressive Load versus Longitudinal Strain for the $[0_2//45_2//0_2//45_2//0_2]_T$-4 Laminate with Clamped Side Boundary Conditions

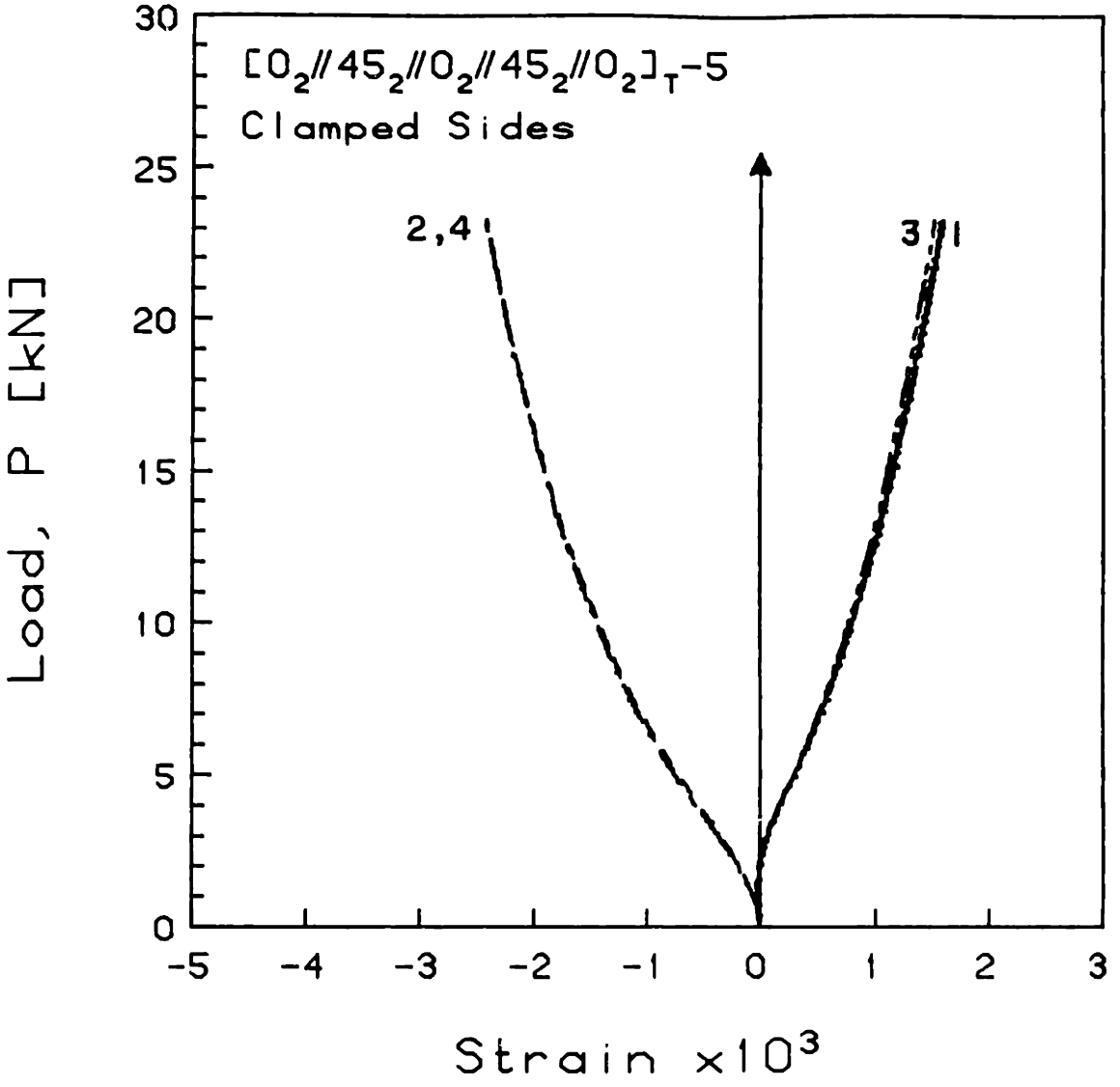

FIGURE F.18 Experimental Plot of Applied Compressive Load versus Longitudinal Strain for the $[O_2//45_2//O_2//45_2//O_2]_T$-5 Laminate with Clamped Side Boundary Conditions

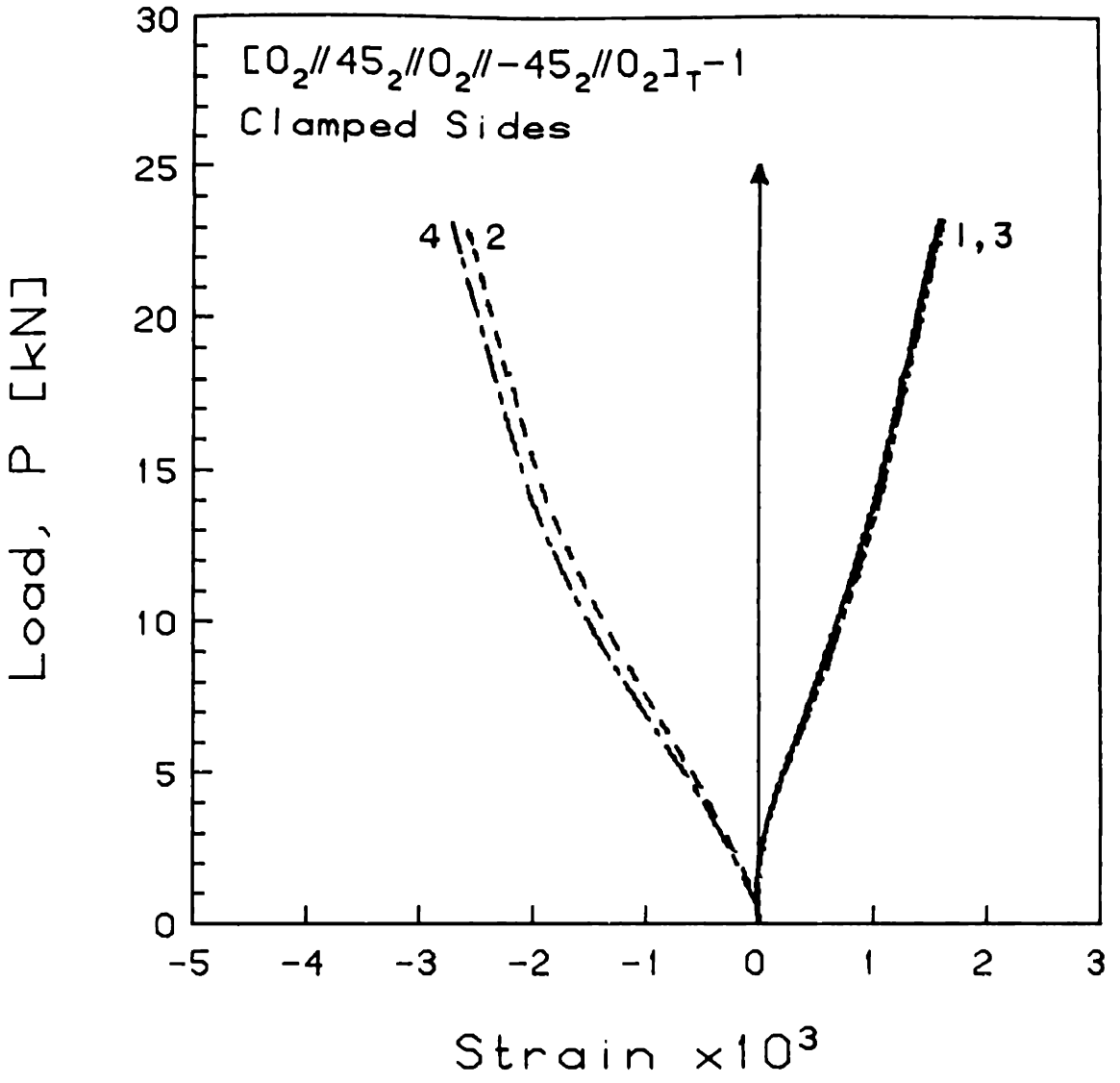

FIGURE F.19 Experimental Plot of Applied Compressive Load versus Longitudinal Strain for the $[0_2//45_2//0_2//-45_2//0_2]_T$-1 Laminate with Clamped Side Boundary Conditions

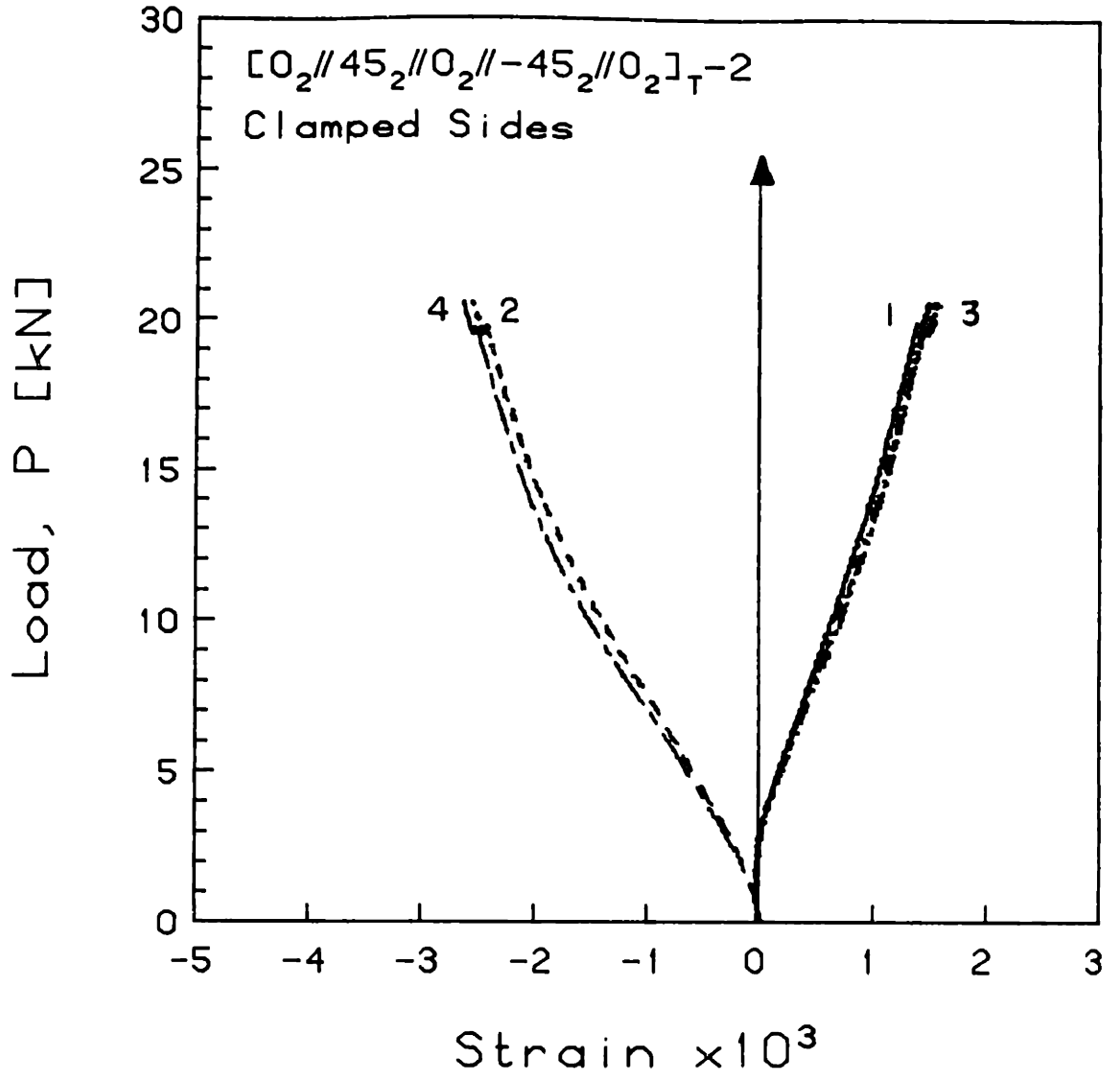

FIGURE F.20 Experimental Plot of Applied Compressive Load versus Longitudinal Strain for the $[O_2//45_2//O_2//-45_2//O_2]_T$-2 Laminate with Clamped Side Boundary Conditions

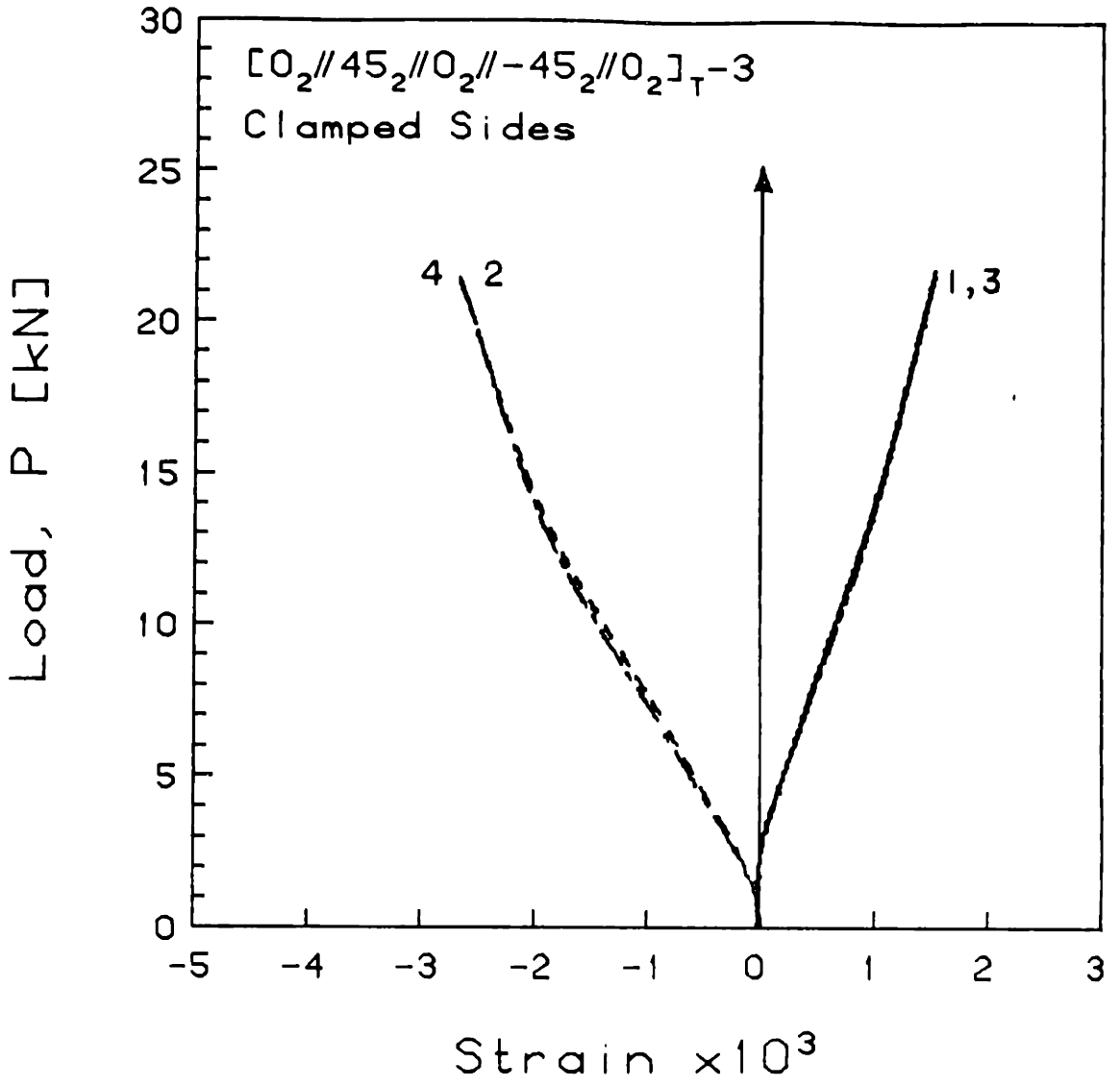

FIGURE F.21 Experimental Plot of Applied Compressive Load versus Longitudinal Strain for the $[0_2//45_2//0_2//-45_2//0_2]_T$-3 Laminate with Clamped Side Boundary Conditions

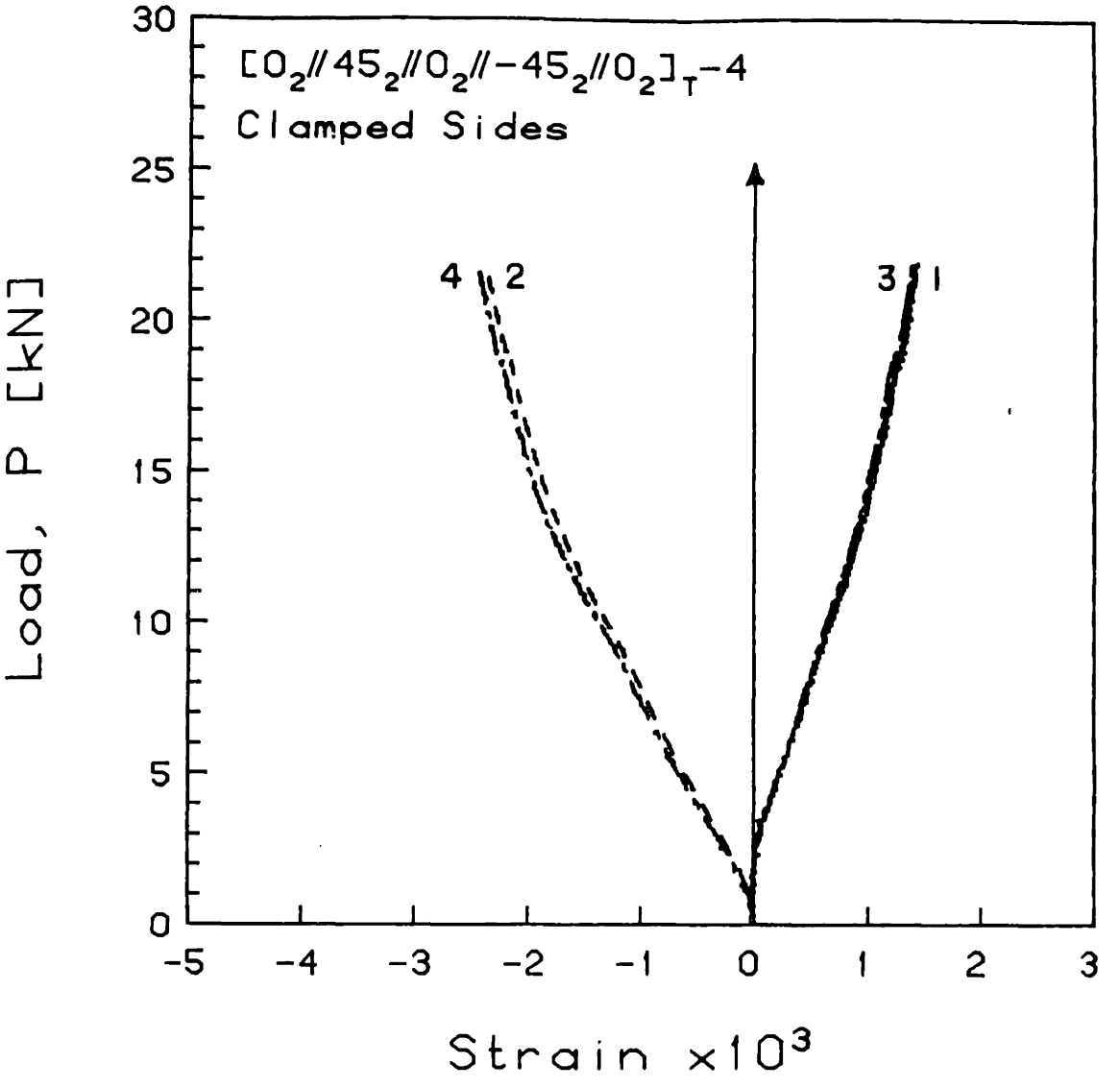

FIGURE F.22 Experimental Plot of Applied Compressive Load versus Longitudinal Strain for the $[0_2//45_2//0_2//-45_2//0_2]_T$-4 Laminate with Clamped Side Boundary Conditions

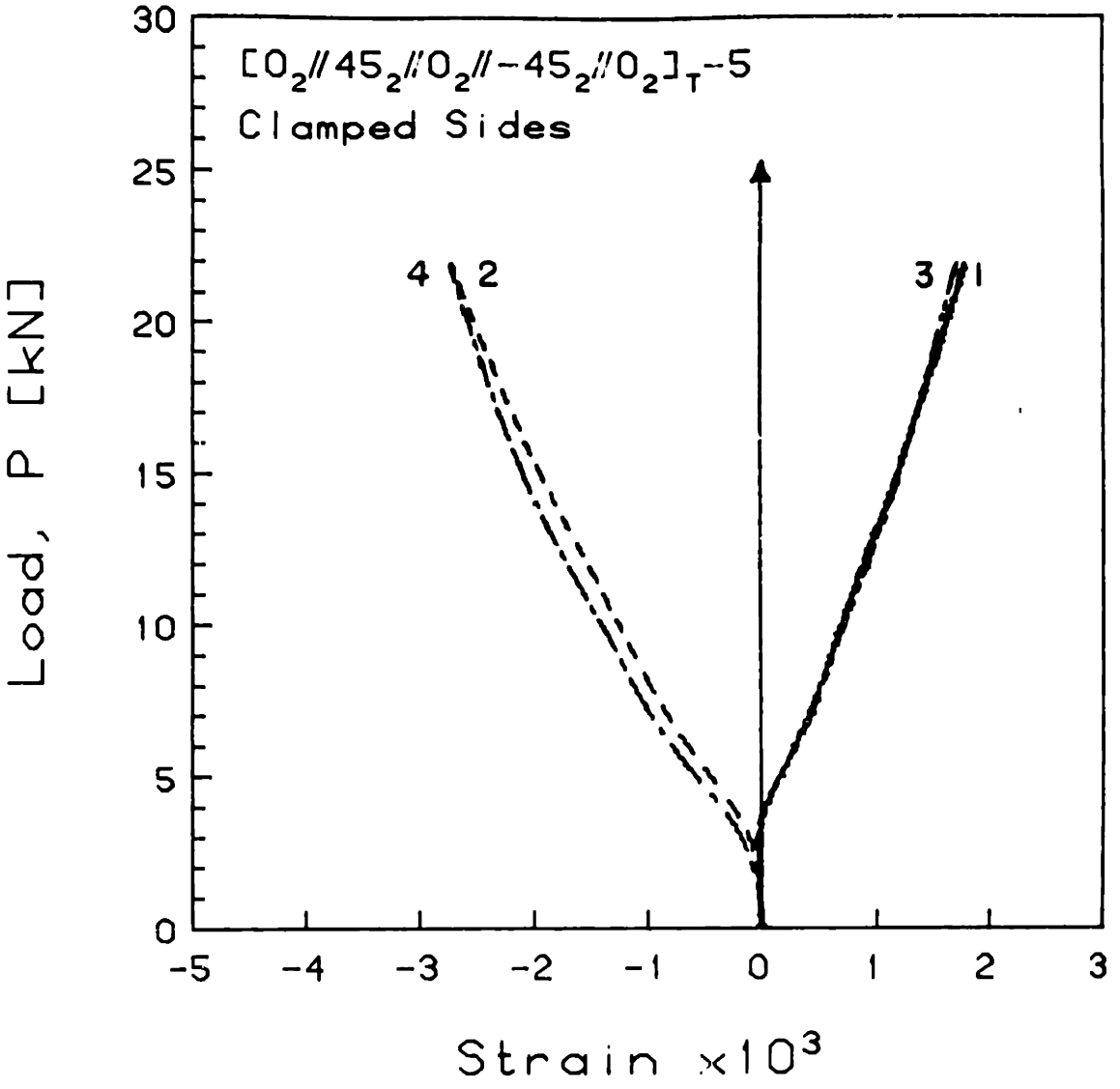

FIGURE F.23 Experimental Plot of Applied Compressive Load versus Longitudinal Strain for the $[O_2//45_2//O_2//-45_2//O_2]_T$-5 Laminate with Clamped Side Boundary Conditions

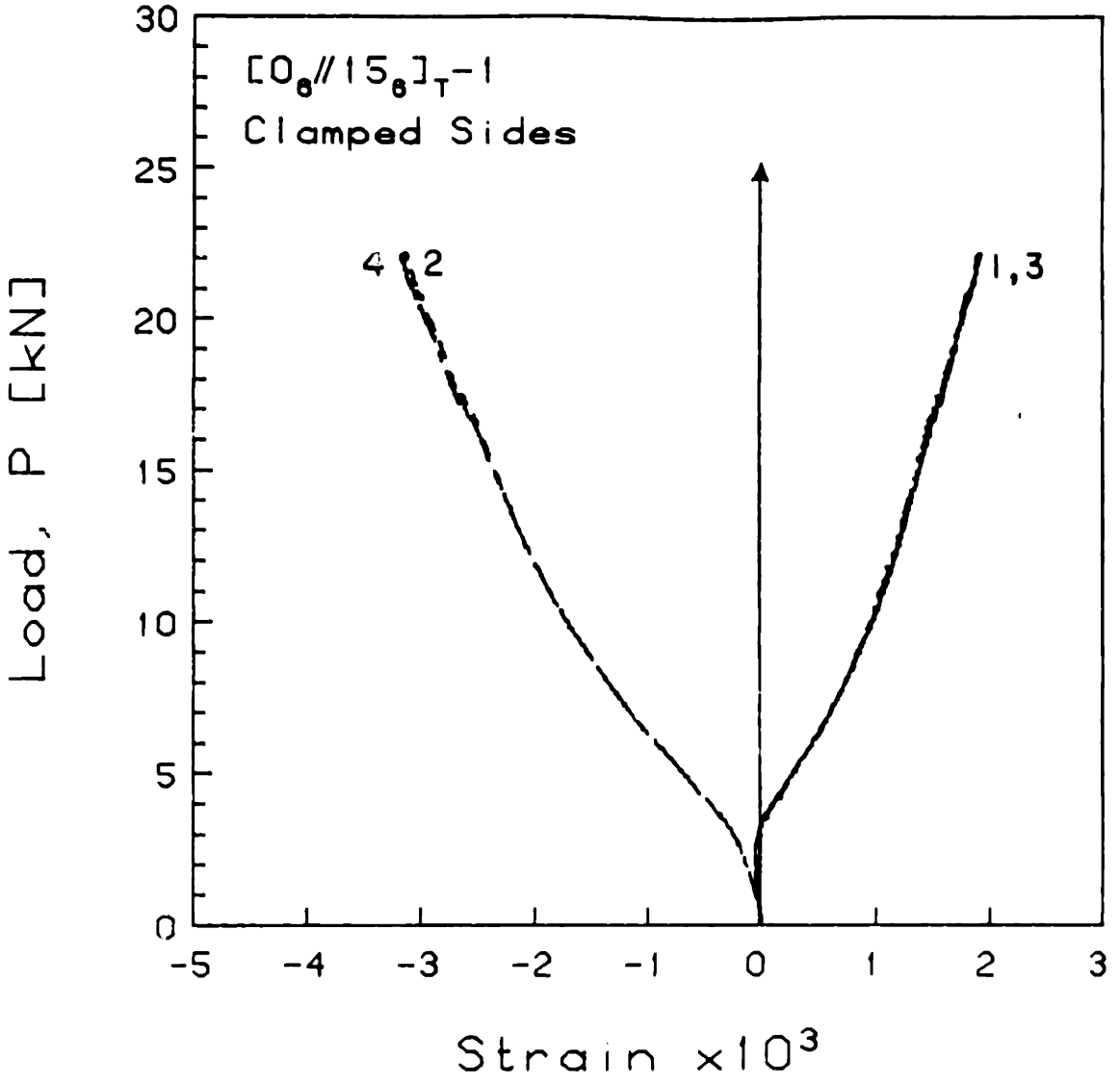

FIGURE F.24 Experimental Plot of Applied Compressive Load versus Longitudinal Strain for the $[O_6//15_6]_T$-1 Laminate with Clamped Side Boundary Conditions

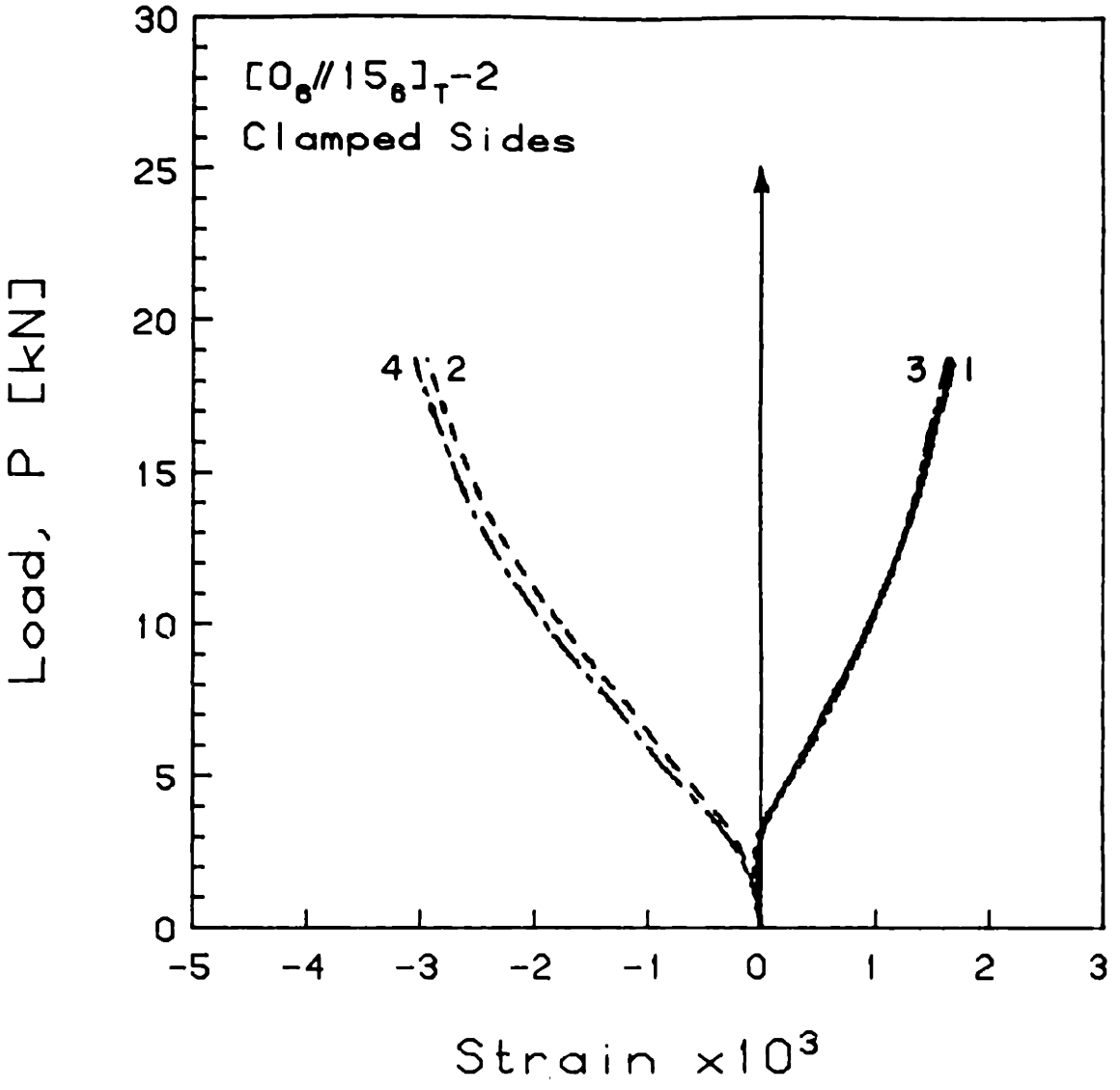

FIGURE F.25 Experimental Plot of Applied Compressive Load versus Longitudinal Strain for the $[0_6//15_6]_T$-2 Laminate with Clamped Side Boundary Conditions

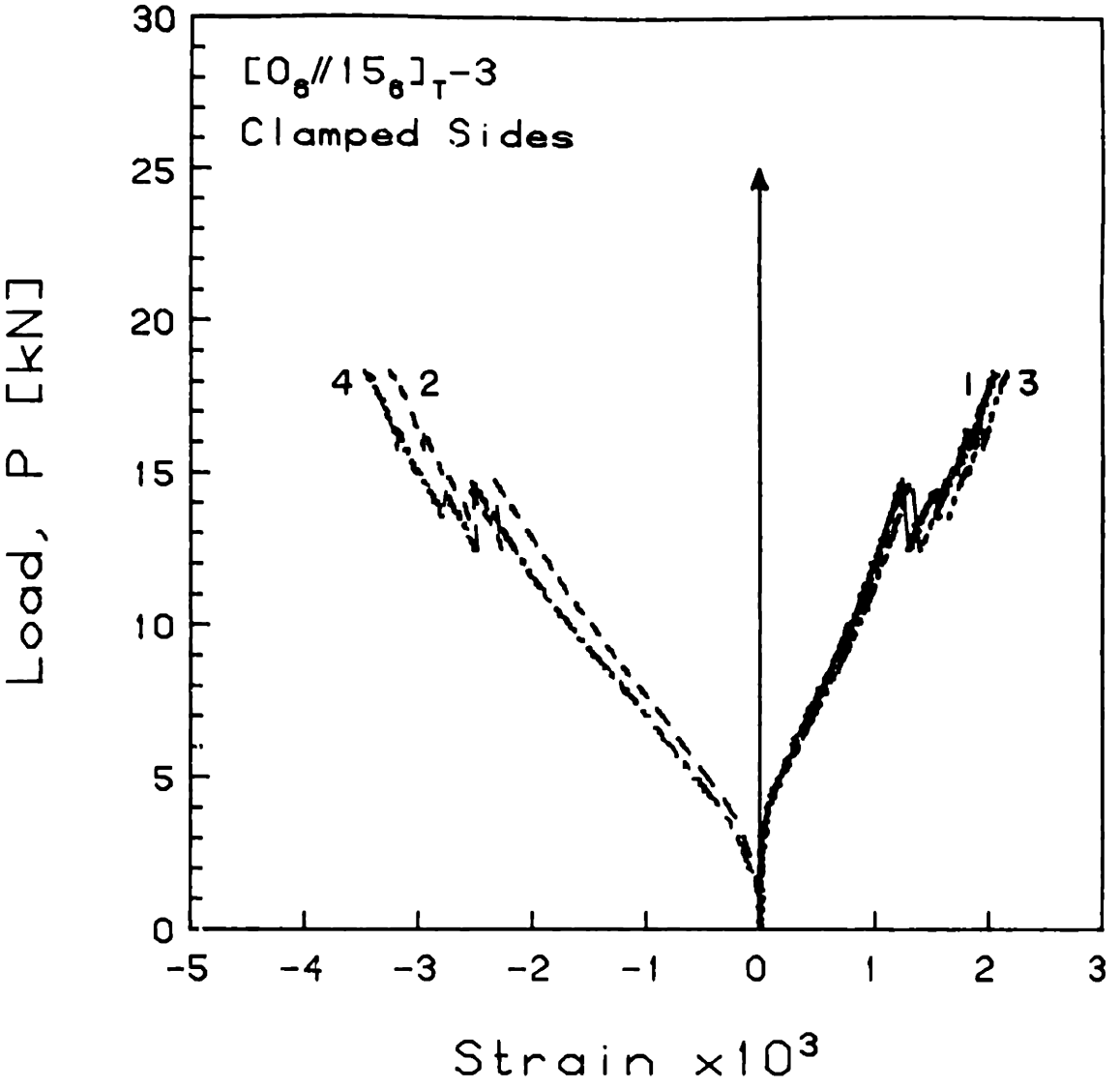

FIGURE F.26 Experimental Plot of Applied Compressive Load versus Longitudinal Strain for the $[O_6//15_6]_T$-3 Laminate with Clamped Side Boundary Conditions

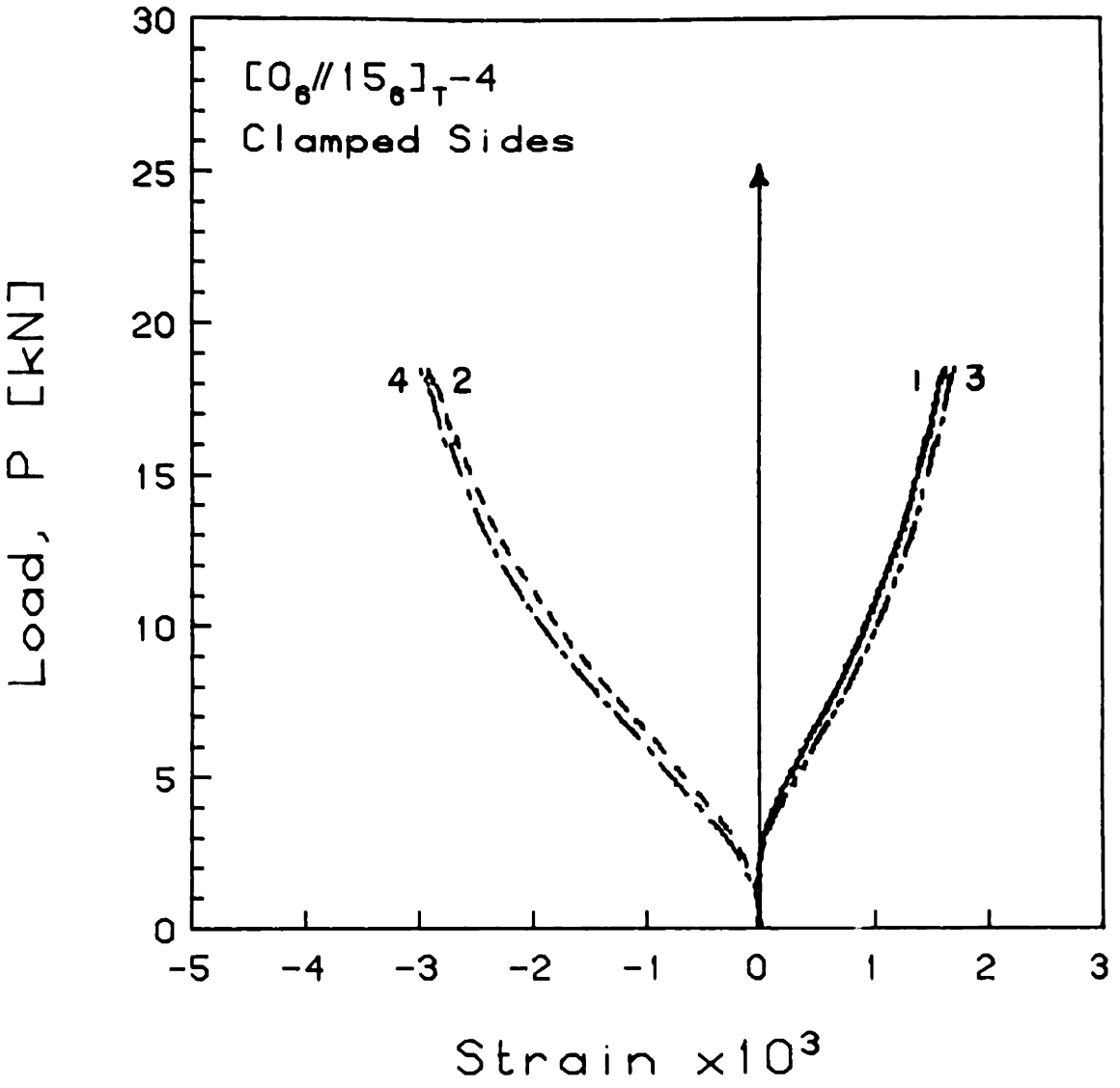

FIGURE F.27 Experimental Plot of Applied Compressive Load versus Longitudinal Strain for the $[O_6//15_6]_T$-4 Laminate with Clamped Side Boundary Conditions

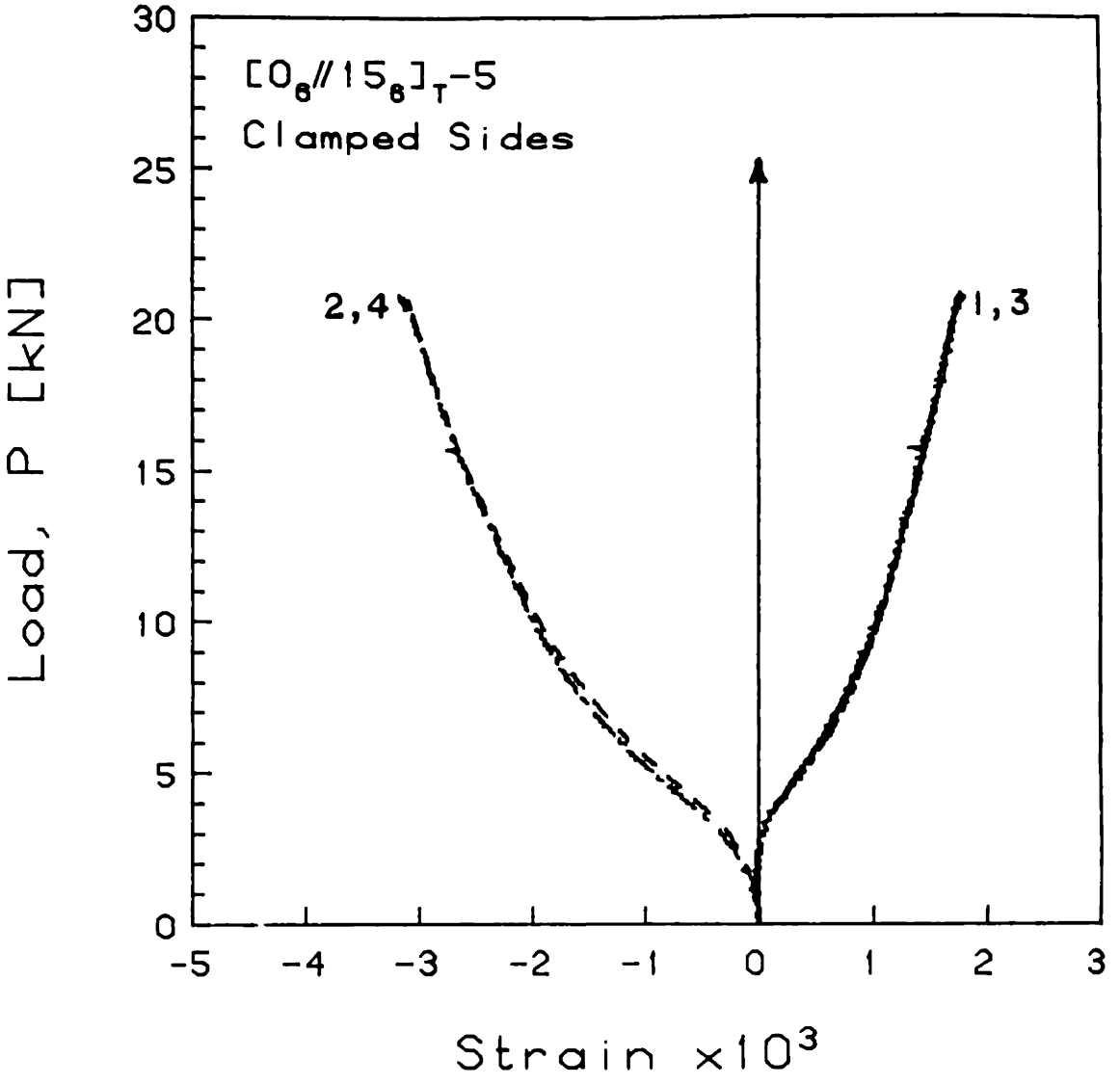

FIGURE F.28 Experimental Plot of Applied Compressive Load versus Longitudinal Strain for the $[0_6//15_6]_T$-5 Laminate with Clamped Side Boundary Conditions

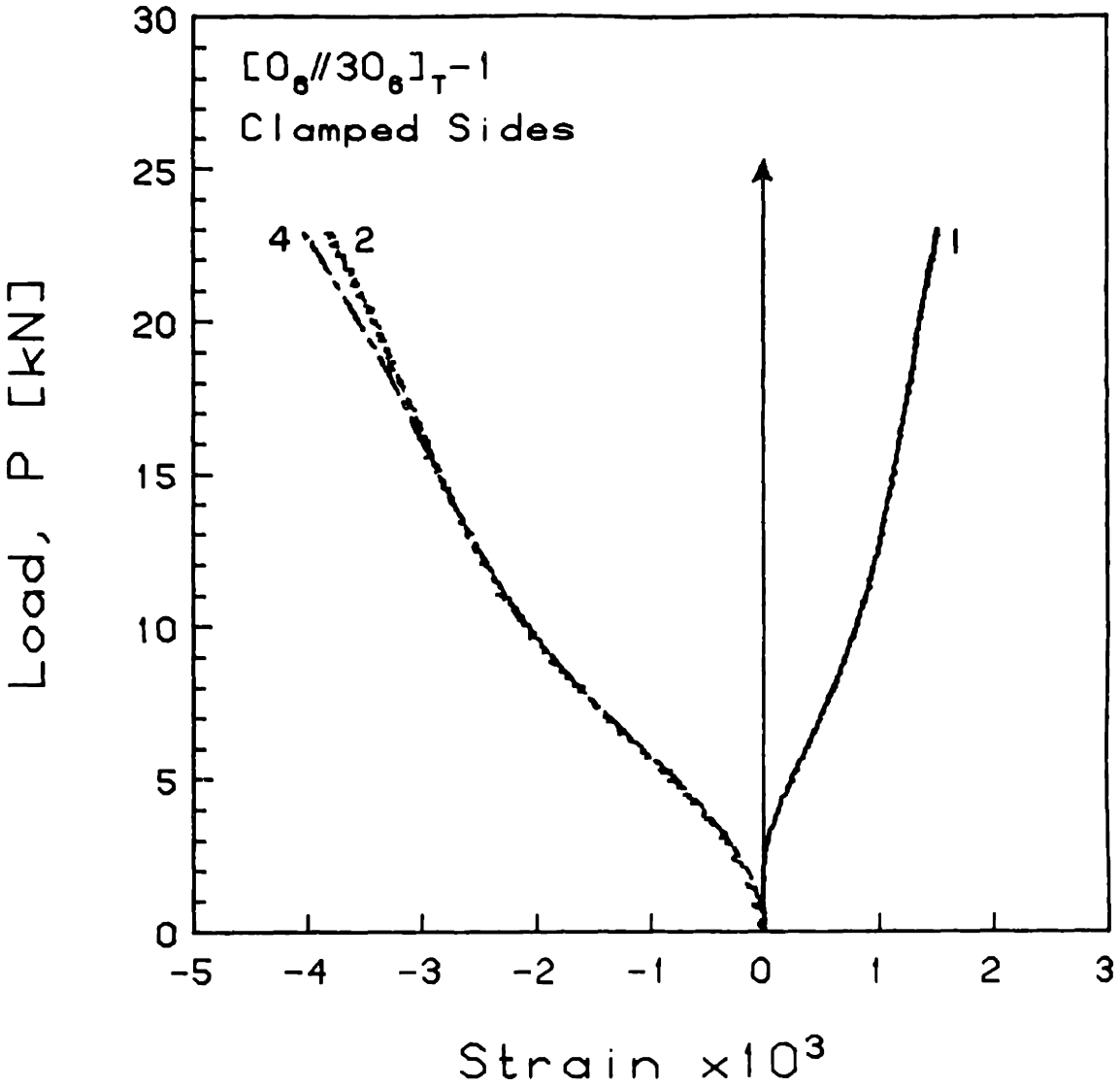

FIGURE F.29 Experimental Plot of Applied Compressive Load versus Longitudinal Strain for the $[0_6//30_6]_T$-1 Laminate with Clamped Side Boundary Conditions

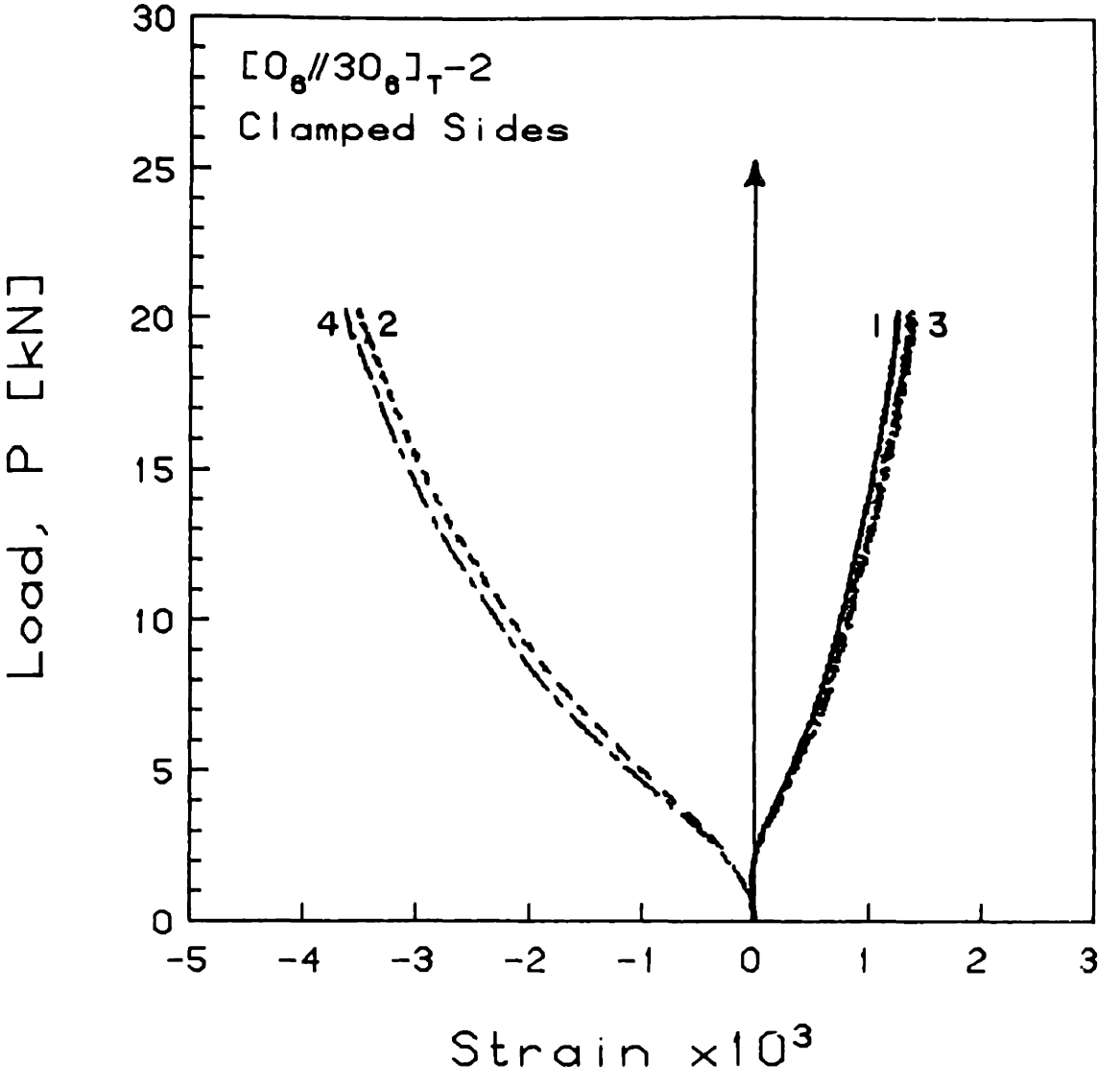

FIGURE F.30 Experimental Plot of Applied Compressive Load versus Longitudinal Strain for the $[0_6//30_6]_T$-2 Laminate with Clamped Side Boundary Conditions

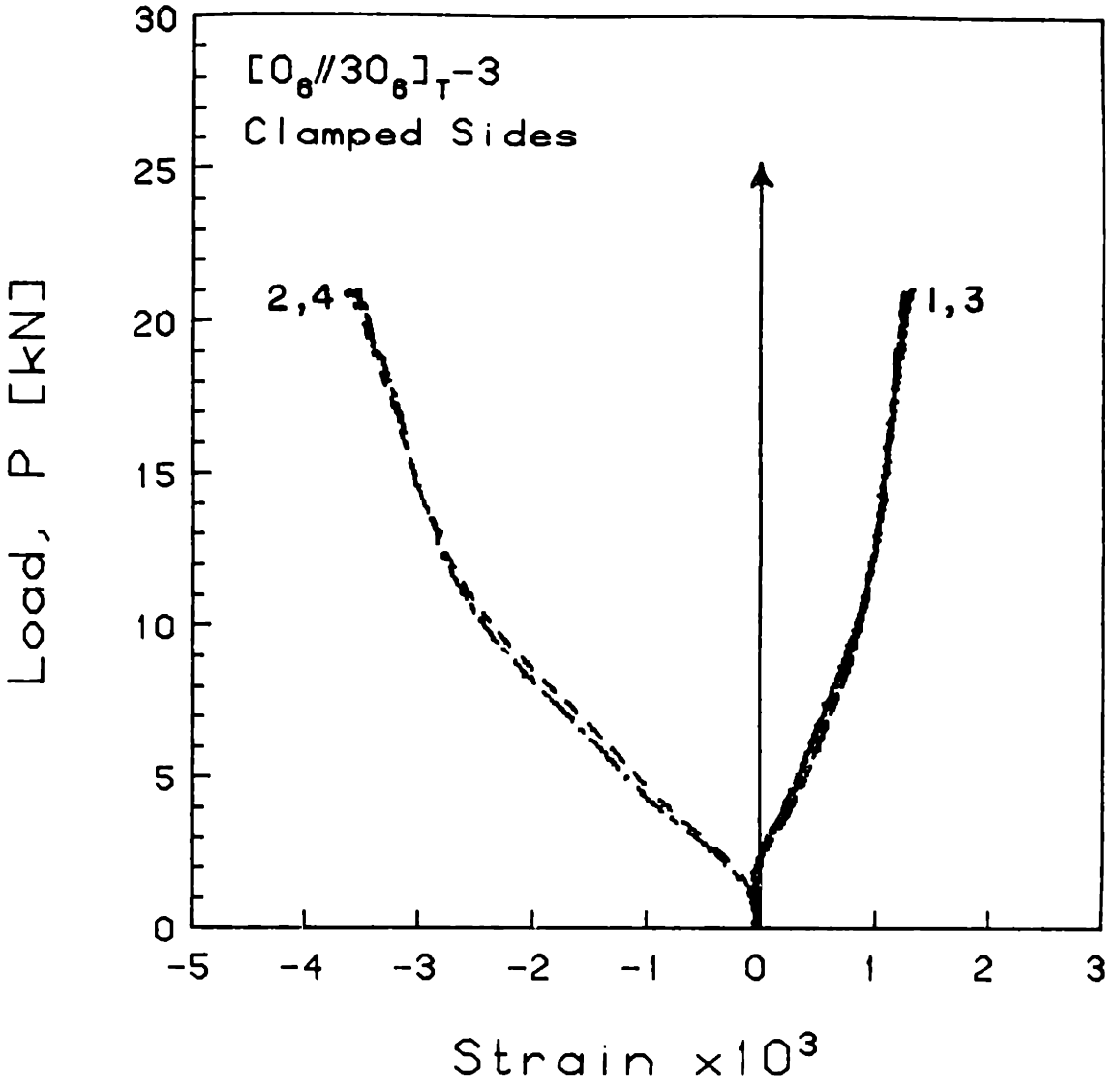

FIGURE F.31 Experimental Plot of Applied Compressive Load versus Longitudinal Strain for the $[0_6//30_6]_T$-3 Laminate with Clamped Side Boundary Conditions

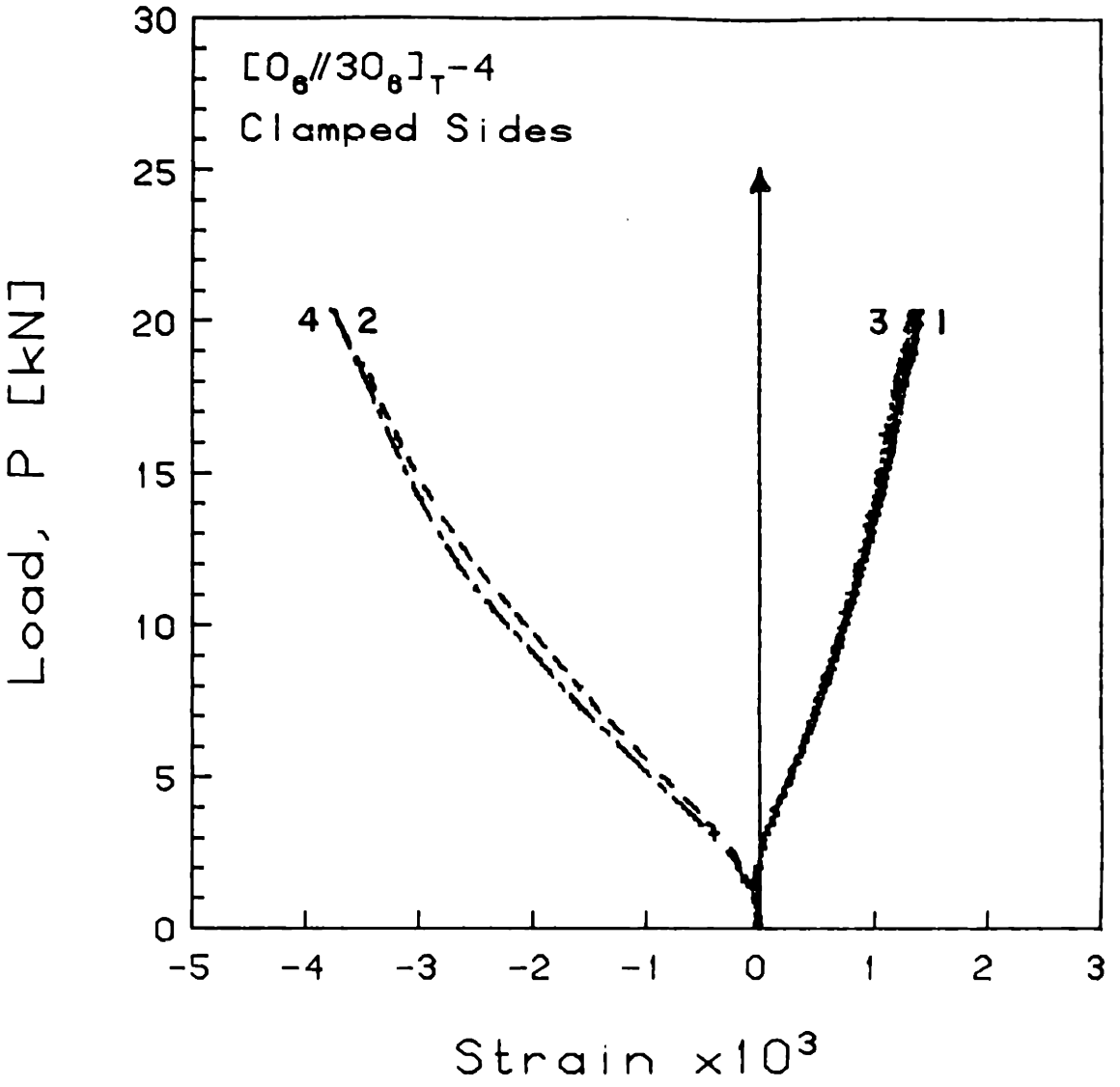

FIGURE F.32 Experimental Plot of Applied Compressive Load versus Longitudinal Strain for the $[0_6//30_6]_T$-4 Laminate with Clamped Side Boundary Conditions

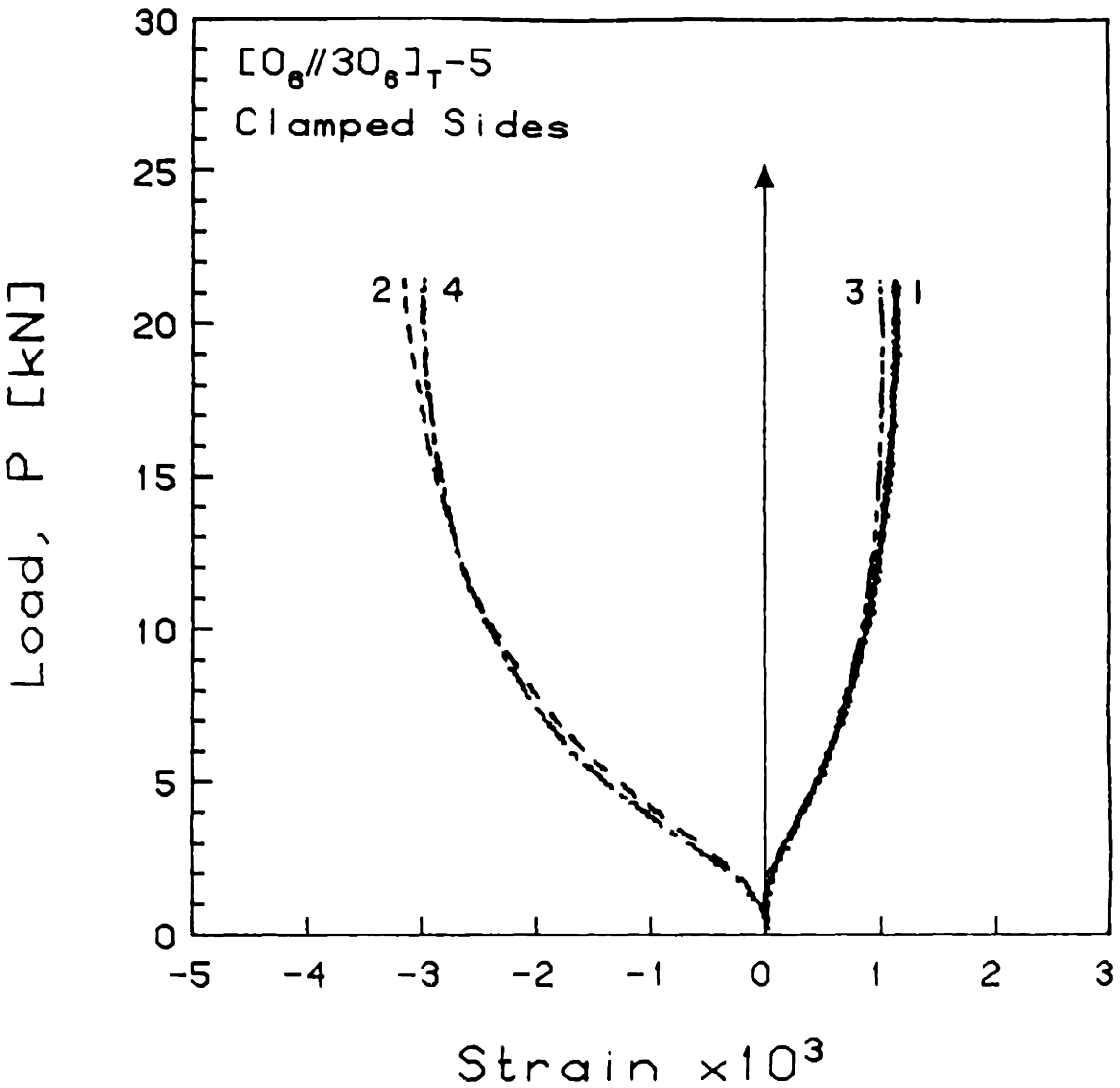

FIGURE F.33 Experimental Plot of Applied Compressive Load versus Longitudinal Strain for the $[0_6//30_6]_T$-5 Laminate with Clamped Side Boundary Conditions

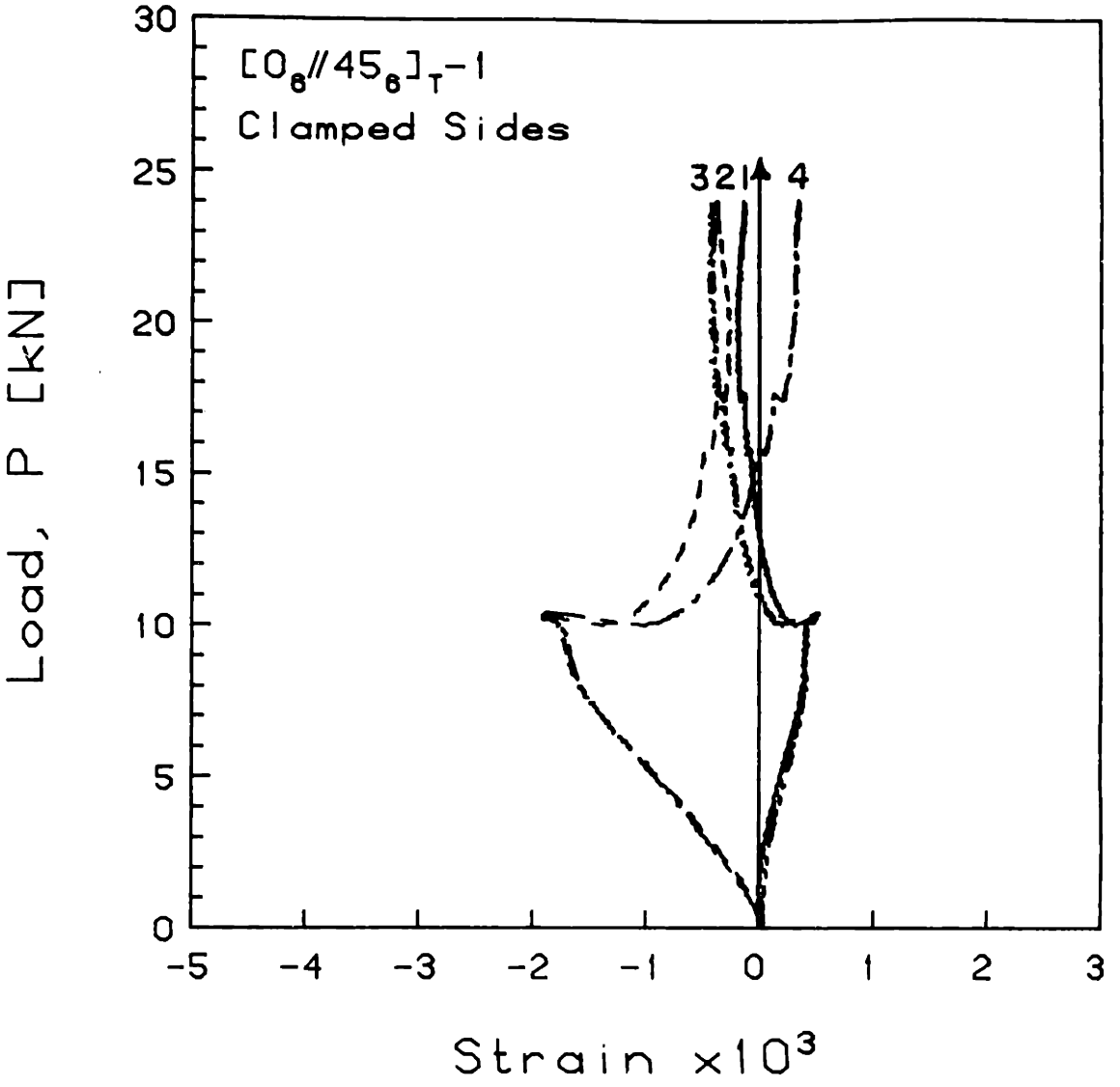

FIGURE F.34 Experimental Plot of Applied Compressive Load versus Longitudinal Strain for the $[O_6//45_6]_T$-1 Laminate with Clamped Side Boundary Conditions

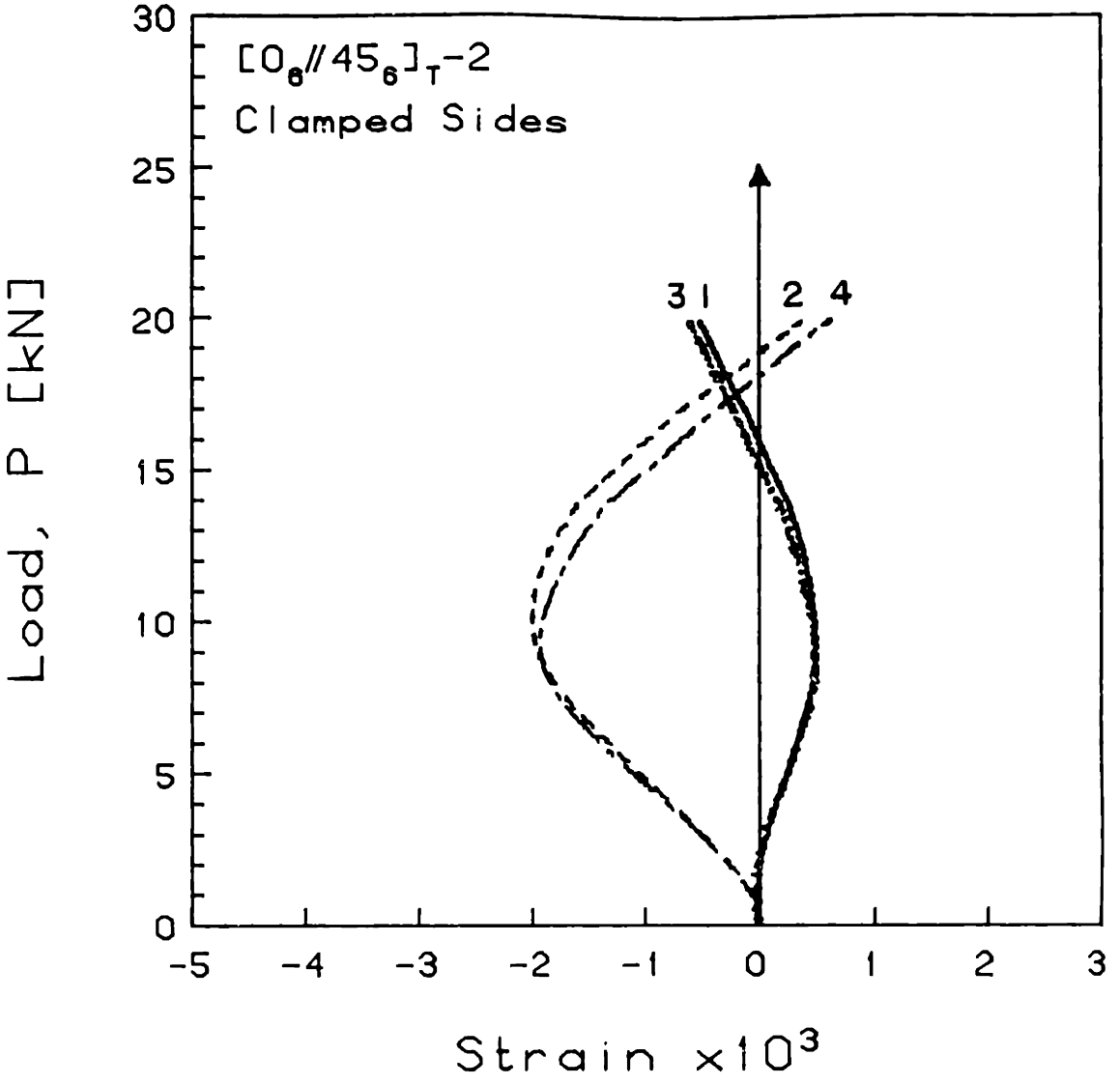

FIGURE F.35 Experimental Plot of Applied Compressive Load versus Longitudinal Strain for the $[0_6//45_6]_T$-2 Laminate with Clamped Side Boundary Conditions

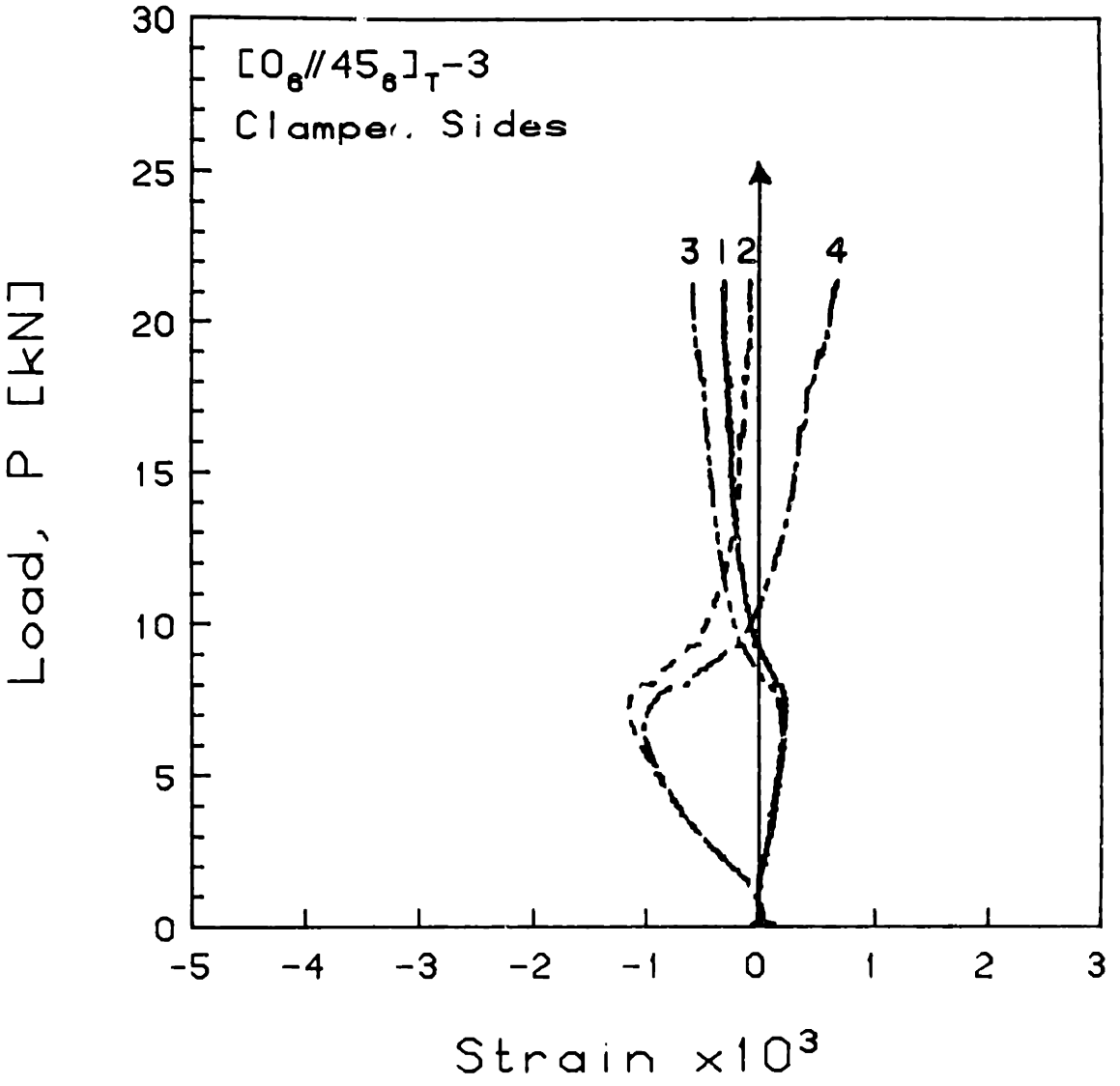

FIGURE F.36 Experimental Plot of Applied Compressive Load versus Longitudinal Strain for the $[O_6//45_6]_T$-3 Laminate with Clamped Side Boundary Conditions

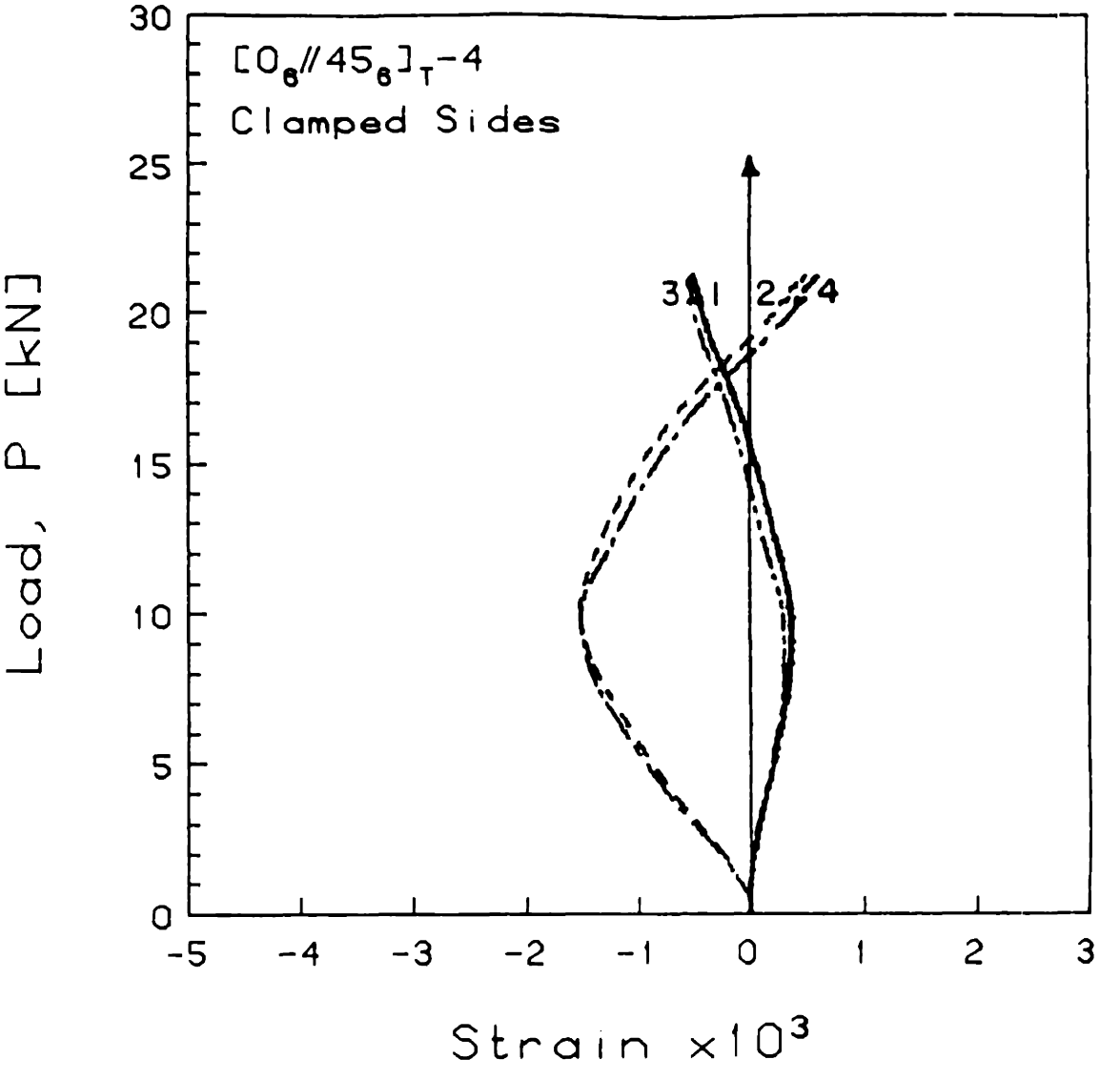

FIGURE F.37 Experimental Plot of Applied Compressive Load versus Longitudinal Strain for the $[0_6//45_6]_T$-4 Laminate with Clamped Side Boundary Conditions

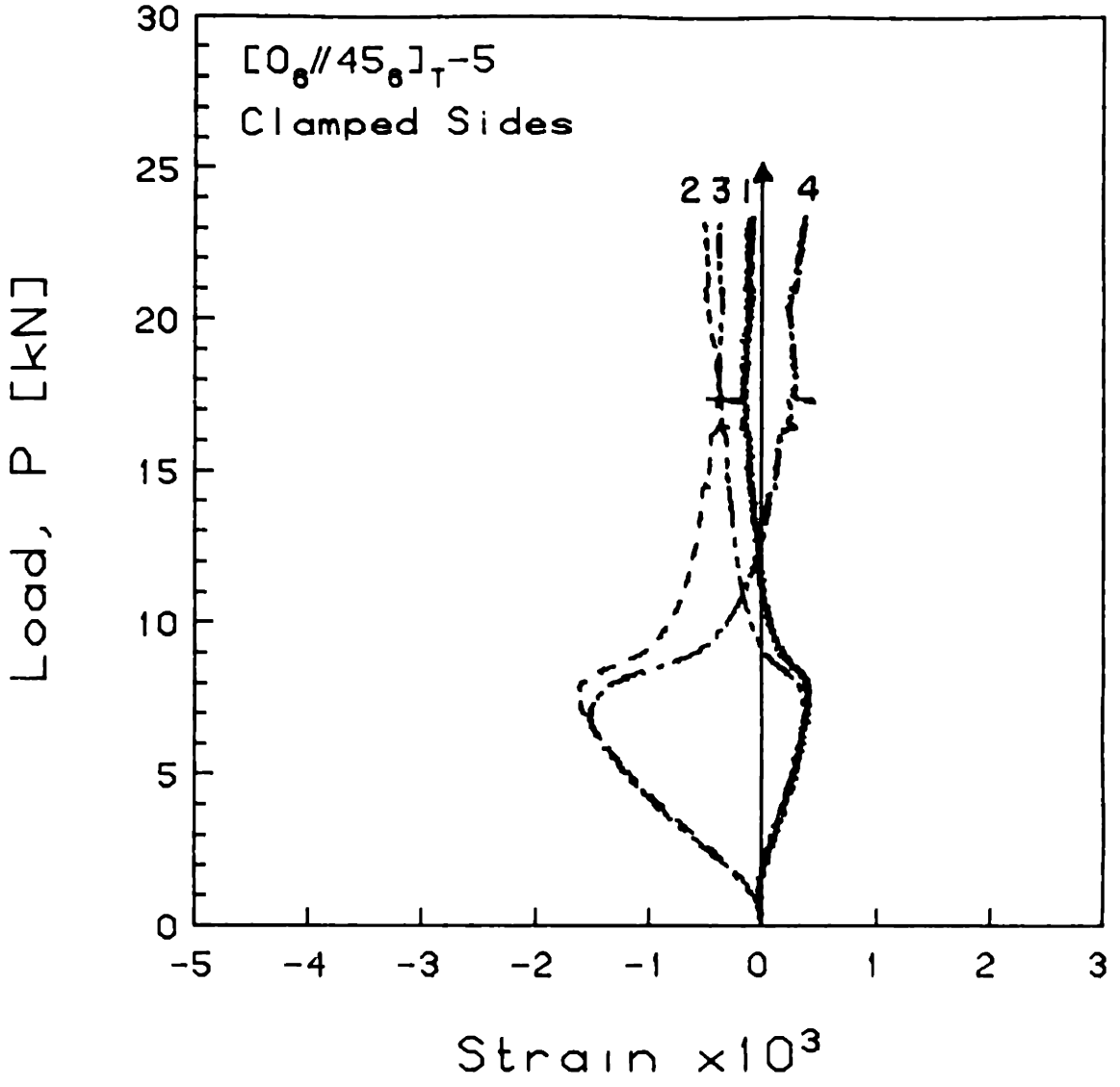

FIGURE F.38 Experimental Plot of Applied Compressive Load versus Longitudinal Strain for the $[0_6//45_6]_T$-5 Laminate with Clamped Side Boundary Conditions

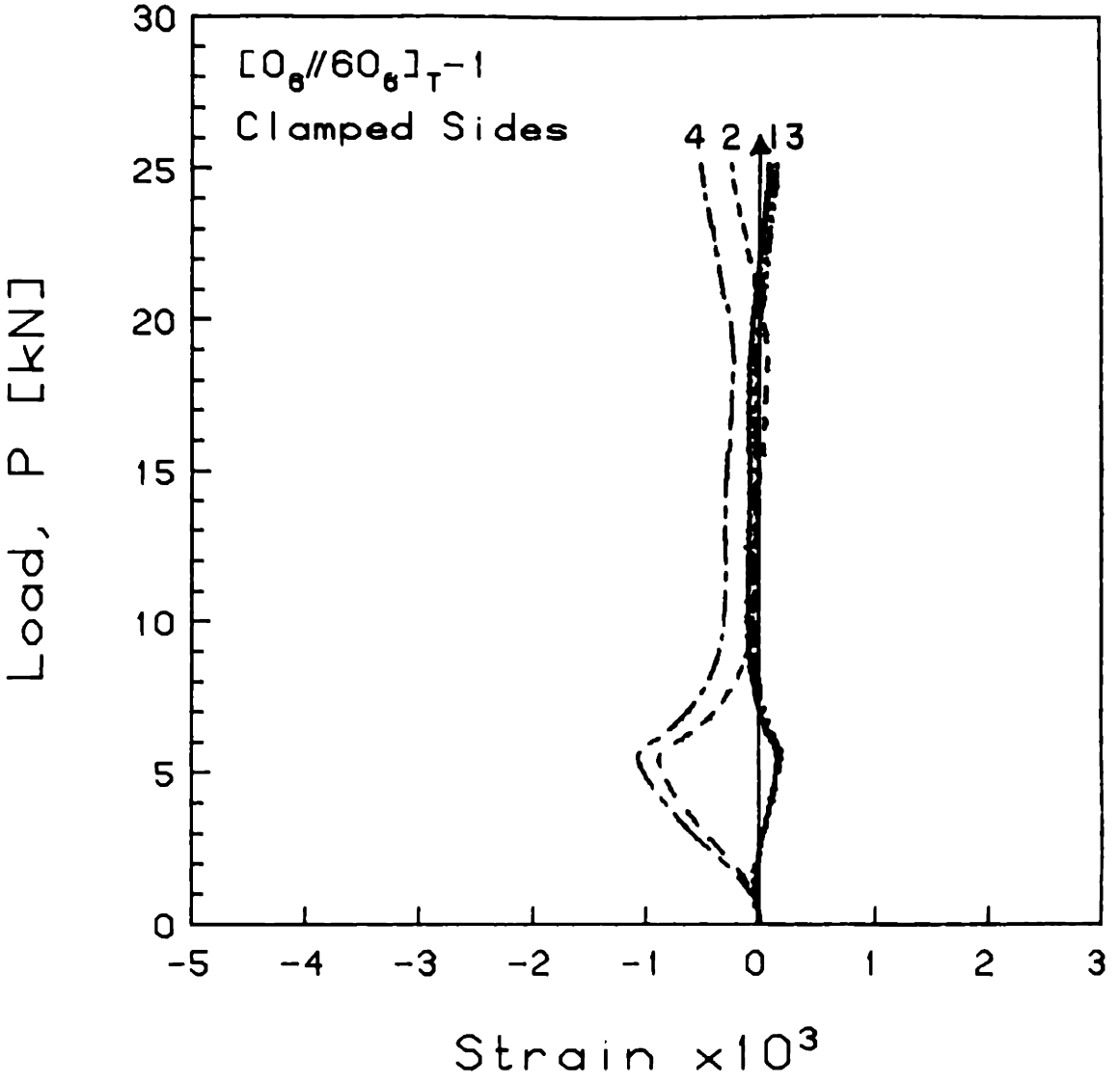

FIGURE F.39 Experimental Plot of Applied Compressive Load versus Longitudinal Strain for the $[0_6//60_6]_T$-1 Laminate with Clamped Side Boundary Conditions

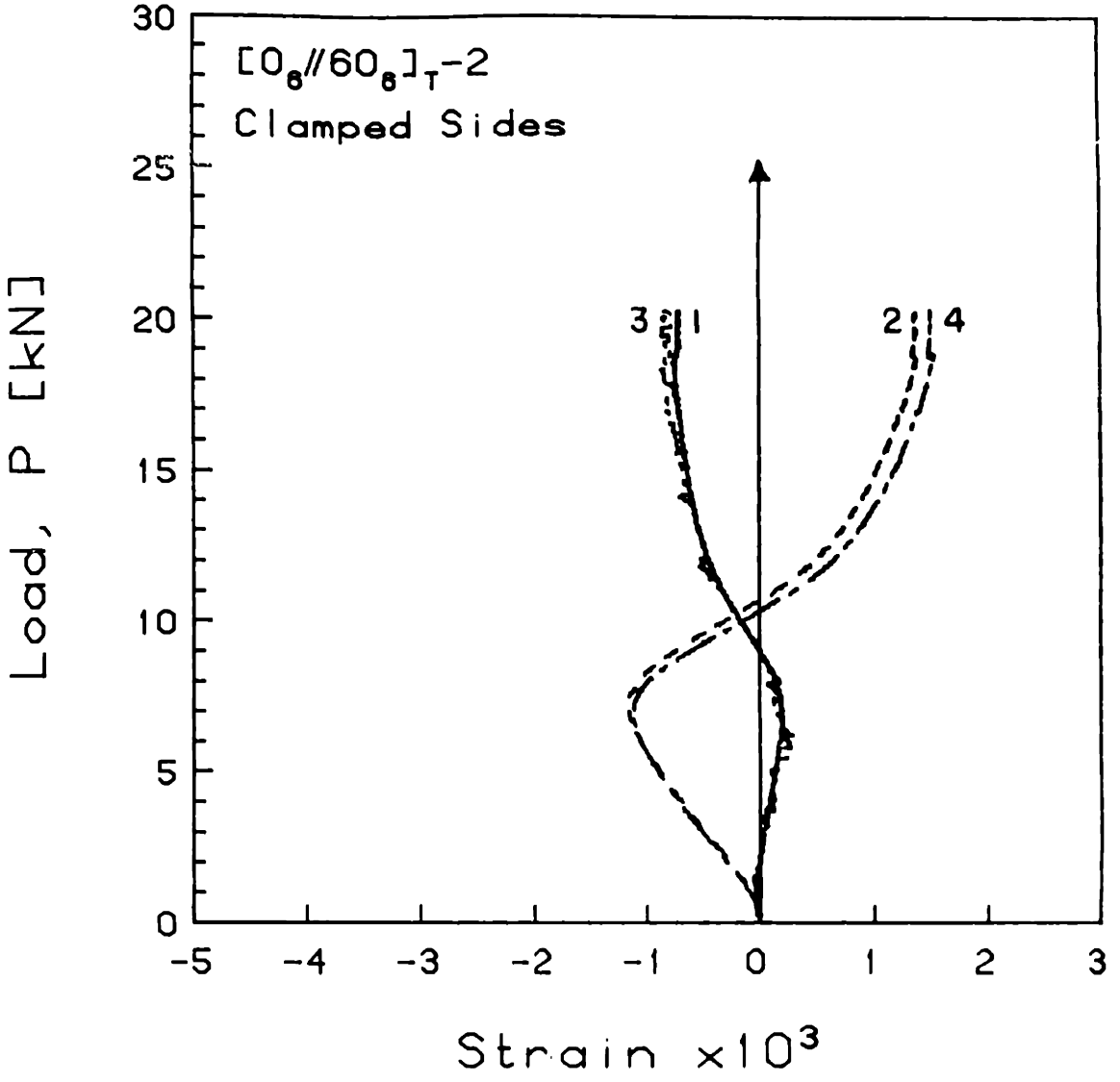

FIGURE F.40 Experimental Plot of Applied Compressive Load versus Longitudinal Strain for the $[O_6//60_6]_T$-2 Laminate with Clamped Side Boundary Conditions

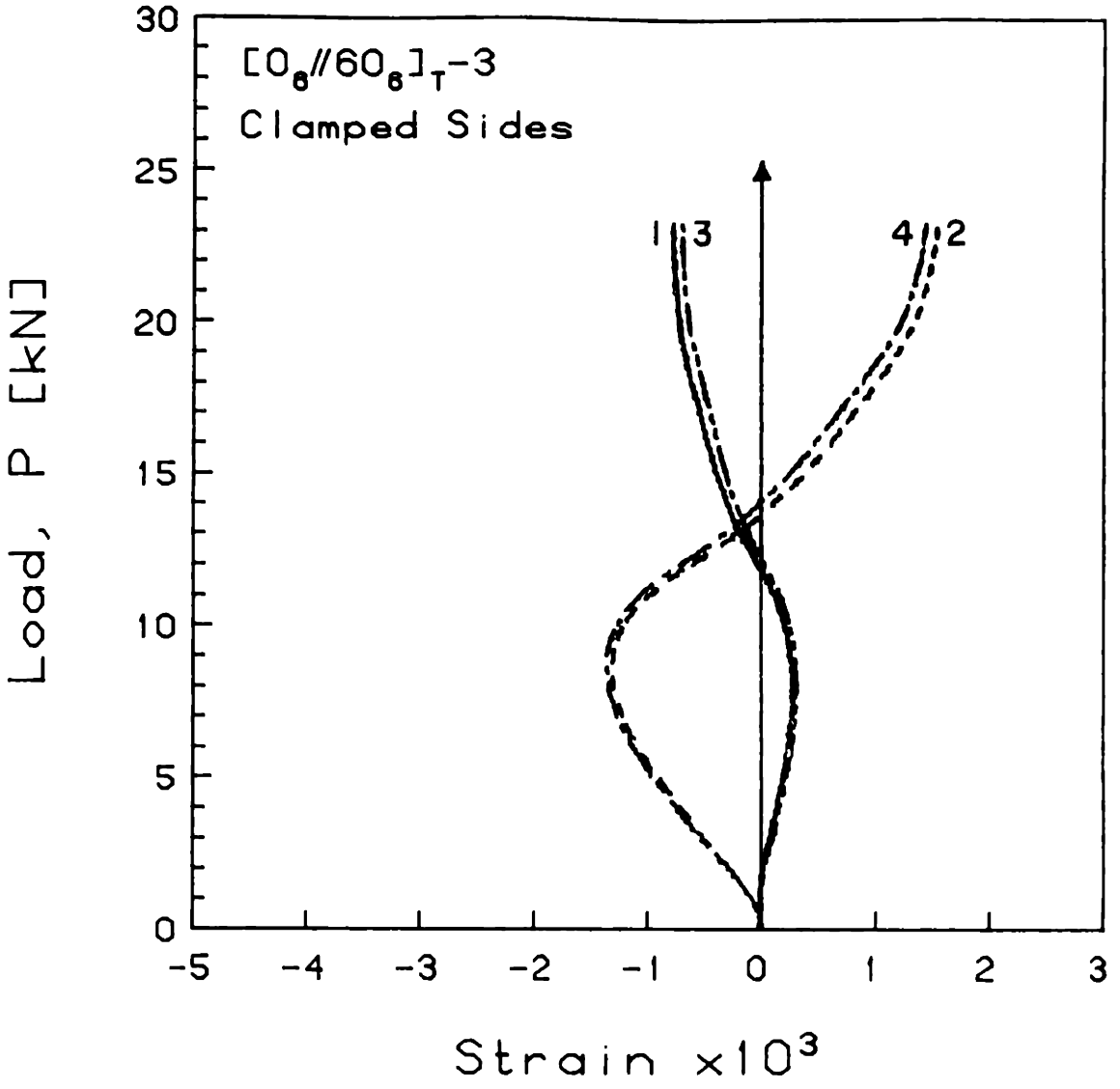

FIGURE F.41 Experimental Plot of Applied Compressive Load versus Longitudinal Strain for the $[0_6//60_6]_T$-3 Laminate with Clamped Side Boundary Conditions

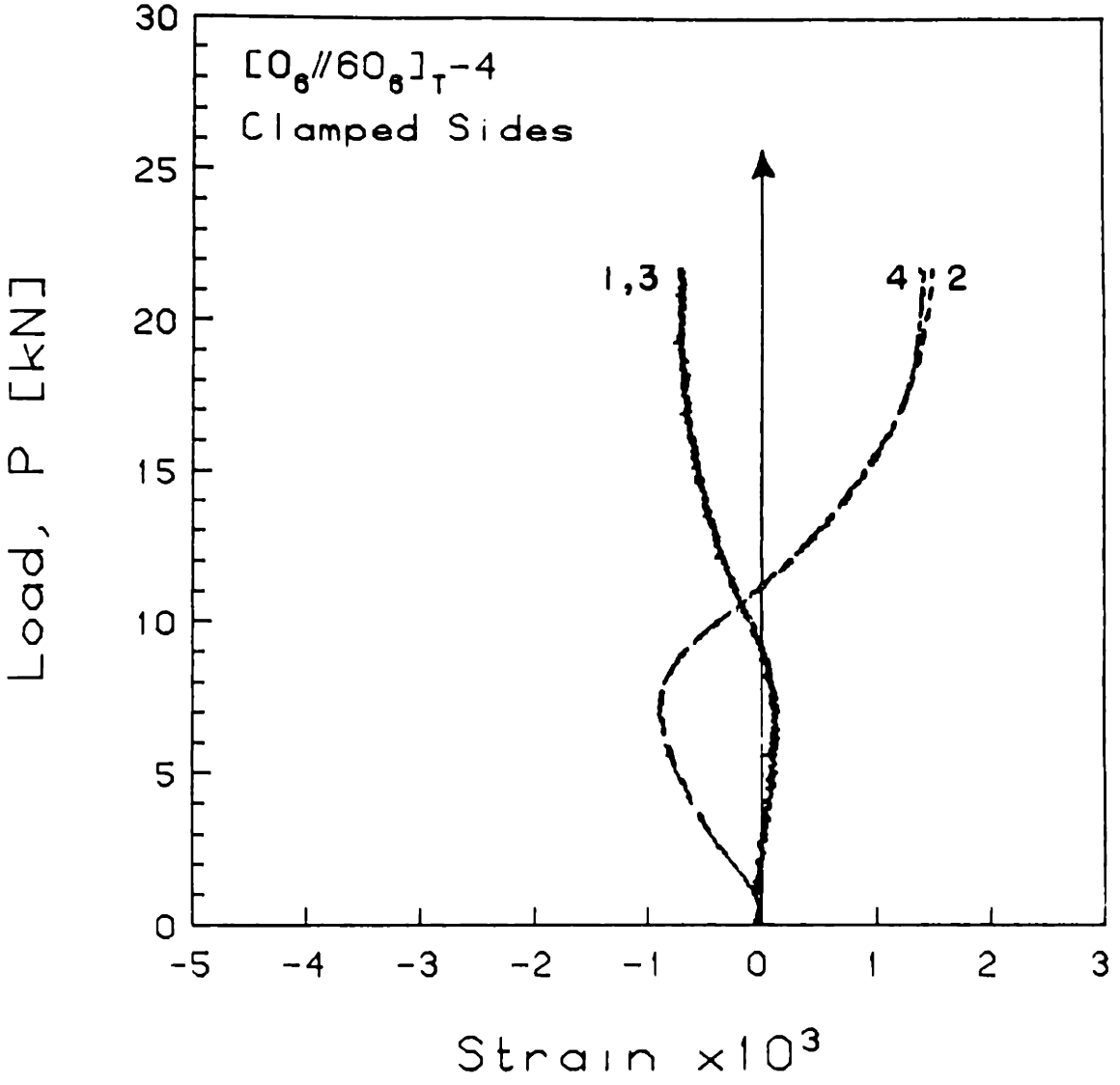

FIGURE F.42 Experimental Plot of Applied Compressive Load versus Longitudinal Strain for the $[0_6//60_6]_T$-4 Laminate with Clamped Side Boundary Conditions

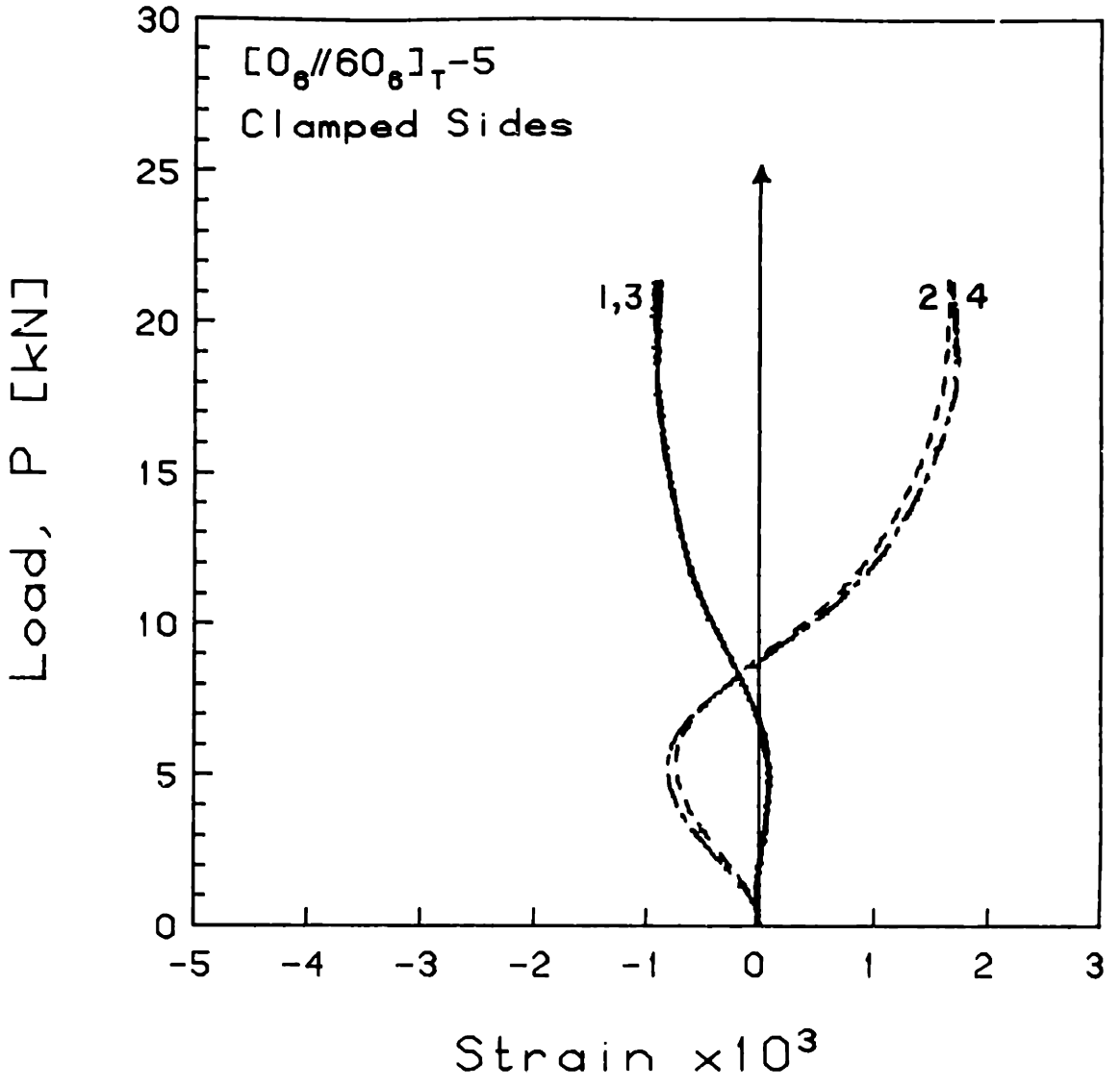

FIGURE F.43 Experimental Plot of Applied Compressive Load versus Longitudinal Strain for the $[O_6//60_6]_T$-5 Laminate with Clamped Side Boundary Conditions

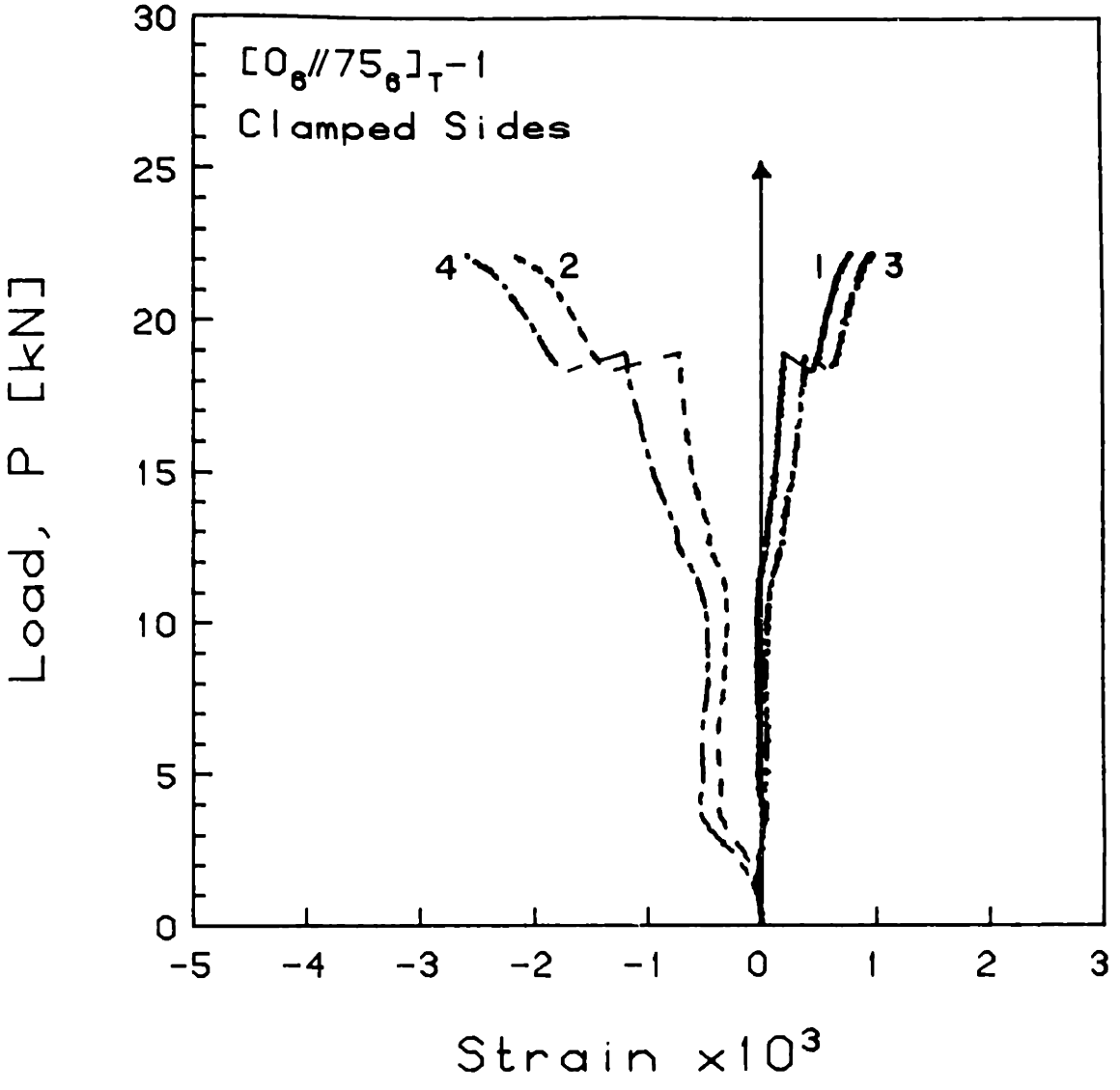

FIGURE F.44 Experimental Plot of Applied Compressive Load versus Longitudinal Strain for the $[0_6//75_6]_T$-1 Laminate with Clamped Side Boundary Conditions

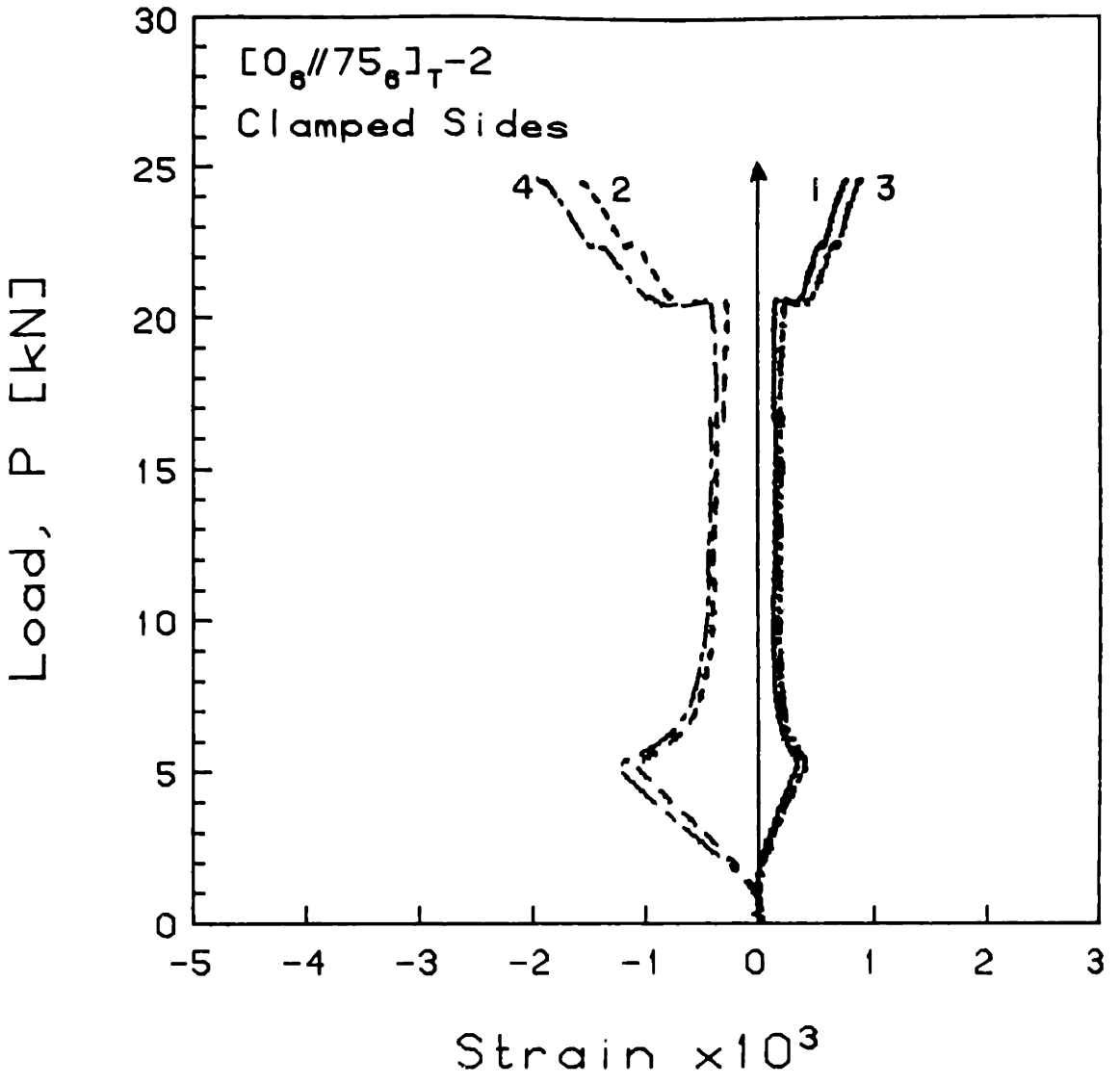

FIGURE F.45 Experimental Plot of Applied Compressive Load versus Longitudinal Strain for the $[0_6//75_6]_T$-2 Laminate with Clamped Side Boundary Conditions

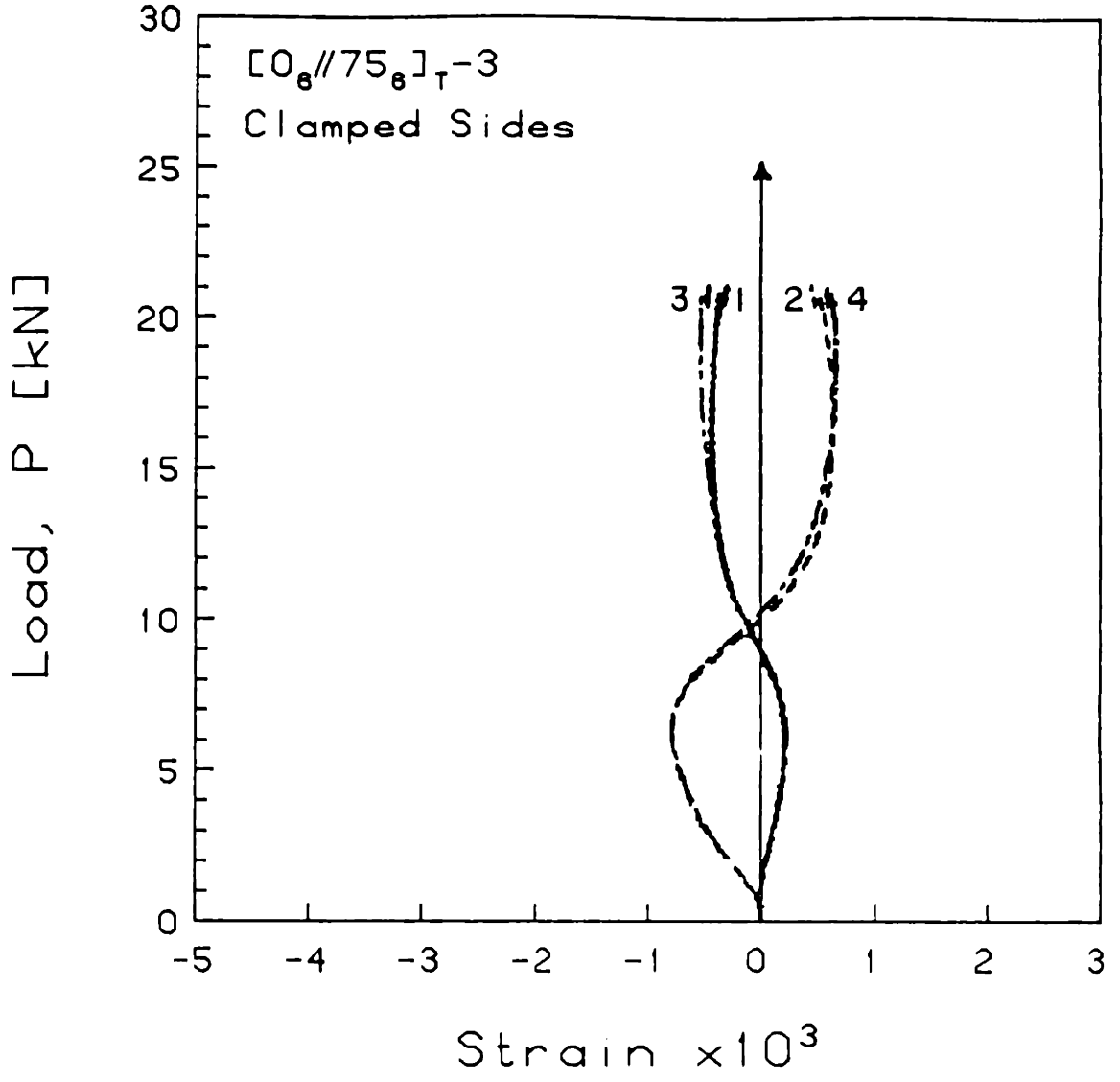

FIGURE F.46 Experimental Plot of Applied Compressive Load versus Longitudinal Strain for the $[0_6//75_6]_T$-3 Laminate with Clamped Side Boundary Conditions

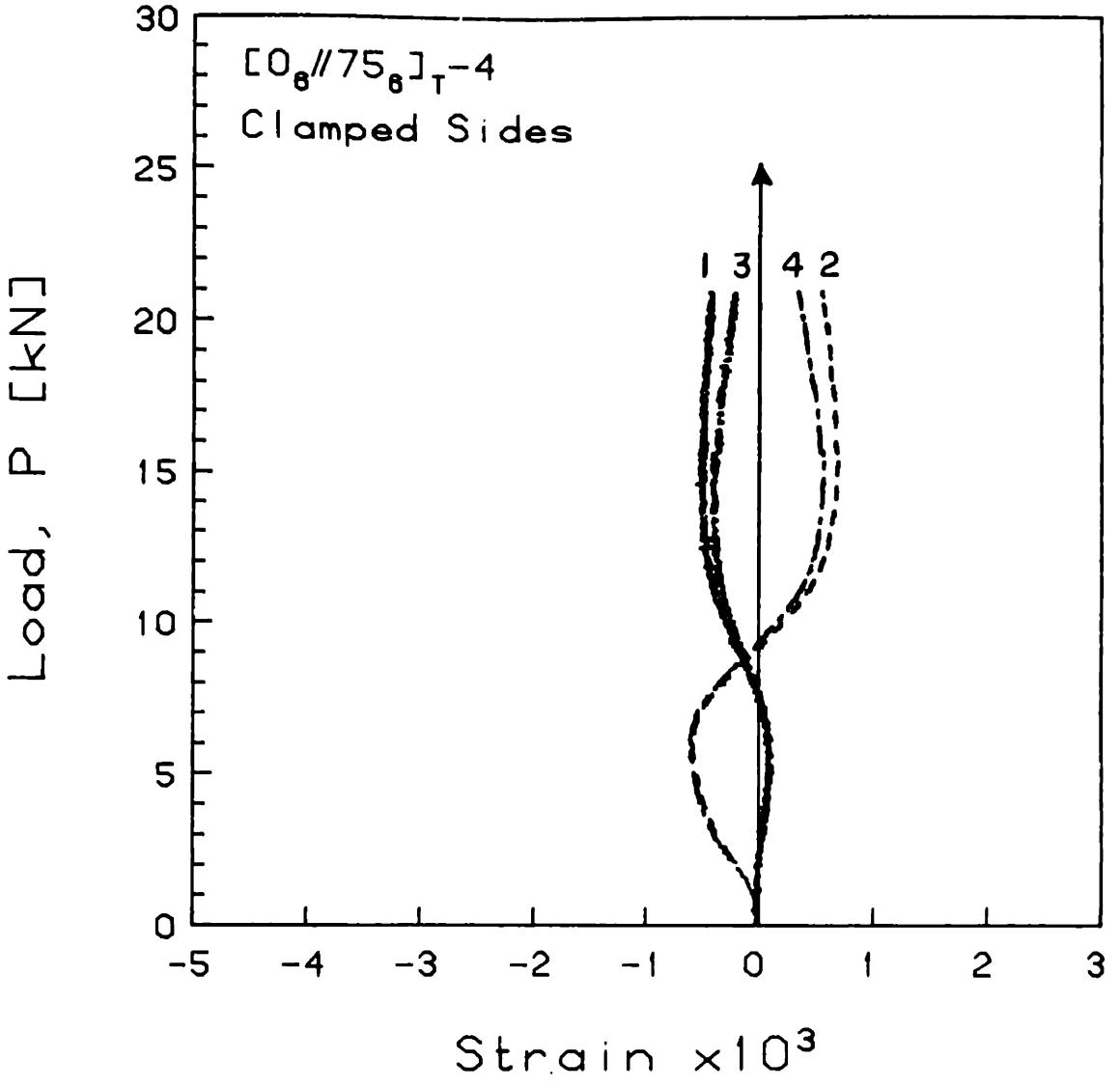

FIGURE F.47 Experimental Plot of Applied Compressive Load versus Longitudinal Strain for the $[0_6//75_6]_T$-4 Laminate with Clamped Side Boundary Conditions

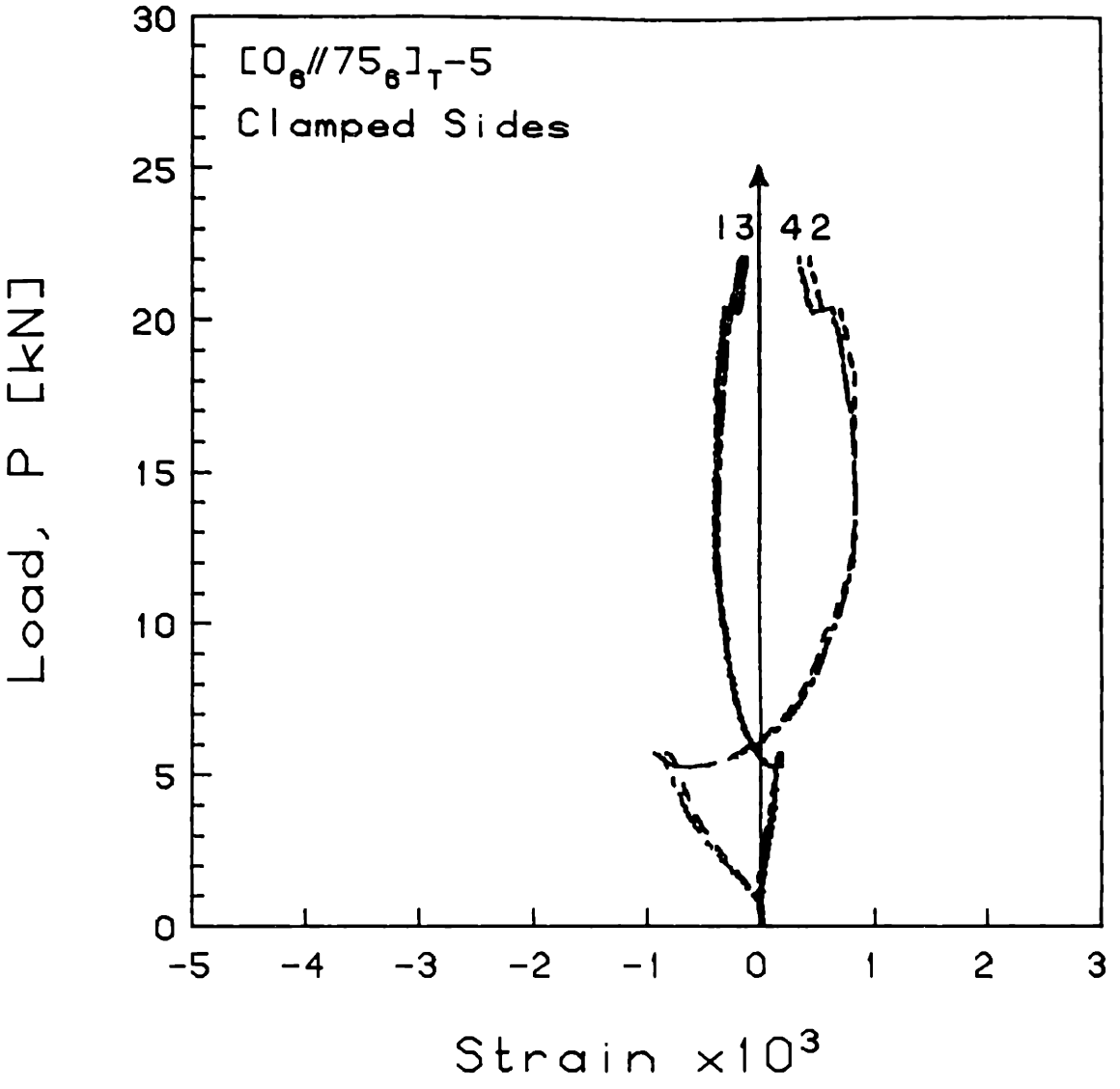

FIGURE F.48 Experimental Plot of Applied Compressive Load versus Longitudinal Strain for the $[0_6//75_6]_T$-5 Laminate with Clamped Side Boundary Conditions

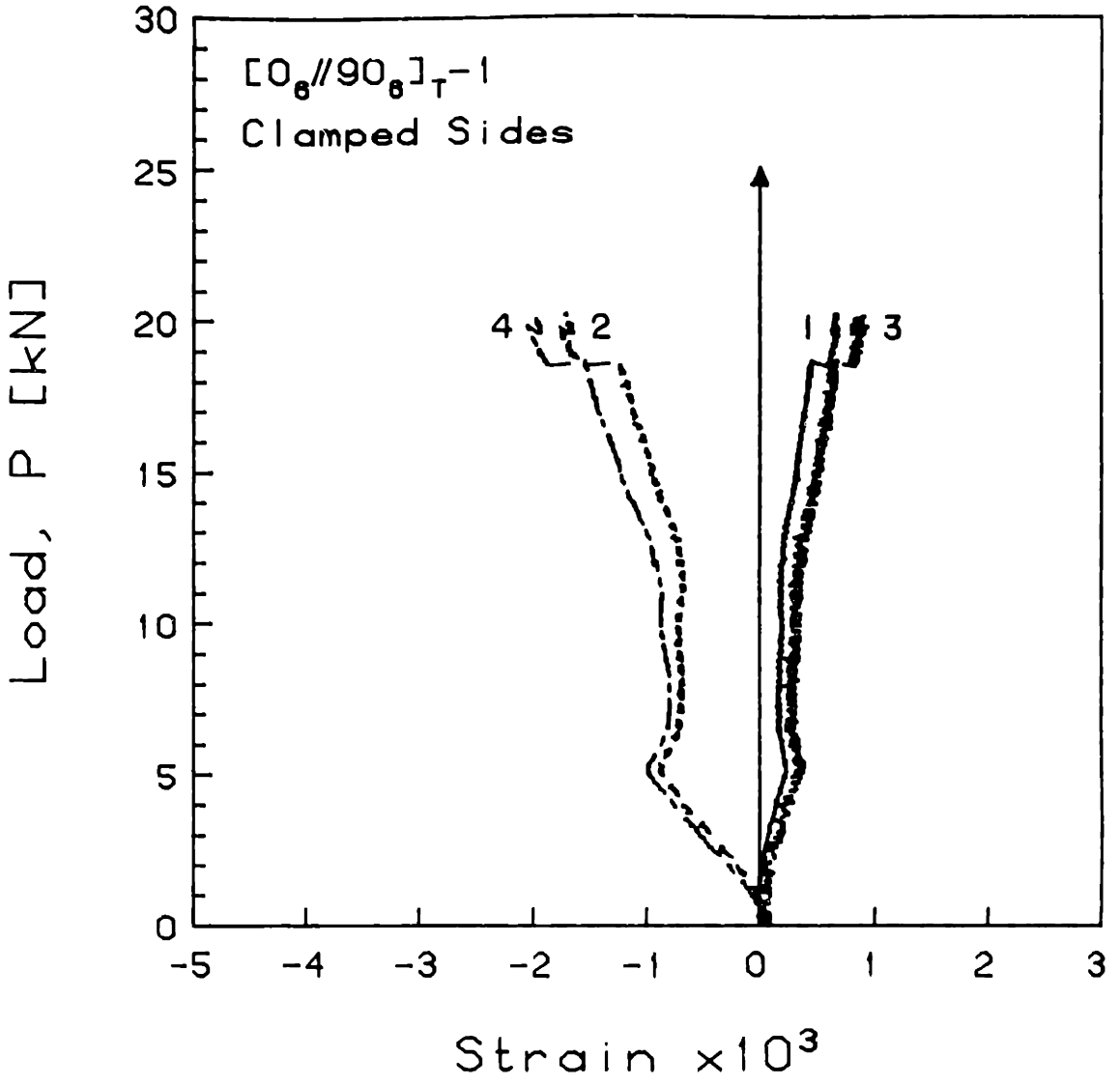

FIGURE F.49 Experimental Plot of Applied Compressive Load versus Longitudinal Strain for the $[0_6//90_6]_T$-1 Laminate with Clamped Side Boundary Conditions

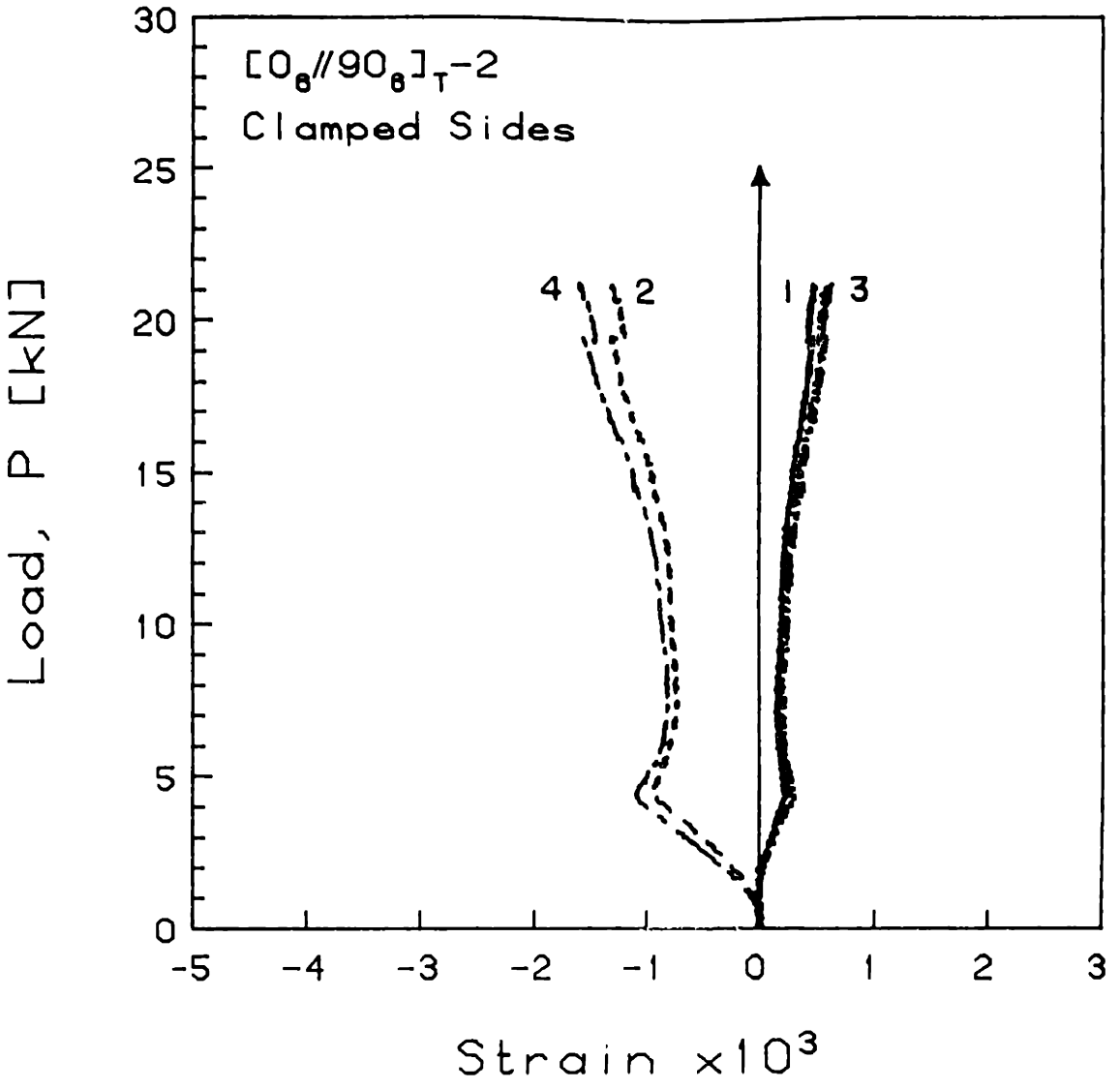

FIGURE F.50 Experimental Plot of Applied Compressive Load versus Longitudinal Strain for the $[0_6//90_6]_T$-2 Laminate with Clamped Side Boundary Conditions

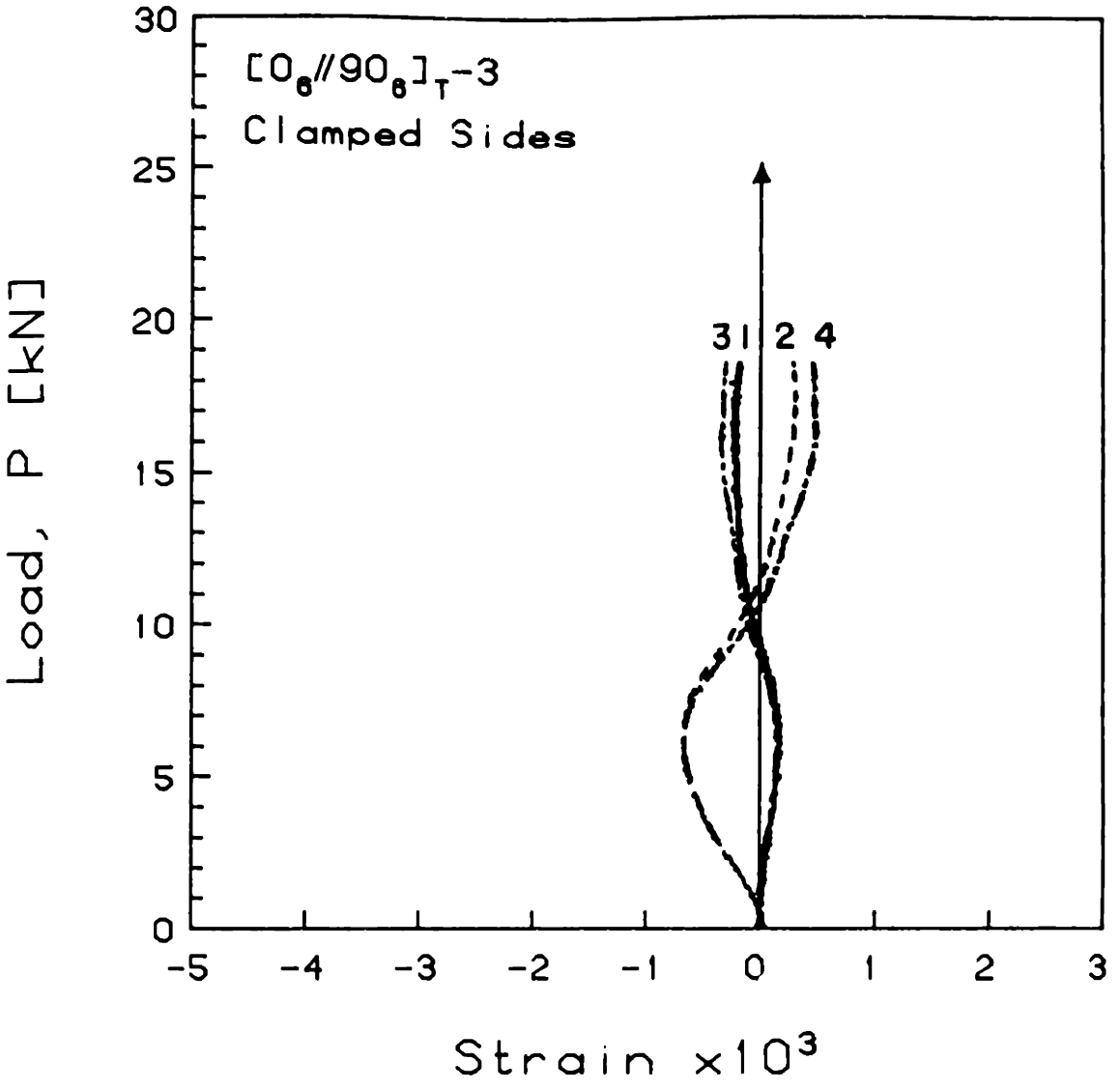

FIGURE F.51 Experimental Plot of Applied Compressive Load versus Longitudinal Strain for the $[O_6//90_6]_T$-3 Laminate with Clamped Side Boundary Conditions

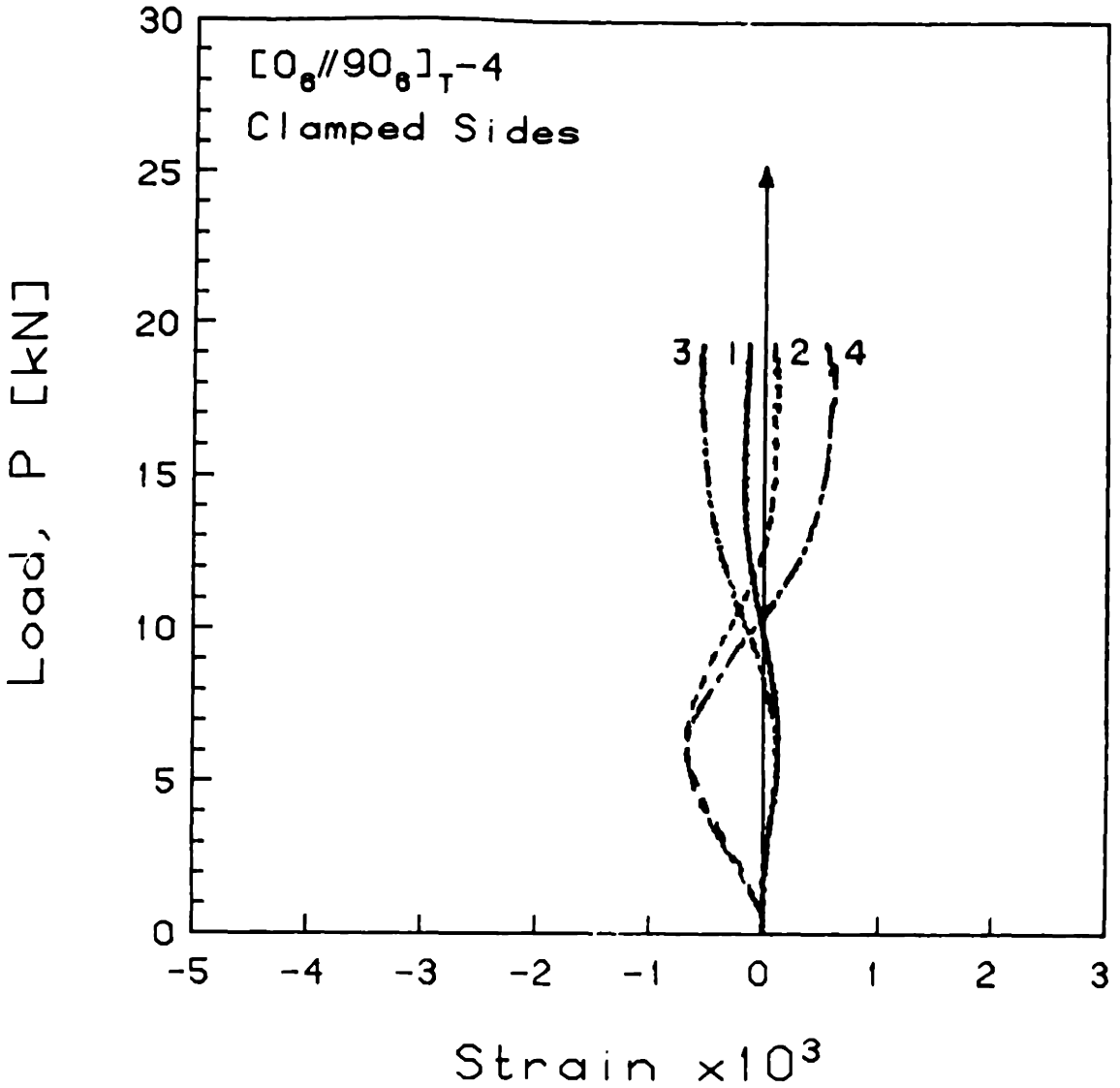

FIGURE F.52 Experimental Plot of Applied Compressive Load versus Longitudinal Strain for the $[0_6//90_6]_T$-4 Laminate with Clamped Side Boundary Conditions

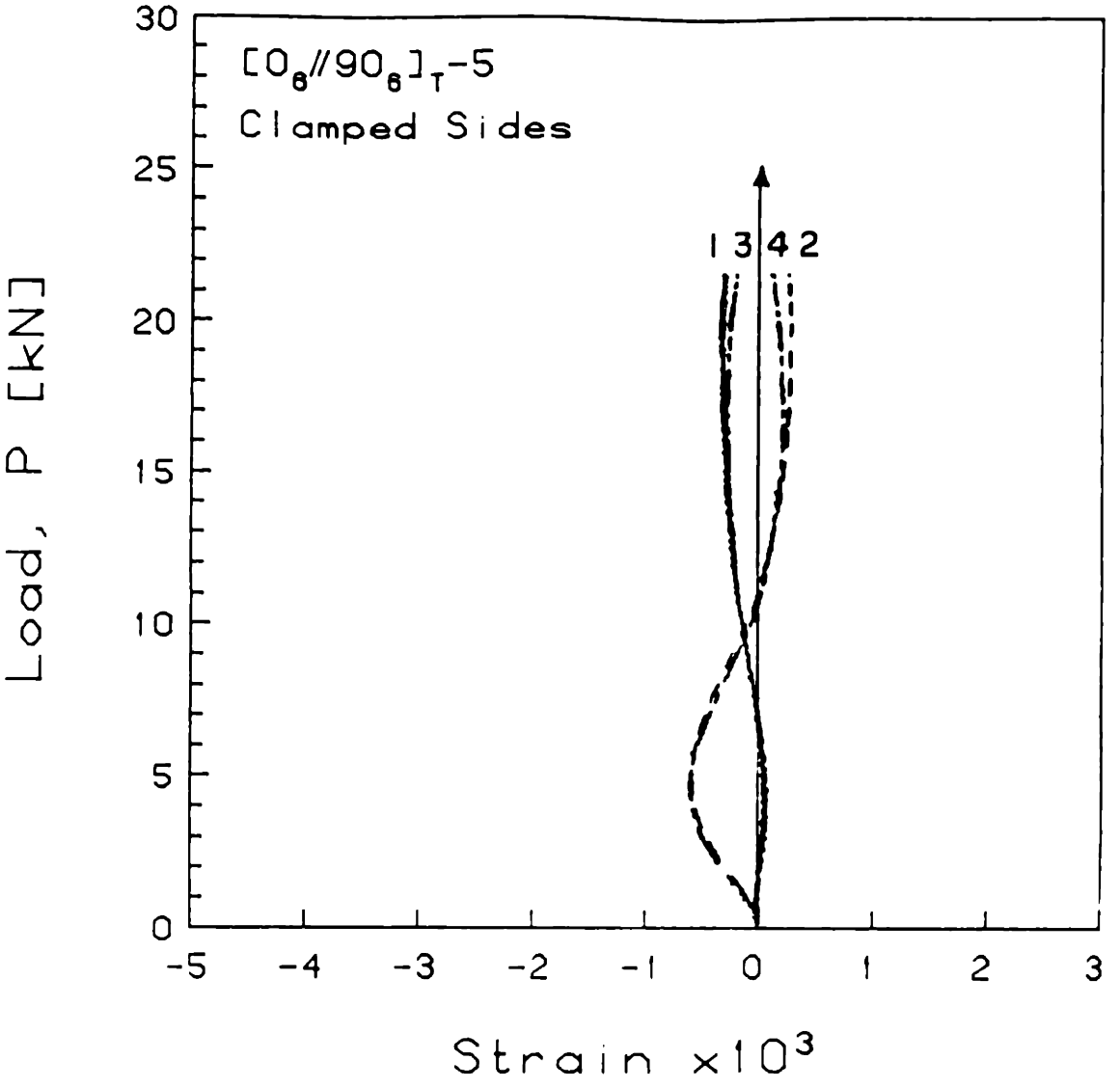

FIGURE F.53 Experimental Plot of Applied Compressive Load versus Longitudinal Strain for the $[0_6//90_6]_T$-5 Laminate with Clamped Side Boundary Conditions

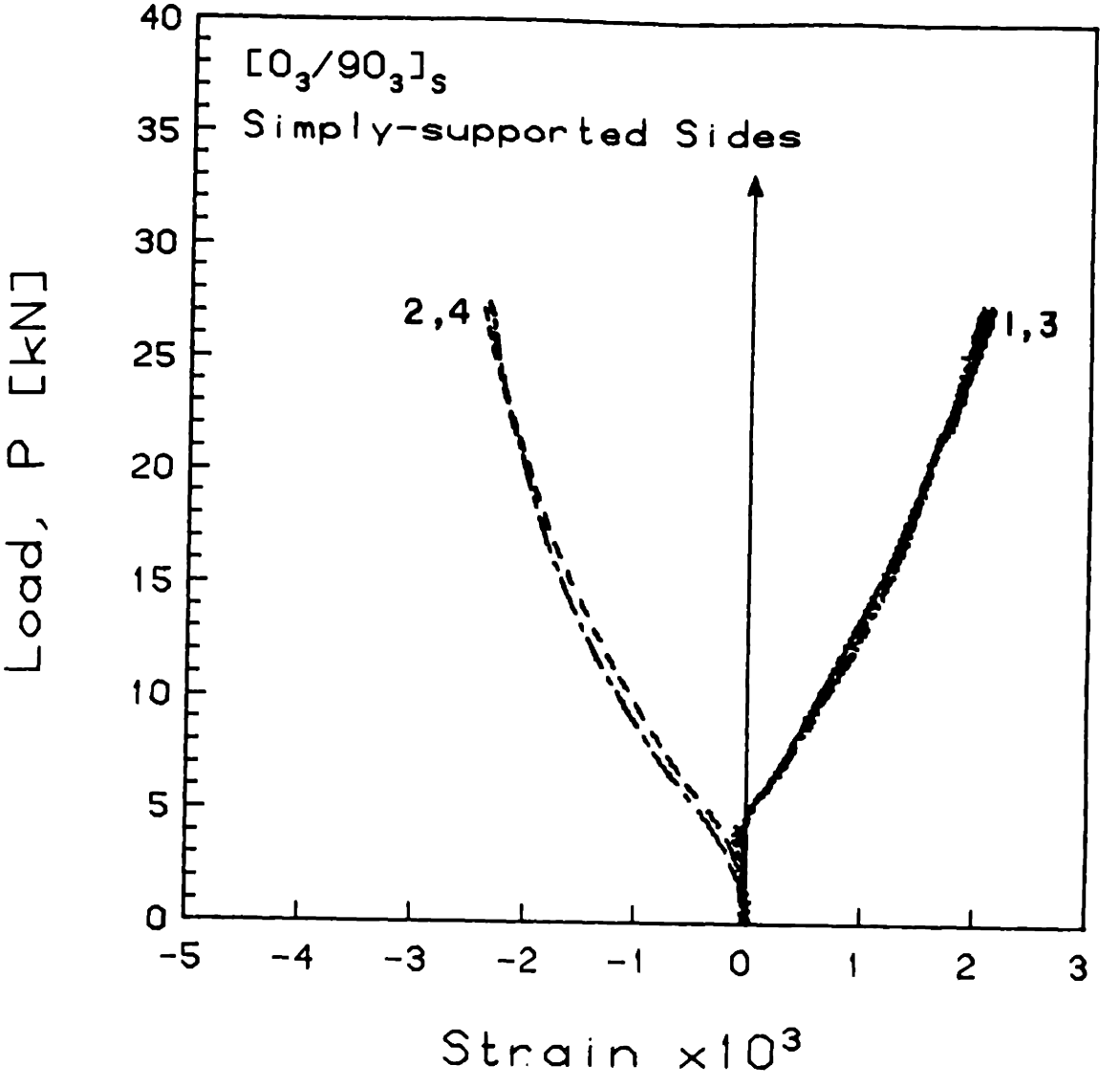

FIGURE F.54 Experimental Plot of Applied Compressive Load versus Longitudinal Strain for the $[0_3/90_3]_S$ Laminate with Simply-Supported Side Boundary Conditions

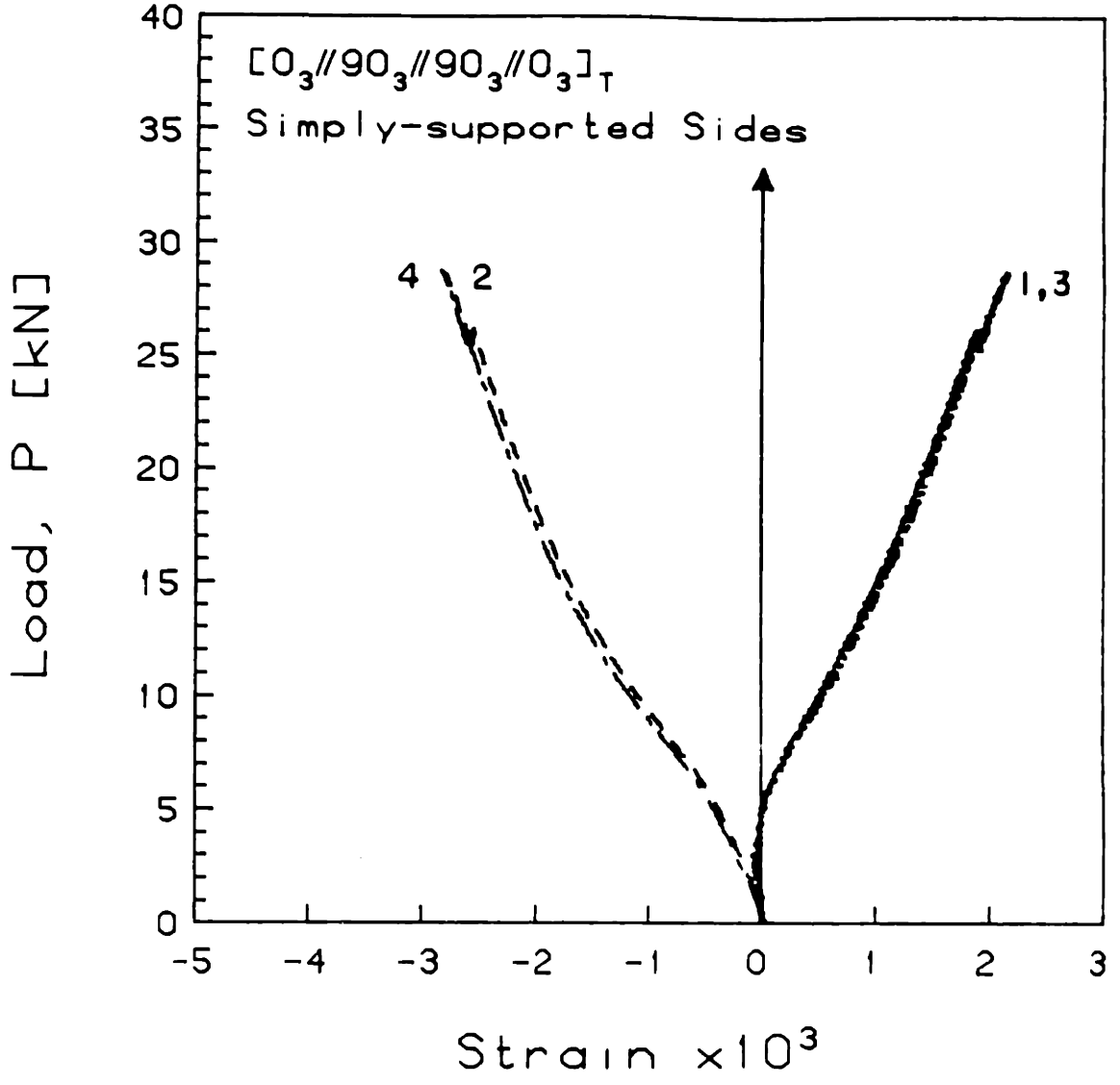

FIGURE F.55 Experimental Plot of Applied Compressive Load versus Longitudinal Strain for the $[0_3//90_3//90_3//0_3]_T$ Laminate with Simply-Supported Side Boundary Conditions

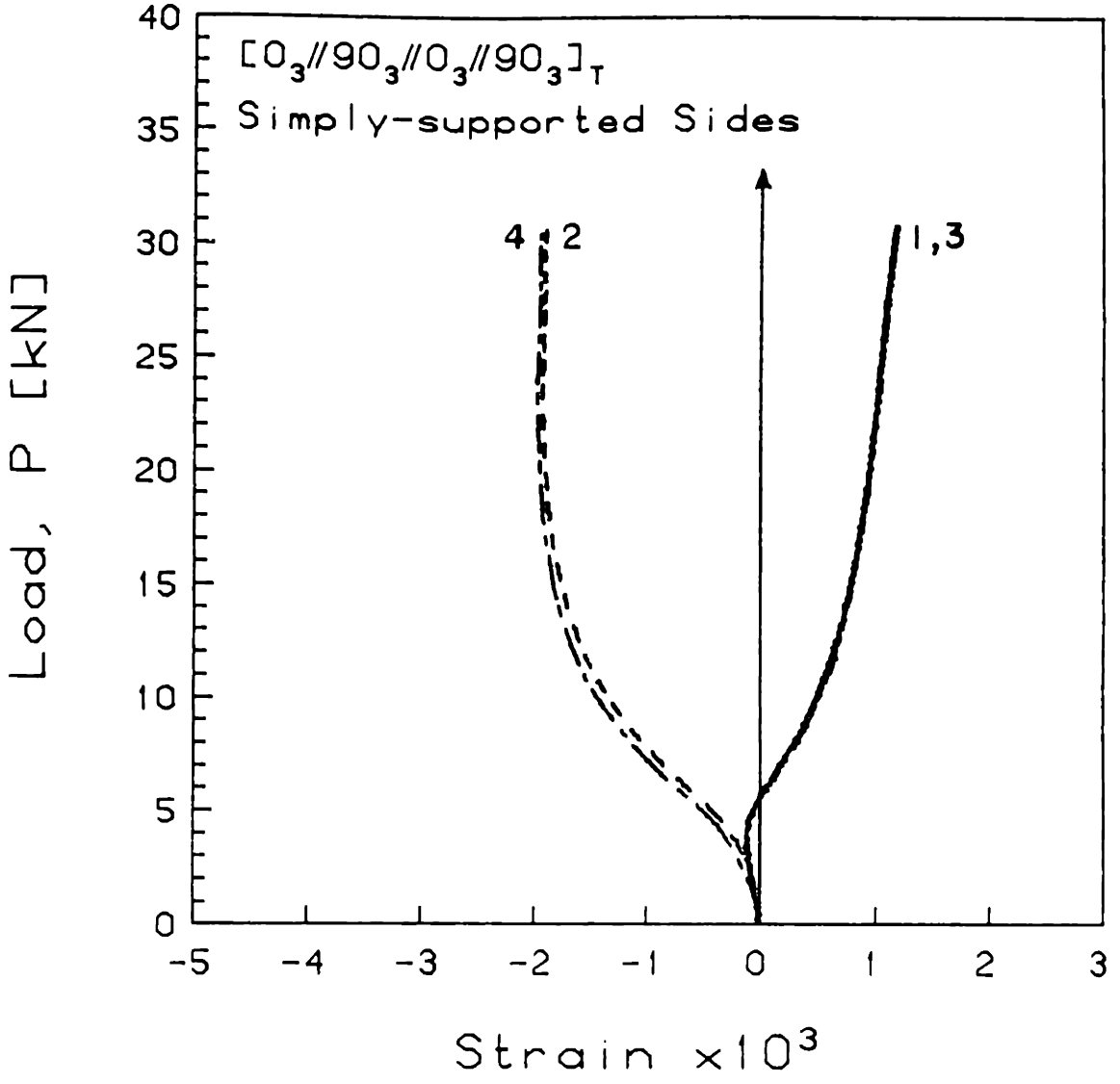

FIGURE F.56 Experimental Plot of Applied Compressive Load versus Longitudinal Strain for the $[0_3//90_3//0_3//90_3]_T$ Laminate with Simply-Supported Side Boundary Conditions

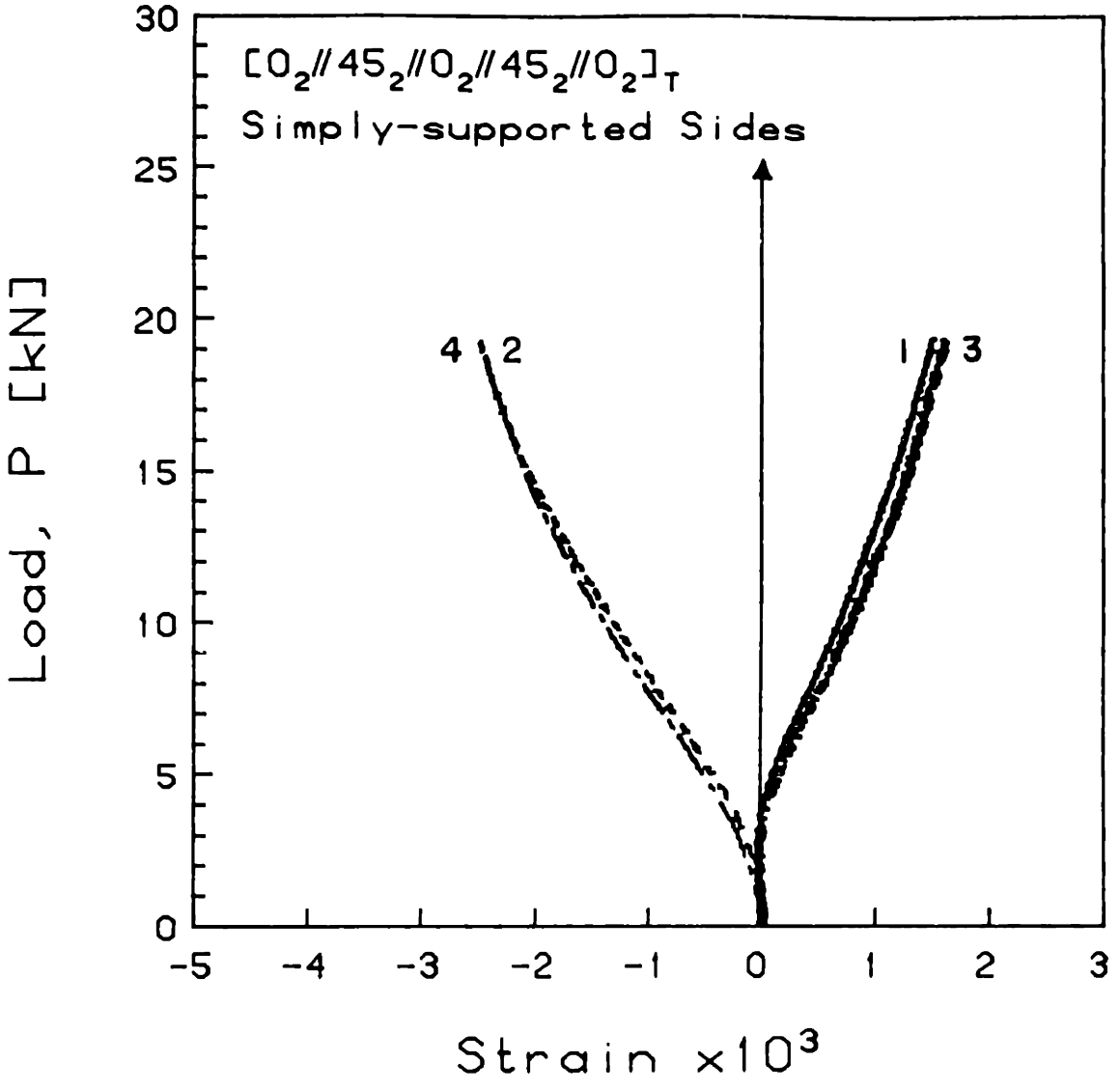

FIGURE F.57 Experimental Plot of Applied Compressive Load versus Longitudinal Strain for the $[0_2//45_2//0_2//45_2//0_2]_T$ Laminate with Simply-Supported Side Boundary Conditions

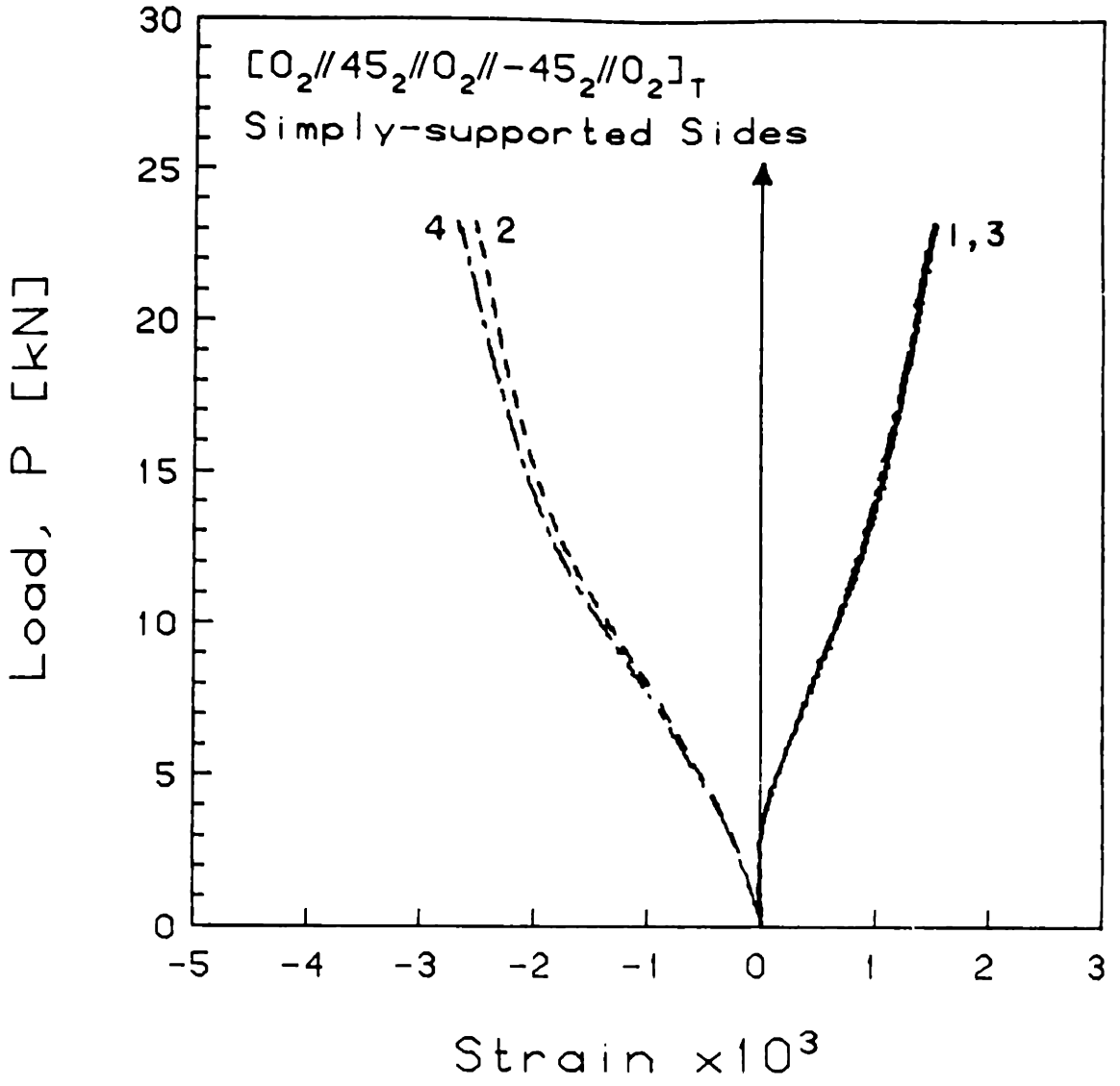

FIGURE F.58 Experimental Plot of Applied Compressive Load versus Longitudinal Strain for the $[O_2//45_2//O_2//-45_2//O_2]_T$ Laminate with Simply-Supported Side Boundary Conditions

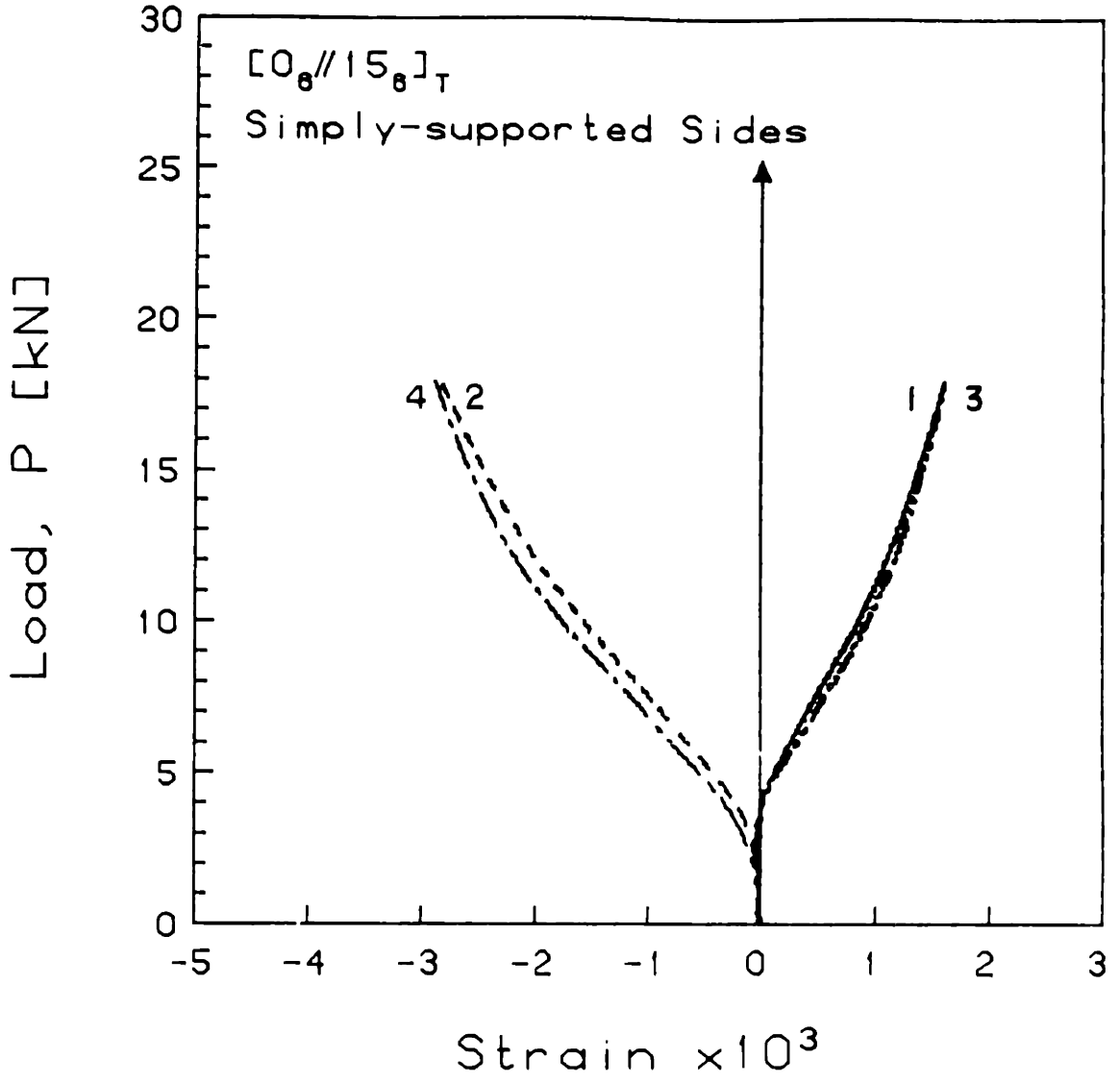

FIGURE F.59 Experimental Plot of Applied Compressive Load versus Longitudinal Strain for the $[0_6//15_6]_T$ Laminate with Simply-Supported Side Boundary Conditions

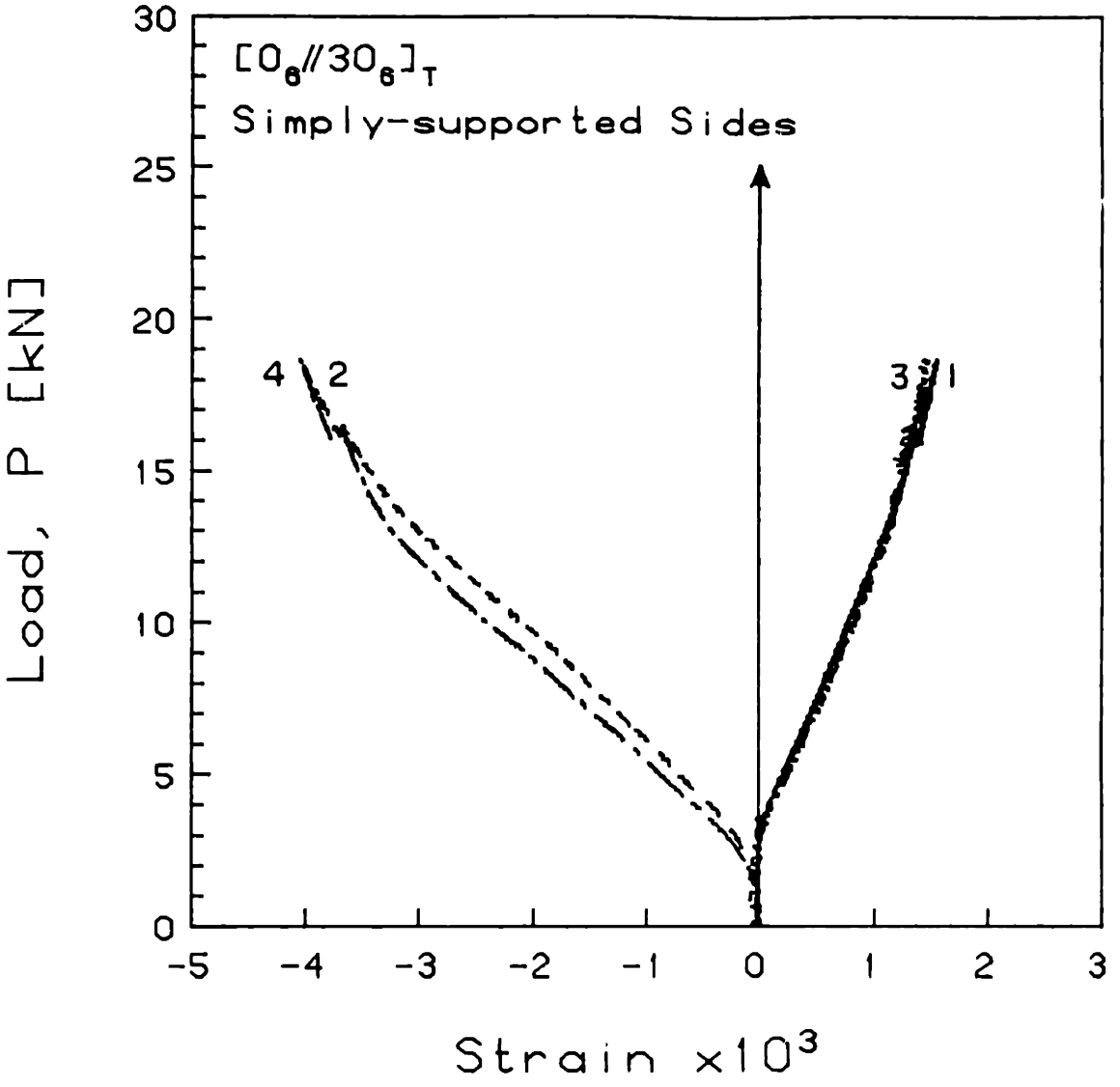

FIGURE F.60 Experimental Plot of Applied Compressive Load versus Longitudinal Strain for the $[0_6//30_6]_T$ Laminate with Simply-Supported Side Boundary Conditions

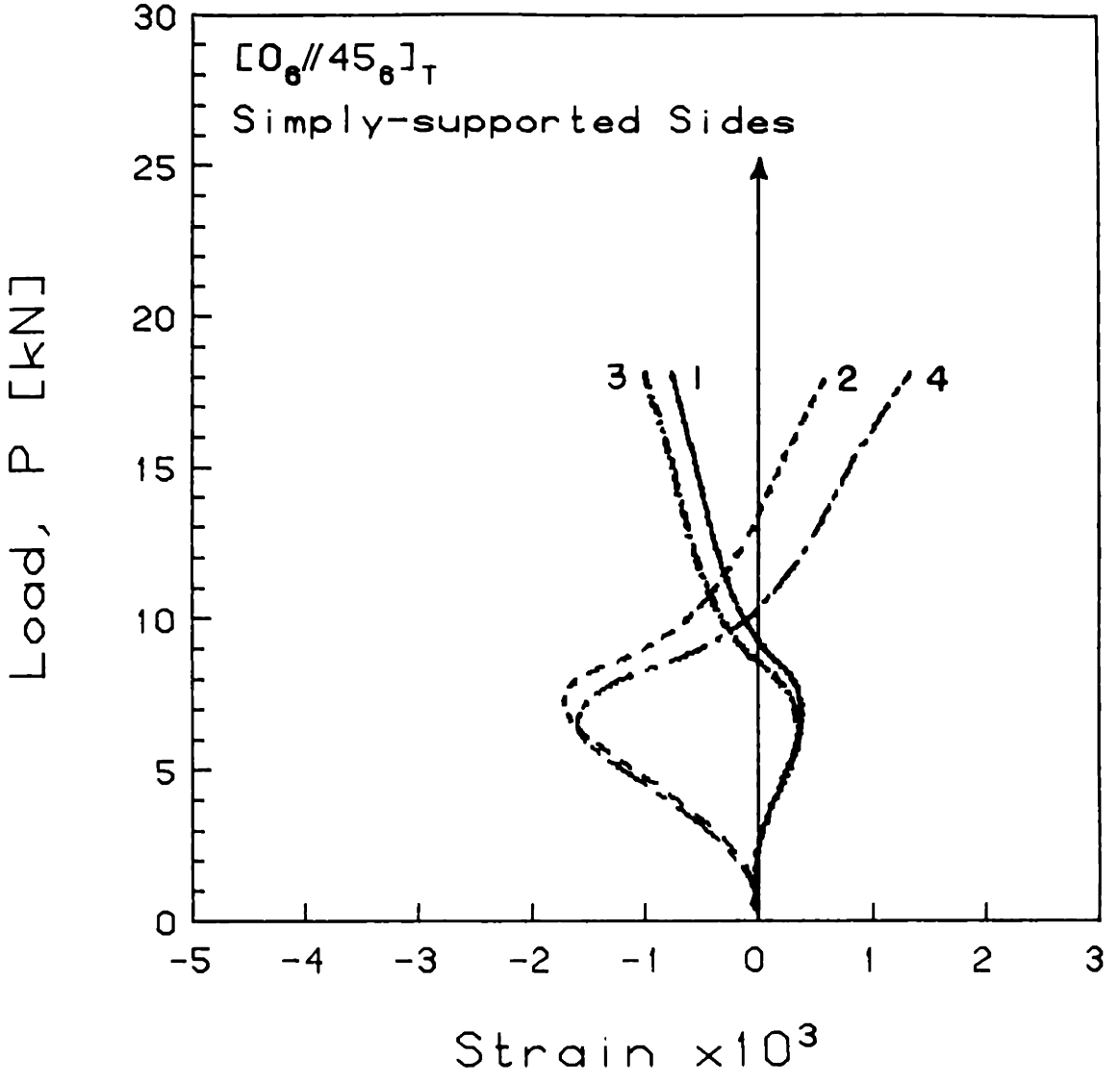

FIGURE F.61 Experimental Plot of Applied Compressive Load versus Longitudinal Strain for the $[0_6//45_6]_T$ Laminate with Simply-Supported Side Boundary Conditions

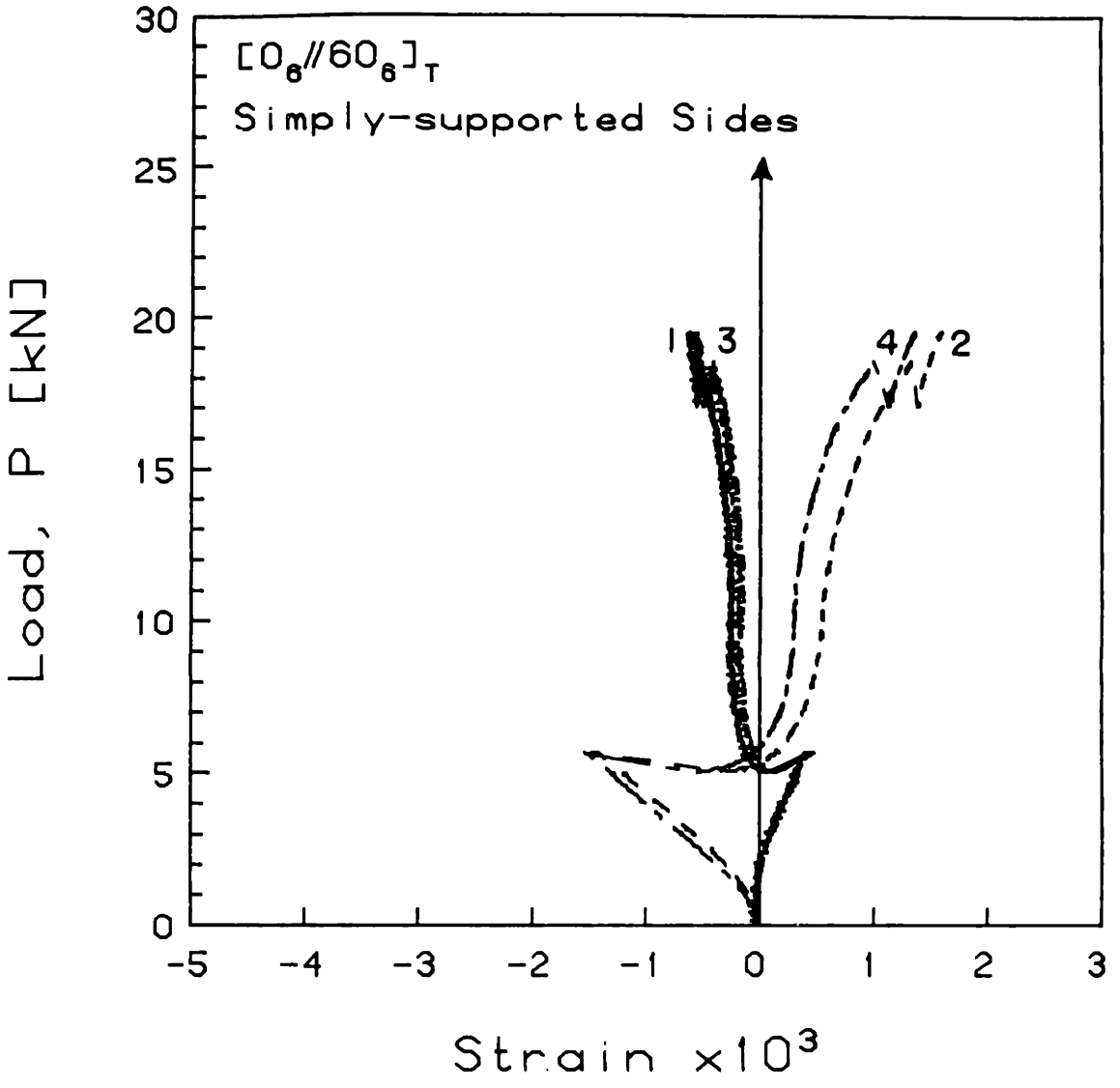

FIGURE F.62 Experimental Plot of Applied Compressive Load versus Longitudinal Strain for the $[0_6//60_6]_T$ Laminate with Simply-Supported Side Boundary Conditions

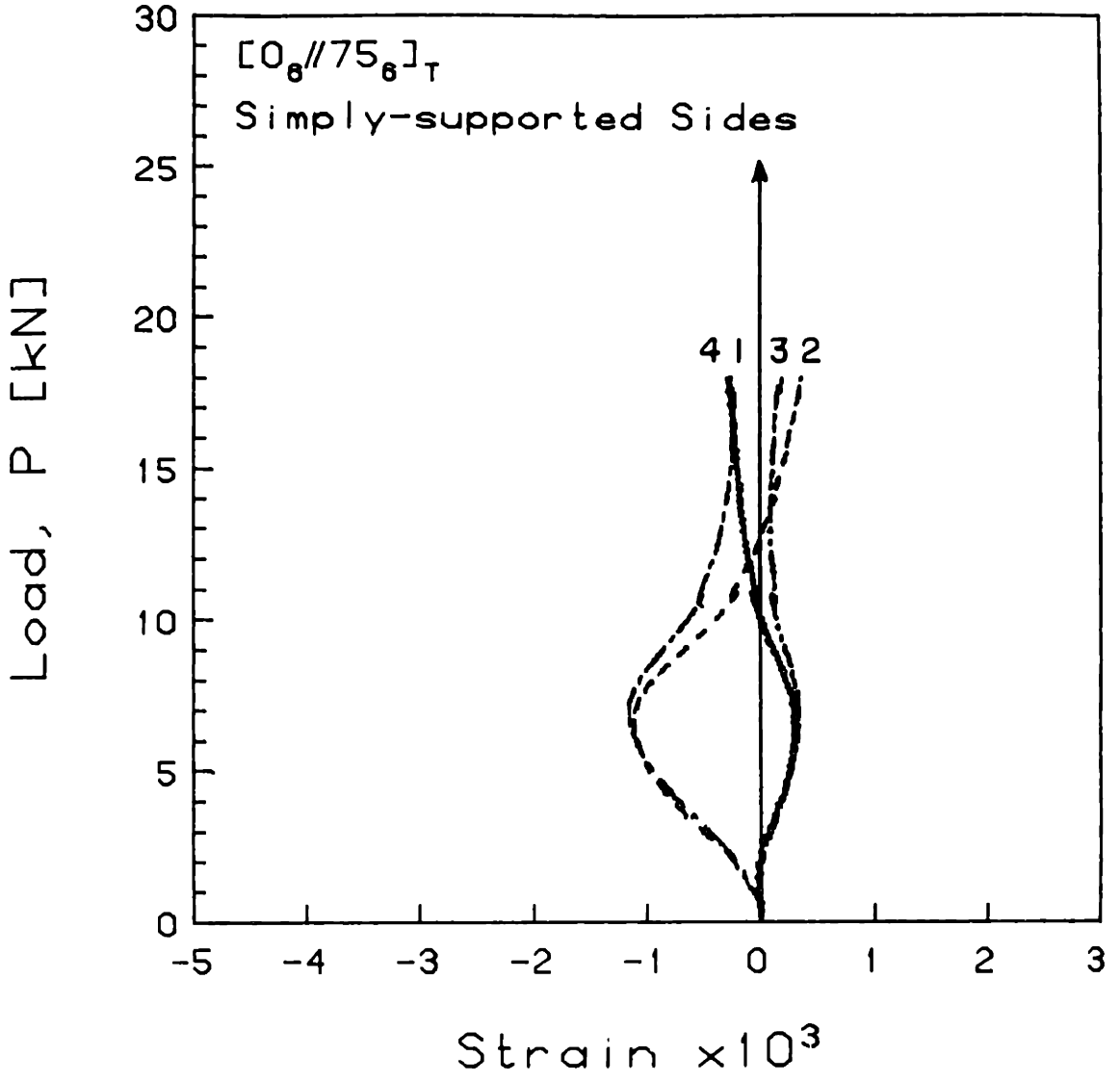

FIGURE F.63 Experimental Plot of Applied Compressive Load versus Longitudinal Strain for the $[0_6//75_6]_T$ Laminate with Simply-Supported Side Boundary Conditions

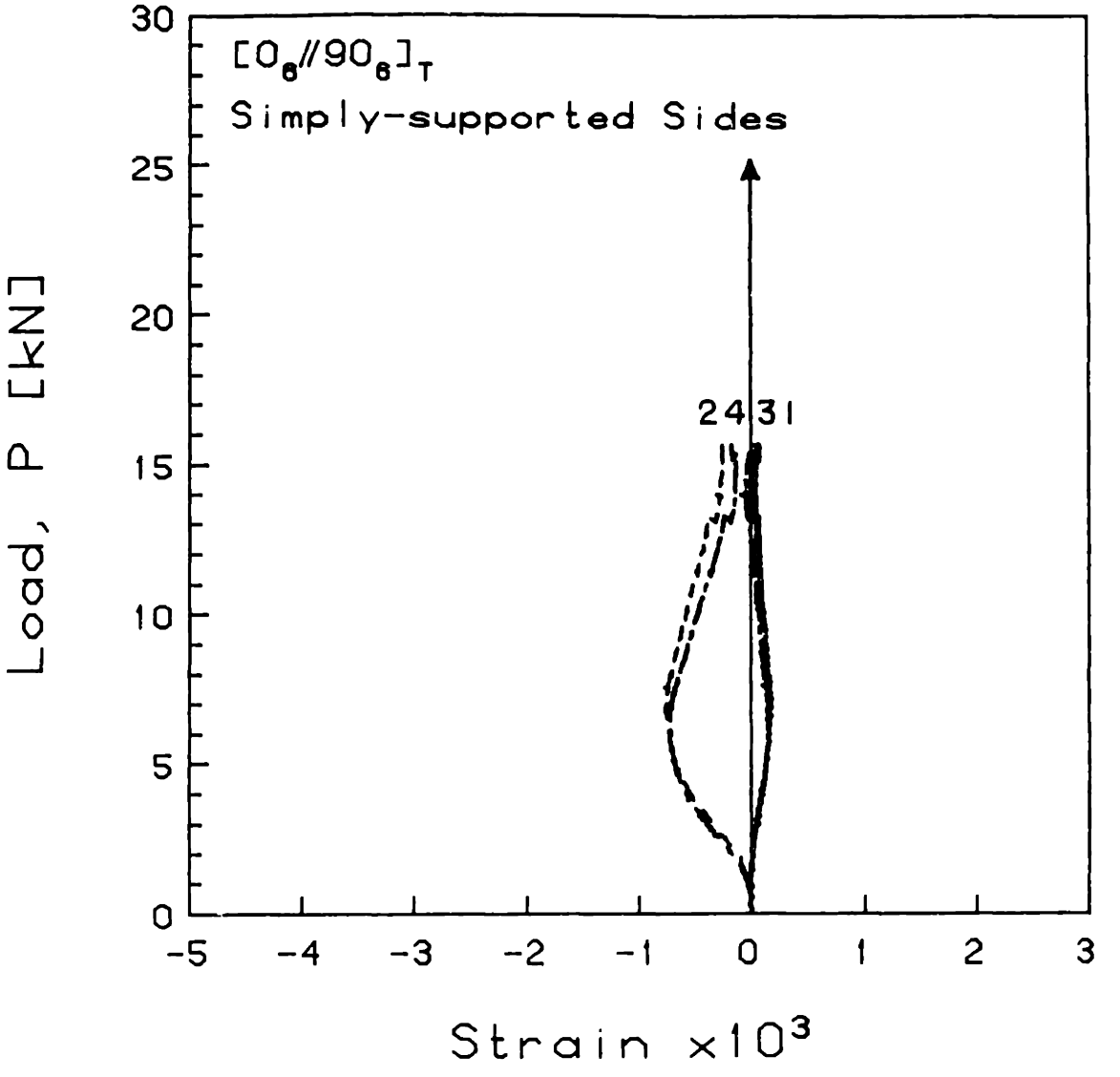

FIGURE F.64 Experimental Plot of Applied Compressive Load versus Longitudinal Strain for the $[0_6//90_6]_T$ Laminate with Simply-Supported Side Boundary Conditions

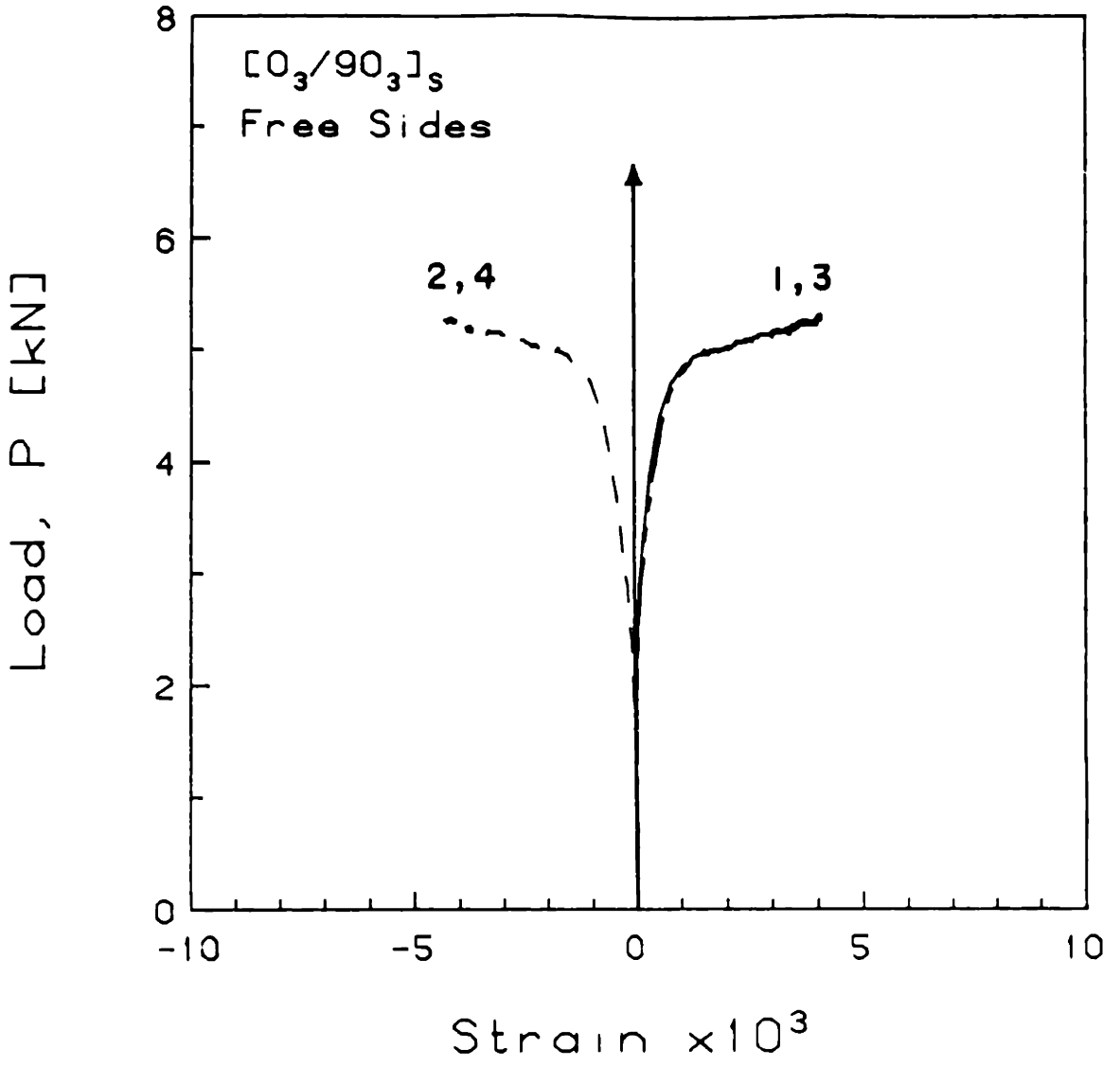

FIGURE F.65 Experimental Plot of Applied Compressive Load versus Longitudinal Strain for the $[0_3/90_3]_S$ Laminate with Free Side Boundary Conditions

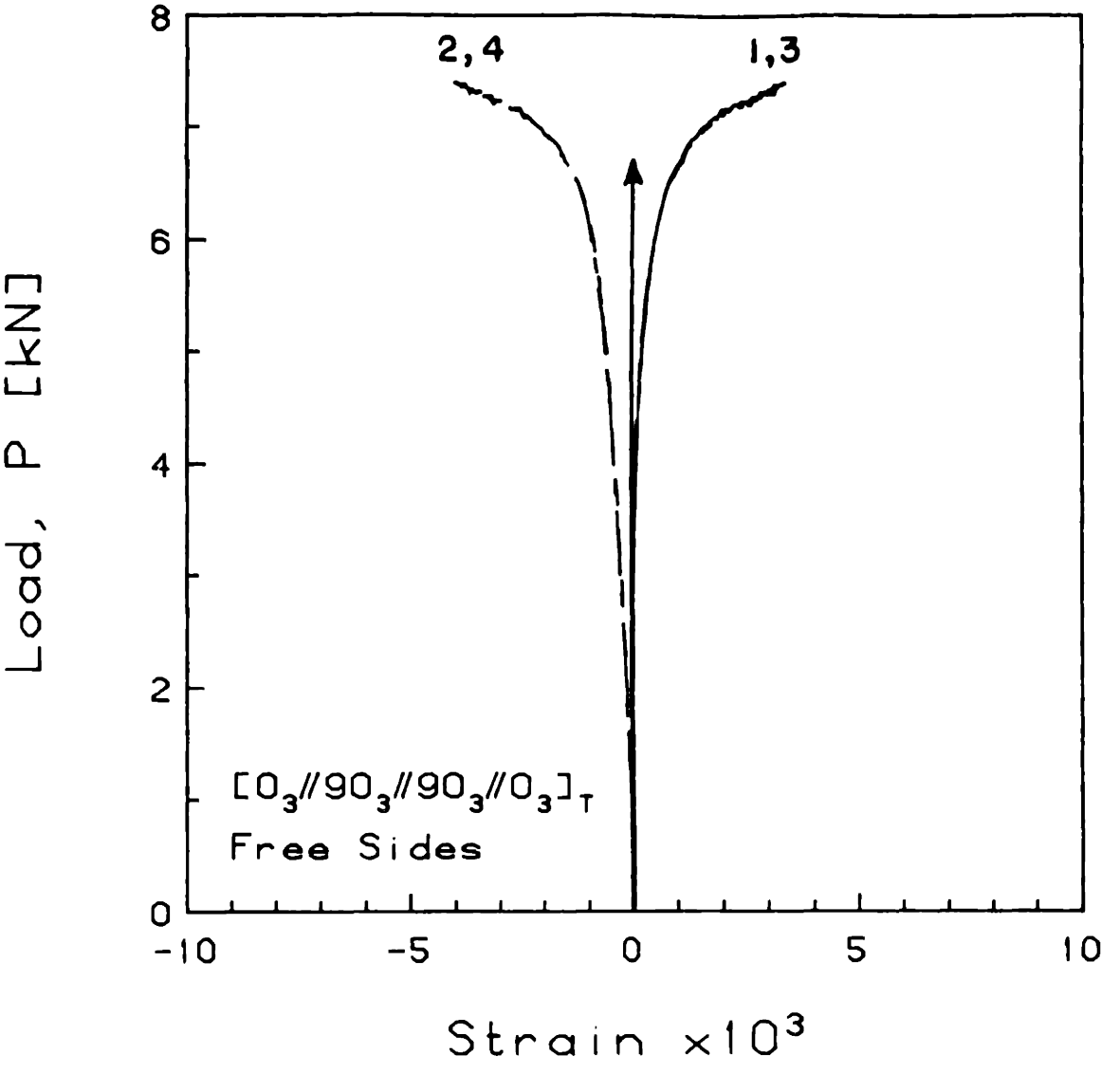

FIGURE F.66 Experimental Plot of Applied Compressive Load versus Longitudinal Strain for the $[0_3//90_3//90_3//0_3]_T$ Laminate with Free Side Boundary Conditions

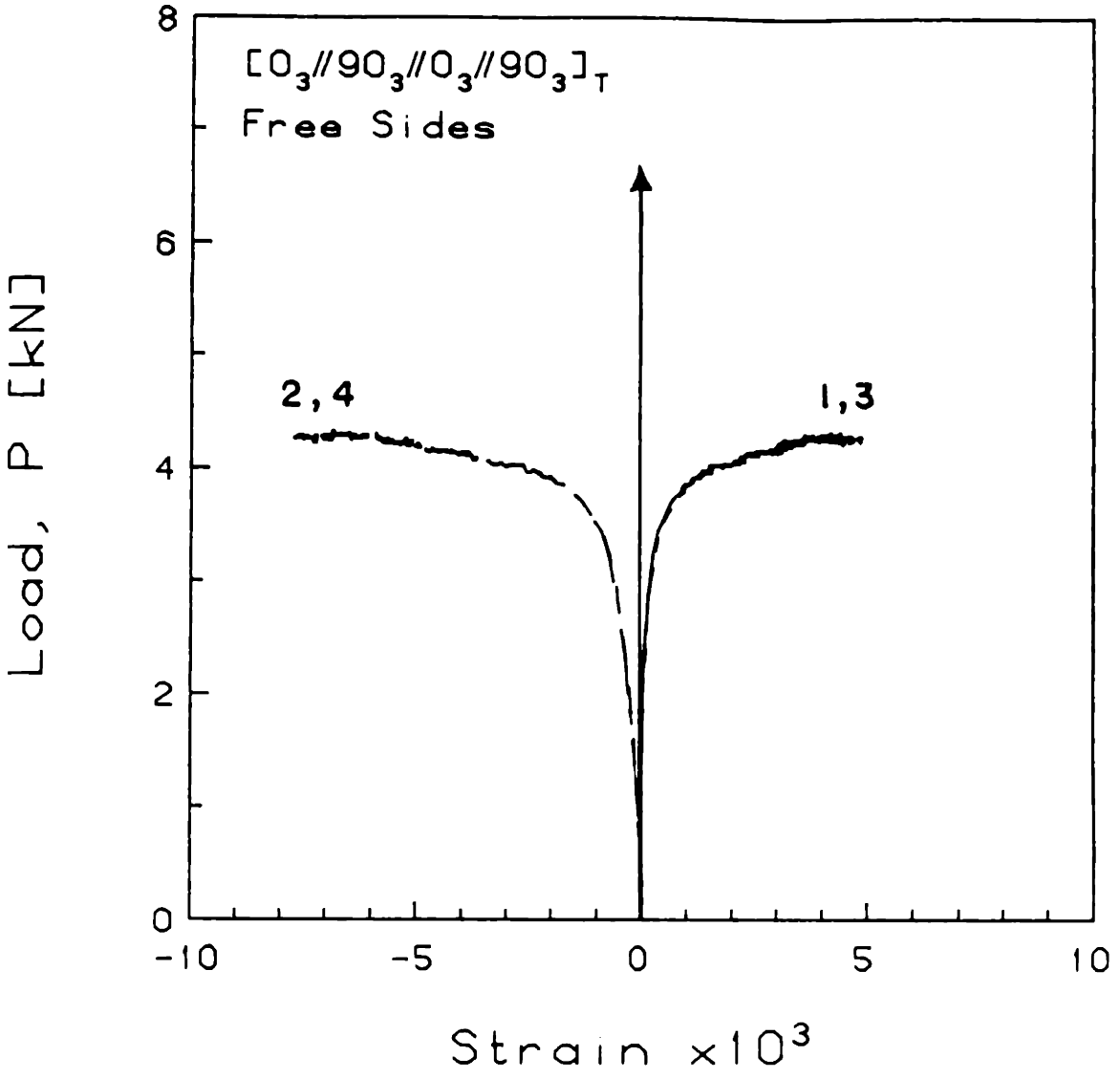

FIGURE F.67 Experimental Plot of Applied Compressive Load versus Longitudinal Strain for the $[0_3//90_3//0_3//90_3]_T$ Laminate with Free Side Boundary Conditions

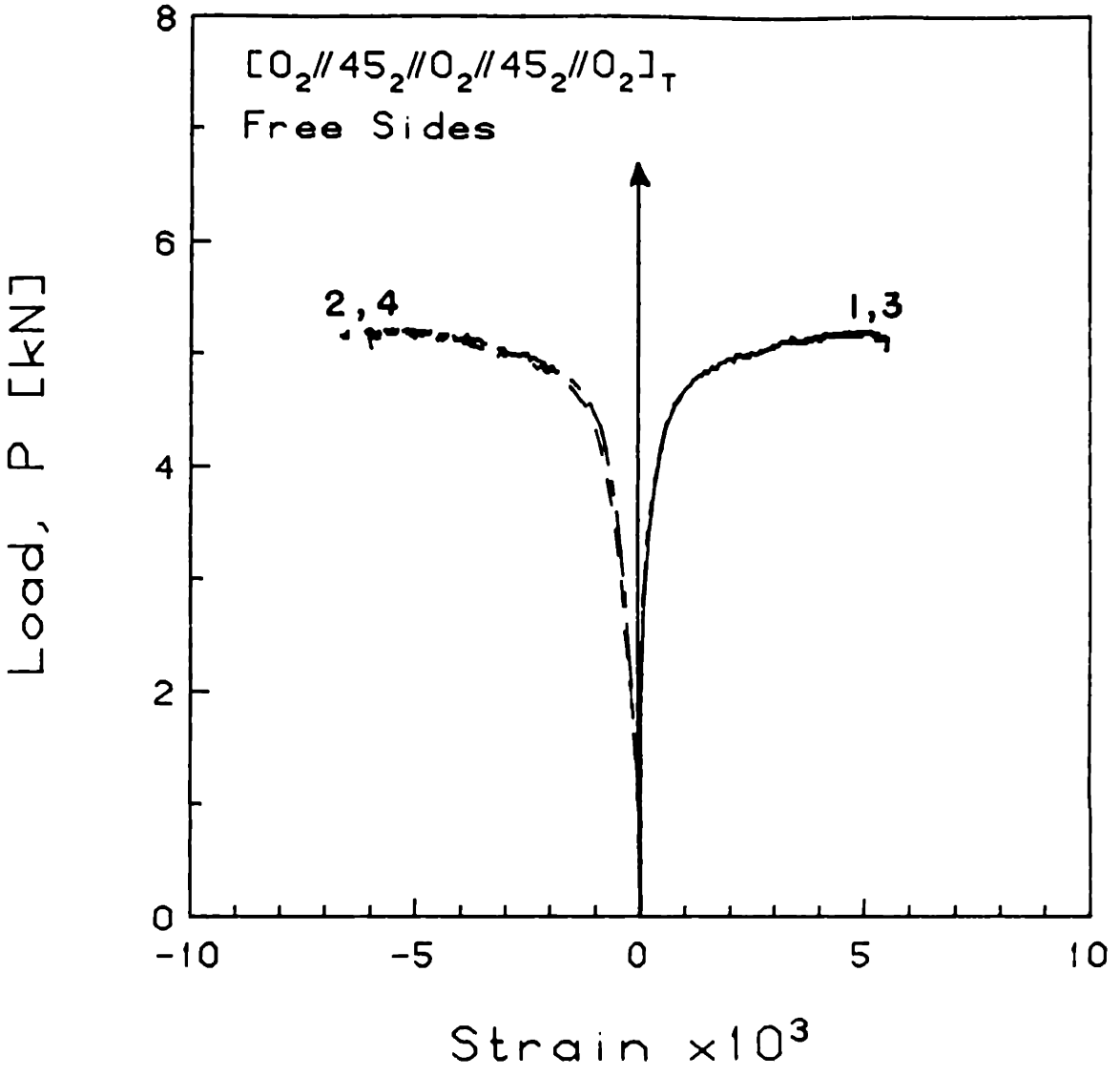

FIGURE F.68 Experimental Plot of Applied Compressive Load versus Longitudinal Strain for the $[O_2//45_2//O_2//45_2//O_2]_T$ Laminate with Free Side Boundary Conditions

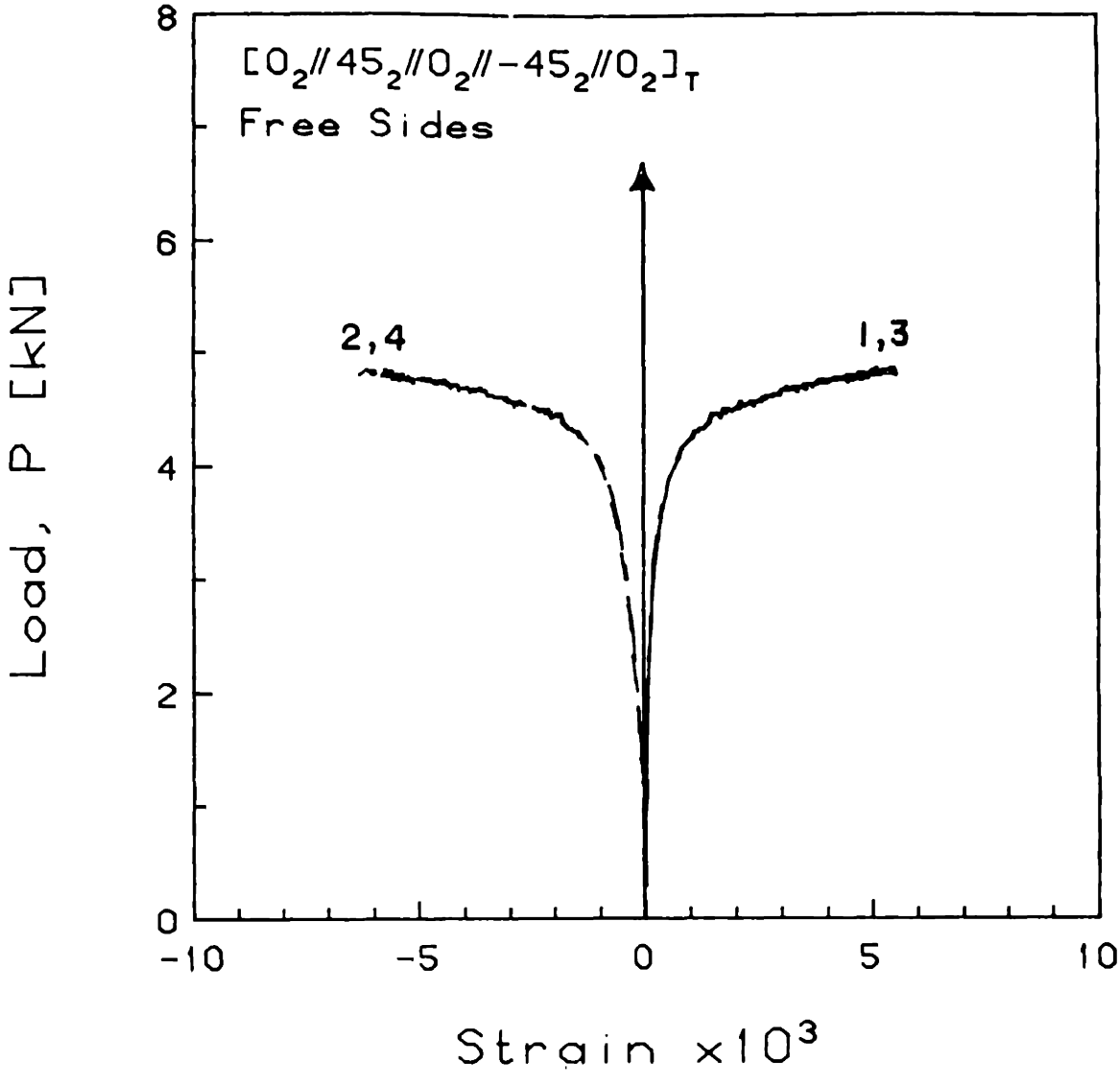

FIGURE F.69 Experimental Plot of Applied Compressive Load versus Longitudinal Strain for the $[0_2//45_2//0_2//-45_2//0_2]_T$ Laminate with Free Side Boundary Conditions

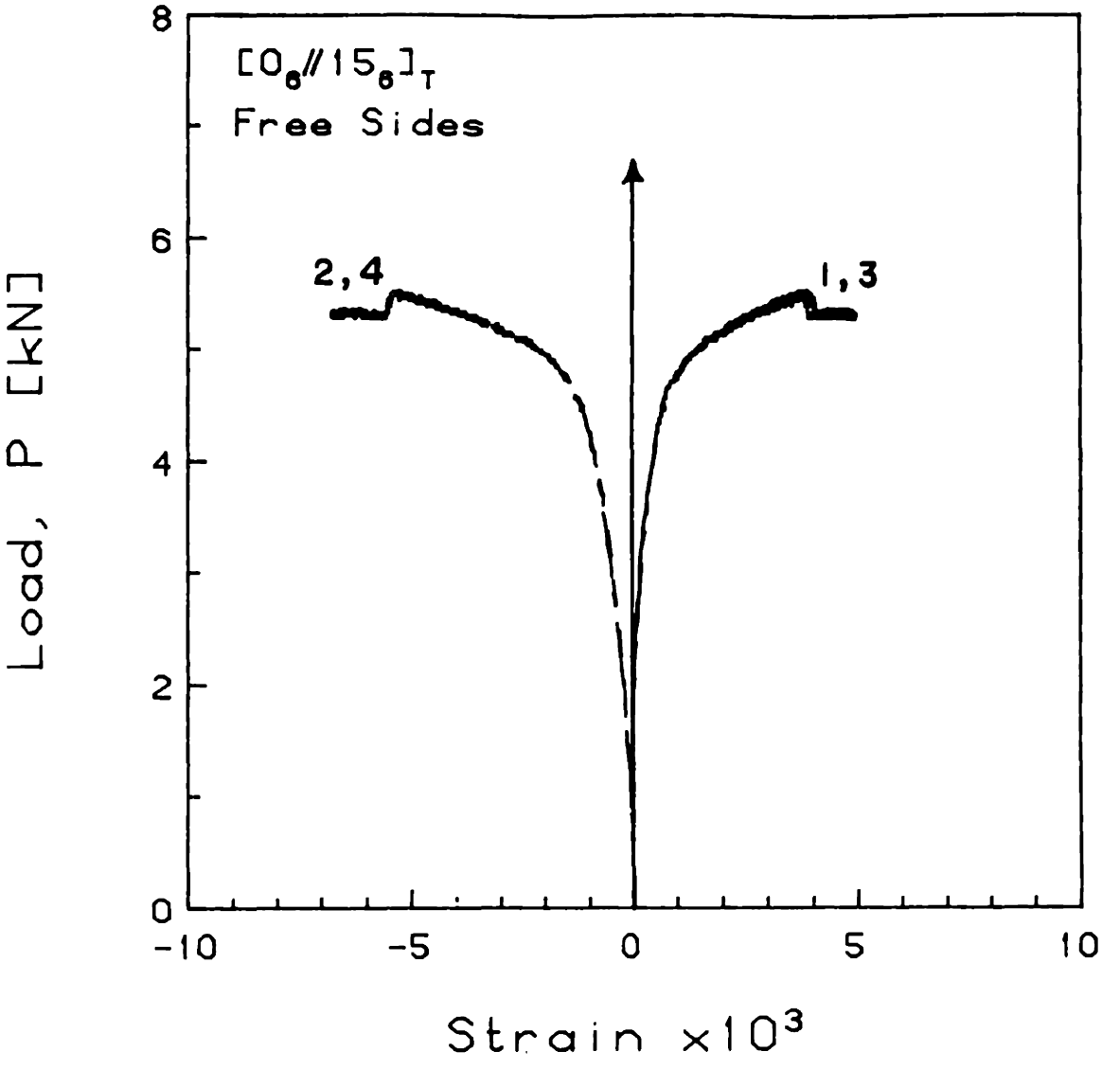

FIGURE F.70 Experimental Plot of Applied Compressive Load versus Longitudinal Strain for the $[0_6//15_6]_T$ Laminate with Free Side Boundary Conditions

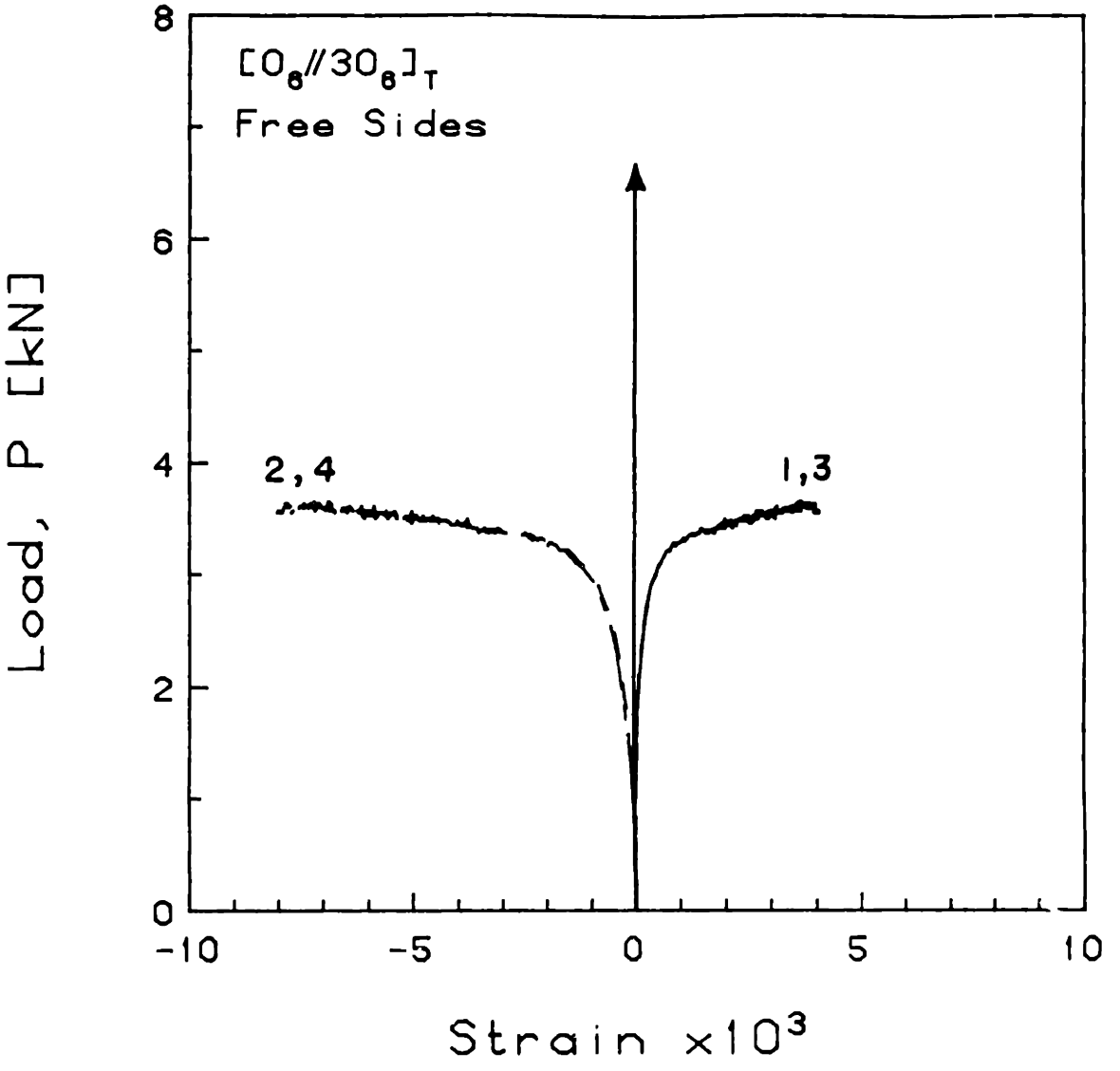

FIGURE F.71 Experimental Plot of Applied Compressive Load versus Longitudinal Strain for the $[0_6//30_6]_T$ Laminate with Free Side Boundary Conditions

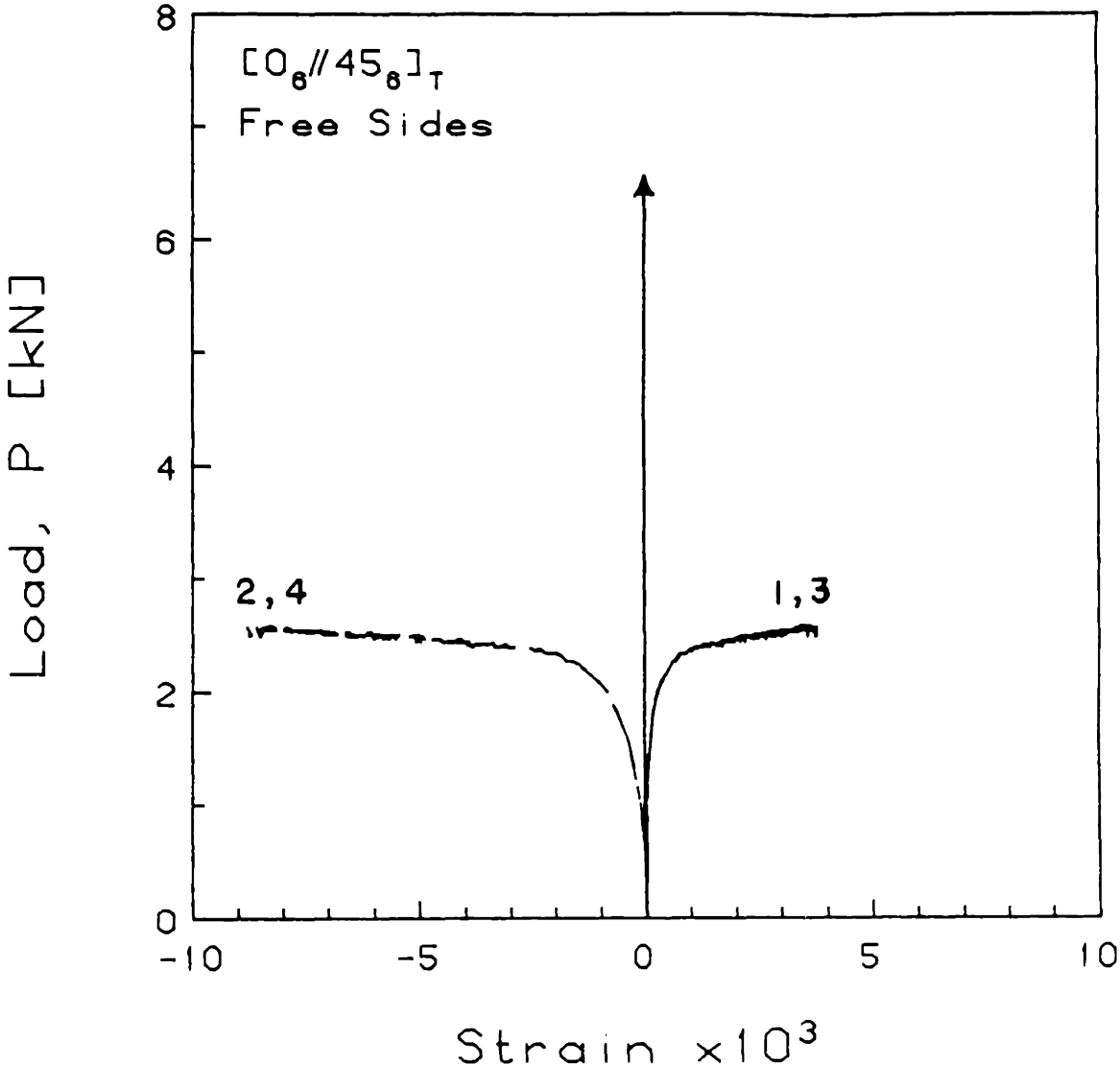

FIGURE F.72 Experimental Plot of Applied Compressive Load versus Longitudinal Strain for the $[0_6//45_6]_T$ Laminate with Free Side Boundary Conditions

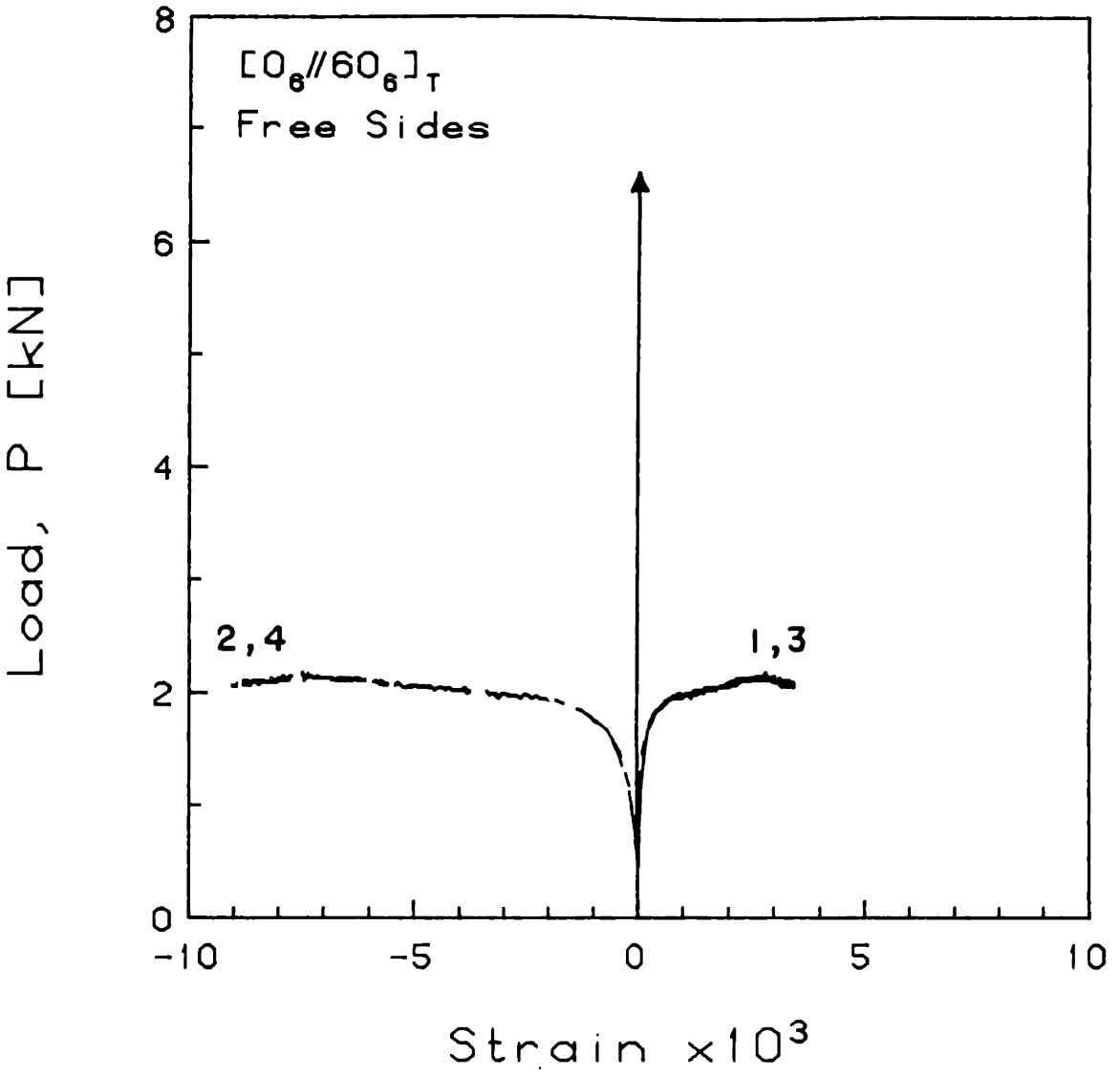

FIGURE F.73 Experimental Plot of Applied Compressive Load versus Longitudinal Strain for the $[0_6//60_6]_T$ Laminate with Free Side Boundary Conditions

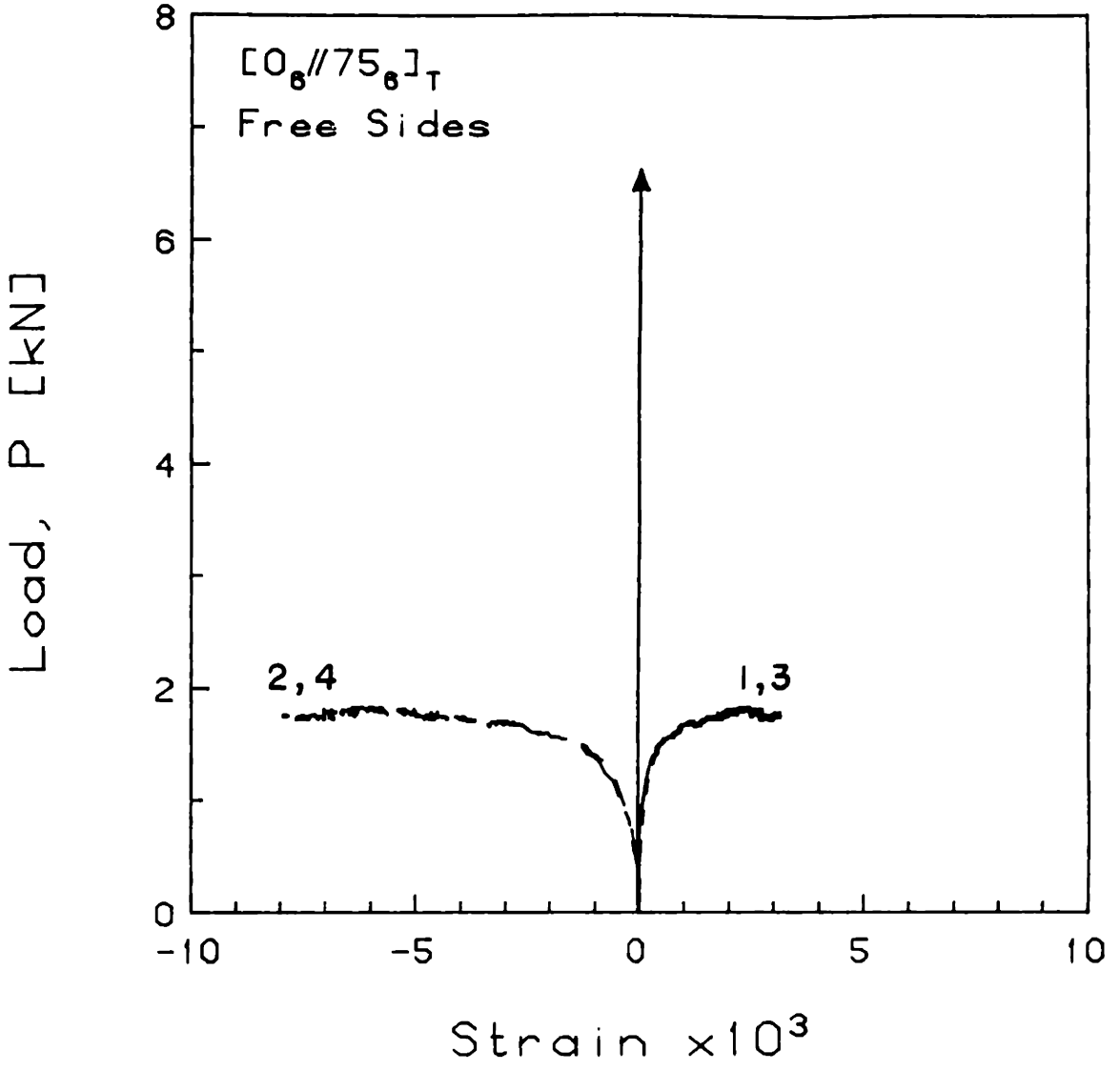

FIGURE F.74 Experimental Plot of Applied Compressive Load versus Longitudinal Strain for the $[0_6//75_6]_T$ Laminate with Free Side Boundary Conditions

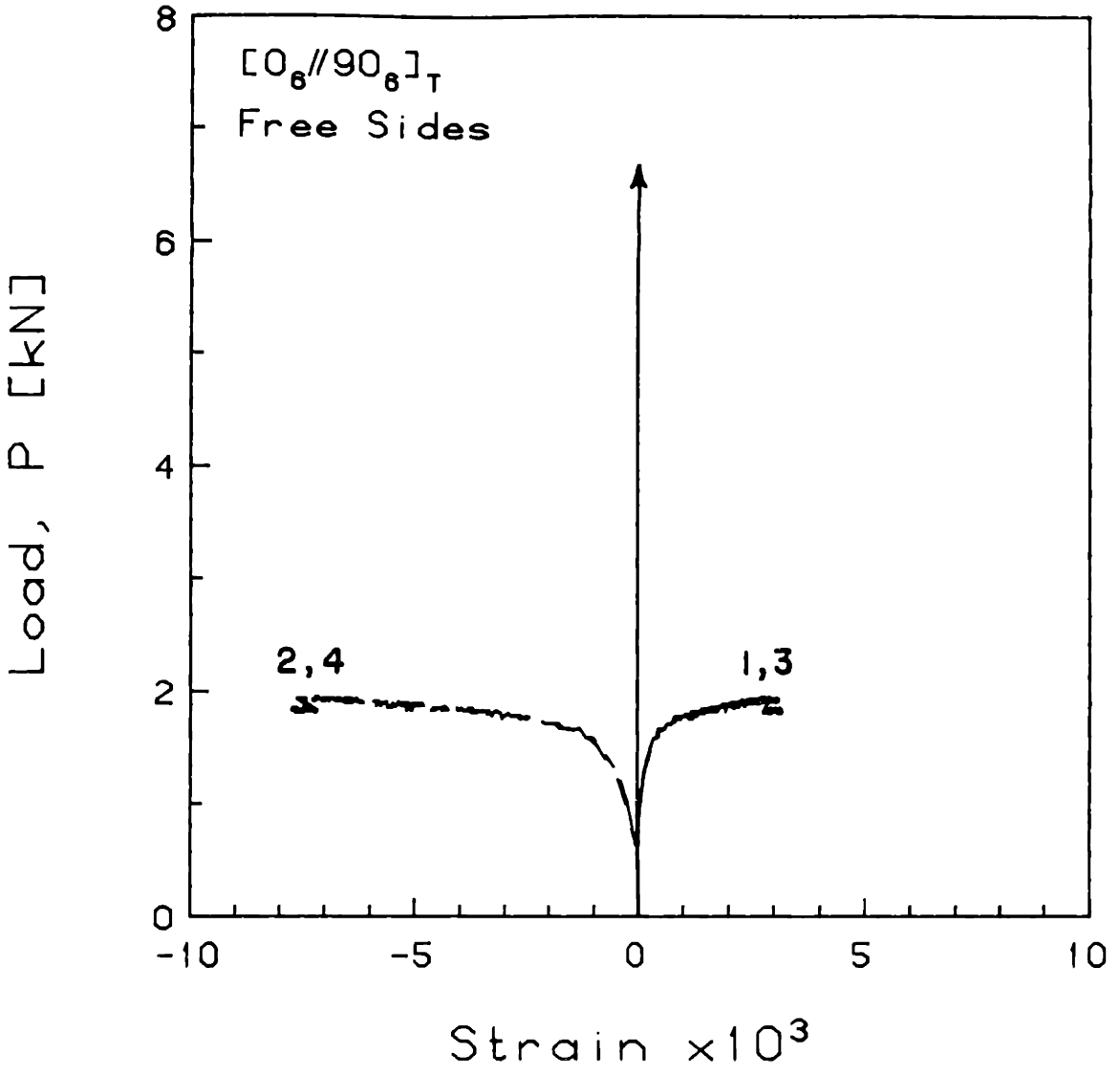

FIGURE F.75 Experimental Plot of Applied Compressive Load versus Longitudinal Strain for the $[0_6//90_6]_T$ Laminate with Free Side Boundary Conditions

APPENDIX G

LOAD VERSUS END-SHORTENING DISPLACEMENT PLOTS

This appendix contains copies of all of the experimental load versus end-shortening displacement data. They are presented in the same order as discussed in the main text, i.e., according to the sequence summarized in Table 4.4. The results for laminates with clamped side boundary conditions are presented first, followed by those with simply-supported side boundary conditions, and, finally, the results for laminates with free sides.

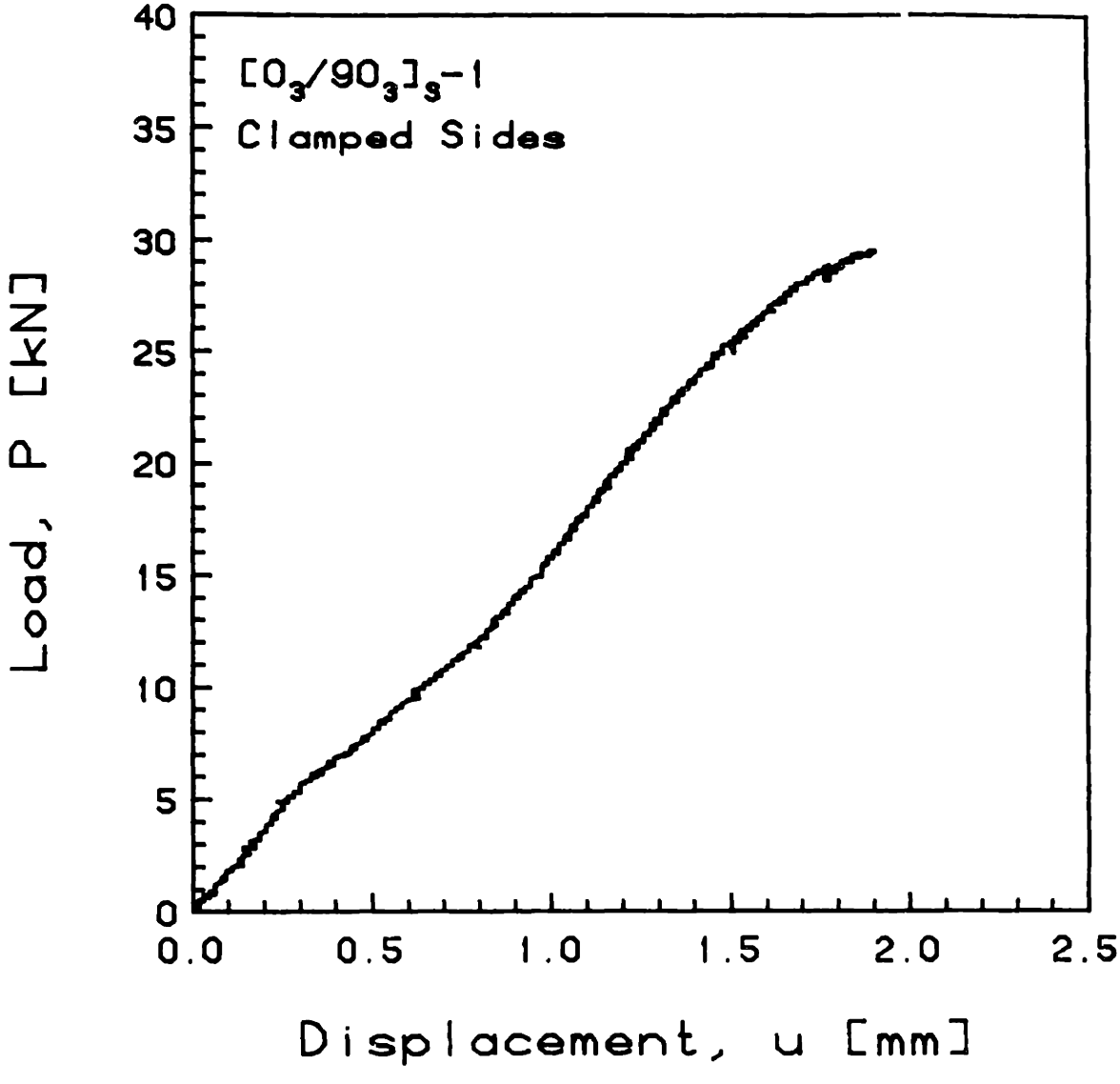

FIGURE G.1 Experimental Plot of Applied Compressive Load versus End-Shortening Displacement for the $[0_3/90_3]_S$-1 Laminate with Clamped Side Boundary Conditions

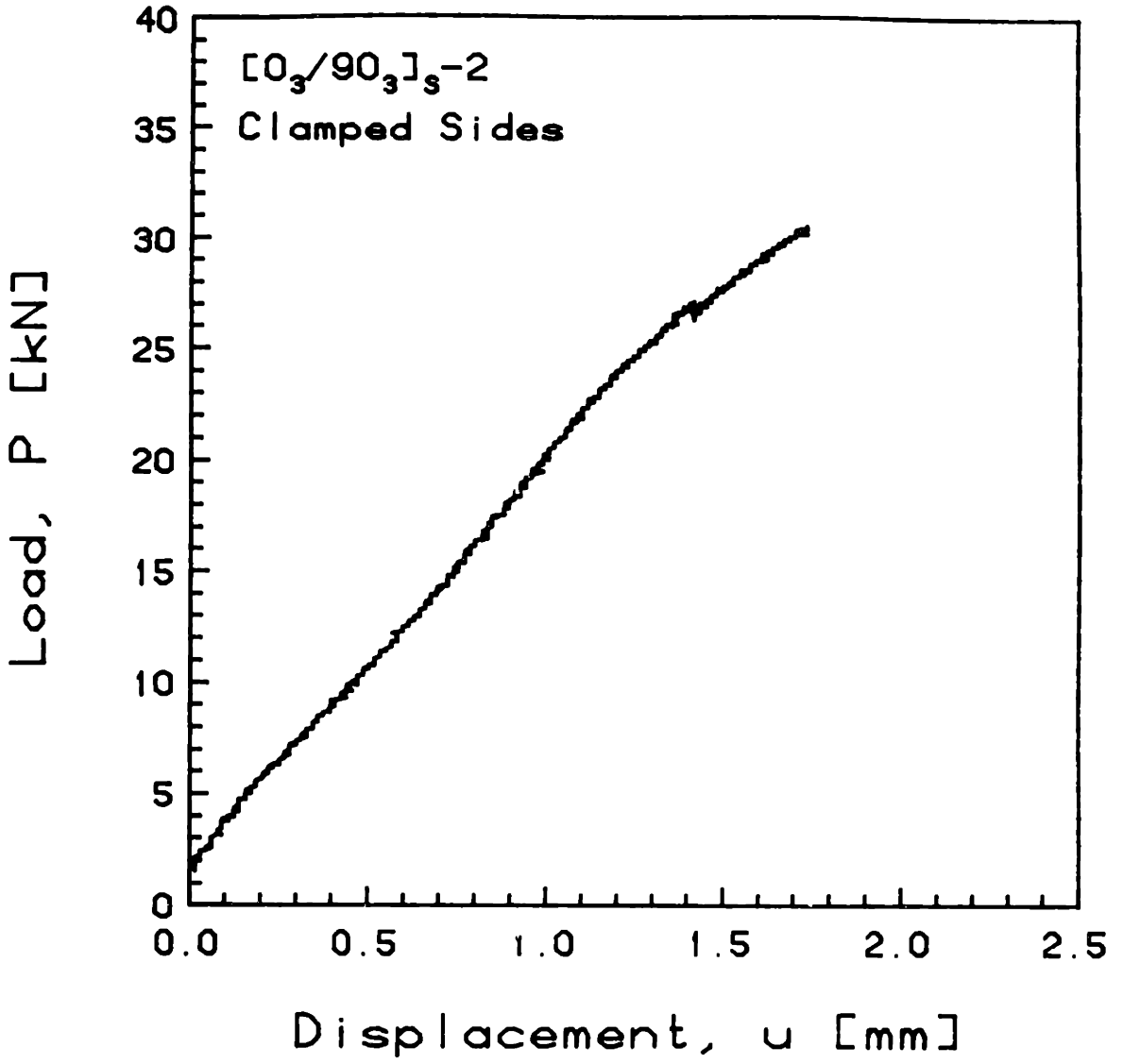

FIGURE G.2 Experimental Plot of Applied Compressive Load versus End-Shortening Displacement for the $[O_3/90_3]_S$-2 Laminate with Clamped Side Boundary Conditions

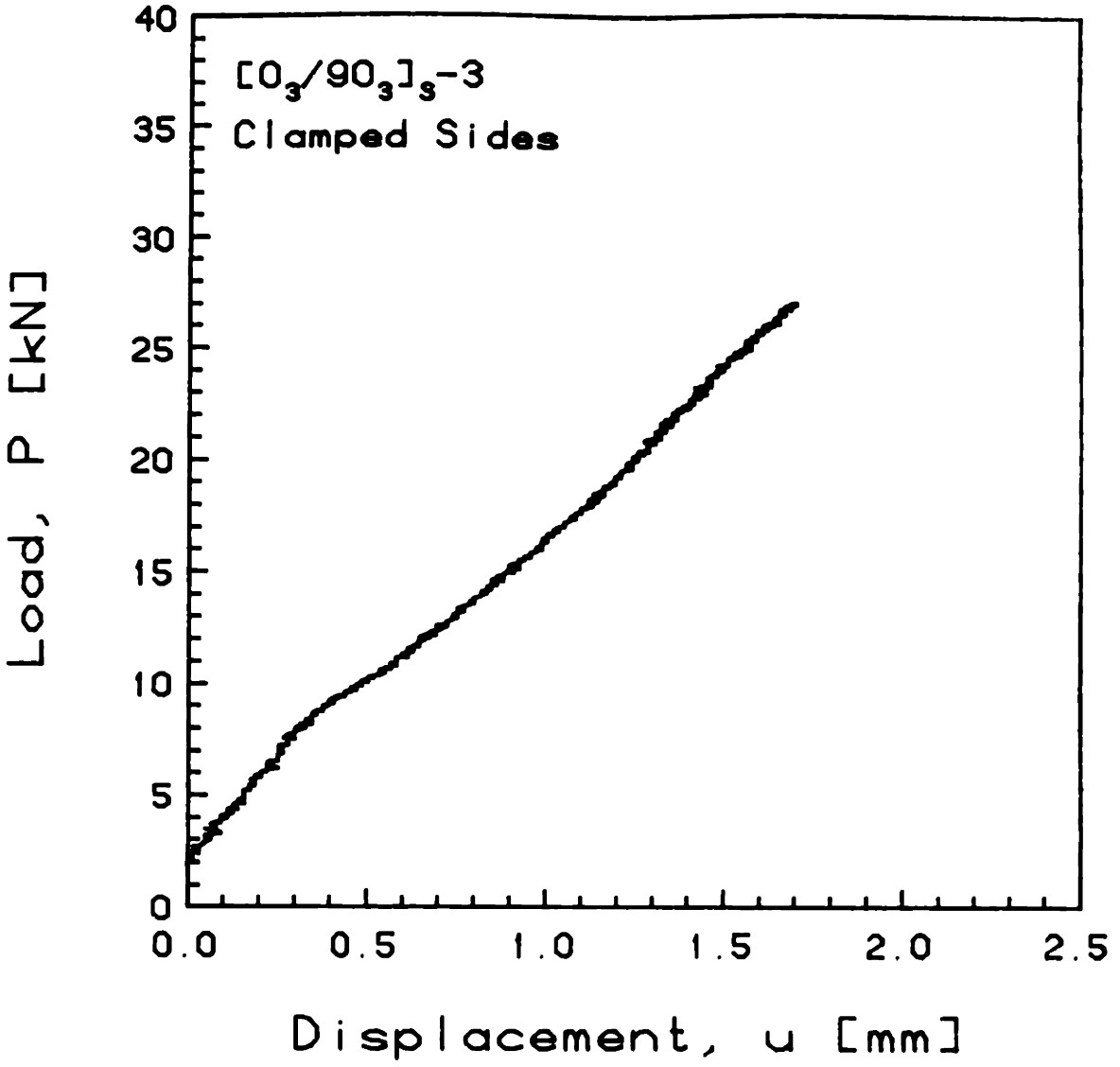

FIGURE G.3 Experimental Plot of Applied Compressive Load versus End-Shortening Displacement for the $[O_3/90_3]_S$-3 Laminate with Clamped Side Boundary Conditions

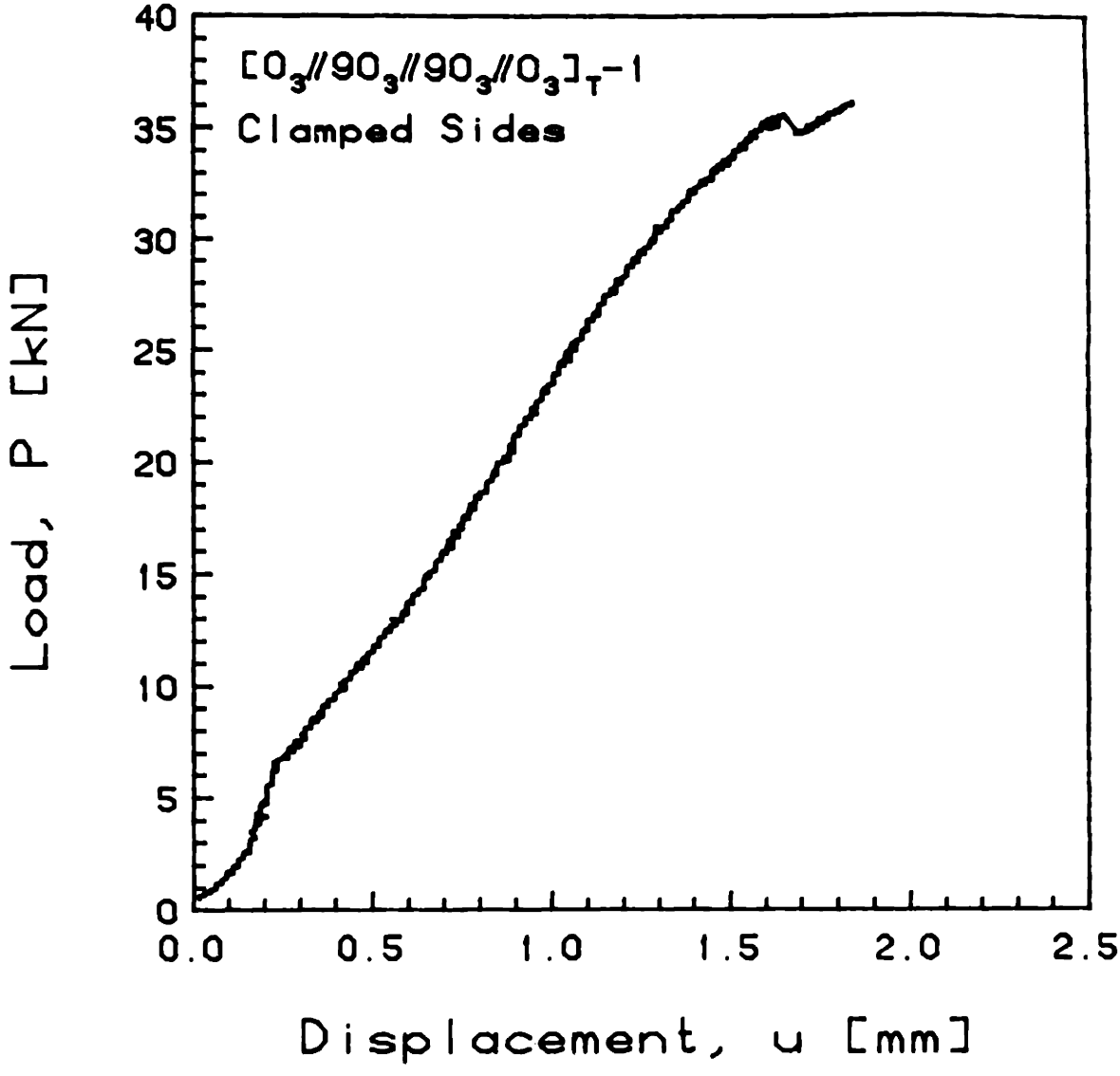

FIGURE G.4 Experimental Plot of Applied Compressive Load versus End-Shortening Displacement for the $[0_3//90_3//90_3//0_3]_T$-1 Laminate with Clamped Side Boundary Conditions

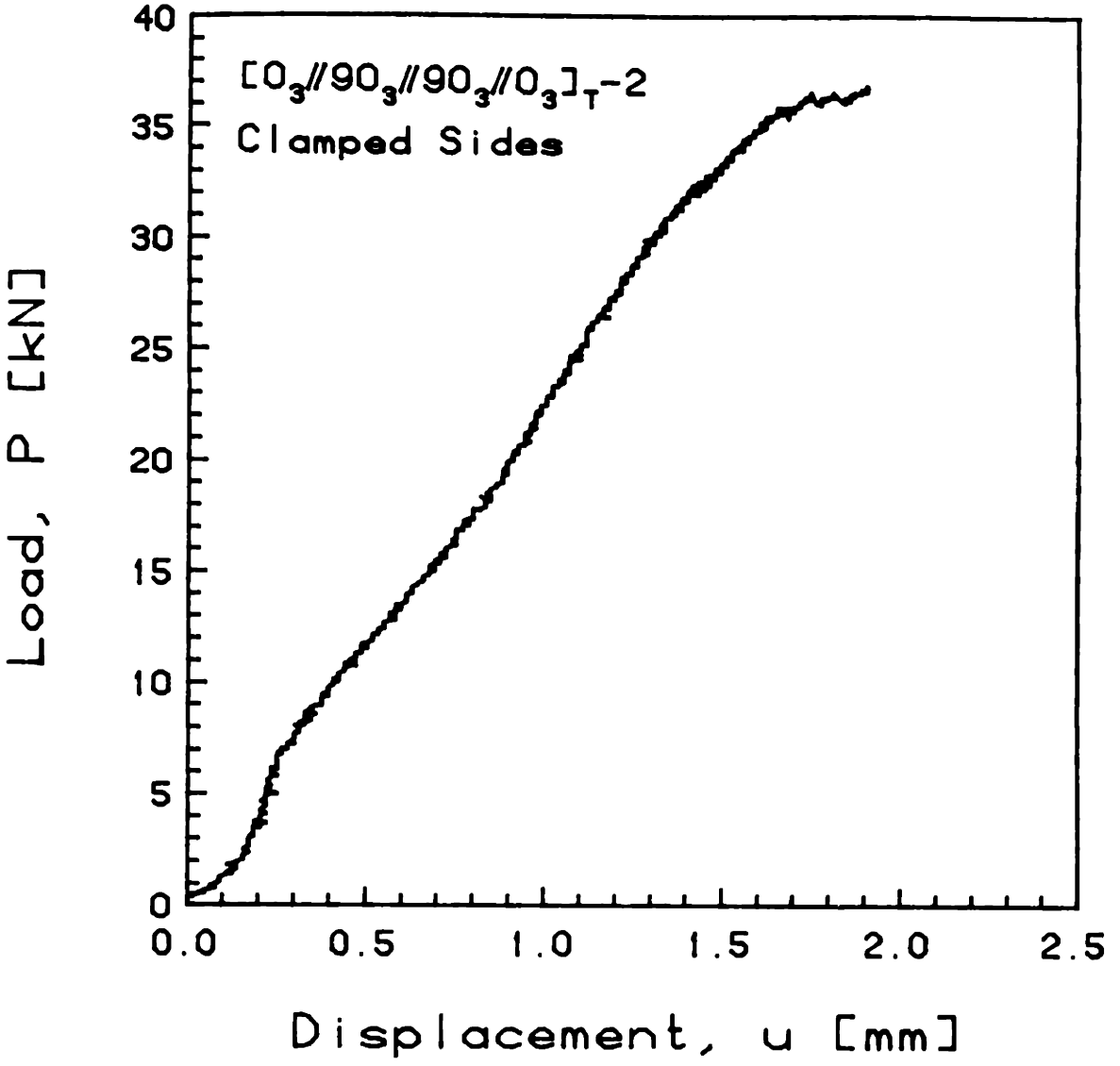

FIGURE G.5 Experimental Plot of Applied Compressive Load versus End-Shortening Displacement for the $[0_3//90_3//90_3//0_3]_T$-2 Laminate with Clamped Side Boundary Conditions

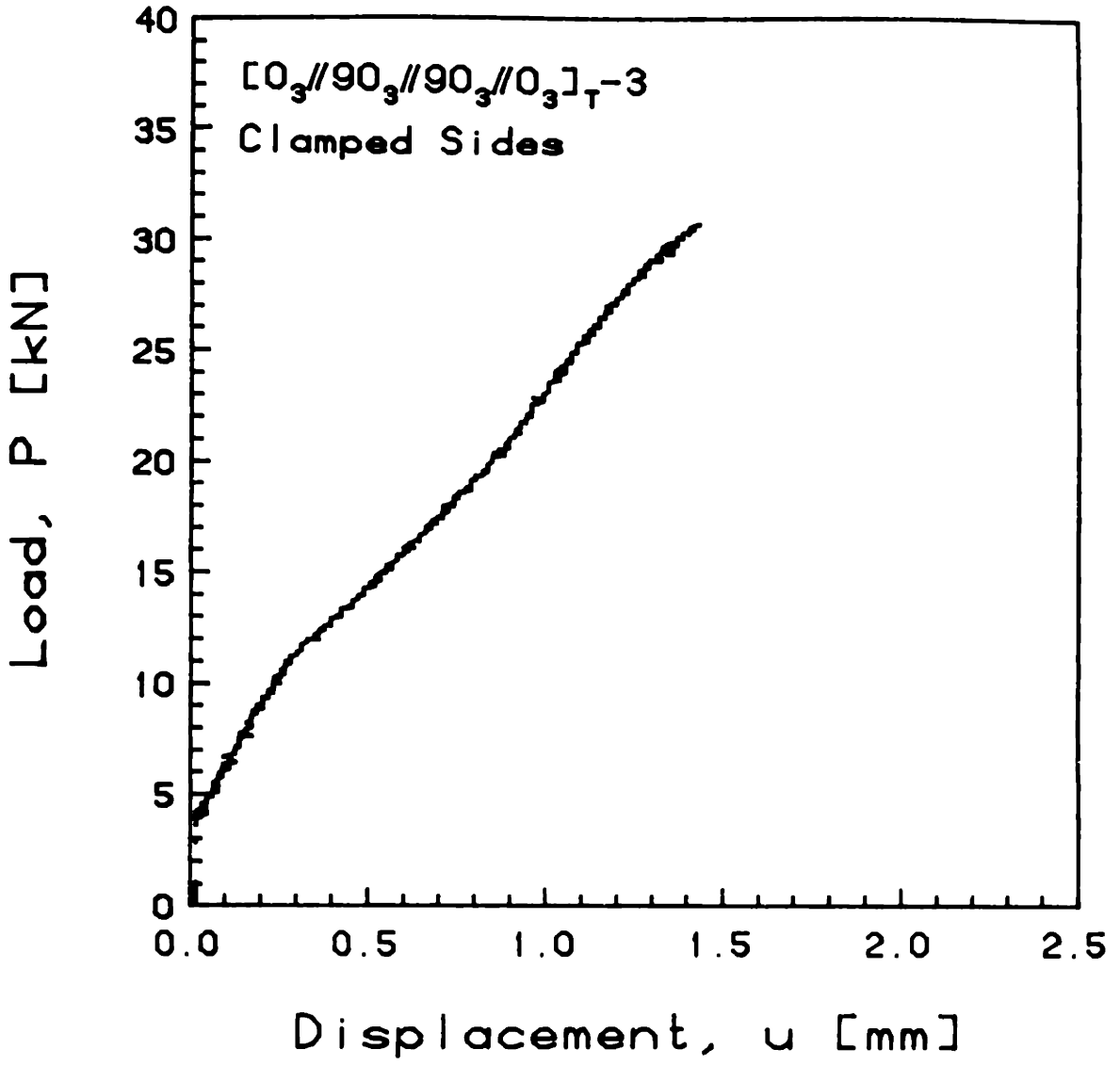

FIGURE G.6 Experimental Plot of Applied Compressive Load versus End-Shortening Displacement for the $[0_3//90_3//90_3//0_3]_T$-3 Laminate with Clamped Side Boundary Conditions

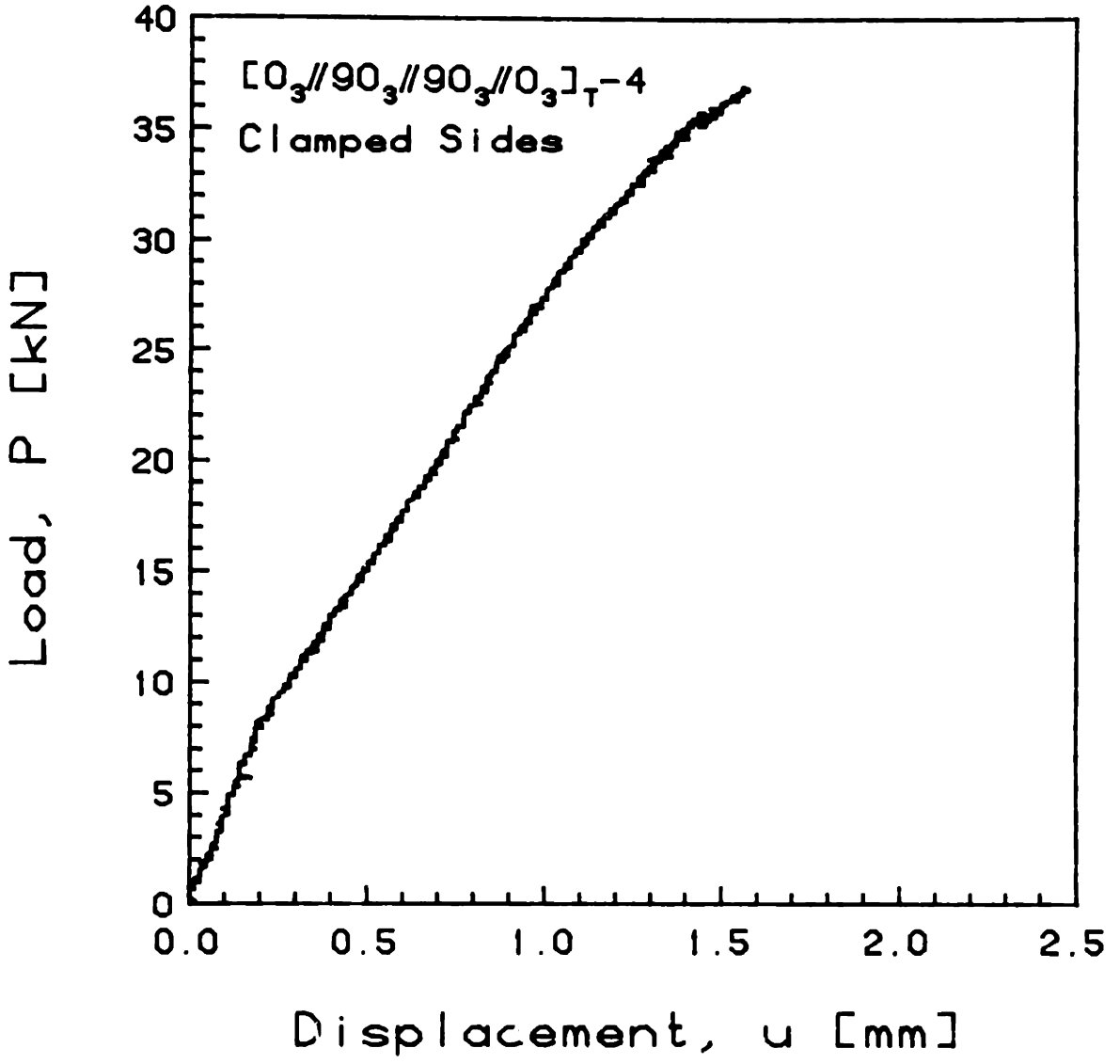

FIGURE G.7 Experimental Plot of Applied Compressive Load versus End-Shortening Displacement for the $[0_3//90_3//90_3//0_3]_T$-4 Laminate with Clamped Side Boundary Conditions

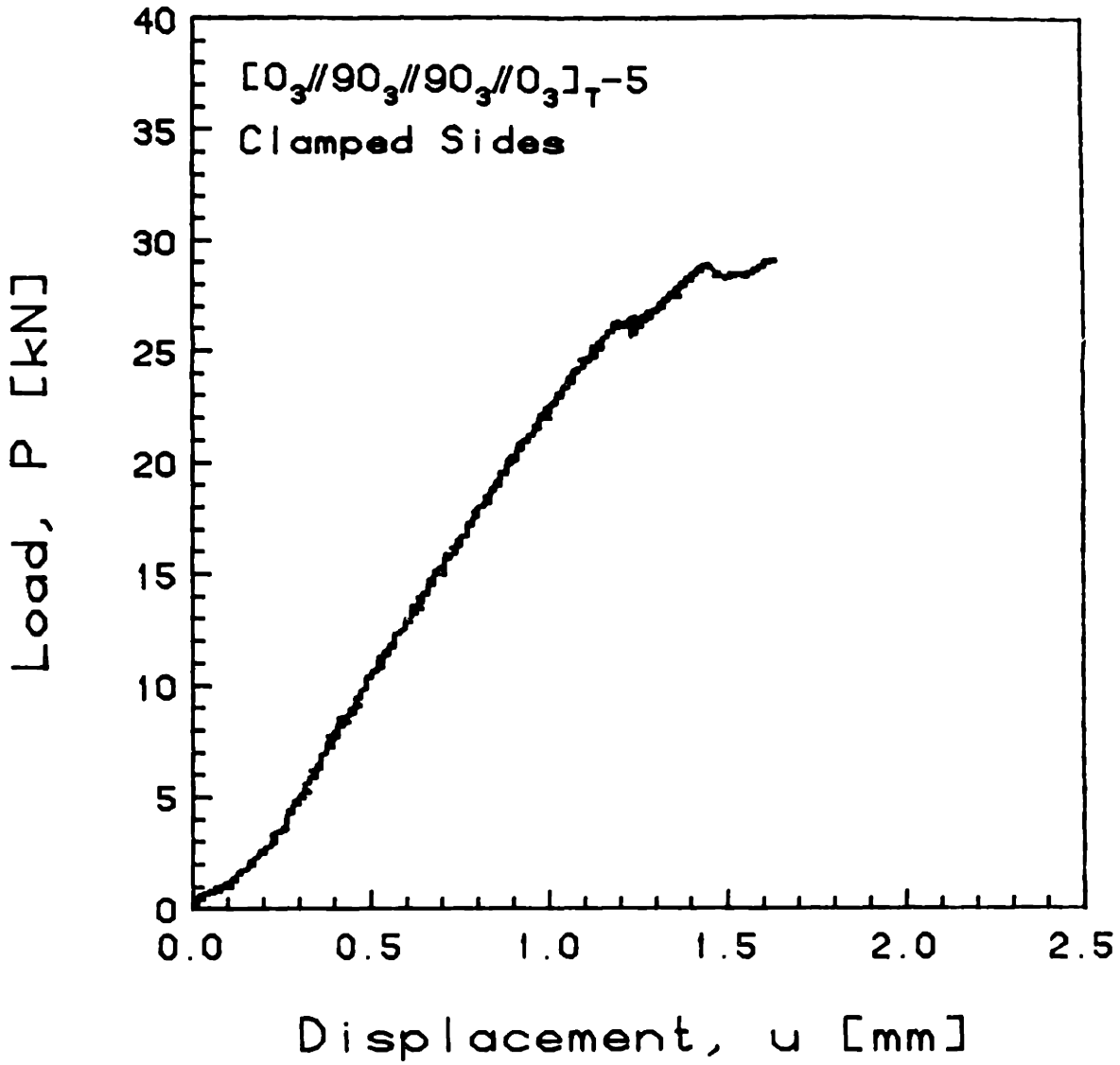

FIGURE G.8 Experimental Plot of Applied Compressive Load versus End-Shortening Displacement for the $[0_3//90_3//90_3//0_3]_T$-5 Laminate with Clamped Side Boundary Conditions

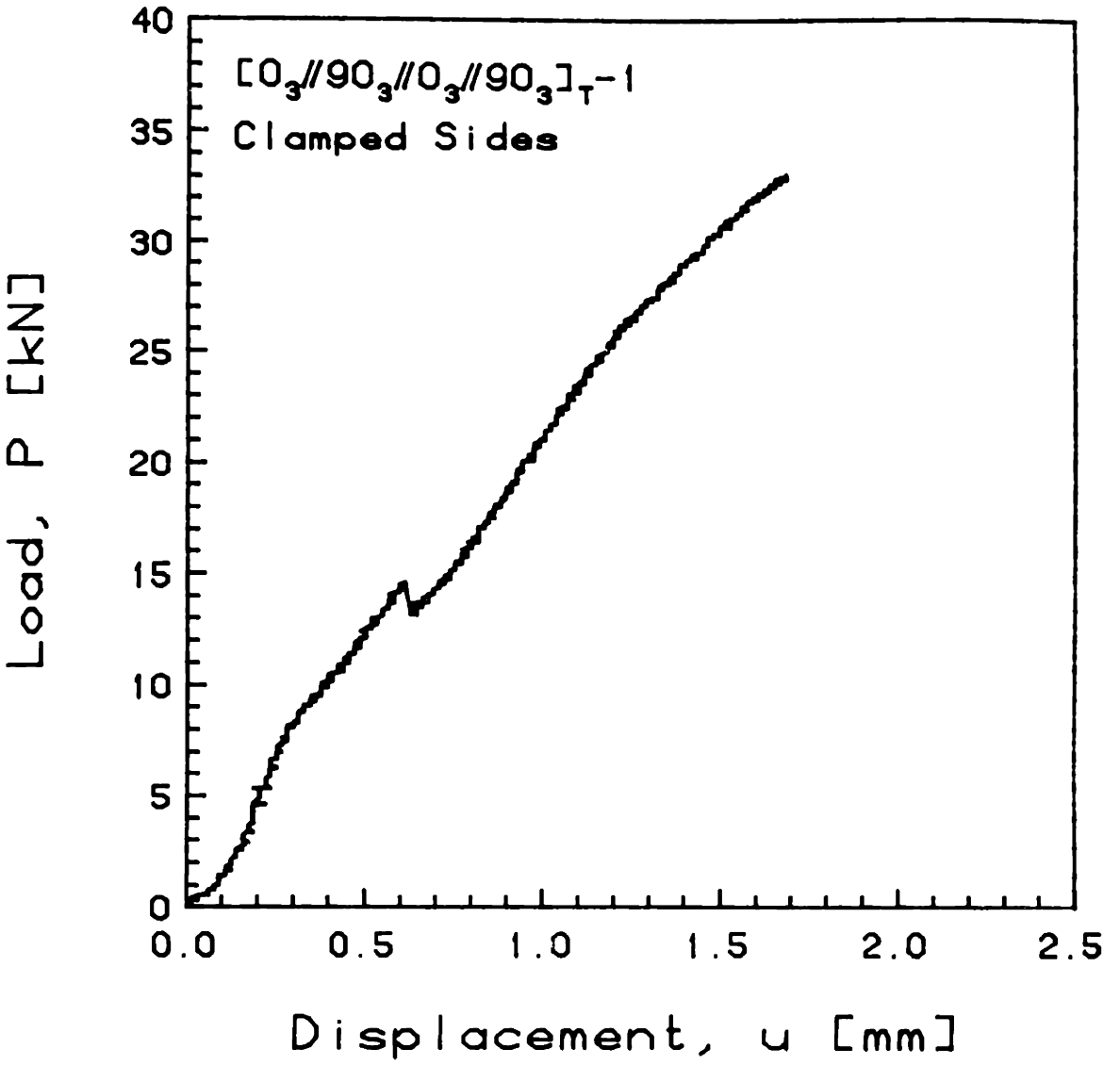

FIGURE G.9 Experimental Plot of Applied Compressive Load versus End-Shortening Displacement for the $[0_3//90_3//0_3//90_3]_T$-1 Laminate with Clamped Side Boundary Conditions

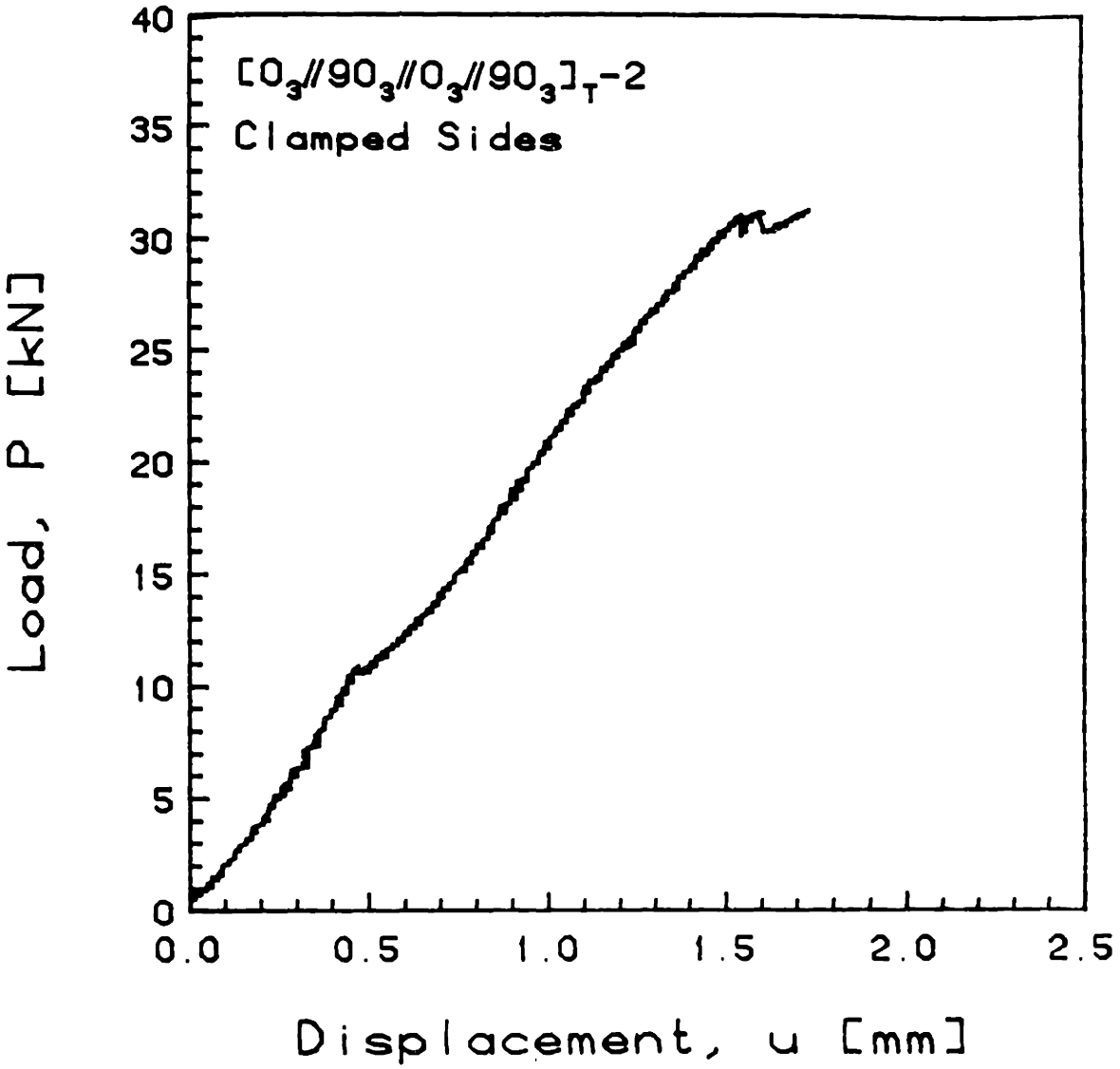

FIGURE G.10 Experimental Plot of Applied Compressive Load versus End-Shortening Displacement for the $[0_3//90_3//0_3//90_3]_T$-2 Laminate with Clamped Side Boundary Conditions

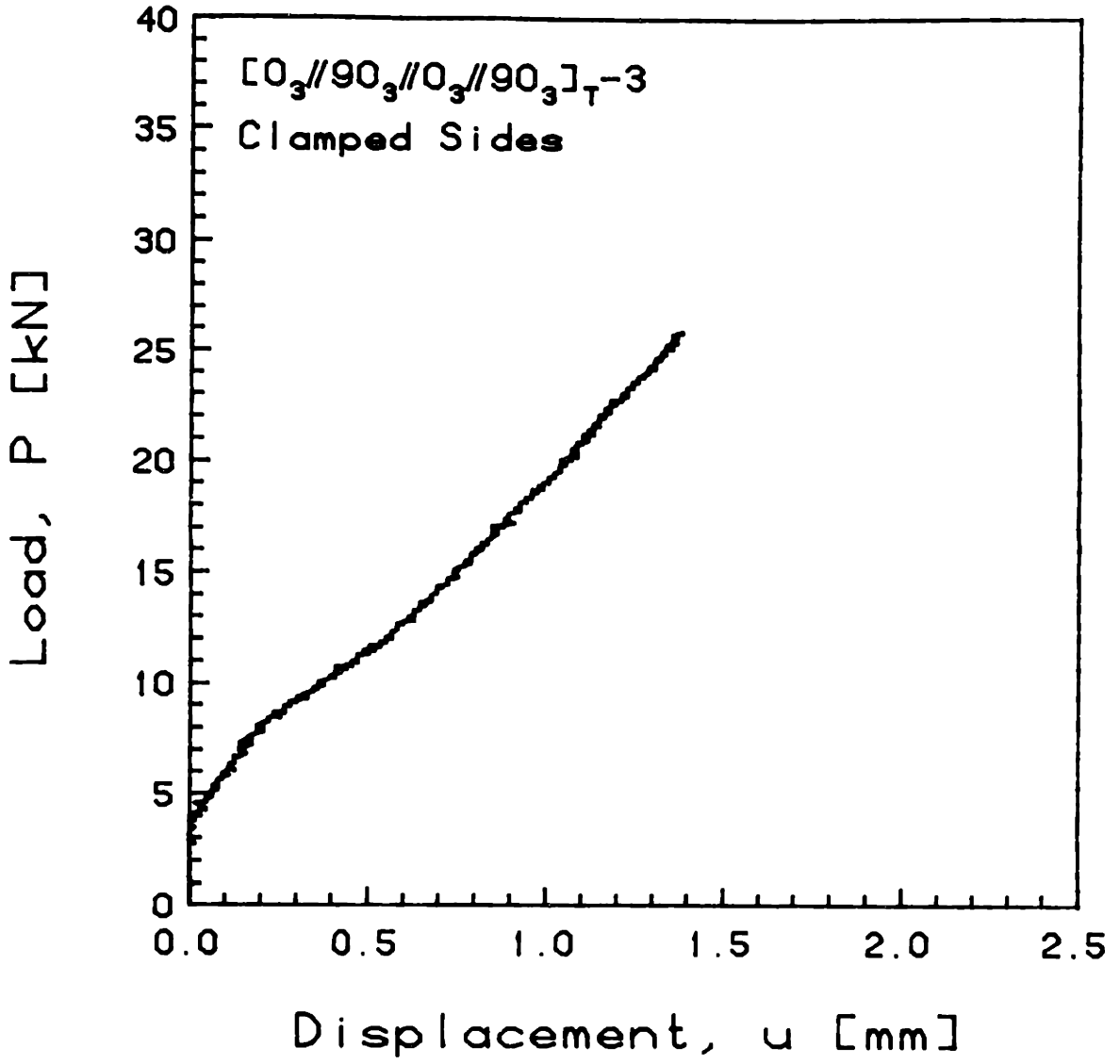

FIGURE G.11 Experimental Plot of Applied Compressive Load versus End-Shortening Displacement for the $[O_3//90_3//O_3//90_3]_T$-3 Laminate with Clamped Side Boundary Conditions

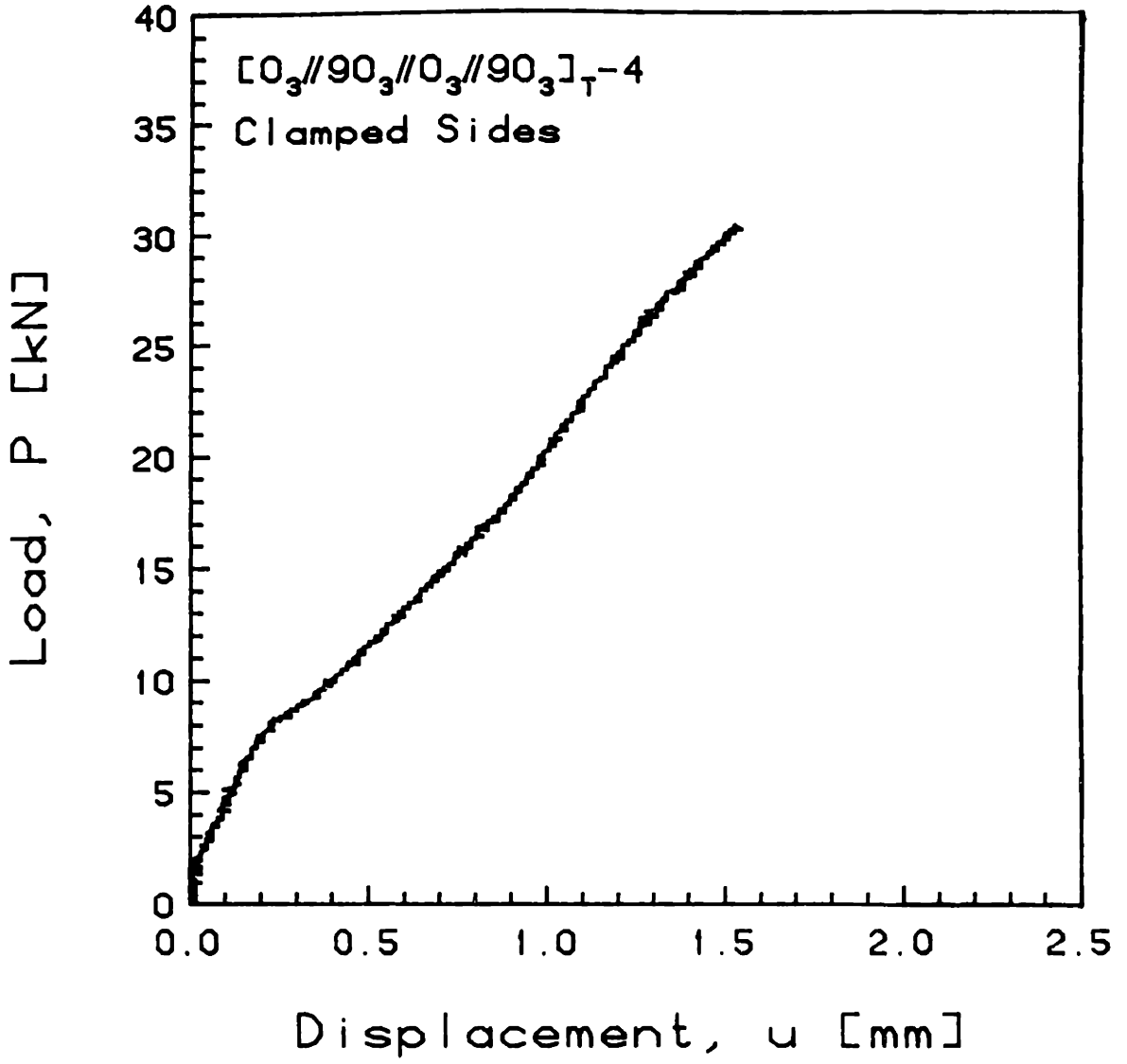

FIGURE G.12 Experimental Plot of Applied Compressive Load versus End-Shortening Displacement for the $[0_3//90_3//0_3//90_3]_T$-4 Laminate with Clamped Side Boundary Conditions

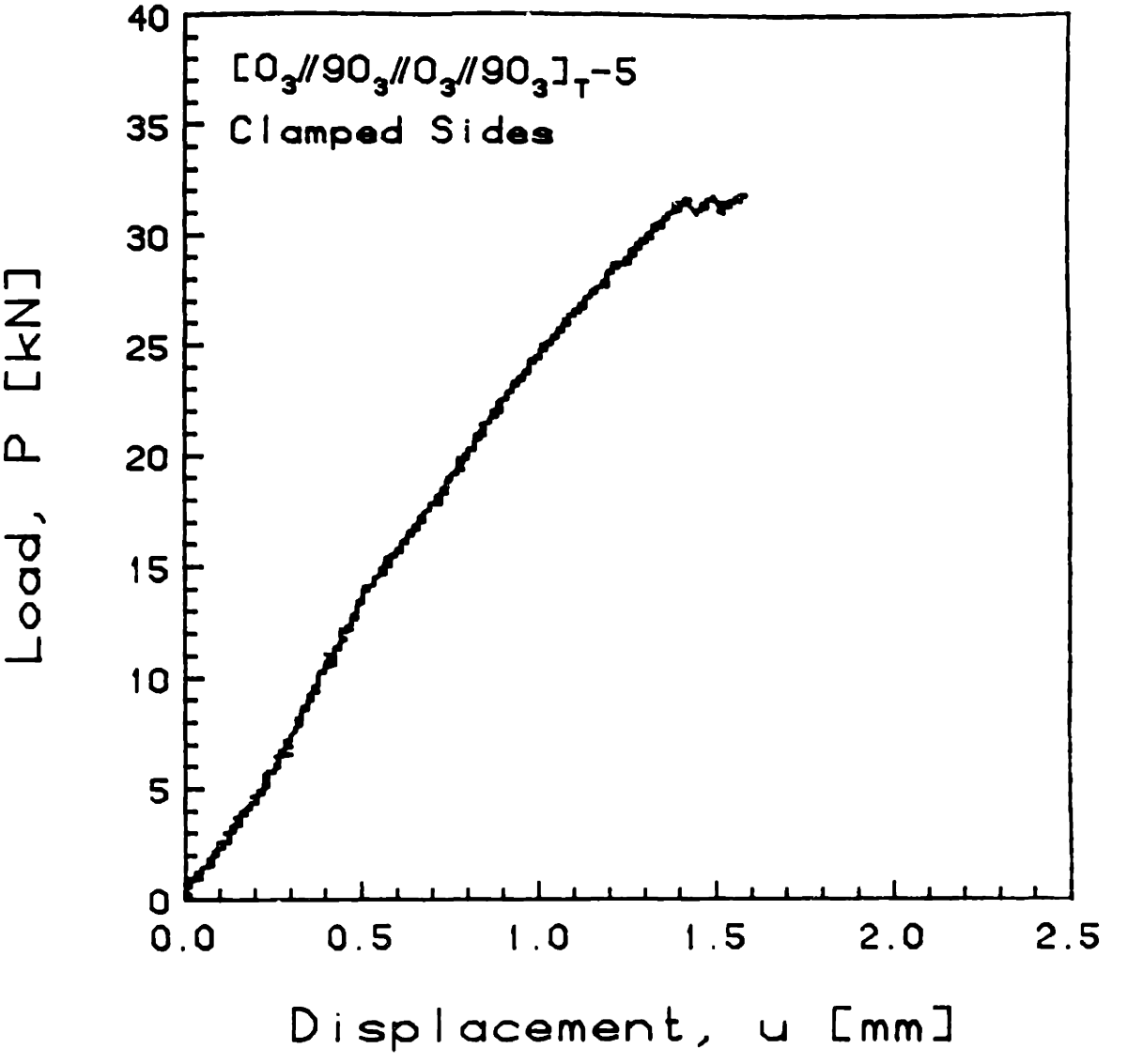

FIGURE G.13 Experimental Plot of Applied Compressive Load versus End-Shortening Displacement for the $[0_3//90_3//0_3//90_3]_T$-5 Laminate with Clamped Side Boundary Conditions

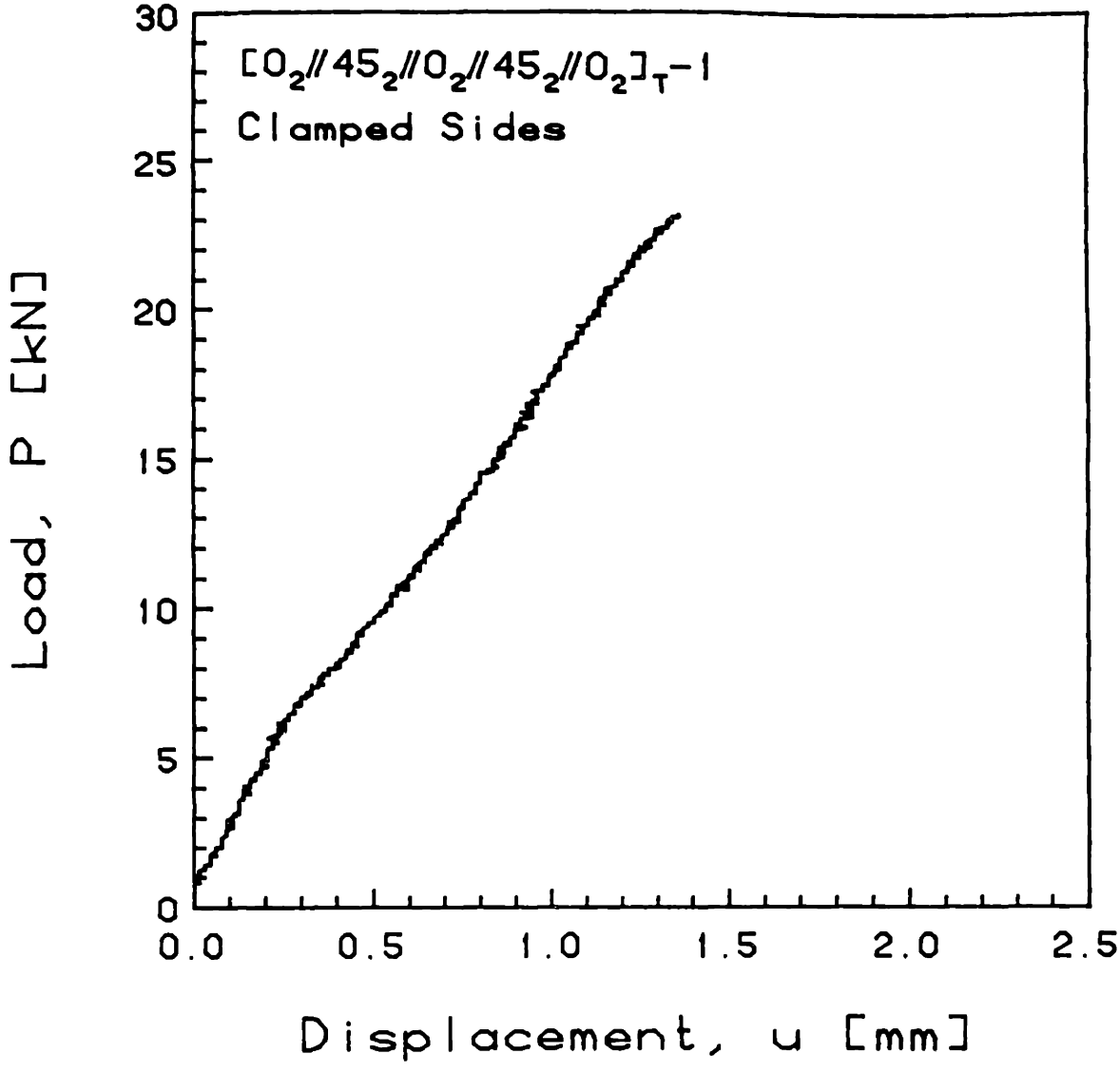

FIGURE G.14 Experimental Plot of Applied Compressive Load versus End-Shortening Displacement for the $[O_2//45_2//O_2//45_2//O_2]_T$-1 Laminate with Clamped Side Boundary Conditions

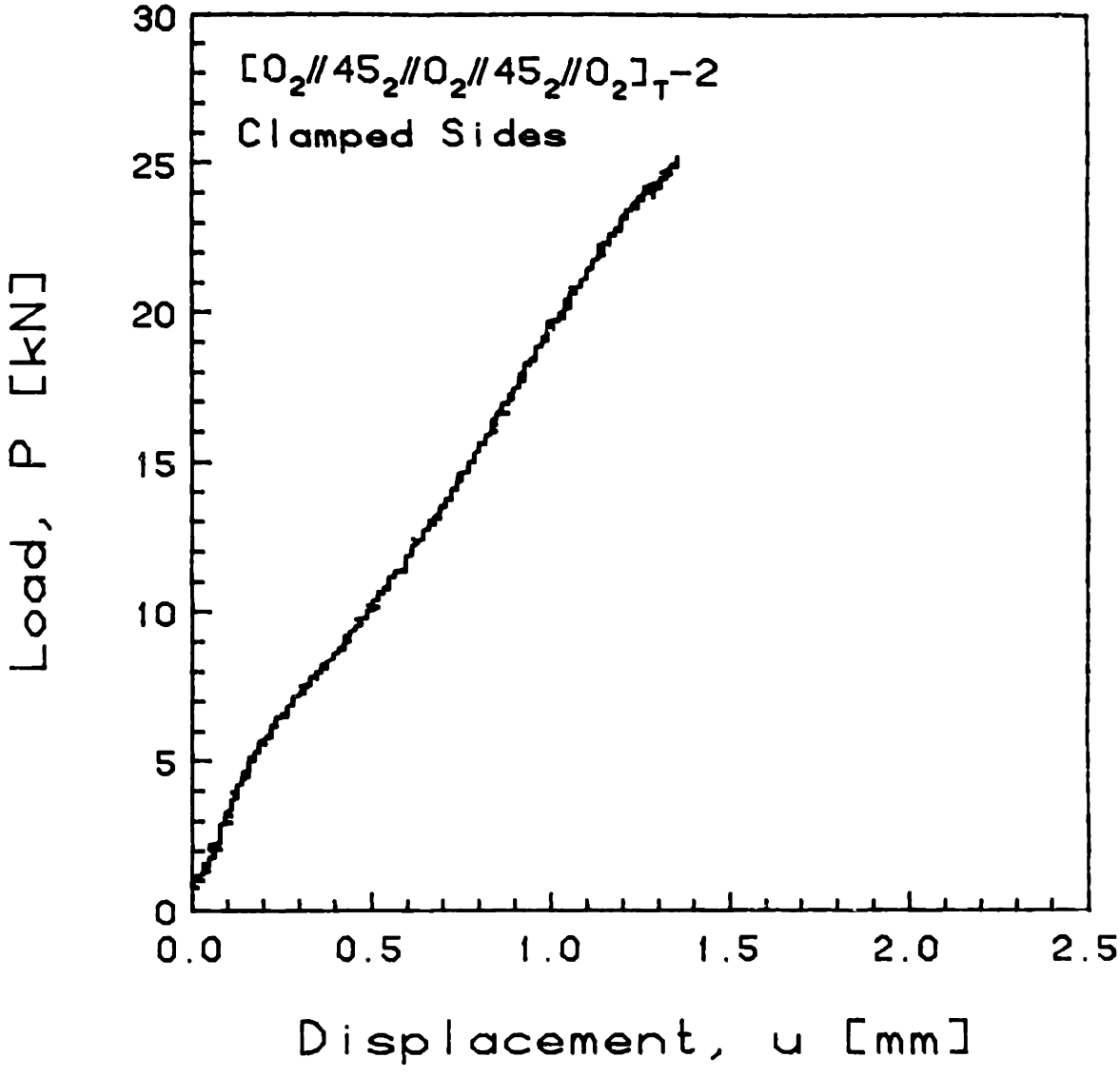

FIGURE G.15 Experimental Plot of Applied Compressive Load versus End-Shortening Displacement for the $[O_2//45_2//O_2//45_2//O_2]_T$-2 Laminate with Clamped Side Boundary Conditions

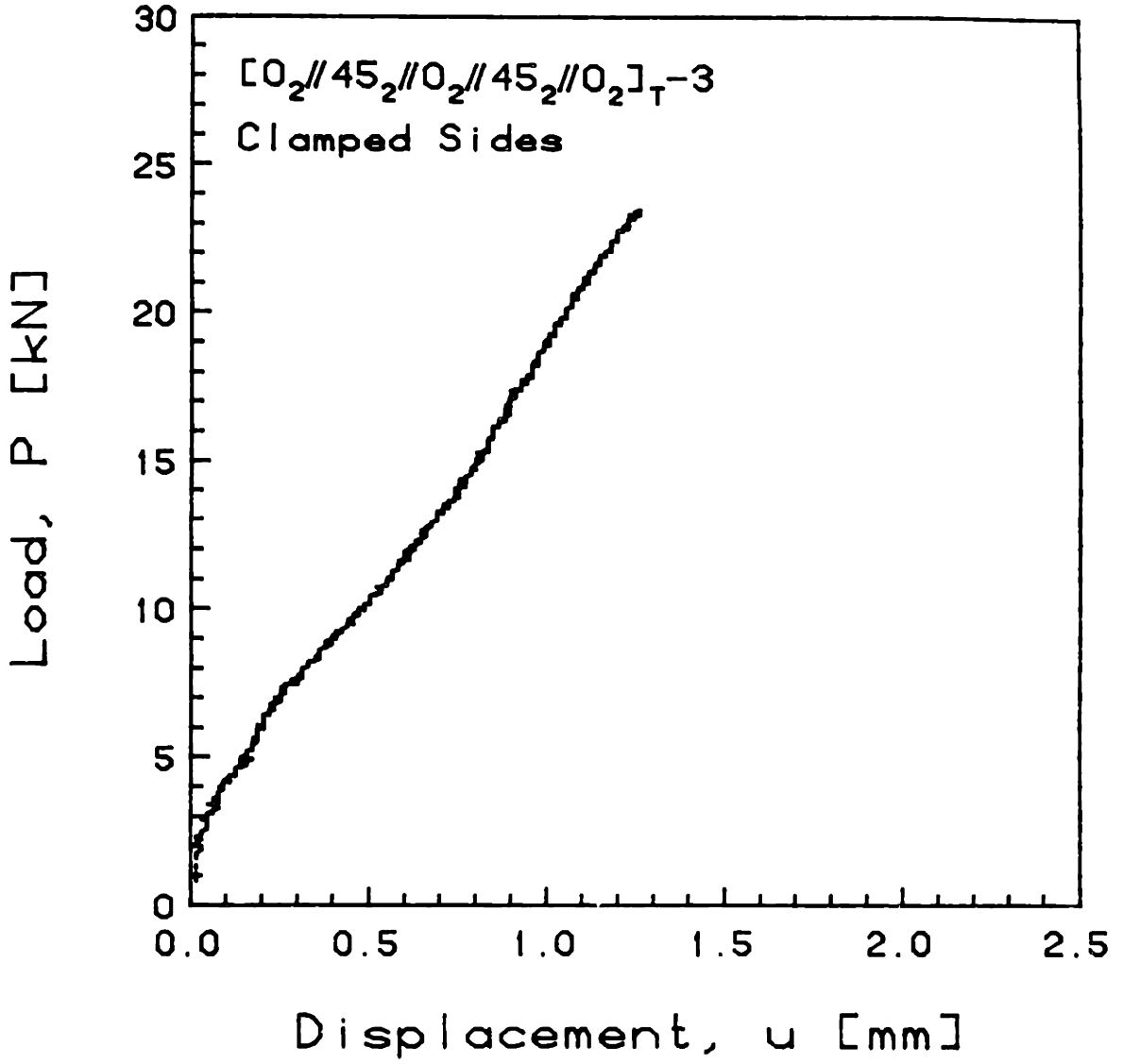

FIGURE G.16 Experimental Plot of Applied Compressive Load versus End-Shortening Displacement for the $[O_2//45_2//O_2//45_2//O_2]_T$-3 Laminate with Clamped Side Boundary Conditions

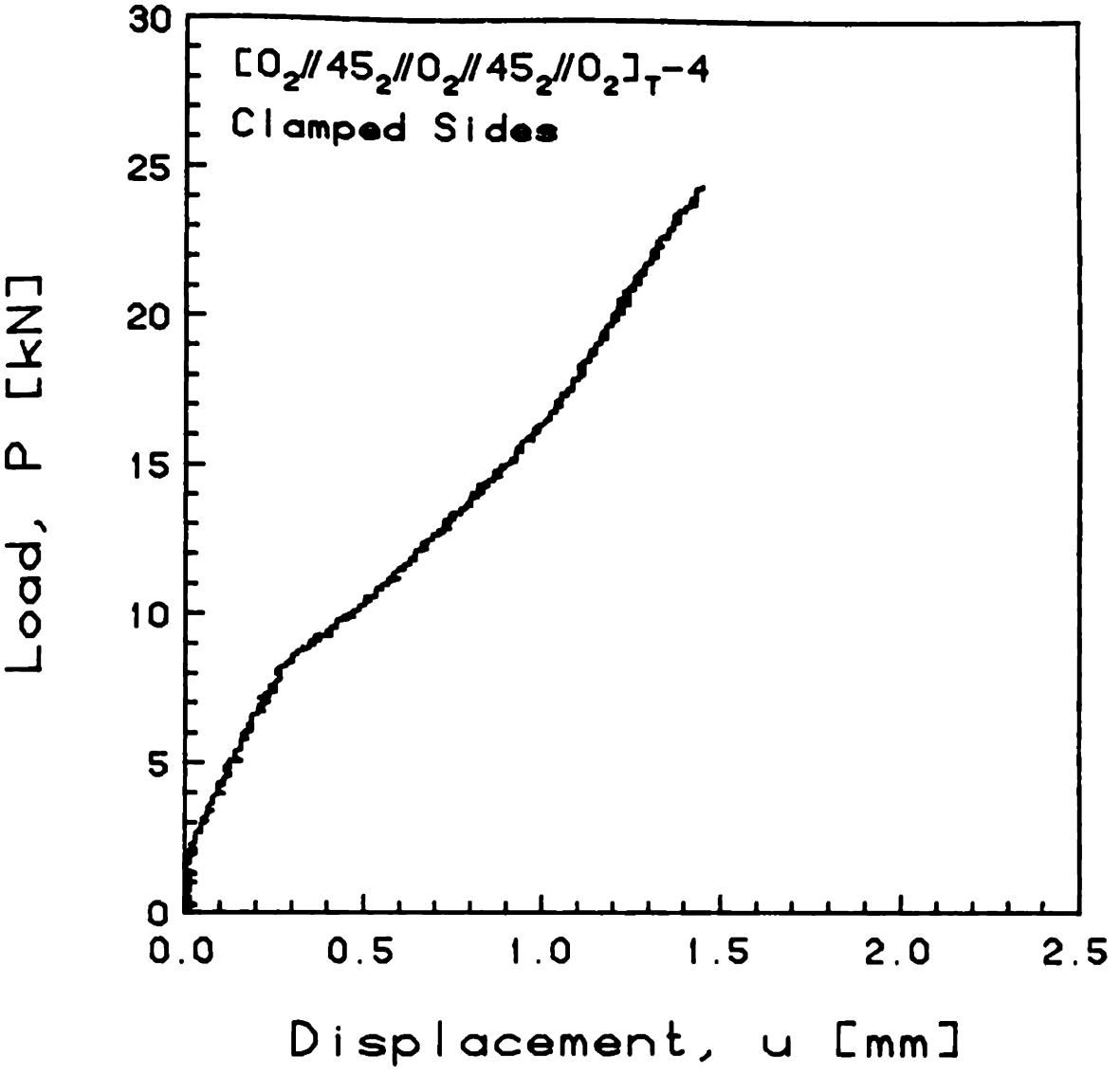

FIGURE G.17 Experimental Plot of Applied Compressive Load versus End-Shortening Displacement for the $[O_2//45_2//O_2//45_2//O_2]_T$-4 Laminate with Clamped Side Boundary Conditions

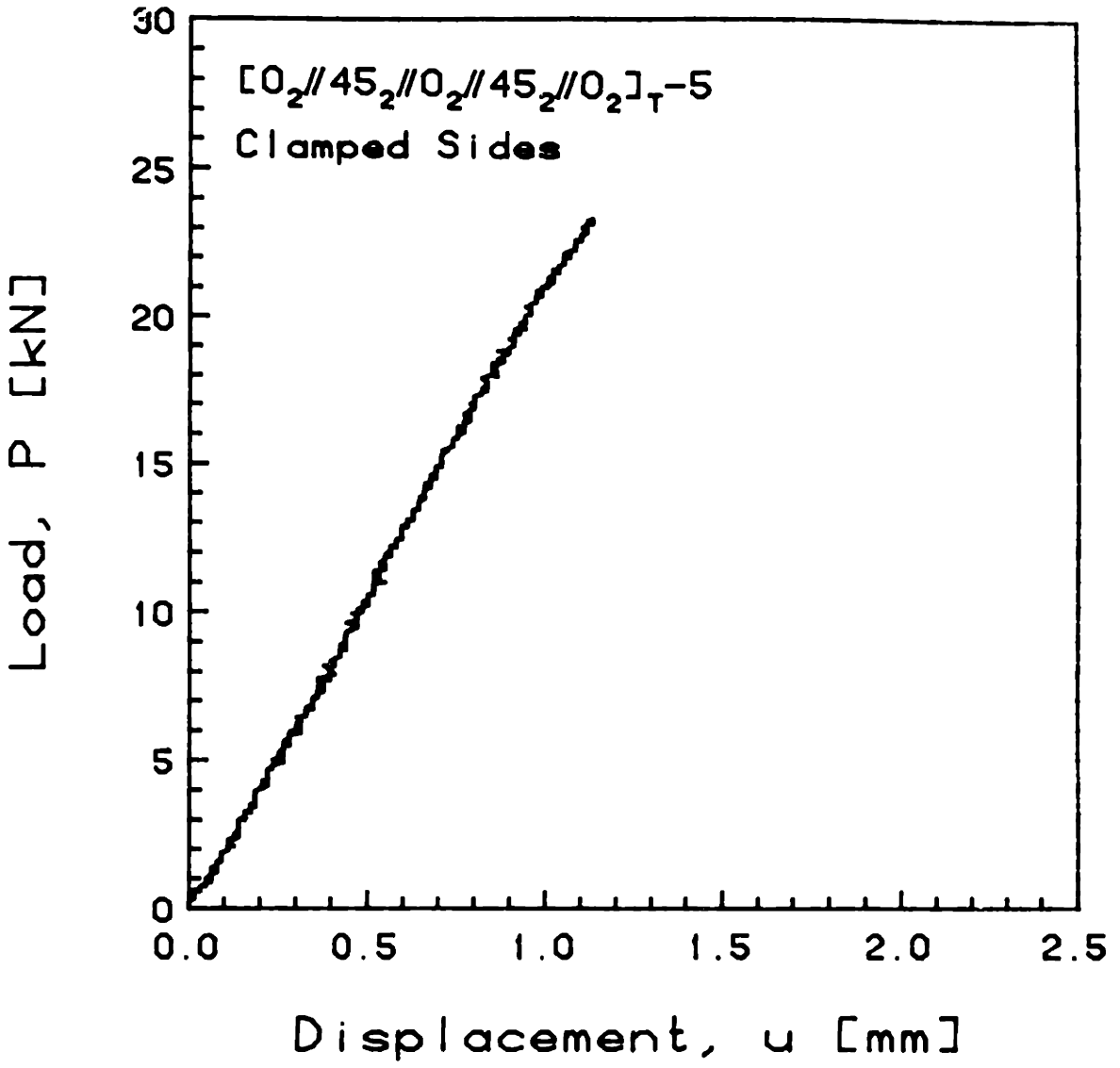

FIGURE G.18 Experimental Plot of Applied Compressive Load versus End-Shortening Displacement for the $[0_2//45_2//0_2//45_2//0_2]_T$-5 Laminate with Clamped Side Boundary Conditions

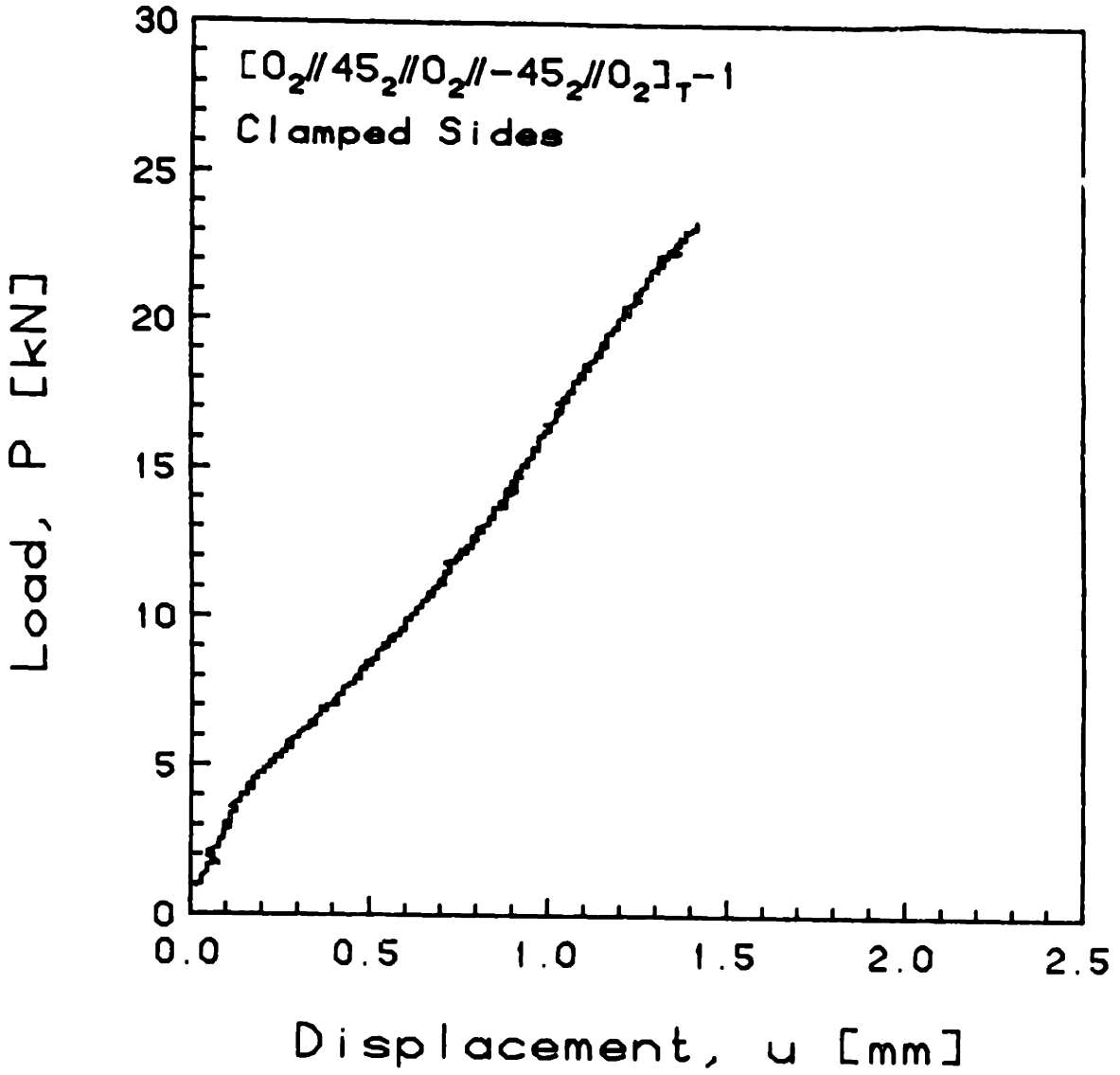

FIGURE G.19 Experimental Plot of Applied Compressive Load versus End-Shortening Displacement for the $[O_2//45_2//O_2//-45_2//O_2]_T$-1 Laminate with Clamped Side Boundary Conditions

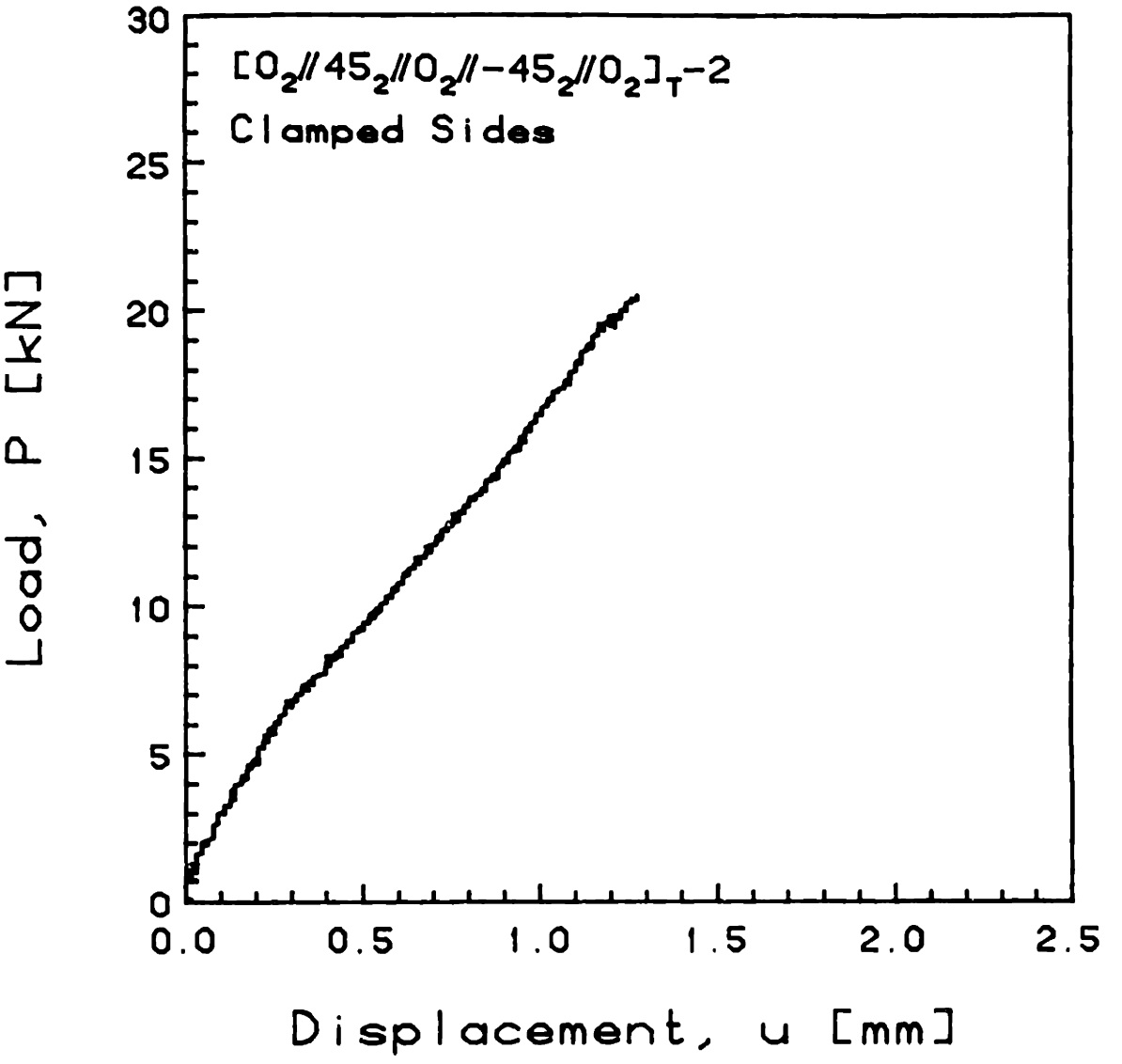

FIGURE G.20 Experimental Plot of Applied Compressive Load versus End-Shortening Displacement for the $[O_2//45_2//O_2//-45_2//O_2]_T$-2 Laminate with Clamped Side Boundary Conditions

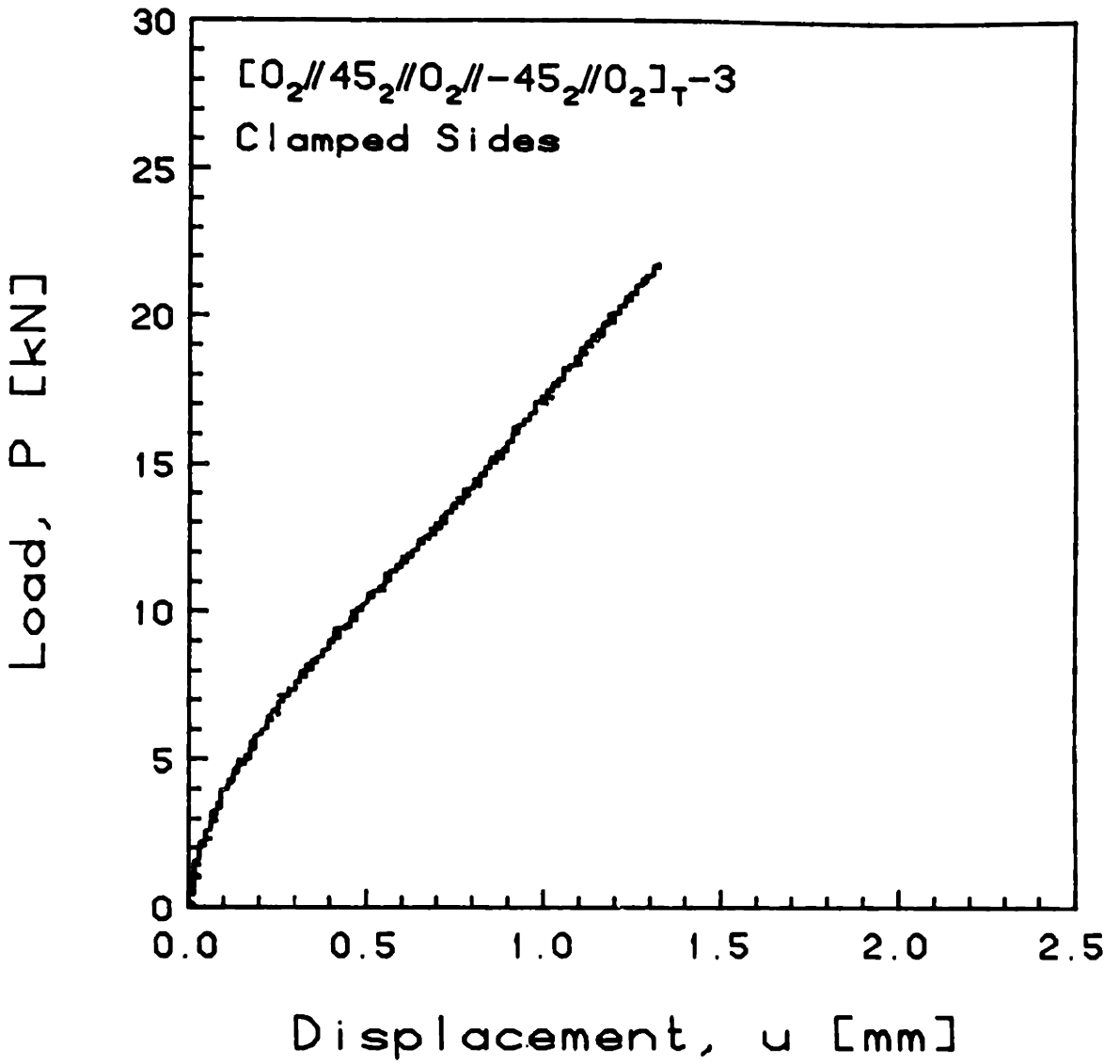

FIGURE G.21 Experimental Plot of Applied Compressive Load versus End-Shortening Displacement for the $[0_2//45_2//0_2//-45_2//0_2]_T$-3 Laminate with Clamped Side Boundary Conditions

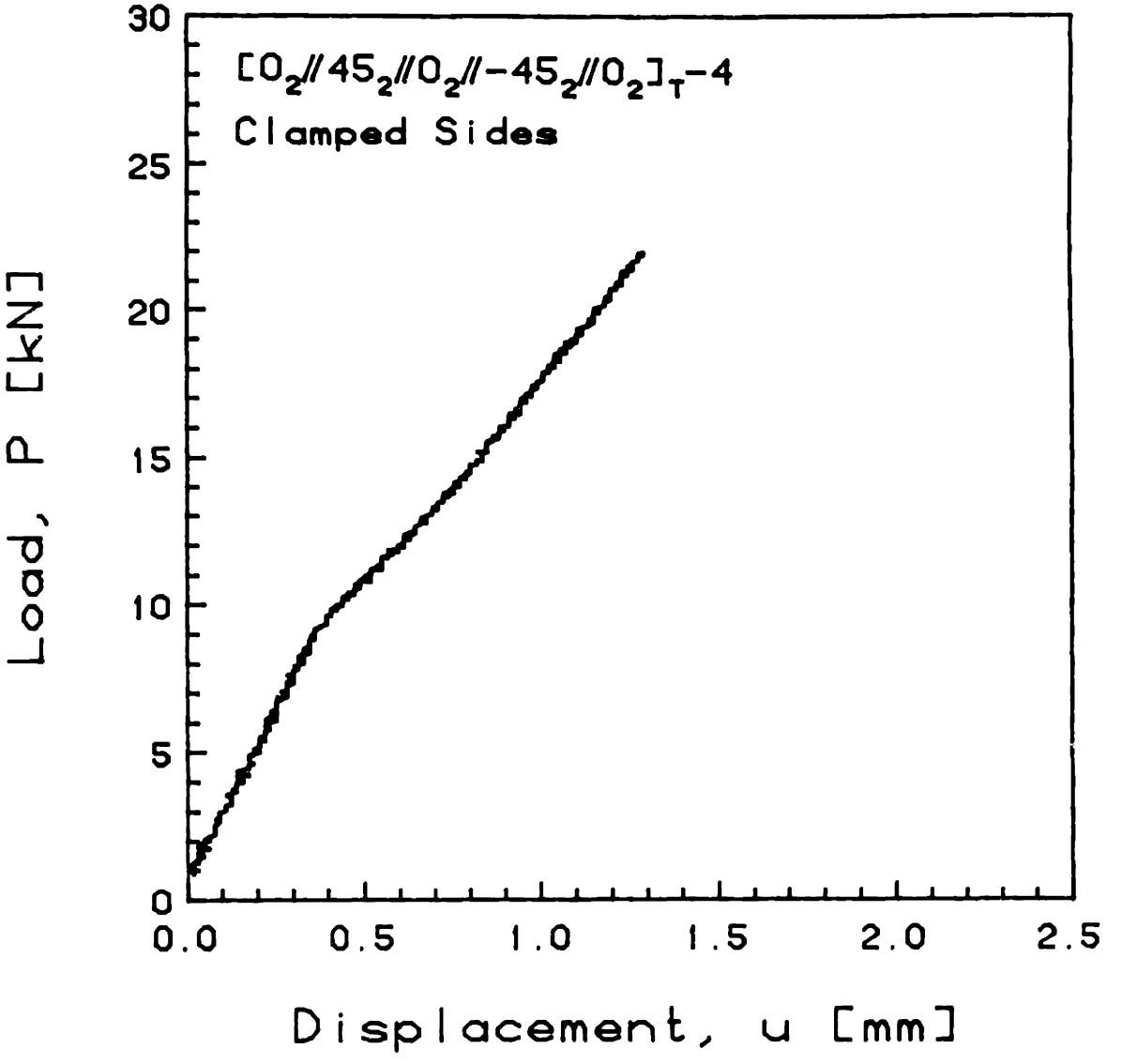

FIGURE G.22 Experimental Plot of Applied Compressive Load versus End-Shortening Displacement for the $[0_2//45_2//0_2//-45_2//0_2]_T$-4 Laminate with Clamped Side Boundary Conditions

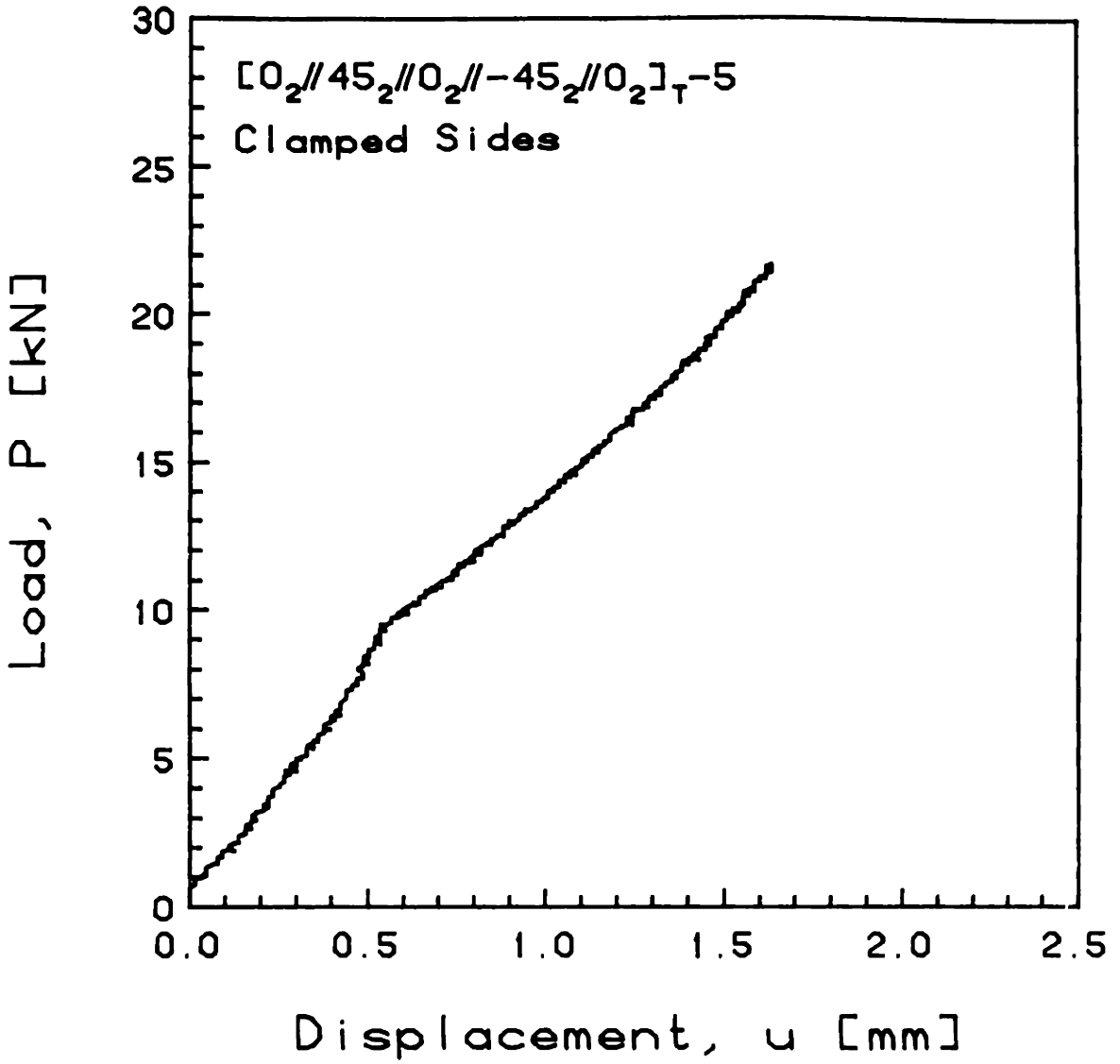

FIGURE G.23 Experimental Plot of Applied Compressive Load versus End-Shortening Displacement for the $[O_2//45_2//O_2//-45_2//O_2]_T$-5 Laminate with Clamped Side Boundary Conditions

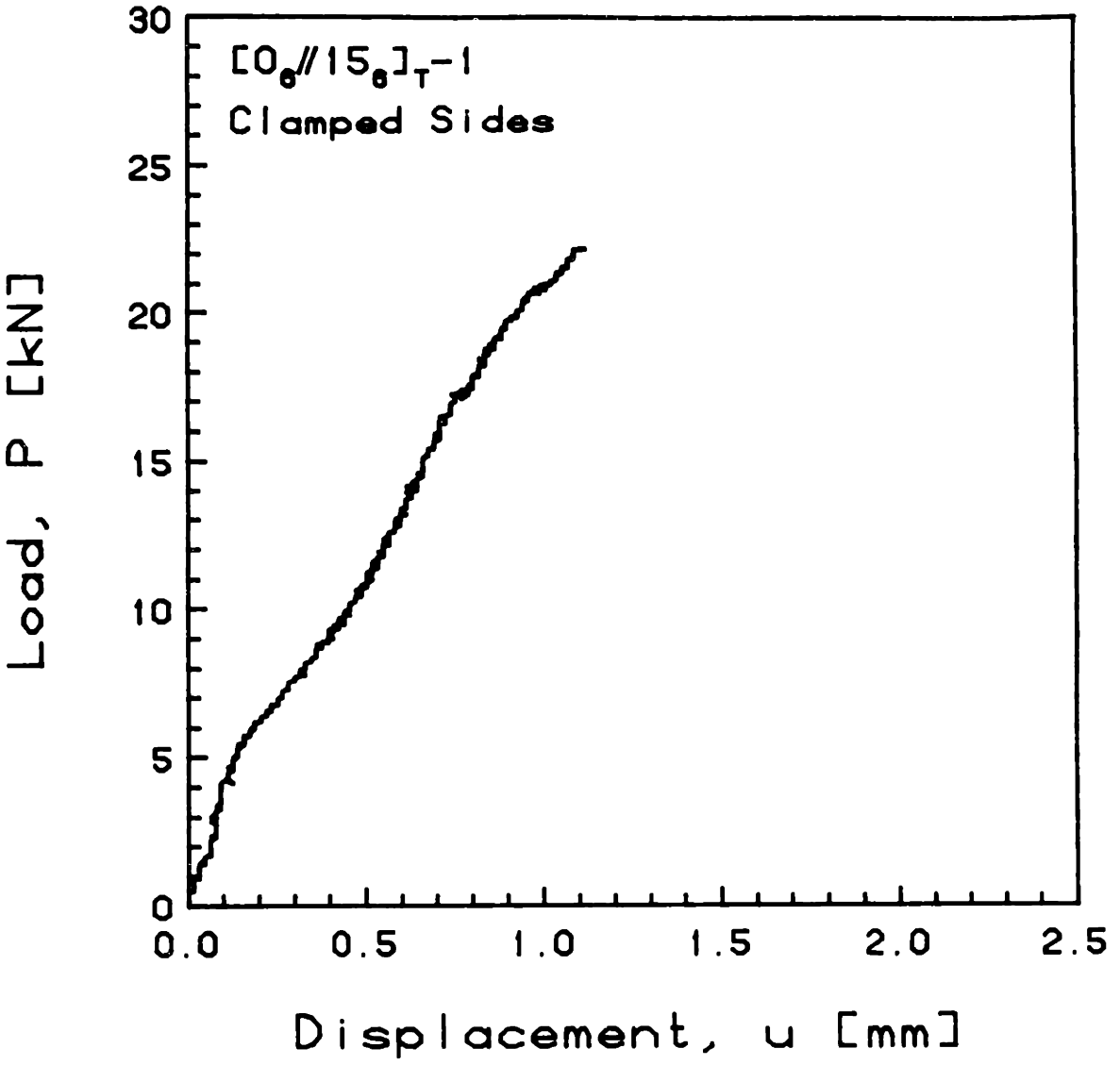

FIGURE G.24 Experimental Plot of Applied Compressive Load versus End-Shortening Displacement for the $[0_6//15_6]_T$-1 Laminate with Clamped Side Boundary Conditions

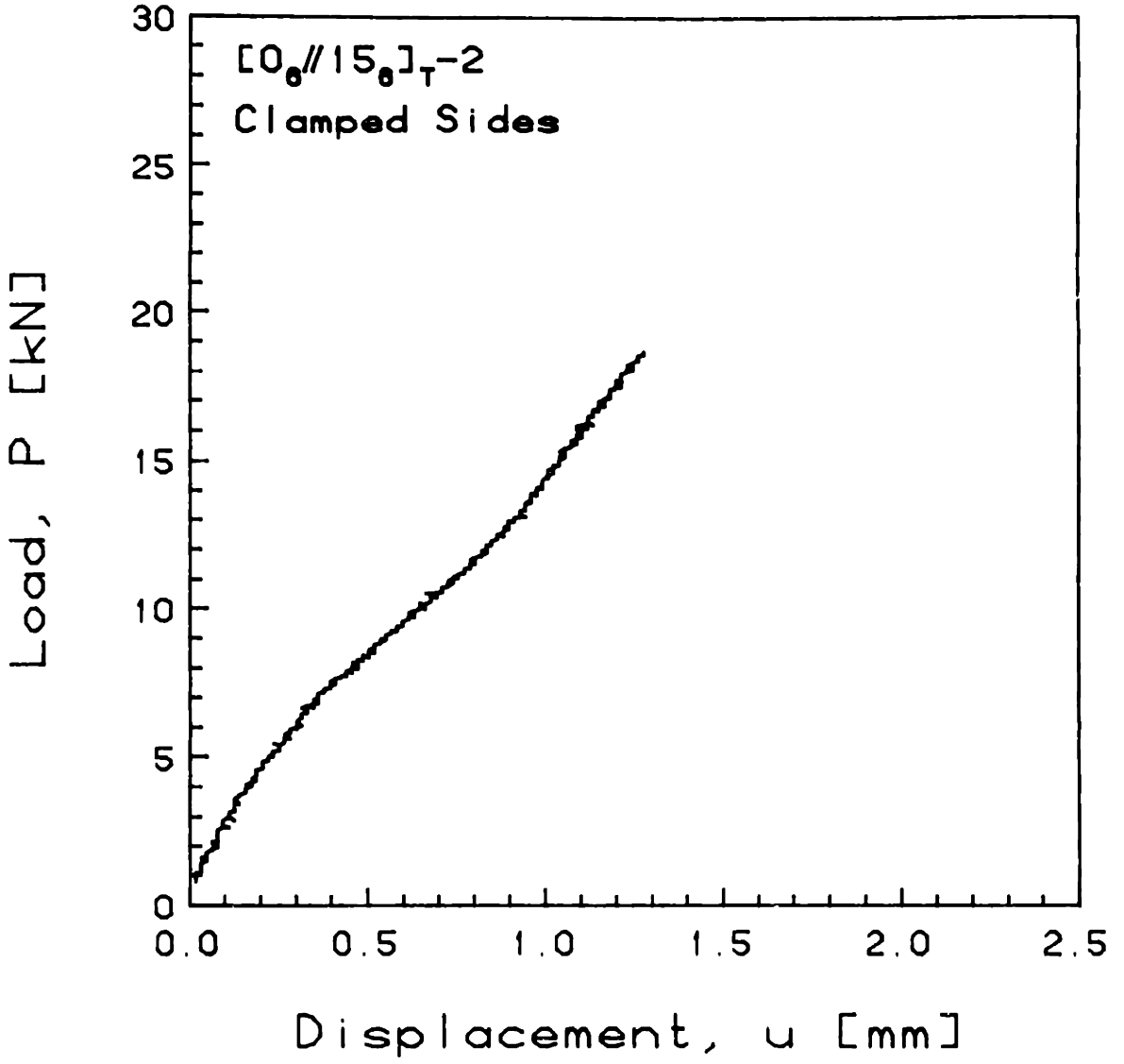

FIGURE G.25 Experimental Plot of Applied Compressive Load versus End-Shortening Displacement for the $[0_6//15_6]_T$-2 Laminate with Clamped Side Boundary Conditions

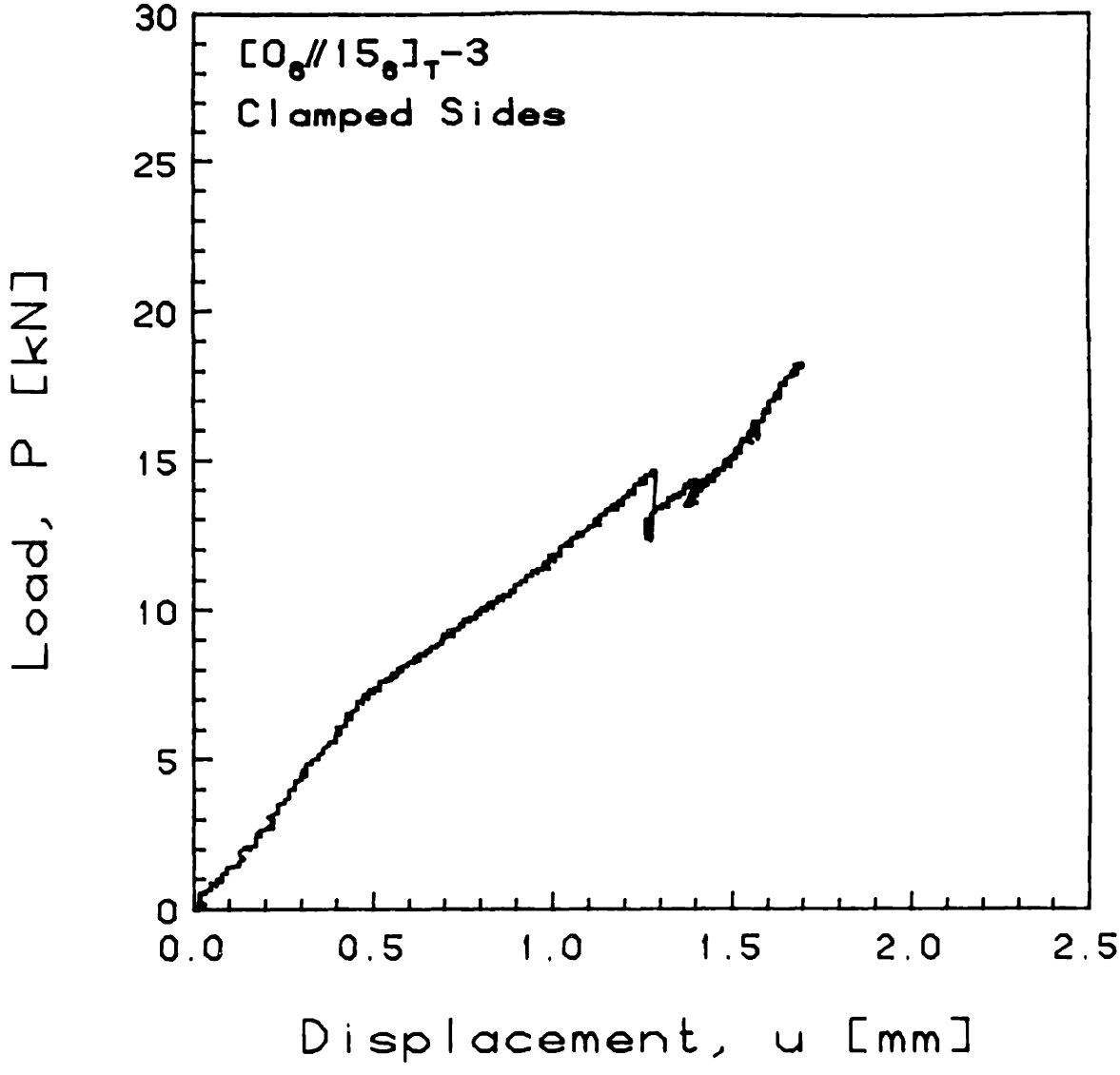

FIGURE G.26 Experimental Plot of Applied Compressive Load versus End-Shortening Displacement for the $[O_6//15_6]_T$-3 Laminate with Clamped Side Boundary Conditions

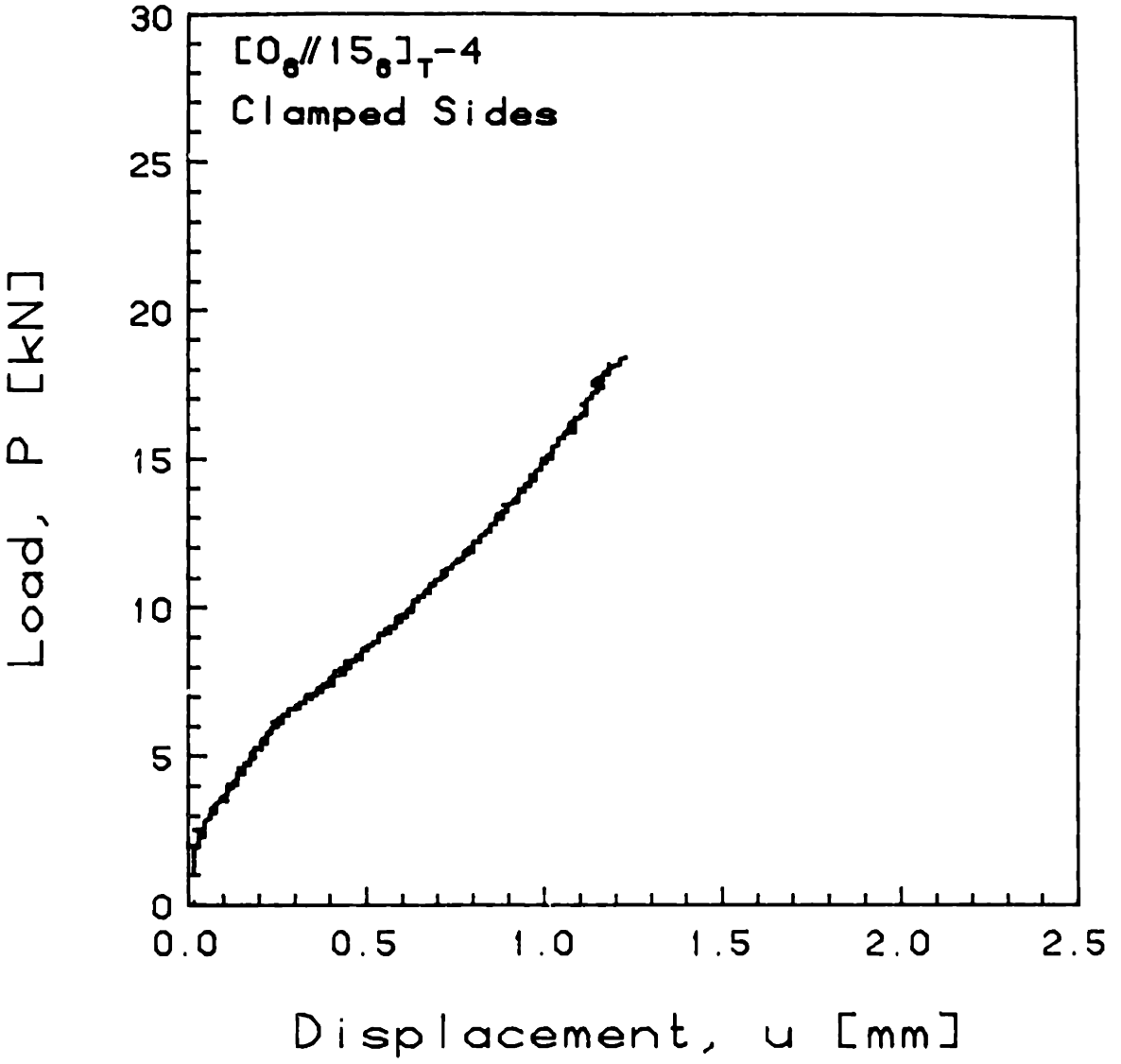

FIGURE G.27 Experimental Plot of Applied Compressive Load versus End-Shortening Displacement for the $[O_6//15_6]_T$-4 Laminate with Clamped Side Boundary Conditions

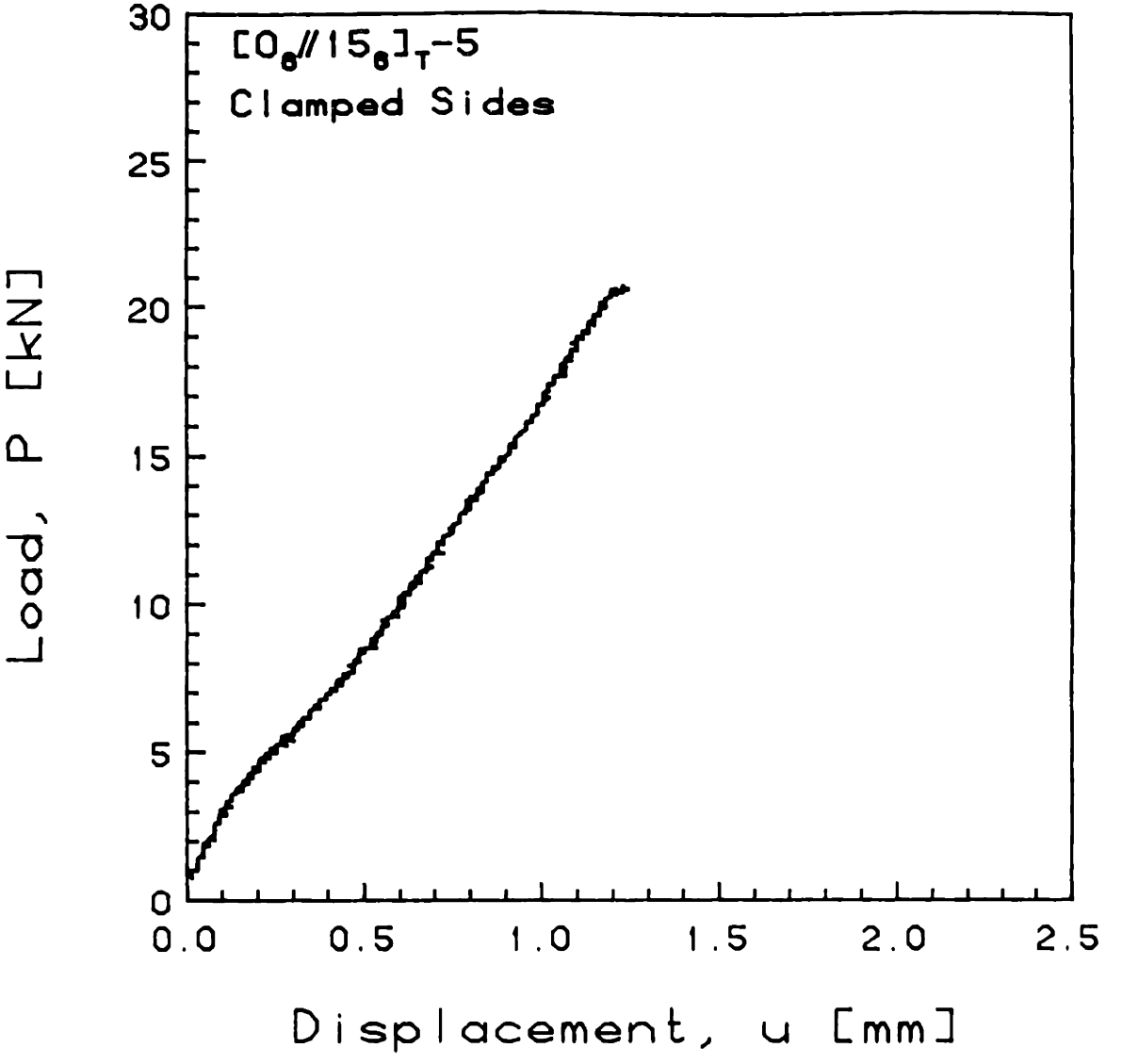

FIGURE G.28 Experimental Plot of Applied Compressive Load versus End-Shortening Displacement for the $[0_6//15_6]_T$-5 Laminate with Clamped Side Boundary Conditions

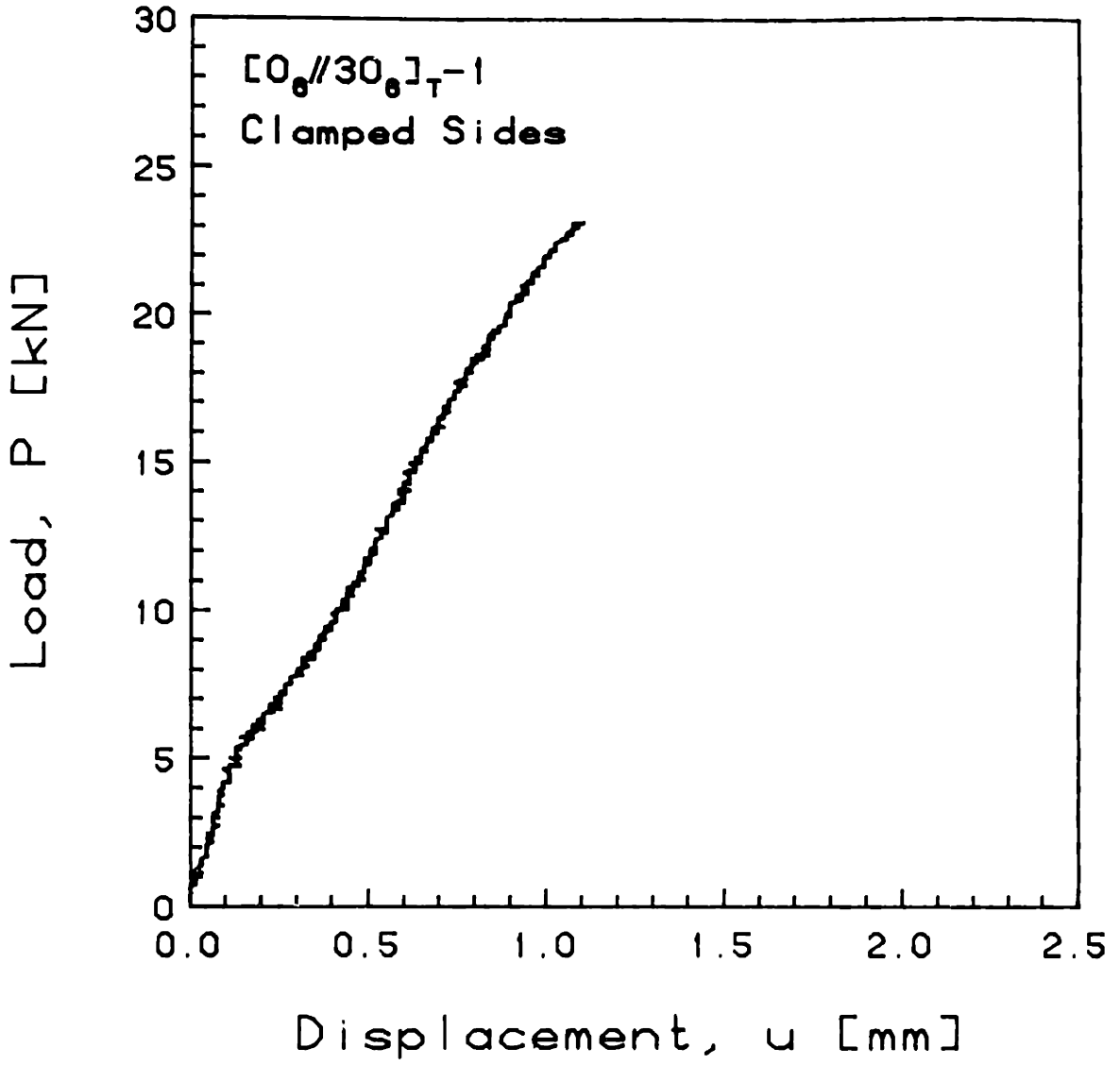

FIGURE G.29 Experimental Plot of Applied Compressive Load versus End-Shortening Displacement for the $[O_6//30_6]_T$-1 Laminate with Clamped Side Boundary Conditions

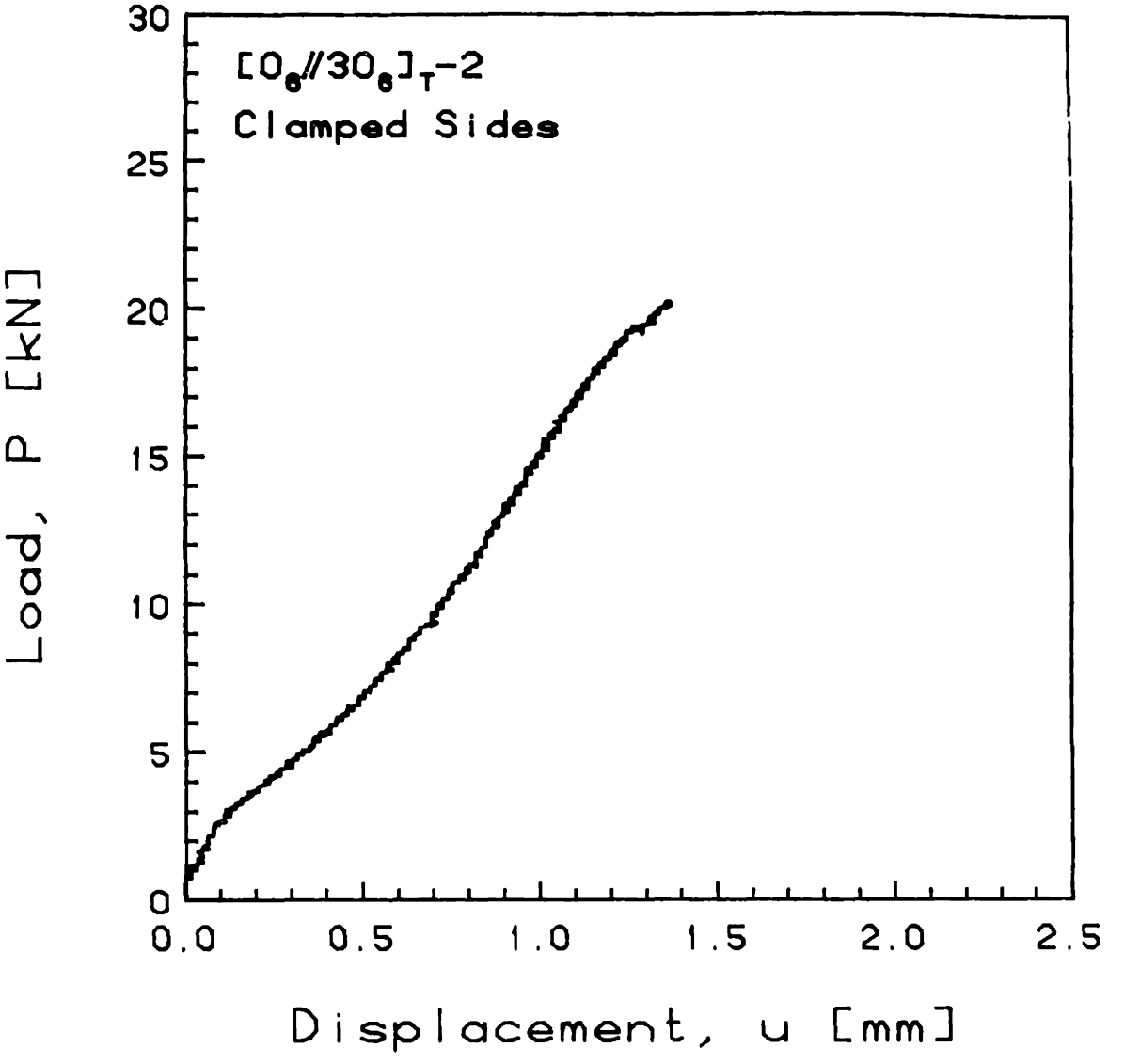

FIGURE G.30 Experimental Plot of Applied Compressive Load versus End-Shortening Displacement for the $[O_6//30_6]_T$-2 Laminate with Clamped Side Boundary Conditions

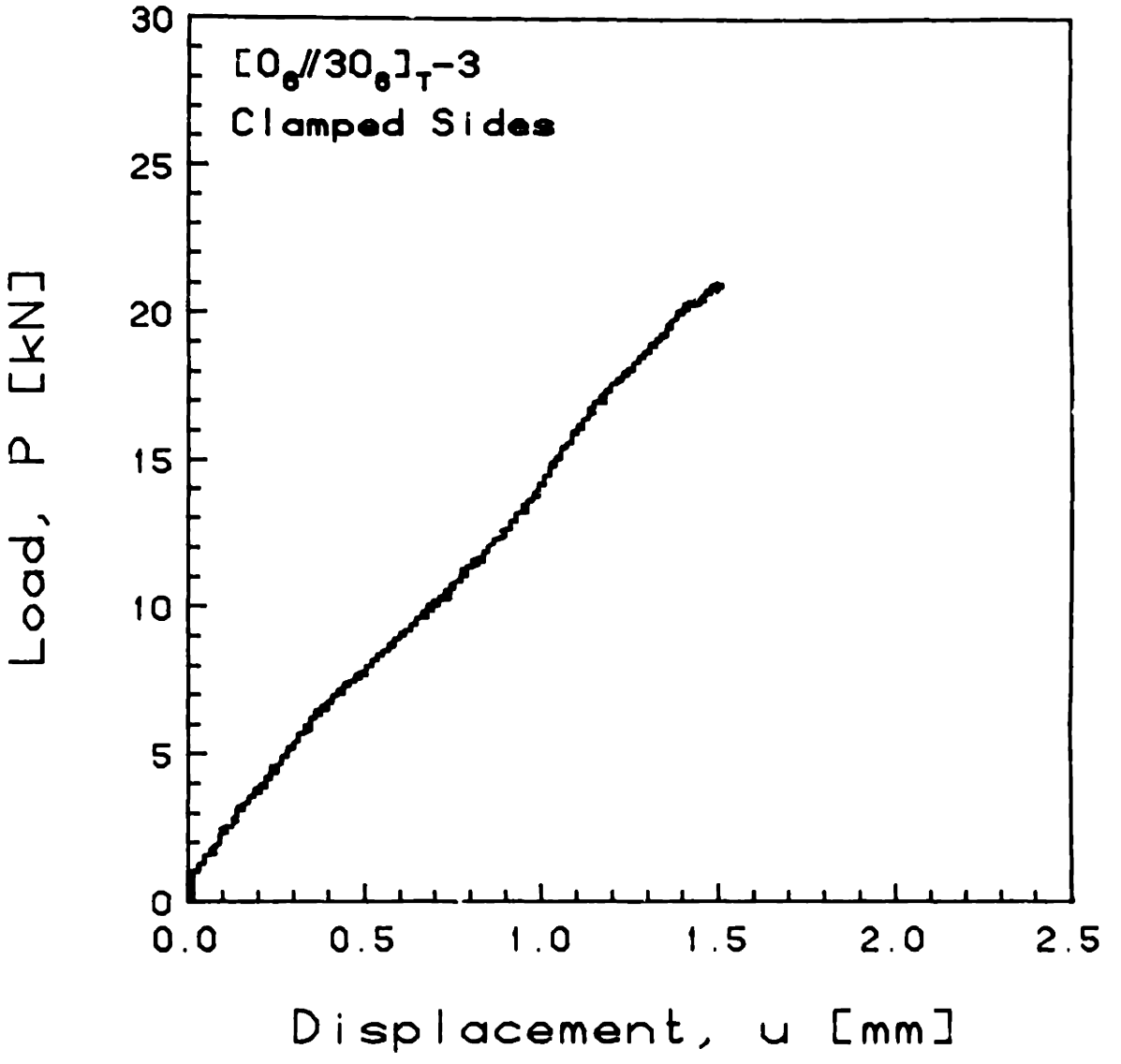

FIGURE G.31 Experimental Plot of Applied Compressive Load versus End-Shortening Displacement for the $[0_6//30_6]_T$-3 Laminate with Clamped Side Boundary Conditions

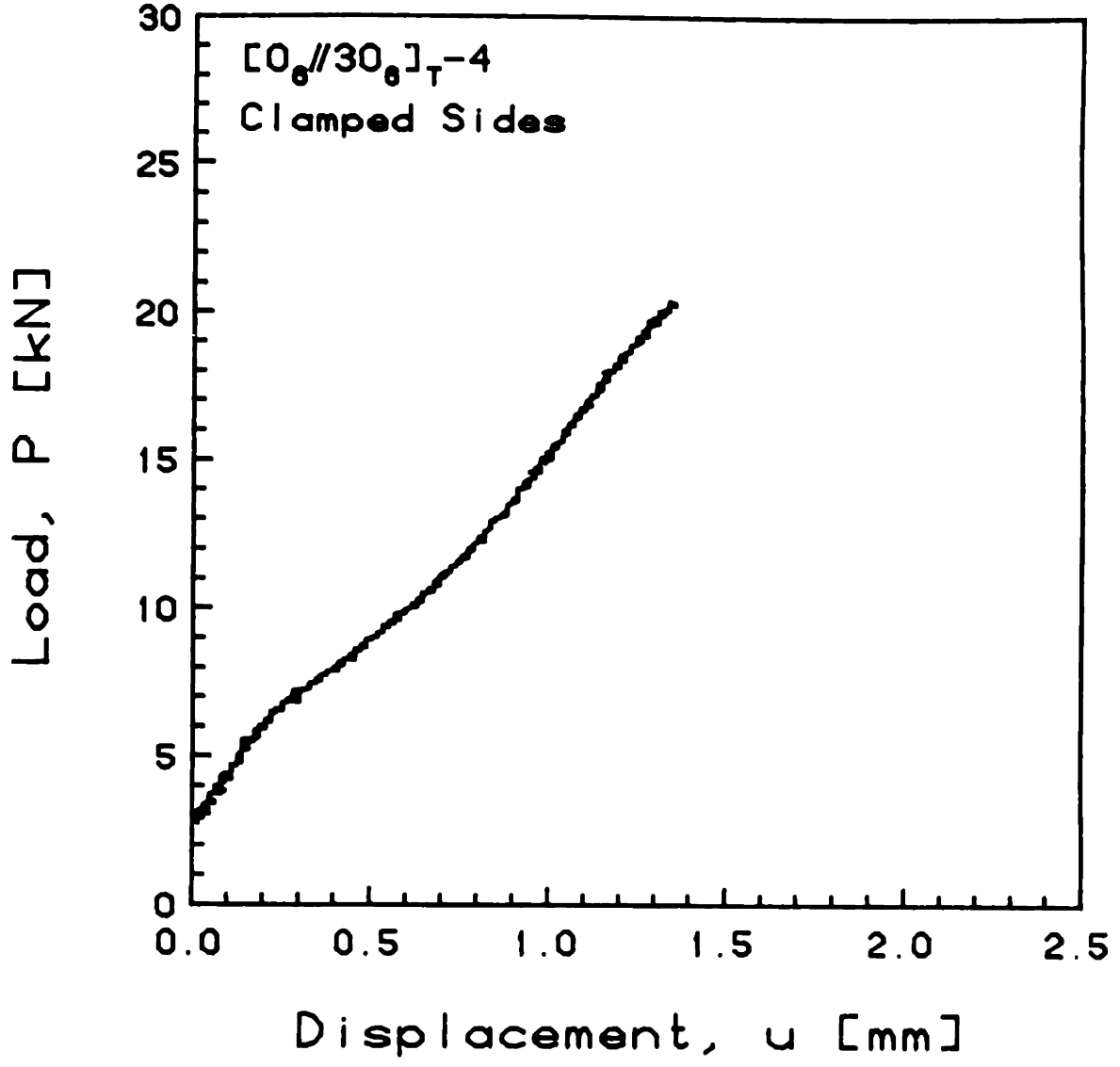

FIGURE G.32 Experimental Plot of Applied Compressive Load versus End-Shortening Displacement for the $[0_6//30_6]_T$-4 Laminate with Clamped Side Boundary Conditions

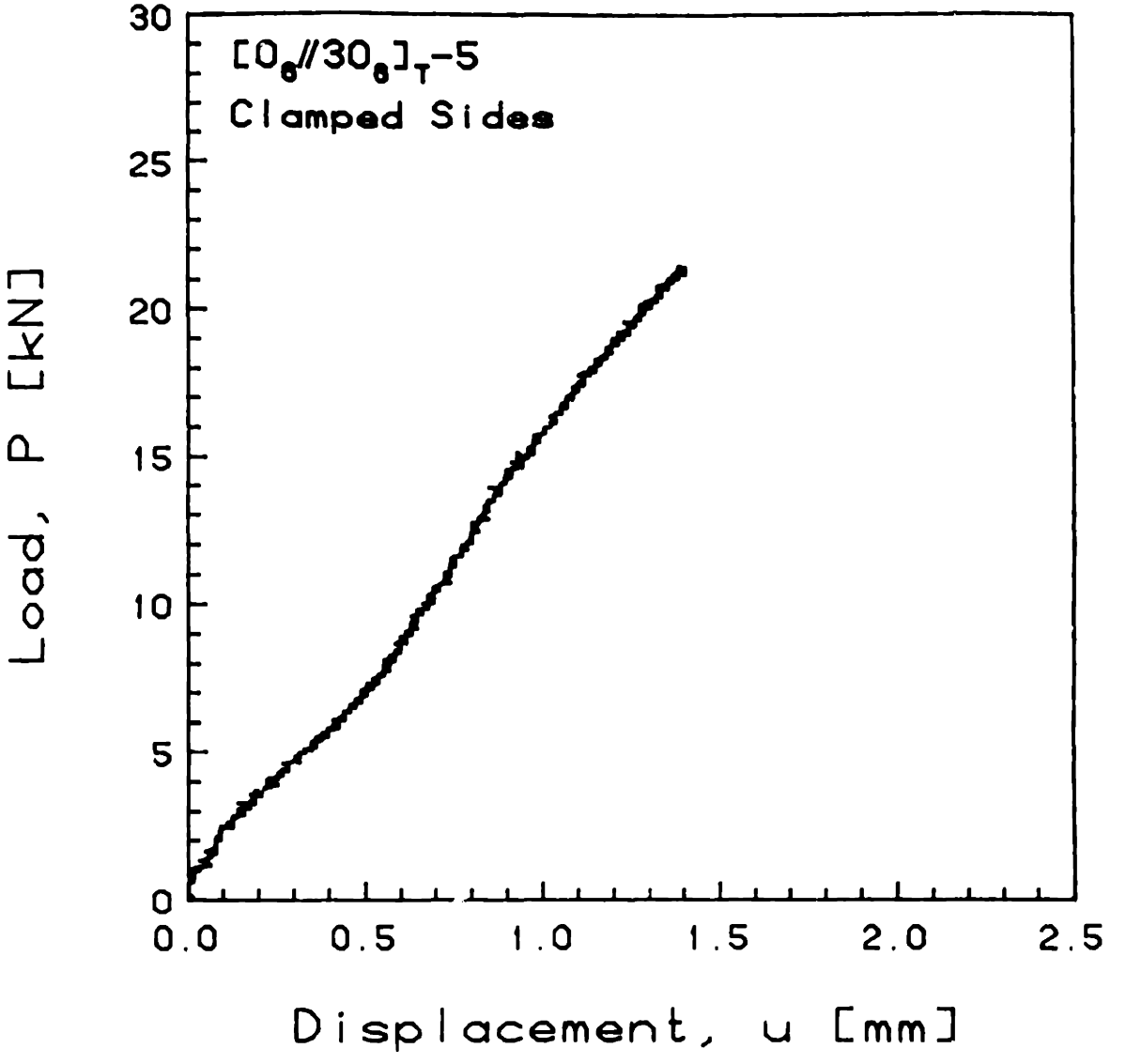

FIGURE G.33 Experimental Plot of Applied Compressive Load versus End-Shortening Displacement for the $[0_6//30_6]_T$-5 Laminate with Clamped Side Boundary Conditions

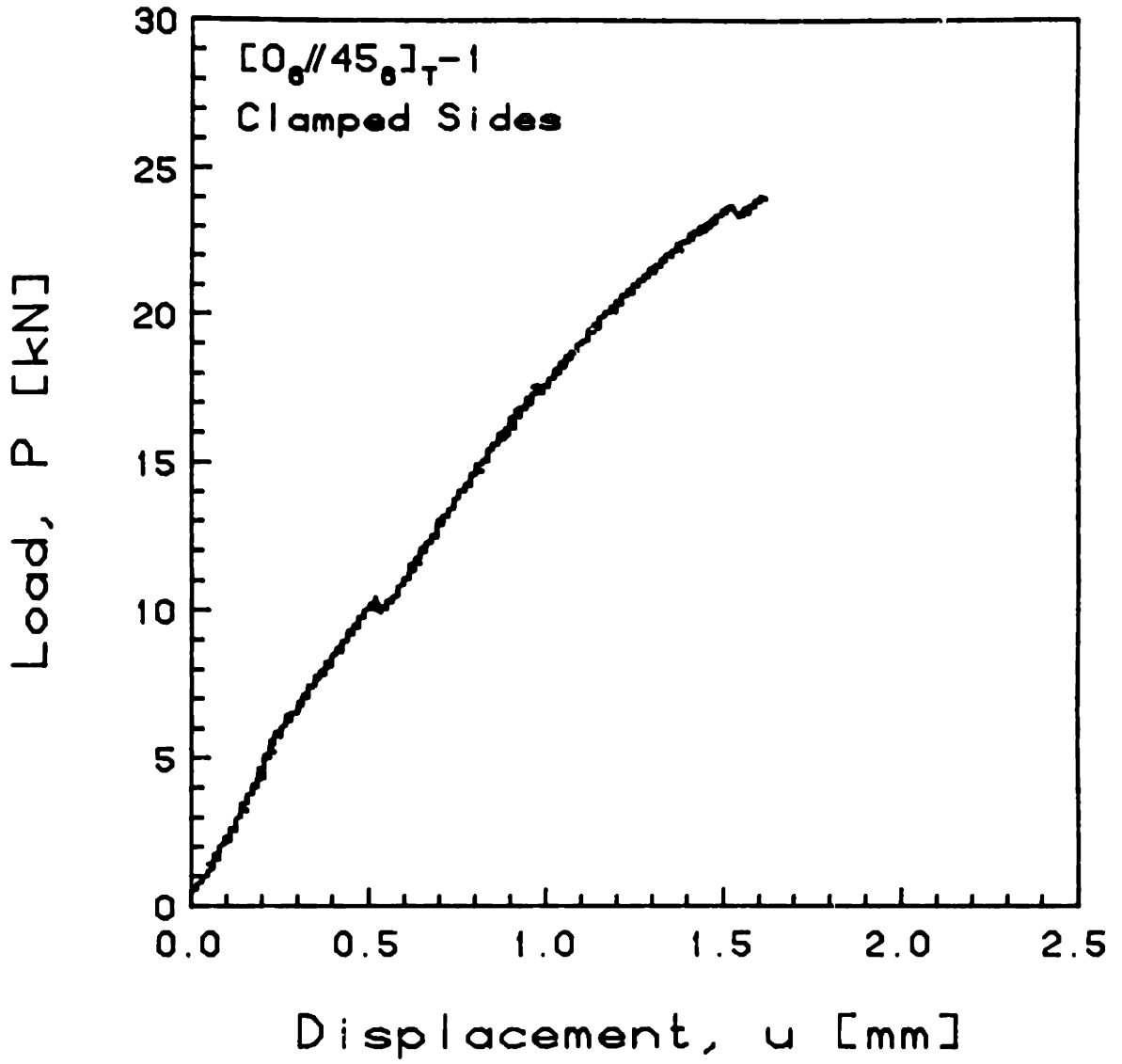

FIGURE G.34 Experimental Plot of Applied Compressive Load versus End-Shortening Displacement for the $[O_6//45_6]_T$-1 Laminate with Clamped Side Boundary Conditions

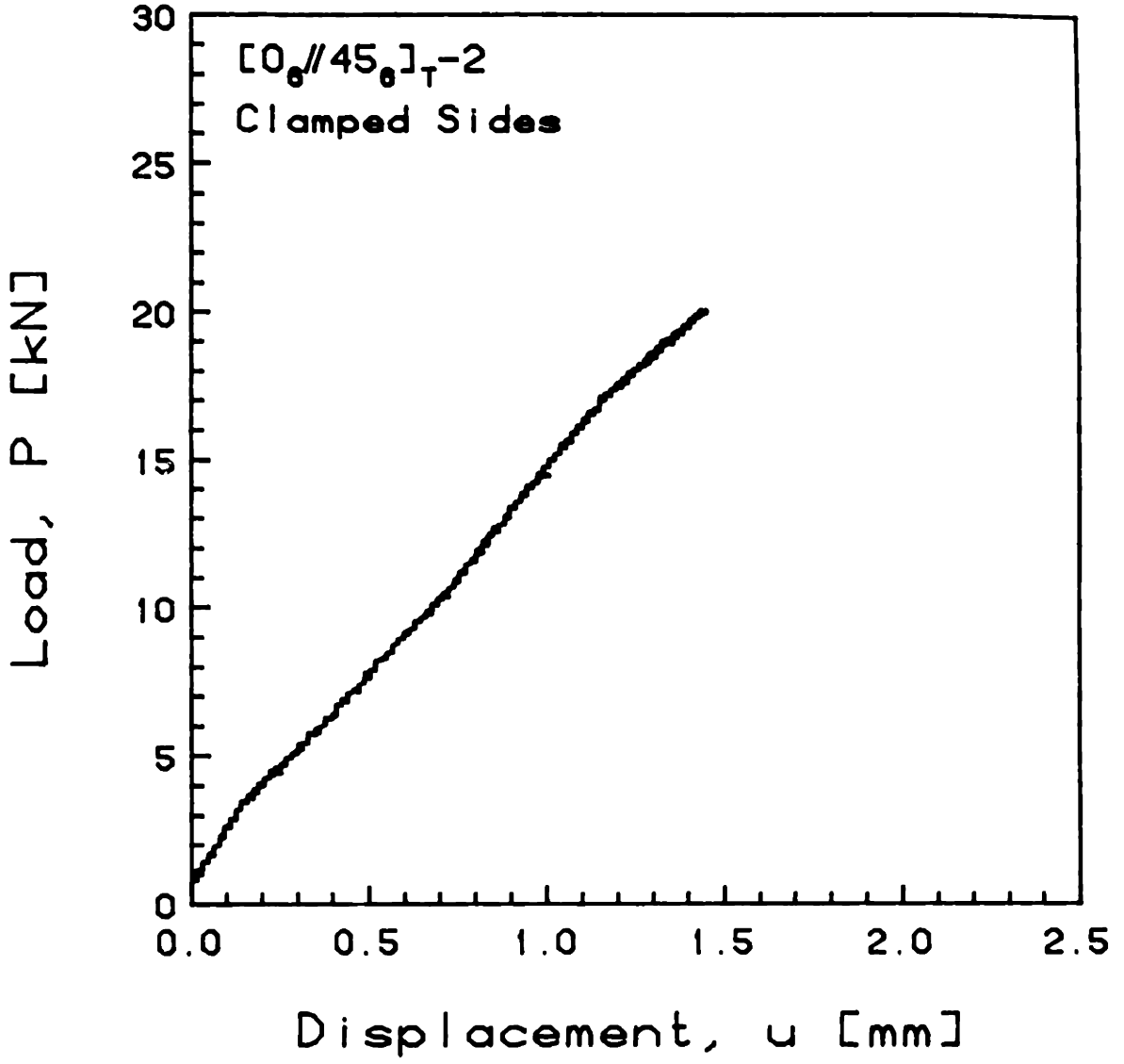

FIGURE G.35 Experimental Plot of Applied Compressive Load versus End-Shortening Displacement for the $[O_6//45_6]_T$-2 Laminate with Clamped Side Boundary Conditions

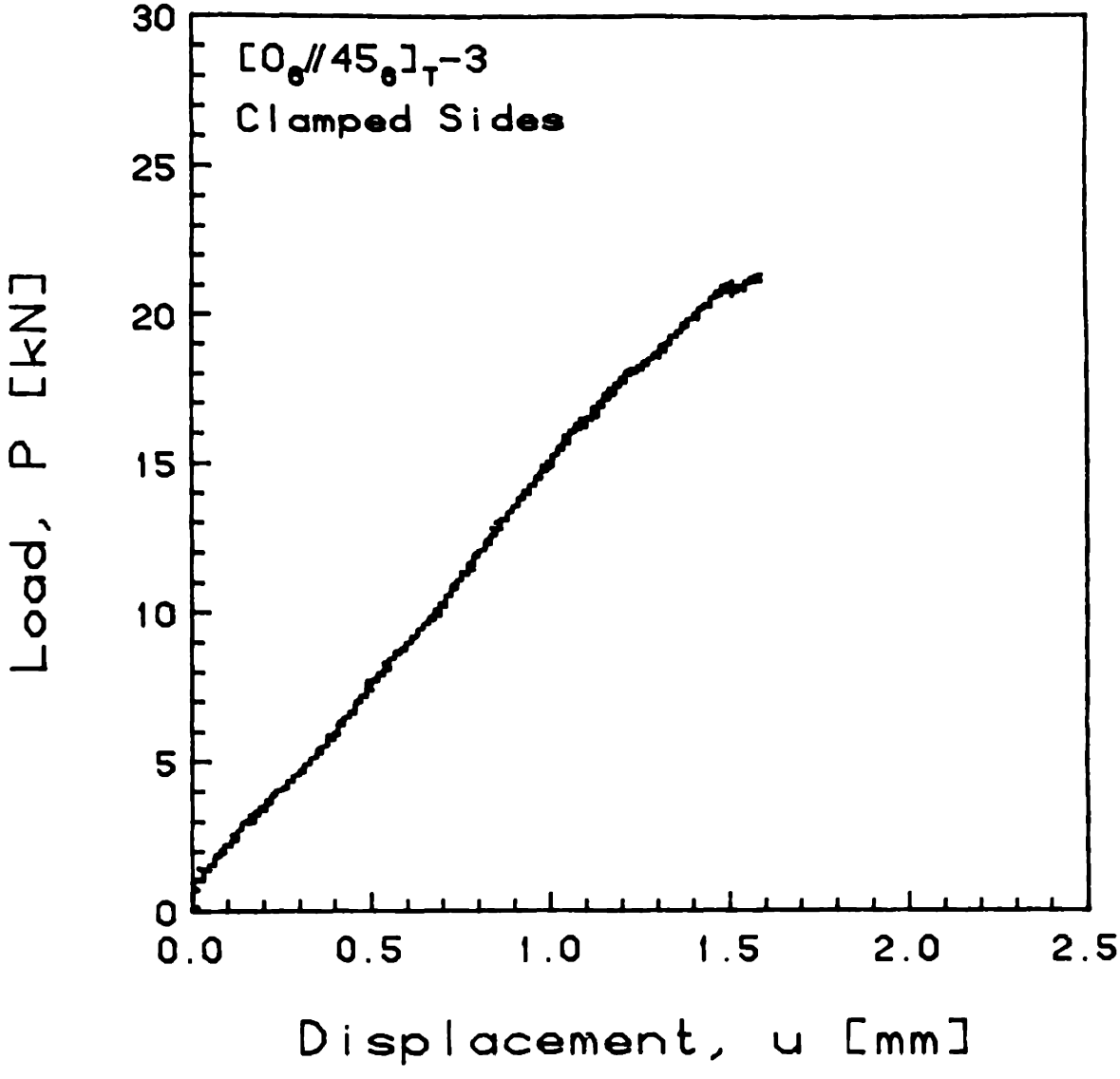

FIGURE G.36 Experimental Plot of Applied Compressive Load versus End-Shortening Displacement for the $[O_6//45_6]_T$-3 Laminate with Clamped Side Boundary Conditions

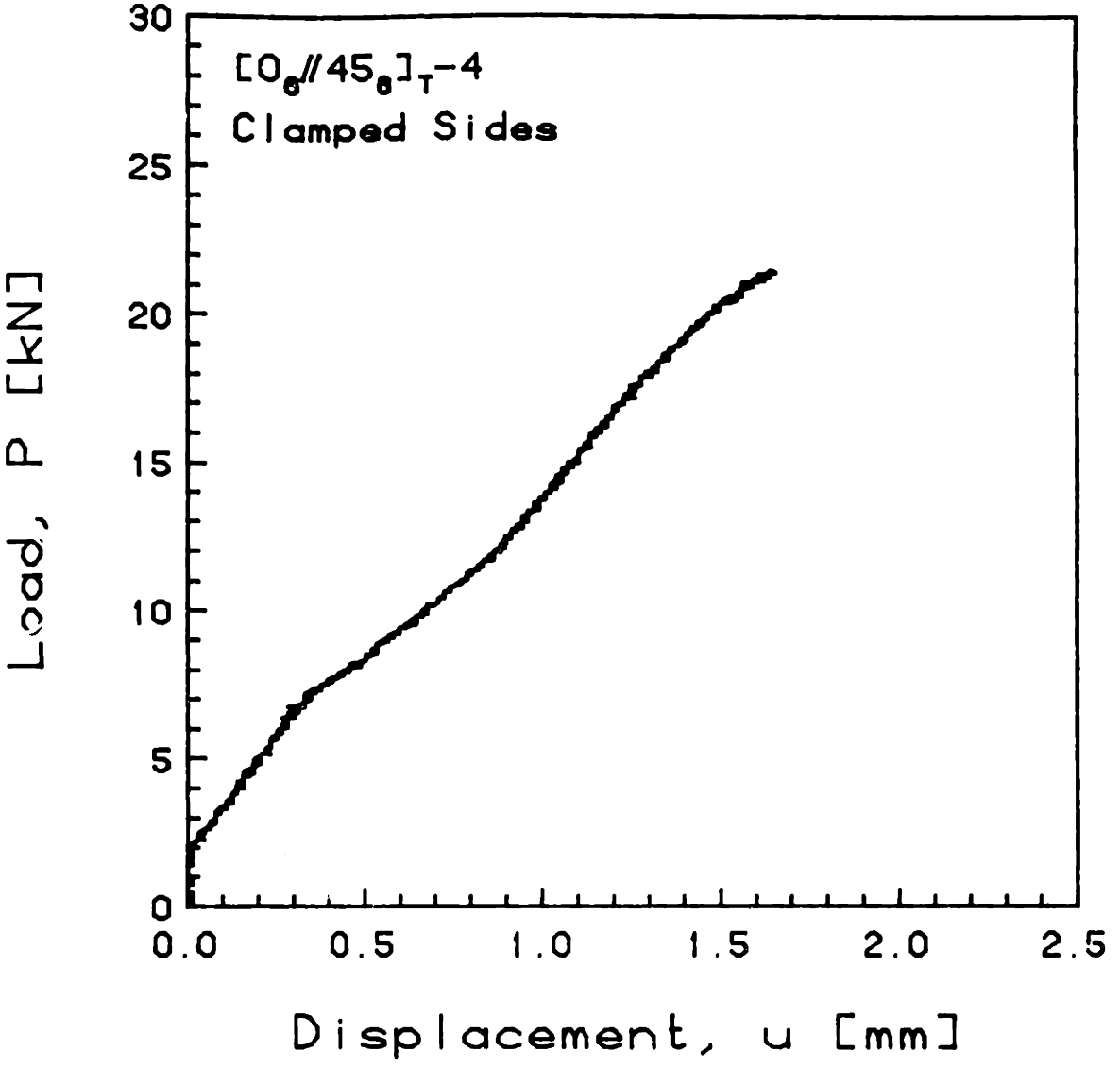

FIGURE G.37 Experimental Plot of Applied Compressive Load versus End-Shortening Displacement for the $[0_6//45_6]_T$-4 Laminate with Clamped Side Boundary Conditions

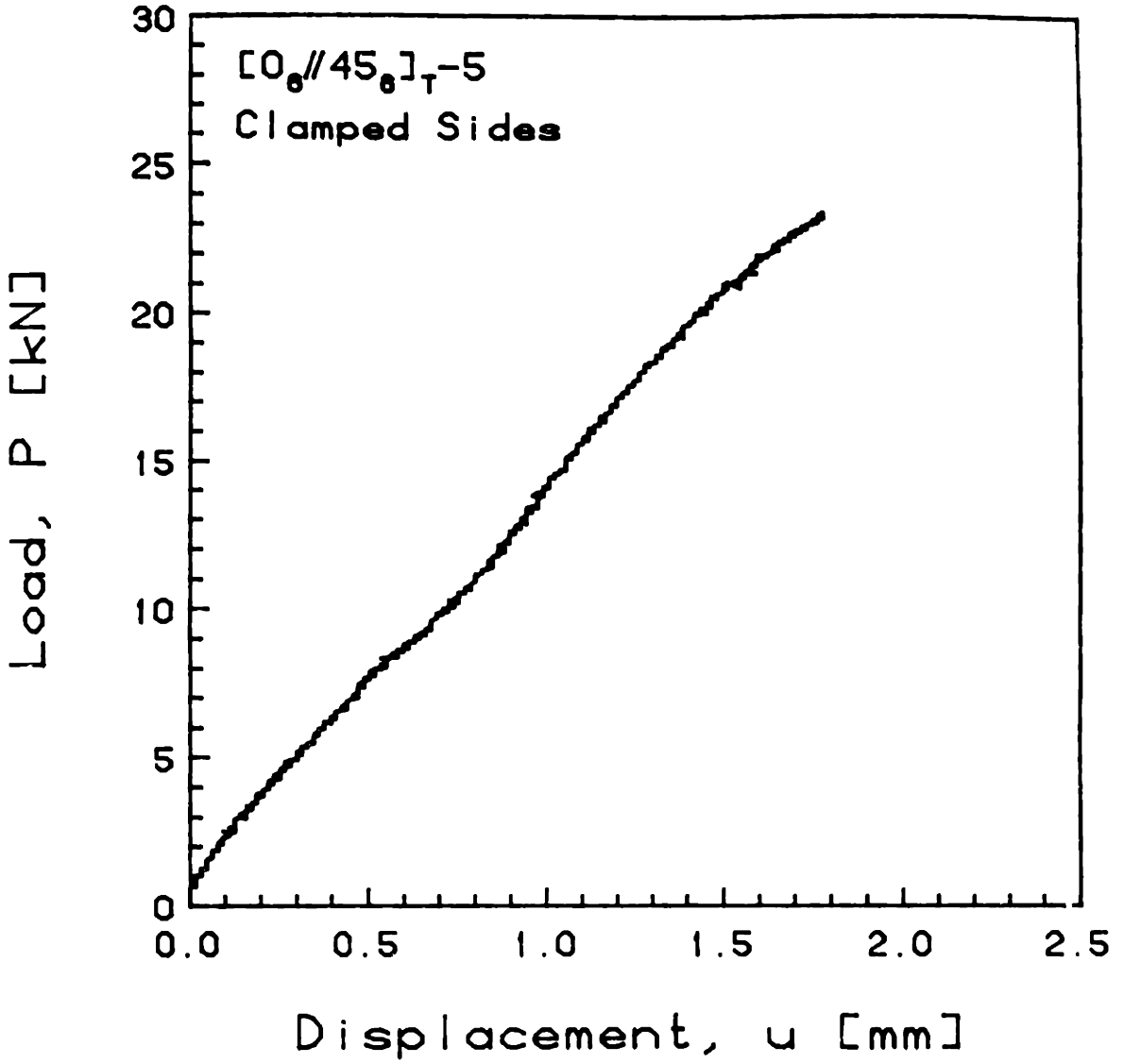

FIGURE G.38 Experimental Plot of Applied Compressive Load versus End-Shortening Displacement for the $[0_6//45_6]_T$-5 Laminate with Clamped Side Boundary Conditions

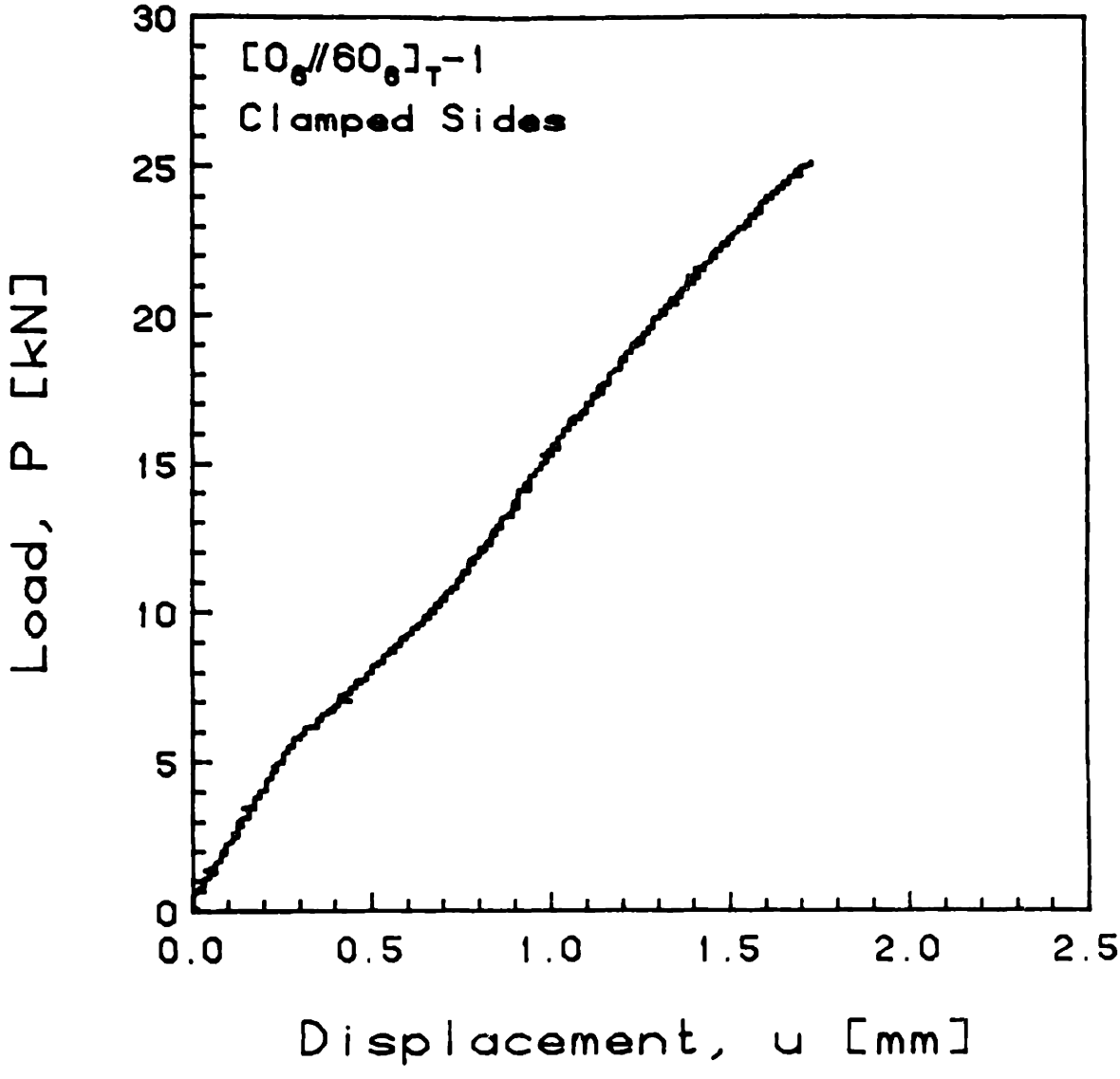

FIGURE G.39 Experimental Plot of Applied Compressive Load versus End-Shortening Displacement for the $[0_6//60_6]_T$-1 Laminate with Clamped Side Boundary Conditions

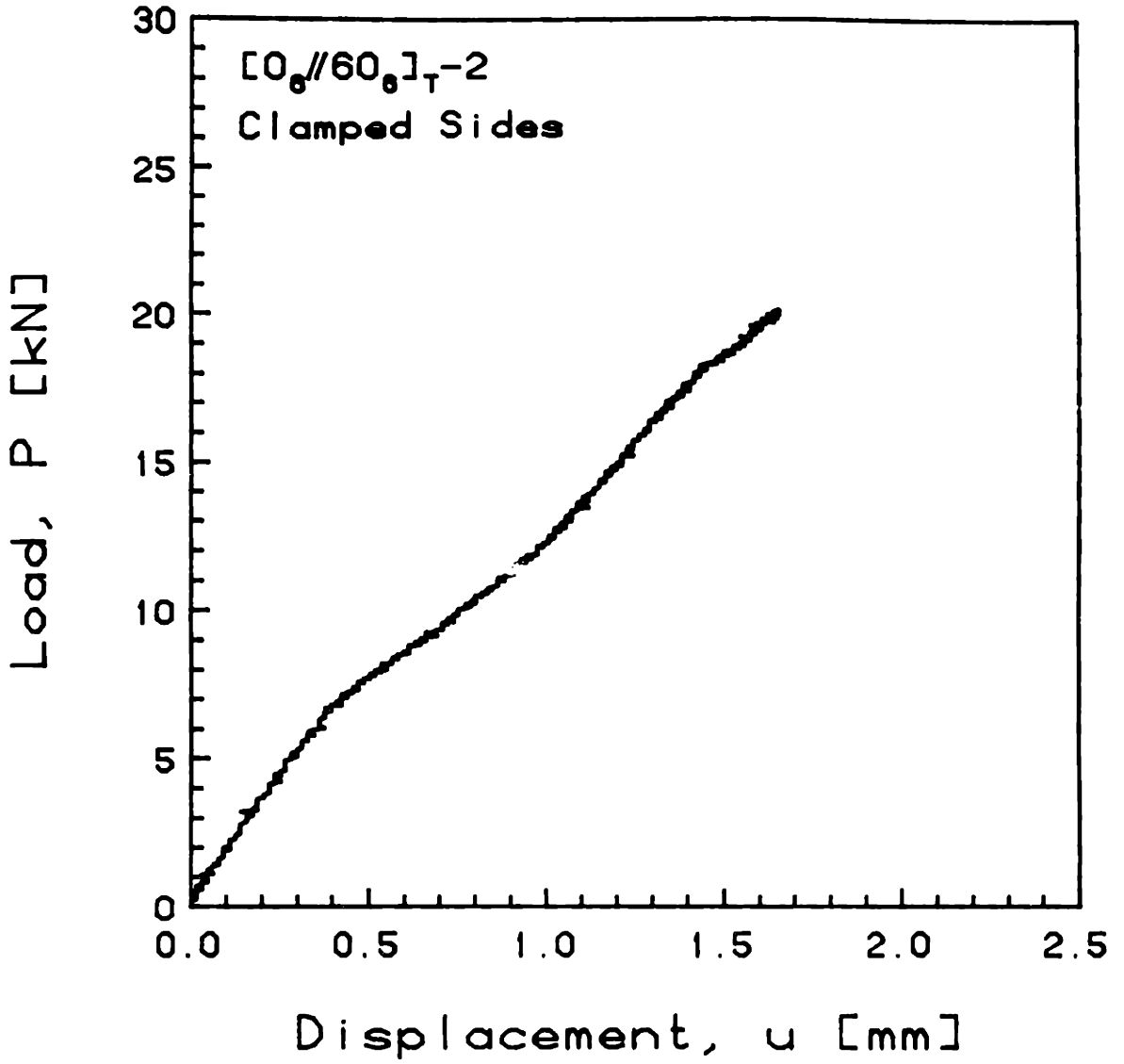

FIGURE G.40 Experimental Plot of Applied Compressive Load versus End-Shortening Displacement for the $[0_6//60_6]_T$-2 Laminate with Clamped Side Boundary Conditions

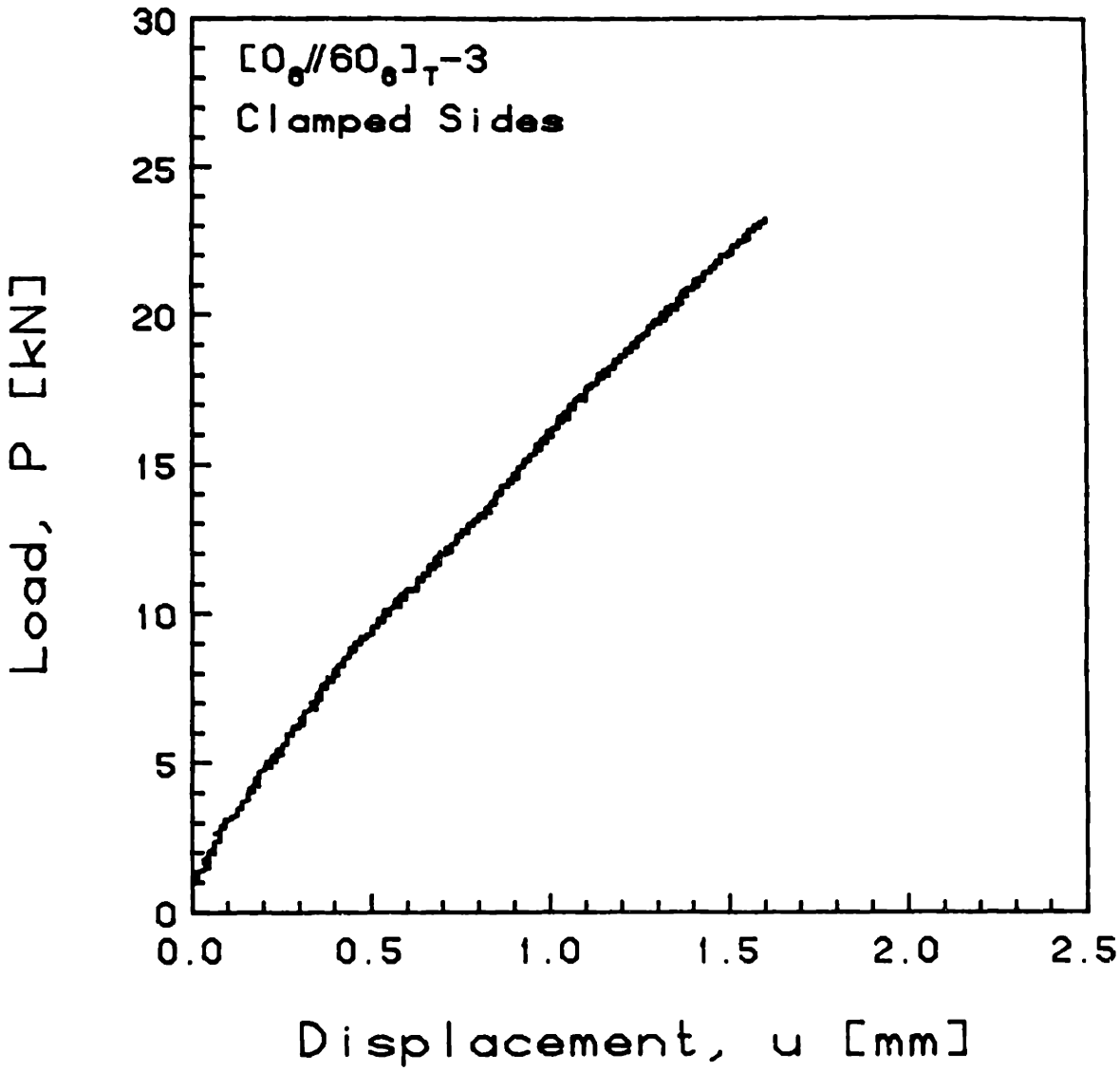

FIGURE G.41 Experimental Plot of Applied Compressive Load versus End-Shortening Displacement for the $[O_6//60_6]_T$-3 Laminate with Clamped Side Boundary Conditions

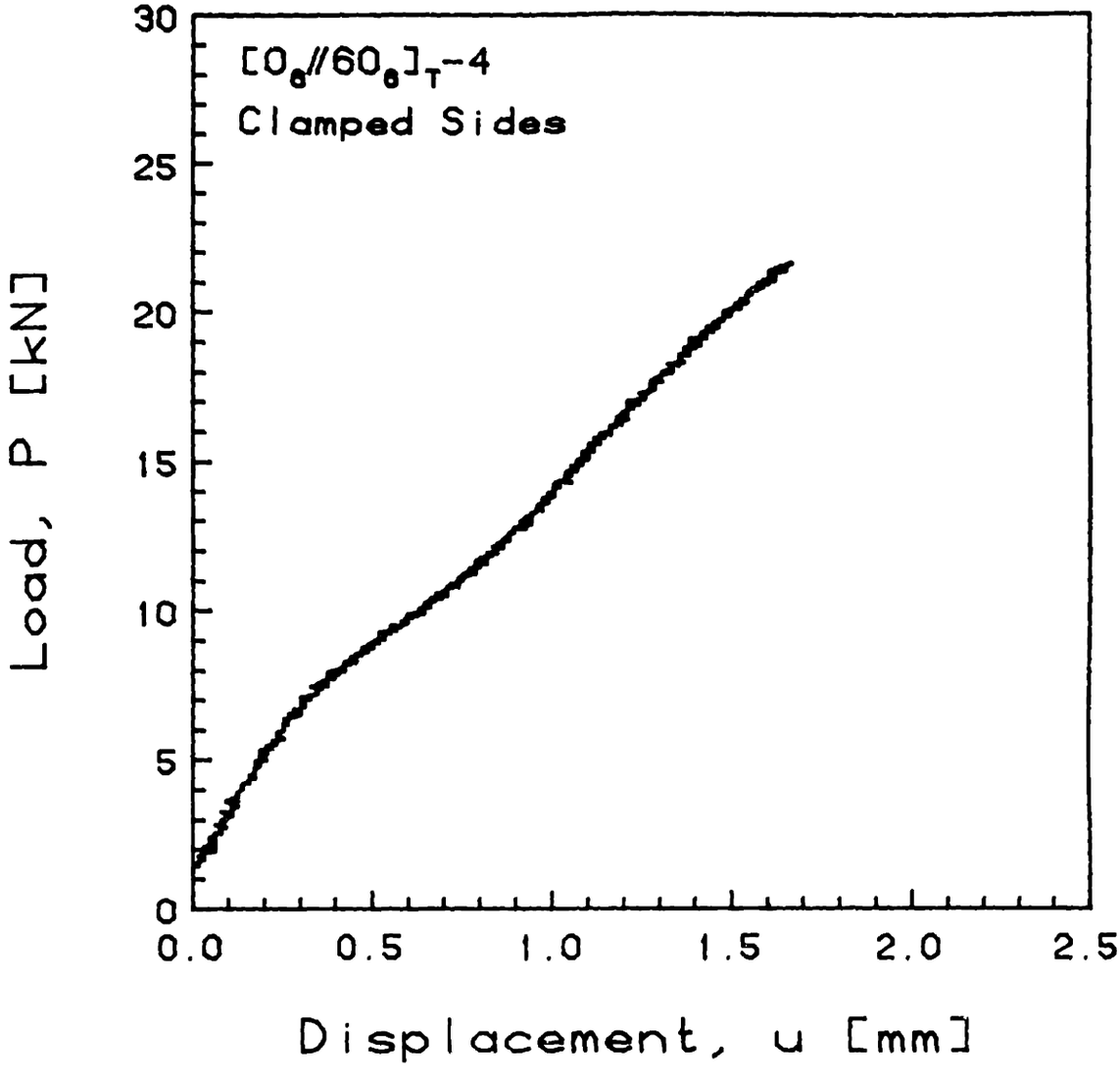

FIGURE G.42 Experimental Plot of Applied Compressive Load versus End-Shortening Displacement for the $[0_6//6C_s]_T$-4 Laminate with Clamped Side Boundary Conditions

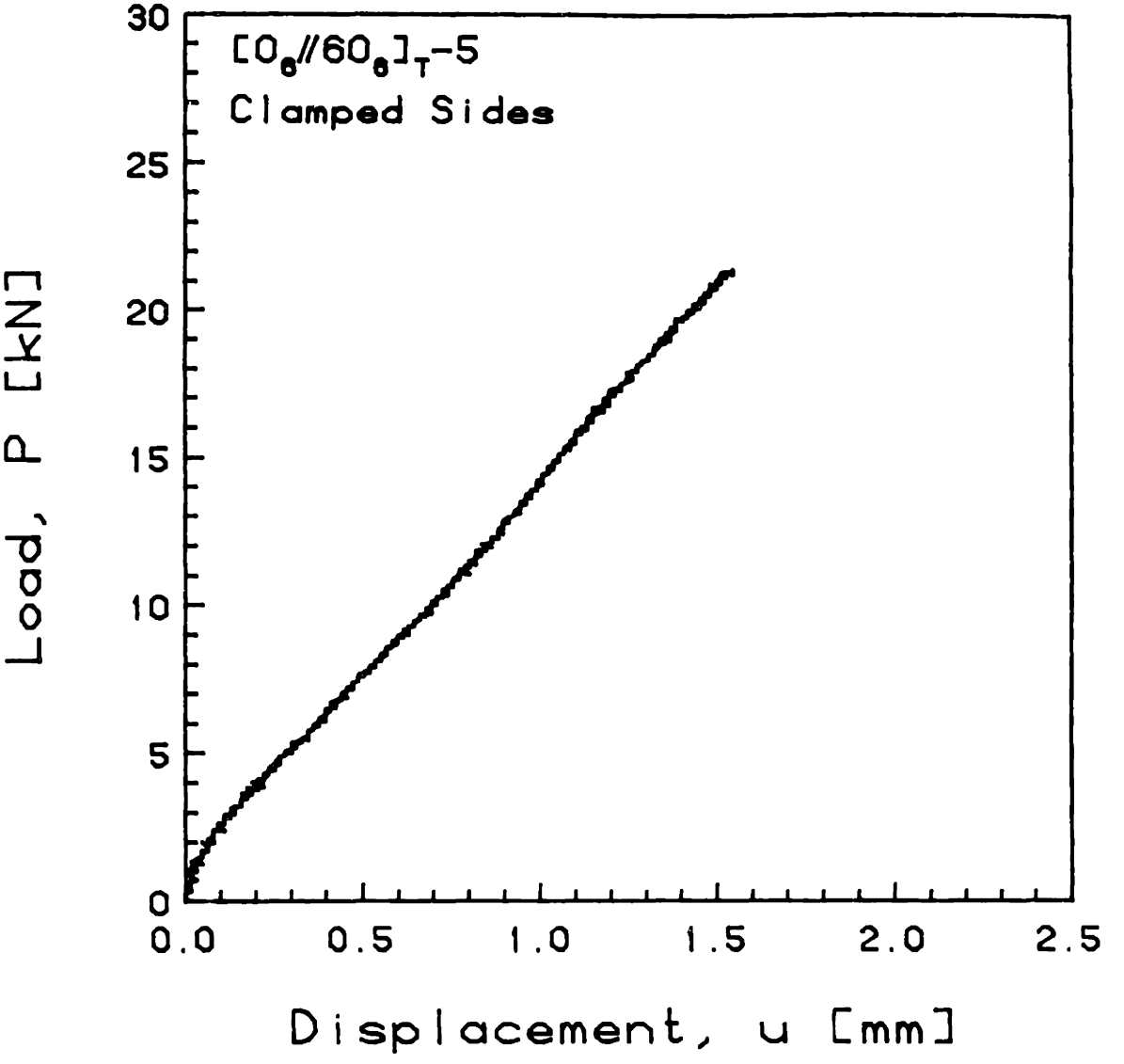

FIGURE G.43 Experimental Plot of Applied Compressive Load versus End-Shortening Displacement for the $[O_6//60_6]_T$-5 Laminate with Clamped Side Boundary Conditions

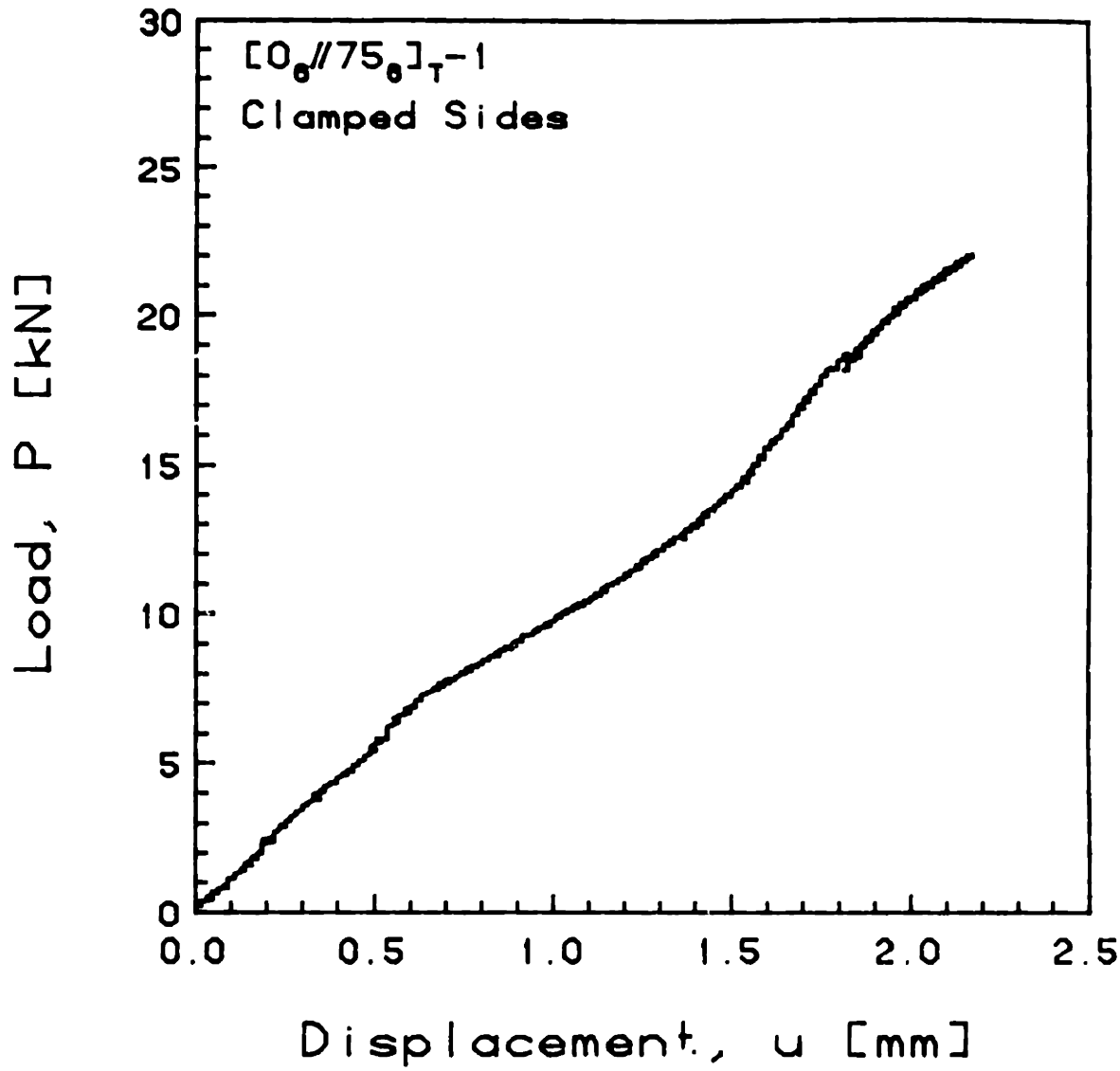

FIGURE G.44 Experimental Plot of Applied Compressive Load versus End-Shortening Displacement for the $[O_6//75_6]_T$-1 Laminate with Clamped Side Boundary Conditions

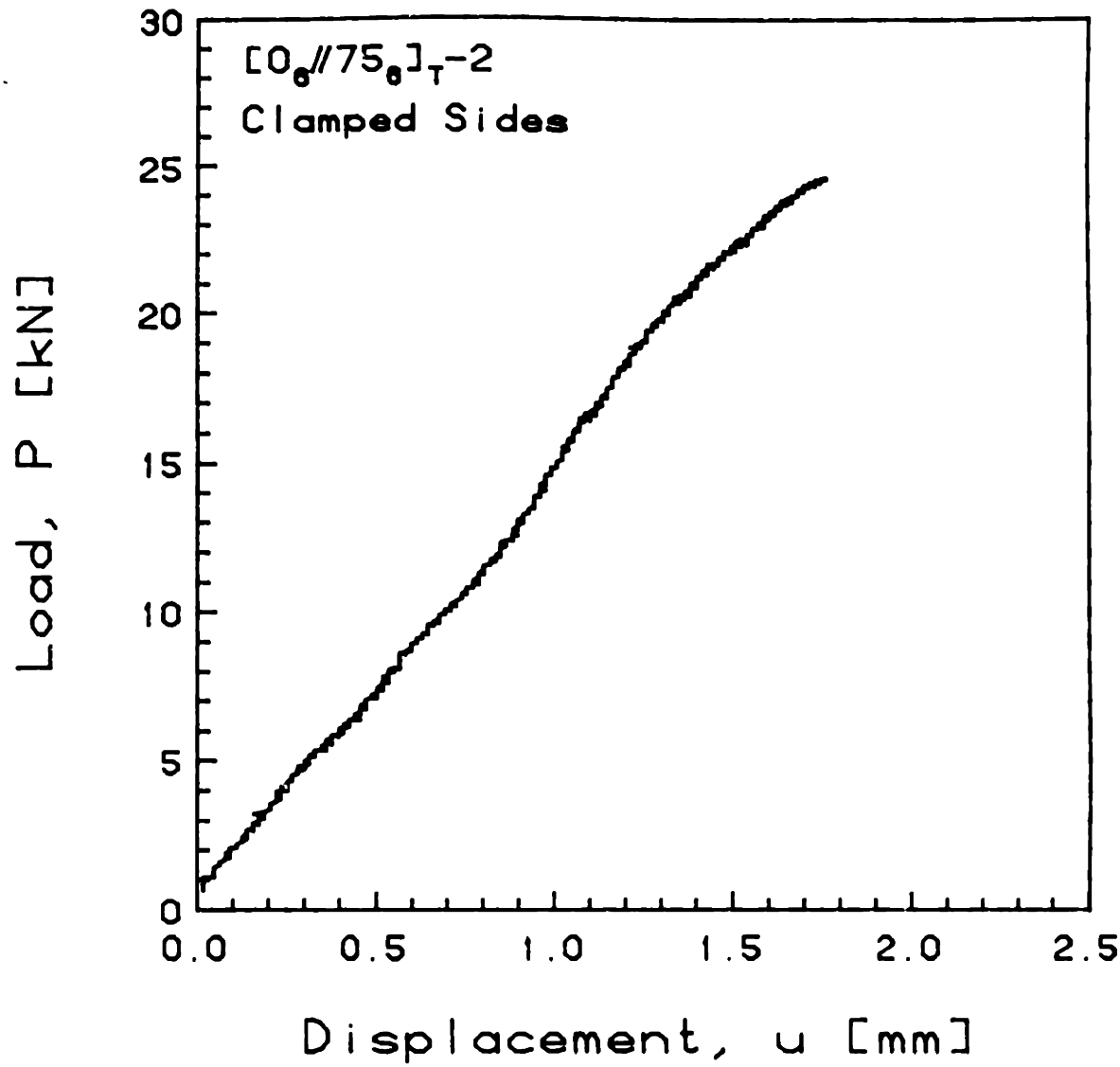

FIGURE G.45 Experimental Plot of Applied Compressive Load versus End-Shortening Displacement for the $[0_6//75_6]_T$-2 Laminate with Clamped Side Boundary Conditions

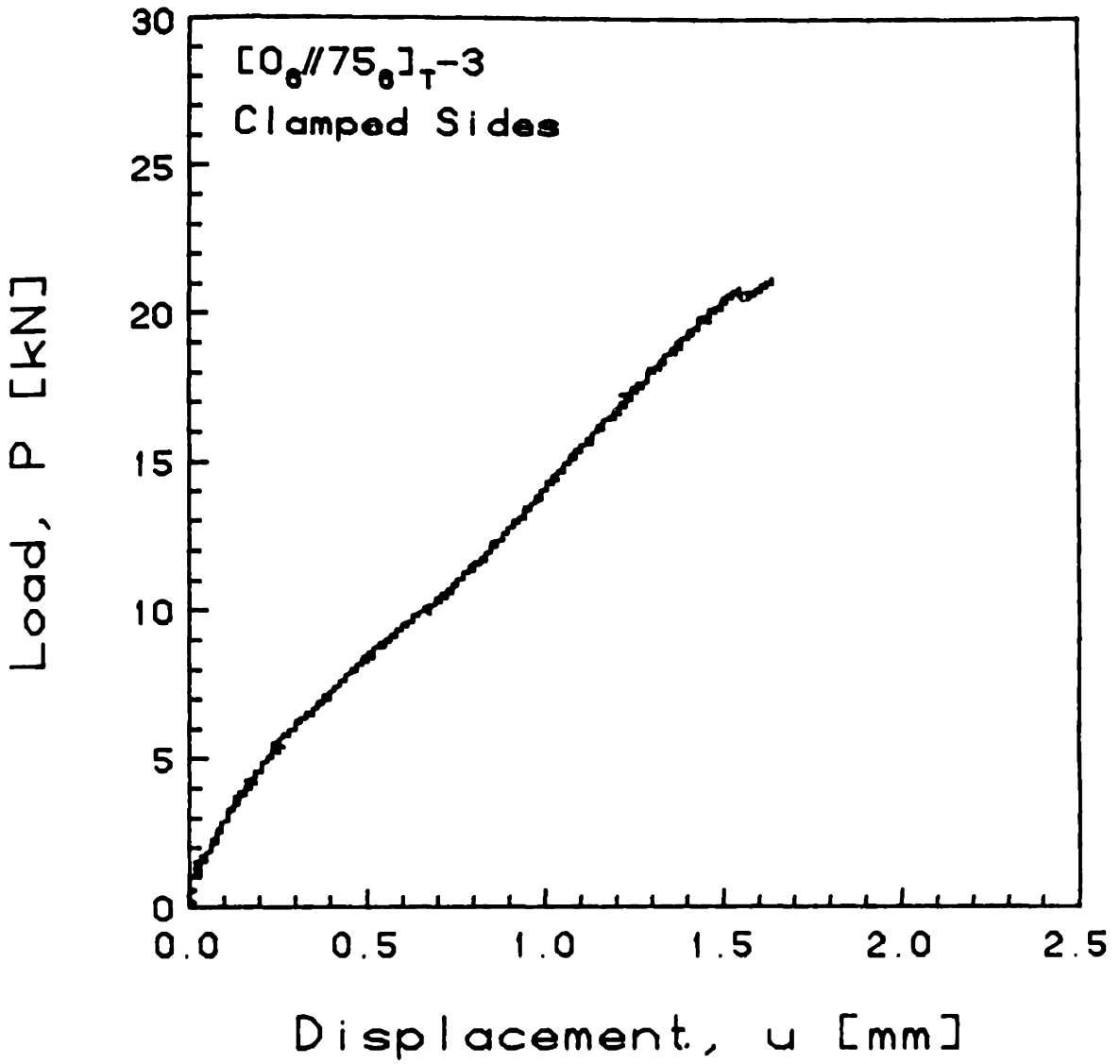

FIGURE G.46 Experimental Plot of Applied Compressive Load versus End-Shortening Displacement for the $[0_6//75_6]_T$-3 Laminate with Clamped Side Boundary Conditions

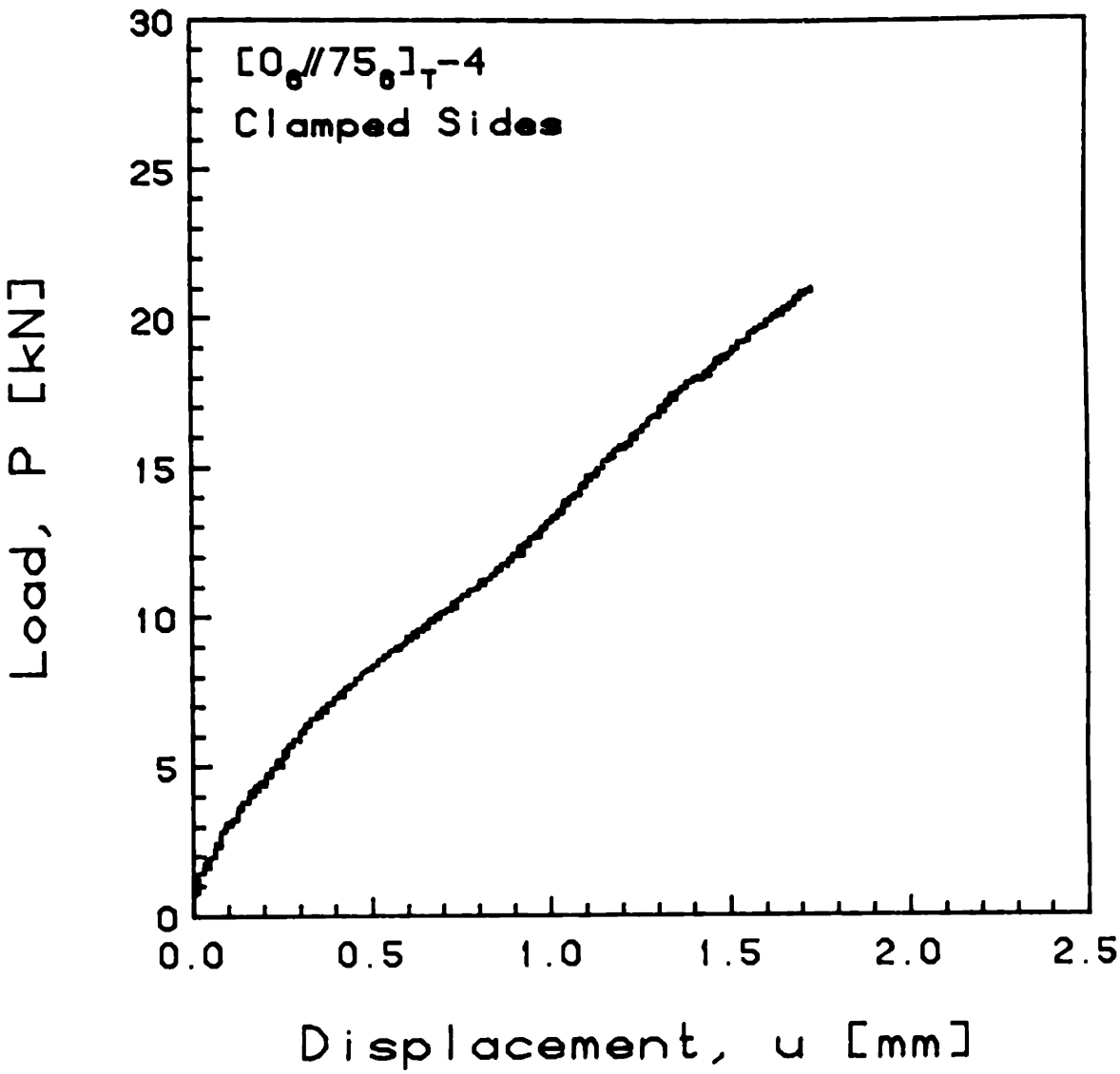

FIGURE G.47 Experimental Plot of Applied Compressive Load versus End-Shortening Displacement for the $[0_6//75_6]_T$-4 Laminate with Clamped Side Boundary Conditions

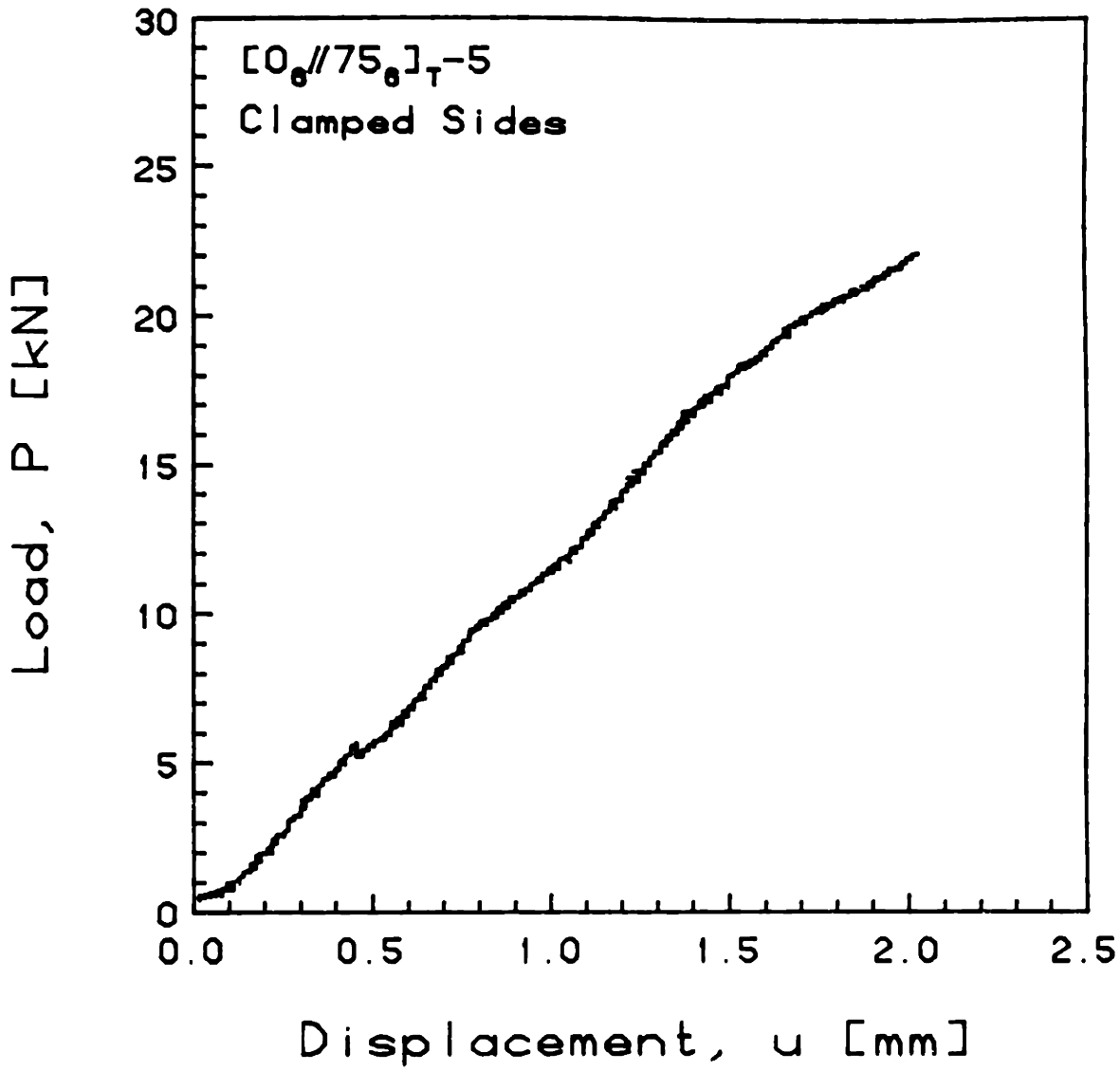

FIGURE G.48 Experimental Plot of Applied Compressive Load versus End-Shortening Displacement for the $[0_6//75_6]_T$-5 Laminate with Clamped Side Boundary Conditions

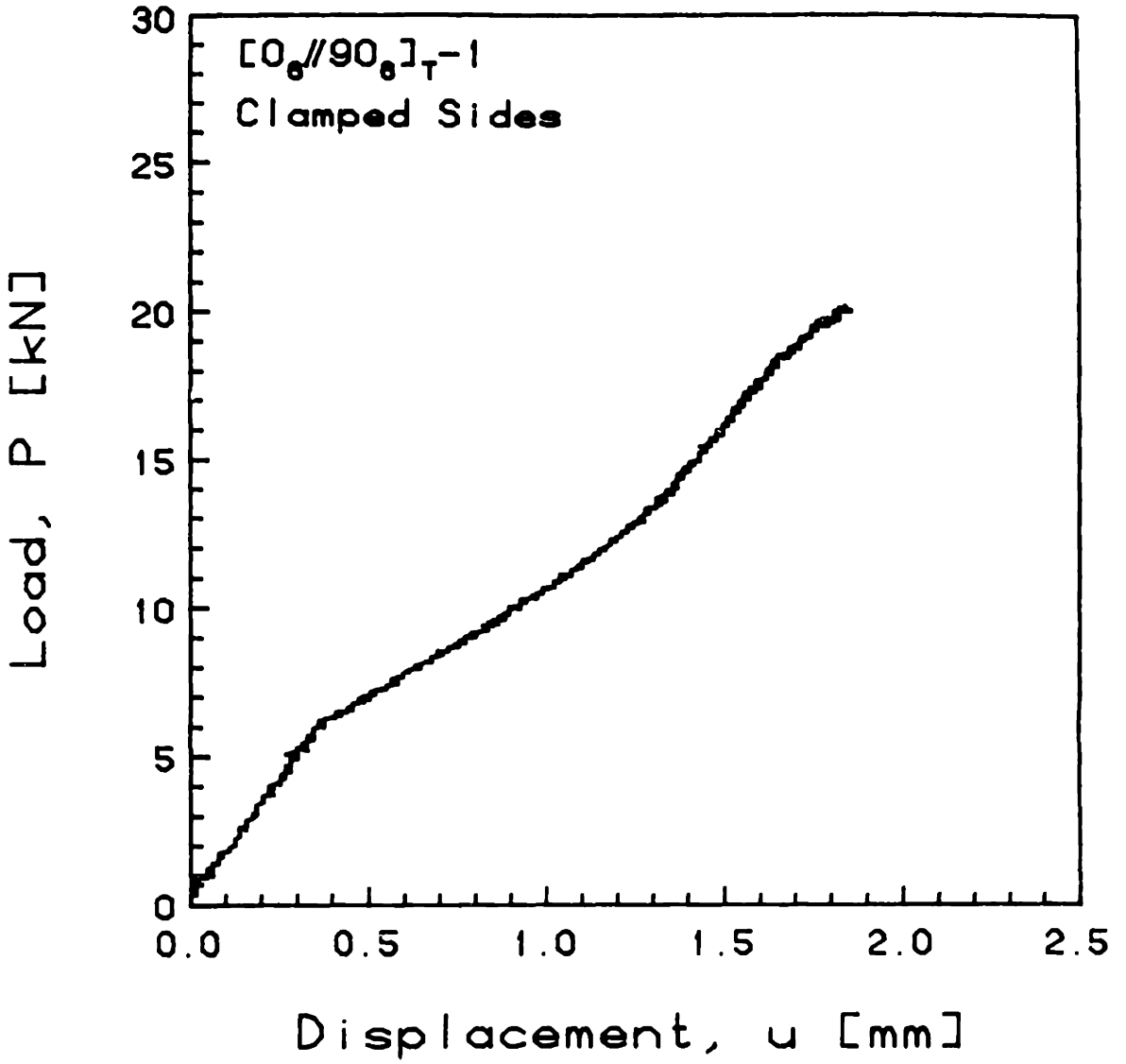

FIGURE G.49 Experimental Plot of Applied Compressive Load versus End-Shortening Displacement for the $[0_6//90_6]_T$-1 Laminate with Clamped Side Boundary Conditions

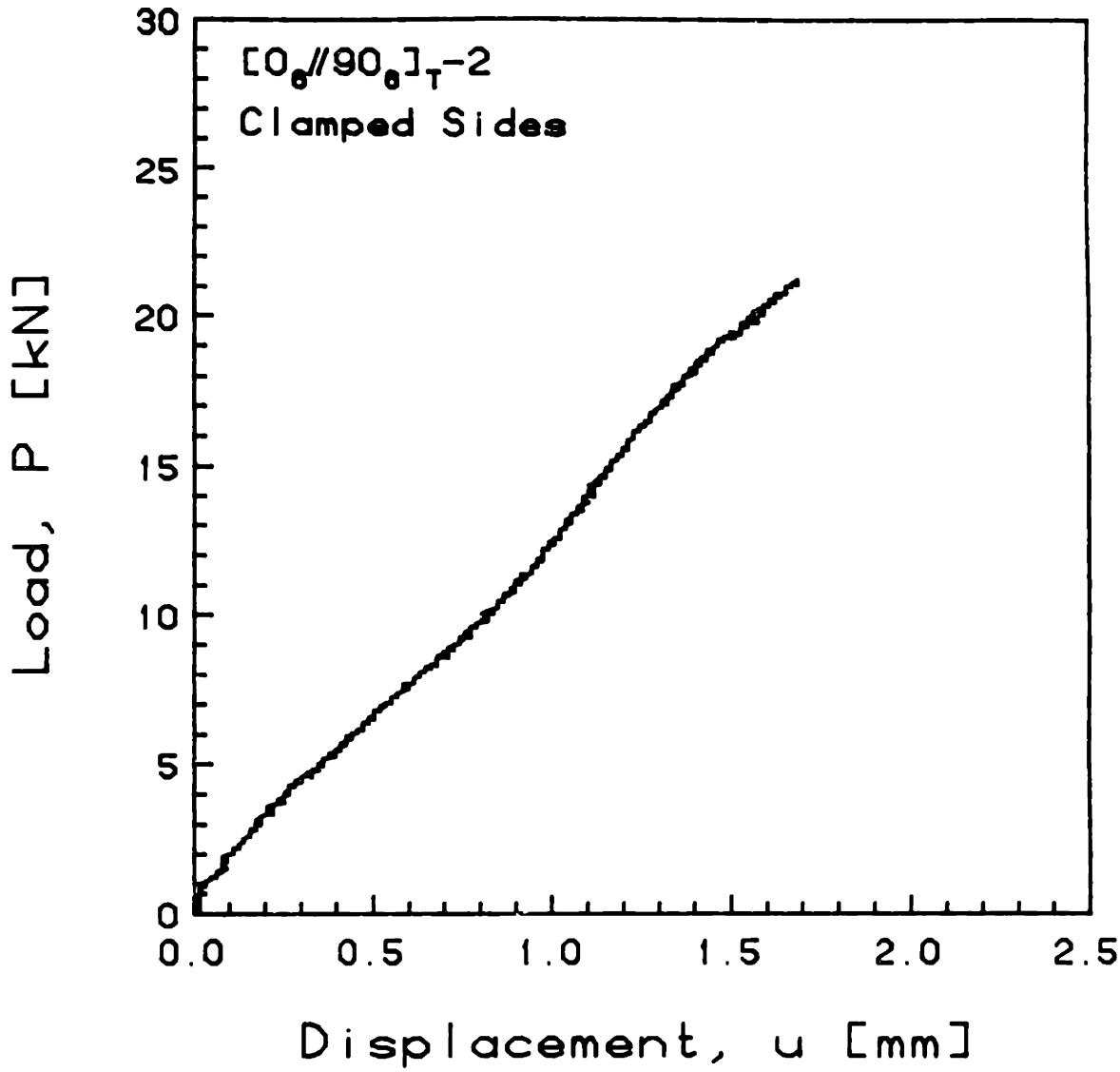

FIGURE G.50 Experimental Plot of Applied Compressive Load versus End-Shortening Displacement for the $[0_6//90_6]_T$-2 Laminate with Clamped Side Boundary Conditions

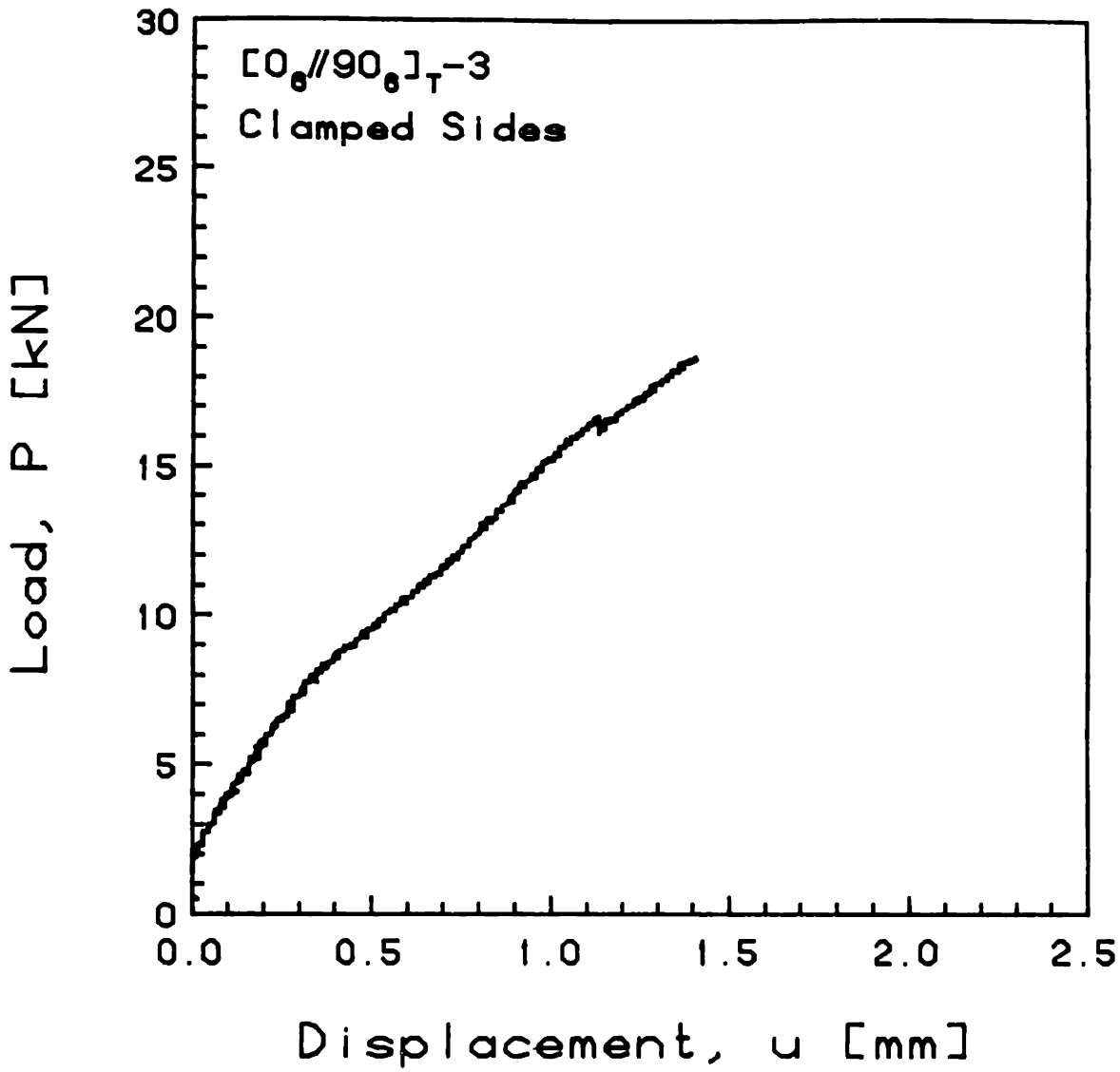

FIGURE G.51 Experimental Plot of Applied Compressive Load versus End-Shortening Displacement for the $[0_6//90_6]_T$-3 Laminate with Clamped Side Boundary Conditions

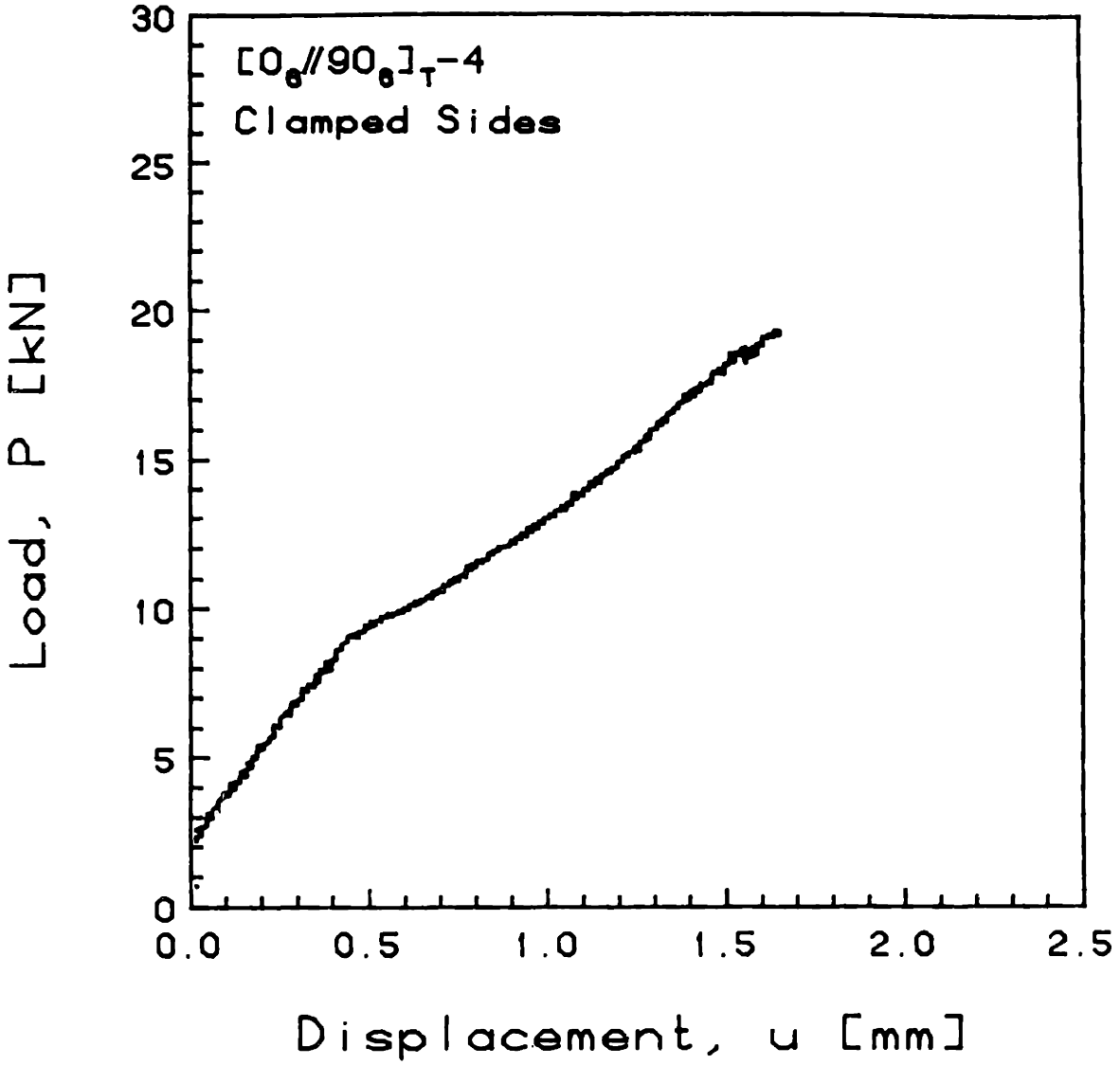

FIGURE G.52 Experimental Plot of Applied Compressive Load versus End-Shortening Displacement for the $[0_6//90_6]_T$-4 Laminate with Clamped Side Boundary Conditions

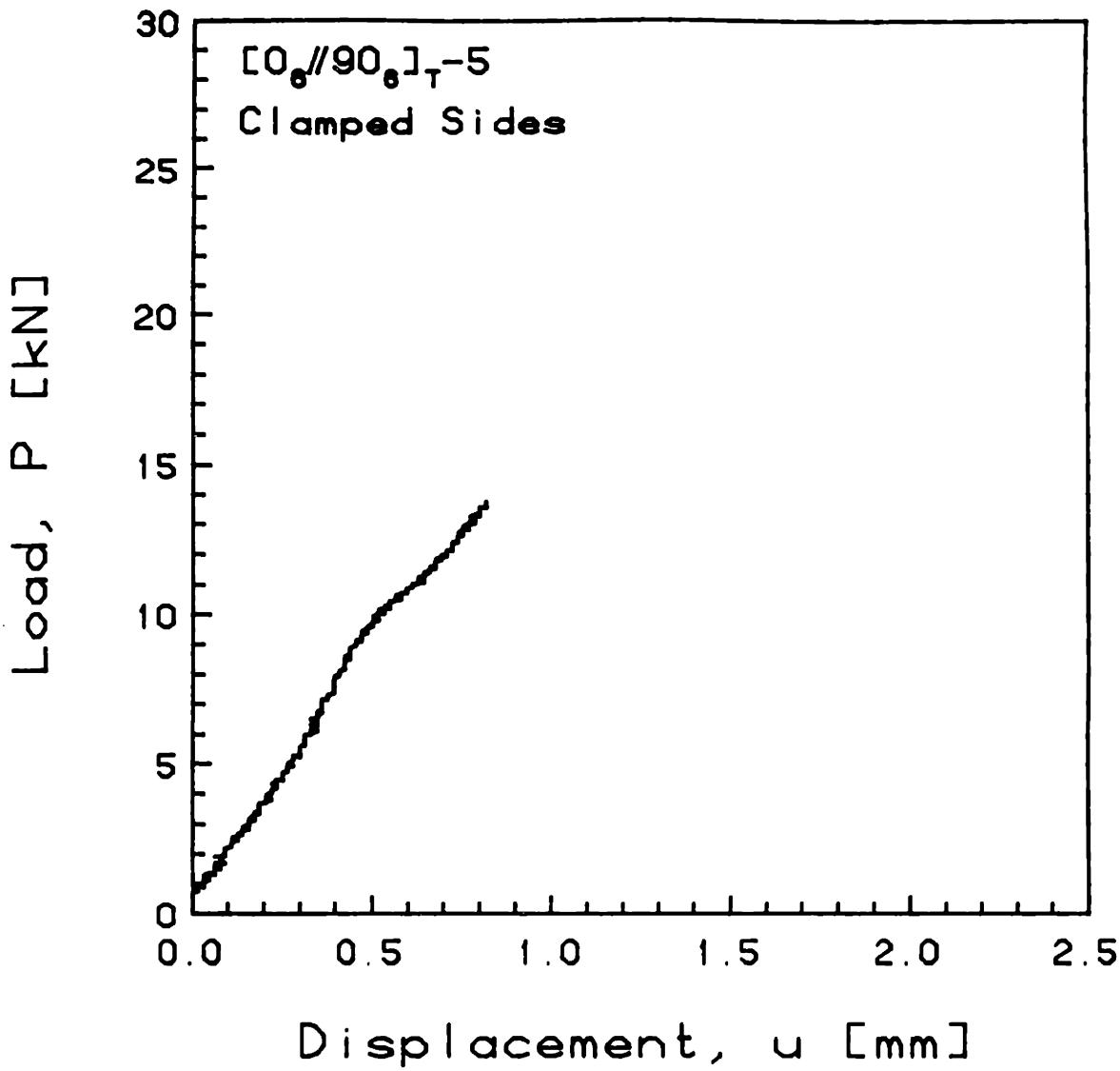

FIGURE G.53 Experimental Plot of Applied Compressive Load versus End-Shortening Displacement for the $[0_6//90_6]_T$-5 Laminate with Clamped Side Boundary Conditions

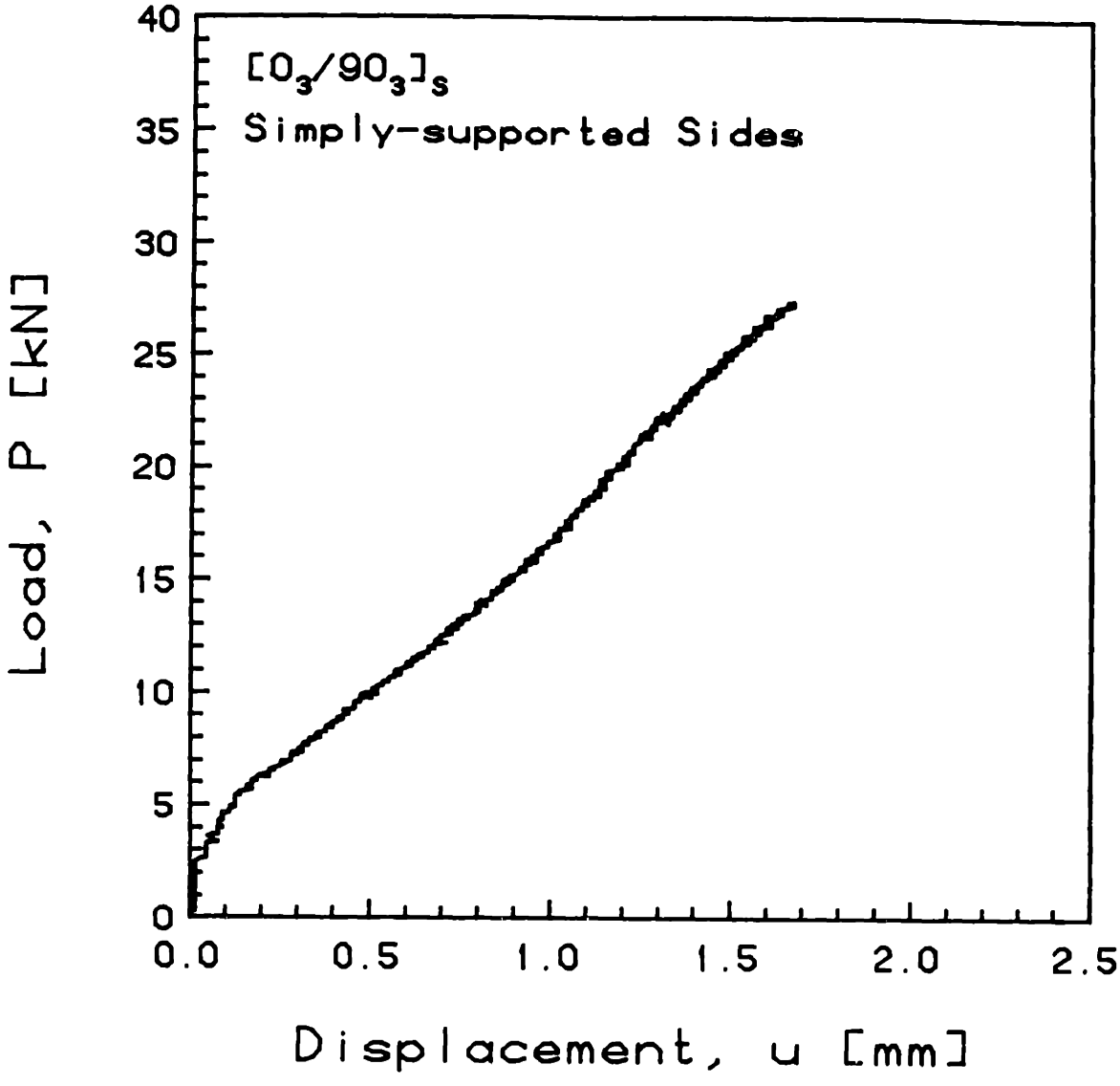

FIGURE G.54 Experimental Plot of Applied Compressive Load versus End-Shortening Displacement for the $[0_3/90_3]_S$ Laminate with Simply-Supported Side Boundary Conditions

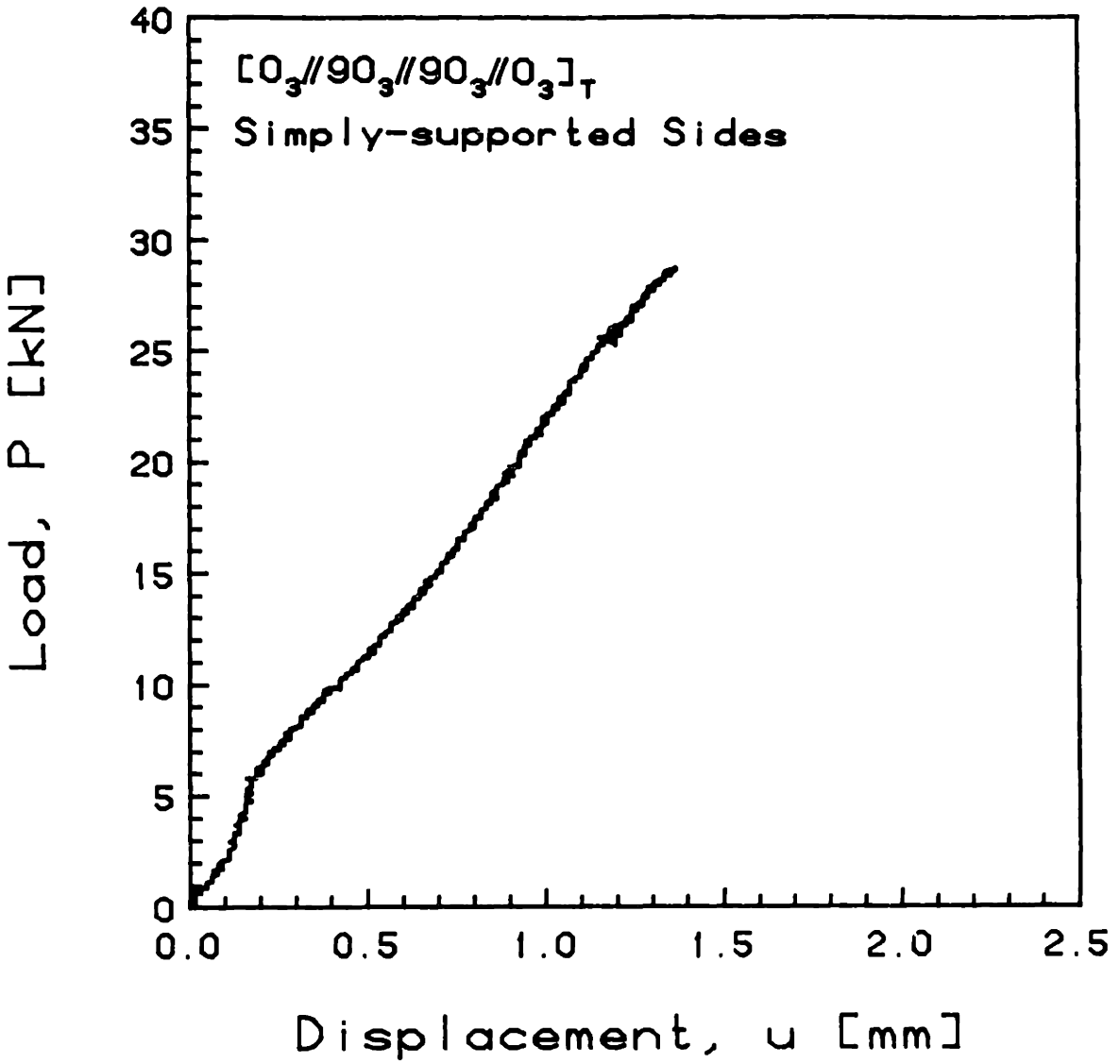

FIGURE G.55 Experimental Plot of Applied Compressive Load versus End-Shortening Displacement for the $[O_3//90_3//90_3//O_3]_T$ Laminate with Simply-Supported Side Boundary Conditions

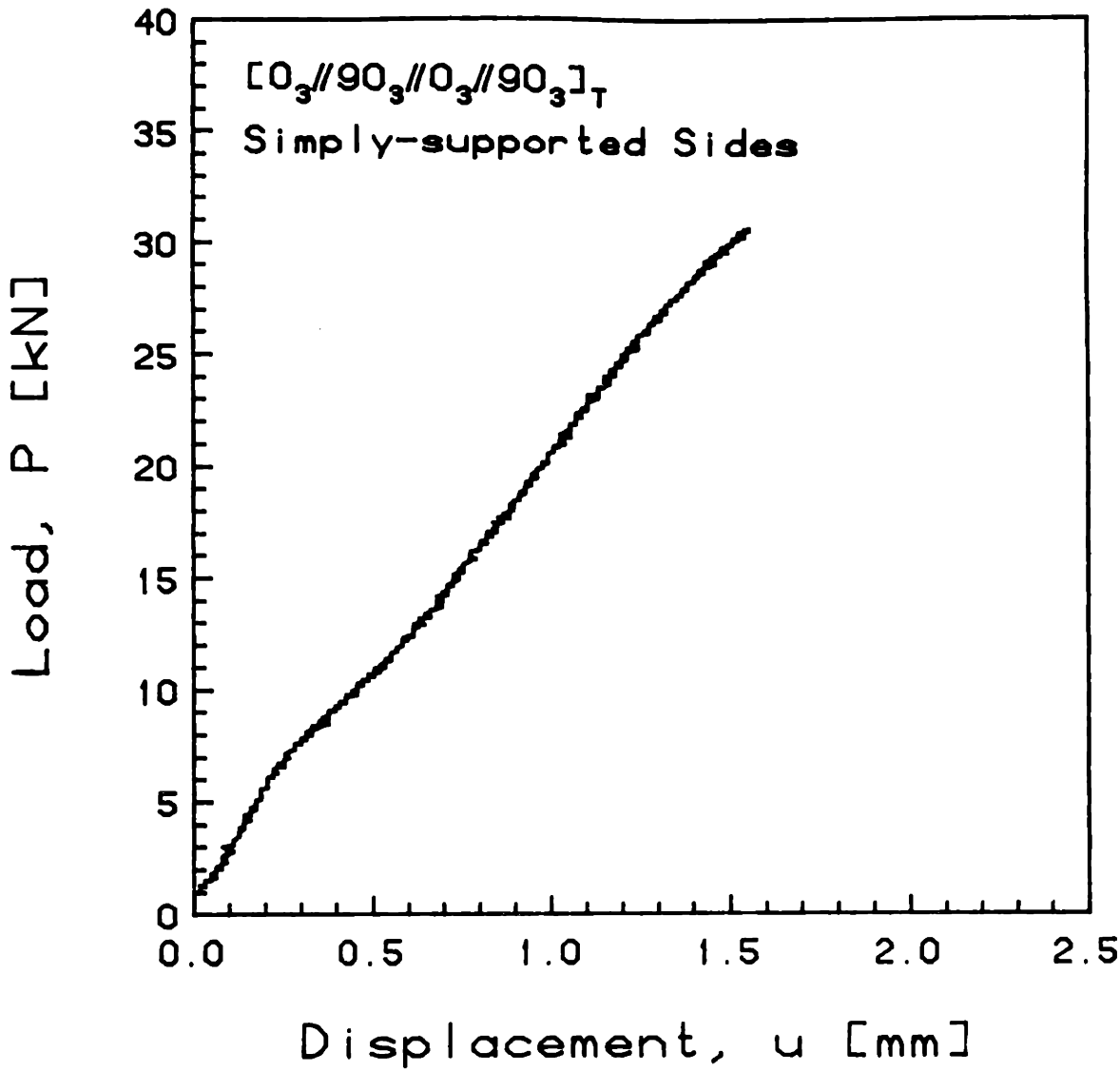

FIGURE G.56 Experimental Plot of Applied Compressive Load versus End-Shortening Displacement for the $[0_3//90_3//0_3//90_3]_T$ Laminate with Simply-Supported Side Boundary Conditions

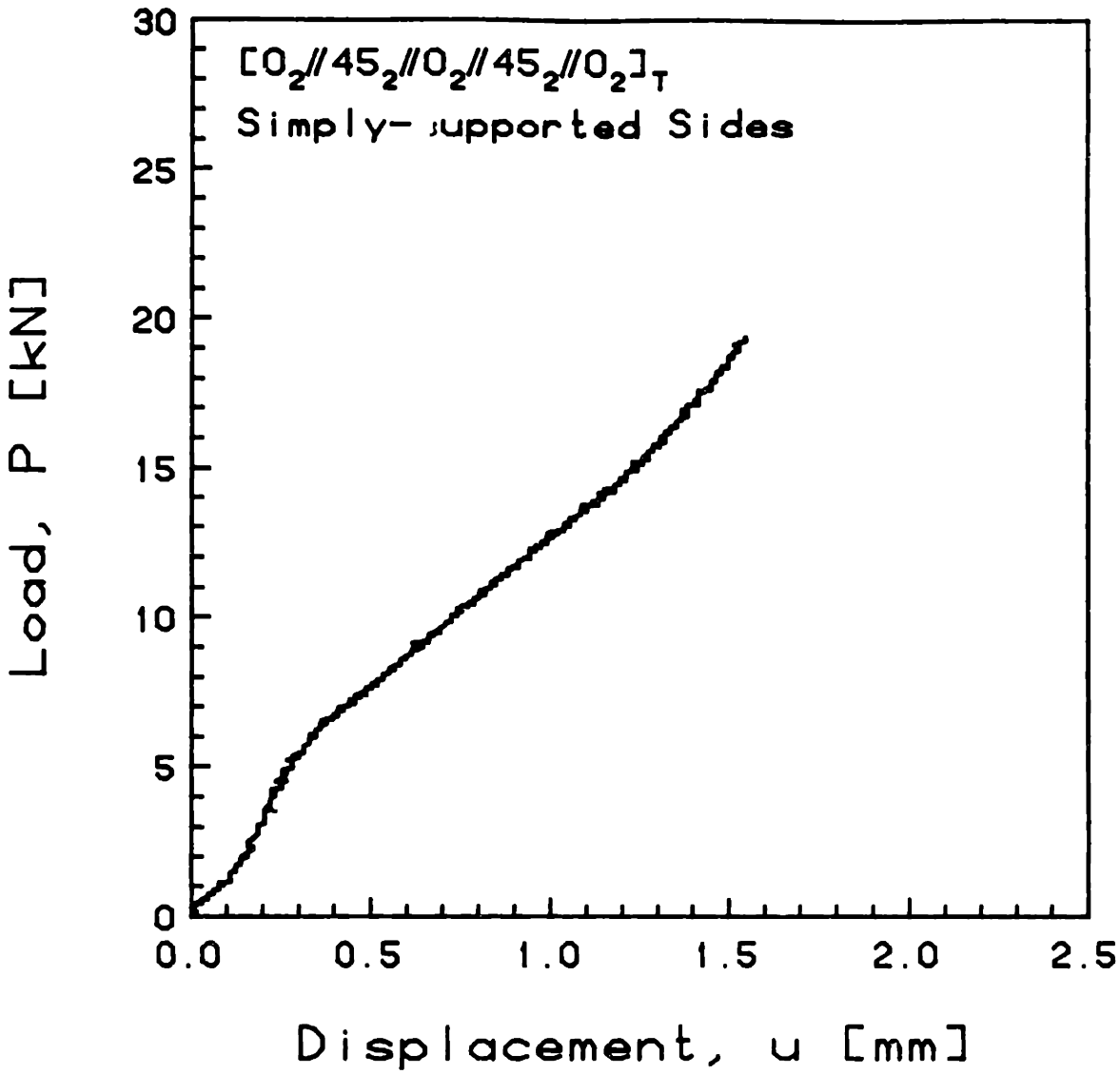

FIGURE G.57 Experimental Plot of Applied Compressive Load versus End-Shortening Displacement for the $[0_2//45_2//0_2//45_2//0_2]_T$ Laminate with Simply-Supported Side Boundary Conditions

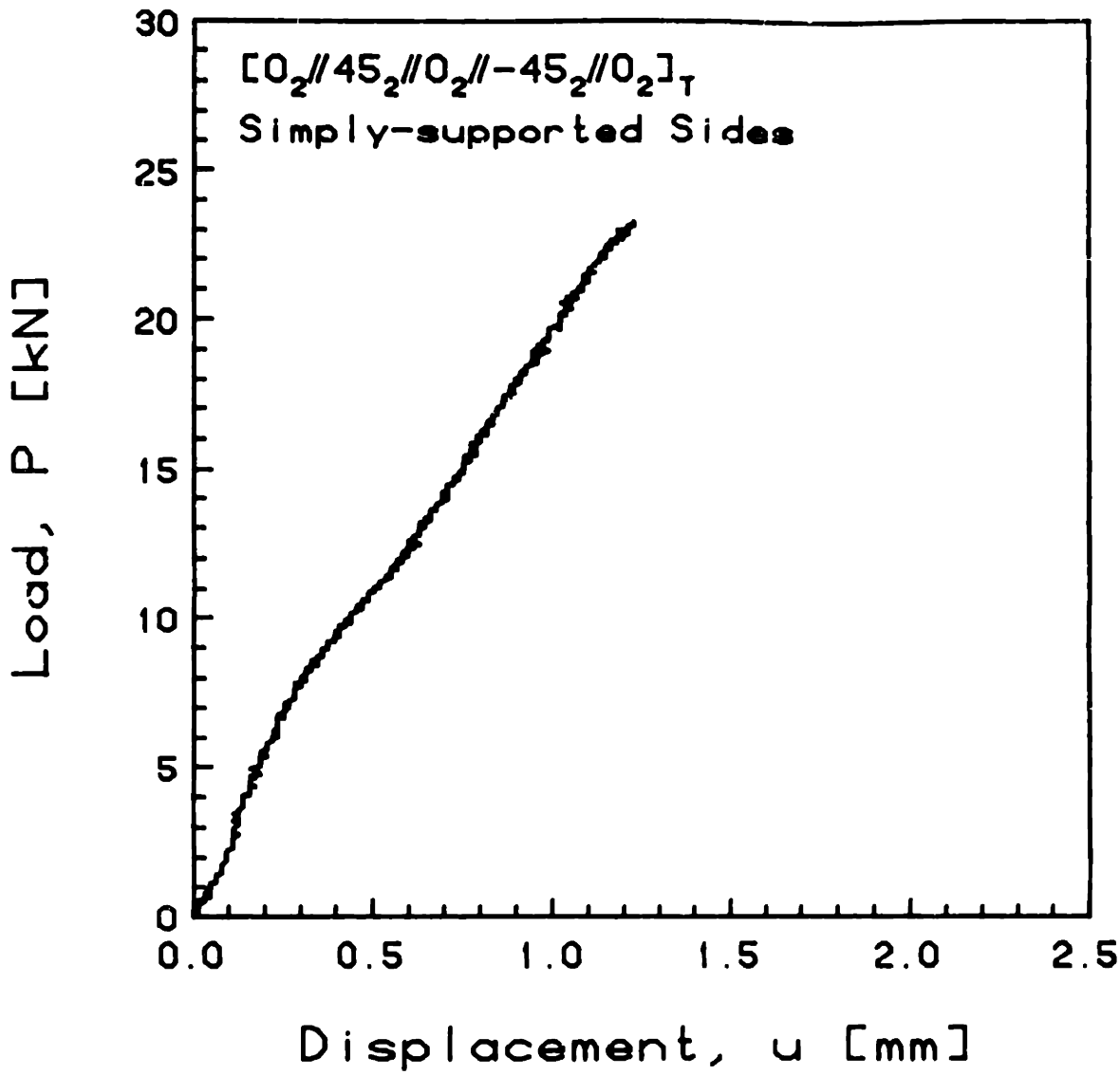

FIGURE G.58 Experimental Plot of Applied Compressive Load versus End-Shortening Displacement for the $[O_2//45_2//O_2//-45_2//O_2]_T$ Laminate with Simply-Supported Side Boundary Conditions

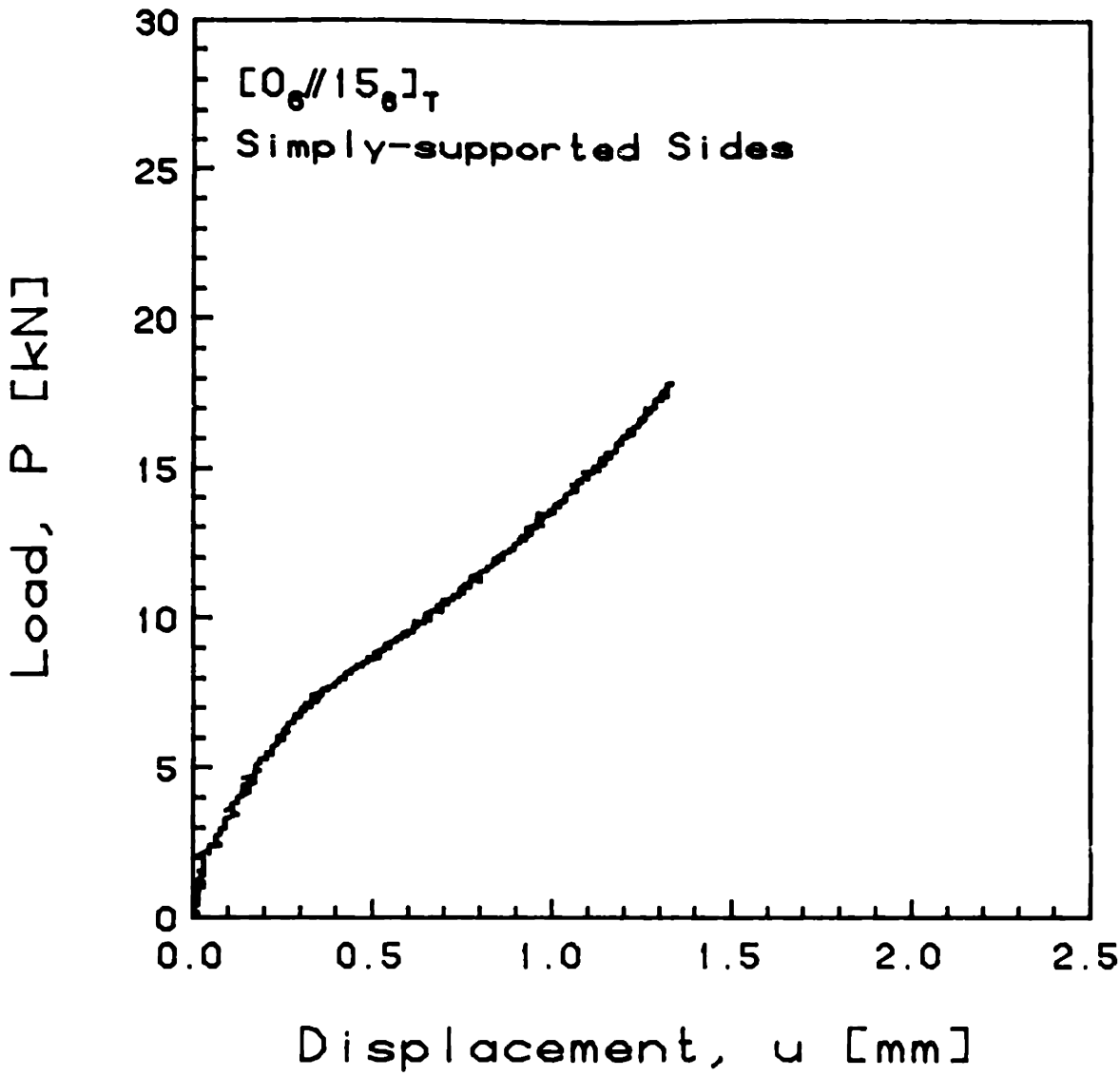

FIGURE G.59 Experimental Plot of Applied Compressive Load versus End-Shortening Displacement for the $[0_6//15_6]_T$ Laminate with Simply-Supported Side Boundary Conditions

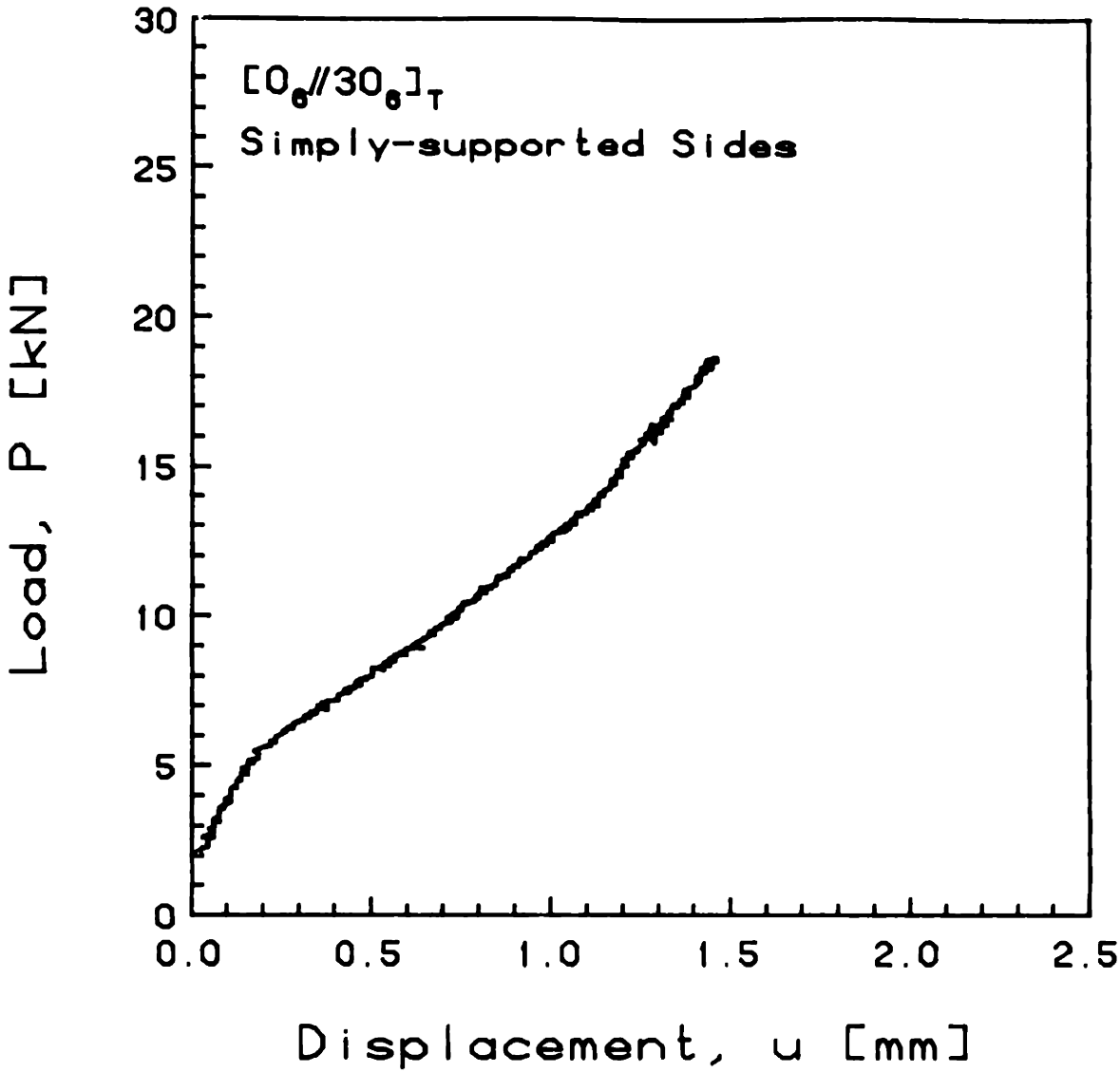

FIGURE G.60 Experimental Plot of Applied Compressive Load versus End-Shortening Displacement for the $[0_6//30_6]_T$ Laminate with Simply-Supported Side Boundary Conditions

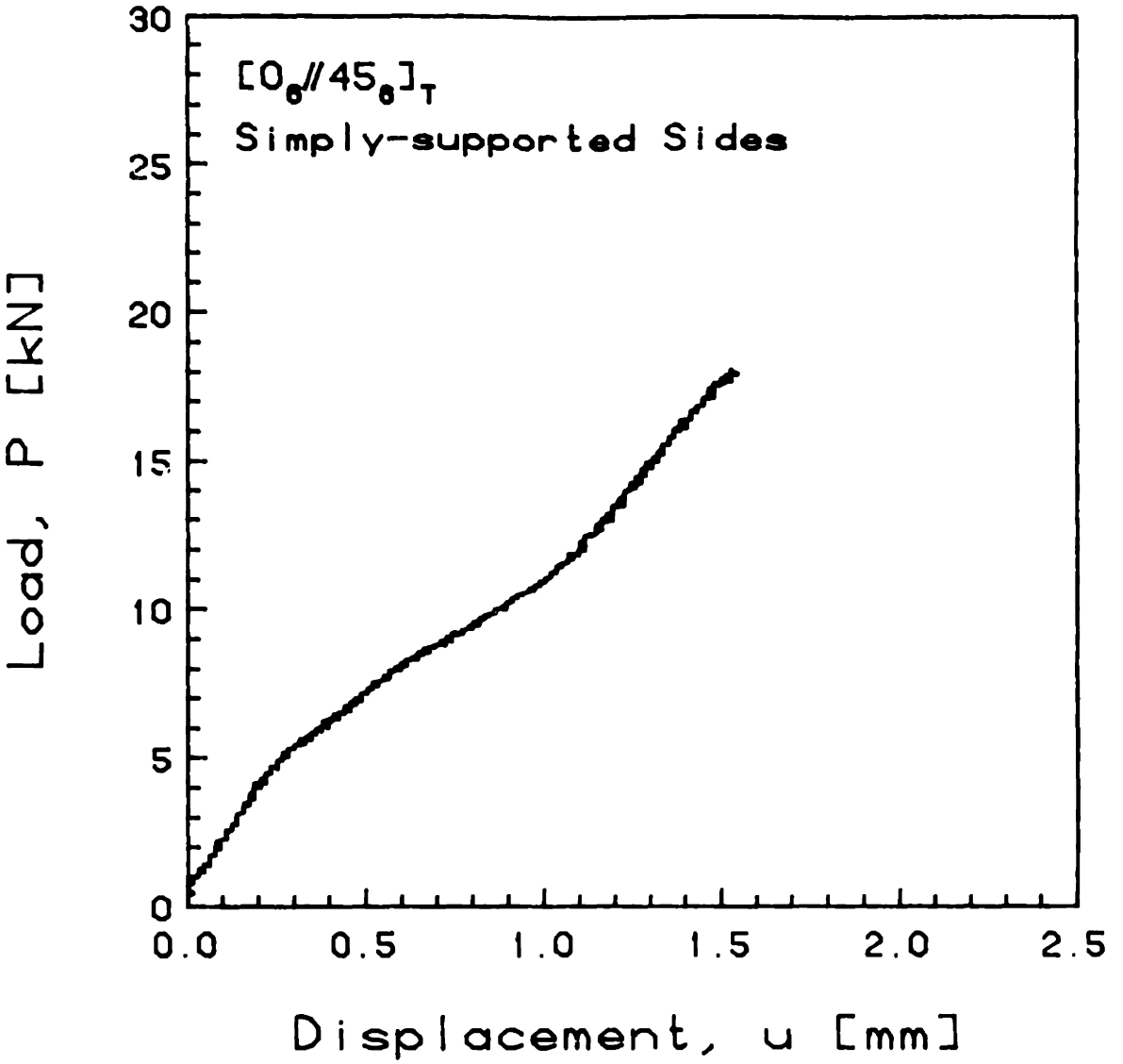

FIGURE G.61 Experimental Plot of Applied Compressive Load versus End-Shortening Displacement for the $[0_6//45_6]_T$ Laminate with Simply-Supported Side Boundary Conditions

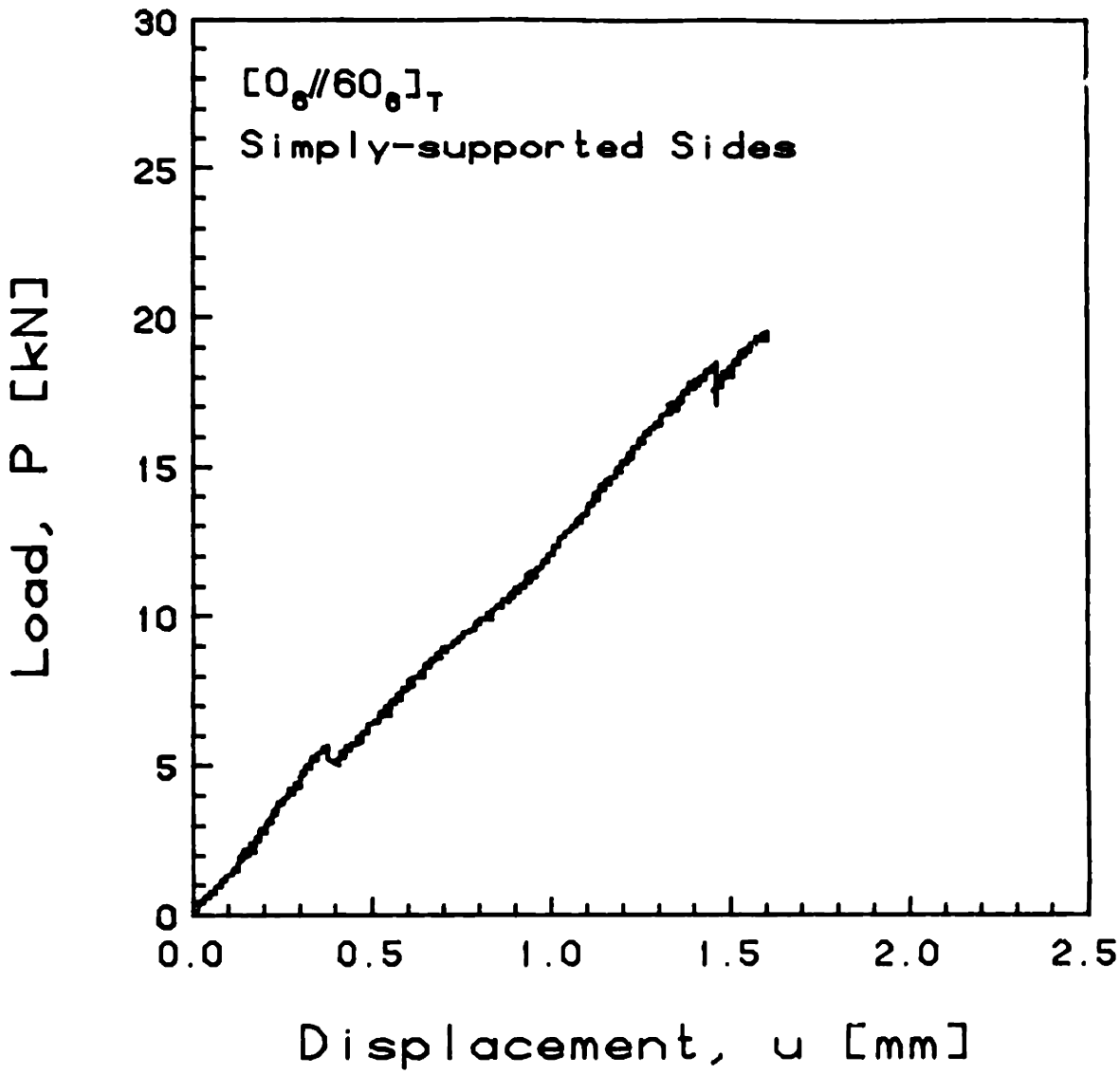

FIGURE G.62 Experimental Plot of Applied Compressive Load versus End-Shortening Displacement for the $[0_6//60_6]_T$ Laminate with Simply-Supported Side Boundary Conditions

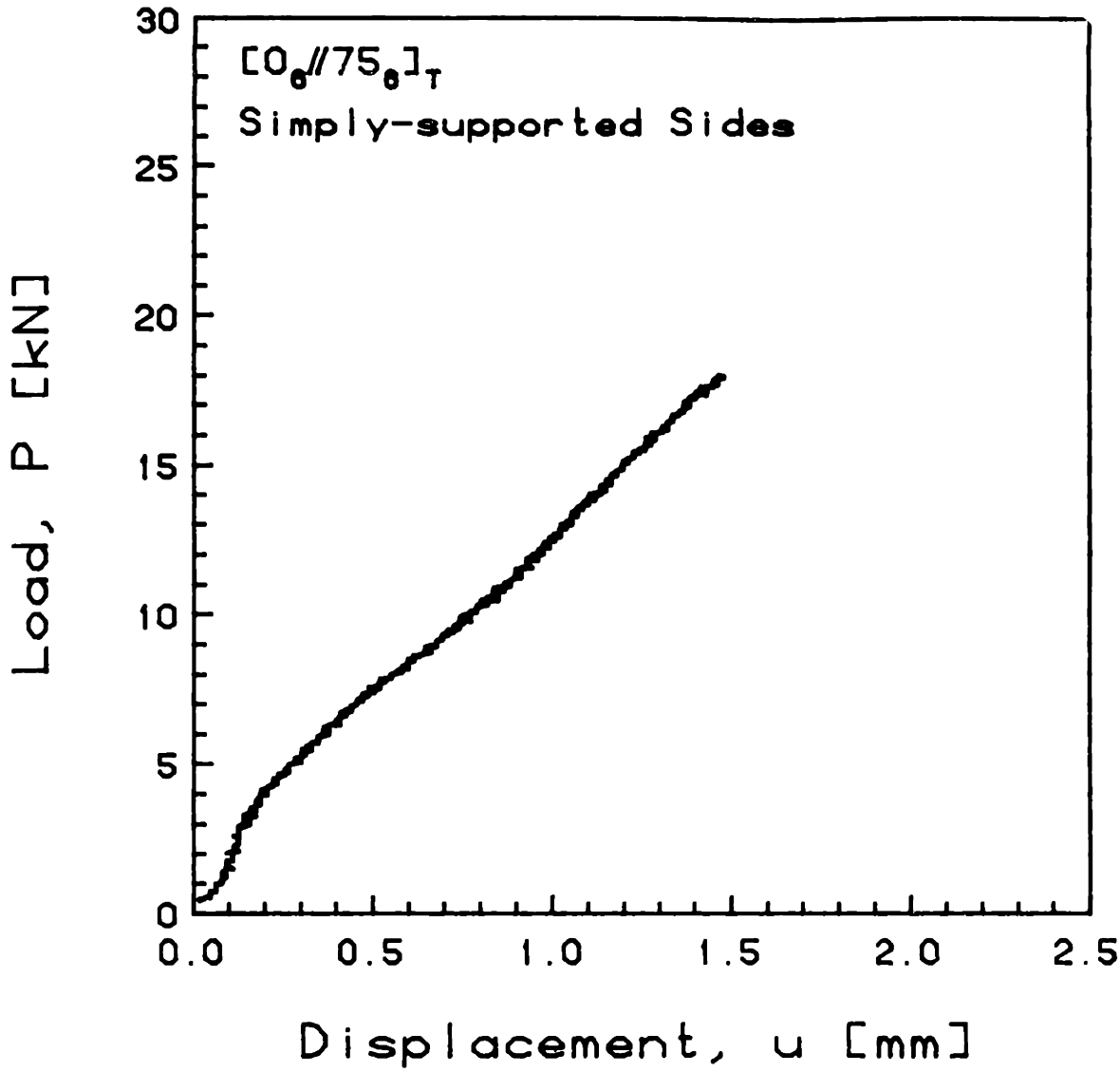

FIGURE G.63 Experimental Plot of Applied Compressive Load versus End-Shortening Displacement for the $[0_6//75_6]_T$ Laminate with Simply-Supported Side Boundary Conditions

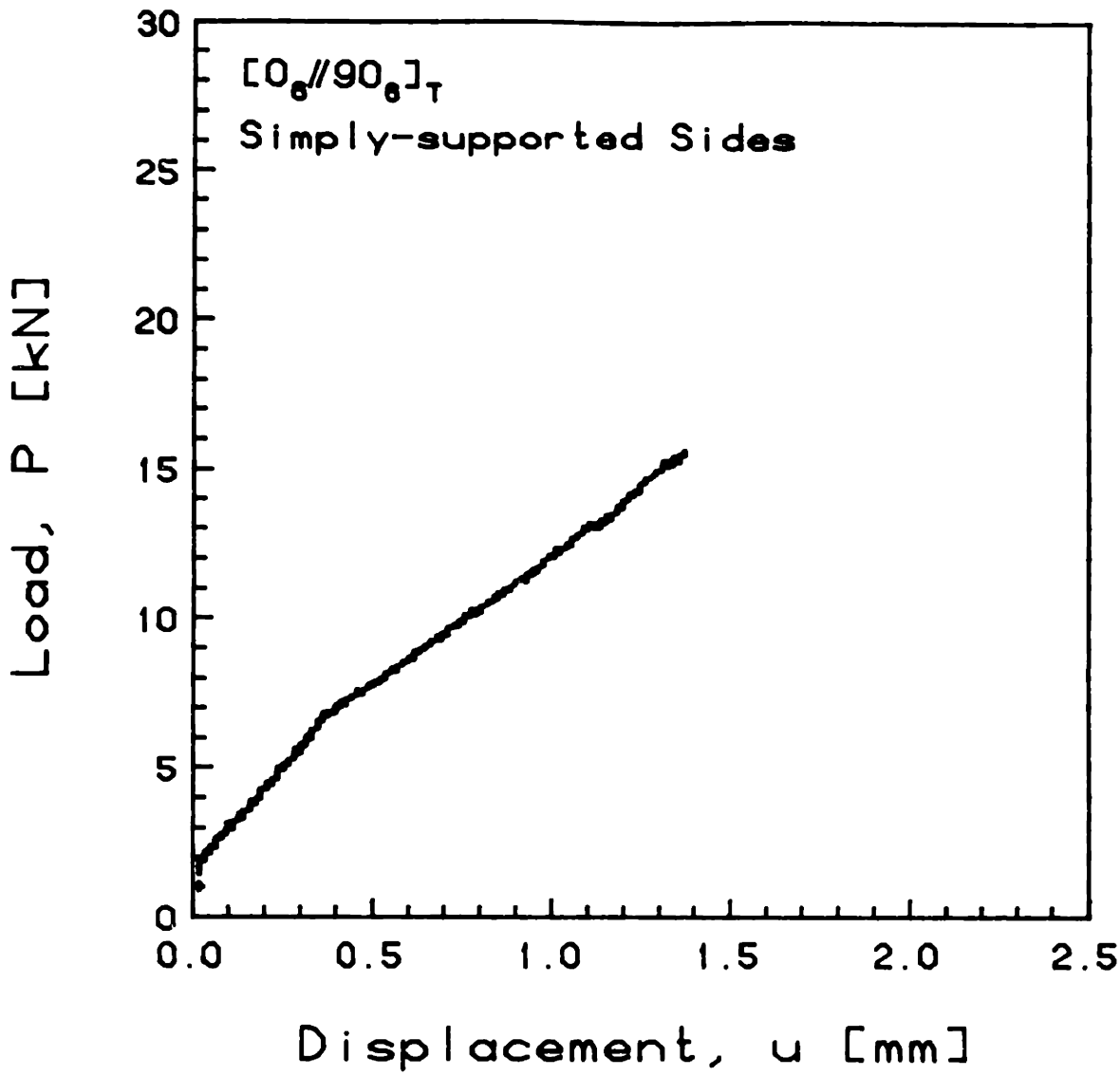

FIGURE G.64 Experimental Plot of Applied Compressive Load versus End-Shortening Displacement for the $[0_6//90_6]_T$ Laminate with Simply-Supported Side Boundary Conditions

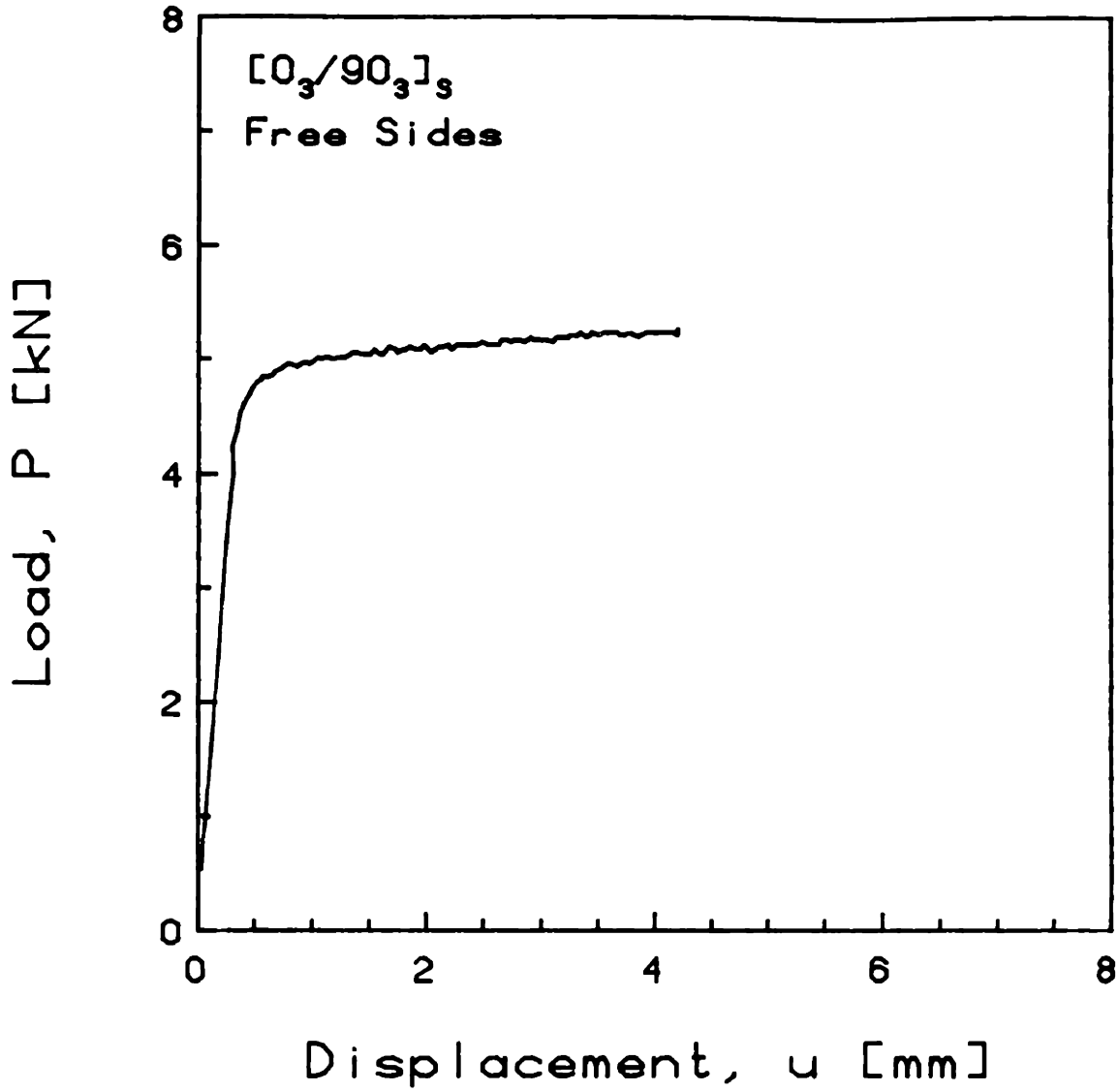

FIGURE G.65 Experimental Plot of Applied Compressive Load versus End-Shortening Displacement for the $[0_3/90_3]_S$ Laminate with Free Side Boundary Conditions

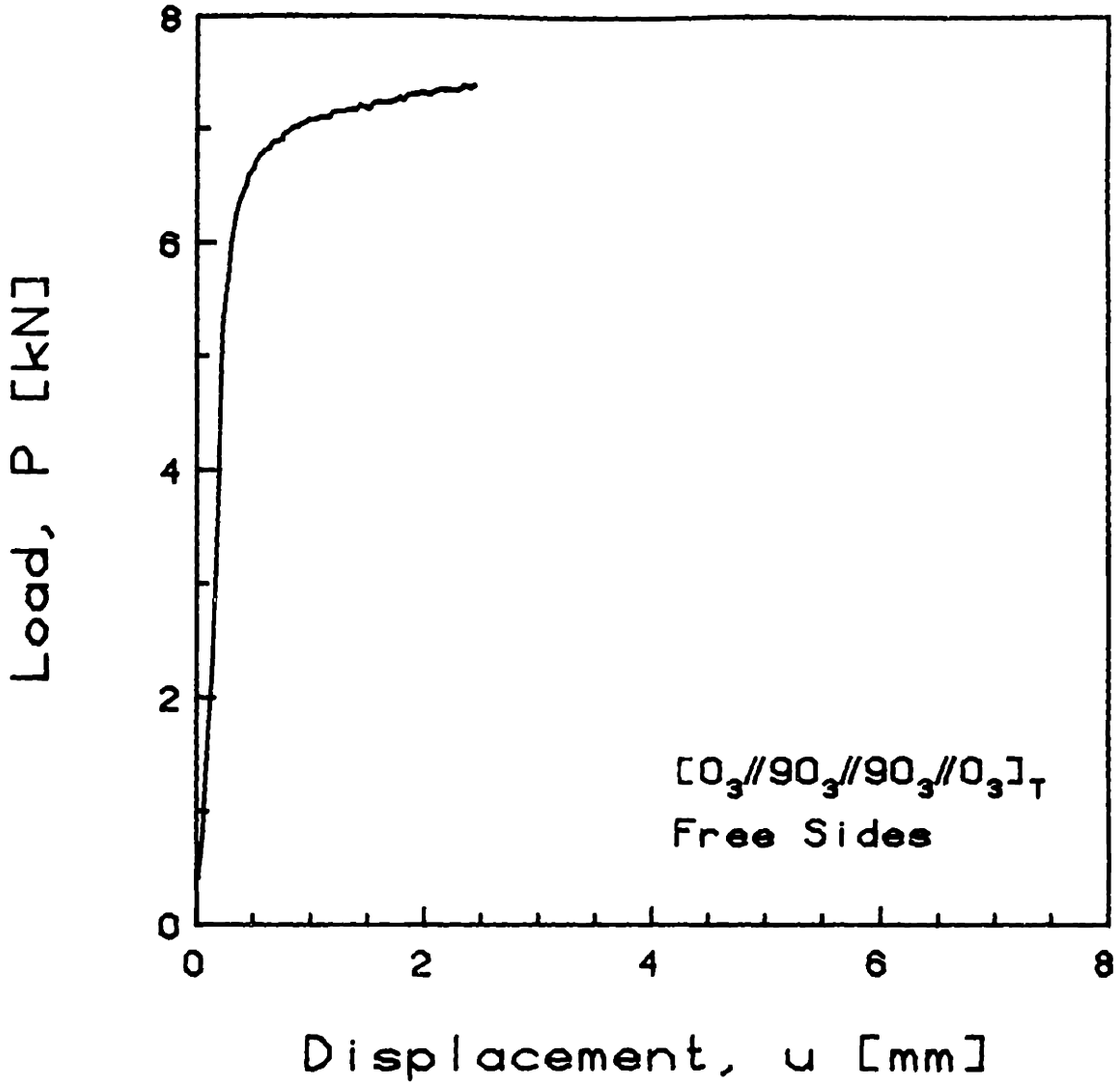

FIGURE G.66 Experimental Plot of Applied Compressive Load versus End-Shortening Displacement for the $[0_3//90_3//90_3//0_3]_T$ Laminate with Free Side Boundary Conditions

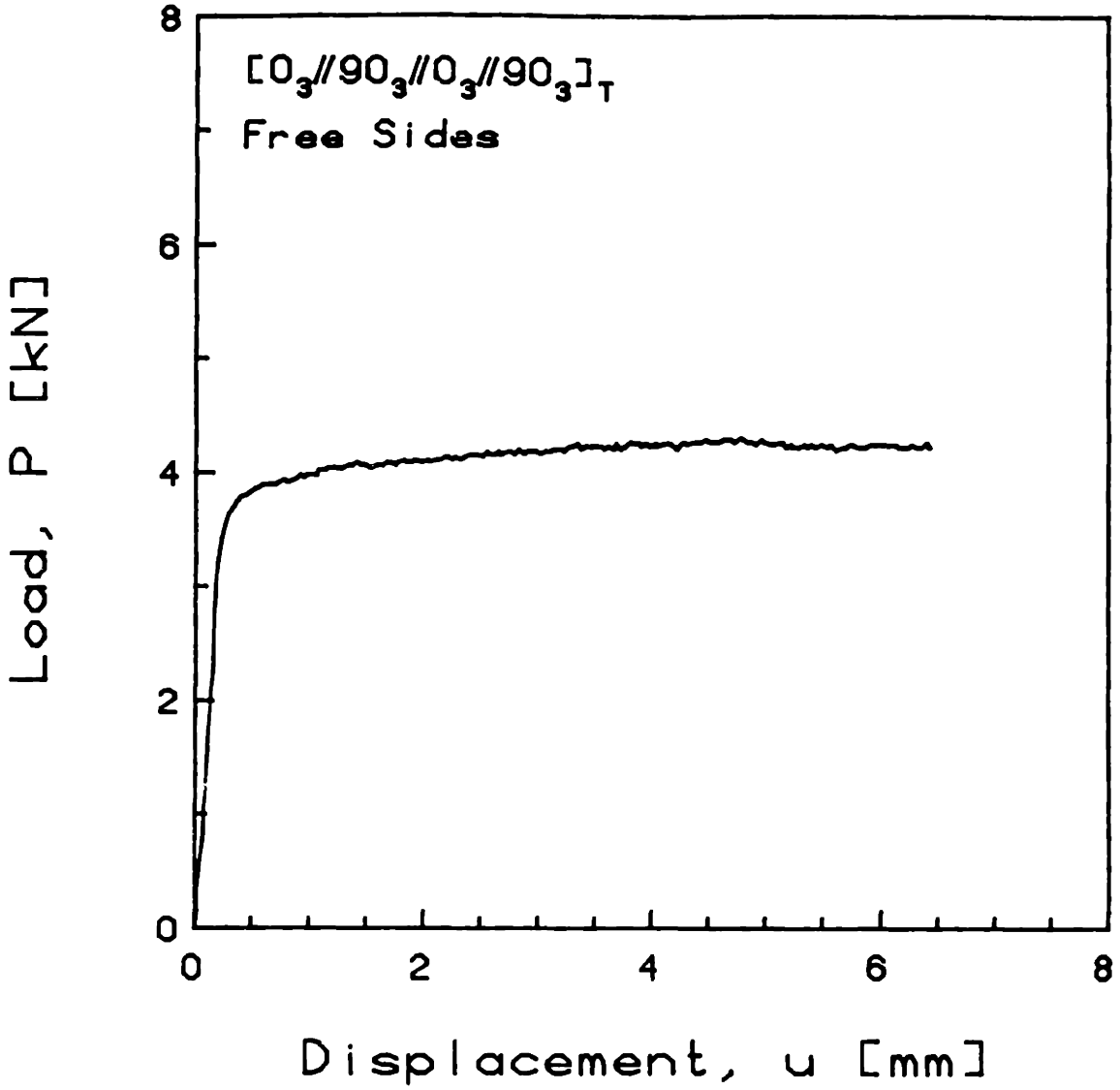

FIGURE G.67 Experimental Plot of Applied Compressive Load versus End-Shortening Displacement for the $[O_3//90_3//O_3//90_3]_T$ Laminate with Free Side Boundary Conditions

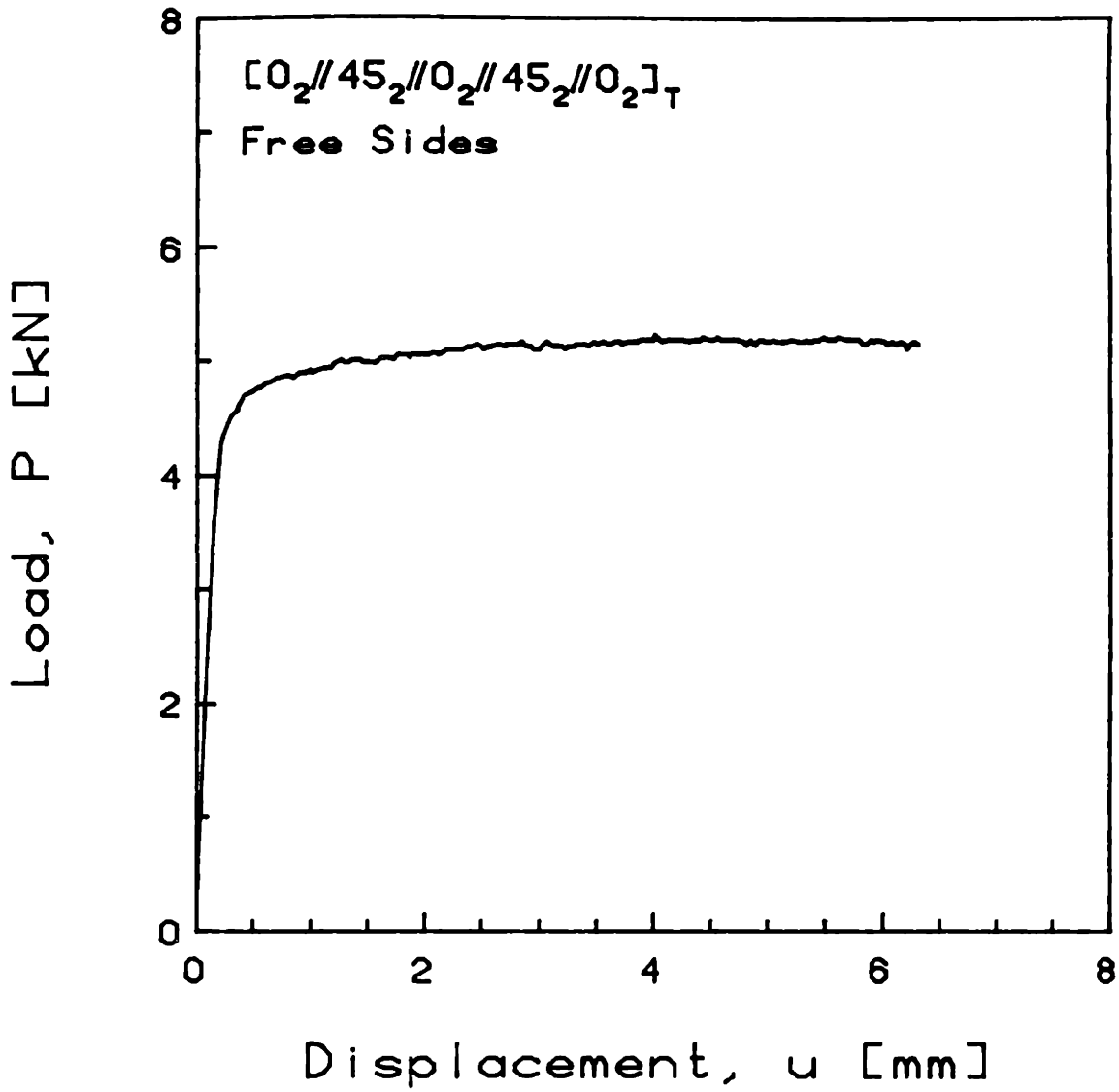

FIGURE G.68 Experimental Plot of Applied Compressive Load versus End-Shortening Displacement for the $[O_2//45_2//O_2//45_2//O_2]_T$ Laminate with Free Side Boundary Conditions

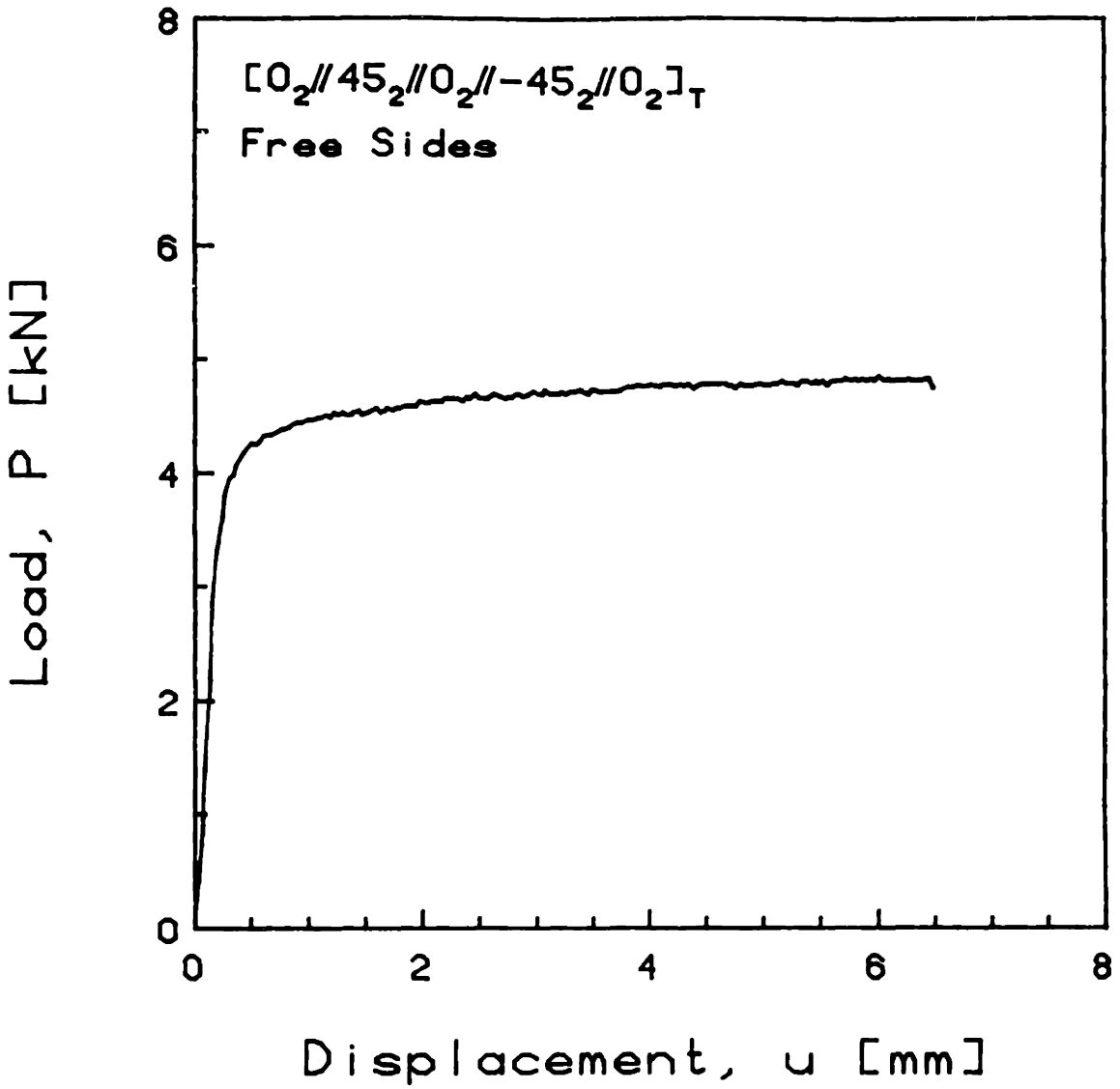

FIGURE G.69 Experimental Plot of Applied Compressive Load versus End-Shortening Displacement for the $[O_2//45_2//O_2//-45_2//O_2]_T$ Laminate with Free Side Boundary Conditions

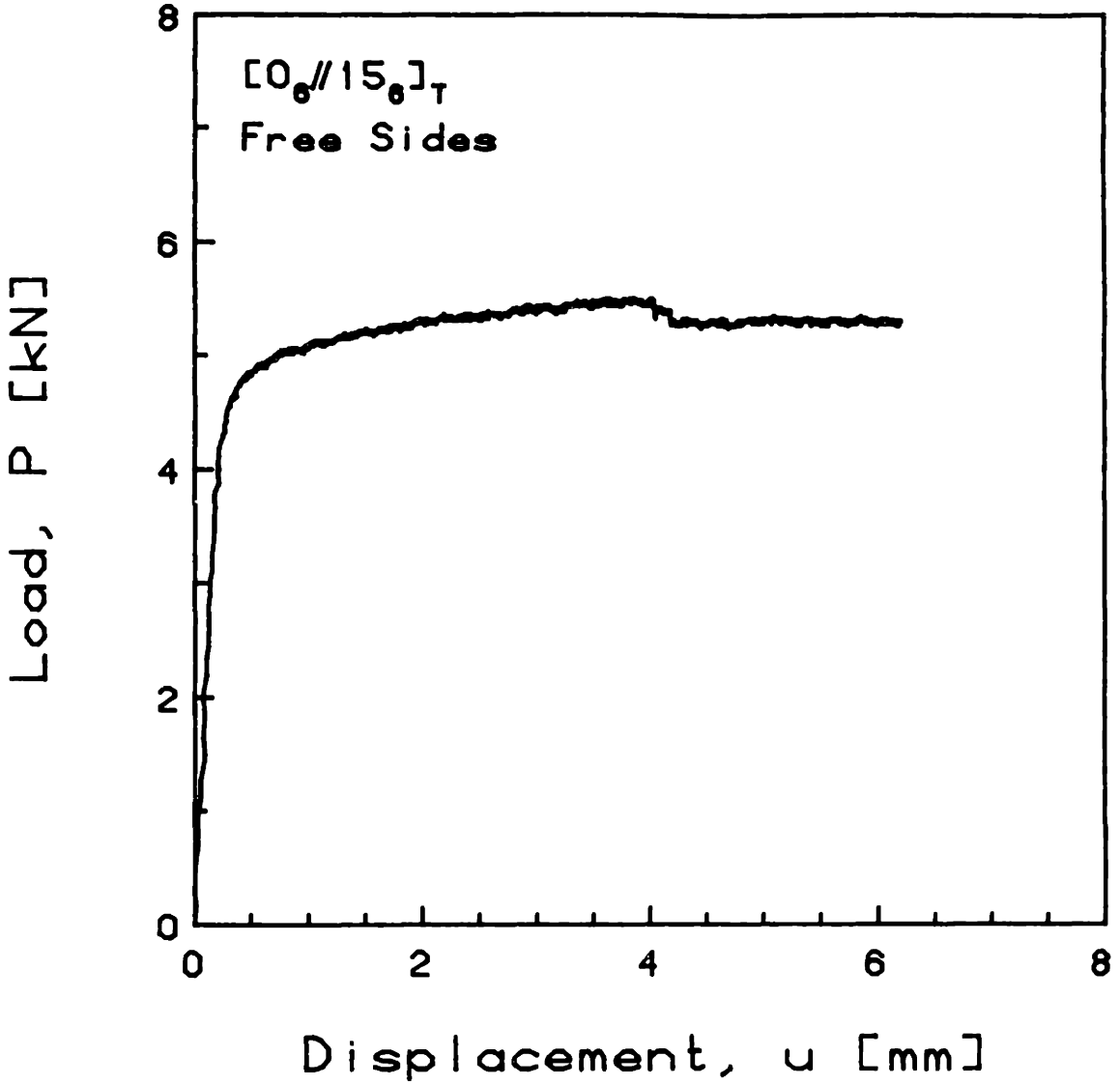

FIGURE G.70 Experimental Plot of Applied Compressive Load versus End-Shortening Displacement for the $[0_6//15_6]_T$ Laminate with Free Side Boundary Conditions

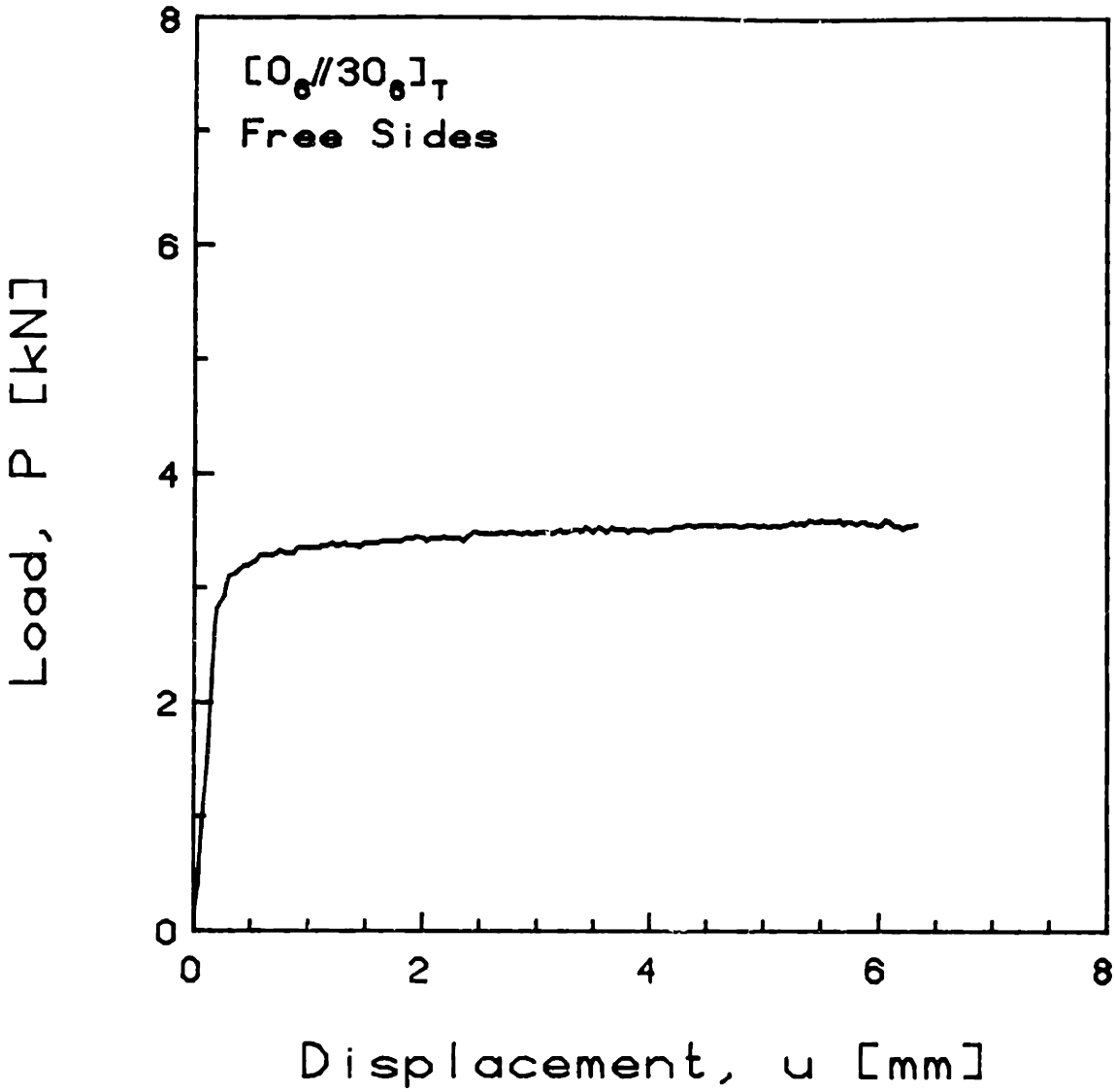

FIGURE G.71 Experimental Plot of Applied Compressive Load versus End-Shortening Displacement for the $[0_6//30_6]_T$ Laminate with Free Side Boundary Conditions

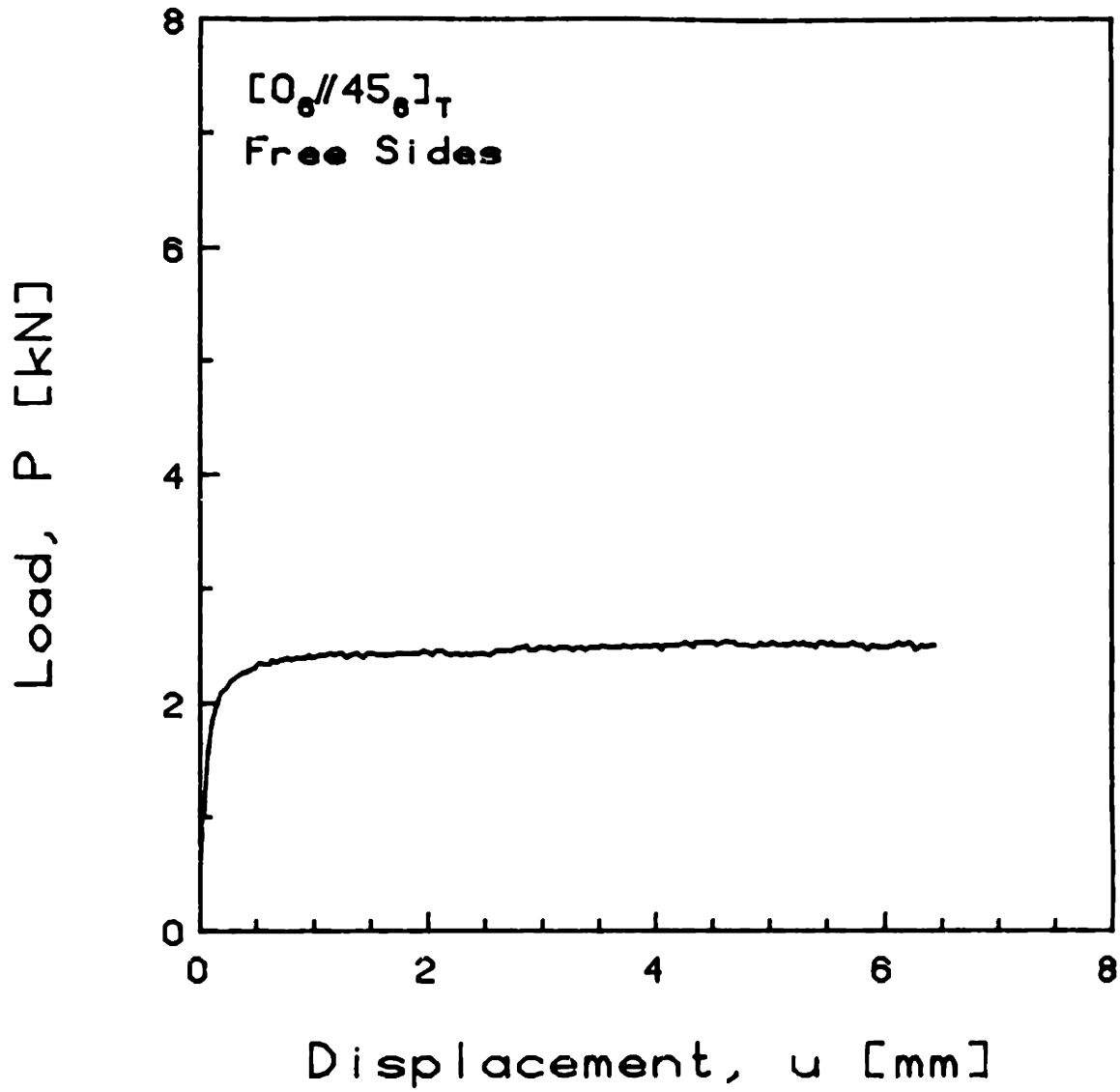

FIGURE G.72 Experimental Plot of Applied Compressive Load versus End-Shortening Displacement for the $[0_6//45_6]_T$ Laminate with Free Side Boundary Conditions

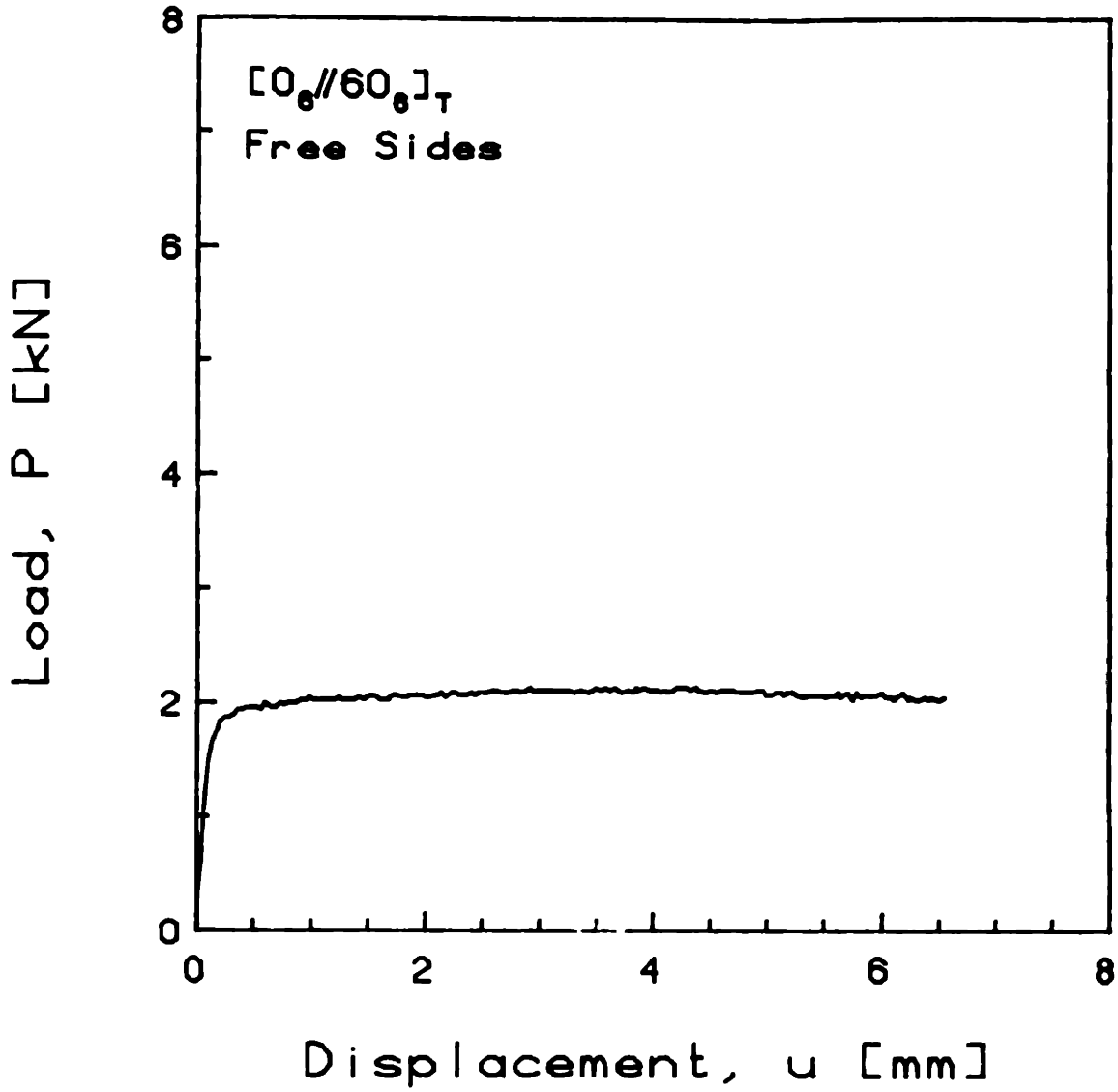

FIGURE G.73 Experimental Plot of Applied Compressive Load versus End-Shortening Displacement for the $[0_6//60_6]_T$ Laminate with Free Side Boundary Conditions

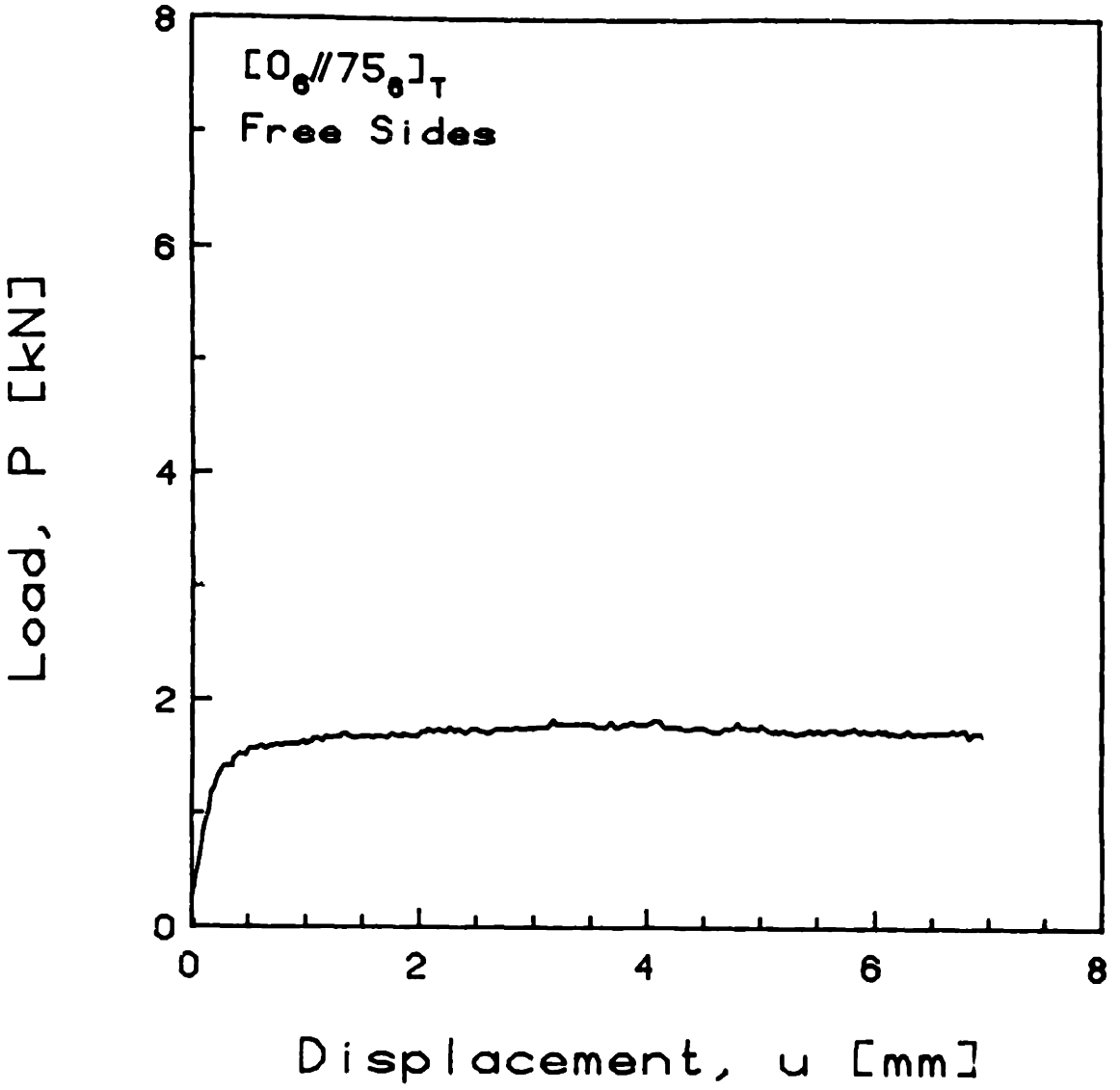

FIGURE G.74 Experimental Plot of Applied Compressive Load versus End-Shortening Displacement for the $[0_6//75_6]_T$ Laminate with Free Side Boundary Conditions

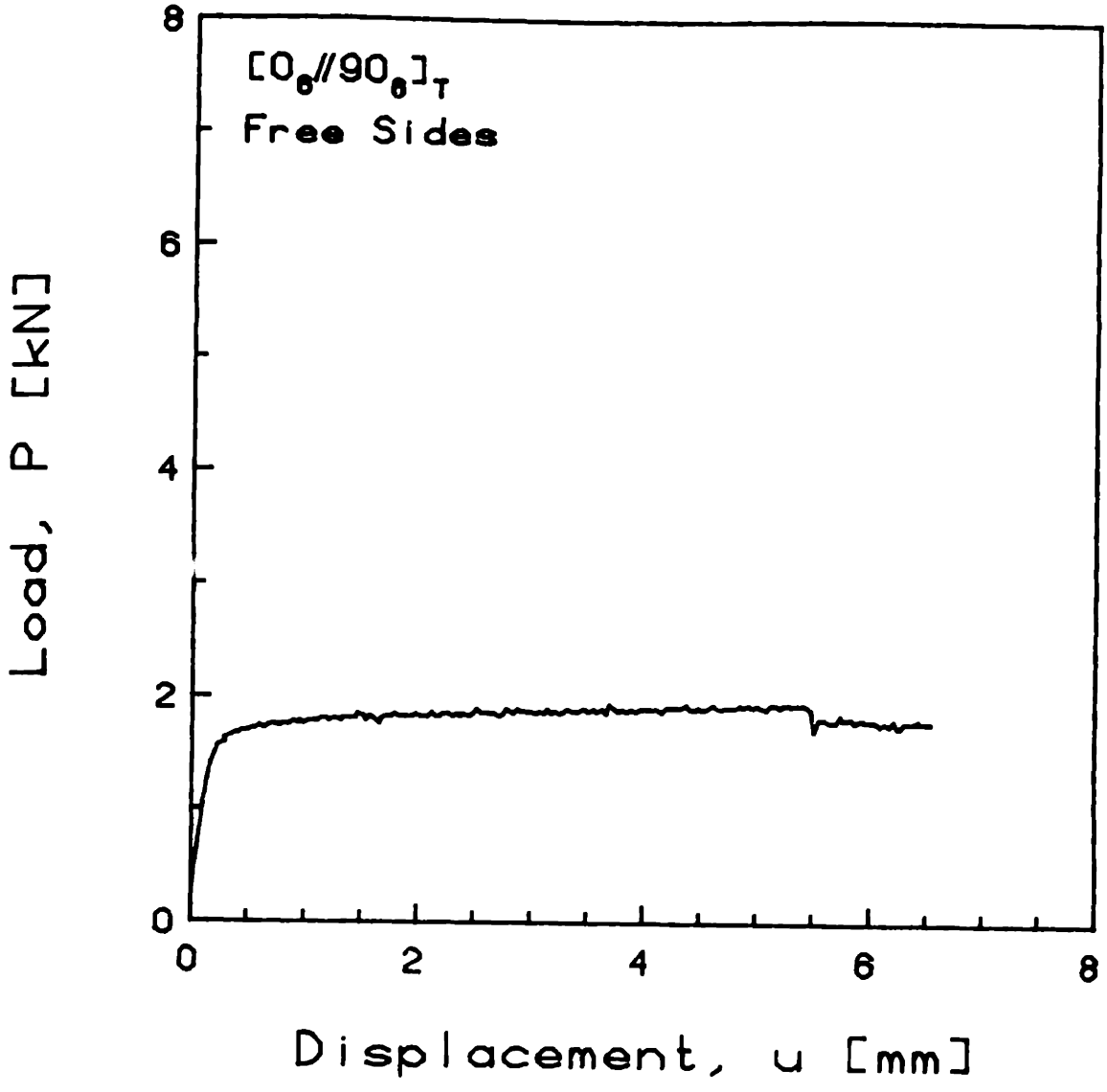

FIGURE G.75 Experimental Plot of Applied Compressive Load versus End-Shortening Displacement for the $[0_6//90_6]_T$ Laminate with Free Side Boundary Conditions

APPENDIX H

ISODEFLECTION CONTOUR MAPS

This appendix contains copies of all of the experimental isodeflection contour maps. They are presented in the same order as discussed in the main text, i.e., according to the sequence summarized in Table 4.4. The results for each laminate type are preceded by the nonlinear Rayleigh-Ritz prediction at 9.0 kN. The predictions for the $[0_6//45_6]_T$ and $[0_6//60_6]_T$ laminate types at 18.0 kN are also included. As before, the results for laminates with clamped side boundary conditions are presented first, followed by those with simply-supported side boundary conditions, and, finally, the results for laminates with free sides are presented.

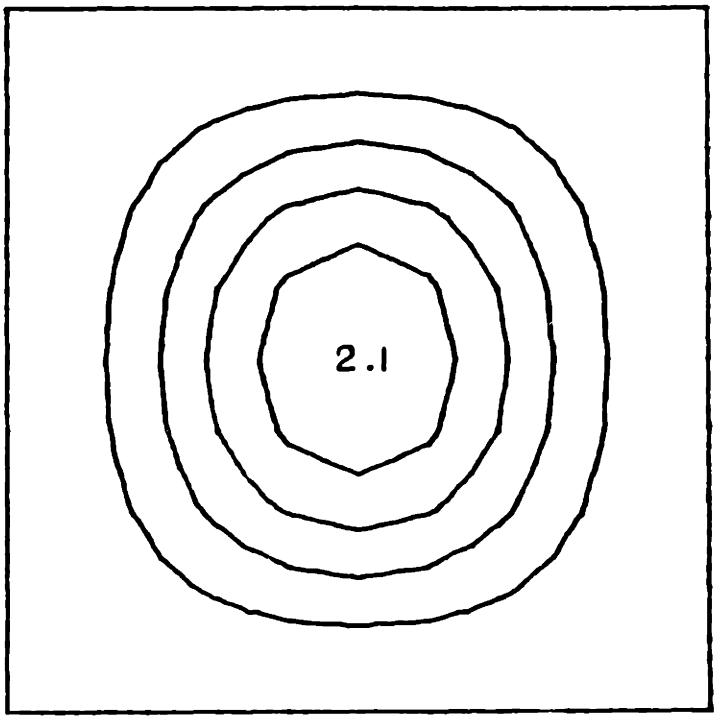

FIGURE H.1 Predicted (via Rayleigh-Ritz) Isodeflection Contour Map for the Laminate Type $[0_3/90_3]_S$ with Clamped Side Boundary Conditions

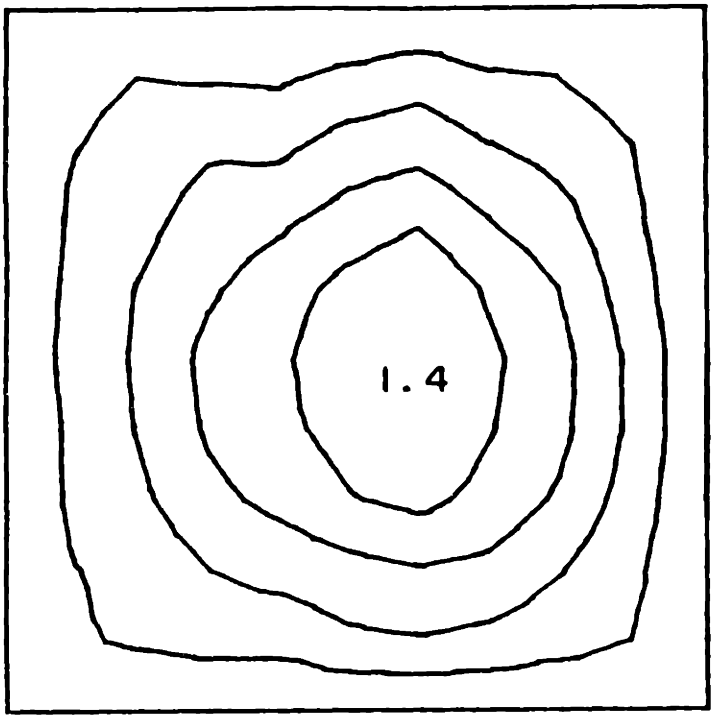

FIGURE H.2 Experimental Isodeflection Contour Map for the $[0_3/90_3]_S$-1 Laminate with Clamped Side Boundary Conditions

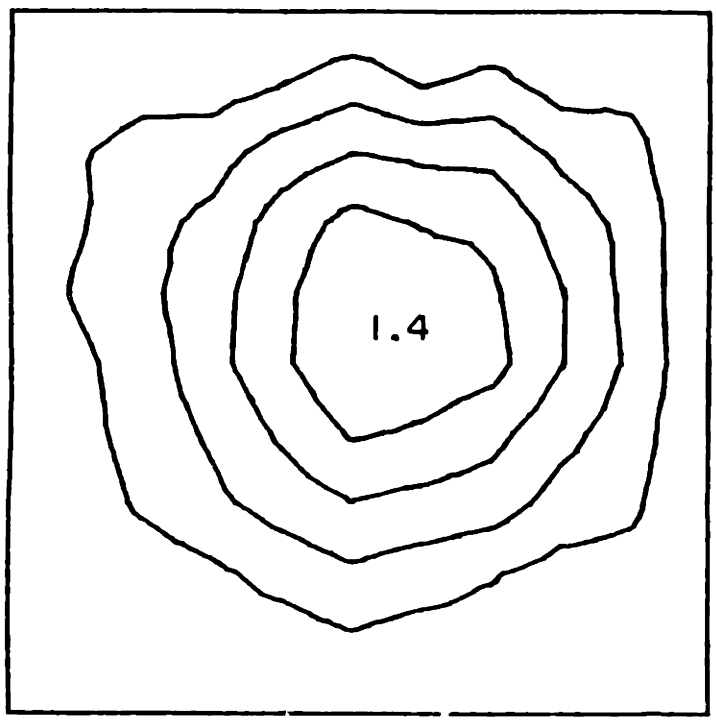

FIGURE H.3 Experimental Isodeflection Contour Map for the $[O_3/90_3]_S$-2 Laminate with Clamped Side Boundary Conditions

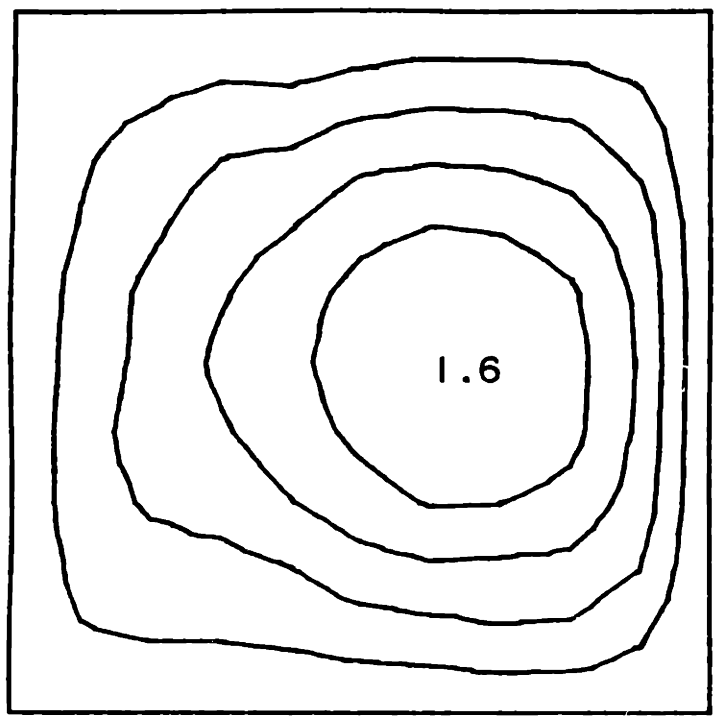

FIGURE H.4 Experimental Isodeflection Contour Map for the $[0_3/90_3]_S$-3 Laminate with Clamped Side Boundary Conditions

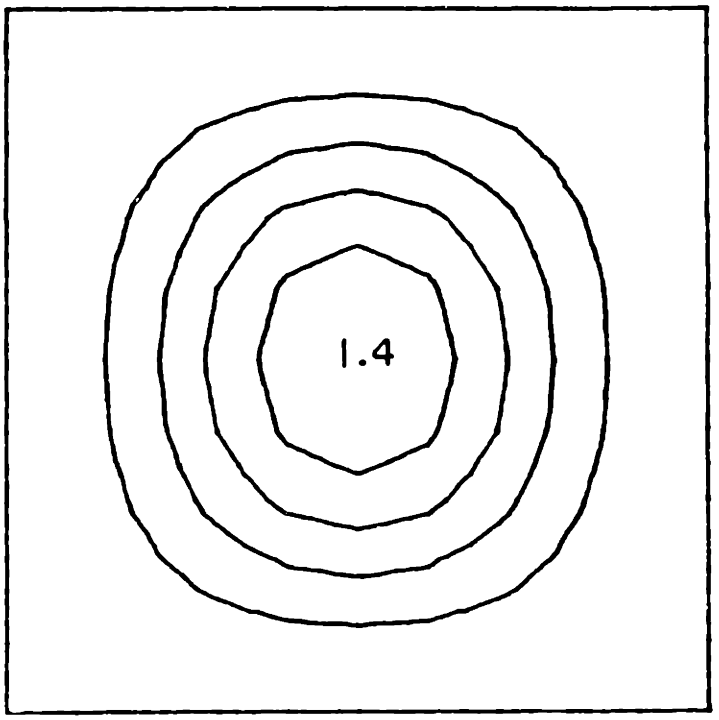

FIGURE H.5 Predicted (via Rayleigh-Ritz) Isodeflection Contour Map for the Laminate Type $[0_3//90_3//90_3//0_3]_T$ with Clamped Side Boundary Conditions

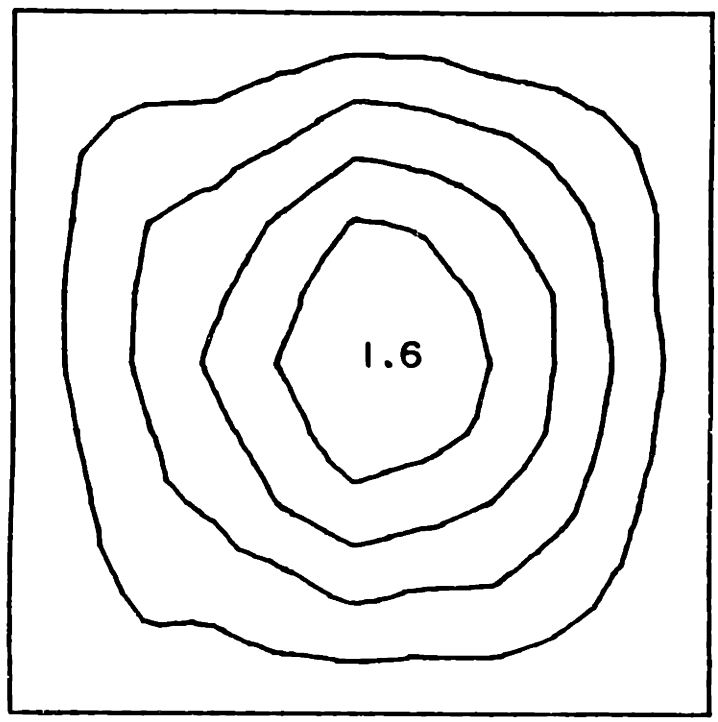

FIGURE H.6 Experimental Isodeflection Contour Map for the $[O_3//90_3//90_3//O_3]_T$-1 Laminate with Clamped Side Boundary Conditions

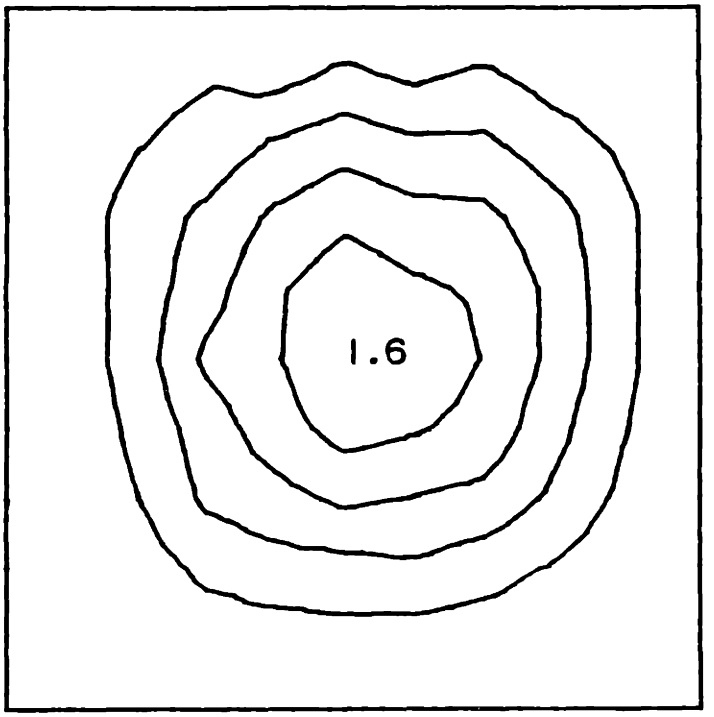

FIGURE H.7 Experimental Isodeflection Contour Map for the $[0_3//90_3//90_3//0_3]_T$-2 Laminate with Clamped Side Boundary Conditions

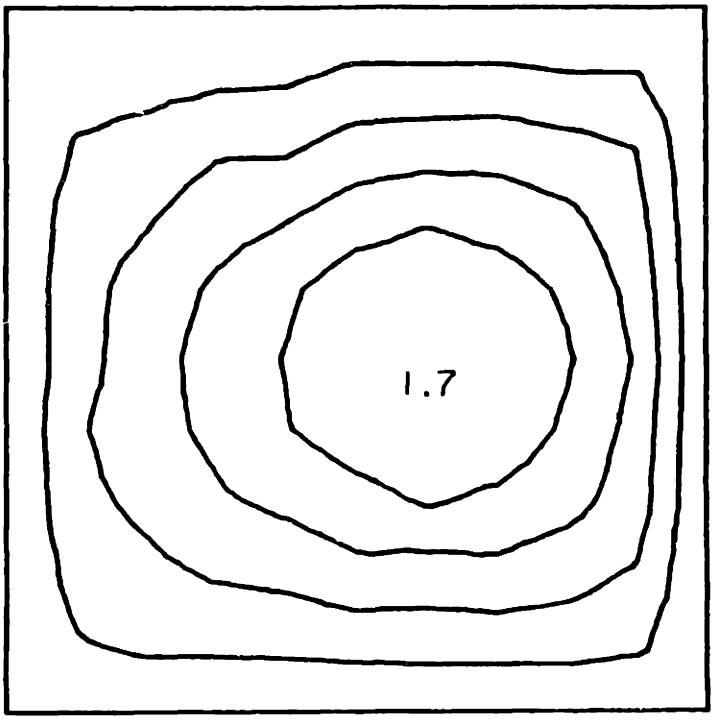

FIGURE H.8 Experimental Isodeflection Contour Map for the $[O_3//90_3//90_3//O_3]_T$-3 Laminate with Clamped Side Boundary Conditions

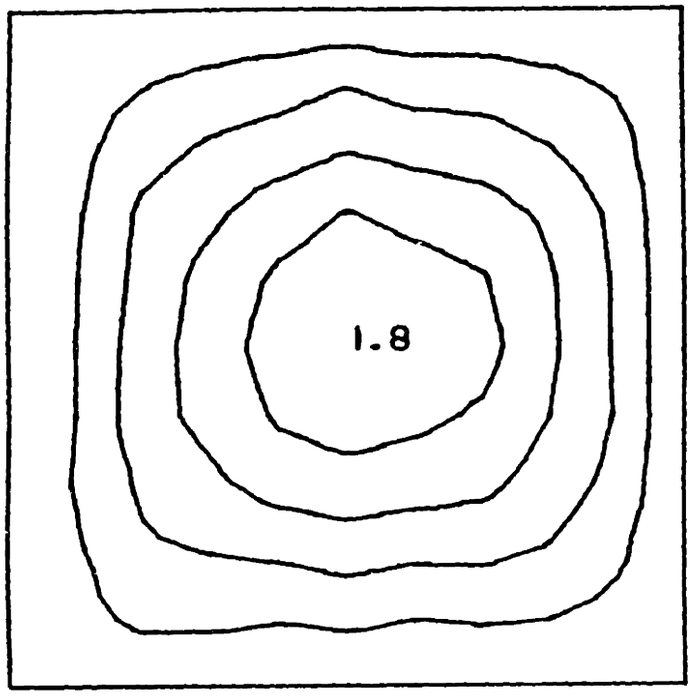

FIGURE H.9 Experimental Isodeflection Contour Map for the $[0_3//90_3//90_3//0_3]_T$-4 Laminate with Clamped Side Boundary Conditions

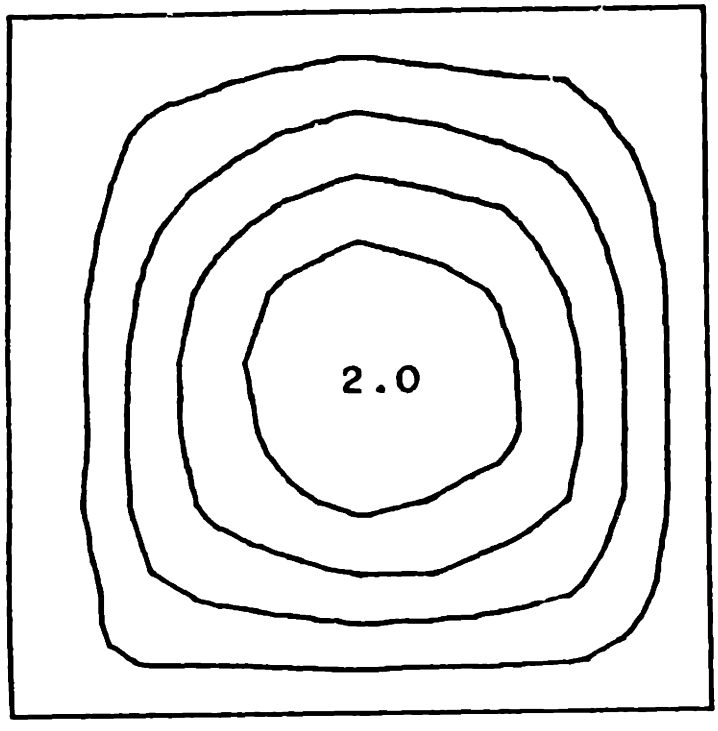

FIGURE H.10 Experimental Phase I Isodeflection Contour Map for the $[O_3//90_3//90_3//O_3]_T$-5 Laminate with Clamped Side Boundary Conditions

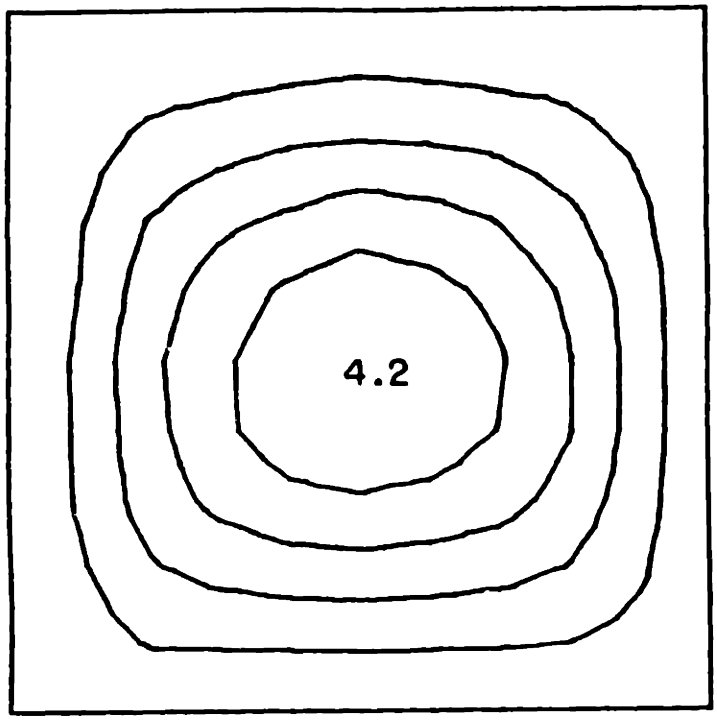

FIGURE H.11 Experimental Phase II Isodeflection Contour Map for the $[0_3//90_3//90_3//0_3]_T$-5 Laminate with Clamped Side Boundary Conditions

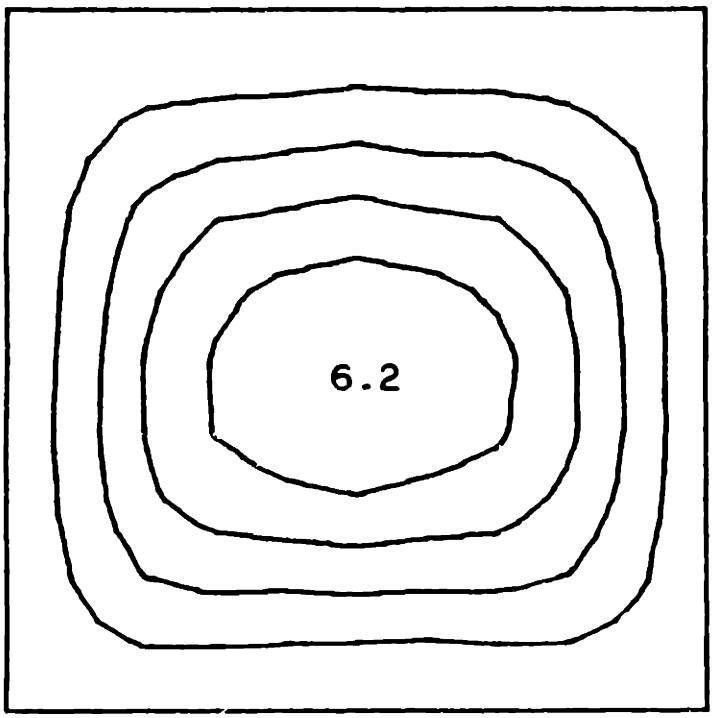

FIGURE H.12 Experimental Phase III Isodeflection Contour Map for the $[O_3//90_3//90_3//O_3]_T$-5 Laminate with Clamped Side Boundary Conditions

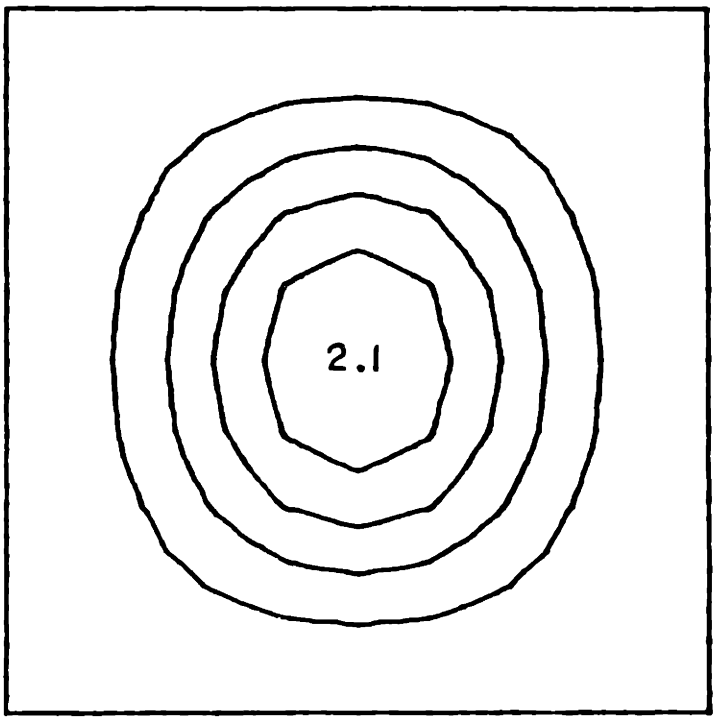

FIGURE H.13 Predicted (via Rayleigh-Ritz) Isodeflection Contour Map for the Laminate Type $[0_3//90_3//0_3//90_3]_T$ with Clamped Side Boundary Conditions

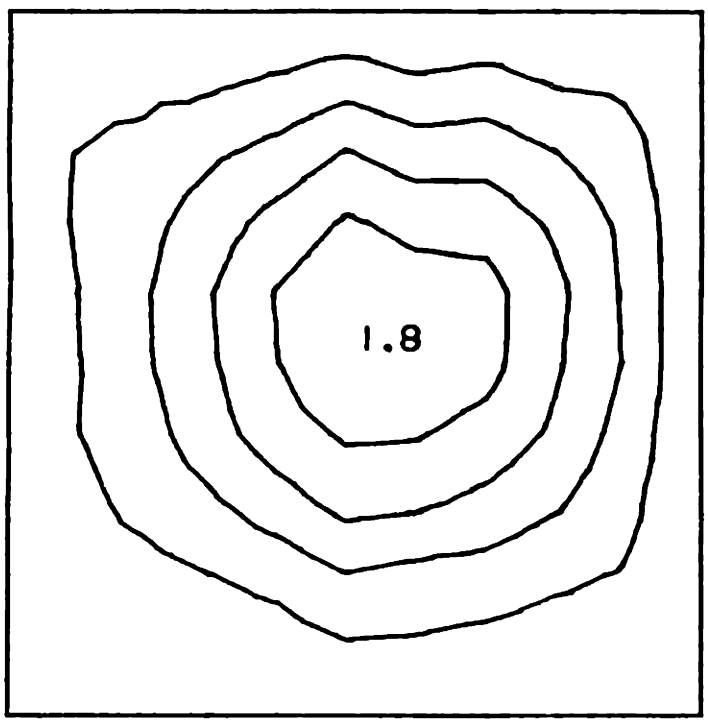

FIGURE H.14 Experimental Isodeflection Contour Map for the $[O_3//90_3//O_3//90_3]_T$-1 Laminate with Clamped Side Boundary Conditions

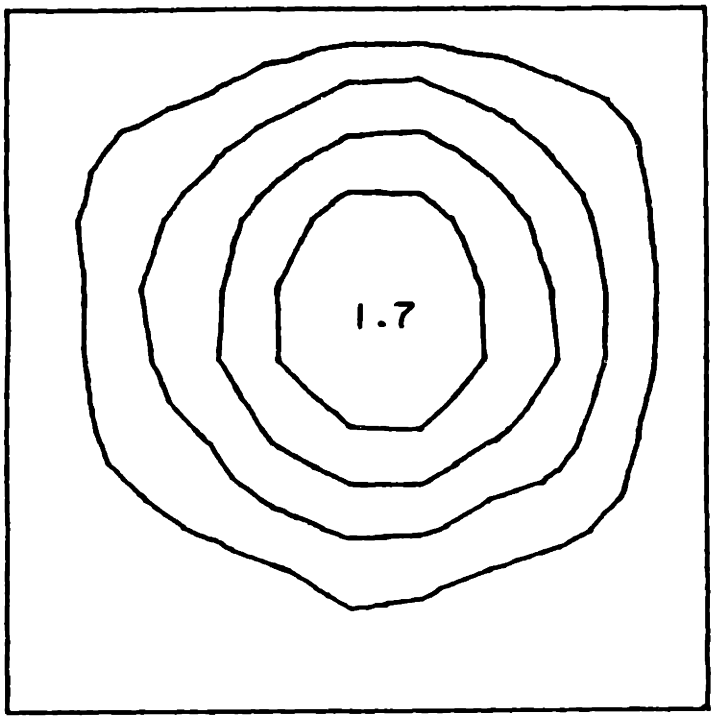

FIGURE H.15 Experimental Phase I Isodeflection Contour Map for the $[0_3//90_3//0_3//90_3]_T$-2 Laminate with Clamped Side Boundary Conditions

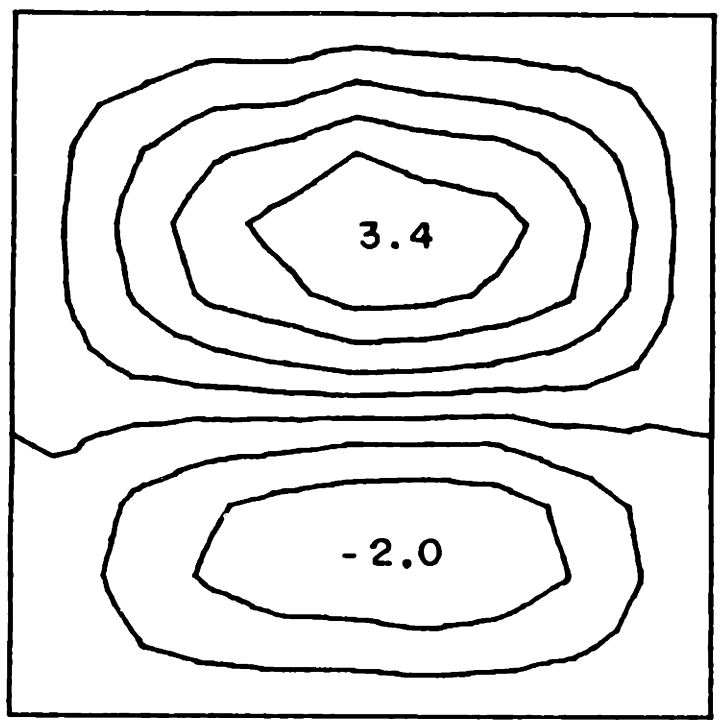

FIGURE H.16 Experimental Phase II Isodeflection Contour Map for the $[0_3//90_3//0_3//90_3]_T$-2 Laminate with Clamped Side Boundary Conditions

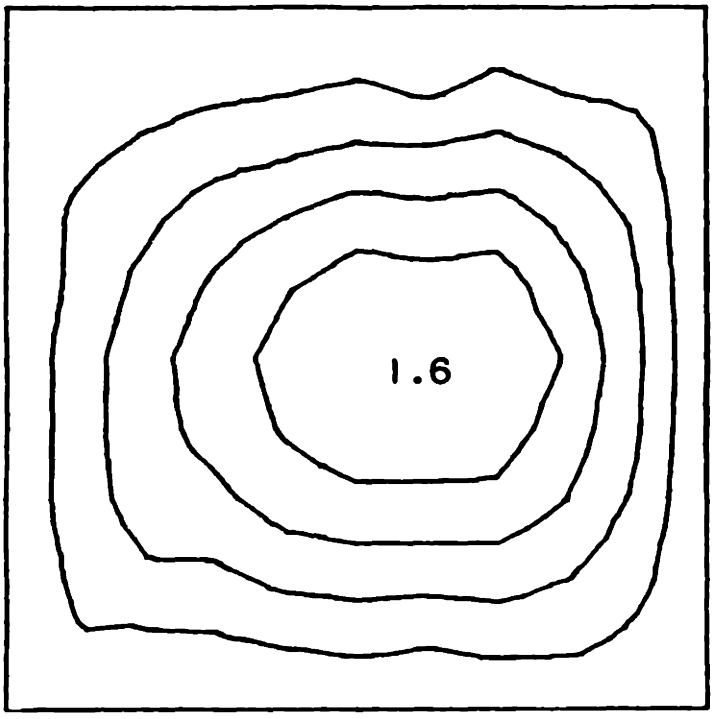

FIGURE H.17 Experimental Isodeflection Contour Map for the $[O_3//90_3//O_3//90_3]_T$-3 Laminate with Clamped Side Boundary Conditions

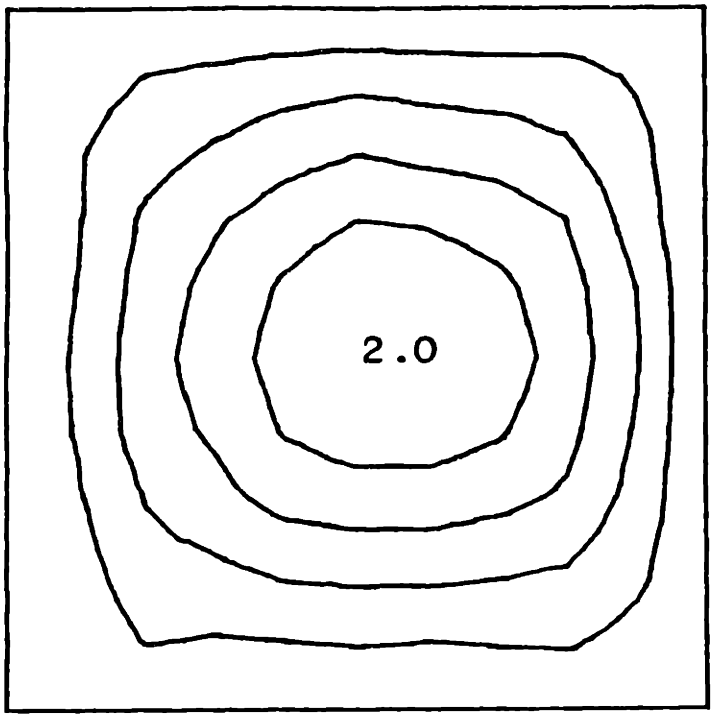

FIGURE H.18 Experimental Isodeflection Contour Map for the $[O_3//90_3//O_3//90_3]_T$-4 Laminate with Clamped Side Boundary Conditions

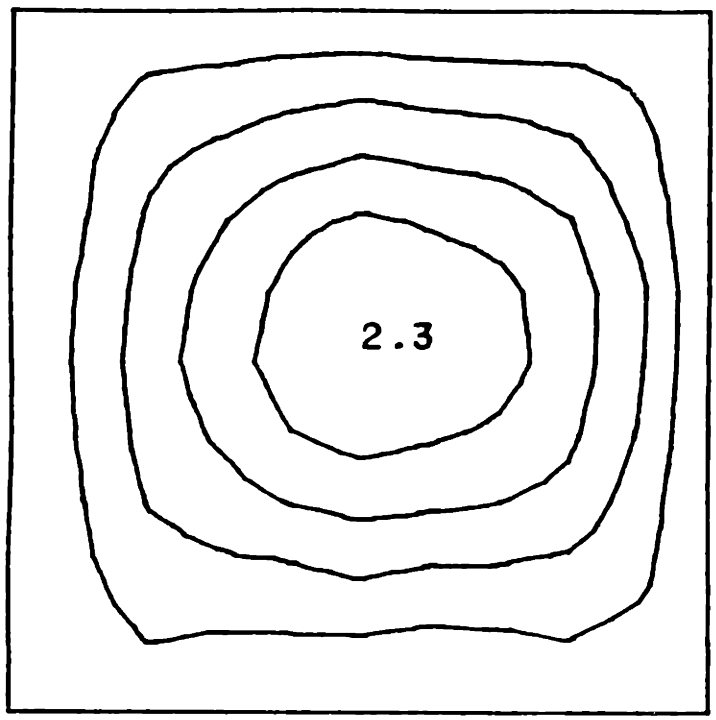

FIGURE H.19 Experimental Phase I Isodeflection Contour Map for the $[O_3//90_3//O_3//90_3]_T$-5 Laminate with Clamped Side Boundary Conditions

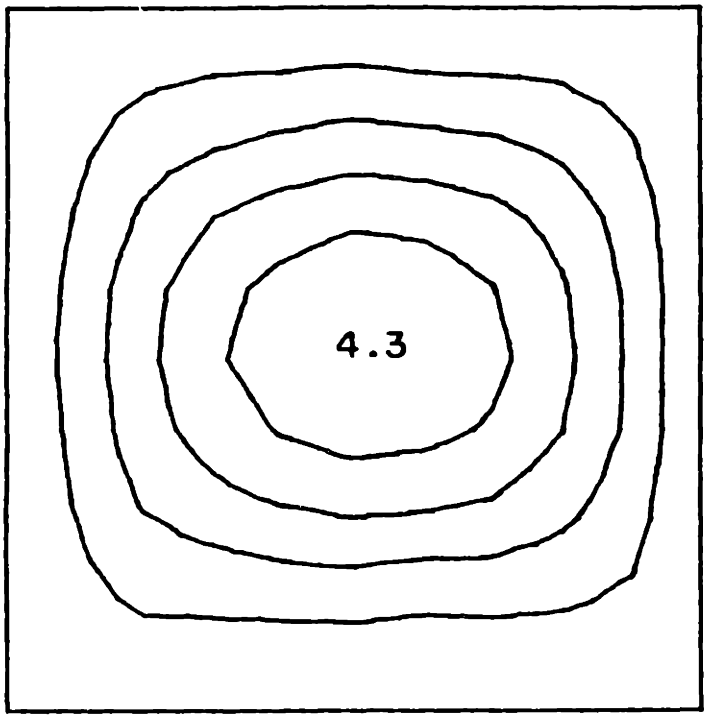

FIGURE H.20 Experimental Phase II Isodeflection Contour Map for the $[O_3//90_3//O_3//90_3]_T$-5 Laminate with Clamped Side Boundary Conditions

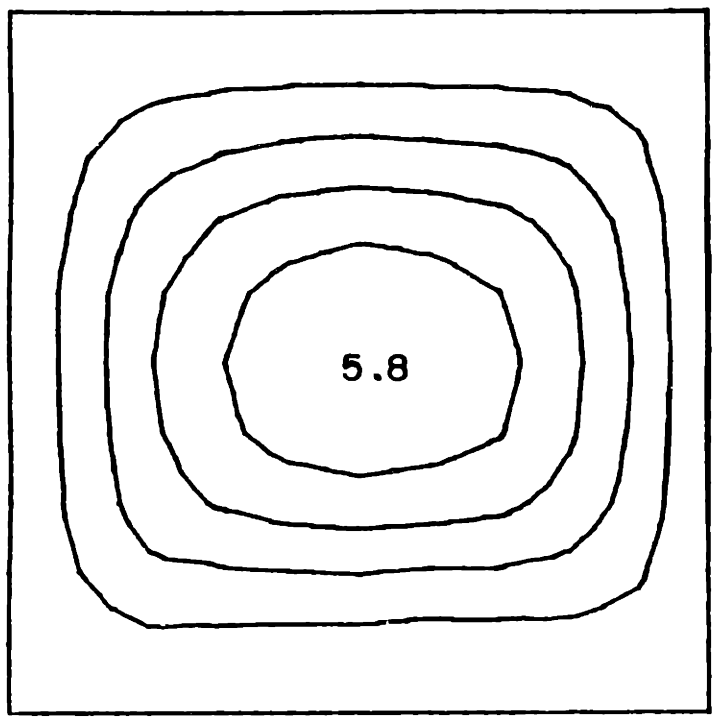

FIGURE H.21 Experimental Phase III Isodeflection Contour Map for the $[O_3//90_3//O_3//90_3]_T$-5 Laminate with Clamped Side Boundary Conditions

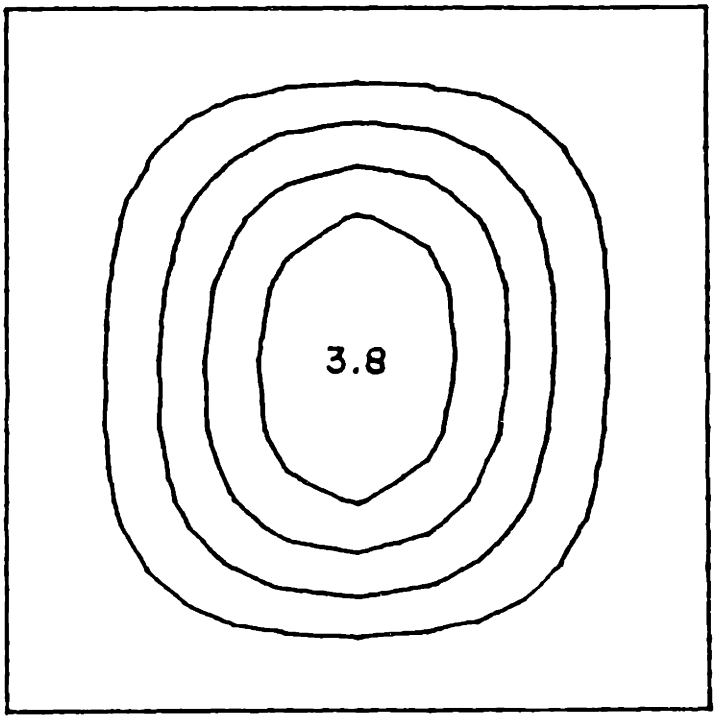

FIGURE H.22 Predicted (via Rayleigh-Ritz) Isodeflection Contour Map for the Laminate Type $[O_2//45_2//O_2//45_2//O_2]_T$ with Clamped Side Boundary Conditions

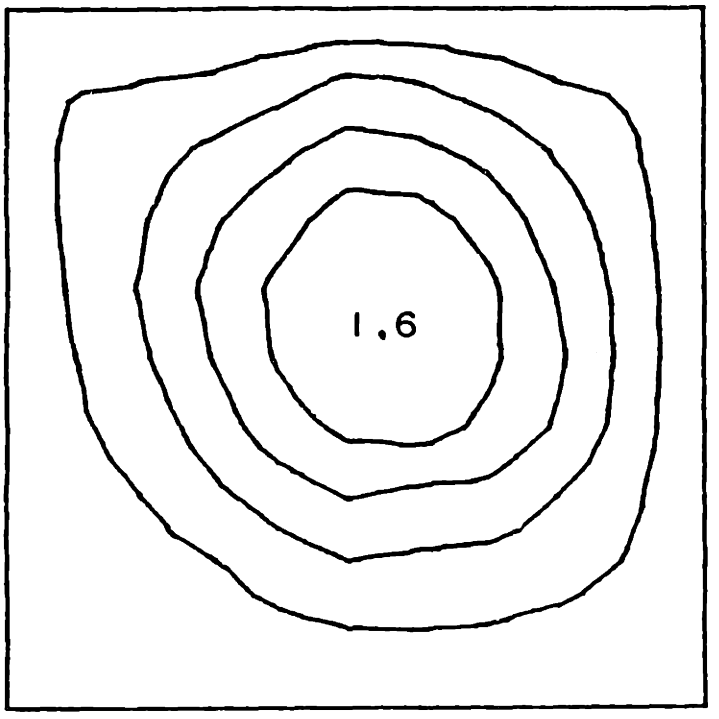

FIGURE H.23 Experimental Isodeflection Contour Map for the $[0_2//45_2//0_2//45_2//0_2]_T$-1 Laminate with Clamped Side Boundary Conditions

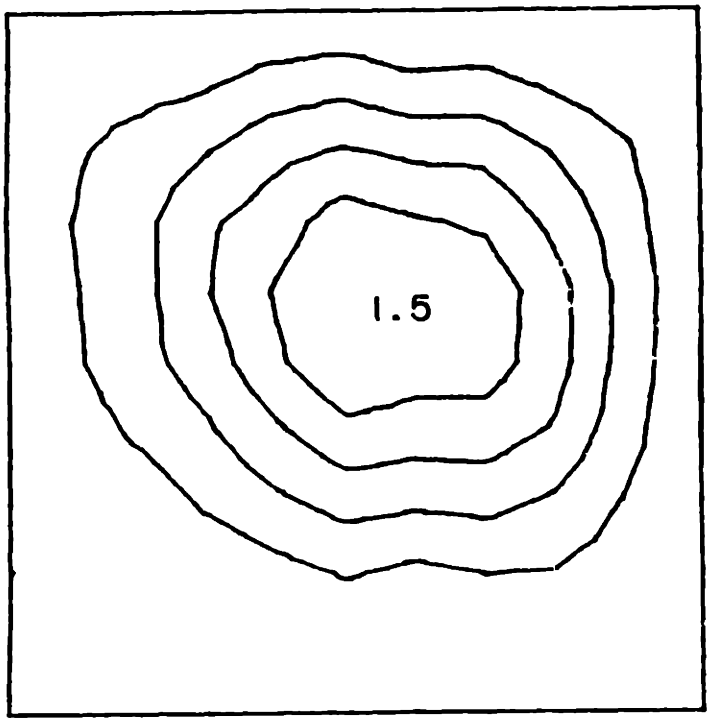

Experimental

$[0_2//45_2//0_2//45_2//0_2]_T$-2

Clamped Sides

3.7 kN

FIGURE H.24 Experimental Isodeflection Contour Map for the $[0_2//45_2//0_2//45_2//0_2]_T$-2 Laminate with Clamped Side Boundary Conditions

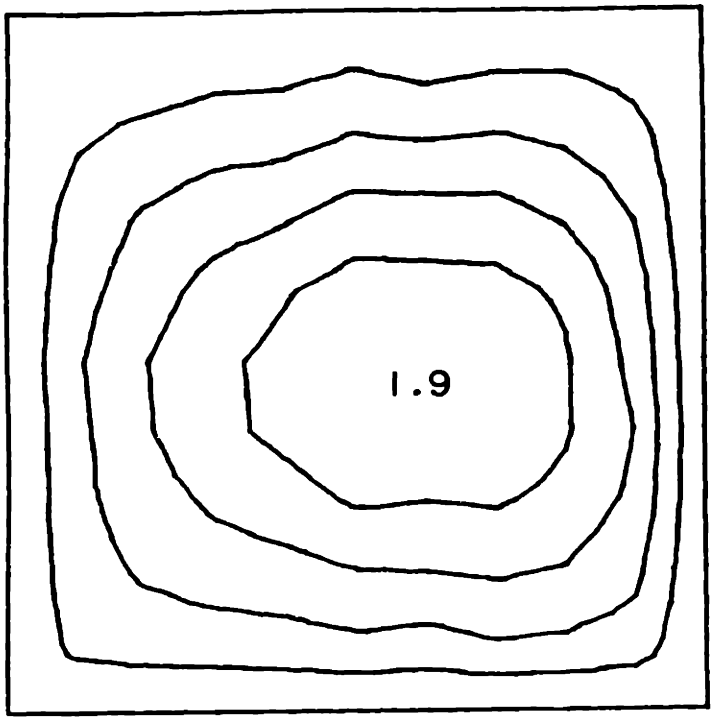

FIGURE H.25 Experimental Isodeflection Contour Map for the $[O_2//45_2//O_2//45_2//O_2]_T$-3 Laminate with Clamped Side Boundary Conditions

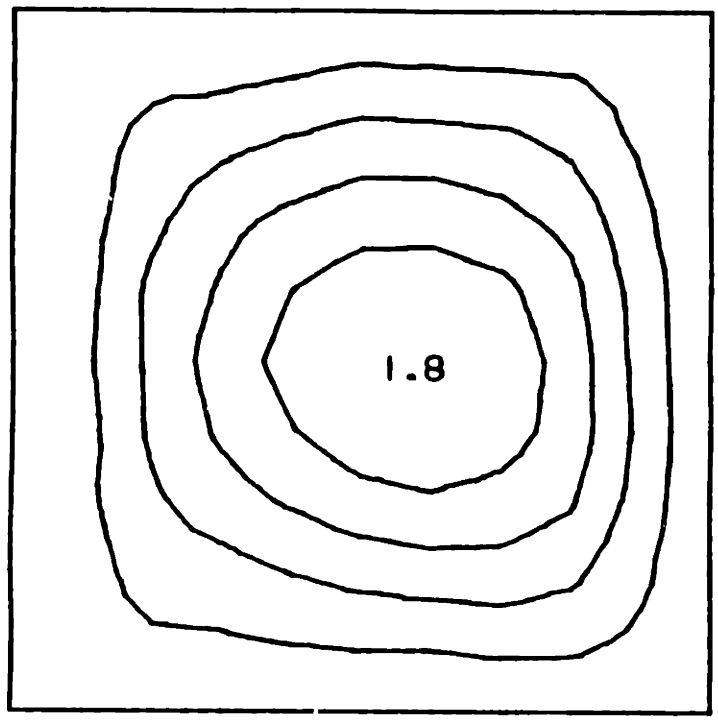

FIGURE H.26 Experimental Isodeflection Contour Map for the $[O_2//45_2//O_2//45_2//O_2]_T$-4 Laminate with Clamped Side Boundary Conditions

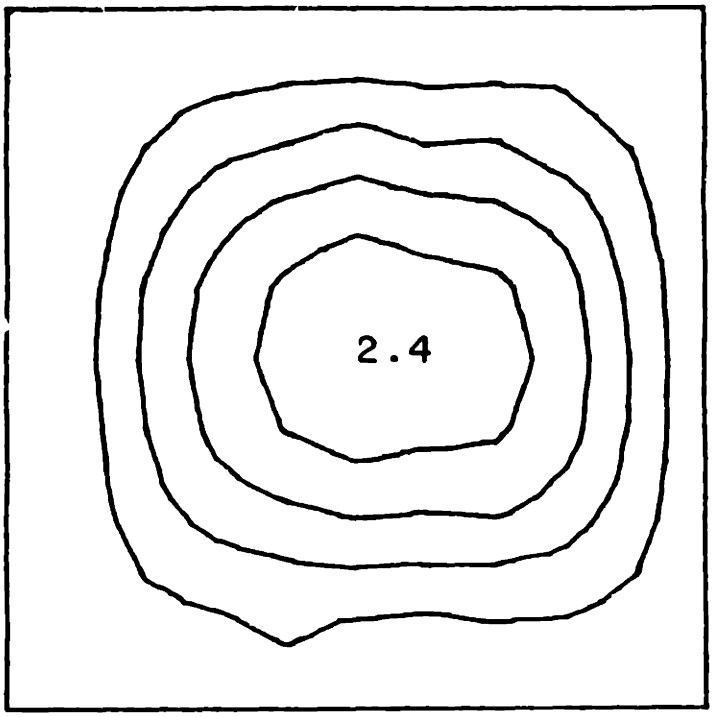

FIGURE H.27 Experimental Phase I Isodeflection Contour Map for the $[0_2//45_2//0_2//45_2//0_2]_T$-5 Laminate with Clamped Side Boundary Conditions

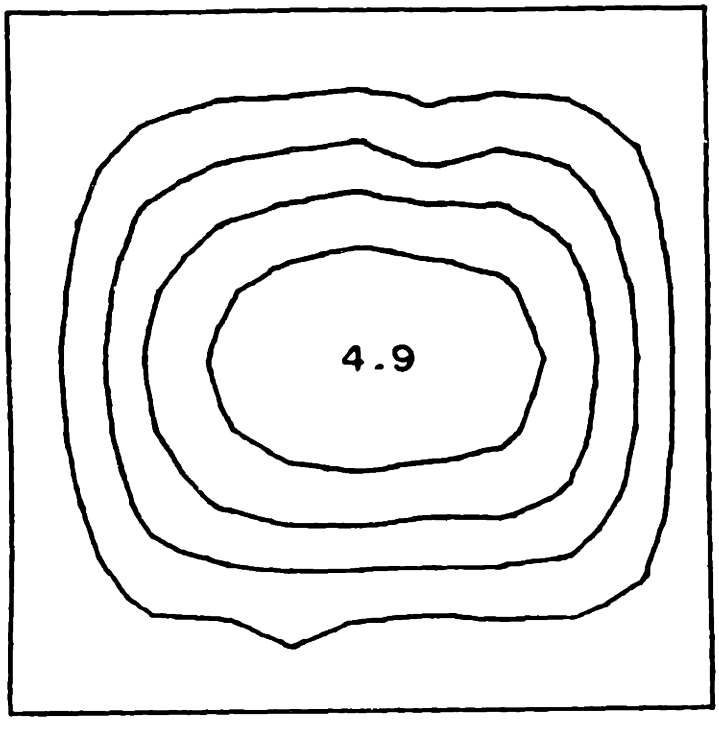

FIGURE H.28 Experimental Phase II Isodeflection Contour Map for the $[O_2//45_2//O_2//45_2//O_2]_T$-5 Laminate with Clamped Side Boundary Conditions

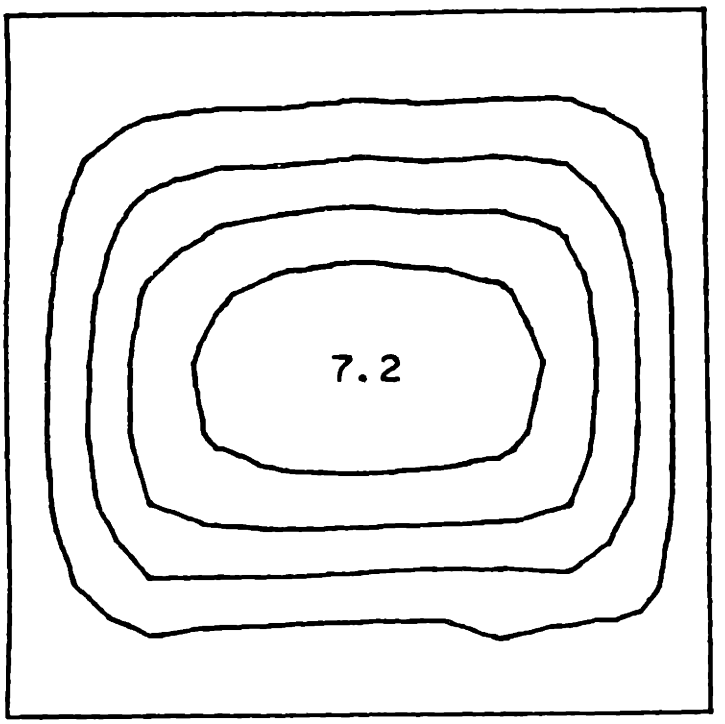

Experimental

$[0_2//45_2//0_2//45_2//0_2]_T$-5

Clamped Sides

13.0 kN

FIGURE H.29 Experimental Phase III Isodeflection Contour Map for the $[0_2//45_2//0_2//45_2//0_2]_T$-5 Laminate with Clamped Side Boundary Conditions

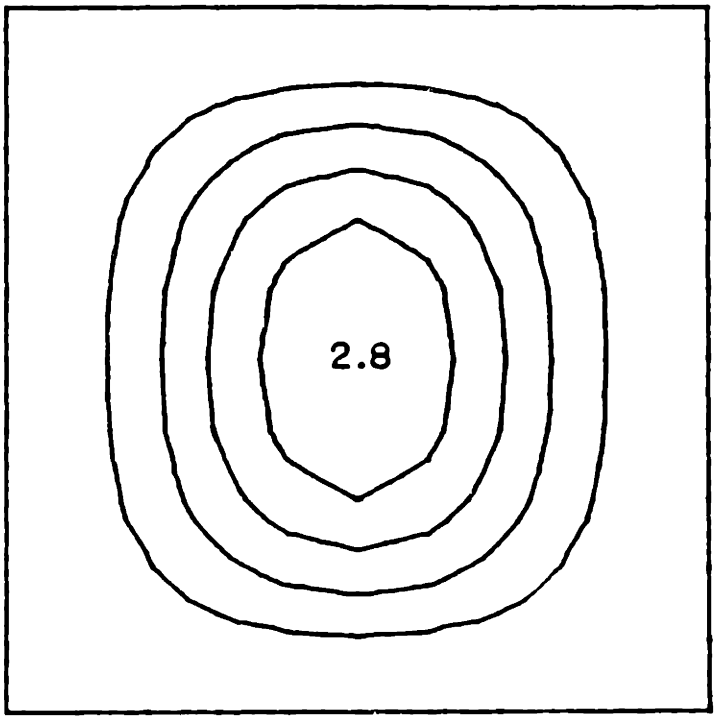

FIGURE H.30 Predicted (via Rayleigh-Ritz) Isodeflection Contour Map for the Laminate Type $[O_2//45_2//O_2//-45_2//O_2]_T$ with Clamped Side Boundary Conditions

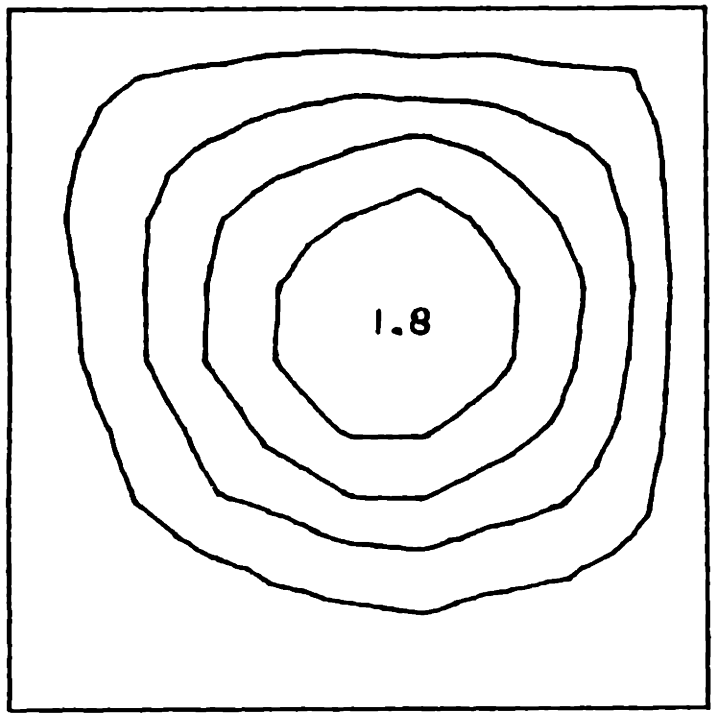

FIGURE H.31 Experimental Isodeflection Contour Map for the $[O_2//45_2//O_2//-45_2//O_2]_T$-1 Laminate with Clamped Side Boundary Conditions

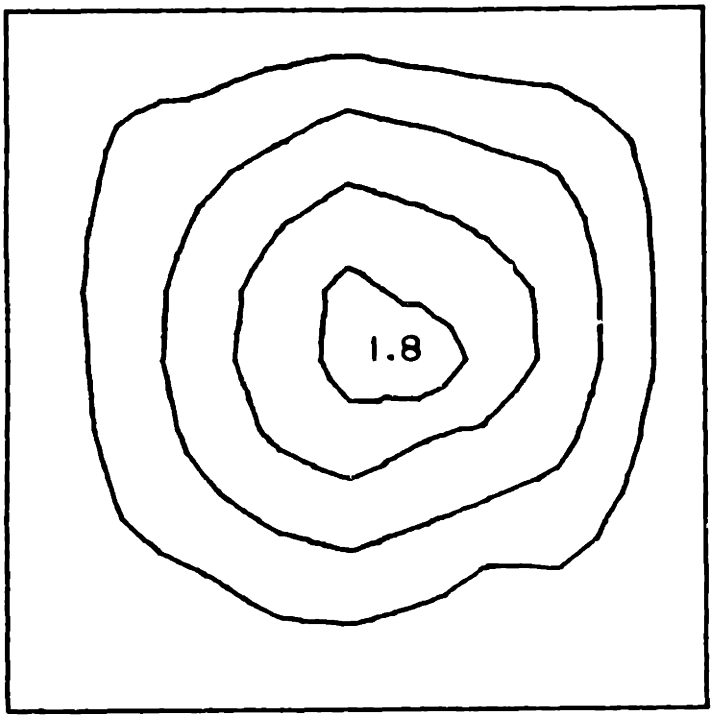

FIGURE H.32 Experimental Isodeflection Contour Map for the $[O_2//45_2//O_2//-45_2//O_2]_T$-2 Laminate with Clamped Side Boundary Conditions

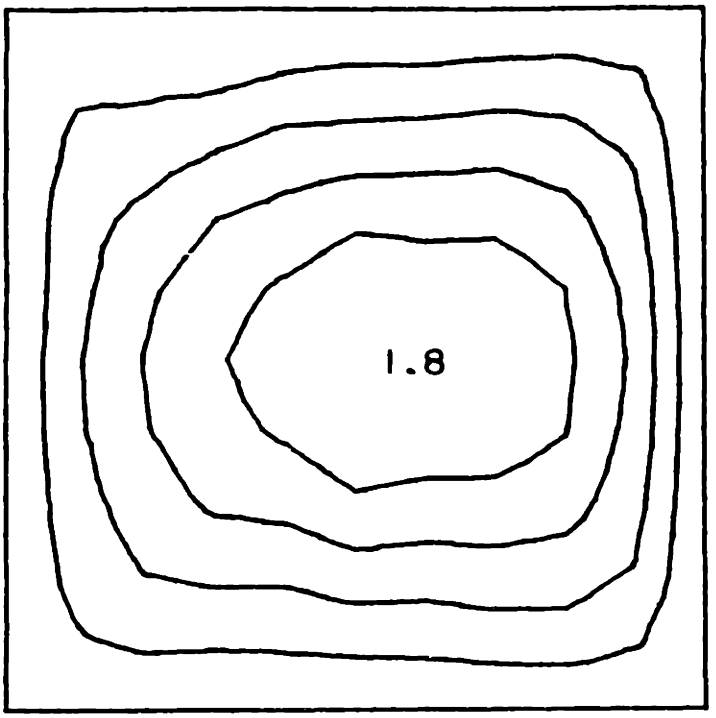

FIGURE H.33 Experimental Isodeflection Contour Map for the $[O_2//45_2//O_2//-45_2//O_2]_T$-3 Laminate with Clamped Side Boundary Conditions

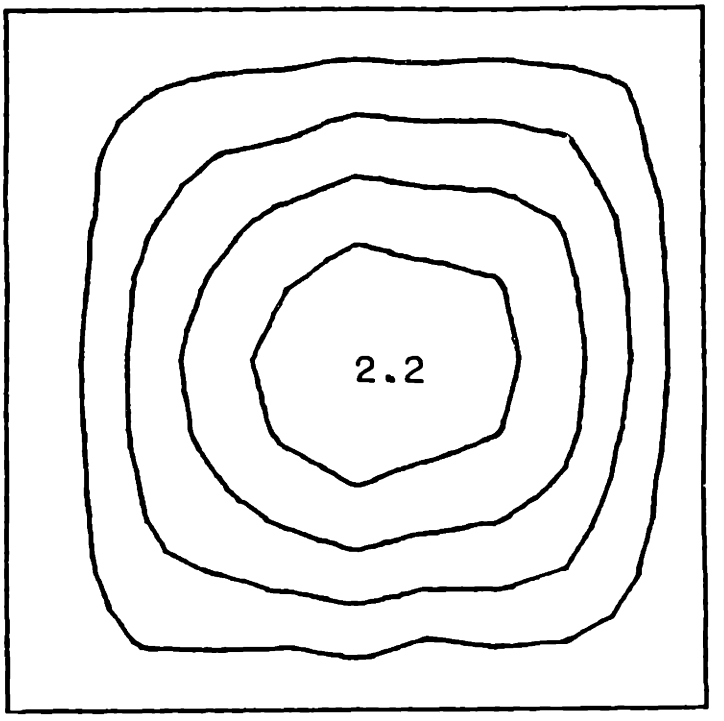

FIGURE H.34 Experimental Isodeflection Contour Map for the $[O_2//45_2//O_2//-45_2//O_2]_T$-4 Laminate with Clamped Side Boundary Conditions

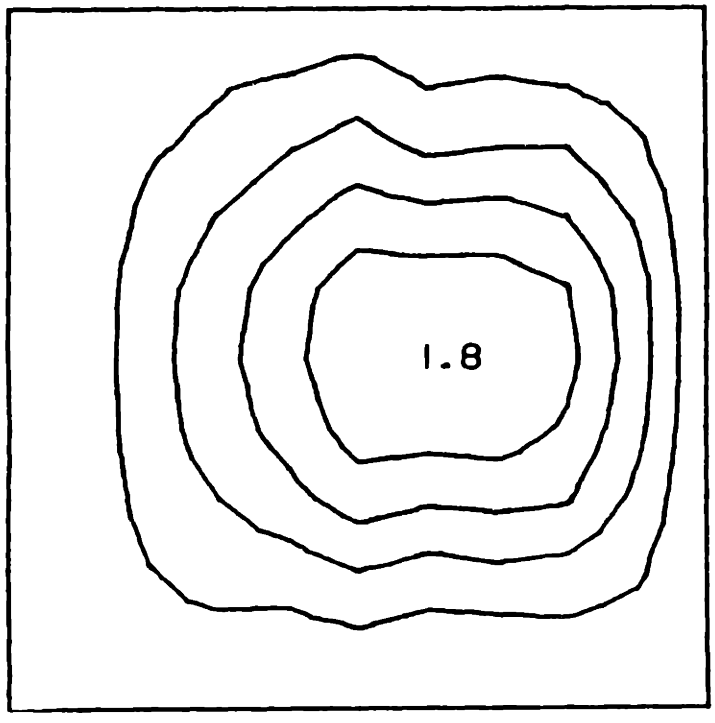

FIGURE H.35 Experimental Phase I Isodeflection Contour Map for the $[0_2//45_2//0_2//-45_2//0_2]_T$-5 Laminate with Clamped Side Boundary Conditions

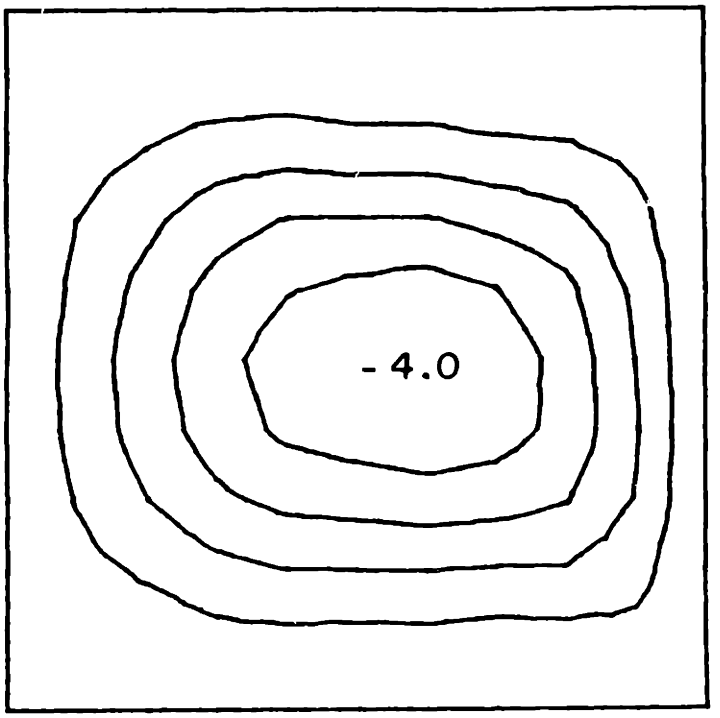

FIGURE H.36 Experimental Phase II Isodeflection Contour Map for the $[O_2//45_2//O_2//-45_2//O_2]_T$-5 Laminate with Clamped Side Boundary Conditions

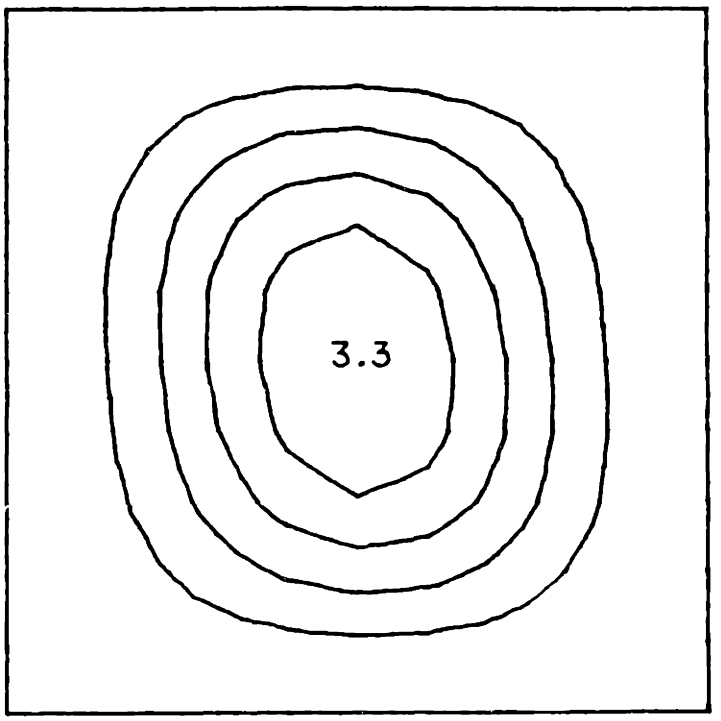

FIGURE H.37 Predicted (via Rayleigh-Ritz) Isodeflection Contour Map for the Laminate Type $[0_6//15_6]_T$ with Clamped Side Boundary Conditions

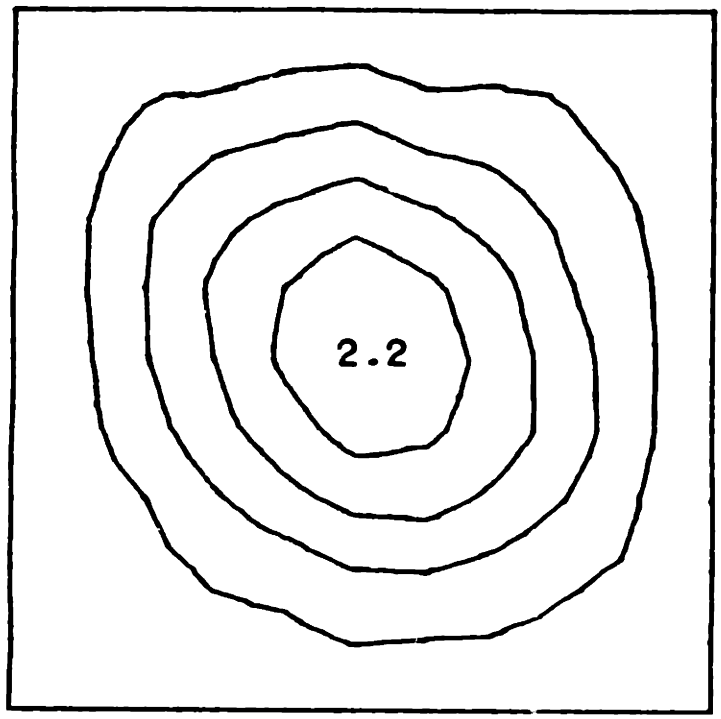

FIGURE H.38 Experimental Isodeflection Contour Map for the $[O_6//15_6]_T$-1 Laminate with Clamped Side Boundary Conditions

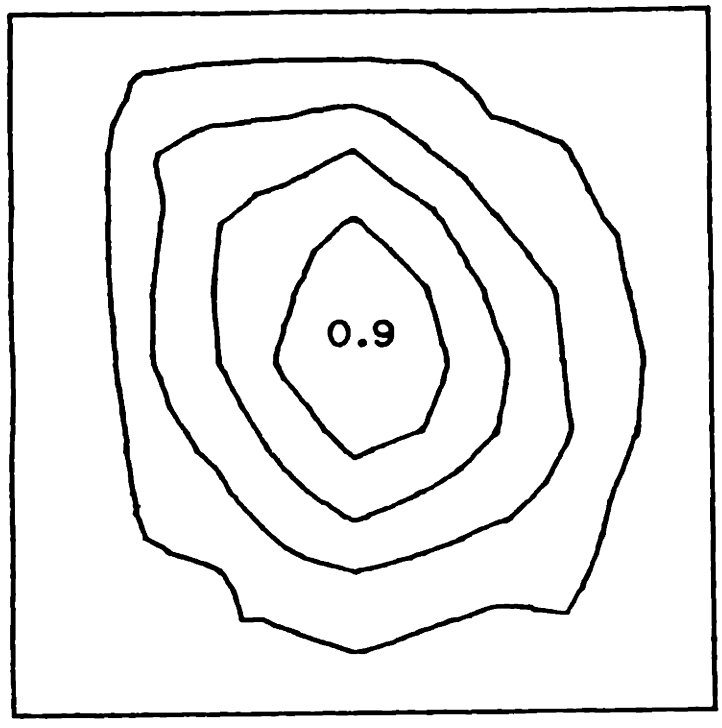

FIGURE H.39 Experimental Isodeflection Contour Map for the $[0_6//15_6]_T$-2 Laminate with Clamped Side Boundary Conditions

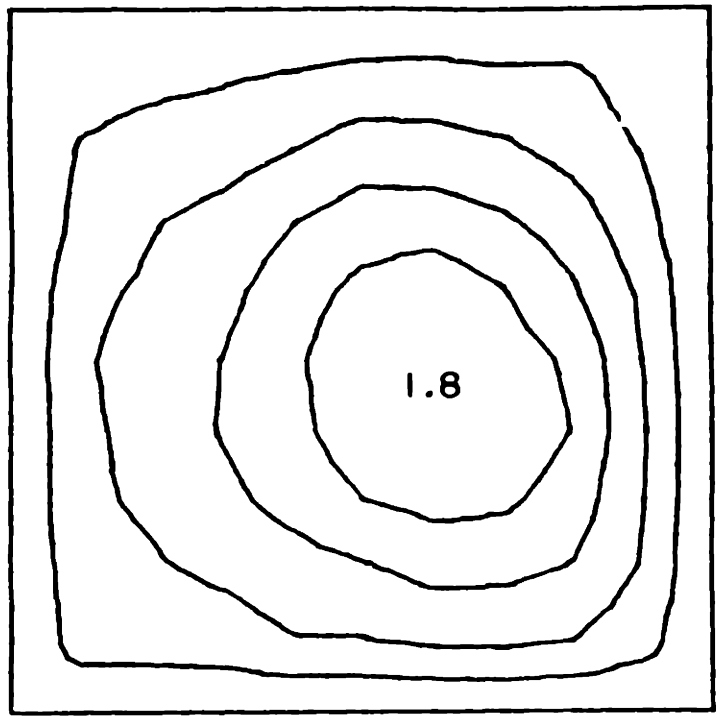

FIGURE H.40 Experimental Isodeflection Contour Map for the $[0_6//15_6]_T$-3 Laminate with Clamped Side Boundary Conditions

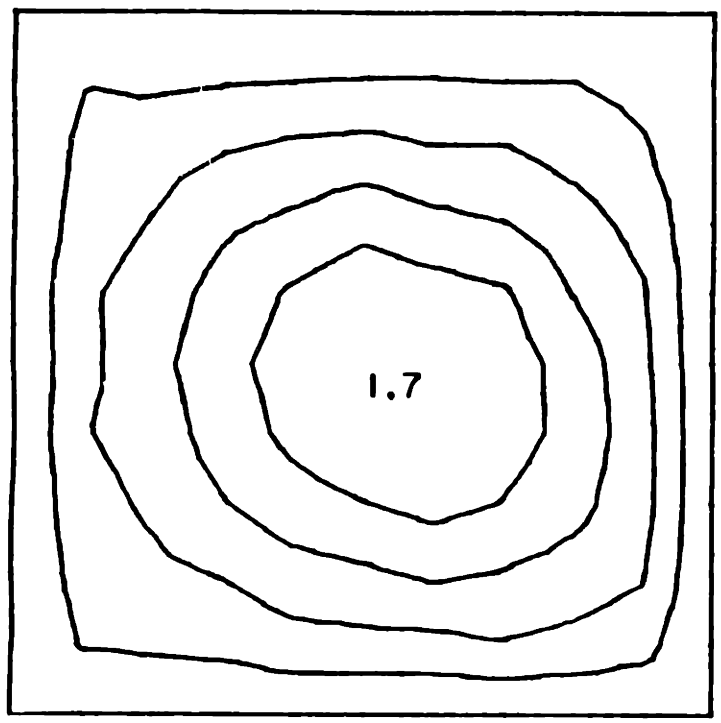

FIGURE H.41 Experimental Isodeflection Contour Map for the $[O_6//15_6]_T$-4 Laminate with Clamped Side Boundary Conditions

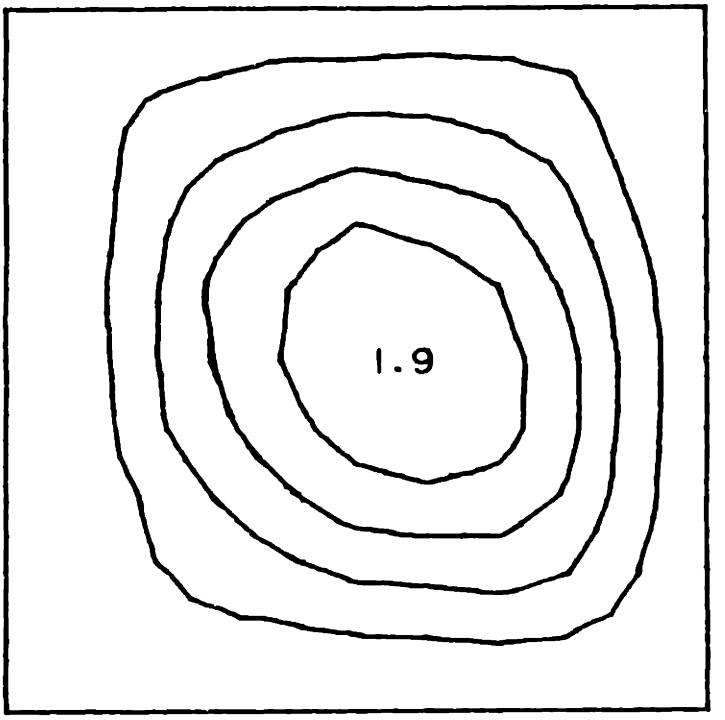

FIGURE H.42 Experimental Phase I Isodeflection Contour Map for the $[O_6//15_6]_T$-5 Laminate with Clamped Side Boundary Conditions

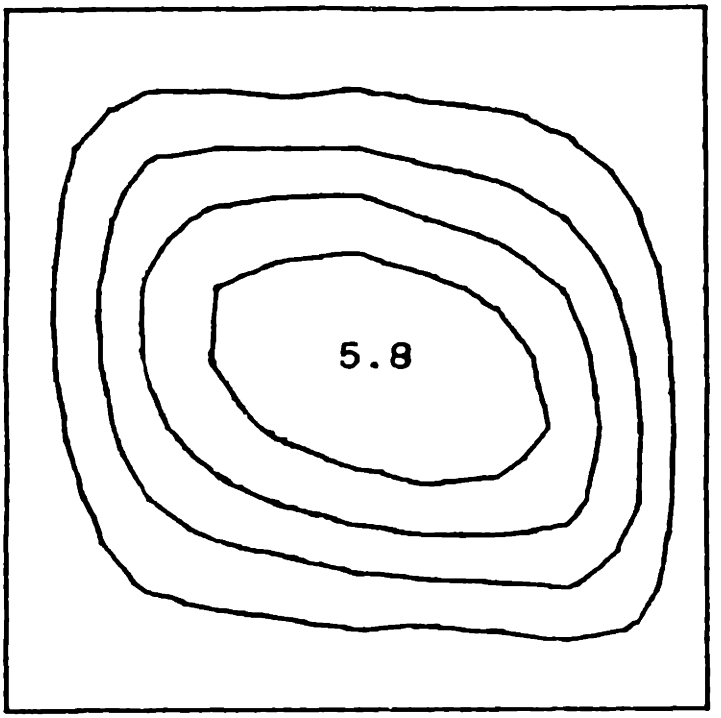

FIGURE H.43 Experimental Phase II Isodeflection Contour Map for the $[0_6//15_6]_T$-5 Laminate with Clamped Side Boundary Conditions

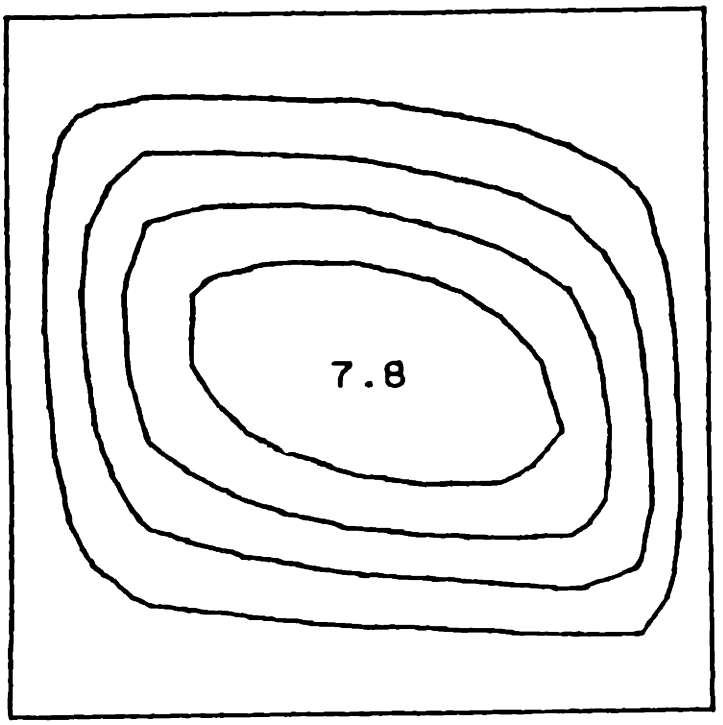

FIGURE H.44 Experimental Phase III Isodeflection Contour Map for the $[0_6//15_6]_T$-5 Laminate with Clamped Side Boundary Conditions

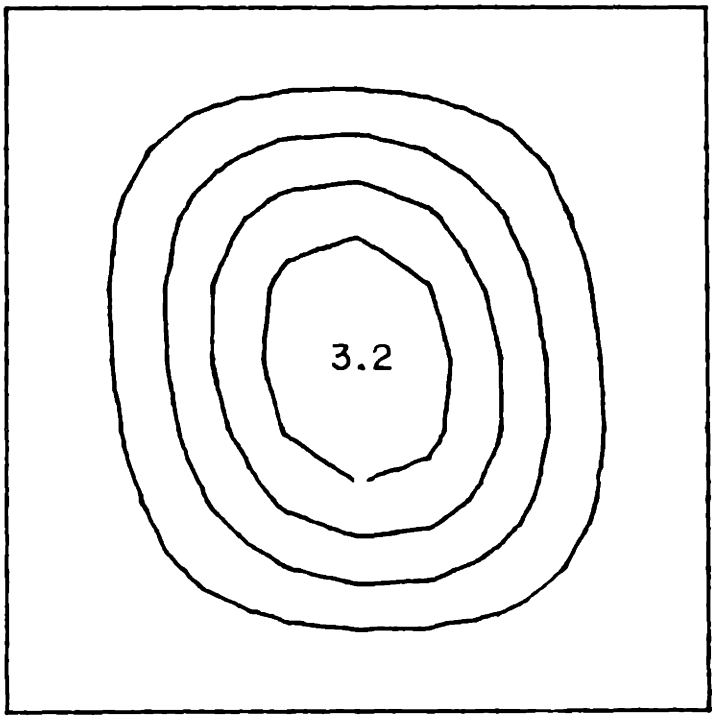

FIGURE H.45 Predicted (via Rayleigh-Ritz) Isodeflection Contour Map for the Laminate Type $[0_6//30_6]_T$ with Clamped Side Boundary Conditions

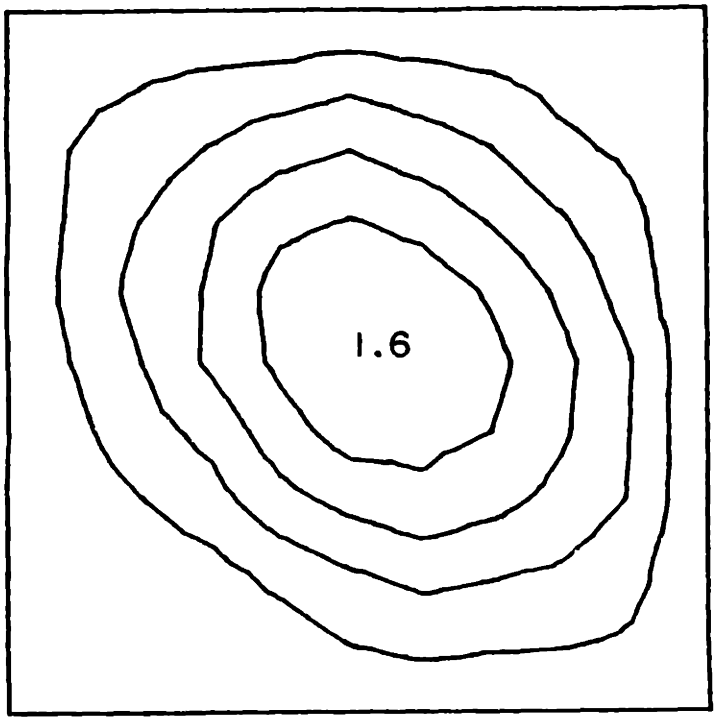

FIGURE H.46 Experimental Isodeflection Contour Map for the $[0_6//30_6]_T$-1 Laminate with Clamped Side Boundary Conditions

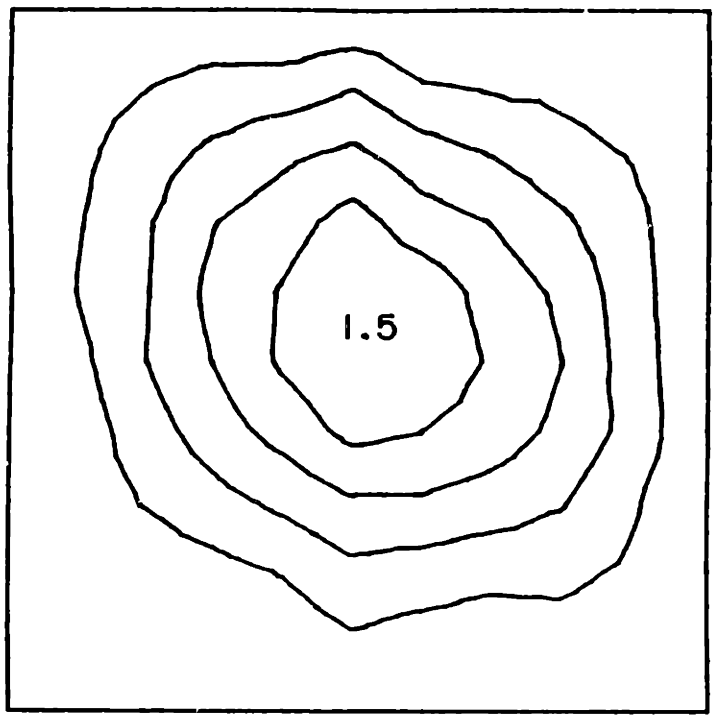

FIGURE H.47 Experimental Isodeflection Contour Map for the $[0_6//30_6]_T$-2 Laminate with Clamped Side Boundary Conditions

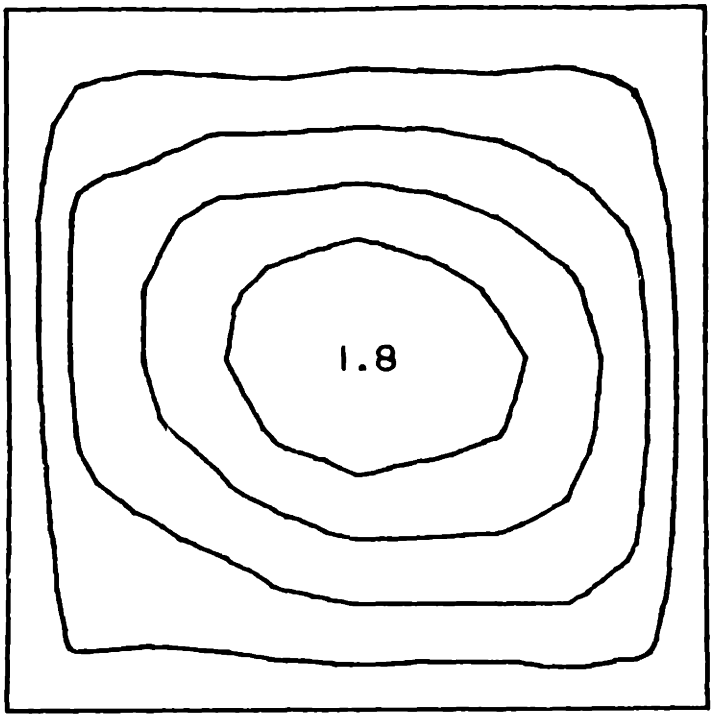

FIGURE H.48 Experimental Isodeflection Contour Map for the $[0_6//30_6]_T$-3 Laminate with Clamped Side Boundary Conditions

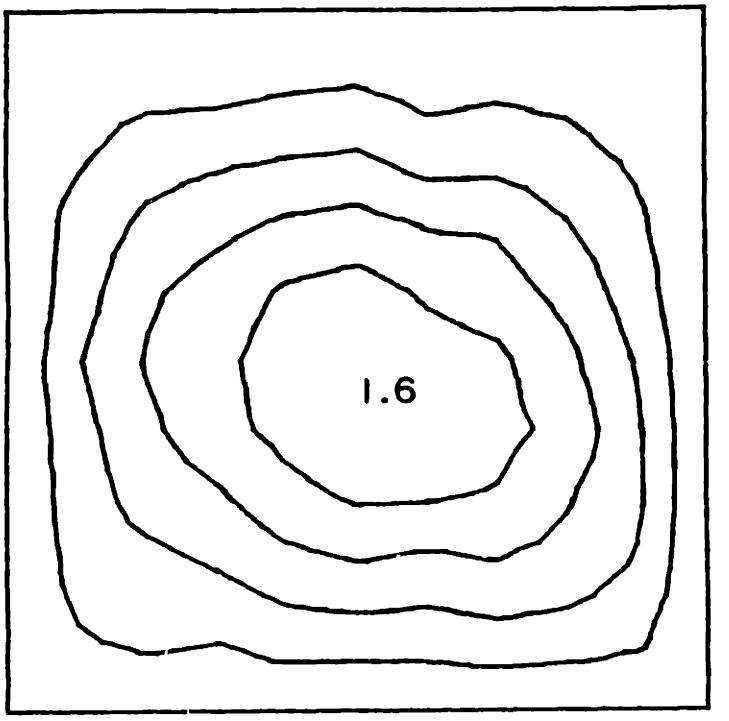

FIGURE H.49 Experimental Isodeflection Contour Map for the $[O_6//30_6]_T$-4 Laminate with Clamped Side Boundary Conditions

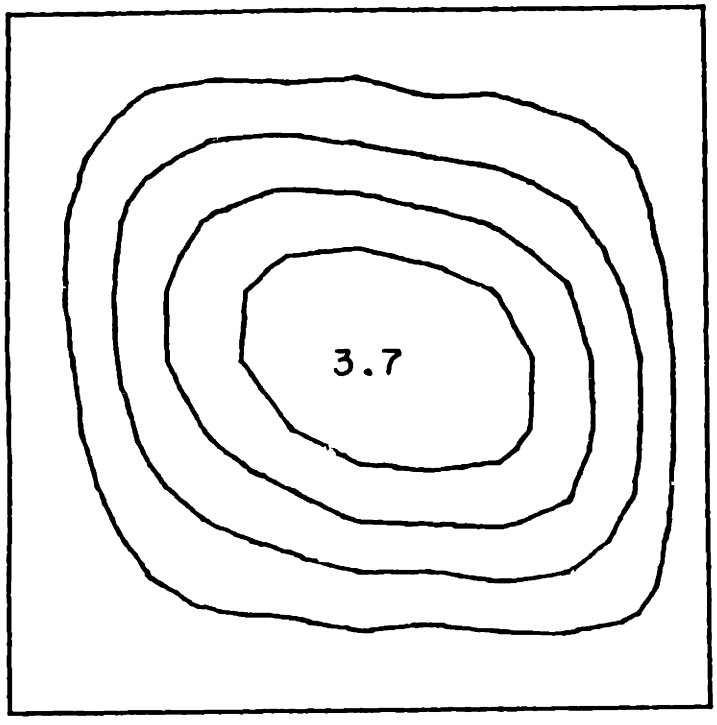

FIGURE H.50 Experimental Phase I Isodeflection Contour Map for the $[0_6//30_6]_T$-5 Laminate with Clamped Side Boundary Conditions

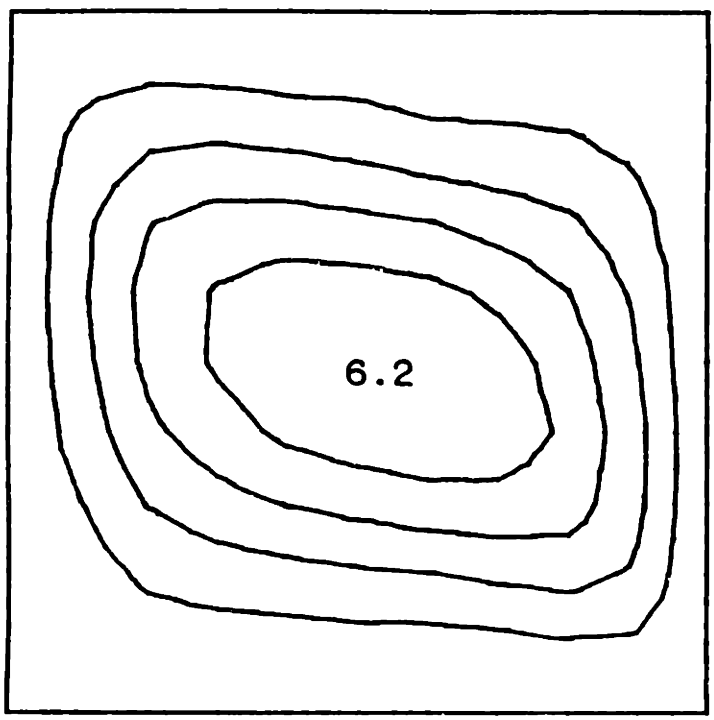

FIGURE H.51 Experimental Phase II Isodeflection Contour Map for the $[0_6//30_6]_T$-5 Laminate with Clamped Side Boundary Conditions

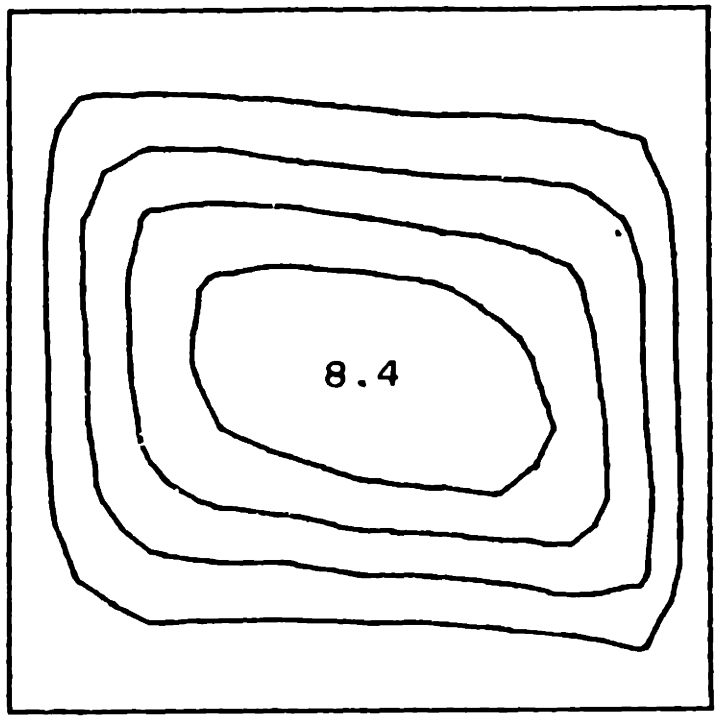

FIGURE H.52 Experimental Phase III Isodeflection Contour Map for the $[0_6//30_6]_T$-5 Laminate with Clamped Side Boundary Conditions

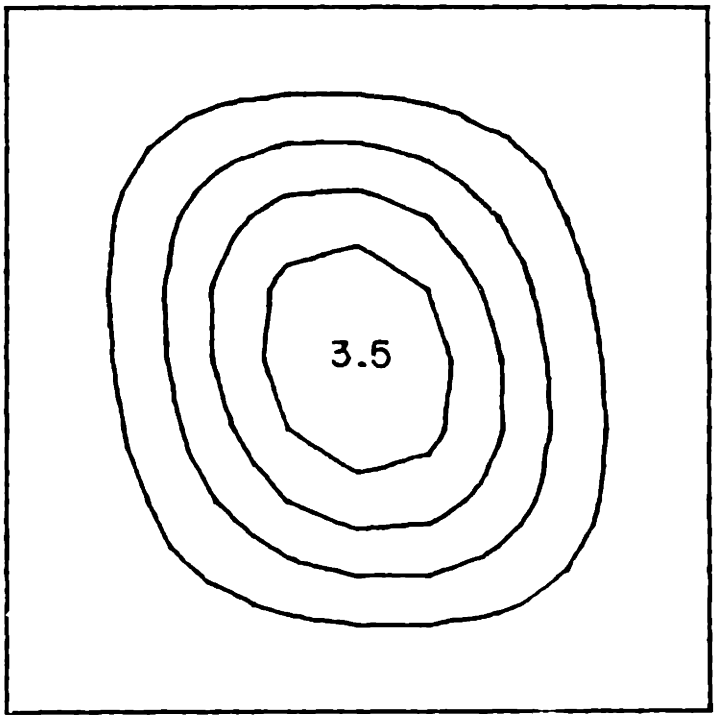

FIGURE H.53 Predicted (via Rayleigh-Ritz) Isodeflection Contour Map for the Laminate Type $[O_6//45_6]_T$ at 9 kN with Clamped Side Boundary Conditions

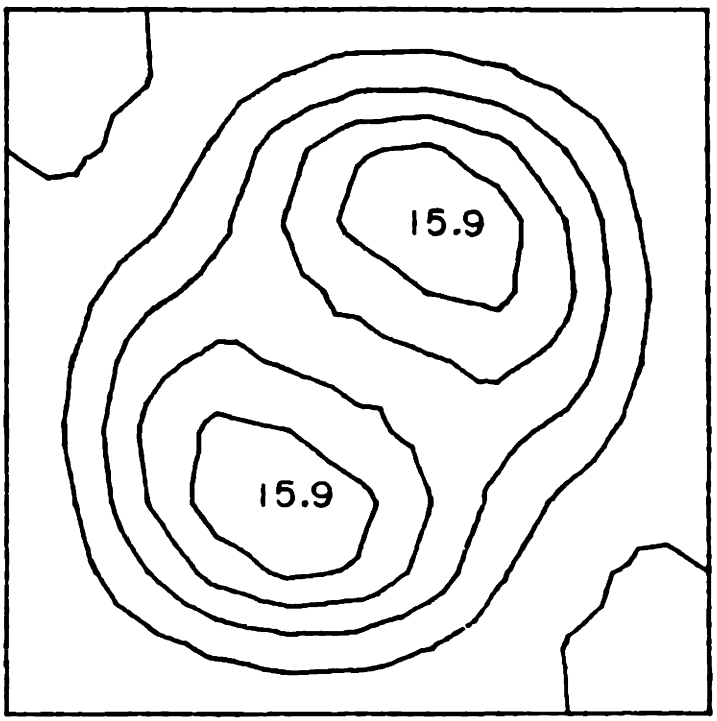

FIGURE H.54 Predicted (via Rayleigh-Ritz) Isodeflection Contour Map for the Laminate Type $[0_6//45_6]_T$ at 18 kN with Clamped Side Boundary Conditions

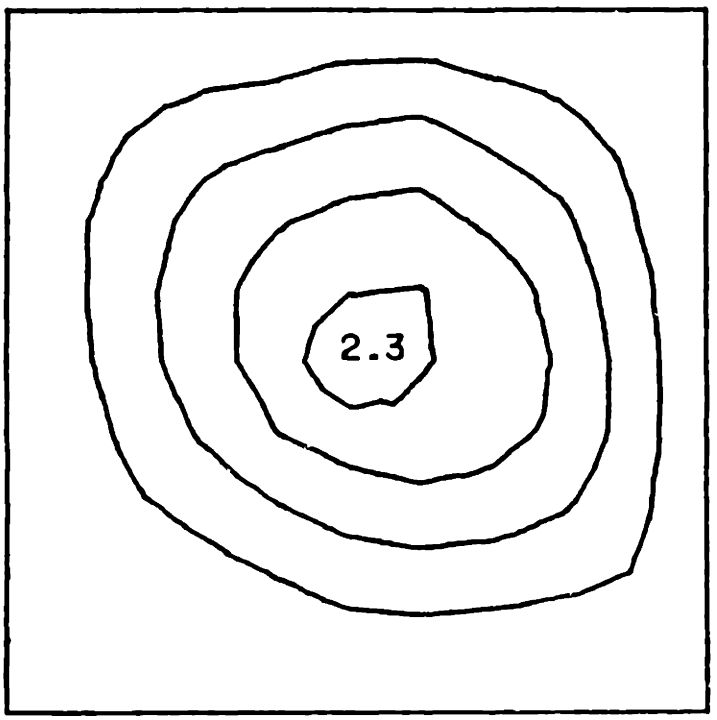

FIGURE H.55 Experimental Isodeflection Contour Map for the $[0_6//45_6]_T$-1 Laminate with Clamped Side Boundary Conditions

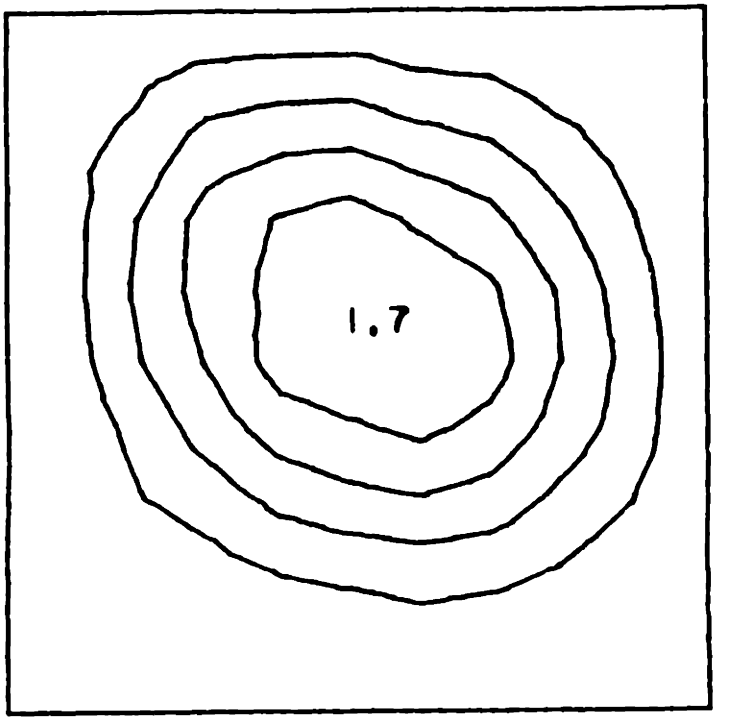

FIGURE H.56 Experimental Isodeflection Contour Map for the $[0_6//45_6]_T$-2 Laminate with Clamped Side Boundary Conditions

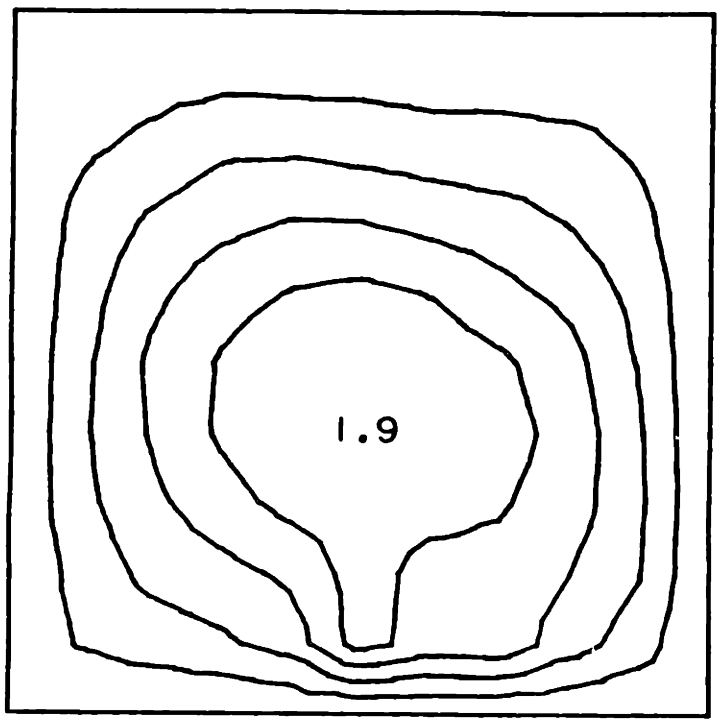

FIGURE H.57 Experimental Phase I Isodeflection Contour Map for the $[0_6//45_6]_T$-3 Laminate with Clamped Side Boundary Conditions

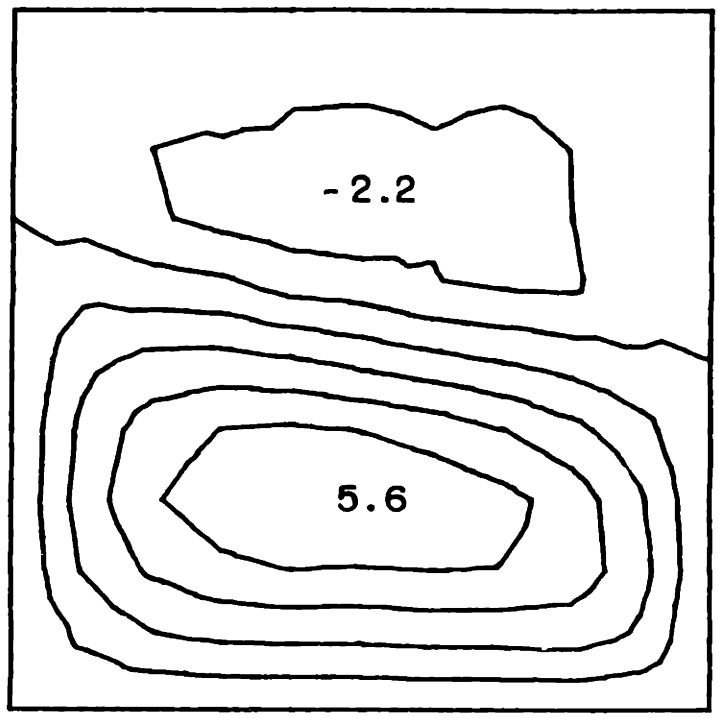

FIGURE H.58 Experimental Phase II Isodeflection Contour Map for the $[0_6//45_6]_T$-3 Laminate with Clamped Side Boundary Conditions

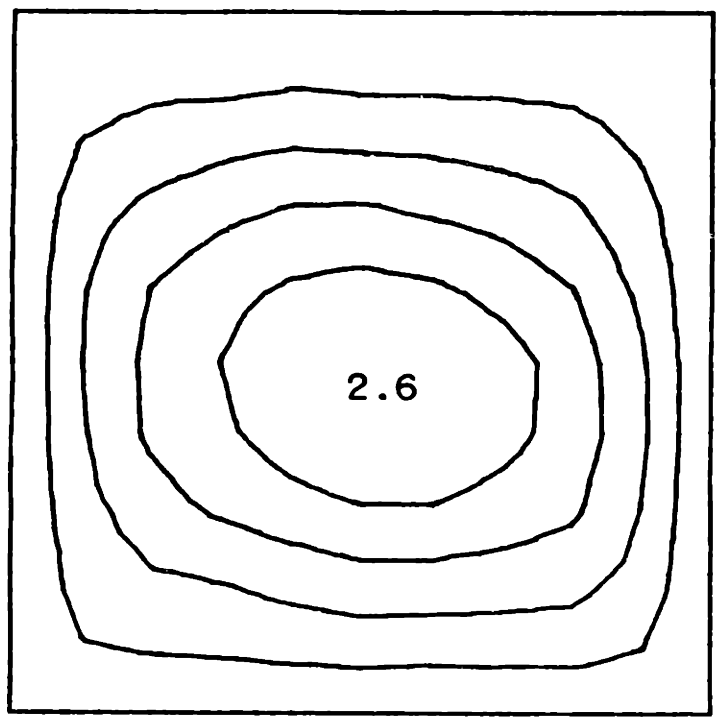

FIGURE H.59 Experimental Isodeflection Contour Map for the $[O_6//45_6]_T$-4 Laminate with Clamped Side Boundary Conditions

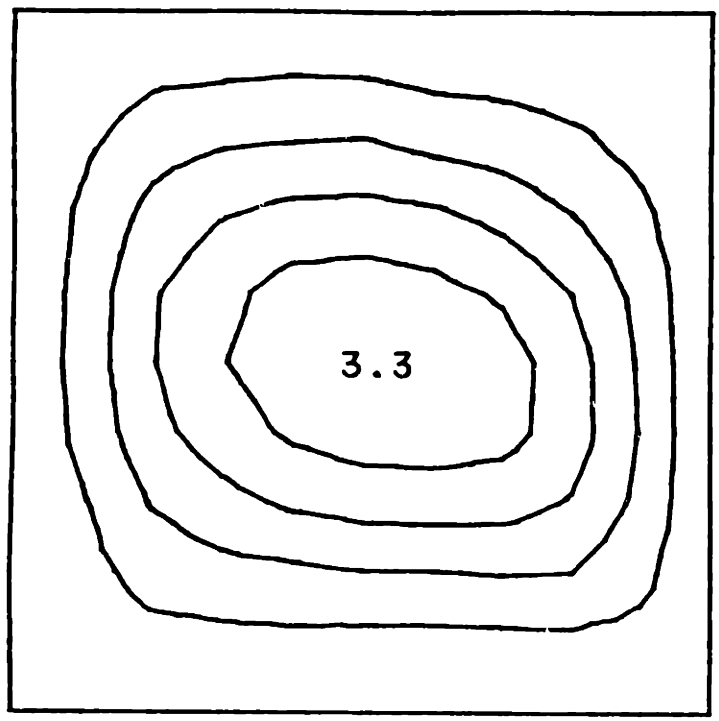

FIGURE H.60 Experimental Phase I Isodeflection Contour Map for the $[0_6//45_6]_T$-5 Laminate with Clamped Side Boundary Conditions

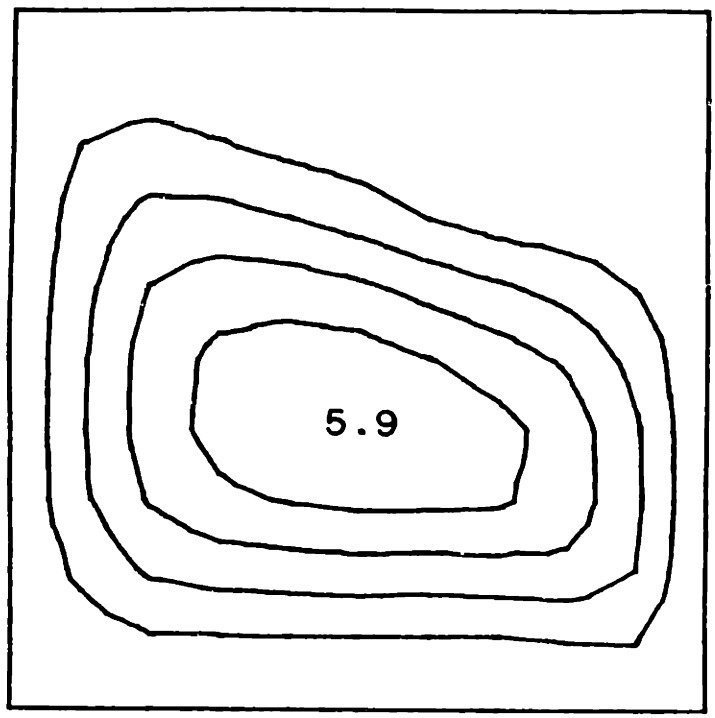

FIGURE H.61 Experimental Phase II Isodeflection Contour Map for the $[O_6//45_6]_T$-5 Laminate with Clamped Side Boundary Conditions

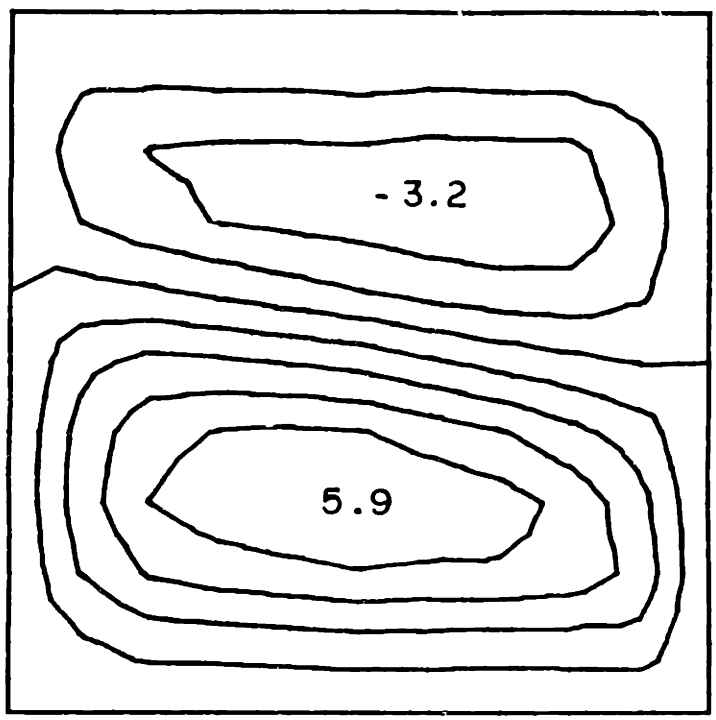

FIGURE H.62 Experimental Phase III Isodeflection Contour Map for the $[O_6//45_6]_T$-5 Laminate with Clamped Side Boundary Conditions

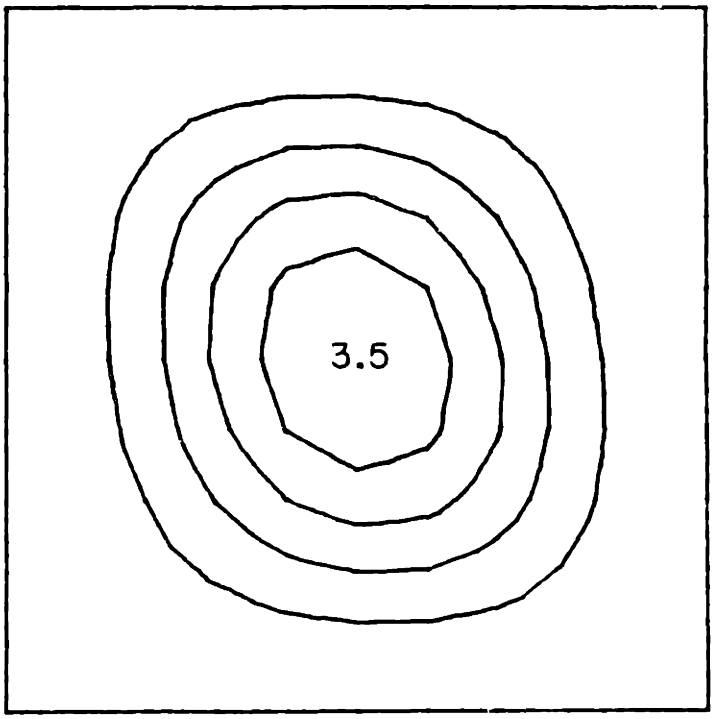

FIGURE H.63 Predicted (via Rayleigh-Ritz) Isodeflection Contour Map for the Laminate Type $[O_6//60_6]_T$ at 9 kN with Clamped Side Boundary Conditions

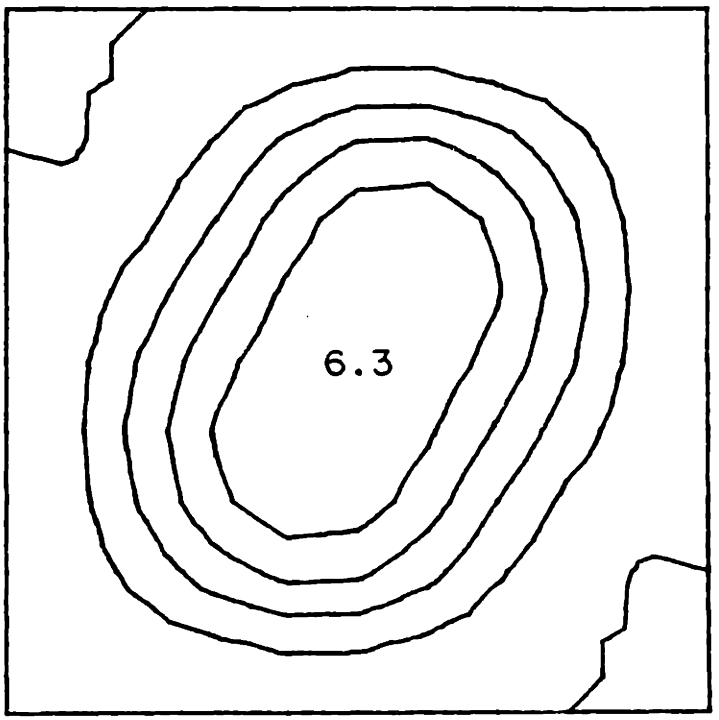

FIGURE H.64 Predicted (via Rayleigh-Ritz) Isodeflection Contour Map for the Laminate Type $[O_6//60_6]_T$ at 18 kN with Clamped Side Boundary Conditions

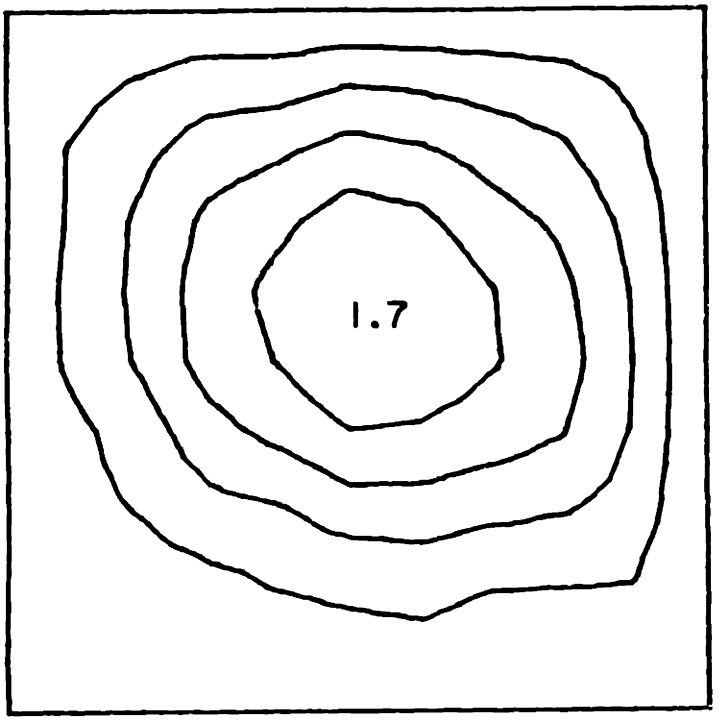

FIGURE H.65 Experimental Isodeflection Contour Map for the $[0_6//60_6]_T$-1 Laminate with Clamped Side Boundary Conditions

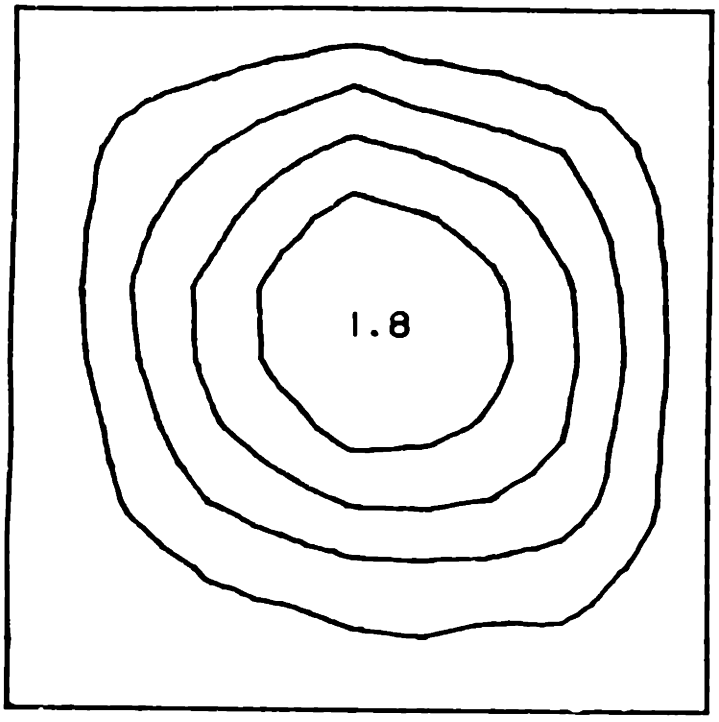

FIGURE H.66 Experimental Isodeflection Contour Map for the $[0_6//60_6]_T$-2 Laminate with Clamped Side Boundary Conditions

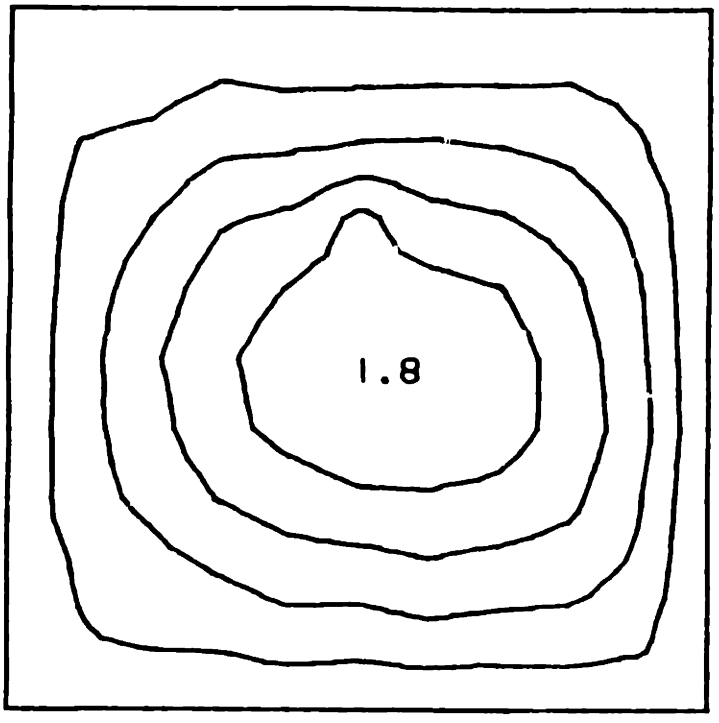

FIGURE H.67 Experimental Isodeflection Contour Map for the $[0_6//60_6]_T$-3 Laminate with Clamped Side Boundary Conditions

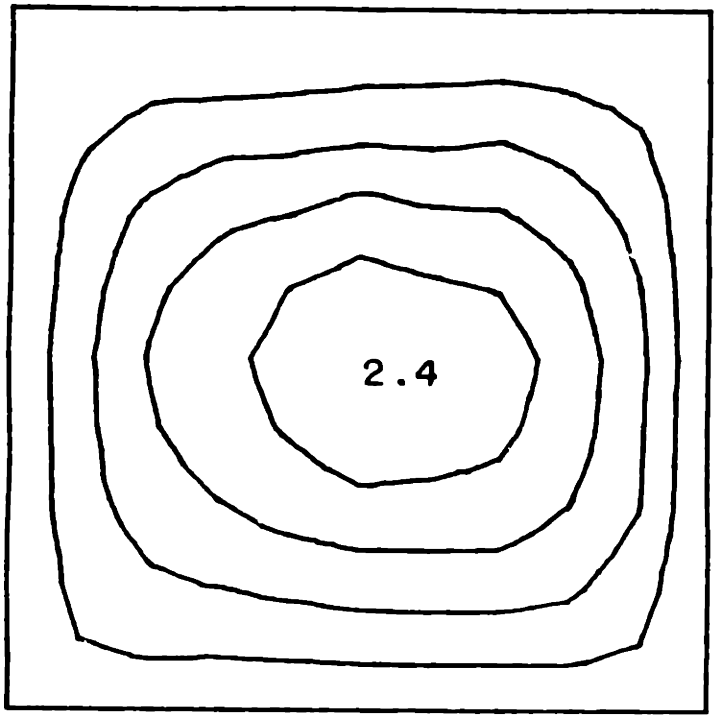

FIGURE H.68 Experimental Isodeflection Contour Map for the $[O_6//60_6]_T$-4 Laminate with Clamped Side Boundary Conditions

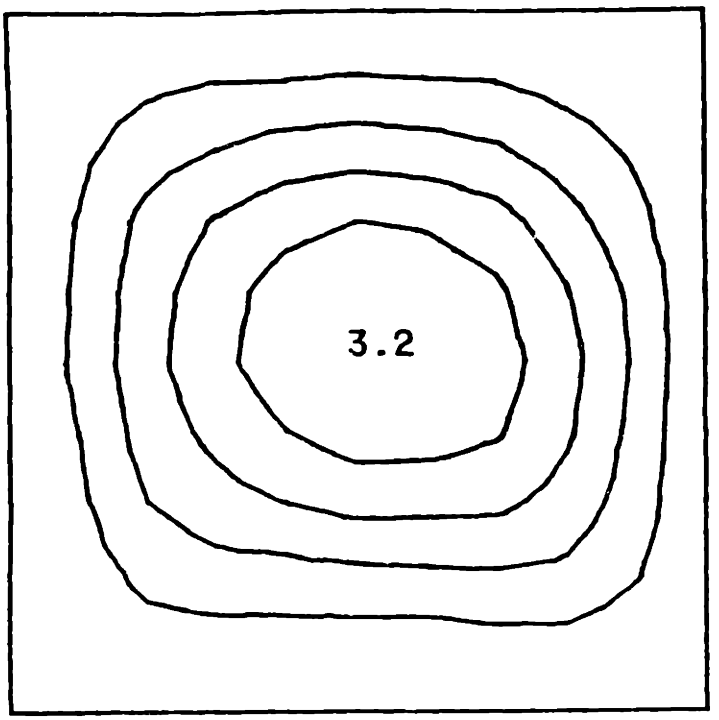

FIGURE H.69 Experimental Phase I Isodeflection Contour Map for the $[O_6//60_6]_T$-5 Laminate with Clamped Side Boundary Conditions

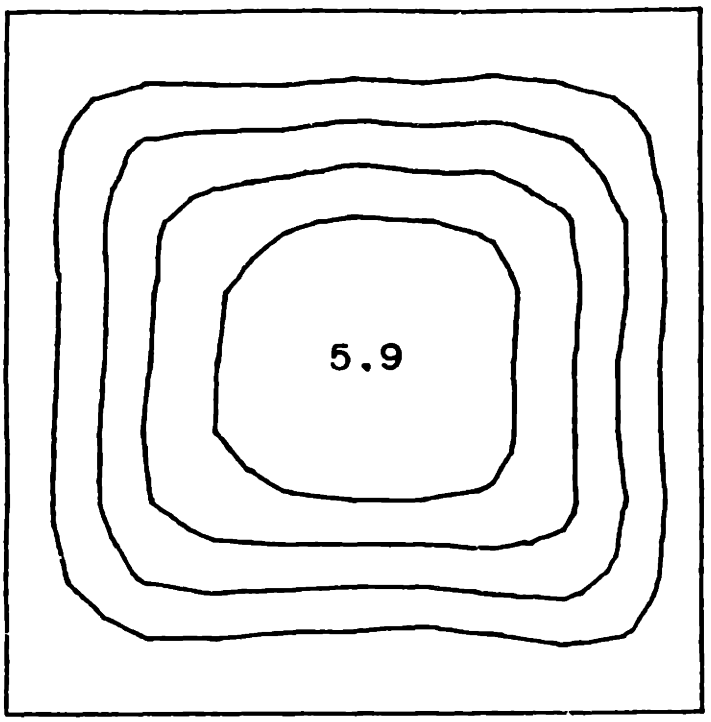

FIGURE H.70 Experimental Phase II Isodeflection Contour Map for the $[0_6//60_6]_T$-5 Laminate with Clamped Side Boundary Conditions

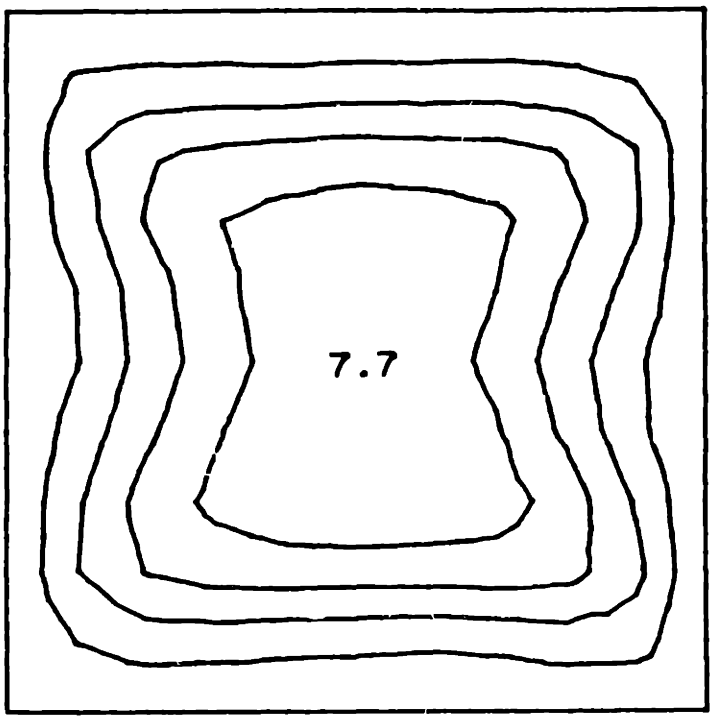

FIGURE H.71 Experimental Phase III Isodeflection Contour Map for the $[0_6//60_6]_T$-5 Laminate with Clamped Side Boundary Conditions

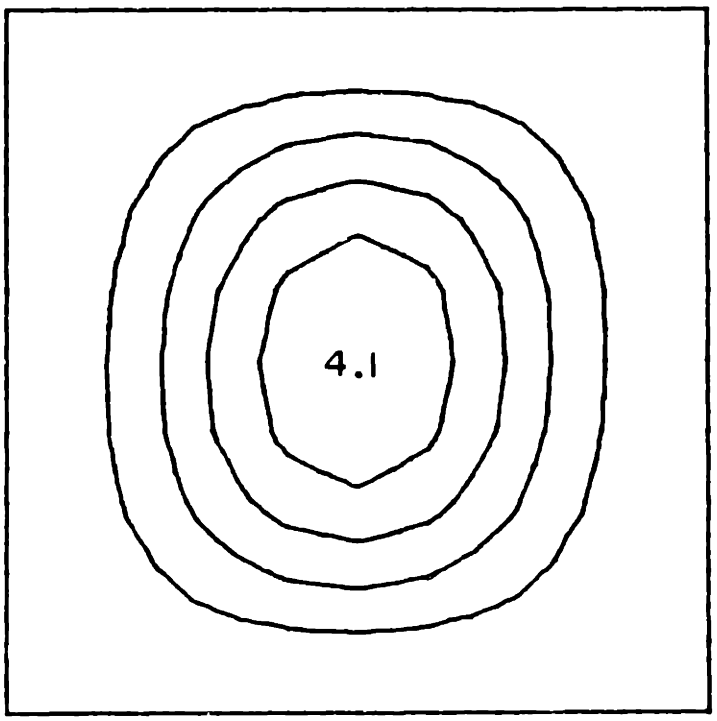

FIGURE H.72 Predicted (via Rayleigh-Ritz) Isodeflection Contour Map for the Laminate Type $[0_6//75_6]_T$ with Clamped Side Boundary Conditions

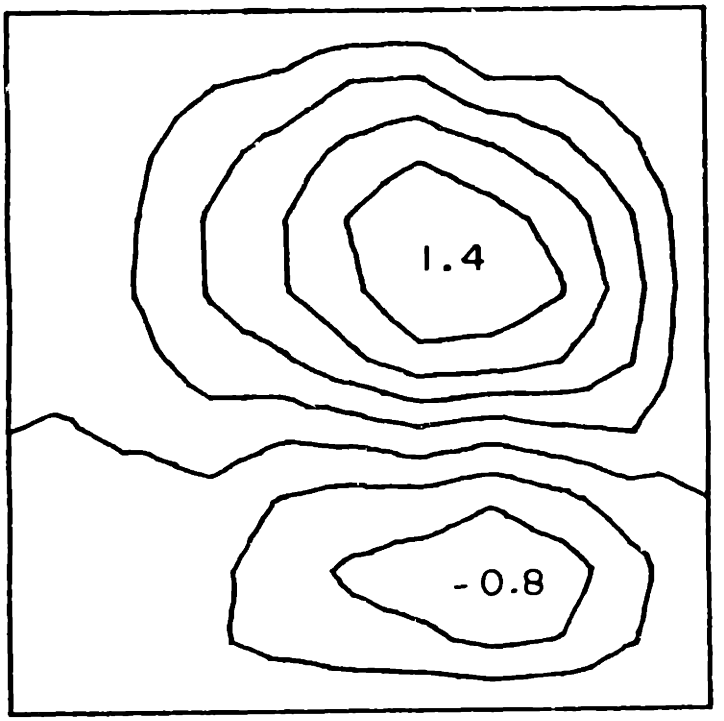

FIGURE H.73 Experimental Isodeflection Contour Map for the $[0_6//75_6]_T$-1 Laminate with Clamped Side Boundary Conditions

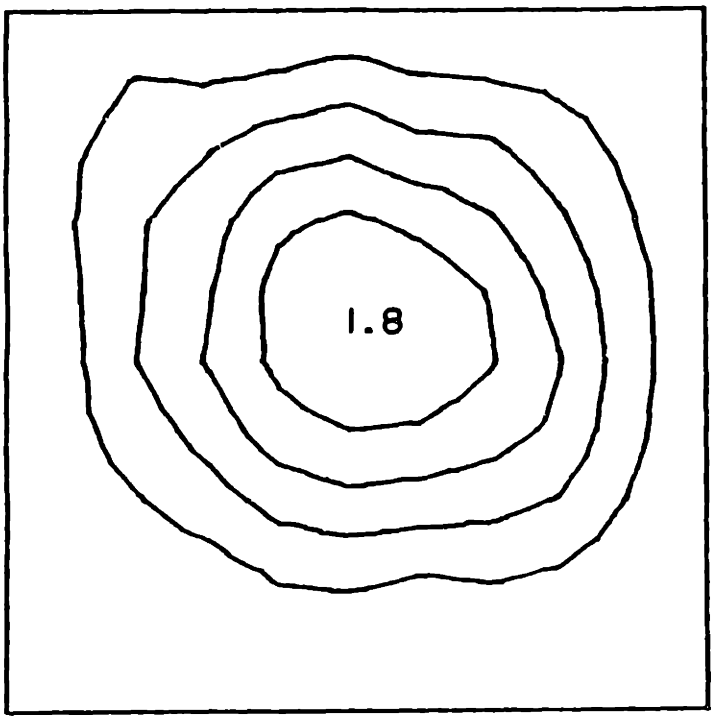

FIGURE H.74 Experimental Phase I Isodeflection Contour Map for the $[0_6//75_6]_T$-2 Laminate with Clamped Side Boundary Conditions

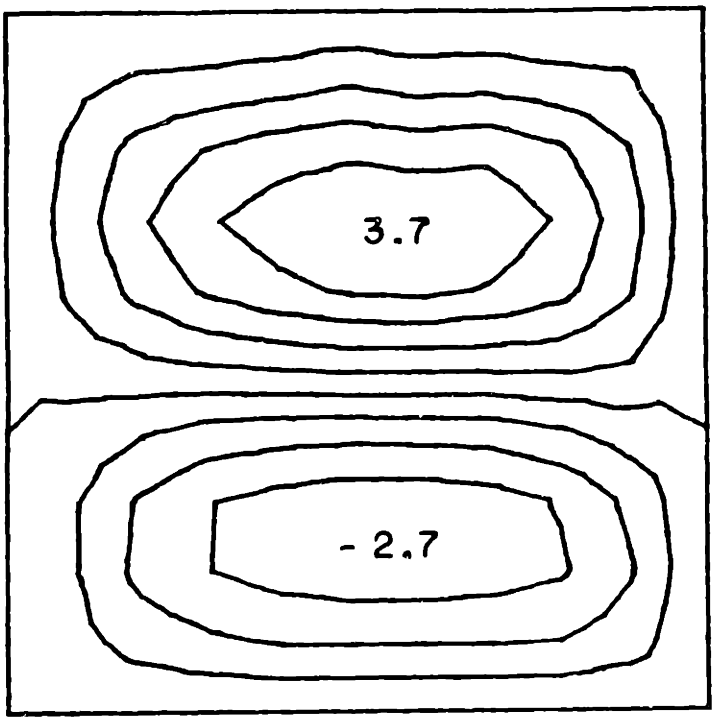

FIGURE H.75 Experimental Phase II Isodeflection Contour Map for the $[0_6//75_6]_T$-2 Laminate with Clamped Side Boundary Conditions

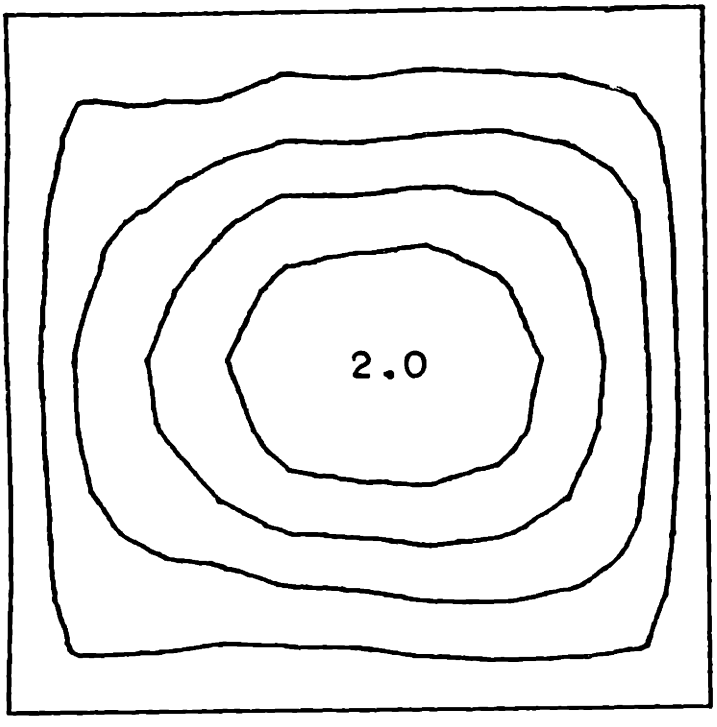

FIGURE H.76 Experimental Isodeflection Contour Map for the $[O_6//75_6]_T$-3 Laminate with Clamped Side Boundary Conditions

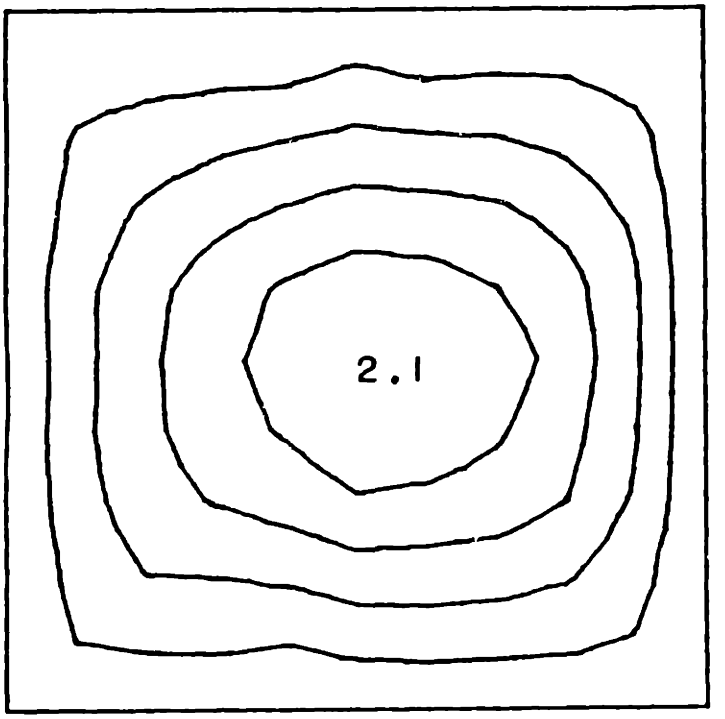

FIGURE H.77 Experimental Isodeflection Contour Map for the $[0_6//75_6]_T$-4 Laminate with Clamped Side Boundary Conditions

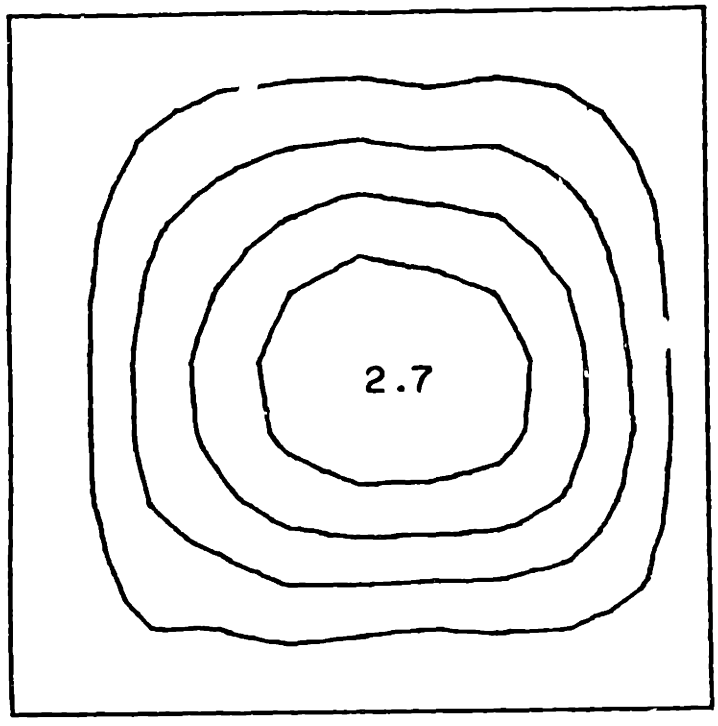

FIGURE H.78 Experimental Phase I Isodeflection Contour Map for the $[0_6//75_6]_T$-5 Laminate with Clamped Side Boundary Conditions

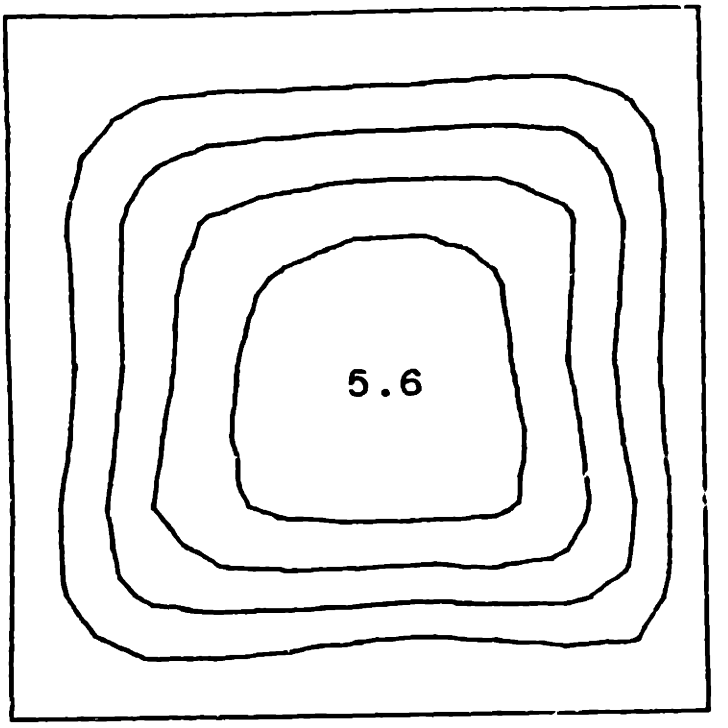

FIGURE H.79 Experimental Phase II Isodeflection Contour Map for the $[O_6//75_6]_T$-5 Laminate with Clamped Side Boundary Conditions

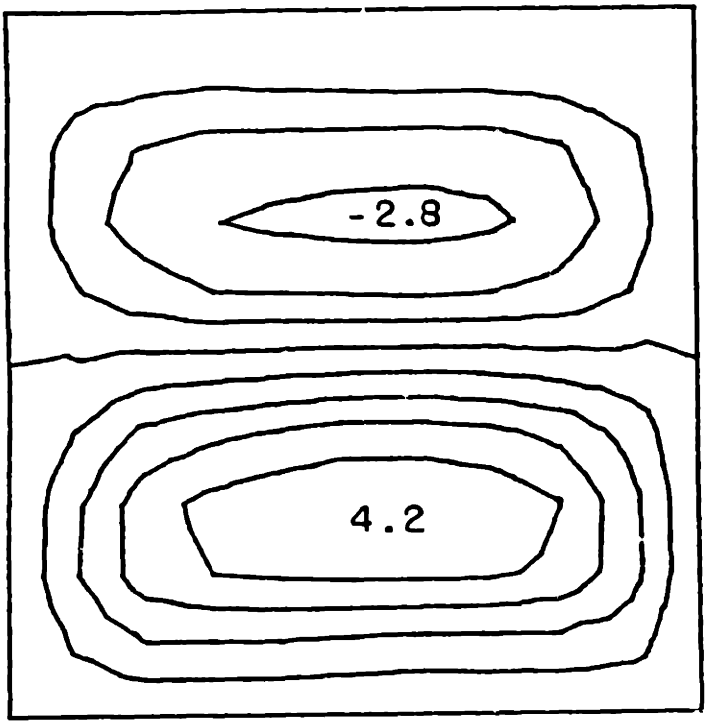

FIGURE H.80 Experimental Phase III Isodeflection Contour Map for the $[0_6//75_6]_T$-5 Laminate with Clamped Side Boundary Conditions

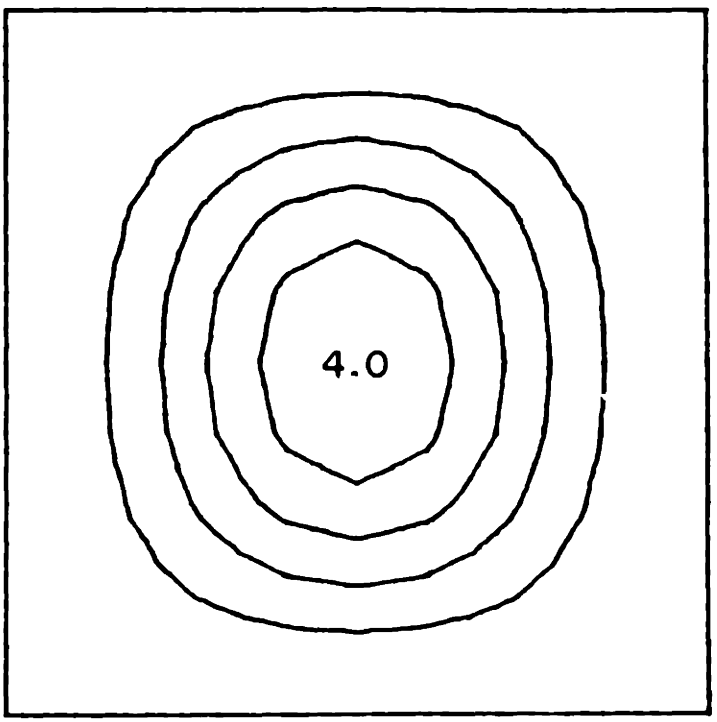

FIGURE H.81 Predicted (via Rayleigh-Ritz) Isodeflection Contour Map for the Laminate Type $[0_6//90_6]_T$ with Clamped Side Boundary Conditions

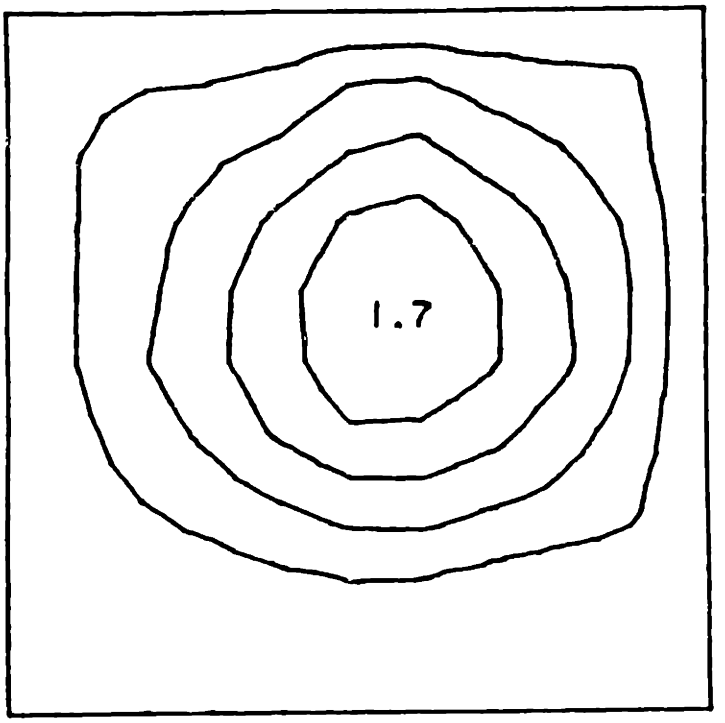

FIGURE H.82 Experimental Isodeflection Contour Map for the $[0_6//90_6]_T$-1 Laminate with Clamped Side Boundary Conditions

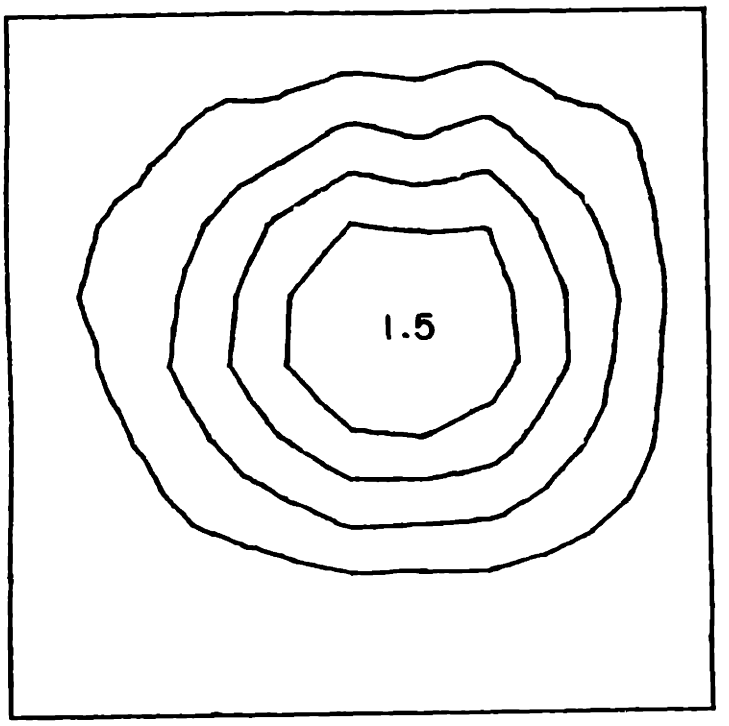

FIGURE H.83 Experimental Phase I Isodeflection Contour Map for the $[O_6//90_6]_T$-2 Laminate with Clamped Side Boundary Conditions

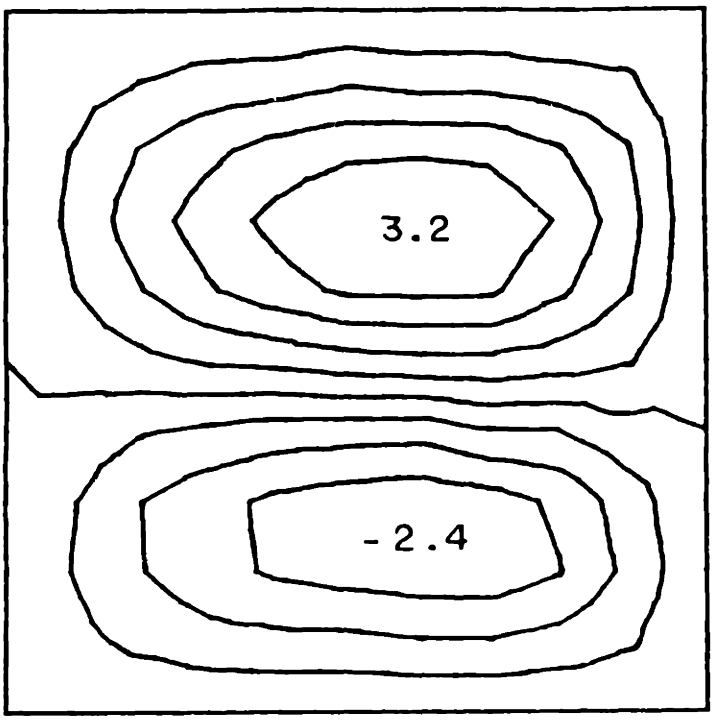

FIGURE H.84 Experimental Phase II Isodeflection Contour Map for the $[0_6//90_6]_T$-2 Laminate with Clamped Side Boundary Conditions

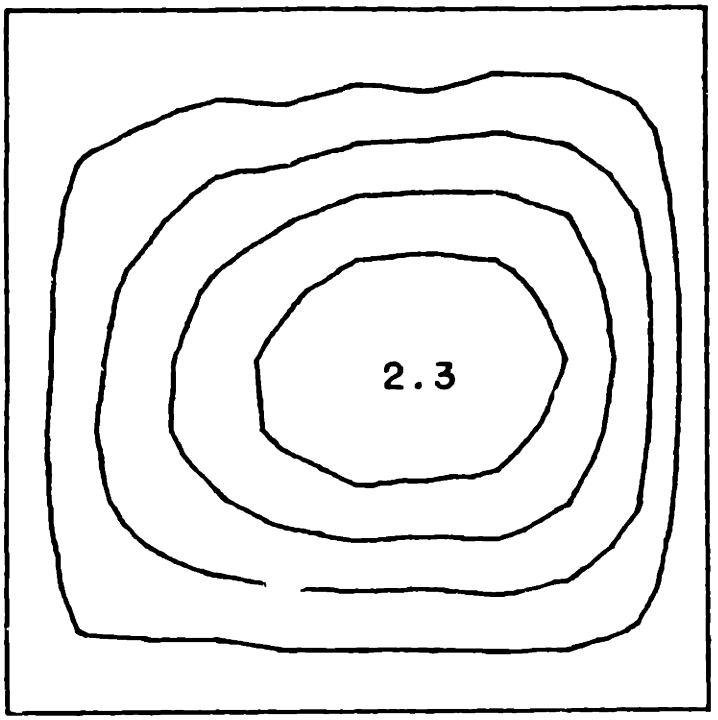

FIGURE H.85 Experimental Isodeflection Contour Map for the $[0_6//90_6]_T$-3 Laminate with Clamped Side Boundary Conditions

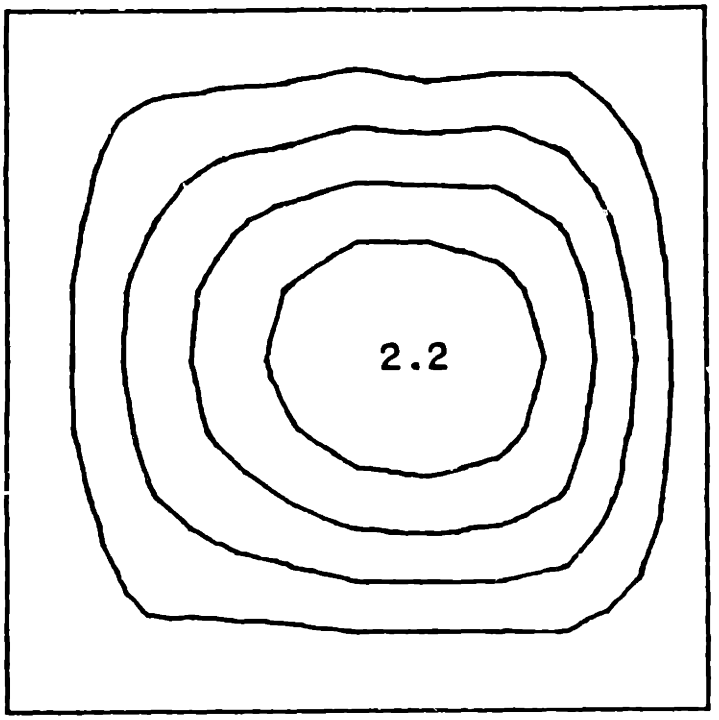

FIGURE H.86 Experimental Isodeflection Contour Map for the $[0_6//90_6]_T$-4 Laminate with Clamped Side Boundary Conditions

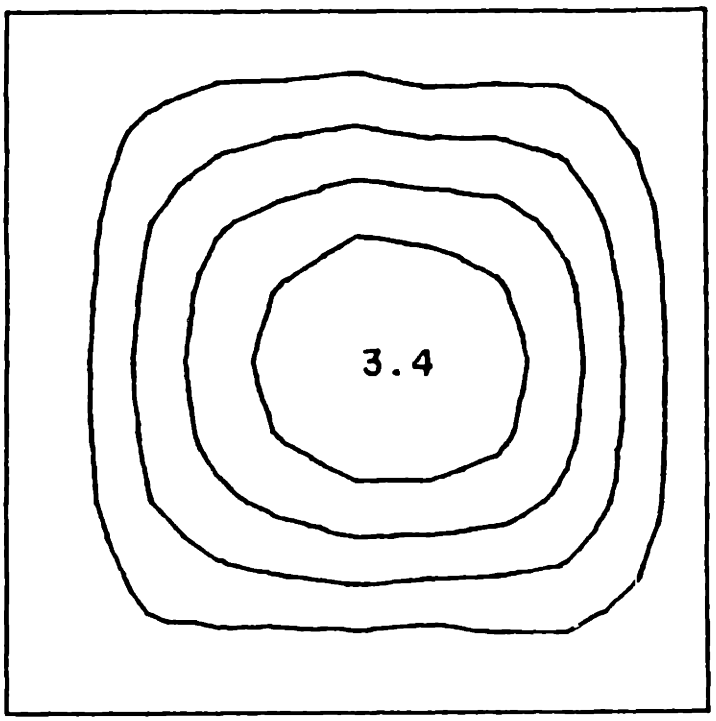

FIGURE H.87 Experimental Phase I Isodeflection Contour Map for the $[O_6//90_6]_T$-5 Laminate with Clamped Side Boundary Conditions

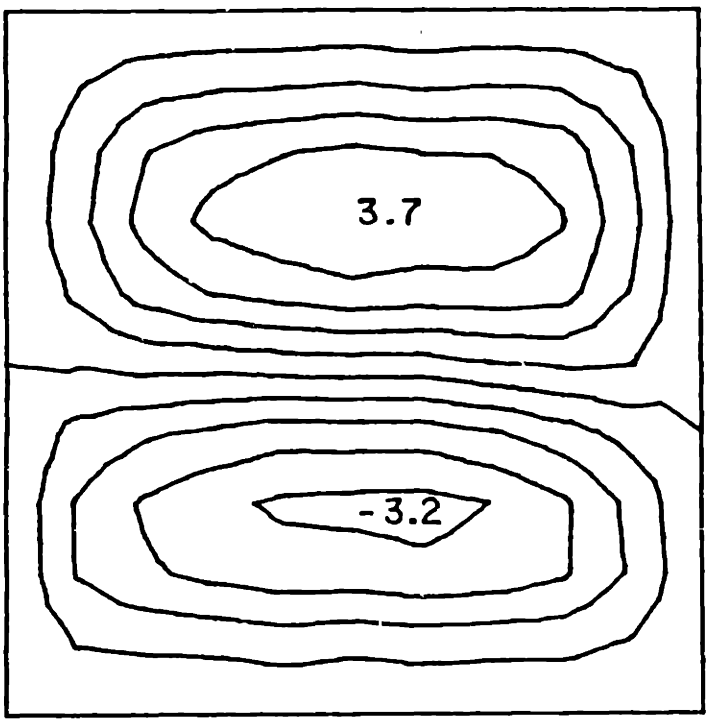

FIGURE H.88 Experimental Phase II Isodeflection Contour Map for the $[O_6//90_6]_T$-5 Laminate with Clamped Side Boundary Conditions

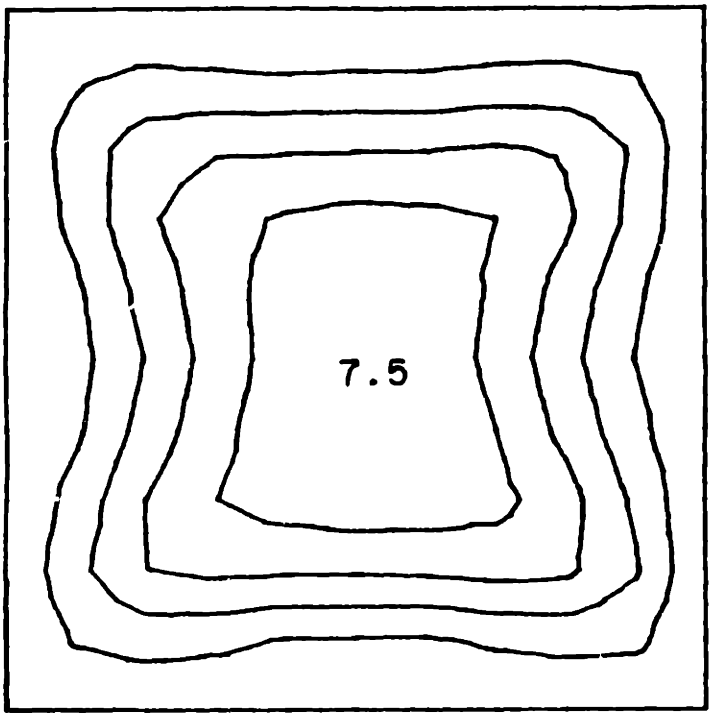

FIGURE H.89 Experimental Phase III Isodeflection Contour Map for the $[C_6//90_6]_T$-5 Laminate with Clamped Side Boundary Conditions

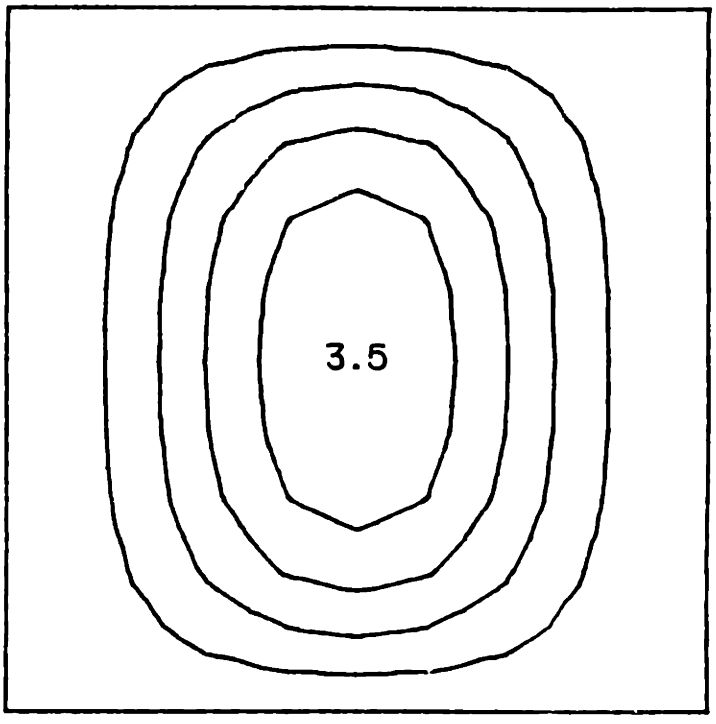

FIGURE H.90 Predicted (via Rayleigh-Ritz) Isodeflection Contour Map for the Laminate Type $[0_3/90_3]_S$ with Simply-Supported Boundary Conditions

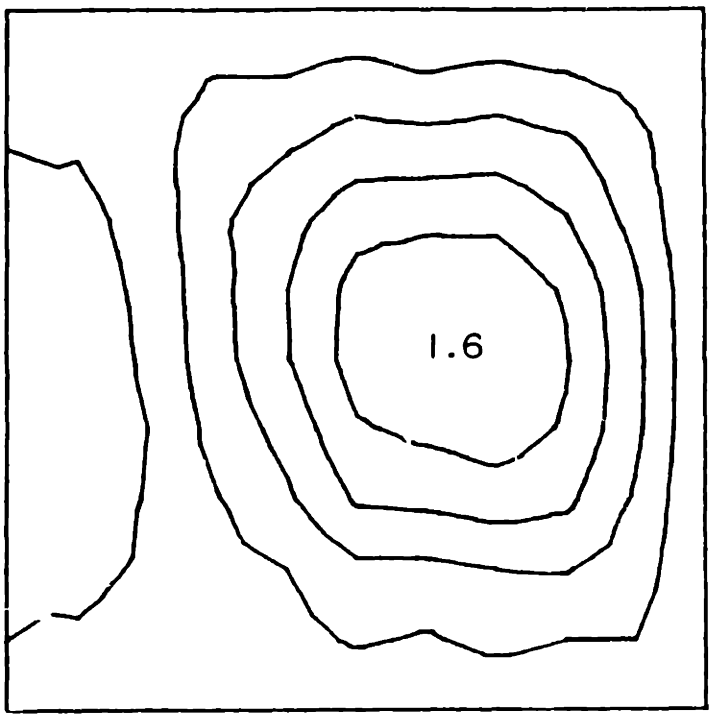

FIGURE H.91 Experimental Isodeflection Contour Map for the $[0_3/90_3]_S$ Laminate with Simply-Supported Boundary Conditions

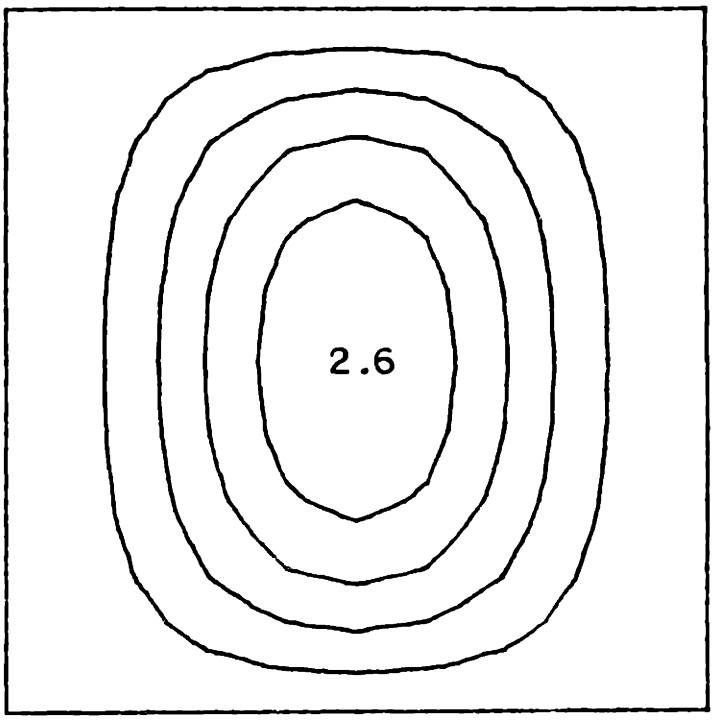

FIGURE H.92 Predicted (via Rayleigh-Ritz) Isodeflection Contour Map for the Laminate Type $[O_3//90_3//90_3//O_3]_T$ with Simply-Supported Boundary Conditions

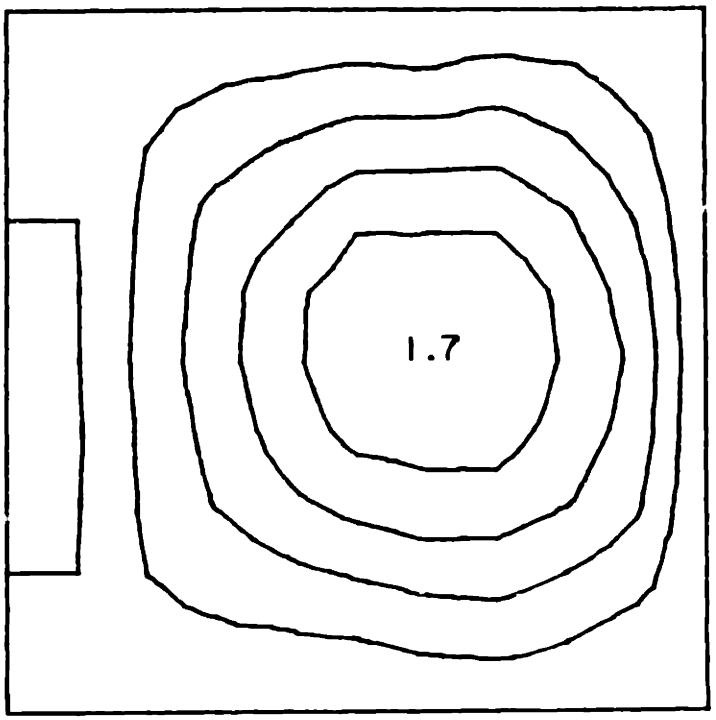

FIGURE H.93 Experimental Isodeflection Contour Map for the $[0_3//90_3//90_3//0_3]_T$ Laminate with Simply-Supported Boundary Conditions

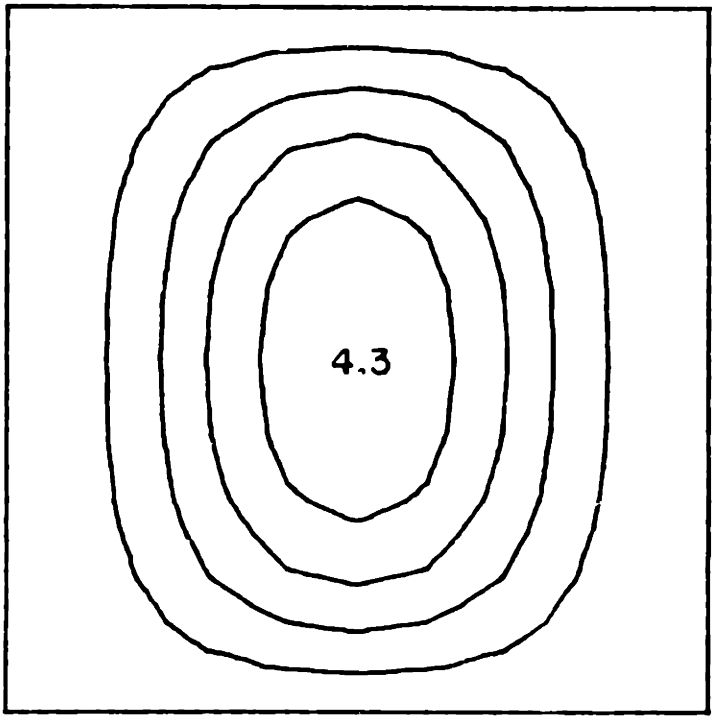

FIGURE H.94 Predicted (via Rayleigh-Ritz) Isodeflection Contour Map for the Laminate Type $[0_3//90_3//0_3//90_3]_T$ with Simply-Supported Boundary Conditions

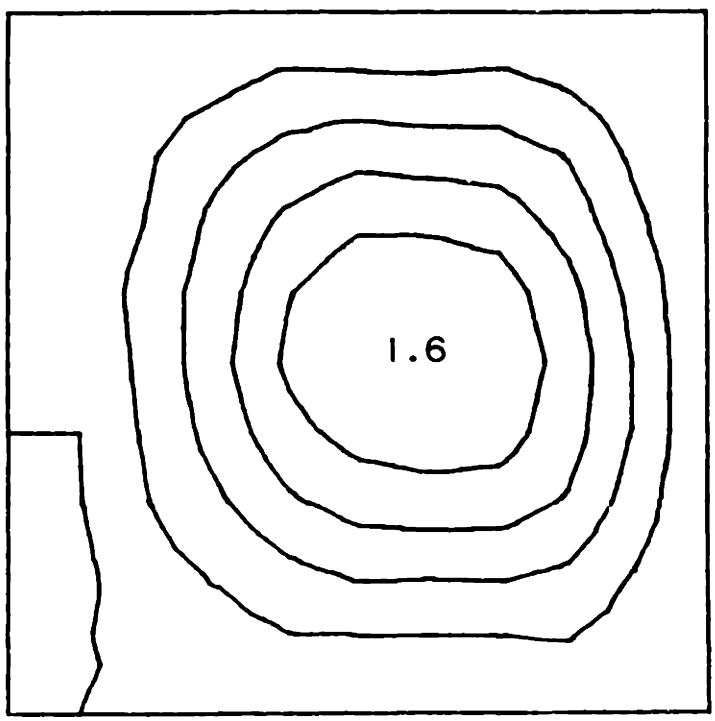

FIGURE H.95 Experimental Isodeflection Contour Map for the $[O_3//90_3//O_3//90_3]_T$ Laminate with Simply-Supported Boundary Conditions

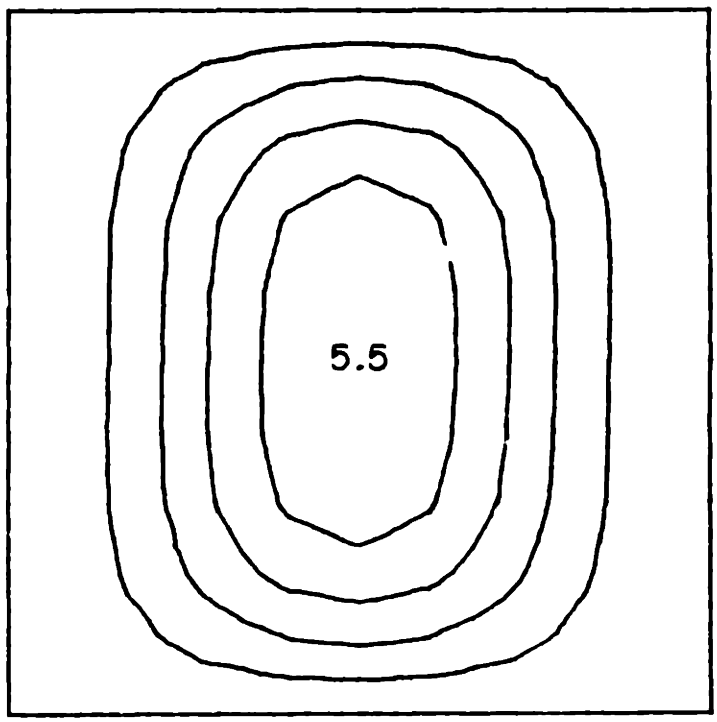

FIGURE H.96 Predicted (via Rayleigh-Ritz) Isodeflection Contour Map for the Laminate Type $[O_2//45_2//O_2//45_2//O_2]_T$ with Simply-Supported Boundary Conditions

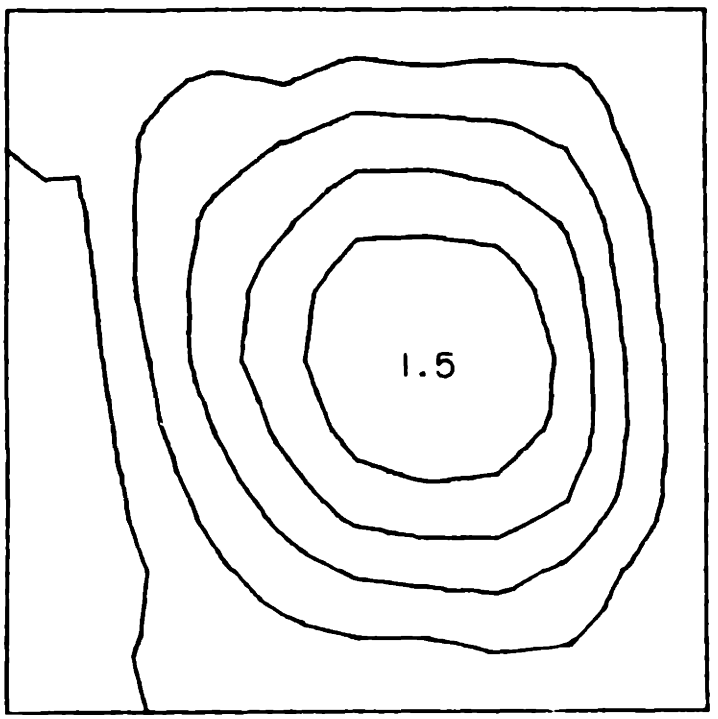

FIGURE H.97 Experimental Isodeflection Contour Map for the $[0_2//45_2//0_2//45_2//0_2]_T$ Laminate with Simply-Supported Boundary Conditions

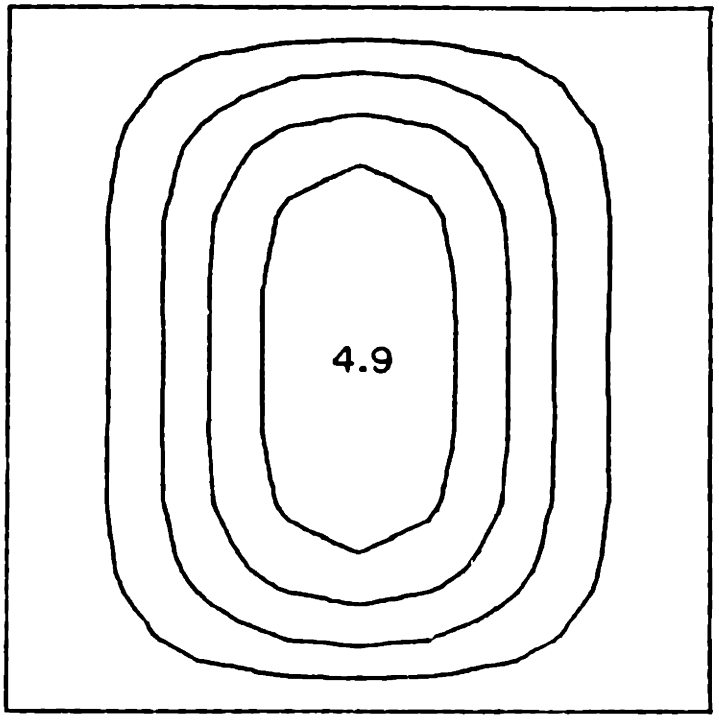

FIGURE H.98 Predicted (via Rayleigh-Ritz) Isodeflection Contour Map for the Laminate Type $[0_2//45_2//0_2//-45_2//0_2]_T$ with Simply-Supported Boundary Conditions

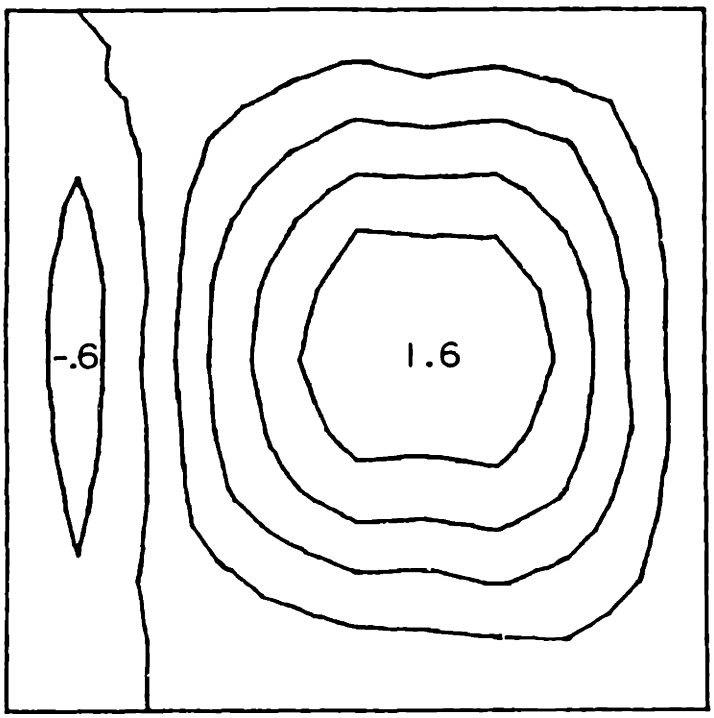

Experimental

$[0_2//45_2//0_2//-45_2//0_2]_T$

Simply-supported Sides

3.2 kN

FIGURE H.99 Experimental Isodeflection Contour Map for the $[0_2//45_2//0_2//-45_2//0_2]_T$ Laminate with Simply-Supported Boundary Conditions

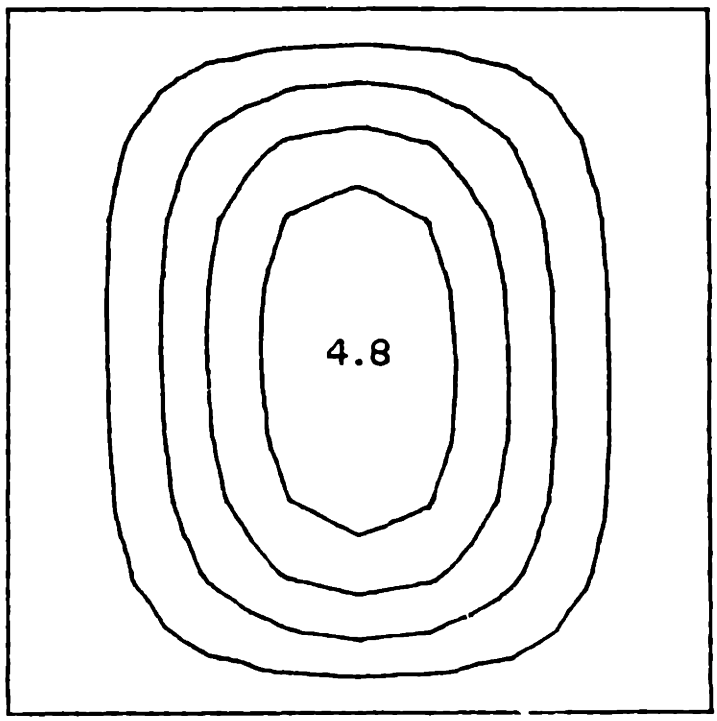

FIGURE H.100 Predicted (via Rayleigh-Ritz) Isodeflection Contour Map for the Laminate Type $[0_6//15_6]_T$ with Simply-Supported Boundary Conditions

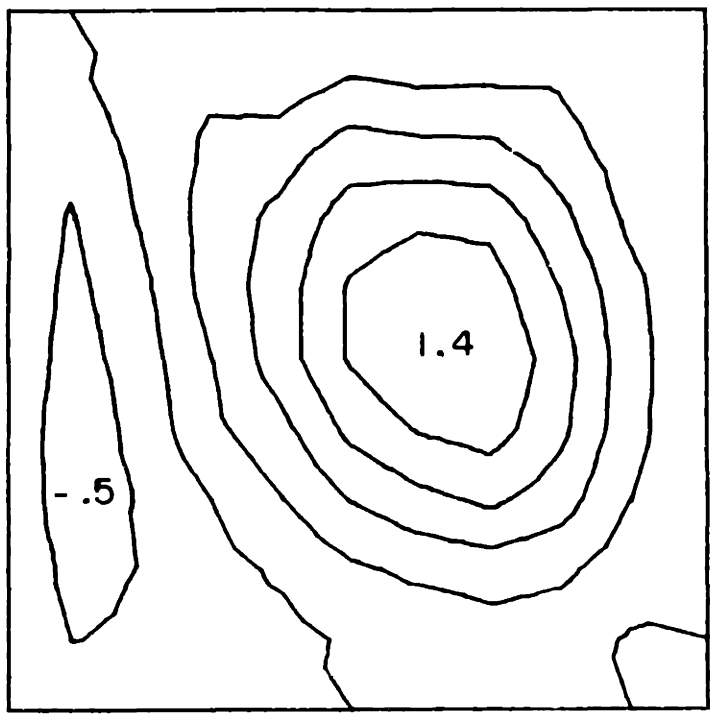

FIGURE H.101 Experimental Isodeflection Contour Map for the $[0_6//15_6]_T$ Laminate with Simply-Supported Boundary Conditions

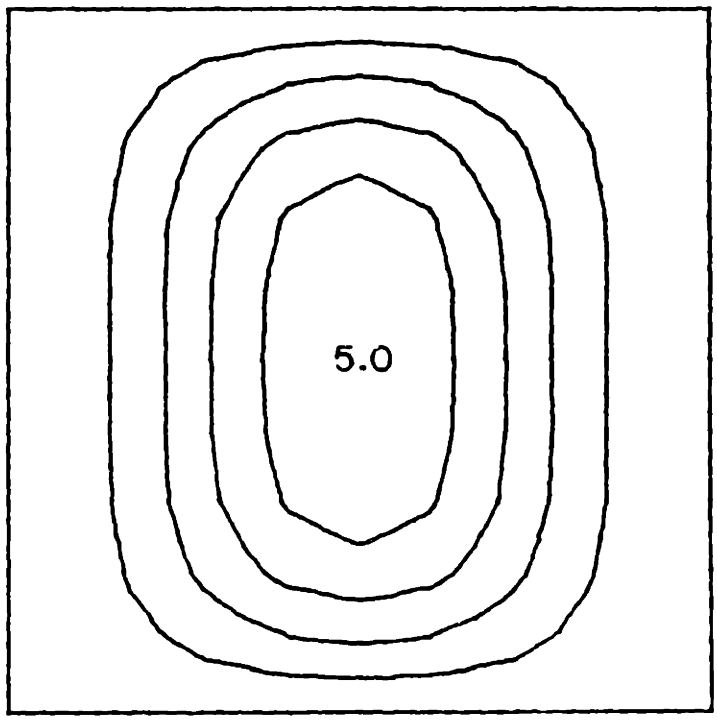

FIGURE H.102 Predicted (via Rayleigh-Ritz) Isodeflection Contour Map for the Laminate Type $[0_6//30_6]_T$ with Simply-Supported Boundary Conditions

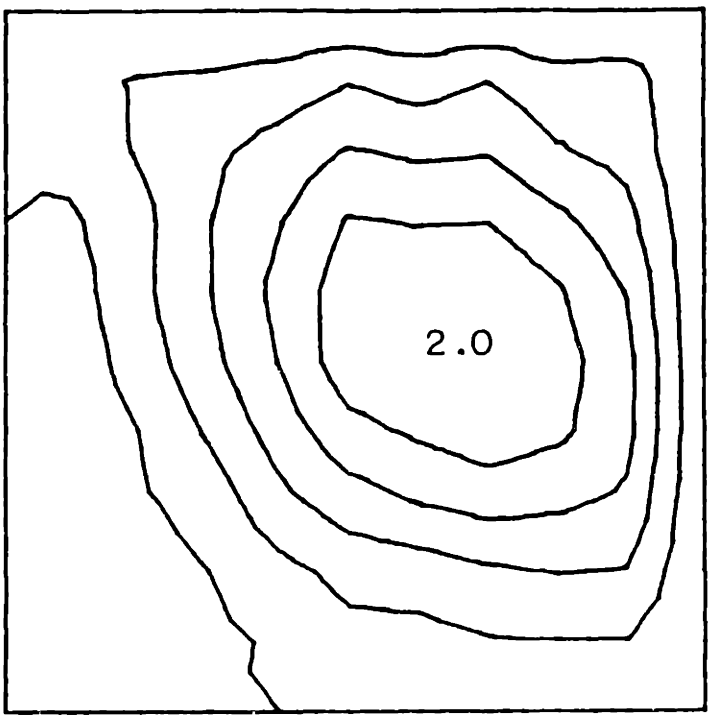

FIGURE H.103 Experimental Isodeflection Contour Map for the $[0_6//30_6]_T$ Laminate with Simply-Supported Boundary Conditions

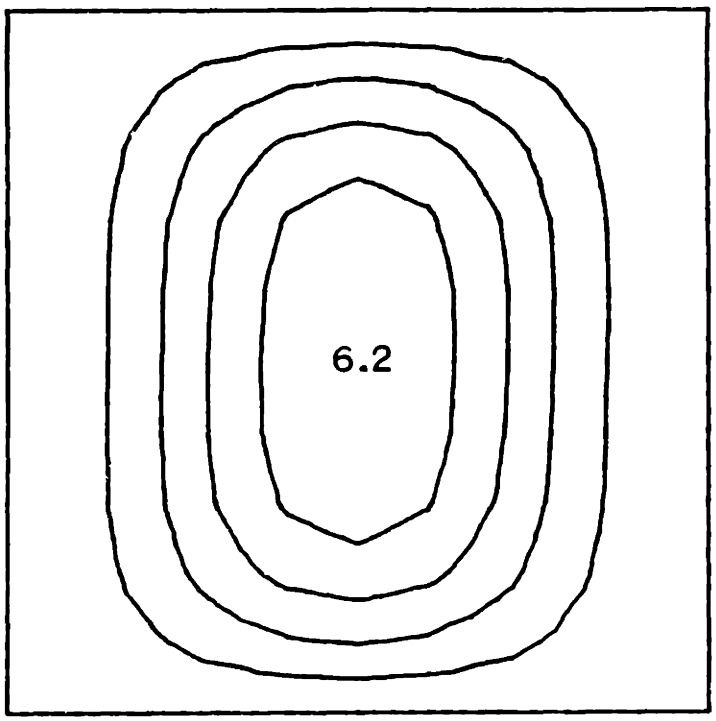

FIGURE H.104 Predicted (via Rayleigh-Ritz) Isodeflection Contour Map for the Laminate Type $[0_6//45_6]_T$ with Simply-Supported Boundary Conditions

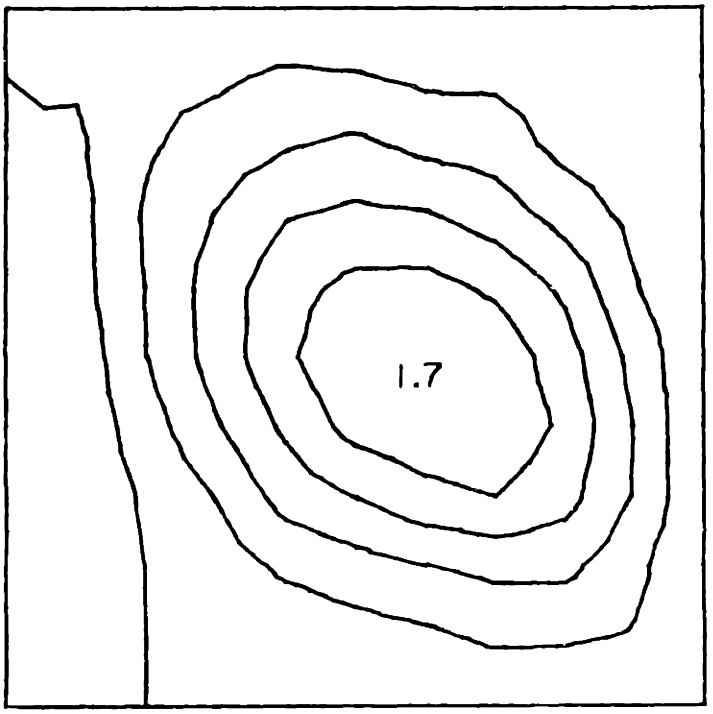

FIGURE H.105 Experimental Isodeflection Contour Map for the $[O_6//45_6]_T$ Laminate with Simply-Supported Boundary Conditions

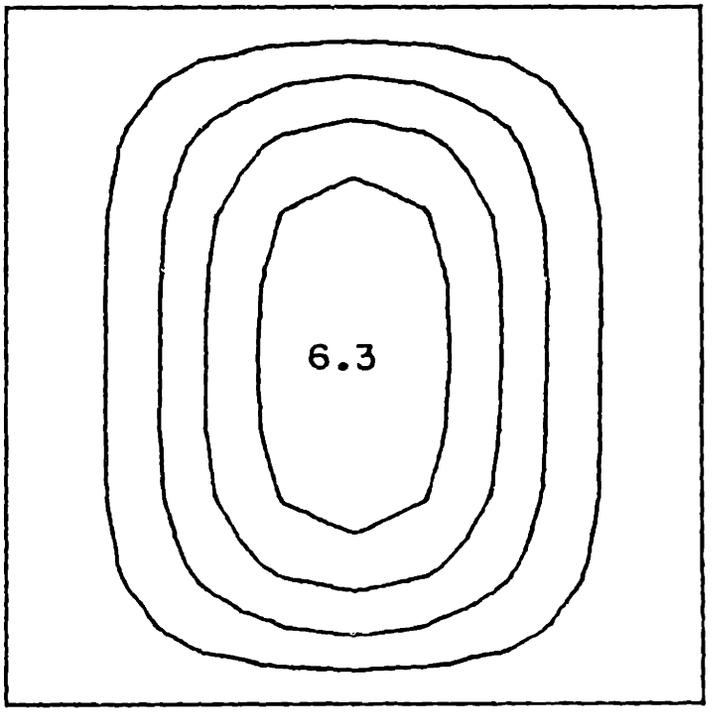

FIGURE H.106 Predicted (via Rayleigh-Ritz) Isodeflection Contour Map for the Laminate Type $[0_6//60_6]_T$ with Simply-Supported Boundary Conditions

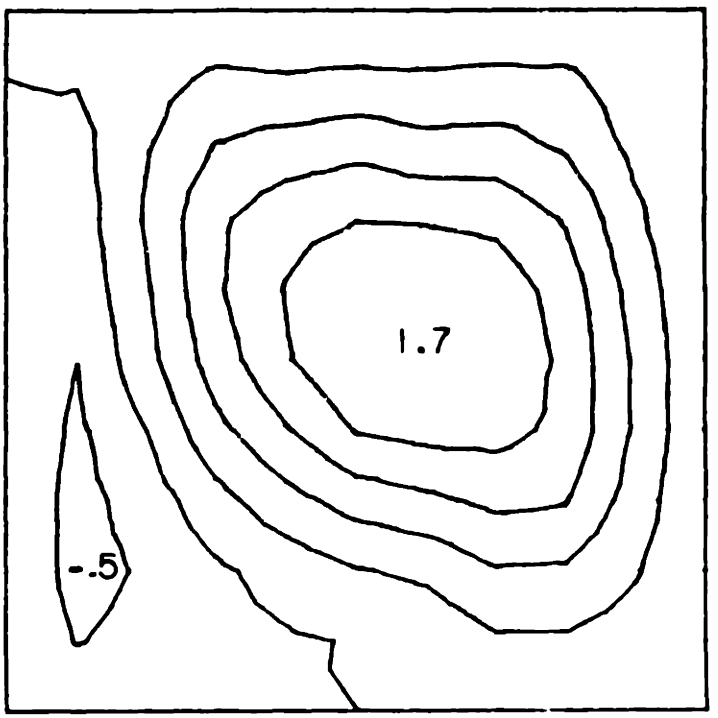

FIGURE H.107 Experimental Phase I Isodeflection Contour Map for the $[0_6//60_6]_T$ Laminate with Simply-Supported Boundary Conditions

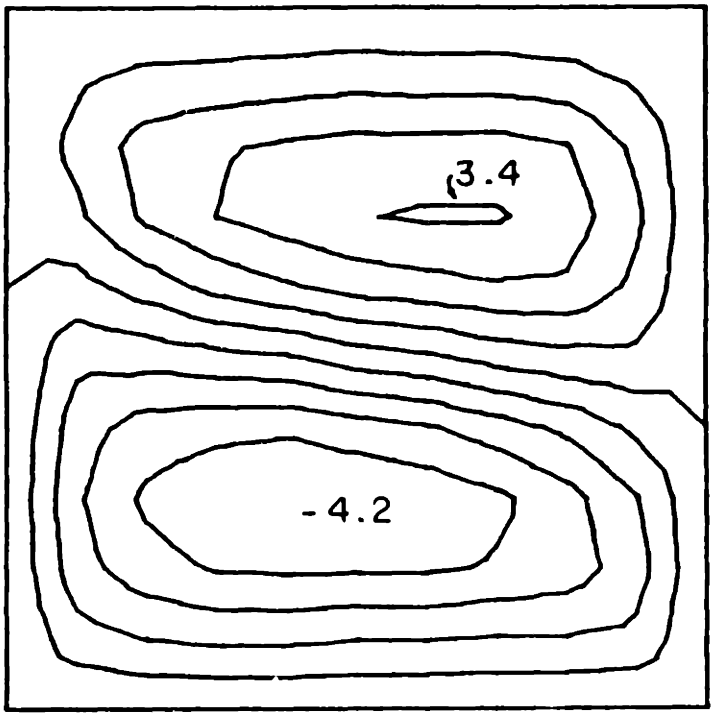

FIGURE H.108 Experimental Phase II Isodeflection Contour Map for the $[0_6//60_6]_T$ Laminate with Simply-Supported Boundary Conditions

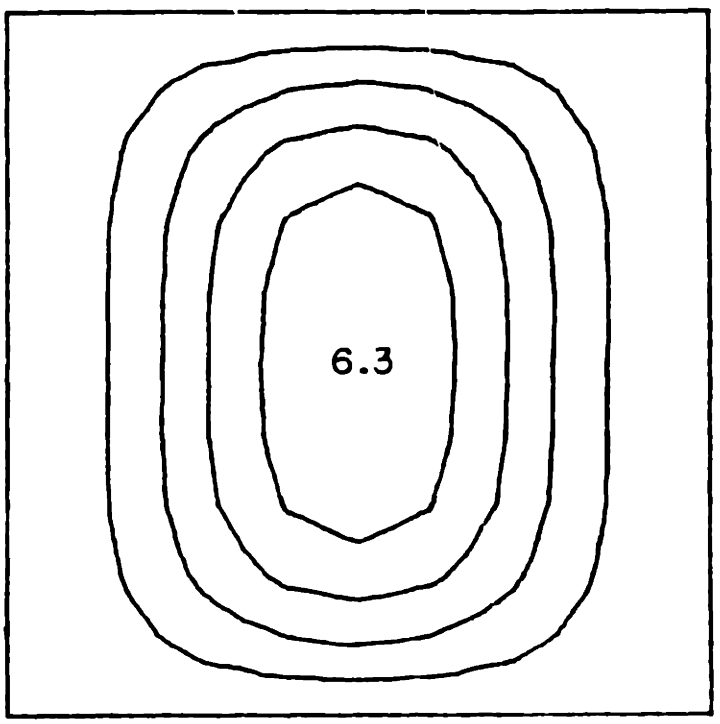

FIGURE H.109 Predicted (via Rayleigh-Ritz) Isodeflection Contour Map for the Laminate Type $[0_6//75_6]_T$ with Simply-Supported Boundary Conditions

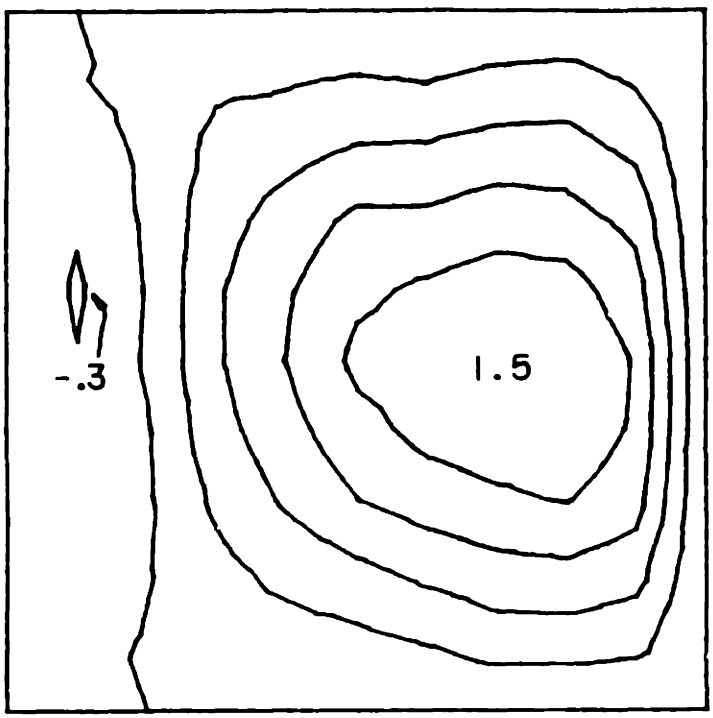

FIGURE H.110 Experimental Isodeflection Contour Map for the $[O_6//75_6]_T$ Laminate with Simply-Supported Boundary Conditions

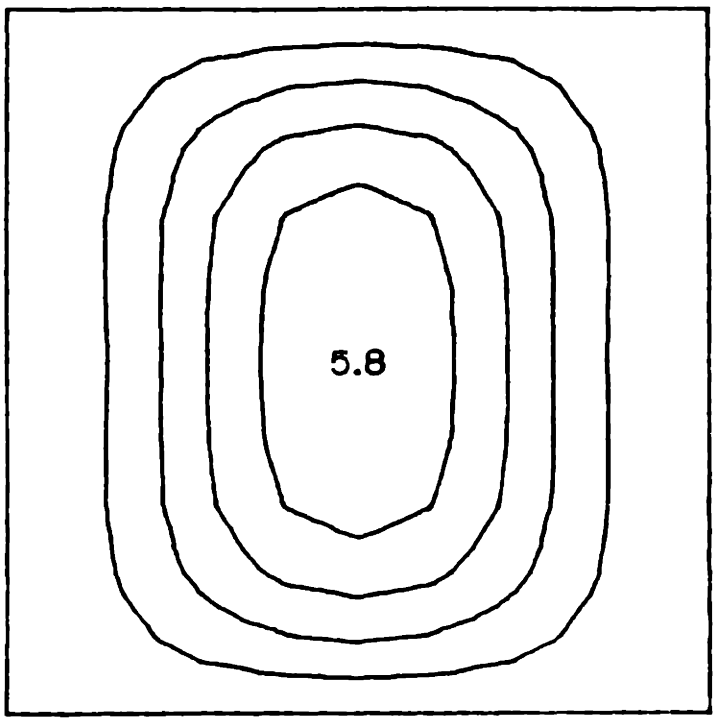

FIGURE H.111 Predicted (via Rayleigh-Ritz) Isodeflection Contour Map for the Laminate Type $[0_6//90_6]_T$ with Simply-Supported Boundary Conditions

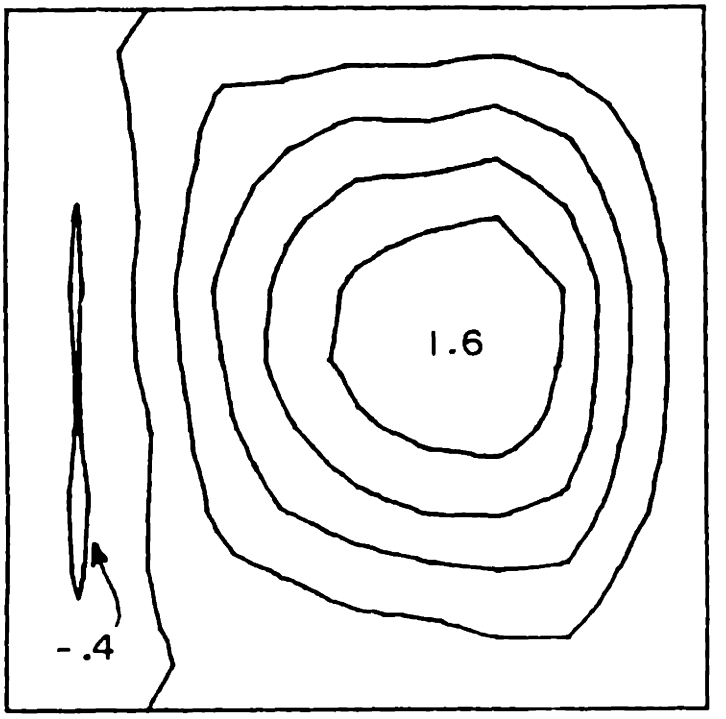

FIGURE H.112 Experimental Isodeflection Contour Map for the $[0_6//90_6]_T$ Laminate with Simply-Supported Boundary Conditions

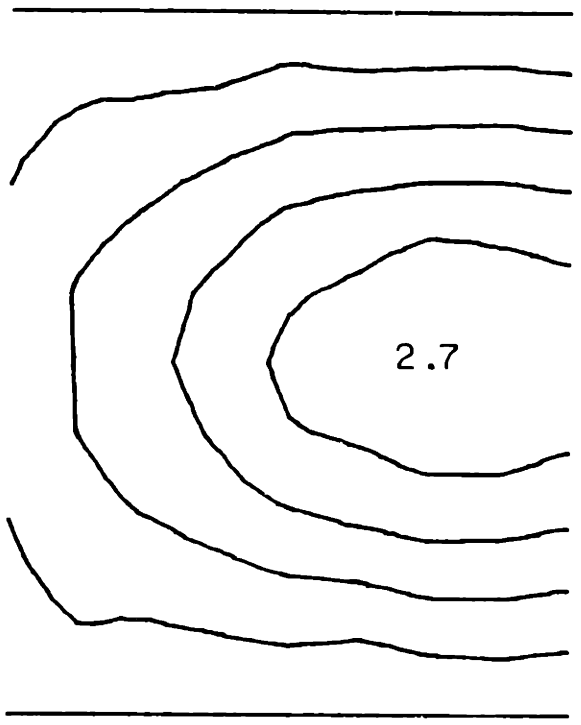

FIGURE H.113 Experimental Isodeflection Contour Map for the $[0_3/90_3]_s$ Laminate with Free Side Boundary Conditions

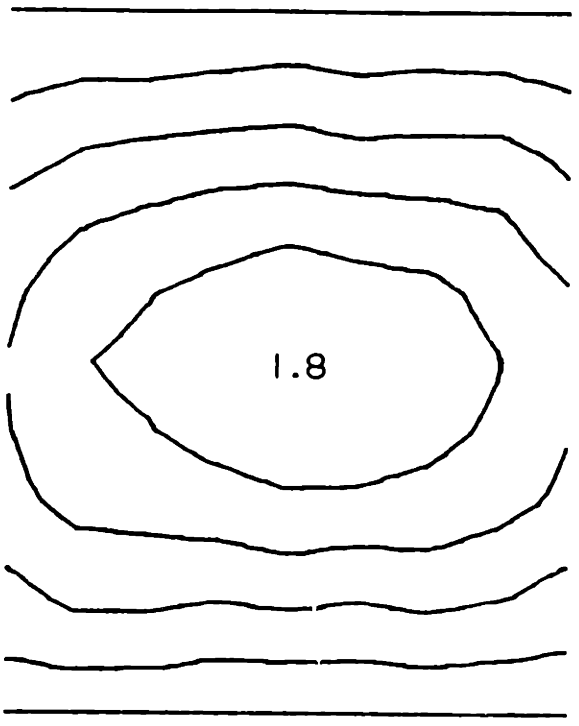

FIGURE H.114 Experimental Isodeflection Contour Map for the $[0_3//90_3//90_3//0_3]_T$ Laminate with Free Side Boundary Conditions

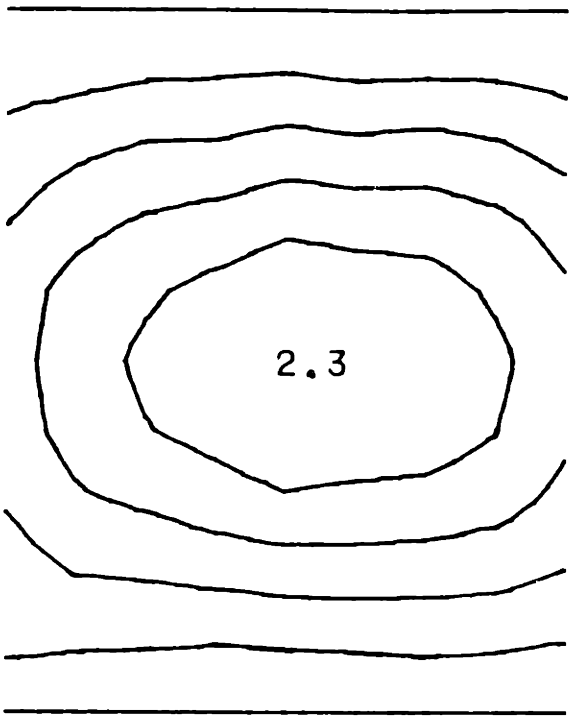

FIGURE H.115 Experimental Isodeflection Contour Map for the $[0_3//90_3//0_3//90_3]_T$ Laminate with Free Side Boundary Conditions

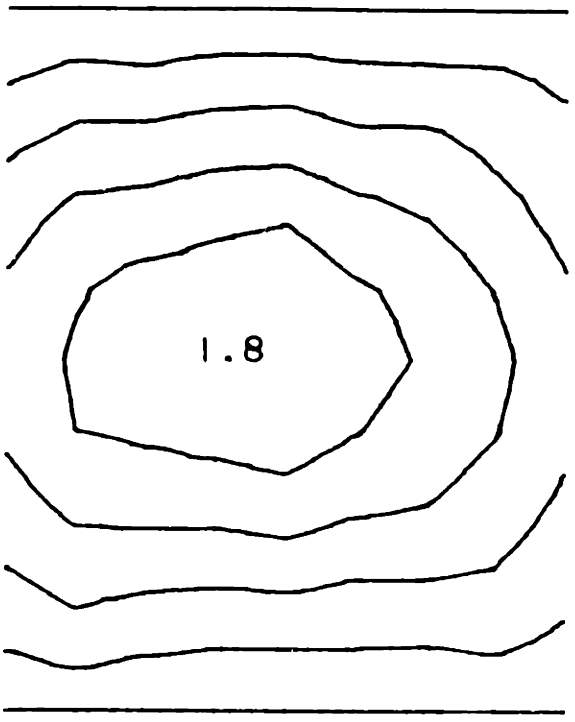

FIGURE H.116 Experimental Isodeflection Contour Map for the $[O_2//45_2//O_2//45_2//O_2]_T$ Laminate with Free Side Boundary Conditions

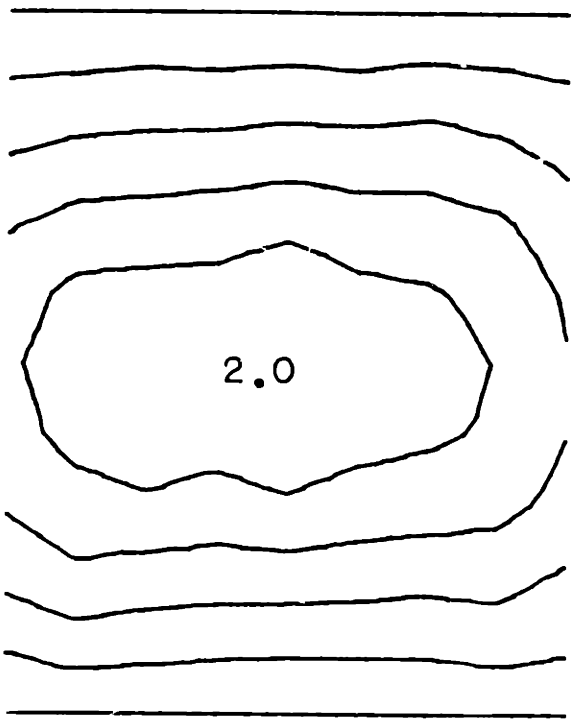

FIGURE H.117 Experimental Isodeflection Contour Map for the $[O_2//45_2//O_2//-45_2//O_2]_T$ Laminate with Free Side Boundary Conditions

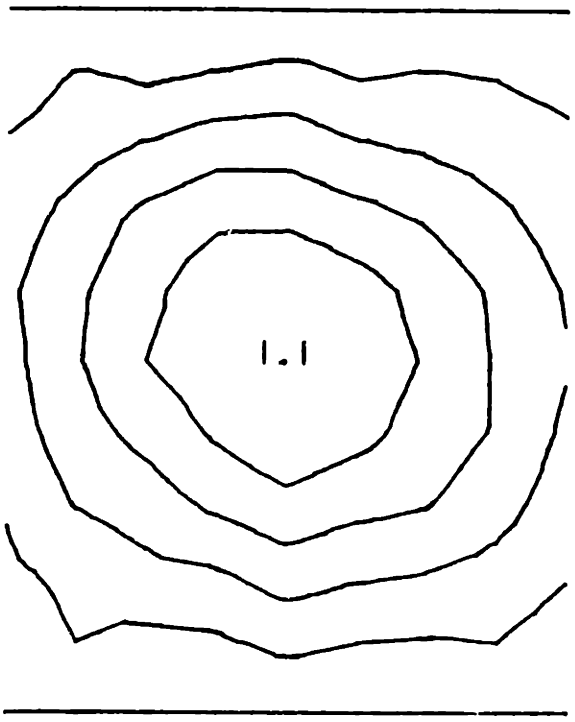

FIGURE H.118 Experimental Phase I Isodeflection Contour Map for the $[0_6//15_6]_T$ Laminate with Free Side Boundary Conditions

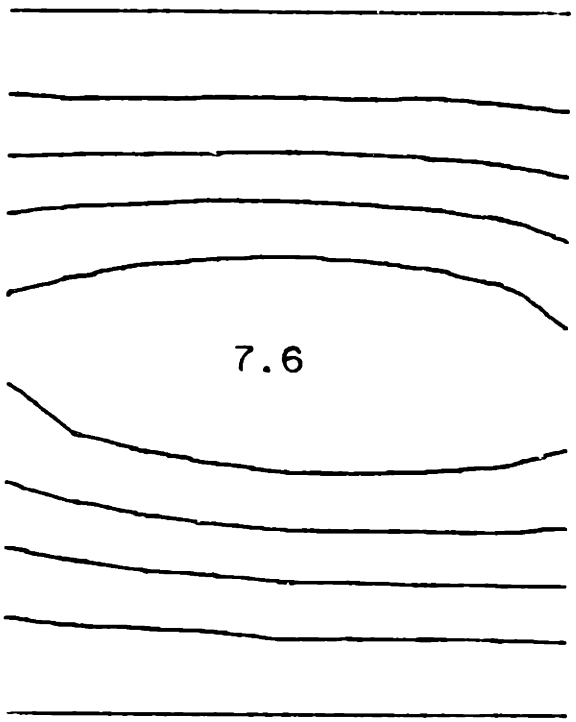

FIGURE H.119 Experimental Phase II Isodeflection Contour Map for the $[0_6//15_6]_T$ Laminate with Free Side Boundary Conditions

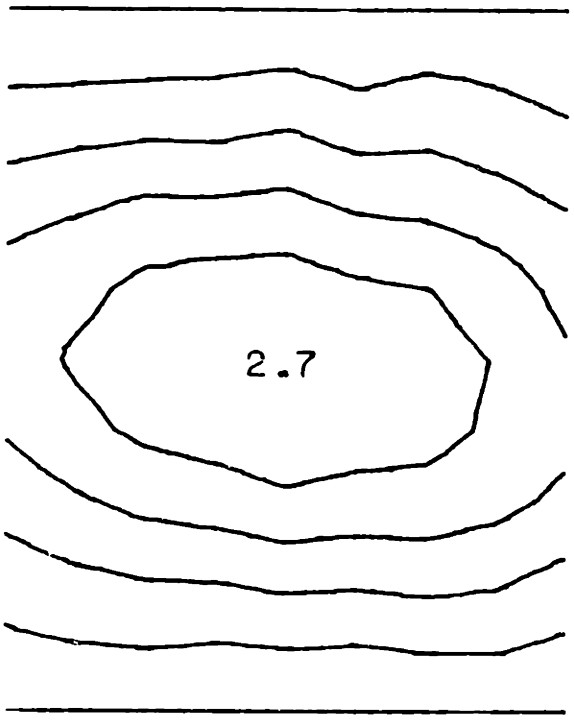

FIGURE H.120 Experimental Isodeflection Contour Map for the $[O_6//30_6]_T$ Laminate with Free Side Boundary Conditions

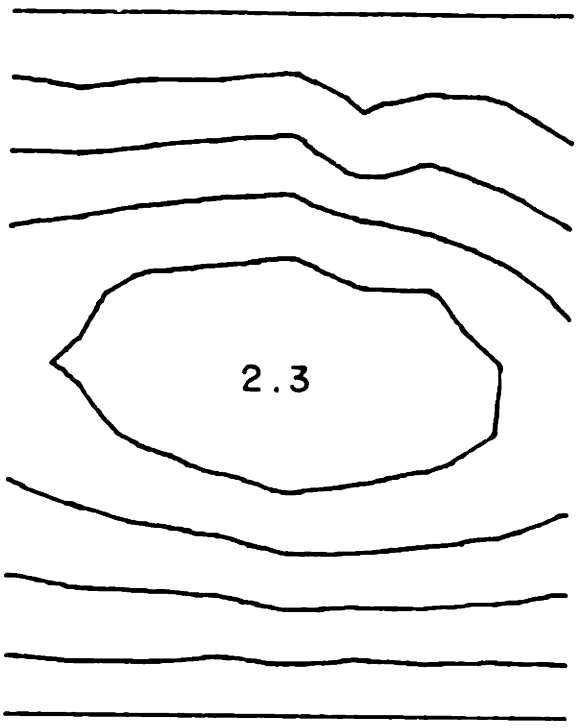

FIGURE H.121 Experimental Isodeflection Contour Map for the $[0_6//45_6]_T$ Laminate with Free Side Boundary Conditions

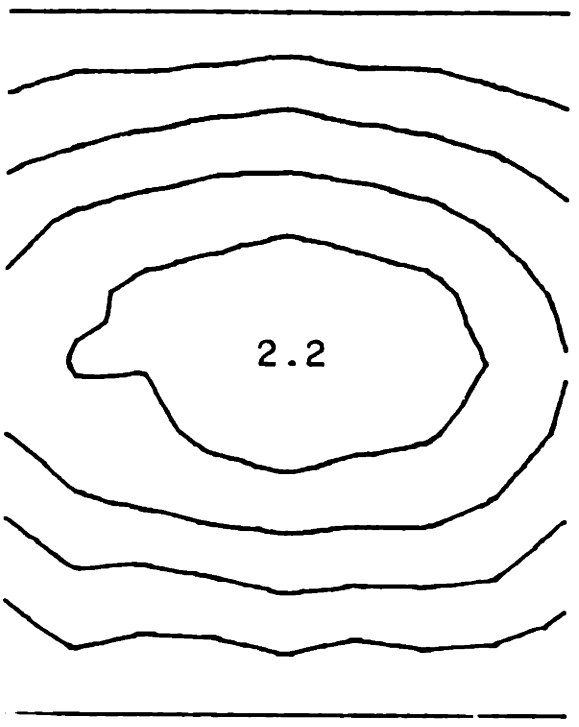

FIGURE H.122 Experimental Isodeflection Contour Map for the $[0_6//60_6]_T$ Laminate with Free Side Boundary Conditions

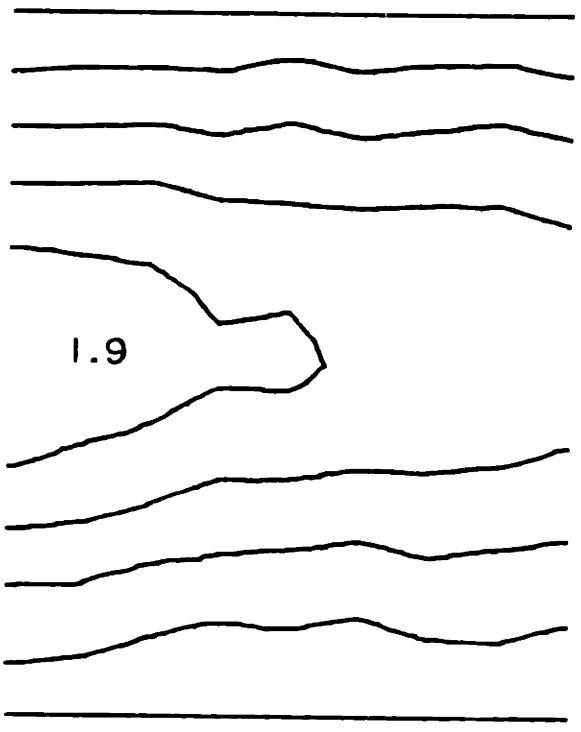

FIGURE H.123 Experimental Phase I Isodeflection Contour Map for the $[0_6//90_6]_T$ Laminate with Free Side Boundary Conditions

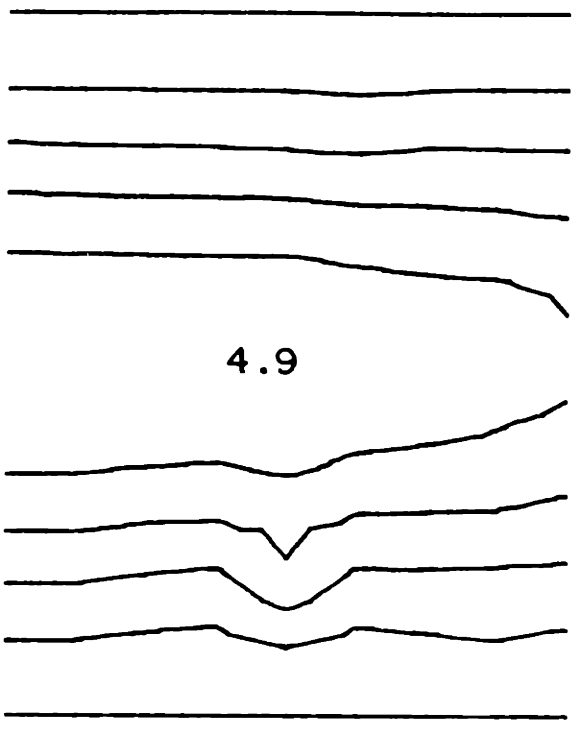

FIGURE H.124 Experimental Phase II Isodeflection Contour Map for the $[O_6//90_6]_T$ Laminate with Free Side Boundary Conditions